

BRIAN L. STEVENS  
FRANK L. LEWIS  
ERIC N. JOHNSON

A white aircraft carrier is shown from a low angle, moving across the water. The ship's hull is white, and it has a dark grey superstructure. The water is a deep blue, and the sky is a lighter blue. The ship is moving towards the right of the frame.

# AIRCRAFT CONTROL AND SIMULATION

THIRD EDITION

**DYNAMICS, CONTROLS DESIGN,  
AND AUTONOMOUS SYSTEMS**

WILEY



# AIRCRAFT CONTROL AND SIMULATION





---

# AIRCRAFT CONTROL AND SIMULATION

## Third Edition

---

Dynamics, Controls Design, and  
Autonomous Systems

**BRIAN L. STEVENS**

**FRANK L. LEWIS**

**ERIC N. JOHNSON**

**WILEY**

Cover image: Space Shuttle Landing© 3Dsculptor/Shutterstock  
Cover design: Wiley

This book is printed on acid-free paper. ∞

Copyright © 2016 by John Wiley & Sons, Inc. All rights reserved

Published by John Wiley & Sons, Inc., Hoboken, New Jersey  
Published simultaneously in Canada

No part of this publication may be reproduced, stored in a retrieval system, or transmitted in any form or by any means, electronic, mechanical, photocopying, recording, scanning, or otherwise, except as permitted under Section 107 or 108 of the 1976 United States Copyright Act, without either the prior written permission of the Publisher, or authorization through payment of the appropriate per-copy fee to the Copyright Clearance Center, 222 Rosewood Drive, Danvers, MA 01923, (978) 750-8400, fax (978) 646-8600, or on the web at [www.copyright.com](http://www.copyright.com). Requests to the Publisher for permission should be addressed to the Permissions Department, John Wiley & Sons, Inc., 111 River Street, Hoboken, NJ 07030, (201) 748-6011, fax (201) 748-6008, or online at [www.wiley.com/go/permissions](http://www.wiley.com/go/permissions).

**Limit of Liability/Disclaimer of Warranty:** While the publisher and author have used their best efforts in preparing this book, they make no representations or warranties with the respect to the accuracy or completeness of the contents of this book and specifically disclaim any implied warranties of merchantability or fitness for a particular purpose. No warranty may be created or extended by sales representatives or written sales materials. The advice and strategies contained herein may not be suitable for your situation. You should consult with a professional where appropriate. Neither the publisher nor the author shall be liable for damages arising herefrom.

For general information about our other products and services, please contact our Customer Care Department within the United States at (800) 762-2974, outside the United States at (317) 572-3993 or fax (317) 572-4002.

Wiley publishes in a variety of print and electronic formats and by print-on-demand. Some material included with standard print versions of this book may not be included in e-books or in print-on-demand. If this book refers to media such as a CD or DVD that is not included in the version you purchased, you may download this material at <http://booksupport.wiley.com>. For more information about Wiley products, visit [www.wiley.com](http://www.wiley.com).

***Library of Congress Cataloging-in-Publication Data is available.***

ISBN 978-1-118-87098-3 (hardback)  
978-1-118-87099-0 (epdf)  
978-1-118-87097-6 (epub)

Typeset in 10/12pt TimesLTStd by SPi-Global, Chennai, India

Printed in the United States of America

10 9 8 7 6 5 4 3 2 1

To Deane, Bill, and Richard  
B.L.S.

To my sons, Chris and Roma  
F.L.

To Amy, Elliot, and Theresa  
E.N.J.



# CONTENTS

---

<b>Preface</b>	<b>xi</b>
<b>1 The Kinematics and Dynamics of Aircraft Motion</b>	<b>1</b>
1.1 Introduction / 1	
1.2 Vector Operations / 3	
1.3 Matrix Operations on Vector Coordinates / 7	
1.4 Rotational Kinematics / 16	
1.5 Translational Kinematics / 20	
1.6 Geodesy, Coordinate Systems, Gravity / 23	
1.7 Rigid-Body Dynamics / 34	
1.8 Advanced Topics / 44	
References / 58	
Problems / 59	
<b>2 Modeling the Aircraft</b>	<b>63</b>
2.1 Introduction / 63	
2.2 Basic Aerodynamics / 64	
2.3 Aircraft Forces And Moments / 75	
2.4 Static Analysis / 101	
2.5 The Nonlinear Aircraft Model / 108	
2.6 Linear Models And The Stability Derivatives / 116	

- 2.7 Summary / 137
- References / 138
- Problems / 139

### **3 Modeling, Design, and Simulation Tools** **142**

- 3.1 Introduction / 142
- 3.2 State-Space Models / 144
- 3.3 Transfer Function Models / 155
- 3.4 Numerical Solution Of The State Equations / 170
- 3.5 Aircraft Models For Simulation / 179
- 3.6 Steady-State Flight / 185
- 3.7 Numerical Linearization / 199
- 3.8 Aircraft Dynamic Behavior / 205
- 3.9 Feedback Control / 213
- 3.10 Summary / 241
- References / 241
- Problems / 243

### **4 Aircraft Dynamics and Classical Control Design** **250**

- 4.1 Introduction / 250
- 4.2 Aircraft Rigid-Body Modes / 257
- 4.3 The Handling-Qualities Requirements / 274
- 4.4 Stability Augmentation / 287
- 4.5 Control Augmentation Systems / 303
- 4.6 Autopilots / 322
- 4.7 Nonlinear Simulation / 344
- 4.8 Summary / 371
- References / 372
- Problems / 374

### **5 Modern Design Techniques** **377**

- 5.1 Introduction / 377
- 5.2 Assignment Of Closed-Loop Dynamics / 381
- 5.3 Linear Quadratic Regulator With Output Feedback / 397
- 5.4 Tracking A Command / 413
- 5.5 Modifying The Performance Index / 428
- 5.6 Model-Following Design / 455
- 5.7 Linear Quadratic Design With Full State Feedback / 470

- 5.8 Dynamic Inversion Design / 477
- 5.9 Summary / 492
  - References / 492
  - Problems / 495

## **6 Robustness and Multivariable Frequency-Domain Techniques 500**

- 6.1 Introduction / 500
- 6.2 Multivariable Frequency-Domain Analysis / 502
- 6.3 Robust Output-Feedback Design / 525
- 6.4 Observers And The Kalman Filter / 529
- 6.5 Linear Quadratic Gaussian/Loop Transfer Recovery / 554
- 6.6 Summary / 577
  - References / 578
  - Problems / 580

## **7 Digital Control 584**

- 7.1 Introduction / 584
- 7.2 Simulation Of Digital Controllers / 585
- 7.3 Discretization Of Continuous Controllers / 588
- 7.4 Modified Continuous Design / 598
- 7.5 Implementation Considerations / 611
- 7.6 Summary / 619
  - References / 620
  - Problems / 620

## **8 Modeling and Simulation of Miniature Aerial Vehicles 623**

- 8.1 Introduction / 623
- 8.2 Propeller/Rotor Forces And Moments / 630
- 8.3 Modeling Rotor Flapping / 640
- 8.4 Motor Modeling / 645
- 8.5 Small Aerobatic Airplane Model / 648
- 8.6 Quadrotor Model / 654
- 8.7 Small Helicopter Model / 655
- 8.8 Summary / 660
  - References / 661
  - Problems / 661

<b>9 Adaptive Control With Application to Miniature Aerial Vehicles</b>	<b>664</b>
9.1 Introduction / 664	
9.2 Model Reference Adaptive Control Based On Dynamic Inversion / 665	
9.3 Neural Network Adaptive Control / 668	
9.4 Limited Authority Adaptive Control / 674	
9.5 Neural Network Adaptive Control Example / 680	
9.6 Summary / 709	
References / 709	
Problems / 711	
 <b>Appendix A F-16 Model</b>	 <b>714</b>
 <b>Appendix B Software</b>	 <b>723</b>
 <b>Index</b>	 <b>733</b>



# PREFACE

---

This book is primarily aimed at students in aerospace engineering, at the senior and graduate level. We hope that it will also prove useful to practicing engineers, both as a reference book and as an update to their engineering education. In keeping with the rising importance of autonomous aircraft systems in the world today, the third edition includes two new chapters that cover principles of unmanned aerial vehicle design and control.

As the subtitle suggests, the book can be viewed as having three Parts. Part I comprises Chapters 1–4 and presents aircraft Kinematics and Dynamics, Modeling, and Simulation, with numerous design examples using classical control methods. Part II, consisting of Chapter 5–7, covers Modern design techniques including Linear Quadratic design, which is based on optimality principles. Also included are LQG/Loop-Transfer Recovery and digital control implementation. Part III contains two newly added Chapters 8 and 9 that detail the modeling, simulation, and control of small unmanned aerial vehicles.

In addressing simulation of aerospace vehicles we have reviewed the relevant parts of classical mechanics and attempted to provide a clear, consistent notation. This has been coupled with a thorough treatment of six-degrees-of-freedom (6-DOF) motion, including a detailed discussion of attitude representation using both Euler angles and quaternions. Simulation of motion over and around the Earth requires some understanding of geodesy and the Earth's gravitation, and these topics have also been discussed in some detail within the framework of the WGS-84 datum. Familiarity with these topics is indispensable to many of the engineers working in the aerospace industry. Given this background the student can independently construct 6-DOF simulations and learn from them.

High-speed motion within the Earth's atmosphere entails aerodynamic forces and moments. We have reviewed aerodynamic modeling, and provided many graphical examples of such forces and moments for real aircraft. The small-perturbation theory of aerodynamic forces and moments is also described in detail. This study of 6-DOF motion and aerodynamic effects culminates in two realistic nonlinear aircraft models, which are then used for design and simulation examples in the rest of the book.

We have provided computer code in both MATLAB and Fortran to perform simulation and design with these models. Involvement with the models and designs will demonstrate many ideas in simulation, control theory, computer-aided design techniques, and numerical algorithms. The design examples are easily reproducible, and offer a great deal of scope to a class of students.

Before starting feedback control design we have reviewed linear systems theory, including the Laplace transform, transfer functions, and the state-space formulation. Transform theory views dynamic systems through their poles and zeros and leads to many convenient graphical and back-of-the-envelope design techniques, while state-space techniques are ideally suited to computer-aided design. We have attempted to pass "seamlessly" between the two formulations.

Classical control design is illustrated through many examples performed on the aircraft models using transform domain techniques supported by an underlying state-space model. Modern design in the later chapters simply uses the state-space models.

Finally, we note that the choice of topics herein is influenced by our experience in the broader area of guidance, navigation, and control (GNC). Very few engineers entering the aerospace industry will find themselves designing flight control systems, and those few will take part in the design of only two or three such systems in their careers. Instead, they will find themselves involved in a broad spectrum of projects, where a good grasp of classical mechanics, dynamics, coordinate transformations, geodesy, and navigation will be invaluable. The importance of modeling and simulation cannot be overstated. Large sums of money are spent on mathematical modeling and digital simulation before any hardware is built.

The first and third authors wish to acknowledge the help of colleagues in Aerospace Engineering at Georgia Tech. Prof. C. V. Smith provided invaluable help with Chapter 1 during many hours of interesting discussion. The computer support of B. H. Hudson at the Georgia Tech Research Institute is also gratefully acknowledged. Both authors wish to thank the staff of John Wiley & Sons for their painstaking preparation of the manuscript.

BRIAN L. STEVENS

*Georgia Institute of Technology*

FRANK L. LEWIS

*University of Texas at Arlington*

ERIC N. JOHNSON

*Georgia Institute of Technology*

# CHAPTER 1

---

## THE KINEMATICS AND DYNAMICS OF AIRCRAFT MOTION

---

### 1.1 INTRODUCTION

In this chapter the end point will be the equations of motion of a rigid vehicle moving over the oblate, rotating Earth. The flat-Earth equations, describing motion over a small area of a nonrotating Earth, with constant gravity, are sufficient for many aircraft simulation needs and will be derived first. To reach this end point we will use the vector analysis of classical mechanics to set up the equations of motion, matrix algebra to describe operations with coordinate systems, and concepts from geodesy (a branch of mathematics dealing with the shape of the Earth), gravitation (the mass attraction effect of the Earth), and navigation, to introduce the effects of Earth's shape and mass attraction.

The moments and forces acting on the vehicle, other than the mass attraction of the Earth, will be abstract until Chapter 2 is reached. At this stage the equations can be used to describe the motion of any type of aerospace vehicle, including an Earth satellite, provided that suitable force and moment models are available. The term *rigid* means that structural flexibility is not allowed for, and all points in the vehicle are assumed to maintain the same relative position at all times. This assumption is good enough for flight simulation in most cases as well as for flight control system design provided that we are not trying to design a system to control structural modes or to alleviate aerodynamic loads on the aircraft structure.

The vector analysis needed for the treatment of the equations of motion often causes difficulties for the student, particularly the concept of the angular velocity vector. Therefore, a review of the relevant topics is provided. In some cases we have gone beyond the traditional approach to flight mechanics. The introduction of topics from geodesy, gravitation, and distance and position calculations allows us

to accurately simulate the trajectories of aircraft that can fly autonomously at very high altitudes and over long distances, including “point-to-point suborbital flight” (e.g., White Knight 2 and SpaceShipTwo). Some topics have been reserved for an “optional” advanced section (e.g., quaternions), Section 1.8.

The equations of motion will be organized as a set of simultaneous first-order differential equations, explicitly solved for the derivatives. For  $n$  independent variables,  $X_i$  (such as components of position, velocity, etc.), and  $m$  control inputs,  $U_i$  (such as throttle, control surface deflection, etc.), the general form will be

$$\begin{aligned}\dot{X}_1 &= f_1(X_1, X_2, \dots, X_n, U_1, U_2, \dots, U_m) \\ \dot{X}_2 &= f_2(X_1, X_2, \dots, X_n, U_1, U_2, \dots, U_m) \\ &\vdots \\ \dot{X}_n &= f_n(X_1, X_2, \dots, X_n, U_1, U_2, \dots, U_m),\end{aligned}\tag{1.1-1}$$

where the functions  $f_i$  are the nonlinear functions that can arise from modeling real systems. If the variables  $X_i$  constitute the smallest set of variables that, together with given inputs  $U_i$ , completely describe the behavior of the system, then the  $X_i$  are a set of *state variables* for the system, and Equations (1.1-1) are a *state-space* description of the system. The functions  $f_i$  are required to be single-valued continuous functions. Equations (1.1-1) are often written symbolically as

$$\dot{X} = f(X, U),\tag{1.1-2}$$

where the *state vector*  $X$  is an  $(n \times 1)$  column array of the  $n$  state variables, the *control vector*  $U$  is an  $(m \times 1)$  column array of the control variables, and  $f$  is an array of nonlinear functions. When  $U$  is held constant, the nonlinear state equations (1.1-1), or a subset of them, usually have one or more *equilibrium points* in the multidimensional state and control space, where the derivatives vanish. The equations are usually approximately linear for small perturbations from equilibrium and can be written in matrix form as the *linear state equation*:

$$\dot{x} = Ax + Bu\tag{1.1-3}$$

Here, the lowercase notation for the state and control vectors indicates that they are perturbations from equilibrium, although the derivative vector contains the actual values (i.e., perturbations from zero). The “*A-matrix*” is square and the “*B-matrix*” has dimensions determined by the number of states and controls.

The state-space formulation will be described in more detail in Chapters 2 and 3. At this point we will simply note that a major advantage of this formulation is that the nonlinear state equations can be solved numerically. The simplest numerical solution method is *Euler integration*, described by

$$X_{k+1} = X_k + f(X_k, U_k) \delta t,\tag{1.1-4}$$

in which  $X_k$  is the  $k$ th value of the state vector computed at discrete times  $k \delta t$ ,  $k = 0, 1, 2, \dots$ , starting from an *initial condition*  $X_0$ . The *integration time step*,  $\delta t$ , must be made small enough that, for every  $\delta t$  interval,  $U$  can be approximated by a constant value, and  $\dot{X} \delta t$  provides a good approximation to the increment in the state vector. This numerical integration allows the state vector to be stepped forward, in time increments of  $\delta t$ , to obtain a *time-history simulation*.

## 1.2 VECTOR OPERATIONS

### Definitions and Notation

Kinematics can be defined as the study of the motion of objects without regard to the mechanisms that cause the motion. The motion of physical objects can be described by means of vectors in three dimensions, and in performing kinematic analysis with vectors we will make use of the following definitions:

*Frame of Reference:* A rigid body or set of rigidly related points that can be used to establish distances and directions (denoted by  $F_i, F_e$ , etc.). In general, a subscript used to indicate a frame will be lowercase, while a subscript used to indicate a point will be uppercase.

*Inertial Frame:* A frame of reference in which Newton's laws apply. Our best inertial approximation is probably a "helio-astronomic" frame in which the center of mass (cm) of the sun is a fixed point, and fixed directions are established by the normal to the plane of the ecliptic and the projection on that plane of certain stars that appear to be fixed in position.

*Vector:* A vector is an abstract geometrical object that has both magnitude and direction. It exists independently of any coordinate system. The vectors used here are Euclidean vectors that exist only in three-dimensional space and come in two main types:

*Bound Vector:* A vector from a fixed point in a frame (e.g., a position vector).

*Free Vector:* Can be translated parallel to itself (e.g., velocity, torque).

*Coordinate System:* A measurement system for locating points in a frame of reference. We may have multiple coordinate systems (with no relative motion) within one frame of reference, and we sometimes loosely refer to them also as "frames."

In choosing a notation the following facts must be taken into account. For position vectors, the notation should specify the two points whose relative position the vector describes. Velocity and acceleration vectors are relative to a frame of reference, and the notation should specify the frame of reference as well as the moving point. The derivative of a vector depends on the observer's frame of reference, and this frame must be specified in the notation. A derivative may be taken in a different frame from

that in which a vector is defined, so the notation may require two frame designators with one vector. We will use the following notation:

**Vectors will be in boldface type fonts.**

*Right subscripts* will be used to designate two points for a position vector, and a point and a frame for a velocity or acceleration vector. A “/” in a subscript will mean “with respect to.”

A *left superscript* will specify the frame in which a derivative is taken, and the dot notation will indicate a derivative.

A *right superscript* on a vector will specify a coordinate system. It will therefore denote an array of the components of that vector in the specified system.

Vector length will be denoted by single bars, for example,  $|\mathbf{p}|$ .

Examples of the notation are:

$\mathbf{p}_{A/B} \equiv$  Position vector of point  $A$  with respect to point  $B$

$\mathbf{v}_{A/i} \equiv$  Velocity vector of point  $A$  in frame  $F_i$

${}^b\dot{\mathbf{v}}_{A/i} \equiv$  Vector derivative of  $\mathbf{v}_{A/i}$  taken in frame  $F_b$

$\mathbf{v}_{A/i}^c \equiv (\mathbf{v}_{A/i})^c \equiv$  Array of components of  $\mathbf{v}_{A/i}$  in coordinate system  $c$

${}^b\dot{\mathbf{v}}_{A/i}^c \equiv$  Components in system  $c$  of the derivative taken in  $F_b$

The individual components of a vector will have subscripts that indicate the coordinate system or be denoted by the vector symbol with subscripts  $x$ ,  $y$ , and  $z$  to indicate the coordinates. All component arrays will be column arrays unless otherwise indicated by the transpose symbol, a right superscript  $T$ . For example, arrays of components in a coordinate system  $b$  could be shown as

$$\mathbf{p}_{A/B}^b = \begin{bmatrix} x_b \\ y_b \\ z_b \end{bmatrix} \quad \text{or} \quad \mathbf{v}_{A/i}^b = \begin{bmatrix} v_x \\ v_y \\ v_z \end{bmatrix} = [v_x \ v_y \ v_z]^T$$

## Vector Properties

Vectors are independent of any Cartesian coordinate system. Addition and subtraction of vectors can be defined independently of coordinate systems by means of geometrical constructions (the “parallelogram law”). Thus, we can draw vectors on charts to determine the *track* of a vehicle through the air or on or under the sea. Some vector operations yield *pseudovectors* that are not independent of a “handedness” convention. For example, the result of the *vector cross-product* operation is a vector whose direction depends on whether a right-handed or left-handed convention is being used. We will always use the right-hand rule in connection with vector direction.

It is usually most convenient to manipulate vectors algebraically by decomposing them into a sum of appropriately scaled unit-length vectors usually written as

$\mathbf{i}, \mathbf{j}, \mathbf{k}$  (i.e.,  $\mathbf{v} = x\mathbf{i} + y\mathbf{j} + z\mathbf{k}$ ). These *unit vectors* are normally chosen to form a right-handed orthogonal set, that is, the right-hand rule applied to  $\mathbf{i}$  and  $\mathbf{j}$  gives the direction of  $\mathbf{k}$  (i.e.,  $\mathbf{i} \times \mathbf{j} = \mathbf{k}$ ). The use of orthogonal unit vectors leads naturally to using Cartesian coordinate systems for their scaling factors and thence to manipulating the coordinates with matrix algebra (next section).

The direction of a vector  $\mathbf{p}$  relative to a coordinate system is commonly described in two different ways: first by rotations in two orthogonal planes, for example, an *azimuth rotation* to point in the right direction and then an *elevation rotation* above the azimuth plane (used with El-over-Az mechanical gimbals), and second by three *direction angles*  $\alpha, \beta, \gamma$  to the coordinate axes (used with some radar antennas). The *direction cosines* of  $\mathbf{p}$ — $\cos \alpha, \cos \beta, \cos \gamma$ —give the projections of  $\mathbf{p}$  on the coordinate axes, and two applications of the theorem of Pythagoras yield

$$\begin{aligned} |\mathbf{p}|^2 \cos^2 \alpha + |\mathbf{p}|^2 \cos^2 \beta + |\mathbf{p}|^2 \cos^2 \gamma &= |\mathbf{p}|^2 \\ \therefore \cos^2 \alpha + \cos^2 \beta + \cos^2 \gamma &= 1 \end{aligned} \quad (1.2-1)$$

The *dot product* of two vectors, say  $\mathbf{u}$  and  $\mathbf{v}$ , is a scalar defined by

$$\mathbf{u} \cdot \mathbf{v} = |\mathbf{u}| |\mathbf{v}| \cos \theta, \quad (1.2-2)$$

where  $\theta$  is the included angle between the vectors (it may be necessary to translate the vectors so that they intersect). The dot product is commutative and distributive; thus,

$$\begin{aligned} \mathbf{u} \cdot \mathbf{v} &= \mathbf{v} \cdot \mathbf{u} \\ (\mathbf{u} + \mathbf{v}) \cdot \mathbf{w} &= \mathbf{u} \cdot \mathbf{w} + \mathbf{v} \cdot \mathbf{w} \end{aligned}$$

The principal uses of the dot product are to find the projection of a vector, to establish orthogonality, and to find length. For example, if (1.2-2) is divided by  $|\mathbf{v}|$ , we have the projection of  $\mathbf{u}$  on  $\mathbf{v}$ ,

$$(\mathbf{u} \cdot \mathbf{v}) / |\mathbf{v}| = |\mathbf{u}| \cos \theta$$

If  $\cos \theta = 0$ ,  $\mathbf{u} \cdot \mathbf{v} = 0$ , and the vectors are said to be *orthogonal*. If a vector is dotted with itself, then  $\cos \theta = 1$ , and we obtain the square of its length. Orthogonal unit vectors satisfy the dot product relationships

$$\begin{aligned} \mathbf{i} \cdot \mathbf{i} &= \mathbf{j} \cdot \mathbf{j} = \mathbf{k} \cdot \mathbf{k} = 1 \\ \mathbf{i} \cdot \mathbf{j} &= \mathbf{j} \cdot \mathbf{k} = \mathbf{k} \cdot \mathbf{i} = 0 \end{aligned}$$

Using these relationships, the dot product of two vectors can be evaluated in terms of components in any convenient orthogonal coordinate system (say  $a$ , with components  $x, y, z$ ),

$$(\mathbf{u} \cdot \mathbf{v})^a = u_x v_x + u_y v_y + u_z v_z \quad (1.2-3)$$

The *cross-product* of  $\mathbf{u}$  and  $\mathbf{v}$ , denoted by  $\mathbf{u} \times \mathbf{v}$ , is a vector  $\mathbf{w}$  that is normal to the plane of  $\mathbf{u}$  and  $\mathbf{v}$  and is in a direction such that  $\mathbf{u}, \mathbf{v}, \mathbf{w}$  (in that order) form

a right-handed system (again, it may be necessary to translate the vectors so that they intersect). The length of  $\mathbf{w}$  is defined to be  $|\mathbf{u} \times \mathbf{v}| = |\mathbf{u}||\mathbf{v}| \sin \theta$ , where  $\theta$  is the included angle between  $\mathbf{u}$  and  $\mathbf{v}$ . It has the following properties:

$$\begin{aligned}
 \mathbf{u} \times \mathbf{v} &= -(\mathbf{v} \times \mathbf{u}) && \text{(anticommutative)} \\
 a(\mathbf{u} \times \mathbf{v}) &= (a\mathbf{u}) \times \mathbf{v} = \mathbf{u} \times (a\mathbf{v}) && \text{(associative; “a” scalar)} \\
 \mathbf{u} \times (\mathbf{v} + \mathbf{w}) &= (\mathbf{u} \times \mathbf{v}) + (\mathbf{u} \times \mathbf{w}) && \text{(distributive)} \\
 \mathbf{u} \cdot (\mathbf{v} \times \mathbf{w}) &= \mathbf{v} \cdot (\mathbf{w} \times \mathbf{u}) = \mathbf{w} \cdot (\mathbf{u} \times \mathbf{v}) && \text{(scalar triple product)} \\
 \mathbf{u} \times (\mathbf{v} \times \mathbf{w}) &= \mathbf{v}(\mathbf{w} \cdot \mathbf{u}) - \mathbf{w}(\mathbf{u} \cdot \mathbf{v}) && \text{(vector triple product)} \quad (1.2-4)
 \end{aligned}$$

As an aid for remembering the form of the triple products, note the *cyclic permutation* of the vectors involved. Alternatively, the vector triple product can be remembered phonetically using “ABC = BAC-CAB.”

The cross-products of the unit vectors describing a right-handed orthogonal coordinate system satisfy the equations

$$\mathbf{i} \times \mathbf{i} = \mathbf{j} \times \mathbf{j} = \mathbf{k} \times \mathbf{k} = 0$$

and, using cyclic permutation,

$$\mathbf{i} \times \mathbf{j} = \mathbf{k}, \quad \mathbf{j} \times \mathbf{k} = \mathbf{i}, \quad \mathbf{k} \times \mathbf{i} = \mathbf{j}$$

Also remember that  $\mathbf{j} \times \mathbf{i} = -(\mathbf{i} \times \mathbf{j}) = -\mathbf{k}$ , and so on.

An example of the use of the cross-product is finding the vector moment  $\mathbf{r} \times \mathbf{F}$  of a force  $\mathbf{F}$  acting at a point whose position vector is  $\mathbf{r}$ .

## Rotation of a Vector

It is intuitively obvious that a vector can be made to point in an arbitrary direction by means of a single rotation around an appropriate axis. Here we follow Goldstein (1980) to derive a formula for vector rotation.

Consider Figure 1.2-1, in which a vector  $\mathbf{u}$  has been rotated to form a new vector  $\mathbf{v}$  by defining a rotation axis along a unit vector  $\mathbf{n}$  and performing a left-handed rotation through  $\mu$  around  $\mathbf{n}$ . The two vectors that must be added to  $\mathbf{u}$  to obtain  $\mathbf{v}$  are shown in the figure and provide a good student exercise in using the vector cross-product (Problem 1.2-4). By doing this addition, we get

$$\mathbf{v} = \mathbf{u} + (1 - \cos \mu)(\mathbf{n} \times (\mathbf{n} \times \mathbf{u})) - (\mathbf{n} \times \mathbf{u}) \sin \mu \quad (1.2-5a)$$

or

$$\mathbf{v} = (1 - \cos \mu)\mathbf{n}(\mathbf{n} \cdot \mathbf{u}) + \mathbf{u} \cos \mu - (\mathbf{n} \times \mathbf{u}) \sin \mu \quad (1.2-5b)$$



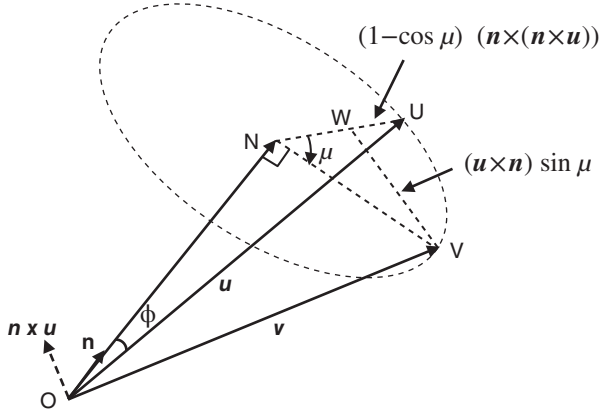


**Figure 1.2-1** Rotation of a vector.

Equations (1.2-5) are sometimes called the *rotation formula*; they show that, after choosing  $\mathbf{n}$  and  $\mu$ , we can operate on  $\mathbf{u}$  with dot and cross-product operations to get the desired rotation; no coordinate system is involved, and the rotation angle can be arbitrarily large.

### 1.3 MATRIX OPERATIONS ON VECTOR COORDINATES

As noted earlier, the coordinate system components of a vector will be written as a  $(3 \times 1)$  column array. Here, we shall show how those components are manipulated in correspondence with operations performed with vectors.

#### The Scalar Product

If  $\mathbf{u}^a$  and  $\mathbf{v}^a$  are column arrays of the same dimension, their scalar product is  $(\mathbf{u}^a)^T \mathbf{v}^a$ , and, for example, in three dimensions,

$$(\mathbf{u}^a)^T \mathbf{v}^a = [u_x \ u_y \ u_z] \begin{bmatrix} v_x \\ v_y \\ v_z \end{bmatrix} = u_x v_x + u_y v_y + u_z v_z \quad (1.3-1a)$$

This result is identical to Equation (1.2-3) obtained from the vector dot product. The scalar product allows us to find the *2-norm* of a column matrix:

$$|\mathbf{v}^a| = \left[ (\mathbf{v}^a)^T \mathbf{v}^a \right]^{\frac{1}{2}} \quad (1.3-1b)$$

In Euclidean space this is the length of the vector.

## The Cross-Product Matrix

From the unit-vector cross-products, given earlier, we can derive a formula for the components of the cross-product of two vectors by writing them in terms of a sum of unit vectors. A convenient mnemonic for remembering the formula is to write it so that it resembles the expansion of a determinant, as follows:

$$\mathbf{u} \times \mathbf{v} = \begin{vmatrix} \mathbf{i} & \mathbf{j} & \mathbf{k} \\ u_x & u_y & u_z \\ v_x & v_y & v_z \end{vmatrix} = \mathbf{i} \begin{vmatrix} u_y & u_z \\ v_y & v_z \end{vmatrix} - \mathbf{j} \begin{vmatrix} u_x & u_z \\ v_x & v_z \end{vmatrix} + \mathbf{k} \begin{vmatrix} u_x & u_y \\ v_x & v_y \end{vmatrix} \quad (1.3-2)$$

where subscripts  $x, y, z$ , indicate components in a coordinate system whose axes are aligned respectively with the unit vectors  $\mathbf{i}, \mathbf{j}, \mathbf{k}$ . We often wish to directly translate a vector equation into a matrix equation of vector components. From the above mnemonic it is easy to see that

$$(\mathbf{u} \times \mathbf{v})^a = \begin{bmatrix} 0 & -u_z & u_y \\ u_z & 0 & -u_x \\ -u_y & u_x & 0 \end{bmatrix} \begin{bmatrix} v_x \\ v_y \\ v_z \end{bmatrix} \equiv \tilde{\mathbf{u}}^a \mathbf{v}^a \quad (1.3-3)$$

A skew-symmetric matrix of the above form will be denoted by the tilde overbar and referred to as the *tilde matrix* or *cross-product matrix*. An example of the use of the cross-product matrix involves the centripetal acceleration at a point described by a position vector  $\mathbf{r}$  rotating with an angular velocity vector  $\boldsymbol{\omega}$  (see also Equation 1):

$$\text{centripetal acceleration} = \boldsymbol{\omega} \times (\boldsymbol{\omega} \times \mathbf{r})$$

In the case of a vector triple product, the vector operation in parentheses must be performed first, but the corresponding matrix operations may be performed collectively in any order:

$$(\mathbf{u} \times (\mathbf{v} \times \mathbf{w}))^a = (\tilde{\mathbf{u}}^a \tilde{\mathbf{v}}^a) \mathbf{w}^a = \tilde{\mathbf{u}}^a (\tilde{\mathbf{v}}^a \mathbf{w}^a)$$

Here, the third term requires only postmultiplication by a column array and hence fewer operations to evaluate than the second term.

## Coordinate Rotation, the DCM

When the rotation formula (1.2-5b) is resolved in a coordinate system  $a$ , the result is

$$\mathbf{v}^a = [(1 - \cos \mu) \mathbf{n}^a (\mathbf{n}^a)^T + (\cos \mu) \mathbf{I} - (\sin \mu) \tilde{\mathbf{n}}^a] \mathbf{u}^a, \quad (1.3-4)$$

where  $\mathbf{n}^a (\mathbf{n}^a)^T$  is a square matrix,  $\mathbf{I}$  is the identity matrix, and  $\tilde{\mathbf{n}}^a$  is a cross-product matrix. This formula was developed as an “active” vector operation in that a vector was being rotated to a new position by means of a left-handed rotation about the specified unit vector. In component form, the new array can be interpreted as the components of a new vector in the same coordinate system, or as the components of the original vector in a new coordinate system, obtained by a right-handed coordinate

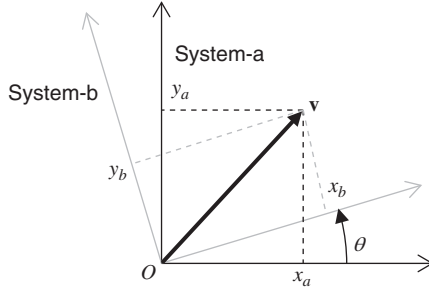


**Figure 1.3-1** A plane rotation of coordinates.

rotation around the specified axis. This can be visualized in Figure 1.3-1, which shows the new components of a vector  $\mathbf{v}$  after a right-handed coordinate system rotation,  $\theta$ , around the  $z$ -axis. Instead, if the vector is given a left-handed rotation of the same amount, then  $(x_b, y_b)$  will become the components of the vector in the original system. Taking the coordinate system rotation viewpoint and combining the matrices in (1.3-4) into a single coefficient matrix, this linear transformation can be written as

$$\mathbf{u}^b = C_{b/a} \mathbf{u}^a \quad (1.3-5)$$

Here  $C_{b/a}$  is a matrix that transforms the coordinates of the vector  $\mathbf{u}$  from system  $a$  to system  $b$  and is called a *direction cosine matrix* (DCM), or simply a *rotation matrix*.

In Figure 1.3-1 a new coordinate system is formed by a *right-handed rotation around the  $z$ -axis* of the original orthogonal coordinate system; the DCM can easily be found by applying Equation (1.3-4) using

$$\mathbf{n}^a = \mathbf{n}^b = [0 \ 0 \ 1]^T, \quad \tilde{\mathbf{n}} = \begin{bmatrix} 0 & -1 & 0 \\ 1 & 0 & 0 \\ 0 & 0 & 0 \end{bmatrix}$$

The DCM and the *components of  $\mathbf{u}$  in system  $b$*  are then found to be

$$\mathbf{u}^b = \begin{bmatrix} x_b \\ y_b \\ z_b \end{bmatrix} = \begin{bmatrix} \cos \theta & \sin \theta & 0 \\ -\sin \theta & \cos \theta & 0 \\ 0 & 0 & 1 \end{bmatrix} \begin{bmatrix} x_a \\ y_a \\ z_a \end{bmatrix} \quad (1.3-6)$$

The direction cosine matrix is so called because its elements are direction cosines between corresponding axes of the new and old coordinate systems. Let  $\mathbf{i}, \mathbf{j}, \mathbf{k}$ , with appropriate subscripts, be unit vectors defining the axes of our orthogonal coordinate systems  $a$  and  $b$ . The  $x_b$ -component of an arbitrary vector  $\mathbf{r}$  can be written as

$$x_b = (\mathbf{r} \cdot \mathbf{i}_b)^b = (\mathbf{r} \cdot \mathbf{i}_b)^a = x_a(\mathbf{i}_a \cdot \mathbf{i}_b) + y_a(\mathbf{j}_a \cdot \mathbf{i}_b) + z_a(\mathbf{k}_a \cdot \mathbf{i}_b)$$

This equation defines the first row of the DCM; the other  $b$ -system components can be found in the same way and consist of dot products of unit vectors, which are equivalent to direction cosines.

The above two methods of constructing a DCM are not very convenient for a general three-dimensional rotation; Euler Rotations (following) provide a more convenient way.

### Direction Cosine Matrix Properties

We will look briefly at some of the properties of the rotation matrix and then at how it may be determined in applications. A coordinate rotation must leave the length of a vector unchanged. The change of length under the rotation above is

$$|\mathbf{u}|^2 = (\mathbf{u}^b)^T \mathbf{u}^b = (C_{b/a} \mathbf{u}^a)^T C_{b/a} \mathbf{u}^a = (\mathbf{u}^a)^T C_{b/a}^T C_{b/a} \mathbf{u}^a$$

and the length is preserved if

$$C_{b/a}^T C_{b/a} = I = C_{b/a} C_{b/a}^T \quad (1.3-7)$$

This is the definition of an *orthogonal matrix*, and it makes the inverse matrix particularly easy to determine ( $C^{-1} = C^T$ ). It also implies that the columns (and also the rows) of the rotation matrix form an orthonormal set:

$$C_{b/a} = [c_1 \quad c_2 \quad c_3] \rightarrow c_i^T c_j = \begin{cases} 0, & i \neq j \\ 1, & i = j \end{cases}$$

Also, since

$$c_1 \equiv C[1 \quad 0 \quad 0]^T$$

columns of the rotation matrix give us the components in the new system of a unit vector in the old system.

If a vector is expressed in a new coordinate system by a sequence of rotations as

$$\mathbf{u}^d = C_{d/c} C_{c/b} C_{b/a} \mathbf{u}^a \quad (1.3-8)$$

then the inverse operation is given by

$$\begin{aligned} \mathbf{u}^a &= (C_{d/c} C_{c/b} C_{b/a})^{-1} \mathbf{u}^d = C_{b/a}^{-1} C_{c/b}^{-1} C_{d/c}^{-1} \mathbf{u}^d = C_{b/a}^T C_{c/b}^T C_{d/c}^T \mathbf{u}^d \\ &= (C_{d/c} C_{c/b} C_{b/a})^T \mathbf{u}^d = C_{d/a}^T \mathbf{u}^d \end{aligned} \quad (1.3-9)$$

### Summary of DCM (Rotation Matrix) Properties

- Successive rotations are described by the product of the individual DCMs; cf. (1.3-8).
- Rotation matrices are not commutative, for example,  $C_{c/b} C_{b/a} \neq C_{b/a} C_{c/b}$ .
- Rotation matrices are orthogonal matrices.
- The determinant of a DCM is unity.
- A nontrivial DCM has one, and only one, eigenvalue equal to unity [see Euler's Rotation Theorem].

## Euler Rotations

Here we will determine the rotation matrix in a way that is better suited to visualizing vehicle orientation.

The orientation of one Cartesian coordinate system with respect to another can always be described by three successive rotations around the orthogonal coordinate axes, and the angles of rotation are called the *Euler angles* (or Eulerian angles). The axes and the order of the rotations are chosen in various ways in different fields of science. When we rule out two successive Euler rotations about the same axis, there are twelve possibilities, six without repetition of an axis (counting both forward and reverse) and six with repetition.

In the aerospace field Euler rotations are performed, in an  $x, y, z$  or  $z, y, x$  order. Each rotation has a form similar to Equation (1.3-6); the zeros and the “1” are placed so that the appropriate coordinate is unchanged (the  $z$ -coordinate in (1.3-6)). The remaining terms are placed with cosines on the main diagonal and sines in the remaining off-diagonal positions, so that the matrix reverts to the identity matrix when the rotation angle is zero. The negative sine term is placed on the row above the “1” term when a positive angle corresponds to a right-handed rotation around the current axis. Henceforth the plane rotation matrix will be written immediately by inspection, and three-dimensional coordinate rotations will be built up as a sequence of plane rotations. The fact that the individual rotations are not commutative can be checked by performing sequences of rotations with any convenient solid object. Therefore, although the order of the sequence can be defined arbitrarily, the same order must be maintained ever after.

The sequence of three Euler rotations leading to a given DCM is not unique, and for a particular DCM we could, in general, find a different set of Euler rotations that would lead to the same final attitude. The Euler angles would then differ from the prescribed angles, and they may be impossible to perform because of physical constraints, for example, aircraft aerodynamic constraints, or mechanical gimbal constraints (think of a simple elevation-over-azimuth sensor-pointing system, where there is a mechanical constraint of zero roll angle). Knowing the Euler rotation convention that was used with the DCM allows the correct Euler angles to be extracted from the DCM, as shown earlier.

Note that Euler angles do not form the components of a vector (though infinitesimal rotations can be treated as such), as will be further elaborated in Section 1.4.

## Rotations Describing Aircraft Attitude

Standard aircraft practice is to describe aircraft orientation by the  $z, y, x$  (also called 3, 2, 1) right-handed Euler rotation sequence that is required to get from a reference system on the surface of Earth into alignment with an aircraft body-fixed coordinate system. The usual choice for the reference system, on Earth, is a North-East-down (*ned*) system, with the  $x$ -axis pointing true North, the  $z$ -axis pointing down, and the  $y$ -axis completing the right-handed set. The exact meaning of “down” will be explained in Section 1.6. The aircraft axes are normally aligned ( $x, y, z$ ), forward,

right, and down (*frd*), with “forward” aligned with the *longitudinal reference line* of the aircraft, and the forward and down axes in the aircraft plane of symmetry. Therefore, starting from the reference system, the sequence of rotations is:

1. Right-handed rotation about the  $z$ -axis, or positive  $\psi$  (compass heading)
2. Right-handed rotation about the new  $y$ -axis, or positive  $\theta$  (pitch)
3. Right-handed rotation about the new  $x$ -axis, or positive  $\phi$  (roll)

The rotations are often described as a yaw-pitch-roll sequence, starting from the reference system.

The plane rotation matrices can be written down immediately with the help of the rules established in the preceding subsection. Thus, abbreviating cosine and sine to  $c$  and  $s$ , we have,

$$C_{frd/nd} = \begin{bmatrix} 1 & 0 & 0 \\ 0 & \cos \phi & \sin \phi \\ 0 & -\sin \phi & \cos \phi \end{bmatrix} \begin{bmatrix} \cos \theta & 0 & -\sin \theta \\ 0 & 1 & 0 \\ \sin \theta & 0 & \cos \theta \end{bmatrix} \begin{bmatrix} \cos \psi & \sin \psi & 0 \\ -\sin \psi & \cos \psi & 0 \\ 0 & 0 & 1 \end{bmatrix}$$

$$C_{frd/nd} = \begin{bmatrix} c\theta c\psi & c\theta s\psi & -s\theta \\ (-c\phi s\psi + s\phi s\theta c\psi) & (c\phi c\psi + s\phi s\theta s\psi) & s\phi c\theta \\ (s\phi s\psi + c\phi s\theta c\psi) & (-s\phi c\psi + c\phi s\theta s\psi) & c\phi c\theta \end{bmatrix} \quad (1.3-10)$$

This matrix represents a standard transformation and will be used throughout the text.

The defined ranges for the rotation angles are

$$\begin{aligned} -\pi < \phi &\leq \pi \\ -\pi/2 &\leq \theta \leq \pi/2 \\ -\pi < \psi &\leq \pi \end{aligned}$$

If the pitch angle,  $\theta$ , had been allowed to have a  $\pm 180^\circ$  range then the airplane could be inverted and heading South with the roll and heading angles reading zero, which is obviously undesirable from a human factors viewpoint! The restriction on theta can be enforced naturally, simply by interpretation of the DCM, as we see in the next subsection

### Euler Angles from the DCM

In a control system it is often necessary to extract the Euler angles, from a continuously computed DCM, for display to a human operator. For the  $z$ - $y$ - $x$  sequence used in Equation (1.3-10), taking account of the chosen angular ranges, the Euler angles are easily seen to be

$$\begin{aligned} \phi &= \text{atan2}(c_{23}, c_{33}), & -\pi < \phi &\leq \pi \\ \theta &= -\text{asin}(c_{13}), & -\pi/2 &\leq \theta \leq \pi/2 \\ \psi &= \text{atan2}(c_{12}, c_{11}), & -\pi < \psi &\leq \pi, \end{aligned} \quad (1.3-11)$$

where  $\text{atan2}(\ast)$  is the four-quadrant inverse tangent function, available in most programming languages. These equations also work for only two Euler rotations (when the order and positive reference directions are the same), for example, the elevation-over-azimuth gimbal system with zero roll angle.

Finite precision computer arithmetic occasionally causes the DCM element  $C_{13}$  to very slightly exceed unit magnitude; in computer code we simply detect this condition and set the pitch attitude to  $90^\circ$ . Since  $\theta$  is usually a low-precision “output” variable, not a state variable, this does not cause any accuracy problems. A more significant problem is the ambiguity introduced into the DCM (1.3-10) at vertical pitch. When  $\theta = \pm\pi/2$  the condition  $C_{11} = C_{12} = C_{23} = C_{33} = 0$  occurs, and the remaining elements can be written as sine and cosine of  $(\phi - \psi)$ , or  $(\phi + \psi)$  when  $\theta = -\pi/2$ . Heading is undefined at vertical pitch, and so roll cannot be computed. For aerobatic aircraft, missiles, and spacecraft, the problem can be avoided by using the quaternion representation of attitude. For most aircraft simulations, the condition  $\theta = 90.000 \dots$  degrees has a very low probability of occurrence and an aircraft simulation can usually fly through vertical pitch without numerical problems.

## Linear Transformations

Linear transformations occur both in the state equation (1.1-3), via the  $A$ -matrix, and in a coordinate rotation. A little knowledge of linear transformations is required in order to use some of the properties of eigenvalues and eigenvectors, described in the next subsection.

Consider the matrix equation

$$v = Au, \quad (1.3-12)$$

where  $v$  and  $u$  are  $n \times 1$  matrices (e.g., vector component arrays) and  $A$  is an  $n \times n$  constant matrix, not necessarily nonsingular. Each element of  $v$  is a linear combination of the elements of  $u$ , and so this equation is a *linear transformation* of the matrix  $u$ . In Euclidean space the geometrical interpretation of the transformation is that a vector is being changed in length and/or direction.

Next, suppose that in an analysis we change to a new set of variables through a reversible linear transformation. If  $L$  is the matrix of this transformation, then  $L^{-1}$  must exist (i.e.,  $L$  is nonsingular) for the transformation to be reversible, and the new variables corresponding to  $u$  and  $v$  are

$$u_1 = Lu, \quad v_1 = Lv$$

Therefore, the relationship between the new variables must be

$$v_1 = LAu = LAL^{-1}u_1 \quad (1.3-13a)$$

The transformation  $LAL^{-1}$  is a *similarity transformation* of the original coefficient matrix  $A$ . A special case of this transformation occurs when the inverse of the matrix  $L$  is given by its transpose (i.e.,  $L$  is an orthogonal matrix) and the similarity

transformation becomes a *congruence transformation*,  $LAL^T$ . An important example of a similarity transformation is a change of state variables,  $z = Lx$ , in the linear state equation (1.1-3), leading to the new state equation

$$\dot{z} = (LAL^{-1})z + (LB)u \quad (1.3-13b)$$

## Eigenvalues and Eigenvectors

Eigenvalues and eigenvectors are introduced here because of the insight they provide into coordinate rotations; they will also be used extensively in Chapter 3 to provide information on the dynamic behavior of systems described by a linear, time-invariant state equation.

A square-matrix linear transformation with an arbitrary matrix  $A(n, n)$  has the property that vectors exist whose components are only scaled by the transformation. If  $\mathbf{v}$  is such an “invariant” vector, its component array,  $v$ , must satisfy the equation

$$Av = \lambda v, \quad v(n \times 1) \quad (1.3-14)$$

where  $\lambda$  is a (scalar) constant of proportionality. A rearrangement of (1.3-14) gives the set of homogeneous linear equations

$$(A - \lambda I)v = 0 \quad (1.3-15)$$

which has a nonnull solution for  $v$  if and only if the determinant of the coefficient matrix is zero (Strang, 1980); that is,

$$|A - \lambda I| = 0 \quad (1.3-16)$$

This determinant is an  $n$ th-order polynomial in  $\lambda$ , called the *characteristic polynomial* of  $A$ , so there may be up to  $n$  distinct solutions for  $\lambda$ . Each solution,  $\lambda_i$ , is known as an *eigenvalue* or *characteristic value* of the matrix  $A$ . The associated invariant vector defined by (1.3-14) is known as a *right eigenvector* of  $A$  (the left eigenvectors of  $A$  are the right eigenvectors of its transpose  $A^T$ ).

In the mathematical model of a physical system, a reversible change of model state variables does not change the behavior of the model if observed at the same outputs. An example of this is the invariance of the eigenvalues of a linear system, described by the state equation (1.1-3), under the similarity transformation (1.3-13). After the similarity transformation, the eigenvalues are given by

$$|\lambda I - LAL^{-1}| = 0,$$

which can be rewritten as

$$|\lambda LL^{-1} - LAL^{-1}| = 0$$

The determinant of a product of square matrices is equal to the product of the individual determinants; therefore,

$$|L| |\lambda I - A| |L^{-1}| = 0 \quad (1.3-17)$$



This equation is satisfied by the eigenvalues of the matrix  $A$ , so the eigenvalues are unchanged by the transformation.

Now consider a special similarity transformation that will reduce the linear equations with square coefficient matrix  $A$  to a canonical (standard) form. First, consider the case when all of the  $n$  eigenvalues of  $A$  are distinct. Then the  $n$  eigenvectors  $v_i$  can be shown to form a linearly independent set; therefore, their components can be used to form the columns of a nonsingular transformation matrix. This matrix is called the *modal matrix*,  $M$ , and

$$M \equiv [v_1 \ v_2 \ \dots \ v_n]$$

Then, according to the eigenvector/eigenvalue defining equation (1.3-14),

$$AM = MJ, \quad \text{where } J = \text{diag}(\lambda_1 \dots \lambda_n)$$

or

$$M^{-1}AM = J \quad (1.3-18)$$

When some of the eigenvalues of  $A$  are repeated (i.e., multiple), it may not be possible to find a set of  $n$  linearly independent eigenvectors. Also, in the case of repeated eigenvalues, the result of the similarity transformation (1.3-18) is in general a *Jordan form matrix* (Wilkinson and Golub, 1976). In this case the matrix  $J$  may have some unit entries on the superdiagonal. These entries are associated with blocks of repeated eigenvalues on the main diagonal.

As an example, the linear state equation (1.1-3), with  $x = Mz$ , becomes

$$\dot{z} = Jz + M^{-1}Bu \quad (1.3-19)$$

This corresponds to a set of state equations with minimal coupling between them. For example, if the eigenvalue  $\lambda_i$  is of multiplicity 2 and the associated Jordan block has a superdiagonal 1, we can write the corresponding equations as

$$\begin{aligned} \dot{z}_i &= \lambda_i z_i + z_{i+1} + b'_i u \\ \dot{z}_{i+1} &= \lambda_i z_i + b'_{i+1} u \end{aligned} \quad (1.3-20)$$

The variables  $z_i$  are called the modal coordinates. In the above case these two equations are coupled; when the eigenvalues are all distinct, the modal coordinates yield a set of uncoupled first-order differential equations. Their homogeneous solutions (i.e., response to initial conditions, with  $u = 0$ ) are the exponential functions  $e^{\lambda_i t}$ , and these are the natural modes of (behavior of) the dynamic system. A disadvantage of the modal coordinates is that the state variables usually lose their original physical significance.

### Euler's Rotation Theorem

A better understanding of coordinate rotations can be obtained by examining the eigenvalues of the DCM. Any nontrivial ( $3 \times 3$ ) rotation matrix has one, and only one,

eigenvalue equal to +1 (see, for example, Goldstein, 1980). The other two eigenvalues are a complex conjugate pair with unit magnitude and can be written as  $(\cos \phi \pm j \sin \phi)$  apart from a special case of two “-1” eigenvalues (see below).

Because the eigenvalues are distinct, the +1 eigenvalue has an associated unique, real eigenvector and, for this eigenvector of an arbitrary rotation matrix  $C$ , Equation (1.3-14) can be written as

$$Cv = v$$

Now, let  $v$  (suitably normalized) be the direction cosine array of an axis passing through the coordinate origin. The only way in which it is possible for the direction cosines to remain unchanged by an arbitrary  $C$  is for  $C$  to be equivalent to a single rotation around the axis given by the eigenvector of eigenvalue +1. Therefore, any compound rotation, made up of rotations about various axes, is equivalent to a single rotation around an axis corresponding to the +1 eigenvector of the compound rotation matrix. (The special case of two “-1” eigenvalues occurs when this rotation is  $180^\circ$ .) This is a modern version of a *fixed-point theorem* proven by Leonhard Euler in 1775.

Euler showed that *if a sphere is rigidly rotated about its center, then there is a diameter that remains fixed*. The principle is fundamentally important and forms the basis of the quaternion representation of rotation that we describe in Section 1.8.

## 1.4 ROTATIONAL KINEMATICS

In this section we will develop kinematic equations for a time-varying orientation, specifically, the relationship between the derivative of a translational vector and angular velocity expressed as a vector. We will follow this with the relationship of the Euler angle derivatives to the angular velocity vector, expressed in state-space form. These relationships will be required when we derive the equations for the six-degrees-of-freedom (6-DoF) motion of a rigid body in Section 1.7. We know from simple mechanics that rotation of a body around an axis induces translational velocities at points away from the axis. We now need to formalize this relationship by expressing the translational velocity as a vector and combining the direction of the axis of rotation with the rate of rotation as a single *angular velocity vector*.

### The Derivative of a Vector

Here we will define the derivative of a vector, show how it depends on the observer's frame of reference, and relate the derivatives of a vector, taken in two different frames, through the relative angular velocity vector of the frames.

In general terms, the derivative of a vector is defined in the same way as the derivative of a scalar:

$$\frac{d}{dt} \mathbf{p}_{A/B} = \lim_{\delta t \rightarrow 0} \left[ \frac{\mathbf{p}_{A/B}(t + \delta t) - \mathbf{p}_{A/B}(t)}{\delta t} \right]$$

This is a new vector created by the changes in length and direction of  $\mathbf{p}_{A/B}$ . If  $\mathbf{p}$  is a free vector (e.g., velocity), then we expect its derivative to be independent of

translation, and the changes in length and direction come from the motion of the tip of  $\mathbf{p}$  relative to its tail. If  $\mathbf{p}$  is a bound vector (e.g., a position vector) in some frame, its derivative in that frame is a free vector, corresponding to motion of the tip of  $\mathbf{p}$ .

### Angular Velocity as a Vector

Using Figure 1.2-1, make a small right-handed rotation,  $\delta\mu \ll 1$  rad, and define  $\mathbf{v} = \mathbf{u} + \delta\mathbf{u}$ ; then Equation (1.2-5a) gives

$$\delta\mathbf{u} \approx -\sin(-\delta\mu)\mathbf{n} \times \mathbf{u} \approx (\mathbf{n} \times \mathbf{u})\delta\mu$$

Now divide by  $\delta t$ , take the limit as  $\delta t \rightarrow 0$ , and define the vector  $\boldsymbol{\omega} \equiv \dot{\mu}\mathbf{n}$ , giving

$$\dot{\mathbf{u}} = \boldsymbol{\omega} \times \mathbf{u} \quad (1.4-1)$$

This equation relates the translational velocity of the tip of the constant-length bound vector  $\mathbf{u}$  to the vector  $\boldsymbol{\omega}$ . The vector  $\boldsymbol{\omega}$  is made up of a unit vector defining the axis of rotation, scaled by the rotation rate; it is the *angular velocity vector* of this rotation. It is a free vector (can be translated parallel to itself) and an axial or pseudovector (it would change direction if we had chosen a left-handed rotation convention).

Because  $\boldsymbol{\omega}$  is a free vector, we associate it with the rigid body (i.e., frame), not just a bound vector in the frame, and give it subscripts to indicate that it is the angular velocity of that body relative to some other body. The orientation of a rotating rigid body is described by a time-varying DCM and it follows from Euler's theorem that the body has a unique *instantaneous axis of rotation*; the angular velocity vector is parallel to this axis and is unique to the body.

### Vector Derivatives and Rotation

To understand the derivative of a vector, observed from another frame, in relative motion, we can proceed as follows.

Figure 1.4-1 shows a frame  $F_b$  in arbitrary motion with respect to another frame  $F_a$  and with angular velocity  $\boldsymbol{\omega}_{b/a}$ . Fixed point  $Q$  has translational velocity  $\mathbf{v}_{Q/a}$  with respect to  $F_a$ , and vector  $\mathbf{p}$  from  $Q$  is the vector of interest. An observer in  $F_b$  watching the tip of this vector would see the new vector  $\mathbf{p}_1$  corresponding to a nonzero derivative  ${}^b\dot{\mathbf{p}}$ . An observer in  $F_a$  would see, in addition, the effect of the angular velocity of  $F_b$  with respect to  $F_a$ , giving the vector  $\mathbf{p}_2$ . The  $F_a$  observer would also see  $\mathbf{p}_2$  translated parallel to itself because of the translational velocity  $\mathbf{v}_{Q/a}$ . However, the derivative in  $F_a$  is a free vector and this translation does not entail a change in length or direction of  $\mathbf{p}_2$ . The derivative  ${}^a\dot{\mathbf{p}}$  is obtained by comparing  $\mathbf{p}_2$  with  $\mathbf{p}$  as  $\delta t \rightarrow 0$ .

In time  $\delta t$ ,  $\mathbf{p}_2 - \mathbf{p}$  is given by

$$\mathbf{p}_2 - \mathbf{p} = {}^b\dot{\mathbf{p}}\delta t + (\boldsymbol{\omega}_{b/a} \times \mathbf{p})\delta t$$

Dividing by  $\delta t$  and taking the limit as  $\delta t \rightarrow 0$  give

$${}^a\dot{\mathbf{p}} = {}^b\dot{\mathbf{p}} + \boldsymbol{\omega}_{b/a} \times \mathbf{p} \quad (1.4-2)$$

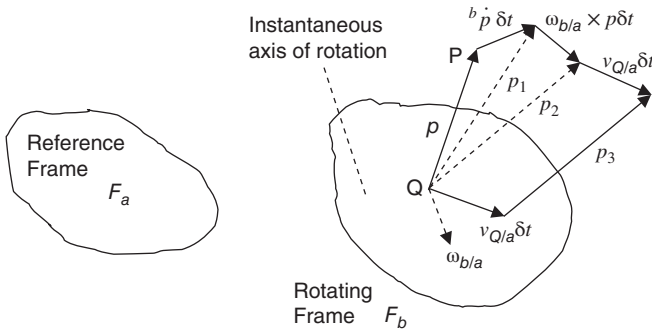


**Figure 1.4-1** A vector derivative in a rotating frame.

Equation (1.4-2) is sometimes called the *equation of Coriolis* (Blakelock, 1965) and will be an essential tool in developing equations of motion from Newton's laws. It is much more general than is indicated above and applies to any physical quantity that has a vector representation. The derivatives need not even be taken with respect to time. Angular velocity can be defined as the vector that relates the derivatives of any arbitrary vector in two different frames, according to (1.4-2). In the interests of having a vector diagram and intuitive feel, we have derived the equation in a rather restricted fashion. A more rigorous derivation (with no diagram) has been given by McGill and King (1995) and a longish derivation with a different kind of diagram by Pestel and Thompson (1968).

Some formal properties of the angular velocity vector are:

- It is a unique vector that relates the derivatives of a vector taken in two different frames.
- It satisfies the relative motion condition  $\omega_{b/a} = -\omega_{a/b}$ .
- It is additive over multiple frames, e.g.,  $\omega_{c/a} = \omega_{c/b} + \omega_{b/a}$  (not true of angular acceleration).
- Its derivative is the same in either frame,  ${}^a\dot{\omega}_{b/a} = {}^b\dot{\omega}_{b/a}$ . [Use (1.4-2) to find the derivative.]

A common problem is the determination of an angular velocity vector after the frames have been defined in a practical application. This can be achieved by finding one or more intermediate frames in which an axis of rotation and an angular rate are physically evident. Then the additive property can be invoked to combine the intermediate angular velocities. An example of this is given later, with the "rotating-Earth" equations of motion of an aerospace vehicle.

The derivative of a vector in some frame can be found from the derivatives of its components in a coordinate system fixed in that frame, that is, if

$$\mathbf{v}^{af} = [v_x \ v_y \ v_z]^T$$

where system  $af$  is fixed in frame  $a$ , then

$${}^a\dot{\mathbf{v}}^{af} = [\dot{v}_x \ \dot{v}_y \ \dot{v}_z]^T$$

If the vector is from a fixed point in that frame, it is a velocity, acceleration, etc., with respect to that frame. If the vector is from a fixed point in a different frame, then it is a relative velocity, acceleration, etc., taken in the derivative frame.

**Example 1.4-1: Centripetal Acceleration on Earth's Surface** If  $\mathbf{p}$  is a position vector from Earth's cm to a fixed point  $P$  on the surface rotating with Earth's (constant) inertial angular velocity  $\boldsymbol{\omega}_{e/i}$ , then the inertial acceleration vector  $\mathbf{a}$  of  $P$  can be found from

$$\begin{aligned} \mathbf{v}_{P/i} &= {}^i\dot{\mathbf{p}} = {}^e\dot{\mathbf{p}} + \boldsymbol{\omega}_{e/i} \times \mathbf{p} \\ \mathbf{a} &= {}^i\dot{\mathbf{v}}_{P/i} = {}^i\dot{\boldsymbol{\omega}}_{e/i} \times \mathbf{p} + \boldsymbol{\omega}_{e/i} \times {}^i\dot{\mathbf{p}} = \boldsymbol{\omega}_{e/i} \times (\boldsymbol{\omega}_{e/i} \times \mathbf{p}) \end{aligned} \quad (1)$$

It is easy to confirm that this *centripetal acceleration* is orthogonal to the angular velocity vector and to show that this equation leads to the well-known scalar formulae ( $v^2/r$  and  $r\omega^2$ ) for centripetal acceleration in a plane perpendicular to the angular velocity vector. ■

## Euler Angle Kinematics

With the idea in mind of relating the Euler angle rates, describing the changing attitude of a body, to its angular velocity, we proceed as follows. We define a reference frame  $F_r$  and a body frame  $F_b$  with a relative angular velocity vector  $\boldsymbol{\omega}_{b/r}$  and a sequence of Euler angles that define the attitude of the body as the orientation of a coordinate system fixed in the body relative to a coordinate system fixed in the reference frame. Each Euler angle rate provides the magnitude and direction information for an individual angular velocity vector (i.e., along a particular coordinate axis). These three vectors can be added to find the resultant angular velocity vector of the vehicle whose Euler angle rates are being considered. Equivalently, we can find the components of the resultant angular velocity vector.

To make this process more concrete we take the common case of motion over Earth, with a *frd* coordinate system in the body, a *ned* system in the reference frame, and a yaw-pitch-roll Euler angle sequence from *ned* to *frd*. In the case of the flat-Earth equations (Section 1.7) the *ned* system is fixed in the Earth as the reference frame, and the relative angular velocity is that of the body with respect to Earth. In the case of the more general 6-DoF equations the *ned* system moves over the Earth, underneath the body, and we must define an abstract reference frame which has its own angular velocity with respect to the Earth frame (determined by latitude and longitude rates).

The coordinate transformations are

$$\boldsymbol{\omega}_{b/r}^{frd} = \begin{bmatrix} \dot{\phi} \\ 0 \\ 0 \end{bmatrix} + C_\phi \left( \begin{bmatrix} 0 \\ \dot{\theta} \\ 0 \end{bmatrix} + C_\theta \begin{bmatrix} 0 \\ 0 \\ \dot{\psi} \end{bmatrix} \right)$$

where  $C_\phi$  and  $C_\theta$  are the right-handed plane rotations through the particular Euler angles, as given in Equations (1.3-10). After multiplying out the matrices, the final result is

$$\boldsymbol{\omega}_{b/r}^{frd} \equiv \begin{bmatrix} P \\ Q \\ R \end{bmatrix} = \begin{bmatrix} 1 & 0 & -\sin \theta \\ 0 & \cos \phi & \sin \phi \cos \theta \\ 0 & -\sin \phi & \cos \phi \cos \theta \end{bmatrix} \begin{bmatrix} \dot{\phi} \\ \dot{\theta} \\ \dot{\psi} \end{bmatrix} \quad (1.4-3)$$

where  $P$ ,  $Q$ ,  $R$ , are standard symbols for, respectively, the roll, pitch, and yaw rate components of the aircraft angular velocity vector in *frd* coordinates. The inverse transformation is

$$\begin{bmatrix} \dot{\phi} \\ \dot{\theta} \\ \dot{\psi} \end{bmatrix} = \begin{bmatrix} 1 & \sin \phi \tan \theta & \cos \phi \tan \theta \\ 0 & \cos \phi & -\sin \phi \\ 0 & \sin \phi / \cos \theta & \cos \phi / \cos \theta \end{bmatrix} \begin{bmatrix} P \\ Q \\ R \end{bmatrix} \quad (1.4-4)$$

For brevity, we will define  $\Phi \equiv [\phi \ \theta \ \psi]^T$  and write (1.4-4) as

$$\dot{\Phi} = H(\Phi) \boldsymbol{\omega}_{b/r}^{frd} \quad (1.4-5)$$

Equations (1.4-3) and (1.4-4) will be referred to as the *Euler kinematical equations*. Note that the coefficient matrices are not orthogonal matrices representing ordinary coordinate rotations. Note also that Equations (1.4-4) have a singularity when  $\theta = \pm\pi/2$ . In addition, if these equations are used in a simulation, the Euler angle rates may integrate up to values outside the Euler angle range. Therefore, logic to deal with this problem must be included in the computer code. Despite these disadvantages the Euler kinematical equations are commonly used in aircraft simulation.

## 1.5 TRANSLATIONAL KINEMATICS

In this section we introduce the equations for relative velocity and relative acceleration between rigid bodies in motion and, in particular, introduce *centripetal* and *Coriolis acceleration*. The equations are then applied to motion over Earth, and the results are used in the 6-DoF motion in Section 1.7.

### Velocity and Acceleration in Moving Frames

Figure 1.5-1 shows a point  $P$  with position vector  $\mathbf{p}$  moving with respect to two frames  $F_a$  and  $F_b$ , in relative motion, and with fixed points  $O$  and  $Q$ , respectively. Suppose that we wish to relate the velocities in the two frames and also the accelerations. We must first relate the position vectors shown in the figure and then take derivatives in  $F_a$  to introduce velocity (we are arbitrarily choosing  $F_a$  to be the “reference” frame):

$$\mathbf{p}_{P/O} = \mathbf{p}_{Q/O} + \mathbf{p}_{P/Q} \quad (1.5-1)$$

$${}^a\dot{\mathbf{p}}_{P/O} = {}^a\dot{\mathbf{p}}_{Q/O} + {}^a\dot{\mathbf{p}}_{P/Q} \quad (1.5-2)$$

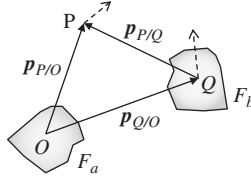


**Figure 1.5-1** Velocity and acceleration in moving frames.

Starting from the left-hand side of Equation (1.5-2), the first two terms are velocities in  $F_a$  but the last term involves the position of  $P$  relative to a fixed point in  $F_b$ , with the derivative taken in  $F_a$ . Let  $\mathbf{v}$  with an appropriate subscript represent a velocity vector. Then, by applying the equation of Coriolis, Equation (1.5-2) gives

$$\mathbf{v}_{P/a} = \mathbf{v}_{Q/a} + (\mathbf{v}_{P/b} + \boldsymbol{\omega}_{b/a} \times \mathbf{p}_{P/Q}) \quad (1.5-3)$$

Note that (1.5-3) can be written as

$$\mathbf{v}_{P/a} = \mathbf{v}_{P/b} + (\mathbf{v}_{Q/a} + \boldsymbol{\omega}_{b/a} \times \mathbf{p}_{P/Q}),$$

where the term in parentheses is the velocity in  $F_a$  of a fixed point in  $F_b$  that is instantaneously coincident with  $P$  and is called the *transport velocity of  $P$  in  $F_a$* .

As an application of Equation (1.5-3), let  $F_a$  be an inertial reference frame and  $F_b$  a body moving with respect to the reference frame. Assume that a navigator on the moving body determines, from an onboard inertial navigation system, his velocity in the inertial reference frame  $\mathbf{v}_{Q/a}$  and his inertial angular velocity vector  $\boldsymbol{\omega}_{b/a}$ . Also, using a radar set, he measures the velocity  $\mathbf{v}_{P/b}$ , of  $P$  in  $F_b$  and the position  $\mathbf{p}_{P/Q}$  of  $P$  with respect to  $Q$ . He can then use Equation (1.5-3), with appropriately chosen coordinate systems, to calculate the velocity of the object in the inertial reference frame and, knowing the equation of motion in the inertial frame, predict its trajectory.

We next find the acceleration of  $P$  by taking derivatives of (1.5-3) in  $F_a$ . Starting from the left, the first two terms are velocities in  $F_a$  and these become accelerations in  $F_a$ . The third term is a velocity in  $F_b$  and must be differentiated by the equation of Coriolis. The last term involving a cross-product can be differentiated by the “product rule,” and the derivative of angular velocity is an angular acceleration vector, denoted by  $\boldsymbol{\alpha}$ . Therefore, denoting translational acceleration by  $\mathbf{a}$ , (1.5-3) yields

$$\mathbf{a}_{P/a} = \mathbf{a}_{Q/a} + (\mathbf{a}_{P/b} + \boldsymbol{\omega}_{b/a} \times \mathbf{v}_{P/b}) + \boldsymbol{\alpha}_{b/a} \times \mathbf{p}_{P/Q} + \boldsymbol{\omega}_{b/a} \times (\mathbf{v}_{P/b} + \boldsymbol{\omega}_{b/a} \times \mathbf{p}_{P/Q})$$

Regrouping terms, we get

$$\begin{aligned} \mathbf{a}_{P/a} = & \underbrace{\mathbf{a}_{P/b} + \mathbf{a}_{Q/a} + \boldsymbol{\alpha}_{b/a} \times \mathbf{p}_{P/Q} + \boldsymbol{\omega}_{b/a} \times (\boldsymbol{\omega}_{b/a} \times \mathbf{p}_{P/Q})}_{\text{Transport Acceleration of P in Frame-a}} \\ & + \underbrace{2\boldsymbol{\omega}_{b/a} \times \mathbf{v}_{P/b}}_{\text{Coriolis Acceleration}} \end{aligned} \quad (1.5-4)$$

Here, the names *total acceleration* and *relative acceleration* apply to the reference and secondary frames, respectively. If  $P$  were fixed in  $F_b$  the first and last right-hand-side terms would vanish, leaving only the *transport acceleration*; this is defined as the acceleration in  $F_a$  of a fixed point in  $F_b$  that is instantaneously coincident with  $P$ . As could be anticipated, the transport acceleration term contains the effects of the motion of  $F_b$  in terms of the acceleration of the reference point  $Q$  and the angular acceleration and angular velocity of the frame [see (1) for more detail of the centripetal term]. A comparison of the acceleration equation with the velocity equation shows that a new type of term has appeared, namely the *Coriolis acceleration*. The significance of Coriolis acceleration is examined in the following subsection.

**Example 1.5-1: Sensor Fixed in A Moving Body** A sensor (e.g., accelerometer, radar, etc.) fixed to a rigid vehicle has no velocity or acceleration in that frame, so according to Equation (1.5-3) or (1.5-4) only the transport term in these equations is nonzero. Sensor motion must often be related analytically to the motion of the vehicle cm (or perhaps some other fixed point). For example, with the same notation as Equation (1.5-4), an accelerometer at position  $P$ , with position vector  $\mathbf{p}_{P/Q}$  relative to the point  $Q$ , has an acceleration given by

$$\mathbf{a}_{P/a} = \mathbf{a}_{Q/a} + \boldsymbol{\alpha}_{b/a} \times \mathbf{p}_{P/Q} + \boldsymbol{\omega}_{b/a} \times (\boldsymbol{\omega}_{b/a} \times \mathbf{p}_{P/Q}),$$

where  $a$  and  $b$  denote, respectively, the reference and vehicle frames. ■

## Acceleration Relative to Earth

This book is concerned with the motion of aerospace vehicles over the Earth, and acceleration relative to Earth is the starting point for equations of motion. Using the results of the previous subsection, let  $F_a$  become an inertial frame  $F_i$  and  $F_b$  become the rigid Earth frame  $F_e$ . Let the points  $Q$  and  $O$  coincide, at Earth's cm (Earth is assumed to have no translational acceleration) so that the acceleration  $\mathbf{a}_{Q/a}$  vanishes and  $\mathbf{p}_{P/Q}$  is a geocentric position vector. Earth's angular velocity is closely constant and so the derivative of  $\boldsymbol{\omega}_{b/a}$  vanishes. This leaves only the relative acceleration, centripetal acceleration, and Coriolis acceleration terms and gives the fundamental equation, relating true (inertial) acceleration to relative acceleration, that we will use in Section 1.7 to apply Newton's laws to motion of a point  $P$  over Earth:

$$\mathbf{a}_{P/i} = \mathbf{a}_{P/e} + \boldsymbol{\omega}_{e/i} \times (\boldsymbol{\omega}_{e/i} \times \mathbf{p}_{P/O}) + 2\boldsymbol{\omega}_{e/i} \times \mathbf{v}_{P/e} \quad (1.5-5)$$

For a particle of mass  $m$  at  $P$ , the relative acceleration  $\mathbf{a}_{P/e}$  corresponds to an “apparent force” on the particle and produces the trajectory observed by a stationary observer on Earth. The true acceleration  $\mathbf{a}_{P/i}$  corresponds to “true” forces (e.g., mass attraction, drag); therefore, writing (1.5-5) in terms of force,

$$\text{Apparent force} = \text{true force} - m[\boldsymbol{\omega}_{e/i} \times (\boldsymbol{\omega}_{e/i} \times \mathbf{p}_{P/O})] - m(2\boldsymbol{\omega}_{e/i} \times \mathbf{v}_{P/e})$$

The second term on the right is the *centrifugal force*, directed normal to the angular velocity vector. The third term is usually referred to as the *Coriolis force* and will cause a ballistic trajectory over Earth to curve to the left or right.



The true force is the sum of the *contact forces*, say  $F$ , and the mass attraction of Earth's gravitational field,  $m\mathbf{G}$  (see next section). The Earth gravity vector is  $\mathbf{g} = \mathbf{G} - \text{centripetal acceleration}$  (see next section), so Equation (1.5-5) is often written (for a body of mass  $m$ ) as

$$\mathbf{a}_{P/e} = \frac{F}{m} + \mathbf{g} - 2\boldsymbol{\omega}_{e/i} \times \mathbf{v}_{P/e} \quad (1.5-6)$$

An often-quoted example of the Coriolis force is the circulation of winds around a low-pressure area (a cyclone) on Earth. The true force is radially inward along the pressure gradient. In the Northern Hemisphere, for example, Earth's angular velocity vector points outward from Earth's surface and, whichever way the velocity vector  $\mathbf{v}_{P/e}$  is directed, the Coriolis force is directed to the right of  $\mathbf{v}_{P/e}$ . Therefore, in the Northern Hemisphere the winds spiral inward in a counterclockwise direction around a cyclone.

The Coriolis acceleration is also significant in high-speed flight; it is zero for an aircraft flying due North or South at the equator and reaches its maximum value at the poles or for flight due East or West at any latitude. Its significance can be estimated by equating its value to the centripetal acceleration, in low, constant-altitude flight, at 45° latitude, and solving for the speed over Earth:

$$2 |\boldsymbol{\omega}_{e/i}| |\mathbf{v}_{cm/e}| \sin(45^\circ) = |\mathbf{v}_{cm/e}|^2 / r_E$$

$$|\mathbf{v}_{cm/e}| = \sqrt{2} r_E |\boldsymbol{\omega}_{e/i}| \approx 657 \text{ m/s (2156 ft/s)}$$

At this speed the Coriolis acceleration is equal to the centripetal acceleration and is very small compared to  $\mathbf{g}$  but causes a position error that grows quadratically with time.

## 1.6 GEODESY, COORDINATE SYSTEMS, GRAVITY

### Introduction

Geodesy is a branch of mathematics that deals with the shape and area of the Earth. Some ideas and facts from geodesy are needed to simulate the motion of an aerospace vehicle around Earth. In addition, some knowledge of Earth's gravitation is required. Useful references are *Encyclopaedia Britannica* (1987), Heiskanen and Moritz (1967), Kuebler and Sommers (1981), NIMA (1997), and Vanicek and Krakiwsky (1982).

### The Shape of the Earth, WGS-84

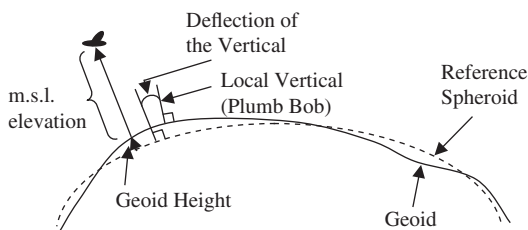
Simulation of high-speed flight over large areas of Earth's surface, with accurate equations of motion and precise calculation of position, requires an accurate model of Earth's shape, rotation, and gravity. Meridional cross sections of Earth are approximately elliptical and the polar radius of Earth is about 21 km less than the equatorial radius, so the solid figure generated by rotating an appropriately scaled ellipse about its minor axis will provide a model of Earth's shape. Organizations from many

countries participate in making accurate measurements of the parameters of these *spheroidal* (i.e., ellipsoids of revolution) models. In the United States the current model is the Department of Defense World Geodetic System 1984, or WGS-84, and the agency responsible for supporting this model is the National Imagery and Mapping Agency (NIMA, 1997). The Global Positioning System (GPS) relies on WGS-84 for the ephemerides of its satellites.

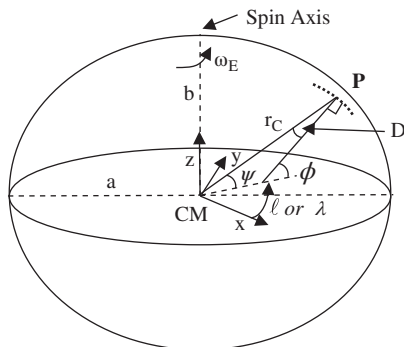
The equipotential surface of Earth's gravity field that coincides with the undisturbed mean sea level extended continuously underneath the continents is called the *geoid*. Earth's irregular mass distribution causes the geoid to be an undulating surface, and this is illustrated in Figure 1.6-1. Note that the *local vertical* is defined by the direction in which a plumb-bob hangs and is accurately normal to the geoid. The angle that it makes with the spheroid normal is called the *deflection of the vertical* and is usually less than 10 arc-s (the largest deflections over the entire Earth are about 1 arc-min).

Figure 1.6-2 shows the *Earth spheroid*, with the oblateness greatly exaggerated. The coordinate system shown has its origin at Earth's center of mass (indirectly determined from satellite orbits),  $z$  up the spin axis, and its  $x$  and  $y$  axes in the equatorial plane. Based on this coordinate system, the equation of the spheroidal model is

$$\frac{x^2 + y^2}{a^2} + \frac{z^2}{b^2} = 1 \quad (1.6-1)$$



**Figure 1.6-1** The geoid and definitions of height.



**Figure 1.6-2** The oblate spheroidal model of the Earth.

In the figure,  $a$  and  $b$  are respectively the semimajor and semiminor axes of the generating ellipse. Two other parameters of the ellipse (not shown) are its *flattening*,  $f$ , and its *eccentricity*,  $e$ .

The WGS-84 spheroid was originally (1976–1979 data) a least-squares best fit to the geoid. More recent estimates have slightly changed the “best fit” parameters, but the current WGS-84 spheroid now uses the original parameters as its defining values. Based on a  $1^\circ \times 1^\circ$  (latitude, longitude) worldwide grid, the root-mean-square (rms) deviation of the geoid from the spheroid is only about 30 m! The WGS-84 defined and derived values are:

$$\begin{aligned}
 a &\equiv 6\,378\,137.0\text{m} && \text{(defined)} \\
 f &= \frac{a-b}{a} \equiv 1/298.257\,223\,563 && \text{(defined)} \\
 b &= 6\,356\,752\text{m} && \text{(derived)} \\
 e &= \frac{(a^2 - b^2)^{\frac{1}{2}}}{a} = .0818\,191\,908\,426 && \text{(derived)} \quad (1.6-2a)
 \end{aligned}$$

Two additional parameters are used to define the complete WGS-84 reference frame; these are the fixed (scalar) Earth rotation rate,  $\omega_E$ , and the Earth’s gravitational constant ( $GM$ ) with the mass of the atmosphere included. In WGS-84 they are defined to be

$$\begin{aligned}
 \omega_E &\equiv 7.292\,1150 \times 10^{-5} \text{ rad/s} \\
 GM &\equiv 398\,6004.418 \times 10^8 \text{ m}^3/\text{s}^2 && (1.6-2b)
 \end{aligned}$$

The  $\omega_E$  value is called the *sidereal rate of rotation* (rate relative to the “fixed” stars); it actually corresponds to a component of Earth’s angular velocity in the heliocentric frame ( $\omega_E = (2\pi/(24 \times 3600)) \times (1 + 1/365.25)$ ), neglecting the inclination of Earth’s axis).

## Frames, Earth-Centered Coordinates, Latitude and Longitude

The *reference frames* used here are the Earth, considered to be a rigid body, and an *inertial frame* (Kaplan, 1981) containing Earth’s cm as a fixed point (this neglects the small centripetal acceleration of Earth’s orbit and any acceleration of the Sun with respect to the Galaxy). An inertial frame must also be nonrotating; so the small, low-amplitude wobble of Earth’s axis will be neglected, and a line from the cm, in the plane of the ecliptic, parallel to a line from the Sun’s cm to a very distant “fixed” star will be taken to be a fixed line. Several polar and Cartesian coordinate systems are defined in these frames; they use Earth’s spin axis and equatorial plane (defined as orthogonal to the spin axis and containing Earth’s cm) for reference.

The Earth-centered–Earth-fixed (ECEF) system is fixed in the Earth frame, has its origin at the cm, its  $z$ -axis up the spin axis, and its  $x$  and  $y$  axes in the equatorial plane (as in Figure 1.6-2) with the  $x$ -axis passing through the Greenwich Meridian (actually a few arc-seconds off the Meridian (see NIMA, 1997)). The Earth-centered

inertial (ECI) system is fixed in the inertial frame, and defined in the same way as ECEF, except that its  $x$ -axis is always parallel to a line from the Sun's cm to Earth's position in orbit at the vernal equinox.

*Terrestrial longitude*,  $\ell$ , and *celestial longitude*,  $\lambda$ , are shown in the figure, measured easterly from the appropriate  $x$ -axis to the projection of the position vector on the equatorial plane. In a given time interval, an increment in celestial longitude is equal to the increment in terrestrial longitude plus the increment in Earth's rotation angle. This can be written as

$$\lambda - \lambda_0 = \ell - \ell_0 + \omega_E t, \quad (1.6-3)$$

where  $\lambda_0$  and  $\ell_0$  are the values at  $t = 0$ . Absolute celestial longitude is often unimportant, and  $\lambda_0 \equiv 0$  can be used. *Latitude angles* are angles subtended by the position vector, above the equatorial plane, and are positive in the Northern Hemisphere.

**Geocentric Coordinates of a Point** The *geocentric coordinates* of a point  $P$ , on the spheroid, are shown in Figure 1.6-2 and, in cross section, for a point above the spheroid in Figure 1.6-3. They are referenced to the common origin of the ECI and ECEF systems and the equatorial plane. They are:

The geocentric latitude of  $P$ : angle  $\psi$

The geocentric radius of  $P$ : distance  $r$

(The geocentric radius of the spheroid is  $r_c$ .)

**Geodetic Coordinates of a Point** The *geodetic coordinates* of point  $P$ , in Figures 1.6-2 and 1.6-3, are used for maps and navigation and are referenced to the normal to the spheroid from point  $P$ . They are:

*Geodetic latitude*,  $\phi$ : the angle of the normal with the equatorial plane.

*Geodetic height*,  $h$ : the height above the spheroid, along the normal.

Geodetic height can be determined from a database of tabulated geoid height versus latitude and longitude plus the elevation above mean sea level (msl). The elevation above msl is in turn obtained from a barometric altimeter or from the land elevation (in a *hypographic database*) plus the altitude above land (e.g., radar altimeter).

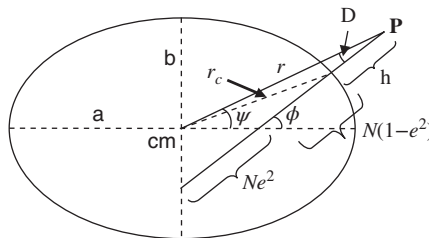


**Figure 1.6-3** The geometry of a point above the spheroid.

In Figure 1.6-3, the triangle that defines latitude shows that

$$\phi = \psi + D \quad (1.6-4)$$

and the very small angle  $D$  is called *the deviation of the normal* and has a maximum value of 11.5 arc-min when  $P$  is on the spheroid and the latitude is  $45^\circ$ .

## Local Coordinate Systems

Local coordinate systems have their origins on the spheroid. The *local geocentric system* (c-system) has its down axis aligned with the geocentric position vector and its “horizontal” axes aligned geographically (usually true North and East). The *local geographic systems* have their down axis aligned with the spheroid normal and are oriented North-East-down (*ned*) or East-North-up (*enu*). These systems move with the vehicle (i.e., origin vertically below the vehicle cm) and the latitude and longitude of the vehicle determine their orientation relative to the Earth-centered systems [see Earth-Related Coordinate Transformations]. If required we could define an imaginary frame in which these systems would be fixed (e.g., a “vehicle-carried” frame) with an angular velocity determined by the vehicle latitude and longitude rates (found from radii of curvature, following). A *tangent-plane coordinate system* is aligned as a geographic system but has its origin fixed at a point of interest on the spheroid; this coordinate system is used with the flat-Earth equations of motion (Section 1.7).

## Radii of Curvature

A *radius of curvature* is a radial length that relates incremental distance along a geometrical arc to an increment in the angle subtended by the arc on a coordinate axis. Discussions of curvature and formulae for radii of curvature can be found in calculus textbooks; the simplest example is a circular arc, where the radius of curvature is the radius of the circle. For the spheroidal model of the Earth, the radii of curvature relating North-South distance along a meridian to an increment in latitude and East-West distance to an increment in longitude are required for estimating distances and speeds over the real Earth.

The *meridian radius of curvature*,  $M$ , of the spheroid is the radius of curvature in a meridian plane that relates North-South distance to increments in geodetic latitude; it is determined by the gradient of the generating ellipse. Applying a general formula for radius of curvature to the generating ellipse, it is easy to show that  $M$  is given by

$$M = \frac{a(1 - e^2)}{(1 - e^2 \sin^2 \phi)^{3/2}}, \quad \frac{b^2}{a} \leq M \leq \frac{a^2}{b} \quad (1.6-5)$$

A radius of curvature, integrated with respect to angle, gives arc length. In this case the integral cannot be found in closed form, and it is much easier to compute distance over the Earth approximately using spherical triangles. The usefulness of this radius of curvature lies in calculating components of velocity. Thus, at geodetic height  $h$ , the

geographic system North component of velocity,  $v_N$ , over Earth is related to latitude rate by

$$v_N = (M + h) \dot{\phi} \quad (1.6-6)$$

The *prime vertical radius of curvature*,  $N$ , is the radius of curvature in a plane perpendicular to the meridian plane and containing the *prime vertical* (the normal to the spheroid at the pertinent latitude). By rotational symmetry, the *center of curvature* (origin for the radius of curvature) is on the minor axis of the generating ellipse, as shown in Figure 1.6-3, and  $N$  is the distance to the ellipse (two parts of  $N$  are shown in the figure). Note that  $N$  occurs in almost all of the geodesy calculations that we will use. The formula for  $N$  is more easily (and instructively) found from the following simple argument than from an algebraically messy application of the standard formula for the radius of curvature. From the figure, we find the radius  $r$  of a *small circle* (of constant latitude) where  $N$  meets the ellipse and, from the rectangular coordinates on the spheroid, the meridian gradient and the gradient of the normal:

$$\begin{aligned} r &= N \cos \phi \\ \text{Meridian gradient} &= \frac{dz}{dr} = -\frac{b^2 r}{a^2 z} \\ \text{Gradient of normal} &= \tan \phi = -\frac{1}{dz/dr} = \frac{a^2 z}{b^2 r} \end{aligned}$$

From these equations, we find that the  $z$ -component on the spheroid at geodetic latitude,  $\phi$ , is

$$z = \frac{b^2}{a^2} N \sin \phi = N(1 - e^2) \sin \phi \quad (1.6-7)$$

Equation (1.6-7) shows the very useful property that  $N$  can be divided into two parts, above and below the equatorial plane, as shown in the figure,

$$N = \underset{\text{(below } x-y)}{Ne^2} + \underset{\text{(above } x-y)}{N(1 - e^2)} \quad (1.6-8)$$

Next, we write the spheroid equation in terms of  $r$  and  $z$ , substitute the above expressions for  $r$  and  $z$ , and solve for  $N$ :

$$N = \frac{a}{(1 - e^2 \sin^2 \phi)^{1/2}}, \quad a \leq N \leq \frac{a^2}{b}, \quad (1.6-9)$$

where  $N$  is needed for coordinate calculations and is useful for calculating velocity components. Using the constant-latitude circle we find that the geographic system East component of velocity over Earth,  $v_E$ , is related to longitude rate by

$$v_E = (N + h) \cos(\phi) \dot{\epsilon} \quad (1.6-10)$$

### Trigonometric Relationships for the Spheroid

Some useful relationships can be derived from the spheroid equation using simple trigonometry. The geocentric radius at any point on the spheroid is given by

$$r_c^2 = \frac{a^2}{1 + \frac{e^2}{1-e^2} \sin^2 \psi} = \frac{b^2}{1 - e^2 \cos^2 \psi} = \frac{a^2 [1 - e^2 (2 - e^2) \sin^2 \phi]}{1 - e^2 \sin^2 \phi} \quad (1.6-11)$$

The deviation of the normal can be found from

$$\tan D = \frac{n \sin \phi \cos \phi}{1 - n \sin^2 \phi} = \frac{n \sin \psi \cos \psi}{1 - n \cos^2 \psi}, \quad \text{where } n = \frac{e^2 N}{N + h} \approx e^2 \quad (1.6-12)$$

and the relationships between geodetic and geocentric latitude are

$$\sin \psi = \frac{(1 - n) \sin \phi}{[1 - n(2 - n) \sin^2 \phi]^{1/2}}, \quad \cos \psi = \frac{\cos \phi}{[1 - n(2 - n) \sin^2 \phi]^{1/2}} \quad (1.6-13)$$

so,

$$\tan \psi = (1 - n) \tan \phi \quad (1.6-14)$$

The geocentric radius to a point  $P$  at geodetic height  $h$  is

$$r = (N + h)[1 - n(2 - n) \sin^2 \phi]^{1/2} \quad (1.6-15)$$

but, because the deviation of the normal,  $D$ , is so small, the geocentric radius at  $P$  is closely equal to the sum of the geocentric radius of the spheroid and the geodetic height:

$$r \approx r_c + h \quad (1.6-16)$$

The error in this approximation is insensitive to altitude and greatest at  $45^\circ$  latitude, where it is still less than  $6 \times 10^{-4} \%$ . The use of the approximation is described in the next subsection.

### Cartesian/Polar Coordinate Conversions

Cartesian position coordinates (ECI or ECEF) can be readily calculated from polar coordinates using the prime vertical radius of curvature. The projection of  $N$  on the  $x$ - $y$  plane gives the  $x$ - and  $y$ -components; the  $z$ -component was given in Equation (1.6-7). Therefore, the ECEF position can be calculated from either geocentric or geodetic coordinates by

$$\mathbf{p}^{ecef} = \begin{bmatrix} r \cos \psi \cos \ell \\ r \cos \psi \sin \ell \\ r \sin \psi \end{bmatrix} = \begin{bmatrix} (N + h) \cos \phi \cos \ell \\ (N + h) \cos \phi \sin \ell \\ [N(1 - e^2) + h] \sin \phi \end{bmatrix} \quad (1.6-17)$$

The position in ECI coordinates is of the same form as (1.6-17), but with celestial longitude  $\lambda$  replacing terrestrial longitude  $\ell$ .

Geocentric coordinates are easily found from the Cartesian coordinates, but geodetic coordinates are more difficult to find. An exact formula exists but requires the solution of a quartic equation in  $\tan \phi$  (Vanicek and Krakiwsky, 1982). Therefore, an iterative algorithm is often used. Referring to Figure 1.6-3, we see that

$$\sin \phi = \frac{z}{N(1 - e^2) + h} \quad (1.6-18)$$

Using the large triangle with hypotenuse  $N + h$  and sides  $\sqrt{x^2 + y^2}$ ,  $[z + Ne^2 \sin \phi]$ , we can write

$$\tan \phi = \frac{[z + Ne^2 \sin \phi]}{\sqrt{x^2 + y^2}} \quad (1.6-19)$$

If (1.6-18) is substituted for  $\sin(\phi)$  in (1.6-19) and simplified, we obtain

$$\tan \phi = \frac{z}{(x^2 + y^2)^{\frac{1}{2}} [1 - Ne^2/(N + h)]}$$

Because  $N$  is a function of  $\phi$ , this formula is implicit in  $\phi$ , but it can be used in the following iterative algorithm for the geodetic coordinates:

$$\begin{aligned} \ell &= \text{atan2}(y, x) \\ h &= 0; \quad N = a \\ \rightarrow \quad \phi &= \tan^{-1} \left[ \frac{z}{(x^2 + y^2)^{1/2}} \left( 1 - \frac{e^2 N}{N + h} \right)^{-1} \right] \\ \uparrow \quad N &= \frac{a}{(1 - e^2 \sin^2 \phi)^{1/2}} \\ \uparrow \quad (h + N) &= \frac{(x^2 + y^2)^{1/2}}{\cos \phi} \\ \leftarrow \quad h &= (N + h) - N \end{aligned} \quad (1.6-20)$$

Latitudes of  $\pm 90^\circ$  must be dealt with as a special case, but elsewhere the iterations converge very rapidly, and accuracy of 10 to 12 decimal digits is easily obtainable. If the algorithm is modified to eliminate the inverse tangent function, convergence is badly affected.

In most practical applications the algorithm can be replaced by the approximation (1.6-16) to find  $h$ , with the geocentric radius of the spheroid found from geocentric latitude  $\psi$  and  $\psi$  found directly from the position vector. Single-precision arithmetic (seven decimal digits) is inadequate when the height above Earth is calculated from the small difference of large quantities (e.g.,  $N$  or  $a$ ). The geodetic latitude can be found from  $\phi = \psi + D$ , where the deviation of the normal,  $D$ , is found from  $\psi$



using (1.6-12) with the approximation  $h \ll N$ . These approximations can also be used to initialize the iterative algorithm above.

## Earth-Related Coordinate Transformations

The rotation from the ECI to the ECEF system is a plane rotation around the  $z$ -axis, and the rotation angle increases steadily as Earth rotates. The conventions chosen for the directions of the two systems (ECEF  $x$ -axis through Greenwich and ECI  $x$ -axis aligned with the line from the Sun to Earth's position in orbit at the vernal equinox) allow the rotation angle to be tabulated as a daily function of *Greenwich Mean Time* (*GMT*). The angle is known as the *Greenwich Hour Angle* (*GHA*, positive East) and tabulated in nautical almanacs published annually for use by navigators. Since the vernal equinox position originally aligned with the First Point of Aries, the angle is given the astronomical symbol for Aries,  $\varphi$ . Therefore, the rotation from ECI to ECEF can be written as

$$C_{ecef/eci} = \begin{bmatrix} c(\text{GHA}_{\varphi}) & s(\text{GHA}_{\varphi}) & 0 \\ -s(\text{GHA}_{\varphi}) & c(\text{GHA}_{\varphi}) & 0 \\ 0 & 0 & 1 \end{bmatrix} \quad (1.6-21)$$

When going from the ECEF to a local system, the convention is to perform the longitude rotation first. For example, consider the coordinate rotation from ECEF to NED. After rotating around the ECEF  $z$ -axis to the correct longitude, a left-handed rotation through  $90^\circ$ , around the  $y$ -axis, is needed to get the  $x$ -axis pointing north and the  $z$ -axis down. It is then only necessary to move to the correct latitude and fall into alignment with the NED system by means of an additional left-handed rotation around the  $y$ -axis, through the latitude angle. Therefore, the transformation is

$$\begin{aligned} C_{ned/ecef} &= \begin{bmatrix} c\phi & 0 & s\phi \\ 0 & 1 & 0 \\ -s\phi & 0 & c\phi \end{bmatrix} \begin{bmatrix} 0 & 0 & 1 \\ 0 & 1 & 0 \\ -1 & 0 & 0 \end{bmatrix} \begin{bmatrix} c\ell & s\ell & 0 \\ -s\ell & c\ell & 0 \\ 0 & 0 & 1 \end{bmatrix} \\ &= \begin{bmatrix} -s\phi c\ell & -s\phi s\ell & c\phi \\ -s\ell & c\ell & 0 \\ -c\phi c\ell & -c\phi s\ell & -s\phi \end{bmatrix} \end{aligned} \quad (1.6-22)$$

The rotation to a geocentric system is found similarly, except that geocentric latitude is used in place of geodetic. For example, a straight replacement of variables in Equation (1.6-22) gives

$$C_{c/eci} = \begin{bmatrix} -s\psi c\lambda & -s\psi s\lambda & c\psi \\ -s\lambda & c\lambda & 0 \\ -c\psi c\lambda & -c\psi s\lambda & -s\psi \end{bmatrix} \quad (1.6-23)$$

## Gravitation and Gravity

The term *gravitation* denotes a mass attraction effect, as distinct from *gravity*, meaning the combination of mass attraction and centrifugal force experienced by a body constrained to move with Earth's surface.

The WGS-84 datum includes an amazingly detailed model of Earth's gravitation. This model is in the form of a (scalar) potential function,  $V$ , such that components of specific mass attraction force along each of three axes can be found from the respective gradients of the potential function. The current potential function, for use with WGS-84, is *Earth Gravitational Model 1996* (EGM96). This has 130,676 coefficients and is intended for very precise satellite and missile calculations. The largest coefficient is two orders of magnitude bigger than the next coefficient and, if we retain only the largest coefficient, the result is still a very accurate model. Neglecting the other coefficients removes the dependence on terrestrial longitude, leaving the following potential function at point  $P(r, \psi)$ :

$$V(r, \psi) = \frac{GM}{r} \left[ 1 - \frac{1}{2} \left( \frac{a}{r} \right)^2 J_2 (3 \sin^2 \psi - 1) \right], \quad (1.6-24)$$

where  $r$  is the length of the geocentric position vector and  $\psi$  is the geocentric latitude. The Earth's *gravitational constant*,  $GM$ , is the product of Earth's mass and the *universal gravitational constant* of the inverse square law. Its EGM96 value, with the mass of the atmosphere included, was given in Equation (1.6-2b). The constant  $J_2$  is given by

$$J_2 = -\sqrt{5} \bar{C}_{2,0} = 1.082\,626\,684 \times 10^{-3}, \quad (1.6-25)$$

where  $\bar{C}_{2,0}$  is the actual EGM96 coefficient.

The gradients of the potential function are easily evaluated in geocentric coordinates. When this is done and the results are transformed into the ECEF system, we obtain the following gravitation model for the *gravitational acceleration*,  $\mathbf{G}$ :

$$\mathbf{G}^{ecef} = -\frac{GM}{r^2} \begin{bmatrix} \left[ 1 + \frac{3}{2} \left( \frac{a}{r} \right)^2 J_2 (1 - 5 \sin^2 \psi) \right] p_x / r \\ \left[ 1 + \frac{3}{2} \left( \frac{a}{r} \right)^2 J_2 (1 - 5 \sin^2 \psi) \right] p_y / r \\ \left[ 1 + \frac{3}{2} \left( \frac{a}{r} \right)^2 J_2 (3 - 5 \sin^2 \psi) \right] p_z / r \end{bmatrix}, \quad (1.6-26)$$

where the geocentric position vector is  $\mathbf{p}$ , with ECEF components  $p_x, p_y, p_z$  and length  $r$ , and the geocentric latitude is given by  $\sin \psi = p_z / r$ . This model is accurate to about  $30 \times 10^{-3}$  to  $35 \times 10^{-3}$  cm/s<sup>2</sup> rms, but local deviations can be quite large. Note that the  $x$ - and  $y$ -components are identical because there is no longitude dependence. The model can also be converted to geodetic coordinates using the relationships given earlier.

The weight of an object on Earth is determined by the gravitational attraction ( $m\mathbf{G}$ ) minus the mass times the centripetal acceleration needed to produce the circular motion in inertial space at geocentric position vector  $\mathbf{p}$ . Dividing the weight

of the object by its mass gives the *gravity vector*  $\mathbf{g}$ . Therefore, the vector equation for  $\mathbf{g}$  is

$$\mathbf{g} = \mathbf{G} - \boldsymbol{\omega}_{e/i} \times (\boldsymbol{\omega}_{e/i} \times \mathbf{p}) \quad (1.6-27)$$

As noted earlier, at Earth's surface  $\mathbf{g}$  is accurately normal to the geoid, points downward, and defines the local vertical. When Equation (1.6-26) is substituted for  $\mathbf{G}$  in (1.6-27) and the equation is resolved in the NED system, we find that  $\mathbf{g}$  is almost entirely along the down axis with a variable *north component* of only a few micro-gs. This is a modeling error, since deflection of the vertical is not explicitly included in the model. The *down component* of  $\mathbf{g}$  given by the model, at Earth's surface, varies sinusoidally from 9.780 m/s<sup>2</sup> at the equator to 9.806 m/s<sup>2</sup> at 45° geodetic latitude and 9.832 m/s<sup>2</sup> at the poles. Our simplified “flat-Earth” equations of motion will use a  $\mathbf{g}$  vector that has only a down component,  $\mathbf{g}_D$ , and is measured at Earth's surface. When a constant value of  $\mathbf{g}_D$  is to be used (e.g., in a simulation), the value at 45° latitude is taken as the standard value of gravity (actually defined to be 9.80665 m/s<sup>2</sup>).

### Gravitation and Accelerometers

The basic principle used in nearly all accelerometers is measurement, indirectly, of the force,  $\mathbf{F}$ , that must be applied (mechanically or by means of a magnetic or electrostatic field) to prevent a known “proof” mass from accelerating with respect to its instrument case when the case is being accelerated. Thus, apart from a small transient and/or steady-state error determined by the dynamics of the proof mass “rebalancing” servo and the type of acceleration signal, the acceleration of the proof mass is the same as the acceleration of the case. An accelerometer is usually a single-axis device, but here we will write vector equations for the acceleration experienced by the accelerometer. The gravitational field always acts on the proof mass,  $m$ , and so the acceleration,  $\mathbf{a}$ , of the proof mass is given by the vector sum:

$$\mathbf{a} = \frac{\mathbf{F}}{m} + \mathbf{G} \equiv \mathbf{f} + \mathbf{G},$$

where  $\mathbf{F}/m$  is the force per unit mass applied to the proof mass, called the *specific force*,  $\mathbf{f}$ . The accelerometer calibration procedure determines the *scale factor*,  $s$ , relating the output quantity to the specific force, and so the accelerometer equation is

$$\text{Accelerometer output} = s\mathbf{f} = s(\mathbf{a} - \mathbf{G}) \quad (1.6-28)$$

Equation (1.6-28) shows that an accelerometer is basically a specific force measuring device. When acceleration must be measured precisely (as in inertial navigation), an accurate model of  $\mathbf{G}$  (as a function of position) is essential. In other, lower precision applications the accelerometer “bias” of  $\mathbf{G}$  is not a limitation.

When an accelerometer's sensitive axis is horizontal, the bias is zero. When an accelerometer, with geocentric position vector  $\mathbf{p}$ , is stationary with respect to Earth,

its acceleration and specific force reading are given by

$$\begin{aligned}\mathbf{a} &= \boldsymbol{\omega}_{e/i} \times (\boldsymbol{\omega}_{e/i} \times \mathbf{p}) \\ \mathbf{f} &= \mathbf{a} - \mathbf{G} = -\mathbf{g}\end{aligned}\tag{1.6-29}$$

This specific force equation shows that the true force acting on the accelerometer has a magnitude equal to the accelerometer weight and is in the negative direction of the  $\mathbf{g}$  vector (i.e., the reaction of the surface on which the accelerometer is sitting). Single-axis accelerometers intended to be used with their sensitive axis vertical can be calibrated in “g-units,” using the standard gravity or the local gravity, so that the specific force reading is

$$\mathbf{f}_D^{ned} = -1 \text{ g-unit}$$

At a different position from the calibration location, the accelerometer could be corrected to the local gravity, but if acceleration is to be calculated accurately, a correction would have to be applied for the different (in general) centripetal acceleration. For accelerometers in motion over Earth, we must evaluate a transport acceleration to relate accelerometer acceleration to vehicle acceleration, as shown in Chapter 4 for the normal-acceleration control augmentation system.

## 1.7 RIGID-BODY DYNAMICS

In this section we finally put together the ideas and equations from the previous sections to obtain a set of state equations that describe the 6-DoF motion of a rigid aerospace vehicle (defined to be frame  $F_b$ ). We shall deal first with the angular motion of the vehicle in response to torques generated by aerodynamic, thrust, or any other forces, whose lines of action do not pass through the vehicle cm. By using the vehicle cm as a reference point, the rotational dynamics of the aircraft can be separated from the translational dynamics (Wells, 1967); we therefore use a body-fixed coordinate system,  $bf$ , with its origin at the cm to compute moments about the origin. A (nonzero) torque vector produces a rate of change of angular momentum vector, but then, to relate angular momentum to the mass distribution of a specific body, we must use the coordinate system  $bf$  and switch to matrix equations to obtain the components of the angular acceleration vector. Angular acceleration components integrate to angular velocity components, but then the three degrees of freedom in angular displacement are obtained from nonlinear equations such as the Euler equations (1.4-4). For an aircraft, the coordinate system  $bf$  is usually forward-right-down,  $frd$ , as described in Section 1.3.

The translational equations are more straightforward, the acceleration of the vehicle cm is obtained from the vector sum of the various forces, and their lines of action do not have to pass through the cm because the effect of any offset is incorporated into the moment equations. The equations are expressed in terms of motion relative to Earth and introduce the usual Coriolis and centripetal terms. Aerodynamic and thrust effects depend on motion relative to the surrounding atmosphere and so, when the

atmosphere is moving relative to Earth, we must introduce an auxiliary equation to compute the *relative wind*.

## Angular Motion

Here, we develop the equations for the rotational dynamics, which will be the same for both the flat-Earth and oblate-rotating-Earth equations of motion. The following definitions will be needed:

$F_i$  = an inertial reference frame

$F_b$  = the body of the rigid vehicle

$\mathbf{v}_{cm/i}$  = velocity of vehicle cm in  $F_i$

$\boldsymbol{\omega}_{b/i}$  = angular velocity of  $F_b$  with respect to  $F_i$

$\mathbf{M}$  = vector sum of all moments about the cm

The moment,  $\mathbf{M}$ , may be generated by aerodynamic effects, any propulsion-force components not acting through the cm, and attitude control devices.

Let the angular momentum vector of a rigid body in the inertial frame and taken about the cm be denoted by  $\mathbf{h}$ . It is shown in textbooks on classical mechanics (Goldstein, 1980) that the derivative of  $\mathbf{h}$  taken in the inertial frame is equal to the vector moment  $\mathbf{M}$  applied about the cm. Therefore, analogously to Newton's law for translational momentum, we write

$$\mathbf{M} = \dot{\mathbf{h}}_{cm/i} \quad (1.7-1)$$

The angular momentum vector can be found by considering an element of mass  $\delta m$  with position vector  $\mathbf{r}$  relative to the cm. Its translational momentum is given by

$$(\mathbf{v}_{cm/i} + \boldsymbol{\omega}_{b/i} \times \mathbf{r})\delta m$$

The angular momentum of this particle about the cm is the moment of the translational momentum about the cm, or

$$\delta \mathbf{h} = \mathbf{r} \times (\mathbf{v}_{cm/i} + \boldsymbol{\omega}_{b/i} \times \mathbf{r})\delta m$$

and for the whole body,

$$\mathbf{h}_{cm/i} = \iiint \mathbf{r} \times (\mathbf{v}_{cm/i} + \boldsymbol{\omega}_{b/i} \times \mathbf{r}) dm$$

In order to integrate this equation over the whole body, we must choose a coordinate system and, to avoid a time-varying integrand, the coordinate system must be fixed in the body. Let the position coordinates in body-fixed axes,  $bf$ , be

$$\mathbf{r}^{bf} = [x \ y \ z]^T$$

The corresponding matrix equation for  $\mathbf{h}$  is obtained by replacing the cross-products by  $\tilde{\mathbf{r}}$  and noting that  $\mathbf{v}$  and  $\boldsymbol{\omega}$  are constants for the purposes of integration. The first

term contains only integrals whose integrands have a position coordinate integrated  $dm$  and, by definition of the cm, they all integrate to zero. The second term is

$$\mathbf{h}_{cm/i}^{bf} = - \iiint \tilde{\mathbf{r}}(\tilde{\mathbf{r}}\boldsymbol{\omega}_{b/i}^{bf}) dm = - \iiint \tilde{\mathbf{r}}^2 dm \boldsymbol{\omega}_{b/i}^{bf}$$

giving

$$\mathbf{h}_{cm/i}^{bf} = \iiint \begin{bmatrix} (y^2 + z^2) & -xy & -xz \\ -xy & (x^2 + z^2) & -yz \\ -xz & -yz & (x^2 + y^2) \end{bmatrix} dm \boldsymbol{\omega}_{b/i}^{bf} \quad (1.7-2)$$

The result of this integration is a  $3 \times 3$  constant matrix that is defined to be the *inertia matrix*  $J^{bf}$  for the rigid body; it contains scalar *moments* and *cross-products of inertia*, for example:

$$\text{Moment of Inertia about } x\text{-axis} = J_{xx} = \int (y^2 + z^2) dm$$

$$\text{Cross-Product of Inertia } J_{xy} \equiv J_{yx} = \int xy dm$$

and so,

$$\mathbf{h}_{cm/i}^{bf} = \begin{bmatrix} J_{xx} & -J_{xy} & -J_{xz} \\ -J_{xy} & J_{yy} & -J_{yz} \\ -J_{xz} & -J_{yz} & J_{zz} \end{bmatrix} \boldsymbol{\omega}_{b/i}^{bf} \equiv J^{bf} \boldsymbol{\omega}_{b/i}^{bf} \quad (1.7-3)$$

It was necessary to choose a coordinate system to obtain this matrix and, consequently, it is not possible to obtain a vector equation of motion that is completely coordinate free. In more advanced treatments this paradox is avoided by the use of tensors. Note also that  $J$  is a real symmetric matrix and therefore has special properties that are discussed below. Various formulae and theorems are available for calculating  $J^{bf}$  for a composite body like an aircraft, and it can be estimated experimentally with the aircraft mounted on a turntable.

With the angular momentum expressed in terms of the inertia matrix and angular velocity vector of the complete rigid body, Equation (1.7-1) can be evaluated. Since the inertia matrix is known, and constant in the body frame, it will be convenient to replace the derivative in (1.7-1) by a derivative taken in the body frame:

$$\mathbf{M} = \dot{\mathbf{h}}_{cm/i} = \dot{\mathbf{h}}_{cm/i}^b + \boldsymbol{\omega}_{b/i} \times \mathbf{h}_{cm/i} \quad (1.7-4)$$

Now, differentiating (1.7-3) in  $F_b$ , with  $J$  constant, and taking body-fixed components, we obtain

$$\mathbf{M}^{bf} = J^{bf} \dot{\boldsymbol{\omega}}_{b/i}^{bf} + \tilde{\boldsymbol{\omega}}_{b/i}^{bf} J^{bf} \boldsymbol{\omega}_{b/i}^{bf}$$

A rearrangement of this equation gives the *state equation for angular velocity*:

$$\dot{\boldsymbol{\omega}}_{b/i}^{bf} = (J^{bf})^{-1} \left[ \mathbf{M}^{bf} - \tilde{\boldsymbol{\omega}}_{b/i}^{bf} J^{bf} \boldsymbol{\omega}_{b/i}^{bf} \right] \quad (1.7-5)$$

This state equation is widely used in simulation and analysis of rigid-body motion from satellites to ships. It can be solved numerically for the angular velocity given the inertia matrix and the torque vector, and its features will now be described.

The assumption that the inertia matrix is constant is not always completely true. For example, with aircraft the inertias will change slowly as fuel is transferred and burned. Also, the inertias will change abruptly if an aircraft is engaged in dropping stores. These effects can usually be adequately accounted for in a simulation by simply changing the inertias in (1.7-5) without accounting for their rates of change. As far as aircraft control system design is concerned, point designs are done for particular flight conditions, and interpolation between point designs can be used when the aircraft mass properties change. This is more likely to be done to deal with movement of the vehicle cm and the resultant effect on static stability (Chapter 2).

The inverse of the inertia matrix occurs in (1.7-5), and because of symmetry this has a relatively simple form:

$$J^{-1} = \frac{1}{\Delta} \begin{bmatrix} k_1 & k_2 & k_3 \\ k_2 & k_4 & k_5 \\ k_3 & k_5 & k_6 \end{bmatrix} \quad (1.7-6)$$

where

$$\begin{aligned} k_1 &= (J_{yy}J_{zz} - J_{yz}^2)/\Delta, & k_2 &= (J_{yz}J_{zx} + J_{xy}J_{zz})/\Delta \\ k_3 &= (J_{xy}J_{yz} + J_{zx}J_{yy})/\Delta, & k_4 &= (J_{zz}J_{xx} - J_{zx}^2)/\Delta \\ k_5 &= (J_{xy}J_{zx} + J_{yz}J_{xx})/\Delta, & k_6 &= (J_{xx}J_{yy} - J_{xy}^2)/\Delta \\ \Delta &= J_{xx}J_{yy}J_{zz} - 2J_{xy}J_{yz}J_{zx} - J_{xx}J_{yz}^2 - J_{yy}J_{zx}^2 - J_{zz}J_{xy}^2 \end{aligned}$$

A real symmetric matrix has real eigenvalues and, furthermore, a repeated eigenvalue of order  $p$  still has associated with it  $p$  linearly independent eigenvectors. Therefore, a similarity transformation can be found that reduces the matrix to a real diagonal form. In the case of the inertia matrix this means that we can find a set of coordinate axes in which the inertia matrix is diagonal. These axes are called the *principal axes*. The inverse of a diagonal matrix is also diagonal and the angular velocity state equation takes its simplest form, known as *Euler's equations of motion*.

At this point it is convenient to be more specific and choose the body-fixed axes to be *frd*, so that we can use standard aircraft yaw, pitch, and roll symbols:

$$M^{frd} = [\ell \ m \ n]^T, \quad \omega_{b/i}^{frd} = [P \ Q \ R]^T \quad (1.7-7)$$

Then Euler's equations of motion are

$$\begin{aligned} \dot{P} &= \frac{(J_y - J_z)QR}{J_x} + \frac{\ell}{J_x} \\ \dot{Q} &= \frac{(J_z - J_x)RP}{J_y} + \frac{m}{J_y} \\ \dot{R} &= \frac{(J_x - J_y)PQ}{J_z} + \frac{n}{J_z} \end{aligned} \quad (1.7-8)$$

and the double-subscript notation on the moments of inertia has been dropped. The equations involve cyclic permutation of the rate and inertia components; they are inherently coupled because angular rates about any two axes produce an angular acceleration about the third. This *inertia coupling* has important consequences for aircraft maneuvering rapidly at high angles of attack; we examine its effects in Chapter 4. The stability properties of the Euler equations are interesting and will be studied in Problem 1.7-3.

The angular velocity state equation is again simplified when applied to aircraft since for most aircraft the *frd*  $x$ - $z$  plane is a plane of symmetry. Under this condition, for every product  $y_i z_j$  or  $y_i x_j$  in an inertia computation there is a product that is identical in magnitude but opposite in sign. Therefore, only the  $J_{xz}$  cross-product of inertia is nonzero. A notable exception is an oblique-wing aircraft (Travassos et al., 1980), which does not have a plane of symmetry. Under the plane-of-symmetry assumption the inertia matrix and its inverse reduce to

$$J^{frd} = \begin{bmatrix} J_x & 0 & -J_{xz} \\ 0 & J_y & 0 \\ -J_{xz} & 0 & J_z \end{bmatrix}, \quad (J^{frd})^{-1} = \frac{1}{\Gamma} \begin{bmatrix} J_z & 0 & J_{xz} \\ 0 & \left( \frac{\Gamma}{J_y} \right) & 0 \\ J_{xz} & 0 & J_x \end{bmatrix} \quad (1.7-9)$$

$$\Gamma = J_x J_z - J_{xz}^2$$

If the angular velocity state equation (1.7-5) is expanded using the torque vector in (1.7-7) and the simple inertia matrix given by (1.7-9), the coupled, nonlinear angular acceleration equations are

$$\begin{aligned} \Gamma \dot{P} &= J_{xz}(J_x - J_y + J_z)PQ - [J_z(J_z - J_y) + J_{xz}^2]QR + J_{xz}\ell + J_{xz}n \\ J_y \dot{Q} &= (J_z - J_x)RP - J_{xz}(P^2 - R^2) + m \\ \Gamma \dot{R} &= -J_{xz}(J_x - J_y + J_z)QR + [J_x(J_x - J_y) + J_{xz}^2]PQ + J_{xz}\ell + J_x n \end{aligned} \quad (1.7-10)$$

In the analysis of angular motion we have so far neglected the angular momentum of any spinning rotors. Technically this violates the rigid-body assumption, but the resulting equations are valid. Note that, strictly, we require axial symmetry of the spinning rotors; otherwise the position of the vehicle cm will vary. This is not a restrictive requirement because it is also a requirement for dynamically balancing the rotors. The effects of the additional angular momentum may be quite significant. For example, a number of World War I aircraft had a single “rotary” engine that had a fixed crankshaft and rotating cylinders. The gyroscopic effects caused by the large angular momentum of the engine gave these aircraft tricky handling characteristics. In the case of a small jet with a single turbofan engine on the longitudinal axis, the effects are smaller. To represent the effect, a constant vector can be added to the



angular momentum vector in (1.7-3); therefore, let

$$\mathbf{h}_{cm/i}^{bf} = J_{bf}^{bf} \boldsymbol{\omega}_{b/i}^{bf} + \begin{bmatrix} h_x \\ h_y \\ h_z \end{bmatrix}_{\text{engines}} \quad (1.7-11a)$$

If this analysis is carried through, the effect is to add the following terms, respectively, to the right-hand sides of the three equations (1.7-10):

$$\begin{aligned} & J_z(Rh_y - Qh_z) + J_{xz}(Qh_x - Ph_y) \\ & - Rh_x + Ph_z \\ & J_{xz}(Rh_y - Qh_z) + J_x(Qh_x - Ph_y) \end{aligned} \quad (1.7-11b)$$

To complete the set of equations for angular motion, an attitude state equation is required. Here, with the flat-Earth equations in mind, we will assume that this will be the Euler kinematical equations (1.4-4). A direction cosine matrix can be computed from the Euler angles and will be needed in the translational equations. Thus, the translational equations will be coupled to the rotational equations. We now have all of the state equations for the angular motion dynamics, and we will turn our attention to the translational motion of the cm.

## Translational Motion of the Center of Mass

**Vector State Equations** We begin by applying Newton's second law to the motion of a constant-mass rigid body near the surface of Earth to find the inertial derivative of velocity under the influence of aerodynamic, propulsion, and mass attraction forces. We shall find state equations, in vector form at first, for position and velocity.

Some considerations for the choice of state variables are that the velocity vector can be chosen for convenience in either navigation over Earth or aerodynamic force and moment calculations on the body. The position vector can be taken from an arbitrary fixed point in the rigid-Earth frame,  $F_e$ . If the variation in gravity is significant over the trajectory, then the position vector should be taken from Earth's cm but will be over six million meters long. For short-range navigation it can more conveniently be taken from an initial point on the surface of Earth, but then latitude and longitude cannot easily be calculated. We will first derive equations for convenience in navigation using velocity of the vehicle cm in  $F_e$  and taking the position vector from Earth's cm.

Earth's cm is a fixed point common to both the inertial frame,  $F_i$ , and the Earth frame,  $F_e$ , so the derivative of a position vector from the cm will give either inertial velocity or Earth velocity, according to the frame in which the derivative is taken. Derivatives in  $F_i$  and  $F_e$  are related through Earth's angular velocity vector,  $\omega_{e/i}$ ,

according to the Coriolis equation. In addition to the above frames, the rigid-body frame  $F_b$  will be required. We also define the following scalars and vectors:

$m \equiv$  Vehicle (constant) mass

$O \equiv$  Earth cm

$\mathbf{p}_{cm/O} \equiv$  Vehicle cm position relative to  $O$

$\mathbf{v}_{cm/i} \equiv \dot{\mathbf{p}}_{cm/O}^i =$  Velocity of the cm in  $F_i$

$\mathbf{v}_{cm/e} \equiv \dot{\mathbf{p}}_{cm/O}^e =$  Velocity of the cm in  $F_e$

$\boldsymbol{\omega}_{x/y} \equiv$  Angular velocity of frame  $x$  with respect to frame  $y$

$\mathbf{F} \equiv$  Vector sum of forces at cm

$\mathbf{G} \equiv$  Earth's gravitation vector

$\mathbf{g} \equiv$  Earth's gravity vector,  $\mathbf{g} = \mathbf{G} - \boldsymbol{\omega}_{e/i} \times (\boldsymbol{\omega}_{e/i} \times \mathbf{p}_{cm/O})$

From the above explanation and definitions, the position and velocity state equations, in vector form, are

$$\begin{aligned} {}^e\dot{\mathbf{p}}_{cm/O} &= \mathbf{v}_{cm/e} \\ {}^e\dot{\mathbf{v}}_{cm/e} &= \mathbf{a}_{cm/e} \end{aligned} \quad (1.7-12)$$

To apply Newton's laws we use Equation (1.5-5), substitute  $(\frac{1}{m}\mathbf{F} + \mathbf{G})$  for the inertial acceleration, and solve for the relative acceleration (i.e., the derivative of the velocity state in  $F_e$ ):

$${}^e\dot{\mathbf{v}}_{cm/e} = \frac{1}{m}\mathbf{F} + \mathbf{G} - \boldsymbol{\omega}_{e/i} \times (\boldsymbol{\omega}_{e/i} \times \mathbf{p}_{cm/O}) - 2\boldsymbol{\omega}_{e/i} \times \mathbf{v}_{cm/e} \quad (1.7-13)$$

This velocity state equation together with the position state equation is suitable for accurate simulation of flight around the oblate, rotating Earth. Latitude and longitude and  $\mathbf{G}$  can be calculated from the geocentric position vector. The Coriolis term was examined in Section 1.5; a rule of thumb is to consider the Coriolis effect significant for speeds over about 2000 ft/s.

Finally, true airspeed is needed for calculating aerodynamic effects and propulsion system performance; therefore we define a relative velocity vector,  $\mathbf{v}_{rel}$ , by

$$\mathbf{v}_{rel} = \mathbf{v}_{cm/e} - \mathbf{v}_{w/e}, \quad (1.7-14)$$

where  $\mathbf{v}_{w/e}$  is the wind velocity taken in  $F_e$ . This is an auxiliary equation that will be needed with the state equations.

The full set of 6-DoF oblate, rotating-Earth matrix equations will be illustrated in Section 1.8, and we will now simplify the vector equations (1.7-12) and (1.7-13) to obtain the much more commonly used *flat-Earth equations*. If the  $\mathbf{g}$  vector can be considered to be independent of latitude and taken to be approximately constant or dependent only on height above Earth's surface, the position vector can be taken from

a point of interest,  $Q$ , on Earth's surface. The position vector then need no longer be six million meters long, but latitude and longitude cannot be calculated from it, and it will give only approximate distances over Earth's surface. If  $Q$  is the fixed point on Earth's surface, then the position state equation is

$${}^e\dot{\mathbf{p}}_{cm/Q} = \mathbf{v}_{cm/e} \quad (1.7-15)$$

As noted at the beginning of this subsection, the velocity state equation can alternatively be expressed in terms of a vector derivative taken in the vehicle body frame, and then when components are taken in a body-fixed coordinate system, we have a set of component derivatives that can be integrated to provide velocity components that determine aerodynamic effects. Changing derivatives in Equation (1.7-13) and substituting for  $\mathbf{g}$ , we have

$$\begin{aligned} {}^b\dot{\mathbf{v}}_{cm/e} + \boldsymbol{\omega}_{b/e} \times \mathbf{v}_{cm/e} &= {}^e\dot{\mathbf{v}}_{cm/e} = \frac{1}{m}\mathbf{F} + \mathbf{g} - 2\boldsymbol{\omega}_{e/i} \times \mathbf{v}_{cm/e} \\ {}^b\dot{\mathbf{v}}_{cm/e} &= \frac{1}{m}\mathbf{F} + \mathbf{g} - (\boldsymbol{\omega}_{b/e} + 2\boldsymbol{\omega}_{e/i}) \times \mathbf{v}_{cm/e} \end{aligned} \quad (1.7-16a)$$

Alternatively, using the additive property of angular velocity vectors,

$${}^b\dot{\mathbf{v}}_{cm/e} = \frac{1}{m}\mathbf{F} + \mathbf{g} - (\boldsymbol{\omega}_{b/i} + \boldsymbol{\omega}_{e/i}) \times \mathbf{v}_{cm/e} \quad (1.7-16b)$$

A further assumption is that Earth is an inertial reference frame; Earth's angular velocity can then be neglected, and  $\boldsymbol{\omega}_{b/i} \equiv \boldsymbol{\omega}_{b/e}$ , and Equations (1.7-16a) and (1.7-16b) both reduce to

$${}^b\dot{\mathbf{v}}_{cm/e} = \frac{1}{m}\mathbf{F} + \mathbf{g} - \boldsymbol{\omega}_{b/e} \times \mathbf{v}_{cm/e} \quad (1.7-16c)$$

These approximations are the basis of the flat-Earth equations of motion, described in the next section.

**The Flat-Earth Equations, Matrix Form** As explained above, the flat-Earth equations are not suitable for precise determination of position over Earth, but they are widely used in simulations to study aircraft performance and dynamic behavior and are used to derive linear state-space models for analytical studies and flight control system design. The assumptions for the flat-Earth equations will now be formally listed:

- (i) The Earth frame is an inertial reference frame.
- (ii) Position is measured in a tangent-plane coordinate system,  $tp$ .
- (iii) The gravity vector is normal to the tangent plane and constant in magnitude.

Some consequent assumptions are:

- (iv) Height above the tangent plane is a good approximation to true height above Earth's surface, and the horizontal projection of the position vector gives a good approximation to distance traveled over Earth's surface (this will be reasonable up to a few hundred miles from the tangent-plane origin).

- (v) The attitude of the vehicle in the tangent-plane coordinate system is a good approximation to true geographic attitude at the position of the vehicle.

Equation (1.7-16c) already incorporates the first flat-Earth assumption, and the position state variable is already referred to the tangent-plane origin; we must now make choices of coordinate systems for the variables in the state equations and make provisions to calculate a rotation matrix to convert from one system to another where necessary.

A *frd* coordinate system fixed in  $F_b$  is very convenient for the velocity vector derivative in  $F_b$ , for the aerodynamic and propulsion forces, and for the vehicle angular velocity vector (which uses body-axes components in the angular motion equations). This choice is less convenient for the  $\mathbf{g}$  vector and Earth angular velocity vector; these are known in Earth-fixed coordinate systems and must be rotated into the body axes using a vehicle-attitude DCM obtained from the attitude state equations. In the flat-Earth equations, the changing attitude of the vehicle is almost invariably adequately modeled with the simple Euler angle kinematical equations, (1.4-4). These relate a *frd* body-fixed system to a *ned* system, here the *ned* system is the *tangent-plane system*, *tp*, fixed in the Earth. The Euler angles can then be used to construct the  $C_{frd/tp}$  DCM, which must be done before the position and velocity state equations can be evaluated.

The set of 6-DoF state equations will be completed by the addition of the angular velocity state equation (1.7-5), with  $\boldsymbol{\omega}_{b/i} \equiv \boldsymbol{\omega}_{b/e}$  as the state variable. The state vector is now

$$\mathbf{X}^T = \left[ \left( \mathbf{p}_{cm/Q}^{tp} \right)^T \quad \boldsymbol{\Phi}^T \quad \left( \mathbf{v}_{cm/e}^{frd} \right)^T \quad \left( \boldsymbol{\omega}_{b/e}^{frd} \right)^T \right] \quad (1.7-17)$$

Using the current values of the state variables we evaluate the state derivatives as follows. The rotation matrix is calculated before the position and velocity state equations as noted above. Aerodynamic angle derivatives can be calculated from the translational velocity derivatives, and therefore the translational velocity state equation is placed ahead of the angular velocity state equation, where those derivatives are more significant (this is explained in detail in Chapter 2) and we have the following set of equations:

$$\begin{aligned} C_{frd/tp} &= fn(\Phi) \\ \dot{\Phi} &= H(\Phi) \boldsymbol{\omega}_{b/e}^{frd} \\ {}^e \dot{\mathbf{p}}_{cm/Q}^{tp} &= C_{tp/frd} \mathbf{v}_{cm/e}^{frd} \\ {}^b \dot{\mathbf{v}}_{cm/e}^{frd} &= \frac{1}{m} \mathbf{F}^{frd} + C_{frd/tp} \mathbf{g}^{tp} - \tilde{\boldsymbol{\omega}}_{b/e}^{frd} \mathbf{v}_{cm/e}^{frd} \\ {}^b \dot{\boldsymbol{\omega}}_{b/e}^{frd} &= (J^{frd})^{-1} \left[ \mathbf{M}^{frd} - \tilde{\boldsymbol{\omega}}_{b/e}^{frd} J^{frd} \boldsymbol{\omega}_{b/e}^{frd} \right] \end{aligned} \quad (1.7-18)$$

The 6-DoF flat-Earth equations contained in (1.7-18) are twelve (scalar) coupled, nonlinear, first-order differential equations and an auxiliary equation. Coupling exists

because angular acceleration integrates to angular velocity, which determines the Euler angle rates, which in turn determine the direction cosine matrix. The direction cosine matrix is involved in the state equations for position and velocity; position (the altitude component) and velocity determine aerodynamic effects which determine angular acceleration. Coupling is also present through the translational velocity. These interrelationships will become more apparent in Chapter 2.

To complete the flat-Earth assumptions,  $\mathbf{g}$  in tangent-plane coordinates will be

$$\mathbf{g}^{tp} = [0 \ 0 \ g_D]^T$$

with the down component,  $g_D$ , equal to the standard gravity ( $9.80665 \text{ m/s}^2$ ), or the local value. Aerodynamic calculations will require the equation for the velocity vector relative to the surrounding air [from Equation (1.7-14)]:

$$\mathbf{v}_{rel}^{frd} = \mathbf{v}_{cm/e}^{frd} - \mathbf{C}_{frd/tp} \mathbf{v}_{W/e}^{tp} \quad (1.7-19)$$

Some additional auxiliary equations will be needed to compute all of the aerodynamic effects, but these will be introduced in Chapter 2.

An interesting alternative to the translational velocity state equation in (1.7-18) can be derived by using relative velocity as the state variable. The vector form of the relative velocity equation is (1.7-14). If this equation is differentiated in the body-fixed frame and used to eliminate  $\mathbf{v}_{cm/e}$  and its derivative from the vector equation for the translational acceleration, we obtain

$${}^b\dot{\mathbf{v}}_{rel} = \frac{1}{m} \mathbf{F} + \mathbf{g} - \boldsymbol{\omega}_{b/e} \times \mathbf{v}_{rel} - (\boldsymbol{\omega}_{b/e} \times \mathbf{v}_{W/e} + {}^b\dot{\mathbf{v}}_{W/e})$$

The term in parentheses is the derivative of the wind velocity, taken in  $F_e$ , so we can write

$${}^b\dot{\mathbf{v}}_{rel} = \frac{1}{m} \mathbf{F} + \mathbf{g} - \boldsymbol{\omega}_{b/e} \times \mathbf{v}_{rel} - {}^e\dot{\mathbf{v}}_{W/e} \quad (1.7-20)$$

The last term on the right can be used as a way of introducing gust inputs into the model or can be set to zero for steady winds. Taking the latter course and introducing components in the body-fixed system give

$${}^b\dot{\mathbf{v}}_{rel}^{frd} = \frac{1}{m} \mathbf{F}^{frd} + \mathbf{C}_{frd/tp} \mathbf{g}^{tp} - \tilde{\boldsymbol{\omega}}_{b/e}^{frd} \mathbf{v}_{rel}^{frd} \quad (1.7-21)$$

This equation is an alternative to the velocity state equation in (1.7-18), and the position state equation therein must then be modified to use the sum of the relative and wind velocities.

The negative of  $\mathbf{v}_{rel}$  is the *relative wind*, which determines the aerodynamic forces and moments on the aerodynamic vehicle and hence its dynamic behavior. In Chapter 2 we will use Equation (1.7-21) to make a model that is suitable for studying the dynamic behavior. Chapter 2 shows how the flat-Earth equations can be “solved” analytically. Chapter 3 shows how they can be solved simultaneously by numerical integration for the purposes of flight simulation.

## 1.8 ADVANCED TOPICS

In this section we have derived two additional sets of kinematical equations for the attitude of a rotating body. The resulting attitude state equations have better numerical properties than the Euler angle state equations [Equations (1.4-4)]. The first set of kinematical equations relates the derivatives of the elements of a direction cosine matrix to the components of the associated angular velocity vector; we will refer to them as the *Poisson kinematical equations* (PKEs). They involve more mathematical operations than the Euler kinematical equations but are free from the singularity at  $90^\circ$  pitch attitude.

The second set of kinematical equations are based on quaternions, a complex number algebra invented by Sir William Rowan Hamilton in 1843 in an attempt to generalize ordinary complex numbers to three dimensions. We have derived many properties of quaternions, applied them to coordinate rotations, and related them to the direction cosine matrix and to Euler angles. Next, we have derived a set of quaternion state equations for the attitude of a rotating body. These quaternion state equations have additional numerical advantages over the PKE.

Finally, we have returned to the 6-DoF equations of motion for a rigid body moving around the oblate, rotating Earth, examined their properties, and explained how they are used. For this motion it is more appropriate to use the PKEs or the quaternion state equations to track the attitude of the rigid body.

### Poisson's Kinematical Equations

Consider, once again, the coordinate transformation,  $C_{bf/rf}$ , between systems fixed in a reference frame,  $\mathbf{F}_r$ , and in a rigid body,  $\mathbf{F}_b$ , when the body has an angular velocity vector  $\boldsymbol{\omega}_{b/r}$  with respect to the reference frame. Applying the transformation to the components of an arbitrary vector,  $\mathbf{u}$ , we have

$$\mathbf{u}^{bf} = C_{bf/rf}(t) \mathbf{u}^{rf}$$

A fixed unit vector in  $\mathbf{F}_r$  corresponds to a unit-length vector with time-varying components in  $\mathbf{F}_b$ . Let this be the vector  $\mathbf{c}_i$ , with components in  $\mathbf{F}_b$  given by the  $i$ th column of  $C_{bf/rf}$ . Now, applying the equation of Coriolis to the derivative of this vector in the two frames, we have

$$0 = {}^r\dot{\mathbf{c}}_i = {}^b\dot{\mathbf{c}}_i + \boldsymbol{\omega}_{b/r} \times \mathbf{c}_i, \quad i = 1, 2, 3$$

Take body-fixed coordinates:

$$0 = {}^b\dot{\mathbf{c}}_i^{bf} + \tilde{\boldsymbol{\omega}}_{b/r}^{bf} \mathbf{c}_i^{bf}, \quad i = 1, 2, 3$$

The term  ${}^b\dot{\mathbf{c}}_i^{bf}$  is the derivative of the  $i$ th column of  $C_{bf/rf}$ . If we combine the three equations into one matrix equation, the result is

$$\dot{C}_{bf/rf} = -\tilde{\boldsymbol{\omega}}_{b/r}^{bf} C_{bf/rf} \quad (1.8-1)$$

These equations are known as *Poisson's kinematical equations*, PKEs, or in inertial navigation as the *strapdown equation*. Whereas Equations (1.4-4) deal with the Euler angles, this equation deals directly with the elements of the rotation matrix. Compared to the Euler kinematical equations, the PKEs have the advantage of being singularity free and the disadvantage of a large amount of redundancy (nine scalar equations). When they are used in a simulation, the Euler angles are not directly available and must be calculated from the direction cosine matrix as in Equations (1.3-11).

## The Equation of Coriolis

In Section 1.4 the equation of Coriolis was derived using vectors; a matrix form can be derived with the use of the PKEs. Starting from a time-varying coordinate transformation of the components of a general vector  $\mathbf{u}$ ,

$$\mathbf{u}^{bf} = C_{bf/af} \mathbf{u}^{af},$$

with coordinate systems  $af$  and  $bf$  fixed in  $\mathbf{F}_a$  and  $\mathbf{F}_b$ , respectively, differentiate the arrays on both sides of the equation. Differentiating the arrays is equivalent to taking derivatives in their respective frames, with components taken in the systems fixed in the frames; therefore,

$${}^b\dot{\mathbf{u}}^{bf} = C_{bf/af} {}^a\dot{\mathbf{u}}^{af} + \dot{C}_{bf/af} \mathbf{u}^{af}$$

or

$${}^b\dot{\mathbf{u}}^{bf} = {}^a\dot{\mathbf{u}}^{bf} + \dot{C}_{bf/af} \mathbf{u}^{af}$$

Now use the Poisson equations to replace  $\dot{C}_{bf/af}$  (note that we used the equation of Coriolis to derive the Poisson equations, but they could have been derived in other ways),

$${}^b\dot{\mathbf{u}}^{bf} = {}^a\dot{\mathbf{u}}^{bf} - \tilde{\boldsymbol{\omega}}_{b/a}^{bf} C_{bf/af} \mathbf{u}^{af}$$

or

$${}^b\dot{\mathbf{u}}^{bf} = {}^a\dot{\mathbf{u}}^{bf} + \tilde{\boldsymbol{\omega}}_{a/b}^{bf} \mathbf{u}^{bf} \quad (1.8-2)$$

Equation (1.8-2) is the equation of Coriolis resolved in coordinate system  $bf$ .

## Quaternions

Quaternions are introduced here because of their “all-attitude” capability and numerical advantages in simulation and control. They are now widely used in simulation, robotics, guidance and navigation calculations, attitude control, and graphics animation. We will review enough of their properties to use them for coordinate rotation in the following subsections. W. R. Hamilton (1805–1865) introduced the quaternion form:

$$x_0 + x_1 i + x_2 j + x_3 k \quad (1.8-3a)$$

with the *imaginary operators* given by

$$i^2 = j^2 = k^2 = -1, \quad ij = k = -ji, \quad ki = j = -ik, \text{ etc.}$$

in an attempt to generalize complex numbers in a plane to three dimensions.

Quaternions obey the normal laws of algebra, except that multiplication is not commutative. Multiplication, indicated by “\*”, is defined by the associative law. For example, if,

$$r = p * q = (p_0 + p_1i + p_2j + p_3k) * (q_0 + q_1i + q_2j + q_3k)$$

then,

$$r = p_0q_0 + p_0q_1i + p_0q_2j + p_0q_3k + p_1q_0i + p_1q_1i^2 + \dots$$

By using the rules for  $i, j, k$ , products, and collecting terms, the answer can be written in various forms, for example,

$$\begin{bmatrix} r_0 \\ r_1 \\ r_2 \\ r_3 \end{bmatrix} = \begin{bmatrix} p_0 & -p_1 & -p_2 & -p_3 \\ p_1 & p_0 & -p_3 & p_2 \\ p_2 & p_3 & p_0 & -p_1 \\ p_3 & -p_2 & p_1 & p_0 \end{bmatrix} \begin{bmatrix} q_0 \\ q_1 \\ q_2 \\ q_3 \end{bmatrix}$$

Alternatively, by interpreting  $i, j, k$  as unit vectors, the quaternion (1.8-3a) can be treated as  $q_0 + \mathbf{q}$ , where  $\mathbf{q}$  is the quaternion vector part, with components  $q_1, q_2, q_3$  along,  $\mathbf{i}, \mathbf{j}, \mathbf{k}$ , respectively. We will write the quaternion as an array, formed from  $q_0$  and the vector components, thus:

$$p = \begin{bmatrix} p_0 \\ p_1 \\ p_2 \\ p_3 \end{bmatrix} \Rightarrow \begin{bmatrix} p_0 \\ \mathbf{p}^r \end{bmatrix}, \quad q = \begin{bmatrix} q_0 \\ q_1 \\ q_2 \\ q_3 \end{bmatrix} \Rightarrow \begin{bmatrix} q_0 \\ \mathbf{q}^r \end{bmatrix}, \quad (1.8-3b)$$

in which the components of the vectors are taken in a reference system  $r$ , to be chosen when the quaternion is applied. The above multiplication can be written as

$$p * q = \begin{bmatrix} p_0q_0 - (\mathbf{p} \cdot \mathbf{q})^r \\ (p_0\mathbf{q} + q_0\mathbf{p} + \mathbf{p} \times \mathbf{q})^r \end{bmatrix} \quad (1.8-4)$$

We will use (1.8-3b) and (1.8-4) as the definitions of quaternions and quaternion multiplication. Quaternion properties can now be derived using ordinary vector operations.



### Quaternion Properties

- (i) **Quaternion Noncommutativity:** Consider the following identity:

$$p * q - q * p = \begin{bmatrix} 0 \\ (\mathbf{p} \times \mathbf{q} - \mathbf{q} \times \mathbf{p})^r \end{bmatrix} = \begin{bmatrix} 0 \\ 2(\mathbf{p} \times \mathbf{q})^r \end{bmatrix}$$

It is apparent that, in general,

$$p * q \neq q * p$$

- (ii) **The Quaternion Norm:** The *norm* of a quaternion is defined to be the sum of the squares of its elements:

$$\text{norm}(q) = \sum_{i=0}^{i=3} q_i^2$$

- (iii) **Norm of a Product:** Using the definition of the norm and vector operations, it is straightforward to show (Problem 1.8-1) that the norm of a product is equal to the product of the individual norms:

$$\text{norm}(p * q) = \text{norm}(p) \text{norm}(q)$$

- (iv) **Associative Property over Multiplication:** The associative property,  $(p * q) * r = p * (q * r)$ , is proven in a straightforward manner.
- (v) **The Quaternion Inverse:** Consider the following product:

$$\begin{bmatrix} q_0 \\ \mathbf{q}^r \end{bmatrix} * \begin{bmatrix} q_0 \\ -\mathbf{q}^r \end{bmatrix} = \begin{bmatrix} q_0^2 + \mathbf{q} \cdot \mathbf{q} \\ (q_0 \mathbf{q} - q_0 \mathbf{q} - \mathbf{q} \times \mathbf{q})^r \end{bmatrix} = \begin{bmatrix} \sum q_i^2 \\ 0 \\ 0 \\ 0 \end{bmatrix}$$

We see that multiplying a quaternion by another quaternion, which differs only by a change in sign of the vector part, produces a quaternion with a scalar part only. A quaternion of the latter form will have very simple properties in multiplication (i.e., multiplication by a constant) and, when divided by the quaternion norm, will serve as the “identity quaternion.” Therefore, the inverse of a quaternion is defined by

$$q^{-1} = \begin{bmatrix} q_0 \\ \mathbf{q}^r \end{bmatrix}^{-1} = \frac{1}{\text{norm}(q)} \begin{bmatrix} q_0 \\ -\mathbf{q}^r \end{bmatrix} \quad (1.8-5)$$

However, we will work entirely with unit-norm quaternions, thus simplifying many expressions.

- (vi) **Inverse of a Product:** The inverse of a quaternion product is given by the product of the individual inverses in the reverse order. This can be seen as follows:

$$\begin{aligned}(p * q)^{-1} &= \frac{1}{\text{norm}(p * q)} \begin{bmatrix} p_0 q_0 - (\mathbf{p} \cdot \mathbf{q})^r \\ -(p_0 \mathbf{q} + q_0 \mathbf{p} + \mathbf{p} \times \mathbf{q})^r \end{bmatrix} \\ &= \frac{1}{\text{norm}(q)} \begin{bmatrix} q_0 \\ -\mathbf{q}^r \end{bmatrix} * \begin{bmatrix} p_0 \\ -\mathbf{p}^r \end{bmatrix} \frac{1}{\text{norm}(p)}\end{aligned}$$

Therefore,

$$(p * q)^{-1} = q^{-1} * p^{-1} \quad (1.8-6)$$

**Vector Rotation by Quaternions** A quaternion can be used to rotate a Euclidean vector in the same manner as the rotation formula, and the quaternion rotation is much simpler in form. The vector part of the quaternion is used to define the rotation axis and the scalar part to define the angle of rotation. The rotation axis is specified by its direction cosines in the reference coordinate system, and it is convenient to impose a unity norm constraint on the quaternion. Therefore, if the direction angles of the axis are  $\alpha, \beta, \gamma$  and a measure of the rotation angle is  $\delta$ , the rotation quaternion is written as

$$q = \begin{bmatrix} \cos \delta \\ \cos \alpha \sin \delta \\ \cos \beta \sin \delta \\ \cos \gamma \sin \delta \end{bmatrix} = \begin{bmatrix} \cos \delta \\ \sin \delta \mathbf{n}^r \end{bmatrix} \quad (1.8-7)$$

where  $\mathbf{n}$  is a unit vector along the rotation axis,

$$\mathbf{n}^r = [\cos \alpha \quad \cos \beta \quad \cos \gamma]^T$$

and

$$\text{norm}(q) = \cos^2 \delta + \sin^2 \delta (\cos^2 \alpha + \cos^2 \beta + \cos^2 \gamma) = 1$$

This formulation also guarantees that there is a unique quaternion for every value of  $\delta$  in the range  $\pm 180^\circ$ , thus encompassing all possible rotations.

Now consider the form of the transformation, which must involve multiplication. For compatibility of multiplication between vectors and quaternions, a Euclidean vector is written as a quaternion with a scalar part of zero; thus

$$u = \begin{bmatrix} 0 \\ \mathbf{u}^r \end{bmatrix}$$

The result of the rotation must also be a quaternion with a scalar part of zero, the transformation must be reversible by means of the quaternion inverse, and Euclidean length must be preserved. The transformation  $v = q * u$  obviously does not satisfy the first of these requirements. Therefore, we consider the transformations

$$v = q * u * q^{-1} \quad \text{or} \quad v = q^{-1} * u * q,$$

which are reversible by performing the inverse operations on  $v$ . The second of these transformations leads to the convention most commonly used:

$$v = q^{-1} * u * q = \left[ \begin{array}{c} q_0(\mathbf{q} \cdot \mathbf{u}) - (q_0\mathbf{u} - \mathbf{q} \times \mathbf{u}) \cdot \mathbf{q} \\ ((\mathbf{q} \cdot \mathbf{u})\mathbf{q} + q_0(q_0\mathbf{u} - \mathbf{q} \times \mathbf{u}) + (q_0\mathbf{u} - \mathbf{q} \times \mathbf{u}) \times \mathbf{q})^r \end{array} \right],$$

which reduces to

$$v = q^{-1} * u * q = \left[ \begin{array}{c} 0 \\ (2\mathbf{q}(\mathbf{q} \cdot \mathbf{u}) + (q_0^2 - \mathbf{q} \cdot \mathbf{q})\mathbf{u} - 2q_0(\mathbf{q} \times \mathbf{u}))^r \end{array} \right] \quad (1.8-8)$$

Therefore, this transformation meets the requirement of zero scalar part. Also, because of the properties of quaternion norms, the Euclidean length is preserved. For a match with the rotation formula, we require agreement between:

Rotation Formula	Quaternion Rotation
$(1 - \cos \mu)\mathbf{n}(\mathbf{n} \cdot \mathbf{u})$	$2 \sin^2 \delta \mathbf{n}(\mathbf{n} \cdot \mathbf{u})$
$\cos \mu \mathbf{u}$	$(\cos^2 \delta - \sin^2 \delta)\mathbf{u}$
$-\sin \mu (\mathbf{n} \times \mathbf{u})$	$-2 \cos \delta \sin \delta (\mathbf{n} \times \mathbf{u})$

The corresponding terms agree if  $\delta = \mu/2$  and half-angle trigonometric identities are applied. Therefore, the quaternion

$$q = \left[ \begin{array}{c} \cos(\mu/2) \\ \sin(\mu/2) \mathbf{n}^r \end{array} \right] \quad (1.8-9a)$$

and transformation

$$u = q^{-1} * u * q \quad (1.8-9b)$$

give a left-handed rotation of a vector  $\mathbf{u}$  through an angle  $\mu$  around  $\mathbf{n}$  when  $\mu$  is positive.

**Quaternion Coordinate Rotation** Refer to the quaternion rotation formulae (1.8-9) and take the viewpoint that positive  $\mu$  is a right-handed coordinate rotation rather than a left-handed rotation of a vector. We will define the quaternion that performs the coordinate rotation to system  $b$  from system  $a$  to be  $q_{b/a}$ ; therefore,

$$q_{b/a} = \left[ \begin{array}{c} \cos(\mu/2) \\ \sin(\mu/2) \mathbf{n}^r \end{array} \right] \quad (1.8-10a)$$

and the coordinate transformation is

$$u^b = q_{b/a}^{-1} * u^a * q_{b/a} \quad (1.8-10b)$$

Equation (1.8-10b) can take the place of the direction cosine matrix transformation (1.3-5), and the coordinate transformation is thus achieved by a single rotation around

an axis aligned with the quaternion vector part,  $\mathbf{n} \sin(\mu/2)$ . Euler's theorem shows that the same coordinate rotation can be achieved by a plane rotation around the unique axis corresponding to an eigenvector of the rotation matrix. Therefore, the vector  $\mathbf{n}$  must be parallel to this eigenvector, and so

$$\mathbf{n}^b = C_{b/a} \mathbf{n}^a = \mathbf{n}^a,$$

which shows that the quaternion vector part has the same components in system  $a$  or system  $b$ . In (1.8-10a) the reference coordinate system  $r$  may be either  $a$  or  $b$ . We will postpone, for the moment, the problem of finding the rotation quaternion without finding the direction cosine matrix and its eigenstructure and instead examine the properties of the quaternion transformation.

Performing the inverse transformation to (1.8-10b) shows that

$$q_{b/a}^{-1} = q_{a/b} \quad (1.8-11)$$

Also, for multiple transformations,

$$u^c = q_{c/b}^{-1} * q_{b/a}^{-1} * u^a * q_{b/a} * q_{c/b} \quad (1.8-12)$$

which, because of the associative property, means that we can also perform this transformation with the single quaternion given by

$$q_{c/a}^{-1} = q_{c/b}^{-1} * q_{b/a}^{-1} \quad (1.8-13a)$$

or

$$q_{c/a} = q_{b/a} * q_{c/b} \quad (1.8-13b)$$

The quaternion coordinate transformation (1.8-10b) actually involves more arithmetical operations than premultiplication of  $\mathbf{u}^a$  by the direction cosine matrix. However, when the coordinate transformation is evolving with time, the time update of the quaternion involves differential equations (following shortly) that are numerically preferable to the Euler kinematical equations and more efficient than the Poisson kinematical equations. In addition, the quaternion formulation avoids the singularity of the Euler equations and is easily renormalized (to reduce error accumulation).

**The Quaternion Kinematical Equations** With the goal of finding an expression for the derivative of a time-varying quaternion, and hence obtaining a state equation for vehicle attitude, we will derive an expression for an incremental increase  $q(t + \delta t)$  from an existing state  $q(t)$  in response to a nonzero angular velocity vector. Following the order of Equation (1.8-13b) for multiplication of two “forward” quaternions, we have

$$q(t + \delta t) = q(t) * \delta q(\delta t)$$

using

$$q(t) = \begin{bmatrix} \cos \frac{\mu}{2} \\ \mathbf{n}^r \sin \frac{\mu}{2} \end{bmatrix}, \quad \delta q(\delta t) \cong \begin{bmatrix} 1 \\ \mathbf{n}^r \frac{\delta \mu}{2} \end{bmatrix},$$

where  $\mu(t)$  is the rotation angle,  $\mathbf{n}$  the Euler axis, and  $r$  the reference coordinate system. The definition of a derivative gives

$$\dot{q} = \lim_{\delta t \rightarrow 0} \frac{q(t + \delta t) - q(t)}{\delta t} = \lim_{\delta t \rightarrow 0} \frac{q(t) * (\delta q - I_{(q)})}{\delta t} = \lim_{\delta t \rightarrow 0} q * \left[ \begin{array}{c} 0 \\ \frac{1}{2} \mathbf{n}^r \frac{\delta \mu}{\delta t} \end{array} \right],$$

where  $I_{(q)}$  is the identity quaternion. Now, take the indicated limit and recognize the angular velocity vector  $\boldsymbol{\omega}$  (as in Section 1.4) associated with the evolving quaternion,

$$\dot{q} = \frac{1}{2} q * \left[ \begin{array}{c} 0 \\ \mathbf{n}^r \frac{d\mu}{dt} \end{array} \right] = \frac{1}{2} q * \left[ \begin{array}{c} 0 \\ \boldsymbol{\omega}^r \end{array} \right]$$

Let this equation be associated with a coordinate rotation from *system a* to *system b*. Then, in terms of our notation, it is written as

$$\dot{q}_{b/a} = \frac{1}{2} q_{b/a} * \boldsymbol{\omega}_{b/a}^b \quad (1.8-14)$$

The above quaternion can also be written as the matrix equation

$$\dot{q}_{b/a} = \frac{1}{2} \begin{bmatrix} 0 & -(\boldsymbol{\omega}_{b/a}^b)^T \\ \boldsymbol{\omega}_{b/a}^b & -\tilde{\boldsymbol{\omega}}_{b/a}^b \end{bmatrix} \begin{bmatrix} q_0 \\ \mathbf{q}^b \end{bmatrix}$$

Writing this out in full using the body system components of  $\boldsymbol{\omega}_{b/a}$  gives

$$\begin{bmatrix} \dot{q}_0 \\ \dot{q}_1 \\ \dot{q}_2 \\ \dot{q}_3 \end{bmatrix} = \frac{1}{2} \begin{bmatrix} 0 & -P & -Q & -R \\ P & 0 & R & -Q \\ Q & -R & 0 & P \\ R & Q & -P & 0 \end{bmatrix} \begin{bmatrix} q_0 \\ q_1 \\ q_2 \\ q_3 \end{bmatrix} \equiv \frac{1}{2} \Omega q \quad (1.8-15)$$

These quaternion state equations (1.8-14) and (1.8-15) are widely used in simulation of rigid-body angular motion, and in discrete form they are used in digital attitude control systems (e.g., for satellites) and for inertial navigation digital processing. We will illustrate their use in 6-DoF simulation for tracking the attitude of a body in motion around the oblate, rotating Earth in the next section.

**Initializing a Quaternion** In simulation and control, we often choose to keep track of orientation with a quaternion and construct the direction cosine matrix and/or Euler angles from the quaternion as needed. It is easy to initialize the quaternion for a simple plane rotation since the Euler axis is evident. For a compound rotation (e.g., yaw, pitch, and roll combined) an eigenvector analysis of the DCM would be needed to formally determine the Euler axis and construct a quaternion. Fortunately, this is not necessary, for a specific rotation the Euler axis is unique and so the quaternion is unique. Therefore, if we construct the quaternion in some other manner, the rotation axis will be implicitly correct. We shall now give two examples of constructing a quaternion for a particular set of rotations.

**Example 1.8-1: Quaternion for a Yaw, Pitch, Roll Sequence** For the yaw, pitch, roll sequence described by (1.3-10) the quaternion formulation is

$$v^{frd} = q_\phi^{-1} * q_\theta^{-1} * q_\psi^{-1} * v^{ned} * q_\psi * q_\theta * q_\phi$$

The rotation axes for the individual quaternions are immediately evident:

$$q_\phi = \begin{bmatrix} \cos \frac{\phi}{2} \\ \sin \frac{\phi}{2} \\ 0 \\ 0 \end{bmatrix}, \quad q_\theta = \begin{bmatrix} \cos \frac{\theta}{2} \\ 0 \\ \sin \frac{\theta}{2} \\ 0 \end{bmatrix}, \quad q_\psi = \begin{bmatrix} \cos \frac{\psi}{2} \\ 0 \\ 0 \\ \sin \frac{\psi}{2} \end{bmatrix}$$

These transformations can be multiplied out, using quaternion multiplication, with only a minor amount of pain. The result is

$$q_{frd/ned} = q_\psi * q_\theta * q_\phi = \begin{bmatrix} \pm \left( \cos \frac{\phi}{2} \cos \frac{\theta}{2} \cos \frac{\psi}{2} + \sin \frac{\phi}{2} \sin \frac{\theta}{2} \sin \frac{\psi}{2} \right) \\ \pm \left( \sin \frac{\phi}{2} \cos \frac{\theta}{2} \cos \frac{\psi}{2} - \cos \frac{\phi}{2} \sin \frac{\theta}{2} \sin \frac{\psi}{2} \right) \\ \pm \left( \cos \frac{\phi}{2} \sin \frac{\theta}{2} \cos \frac{\psi}{2} + \sin \frac{\phi}{2} \cos \frac{\theta}{2} \sin \frac{\psi}{2} \right) \\ \pm \left( \cos \frac{\phi}{2} \cos \frac{\theta}{2} \sin \frac{\psi}{2} - \sin \frac{\phi}{2} \sin \frac{\theta}{2} \cos \frac{\psi}{2} \right) \end{bmatrix} \quad (1)$$

A plus or minus sign has been added to these equations because neither (1.8-10b) nor (1.8-15) is affected by the choice of sign. The same choice of sign must be used in all of Equations (1). ■

**Example 1.8-2: Quaternion for an ECEF-to-NED Rotation** The sequence of rotations required to arrive at an NED orientation, starting from the ECEF system is:

- (i) A right-handed rotation about the ECEF  $z$ -axis to a positive longitude,  $\ell$ .
- (ii) A left-handed rotation of  $(90 + \phi)$  degrees, around the new  $y$ -axis, to a positive geodetic latitude of  $\phi$ . (This is easily seen by letting  $\ell$  be zero.)

The quaternion description is

$$q_{ned/ecf} = q_\ell * q_{(-90-\phi)} = \begin{bmatrix} \cos \frac{\ell}{2} \\ 0 \\ 0 \\ \sin \frac{\ell}{2} \end{bmatrix} * \begin{bmatrix} \cos \left( \frac{\phi}{2} + 45^\circ \right) \\ 0 \\ -\sin \left( \frac{\phi}{2} + 45^\circ \right) \\ 0 \end{bmatrix}$$

Following the rules of quaternion multiplication, with a cross-product matrix used on the vector part, gives

$$q_{ned/ecf} = \begin{bmatrix} \cos \frac{\ell}{2} \cos \left( \frac{\phi}{2} + 45^\circ \right) \\ \sin \frac{\ell}{2} \sin \left( \frac{\phi}{2} + 45^\circ \right) \\ -\cos \frac{\ell}{2} \sin \left( \frac{\phi}{2} + 45^\circ \right) \\ \sin \frac{\ell}{2} \cos \left( \frac{\phi}{2} + 45^\circ \right) \end{bmatrix} \quad (1)$$

■

**Direction Cosine Matrix from Quaternion** If we write the quaternion rotation formula (1.8-8) in terms of array operations, using the vector part of the quaternion, we get

$$\mathbf{u}^b = \left[ 2\mathbf{q}^a(\mathbf{q}^a)^T + (q_0^2 - (\mathbf{q}^a)^T \mathbf{q}^a) \mathbf{I} - 2q_0 \tilde{\mathbf{q}}^a \right] \mathbf{u}^a \equiv C_{b/a} \mathbf{u}^a \quad (1.8-16)$$

The cross-product matrix  $\tilde{\mathbf{q}}^a$  is given by

$$\tilde{\mathbf{q}}^a = \begin{bmatrix} 0 & -q_3 & q_2 \\ q_3 & 0 & -q_1 \\ -q_2 & q_1 & 0 \end{bmatrix} \quad (1.8-17)$$

Now, evaluating the complete transformation matrix in (1.8-16), we find that

$$C_{b/a} = \begin{bmatrix} (q_0^2 + q_1^2 - q_2^2 - q_3^2) & 2(q_1q_2 + q_0q_3) & 2(q_1q_3 - q_0q_2) \\ 2(q_1q_2 - q_0q_3) & (q_0^2 - q_1^2 + q_2^2 - q_3^2) & 2(q_2q_3 + q_0q_1) \\ 2(q_1q_3 + q_0q_2) & 2(q_2q_3 - q_0q_1) & (q_0^2 - q_1^2 - q_2^2 + q_3^2) \end{bmatrix} \quad (1.8-18)$$

This expression for the rotation matrix, in terms of quaternion parameters, corresponds to Equations (1.8-10) and the single right-handed rotation around  $\mathbf{n}$  through the angle  $\mu$ . Equation (1.8-18) is independent of any choice of Euler angles. Depending on the coordinate rotation that it represents, we can determine a set of Euler angles as in Equation (1.3-11).

**Quaternion from Direction Cosine Matrix** The quaternion parameters can also be calculated from the elements  $\{c_{i,j}\}$  of the general direction cosine matrix. If terms on the main diagonal of (1.8-18) are combined, the following relationships are obtained:

$$\begin{aligned} 4q_0^2 &= 1 + c_{11} + c_{22} + c_{33} \\ 4q_1^2 &= 1 + c_{11} - c_{22} - c_{33} \\ 4q_2^2 &= 1 - c_{11} + c_{22} - c_{33} \\ 4q_3^2 &= 1 - c_{11} - c_{22} + c_{33} \end{aligned} \quad (1.8-19a)$$

These relationships give the magnitudes of the quaternion elements but not the signs. The off-diagonal terms in (1.8-18) yield the additional relationships

$$\begin{aligned} 4q_0q_1 &= c_{23} - c_{32}, & 4q_1q_2 &= c_{12} + c_{21} \\ 4q_0q_2 &= c_{31} - c_{13}, & 4q_2q_3 &= c_{23} + c_{32} \\ 4q_0q_3 &= c_{12} - c_{21}, & 4q_1q_3 &= c_{31} + c_{13} \end{aligned} \quad (1.8-19b)$$

From the first set of equations, (1.8-19a), the quaternion element with the largest magnitude (at least one of the four must be nonzero) can be selected. The sign associated with the square root can be chosen arbitrarily, and then this variable can be used as a divisor with (1.8-19b) to find the remaining quaternion elements. An interesting

quirk of this algorithm is that the quaternion may change sign if the algorithm is restarted with a new set of initial conditions. This will have no effect on the rotation matrix given in (1.8-18). Algorithms like this are discussed by Shoemaker (1985) and Shepperd (1978).

### The Oblate Rotating-Earth 6-DoF Equations

The starting point here will be the position and velocity state equations (1.7-12) and (1.7-13) and the angular velocity state equation (1.7-4):

$$\begin{aligned}\mathbf{e}\dot{\mathbf{p}}_{cm/O} &= \mathbf{v}_{cm/e} \\ \mathbf{e}\dot{\mathbf{v}}_{cm/e} &= \frac{1}{m}\mathbf{F} + \mathbf{G} - \boldsymbol{\omega}_{e/i} \times (\boldsymbol{\omega}_{e/i} \times \mathbf{p}_{cm/O}) - 2\boldsymbol{\omega}_{e/i} \times \mathbf{v}_{cm/e} \\ \mathbf{M} &= \mathbf{h}_{cm/i}^i = \mathbf{h}_{cm/i}^b + \boldsymbol{\omega}_{b/i} \times \mathbf{h}_{cm/i}\end{aligned}$$

This time, we will resolve the position and velocity equations on the coordinate axes of the ECEF system (abbreviated in the equations to *ecf*), instead of the tangent-plane system. The reference point, *O*, for the position vector will then be at Earth's cm, and latitude and longitude will then be easily calculated. The angular velocity equation must, as usual, be resolved in a body-fixed coordinate system in order to avoid a time-varying inertia matrix, and we will use the forward-right-down system, *frd*. A coordinate transformation will therefore be needed, and this time it will be obtained from a quaternion,  $q_{frd/ecf}$ . With these choices of coordinate systems the state vector, for the set of 6-DoF equations, will be

$$\mathbf{X} = \left[ q_{frd/ecf}, \mathbf{p}_{cm/O}^{ecf}, \mathbf{v}_{cm/e}^{ecf}, \boldsymbol{\omega}_{b/i}^{frd} \right]^T$$

Note that, here, the transpose designation is only meant to indicate that the element column arrays inside the brackets should be stacked into a single column.

The matrix state equations now follow from this choice of state vector as

$$\begin{aligned}\dot{q}_{frd/ecf} &= \frac{1}{2} q_{frd/ecf} * \left( \boldsymbol{\omega}_{b/i}^{frd} - \boldsymbol{\omega}_{e/i}^{frd} \right) \\ \mathbf{e}\dot{\mathbf{p}}_{cm/o}^{ecf} &= \mathbf{v}_{cm/e}^{ecf} \\ \mathbf{e}\dot{\mathbf{v}}_{cm/e}^{ecf} &= \frac{\mathbf{F}^{ecf}}{m} - 2\tilde{\boldsymbol{\omega}}_{e/i}^{ecf} \mathbf{v}_{cm/e}^{ecf} + \mathbf{g}^{ecf} \\ \mathbf{b}\dot{\boldsymbol{\omega}}_{b/i}^{frd} &= (\mathbf{J}^{frd})^{-1} \left( \mathbf{M}^{frd} - \tilde{\boldsymbol{\omega}}_{b/i}^{frd} \mathbf{J}^{frd} \boldsymbol{\omega}_{b/i}^{frd} \right)\end{aligned}\quad (1.8-20)$$

The following auxiliary equations must be executed first to compute Earth's angular velocity in body-fixed coordinates for the quaternion equation and the aerodynamic forces in Earth-fixed coordinates for the velocity state equation:

$$\begin{bmatrix} 0 \\ \boldsymbol{\omega}_{e/i}^{frd} \end{bmatrix} = q_{frd/ecf}^{-1} * \begin{bmatrix} 0 \\ \boldsymbol{\omega}_{e/i}^{ecf} \end{bmatrix} * q_{frd/ecf} \quad \begin{bmatrix} 0 \\ \frac{\mathbf{F}^{ecf}}{m} \end{bmatrix} = q_{frd/ecf} * \begin{bmatrix} 0 \\ \frac{\mathbf{F}^{frd}}{m} \end{bmatrix} * q_{ecf/frd}\quad (1.8-21)$$



The gravity term will be calculated from the centripetal acceleration and  $\mathbf{G}$  as a function of the geocentric position vector.

A short digression will be used here to bring out useful information contained in the velocity equation. We shall set the applied force,  $\mathbf{F}$ , to zero and look for a steady-state Earth orbit around the equator, i.e.,  $p_z \equiv 0$  (this is the only Great Circle possibility). Also, let the  $y$ -component of position,  $p_y$ , be zero, so that the vehicle is crossing the *ecf*  $x$ -axis (zero longitude), and set the  $y$  and  $z$  acceleration components to zero. The *ecf*  $x$ -acceleration component will be set to the centripetal acceleration for a circular orbit at geodetic height  $h$  above the WGS-84 spheroid,  $\dot{v}_x = -v_y^2/(a + h)$ . Therefore, the  $x$ -axis equation of motion will be

$$-v_y^2/(a + h) = 2\omega_z v_y - G_D + \omega_z^2(a + h),$$

where  $\omega_z$  is the  $z$ -component of  $\omega_{e/j}$ . When this quadratic equation is solved for the velocity, we obtain the *circular orbit condition*,

$$v_y = \sqrt{G_D(a + h)} - \omega_z(a + h) \quad (1.8-22)$$

The first term on the right-hand side is the inertial velocity component, and the second is the easterly component of Earth's velocity at the equator. The inertial term simply boils down to the centripetal acceleration condition  $v^2/r = G$ . Some idea of the numbers involved can be obtained by using the value of  $a$  given in Section 1.6 and the  $\mathbf{G}$  model given there and choosing a geodetic height. At 422 km above the spheroid the inertial component is 7.662 km/s. The International Space Station is stated to be in a nearly circular orbit, at an average height of 422 km above msl, and inclined at about  $55^\circ$  to the equatorial plane, and its orbital speed is stated to be 7.661 km/s (17,100 mph). The orbital velocity is quite insensitive to the orbit inclination and height, and most objects in low-Earth orbit (LEO) have about this velocity.

Returning to the 6-DoF equations, the relative wind, defined in Equation (1.7-14), could be computed for use in finding the aerodynamic forces and moments as

$$\begin{bmatrix} 0 \\ \mathbf{v}_{rel}^{frd} \end{bmatrix} = q_{frd/ecf}^{-1} * \begin{bmatrix} 0 \\ \mathbf{v}_{cm/e}^{ecf} - \mathbf{v}_{w/e}^{ecf} \end{bmatrix} * q_{frd/ecf} \quad (1.8-23)$$

The components of  $\mathbf{v}_{rel}^{frd}$  determine the aerodynamic angles and these, together with the magnitude of this velocity vector, determine the aerodynamic forces and moments on the vehicle. There would be practical difficulties in providing the wind information for a simulation, unless it could be neglected for high-speed, high-altitude flight or taken as piecewise constant over different segments of a flight. Onboard a real vehicle the situation would be reversed, in that the velocity over Earth would be known from the INS (Inertial Navigation System), and the major component of the relative wind would be known from the aircraft pitot-static air-data system, so that some estimate of atmospheric wind could be calculated.

Output equations that are likely to be needed with the 6-DoF equations are a calculation of vehicle attitude in a geographic coordinate system and calculation of geodetic position coordinates. Referring to Section 1.6, longitude is easily

calculated from the ECEF coordinates of the geocentric position vector in Equations (1.8-20),

$$\ell = \text{atan2}(p_y, p_x), \quad (1.8-24)$$

while geodetic latitude and height can be calculated from the approximations described in Section 1.6. The usual attitude reference for the vehicle is a geographic coordinate system (i.e., NED or ENU, and moving over the Earth with the vehicle) and the attitude is specified by the Euler angles of the vehicle body axes relative to the geographic system. We will choose the NED system, and the roll, pitch, and heading angles of the vehicle can be calculated as follows. First, calculate  $q_{ned/ecf}$  from latitude and longitude, as in Example 1.8-2. Then, using the quaternion state variable, we can calculate the quaternion  $q_{frd/ned}$ . This quaternion determines the DCM,  $C_{frd/ned}$ , and from this we can find the Euler angles, as in (1.3-11). The equations are

$$\begin{aligned} q_{frd/ned}^{-1} &= q_{frd/ecf}^{-1} * q_{ecf/ned}^{-1} \\ C_{frd/ned} &= fn(q_{frd/ned}) \\ \phi &= \text{atan2}(c_{23}, c_{33}) \\ \theta &= -\text{asin}(c_{13}) \\ \psi &= \text{atan2}(c_{12}, c_{11}) \end{aligned} \quad (1.8-25)$$

This completes the discussion of the oblate, rotating-Earth 6-DoF simulation equations, and the following simulation example will illustrate their use.

**Example 1.8-3: Simulation of Motion around Earth** Equations (1.8-20), (1.8-21), (1.8-24), and (1.8-25) were programmed as a subroutine, with the state and derivative vectors as its arguments. The programming is almost trivially easy in a language that handles matrix operations (e.g., Fortran-95; MATLAB<sup>TM</sup>). It is only necessary to write two additional routines, for quaternion multiplication and for the tilde matrix from vector elements. The “vehicle” was simply a “brick” with dimensions  $2 \times 5 \times 8$  units, and the coordinate origin was at the center of mass with the  $x$ -axis parallel to the eight-unit side and  $y$  parallel to the five-unit side. For this simulation no aerodynamic effects were modeled, and the applied torque and applied specific force components were set to zero. A simple driver program was written to use the fourth-order Runge-Kutta routine in Chapter 2 to integrate the equations and handle input and output operations. The initial-condition inputs were geodetic position (latitude, longitude, and altitude), Euler angles, velocity over Earth in  $frd$  coordinates, simulation run time, and integration time step. Note that, because the equations are in terms of velocity over Earth, no input of Earth’s inertial velocity components is required; inertial effects are accounted for with the Coriolis term in the state equation.

Much can be learned from running this simulation; the brick can be fired vertically to observe Coriolis effects, spun around its intermediate-inertia axis to observe its instability to small additional angular rate disturbances, or put into Earth orbit to study steady-state conditions, escape velocity, etc. Here, we have simulated an orbit starting from zero latitude and longitude and an altitude of  $10^5$  m. This low-altitude orbit

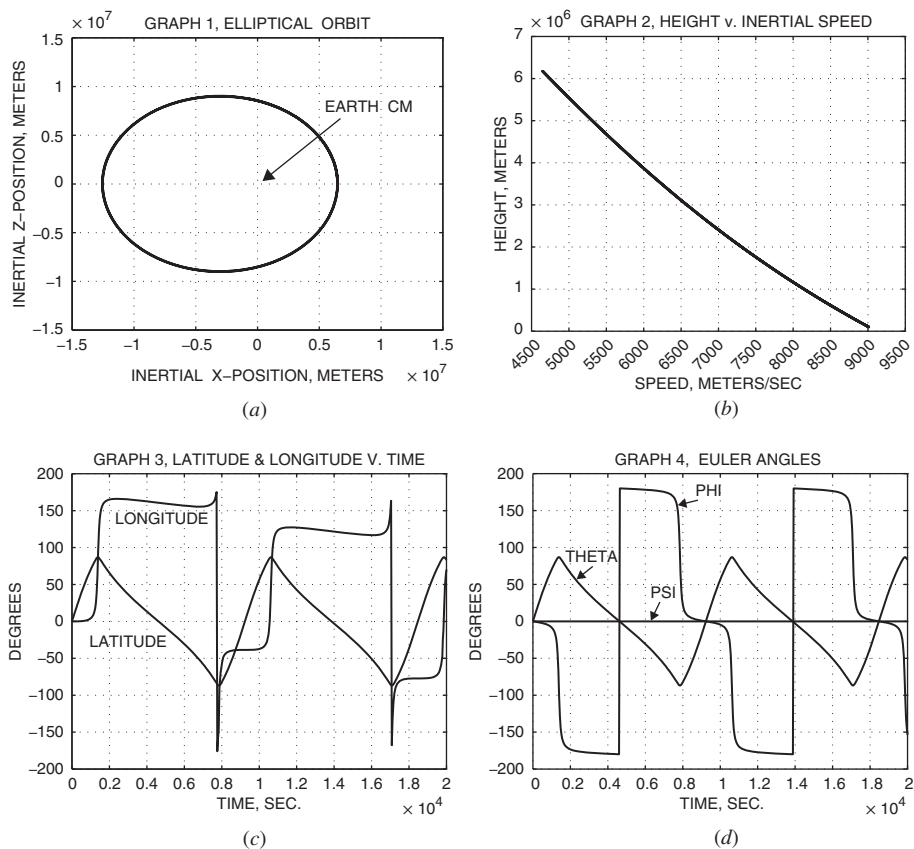


Figure 1.8-1

(below the usual “LEO” range) would show a rapid decay if atmospheric drag were modeled. The other initial conditions are a heading angle of zero degrees (aiming for the North Pole); zero pitch and roll, a forward component of velocity of 9.0 km/s (enough to give a moderately elliptical orbit), and zero initial angular rates. Integration step size is not critical; 0.01, 0.10, and 1.0 s step sizes give identical graphs (small step size would be needed for the spinning brick stability experiment).

Graph 1 shows a plot of the orbit in an inertial coordinate system initialized from the *ecf* system at  $t = 0$ . Earth’s cm is at the origin (a focus of the ellipse). Orbits that pass through high latitudes are significantly affected by the variation of Earth’s gravity with latitude, especially very low orbits such as this one. Thus, if the simulation is run for two or more orbits an inertial precession of the orbital plane will be observed.

Graph 2 shows height above the Spheroid versus the inertial speed, and this reaches minimum speed and maximum height at the Apogee (zero latitude, and 180° longitude).

Graph 3 shows latitude and longitude. The orbit will pass to the right of the North Pole because added to the initial Earth-velocity of 9 km/s North it has an initial inertial velocity of 465.1 m/s to the East, imparted at the Equator by the spin of the Earth. The orbital plane must contain the Earth's cm and so the orbit is tilted away from the poles, and the latitude never reaches  $\pm 90^\circ$ . Longitude will decrease steadily as the Earth rotates under the inertially fixed orbit. The rate of change of longitude is determined by the eastward component of the relative inertial velocity of the orbit and points on the Earth below, and the convergence of the Meridians near the Poles. Therefore, longitude changes very slowly at first, and then changes rapidly near  $90^\circ$  latitude. At the maximum negative latitude the longitude changes by  $180^\circ$ , in the same way as near the North Pole, but the change is disguised by the  $180^\circ$  ambiguity.

The Euler angle graphs show the attitude of the brick relative to a local NED system. The brick maintains a fixed inertial orientation as it circles Earth (initial rates were zero, and no torques were applied), and so the Euler angle variations are caused by changing orientation of the NED system as it follows the trajectory. The local NED system never reaches zero tilt with respect to the equatorial plane since the trajectory does not pass over the poles. Consequently, the pitch attitude angle of the brick never reaches  $90^\circ$  as the brick approaches the poles. The roll angle of the brick shows the expected  $180^\circ$  transitions, and the shape of these closely matches the shape of changes in the longitude graph. The heading angle remains unchanged, at zero. ■

In concluding this chapter, we note that practically all of the concepts introduced in the chapter are used in Example 1.8-3, and a number of significantly different orbits and initial condition combinations can be simulated, leading to graphical results that are quite demanding in their interpretation. Lack of space prevented the use of the simulation to illustrate properties of spinning bodies, which is also very instructive.

## REFERENCES

- Blakelock, J. H. *Automatic Control of Aircraft and Missiles*. New York: Wiley, 1965.
- Encyclopaedia Britannica*. 15th ed., vol. 17, *Macropaedia*. Chicago: Encyclopaedia Britannica, 1987, pp. 530–539.
- Goldstein, H. *Classical Mechanics*. 2d ed. Reading, Mass.: Addison-Wesley, 1980.
- Heiskanen, W. A., and H. Moritz. *Physical Geodesy*. San Francisco and London: W. H. Freeman, 1967.
- Kane, T. R., P. W. Likins, and D. A. Levinson. *Spacecraft Dynamics*. New York: McGraw-Hill, 1983.
- Kaplan, G. H. The IAU Resolutions on Astronomical Constants, Time Scales, and the Fundamental Reference Frame. Circular no. 163. United States Naval Observatory, Washington, D.C., December 10, 1981.
- Kuebler, W., and S. Sommers. "The Role of the Earth's Shape in Navigation: An Example." *Journal of the Institute of Navigation* 28, no. 1 (spring 1981): 29–33.
- McGill, D. J., and W. W. King. *An Introduction to Dynamics*. 3d ed. Boston: PWS Engineering, 1995.

- NIMA. "Department of Defense World Geodetic System 1984, Its Definition and Relationships with Local Geodetic Systems." Technical Report 8350.2. 3d ed. National Imagery and Mapping Agency, July 4, 1997 (Freely available by online download).
- Pestel, E. C., and W. T. Thompson. *Dynamics*. New York: McGraw-Hill, 1968.
- Shepperd, S. W. "Quaternion from Rotation Matrix." *AIAA Journal of Guidance and Control* 1, no. 3 (May–June 1978): 223–224.
- Shoemake, K. "Animating Rotation with Quaternion Curves." *Computer Graphics* 19, no. 3 (1985): 245–254.
- Strang, G. *Linear Algebra and Its Applications*. New York: Academic, 1980.
- Travassos, R. H., N. K. Gupta, K. W. Iliffe, and R. Maine. "Determination of an Oblique Wing Aircraft's Aerodynamic Characteristics." Paper no. 80-1630. *AIAA Atmospheric Flight Mechanics Conference*, 1980, p. 608.
- Vanicek, P., and E. J. Krakiwsky. *Geodesy: The Concepts*. Amsterdam: North-Holland, 1982.
- Wells, D. *Theory and Problems of Lagrangian Dynamics*. Schaum's Outline Series. New York: McGraw-Hill, 1967.
- Wilkinson, J. H., and G. Golub. "Ill Conditioned Eigensystems and the Computation of the Jordan Canonical Form." *SIAM Review* 18 (October 1976): 578–619.

## PROBLEMS

### Section 1.2

- 1.2-1** If vectors  $\mathbf{u}, \mathbf{v}, \mathbf{w}$ , from a common point, define the adjacent edges of a parallelepiped, show that  $\mathbf{u} \cdot (\mathbf{v} \times \mathbf{w})$  represents the signed volume of the parallelepiped.
- 1.2-2** Show that  $\mathbf{u} \times (\mathbf{v} \times \mathbf{w}) + \mathbf{v} \times (\mathbf{w} \times \mathbf{u}) + \mathbf{w} \times (\mathbf{u} \times \mathbf{v}) = \mathbf{0}$ .
- 1.2-3** Two particles moving with constant velocity are described by the position vectors

$$\mathbf{p} = \mathbf{p}_0 + \mathbf{v}t, \quad \mathbf{s} = \mathbf{s}_0 + \mathbf{w}t$$

- (a) Show that the shortest distance between their trajectories is given by

$$d = |(\mathbf{s}_0 - \mathbf{p}_0) \cdot (\mathbf{w} \times \mathbf{v})| / |\mathbf{w} \times \mathbf{v}|$$

- (b) Find the shortest distance between the particles themselves.

- 1.2-4** Derive the vector expressions shown in Figure 1.2-1.

### Section 1.3

- 1.3-1** Derive the cross-product matrix used in Equation (1.3-3).
- 1.3-2** Start with an airplane heading north in level flight and draw two sequences of pictures to illustrate the difference between a yaw, pitch, roll sequence and a roll, yaw, pitch sequence. Let the rotations (Euler angles) be yaw  $\psi = -90^\circ$ , pitch  $\theta = -45^\circ$ , and roll  $\phi = 45^\circ$ . State the final orientation.

- 1.3-3** Find the rotation matrix corresponding to (1.3-10) but for a heading, roll, pitch sequence. Find the formulae for the Euler angles and specify their ranges.
- 1.3-4** For the rotation in Equation (1.3-10), with heading, pitch, and roll angles all equal to  $-90^\circ$ , find, by hand:
- (a) The eigenvalues
  - (b) The eigenvector for the +1 eigenvalue
  - (c) The direction of the Euler axis in terms of an azimuth and an elevation angle
  - (d) The equivalent rotation around the Euler axis (by physical experiment)
- 1.3-5** Show that the rotation matrix between two coordinate systems can be calculated from a knowledge of the position vectors of two different objects if the position vectors are known in each system.
- (a) Specify the rotation matrix in terms of the solution of a matrix equation.
  - (b) Show how the matrix equation can be solved for the rotation matrix.

## Section 1.4

- 1.4-1** Prove that the derivative of the angular velocity vector of a frame  $F_b$  relative to frame  $F_a$  is the same when taken in either  $F_a$  or  $F_b$ .
- 1.4-2** Prove that the centripetal acceleration vector is always orthogonal to the angular velocity vector.
- 1.4-3** Find the Euler angle rates as in Equation (1.4-4) but for the rotation sequence heading, roll, pitch.

## Section 1.5

- 1.5-1** Start from the vector equation (1.5-6).
- (a) Obtain the matrix equation for the NED coordinates of the vectors. Assume that  $\mathbf{g}$  has a *down component* only.
  - (b) Neglecting North motion, and the *y-dot* contribution to vertical acceleration, integrate the equations to obtain the *y* and *z* displacement equations (include initial condition terms with the indefinite integrals).
  - (c) Compare the Coriolis deflections of a mass reaching the ground for the following two cases: (i) thrown vertically upward with initial velocity  $u$ ; (ii) dropped, with zero initial velocity, from the maximum height reached in (i).

## Section 1.6

- 1.6-1** Starting from a calculus textbook definition of radius of curvature and the equation of an ellipse, derive the formula (1.6-5) for the meridian radius of curvature.

- 1.6-2** Derive the formulae (1.6-13) and hence the formula (1.6-14) for geocentric latitude in terms of geodetic latitude by using the geometry of the generating ellipse.
- 1.6-3** Derive the formula (1.6-26) for  $\mathbf{G}$  starting from the potential function  $V$  in Equation (1.6-24). Use a geocentric coordinate system as mentioned in the text.
- 1.6-4** Starting from (1.6-26), write and test a program to evaluate  $|\mathbf{g}|$  and  $|\mathbf{G}|$  as functions of geodetic latitude and altitude. Plot them both on the same axes against latitude ( $0 \rightarrow 90^\circ$ ). Do this for  $h = 0$  and 30,000 m.
- 1.6-5** Derive the conditions for a body to remain in a geostationary orbit of Earth. Use the gravity model and geodetic data to determine the geostationary altitude. What are the constraints on the latitude and inclination of the orbit?

## Section 1.7

- 1.7-1** An aircraft is to be mounted on a platform with a torsional suspension so that its moment of inertia,  $I_{zz}$ , can be determined. Treat the wings as one piece equal to one-third of the aircraft weight and placed on the fuselage one-third back from the nose.
- Find the distance of the aircraft cm from the nose as a fraction of the fuselage length.
  - The aircraft weight is 80,000 lb, the wing planform is a rectangle 40 ft by 16 ft, and the planview of the fuselage is a rectangle 50 ft by 12 ft. Assuming uniform density, calculate the aircraft moment of inertia (in slug-ft<sup>2</sup>).
  - Calculate the period of oscillation (in seconds) of the platform if the torsional spring constant is 10,000 lb-ft/rad.
- 1.7-2** Use Euler's equations of motion (1.7-8) and the Euler kinematical equations (1.4-4) to simulate the angular motion of a brick tossed in the air and spinning. Write a MATLAB program using Euler integration (1.1-4) to integrate these equations over a 300-s interval using an integration step of 10 ms. Add logic to the program to restrict the Euler angles to the ranges described in Section 1.3. Let the brick have dimensions  $8 \times 5 \times 2$  units, corresponding to  $x, y, z$  axes at the center of mass. The moments  $\ell, m, n$  are all zero, and the initial conditions are:
- $\phi = \theta = \psi = 0, \quad P = 0.1, \quad Q = 0, \quad R = 0.001 \text{ rad/s}$
  - $\phi = \theta = \psi = 0, \quad P = 0.001, \quad Q = 0, \quad R = 0.1 \text{ rad/s}$
  - $\phi = \theta = \psi = 0, \quad P = 0.0, \quad Q = 0.1, \quad R = 0.001 \text{ rad/s}$
- Plot the three angular rates (deg/s) on one graph, and the three Euler angles (in deg) on another. Which motion is stable and why?
- 1.7-3** Derive a set of linear state equations from Equations (1.7-8) by considering perturbations from a steady-state condition with angular rates  $P_e, Q_e,$  and  $R_e$ .

Find expressions for the eigenvalues of the coefficient matrix when only one angular rate is nonzero and show that there is an unstable eigenvalue if the moment of inertia about this axis is either the largest or the smallest of the three inertias. Deduce any practical consequences of this result.

- 1.7-4** The propeller and crankshaft of a single-engine aircraft have a combined moment of inertia of  $45 \text{ slug-ft}^2$  about the axis of rotation and are rotating at 1500 rpm clockwise when viewed from in front. The moments of inertia of the aircraft are roll:  $3000 \text{ slug-ft}^2$ , pitch:  $6700 \text{ slug-ft}^2$ , yaw:  $9000 \text{ slug-ft}^2$ . If the aircraft rolls at  $100 \text{ deg/s}$ , while pitching at  $20 \text{ deg/s}$ , determine the angular acceleration in yaw. All inertias and angular rates are body-axes components.
- 1.7-5** Analyze the height and distance errors of the flat-Earth equations.

## Section 1.8

- 1.8-1** Show that, for a quaternion product, the norm of the product is equal to the product of the individual norms.
- 1.8-2** Compare the operation count (+, −, ×, ÷) of the vector rotation formula (1.2-5b) with that of the quaternion formula (1.8-9b).
- 1.8-3** If a coordinate system  $b$  is rotating at a constant rate with respect to a system  $a$  and only the components of the angular velocity vector in system  $b$  are given, find an expression for the quaternion that transforms coordinates from  $b$  to  $a$ .
- 1.8-4** (a) Write a subroutine or an M-file for the Round the Earth 6-DoF equations of motion as described in Example 1.8-3.  
 (b) Write a driver program to use these 6-DoF equations and reproduce the results of Example 1.8-3.



## CHAPTER 2

---

# MODELING THE AIRCRAFT

---

### 2.1 INTRODUCTION

Model building is a fundamental process. An aircraft designer has a mental model of the type of aircraft that is needed, uses physical models to gather wind tunnel data, and designs with mathematical models that incorporate the experimental data. The modeling process is often iterative; a mathematical model based on the laws of physics will suggest what experimental data should be taken, and the model may then undergo considerable refinement in order to fit the data. In building the mathematical model we recognize the onset of the law of diminishing returns and build a model that is good enough for our purposes but has known limitations. Some of these limitations involve uncertainty in the values of parameters. Later we attempt to characterize this uncertainty mathematically and allow for it in control system design.

Actually, because of the high cost of building and flight testing a real aircraft, the importance of the mathematical models goes far beyond design. The mathematical model is used, in conjunction with computer simulation, to evaluate the performance of the prototype aircraft and hence improve the design. It can also be used to drive training simulators, to reconstruct the flight conditions involved in accidents, and to study the effects of modifications to the design. Furthermore, mathematical models are used in all aspects of the aircraft design (e.g., structural models for studying stress distribution and predicting fatigue life).

All of the chapters following this one will make use of the mathematical models presented in this chapter in some form and thus demonstrate the importance of modeling in the design of aircraft control systems. The rigid-body equations of motion that were derived in Chapter 1 form the skeleton of the aircraft model. In this chapter we add some muscles to the skeleton by modeling the aerodynamic forces and moments

that drive the equations. By the end of the chapter we will have the capability, given the basic aerodynamic data, to build mathematical models that can be used for computer simulation or for control systems design. We start by considering some basic elements of aerodynamics.

## 2.2 BASIC AERODYNAMICS

In the aerospace industry it is necessary for a wide range of specialists to work together; thus flight control engineers must be able to work with the aerodynamicists as well as with structural and propulsion engineers. Each must have some understanding of the terms and mathematical models used by the other. This is becoming increasingly important as designers seek to widen aircraft performance envelopes by integrating the many parts of the whole design process. Furthermore, at the prototype stage the controls designer must work closely with the test pilots to make the final adjustments to the control systems. This may take many hours of simulator time and flight testing.

### Airfoil Section Aerodynamics

The mathematical model used by the control engineer will usually contain aerodynamic data for the aircraft as a whole. However, to gain the necessary insight, we start by examining the aerodynamic forces on an airfoil.

Figure 2.2-1 shows the cross section of an airfoil (a theoretical body of infinite length shaped to produce lift when placed in an airflow) and defines some of the terms used. The flowfield around the airfoil is represented by the *streamlines* shown in the figure (for a steady flow, the flow direction at any point is tangential to the streamline passing through that point). The figure illustrates attached flow, that is, the streamlines follow the surface of the airfoil and do not reverse direction anywhere over the surface. This is a two-dimensional situation; the cross section is constant and the length of this airfoil is infinite, so that the flowfield does not change in the direction perpendicular to the plane of the diagram. The initial direction of the flowfield is defined

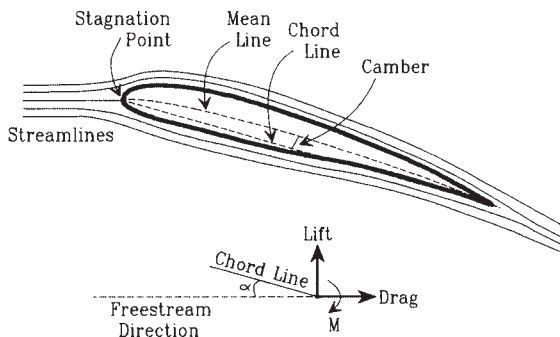


**Figure 2.2-1** Definitions associated with an airfoil.

by the freestream velocity vector. This is the velocity measured ahead of the airfoil at a sufficient distance that the flow there is unaffected by the presence of the airfoil.

The shape of the airfoil determines its aerodynamic properties, and some of the important geometrical parameters are shown in the figure. The *chord line* is a straight line drawn from the leading edge to the trailing edge and is the reference line for describing the shape. An airfoil may be symmetric or, more usually, asymmetric with respect to the chord line. The *mean line* (or *camber line*) is a line joining the leading edge to the trailing edge and having a desired shape. The airfoil is constructed on this camber line by drawing perpendiculars and placing the upper and lower surfaces equal distances above and below the camber line according to a chosen distribution of airfoil thickness. The shape of the camber line, the thickness distribution, and the leading-edge radius combine to determine the aerodynamic properties and the useful speed range.

Two different physical mechanisms contribute to producing an aerodynamic force. First, each element of surface area, multiplied by the pressure at that position, leads to an elemental force normal to the airfoil surface. When this calculation is integrated over the whole surface, the resultant force is, in general, nonzero, except, for example, in the idealized case of laminar flow around a symmetrical airfoil pointed directly into the flow. Second, for each element of surface area there is a layer of the fluid (air) in contact with the surface and not moving relative to the surface. When the flow is laminar, we can visualize layers of fluid farther from the surface moving progressively faster, and the molecular forces between layers, per unit area, constitute the *shear stress*. Shear stress multiplied by the element of area leads to an elemental force tangential to the surface. When the shear forces are integrated over the whole surface, the resultant force is defined to be the *skin friction*. The skin friction force will be proportional to the *wetted area* (area in contact with the fluid) of the airfoil. When the flow is *turbulent* (i.e., the motion at any point is irregular and eddies are formed) over some or all of the airfoil surface, the physical mechanism is harder to visualize but we still define a skin friction force, although the mathematical model is different. The combination of the pressure force and the skin friction force is the resultant aerodynamic force on the airfoil.

Now imagine that the airfoil is pivoted about an axis perpendicular to the cross section, passing through the chord line at an arbitrary distance back from the leading edge. The angle that the chord line makes with the freestream velocity vector is the airfoil *angle of attack*, usually denoted by  $\alpha$  (hereinafter referred to as “alpha”) and shown as a positive quantity in the figure. In our hypothetical experiment, let the freestream velocity vector be constant in magnitude and direction and the ambient temperature and pressure be constant. In this situation, the only remaining variable that influences the aerodynamic forces is alpha. Also, elementary mechanics tells us that in this situation the aerodynamic effects can be represented by a force acting at the axis and normal to it (because of symmetry) and a couple acting around the axis.

The aerodynamic force is conventionally resolved into two perpendicular components, the *lift* and *drag* components, shown in the figure. Lift is defined to be perpendicular to the freestream velocity vector, and drag is parallel to it. Lift and

drag normally increase as  $\alpha$  is increased. An aerodynamic moment is also indicated in the figure, and the positive reference direction is shown there. By definition, the moment is zero when the axis is chosen to pass through the center of pressure (cp) of the airfoil (i.e., the cp is the point through which the total force can be thought to be acting). This is not a particularly convenient location for the axis since experiments show that the location of the cp changes significantly with  $\alpha$ . There is another special location for the axis: the *aerodynamic center* (ac) of the airfoil. The ac is a point at which the aerodynamic moment tends to be invariant with respect to  $\alpha$  (within some range of  $\alpha$ ). It is normally close to the chord line, about one quarter-chord back from the leading edge, and moves back to the half-chord position at supersonic speeds. As  $\alpha$  is varied through positive and negative values, the cp moves in such a way that the moment about the ac remains constant. For the cambered airfoil shown in Figure 2.2-1, the moment about the ac will be a nose-down (negative) moment, as shown in Figure 2.2-2, curve 1.

The aerodynamic center is important when we come to consider the stability of the airfoil in an airflow. It is obvious (by *reductio ad absurdum*) that if we move the pivot axis forward of the ac we will measure a negative pitching moment that becomes more negative as  $\alpha$  is increased. This is shown in curve 2 of Figure 2.2-2; point  $B$  on this curve is the angle of attack where the pitching moment becomes zero. If we attempt to increase  $\alpha$  away from point  $B$ , a negative pitching moment is generated; conversely, decreasing  $\alpha$  generates a positive moment. These are restoring moments that tend to hold  $\alpha$  at the value  $B$ . Therefore, neglecting any moment due to its weight, the airfoil will settle into a *stable equilibrium* condition at point  $B$  when allowed to pivot freely about a point forward of the aerodynamic center.

When the axis is at the aerodynamic center, as in curve 1 of the figure, there is a stable equilibrium at point  $A$ . This point is at a large negative value of  $\alpha$  outside the normal range of operation. When we place the pivot axis behind the ac, as in curve 3, the pitching moment increases with  $\alpha$ . There is an equilibrium condition

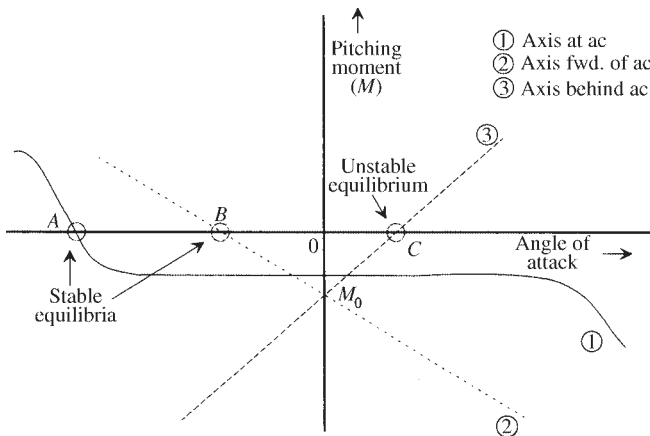


Figure 2.2-2 Airfoil moment about different axes.

at point  $C$ , but this is an *unstable equilibrium* because any small perturbation in  $\alpha$  creates a moment that drives the angle of attack out of this region. With the sign conventions we have chosen, we see that a stable equilibrium is associated with a negative slope to the pitching moment curve and unstable equilibrium with a positive slope. If the airfoil had to support the weight of an aircraft, a stable equilibrium point would normally have to occur at a positive angle of attack. This would require curve 2 to be shifted upward (i.e.,  $M_0$  positive); in practice, the horizontal tail of the aircraft provides the additional positive pitching moment required.

The stability of this hypothetical experiment has been analyzed by considering the *static* balance of the pitching moment and the effect of small perturbations. The condition of a steady-state moment tending to restore equilibrium is known as *positive stiffness* and, in this case, positive pitch stiffness is associated with a *negative slope* of the pitching moment– $\alpha$  curve. In this experiment only a single degree of freedom was involved: rotation around a fixed axis. The static analysis was sufficient to determine whether the equilibrium was stable or unstable (and to determine the stability boundary), but not sufficient to determine the dynamics of the motion when the equilibrium was disturbed.

The motion of an airplane in the vertical plane involves three degrees of freedom, one rotational (the pitching motion described above) and two translational (horizontal and vertical velocity components). An analysis of the stability of the motion requires that a steady-state trajectory be defined and an analysis of small perturbations in the motion be performed. From this analysis the *dynamic modes* (i.e., the time-dependent behavior of the system in response to an impulsive input) can be determined. A pilot's ability to control an airplane is linked to the stability of the modes, so *dynamic stability* is of critical importance. Dynamic stability analyses will be performed in later chapters. Here we simply note that positive stiffness is not sufficient to ensure dynamic stability, but the aircraft dynamic stability conditions will later be seen to be dominated by the static stability condition.

We must now describe the mathematical models for the forces and moments on an airfoil and include the situation where the parameters of the flowfield may vary. It is shown in textbooks on aerodynamics (Kuethe and Chow, 1984) that, for a body of given shape with a given orientation to the freestream flow, the forces and moments are proportional to the product of freestream mass density,  $\rho$ , the square of the freestream airspeed,  $V_T$ , and a characteristic area for the body. The product of the first two quantities has the dimensions of pressure and it is convenient to define the *dynamic pressure*,  $\bar{q}$ , by

$$\bar{q} = \frac{1}{2} \rho V_T^2 \quad (\text{pressure units}) \quad (2.2-1)$$

and note that this is also the kinetic energy per unit volume. In the *standard atmosphere* model (U.S. Standard Atmosphere, 1976) the mass density  $\rho$  is  $2.3769 \times 10^{-3}$  slugs/ft<sup>3</sup> at sea level (1.2250 kg/m<sup>3</sup>) and, as an example, the dynamic pressure at 300 mph (440 ft/s) at sea level is

$$\bar{q} = 0.5 \times 0.002377 \times 440^2 = 230 \text{ lb/ft}^2 \text{ (psf)}$$

This dynamic pressure of about  $1.6 \text{ lb/in.}^2$  (psi) is to be compared with the static pressure of approximately 14.7 psi at sea level. By dividing a measured (or calculated) aerodynamic force by the product of dynamic pressure and an arbitrarily chosen reference area, we determine dimensionless coefficients that represent the ability of the airfoil to produce lift or drag. In the case of an aerodynamic moment we must also divide by an arbitrarily chosen reference length. The dimensionless coefficients are called *aerodynamic coefficients* and depend on the shape of the airfoil and its angle of attack.

An aerodynamic coefficient is also a function of the freestream viscosity, which is a measure of a fluid's resistance to rate of change of shape. In addition, the aerodynamic coefficient depends on how much the fluid is compressed in the flow around the airfoil. If this dependence is expressed in terms of two appropriate parameters, then *geometrically similar* airfoils (i.e., same shape, same definition of reference area, but not necessarily the same size) will have the same aerodynamic coefficient when they are at the same angle of attack in two different flowfields, providing that the two *similarity parameters* are the same for each. This assumes that the effect of surface roughness is negligible and that there is no effect from turbulence in the freestream airflow. Matching of the two sets of similarity parameters is required for wind tunnel results to carry over to full-sized aircraft. The two conventional similarity parameters will now be described.

The nature of the boundary layer viscous flow is determined by a single freestream dimensionless parameter, the *Reynolds number*,  $R_e$ , given by

$$R_e = (\rho \ell V_T) / \mu, \quad (2.2-2)$$

where  $\ell$  is some characteristic length and  $\mu$  is the viscosity of the fluid. Note that the viscosity varies greatly with the temperature of the fluid but is practically independent of the pressure. The characteristic length is usually the airfoil chord or, for an aircraft, the mean chord of the wing. Reynolds numbers obtained in practice vary from a few hundred thousand to several million. The flow in the boundary layer is laminar at low Reynolds numbers and, at some critical Reynolds number of the order of a few hundred thousand, it transitions to turbulent flow with a corresponding increase in the skin friction drag.

For most airplanes in flight, the boundary layer flow is turbulent over most of the wing airfoil, except for close to the leading edge. The NACA 6-series airfoils, designed in the 1930s and 1940s to promote laminar flow, showed a significant drag reduction in wind tunnel tests, but this usually could not be maintained in the face of the surface contamination and production roughness of practical wings.

The dynamic pressure is an increment of pressure on top of the static pressure. The fractional change in volume, which is a measure of how much the fluid is compressed, is given by dividing the dynamic pressure by the bulk modulus of elasticity (which has the units of pressure). Physics texts show that the speed of sound in a fluid is given by the square root of the quotient of the modulus of elasticity over the mass density. Therefore, when the dynamic pressure is divided by the modulus of elasticity, we obtain a dimensionless quantity equal to one-half of the square of the *freestream Mach number*,  $M$ , defined by

$$M = V_T / a, \quad (2.2-3)$$

where  $a$  is the speed of sound at the ambient conditions. At sea level in the standard atmosphere,  $a$  is equal to 1117 ft/s (340 m/s, 762 mph). Freestream Mach number is the second similarity parameter, and the aerodynamic coefficients are written as functions of  $\alpha$ , Reynolds number, and Mach number. The Mach number ranges of interest in aerodynamics are

$$\begin{aligned} \text{subsonic speeds:} \quad & M < 1.0 \\ \text{transonic speeds:} \quad & 0.8 \leq M \leq 1.2 \\ \text{supersonic speeds:} \quad & 1.0 < M < 5.0 \\ \text{hypersonic speeds:} \quad & 5.0 \leq M \end{aligned} \quad (2.2-4)$$

The *compressibility effects*, described above, may begin to have a noticeable influence on an aerodynamic coefficient at a freestream Mach number as low as 0.3. By definition pressure disturbances propagate through a fluid at the speed of sound, and an approaching low-speed aircraft can be heard when it is still some distance from the observer. When the Mach number reaches unity at some point in the flow, pressure disturbances at that point can no longer propagate ahead. The wavefront remains fixed to the aerodynamic body at that point and is called a *shock wave*. At still higher Mach numbers the wavefront is inclined backward in the flow and forms a *Mach cone* with its apex at the source of the pressure disturbance. The Mach number will in general reach unity at some point on the airfoil surface when the freestream velocity is still subsonic. This freestream Mach number, called the *critical Mach number*, defines the beginning of *transonic flow* for an airfoil or wing. Because of the formation of shock waves and their interaction with the boundary layer, the aerodynamic coefficients can vary with Mach number in a complex manner in the transonic regime. For example, at a freestream Mach number slightly greater than the critical Mach number, a sharp increase in drag coefficient occurs. This is called the *drag divergence Mach number*. In the supersonic regime the aerodynamic coefficients tend to change less erratically with Mach number, and in the hypersonic regime the aerodynamic effects eventually become invariant with Mach number.

We are now in a position to write down the mathematical models for the magnitudes of the forces and moments shown in Figure 2.2-1. The measurements are typically made at some point in the airfoil close to the ac (usually at the quarter-chord point). The force components and the moment of the couple are modeled by the following equations, involving lift, drag, and moment *section coefficients*  $C_\ell$ ,  $C_d$ , and  $C_m$ , respectively:

$$\begin{aligned} \text{lift per unit span} &= \bar{q} c C_\ell (\alpha, M, R_e) \\ \text{drag per unit span} &= \bar{q} c C_d (\alpha, M, R_e) \\ \text{pitching moment per unit span} &= \bar{q} c^2 C_m (\alpha, M, R_e) \end{aligned} \quad (2.2-5)$$

The reference length for this infinitely long airfoil section is the chord length,  $c$ , and the product  $\bar{q}c$  has the dimensions of force per unit length.

Consider first the variation of section aerodynamic coefficients with  $\alpha$ . The dimensionless *lift coefficient*,  $C_l$ , measures the effectiveness of the airfoil at producing lift. This coefficient is linear in  $\alpha$  at low values of  $\alpha$  and positive at zero angle of attack for cambered airfoils. The *lift-curve slope* has a theoretical value of  $2\pi$  per radian for thin airfoils at low subsonic Mach numbers. The drag equation has the same form as the lift equation, and the *drag coefficient*,  $C_d$ , is usually parabolic in  $\alpha$ , in the region where the lift coefficient is linear in  $\alpha$ . The drag coefficient is commonly presented as a function of lift coefficient. Typical plots of lift and drag coefficients, with representative values, are shown, respectively, in Figures 2.2-3a and b. The moment equation is different from the lift and drag equations in that it requires an additional length variable to make it dimensionally correct. The airfoil chord,  $c$ , is used once again for this purpose. A typical plot of the *pitching moment coefficient*,  $C_m$ , is also shown in Figure 2.2-3a.

Now consider the variation of these coefficients at higher values of  $\alpha$ . Wind tunnel flow visualization studies show that, at high values of  $\alpha$ , the flow can no longer follow the upper surface of the airfoil and becomes detached. There is a region above the upper surface, near the trailing edge, where the velocity is low and the flow reverses direction in places in a turbulent motion. As the angle of attack is increased farther, the beginning of the region of separated flow moves toward the leading edge of the airfoil. The pressure distribution over the airfoil is changed in such a way that the lift component of the aerodynamic force falls off rapidly and the drag component increases rapidly. The airfoil is said to be *stalled*, and this condition is normally avoided in flight. The pitching moment (about the axis through the aerodynamic center) also changes rapidly, typically becoming more negative.

Next consider the effect of Reynolds number. The lift-curve slope is essentially independent of  $R_e$  when  $R_e \approx 10^6$  to  $10^7$  (where normal, manned aircraft fly) but is significantly reduced when  $R_e \approx 10^5$  (which may be reached by miniature and

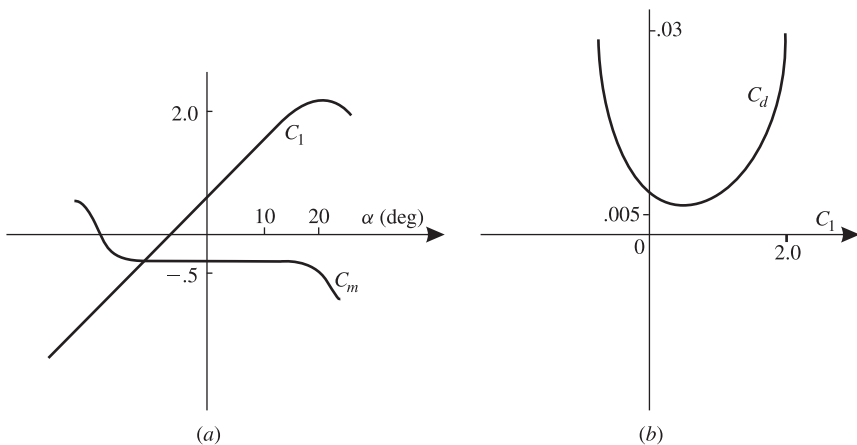


**Figure 2.2-3** Typical plots of lift, drag, and moment coefficients.



unmanned vehicles). The maximum (stall) lift coefficient tends to increase with  $R_e$ , even at high values. The drag curve is affected by  $R_e$  in that its minimum value is larger at lower  $R_e$ ; also, near stall the drag coefficient is increased by lower  $R_e$ . The pitching moment is similar to the lift coefficient in that it is independent of Reynolds number in the linear region, at high  $R_e$ , but not independent in the stall region.

Finally, consider the effect of Mach number on the aerodynamic coefficients. In the case of the lift coefficient, both the lift-curve slope and the maximum lift are changed when compressibility effects begin to occur. The theoretical values for lift-curve slope are modified by the Prandtl-Glauert correction (Anderson, 1991; Kuethe and Chow, 1984):

$$\frac{\partial C_L}{\partial \alpha} = \frac{2\pi}{\sqrt{(1 - M^2)}}, \quad M < 1 \quad (2.2-6a)$$

$$\frac{\partial C_L}{\partial \alpha} = \frac{4}{\sqrt{(M^2 - 1)}}, \quad M > 1 \quad (2.2-6b)$$

In the transonic region, the lift-curve slope of a thin airfoil will generally pass through a smooth peak, while that of a thick airfoil will show a more complicated variation. The maximum lift coefficient falls with increasing Mach number in the supersonic regime. For the drag coefficient, the effect of increasing subsonic Mach number is to bodily raise the drag curve shown in Figure 2.2-3b; the drag coefficient then falls off somewhat with increasing supersonic Mach number.

The effect of Mach number on the pitching moment coefficient is due to a rearward shift of the airfoil  $c_p$  with Mach number. This causes a shift in position of the airfoil aerodynamic center. At low subsonic Mach numbers it is usually at a distance back from the leading edge equal to about 25% of the chord. In the transonic region its position may change erratically, and at higher speeds it tends to shift aft to the 50% chord position. Therefore, if the pitching moment is measured at the quarter-chord position, the slope, with  $\alpha$ , changes from zero to a negative value as the Mach number is increased from subsonic to supersonic values.

## Finite Wings

Real wings are finite in length and involve “three-dimensional” aerodynamics. When a wing is producing lift, the air tends to flow around the tip, from the high-pressure region under the wing to the low-pressure region above the upper surface. This circulation of the air creates a vortex motion at the tips so that, behind the wing, the sheet of air that is deflected downward by airfoil action curls up at the edges to form a *vortex sheet*. The energy that goes into creating the vortex motion leads to an increase in the force needed to push the wing through the air, that is, an increase in drag. In addition, the leakage around the tips creates a spanwise component of flow and reduces the lift-curve slope compared to that of a “two-dimensional” airfoil. Thus, there is a decrease in the *lift-over-drag* ratio compared to the airfoil. Many aircraft use wing-tip devices and aerodynamic “fences” on the wing to reduce these detrimental effects.

A complete wing may have straight or curved leading and trailing edges or it may consist of two identical halves that are swept back toward the tips. The chord may be constant or reduced toward the wing tip (wing taper), and different airfoil sections may be used over different parts of the span. The “planform” of a wing has a large impact on its aerodynamic properties. Among the most important parameters of the planform are the aspect ratio and the leading-edge sweep angle. These and other parameters are defined in Table 2.2-1.

An explanation of the calculation of the mean aerodynamic chord can be found in various aerodynamics texts (e.g., Dommasch et al., 1967). The aspect ratio is equivalent to a measure of span relative to chord; for complete aircraft, values range from about 30 (some sailplanes), through 14 (Lockheed U-2) and 7 (Boeing 747), down to about 3 (fighter aircraft), and even lower for delta wings. High-aspect-ratio wings act more like the “two-dimensional” airfoil, while low-aspect wings have greatly reduced lift-curve slope and lift-over-drag ratio. High lift-over-drag ratio is needed for efficient cruise performance (passenger jets), long-duration flight (military reconnaissance), and shallow glide angle (sailplanes). A low aspect ratio simplifies structural design problems for high- $g$  aircraft, permits very high roll rates, and reduces *supersonic wave drag* (described later).

*Prandtl’s lifting line theory* (Anderson, 1991) provides a simple expression for the lift-curve slope of a straight high-aspect-ratio finite wing in incompressible flow, in terms of aspect ratio and the lift-curve slope of the corresponding airfoil section. This formula can be combined with the Prandtl-Glauert corrections of Equations (2.2-6) to give a formula that applies to subsonic compressible flow. The transonic lift-curve slope is hard to predict but, in the supersonic regime, the lift-curve slope can be approximated as a constant (4.0) divided by the Prandtl-Glauert correction factor, as in Equation (2.2-6b). For low-aspect-ratio wings ( $AR < 4$ ), slightly more complicated formulas are available (Anderson, 1999). Wing sweep further complicates the picture. A lift-curve slope formula can be derived for subsonic swept wings by introducing the cosine of the sweep angle into the above-described formulas. For supersonic swept wings the behavior of the lift-curve slope depends on whether the sweep of the wing puts its leading edge inside or outside of the shock wave from the apex of the swept wing, and no convenient formulas are available. The above facts are clearly described in much more detail by Anderson (1999).

Delta-shaped wing planforms behave in a fundamentally different way than conventional wings. When producing lift, a delta wing has a strong vortex rolling over the full length of each leading edge. The vortices are stable, in the sense that they remain

**TABLE 2.2-1 Important Wing Planform Parameters**

$b$ = wing span (i.e., tip to tip)	$\lambda$ = taper ratio (tip chord/root chord)
$c$ = wing chord (varies along span)	
$\bar{c}$ = mean aerodynamic chord (mac)	$\Lambda$ = leading-edge sweep angle
$S$ = wing area (total)	$AR = b^2/S$ = aspect ratio

in place over a wide range of  $\alpha$ , and contribute to lower pressure over the upper surface. The lift curve of the delta wing is slightly nonlinear, with the slope increasing at first as  $\alpha$  increases. The average lift-curve slope is only about half that of a conventional wing, but the stall angle of attack is about twice as big. A delta wing has been used on various fighter aircraft because it can provide the large sweep angle needed for supersonic flight and can also attain a normal peak lift coefficient through the *vortex lift*. A degree of vortex lift similar to that of a delta wing can be obtained from a conventional swept wing if, near the wing root, the leading edge is carried forward with a sharp-edged extension having a sweep angle near  $90^\circ$ . This leading-edge extension generates a vortex that trails back over the inboard wing panels and keeps the flow attached to the wing at high  $\alpha$ .

### Aircraft Configurations

A conventional aircraft uses airfoil sections for the wings, horizontal tail, vertical tail, and possibly additional surfaces such as horizontal canards [notable exceptions to this configuration are the flying wing aircraft, such as the Northrop YB series (Anderson, 1976) and the more modern B-2 bomber]. The close proximity of the wings and fuselage, and of the wing and tail surfaces, creates interference effects, so that the total aerodynamic force is not given by the sum of the forces that would be obtained from the individual surfaces acting alone. In addition, the fuselage of the airplane provides some lift and a considerable amount of drag. Therefore, the aerodynamic coefficients of a complete aircraft must be found from wind tunnel measurements and computational fluid dynamics (CFD). Anderson (1999) cites a study that measured the subsonic lift-curve slope of a wing-fuselage combination as a function of the ratio of fuselage diameter to wingspan ( $d/b$ ). The study showed that for a range of  $d/b$  from zero to 0.6, the lift-curve slope was within 5% of that of the wing alone. This was because of the lift of the fuselage, and because of favorable cross-flows induced on the wing by the fuselage. A further conclusion was that the lift of the wing-body combination could be approximated by using the lift coefficient of the wing alone, with a reference area given by the planform area of the wing projected through the fuselage. This is the usual definition of the wing planform reference area.

Figure 2.2-4 shows a number of distinctive planforms. Low-speed aircraft, ranging from light general aviation types to military heavy-lift transport aircraft, have stiff moderate-aspect-ratio wings with no sweepback (cf. Figure 2.2-4d). Aircraft designed to reach transonic speeds and beyond have highly swept wings. The effect of the sweep is to postpone the *transonic drag rise*, since the component of the airflow perpendicular to the leading edge has its speed reduced by the cosine of the sweep angle. Large jet airliners designed to cruise efficiently at high subsonic Mach numbers have swept wings with a high aspect ratio (Figure 2.2-4e). This produces the highest ratio of lift to induced drag (the increase in drag that occurs when lift is produced). In the case of high-speed fighter aircraft, the requirement for low supersonic wave drag and high maneuverability causes a dramatic change to very-low-aspect-ratio wings (Figure 2.2-4b). The stubby wings allow the aircraft structure to be designed to withstand very high lift forces during maneuvers. They also reduce the moment of inertia

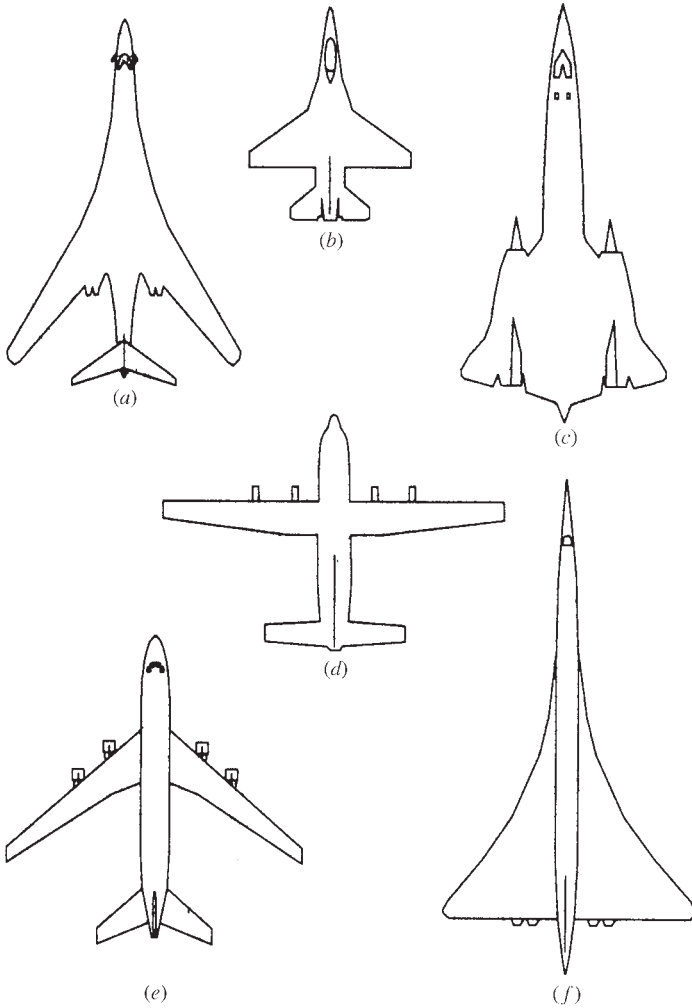


**Figure 2.2-4** Types of aircraft wing planform.

about the longitudinal axis and the aerodynamic damping moments during rolling, thus promoting a high roll acceleration and a high maximum roll rate.

Wing sweep has the disadvantage of reducing the lift-curve slope of the wing (i.e., less lift at a given  $\alpha$ ) and producing suboptimal performance at low speeds. A way to overcome this when a high lift-to-drag ratio is required over a wide envelope is to use a variable-sweep wing, as exemplified by the F-14 and B-1B aircraft (Figure 2.2-4a). This is a heavy and costly solution. For commercial aircraft that are usually optimized for one cruise condition, the most common method of achieving adequate lift at low speeds is to increase the camber and area of the wing by means of leading- and trailing-edge devices (slats and flaps). These may then be

deployed manually for landing. More specialized solutions are to use an automatic maneuvering flap, as in the case of the F-16 leading-edge flap, which is deployed automatically as a function of angle of attack when the Mach number is low. More recently the concept has been taken to its logical conclusion in the *mission adaptive wing* (DeCamp et al., 1987), tested on an F-111 aircraft.

Wing planforms that create vortex lift are shown in Figures 2.2-4*b*, *c*, and *f*, representing the F-16, SR-71, and Concorde aircraft, respectively.

The F-16 has sharp-edged, highly swept forebody *strakes* to generate the vortices. The design goal was to achieve maximum maneuverability through the use of vortex lift. The Concorde has an *ogee* wing with very large initial sweep angle, with the design aim of increasing the lift at low speed and reducing the movement of the aerodynamic center between low-speed and supersonic cruise conditions. The high angle of attack needed to get the low-speed vortex lift would obscure the pilot's view of the runway, and this problem was solved by using the droop nose. Some description of the design of these wings can be found in the American Institute of Aeronautics and Astronautics (AIAA) case studies (Droste and Walker, no date; Rech and Leyman, no date). The SR-71 Mach 3-plus, high-altitude, strategic reconnaissance aircraft (Drendel, 1982) has a blended wing-body with chines. This blending reduces wing-body wave interference drag at cruise speed, while vortex lift effects may be useful during takeoff and landing.

Vortices are also shed from a conventional forebody at high  $\alpha$ , and a long forebody overhang (as in the case of the shark nose on the F-5) presents difficult design problems. This is because any slight asymmetry in the shed vortices causes pressure differentials at the nose and leads to a relatively large (and unpredictable) yawing moment because of the long lever arm from the aircraft center of mass.

## 2.3 AIRCRAFT FORCES AND MOMENTS

The equations of motion derived in Chapter 1 are driven by the aerodynamic forces and moments acting at the cm of the complete rigid aircraft. In Section 2.2 we have covered enough basic aerodynamics to understand how these forces and moments come about. We now begin to examine how they can be measured and expressed.

### Definition of Axes and Angles

The aerodynamic forces and moments on an aircraft are produced by the relative motion with respect to the air and depend on the orientation of the aircraft with respect to the airflow. In a uniform airflow these forces and moments are unchanged after a rotation around the freestream velocity vector. Therefore, only two orientation angles (with respect to the relative wind) are needed to specify the aerodynamic forces and moments. The angles that are used are the *angle of attack* ( $\alpha$ ) and the *sideslip angle* ( $\beta$ ). They are known as the *aerodynamic angles* and will now be formally defined for an aircraft. Note that the aerodynamic forces and moments are also dependent on angular rates, but for the moment we are concerned only with orientation.

Figure 2.3-1 shows an aircraft with the relative wind on its right side (i.e., sideslip-ping), with three *frd* (forward, right, down) coordinate systems with a common origin at the aircraft cm, and with aerodynamic angles  $\alpha$  and  $\beta$ . The *body-fixed coordinate system*, *bf*, has its *x*-axis parallel to the fuselage reference line (used in the blueprints) and its *z*-axis in the (conventional) aircraft plane of symmetry. The angle of attack is denoted by  $\alpha_{frl}$  when measured to the fuselage reference line from the projection of the relative wind on the body *x-z* plane. It is positive when the relative wind is on the underside of the aircraft. The sideslip angle is measured to the relative wind vector from the same projection. It is positive when the relative wind is on the right side of the airplane.

The angle of attack is also given the symbol  $\alpha_0$  when measured to the aircraft zero-lift line (where aircraft lift is zero, with neutral controls and no sideslip). We will simply write “ $\alpha$ ” throughout and mean  $\alpha_{frl}$  unless otherwise stated. For an aircraft in steady-state flight (Section 2.6) the “equilibrium” angle of attack will be denoted by  $\alpha_e$ , and the equilibrium sideslip angle is normally zero.

In Figure 2.3-1,  $\alpha_e$  defines the orientation of the *stability-axes* coordinate system, *s*, which is used for analyzing the effect of perturbations from steady-state flight. As can be seen from the figure, it is obtained from the body-fixed system by a left-handed rotation, through  $\alpha_e$ , around the body *y*-axis. The *wind-axes* system, *w*, is obtained from the stability-axes system by a rotation around the *z*-axis that aligns the wind *x*-axis directly into the relative wind. A left-handed wind-axes system, aligned backward, left, and “up” relative to the aircraft, has been used in the past for wind tunnel

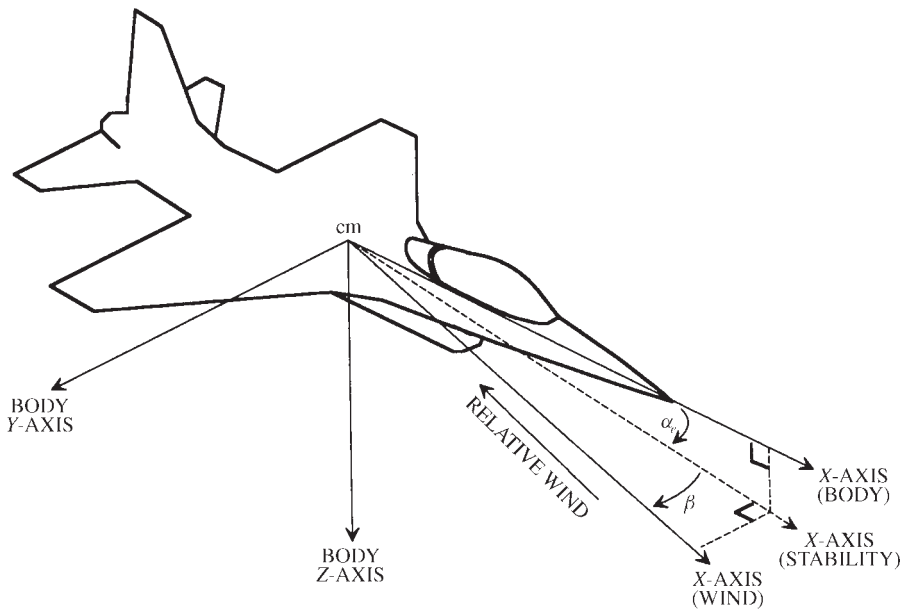


**Figure 2.3-1** Definitions of axes and aerodynamic angles.

data (Pope, 1954). *Lift*  $L$ , *drag*  $D$ , and *cross-wind force*  $C$  were defined naturally in these axes as the aerodynamic force components along the respective positive axes. The notation for our right-handed coordinate systems is given in Table 2.3-1, in the next subsection.

Following the rules for finding rotation matrices, the rotation matrices from body fixed to stability and stability to wind axes are

$$C_{s/bf} = \begin{bmatrix} \cos \alpha_e & 0 & \sin \alpha_e \\ 0 & 1 & 0 \\ -\sin \alpha_e & 0 & \cos \alpha_e \end{bmatrix} \quad (2.3-1a)$$

$$C_{w/s} = \begin{bmatrix} \cos \beta & \sin \beta & 0 \\ -\sin \beta & \cos \beta & 0 \\ 0 & 0 & 1 \end{bmatrix} \quad (2.3-1b)$$

and the combined rotation from body fixed to wind is

$$C_{w/bf} = \begin{bmatrix} \cos \alpha_e \cos \beta & \sin \beta & \sin \alpha_e \cos \beta \\ -\cos \alpha_e \sin \beta & \cos \beta & -\sin \alpha_e \sin \beta \\ -\sin \alpha_e & 0 & \cos \alpha_e \end{bmatrix} \quad (2.3-2)$$

This transformation will also be used without the subscript  $e$  when converting instantaneous wind-axes components into body axes, and vice-versa.

## Definition of Forces and Moments

Table 2.3-1 defines the symbols that will be needed for aircraft force, moment, and velocity components. The subscripts  $A$  or  $T$  on the force and moment vectors indicate, respectively, aerodynamic or thrust effects. In the case of the aerodynamic forces, there are no specific symbols for stability-axes components but, as indicated in (2.3-3b), the stability axes have two components that are unchanged from the other axes. These dimensionless coefficients are defined in the next section. Note that  $C_N$  and  $C_X$  are, respectively, the *normal force* and *axial force* coefficients;  $C_N$  is the negative of the body-axes force coefficient  $C_Z$ .

A useful notation scheme is to use lowercase symbols to indicate small perturbations on the “uppercase” variables. Unfortunately, aircraft moments are almost universally denoted by lowercase symbols, as shown in (2.3-4) and (2.3-5). Also, the same symbols are commonly used for the dimensionless moment coefficients regardless of coordinate system, and the coordinate system must be explicitly stated.

Thrust components are shown in (2.3-5); note that a sideforce component can be produced by unbalanced engine power because in a multiengine aircraft the engines may be toed-in to align them with the airflow from the forebody. Also, the thrust axis is often slightly tilted with respect to the body  $x$ -axis, and so a  $z$ -component of thrust can result. In the case of VTOL or V/STOL aircraft, the  $z$ -component of thrust will

**TABLE 2.3-1 Force, Moment, and Velocity Definitions**

Aerodynamic forces:

$$\mathbf{F}_A^w \equiv \begin{bmatrix} -D \\ -C \\ -L \end{bmatrix} = C_{w/bf} \begin{bmatrix} X_A \\ Y_A \\ Z_A \end{bmatrix} \equiv C_{w/bf} \mathbf{F}_A^{bf} \quad (2.3-3a)$$

Dimensionless force coefficients:

$$\begin{array}{lll} \text{Wind :} & C_D & C_C & C_L \\ \text{Stability :} & * & C_Y & C_L \\ \text{Body :} & C_X & C_Y & C_Z \quad (-C_N) \end{array} \quad (2.3-3b)$$

Aerodynamic moments:

$$\mathbf{M}_A^{bf} \equiv \begin{bmatrix} \ell \\ m \\ n \end{bmatrix}, \quad \mathbf{M}_A^s \equiv \begin{bmatrix} \ell_s \\ m \\ n_s \end{bmatrix}, \quad \mathbf{M}_A^w \equiv \begin{bmatrix} \ell_w \\ m_w \\ n_w \end{bmatrix} \quad (n_w = n_s) \quad (2.3-4a)$$

Dimensionless moment coefficients:

$$C_\ell, C_m, C_n$$

(same notation in all systems) (2.3-4b)

Thrust force and moment:

$$\mathbf{F}_T^{bf} \equiv \begin{bmatrix} X_T \\ Y_T \\ Z_T \end{bmatrix}, \quad \mathbf{M}_T^{bf} \equiv \begin{bmatrix} m_{x,T} \\ m_{y,T} \\ m_{z,T} \end{bmatrix} \quad (2.3-5)$$

Relative velocity components:

$$\mathbf{v}_{rel}^{bf} \equiv \begin{bmatrix} U' \\ V' \\ W' \end{bmatrix} = C_{bf/w} \mathbf{v}_{rel}^w \equiv C_{bf/w} \begin{bmatrix} V_T \\ 0 \\ 0 \end{bmatrix} = \begin{bmatrix} V_T \cos \alpha \cos \beta \\ V_T \sin \beta \\ V_T \sin \alpha \cos \beta \end{bmatrix} \quad (2.3-6a)$$

Aerodynamic angles:

$$\tan \alpha = \frac{W'}{U'}, \quad \sin \beta = \frac{V'}{V_T}, \quad V_T = |\mathbf{v}_{rel}| \quad (2.3-6b)$$

Absolute velocity components:

$$\mathbf{v}_{cm/e}^{bf} \equiv \begin{bmatrix} U \\ V \\ W \end{bmatrix} \quad (2.3-6c)$$

Angular velocity components ( $r$  denotes any ref. frame):

$$\boldsymbol{\omega}_{b/r}^{bf} \equiv \begin{bmatrix} P \\ Q \\ R \end{bmatrix}, \quad \boldsymbol{\omega}_{b/r}^s \equiv \begin{bmatrix} P_s \\ Q \\ R_s \end{bmatrix}, \quad \boldsymbol{\omega}_{b/r}^w \equiv \begin{bmatrix} P_w \\ Q_w \\ R_w \end{bmatrix} \quad (R_w = R_s) \quad (2.3-7)$$

Control surface deflections:

Elevator:  $\delta_e$  Aileron:  $\delta_a$  Rudder:  $\delta_r$  Flap:  $\delta_F$ Throttle position:  $\delta_t$ Control vector:  $\overline{U} = [\delta_t \delta_e \delta_a \delta_r \delta_F \dots]^T$



be particularly important. Models of propeller-driven aircraft must include several important force and moment effects.

In Equation (2.3-6) primes are used to denote velocity components relative to the atmosphere, as opposed to “inertial” components. In the wind system the relative velocity vector  $\mathbf{v}_{rel}$  has only an  $x$ -component  $V_T$ , and so  $V_T = |\mathbf{v}_{rel}|$ . In (2.3-6b) the aerodynamic angles have been found from the interrelationships of the components in (2.3-6a). The control vector of the nonlinear state-space model has been denoted by  $\bar{U}$ , in this chapter only, to distinguish it from a velocity component.

## Force and Moment Coefficients

The forces and moments acting on the complete aircraft are defined in terms of dimensionless aerodynamic coefficients in the same manner as for the airfoil section. The situation is now three dimensional, and the coefficients are functions of the two aerodynamic angles, as well as Mach and Reynolds numbers. Furthermore, an aircraft is a flexible structure and its shape is deformed by the influence of high dynamic pressure, with consequent changes in the aerodynamic coefficients. If Mach and altitude are specified, together with a temperature and density model of the atmosphere, then Reynolds number and dynamic pressure can be determined. Therefore, the aircraft aerodynamic coefficients are, in practice, specified as functions of the aerodynamic angles, Mach, and altitude (in the standard atmosphere). In addition, control surface deflections and propulsion system effects cause changes in the coefficients. A control surface deflection,  $\delta_s$ , effectively changes the camber of a wing, which changes the lift, drag, and moment. Consequently, we write the dependence of an aerodynamic coefficient as

$$C_{(\ )} = C_{(\ )} (\alpha, \beta, M, h, \delta_s, T_c), \quad (2.3-8a)$$

where  $T_c$  is a *thrust coefficient* (defined later). Other factors that change the coefficients are configuration changes (e.g., landing gear, external tanks, etc.) and ground proximity effects. In terms of wind-axes components, we have the following coefficients:

$$\begin{aligned} \text{drag, } D &= \bar{q} S C_D \\ \text{lift, } L &= \bar{q} S C_L \\ \text{crosswind force, } C &= \bar{q} S C_C \\ \text{rolling moment, } \ell_w &= \bar{q} S b C_\ell \\ \text{pitching moment, } m_w &= \bar{q} S \bar{c} C_m \\ \text{yawing moment, } n_w &= \bar{q} S b C_n \end{aligned} \quad (2.3-8b)$$

Exactly equivalent definitions are used for body- or stability-axes components, with the symbols given in Table 2.3-1. In Equation (2.3-8a), as a rough generality, *longitudinal coefficients* (lift, drag, pitching moment) are primarily dependent on alpha, and in the *lateral-directional coefficients* (roll, yaw, and sideforce) beta is equally as important as alpha.

Equation (2.3-8a) implies a complicated functional dependence that would have to be modeled as a “lookup-table” in a computer. The vast majority of aircraft have flight envelopes restricted to small angles of attack and/or low Mach numbers. For these aircraft, the functional dependence will be simpler and any given coefficient might be broken down into a sum of simpler terms, with linearity assumed in some terms.

The coefficients considered so far are *static coefficients*, that is, they would be obtained from measurements on a stationary model in a wind tunnel (other methods are considered later). It is also necessary to model the aerodynamic effects when an airplane maneuvers. In general terms this requires a differential equation model of the aerodynamic force or moment. To determine if this level of complexity is warranted, we examine maneuvering flight more closely, in two categories. First, consider maneuvers that are slow enough that the flowfield around the aircraft is able to adjust in step with the maneuver and so the maneuver-induced translational velocities of points on the aircraft cause changes in the local aerodynamic angles that are still in the linear regime. The aerodynamic forces or moments can then be modeled as linearly proportional to the angular rate that produced them. Linearization is usually associated with taking a partial derivative, and in this case the coefficient of proportionality is called an *aerodynamic derivative*. The aerodynamic derivatives will be described in the next subsection.

In the second category are maneuvers in which an airplane can significantly change its orientation in a time interval that is comparable with the time required for the flowfield around the aircraft to readjust. These *unsteady aerodynamic effects* lead to time dependence in the aerodynamic coefficients and much more complicated mathematical models. For example, when a very maneuverable aircraft is pitched up rapidly and the angle of attack reaches a value near to stall, the lift generated by the wing may briefly exceed that predicted by the static lift curve. This *dynamic lift* occurs because flow separation takes a finite time to progress from the trailing edge of the wing to the leading edge. The effect can be modeled by making the lift coefficient satisfy a first-order differential equation involving angle-of-attack rate, “alpha-dot” (Goman and Khrabrov, 1994). Another example of possible unsteady aerodynamic behavior is *wing-rock* (McCormick, 1995).

## The Aerodynamic Derivatives

The aerodynamic derivatives can be subdivided into two categories. First, when the body frame has a constant angular velocity vector, every point on the aircraft has a different translational velocity in the geographic frame and, taking body-axes components, the aerodynamic angles could be computed at any point using the equivalent of Equation (2.3-6b). For example, a roll rate  $P$  would create translational velocity components  $\pm Pb/2$  at the wing tips. When  $P > 0$  this would cause the angle of attack to be reduced by approximately  $Pb/(2V_T)$  at the left wing tip and increased by the same amount at the right wing tip. This would in turn create a skew-symmetric variation in lift across the full span of the wings and, assuming that the wing is not stalled across most of the span, produce a negative rolling moment. Because the moment

opposes the roll rate  $P$ , the coefficient relating the rolling moment to the roll rate is called a *damping derivative*.

The quantity  $Pb/(2V_T)$  is given the symbol  $\hat{p}$  and is thought of as a dimensionless roll rate. In a continuous roll, with the aircraft cm moving in a straight line, the wing tips move along a helical path and  $Pb/(2V_T)$  is the *helix angle*. The helix angle is a useful figure of merit for roll control power and has been evaluated and compared for a variety of aircraft (Perkins and Hage, 1949; Stinton, 1996). The mathematical model for the dimensionless damping force, or moment  $\Delta C$ , is of the form

$$\Delta C_{(\cdot)} = C_{(\cdot)}(\alpha, \beta, M, h, \delta_s, T_c) \times \frac{k}{2V_T} \times \text{rate} \quad (2.3-9a)$$

The constant  $k$  in the dimensionless rate, in Equation (2.3-9a), is either the wingspan (for roll and yaw rates) or the wing mean aerodynamic chord (for pitch rate). The coefficient  $C_{(\cdot)}$  is one of the following  $p$ ,  $q$ , or  $r$  derivatives,

$$C_{\ell_p} \quad C_{m_q} \quad C_{n_r} \quad (2.3-9b)$$

$$C_{\ell_r} \quad C_{n_p} \quad (2.3-9c)$$

$$C_{L_q} \quad C_{Y_p} \quad C_{Y_r}, \quad (2.3-9d)$$

which relate the increments in the moments or forces to the yawing, pitching, and rolling rates. Names are given to the derivatives later. The dimensionless forces and moments are converted to actual forces and moments as in Equations (2.3-8b). Some possible derivatives have been omitted, for example, the effect of pitch rate on drag is usually insignificant. The moment derivatives are the source of the important damping effects on the natural modes of the aircraft.

The second category of aerodynamic derivatives is the *acceleration derivatives*. When the aircraft has translational acceleration, the aerodynamic angles have nonzero first derivatives that can be found by differentiating Equations (2.3-6b). Thus,

$$\dot{\alpha} = \frac{U' \dot{W}' - W' \dot{U}'}{(U')^2 + (W')^2} \quad (2.3-10a)$$

and

$$\dot{\beta} = \frac{\dot{V}' V_T - V' \dot{V}_T}{V_T [(U')^2 + (W')^2]^{1/2}} \quad (2.3-10b)$$

where

$$\dot{V}_T = \frac{U' \dot{U}' + V' \dot{V}' + W' \dot{W}'}{V_T} \quad (2.3-10c)$$

The main steady aerodynamic effect of the changing aerodynamic angles is that, as the flowfield around the wings and fuselage changes, there is a small airspeed-dependent delay before the changes in downwash and sidewash are felt at

the tail. A first-order approximation in modeling these effects is to make the resulting force and moment increments directly proportional to the aerodynamic angle rates. Therefore, the following acceleration derivatives are commonly used:

$$\text{alpha-dot derivatives: } C_{L_{\dot{\alpha}}} C_{m_{\dot{\alpha}}} \quad (2.3-11)$$

These derivatives are used in an equation of exactly the same form as Equation (2.3-9a). The beta-dot derivatives, used to model the delay in the change in sidewash at the vertical tail, are less commonly used.

## Aerodynamic Coefficient Measurement and Estimation

The static aerodynamic coefficients can be measured in a wind tunnel using an aircraft scale model mounted on a rigid “sting,” to which strain gages have been attached. An older wind tunnel may use a “balance” rather than strain gages. Rigid mounting in a wind tunnel allows *untrimmed coefficients* to be measured, that is, nonzero aerodynamic moments can be measured as the aerodynamic angles are changed or control surfaces are moved.

Specially equipped wind tunnels allow the model to be subjected to an oscillatory motion (Queijo, 1971) so that damping and acceleration derivatives can be measured. Unfortunately, as might be expected, the results are dependent on the frequency of the oscillation. Empirical criteria have been formulated to determine frequency limits below which a quasi-steady assumption (i.e., instantaneous flowfield readjustment) can be made about the flow (Duncan, 1952).

The second important method of measuring aerodynamic coefficients is through *flight test*. In this case *trimmed coefficients* are measured by using the control surfaces to make perturbations from the trimmed steady-state flight condition (Maine and Iliffe, 1980). The typical results are curves of a coefficient plotted against Mach, with altitude as a parameter, for a specified aircraft weight and cm position. The dependence on altitude comes about through the variation of alpha with altitude for a given Mach number, through aeroelastic effects changing with dynamic pressure and, possibly, through Reynolds number effects. To convert to untrimmed coefficients, which are functions of the aerodynamic angles, Mach, and altitude, the trimmed angle of attack must also be recorded in the same form. The flight test results can then be cross-plotted to obtain untrimmed coefficients. The untrimmed coefficients are required when building an aircraft model that is intended to function over a wide range of flight conditions; the trimmed coefficients are used to build small-perturbation models for control systems design or *handling qualities* studies.

Other ways of determining aerodynamic coefficients include the use of CFD computer codes or a combination of empirical data and theory built into a computer program such as the Stability and Control Datcom (Hoak et al., 1970). The input data must include a geometrical description of the aircraft. There are also simple formulas based on assumptions of linearity that can be used to estimate the aerodynamic derivatives. Some of these will be described in subsequent sections.

Component Buildup

The aerodynamic coefficients have a complex dependence on a large number of variables, and this creates both modeling problems and measurement problems. For example, a computer model might be created in the form of a data lookup table in five dimensions (five independent variables). It would be difficult to design an interpolation algorithm for this table or to set up a data measurement system (e.g., wind tunnel measurements), and very little physical insight would be available to help. It is advantageous to build up an aerodynamic coefficient from a sum of components that provide physical insight, require just a single type of test and wind tunnel model, and are convenient to handle mathematically (e.g., fewer dimensions, linearizable, etc.). We will now take each of the aerodynamic coefficients in turn and examine their functional dependence and how this can be modeled.

Drag Coefficient,  $C_D$

The drag coefficient of the complete aircraft is of paramount importance to the aircraft designer. Low drag provides better performance in terms of range, fuel economy, and maximum speed, and designers take pains to estimate the total drag accurately. By the same token we should understand how to make a good mathematical model of the drag. In general, the drag force is a combination of friction drag and drag caused when the integral of pressure over the whole surface area of the body is nonzero. Table 2.3-2 shows the total drag of an aircraft, composed of friction drag and various constituent parts of the pressure drag.

This is not a linear superposition of independent effects; the proportions of the three components will change with flight conditions, and they cannot necessarily be separated and measured individually. The *parasite drag* is called *profile drag* when applied to an airfoil section; it is the sum of skin friction and *form drag*. Form drag is simply the pressure drag caused by flow separation at high alpha. *Induced drag* (also called *vortex drag*) is the pressure drag caused by the tip vortices of a finite wing when it is producing lift. *Wave drag* is the pressure drag when shock waves are present over the surface of the aircraft. The total drag may be broken down into other different components according to the experimental situation. The resulting components will only be meaningful when used in the correct context. For example, *interference drag* is the difference between the summed drag of separate parts of the aircraft and the total drag when these parts are combined. It is a result of mutual interference between the flows over the different parts of the aircraft. Other terms include *drag due to lift* and *zero-lift drag* used for the complete aircraft.

TABLE 2.3-2 Aircraft Drag Components

Parasite Drag = Friction Drag + Form Drag (flow separation)	
+ Induced Drag	(effect of wing-tip vortices, finite wing)
+ Wave Drag	(effect of shock waves on pressure distribution)
Total Drag	

Now consider, one by one, the drag terms from Table 2.3-2. The aircraft parasite drag is virtually all skin friction drag when the aircraft wing is not stalled. The amount of skin friction drag will depend on the wetted area of the aircraft. The wetted area can range from several times the wing planform area, down to approximately twice the planform area in the case of a flying-wing aircraft. However, as we have already seen, the value of the airplane drag coefficient is calculated based on the wing planform area. The flow in the boundary layer will ordinarily be mostly turbulent in normal flight, but this will depend to a small extent on the lift coefficient. In laminar flow the drag coefficient for skin friction is inversely proportional to the square root of the Reynolds number; in turbulent flow it decreases more slowly as the Reynolds number increases. The Reynolds number increases in proportion to airspeed, but dynamic pressure increases with the square of airspeed. Therefore, we expect to see an increase in skin friction drag with airspeed, although it will become a smaller fraction of the total drag at higher speeds. For example, the skin friction of a supersonic fighter may be about 50% of the total drag at subsonic speed and about 25% at supersonic speed (Whitford, 1987). The skin friction drag coefficient is found to vary parabolically with lift coefficient (Perkins and Hage, 1949).

Turning now to induced drag, the drag coefficient for the induced drag of a high-aspect unswept wing, in subsonic flow, can be modeled as (Perkins and Hage, 1949; Anderson, 1999)

$$C_{D_i} = C_L^2 / (\pi e AR) \quad (2.3-12)$$

The *efficiency factor*,  $e$ , is close to unity, and aspect ratio is the important design parameter. This equation provides a guide to minimizing the induced drag of a complete aircraft, but the difficulties of constructing a light, high-aspect wing tend to limit the aspect ratio to values of 10 or lower, with the exceptions mentioned earlier.

Finally, consider wave drag. As in the case of an airfoil, an airplane will have a critical Mach number when the flow reaches supersonic speed at some point on the surface, and the airplane drag coefficient begins to rise. The drag divergence Mach number is the corner point or “knee” of the increasing drag coefficient curve and is reached next. A shock wave pattern is now established over the airplane and the total drag now includes wave drag. The drag coefficient continues to rise, peaks at about the end of the transonic regime, and falls off in the manner of the Prandtl-Glauert formula. Figure 2.3-2a shows the transonic drag rise for a particular fighter aircraft. The peak drag can be minimized by using a combination of three techniques. First, wing sweep (up to about  $70^\circ$ ) is used to reduce the component of the relative wind that is normal to the leading edge of the wing. This has the effect of shifting the drag rise curve to the right and merging it into the supersonic part. The drag rise becomes less steep, the peak of the curve becomes less sharp, and its height is reduced. Second, supersonic aircraft use thin airfoils, with thickness-over-chord ratios down to about 5%; these airfoils have lower wave drag and higher critical Mach numbers than thick airfoils. Finally, if the cross-sectional area of the complete airplane is made to vary smoothly with the distance from nose or tail, then the drag peak can be significantly reduced. This is R. T. Whitcomb’s famous *area rule* (Anderson, 1999), and it leads to a fighter fuselage with a pinched waist at the point where the wings begin.

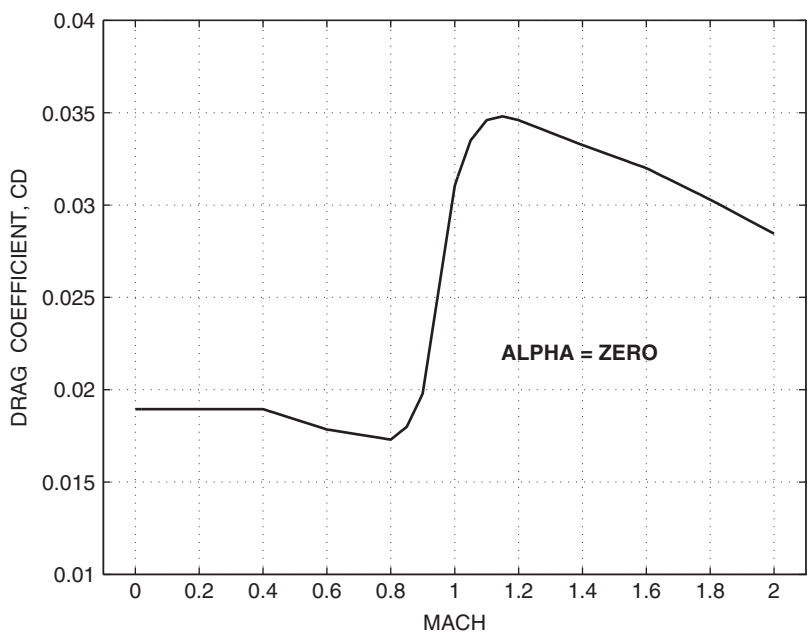


**Figure 2.3-2a** Transonic drag rise for a fighter aircraft.

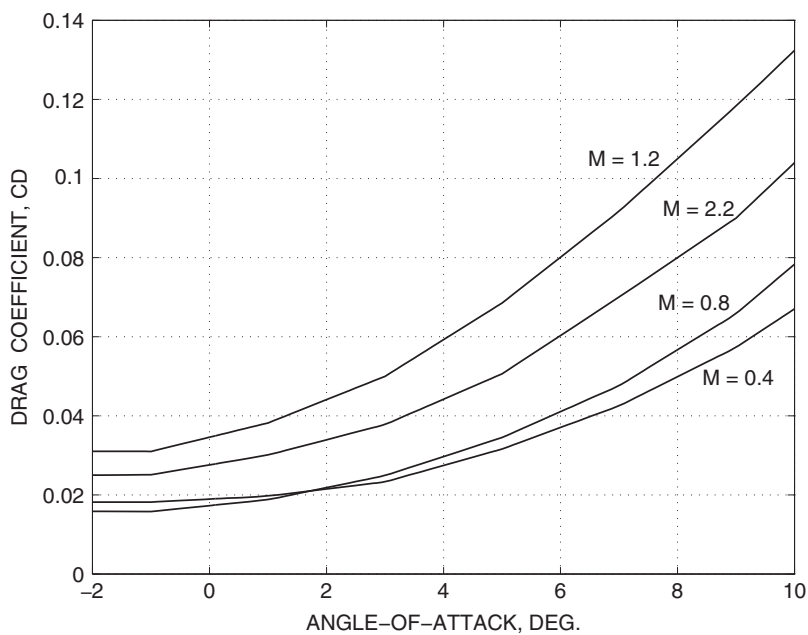


**Figure 2.3-2b** Drag coefficient of a fighter aircraft.

At constant Mach and below stall, the three types of drag described above each have a component that varies with the square of lift coefficient and a component that is independent of lift coefficient. Therefore, below stall, the complete airplane drag can be written as

$$C_D(C_L, M) = k(M) (C_L - C_{L_{DM}})^2 + C_{DM}(M), \quad (2.3-13)$$

where  $k(M)$  is a proportionality constant that changes with Mach. This parabolic equation matches the actual drag variation quite accurately; it is known as the *drag polar*. Note that the minimum drag  $C_{DM}$  can occur at a nonzero value  $C_{L_{DM}}$  of the lift coefficient.

If we consider lift beyond the stall, up to an angle of attack of  $90^\circ$ , two or possibly three values of  $\alpha$  can correspond to a given lift coefficient, and the drag is in general different for each of these values of  $\alpha$ . Therefore, for high- $\alpha$  simulation, we model drag as a function of  $\alpha$ . Because lift is quite linear as a function of  $\alpha$  below stall, the plot of drag coefficient is still parabolic in this region. Figure 2.3-2b shows the untrimmed baseline drag coefficient of the same supersonic fighter aircraft as used for Figure 2.3-2a, plotted against  $\alpha$  with Mach as a parameter. In the figure, the drag varies parabolically with  $\alpha$  and varies with Mach number in the same way as in Figure 2.3-2a.

In addition to the above effects, we can expect the drag coefficient to be dependent on altitude, sideslip, control surface and flap deflections, landing gear extension, and possibly ground effect. Altitude dependence (with Mach) allows for the effect of Reynolds number on the skin friction drag.

With the above facts and Equation (2.3-8a) in mind, we might expect a drag coefficient model consisting of a “baseline” component plus drag increments for control surfaces and gear of the form

$$\begin{aligned} C_D = & C_D(\alpha, \beta, M, h) + \Delta C_D(M, \delta_e) + \Delta C_D(M, \delta_r) + \Delta C_D(\delta_F) \\ & + \Delta C_D(\text{gear}) + \dots \end{aligned} \quad (2.3-14)$$

With aircraft that operate with little sideslip, the sideslip dependence can be treated as a separate increment.

## Lift Coefficient, $C_L$

The lift coefficient of the complete aircraft is determined by the wings, fuselage, and horizontal tail and their mutual interference effects. Nevertheless, it varies with  $\alpha$  and Mach in a way similar to that described earlier for the finite wing. The variation of lift coefficient with  $\alpha$  is usually quite linear until near the stall, when it drops sharply and then may rise again, before falling to zero when  $\alpha$  is near  $90^\circ$ . The peak value of the lift coefficient may be as great as 3 for a highly cambered wing, but the increased drag of a highly cambered wing is not acceptable for high-speed aircraft. These aircraft use thin wings with not much camber and get their lift from the



higher dynamic pressure or from effectively increasing the camber with leading- and trailing-edge flaps to get lift at low speed. Ground effect produces greater lift for a given drag; it is usually negligible beyond one wingspan above the ground.

The slope of the lift curve increases with aspect ratio and with reduction in the wing leading-edge sweep angle. Light aviation aircraft and large passenger jets can have wing aspect ratios greater than 7, compared to 3 to 4 for a fighter aircraft. Increasing the wing sweep angle has the desirable (for high-speed aircraft) effect of delaying the transonic drag rise, and the sweep angle may lie between roughly  $25^\circ$  and  $60^\circ$ . Since lift-curve slope is an important factor in determining the response to turbulence, some military aircraft with a requirement for very-low-altitude high-speed flight tolerate the expense and weight of variable-sweep wings. Compressibility effects also change the slope of the lift curve. Airfoil section theory predicts that at subsonic Mach numbers the slope should vary as  $(1 - M^2)^{-1/2}$  and at supersonic Mach numbers as  $(M^2 - 1)^{-1/2}$ , and this kind of behavior is observed in practical wings.

Dependence of lift on sideslip is usually small until the magnitude of the sideslip reaches several degrees, and since large values of sideslip only occur at low speed, this effect will typically be modeled as a separate Mach-independent correction to the baseline lift. The dependence on altitude is small and will be neglected here, and the dependence on control surface deflection is specific to the particular surface. Therefore, we will focus on the remaining three variables.

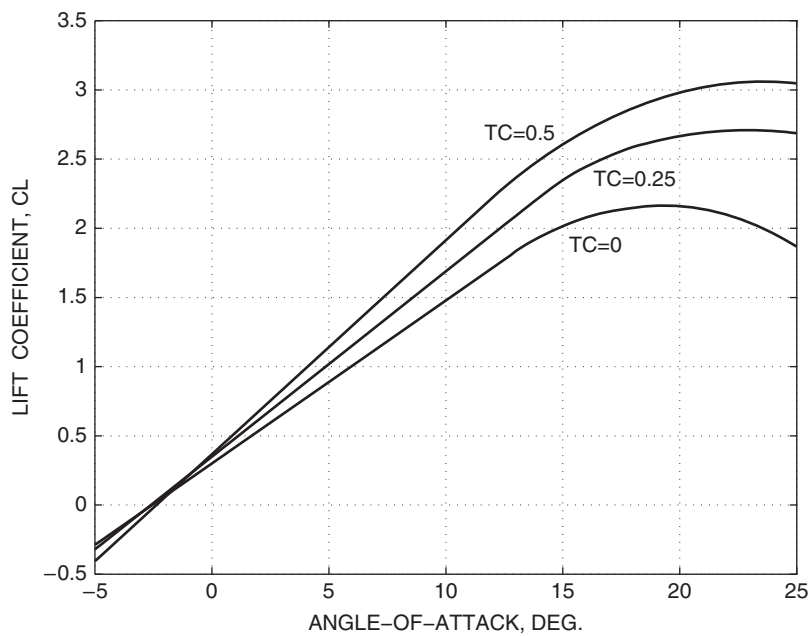
The *thrust coefficient*,  $T_C$ , normally applies to propeller aircraft and is used to account for propeller wash over the wings, fuselage, and vertical fin. It is defined by normalizing engine thrust in the same way as the nondimensional coefficients; thus,

$$T_C = \text{thrust} / \bar{q} S_D, \quad (2.3-15)$$

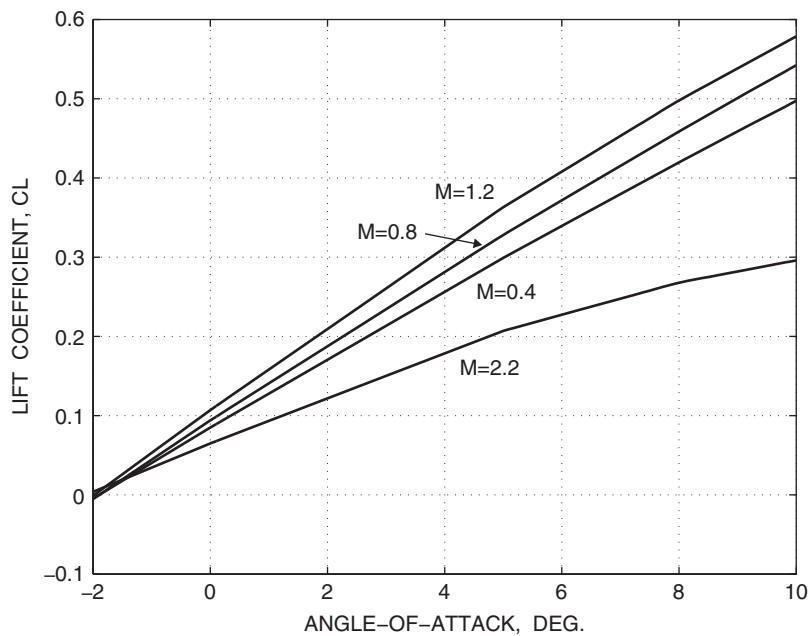
where  $S_D$  is the area of the disc swept out by a propeller blade. The propeller slip stream increases the airspeed over the wings, changes the angle of downwash behind the wing (which affects the angle of attack of the horizontal tail), and changes the dynamic pressure at the tail. The effect on the airplane lift curve can be very significant; Figure 2.3-3a shows the lift curve of a turboprop transport aircraft with four engines mounted directly on the wing. At high thrust coefficient, the figure shows a major increase in the peak lift coefficient and a shift of the peak to higher  $\alpha$ . More information on power effects can be found in the work of Perkins and Hage (1949) and Stinton (1983).

Figure 2.3-3b shows the effect of Mach number on the lift curve of a fighter aircraft. Note that the slope of the lift curve at first increases with Mach number and then decreases. An additional effect (not shown) is that the peak lift coefficient decreases with increasing supersonic Mach number.

The normal force coefficient is often a more convenient quantity than lift coefficient. The normal force coefficient will usually rise with  $\alpha$ , nearly monotonically, all the way to  $90^\circ$  angle of attack, whereas lift coefficient shows the complicated stall behavior. Unfortunately, its partner, the axial force coefficient, displays very complicated behavior in the same range of  $\alpha$  and may change sign a few times over the range of  $\alpha$ . The rotation matrix (2.3-2) and the definitions in Table 2.3-1 give



**Figure 2.3-3a** Lift coefficient of a low-speed transport aircraft.



**Figure 2.3-3b** Lift coefficient of a fighter aircraft.

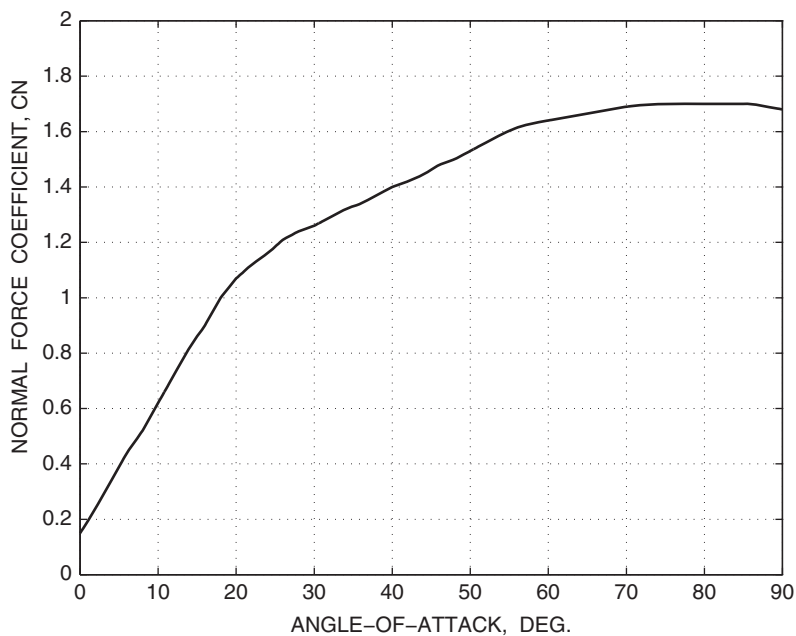


**Figure 2.3-3c** Normal force coefficient of the F-4E aircraft.

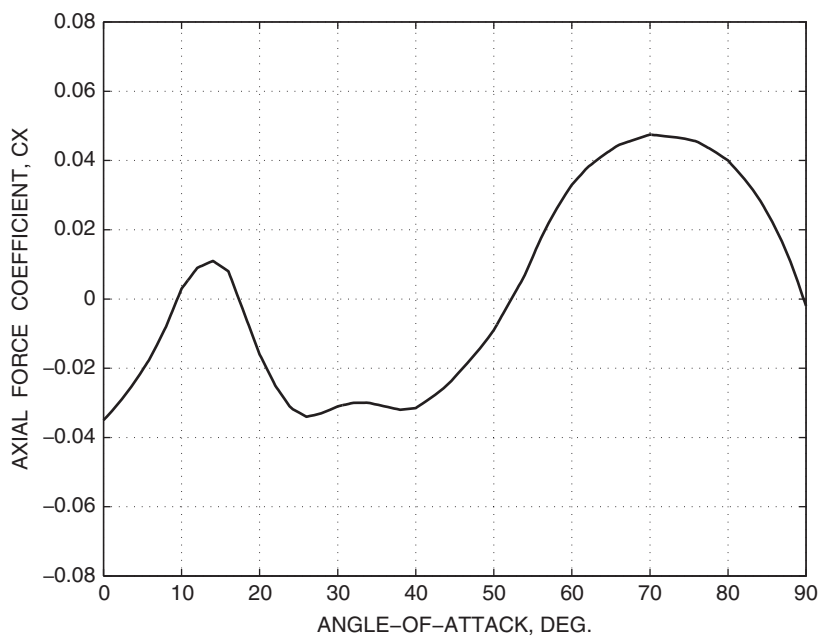


**Figure 2.3-3d** Axial force coefficient of the F-4E aircraft.

the following expressions for the lift and drag coefficients in terms of the body-axes coefficients:

$$C_D = -\cos \alpha \cos \beta C_X - \sin \beta C_Y + \sin \alpha \cos \beta C_N$$

$$C_L = \sin \alpha C_X + \cos \alpha C_N$$

and at low alpha  $C_L \approx C_N$ . Figures 2.3-3*c* and *d* show the low-Mach, high-alpha, normal and axial force coefficients for the F-4E aircraft.

A general model for lift coefficient may be of the form

$$C_L = C_L(\alpha, \beta, M, T_c) + \Delta C_L(\delta_F) + \Delta C_{L_{ge}}(h), \quad (2.3-16)$$

where  $\Delta C_{L_{ge}}(h)$  is the increment of lift in ground effect.

### Sideforce Coefficient, $C_Y$

In the case of a symmetrical aircraft, sideforce is created mainly by sideslipping motion (i.e.,  $\beta \neq 0$ ) and by rudder deflection. Figure 2.3-4 shows the sideforce coefficient for the F-4B and -C aircraft (Chambers and Anglin, 1969) for alpha equal to zero and  $40^\circ$  and with linear interpolation for other values of alpha. Note that positive sideslip leads to negative sideforce because positive sideslip corresponds to

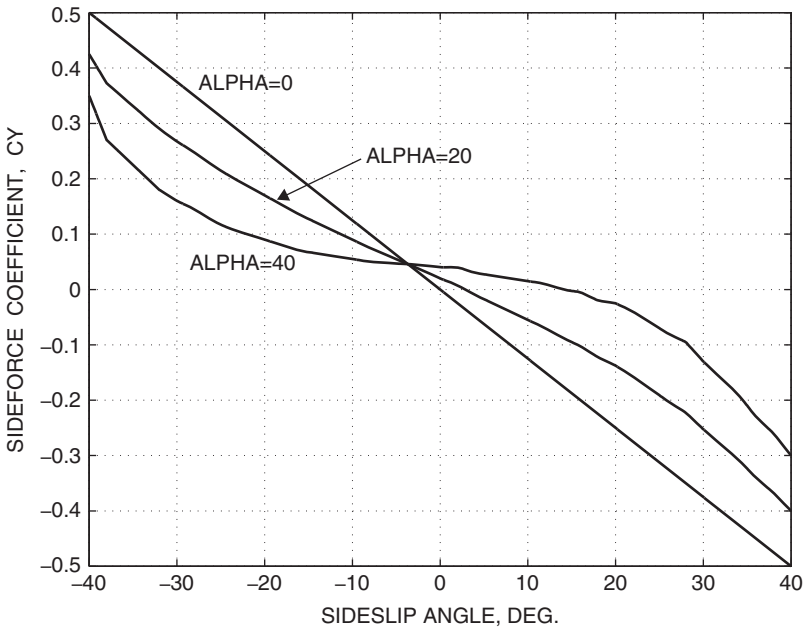


Figure 2.3-4 Sideforce coefficient of the F-4B, C aircraft.

the relative wind on the right-hand side of the nose. The high-alpha curve does not pass through the origin possibly because of asymmetry in the wind tunnel model or anomalies in the measurements. Note that at high subsonic speeds very little sideslip is possible without exceeding the hinge moment limit of the rudder or the structural limit of the vertical fin.

The sideforce model for a high-performance aircraft is typically of the form

$$C_Y = C_Y(\alpha, \beta, M) + \Delta C_{Y_{\delta r}}(\alpha, \beta, M, \delta_r) + \Delta C_{Y_{\delta a}}(\alpha, \beta, M, \delta_a) + \frac{b}{2V_T} \left[ C_{Y_p}(\alpha, M)P + C_{Y_r}(\alpha, M)R \right] \quad (2.3-17a)$$

Additional corrections are added for flaps, gear, and the like. The last two terms are linear in the angular rates, and the other terms are linearized whenever acceptable accuracy is achieved; thus,

$$\begin{aligned} C_Y(\alpha, \beta, M) &\approx C_{Y_\beta}(\alpha, M) \times \beta \\ \Delta C_{Y_{\delta r}}(\alpha, \beta, M, \delta_r) &\approx C_{Y_{\delta r}}(\alpha, \beta, M) \times \delta_r \\ \Delta C_{Y_{\delta a}}(\alpha, \beta, M, \delta_a) &\approx C_{Y_{\delta a}}(\alpha, \beta, M) \times \delta_a \end{aligned} \quad (2.3-17b)$$

These terms have been linearized “around the origin,” that is, for a symmetrical aircraft, the sideforce can be expected to go to zero when the sideslip is zero and the rudder and aileron are in their neutral positions.

## Rolling Moment

Rolling moments are created by sideslip alone, by the control action of the ailerons and the rudder, and as damping moments resisting rolling and yawing motion. Consider first the effect of sideslip; if a right-wing-down roll disturbance occurs and is not corrected (stick fixed), then the effect of gravity will be to start a positive sideslip. If the aircraft aerodynamics are such that positive sideslip causes a positive rolling moment, then the roll angle will increase further. This is an unstable situation. We see that, for positive stiffness in roll, the slope of the rolling moment–sideslip curve should be negative. Therefore, it is useful to understand the aerodynamic effects that determine the behavior of the rolling moment coefficient with sideslip; this will be our baseline term in the rolling moment coefficient buildup.

The baseline rolling moment coefficient is primarily a function of sideslip, alpha, and Mach and can be written as  $C_\ell(\beta, \alpha, M)$ . Figure 2.3-5 is a plot of the rolling moment coefficient for the F-4B at low Mach number; it shows that, for small sideslip, the coefficient is approximately linear with beta, but changes in alpha can cause a significant change in slope. Also, at low alpha, sideslip greater than  $20^\circ$  can cause a loss of stability in roll. In general, the effect of sideslip is to create a lateral component of the relative wind, and there are three separate effects of this lateral component on the horizontal aerodynamic surfaces. These will now be described.

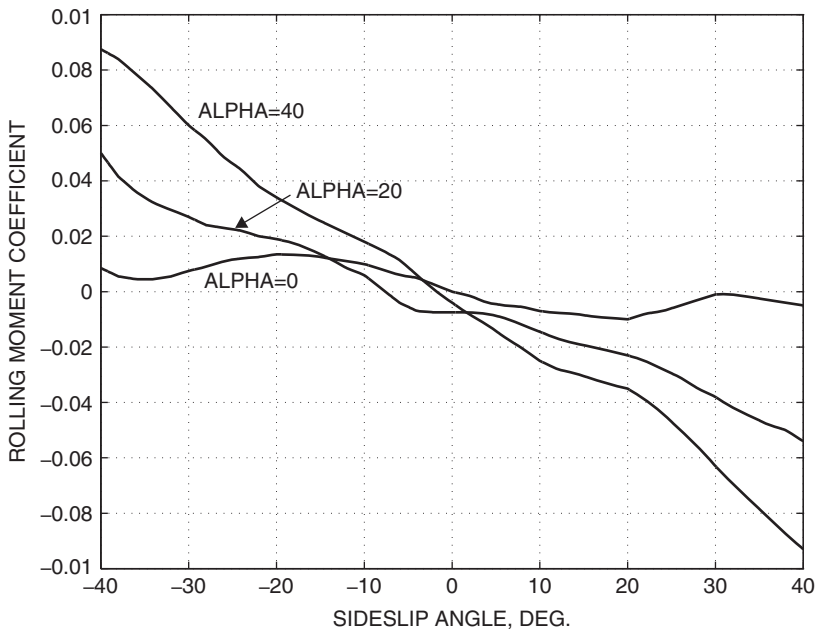


**Figure 2.3-5** Rolling moment coefficient of the F-4B aircraft.

First, note that the angle by which the wings of an aircraft are canted up above the body-axes  $x-y$  plane is called the *dihedral angle*, and a negative dihedral angle is called an *anhedral angle*. Dihedral is often very noticeable on small low-wing (wing root attached at the bottom of the fuselage) aircraft, while a well-known example of anhedral is the Harrier (AV-8B) aircraft. Dihedral (or anhedral) angles give one wing a positive angle of attack (in a spanwise direction) to the lateral component of the relative wind, and the other wing receives a similar negative angle of attack. Referring to Figure 2.3-1, it is easy to see that positive beta creates a negative rolling moment when the wings have positive dihedral. This same effect applies to the horizontal tail.

The second effect of sideslip on the horizontal surfaces occurs when they are swept back. In this case the relative wind is more nearly perpendicular to the leading edge of the windward wing than is the case for the leeward wing. Therefore, the windward wing develops more lift, and the outcome is again a negative rolling moment for positive beta.

The third effect of sideslip on the horizontal surfaces is that on the windward side of the fuselage some of the lateral airflow is diverted up and over the fuselage and some is diverted under the fuselage. This flow will modify the angle of attack of the wings, depending on their position on the fuselage. Above the centerline of the fuselage, the upward component of the relative wind is increased. Therefore, for a high-wing aircraft, the angle of attack of that wing is increased (assuming that it was operating at a positive alpha). For a low-wing aircraft the upward component of the relative wind would be reduced by the effect of the air flowing down and under the

fuselage, and the angle of attack of that wing would be reduced. Thus, for low-wing aircraft, positive sideslip creates a positive contribution to rolling moment, and for high-wing aircraft it creates a negative contribution.

Finally, the lateral component of the relative wind acting on the vertical tail will generate a rolling moment about the cm. Depending on the aircraft angle of attack and the location of the center of pressure of the vertical tail, this rolling moment could be positive or negative. Usually positive beta will produce a negative rolling moment component.

Of all the above effects, only the fuselage effect on a low-wing airplane led to a positive increment in rolling moment in response to a positive increment in beta. This can be a strong effect and is responsible for a loss of stability in roll. Low-wing airplanes usually have noticeable positive dihedral in order to provide positive roll stiffness. The airplanes will then have an inherent tendency to fly with wings level.

For a high-performance aircraft the rolling moment model will typically be of the form

$$C_\ell = C_\ell(\alpha, \beta, M) + \Delta C_{\ell_{\delta a}}(\alpha, \beta, M, \delta_a) + \Delta C_{\ell_{\delta r}}(\alpha, \beta, M, \delta_r) + \frac{b}{2V_T} \left[ C_{\ell_p}(\alpha, M)P + C_{\ell_r}(\alpha, M)R \right], \quad (2.3-18a)$$

where  $C_{\ell_p}$  is the *roll damping derivative*. The rolling moment dependence on  $\beta$ , and the aileron and rudder, can often be linearized around the origin:

$$\begin{aligned} C_\ell(\alpha, \beta, M) &\approx C_{\ell_\beta}(\alpha, M) \times \beta \\ \Delta C_{\ell_{\delta a}}(\alpha, \beta, M, \delta_a) &\approx C_{\ell_{\delta a}}(\alpha, \beta, M) \times \delta_a \\ \Delta C_{\ell_{\delta r}}(\alpha, \beta, M, \delta_r) &\approx C_{\ell_{\delta r}}(\alpha, \beta, M) \times \delta_r, \end{aligned} \quad (2.3-18b)$$

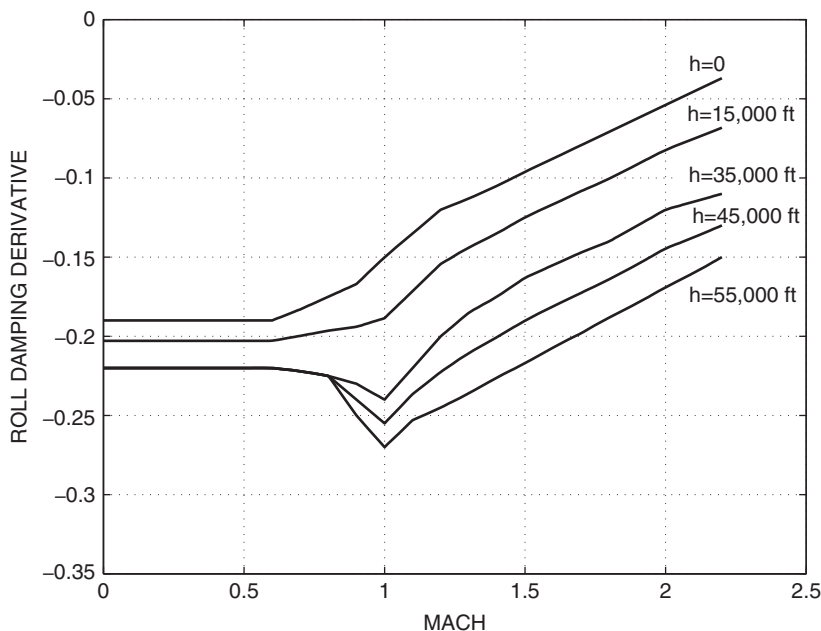
where  $C_{\ell_\beta}$  is the *dihedral derivative* that determines static stability in roll and  $C_{\ell_{\delta a}}$  and  $C_{\ell_{\delta r}}$  are *roll control derivatives*.

Figure 2.3-6 shows the stability-axes, trimmed, roll damping derivative for the F-4C. The data are Mach dependent because of compressibility and altitude dependent because the trimmed angle of attack changes with altitude and because of aeroelastic changes with dynamic pressure.

## Control Effects on Rolling Moment

We now briefly examine the control moment terms in Equations (2.3-18) with respect to their dependence on alpha and Mach. The rudder is intended to provide directional control (yaw), so the “cross-control” effect on rolling moment is an unwanted effect. This effect comes about because the center of pressure of the rudder is normally above the longitudinal axis.

Conventional ailerons mounted outboard on the trailing edge of the wings become ineffective and can reverse their net effect as high subsonic speeds are approached.



**Figure 2.3-6** Roll damping derivative of the F-4C aircraft.

This is because the aileron lift component produced by a downward deflection twists the wing in the direction that reduces its angle of attack and hence reduces the wing lift component. Spoilers, which are uncambered surfaces deflected upward above the aft surface of the wing, “spoil” the lift on that portion of the wing and thus provide roll control. The twisting effect on the wing is reduced and control reversal can be avoided. Spoilers are commonly combined with ailerons in such a way that one aileron and the opposite spoiler operate simultaneously, and the ailerons deflect downward only. Mounting the ailerons farther inboard reduces the effect of wing twist but also reduces their moment arm. However, the X-29 forward-swept-wing aircraft is an example of combined inboard and outboard “flaperons” being made to work very effectively up to high  $\alpha$  (Kandebo, 1988).

The effectiveness of both ailerons and spoilers is reduced by cross-flows on the wing and hence by wing sweep. Therefore, for swept-wing aircraft, an additional rolling moment is obtained by using differential control of the horizontal-tail control surfaces (e.g., most modern fighter aircraft).

## Pitching Moment

The baseline pitching moment coefficient may typically be written as  $C_m(\alpha, M, T_c)$  for a low-speed aircraft or  $C_m(\alpha, M, h)$  for a high-speed jet aircraft where aeroelastic effects are included. Figure 2.3-7a illustrates the dependence of this coefficient on  $\alpha$  and  $T_c$  for the low-speed turboprop transport aircraft. The figure shows that, as



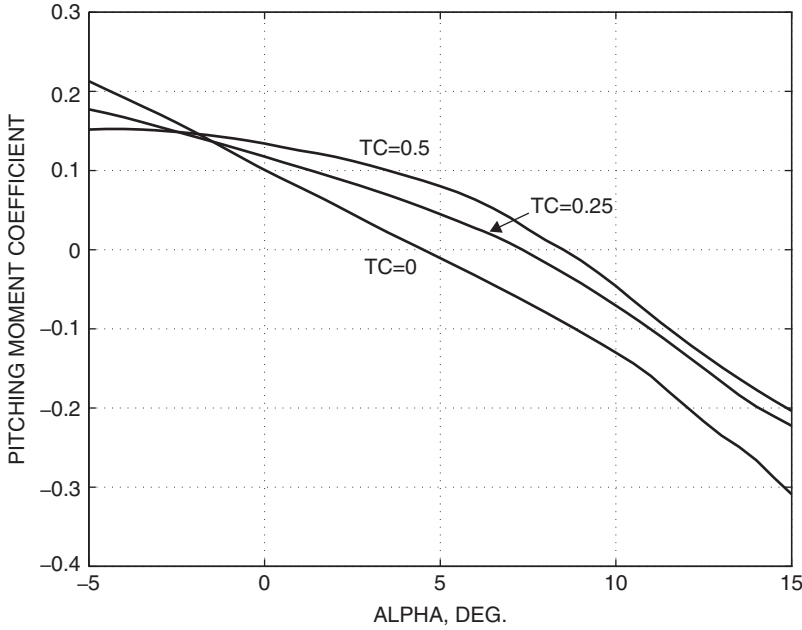


**Figure 2.3-7a** Pitching moment coefficient of a low-speed transport aircraft.

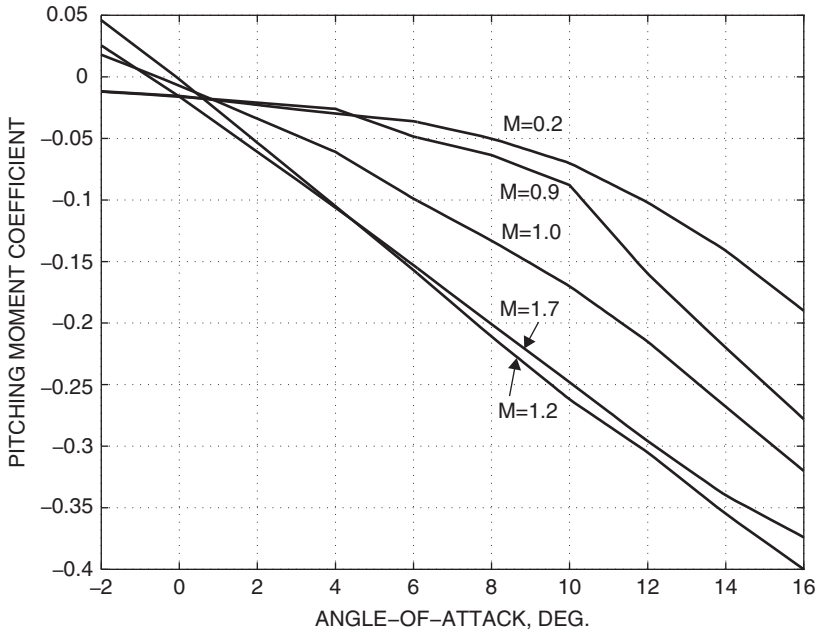
alpha increases, the nose-down (restoring) moment becomes steadily stronger. At low freestream angles of attack and high thrust coefficient, the propeller wash tends to make the effective angle of attack independent of the freestream direction, and the moment curve has only a small negative slope (reduced pitch stiffness).

Figure 2.3-7b shows a baseline moment coefficient that is representative of a supersonic jet-trainer. In this case the parameter is Mach number, and the slope of the moment curve gets steeper with increasing Mach because of the rearward shift of the wing-body aerodynamic center. This increasing pitch stiffness is detrimental to maneuverability and to the lift-over-drag ratio; it is discussed further in the pitch static stability section.

For a high-performance aircraft the pitching moment coefficient will be built up in the form

$$\begin{aligned}
 C_m = & C_m(\alpha, M, h, \delta_F, T_c) + \Delta C_{m_{\delta_e}}(\alpha, M, h, \delta_e) + \frac{\bar{c}}{2V_T} [C_{m_q} \dot{Q} + C_{m_{\dot{\alpha}}} \dot{\alpha}] \\
 & + \frac{x_R}{\bar{c}} C_L + \Delta C_{m_{\text{thrust}}}(\delta_t, M, h) + \Delta C_{m_{\text{gear}}}(h)
 \end{aligned} \tag{2.3-19a}$$

In the baseline term, all five variables are unlikely to be present simultaneously. The  $M$  and  $h$  variables imply a high-speed aircraft, while  $T_c$  implies a low-speed propeller aircraft. Also, the effect of wing flap deflection,  $\delta_F$ , may be treated as



**Figure 2.3-7b** Pitching moment coefficient of a jet trainer aircraft.

a separate increment. The elevator increment term may often be linearized around the origin:

$$\Delta C_{m_{\delta_e}}(\alpha, M, h, \delta_e) \approx C_{m_{\delta_e}}(\alpha, M, h) \times \delta_e, \quad (2.3-19b)$$

where  $C_{m_{\delta_e}}$  is the *elevator control power*. The pitch damping derivative  $C_{m_q}$  and the alpha-dot acceleration derivative will also be functions of alpha, Mach, and altitude and are discussed in Section 2.6. The purpose of the term  $(x_R C_L)/\bar{c}$  is to correct for any  $x$ -displacement ( $x_R$ ) of the aircraft cm from the aerodynamic data reference position. If  $x_R$  is not zero, the lift force will provide a contribution to the pitching moment. This is considered in more detail in the next section. The last two terms represent, respectively, the effect of the engine thrust vector not passing through the aircraft cm and the moment due to landing gear doors and landing gear. This last term is dependent on height above ground because of ground effect.

## Control Effects on Pitching Moment

A conventional elevator for a subsonic aircraft consists of a movable surface at the trailing edge of the horizontal tail. In addition, the horizontal tail may move as a whole, or a “tab” on the elevator may move, so that the elevator deflection can be trimmed to zero in various flight conditions. In transonic and supersonic

flight a shock wave attached to the horizontal tail would render this type of elevator ineffective. Therefore, on supersonic aircraft the complete horizontal stabilizer surface moves (i.e., a “stabilator”) in response to control stick or trim button signals. As indicated above, elevator (or stabilator) control power is dependent on Mach and altitude because compressibility and aeroelastic effects cause the elevator effectiveness to decrease with increasing Mach number and dynamic pressure.

An aft tail experiences a downwash effect from the wing and a reduction in dynamic pressure. These are alpha-dependent effects and can be included in the control power term as implied above. However, for a propeller aircraft, the dynamic pressure at the tail is strongly dependent on thrust coefficient and may be greatly increased. This can be modeled by multiplying the elevator control power by a *tail efficiency factor*,  $\eta$ , which is a function of alpha, thrust coefficient, flap deflection, and ground effect:

$$\eta(\alpha, T_c, \delta_F, h) \equiv \bar{q}_{TAIL}/\bar{q} \quad (2.3-20)$$

The tail efficiency factor of a propeller aircraft may exceed 2.0 at high values of thrust coefficient.

## Yawing Moment

Yawing moments are created by sideslip, by the action of the rudder, by propeller effects, by unbalanced thrust in a two-engine aircraft, and, to a lesser extent, by differences in drag between the ailerons and by asymmetric aerodynamic effects at high alpha (e.g., “vortex shedding”).

The sideslip dependence has three components. A small component is created by wing sweep: Positive sideslip creates a positive yawing moment because the right wing becomes more nearly perpendicular to the freestream direction and develops more lift and drag. Second, the fuselage produces a strong negative yawing moment when in positive sideslip (see, for example, Perkins and Hage, 1949). Third, directional stability demands that the aircraft should tend to weathercock into the relative wind; therefore, it is the job of the vertical tail to provide a strong yawing moment of the same sign as beta. This moment is computed from the moment arm of the tail about the cm and the “lift” generated by the vertical tail when in sideslip. The overall result of these effects is that the yawing moment is quite linear in beta for low values of sideslip.

When the aircraft is at a high angle of attack, the fuselage yawing moment can become more adverse, and at the same time the dynamic pressure at the tail may be reduced, eventually resulting in a loss of directional stability. Figure 2.3-8a shows low-speed, high-alpha, yawing moment data for the F-4B, C aircraft, and clearly shows the loss of directional stability at high alpha.

A rotating propeller produces several different “power effects,” which are best included in the propulsion model (Perkins and Hage, 1949; Ribner, 1943). A conventional tractor propeller has a destabilizing effect in yaw, while a pusher propeller has a stabilizing effect. The slipstream of a tractor propeller strongly affects the dynamic pressure at the tail of the airplane, and the swirl of the slipstream modifies the flow

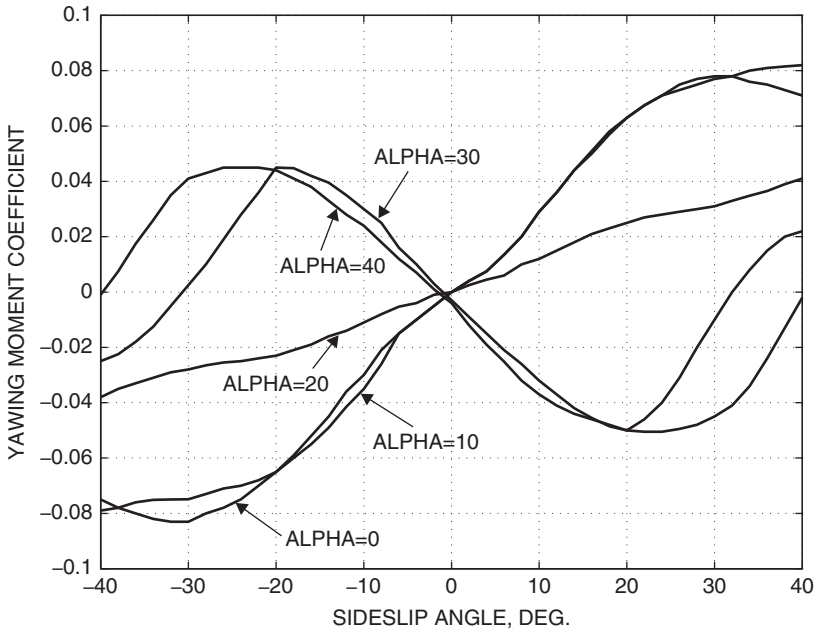


**Figure 2.3-8a** Yawing moment coefficient of the F-4B, C aircraft.

over the fuselage and tail. Thus, the baseline yawing moment can have a strong dependence on thrust coefficient.

Finally, with a high-speed aircraft, compressibility effects can cause the slope of the yawing moment–beta curve to be a function of Mach number. Figure 2.3-8b shows the effect of Mach on the yawing moment of the jet trainer aircraft at low alpha.

The yawing moment coefficient for a high-performance aircraft will be of the form

$$C_n = C_n(\alpha, \beta, M, T_c) + \Delta C_{n_{\delta_r}}(\alpha, \beta, M, \delta_r) + \Delta C_{n_{\delta_a}}(\alpha, \beta, M, \delta_a) + \frac{b}{2V_T} \left[ C_{n_p}(\alpha, M)P + C_{n_r}(\alpha, M)R \right], \quad (2.3-21a)$$

where  $C_{n_r}$  is the yaw damping derivative. The thrust coefficient in the baseline term is appropriate for a propeller aircraft. The yawing moment dependence on  $\beta$ , and the rudder and aileron, can often be linearized around the origin:

$$\begin{aligned} C_n(\alpha, \beta, M, T_c) &\approx C_{n_\beta}(\alpha, M, T_c) \times \beta \\ \Delta C_{n_{\delta_r}}(\alpha, \beta, M, \delta_r) &\approx C_{n_{\delta_r}}(\alpha, \beta, M) \times \delta_r \\ \Delta C_{n_{\delta_a}}(\alpha, \beta, M, \delta_a) &\approx C_{n_{\delta_a}}(\alpha, \beta, M) \times \delta_a, \end{aligned} \quad (2.3-21b)$$

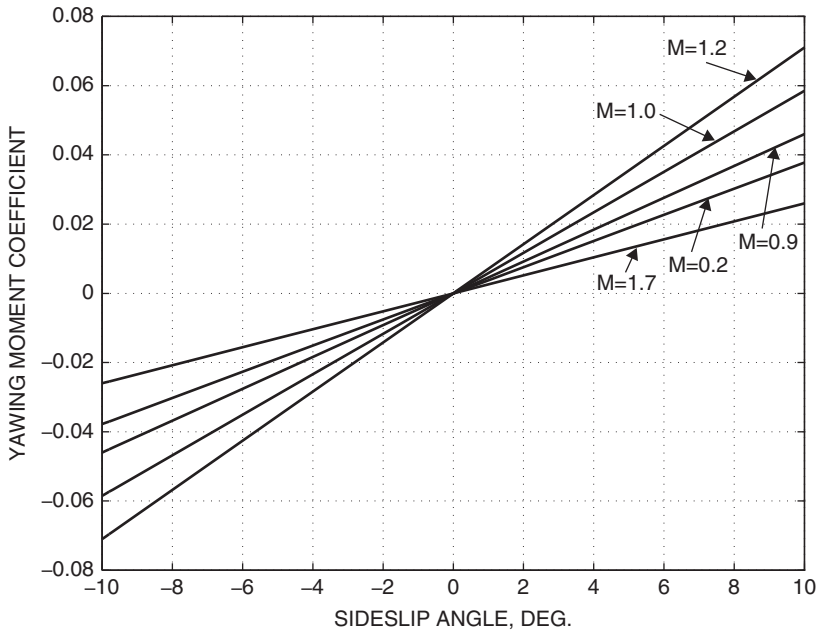


Figure 2.3-8b Yawing moment coefficient of a jet trainer aircraft.

where  $C_{n_\beta}$  is the *yaw stiffness derivative* that determines the directional stability and  $C_{n_{\delta r}}$ ,  $C_{n_{\delta a}}$  are yaw control derivatives.

### Control Effects on Yawing Moment

The rudder usually forms a part of the trailing edge of the vertical tail; when deflected, it provides a strong yawing moment and some rolling moment. Its purpose is to create sideslip (e.g., for cross-wind landing) or remove sideslip (e.g., to coordinate a turn). The vertical tail is no longer a symmetric airfoil section when the rudder is deflected and then begins to produce “lift.” The resulting sideforce is such that deflection of the rudder trailing edge to the right produces a positive yawing moment. All-moving vertical fins are sometimes used for rudder control, as, for example, on the SR-71, where large yawing moments can occur as a result of an engine “unstart.”

Like the horizontal tail, the vertical tail and rudder can be affected by wing downwash and blanketed at high angles of attack. A tail efficiency factor can be used to model the effect, as in the pitching moment equation. Wing flap deflection can also significantly change the downwash at the rudder.

Differential deflection of the ailerons and spoilers also produces a yawing moment because of the difference in drag between the two sets. As described earlier, roll control can be obtained in a number of different ways, and the cross-control effects on yawing moment can vary.

## Data Handling

It should be clear from the foregoing description of aerodynamic forces and moments that the aerodynamic database for a given aircraft can become rather large. It may range from roughly fifty data tables for a relatively simple piloted simulation model to several thousand tables for an aircraft like the Lockheed-Martin F-22. Many of the tables will have four independent variables and could contain over 10,000 data points; the whole database could contain a few million points.

A large aerodynamic database must be handled efficiently within an organization; it represents thousands of hours of planning, model testing, flight testing, and computer simulation. It must be kept current, with all changes fully documented, and be accessible to different users. The control engineer will have access to the database through a computer workstation and will be able to call up the appropriate force and moment routines for the equations of motion. An example of a small database has been given by Nguyen et al. (1979) for low-speed F-16 model data, taken at the NASA Dryden and Langley Research Centers. A three-dimensional plot made from one of the two-dimensional (two independent variables) tables of this F-16 data is shown in Figure 2.3-9. A reduced data set derived from this report is listed in the appendices and is used for the F-16 model given in Chapter 3.

Aerodynamic lookup table data are discrete, whereas aircraft models require data at arbitrary values of the independent variables. This problem is solved by using an

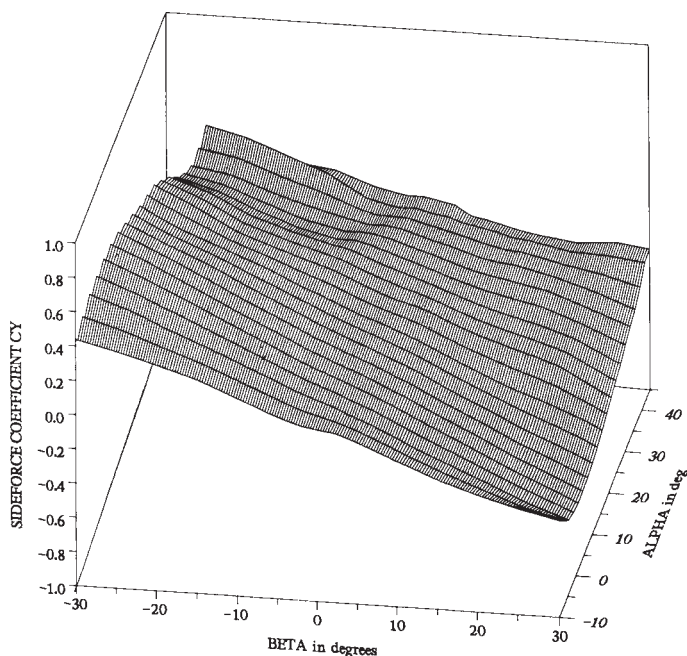


**Figure 2.3-9** Sideforce coefficient of the F-16 model.

interpolation algorithm with the data. In the appendices we have provided a simple interpolation algorithm for use with the F-16 data.

Basic aerodynamic data are often rough (scattered data points). This is because of the inaccuracies associated with measuring aerodynamic data, the sensitivity to small changes in the independent variables, and fusion of data from different sources or test runs. The data can be smoothed and regenerated at new uniform increments of the independent variables as required, for example, by means of a “spline” algorithm [International Mathematical and Statistical Libraries (IMSL), 1980; Press et al., 1989].

## 2.4 STATIC ANALYSIS

In steady-state flight the forces and moments acting on an aircraft are constant (i.e., static) when taken in the body frame. Static analysis provides the basic information for sizing and configuring the aircraft and evaluating its performance and lays the groundwork for dynamic analysis. A “static stability” analysis is used to determine if the aircraft will return to a steady-state flight condition after being subjected to a small atmospheric disturbance. For example, an incremental increase in Mach number can produce a net increase in thrust minus drag and cause a relatively slow departure, in speed, from the equilibrium condition. In contrast, an unstable departure in pitch could be too fast for the pilot to control and could lead to structural failure. The static stability analysis is so-called because rate-dependent effects are not considered, and it is usually performed for the special case of wings-level, nonturning flight. Dynamic stability in all of the motion variables can be determined from the eigenvalues of the linearized equations of motion and is considered in Chapters 3 and 4. It can easily be performed in other steady-state flight conditions, for example, a steady turn.

### Static Equilibrium

Here we consider only wings-level, zero-sideslip flight. Suitable coordinate systems for this analysis are the body-fixed axes and the stability axes (now coincident with the wind axes). We must bear in mind that the origin of these systems, the aircraft cm, is not a fixed point. The cm will move as fuel is drawn from different tanks or because of cargo movement or stores being dropped. Aerodynamic data are referred to a fixed point, typically the point inside the fuselage where a line joining the quarter-chord points, in the wing roots, intersects the plane of symmetry.

Figure 2.4-1 shows the forces and moments on the aircraft. In the figure,  $R(x_R, 0, z_R)$  is the reference point for the aerodynamic moment data,  $C$  is the aircraft cm, and  $T$  is the quarter-chord point (in the plane of symmetry) of the horizontal tail. The term  $\mathbf{F}_R$  is the resultant aerodynamic force on the aircraft,  $L$  and  $D$  are its lift and drag components, and  $\mathbf{M}_R$  is the total aerodynamic moment at  $R$ . With respect to the aircraft cm, the position vectors of  $R$  and the quarter-chord point in the horizontal tail are, respectively,  $\mathbf{r}_R$  and  $\mathbf{r}_T$ . The chord line of the horizontal tail has an incidence

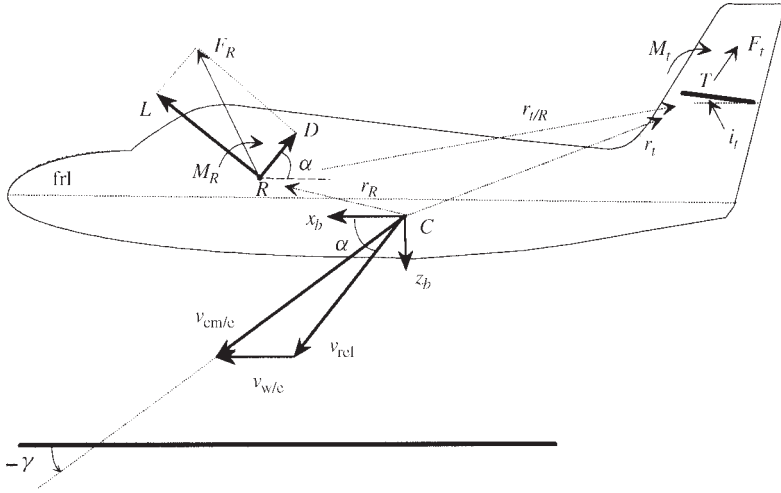


**Figure 2.4-1** Diagram for calculating pitching moment.

angle  $i_t$  to the fuselage reference line. The thrust vector  $\mathbf{F}_T$  (not shown) is assumed to lie in the plane of symmetry, tilted up at an angle  $\alpha_T$  to the fuselage reference line, and does not necessarily pass through the cm.

To determine the equilibrium conditions, the direction of the gravity vector must be known relative to the aircraft. The *flight-path angle*  $\gamma$  shown in the figure is the angle that the velocity vector  $\mathbf{v}_{CM/e}$  makes with the NE plane and is positive when the aircraft is climbing. For simplicity the wind velocity will be taken to be zero so that  $\mathbf{v}_{rel} = \mathbf{v}_{CM/e}$ , and alpha and the flight-path angle will determine orientation relative to the gravity vector. Then summing force components along the  $x$  and  $z$  stability axes yields

$$F_T \cos(\alpha_{frl} + \alpha_T) - D - mg_D \sin \gamma = 0 \quad (2.4-1a)$$

$$F_T \sin(\alpha_{frl} + \alpha_T) + L - mg_D \cos \gamma = 0 \quad (2.4-1b)$$

The moment at the cm is given by

$$\mathbf{M}_{CM} = \mathbf{M}_R + \mathbf{r}_R \times \mathbf{F}_R + \mathbf{M}_p, \quad (2.4-2)$$

where  $\mathbf{M}_p$  is the pitching moment created directly by the engines. Using body-axes components in the cross-product yields the equilibrium equation

$$0 = M_{CM} = M_R + x_R F_N + z_R F_X + M_p, \quad (2.4-3)$$

where the normal force,  $F_N$ , and axial force,  $F_X$ , are given by

$$F_N = L \cos \alpha_{frl} + D \sin \alpha_{frl}$$

$$F_X = L \sin \alpha_{frl} - D \cos \alpha_{frl}$$



Now divide (2.4-3) by  $(\bar{q}S\bar{c})$  to obtain dimensionless moment coefficients,

$$C_{m_{CM}} = C_{m_R} + \frac{x_R}{\bar{c}} C_N + \frac{z_R}{\bar{c}} C_X + C_{m_p}, \quad (2.4-4)$$

where  $C_{m_p}$  is thrust moment made dimensionless by dividing by  $(\bar{q}S\bar{c})$ , and

$$\begin{aligned} C_N &= [C_L \cos \alpha_{frl} + C_D \sin \alpha_{frl}] \approx C_L \text{ in cruise,} \\ C_X &= [C_L \sin \alpha_{frl} - C_D \cos \alpha_{frl}] \end{aligned} \quad (2.4-5)$$

In equilibrium, the left-hand side of Equation (2.4-4) is zero, and in cruise conditions,  $\cos \alpha_{frl} \approx 1$ ,  $\sin \alpha_{frl} \approx \alpha_{frl}$ ,  $C_L \gg C_D$ ,  $C_N \gg C_X$ . Normally, the coordinates  $x_R$  and  $z_R$  are both small, and either one could be zero.

In *performance analysis* we solve the nonlinear equilibrium equations (2.4-1) and (2.4-4) for a given flight condition (true airspeed and altitude) using an iterative computer algorithm [(Problem (2.4-1))]. The data required are  $F_T(M, h, \delta_i)$ , aerodynamic data— $C_L(\alpha, M, \delta e)$ ,  $C_D(\alpha, M, \delta e)$ ,  $C_{m_R}(\alpha, M, \delta e)$ —and an atmosphere model to determine mass density and the speed of sound at any altitude. Effects such as flaps and gear can be included if required. If the effect of elevator deflection on lift and drag is ignored, then the force equations are independent of the moment equation.

### Effect of the Horizontal Tail

Now suppose that  $\mathbf{F}_{wb}$  and  $\mathbf{M}_{R,wb}$  are the aerodynamic force and moment vectors at  $R$  when the horizontal tail is removed from the aircraft. The flow over the wing-body combination creates a downwash effect at the horizontal-tail position and a change in dynamic pressure, both of which are dependent on flight conditions. These effects will be modeled later. Let  $\mathbf{F}_t$  and  $\mathbf{M}_{c/4,t}$  be the force and moment vectors measured at the quarter-chord point of the isolated horizontal tail when it is placed in the same flow-field that exists at the tail position of the wing-body combination. Also, assume that putting the horizontal tail back on the wing-body combination does not significantly modify the wing-body flowfield. With these assumptions, we can write

$$\mathbf{M}_{CM} = \mathbf{M}_{R,wb} + \mathbf{M}_{c/4,t} + \mathbf{r}_R \times \mathbf{F}_{wb} + \mathbf{r}_t \times \mathbf{F}_t + \mathbf{M}_p \quad (2.4-6a)$$

$$\mathbf{F}_R = \mathbf{F}_{wb} + \mathbf{F}_t \quad (2.4-6b)$$

In order to have the tail position specified in terms of a fixed vector, let

$$\mathbf{r}_t = \mathbf{r}_R + \mathbf{r}_{t/R},$$

where  $\mathbf{r}_{t/R}$  is shown in the figure. Then from Equations (2.4-6a) and (2.4-6b),

$$\mathbf{M}_{CM} = \mathbf{M}_{R,wb} + \mathbf{M}_{c/4,t} + \mathbf{r}_R \times \mathbf{F}_R + \mathbf{r}_{t/R} \times \mathbf{F}_t + \mathbf{M}_p \quad (2.4-7)$$

The aerodynamic moment vector at the cm has the same  $y$  component  $M$  in either body or stability axes; other components are zero because of the symmetrical flight

condition. Equation (2.4-7) will be evaluated using the body-fixed components of the reference point and the horizontal tail. It will be assumed that the aerodynamic data reference point, tail quarter-chord point, and center of mass are at the same height in the fuselage, so that the  $z$ -components disappear from the equation. This allows conclusions to be drawn about the effect of the longitudinal position of the cm on static stability, with much less cumbersome equations; it is also usually a good approximation in practice. Equation (2.4-7) then yields the scalar equation:

$$\begin{aligned} M_{CM} = & M_{R,wb} + M_{c/4,t} + x_R[L \cos(\alpha_{frl}) + D \sin(\alpha_{frl})] \\ & + (x_t - x_R)[L_t \cos(\alpha_{frl} - \epsilon) + D_t \sin(\alpha_{frl} - \epsilon)] + M_p \end{aligned} \quad (2.4-8)$$

In this equation  $\epsilon$  is the *downwash angle* at the horizontal tail and is usually positive with a magnitude of a few degrees. It represents the effect of the wings and fuselage on the direction of flow at the tail and is a function of the aircraft angle of attack and thrust effects (Roskam, 1979). The tail lift,  $L_t$ , and drag,  $D_t$ , are defined relative to the direction  $(\alpha_{frl} - \epsilon)$ . In addition to the downwash effect at the tail, the airflow over the tail is modified in speed by the effect of the wings and body. This effect is modeled by the tail efficiency  $[\eta]$ , Equation (2.3-20)].

The tail lift and drag are computed from  $\bar{q}_t$  and tail reference area  $S_t$ . Therefore, dividing Equation (2.4-8) by  $(\bar{q}\bar{c}S)$  yields

$$\begin{aligned} C_{m_{CM}} = & C'_m m_R + \frac{x_R}{\bar{c}}[C_L \cos(\alpha_{frl}) + C_D \sin(\alpha_{frl})] \\ & - \eta \bar{V}_H[C_{L_t} \cos(\alpha_{frl} - \epsilon) + C_{D_t} \sin(\alpha_{frl} - \epsilon)] + C_{m_p}, \end{aligned} \quad (2.4-9)$$

where

$$C'_m = C_{m_{R,wb}} + \eta \frac{\bar{c}_t S_t}{\bar{c} S} C_{m_{c/4,t}} \quad (2.4-10)$$

and  $\bar{V}_H$  is a modification of the *horizontal-tail volume ratio* [Equation (2.6-35)], given by

$$\bar{V}_H = -\frac{(x_t - x_R)S_t}{\bar{c}S} \quad (2.4-11)$$

$\bar{V}_H$  is constant and positive for an aft tail because its numerator contains the distance of the reference point ahead of the tail. Note that, in the normal range of  $\alpha$ , the drag terms in (2.4-9) can be discarded. A study of the moment equation will tell us how much elevator deflection is required to trim the aircraft and the effect of movement of the aircraft cm on trimmed elevator deflection.

## Static Stability Analysis in Pitch

We focus here on the pitching moment equation and the requirements on the aircraft configuration for static stability in pitch. Static directional and rolling stability are considered in Section 2.6, in conjunction with the stability derivatives.

The moment balance around the pitch axis of the aircraft is critical to both performance and stability. If the lift force generated by the wings and body creates a large moment about the cm, the horizontal tail must carry a significant load. If this is a download, the overall effect is additional drag with a net reduction in lift and reduced load-carrying efficiency. In Section 2.2 we saw that the moment about the airfoil aerodynamic center was constant and relatively small, and for positive pitch stiffness, the axis about which the airfoil pivoted needed to be ahead of the ac. Therefore, the cm of the aircraft should be ahead of the ac of the wing-body combination, and the pitch stiffness of the complete aircraft must be analyzed. We also saw in Section 2.2 that the zero-alpha moment  $M_0$  needed to be positive in order to obtain equilibrium with a positive angle of attack (and therefore provide the design lift). For a conventional aircraft this is achieved by giving the horizontal tail a negative incidence, so that it provides a positive contribution to the total pitching moment. Efficiency can be improved by reducing the pitch stiffness [this is done in relaxed static stability (RSS) designs], but then the movement of the cm must be more carefully controlled and the flight control system may need to be designed to provide artificial stability.

As in Section 2.2, to determine the static stability in pitch we need to find the slope of the pitching moment–alpha curve. Therefore, we must differentiate, with respect to  $\alpha_{frl}$ , the total pitching moment at the center of mass as given by (2.4-9). In this equation each trigonometric function is multiplied by an aerodynamic coefficient that is also a function of alpha. In addition, tail efficiency and downwash angle are functions of alpha, and differentiation produces a very cumbersome expression. Nevertheless, the expression can be simplified by making use of the relationships

$$\begin{aligned}\alpha_t &= \alpha_{frl} + i_t - \epsilon \\ \partial\alpha_t / \partial\alpha_{frl} &= 1 - \partial\epsilon / \partial\alpha_{frl}\end{aligned}\tag{2.4-12a}$$

and, for the wing and body, the approximations

$$\left. \begin{array}{l} C_L \sin \alpha_{frl} \\ C_D \cos \alpha_{frl} \\ C_{D_\alpha} \sin \alpha_{frl} \end{array} \right\} \ll C_{L_\alpha} \cos \alpha_{frl}\tag{2.4-12b}$$

and for the tail

$$\left. \begin{array}{l} (\partial\epsilon / \partial\alpha_{frl}) C_{L_t} \sin(\alpha_{frl} - \epsilon) \\ (\partial\epsilon / \partial\alpha_{frl}) C_{D_t} \cos(\alpha_{frl} - \epsilon) \\ (1 - \partial\epsilon / \partial\alpha_{frl}) C_{D_{\alpha,t}} \sin(\alpha_{frl} - \epsilon) \end{array} \right\} \ll (1 - \partial\epsilon / \partial\alpha_{frl}) C_{L_{\alpha,t}} \cos(\alpha_{frl} - \epsilon)\tag{2.4-12c}$$

These are normally very good approximations. Equation (2.4-9) can now be differentiated with respect to  $\alpha_{frl}$ , and the above approximations applied, leading to

$$C_{m_\alpha} = \frac{\partial C'_{m_R}}{\partial \alpha} + \frac{x_R}{\bar{c}} C_{L_\alpha} \cos(\alpha_{frl}) - \bar{V}_H \left[ \eta \left( 1 - \frac{\partial \varepsilon}{\partial \alpha} \right) C_{L_{\alpha,t}} + \frac{\partial \eta}{\partial \alpha} C_{L_t} \right] \cos(\alpha_{frl} - \varepsilon) + \frac{\partial C_{m_p}}{\partial \alpha}, \quad (2.4-13)$$

where the first term in this equation is given by

$$\frac{\partial C'_{m_R}}{\partial \alpha} = \frac{\partial C_{m_{R,wb}}}{\partial \alpha} + \frac{\bar{c}_t S_t}{\bar{c} S} \left[ \frac{\partial \eta}{\partial \alpha} C_{m_{c/4,t}} + \eta \frac{\partial C_{m_{c/4,t}}}{\partial \alpha} \right] \quad (2.4-14)$$

We will also make use of (2.4-9) with the drag terms neglected:

$$C_{m_{CM}} \approx C'_{m_R} + \frac{x_R}{\bar{c}} C_L \cos(\alpha_{frl}) - \eta \bar{V}_H C_{L_t} \cos(\alpha_{frl} - \varepsilon) + C_{m_p} \quad (2.4-15)$$

For positive stiffness in pitch, of a conventional aircraft, Equation (2.4-13) must yield a negative value for  $C_{m_\alpha}$ , and this must occur in equilibrium [ $C_{m_{CM}} = 0$  in Equation (2.4-15)] at a positive angle of attack. An examination of the terms in these equations will show how this is possible.

On the right-hand side of Equation (2.4-15), the first term ( $C'_{m_R}$ ) will be small and negative for a normally cambered airfoil, the second term will be negative when the cm is forward of the reference point (which is a requirement for  $C_{m_\alpha} < 0$ ), and so the third term must be chosen to overcome these negative contributions. The volume coefficient  $\bar{V}_H$  is positive, and so  $C_{L_t}$  is made negative by giving the tail a negative incidence and/or using an upside-down cambered airfoil. The incidence is chosen so that the total pitching moment is positive at small angles of attack and becomes zero at the desired positive value of  $\alpha_{frl}$ . Trim adjustments are made with an elevator “tab” or by using an “all-flying” tail, and control adjustments are made by using the elevator to effectively change the camber of the horizontal-tail airfoil. The remaining term  $C_{m_p}$  will be variable with flight conditions, but the thrust line must be kept close enough to the cm to keep it small.

In the  $C_{m_\alpha}$  equation (2.4-13), the first term on the right-hand side is small because the reference points are close to aerodynamic centers. The second term is of major importance; if the cm is aft of the aerodynamic reference point,  $x_R$  is positive and this term provides a positive (destabilizing) contribution to  $C_{m_\alpha}$ .

The third term contains tail efficiency (always positive) and the complement of the “downwash slope.” A good deal of information is available about the derivative of the downwash angle with respect to alpha (Roskam, 1979). Its value depends on the distance of the tail from the wing and on Mach number and is typically about 0.5 at low subsonic Mach numbers. Since the lift-curve slope is always positive below the stall, the term will provide a negative contribution to  $C_{m_\alpha}$ .

The fourth term contains the derivative of tail efficiency with respect to  $\alpha_{frl}$ . Tail efficiency can be strongly dependent on alpha, thrust coefficient, and flap setting. For

example, the four-engine, turboprop heavy transport aircraft, whose pitching moment is given in Figure 2.3-7a, has the tail at the same height on the fuselage as the wing and relatively close to the wing. For this aircraft the tail efficiency rises rapidly to a peak at several degrees  $\alpha$  and then falls rapidly. The height of the peak increases strongly with thrust coefficient and can be higher than  $\eta = 2.0$  but is reduced by increasing amounts of flap. The slope  $\partial\eta/\partial\alpha$  can be greater than 10/rad, with no flaps, high  $T_c$ , and at a few degrees  $\alpha$ . At zero thrust coefficient, the tail efficiency is slightly less than unity, and the slope  $\partial\eta/\partial\alpha$  is approximately constant and slightly negative. Since  $C_{L_t}$  had to be made negative, this fourth term is destabilizing for normal thrust coefficients and  $\alpha$ . This could have been observed from physical reasoning, since we know that the tail efficiency behavior makes the tail more effective at producing a download as  $\alpha$  increases.

The fifth term in (2.4-13) is the derivative of the propulsion system moment coefficient with angle of attack. Power effects are very complex, especially for propeller aircraft. The existing mathematical models do not necessarily give very good results, and experimental data from powered models are needed. The reader is referred to the literature for more details (Perkins and Hage, 1949; Ribner, 1943; Stinton, 1983).

In summary, an aft-tail aircraft will become statically unstable in pitch if the cm is moved too far aft by incorrect loading. Conversely, if we regard the aerodynamic data reference point as movable and at the aircraft aerodynamic center, then as the aerodynamic center moves aft with increasing subsonic Mach number, an aircraft will become more stable in pitch. The lift-to-drag penalty becomes worse as the aerodynamic center moves aft, and for high-performance military aircraft there is a strong incentive to use “relaxed static stability.”

## Neutral Point

The *neutral point* is the cm position for which  $C_{m_\alpha} = 0$ . It is therefore an “aerodynamic center” for the whole aircraft. To find a relationship involving the neutral point, we return to the tail-on moment equation, Equation (2.4-4). If we now differentiate this equation with respect to  $\alpha_{fr}$ , we obtain

$$C_{m_\alpha} = \frac{\partial C_{m_R}}{\partial \alpha} + \frac{x_R}{\bar{c}} C'_N(\alpha) + \frac{z_R}{\bar{c}} C'_X(\alpha) + \frac{\partial C_{m_P}}{\partial \alpha}, \quad (2.4-16)$$

where the primes on  $C_N$  and  $C_X$  denote their derivatives with respect to  $\alpha$ , which can be calculated by differentiating Equations (2.4-5).

Let  $x_{R/np}$  and  $z_{R/np}$  be the coordinates of the reference point when the body-fixed coordinate system has its origin at the neutral point. Then by definition of the neutral point,  $C_{m_\alpha}$  becomes zero when we insert these coordinates into Equation (2.4-16). If we solve the resulting equation for the derivative of  $C_{m_R}$  and substitute it into Equation (2.4-16), we obtain

$$C_{m_\alpha} = \frac{(x_R - x_{R/np})}{\bar{c}} C'_N(\alpha) + \frac{(z_R - z_{R/np})}{\bar{c}} C'_X(\alpha) \quad (2.4-17)$$

This equation for  $C_{m_\alpha}$  holds over the complete range of  $\alpha$  and Mach. An additional independent equation is needed if we require a solution for the coordinates of the neutral point. A universally used approximation is obtained by neglecting the  $z$ -component in this equation and using the approximations (2.4-12) in  $C'_N$ . The result is

$$C_{m_\alpha} = \frac{(x_R - x_{R/np})}{\bar{c}} C_{L_\alpha} \cos(\alpha_{frl}) \quad (2.4-18)$$

The  $x$ -difference in this equation is the position of the aerodynamic data reference point with respect to the neutral point. It can be written in terms of distances measured in the aft direction, from the leading edge of the wing mean aerodynamic chord (mac) to the cm and to the neutral point. Thus, let distance measured aft from the leading edge be divided by  $\bar{c}$  and denoted by  $h$ . Then, Equation (2.4-18) becomes

$$C_{m_\alpha} = -(h_{np} - h_{cm}) C_{L_\alpha} \cos(\alpha_{frl}) \quad (2.4-19)$$

In this equation the  $h$ -difference in parentheses is called the *static margin*;  $h_{cm}$  might typically be 0.25 (chords), and  $h_{np}$  might typically be 0.30 (chords), and then the static margin would be 0.05.

A conventionally balanced aircraft is usually designed to have a minimum (worst-case loading) positive static margin of between 3 and 5% (0.03 to 0.05). This is for safety reasons and to allow some margin for cm variations with load conditions. Aircraft that operate into the transonic and supersonic regions pay a price for this low-speed static stability. The aerodynamic center of an airfoil tends to shift aft from  $0.25\bar{c}$  toward  $0.5\bar{c}$  in going from high subsonic speeds to supersonic speeds (see Section Basic Aerodynamics). This causes a corresponding movement in the aircraft neutral point and a large increase in the static margin. The undesirable consequences are increased trim drag (and therefore reduced range or fuel economy) and reduced maneuverability. Some modern military aircraft (notably the F-16) have minimized these penalties by using a reduced, or negative, static margin at subsonic speeds. Since negative pitch stiffness normally leads to dynamic instability in pitch, these aircraft use an automatic control system to restore pitch stability. This is described in later chapters.

## 2.5 THE NONLINEAR AIRCRAFT MODEL

In this section the aerodynamic force and moment models will be combined with the vector equations of motion to obtain aircraft models for simulation and for analytical purposes. For simplicity, the treatment will be limited to the flat-Earth equations of motion. First, the vector equations will be expanded with the translational velocity state equation expressed in terms of velocity components in the aircraft body-fixed system. The resulting equations are well conditioned when all of these components become zero (e.g., hovering motion or sitting on the runway), and body-axes equations are the best choice for general flight simulation.

On the other hand, for the purposes of linearizing the equations of motion and studying the dynamic behavior, it is better to have the velocity equation in terms of stability or wind-axes variables: airspeed and aerodynamic angles. A convenient way to introduce these variables is to treat the stability and wind axes as being fixed to frames that are rotating relative to the vehicle-body frame. The angular velocity vector then involves alpha-dot or beta-dot, and these become state derivatives in the state-space model. In addition, the drag, lift, and cross-wind force each appear in separate state equations and, under certain conditions, the equations decouple into two sets describing, separately, the *longitudinal motion* (pitching and translation in the geographic vertical plane) and *lateral-directional motion* (rolling, sideslipping, and yawing). The “stability” or “wind-axes” equations are therefore useful for deriving simpler, small perturbation models that can be used for linear analysis and design.

## Model Equations

(i) **Body-Axes Equations** For convenience the flat-Earth equations of motion (1.7-18) are repeated here:

$$\begin{aligned}
 C_{frd/tp} &= fn(\Phi) \\
 \dot{\Phi} &= H(\Phi) \omega_{b/e}^{frd} \\
 {}^e \mathbf{p}_{cm/Q}^{tp} &= C_{tp/frd} \mathbf{v}_{cm/e}^{frd} \\
 {}^b \dot{\mathbf{v}}_{cm/e}^{frd} &= \frac{1}{m} \mathbf{F}^{frd} + C_{frd/tp} \mathbf{g}^{tp} - \tilde{\omega}_{b/e}^{frd} \mathbf{v}_{cm/e}^{frd} \\
 {}^b \dot{\omega}_{b/e}^{frd} &= (\mathbf{J}^{frd})^{-1} \left[ \mathbf{M}^{frd} - \tilde{\omega}_{b/e}^{frd} \mathbf{J}^{frd} \omega_{b/e}^{frd} \right]
 \end{aligned} \tag{2.5-1}$$

with the auxiliary equation

$$\mathbf{v}_{rel}^{frd} = \mathbf{v}_{cm/e}^{frd} - C_{frd/tp} \mathbf{v}_{W/e}^{tp} \tag{2.5-2}$$

Let the tangent-plane components of the position vector and the *frd* components of the velocity vector be given by, respectively,

$$\mathbf{p}_{cm/Q}^{tp} \equiv [p_N \ p_E \ p_D]^T, \quad \mathbf{v}_{cm/e}^{frd} \equiv [U \ V \ W]^T$$

The body-axes components of the angular velocity vector and the Euler angles are

$$\omega_{b/e}^{frd} \equiv [P \ Q \ R]^T, \quad \Phi \equiv [\phi \ \theta \ \psi]^T$$

Therefore, the state vector for the body-axes equations is

$$\mathbf{X} = [p_N \ p_E \ p_D \ \phi \ \theta \ \psi \ U \ V \ W \ P \ Q \ R]^T \tag{2.5-3}$$

Given a value for the state vector, the Euler angle and position derivatives can be evaluated immediately. They are shown in expanded form in Table 2.5-1, with the substitution  $\dot{h} = -\dot{p}_D$  for vertical velocity.

The remaining translational and angular velocity state equations require the aerodynamic forces and moments and therefore a calculation of the relative wind. Let the wind have tangent-plane components

$$\mathbf{v}_{W/e}^{ip} = [W_N \ W_E \ W_D]^T$$

Then (2.5-2) can be used to find the vehicle velocity relative to the surrounding air:

$$\mathbf{v}_{rel}^{frd} = [U' \ V' \ W']^T$$

For lack of a convenient alternative, let the wind enter the model through the control vector, so a typical control vector will be

$$\bar{U} = [\delta_t, \delta_e, \delta_a, \delta_r, W_N, W_E, W_D]^T \quad (2.5-4)$$

Additional inputs can be created as needed for flaps, gear, speed brake, and so on, and for derivatives of wind velocity components.

The dynamic pressure, Mach number, and aerodynamic angles must now be calculated from the true airspeed (Table 2.3-1):

$$V_T = |\mathbf{v}_{rel}| \quad (2.5-5a)$$

$$\bar{q} = \frac{1}{2} \rho(h) V_T^2 \quad (2.5-5b)$$

$$M = M(V_T, h) \quad (2.5-5c)$$

$$\alpha = \tan^{-1} (W' / U') \quad (2.5-5d)$$

$$\beta = \sin^{-1} (V' / V_T), \quad (2.5-5e)$$

where a model of the standard atmosphere is used to calculate  $\rho(h)$  and  $M(V_T, h)$ . Next compute installed thrust and the body-axes aerodynamic coefficients, transforming from stability or wind axes, as necessary, and using the component buildup equations from Section 2.3. The state derivatives alpha-dot and beta-dot cannot yet be calculated, so we must either neglect  $C_{L_{\dot{\alpha}}}$  and  $C_{Y_{\dot{\beta}}}$  or use approximate values of alpha-dot and beta-dot (e.g., from the last simulation time step). Control surface deflections must come either directly from the pilot via the control vector or from additional state-variable models representing actuator dynamics. The aerodynamic and thrust forces can now be calculated (subscripts  $A$  and  $T$  will be used, respectively, to denote aerodynamic and thrust components):

$$C_{(\ )} = C_{(\ )}(\alpha, \beta, M, h, \delta_S, P, Q, R) \quad (2.5-6a)$$

$$\mathbf{F}_{A,T}^{frd} = \mathbf{F}_T^{frd} + \bar{q} S [C_X \ C_Y \ C_Z]^T \quad (2.5-6b)$$

and the translational velocity state equation can be expanded as shown in Table 2.5-1.



The aerodynamic angle rates,  $\alpha$ -dot, and  $\beta$ -dot [(Equations (2.3-10))] must now be found. If the gust response of the aircraft must be modeled, then the relative wind equation (2.5-2) must be differentiated, and the derivative of the direction cosine matrix can be found from Poisson's kinematical equations (Section 1.8). Otherwise, when studying the dynamics of the aircraft, it is usual to set the wind to zero and use the derivatives of  $U$ ,  $V$ , and  $W$  to find the aerodynamic angle rates. The aerodynamic and thrust moments can be calculated in the form

$$C_{(\cdot)} = C_{(\cdot)}(\alpha, \beta, M, h, \delta_S, \dot{\alpha}, \dot{\beta}, P, Q, R) \quad (2.5-7a)$$

$$\mathbf{M}_{A,T}^{frd} = \mathbf{M}_T^{frd} + \bar{q}S[\mathbf{b}C_\ell \quad \bar{c}C_m \quad bC_n]^T \quad (2.5-7b)$$

and the angular velocity state equation can be evaluated. The expansion of this "moment equation" is repeated in Table 2.5-1. This completes the body-axis 6-DoF equations.

**(ii) Wind- or Stability-Axes Equations** A nonlinear model in terms of the state variables

$$\mathbf{X}^T = [V_T \ \beta \ \alpha \ \phi \ \theta \ \psi \ P_s \ Q \ R_s] \quad (2.5-8)$$

will be constructed here and, as described in the Section 2.5 introduction, will be found to have advantages for linearization and decoupling. Equations (1.7-20) show that the flat-Earth force equations (velocity state equations) are dependent only on the relative velocity,  $\mathbf{v}_{rel}$ , and they are an appropriate starting point here.

**TABLE 2.5-1 The Flat-Earth, Body-Axes 6-DoF Equations**

Force equations

$$\begin{aligned} \dot{U} &= RV - QW - g_D \sin \theta + (X_A + X_T)/m \\ \dot{V} &= -RU + PW + g_D \sin \phi \cos \theta + (Y_A + Y_T)/m \\ \dot{W} &= QU - PV + g_D \cos \phi \cos \theta + (Z_A + Z_T)/m \end{aligned}$$

Kinematic equations

$$\begin{aligned} \dot{\phi} &= P + \tan \theta (Q \sin \phi + R \cos \phi) \\ \dot{\theta} &= Q \cos \phi - R \sin \phi \\ \dot{\psi} &= (Q \sin \phi + R \cos \phi) / \cos \theta \end{aligned}$$

Moment equations

$$\begin{aligned} \Gamma \dot{P} &= J_{xz} [J_x - J_y + J_z] PQ - [J_z(J_z - J_y) + J_{xz}^2] QR + J_z \ell + J_{xz} n \\ J_y \dot{Q} &= (J_z - J_x) PR - J_{xz}(P^2 - R^2) + m \\ \Gamma \dot{R} &= [(J_x - J_y)J_x + J_{xz}^2] PQ - J_{xz}[J_x - J_y + J_z] QR + J_{xz} \ell + J_x n \\ \cdot \Gamma &= J_x J_z - J_{xz}^2 \end{aligned}$$

Navigation equations

$$\begin{aligned} \dot{p}_N &= U c \theta c \psi + V (-c \phi s \psi + s \phi s \theta c \psi) + W (s \phi s \psi + c \phi s \theta c \psi) \\ \dot{p}_E &= U c \theta s \psi + V (c \phi c \psi + s \phi s \theta s \psi) + W (-s \phi c \psi + c \phi s \theta s \psi) \\ \dot{h} &= U s \theta - V s \phi c \theta - W c \phi c \theta \end{aligned}$$

(a) *Force Equations:* As an expedient way of deriving these equations, imagine the stability axes as fixed in a new “stability frame” with angular velocity vector  $-\dot{\alpha} \mathbf{j}$  with respect to the body frame. Similarly, imagine the wind axes as fixed in a new “wind frame” with angular velocity  $\dot{\beta} \mathbf{k}$  with respect to the stability frame. The flat-Earth force equation (1.7-20), with steady wind, reduces to

$${}^b \dot{\mathbf{v}}_{rel} = (1/m) \mathbf{F}_{A,T} + \mathbf{g} - \boldsymbol{\omega}_{b/e} \times \mathbf{v}_{rel} \quad (2.5-9)$$

Let the derivative taken in the body frame be replaced with a derivative taken in the wind frame:

$${}^w \dot{\mathbf{v}}_{rel} + \boldsymbol{\omega}_{w/b} \times \mathbf{v}_{rel} = (1/m) \mathbf{F}_{A,T} + \mathbf{g} - \boldsymbol{\omega}_{b/e} \times \mathbf{v}_{rel} \quad (2.5-10)$$

Resolving these vectors in wind axes gives the matrix equation

$${}^w \dot{\mathbf{v}}_{rel}^w + \tilde{\boldsymbol{\omega}}_{w/b}^w \mathbf{v}_{rel}^w = (1/m) \mathbf{F}_{A,T}^w + C_{w/b} C_{b/n} \mathbf{g}^n - \tilde{\boldsymbol{\omega}}_{b/e}^w \mathbf{v}_{rel}^w \quad (2.5-11)$$

The cross-product matrix on the left-hand side can be determined as follows. If  $\alpha$ -dot is greater than zero, the angle of attack is increasing and the stability frame is undergoing a left-handed rotation about the body  $y$ -axis, relative to the body frame. Also, if  $\beta$ -dot is greater than zero, the wind frame is undergoing a right-handed rotation around the stability  $z$ -axis, relative to the stability frame. Therefore,

$$\boldsymbol{\omega}_{s/b}^s = \boldsymbol{\omega}_{s/b}^b = \begin{bmatrix} 0 & -\dot{\alpha} & 0 \end{bmatrix}^T \quad (2.5-12a)$$

$$\boldsymbol{\omega}_{w/s}^w = \boldsymbol{\omega}_{w/s}^s = \begin{bmatrix} 0 & 0 & \dot{\beta} \end{bmatrix}^T \quad (2.5-12b)$$

Now

$$\boldsymbol{\omega}_{w/b} = \boldsymbol{\omega}_{w/s} + \boldsymbol{\omega}_{s/b} \quad (2.5-13)$$

and so

$$\boldsymbol{\omega}_{w/b}^w = \begin{bmatrix} 0 \\ 0 \\ \dot{\beta} \end{bmatrix} + \begin{bmatrix} c\beta & s\beta & 0 \\ -s\beta & c\beta & 0 \\ 0 & 0 & 1 \end{bmatrix} \begin{bmatrix} 0 \\ -\dot{\alpha} \\ 0 \end{bmatrix} = \begin{bmatrix} -\dot{\alpha} s\beta \\ -\dot{\alpha} c\beta \\ \dot{\beta} \end{bmatrix} \quad (2.5-14)$$

Then the left-hand side of the force equation becomes

$${}^w \dot{\mathbf{v}}_{rel}^w + \tilde{\boldsymbol{\omega}}_{w/b}^w \mathbf{v}_{rel}^w = \begin{bmatrix} \dot{V}_T \\ \dot{\beta} V_T \\ \dot{\alpha} V_T \cos \beta \end{bmatrix} \quad (2.5-15)$$

This array contains the derivatives of the first three state variables in (2.5-8).

The aerodynamic and thrust force term can now be calculated as follows. Again, for simplicity, assume that the thrust vector lies in the  $x_b$ - $z_b$  plane but is inclined at an angle  $\alpha_T$  to the fuselage reference line (so that positive  $\alpha_T$  corresponds to a component of thrust in the negative  $z_b$  direction). Then it is easy to write the stability-axis components of thrust and transform to wind axes:

$$\mathbf{F}_{A,T}^w = \begin{bmatrix} c\beta & s\beta & 0 \\ -s\beta & c\beta & 0 \\ 0 & 0 & 1 \end{bmatrix} \begin{bmatrix} \mathbf{F}_T \cos(\alpha + \alpha_T) \\ 0 \\ \mathbf{F}_T \sin(\alpha + \alpha_T) \end{bmatrix} - \begin{bmatrix} D \\ C \\ L \end{bmatrix} \quad (2.5-16)$$

where

$$F_T = |\mathbf{F}_T|$$

In wind axes the gravity term is given by

$$\mathbf{g}^w = C_{w/b} C_{b/n} \begin{bmatrix} 0 \\ 0 \\ g_D \end{bmatrix} \equiv \begin{bmatrix} g_1 \\ g_2 \\ g_3 \end{bmatrix},$$

where the components are

$$\begin{aligned} g_1 &= g_D(-c\alpha c\beta s\theta + s\beta s\phi s\theta + s\alpha c\beta c\phi c\theta) = -g_D \sin(\gamma) \\ g_2 &= g_D(c\alpha s\beta s\theta + c\beta s\phi c\theta - s\alpha s\beta c\phi c\theta) \\ g_3 &= g_D(s\alpha s\theta + c\alpha c\phi c\theta) \end{aligned} \quad (2.5-17)$$

[See (3.6-2) to introduce  $\gamma$  into the first equation.] The remaining cross-product is given by

$$\boldsymbol{\omega}_{b/e}^w \mathbf{v}_{rel}^w = [0 \quad V_T R_w \quad -V_T Q_w]^T, \quad (2.5-18)$$

where  $R_w = R_s$  and  $Q_w = (-P_s \sin \beta + Q \cos \beta)$ .

When all of these terms are assembled, the force equations are

$$\begin{aligned} m \dot{V}_T &= F_T \cos(\alpha + \alpha_T) \cos \beta - D + m g_1 \\ m \dot{\beta} V_T &= -F_T \cos(\alpha + \alpha_T) \sin \beta - C + m g_2 - m V_T R_s \\ m \dot{\alpha} V_T \cos \beta &= -F_T \sin(\alpha + \alpha_T) - L + m g_3 + m V_T (Q \cos \beta - P_s \sin \beta) \end{aligned} \quad (2.5-19)$$

It is evident that, if lift and cross-wind force include a linear dependence on the state derivatives  $\alpha$ -dot and  $\beta$ -dot, respectively, the equations can be solved for these state derivatives. Unfortunately, this requires a nonzero airspeed  $V_T$ . However, we will show that these equations are useful for constructing a small-perturbation model of aircraft dynamics.

**(b) Moment Equations:** In the moment equation (2.5-1e) the derivative taken in the body frame can be replaced with a derivative taken in the stability or wind frame; the

form of the equation is the same in either case. The stability frame will be shown later to be a more convenient choice; thus,

$${}^s\dot{\mathbf{w}}_{b/e}^{bf} + (\mathbf{w}_{s/b} \times \mathbf{w}_{b/e})^{bf} = (J^{bf})^{-1} [\mathbf{M}_{A,T}^{bf} - \tilde{\mathbf{w}}_{b/e}^{bf} J^{bf} \mathbf{w}_{b/e}^{bf}] \quad (2.5-20)$$

Now change from body-axes to stability-axes components, insert a cross-product matrix for  $(\mathbf{w} \times)^s$ , and solve for the derivatives:

$${}^s\dot{\mathbf{w}}_{b/e}^s = -\tilde{\mathbf{w}}_{s/b}^s \mathbf{w}_{b/e}^s + (J^s)^{-1} [\mathbf{M}_{A,T}^s - \tilde{\mathbf{w}}_{b/e}^s J^s \mathbf{w}_{b/e}^s] \quad (2.5-21)$$

where the stability-axes inertia matrix is

$$J^s = C_{s/b} J^b C_{b/s} \quad (2.5-22)$$

Equation (2.5-22) has an extra term compared to the body-axes moment equation and offers no advantages for simulation. It does have advantages for deriving a small-perturbation model because it introduces alpha-dot into the small-perturbation moment equations in a formal manner, as will be shown in the next section. If we had wished to introduce beta-dot, it would have been necessary to convert to wind axes (Stevens and Lewis, 1992).

Consider the terms in the stability-axes moment equation; starting with the inertia matrix. We will restrict ourselves to aircraft having a plane of symmetry, so that the body-axes inertia matrix is given by Equation (1.7-9). When the transformation (2.5-22) is performed, the matrix is found to have the same structure in stability axes:

$$J^s = \begin{bmatrix} J'_x & 0 & -J'_{xz} \\ 0 & J'_y & 0 \\ -J'_{xz} & 0 & J'_z \end{bmatrix}, \quad (2.5-23)$$

where

$$J'_x = J_x \cos^2 \alpha + J_z \sin^2 \alpha - J_{xz} \sin 2\alpha$$

$$J'_y = J_y$$

$$J'_z = J_x \sin^2 \alpha + J_z \cos^2 \alpha + J_{xz} \sin 2\alpha$$

$$J'_{xz} = \frac{1}{2} (J_x - J_y) \sin 2\alpha + J_{xz} \cos 2\alpha$$

Furthermore, the inverse of this matrix is easily found and is again of the same form:

$$(J^s)^{-1} = \frac{1}{\Gamma} \begin{bmatrix} J'_z & 0 & J'_{xz} \\ 0 & \Gamma/J'_y & 0 \\ J'_{xz} & 0 & J'_x \end{bmatrix} \quad (2.5-24)$$

with

$$\Gamma = J'_x J'_z - J'^2_{xz} \quad (= J_x J_z - J_{xz}^2, \quad \text{Problem 2.5-3})$$

Note that in wind axes  $J^w$  is a full matrix, so that working in stability axes is considerably more convenient, provided that we can neglect beta-dot derivatives in the moment equations. Other terms in the moment equation are

$$\begin{aligned} {}^s\dot{\omega}_{b/e}^s &= [\dot{P}_s \quad \dot{Q} \quad \dot{R}]^T \\ \omega_{s/b}^s &= [0 - \dot{\alpha} \quad 0]^T \\ \tilde{\omega}_{s/b}^s \omega_{b/e}^s &= \dot{\alpha} [-R_s \quad 0 \quad P_s]^T \end{aligned} \quad (2.5-25)$$

The stability-axes moment equations (2.5-21) can now be written in component form as

$$\begin{bmatrix} \dot{P}_s \\ \dot{Q} \\ \dot{R}_s \end{bmatrix} = -\dot{\alpha} \begin{bmatrix} -R_s \\ 0 \\ P_s \end{bmatrix} + \frac{1}{\Gamma} \begin{bmatrix} J'_z & 0 & J'_{xz} \\ 0 & \Gamma/J'_y & 0 \\ J'_{xz} & 0 & J'_x \end{bmatrix} \begin{bmatrix} \ell_s \\ m \\ n_s \end{bmatrix} - \tilde{\omega}_{b/e}^s J^s \omega_{b/e}^s \quad (2.5-26)$$

The last term is of the same form as the corresponding term in the body-axes moment equations; it will not need to be expanded.

### Decoupling of the Nonlinear Equations/3-DOF Longitudinal Model

Most aircraft spend most of their flying time in a wings-level steady-state flight condition and, since the model of the 3-DoF motion in a vertical plane is much simpler than the 6-DoF model, it is worthwhile investigating the equations of motion under the wings-level flight condition. Referring to the force equations (2.5-19), if the roll angle  $\phi$  is zero, the gravity terms are greatly simplified:

$$\begin{aligned} g_1 &= -g_D \sin \gamma = -g_D \cos \beta \sin(\theta - \alpha) \\ g_2 &= g_D [\sin \theta \cos \alpha - \cos \theta \sin \alpha] \sin \beta = g_D \sin \beta \sin(\theta - \alpha) \\ g_3 &= g_D [\sin \alpha \sin \theta - \cos \alpha \cos \theta] = g_D \cos(\theta - \alpha) \end{aligned} \quad (2.5-27)$$

When the sideslip is small, the flight-path angle is given by the difference between pitch attitude and angle of attack, and so the gravity terms become

$$\begin{aligned} g_1 &= -g_D \sin(\gamma) \\ g_2 &= \beta g_D \sin(\gamma) \\ g_3 &= g_D \cos(\gamma) \end{aligned} \quad (2.5-28)$$

and the force equations (2.5-19) reduce to

$$\begin{aligned} m \dot{V}_T &= F_T \cos(\alpha + \alpha_T) - D - m g_D \sin \gamma \\ m \dot{\beta} V_T &= -\beta F_T \cos(\alpha + \alpha_T) - C + \beta m g_D \sin \gamma - m V_T R_s \\ m \dot{\alpha} V_T &= -F_T \sin(\alpha + \alpha_T) - L + m g_D \cos \gamma + m V_T (Q - \beta P_s) \end{aligned} \quad (2.5-29)$$

The first and third equations describe longitudinal motion and, when beta is negligible, are independent of the second (sideslip) equation.

Decoupling of the longitudinal motion also occurs in the attitude equations and the moment equations. It can be seen from the kinematic equations in Table 2.5-1 that when the roll angle is zero,

$$\dot{\theta} = Q \quad (2.5-30)$$

The body-axes moment equations in Table 2.5-1 show that, if the roll and yaw rates ( $P$  and  $R$ ) are small, the pitching moment equation is not coupled to the rolling and yawing moment equations, and

$$J_Y \dot{Q} = m \quad (2.5-31)$$

Therefore, we can obtain a model for pure longitudinal motion by adding Equations (2.5-30) and (2.5-31) to the decoupled longitudinal force equations:

$$\begin{aligned} m \dot{V}_T &= F_T \cos(\alpha + \alpha_T) - D - m g_D \sin(\theta - \alpha) \\ m \dot{\alpha} V_T &= -F_T \sin(\alpha + \alpha_T) - L + m g_D \cos(\theta - \alpha) + m V_T Q \\ \dot{\theta} &= Q \\ \dot{Q} &= m/J_y \end{aligned} \quad (2.5-32)$$

The state vector for these equations is

$$X = [V_T \quad \alpha \quad \theta \quad Q]^T \quad (2.5-33)$$

A common alternative model uses flight-path angle as a state variable in place of pitch attitude:

$$\begin{aligned} m \dot{V}_T &= F_T \cos(\alpha + \alpha_T) - D - m g_D \sin \gamma \\ m \dot{\gamma} V_T &= F_T \sin(\alpha + \alpha_T) + L - m g_D \cos \gamma \\ \dot{\alpha} &= Q - \dot{\gamma} \\ \dot{Q} &= m/J_y \end{aligned} \quad (2.5-34)$$

These longitudinal models are used for a variety of purposes, from performance analysis to automatic control system design. If the lift and drag forces are linearized for small perturbations from a specified flight condition, we obtain linear longitudinal equations that are the same as those derived in the next section by a formal linearization of the complete 6-DoF equations followed by decoupling.

## 2.6 LINEAR MODELS AND THE STABILITY DERIVATIVES

When we perform a computer simulation to evaluate the performance of an aircraft with its control systems, we almost invariably use a nonlinear model. Also, the linear equations needed for control systems design will mostly be derived by numerical

methods from the nonlinear computer model. Because the nonlinear state models are difficult to handle without the use of a digital computer, most of the early progress in understanding the dynamics of aircraft and the stability of the motion came from studying linear algebraic small-perturbation equations. G. H. Bryan (1911) introduced the idea of perturbed forces and moments with respect to a “steady-state” flight condition, and this approach is still in use. The small-perturbation equations are linear equations derived algebraically from nonlinear equations like those of Section 2.5. In these equations the nonlinear aerodynamic coefficients are replaced by terms involving the aerodynamic derivatives described briefly in Section 2.3.

There are two good reasons, apart from their historical importance, for algebraically deriving the small-perturbation equations. First, the aerodynamic derivatives needed for the linear equations can be estimated relatively quickly (Hoak et al., 1970) before nonlinear aerodynamic data become available. Second, the algebraic small-perturbation equations provide a great deal of insight into the relative importance of the various aerodynamic derivatives under different flight conditions and their effect on the stability of the aircraft motion. In preparation for deriving the linear equations we now examine the concept of a steady-state flight condition.

### Singular Points and Steady-State Flight

In the preceding section, when the body-axes force equations were used,  $\alpha$ -dot or  $\beta$ -dot force dependence created a difficulty in that the state equations became implicit in the derivatives of the states  $\alpha$  and  $\beta$ . This problem was solved in an ad hoc manner by using the wind-axes equations and collecting linear  $\alpha$ -dot or  $\beta$ -dot terms on one side of the equations. In this section where the goal is to derive linear equations algebraically, we take a more general approach, starting with *implicit state equations* in the general form

$$f(\dot{X}, X, \bar{U}) = 0, \quad (2.6-1)$$

where  $f$  is an array of  $n$  scalar nonlinear functions  $f_i$ , as in (1.1-1).

In the theory of nonlinear systems (Vidyasagar, 1978) the concept of a *singular point*, or *equilibrium point*, of an autonomous (no external control inputs) time-invariant system is introduced. The coordinates of a singular point of the implicit nonlinear state equations are given by a solution,  $X = X_e$ , which satisfies

$$f(\dot{X}, X, \bar{U}) = 0, \quad \text{with } \dot{X} \equiv 0; \bar{U} \equiv 0 \text{ or constant} \quad (2.6-2)$$

This idea has strong intuitive appeal; the system is “at rest” when all of the derivatives are identically zero, and then one may examine the behavior of the system near the singular point by slightly perturbing some of the variables. If, in the case of an aircraft model, the state trajectory departs rapidly from the singular point in response to a small perturbation in, say, pitch attitude, the human pilot is unlikely to be able to control this aircraft.

Steady-state aircraft flight can be defined as a condition in which all of the force and moment components in the body-fixed coordinate system are constant or zero.

It follows that the aerodynamic angles and the angular rate components must be constant, and their derivatives must be zero. It must be assumed that the aircraft mass remains constant. In the case of the round-Earth equations, minor circles (and the major circle around the equator) are the only trajectories along which gravity remains constant in magnitude.

Assuming that the flat-Earth equations are satisfactory for all of our control system design purposes, the definition allows steady wings-level flight and steady turning flight. Furthermore, if the change in atmospheric density with altitude is neglected, a wings-level climb and a climbing turn are permitted as steady-state flight conditions. In this case the *ned* position equations do not couple back into the equations of motion and need not be used in finding a steady-state condition. Therefore, the steady-state conditions that are important to us for control system design can be defined in terms of the remaining nine state variables of the flat-Earth equations as follows:

### Steady-State Flight

$$\dot{P}, \dot{Q}, \dot{R}, \text{ and } \dot{U}, \dot{V}, \dot{W} \text{ (or } \dot{V}_T, \dot{\beta}, \dot{\alpha}) \equiv 0, \text{ controls fixed} \quad (2.6-3a)$$

with the following additional constraints according to the flight condition:

$$\begin{aligned} \text{STEADY WINGS-LEVEL FLIGHT:} \quad & \phi, \dot{\phi}, \dot{\theta}, \dot{\psi} \equiv 0 \quad (\because P, Q, R \equiv 0) \\ \text{STEADY TURNING FLIGHT:} \quad & \dot{\phi}, \dot{\theta} \equiv 0, \quad \dot{\psi} \equiv \text{TURN RATE} \\ \text{STEADY PULL-UP:} \quad & \phi, \dot{\phi}, \dot{\psi} \equiv 0, \quad \dot{\theta} \equiv \text{PULL-UP RATE} \\ \text{STEADY ROLL:} \quad & \dot{\theta}, \dot{\psi} \equiv 0, \quad \dot{\phi} \equiv \text{ROLL RATE} \end{aligned} \quad (2.6-3b)$$

The steady-state conditions  $\dot{P}, \dot{Q}, \dot{R} \equiv 0$  require the angular rates to be zero or constant (as in steady turns), and therefore the aerodynamic and thrust moments must be zero or constant. The conditions  $\dot{U}, \dot{V}, \dot{W} \equiv 0$  require the airspeed, angle of attack, and sideslip angle to be constant, and hence the aerodynamic forces must be zero or constant. Therefore, the steady-state pull-up (or push-over) and steady-state roll conditions can only exist instantaneously. However, it is useful to be able to linearize the aircraft dynamics in these flight conditions since the control systems must operate there.

While a pilot may not find it very difficult to put an aircraft into a steady-state flight condition, the mathematical model requires the solution of the simultaneous nonlinear equations (2.6-2). In general, because of the nonlinearity, a steady-state solution can only be found by using a numerical method on a digital computer. Multiple solutions can exist, and a feasible solution will emerge only when practical constraints are placed on the variables. We consider this problem in Chapter 3 and assume here that a solution  $X_e, \bar{U}_e$  is known for the desired flight condition.



## Linearization

The implicit nonlinear equations will be written as

$$\begin{aligned} f_1(\dot{X}, X, \bar{U}) &= 0 \\ f_2(\dot{X}, X, \bar{U}) &= 0 \\ &\vdots \\ f_9(\dot{X}, X, \bar{U}) &= 0 \end{aligned} \tag{2.6-4}$$

and will be obtained from the wind-axes force equations, kinematic equations, and stability-axes moment equations, by moving all nonzero terms to the right-hand side of the equations. The reduced state vector is

$$X = [V_T \ \beta \ \alpha \ \phi \ \theta \ \psi \ P_s \ Q_s \ R_s]^T \tag{2.6-5a}$$

The control vector, given by (2.5-4), is reduced here to

$$\bar{U} = [\delta_i \ \delta_e \ \delta_a \ \delta_r]^T \tag{2.6-5b}$$

We now consider small perturbations from the steady-state condition  $X_e, \bar{U}_e$  and derive a set of linear constant-coefficient state equations. If we expand the nonlinear state equations (2.6-4) in a Taylor series about the equilibrium point  $(X_e, \bar{U}_e)$  and keep only the first-order terms, we find that the perturbations in the state, state derivative, and control vectors must satisfy

$$\begin{aligned} \nabla_{\dot{X}} f_1 \ \delta \dot{X} + \nabla_X f_1 \ \delta X + \nabla_{\bar{U}} f_1 \ \delta \bar{U} &= 0 \\ \vdots \quad \vdots \quad \quad \quad \vdots \quad \vdots \quad \quad \quad \vdots \quad \vdots \\ \nabla_{\dot{X}} f_9 \ \delta \dot{X} + \nabla_X f_9 \ \delta X + \nabla_{\bar{U}} f_9 \ \delta \bar{U} &= 0 \end{aligned} \tag{2.6-6}$$

In this equation,  $\nabla$  (del, or nabla) represents a row array of first partial derivative operators, for example,

$$\nabla_X f_i \equiv \left[ \frac{\partial f_i}{\partial X_1} \ \frac{\partial f_i}{\partial X_2} \quad \cdots \quad \frac{\partial f_i}{\partial X_n} \right]$$

Each term in (2.6-6) is a scalar product; thus,  $\nabla_X f_1 \ \delta X$  is the total differential of  $f_1$  due to simultaneous perturbations in all the elements of the state vector.

Equations (2.6-6) can now be written in implicit linear state-variable form as

$$E\dot{x} = Ax + Bu \tag{2.6-7}$$

Lowercase notation has been used to indicate that  $x$  and  $u$  are perturbations from the equilibrium values of the state and control vectors. The coefficient matrices

$$E = - \begin{bmatrix} \nabla_{\dot{X}} f_1 \\ \vdots \\ \nabla_{\dot{X}} f_9 \end{bmatrix}_{\substack{\bar{U}=\bar{U}_e \\ X=X_e}} \quad A = \begin{bmatrix} \nabla_x f_1 \\ \vdots \\ \nabla_x f_9 \end{bmatrix}_{\substack{\bar{U}=\bar{U}_e \\ X=X_e}} \quad B = \begin{bmatrix} \nabla_U f_1 \\ \vdots \\ \nabla_U f_9 \end{bmatrix}_{\substack{\bar{U}=\bar{U}_e \\ X=X_e}} \quad (2.6-8)$$

are called *Jacobian matrices* and must be calculated at the equilibrium point. If  $E$  is nonsingular, (2.6-7) can be rewritten as an explicit set of linear state equations, but we will see later that this is not necessarily the most convenient way to use the implicit state equations.

The Jacobian matrices  $E, A, B$  will be evaluated three rows at a time, corresponding, respectively, to the wind-axes force equations ( $f_1$  to  $f_3$ ), kinematic equations ( $f_4$  to  $f_6$ ), and moment equations ( $f_7$  to  $f_9$ ). The evaluation will be for the steady, level flight condition, with the additional constraint of no sideslip ( $\beta = 0$ ). The latter condition greatly simplifies the algebra involved in the linearization and leads to “lateral-longitudinal” decoupling. Therefore, the equilibrium (steady-state) conditions are

STEADY-STATE CONDITIONS FOR LINEARIZATION:

$$\beta, \phi, P, Q, R \equiv 0$$

$$\text{All derivatives} \equiv 0 \quad (2.6-9)$$

$$V_T = V_{T_e}, \alpha = \alpha_e, \theta = \theta_e, \psi \equiv 0, \gamma_e \equiv 0$$

The algebra can be further reduced by taking advantage of some features of the equations. Thus, when differentiating products containing  $\cos \beta$  or  $\cos \phi$ , all of the resulting  $\sin \beta$  or  $\sin \phi$  terms will disappear when we apply the  $\beta = 0$  and  $\phi = 0$  equilibrium conditions. Therefore, the  $\cos \beta$  or  $\cos \phi$  terms can be set to unity before differentiation. Similarly, a  $\cos \beta$  or  $\cos \phi$  in the denominator of a quotient term can be set to unity. Also, if two or more terms with equilibrium values of zero (e.g.,  $\sin \beta$ ,  $\sin \phi$ ) occur in a product term, this product can be discarded before differentiation.

**The Linearized Force Equations** The first three rows of the linear equations (2.6-7) will now be obtained by performing the gradient operations, shown in (2.6-8), on the nonlinear force equations (2.5-19). All of the terms in (2.5-19) will be moved to the right-hand side of the equations. First, we find the partial derivatives with respect to  $\dot{X}$  and use the steady-state condition (2.6-9). The thrust is assumed to be independent of the state derivatives; this gives

$$- \begin{bmatrix} \nabla_{\dot{X}} f_1 \\ \nabla_{\dot{X}} f_2 \\ \nabla_{\dot{X}} f_3 \end{bmatrix}_{X=X_e} = \begin{bmatrix} m \nabla_{\dot{X}} \dot{V}_T + \nabla_{\dot{X}} D \\ m V_T \nabla_{\dot{X}} \dot{\beta} + \nabla_{\dot{X}} C \\ m V_T \nabla_{\dot{X}} \dot{\alpha} + \nabla_{\dot{X}} L \end{bmatrix} \quad (2.6-10)$$

A term such as  $\nabla_{\dot{X}} \dot{V}_T$  is simply a row array with unity in the position corresponding to the  $\dot{V}_T$  state derivative and zeros elsewhere. The other terms, such as  $\nabla_{\dot{X}} L$ , are row arrays containing all of the partial derivatives of the forces with respect to the state derivatives.

The partial derivatives of the aerodynamic forces and moments with respect to other variables are the *aerodynamic derivatives*, first introduced in Section 2.3. Table 2.6-1 defines the derivatives that are normally significant in the force equations. These derivatives are called the *dimensional derivatives*, and later we will introduce a related set of derivatives that have been made dimensionless in the same way that the aerodynamic coefficients are made dimensionless. The dimensional derivatives are given the symbols  $X$ ,  $Y$ , and  $Z$  to indicate which force component is involved (the symbols  $D$ ,  $C$ , and  $L$  are also used). Their subscripts indicate the quantity with respect to which the derivative is taken [subscripts for the controls were defined in (2.6-5b)].

For the purpose of deriving the linear equations, only the derivatives shown in the table will be assumed to be nonzero. Therefore, the terms  $\nabla_{\dot{X}} D$  and  $\nabla_{\dot{X}} C$  in (2.6-10) will now be dropped (additional terms will be dropped later). Note that the components involved in the partial derivatives are wind-axes components, except for the engine thrust  $F_T$ . This force belongs naturally to the aircraft-body axes, and it only appears in the wind-axes equations in conjunction with trigonometric functions of the aerodynamic angles.

We will interpret (2.6-10) in terms of the dimensional derivatives. The array  $\nabla_{\dot{X}} L$  contains only the derivative  $Z_{\dot{\alpha}}$  (multiplied by  $m$ ) in the  $\dot{\alpha}$  position, so (2.6-10) can now be rewritten as

$$- \begin{bmatrix} \nabla_{\dot{X}} f_1 \\ \nabla_{\dot{X}} f_2 \\ \nabla_{\dot{X}} f_3 \end{bmatrix}_{X=X_e} = m \begin{bmatrix} 1 & 0 & 0 & 0 & 0 & 0 & 0 & 0 & 0 \\ 0 & V_{T_e} & 0 & 0 & 0 & 0 & 0 & 0 & 0 \\ 0 & 0 & V_{T_e} - Z_{\dot{\alpha}} & 0 & 0 & 0 & 0 & 0 & 0 \end{bmatrix} \quad (2.6-11)$$

**TABLE 2.6-1 The Force Dimensional Derivatives**

X-AXIS	Y-AXIS	Z-AXIS
$X_V = \frac{-1}{m} \frac{\partial D}{\partial V_T}$	$Y_{\beta} = -\frac{1}{m} \left( \frac{\partial C}{\partial \beta} + D_e \right)$	$Z_V = \frac{-1}{m} \frac{\partial L}{\partial V_T}$
$X_{T_V} = \frac{1}{m} \frac{\partial F_T}{\partial V_T}$	$Y_p = -\frac{1}{m} \frac{\partial C}{\partial P_s}$	$Z_{\alpha} = \frac{-1}{m} \left( D_e + \frac{\partial L}{\partial \alpha} \right)$
$X_{\alpha} = \frac{1}{m} \left( L_e - \frac{\partial D}{\partial \alpha} \right)$	$Y_r = -\frac{1}{m} \frac{\partial C}{\partial R_s}$	$Z_{\dot{\alpha}} = \frac{-1}{m} \frac{\partial L}{\partial \dot{\alpha}}$
$X_{\delta_e} = \frac{-1}{m} \frac{\partial D}{\partial \delta_e}$	$Y_{\delta_r} = -\frac{1}{m} \frac{\partial C}{\partial \delta_r}$	$Z_q = \frac{-1}{m} \frac{\partial L}{\partial Q}$
$X_{\delta_t} = \frac{1}{m} \frac{\partial F_T}{\partial \delta_t}$	$Y_{\delta_a} = -\frac{1}{m} \frac{\partial C}{\partial \delta_a}$	$Z_{\delta_e} = \frac{-1}{m} \frac{\partial L}{\partial \delta_e}$

Next, using (2.5-19), form the partial derivatives with respect to  $X$  and apply the steady-state conditions (2.6-9). The result is

$$\begin{bmatrix} \nabla_X f_1 \\ \nabla_X f_2 \\ \nabla_X f_3 \end{bmatrix} = \begin{bmatrix} -F_T \sin(\alpha_e + \alpha_T) \nabla_X \alpha + \cos(\alpha_e + \alpha_T) \nabla_X F_T - mg_D \cos \gamma_e \nabla_X (\theta - \alpha) - \nabla_X D \\ -F_T \cos(\alpha_e + \alpha_T) \nabla_X \beta + mg_D (\sin \gamma_e \nabla_X \beta + \cos \theta_e \nabla_X \phi) - \nabla_X C - mV_{T_e} \nabla_X R_s \\ -F_T \cos(\alpha_e + \alpha_T) \nabla_X \alpha - \sin(\alpha_e + \alpha_T) \nabla_X F_T + mg_D \sin \gamma_e \nabla_X (\alpha - \theta) - \nabla_X L + mV_{T_e} \nabla_X Q \end{bmatrix} \quad (2.6-12)$$

This result can be further reduced by using the steady-state conditions, obtained by setting the left-hand side of (2.5-19) to zero, to replace some groups of terms by the steady-state lift and drag forces. Thus, the partial derivatives evaluated at the equilibrium point are

$$\begin{bmatrix} \nabla_X f_1 \\ \nabla_X f_2 \\ \nabla_X f_3 \end{bmatrix}_{\substack{\bar{U}=\bar{U}_e \\ X=X_e}} = \begin{bmatrix} \cos(\alpha_e + \alpha_T) \nabla_X F_T - \nabla_X D + L_e \nabla_X \alpha - mg_D \cos \gamma_e \nabla_X \theta \\ -\nabla_X C - D_e \nabla_X \beta + mg_D \cos \theta_e \nabla_X \phi - mV_{T_e} \nabla_X R_s \\ -\sin(\alpha_e + \alpha_T) \nabla_X F_T - \nabla_X L - D_e \nabla_X \alpha - mg_D \sin \gamma_e \nabla_X \theta + mV_{T_e} \nabla_X Q \end{bmatrix} \quad (2.6-13)$$

where  $\alpha_e$ ,  $\theta_e$ ,  $\gamma_e$ ,  $L_e$ , and  $D_e$  are the steady-state values. Note that there is no steady-state sideforce. If this expression is interpreted in terms of the derivatives from Table 2.6-1, we obtain for the right-hand side:

$$m \begin{bmatrix} X_V + X_{T_V} \cos(\alpha_e + \alpha_T) & 0 & X_\alpha & 0 & -g_D \cos \gamma_e & 0 & 0 & 0 & 0 \\ 0 & Y_\beta & 0 & g_D \cos \theta_e & 0 & 0 & Y_p & 0 & Y_r - V_{T_e} \\ Z_V - X_{T_V} \sin(\alpha_e + \alpha_T) & 0 & Z_\alpha & 0 & -g_D \sin \gamma_e & 0 & 0 & V_{T_e} + Z_q & 0 \end{bmatrix} \quad (2.6-14)$$

This matrix constitutes the top three rows of  $A$  in (2.6-7).

It only remains to obtain the partial derivatives of the force equations with respect to the control vector  $\bar{U}$ . The partial derivatives are

$$\begin{bmatrix} \nabla_U f_1 \\ \nabla_U f_2 \\ \nabla_U f_3 \end{bmatrix} = \begin{bmatrix} \cos(\alpha + \alpha_T) \nabla_U F_T - \nabla_U D \\ \nabla_U Y \\ -\sin(\alpha + \alpha_T) \nabla_U F_T - \nabla_U L \end{bmatrix} \quad (2.6-15)$$

Now, inserting the relevant dimensional derivatives and the equilibrium values of the angles, we obtain

$$\begin{bmatrix} \nabla_U f_1 \\ \nabla_U f_2 \\ \nabla_U f_3 \end{bmatrix}_{\substack{X=X_e \\ \bar{U}=\bar{U}_e}} = m \begin{bmatrix} X_{\delta t} \cos(\alpha_e + \alpha_T) & X_{\delta e} & 0 & 0 \\ 0 & 0 & Y_{\delta a} & Y_{\delta r} \\ -X_{\delta t} \sin(\alpha_e + \alpha_T) & Z_{\delta e} & 0 & 0 \end{bmatrix} \quad (2.6-16)$$

and these are the top three rows of  $B$  in (2.6-7).

This completes the linearization of the force equations. Note that the positions of the zero elements correspond to the beginnings of the anticipated decoupling in (2.6-7). One of the assumptions contributing to this decoupling is that the partial derivatives of drag with respect to the lateral-directional controls (ailerons and rudder) can be neglected. In practice aileron and rudder deflections do cause nonnegligible changes in drag, but this assumption does not have any significant consequences on the linearized dynamics.

**The Linearized Kinematic Equations** We will now determine the second block of three rows in (2.6-7). The nonlinear kinematic relationship between the Euler angle rates and the stability-axes rates  $P_s$ ,  $Q$ , and  $R_s$  is obtained from Table 2.5-1 and the transformation matrices  $C_{bf/s}$ . Thus,

$$\dot{\Phi} = H(\Phi) C_{bf/s} \omega_{b/e}^s \quad (2.6-17)$$

There are no aerodynamic forces or moments involved in these equations, and it is easy to see that the contribution to the  $E$ -matrix is given by

$$-\begin{bmatrix} \nabla_{\dot{X}} f_4 \\ \nabla_{\dot{X}} f_5 \\ \nabla_{\dot{X}} f_6 \end{bmatrix} = \begin{bmatrix} 0 & 0 & 0 & 1 & 0 & 0 & 0 & 0 & 0 \\ 0 & 0 & 0 & 0 & 1 & 0 & 0 & 0 & 0 \\ 0 & 0 & 0 & 0 & 0 & 1 & 0 & 0 & 0 \end{bmatrix} \quad (2.6-18)$$

Next we determine the contributions of the kinematic equations to the  $A$ -matrix. Equations (2.6-17) are linear in  $P_s$ ,  $Q$ , and  $R_s$ , so all partial derivatives of the coefficient matrix elements will be eliminated when we set  $P_s = Q = R_s = 0$ . It only remains to evaluate the coefficient matrices under the steady-state conditions. The result is

$$H(\Phi) C_{bf/s} = \begin{bmatrix} c\alpha + t\theta c\varphi s & t\theta s\varphi & -s\alpha + t\theta c\varphi c\alpha \\ -s\varphi s\alpha & c\varphi & -s\varphi c\alpha \\ c\varphi s\alpha/c\theta & s\varphi/c\theta & c\varphi c\alpha/c\theta \end{bmatrix} \quad (2.6-19)$$

Inserting the steady-state conditions in this matrix and applying some trigonometric identities, we see that

$$\begin{bmatrix} \nabla_X f_4 \\ \nabla_X f_5 \\ \nabla_X f_6 \end{bmatrix}_{\substack{\bar{U}=\bar{U}_e \\ X=X_e}} = \begin{bmatrix} 0 & 0 & 0 & 0 & 0 & 0 & c\gamma_e/c\theta_e & 0 & s\gamma_e/c\theta_e \\ 0 & 0 & 0 & 0 & 0 & 0 & 0 & 1 & 0 \\ 0 & 0 & 0 & 0 & 0 & 0 & s\alpha_e/c\theta_e & 0 & c\alpha_e/c\theta_e \end{bmatrix} \quad (2.6-20)$$

The partial derivatives of the kinematic variables with respect to the control vector are all zero, so this completes the linearization of the kinematic equations. Note that the force and moment equations are independent of the heading angle  $\psi$  in the *ned* tangent plane, so the third kinematic equation is not really needed in the linear model.

**The Linearized Moment Equations** Here we determine the last three rows of the linear state equations (2.6-7). The starting point for this linearization is the stability-axes moment equations (2.5-26), with all terms moved to the right-hand side. The moment partial derivatives that are normally considered important are contained in Table 2.6-2; the table defines the moment dimensional derivatives. These dimensional derivatives are given the symbols  $L$ ,  $M$ , and  $N$  to denote, respectively, rolling, pitching, and yawing moments, and their subscripts indicate the quantity with respect to which the derivative is taken. These include all six of the state variables that determine the translational and rotational rates, the four control variables, and the angular rate  $\alpha$ -dot. The derivatives with respect to  $\beta$ -dot have been omitted from the table because they are usually unimportant and are difficult to measure. The effect of  $\beta$ -dot on yawing moment may sometimes be important, and the derivative can be estimated with methods given in the USAF DATCOM (Hoak et al., 1970). It is convenient to include the moment of inertia for the corresponding axis in the definition of the dimensionless coefficient. Therefore, each derivative has the dimensions of angular acceleration divided by the independent variable dimensions ( $s^{-1}$ ,  $s^{-2}$ ,  $ft^{-1}s^{-1}$ , or none).

We will assume, as in Section 2.5, that the engine thrust vector lies in the  $x_b$ - $z_b$  plane and therefore contributes only a pitching moment  $m_{y,T}$  to the stability-axes moment equations. This is not an accurate assumption for a propeller aircraft, and

**TABLE 2.6-2    The Moment Dimensional Derivatives**

ROLL	PITCH	YAW
$L_\beta = \frac{1}{J'_x} \frac{\partial \mathcal{L}}{\partial \beta}$	$M_V = \frac{1}{J'_y} \frac{\partial m_A}{\partial V_T}$	$N_\beta = \frac{1}{J'_z} \frac{\partial n_A}{\partial \beta}$
$L_P = \frac{1}{J'_x} \frac{\partial \mathcal{L}}{\partial P}$	$M_\alpha = \frac{1}{J'_y} \frac{\partial m_A}{\partial \alpha}$	$N_p = \frac{1}{J'_z} \frac{\partial n_A}{\partial P}$
$L_r = \frac{1}{J'_x} \frac{\partial \mathcal{L}}{\partial R}$	$M_{\dot{\alpha}} = \frac{1}{J'_y} \frac{\partial m_A}{\partial \dot{\alpha}}$	$N_r = \frac{1}{J'_z} \frac{\partial n_A}{\partial R}$
$L_{\delta a} = \frac{1}{J'_x} \frac{\partial \mathcal{L}}{\partial \delta_a}$	$M_q = \frac{1}{J'_y} \frac{\partial m_A}{\partial Q}$	$N_{\delta a} = \frac{1}{J'_z} \frac{\partial n_A}{\partial \delta_a}$
$L_{\delta r} = \frac{1}{J'_x} \frac{\partial \mathcal{L}}{\partial \delta_r}$	$M_{\delta e} = \frac{1}{J'_y} \frac{\partial m_A}{\partial \delta_e}$	$N_{\delta r} = \frac{1}{J'_z} \frac{\partial n_A}{\partial \delta_r}$
	$M_{T_V} = \frac{1}{J'_y} \frac{\partial m_T}{\partial V_T}$	$N_{T_\beta} = \frac{1}{J'_z} \frac{\partial n_T}{\partial \beta}$
	$M_{T_\alpha} = \frac{1}{J'_y} \frac{\partial m_T}{\partial \alpha}$	
	$M_{\delta t} = \frac{1}{J'_y} \frac{\partial m_T}{\partial \delta_t}$	

there will be a number of power effects (Stinton, 1983; Ribner, 1943). These include a rolling moment due to propeller torque reaction, which is a function of throttle setting, and moments and forces that depend on the total angle of attack of the propeller, which is a function of  $\alpha$  and  $\beta$ . The table shows derivatives for thrust moment varying with speed,  $\alpha$ , throttle position, and sideslip. For simplicity, the derivatives with respect to  $\alpha$  and  $\beta$  will be omitted from our equations.

The stability-axes moment equations (2.5-26) are repeated here, with all nonzero terms moved to the right-hand side:

$$0 = \begin{bmatrix} f_7 \\ f_8 \\ f_9 \end{bmatrix} = \begin{bmatrix} -\dot{P}_s + \dot{\alpha} R_s \\ -\dot{Q} \\ -\dot{R}_s - \dot{\alpha} P_s \end{bmatrix} + \frac{1}{\Gamma} \begin{bmatrix} J'_z & 0 & J'_{xz} \\ 0 & \Gamma/J'_y & 0 \\ J'_{xz} & 0 & J'_x \end{bmatrix} \begin{bmatrix} \ell_s \\ m \\ n_s \end{bmatrix} - \tilde{\omega}_{b/e}^s J^s \omega_{b/e}^s \quad (2.6-21)$$

To find the block of  $E$ -matrix terms, all the moment equation terms that involve state derivatives must be examined. These are

$$\dot{P}_s, \dot{Q}, \dot{R}_s, \dot{\alpha} R_s, \dot{\alpha} P_s, m$$

The two  $\alpha$ -dot terms are of degree 2 in the variables that are set to zero in the steady state. Therefore, the corresponding partial derivatives vanish from the  $E$ -matrix, leaving only four terms:

$$-\left[ \begin{array}{c} \nabla_{\dot{X}} f_7 \\ \nabla_{\dot{X}} f_8 \\ \nabla_{\dot{X}} f_9 \end{array} \right]_{\substack{\bar{U}=\bar{U}_e \\ X=X_e}} = \begin{bmatrix} \dot{v}_T & \dot{\beta} & \dot{\alpha} & \dot{\phi} & \dot{\theta} & \dot{\psi} & \dot{P}_s & \dot{Q} & \dot{R}_s \\ 0 & 0 & 0 & 0 & 0 & 0 & 1 & 0 & 0 \\ 0 & 0 & -M_{\dot{\alpha}} & 0 & 0 & 0 & 0 & 1 & 0 \\ 0 & 0 & 0 & 0 & 0 & 0 & 0 & 0 & 1 \end{bmatrix} \quad (2.6-22)$$

The contributions of the moment equations to the  $A$ - and  $B$ -matrices must now be found. In Equation (2.6-21), on the right, the derivatives of the angular rates are constants for the purposes of partial differentiation; the  $\alpha$ -dot terms are of degree 2 in the variables of the steady-state condition, as is the last term on the right. This leaves only the term comprising the product of the inertia matrix and the moment array. The stability-axes inertia matrix is a function of  $\alpha$ , but its derivative will be multiplied by a moment array that is null in steady-state nonturning flight. Therefore, the only partial derivatives that are of interest are given by the inertia matrix terms multiplied by the partial derivatives of the moments:

$$\left[ \begin{array}{c} \nabla_{\dot{X}} f_7 \\ \nabla_{\dot{X}} f_8 \\ \nabla_{\dot{X}} f_9 \end{array} \right]_{\substack{\bar{U}=\bar{U}_e \\ X=X_e}} = \begin{bmatrix} (J'_Z \nabla_X \ell_s + J'_{XZ} \nabla_X n_s) / \Gamma \\ (\nabla_X m) / J'_y \\ (J'_{XZ} \nabla_X \ell_s + J'_X \nabla_X n_s) / \Gamma \end{bmatrix} \quad (2.6-23)$$

and

$$\begin{bmatrix} \nabla_U f_7 \\ \nabla_U f_8 \\ \nabla_U f_9 \end{bmatrix}_{\substack{\bar{U}=\bar{U}_e \\ X=X_e}} = \begin{bmatrix} (J'_Z \nabla_U \ell_s + J'_{XZ} \nabla_U n_s) / \Gamma \\ (\nabla_U m) / J'_Y \\ (J'_{XZ} \nabla_U \ell_s + J'_X \nabla_U n_s) / \Gamma \end{bmatrix} \quad (2.6-24)$$

When the partial derivatives in (2.6-23) and (2.6-24) are interpreted in terms of the dimensional derivatives in Table 2.6-2, we obtain the last three rows of the  $A$ -matrix,

$$\begin{bmatrix} \nabla_X f_7 \\ \nabla_X f_8 \\ \nabla_X f_9 \end{bmatrix}_{\substack{\bar{U}=\bar{U}_e \\ X=X_e}} = \begin{bmatrix} 0 & \mu L_\beta + \sigma_1 N_\beta & 0 & 0 & 0 & 0 & \mu L_p + \sigma_1 N_p & 0 & \mu L_r + \sigma_1 N_r \\ M_V + M_{T_V} & 0 & M_\alpha + M_{T_\alpha} & 0 & 0 & 0 & 0 & M_q & 0 \\ 0 & \mu N_\beta + \sigma_2 L_\beta & 0 & 0 & 0 & 0 & \mu N_p + \sigma_2 L_p & 0 & \mu N_r + \sigma_2 L_r \end{bmatrix} \quad (2.6-25)$$

and the last three rows of the  $B$ -matrix,

$$\begin{bmatrix} \nabla_U f_7 \\ \nabla_U f_8 \\ \nabla_U f_9 \end{bmatrix}_{\substack{\bar{U}=\bar{U}_e \\ X=X_e}} = \begin{bmatrix} 0 & 0 & \mu L_{\delta a} + \sigma_1 N_{\delta a} & \mu L_{\delta r} + \sigma_1 N_{\delta r} \\ M_{\delta t} & M_{\delta e} & 0 & 0 \\ 0 & 0 & \mu N_{\delta a} + \sigma_2 L_{\delta a} & \mu N_{\delta r} + \sigma_2 L_{\delta r} \end{bmatrix} \quad (2.6-26)$$

In these equations, the constants  $\mu$  and  $\sigma_i$  are given by

$$\mu = (J'_Z J'_X) / \Gamma \quad \sigma_1 = (J'_Z J'_{XZ}) / \Gamma \quad \sigma_2 = (J'_X J'_{XZ}) / \Gamma \quad (2.6-27)$$

The cross-product of inertia is normally small in magnitude compared to the moments of inertia, so the parameter  $\mu$  is quite close to unity, and the  $\sigma_i$  are much smaller than unity.

## The Decoupled Linear State Equations

All of the information for the coefficient matrices of the linear state equations (2.6-7) has now been obtained. An inspection of the coefficient blocks shows that the longitudinal- and lateral-directional equations are decoupled (although the lateral-directional equations do depend on steady-state longitudinal quantities such as  $\gamma_e$  and  $\theta_e$ ). Therefore, rather than attempt to assemble the complete equations, we will collect the longitudinal- and lateral-directional equations separately.

If the longitudinal state and control variables are ordered as follows, additional potential decoupling will become apparent. Thus, we choose the longitudinal state and input vectors as

$$x = [\alpha \quad q \quad v_T \quad \theta]^T \quad u = [\delta_e \quad \delta_t]^T \quad (2.6-28)$$



The longitudinal equations are obtained from the first and last rows of (2.6-11), (2.6-14), and (2.6-16) (divided through by  $m$ ); the middle rows of (2.6-18) and (2.6-20); and the middle rows of (2.6-22), (2.6-25), and (2.6-26). The longitudinal coefficient matrices are now given by

$$\begin{aligned}
 E &= \begin{bmatrix} V_{T_e} - Z_{\dot{\alpha}} & 0 & 0 & 0 \\ -M_{\dot{\alpha}} & 1 & 0 & 0 \\ 0 & 0 & 1 & 0 \\ 0 & 0 & 0 & 1 \end{bmatrix} \quad B = \begin{bmatrix} Z_{\delta_e} & -X_{\delta_t} \sin(\alpha_e + \alpha_T) \\ M_{\delta_e} & M_{\delta_t} \\ X_{\delta_e} & X_{\delta_t} \cos(\alpha_e + \alpha_T) \\ 0 & 0 \end{bmatrix} \\
 A &= \begin{bmatrix} Z_{\alpha} & V_{T_e} + Z_q & Z_V - X_{T_V} \sin(\alpha_e + \alpha_T) & -g_D \sin \gamma_e \\ M_{\alpha} + M_{T_{\alpha}} & M_q & M_V + M_{T_V} & 0 \\ X_{\alpha} & 0 & X_V + X_{T_V} \cos(\alpha_e + \alpha_T) & -g_D \cos \gamma_e \\ 0 & 1 & 0 & 0 \end{bmatrix} \quad (2.6-29)
 \end{aligned}$$

We see that  $E$  is block diagonal and does not contribute to any coupling between the  $\alpha$ ,  $q$ , and  $v_T$ ,  $\theta$  pairs of variables. Furthermore,  $E$  is nonsingular for nonhovering flight because, although  $Z_{\dot{\alpha}}$  can be positive, it is normally much smaller in magnitude than  $V_{T_e}$ .

The  $A$ -matrix has several null elements and, in level flight, the (1, 4) element is zero. In trimmed flight, at low Mach numbers, the moment derivatives in element (2, 3) are zero (see next section). Finally, the (1, 3) element is small compared to the other elements of the first row and can often be neglected. Under the above conditions, the angle-of-attack and pitch-rate differential equations have no dependence on the speed, pitch-attitude perturbations (but not vice-versa). The solution of these equations, with the elevator and throttle inputs fixed, is a “stick-fixed” mode of oscillation known as the short-period mode (Chapter 3).

In the same vein, the (3, 1) element of the  $B$ -matrix (drag due to elevator deflection) is usually negligible, and the pitching moment due to throttle inputs, element (2, 2), is zero if the  $x$ - $z$  plane component of the engine thrust vector passes through the aircraft center of mass [this is not true for aircraft such as the B-747 and B-767 (Roskam, 1979)]. Also, the (1, 2) element of  $B$  may often be neglected because of the small sine component. Under these conditions, the elevator input controls only the  $\alpha$ -pitch-rate dynamics, the throttle input controls only the speed-pitch-attitude dynamics, and transfer function analysis is simplified (Chapter 4).

The lateral-directional states and controls are

$$x = [\beta \quad \phi \quad p_s \quad r_s]^T \quad u = [\delta_a \quad \delta_r]^T, \quad (2.6-30)$$

where the state  $\psi$  has been dropped. The state equations are obtained from the second rows of (2.6-11), (2.6-14), and (2.6-16); the first rows of (2.6-18) and (2.6-20); and

the first and third rows of (2.6-22), (2.6-25), and (2.6-26). The resulting coefficient matrices are

$$\begin{aligned}
 E &= \begin{bmatrix} V_{T_e} & 0 & 0 & 0 \\ 0 & 1 & 0 & 0 \\ 0 & 0 & 1 & 0 \\ 0 & 0 & 0 & 1 \end{bmatrix} & B &= \begin{bmatrix} Y_{\delta a} & Y_{\delta r} \\ 0 & 0 \\ L'_{\delta a} & L'_{\delta r} \\ N'_{\delta a} & N'_{\delta r} \end{bmatrix} \\
 A &= \begin{bmatrix} Y_\beta & g_D \cos \theta_e & Y_p & Y_r - V_{T_e} \\ 0 & 0 & c\gamma_e/c\theta_e & s\gamma_e/c\theta_e \\ L'_\beta & 0 & L'_p & L'_r \\ N'_\beta & 0 & N'_p & N'_r \end{bmatrix}, \quad (2.6-31)
 \end{aligned}$$

where primed moment derivatives are defined (McRuer et al., 1973) by

$$\begin{aligned}
 L'_\beta &= \mu L_\beta + \sigma_1 N_\beta & L'_p &= \mu L_p + \sigma_1 N_p & L'_r &= \mu L_r + \sigma_1 N_r \\
 N'_\beta &= \mu N_\beta + \sigma_2 L_\beta & N'_p &= \mu N_p + \sigma_2 L_p & N'_r &= \mu N_r + \sigma_2 L_r \\
 L'_{\delta a} &= \mu L_{\delta a} + \sigma_1 N_{\delta a} & L'_{\delta r} &= \mu L_{\delta r} + \sigma_1 N_{\delta r} \\
 N'_{\delta a} &= \mu N_{\delta a} + \sigma_2 L_{\delta a} & N'_{\delta r} &= \mu N_{\delta r} + \sigma_2 L_{\delta r}
 \end{aligned} \quad (2.6-32)$$

The inverse of the  $E$ -matrix is diagonal and exists for nonzero airspeed. Its effect is simply to divide the right-hand side of the beta-dot equation by airspeed. Therefore, although the original nonlinear equations were assumed implicit, the linear equations can now be made explicit in the derivatives. The coefficient matrices depend on the steady-state angle of attack and pitch attitude in both cases. Although they nominally apply to small perturbations about a wings-level, steady-state flight condition, the equations can be used satisfactorily for perturbed roll angles of several degrees.

In this chapter we will be content with simply deriving the coefficient matrices for the linear state equations; the equations will not be used until Chapter 3. The remainder of the chapter will be devoted to expressing the dimensional stability derivatives, used in the coefficient matrices, in terms of derivatives of the dimensionless aerodynamic coefficients defined in (2.3-8b). The resulting “dimensionless derivatives” have the advantage that they are less dependent on the specific aircraft and flight condition and more dependent on the geometrical configuration of an aircraft. Methods have been developed to estimate the dimensionless derivatives, and they can be used to compare and assess different design configurations.

## The Dimensionless Stability and Control Derivatives

The dimensional aerodynamic derivatives are simply a convenient set of coefficients for the linear equations. We must now relate them to the *dimensionless stability*

*derivatives* used by stability and control engineers and found in aerodynamic data. The way in which the stability derivatives are made dimensionless depends on whether the independent variable for the differentiation is angle, angular rate, or velocity. This will be illustrated by example before we tabulate the derivatives.

Consider the derivative  $X_V$  in Table 2.6-1; this derivative is taken with respect to airspeed. The drag force depends on airspeed both through dynamic pressure and through the variation of the aerodynamic drag coefficient with airspeed. Therefore, using the definition of  $X_V$  and the drag equation from (2.3-8b), we have

$$X_V = \frac{-1}{m} \left[ \frac{\partial \bar{q}}{\partial V_T} S C_D + \bar{q} S \frac{\partial C_D}{\partial V_T} \right] = \frac{-\bar{q} S}{m V_{T_e}} (2C_D + C_{D_V}),$$

where  $C_{D_V} \equiv V_{T_e} (\partial C_D / \partial V_T)$  is the dimensionless speed damping derivative.

Next consider a derivative that is taken with respect to angular rate,  $C_{m_q}$ . The dimensionless rate damping derivatives were defined in Section 2.3 and can now be related to the dimensional derivatives. Making use of the definition of pitching moment coefficient in (2.3-8b), we have

$$M_q = \frac{\bar{q} S \bar{c}}{J'_Y} \frac{\partial C_m}{\partial Q} = \frac{\bar{q} S \bar{c}}{J'_Y} \frac{\bar{c}}{2V_{T_e}} C_{m_q}, \quad \text{where} \quad C_{m_q} \equiv \frac{2V_{T_e}}{\bar{c}} \frac{\partial C_m}{\partial Q}$$

The “dimensionless” stability derivatives taken with respect to angle actually have dimensions of  $\text{deg}^{-1}$  when expressed in degrees rather than radians.

Tables 2.6-1 and 2.6-2 include six thrust derivatives ( $X_{T_V}$ ,  $X_{\delta_t}$ ,  $M_{T_V}$ ,  $M_{T_\alpha}$ ,  $M_{\delta_t}$ ,  $N_{T_\beta}$ ). The corresponding dimensionless derivatives can be defined by expressing the thrust force and moment components in terms of dimensionless coefficients. For example, a pitching moment component due to thrust can be written as  $M_T = \bar{q} S \bar{c} C_{m_T}$ . Values for the thrust derivatives would be found by referring to the “installed thrust” data for the specific engine and determining the change in thrust due to a perturbation in the variable of interest. In the case of the derivatives with respect to  $V_T$  and throttle setting, it is probably most convenient to work directly with the dimensional derivatives. Determination of the thrust derivatives with respect to  $\alpha$  and  $\beta$  is more complicated; a readable explanation is given by Roskam (1979).

Following the lines of the examples above, the longitudinal dimensionless stability and control derivatives and the lateral-directional dimensionless stability and control derivatives corresponding to Tables 2.6-1 and 2.6-2 are given in Tables 2.6-3 and 2.6-4. Some of the thrust derivatives have been omitted because of lack of space and because of their limited utility.

The dimensionless stability derivatives are in general very important to both the aircraft designer and the stability and control engineer. They provide information about the natural stability of an aircraft, about the effectiveness of the control surfaces, and about the maneuverability. They correlate with the geometrical features of the aircraft and thereby facilitate the preliminary design process. The typical variation of many of the stability derivatives with flight conditions (e.g., speed, angle of attack, sideslip angle) is known to the designer, and he or she can therefore

**TABLE 2.6-3 Longitudinal Dimensional versus Dimensionless Derivatives**

$X_V = \frac{-\bar{q}S}{mV_{T_e}}(2C_{D_e} + C_{D_V})$	$C_{D_V} \equiv V_{T_e} \frac{\partial C_D}{\partial V_T}$
$X_{T_V} = \frac{\bar{q}S}{mV_{T_e}}(2C_{T_e} + C_{T_V})$	$C_{T_V} \equiv V_{T_e} \frac{\partial C_T}{\partial V_T}$
$X_\alpha = \frac{\bar{q}S}{m}(C_{L_e} - C_{D_\alpha})$	$C_{D_\alpha} \equiv \frac{\partial C_D}{\partial \alpha}$
$X_{\delta e} = \frac{-\bar{q}S}{m}C_{D_{\delta e}}$	$C_{D_{\delta e}} \equiv \frac{\partial C_D}{\partial \delta_e}$
$Z_V = \frac{-\bar{q}S}{mV_{T_e}}(2C_{L_e} + C_{L_V})$	$C_{L_V} \equiv V_{T_e} \frac{\partial C_L}{\partial V_T}$
$Z_\alpha = \frac{-\bar{q}S}{m}(C_{D_e} + C_{L_\alpha})$	$C_{L_\alpha} \equiv \frac{\partial C_L}{\partial \alpha}$
$Z_{\dot{\alpha}} = \frac{-\bar{q}S\bar{c}}{2mV_{T_e}}C_{L_{\dot{\alpha}}}$	$C_{L_{\dot{\alpha}}} \equiv \frac{2V_{T_e}}{\bar{c}} \frac{\partial C_L}{\partial \dot{\alpha}}$
$Z_q = \frac{-\bar{q}S\bar{c}}{2mV_{T_e}}C_{L_q}$	$C_{L_q} \equiv \frac{2V_{T_e}}{\bar{c}} \frac{\partial C_L}{\partial Q}$
$Z_{\delta e} = \frac{-\bar{q}S}{m}C_{L_{\delta e}}$	$C_{L_{\delta e}} \equiv \frac{\partial C_L}{\partial \delta_e}$
$M_V = \frac{\bar{q}S\bar{c}}{J_Y V_{T_e}}(2C_{m_e} + C_{m_V})$	$C_{m_V} \equiv V_{T_e} \frac{\partial C_m}{\partial V_T}$
$M_{T_V} = \frac{\bar{q}S\bar{c}}{J_Y V_{T_e}}(2C_{m_T} + C_{m_{T_V}})$	$C_{m_{T_V}} \equiv V_{T_e} \frac{\partial C_m}{\partial V_T}$
$M_\alpha = \frac{\bar{q}S\bar{c}}{J_Y}C_{m_\alpha}$	$C_{m_\alpha} \equiv \frac{\partial C_m}{\partial \alpha}$
$M_{\dot{\alpha}} = \frac{\bar{q}S\bar{c}}{J_Y} \frac{\bar{c}}{2V_{T_e}}C_{m_{\dot{\alpha}}}$	$C_{m_{\dot{\alpha}}} \equiv \frac{2V_{T_e}}{\bar{c}} \frac{\partial C_m}{\partial \dot{\alpha}}$
$M_q = \frac{\bar{q}S\bar{c}}{J_Y} \frac{\bar{c}}{2V_{T_e}}C_{m_q}$	$C_{m_q} \equiv \frac{2V_{T_e}}{\bar{c}} \frac{\partial C_m}{\partial Q}$
$M_{\delta e} = \frac{\bar{q}S\bar{c}}{J_Y}C_{m_{\delta e}}$	$C_{m_{\delta e}} \equiv \frac{\partial C_m}{\partial \delta_e}$

anticipate the design problems in different parts of the flight envelope. Information on the importance of the stability derivatives, the accuracy with which they can be estimated, and their variation with flight conditions can be found in stability and control textbooks (Roskam, 1979; Etkin, 1972; Perkins and Hage, 1949) and in the USAF DATCOM (Hoak et al., 1970). Stability derivatives at certain flight conditions, for a number of different aircraft, are also given in these books, by Blakelock (1965), by McRuer et al. (1973), and in various other texts.

**TABLE 2.6-4 Lateral-Directional Dimensional versus Dimensionless Derivative**

$Y_{\beta} = \frac{\bar{q}S}{m} C_{Y_{\beta}}$	$C_{Y_{\beta}} = - \left( \frac{\partial C_C}{\partial \beta} + C_{D_e} \right)$
$Y_p = \frac{\bar{q}Sb}{2mV_{T_e}} C_{Y_p}$	$C_{Y_p} \equiv - \frac{2V_{T_e}}{b} \frac{\partial C_C}{\partial P_S}$
$Y_r = \frac{\bar{q}Sb}{2mV_{T_e}} C_{Y_r}$	$C_{Y_r} \equiv - \frac{2V_{T_e}}{b} \frac{\partial C_C}{\partial R_S}$
$Y_{\delta r} = \frac{\bar{q}S}{m} C_{Y_{\delta r}}$	$C_{Y_{\delta r}} \equiv - \frac{\partial C_C}{\partial \delta_r}$
$Y_{\delta a} = \frac{\bar{q}S}{m} C_{Y_{\delta a}}$	$C_{Y_{\delta a}} \equiv - \frac{\partial C_C}{\partial \delta_a}$
$L_{\beta} = \frac{\bar{q}Sb}{J'_X} C_{\ell_{\beta}}$	$C_{\ell_{\beta}} \equiv \frac{\partial C_{\ell}}{\partial \beta}$
$L_p = \frac{\bar{q}Sb}{J'_X} \frac{b}{2V_{T_e}} C_{\ell_p}$	$C_{\ell_p} \equiv \frac{2V_{T_e}}{b} \frac{\partial C_{\ell}}{\partial P}$
$L_r = \frac{\bar{q}Sb}{J'_X} \frac{b}{2V_{T_e}} C_{\ell_r}$	$C_{\ell_r} \equiv \frac{2V_{T_e}}{b} \frac{\partial C_{\ell}}{\partial R}$
$L_{\delta a} = \frac{\bar{q}Sb}{J'_X} C_{\ell_{\delta a}}$	$C_{\ell_{\delta a}} \equiv \frac{\partial C_{\ell}}{\partial \delta_a}$
$L_{\delta r} = \frac{\bar{q}Sb}{J'_X} C_{\ell_{\delta r}}$	$C_{\ell_{\delta r}} \equiv \frac{\partial C_{\ell}}{\partial \delta_r}$
$N_{\beta} = \frac{\bar{q}Sb}{J'_Z} C_{n_{\beta}}$	$C_{n_{\beta}} \equiv \frac{\partial C_n}{\partial \beta}$
$N_p = \frac{\bar{q}Sb}{J'_Z} \frac{b}{2V_{T_e}} C_{n_p}$	$C_{n_p} \equiv \frac{2V_{T_e}}{b} \frac{\partial C_n}{\partial P}$
$N_r = \frac{\bar{q}Sb}{J'_Z} \frac{b}{2V_{T_e}} C_{n_r}$	$C_{n_r} \equiv \frac{2V_{T_e}}{b} \frac{\partial C_n}{\partial R}$
$N_{\delta a} = \frac{\bar{q}Sb}{J'_Z} C_{n_{\delta a}}$	$C_{n_{\delta a}} \equiv \frac{\partial C_n}{\partial \delta_a}$
$N_{\delta r} = \frac{\bar{q}Sb}{J'_Z} C_{n_{\delta r}}$	$C_{n_{\delta r}} \equiv \frac{\partial C_n}{\partial \delta_r}$

In the next subsection we briefly describe the significance of various dimensionless derivatives and their variation with flight conditions. This information will be utilized in Chapter 4 when aircraft dynamic modes are analyzed.

### Description of the Longitudinal Dimensionless Derivatives

The names and relative importance of the longitudinal stability derivatives are shown in Table 2.6-5, starting with the most important.

**TABLE 2.6-5 Importance of Longitudinal Stability Derivatives**

$C_{L\alpha}$	Lift-curve slope (determines response to turbulence)
$C_{m\alpha}$	Pitch stiffness ( $< 0$ for static stability)
$C_{m\dot{q}}$	Pitch damping ( $< 0$ for short-period damping)
$C_{m\dot{V}}$	Tuck derivative ( $< 0$ gives unstable tuck)
$C_{m\dot{\alpha}}$	Alpha-dot derivative (less important than $C_{m\dot{q}}$ )
$C_{D\dot{V}}$	Speed damping (if $> 0$ can mitigate unstable $C_{m\dot{V}}$ )
$C_{D\alpha}$	Drag versus alpha slope
$C_{L\dot{V}}$	Lift versus speed slope
$C_{L\dot{\alpha}}$	Acceleration derivative for lift
$C_{L\dot{q}}$	Pitch-rate-dependent lift

The stability derivatives are estimated from geometrical properties, from the slopes of the aerodynamic coefficients, or from perturbed motion of an aircraft in flight test or a model in a wind tunnel. The aerodynamic coefficients are, in general, nonlinear functions, and so for a given aircraft the stability derivatives vary with the aerodynamic angles ( $\alpha, \beta$ ), Mach number (compressibility effect), thrust (power effect), and dynamic pressure (aeroelastic effects). Descriptions of these variations and methods of estimating the derivatives can be found in the literature (Roskam, 1979; Perkins and Hage, 1949; Queijo, 1971). Stability derivatives obtained from flight test are usually presented in graphs that apply to trimmed-flight conditions at, for example, a given altitude with varying Mach number. Therefore, a sequence of points along a particular curve would correspond to different combinations of thrust, angle of attack, and elevator setting. This is acceptable to the flying-qualities engineer but presents a difficulty to the simulation engineer seeking to build a lookup table for that derivative.

Plots of aerodynamic coefficients, particularly those of high-speed aircraft, can exhibit both small-scale fluctuations and regimes of widely different behavior. Differentiation exaggerates such effects, and so it is easier to generalize about the behavior of aerodynamic coefficients than about the stability derivatives. Furthermore, the stability derivatives do not provide an adequate model of aircraft behavior for large-amplitude maneuvers and very nonlinear regimes such as stall. Stability derivative information is more readily available than aerodynamic coefficient data and is appropriate for linear models for stability analysis and flight control system design but is limited in its applicability to flight simulation. We now summarize the typical behavior of the most important derivatives in the normal flight regimes.

**Lift-Curve Slope** The derivative  $C_{L\alpha}$  is called the lift-curve slope; it is important because it determines how turbulent changes in alpha translate into changes in lift and hence determines the level of comfort for the pilot. In the same manner, it affects the maneuverability of the aircraft. It also affects the damping of the pitching motion of the aircraft when subjected to sudden disturbances, as will be shown in Chapter 4. This influences the pilot’s opinion of the *handling qualities* of the airplane.

The lift-curve slope is approximately independent of  $\alpha$  and typically in the range 1 to 8 (per radian) for the linear region of the lift curve below stall. When the wing is producing a large amount of lift, wing twist will reduce the local angle of attack of the wing panels according to distance out from the wing root. This will tend to reduce the lift-curve slope as  $\alpha$  increases.

As explained in Section 2.3, compressibility effects also change  $C_{L_\alpha}$  significantly; below the critical Mach number it increases with Mach, and at supersonic speeds it decreases with Mach. In the transonic range it may pass smoothly through a maximum (e.g., fighter-type wings) or may show a dip (thick, higher-aspect wings with no sweep). Wing sweep-back has the effect of reducing the lift-curve slope and making the curve of  $C_{L_\alpha}$  versus Mach less peaked. The propulsion system can also have a strong effect on the  $C_{L_\alpha}$ , as can be visualized from Figure 2.3-3a.

***Pitch Stiffness Derivative*** The derivative  $C_{m_\alpha}$  is the slope of the curve of the static pitching moment coefficient, around the cm, versus  $\alpha$ , with controls neutral. Figures 2.3-7 show pitching moment– $\alpha$  curves, and Section 2.4 explains the factors that contribute to the derivative. This derivative is of critical importance for aircraft pitch stability; it also plays an important role in the dynamic behavior of pitching motion, as shown in Chapter 4.

Section 2.4 shows that the pitch stiffness will increase as the aerodynamic center moves aft with increasing Mach number and, depending on cm position, will also be affected by changes in wing  $C_{L_\alpha}$  with Mach. The second important component of  $C_{m_\alpha}$  contains the lift-curve slope of the horizontal tail. Again, the lift-curve slope varies with Mach, but this may not have a very great effect on  $C_{m_\alpha}$ , particularly in the case of a thin, swept, low-aspect “all-flying” tail. The lift-curve slope is multiplied by the tail efficiency factor, and this will tend to decrease with increasing  $\alpha$ , to an extent depending on the degree of coupling between wing and tail. The third component of  $C_{m_\alpha}$  is the derivative with respect to  $\alpha$  of the pitching moment at the “wing-body aerodynamic center.” A true wing-body aerodynamic center may not exist, and so this term is nonzero and difficult to determine. Roskam (1979) states that  $C_{m_\alpha}$  will normally lie in the range  $-3$  to  $+1 \text{ rad}^{-1}$ .

***Pitch Damping Derivative,  $C_{m_q}$***  The pitch damping derivative,  $C_{m_q}$ , was introduced in Section 2.3. This derivative is normally negative and determines the moment that opposes any pitch rate. It provides the most important contribution to the damping of the dynamic behavior in pitch (see Chapter 4) and hence is intimately involved in aircraft handling qualities.

The pitch damping is not given by the slope of an aerodynamic coefficient; it must be estimated from oscillatory motion of the aircraft or aircraft model or calculated. The main physical mechanism involved is that pitch rate determines translational rate of the horizontal tail perpendicular to the relative wind. This changes the tail angle of attack, tail “lift,” and hence the tail moment about the cm. When the induced translational rate is small compared to true airspeed, the change in tail angle of attack will

be linearly related to pitch rate. Therefore, the pitch damping moment is invariably modeled as linearly proportional to pitch rate through  $C_{m_q}$ .

A very simple expression for the pitch damping derivative  $C_{m_q}$  can be obtained by calculating the horizontal-tail increment in lift due to a pitch-rate-induced translational velocity at the tail. Equation (2.3-9a) gives this derivative as

$$C_{m_q} = \frac{2V_{T_e}}{\bar{c}} \frac{\Delta C_m}{Q} \quad (2.6-33)$$

Let the moment arm of the tail ac about the aircraft cm be  $\ell_t$ . The increment in lift of the tail is, in dimensionless form,

$$\Delta C_{L_t} = C_{L_{\alpha,t}} \tan^{-1}(Q\ell_t/V_{T_e}) \approx C_{L_{\alpha,t}}(Q\ell_t/V_{T_e}) \quad (2.6-34)$$

Now remember that the dimensional pitching moment coefficient is obtained by multiplying the dimensionless moment coefficient by  $(S\bar{c})$ . Therefore, this lift must be converted to a nondimensional pitching moment by multiplying by the *horizontal-tail volume ratio*,

$$V_H = (S_t\ell_t)/(S\bar{c}) \quad (2.6-35)$$

From the above three equations, noting that a positive pitch rate gives the tail a downward motion, a positive lift component, and therefore a negative contribution to aircraft pitching moment, we obtain

$$C_{m_q} = -2V_H C_{L_{\alpha,t}}(\ell_t/\bar{c}) \quad (2.6-36)$$

This equation neglects any pitch damping effect from the wings and fuselage, applies only for small alpha, and does not model any compressibility, aeroelastic, or thrust-dependent effects. It can be made to include some thrust and wing-downwash effects by including the tail efficiency factor [Equation (2.3-20)].

Figure 2.6-1 shows the variation of the pitch damping and acceleration derivatives for the jet trainer. These derivatives change quite dramatically with Mach in the transonic region, they are independent of alpha until stall is approached, and the pitch damping is somewhat dependent on altitude through aeroelastic effects. They can also be expected to be dependent on elevator deflection and movement of the tail aerodynamic center.

**Tuck Derivative** The effect of speed variations on pitching moment is contained in the “tuck derivative,”  $C_{m_v}$ . This derivative can also be written in terms of Mach:

$$C_{m_v} = \frac{V_{T_e}}{a} \frac{\partial C_m}{\partial (V_T/a)} = M \frac{\partial C_m}{\partial M} \quad (2.6-37)$$

The derivative will be negligible at low subsonic speeds when compressibility effects are absent and at supersonic speeds when the aerodynamic center has ceased to



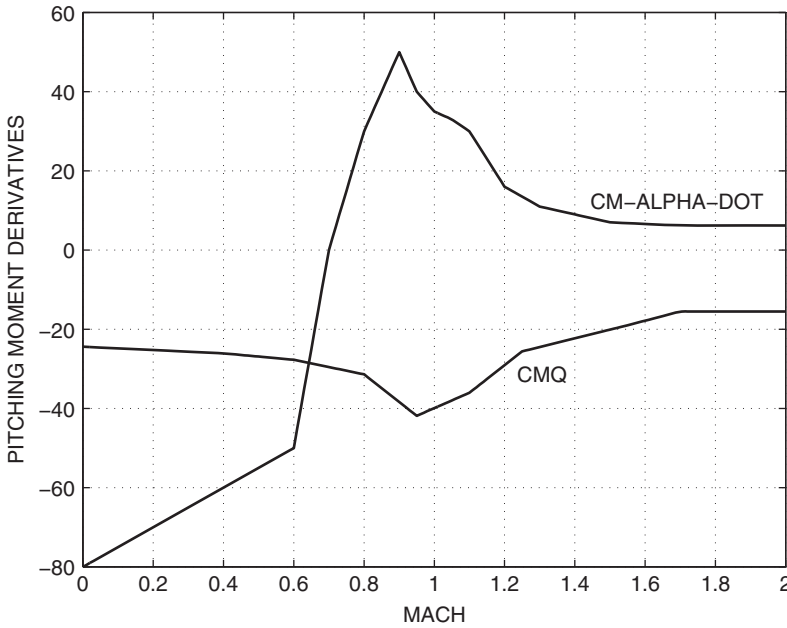


**Figure 2.6-1** Pitching moment derivatives of a jet trainer aircraft.

move. In the transonic region we would expect to find a negative value as the ac moves aft but, in fact,  $C_{m_v}$  can be positive for some aircraft. The derivative changes quite abruptly as the transonic regime is reached and, if it is negative, the aircraft will tend to pitch down as speed increases. Gravity will then tend to further increase the speed, leading to an unstable pitch-down or “tuck-under” effect. The tuck may be particularly troublesome if the elevator control effectiveness is simultaneously decreasing with Mach. The transonic drag rise helps to mitigate an unstable tuck characteristic. Values of the tuck derivative range between about  $-0.4$  and  $+0.6$  (Roskam, 1979).

**Speed Damping Derivative** The speed damping derivative,  $C_{D_v}$ , can also be written in terms of Mach:

$$C_{D_v} = \frac{V_T}{a} \frac{\partial C_D}{\partial (V_T/a)} = M \frac{\partial C_D}{\partial M} \quad (2.6-38)$$

Like the tuck derivative, the speed damping derivative is a compressibility effect. It is negligible at low Mach numbers, rises to a peak with the transonic drag rise, then changes rapidly to negative values as the drag coefficient peaks and falls off with Mach, after the transonic regime. Values typically lie in the range  $-0.01$  to  $+0.30$  (Roskam, 1979).

**TABLE 2.6-6 Importance of Lateral-Directional Derivatives**

$C_{\ell_\beta}$	Dihedral derivative (< 0 for positive stiffness)
$C_{n_\beta}$	Yaw stiffness (> 0 for positive stiffness)
$C_{\ell_p}$	Roll damping (< 0 for roll damping)
$C_{n_r}$	Yaw damping (< 0 for yaw damping)
$C_{n_p}$	Yawing moment due to roll rate
$C_{\ell_r}$	Rolling moment due to yaw rate
$C_{Y_\beta}$	Sideforce due to sideslip
$C_{Y_r}$	Sideforce due to yaw rate
$C_{Y_p}$	Sideforce due to roll rate
$C_{n_{\dot{\beta}}}$	Yawing moment due to sideslip rate
$C_{Y_{\dot{\beta}}}$	Sideforce due to sideslip rate
$C_{\ell_{\dot{\beta}}}$	Rolling moment due to sideslip rate

### Description of the Lateral-Directional Dimensionless Derivatives

The lateral-directional stability derivatives are shown in Table 2.6-6, starting with the most important. The more important derivatives are discussed below.

**Dihedral Derivative** The *dihedral derivative*,  $C_{\ell_\beta}$ , is the slope of the rolling moment versus sideslip curve. Section 2.3 showed that this slope should be negative to achieve positive stiffness in roll and that positive wing dihedral could provide this. However, too much positive stiffness in roll tends to reduce the damping of the aircraft dynamic behavior in a yawing-rolling motion (the dutch roll mode, see Chapter 4), and the designer must find a compromise in the value of  $C_{\ell_\beta}$ . In some aircraft, wing sweep produces a  $C_{\ell_\beta}$  that is too negative and the aircraft may have negative dihedral (anhedral) of the wings or horizontal tail to offset this effect (e.g., F-4 and AV8-B aircraft). The value of  $C_{\ell_\beta}$  is typically in the range  $-0.4$  to  $+0.1$  per radian (Roskam, 1979) and may change significantly with Mach number in the transonic range.

**Yaw Stiffness Derivative** The *yaw stiffness derivative*,  $C_{n_\beta}$ , is the slope of the curve of yawing moment due to sideslip (Section 2.3), and it is associated with weathercock stability (tendency to head into the relative wind). It must be positive for positive stiffness in yaw, and it is principally determined by the size of the vertical tail. Weathercock stability can be lost at high dynamic pressure, due to structural deformation of the vertical tail, and aircraft have been known to “swap ends” in flight.

$C_{n_\beta}$  plays a major role in the aircraft dutch roll mode (Chapter 4). Its value is typically in the range  $0$  to  $0.4 \text{ rad}^{-1}$  (Roskam, 1979), tending to fall off and possibly even become negative at transonic to supersonic Mach numbers. It may also become

negative at high angles of attack when the vertical tail becomes immersed in the wake from the wings and body. Achieving a suitable value of  $C_{n_\beta}$  is a consideration in the initial sizing of the vertical tail of an aircraft.

**Roll Damping Derivative** The *roll damping derivative*,  $C_{\ell_p}$ , was introduced in Section 2.3 and is chiefly due to the variation of angle of attack along the wing span when the aircraft is rolling. The rolling moment produced by the differential lift between the two wings will be linearly proportional to roll rate until stall begins on the outer wing panels. This derivative is positive, except possibly in a spin, and usually lies in the range  $-0.8$  to  $-0.1$  per radian. It thus provides a moment that damps rolling motion, plays the major roll in the response of the aircraft to aileron inputs (see roll time constant, Chapter 4), and determines the associated handling qualities. It is determined from small-amplitude rolling motion measurements. When considering maximum roll rate, the helix angle (Section 2.3) is the more important parameter. In general,  $C_{\ell_p}$  is a function of Mach number, altitude (because of aeroelastic effects), and  $\alpha$ .

**Yaw Damping Derivative** The *yaw damping derivative*,  $C_{n_r}$ , was introduced in Section 2.3 and assumes a linear relationship between yaw rate and the yawing moment it produces. It is mainly determined by the vertical tail and is always negative except possibly in a spin. A simple calculation, analogous to the calculation of pitch damping, gives

$$C_{n_r} = -2V_v C_{L_{\alpha,vt}} (\ell_t/b), \quad (2.6-39)$$

where  $V_v$  is a volume ratio for the vertical tail. It is the most important parameter in the airplane dutch roll mode (Chapter 4), and many aircraft must use an automatic control system to augment  $C_{n_r}$  (Chapter 4) because of inadequate dutch roll damping.

## 2.7 SUMMARY

In this chapter we have described how the aerodynamic forces and moments acting on an aircraft are created, how they are modeled mathematically, and how the data for the models are gathered. We have related these forces and moments to the equations of motion of a rigid aircraft that were derived in Chapter 1. The transformation of the equations of motion into a different set of coordinates has been demonstrated and also the derivation of a nonlinear model for longitudinal motion only. Steady-state flight conditions have been defined. It has been shown that the equations of motion can be linearized around a steady-state condition and that they can then be separated into two decoupled sets. One of these sets describes the longitudinal motion of an aircraft, and the other describes the lateral-directional motion. The linear equations have been expressed in terms of the aerodynamic derivatives, and the significance of these derivatives has been explained. In Chapter 3 we develop a number of powerful analytical and computational tools and use them in conjunction with the aircraft models developed here.

## REFERENCES

- Anderson, F. *Northrop: An Aeronautical History*. Los Angeles: Northrop Corporation, 1976.
- Anderson, J. D., Jr. *Fundamentals of Aerodynamics*. 2d ed. New York: McGraw-Hill, 1991.
- . *Aircraft Performance and Design*. New York: McGraw-Hill, 1999.
- Babister, A. W. *Aircraft Stability and Control*. Oxford: Pergamon, 1961.
- Blakelock, J. H. *Automatic Control of Aircraft and Missiles*. New York: Wiley, 1965.
- Bryan, G. H. *Stability in Aviation*. London: Macmillan, 1911.
- Chambers, J. R., and E. L. Anglin. "Analysis of Lateral-Directional Stability Characteristics of a Twin-Jet Fighter Airplane at High Angles of Attack." *NASA Technical Note D-5361*. Washington, D.C.: NASA, 1969.
- DeCamp, R. W., R. Hardy, and D. K. Gould. "Mission Adaptive Wing." *Paper 872419*, Society of Automotive Engineers, 1987.
- Dommasch, D. O., S. S. Sherby, and T. F. Connolly. *Airplane Aerodynamics*. 4th ed. New York: Pitman, 1967.
- Drendel, L. *SR-71 Blackbird in Action*. Carrollton, Tex.: Squadron/Signal Publications, 1982.
- Droste, C. S., and J. E. Walker. "The General Dynamics Case Study on the F-16 Fly-by-Wire Flight Control System." *AIAA Professional Case Studies*, no date.
- Duncan, W. J. *The Principles of the Control and Stability of Aircraft*. Cambridge: Cambridge University Press, 1952.
- Etkin, B. *Dynamics of Atmospheric Flight*. New York: Wiley, 1972.
- Goman, M., and A. Khrabrov. "State-Space Representation of Aerodynamic Characteristics of an Aircraft at High Angles of Attack." *Journal of Aircraft* 31, no. 5 (September–October 1994): 1109–1115.
- Hoak, D. E., et al. *USAF Stability and Control DATCOM*. Wright Patterson Air Force Base, Ohio: Flight Control Division, Air Force Flight Dynamics Laboratory, September 1970.
- IMSL. *Library Contents Document*. 8th ed. Houston, Tex.: International Mathematical and Statistical Libraries, 1980.
- Kandebo, S. W. "Second X-29 Will Execute High-Angle-of-Attack Flights." *Aviation Week and Space Technology* (October 31, 1988): 36–38.
- Kuethe, A. M., and C. Y. Chow. *Foundations of Aerodynamics*. 4th ed. New York: Wiley, 1984.
- Maine, R. E., and K. W. Iliffe. "Formulation and Implementation of a Practical Algorithm for Parameter Estimation with Process and Measurement Noise." *Paper 80-1603. AIAA Atmospheric Flight Mechanics Conference*, August 11–13, 1980, pp. 397–411.
- McCormick, B. W. *Aerodynamics, Aeronautics, and Flight Mechanics*. New York: Wiley, 1995.
- McFarland, R. E. "A Standard Kinematic Model for Flight Simulation at NASA Ames." *NASA CR-2497*. Washington, D.C.: NASA, January 1975.
- McRuer, D., I. Ashkenas, and D. Graham. *Aircraft Dynamics and Automatic Control*. Princeton, N.J.: Princeton University Press, 1973.
- Nguyen, L. T., et al. "Simulator Study of Stall/Post-Stall Characteristics of a Fighter Airplane with Relaxed Longitudinal Static Stability." *NASA Technical Paper 1538*. Washington, D.C.: NASA, December 1979.
- Perkins, C. D., and R. E. Hage. *Airplane Performance Stability and Control*. New York: Wiley, 1949.

- Pope, A. *Wind Tunnel Testing*. New York: Wiley, 1954.
- Press, W. H., B. P. Flannery, S. A. Teukolsky, and W. T. Vetterling. *Numerical Recipes: The Art of Scientific Computing*. New York: Cambridge University Press, 1989.
- Queijo, M. J. "Methods of Obtaining Stability Derivatives." *Performance and Dynamics of Aerospace Vehicles*. Washington, D.C.: NASA-Langley Research Center, NASA, 1971.
- Rech, J., and C. S. Leyman. "A Case Study by Aerospatiale and British Aerospace on the Concorde." *AIAA Professional Case Studies*, no date.
- Ribner, H. S. *NACA Reports 819, 820*. Langley, Va.: NACA, 1943.
- Roskam, J. *Airplane Flight Dynamics and Automatic Flight Controls*. Lawrence, Kans.: Roskam Aviation and Engineering Corp., 1979.
- Scott, W. B. "X-28 Proves Viability of Forward-Swept Wing." *Aviation Week and Space Technology* (October 31, 1988): 36–42.
- Stevens, B. L., and F. L. Lewis. *Aircraft Control and Simulation*. 1st ed. New York: Wiley, 1992.
- Stinton, D. *Design of the Airplane*. Washington, D.C.: AIAA, 1983.
- . *Flying Qualities and Flight Testing of the Airplane*. AIAA Educational Series. Washington, D.C.: AIAA, 1996.
- U.S. Standard Atmosphere. *U.S. Extensions to the ICAO Standard Atmosphere*. Washington, D.C.: U.S. Government Printing Office, 1976.
- Vidyasagar, M. *Nonlinear Systems Analysis*. Englewood Cliffs, N.J.: Prentice Hall, 1978.
- Whitford, R. *Design for Air Combat*. London: Jane's, 1987.
- Yuan, S. W. *Foundations of Fluid Mechanics*. Englewood Cliffs, N.J.: Prentice Hall, 1967.

## PROBLEMS

### Section 2.2

- 2.2-1** An airfoil is tested in a subsonic wind tunnel. The lift is found to be zero at a geometrical angle of attack  $\alpha = -1.5^\circ$ . At  $\alpha = 5^\circ$ , the lift coefficient is measured as 0.52. Also, at  $\alpha = 1^\circ$  and  $7.88^\circ$ , the moment coefficients about the center of gravity are measured as  $-0.01$  and  $0.05$ , respectively. The center of gravity is located at  $0.35c$ . Calculate the location of the aerodynamic center and the value of  $Cm_{ac}$ .

### Section 2.3

- 2.3-1** An aircraft is flying wings level at constant altitude, at a speed of 500 ft/s, with an angle of attack of  $8^\circ$  and a sideslip angle of  $-5^\circ$ , when it runs into gusty wind conditions. Determine the new "instantaneous" angles of attack and sideslip angle for the following cases:
- (i) A horizontal gust of 20 ft/s from *left to right* along the body  $y$ -axis
  - (ii) A horizontal gust of 50 ft/s from dead astern
  - (iii) A gust of 30 ft/s, *from the right*, with velocity vector in the  $y$ - $z$  plane, and at an angle of  $70^\circ$  below the  $x$ - $y$  plane

- 2.3-2** Derive expressions for the derivatives of  $V_T$ , alpha, and beta, in terms of  $U'$ ,  $V'$ , and  $W'$  and their derivatives. Check the results against Equations (2.3-10).
- 2.3-3** Consult the literature to find information on the significance and numerical values of the helix angle achieved by different types of fighter aircraft. Find some graphs of roll rate versus equivalent airspeed and calculate some values of helix angle. Explain the shape of the graph.
- 2.3-4** Program the functions for the body-axes force coefficients  $C_X$  and  $C_Z$ , as given in Appendix A, for the F-16 model. Write another program to use these data and plot a set of curves of lift coefficient as a function of alpha (for  $-10^\circ \leq \alpha \leq 50^\circ$ ), with elevator deflection as a parameter (for  $\delta_e = -25^\circ, 0^\circ, 25^\circ$ ). Determine the angle of attack at which maximum lift occurs.
- 2.3-5** Program the body-axes moment coefficient  $C_M$ , as given in Appendix A, for the F-16 model. Write another program to plot a set of curves of pitching moment as a function of alpha (for  $-10^\circ \leq \alpha \leq 50^\circ$ ), with elevator deflection as a parameter (for  $\delta_e = -25^\circ, 0^\circ, 25^\circ$ ). Comment on the pitch stiffness and on the elevator control power.
- 2.3-6** Program the F-16 engine thrust model, function THRUST, in Appendix A. Write a program to plot the thrust as a function of power setting (0 to 100%), with altitude as a parameter (for  $h = 0, 25 \text{ kft}, 50 \text{ kft}$ ), at Mach 0.6. Also, plot thrust against Mach number, at 100% power, with altitude as a parameter (for  $h = 0, 25 \text{ kft}, 50 \text{ kft}$ ). Comment on these characteristics of the jet engine.

## Section 2.4

- 2.4-1** Solve numerically the nonlinear longitudinal-equilibrium equations to determine the angle of attack and elevator deflection (both in degrees) of the following small airplane, for level ( $\gamma = 0$ ) steady-state flight at 90 ft/s. Assume  $g = 32.2 \text{ ft/s}$ .

Atmospheric density =  $2.377 \times 10^{-3} \text{ slugs/ft}^3$  (assumed constant)

Weight = 2300 lb, inertia (slug-ft<sup>2</sup>):  $I_{yy} = 2094$

Wing reference area,  $S = 175 \text{ ft}^2$

Mean aerodynamic chord,  $\bar{c} = 4.89 \text{ ft}$

Thrust angle,  $\alpha_T = 0$

Lift:  $C_L = 0.25 + 4.58 * \alpha$  (alpha in radians)

Drag:  $C_D = 0.038 + 0.053 * C_L * C_L$

Pitch:  $C_m = 0.015 - 0.75 * \alpha - 0.9 * \delta_e$  (alpha,  $\delta_e$ , in radians)

Pitch damping coefficient,  $C_{m_q} = -12.0$  (per rad/s)

- 2.4-2** Derive Equation (2.4-13), including all of the missing steps.

- 2.4-3** An aircraft is flying at 30,000 ft ( $\rho = 8.9068 \times 10^{-4}$ ) and has a wing lift coefficient of 1.0 and a tail lift coefficient of 1.2. The wing surface area and tail surface area are 600 ft<sup>2</sup> and 150 ft<sup>2</sup>, respectively. The mean aerodynamic chord of the wing is 10 ft. The mean aerodynamic center of the wing is 10 ft ahead of the cm. The pitching moment coefficient about the aerodynamic center of the wing is  $-0.05$ . The tail is made up of a symmetric airfoil cross section; take the tail efficiency as  $\eta = 1.0$ . Determine the distance of the tail aerodynamic center from the cm for trimmed flight. If the aircraft weighs 50,000 lb, calculate the air speed for trimmed level flight.

## Section 2.5

- 2.5-1** Make a block diagram of the flat-Earth vector equations of motion (2.5-1), including wind inputs, pilot control inputs, and terrestrial position calculations. Blocks included should be vector integration, moment generation, force generation, atmosphere model with Mach and dynamic pressure calculation, addition, subtraction, and cross product. The diagram should show all of the variables that would be needed in a high-fidelity simulation.
- 2.5-2** Repeat Problem 2.5-1 for the oblate rotating-Earth equations of motion.
- 2.5-3** Show that the quantity  $\Gamma$  in Equation (2.5-24) can be calculated from either body-axes or wind-axes quantities, with the same formula.
- 2.5-4** Expand the flat-Earth vector form equations of motion, Equations (2.5-1), into scalar equations. Check the results against Table 2.5-1.

## Section 2.6

- 2.6-1** Work through the derivation of the coefficient matrices for the linearized force equations (2.6-11), (2.6-14), and (2.6-16), filling in all of the steps.
- 2.6-2** Fill in all of the steps in the derivation of the coefficient matrix, Equation (2.6-20), for the linearized kinematic equations.
- 2.6-3** Fill in all of the steps in the derivation of the coefficient matrices for the linearized moment equations (2.6-22), (2.6-25), and (2.6-26).
- 2.6-4** Write a program to calculate (approximately) the derivative of a function of a single variable (assumed to be continuous), given discrete values of the function. Use the program with the lookup table from Problem 2.3-5 to estimate the derivative  $C_{m_\alpha}$  at the values of  $\alpha = 0^\circ, 10^\circ, 20^\circ$ , and  $30^\circ$  (when  $\delta e = 0^\circ$ ). Determine whether the aircraft has positive pitch stiffness at these angles of attack.

## CHAPTER 3

---

# MODELING, DESIGN, AND SIMULATION TOOLS

---

### 3.1 INTRODUCTION

In this chapter we will look more closely at continuous-time state-space models, their properties, and how they are derived from physical systems. This will lead to numerical methods and algorithms for computer software that can be applied to the many tasks associated with the simulation of an aerospace vehicle and design of its control systems. The software tools will provide the capability to trim aircraft models for steady-state flight, perform digital flight simulation, extract linear state-space and transfer function descriptions of aircraft models, and perform linear control system design. These operations are illustrated in Figure 3.1-1.

In the figure the nonlinear state and output equations are, respectively,

$$\dot{X} = f(X, U), X(n \times 1), U(m \times 1) \quad (3.1-1a)$$

$$Y = g(X, U), Y(p \times 1), \quad (3.1-1b)$$

where  $f$  and  $g$  represent arrays of continuous, single-valued functions. The linear versions of these equations are

$$\dot{x} = Ax + Bu \quad (3.1-2a)$$

$$y = Cx + Du \quad (3.1-2b)$$

An output equation is required because the state variables may not all be physical variables or directly accessible. Hence there is a need to represent physically measurable quantities by the output variables  $Y_i$  or  $y_i$ .



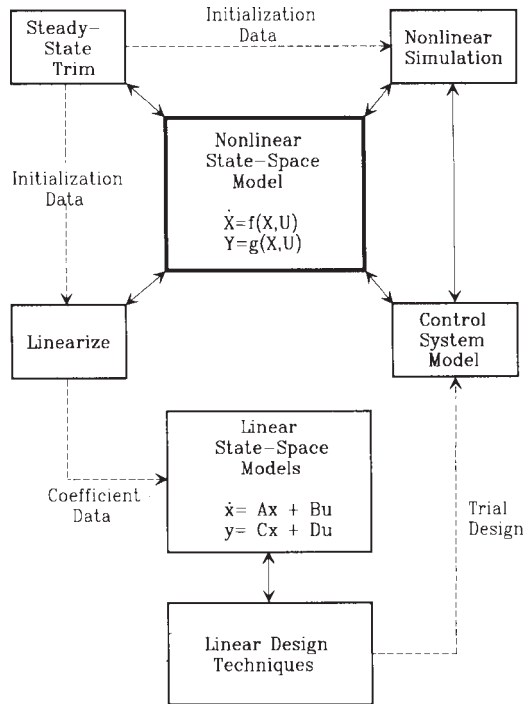


**Figure 3.1-1** State-space operations.

Referring to Figure 3.1-1, the behavior of a real system can be simulated by solving the nonlinear model equations. The mathematical theory for numerical solution of ordinary differential equations (ODEs) is mature and is cast in the state-space canonical form. Therefore, a state-space model is a prerequisite for simulation. Second, real systems operate around design points or equilibrium conditions and are nonlinear to varying degrees as they deviate from equilibrium. By linearizing the nonlinear model around these design points the powerful tools of linear systems theory can be used to analyze the system and perform control systems design. The state-space formulation lends itself to linearization around equilibrium points. Third, the matrix formulation of the linear state equations readily handles multiple-input, multiple-output (MIMO) systems with single-input, single-output (SISO) systems as a special case. We will see that the MIMO description is essential for some aspects of aircraft dynamics. Lastly, if additional equations are to be coupled to the model, for example, to simulate an automatic control system, this is easily done when the controller equations are also in state-space form.

Also in this chapter, we have provided source code for state-space models of two different aircraft. These models will be used to illustrate aircraft dynamic behavior and for control system design examples in Chapter 4. The final topic of the chapter is a review of the classical control theory and design techniques that will be used in Chapter 4.

### 3.2 STATE-SPACE MODELS

ODEs are our most powerful method for modeling continuous-time lumped-parameter dynamic systems. Continuous time implies that the variables are uniquely defined at all moments in time within a specified interval, except possibly at a countable set of points. *Lumped parameter* implies that each of the interconnected elements that make up the model responds immediately to its excitation. This is in contrast to distributed-parameter systems, in which disturbances propagate through the system as waves. Distributed-parameter systems are described by partial differential equations. Real dynamic systems can behave as lumped- or distributed-parameter systems, depending on the frequency spectrum of their excitation. For example, an aircraft will respond partly as a distributed-parameter system to a sudden wind gust that excites the flexible bending modes of the wings and fuselage. For wind disturbances that are less abrupt, it will respond according to our rigid-body equations of motion. For large, flexible aircraft such as passenger jets, the flexible modes can be low enough in frequency to approach or overlap with the rigid-body modes. We will restrict ourselves to lumped-parameter models described by ODEs, and these ODEs allow us to describe a wide range of nonlinear and time-varying systems.

The continuous-time state-space equations are a “canonical form” of the ODE description of continuous-time lumped-parameter dynamic systems. That is, they represent a form to which all the members of the class can be reduced by appropriate transformations. Reduction to this canonical form allows a wide range of modeling, simulation, and design problems to be handled within a common framework of algorithms and software tools, as shown in Figure 3.1-1.

#### Models of Mechanical and Electrical Systems

There are many ways of deriving state equations for these systems. Here we give two examples in which we choose the state variables according to the energy storage elements and then use an appropriate technique for finding the state equations.

**Example 3.2-1: State Equations for a Mechanical System** Figure 3.2-1 shows a simple mechanical system to illustrate the derivation of state equations. The input to the system is the spring displacement  $u(t)$ , and the output is the displacement  $y(t)$  of the mass  $m$ . The mass slides with negligible friction, and the springs are linear with stiffness  $k_i$  and zero mass. The dampers also have no mass and only dissipate energy. They produce a reaction force equal to the viscous constant,  $d_i$ , times the rate at which they are extending or contracting. The auxiliary variable  $w(t)$  is needed so that equations can be written for the associated spring and damper. There are three independent energy storage elements, and state variables can be assigned accordingly:

$$\begin{aligned} x_1 &= (u - y), && \text{compression of spring } k_1 \\ x_2 &= (y - w), && \text{compression of spring } k_2 \\ x_3 &= \dot{y}, && \text{translational rate of } m \end{aligned}$$

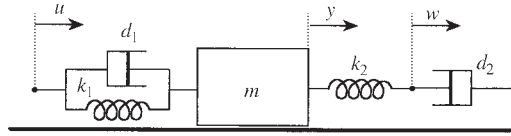


**Figure 3.2-1** A mechanical system.

Equations involving the state variables can now be written by inspection:

$$\begin{aligned}\dot{x}_1 &= \dot{u} - x_3 \\ d_2(x_3 - \dot{x}_2) &= k_2 x_2 \\ m\dot{x}_3 &= k_1 x_1 + d_1(\dot{u} - x_3) - k_2 x_2\end{aligned}$$

These equations can be put into the form

$$\dot{x} = Ax + B_1 \dot{u}$$

To reduce this to state-space form, let

$$z = x - B_1 u$$

Then

$$\dot{z} = Ax = Az + (AB_1)u$$

and these are state equations in standard form. This approach will work for most simple mechanical systems. The technique used to remove  $\dot{u}$  from the first set of equations will also work for the equation:

$$\dot{x} = Ax + B_1 \dot{u} + B_0 u \quad \blacksquare$$

In any physical system, the stored energy cannot be changed instantaneously because this would require infinite power. This provides a way of directly finding the coefficient matrices of the linear state equations, which is most easily illustrated with an electrical circuit.

In an electrical circuit, energy is stored in the magnetic fields of inductors and in the electric fields of capacitors. Inductor currents and capacitor voltages can be chosen as state variables because these quantities determine the stored energy. Therefore, the current through an inductor, or voltage across a capacitor, cannot change instantaneously.

For any given unexcited circuit, if we could place an ideal unit-step voltage generator in series with each capacitor in turn, inside its terminals, its state variable would jump to 1.0 volts at  $t = 0$ . Instantaneously, all of the capacitors would act like short circuits and all of the inductors like open circuits. The capacitor currents and inductor voltages are proportional to the derivatives of their state variables ( $i = C(dv/dt)$ ),

$v = L(di/dt)$ ). Therefore, all of the state derivatives can be found, when all but one of the state variables are zero, by analyzing a much simpler circuit in which capacitors have been replaced by short circuits and inductors by open circuits. This gives one column of the  $A$ -matrix. Similarly, placing a unit-step current generator in parallel with each inductor in turn gives the columns of the  $A$ -matrix corresponding to the inductor current state variables. This procedure is illustrated in our second example.

**Example 3.2-2: State Equations for an Electrical System** Here we will find the  $A$ - and  $B$ -matrix elements  $a_{ij}$ ,  $b_i$  for the “bridged-T” circuit shown in Figure 3.2-2. In the figure the state variables  $x_1$ ,  $x_2$ , and  $x_3$  have been assigned to the capacitor voltages and inductor current. Imagine a unit-step voltage generator placed in series with  $C_1$ , as indicated by the dashed circle, and let  $t = 0^+$  indicate that the generator has switched from zero to 1 volt. Then, at  $t = 0^+$ ,

$$x_1(0^+) = 1.0, \quad x_2(0^+) = 0.0, \quad x_3(0^+) = 0.0$$

The defining equation for a capacitor and the linear state equation then give

$$i_1(0^+) \equiv C_1 \dot{x}_1(0^+) = C_1 a_{11} x_1(0^+) \quad \text{or} \quad a_{11} = \frac{1}{C_1} \frac{i_1(0^+)}{x_1(0^+)}$$

The conductance  $i_1(0^+)/x_1(0^+)$  is easily found from the resistive circuit obtained when  $C_2$  is replaced by a short circuit and  $L$  by an open circuit. The result is

$$a_{11} = \frac{-1}{C_1 \left( R_1 + \frac{R_2 R_4}{R_2 + R_4} \right)}$$

The same voltage generator also gives

$$v_2(0^+) \equiv L \dot{x}_2(0^+) = L a_{21} x_1(0^+) \quad \text{or} \quad a_{21} = \frac{1}{L} \frac{v_2(0^+)}{x_1(0^+)} = \frac{1}{L}$$

and

$$a_{31} = \frac{i_2(0^+)}{C_2 x_1(0^+)} = \frac{-1}{C_2 (R_1 + R_4 + (R_1 R_4)/R_2)}$$

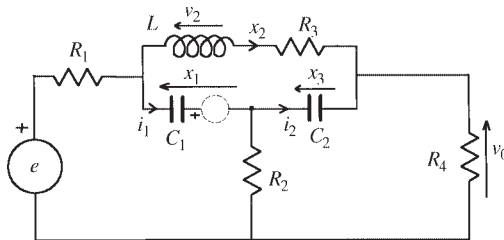


**Figure 3.2-2** State variables for an electrical circuit.

The second and third columns of the  $A$ -matrix can be found, respectively, by putting a unit-step current generator in parallel with  $L$  and a unit-step voltage generator in series with  $C_2$ . In the same manner, the  $B$ -matrix can be found by letting the input voltage  $e(t)$  come from a unit-step voltage generator. The  $C$ - and  $D$ -matrices can be found in an ad hoc way; in this case an expression for the output voltage is

$$v_o = (x_2 + C_2 \dot{x}_3) R_4$$

Substitution of the state equation for  $\dot{x}_3$  into this expression yields  $C$  and  $D$ . ■

This technique will always work for linear time-invariant electric circuits, though any mutual-induction coupling causes complications. Alternative techniques include setting up the Kirchhoff loop or nodal equations and reducing these to state equations (Nise, 1995).

## Reduction of Differential Equations to State-Space Form

Consider the following nonlinear, scalar ODE:

$$\ddot{y} + f(\dot{y}) + g(y) = h(u) \quad (3.2-1)$$

Here  $u(t)$  is a known input and  $y(t)$  is the response of the system described by this ODE. The functions  $f$ ,  $g$ ,  $h$  are arbitrary, known nonlinear functions and may be the result of manipulating a preceding nonlinear equation to reduce the coefficient of the highest derivative to unity. Suppose that we convert this differential equation to two simultaneous integral equations by writing

$$\begin{aligned} y &= \int \dot{y} dt \\ \dot{y} &= \int [h(u(t)) - f(\dot{y}) - g(y)] dt \end{aligned} \quad (3.2-2)$$

Now consider how these equations might be solved. The variable  $y$  may be, for example, a position variable, but the functional form of the solution is the same if we use any other quantity as an *analog* of position. In an *analog computer* a device is available to perform integration of voltages with respect to time, and voltage is the analog of whatever physical variable we wish to simulate. We can make a diagram of the analog computer connections if we draw a box representing the integration operation, symbols representing summation and multiplication of variables, and lines showing which variables are subjected to each operation. Thus, Figure 3.2-3 shows a *simulation diagram* (or simply a *block diagram*) of Equations (3.2-2). If an analog computer is connected in this way and switched on with the correct initial conditions on the integrators, it will effectively solve Equations (3.2-1) or (3.2-2).

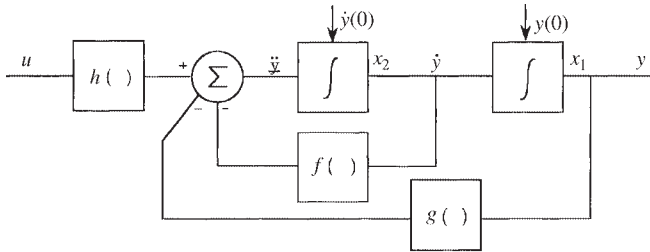


**Figure 3.2-3** A SISO simulation diagram.

Referring to Figure 3.2-3, if we simultaneously break the input connections of all of the integrators (in an analog computer the inputs would be connected to “signal ground”), the outputs of the integrators will remain constant at the values they had at the instant of breaking the connections. If the continuation of the input signal  $u(t)$  is available, the analog computer simulation can be restarted at any time and all of the signals will assume the values they had when the connections were broken, and the simulation can continue with no information lost. Therefore, the integrator output variables satisfy our earlier definition of state variables. Knowledge of their values at any time instant, together with the input signal, completely defines the state of the system.

Now starting from the right-hand side of Figure 3.2-3, let state variables  $x_1$  and  $x_2$  be defined as the integrator outputs. Therefore, by inspection of the diagram, or Equations (3.2-2), the state equations for the second-order ODE (3.2-1) are

$$\begin{aligned}\dot{x}_1 &= x_2 \\ \dot{x}_2 &= h(u) - f(x_2) - g(x_1)\end{aligned}\tag{3.2-3}$$

This technique can easily be extended to find  $n$  state variables for an  $n$ th-order differential equation. It is not necessary to draw the block diagram, because the technique simply amounts to defining  $y(t)$  and its derivatives up to the  $(n - 1)$ th as state variables and then writing the equation for the  $n$ th derivative by inspection. State variables chosen in this way are often called *phase variables*.

Next consider a more difficult example where the block diagram will be helpful. This time the ODE model will involve derivatives of the input variable but will be linear with constant coefficients, as in the following second-order example:

$$\ddot{y} + a_1 \dot{y} + a_0 y = b_2 \ddot{u} + b_1 \dot{u} + b_0 u\tag{3.2-4}$$

The coefficient of the highest derivative of  $y$  can always be made equal to unity by dividing all of the other coefficients. Let the operator  $p^n$  indicate differentiation  $n$  times with respect to time and write this equation as

$$p^2(y - b_2 u) + p(a_1 y - b_1 u) + (a_0 y - b_0 u) = 0$$

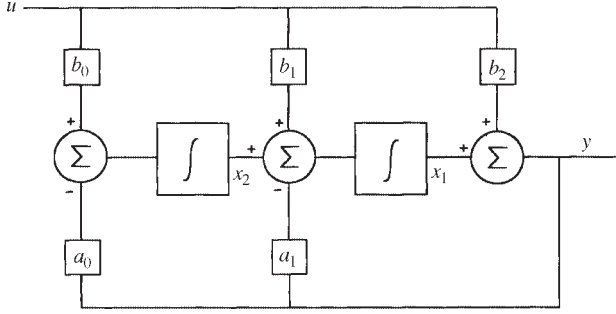


**Figure 3.2-4** A general second-order SISO simulation diagram.

Now turn this into an integral equation for  $y$ ,

$$y = b_2 u + \int (b_1 u - a_1 y) dt + \iint (b_0 u - a_0 y) d\tau dt$$

A simulation diagram can be drawn by inspection of this equation and is shown in Figure 3.2-4. A set of state equations can again be found by assigning state variables to the outputs of the integrators.

This example can be extended to the general case of an  $n$ th-order differential equation, with all derivatives of the input present. The differential equation for the general case is

$$p^n y + \sum_{i=0}^{n-1} a_i p^i y = \sum_{i=0}^n b_i p^i u \quad (3.2-5)$$

and the state equations are

$$\frac{d}{dt} \begin{bmatrix} x_1 \\ x_2 \\ \vdots \\ \vdots \\ x_n \end{bmatrix} = \begin{bmatrix} -a_{n-1} & 1 & 0 & \dots & 0 \\ -a_{n-2} & 0 & 1 & \dots & 0 \\ \vdots & \vdots & \vdots & \ddots & \vdots \\ -a_1 & 0 & 0 & \dots & 1 \\ -a_0 & 0 & 0 & \dots & 0 \end{bmatrix} \begin{bmatrix} x_1 \\ x_2 \\ \vdots \\ \vdots \\ x_n \end{bmatrix} + \begin{bmatrix} (b_{n-1} - a_{n-1}b_n) \\ (b_{n-2} - a_{n-2}b_n) \\ \vdots \\ \vdots \\ (b_0 - a_0b_n) \end{bmatrix} u(t) \quad (3.2-6)$$

If the highest derivative on the right-hand side of (3.2-5) is the  $m$ th, then for real systems  $m \leq n$ . In the cases where  $m = n$  this is a practical approximation in situations when very-high-frequency effects can be neglected. Therefore,  $b_i \equiv 0$  for  $i > m$ , and when  $m < n$  a group of  $n$  terms disappears from the right-hand side of (3.2-6).

This form of the linear state equations is known as the *observer canonical form*. The  $A$ -matrix has a structure called a *companion form*, which is known to be “ill conditioned” for numerical computation but is useful for theoretical results. The technique used here to obtain the simulation and state equations can be extended to include time-varying ODE coefficients (Laning and Battin, 1956), but there is no general method for deriving the simulation diagram when the ODE is nonlinear.

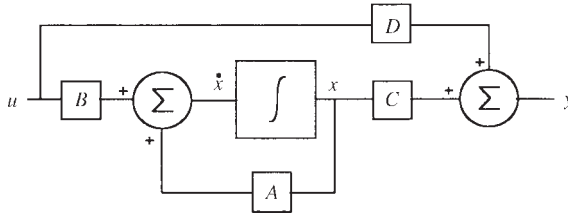


**Figure 3.2-5** State equation simulation diagram.

Finally, let us take a look at a simulation diagram representation of the linear state equations. Figure 3.2-5 shows a diagram that represents the linear state and output equations, as given by Equations (3.1-2). In this diagram the lines, or signal paths, carry several variables simultaneously, the coefficient boxes represent matrix operations, and the integrator box represents multiple integrators simultaneously processing all of the input signals individually. This also represents a valid way to wire up an analog computer; the advantages of this form of system model will become apparent in this chapter.

### Time-Domain Solution of LTI State Equations

When the state equations are linear and time invariant (LTI), they can be solved analytically. Elementary differential equation texts show that a linear first-order ODE can be solved by using an exponential “integrating factor” to yield an exact derivative. When the equation is also time invariant, the integrating factor reduces to a simple exponential function. An analogous method can be used to solve the set of  $n$  first-order LTI state equations.

The matrix exponential  $e^{At}$ , where  $A$  is a square constant matrix, is defined by the matrix series

$$e^{At} \equiv I + At + \frac{A^2 t^2}{2!} + \frac{A^3 t^3}{3!} + \dots \quad (3.2-7)$$

The series is uniformly convergent and can be differentiated or integrated term by term, resulting in properties analogous to the scalar exponential function

$$\frac{d}{dt}(e^{At}) = Ae^{At}$$

and

$$A \int e^{At} dt = e^{At} - I$$

It is also evident from (3.2-7) that  $\exp(At)$  is commutative with  $A$ , that is,

$$Ae^{At} = e^{At}A$$



Now using  $e^{At}$  as an integrating factor, the state equation (3.1-2a) can be written as

$$\frac{d}{dt} (e^{-At} x(t)) = e^{At} B u(t)$$

If this equation is integrated, with the constant of integration determined from initial conditions at  $t = t_0$ , we obtain

$$x(t) = e^{A(t-t_0)} x(t_0) + \int_{t_0}^t e^{A(t-\tau)} B u(\tau) d\tau \quad (3.2-8)$$

The first component of this solution is the *homogeneous component*, which is the response to the initial conditions  $x(t_0)$ , and  $e^{A(t-t_0)}$  takes the state from time  $t_0$  to  $t$  and is called the *transition matrix*. The second component is the *forced component*, which is the response to the input  $u(t)$ . The integral on the right-hand side of (3.2-8) is a *convolution integral*, the time-domain equivalent of transform multiplication in the frequency domain.

The solution (3.2-8) is of little computational value to us because of the difficulties of finding analytical expressions for the transition matrix for systems of all but the lowest order. Also the convolution integral is inconvenient to evaluate for any but the simplest input functions. However, this solution does lead to a discrete-time recursion formula that is useful. A recursion formula becomes practical when we consider a short time interval  $T$ , over which the input can be approximated by a simple function. Therefore, we look for a discrete-time formula by considering a time interval from  $t = kT$  to  $t = (k+1)T$ , where  $k$  is a positive integer. In Equation (3.2-8), let  $t_0 = kT$  and  $t = (k+1)T$  and make a change of variable  $\lambda = (\tau - kT)$ ; then

$$x(k+1) = e^{AT} x(k) + e^{AT} \int_0^T e^{-A\lambda} B u(\lambda + kT) d\lambda, \quad (3.2-9)$$

where  $T$  is implied in the argument of  $x$ .

The integral in (3.2-9) can be evaluated by a variety of methods, for example, the trapezoidal rule or Simpson's rule. We will take a simple stepped approximation to  $u(t)$  such that  $u(\lambda + kT) \approx u(kT)$  for  $0 \leq \lambda < T$  [this is called a *zero-order hold (ZOH) approximation*];  $u(kT)$  can then be taken out of the integrand. The remaining integral can be evaluated by considering term-by-term integration of the matrix exponential, and the result is

$$x(k+1) = e^{AT} x(k) + Q(T) B u(k), \quad (3.2-10)$$

where  $Q(T)$  is given by

$$Q(T) = T \left[ I + \frac{AT}{2!} + \frac{A^2 T^2}{3!} + \frac{A^3 T^3}{4!} + \cdots \right] \quad (3.2-11a)$$

or, when  $A^{-1}$  exists,

$$Q(T) = A^{-1} (e^{AT} - I) \quad (3.2-11b)$$

Equation (3.2-10) is a discrete-time recursion formula. It can be used as an alternative to numerical integration of the state equations when the equations are linear and  $e^{AT}$  has been found analytically or numerically. The matrix exponential  $e^{AT}$  is called the *discrete-time transition matrix*. Methods of computing the transition matrix are described in the literature (Healey, 1973; Moler and Van Loan, 1978; Zakian, 1970), and methods of computing integrals involving the matrix exponential (e.g.,  $Q(T)$ ) are described by Van Loan (1978). Commercial software is available to compute the transition matrix (e.g., MATLAB “expm”).

### Modal Decomposition

In Section 1.3 the modal coordinates were introduced to show the connection between eigenvalues and the natural modes of a dynamic system. It is possible to use the additional information contained in the eigenvectors to determine which variables are involved in a given mode and what inputs will excite the mode. The time-domain solution (3.2-8) of the LTI state equation can be used for this purpose.

The continuous-time transition matrix can be expressed in terms of eigenvalues and eigenvectors in the following way. The similarity between the  $A$  matrix and (in general) a Jordan form matrix can be used to express an arbitrary power of  $A$  as

$$A^k = (MJM^{-1}) (MJM^{-1}) \dots = MJ^k M^{-1}$$

When this is done for every term in the matrix exponential series and when  $J$  is assumed to be diagonal (distinct eigenvalues), the result is

$$e^{At} = Me^{Jt}M^{-1} = [v_1 \ v_2 \ \dots v_n] \begin{bmatrix} e^{\lambda_1 t} & 0 & 0 & 0 & \dots \\ 0 & e^{\lambda_2 t} & 0 & 0 & \dots \\ 0 & 0 & e^{\lambda_3 t} & 0 & \dots \\ \dots & \dots & \dots & \dots & \dots \\ 0 & \dots & \dots & 0 & e^{\lambda_n t} \end{bmatrix} \begin{bmatrix} w_1^T \\ w_2^T \\ w_3^T \\ \dots \\ w_n^T \end{bmatrix}, \quad (3.2-12)$$

where  $v_i$  is the  $i$ th column of  $M$  (the  $i$ th eigenvector) and  $w_i^T$  is the  $i$ th row of  $M^{-1}$ . Then, by definition, “vectors”  $w_i$  are orthonormal with the eigenvectors, that is,

$$w_i^T v_j = \begin{cases} 0, & i \neq j \\ 1, & i = j \end{cases} \quad (3.2-13)$$

It is also easy to show that the vectors  $w_i$  are actually the *left eigenvectors* of  $A$ , that is, the right eigenvectors of  $A^T$ . If (3.2-12) is postmultiplied by the initial-condition

vector  $x_0$ , the homogeneous part of the solution of the continuous-time state equation is obtained:

$$e^{At}x_0 = [v_1 \ v_2 \ \cdots \ v_n] \begin{bmatrix} e^{\lambda_1 t} (w_1^T x_0) \\ e^{\lambda_2 t} (w_2^T x_0) \\ \dots\dots\dots \\ e^{\lambda_n t} (w_n^T x_0) \end{bmatrix}, \quad (3.2-14)$$

where the terms  $(w_i^T x_0)$  are scalar products. Equation (3.2-14) can be rewritten as

$$e^{At}x_0 = \sum_{i=1}^n (w_i^T x_0) e^{\lambda_i t} v_i$$

If this same procedure is followed but with (3.2-12) postmultiplied by  $Bu(\tau)$ , the forced component of the response is obtained. The complete response is therefore given by

$$x(t) = \sum_{i=1}^n v_i e^{\lambda_i t} (w_i^T x_0) + \sum_{i=1}^n v_i \int_0^t e^{\lambda_i(t-\tau)} (w_i^T B u(\tau)) d\tau \quad (3.2-15)$$

In effect, Equation (3.2-15) uses the  $n$  linearly independent eigenvectors as a basis for the  $n$ -dimensional space, associates a characteristic mode with each basis vector, and shows the fixed component of  $x(t)$  in each direction. If, for example, the initial-condition vector lies in a direction such that a scalar product  $(w_i^T x_0)$  is zero, the mode  $e^{\lambda_i t}$  will not appear in the homogeneous response. According to (3.2-13), this will occur if the initial-condition vector lies along any eigenvector other than the  $i$ th. Similarly, if the scalar product  $(w_i^T B u(\tau))$  is zero, the mode  $e^{\lambda_i t}$  will not be excited by the input. In Chapters 5 and 6 we discuss the related idea of *controllability* of the modes and show how it is determined by the  $A$ - and  $B$ -matrices. If we form the output vector by premultiplying (3.2-15) by the  $C$ -matrix, we see that whether or not a mode appears in the output depends on the  $C$ - and  $A$ -matrices. This is the concept of *observability*, also described in Chapters 5 and 6.

Equation (3.2-15) also shows that if we examine the  $i$ th eigenvector, its nonzero elements will indicate to what extent each state variable participates in the  $i$ th mode. The relative involvement of the different variables is complicated by the fact that the eigenvector elements can, in general, each have different units.

## Laplace Transform Solution of LTI State Equations

The Laplace transform (LT) maps real functions of time into functions of the complex variable  $s$ , which is written in terms of its real and imaginary parts as  $s = \sigma + j\omega$  and has the dimensions of a complex frequency variable. In the complex frequency domain (or  $s$ -domain) the functions of  $s$  can be manipulated algebraically into recognizable, known transforms and then mapped back into the time domain. Laplace

transform theory is thoroughly covered in many undergraduate texts (Ogata, 1998), and here we will only review two important points concerning applicability.

Two different ways of applying the LT will now be described. First, in general, analysis of a dynamic system will produce a set of simultaneous integro-differential equations. These equations should be transformed immediately, so that the initial-condition terms that appear from applying the LT differentiation and integration theorems represent the initial stored energy. If the integral terms are removed by differentiation, derivatives of the system input may appear. These give rise to extra initial-condition terms when the differential equations are transformed and can make it difficult to solve for all of the required initial conditions on the dependent variable. Therefore, we avoid transforming the general ODE in Equation (3.2-5) if there are nonzero initial conditions and derivatives on the right-hand side.

The second method of using the LT applies to initially unexcited systems; no initial-condition terms appear after transforming. If the equations have been differentiated so that derivatives of the input appear, the input initial-condition terms must cancel with the initial conditions on the output. Therefore, if the system is described by the differential equation (3.2-15), this equation can be transformed with zero initial conditions. For circuits there is actually no need to write the differential equations because, with no initial stored energy, the system elements can be represented by transform impedances (or admittances). Circuit analysis rules will then yield  $s$ -domain equations that can be solved for the output transform. This method will be addressed in the next section.

We will denote Laplace transforms by uppercase symbols, thus

$$X(s) = \mathcal{L}[x(t)], \quad U(s) = \mathcal{L}[u(t)]$$

The LTI state equations have no derivatives of  $u(t)$  and can be solved by Laplace transforming (3.1-2a):

$$sX(s) - x(0^+) = AX(s) + BU(s) \quad (3.2-16)$$

$$\therefore X(s) = (sI - A)^{-1}[x(0^+) + BU(s)]$$

$$Y(s) = C(sI - A)^{-1}[x(0^+) + BU(s)] + DU(s) \quad (3.2-17)$$

Because there are no input derivatives, this solution requires  $n$  initial conditions on  $x(t)$  only, and these would specify the initial stored energy in our earlier examples. The symbol  $0^+$  indicates the limit when the time origin is approached from the right-hand side.

If we compare the transform solution for  $X(s)$  with the time-domain solution for  $x(t)$ , Equation (3.2-8), we see that the transition matrix is given by

$$e^{At} = \mathcal{L}^{-1}[(sI - A)^{-1}] \quad (3.2-18)$$

The LT solutions (3.2-16) and (3.2-17) are not well suited to machine computation, and hand computation involves a prohibitive amount of labor for other than low-order dynamic systems. Therefore, the LT solutions are mainly of interest as a complex number description of system properties, as we will now see.

### 3.3 TRANSFER FUNCTION MODELS

#### Derivation of Transfer Functions; Poles and Zeros

Consider the system described by the  $n$ th-order ODE (3.2-5) and transform with zero initial conditions. Solving algebraically for  $Y(s)$ ,

$$Y(s) = \frac{b_m s^m + b_{m-1} s^{m-1} + \dots + b_1 s + b_0}{s^n + a_{n-1} s^{n-1} + \dots + a_1 s + a_0} U(s), m \leq n \quad (3.3-1)$$

The polynomial rational function relating  $Y(s)$  to  $U(s)$  is the *transfer function* of this SISO system. If we have obtained the transform  $U(s)$ , then, using the partial fraction technique (see below), the right-hand side of (3.3-1) can be broken down into a sum of transforms corresponding to known time functions, and hence  $y(t)$  can be found as a sum of time functions.

From (3.2-17) we see that the transfer function obtained from the LTI state equations is a matrix expression and, for a MIMO system with  $p$  outputs and  $m$  inputs, the  $(p \times m)$  transfer function matrix is given by

$$G(s) = C(sI - A)^{-1}B + D \quad (3.3-2)$$

It is easy to show that a transfer function matrix is unchanged by a nonsingular transformation of the state variables. Equation (1.3-13b) represents such a transformation, and if the coefficient matrices from that equation are substituted into (3.3-2), the result is

$$\begin{aligned} G(s) &= CL^{-1}(sI - LAL^{-1})^{-1}LB + D \\ &= C[L^{-1}(sI - LAL^{-1})L]^{-1}B + D \\ &= C(sI - A)^{-1}B + D, \end{aligned}$$

which is (3.3-2) again. Therefore, we can choose a new set of state variables for a system, and the transfer function will be unchanged.

We will now review some other important properties of transfer functions. A matrix inverse can be expressed in terms of the adjoint matrix with its elements divided by its determinant, and so (3.3-2) can be written as

$$G(s) = \frac{C \operatorname{adj} (sI - A)B + D |sI - A|}{|sI - A|} \quad (3.3-3)$$

The transfer function from the  $j$ th input to the  $i$ th output is the  $(i, j)$ th element of  $G(s)$ , and this is the SISO transfer function  $G_{ij}(s)$ . A SISO transfer function can therefore be written as

$$G_{ij}(s) = \frac{c_i \operatorname{adj} (sI - A)b_j + d_{ij}|sI - A|}{|sI - A|}, \quad (3.3-4)$$

where  $c_i$  and  $b_j$  are, respectively, the  $i$ th row of  $C$  and the  $j$ th column of  $B$ . This transfer function is a rational function of two polynomials. The elements of the adjoint  $\text{adj}(sI - A)$  are, by definition, cofactors of  $|sI - A|$  and are therefore polynomials in  $s$  of degree  $n - 1$  or lower. The determinant  $|sI - A|$  is a polynomial of degree  $n$ . When (3.3-4) is written out as the ratio of two polynomials, it will correspond exactly to the SISO transfer function in (3.3-1) that we obtained from the  $n$ th-order ODE.

In (3.3-4), when  $d_{ij} = 0$ , the *relative degree* (denominator degree minus numerator degree) of this transfer function is unity or higher. When  $d_{ij} \neq 0$ , the relative degree is zero and, referring to the simulation diagram in Figure 3.2-5, we see that  $d_{ij}$  forms a “direct-feed” path from input to output. This means that the system output immediately begins to follow an input, and then the modes of the system respond and begin to modify the output.

If the polynomials in the transfer function (3.3-4) are factored, we obtain

$$G_{ij}(s) = \frac{k(s + z_1)(s + z_2) \dots (s + z_m)}{(s + p_1)(s + p_2) \dots (s + p_n)} \quad (3.3-5a)$$

Or, equivalently,

$$G_{ij}(s) = \frac{a_1}{s + p_1} + \frac{a_2}{s + p_2} + \dots + \frac{a_n}{s + p_n} \quad (3.3-5b)$$

The denominator factors are the factors of  $|sI - A|$ , and it is evident from (3.3-3) and (3.3-4) that all of the individual SISO transfer functions have the same denominator factors, given by the roots of the  $n$ th-degree polynomial equation

$$|sI - A| = 0 \quad (3.3-6)$$

The roots  $\{-p_i\}$  are called the *poles* of the transfer function and, at these values of  $s$ , the transfer function becomes infinite in magnitude.

Equation (3.3-6) is also the defining equation for the eigenvalues of the  $A$ -matrix. Therefore, the system poles are given by the eigenvalues of  $A$ . We know from Chapter 1 that the eigenvalues of a real system are real or occur in complex conjugate pairs and, according to Equation (3.2-15), determine the natural modes of a system. The position of the poles in the complex  $s$ -plane will determine the time constant of a real mode or the frequency of oscillation and exponential damping factor of a complex mode. Also, poles in the right-half  $s$ -plane will correspond to exponentially growing functions (unstable behavior). For this reason graphical operations in the  $s$ -plane are important to us.

Equation (3.3-5b) is the *partial fraction expansion* of the transfer function, and a coefficient  $a_i$  is the *residue* in the pole at  $-p_i$  (Ogata, 1998). In the case of complex poles the partial fractions combine as conjugate pairs. Poles of multiplicity  $k$  require a numerator of degree  $(k - 1)$  and can be further broken down into a finite expansion in inverse powers of  $(s + p_i)$ .

The *zeros* of the individual SISO transfer functions are the positions in the  $s$ -plane where their magnitudes become zero, that is, the roots  $\{-z_i\}$  of the numerator polynomial of (3.3-4). The number of zeros of each SISO transfer function will

range from zero to  $n$ , depending on the relative degree of the transfer function. Equations (3.3-3) and (3.3-4) show that the transfer function zeros depend on the  $B$ ,  $C$ , and  $D$  matrices, and Equation (3.2-15) shows how the  $B$  and  $C$  matrices, respectively, play a role in the excitation of a mode and its appearance in the system output. When a response transform is expanded in partial fractions, we see that the partial fraction coefficients depend on the numerator polynomial and hence on the zeros. The partial fraction terms correspond to the modes, and the zeros determine how strongly the modes are represented in the response. If all of the poles of the transform of the system input coincide with zeros of the SISO transfer function, there will be no forced response at the output of the system.

It is known that the values of polynomial roots are very sensitive to changes in the polynomial coefficients, and Equations (3.3-3) and (3.3-4) are the starting points of algorithms used to change the computation of zeros into a much more numerically stable eigenvalue problem (Emami-Naeini and Van Dooren, 1982). Transfer function-related analysis and design tools are based on poles and zeros, and we will have little use for the polynomial form of the transfer function.

When  $G_{ij}(s)$  is in the factored form (3.3-5a), with all coefficients of  $s$  equal to unity, or expressed as the ratio of two monic polynomials, the coefficient  $k$  is known as the *static loop sensitivity*. Note that if there are no poles or zeros at the  $s$ -plane origin, then, when  $s = 0$ , the magnitude of the transfer function (the dc gain) is finite and is determined by  $k$  and the zero and pole positions. If the relative degree is zero,  $k$  is the value of the transfer function at large values of  $s$  (the high-frequency gain).

From this point on we will drop the subscripts on  $G(s)$ , and it will be obvious from the context whether  $G$  represents a matrix or a scalar transfer function.

## Interpretation of the SISO Transfer Function

The complex exponential function  $e^{st}$ ,  $s = \sigma + j\omega$ , possesses time derivatives of all orders, all of the same form, and if we could apply it as an input to the SISO system described by the ODE (3.2-5), the particular solution of the ODE would be a time function of the same form. Furthermore, the solution would be given by an expression exactly like the transfer function (3.3-1), and we could use the response to  $e^{st}$  as a definition of a transfer function. The effect of the system on a specific exponential function  $e^{s_1 t}$  could be found by evaluating  $G(s_1)$ , given by

$$G(s_1) = \frac{k(s_1 + z_1)(s_1 + z_2) \dots (s_1 + z_m)}{(s_1 + p_1)(s_1 + p_2) \dots (s_1 + p_n)} \quad (3.3-7)$$

The numerator and denominator factors in this transfer function can be represented in magnitude and phase by vectors in the  $s$ -plane, drawn from the zeros and poles, respectively, to the point  $s_1$ . This is illustrated by the example shown in Figure 3.3-1 and, in general,

$$|G(s_1)| = k \frac{\text{product of lengths of vectors from zeros to } s_1}{\text{product of lengths of vectors from poles to } s_1} \quad (3.3-8a)$$

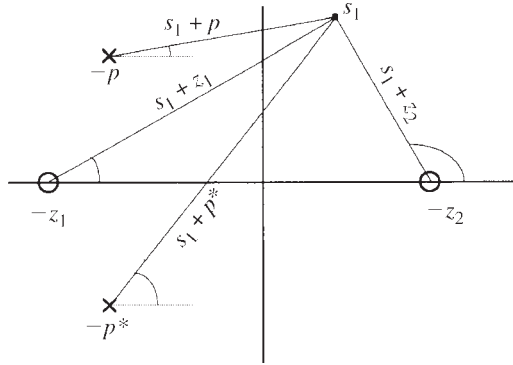


**Figure 3.3-1**  $s$ -Plane vectors representing pole-zero factors.

and

$$\begin{aligned} \angle G(s_1) = & \text{sum of angles of vectors from zeros to } s_1 \\ & - \text{sum of angles of vectors from poles to } s_1 \end{aligned} \quad (3.3-8b)$$

Because complex poles and zeros occur in conjugate pairs,

$$G(s_1^*) = G^*(s_1), \quad (3.3-9)$$

where “\*” denotes the conjugate, and this is clearly illustrated by drawing the appropriate vectors. This interpretation of the transfer function is particularly useful when  $s_1$  is a point on the  $s$ -plane  $j\omega$  axis. A real sinusoid can be represented as

$$\cos(\omega_1 t) = \frac{1}{2}(e^{j\omega_1 t} + e^{-j\omega_1 t}) \quad (3.3-10)$$

The particular solution of the ODE, with this input, is given by

$$\begin{aligned} y(t) &= \frac{1}{2} \left[ G(j\omega_1) e^{j\omega_1 t} + G(-j\omega_1) e^{-j\omega_1 t} \right] \\ \therefore y(t) &= \text{Re}\{G(j\omega_1) e^{j\omega_1 t}\} = |G(j\omega_1)| \cos(\omega_1 t + \angle G(j\omega_1)), \end{aligned} \quad (3.3-11)$$

where  $\text{Re}$  is the real-part operator, and we have made use of (3.3-9). The sinusoidal input (3.3-10) was not switched on at some particular time; mathematically it has existed for all time, and the solution (3.3-11) represents the *steady-state response* to a sinusoidal input of the system whose transfer function is  $G(s)$ .

The plots of  $|G(j\omega)|$  and  $\angle G(j\omega)$ , as  $\omega$  is varied from low to high frequency, are called the *magnitude* and *phase* of the system *frequency response*. The vector interpretation (3.3-8) shows that if there is a pair of complex poles near the imaginary axis, the vectors drawn from these poles will become very short in length over some range of frequencies, and there will be a peak in the magnitude of  $G(j\omega)$  and rapid changes in its phase. This is the phenomenon of *resonance*, in which a natural mode



of a system is excited by the input to the system. Conversely, if there is a pair of complex zeros close to the  $j\omega$  axis, the magnitude will pass through a minimum and the phase will again change rapidly. These effects are discussed more thoroughly in the section on frequency response.

A transfer function carries some very basic information about the way in which an aircraft (or any other system) will respond that is usually not obvious to the student. Two theorems that are fundamental in interpreting the transfer function are the Laplace transform initial- and final-value theorems:

$$\text{initial value : } f(0^+) \equiv \lim_{t \rightarrow 0} f(t) = \lim_{s \rightarrow \infty} sF(s) \quad (3.3-12a)$$

$$\text{final value : } f(\infty) \equiv \lim_{t \rightarrow \infty} f(t) = \lim_{s \rightarrow 0} sF(s) \quad (3.3-12b)$$

As an example of these theorems, consider the response of a system to a unit-step function. A useful notation for functions that start at  $t=0$  has been given by (DeRusso et al., 1965), and includes the unit step function

$$U_{-1}(t) \equiv \begin{cases} 0, & t < 0 \\ 1, & t > 0 \end{cases}$$

$U_{-1}(t)$  is undefined at  $t = 0$  and has a Laplace transform  $1/s$  (Ogata, 1998). The symbols  $U_{-2}$ ,  $U_{-3}$  denote, respectively, a unit ramp and unit parabola, and  $U_0$  denotes a unit impulse function. Now let the unit step, occurring at  $t = 0$ , be the input to the transfer function:

$$G(s) = \frac{-(s - \alpha)}{s^2 + s + 1}, \quad \alpha > 0 \quad (3.3-13)$$

The transfer function has a relative degree  $r = 1$ , and this makes the initial value of the step response zero:

$$f(0^+) = \lim_{s \rightarrow \infty} \left[ s \frac{-(s - \alpha)}{s^2 + s + 1} \frac{1}{s} \right] = 0$$

The transform of the derivative is :

$$\mathcal{L}[\dot{f}(t)] = sF(s) - f(0^+) \Rightarrow sF(s)$$

and the initial value of the derivative is

$$\dot{f}(0^+) = \lim_{s \rightarrow \infty} [s^2 F(s)] = -1$$

The final value of the step response is

$$f(\infty) = \lim_{s \rightarrow 0} [sF(s)] = \alpha$$

The transfer function (3.3-13) has a sign difference between its behavior at small and large  $s$ ;  $G(0) = \alpha$  (positive dc gain) and  $G(\infty) = -1/s$ . From the above analysis, the consequences are that the step response starts out in the negative direction but finishes with a positive value. The transfer function numerator factor  $(s - \alpha)$ ,  $\alpha > 0$ , corresponds to a zero in the right-half  $s$ -plane, and this is the cause of the above behavior.

If a transfer function contains right-half-plane zeros, it is called *non-minimum phase* (NMP), and the initial response to a step input may have the opposite sign to the final response (depending on the number of NMP zeros). This is an undesirable type of response from the point of view of a human operator. NMP zeros are also undesirable in feedback controller design since, as we will see later from “root-locus” plots, a right-half-plane zero tends to attract the closed-loop poles to the right-half  $s$ -plane. These types of zeros occur when there are two or more different paths to the system output, or two or more different physical mechanisms, producing competing output components.

When there are left-half-plane zeros near the origin, these tend to promote an overshoot in the response to a step input, which is again undesirable. Problem 3.3-2 illustrates the effects of both NMP zeros and left-half-plane zeros close to the origin.

By writing the simple differential equations for an ideal integrator or differentiator, and transforming them, we can derive their transfer functions. Thus, the transfer function of an integrator consists of a single pole at the origin, and a differentiator corresponds to a single zero at the origin. In a block diagram using transform-domain quantities, we will represent integrators and differentiators by boxes containing, respectively,  $1/s$  and  $s$ .

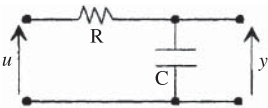
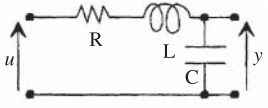
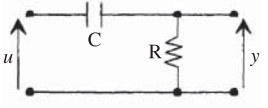
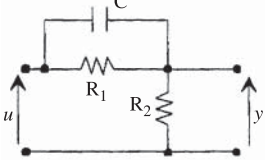
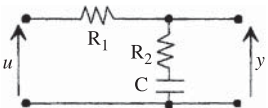
Finally, when transfer function poles and zeros are close together in the  $s$ -plane, the residue in the poles tends to be small (i.e., the coefficients of the corresponding partial fraction terms are small). A pole can be effectively canceled out of the transfer function by a nearby zero in this way.

## Transfer Function Examples and Standard Forms

Table 3.3-1 shows a number of standard transfer functions, and their state equations, that are used as either models or compensating networks in control systems design (see Chapter 4). Simple electrical networks that can be used to realize these transfer functions are also shown. The voltage transfer functions (assuming no source and output loading effects) can be derived from the networks by representing the network elements by their Laplace transform impedances (i.e.,  $1/sC$  for a capacitor,  $sL$  for an inductor). They can then be analyzed in the same way as dc circuits. The transfer functions are written here in *standard form*. This requires all numerator and denominator factors to be written as either  $(s\tau)$ ,  $(s\tau + 1)$ , where  $\tau$  is a time constant, or the second-order standard form given below. The state equations can be derived from the transfer functions by the methods given earlier.

Four of the networks in Table 3.3-1 have only a single energy storage element, are modeled with a single state variable, and hence have only a single real pole in their transfer functions. The standard form for a transfer function factor corresponding to

TABLE 3.3-1 Network Transfer Functions and State Equations

Network	Transfer Function	State Equations
 <p>SIMPLE LAG</p>	$\frac{1}{1 + s\tau}, \quad \tau = CR$	$\dot{x} = \frac{u - x}{\tau}$ $y = x$
 <p>QUADRATIC LAG</p>	$\frac{\omega_n^2}{s^2 + 2\zeta\omega_n s + \omega_n^2}$ $\omega_n^2 = \frac{1}{LC}, \quad \zeta = \frac{R}{2} \sqrt{\frac{C}{L}}$	$\dot{x}_1 = x_2$ $\dot{x}_2 = -\omega_n^2 x_1 - 2\zeta\omega_n x_2 + \omega_n^2 u$ $y = x_1$
 <p>SIMPLE LEAD</p>	$\frac{s\tau}{1 + s\tau}, \quad \tau = CR$	$\dot{x} = \frac{u - x}{\tau}$ $y = u - x$
 <p>LEAD COMPENSATOR</p>	$\frac{s + z}{s + p}, \quad z = \frac{1}{CR_1},$ $\frac{z}{p} = \frac{R_2}{R_1 + R_2}$	$\dot{x} = u - px$ $y = u + (z - p)x$
 <p>LAG COMPENSATOR</p>	$\frac{p}{z} \frac{s + z}{s + p}, \quad z = \frac{1}{CR_2},$ $\frac{p}{z} = \frac{R_2}{R_1 + R_2}$	$\dot{x} = u - px$ $y = \frac{p}{z}[u + (z - p)x]$

a single real pole or zero is the dimensionless factor  $(\tau s + 1)$ , and the pole or zero is at  $s = -1/\tau$ . As an example, we will derive the transfer function of the network identified as a “simple lead.”

With the restriction that any load connected to the output of the network must draw negligible current, the same current flows in the series (connecting input and output) branch as in the shunt (across the output terminals) branch. The voltage transfer function  $G(s)$  is then simply the impedance of the shunt branch divided by the sum of the shunt and series impedances:

$$G(s) = \frac{Y(s)}{U(s)} = \frac{R}{R + 1/sC} = \frac{s\tau}{s\tau + 1}, \quad \text{where } \tau = CR \quad (3.3-14)$$

This transfer function has a zero at the  $s$ -plane origin and a pole at  $s = -1/\tau$ . We could immediately write down the differential equation relating input and output voltages and recognize that the derivative of the input is present (the transfer function relative degree is zero). We will therefore find the state equations by a method that is similar to that used for Equation (3.2-6).

Rewrite (3.3-14) with an auxiliary variable  $Z(s)$  as

$$\frac{Y(s)}{s\tau} = \frac{U(s)}{s\tau + 1} \equiv Z(s) \quad (3.3-15)$$

Now draw a simulation diagram with, in general, a chain of integrators whose outputs, starting from the last one, are  $Z$ ,  $sZ$ ,  $s^2Z$ , and so on. Here we need only a single integrator. The  $U(s)$  equation in (3.3-15) gives

$$s\tau Z(s) = U(s) - Z(s),$$

which allows the input connections of the integrator to be established, as shown in Figure 3.3-2. Similarly, the  $Y(s)$  equation in (3.3-15) allows the simulation diagram output connections to be established. The final step is to assign state variables to the outputs of the integrators and write the state equations by inspection of the simulation diagram. In this case, Figure 3.3-2 gives the result shown in Table 3.3-1,

$$\dot{x} = (u - x)/\tau, \quad y = (u - x)$$

This method of finding state equations from transfer functions or ODEs extends readily to higher-order systems; it leads to an  $A$ -matrix in companion form. Therefore, for practical purposes we restrict it to low-order systems.

Next consider the *quadratic-lag* circuit in Table 3.3-1. This has two energy storage elements and requires two state variables. Because there is again only a single loop, the voltage transfer function can again be found from the branch impedances:

$$G(s) = \frac{1/sC}{sL + R + 1/sC} = \frac{1/(LC)}{s^2 + s(R/L) + 1/(LC)}$$

When a transfer function has the possibility of a pair of complex poles or zeros, it is usually convenient to represent these by a real second-order factor rather than a pair of complex first-order factors. A second-order transfer function factor is written

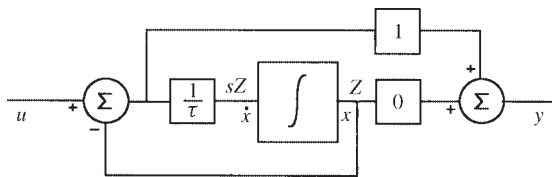


**Figure 3.3-2** Simulation diagram for a simple lead.

as  $(s^2 + 2\zeta\omega_n s + \omega_n^2)$ , where  $\omega_n$  is called the *natural frequency* and  $\zeta$  is called the *damping ratio*. Using this form, the above transfer function becomes

$$G(s) = \frac{\omega_n^2}{s^2 + 2\zeta\omega_n s + \omega_n^2}, \quad (3.3-16)$$

where

$$\omega_n = 1/\sqrt{LC}, \quad \zeta = \frac{1}{2}R\sqrt{C/L}$$

Equation (3.3-16) is the standard second-order form for a complex pole pair; for complex zeros this form is inverted. Note that it has a dc gain of unity. Transfer functions can always be written in terms of the standard forms, and in the next sections we explore the properties of some standard forms rather than specific systems.

## Frequency Response

Frequency response was defined in connection with Equations (3.3-10) and (3.3-11). Here we look at the frequency response of some standard-form transfer functions. An example of a first-order transfer function is

$$G(s) = \frac{s\tau_1}{s\tau_2 + 1} \quad \text{or} \quad G(s) = \frac{s\tau_1/\tau_2}{s + 1/\tau_2} \quad (3.3-17)$$

The first transfer function is in standard form for plotting frequency response, and the second matches the vector representation described earlier. Visualizing the vectors, we can see immediately that the frequency response starts from zero magnitude and  $90^\circ$  leading phase and, at high frequencies, it becomes constant in magnitude with zero phase angle. The transfer function itself shows that the high-frequency value of the magnitude is equal to  $\tau_1/\tau_2$ .

Using the first form of the transfer function, with  $s = j\omega$ , the magnitude and phase are given by

$$|G(j\omega)| = \frac{\omega\tau_1}{\sqrt{(1 + \omega^2\tau_2^2)}}, \quad \angle G(j\omega) = \pi/2 - \tan^{-1}(\omega\tau_2) \quad (3.3-18)$$

An octave is a two-to-one frequency interval, and a decade is a ten-to-one interval; experience shows that the extent of the frequency range of interest for practical systems is usually a few decades. If the frequency-response plots are made with a logarithmically spaced frequency scale, each decade occupies the same width, and features that would be lost on a linear scale are visible.

In the case of the magnitude plot, it is found that plotting the logarithm of the magnitude is very convenient for engineering purposes. This is because overall gain can be found by adding log-magnitudes, but also because very often mechanical, electrical, or physiological effects are more nearly linearly related to the logarithm of a power ratio than to the direct power ratio. An example is the Weber-Fechner law of psychology, which states that the human ear responds logarithmically. The

logarithmic units most commonly used are the bel and the decibel (1 bel = 10 dB); the decibel is given by 10 times the common logarithm of the relevant power ratio, or 20 times the corresponding amplitude ratio. In engineering measurements, 0.1 dB represents good resolution, and a 60- to 80-dB range is roughly the limit of linear operation for many systems. Plots of decibel magnitude and linear phase, plotted against logarithmically spaced frequency, are known as *Bode plots*.

Taking the log-magnitude in Equation (3.3-18) gives

$$20 \log_{10}(|G(j\omega)|) = 20 \log_{10}(\omega\tau_1) - 10 \log_{10}(1 + \omega^2\tau_2^2)$$

The first term on the right increases by 20 dB for every tenfold increase in  $\omega$ ;  $k$ -fold increases in frequency all occupy the same width on a logarithmic-spaced frequency scale. Therefore, this term has a straight-line Bode plot with a slope of 20 dB/decade (6 dB/octave). The second term on the right can be approximated as follows:

$$10 \log_{10}(1 + \omega^2\tau_2^2) \begin{cases} \approx 20 \log_{10}(\omega\tau_2), & \omega^2\tau_2^2 \gg 1 \\ = 3.01 \text{ dB}, & \omega\tau_2 = 1 \\ \approx 0 \text{ dB} & \omega^2\tau_2^2 \ll 1 \end{cases}$$

These results show that this term has asymptotes given by a 0-dB line at low frequency and a line with a slope of 20 dB/decade at high frequency. At the “corner frequency” (or break frequency),  $\omega = 1/\tau_2$ , the term is 3 dB from the 0-dB asymptote, and at an octave above and below the corner frequency, it is 1 dB from its asymptotes. The phase plot asymptotically approaches  $90^\circ$  at low frequencies and zero at high frequencies and passes through  $45^\circ$  at the corner frequency. It is much more spread out, being about  $6^\circ$  from its asymptotic values at a decade above and below the corner frequency. These decibel values and phase values are to be subtracted because this term came from the denominator of the transfer function. Exact Bode plots of the transfer function (3.3-17), with  $\tau_1 = 10$  and  $\tau_2 = 2$ , are shown in Figure 3.3-3.

Consider next a quadratic transfer function factor:

$$s^2 + 2\zeta\omega_n s + \omega_n^2 \quad (3.3-19a)$$

$$= (s + \zeta\omega_n)^2 + \omega_n^2(1 - \zeta^2) \quad (3.3-19b)$$

The quadratic formula shows that this factor represents complex conjugate roots when  $\zeta^2 < 1$ , and (3.3-19b) shows that the roots are given by

$$s = -\zeta\omega_n \pm j\omega_n \sqrt{1 - \zeta^2} \equiv -\zeta\omega_n \pm j\omega_d, \quad (3.3-20)$$

where  $\omega_d \equiv \omega_n(1 - \zeta^2)^{1/2}$  is the *damped frequency*. Figure 3.3-4 shows the  $s$ -plane vectors that could be used to evaluate the frequency response of a quadratic factor with complex roots. Complex poles are shown in the figure, but the following

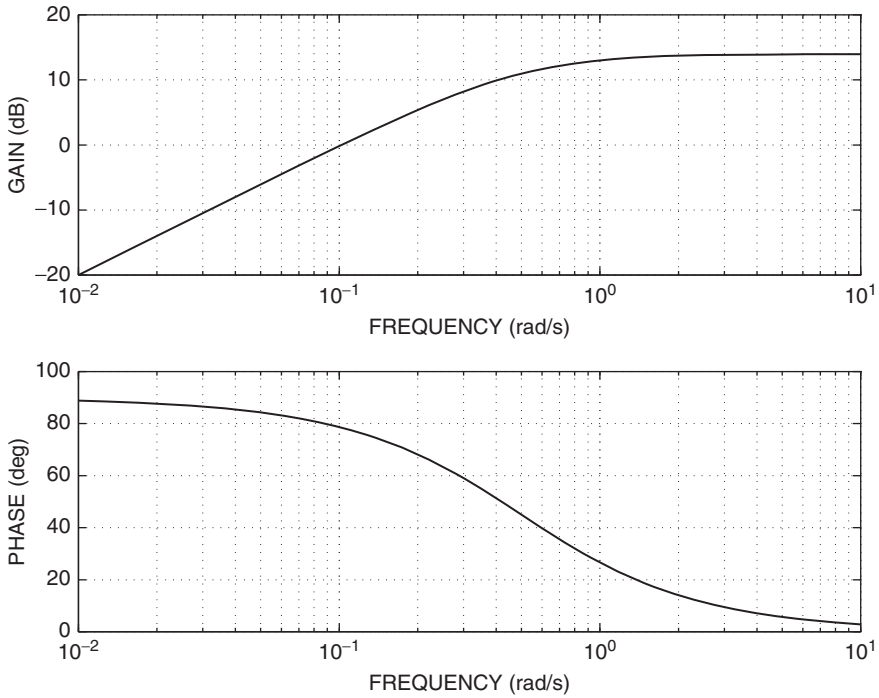


**Figure 3.3-3** Bode plots for a simple lead.

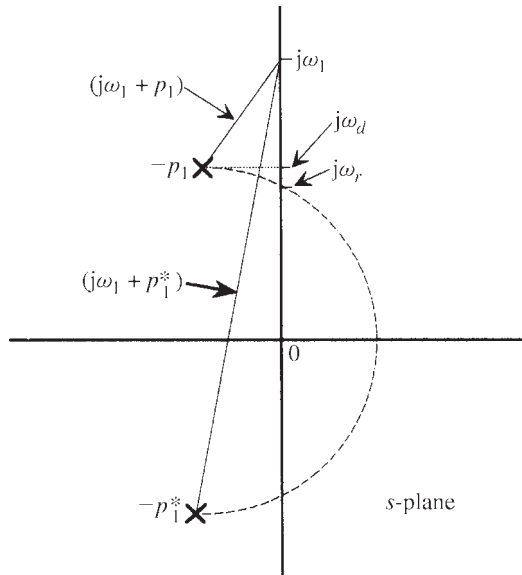


**Figure 3.3-4** Geometrical properties of a quadratic lag.

results also apply to complex zeros. The *resonant frequency*,  $\omega_r$ , is the frequency at which the product of the lengths of the vectors is at a minimum and is given by the imaginary-axis intersection of the semicircle whose diameter is the line joining the poles. This is because the vectors drawn to an imaginary-axis point are the sides of a constant-area triangle (constant base, constant height). At the point  $j\omega_r$ , the angle at the apex of the triangle reaches a maximum of  $90^\circ$ , so the product of its two sides is at a minimum (area = product of two sides and sine of included angle). By constructing another right triangle whose hypotenuse is a line from  $-\zeta\omega_n$  on the real axis to  $j\omega_r$  on the imaginary axis, we find that  $\omega_r$  is given by

$$\omega_r = \omega_n \sqrt{1 - 2\zeta^2} \quad (3.3-21)$$

and so the resonant frequency approaches the natural frequency as the damping ratio becomes small. There is no peak or dip in the frequency response of a complex pair of poles or zeros when  $\zeta > 1/\sqrt{2}$ .

We can apply these results to the quadratic-lag standard form, (3.3-16). Its magnitude and phase are given by

$$|G(j\omega)| = \frac{\omega_n^2}{\sqrt{[(\omega_n^2 - \omega^2)^2 + 4\zeta^2\omega^2\omega_n^2]}} \quad (3.3-22a)$$

$$\angle G(j\omega) = -\tan^{-1}(2\zeta\omega/\omega_n, 1 - \omega^2/\omega_n^2) \quad (3.3-22b)$$

The four-quadrant inverse-tangent function is necessary because the phase angle, by which the output lags behind the input, lies between zero and  $180^\circ$ . At resonance, the magnitude of the quadratic-lag standard form is found by substituting (3.3-21) into (3.3-22a):

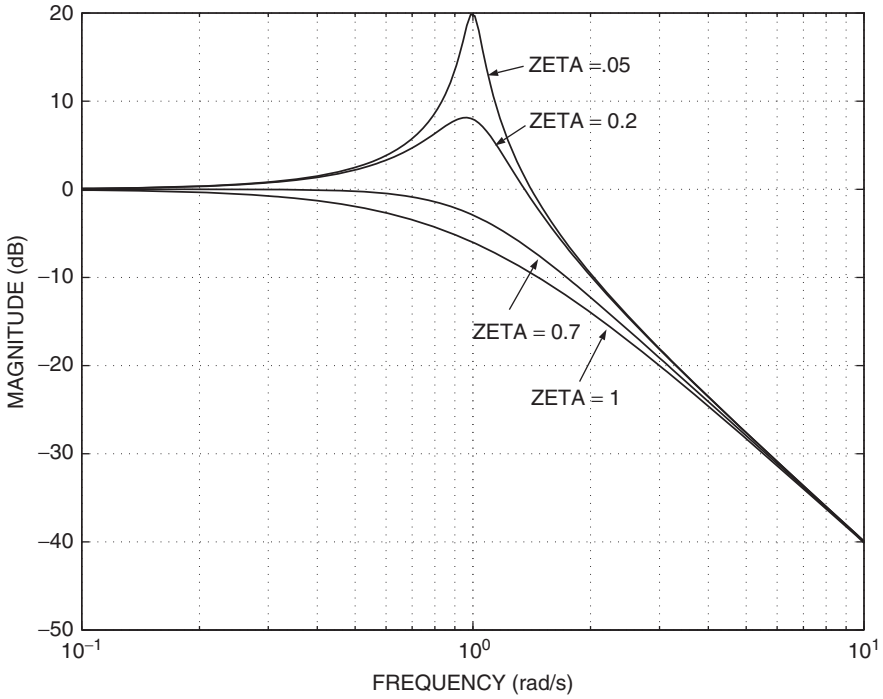
$$|G(j\omega_r)| = \frac{1}{2\zeta\sqrt{1 - \zeta^2}}, \quad \zeta < 1/\sqrt{2} \quad (3.3-23)$$

Figure 3.3-5 shows the Bode magnitude and phase plots for a quadratic lag, with  $\omega_n = 1.0$ . The asymptotes of the magnitude plot are now found to be a 0-dB line and a line with a slope of  $-40$  dB/decade, intersecting the 0-dB line at  $\omega_n$ . When the damping ratio is small, there is a large deviation from the asymptotes near  $\omega_n$ .

Finally, consider a transfer function  $(s + z)/(s + p)$ . This has corner frequencies at  $\omega = z$  and  $\omega = p$ , and the  $s$ -plane vectors show that its gain varies from  $z/p$  at zero frequency to unity at infinite frequency. If  $z < p$ , the gain will rise to unity and, if  $z > p$ , the gain will fall to unity. Rising gain is accompanied by a leading phase angle, and vice versa. On a logarithmic frequency scale, the maximum or minimum of the phase shift occurs midway between the pole and zero frequencies, and this is the geometric mean  $\sqrt{pz}$ . Other properties of this transfer function are derived in Section 3.9, where it is used for control system *compensation*. Figure 3.3-6 shows Bode plots for the leading-phase case,  $z < p$ .

Various systems, including control systems, audio amplifiers, and sensors and measurement devices, can have their performance specified in terms of frequency response. The usual criteria are the *bandwidth*, *peak magnification*, and amount of





**Figure 3.3-5a** Bode gain plot for a quadratic lag.

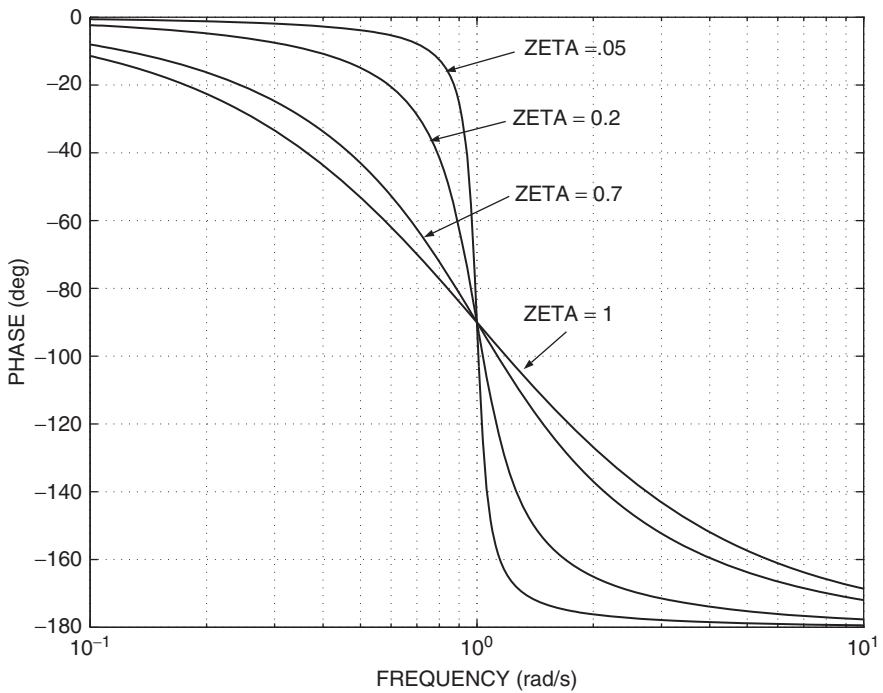


**Figure 3.3-5b** Bode phase plot for a quadratic lag.

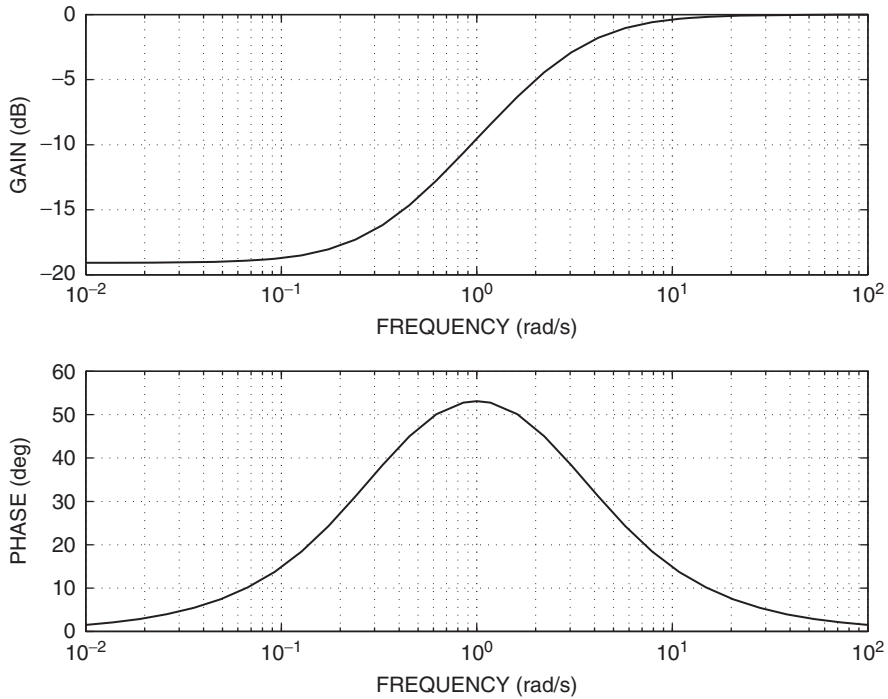


**Figure 3.3-6** Bode plots for a lead compensator.

phase shift at some frequency. A system whose frequency response extends down to zero frequency and “rolls off” with increasing frequency (e.g., an integrator or a simple lag) is called a *low-pass* system. Most control systems behave in this way. Similar definitions apply to *high-pass* and *band-pass* systems. If a low-pass system has a level frequency response at low frequency, we define the bandwidth to be the frequency at which the gain has fallen by 3 dB from its low-frequency value. As an example, the quadratic lag is a low-pass transfer function, it may have a resonant peak before it rolls off, and it can be shown to be “3 dB down” at the frequency

$$\omega_B = \omega_n \sqrt{[(1 - 2\zeta^2) + \sqrt{(4\zeta^4 - 4\zeta^2 + 2)}]} \quad (3.3-24)$$

## Time Response

Here we will look briefly at the step response of the simple-lag and quadratic-lag transfer functions. The transfer function of the simple lag is given in Table 3.3-1; the transform of a unit step input, occurring at  $t = 0$ , is  $U(s) = 1/s$ , and so the output transform is

$$Y(s) = \frac{1/\tau}{s + 1/\tau} \frac{1}{s} \equiv \frac{1}{s} + \frac{-1}{s + 1/\tau}$$

The partial fraction terms on the right correspond to known time functions, and so  $y(t)$  can be written down directly:

$$y(t) = (1 - e^{-t/\tau})U_{-1}(t), \quad (3.3-25)$$

where the unit step  $U_{-1}(t)$  serves to define the answer to be zero for  $t < 0$ . Equation (3.3-25) shows that the response of a simple real-pole transfer function to a step input is an exponential growth from zero to a final value given by the dc gain times the magnitude of the step.

The unit-step response of the quadratic lag (3.3-16) is given by

$$Y(s) = \frac{\omega_n^2}{(s + \zeta\omega_n)^2 + \omega_n^2(1 - \zeta^2)} \frac{1}{s} \equiv \frac{1}{s} - \frac{s + 2\zeta\omega_n}{(s + \zeta\omega_n)^2 + \omega_n^2(1 - \zeta^2)},$$

where the partial fraction coefficients were determined by the method of “comparing coefficients.” The solution can now be written down from a knowledge of the Laplace transforms of sine and cosine functions of time and the complex domain shifting theorem. Using a trigonometric identity to combine the sine and cosine terms gives

$$y(t) = \left[ 1 - \frac{e^{-\zeta\omega_n t}}{\sqrt{1 - \zeta^2}} \sin(\omega_d t + \phi) \right] U_{-1}(t), \quad (3.3-26)$$

where

$$\phi = \cos^{-1}(\zeta)$$

Plots of this answer are shown in Figure 3.3-7 for several values of  $\zeta$ . The graphs were plotted with  $\omega_n = 1$ ; they apply to any natural frequency if the horizontal scale

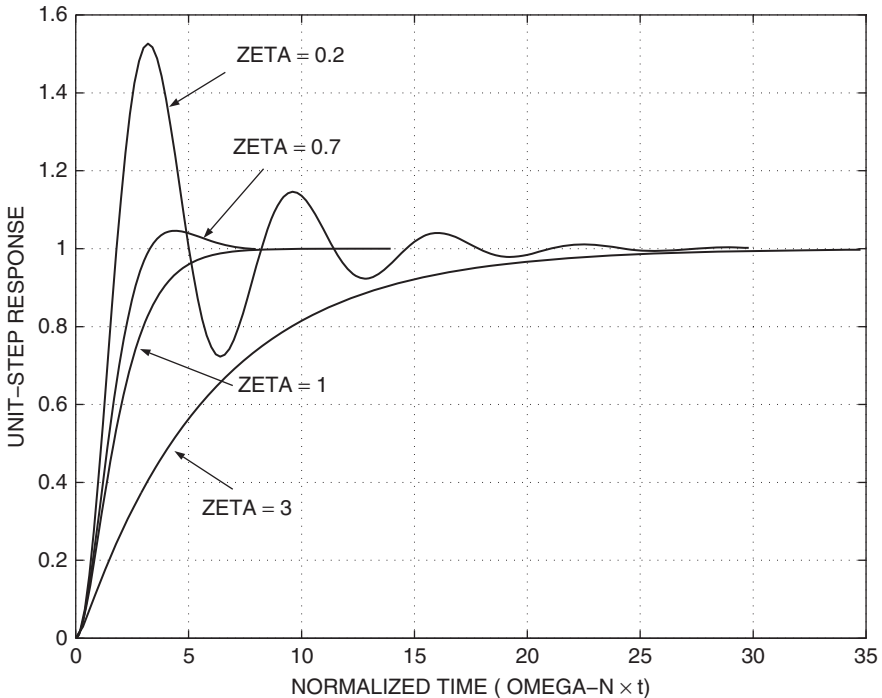


Figure 3.3-7 Step response of a quadratic lag.

is treated as “normalized time”  $\omega_n t$ . The case  $\zeta = 1$  is defined to be *critically damped*; when the damping ratio is less than 1, the step response has an overshoot and the poles are complex.

These results are useful because very often a dynamic system has a *dominant pair* of complex poles (Nise, 1995), which essentially determine its behavior. The damping of a system can be specified by the *maximum overshoot*, or *settling time*, of its step response, while system speed of response can be specified by the *rise time*, or the *peak time*, of its step response. These performance figures can be related to the damping ratio and natural frequency of a dominant pair (Dorf and Bishop, 2001).

### 3.4 NUMERICAL SOLUTION OF THE STATE EQUATIONS

#### Introduction

The aircraft state equations are nonlinear, depend on experimentally determined data, and are subjected to arbitrary input signals. An analytical solution is out of the question, and numerical methods must be used to compute an aircraft trajectory. In general, the state vector of a physical system will move in a smooth, continuous manner in the  $n$ -dimensional state space because the state variables describe the energy stored in a physical system, and an instantaneous change in energy would require infinite power. Therefore, derivatives of the state variables will exist, and a Taylor series expansion can be used to predict the motion.

Numerical evaluation of the continuous trajectory implies that, given the initial condition  $X(t_0)$  and control input  $U(t)$ , we must calculate discrete sequential values of the state:

$$X(t_0 + kT), \quad k = 1, 2 \dots \quad (3.4-1a)$$

that satisfy the state equations

$$\dot{X}(t) = f(X(t), U(t)) \quad (3.4-1b)$$

This is called the *initial-value problem*, and the *time step*  $T$  is usually chosen to be a fixed size. The state equations are not autonomous since the control input is an external input, and the time step must be made small enough that the control input can be approximated by a constant value during any interval  $kT$  to  $(k + 1)T$ . There are two classes of numerical solution methods for the initial-value problem, Runge-Kutta (RK) methods and linear multistep methods (LMMs), and these will now be described.

#### Runge-Kutta Methods

Consider the simplest ODE initial-value problem: a single first-order autonomous differential equation with a specified boundary condition,

$$\frac{dx}{dt} = f(x, t), \quad x(t_0) = x_0 \quad (3.4-2)$$

The problem of finding the discrete-solution values for (3.4-2) has an obvious connection to the Taylor series:

$$x(t_0 + T) = x(t_0) + T\dot{x}(t_0) + \frac{T^2}{2!}\ddot{x}(t_0) + \dots \quad (3.4-3)$$

The simplest RK method is *Euler integration*, which merely truncates the Taylor series after the first derivative. The Euler formula applied to (3.4-2) is

$$x_E(t_0 + T) \approx x(t_0) + Tf(x(t_0), t_0) \quad (3.4-4)$$

This formula is not very accurate unless very small time steps are used, and furthermore it can easily be improved upon, as follows.

In *trapezoidal integration* an estimate of the function derivative at the end of the time step is obtained from the Euler formula; then the average of the derivatives at the beginning and end of the time step is used to make a more accurate Euler step. The equations for a step forward from time  $t$  to  $t + T$  are

$$\begin{aligned} x_E(t + T) &= x(t) + Tf(x(t), t) \\ \dot{x}_E(t + T) &= f(x_E(t + T), t + T) \\ x_T(t + T) &= x(t) + \frac{T}{2} [\dot{x}(t) + \dot{x}_E(t + T)], \end{aligned} \quad (3.4-5)$$

where subscripts  $E$  and  $T$  indicate, respectively, Euler and trapezoidal steps. For reasons that will soon become clear, these equations are commonly written as

$$\begin{aligned} k_1 &= Tf(x, t) \\ k_2 &= Tf(x + k_1, t + T) \\ x_T(t + T) &= x(t) + \frac{1}{2}(k_1 + k_2) \end{aligned} \quad (3.4-6)$$

This algorithm can be shown to agree with the first three Taylor series terms, that is, up to and including the second derivative term. Therefore, this trapezoidal integration formula is said to be of order 2, and it gives an improvement in accuracy over the Euler first-order method. RK algorithms are an extension of (3.4-6) to higher orders, and the general form is

$$\begin{aligned} k_1 &= Tf(x, t) \\ k_2 &= Tf(x + \beta_1 k_1, t + \alpha_1 T) \\ k_3 &= Tf(x + \beta_2 k_1 + \beta_3 k_2, t + \alpha_2 T) \\ k_4 &= Tf(x + \beta_4 k_1 + \beta_5 k_2 + \beta_6 k_3, t + \alpha_3 T) \\ &\vdots \\ x_{RK}(t + T) &= x(t) + \gamma_1 k_1 + \gamma_2 k_2 + \gamma_3 k_3 + \dots \end{aligned} \quad (3.4-7)$$

Implicit RK algorithms also exist, wherein a coefficient  $k_i$  occurs on both sides of one of the equations above. The constants  $\alpha_i$ ,  $\beta_i$ , and  $\gamma_i$  are chosen so that a particular RK scheme agrees with the Taylor series to as high an order as possible. A great deal of algebraic effort is needed to derive higher-order (greater than 4) RK algorithms, and the constants are not unique for a given order. An algorithm that dates from the end of the nineteenth century and is still popular is Runge's fourth-order rule, which uses the constants

$$\begin{aligned}\alpha_1 &= \alpha_2 = \beta_1 = \beta_3 = \frac{1}{2} \\ \alpha_3 &= \beta_6 = 1 \\ \beta_2 &= \beta_4 = \beta_5 = 0 \\ \gamma_1 &= \gamma_4 = 1/6, \quad \gamma_2 = \gamma_3 = 1/3\end{aligned}\tag{3.4-8}$$

In this case only one previous  $k$  value appears in each of the  $k$  equations in (3.4-7), thus making a simpler algorithm. This algorithm has been used for most of our examples, and computer code for the general case of  $n$  simultaneous nonlinear state equations is given in the example below.

An important feature of the RK methods is that the only value of the state vector that is needed is the value at the beginning of the time step; this makes them well suited to the ODE initial-value problem. The amount of computation involved is governed by the number of derivative evaluations using the state equations performed during each time step. The number of derivative evaluations depends on the order chosen. For example, a fourth-order RK algorithm cannot be achieved with fewer than four derivative evaluations. For a given overall accuracy in a time-response calculation, there is a trade-off between many small steps with a low-order method and fewer steps but more derivative evaluations with a higher-order method. This led mathematicians to consider the problem of estimating the error in the computed solution function at each time step. Such an error estimate can be used to control the step size automatically in order to meet a specified accuracy. Algorithms that combine RK integration with error estimation include Runge-Kutta-Merson (RKM), Runge-Kutta-England, and Runge-Kutta-Gill; computer codes are commonly available. In terms of (3.4-7) the coefficients for the RKM scheme, for example, are

$$\begin{aligned}\alpha_1 &= \beta_1 = 1/3 \\ \alpha_2 &= 1/3, \quad \beta_2 = \beta_3 = 1/6 \\ \alpha_3 &= 1/2, \quad \beta_4 = 1/8, \quad \beta_5 = 0, \quad \beta_6 = 3/8 \\ \alpha_4 &= 1, \quad \beta_7 = 1/2, \quad \beta_8 = 0, \quad \beta_9 = -3/2, \quad \beta_{10} = 2 \\ \gamma_1 &= 1/6, \quad \gamma_2 = \gamma_3 = 0, \quad \gamma_4 = 2/3, \quad \gamma_5 = 1/6\end{aligned}\tag{3.4-9}$$

and the estimated error is

$$E \approx \frac{1}{30}[2k_1 - 9k_3 + 8k_4 - k_5]$$

## Linear Multistep Methods

In the LMMs the solution function is a linear combination of past values of the function and its derivatives, as described by the linear difference equation

$$x(n+1) = \sum_{r=0}^n \alpha_r x(n-r) + T \sum_{r=-1}^n \beta_r \dot{x}(n-r), \quad (3.4-10)$$

where  $x(i)$  indicates the value of  $x$  at time  $iT$ , with  $i$  an integer. If  $\beta_{-1}$  is nonzero, the algorithm is an implicit algorithm because the solution  $x(n+1)$  is needed to evaluate  $\dot{x}(n+1)$  on the right-hand side. Otherwise the algorithm is explicit. The implicit equation must be solved at each time step. LMMs can be designed to require less computation than RK methods because a number of past values can be kept in storage as the computation proceeds. Because of the requirements for past values, the LMMs are not self-starting, and an RK method, for example, could be used to generate the starting values.

The LMM algorithms can be created in a number of different ways. For instance, if the scalar state equation (3.4-2) is written as an integral equation over the time interval  $nT$  to  $(n+k)T$ , the result is

$$x(n+k) = x(n) + \int_{nT}^{(n+k)T} f(x, t) dt \quad (3.4-11)$$

There are many finite-difference formulae for evaluating a definite integral, and this approach leads to the *Newton-Coates integration formulae* (Isaacson and Keller, 1966; Ralston, 1965). Two examples are

$$x(n+1) = x(n-1) + 2T\dot{x}(n) \quad (3.4-12a)$$

$$x(n+1) = x(n-1) + \frac{T}{3}[\dot{x}(n+1) + 4\dot{x}(n) + \dot{x}(n-1)] \quad (3.4-12b)$$

The first formula uses the *midpoint rule* for the area represented by the integral and is explicit, while the second uses *Simpson's rule* and is implicit. Implicit and explicit formulae can be used together in a *predictor-corrector algorithm* (Hamming, 1962). The explicit formula is the predictor, used to obtain an approximate value of the solution, and the implicit formula is the corrector equation, which is solved (by iteration) to obtain a more accurate solution.

LMMs of any order can be derived directly from (3.4-10). When  $\alpha_r \equiv 0$  for  $r > 0$ , the *Adams-Bashforth-Moulton (ABM) formulae* are obtained.

We now give two examples. Assume that Equation (3.4-10) has the terms

$$x(n+1) = \alpha_0 x(n) + T[\beta_0 \dot{x}(n) + \beta_1 \dot{x}(n-1)] \quad (3.4-13)$$

Now write Taylor series expansions for the terms that are not taken at time  $nT$ :

$$\begin{aligned} x(n+1) &= x(n) + T\dot{x}(n) + \frac{T^2}{2!}\ddot{x}(n) + \dots \\ \dot{x}(n-1) &= \dot{x}(n) - T\ddot{x}(n) + \frac{T^2}{2!}\ddot{\ddot{x}}(n) \dots \end{aligned}$$

Substitute these expressions in (3.4-13) and equate powers of  $T$  on both sides of the resulting equation; this gives

$$\begin{aligned} T^0 : \quad 1 &= \alpha_0 \\ T^1 : \quad 1 &= \beta_0 + \beta_1 \\ T^2 : \quad \frac{1}{2} &= -\beta_1 \end{aligned}$$

Therefore, (3.4-13) yields the second-order ABM formula

$$x(n+1) = x(n) + \frac{T}{2}[3\dot{x}(n) - \dot{x}(n-1)] \quad (3.4-14)$$

This requires only one state equation evaluation per time step, and it has often been used for simulation. The higher-order methods also require only one derivative evaluation per time step, and the third-order ABM is

$$x(n+1) = x(n) + \frac{T}{12}[23\dot{x}(n) - 16\dot{x}(n-1) + 5\dot{x}(n-2)] \quad (3.4-15)$$

The implicit formulae may be derived in the same way; they give improved accuracy and can also provide an error estimate. They are commonly used in the predictor-corrector form, and this requires two derivative evaluations per step.

### Stability, Accuracy, and Stiff Systems

In developing numerical algorithms it is always necessary to consider how computational errors are magnified. If, in pursuit of greater accuracy, one blindly attempts to create higher-order LMM formulae, it is quite possible that the algorithm will be unstable and errors will grow with time. Stability can be determined by analyzing a finite-difference equation associated with the integration algorithm. This analysis (Shampine and Gordon, 1975) is beyond the scope of this chapter and we simply note that the specific algorithms described above are stable.

The RK stability properties are different from those of the LMMs. In the case of the RK algorithms, a reduction in time-step size will eventually eliminate an instability, although the required step size may be unreasonably small. Example 3.6-5 is an example of a reduction in step size eliminating an instability. When a set of state equations is being integrated, the required step size will be determined by the smallest time constant (i.e., the fastest component) of the solution function. A system with a very wide spread of time constants is known as a *stiff system*, and a very large number of RK steps may be necessary to yield only a small part of the complete solution. Other techniques are required for stiff systems (see below).

### Choice of Integration Algorithm

The most important feature of the RK methods is that they directly solve the initial-value problem. That is, no past values are needed to start the integration.



This, of course, exactly matches the philosophy of the state-space formulation in which all of the information describing the “state” of the system is contained in the state vector at any given time instant. The full significance of these facts can only be appreciated when a simulation containing discrete events is considered. This is a common practical engineering situation. For instance, at a given time a new subsystem may be activated or at a certain value of some variable the equations of motion may change because limiting or saturation behavior occurs. This means that previous states are less relevant; the information they carry may now apply to only a part of the complete system. This fact favors the RK methods over the multistep methods, and we will return to these points later. The disadvantages of the RK methods are that the error expressions are complex, they are inefficient when dealing with stiff systems, and more derivative evaluations are required for a given order than is the case with LMMs. The tremendous increases in computing power in recent years have made these disadvantages much less significant for small- to medium-sized simulations. Such simulations are commonly run with a fixed time step that has been found (by trial and error) to be adequate for the required accuracy and is also determined by other discrete-event considerations.

The important features of LMMs are that higher-order methods are obtained for a given number of derivative evaluations, and an accurate expression for the integration error can usually be obtained. These methods come into their own on very large systems of equations and large stiff systems and when there is no hard-limiting behavior or topological changes due to switching. The software package ODE-PACK (Hindmarsh, 1982) is available for large and stiff problems, and it handles equations in standard explicit form or in linearly implicit form. For nonstiff problems it uses the implicit ABM methods, and for stiff problems it uses a backward-difference formula and improves on the Gear algorithms (Gear, 1971) that have long been used for stiff systems. These algorithms have been used on atmosphere models with more than 10,000 simultaneous ODEs; the spread of time constants in the problem ranged from milliseconds to years, thus making the equations extremely stiff.

### Time-History Simulation

Here we will show how the integration techniques can be used to determine a *state trajectory*, that is, the motion of the tip of the state vector as a function of time in the  $n$ -dimensional space. This is usually called *time-history simulation*. Our state-space dynamic equations are already in the best form for simulation, either non-real-time simulation or real-time simulation (e.g., in a flight simulator); it is only necessary to couple them with the integration algorithm.

In general, a simulation will also need to process discrete-time calculations, that is, calculations in which the signals are only defined at the “sample instants.” Such signals may arise from simulating a digital computer or sampling external signals. The numerical integration algorithms are based on the assumption that external inputs to the state equations will remain constant during an integration step. Therefore, the integration routines effectively impose a “zero-order data-hold” (ZOH) on the sampled signals. The ZOH is described in more detail in Chapter 7.

Figure 3.4-1 shows how a non-real-time simulation program may be organized. Two separate functions or subroutines are needed for the dynamic models. One

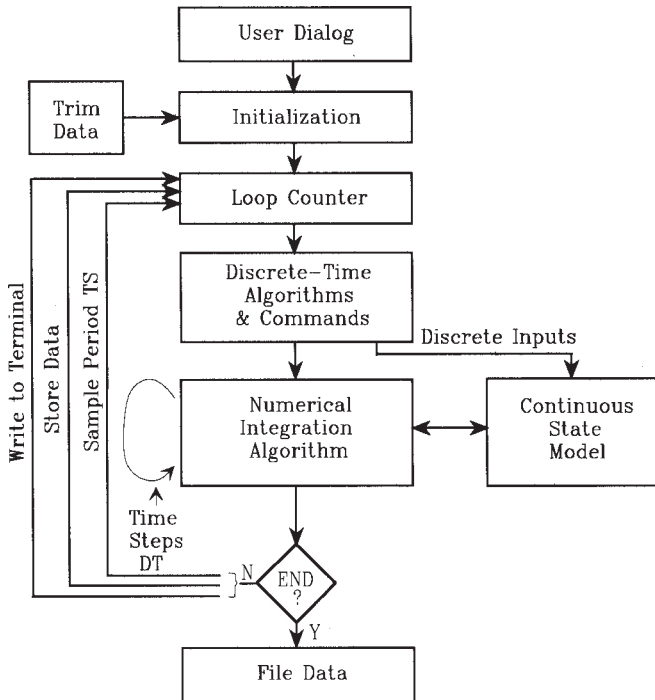


**Figure 3.4-1** Time-history simulation.

function contains the continuous-time state equations, and another function contains preprogrammed discrete-time commands and any discrete-time algorithms used for digital control. Simulation time is controlled by a for-loop, and the basic increment of time is the integration time step  $DT$ . The *sample period* for the discrete dynamics  $TS$  can conveniently be chosen to be an integer multiple of  $DT$ . Alternatively,  $TS$  may be the basic time increment, and the integration algorithm may integrate over  $TS$  while adaptively adjusting its step size to attain a specified integration accuracy. Periodic sampling is not essential, and the adaptive integration may continue until a discrete input occurs. The following example shows that a simple time-history simulation is very easy to perform.

**Example 3.4-1: Integration of the Van der Pol Equation** A simple time-history program “NLSIM” written in MATLAB code is shown below; it prompts the user for the name of the m-file containing the state equations and the name of an initial-condition file. The convention used is that the state equation function will always have the arguments “time,”  $X$ , and  $U$ , in that order. The initial condition file will be a text file with a “.dat” extension, which can also be read by other programming languages; it should have a different name from the state-equations file. The “.dat” extension must be entered at the MATLAB prompt because otherwise MATLAB assumes an “.m” extension.

```
% NLSIM.M Nonlinear Simulation
clear all
```

```

% global % add variables as needed
name= input('Enter Name of State Equations m-file : ','s');
icfile= input('Enter Name of i.c. File : ','s');
tmp= dlmread(icfile,',' );
n=tmp(1); m=tmp(2);
x=tmp(3:n+2); u=tmp(n+3:n+m+2);
stat=fclose('all');
runtime= input('Enter Run-Time : ');
dt = input('Enter Integration Time-step : ');
N=runtime/dt; k=0; NP= fix ( max(1,N/500) ); time=0.;
xd= feval(name,time,x,u); % Set variables in state equations
save=u(2); % For Example 3.6-3 only
for i=0:N
    time=i*dt;
    if rem(i,NP)==0
        k=k+1;
        y(k,1)= x(1); % record data as needed
        y(k,2)= x(2);
        %y(k,3)=
    end
    %if time>=2 % For Example 3.6-3
    % u(2)=save;
    %elseif time>=1.5
    % u(2)=save-2;
    %elseif time>=1.0
    % u(2)=save+2;
    %else
    % u(2)=save;
    %end
    [x]= RK4(name,time,dt,x,u);
end
t= NP*dt*[0:k-1];
figure(1)
plot(y(:,1), y(:,2)) % For Van der Pol
grid on
axis([-3,3,-4,5])
xlabel('X(1)')
ylabel('X(2)')
text(-1.8,3.2,'(-2,3)')

```

The fourth-order RK algorithm, with the constants given in (3.4-8) is

```

function [xnew]= RK4(f,time,dt,xx,u)
xd=feval(f,time,xx,u);
xa=xd*dt;
x =xx + 0.5*xa;
t =time + 0.5*dt;
xd=feval(f,t,x,u);
q = xd*dt;
x = xx + 0.5*q;
xa= xa + 2.0*q;
xd= feval(f,t,x,u);
q = xd*dt;
x = xx + q;
xa= xa + 2.0*q;

```

```

time= time + dt;
xd= feval(f,time,x,u);
xnew= xx + (xa + xd*dt)/6.0;

```

The state equations used as an example are those of the Van der Pol oscillator, which exhibits interesting nonlinear behavior,

```

% File VDPOL.m
function [xd]= vdpol(time,x,u)
xd= [x(2)    -u(1)*(x(1)^2-1)*x(2)-x(1)];

```

The control input  $u = 0.8$  was used as the parameter that controls the dynamic behavior of the Van der Pol oscillator. For this example the initial condition file VDP.dat contained the number of states and controls, the initial state, and the control input as follows:

2, 1, .1, .1, .8

Figure 3.4-2 shows state  $x_2$  plotted against state  $x_1$  and is called a *phase portrait*. Two different sets of initial conditions are shown in the figure, and in both cases the state trajectories approach the same closed contour. The resulting constant-amplitude oscillation is called a *limit cycle*. This example is studied further in Problem 3.4-1, and NLSIM.m is used for aircraft simulation in Section 3.6.

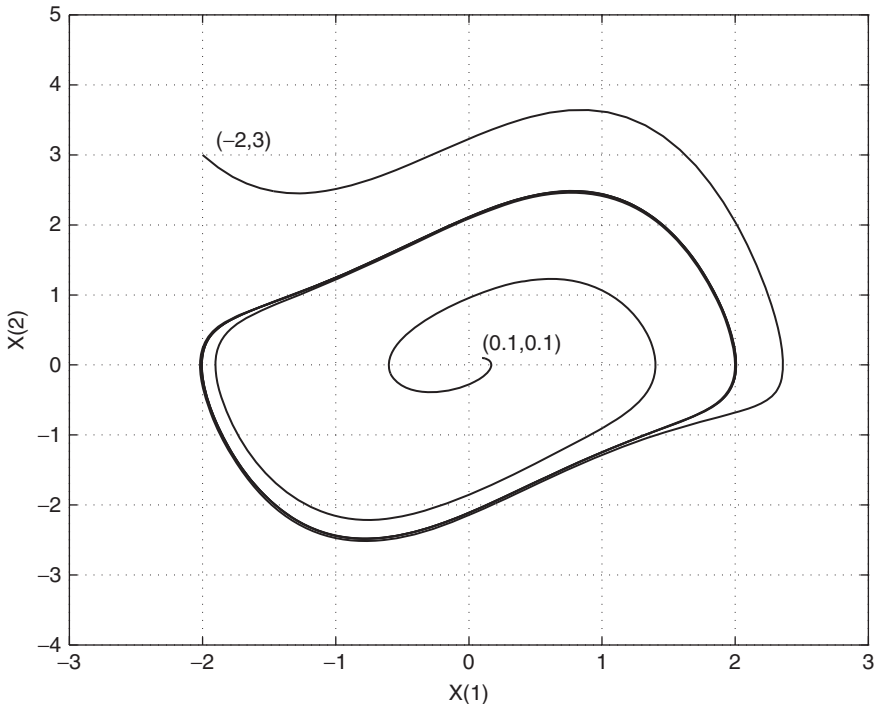


**Figure 3.4-2** A Van der Pol limit cycle.

### 3.5 AIRCRAFT MODELS FOR SIMULATION

#### Simulation Issues

In Section 3.4 we used MATLAB to illustrate simple nonlinear simulation, but this *interpreted* code executes one to two orders of magnitude more slowly than *compiled* code. In time-history simulation we wish to use a fixed sample period of 5 to 50 ms for the purposes of adequately sampling external inputs, generating random inputs, and interfacing with discrete-time controllers. The integration step size must be less than or equal to the discrete-time sample period and depends on the accuracy required and the stiffness of the dynamics. With this constraint, any improvement in speed of execution must come from linking MATLAB with compiled code. Rather than use this approach we have chosen to present a simple aircraft model in MATLAB code and a more complicated model in Fortran code. The choice of Fortran produces readable code. The reader has the option of converting the Fortran code to MATLAB (which is relatively easy to do), using MATLAB with compiled code (free compilers can be found), or running the Fortran code. A Fortran simulation program, TRESP, was written in the same form as the MATLAB program in Example 3.4-1 and using the RK4 integrator but using subroutines for the continuous dynamics and the discrete dynamics and with more comprehensive interactive capabilities. This program was used for the F-16 flight simulation examples in Section 3.6 and Chapter 4.

#### A Simple Longitudinal Model

This model has only three degrees of freedom (i.e., translation and pitching motion in the vertical plane): it has fixed aerodynamic coefficients and is representative of a medium-size transport aircraft at a low-speed flight condition. Data are also provided for the effects of extending landing gear and flaps. The aircraft weighs 162,000 lb (one-half fuel, partial cargo), and it has two turboprop engines, each developing 30,000 lb of static thrust at sea level. The wing area is 2170 ft<sup>2</sup>, wing span 140 ft, length 90 ft, and pitch-axis inertia  $4.1 \times 10^6$  slug-ft<sup>2</sup>. The model is illustrated in Figure 3.5-1, programmed as a MATLAB function.

This MATLAB function calculates the state derivative vector  $\dot{x}$  from the state vector  $x$  and the control vector  $u$ ; the formal argument “time” is unused. It is compatible with the time-history program given in Example 3.4-1. The control inputs  $u(3)$  and  $u(4)$  are used, respectively, to set the  $x$ -axis position of the cg and the landing configuration switch. For the aircraft models we will use the customary term *center of gravity* (cg) synonymously with cm, although technically a cg does not exist if a body does not have a spherically symmetrical distribution of mass.

Miscellaneous model outputs can be made available by setting up global variables. The aerodynamic derivatives are in stability axes and have “per degree” units except for the pitch damping coefficients ( $C_{m_q}$ ,  $C_{m_{\dot{\alpha}}}$ ), which are per radian per second. There is provision for a  $C_{L_{\dot{\alpha}}}$  derivative, but it is zero in this case. Lift is calculated from a linear lift curve and the stall is not modeled, while drag is calculated from the nonlinear drag polar. The elevator deflection is in degrees, and the throttle input is in the zero to

```

function [xd]= transp(time,x,u)
% Medium-sized transport aircraft, longitudinal dynamics.
%
S=2170.0; CBAR=17.5; MASS=5.0E3; IYY= 4.1E6;
TSTAT=6.0E4; DTDV =-38.0; ZE = 2.0; CDCLS= .042;
CLA = .085; CMA =-.022; CMDE =-.016; % per degree
CMQ =-16.0; CMADOT= -6.0; CLADOT= 0.0; % per radian
RTOD = 57.29578; GD=32.17;
THTL =u(1);
ELEV =u(2);
XCG = u(3);
LAND = u(4);
VT = x(1); % TAS in fps
ALPHA= RTOD*x(2); % A.O.A.
THETA= x(3); % PITCH ATTITUDE
Q = x(4); % PITCH RATE
H = x(5); % ALTITUDE
%
[MACH,QBAR]= ADC(VT,H);
QS = QBAR*S;
SALP= sin (x(2)); CALP= cos(x(2));
GAM = THETA - x(2); SGAM= sin (GAM); CGAM= cos(GAM);
if LAND == 0 % CLEAN
CLO= .20; CDO= .016;
CMO= .05; DCDG= 0.0; DCMG= 0.0;
elseif LAND == 1 % LANDING FLAPS & GEAR
CLO= 1.0; CDO= .08;
CMO= -.20; DCDG= .02; DCMG= -.05;
else
disp('Landing Gear & Flaps ?')
end
THR= (TSTAT+VT*DTDV) * max(THTL,0); % THRUST
CL=CLO+CLA*ALPHA; % NONDIM. LIFT
CM=DCMG+CMO+CMA*ALPHA+CMDE*ELEV+CL* (XCG-.25); % MOMENT
CD=DCDG+CDO+CDCLS*CL*CL; % DRAG POLAR
%
% STATE EQUATIONS NEXT
xd(1) = (THR*CALP-QS*CD)/MASS - GD*SGAM;
xd(2)=(-THR*SALP-QS*CL+MASS*(VT*Q+GD*CGAM))/(MASS*VT+QS*CLADOT);
Xd(3) = Q;
D = .5*CBAR*(CMQ*Q+CMADOT*xd(2))/VT; % PITCH DAMPING
Xd(4) = (QS*CBAR*(CM + D) + THR*ZE)/IYY; % Q-DOT
Xd(5) = VT*SGAM; % VERTICAL SPEED
Xd(6) = VT*CGAM; % HORIZNTL. SPEED

```

**Figure 3.5-1** Transport aircraft model.

unity range. Atmospheric density (and hence dynamic pressure) is calculated in the function ADC (air data computer, see Appendix A) from the temperature variation of the standard atmosphere (Yuan, 1967). The engine thrust is modeled as decreasing linearly with airspeed, to approximate the characteristics of a propeller-driven aircraft. The thrust vector does not pass through the cg (the perpendicular distance

from this vector to the cg is  $Z_E$ ), and therefore throttle changes will tend to cause pitching motion of the aircraft. Other parts of the model are either self-evident or can be understood by referring to the descriptions of aerodynamic effects in Chapter 2. This model will be used later for illustrative examples.

### A Six-Degree-of-Freedom Nonlinear Aircraft Model

The mathematical model given here uses the wind tunnel data from NASA-Langley wind tunnel tests on a subscale model of an F-16 airplane (Nguyen et al., 1979). The data apply to the speed range up to about  $M = 0.6$  and were used in a NASA-piloted simulation to study the maneuvering and stall/poststall characteristics of a relaxed static stability airplane. Because of the application and the ease of automated data collection, the data cover a very wide range of angle of attack ( $-20^\circ$  to  $90^\circ$ ) and sideslip angle ( $-30^\circ$  to  $30^\circ$ ). However, the present state of the art does not allow accurate dynamic modeling in the poststall region, and in addition the aircraft has insufficient pitching moment control for maneuvering at angles of attack beyond about  $25^\circ$ . Therefore, for use here, we have reduced the range of the data to  $-10^\circ \leq \alpha \leq 45^\circ$  and approximated the beta dependence in some cases.

The F-16 has a leading-edge flap that is automatically controlled as a function of alpha and Mach and responds rapidly as alpha changes during maneuvering. In the speed range for which the data are valid, the Mach-dependent variation of the flap is small, and so we have eliminated this dependence. Then, neglecting the dynamics of the flap actuator and assuming that the flap is dependent on alpha only, we have merged all of the independent flap data tables into the rest of the tabular aerodynamic data. The effect of the flap deflection limits (but not the rate limits) is still present in the reduced data. These steps have greatly reduced the size of the database and made it feasible to present the data here (Appendix A). The approximate model constructed from these data exhibits steady-state flight trim conditions, and corresponding dynamic modes, that are close to those of the full (50-lookup-table) model.

The F-16 model has been programmed as a Fortran subroutine in a form similar to the MATLAB model. The code is shown in Figure 3.5-2; all subroutines and functions called by the model are included in Appendix A. Note that English units have been used here, rather than SI units. State variables  $V_T$ ,  $\alpha$ , and  $\beta$  have been used instead of the velocity components  $U$ ,  $V$ , and  $W$  for ease of comparison with the linear small-perturbation equations. For serious simulation purposes it would be preferable to change to states  $U$ ,  $V$ , and  $W$ . The quantities XCGR and HX are, respectively,  $x$ -coordinates of the reference cg position and engine angular momentum (assumed constant at 160 slug-ft<sup>2</sup>/s).

The aerodynamic force and moment component buildup follows the outline presented in Section 2.3 except that body axes are used. For example, CX(alpha, EL) is a function subprogram that computes the nondimensional force coefficient for the body  $x$ -axis and is a function of angle of attack and elevator deflection. The total force coefficients for the three axes are CXT, CYT, and CZT. As shown in the appendix, the component functions typically contain a two-dimensional data lookup table

```

SUBROUTINE F (TIME,X,XD)
REAL X(*), XD(*), D(9), MASS
COMMON/PARAM/XCG
COMMON/CONTROLS/THTL,EL,AIL,RDR
COMMON/OUTPUT/AN,ALAT,AX,QBAR,AMACH,Q,ALPHA
PARAMETER (AXX=9496.0, AYY= 55814.0, AZZ=63100.0, AXZ= 982.0)
PARAMETER (AXZS=AXZ**2, XPQ=AXZ*(AXX-AYY+AZZ),
& GAM=AXX*AZZ-AXZ**2)
PARAMETER (XQR= AZZ*(AZZ-AYY)+AXZS, ZPQ=(AXX-AYY)*AXX+AXZS)
PARAMETER ( YPR= AZZ - AXX )
PARAMETER (WEIGHT= 25000.0, GD= 32.17, MASS= weight/gd)

DATA S,B,CBAR,XCGR,HX/300,30,11.32,0.35,160.0/
DATA RTOD / 57.29578/

C
C Assign state & control variables
C
VT= X(1); ALPHA= X(2)*RTOD; BETA= X(3)*RTOD
PHI=X(4); THETA= X(5); PSI= X(6)
P= X(7); Q= X(8); R= X(9); ALT= X(12); POW= X(13)

C
C Air data computer and engine model
C
CALL ADC(VT,ALT,AMACH,QBAR); CPOW= TGEAR(THTL)
XD(13) = PDOT(POW,CPOW); T= THRUST(POW,ALT,AMACH)

C
C Look-up tables and component buildup
C
CXT = CX (ALPHA,EL)
CYT = CY (BETA,AIL,RDR)
CZT = CZ (ALPHA,BETA,EL)
DAIL= AIL/20.0; DRDR= RDR/30.0
CLT = CL(ALPHA,BETA) + DLDA(ALPHA,BETA)*DAIL
& + DLDR(ALPHA,BETA)*DRDR
CMT = CM(ALPHA,EL)
CNT = CN(ALPHA,BETA) + DNDA(ALPHA,BETA)*DAIL
& + DNDR(ALPHA,BETA)*DRDR

C
C Add damping derivatives :
C
TVT= 0.5/VT; B2V= B*TVT; CQ= CBAR*Q*TVT
CALL DAMP(ALPHA,D)
CXT= CXT + CQ * D(1)
CYT= CYT + B2V * ( D(2)*R + D(3)*P )
CZT= CZT + CQ * D(4)
CLT= CLT + B2V * ( D(5)*R + D(6)*P )
CMT= CMT + CQ * D(7) + CZT * (XCGR-XCG)
CNT= CNT + B2V*(D(8)*R + D(9)*P) - CYT*(XCGR-XCG) * CBAR/B

C
C Get ready for state equations
C
CBTA = COS(X(3)); U=VT*COS(X(2))*CBTA
V= VT * SIN(X(3)); W=VT*SIN(X(2))*CBTA

```

**Figure 3.5-2** Model of the F-16 aircraft.



```

      STH  = SIN(THETA); CTH= COS(THETA);   SPH= SIN(PHI)
      CPH  = COS(PHI) ; SPSI= SIN(PSI);     CPSI= COS(PSI)
      QS   = QBAR * S ; QSB= QS * B;        RMQS= QS/MASS
      GCTH = GD * CTH ; QSPH= Q * SPH
      AY   = RMQS*CYT ; AZ= RMQS * CZT

C
C Force equations
C
      UDOT  = R*V - Q*W - GD*STH + (QS * CXT + T)/MASS
      VDOT  = P*W - R*U + GCTH * SPH + AY
      WDOT  = Q*U - P*V + GCTH * CPH + AZ
      DUM   = (U*U + W*W)
      xd(1) = (U*UDOT + V*VDOT + W*WDOT)/VT
      xd(2) = (U*WDOT - W*UDOT) / DUM
      xd(3) = (VT*VDOT- V*XD(1)) * CBTA / DUM

C
C Kinematics
C
      xd(4) = P + (STH/CTH)*(QSPH + R*CPH)
      xd(5) = Q*CPH - R*SPH
      xd(6) = (QSPH + R*CPH)/CTH

C
C Moments
C
      ROLL  = QSB*CLT
      PITCH = QS *CBAR*CMT
      YAW   = QSB*CNT
      PQ    = p*Q
      QR    = Q*R
      QHX   = Q*HX
      xd(7) = ( XPQ*PQ - XQR*QR + AZZ*ROLL + AXZ*(YAW + QHX) )/GAM
      xd(8) = ( YPR*P*R - AXZ*(P**2 - R**2) + PITCH - R*HX )/AYY
      xd(9) = ( ZPQ*PQ - XPQ*QR + AXZ*ROLL + AXX*(YAW + QHX) )/GAM

C
C Navigation
C
      T1= SPH * CPSI; T2= CPH * STH; T3= SPH * SPSI
      S1= CTH * CPSI; S2= CTH * SPSI; S3= T1 * STH - CPH * SPSI
      S4= T3 * STH + CPH * CPSI; S5= SPH * CTH; S6= T2*CPSI + T3
      S7= T2 * SPSI - T1; S8= CPH * CTH

C
      xd(10) = U * S1 + V * S3 + W * S6      ! North speed
      xd(11) = U * S2 + V * S4 + W * S7      ! East speed
      xd(12) = U * STH -V * S5 - W * S8      ! Vertical speed

C
C Outputs
C
      AN -AZ/GD; ALAT= AY/GD
      RETURN
      END

```

Figure 3.5-2 (Continued)

and a linear interpolation routine. We have used as much commonality as possible in the data tables and interpolation routines and have provided an interpolator that will also extrapolate beyond the limits of the tables. Therefore, a simulation may recover without loss of all data despite temporarily exceeding the limits of a lookup table.

**Engine Model** The NASA data include a model of the F-16 afterburning turbofan engine in which the thrust response is modeled with a first-order lag and the lag time constant is a function of the actual engine power level (POW) and the commanded power (CPOW). This time constant is calculated in the function PDOT, whose value is the rate of change of power, while the state variable  $X_{13}$  represents the actual power level. The function TGEAR (throttle gearing) relates the commanded power level to the throttle position (0 to 1.0) and is a linear relationship apart from a change of slope when the military power level is reached at 0.77 throttle setting. The variation of engine thrust with power level, altitude, and Mach number is contained in the function THRUST.

**Sign Convention for Control Surfaces** The sign conventions used in the model follow a common industry convention and are given in Table 3.5-1.

**Testing the Model** When constructing this model, a simple program should be written to exercise each of the aerodynamic lookup tables individually and plot the data before the tables are used with the model. The range of the independent variables should be chosen to ensure that both extrapolation and interpolation are performed correctly. A simple check on the complete model can be obtained by writing another program to set the parameter, input, and state vectors to the arbitrarily chosen values given in Table 3.5-2. The resulting values of the derivative vector should then agree with those given in the table.

Next we must bring this model under control by finding a combination of values of the state and control variables that correspond to a steady-state flight condition. Unlike a real pilot who is constantly receiving visual and other cues, this is quite difficult for us and will be the subject of the next section. In the next section steady-state trim data will be given for both wings-level, non-sideslipping flight and turning flight. Therefore, the longitudinal equations can be tested alone before all the equations are brought into play.

TABLE 3.5-1    Aircraft Control Surface Sign Conventions

	Deflection	Sense	Primary Effect
Elevator	trailing edge down	positive	negative pitching moment
Rudder	trailing edge left	positive	negative yawing moment
Ailerons	right-wing trailing edge down	positive	negative rolling moment

TABLE 3.5-2 F-16 Model Test Case

Index (i)	PARAM	$U(i)$	$X(i)$	$\dot{X}(i)$
1	.4	0.9	500	-75.23724
2		20	0.5	-0.8813491
3		-15	-0.2	-0.4759990
4		-20	-1	2.505734
5			1	0.3250820
6			-1	2.145926
7			0.7	12.62679
8			-0.8	0.9649671
9			0.9	0.5809759
10			1000	342.4439
11			900	-266.7707
12			10000	248.1241
13			90	-58.68999

### 3.6 STEADY-STATE FLIGHT

Steady-state flight is important because it provides an initial condition for flight simulation and a flight condition in which we can linearize the aircraft dynamics (see Section Numerical Linearization). Figure 3.1-1 shows how a steady-state “trim” program fits into the state-space context. A generic trim program links to any nonlinear model and produces a file containing the steady-state values of the control and state vectors for use by the time-history and linearization programs. Steady-state flight was defined in Section 2.6 and was shown to require the solution of a set of nonlinear simultaneous equations derived from the state model. Now we are faced with the problem of actually calculating the values of the state and control vectors that satisfy these equations. This cannot be done analytically because of the very complex functional dependence of the aerodynamic data. Instead, it must be done with a numerical algorithm that iteratively adjusts the independent variables until some solution criterion is met. The solution will be approximate but can be made arbitrarily close to the exact solution by tightening up the criterion. Also, the solution may not be unique—for example, steady-state level flight at a given engine power level can in general correspond to two different airspeeds and angles of attack. Our knowledge of aircraft behavior will allow us to specify the required steady-state condition so that the trim algorithm converges on an appropriate, if not unique, solution.

One of the first things that must be decided is how to specify the steady-state condition, how many of the state and control variables can be chosen independently, and what constraints exist on the remaining variables. A computer program can then be written so that the specification variables are entered from the keyboard, and the independent variables are adjusted by the numerical algorithm that solves the nonlinear equations, while the remaining variables are determined from the constraint equations.

For steady-state flight we expect to be able to specify the altitude and the velocity vector (i.e., speed and flight-path angle) within the limits imposed by engine power. Then, assuming that the aircraft configuration (i.e., flap settings, landing gear up or down, speed brake deployed, etc.) is prespecified, for a conventional aircraft we expect that a unique combination of the control inputs and the remaining state variables will exist. All of the control variables (throttle, elevator, aileron, and rudder) enter the model only through tabular aerodynamic data, and we cannot, in general, determine any analytical constraints on these control inputs. Therefore, these four control inputs must be adjusted by our numerical algorithm. This is not the case for the state variables.

Since only the NED altitude component of the tangent-plane position vector is relevant and can be prespecified, we can temporarily eliminate the three position states from consideration. Consider first steady translational flight. The state variables  $\phi$ ,  $P$ ,  $Q$ ,  $R$  are all identically zero, and the orientation  $\psi$  can be specified freely; this only leaves  $V_T$ ,  $\alpha$ ,  $\beta$  (or  $U$ ,  $V$ ,  $W$ ), and  $\theta$  to be considered. The sideslip angle cannot be specified freely; it must be adjusted by our trim algorithm to zero out any sideforce. This leaves the variables  $V_T$ ,  $\alpha$ , and  $\theta$ ; the first two are interrelated through the amount of lift needed to support the weight of the aircraft; therefore, only two may be specified independently ( $\theta$  and either  $V_T$  or  $\alpha$ ). We usually wish to impose a flight-path angle ( $\gamma$ ) constraint on the steady-state condition, so we will finally choose to specify  $V_T$  and  $\gamma$ .

Because the atmospheric density changes with altitude, a steady-state flight condition does not strictly include a nonzero flight-path angle. Nevertheless, it is useful to be able to determine a trimmed condition for a nonzero flight-path angle at any given altitude, since rate of climb (ROC) can then be determined and linearized dynamic models can be obtained for nonzero flight-path angles. We will therefore derive a general ROC constraint; this constraint will allow a nonzero roll angle so that it can also be applied to steady-state turning flight.

Steady-state turning flight must now be considered; the variables  $\phi$ ,  $P$ ,  $Q$ , and  $R$  will no longer be set to zero. The turn can be specified by the Euler angle rate  $\dot{\psi}$ ; this is the rate at which the aircraft's heading changes (the initial heading can still be freely specified). Then, given values of the attitude angles  $\phi$  and  $\theta$ , the state variables  $P$ ,  $Q$ , and  $R$  can be determined from the kinematic equation (1.4-4). The required value of  $\theta$  can be obtained from the ROC constraint if the value of  $\phi$  is known, and we next consider the determination of  $\phi$ .

The roll angle ( $\phi$ ) for the steady-state turn can be freely specified, but then, in general, there will be a significant sideslip angle and the turn will be a "skidding" turn. The pilot will feel a force pushing him or her against the side of the cockpit, the passengers' drinks will spill, and the radius of the turn will be unnecessarily large. In a "coordinated" turn the aircraft is rolled at an angle such that there is no component of aerodynamic force along the body  $y$ -axis. This condition is used as the basis of the turn coordination constraint derived below. The turn coordination constraint will be found to involve both  $\theta$  and  $\phi$ ; therefore, it must be solved simultaneously with the ROC constraint.

Chapters 1 and 2 have shown, via the flat-Earth equations, that the dynamic behavior of the aircraft is determined by the relative wind ( $-\mathbf{v}_{rel}$ ) and height in the

atmosphere and hence by the variables  $V_T$ ,  $\alpha$ ,  $\beta$ , and  $h$ . The behavior is essentially independent of the wind velocity  $\mathbf{v}_{W/e}$ . Therefore, when we wish to determine a steady-state flight condition for studying the dynamics, we will set the wind velocity to zero.

### The Rate-of-Climb Constraint

With no wind, the velocity relative to the atmosphere is just the velocity over Earth, and

$$\mathbf{v}_{cm/e}^{tp} = C_{tp/bf} C_{bf/w} \mathbf{v}_{rel}^w$$

In the flat-Earth equations the rate of climb is simply  $V_T \sin \gamma$ , and this is the  $-z$ -component of the velocity in tangent-plane coordinates. Therefore, the above equation yields

$$V_T \begin{bmatrix} * \\ * \\ -\sin \gamma \end{bmatrix} = C_{tp/bf} C_{bf/w} \begin{bmatrix} V_T \\ 0 \\ 0 \end{bmatrix} \quad (3.6-1)$$

The asterisks indicate “don’t care” components, and if this equation is expanded and then arranged to solve for  $\theta$  (Problem 3.6-3), the results are

$$\sin \gamma = a \sin \theta - b \cos \theta, \quad (3.6-2)$$

where

$$a = \cos \alpha \cos \beta, \quad b = \sin \phi \sin \beta + \cos \phi \sin \alpha \cos \beta$$

Now, solving for  $\theta$ , we find

$$\tan \theta = \frac{ab + \sin \gamma \sqrt{a^2 - \sin^2 \gamma + b^2}}{a^2 - \sin^2 \gamma}, \quad \theta \neq \pm \pi/2 \quad (3.6-3)$$

As a check, in wings-level, non-sideslipping flight this equation reduces to  $\theta = \alpha + \gamma$ .

### The Turn Coordination Constraint

In a perfectly coordinated turn the components of force along the aircraft body-fixed  $y$ -axis sum to zero, and in addition we have the steady-state condition  $\dot{V} = 0$ . Then, from Table 2.5-1,

$$0 = -RU + PW + g_D \sin \phi \cos \theta$$

Now use Equation (1.4-4), with  $\dot{\phi} = \dot{\theta} = 0$ , to introduce the *turn rate*  $\dot{\psi}$  in place of  $P$  and  $R$ . Also use Equation (2.3-6a) to introduce  $V_T$  in place of  $U$  and  $W$ ; the result is

$$-V_T \dot{\psi} \cos \beta [\cos \alpha \cos \theta \cos \phi + \sin \alpha \sin \theta] = g_D \sin \phi \cos \theta$$

If we define

$$\mathcal{G} \equiv \dot{\psi} V_T / g_D,$$

which is the centripetal acceleration (in  $g$ 's), then the constraint can be written as

$$\sin \phi = \mathcal{G} \cos \beta (\sin \alpha \tan \theta + \cos \alpha \cos \phi) \quad (3.6-4)$$

This is the required coordination constraint; it can be used in conjunction with (3.6-3) to trim the aircraft for turning flight with a specified rate of climb. If we can now solve (3.6-3) and (3.6-4) simultaneously for the state variables  $\phi$  and  $\theta$ , our numerical trim algorithm need only vary  $\alpha$  and  $\beta$  (in addition to the four controls). The simultaneous solution is quite cumbersome but can be shown to be

$$\tan \phi = \mathcal{G} \frac{\cos \beta}{\cos \alpha} \frac{(a - b^2) + b \tan \alpha [c(1 - b^2) + \mathcal{G}^2 \sin^2 \beta]^{\frac{1}{2}}}{a^2 - b^2 (1 + c \tan^2 \alpha)}, \quad (3.6-5)$$

where

$$a = 1 - \mathcal{G} \tan \alpha \sin \beta, \quad b = \sin \gamma / \cos \beta, \quad c = 1 + \mathcal{G}^2 \cos^2 \beta$$

The value of  $\phi$  given by (3.6-5) can now be used to solve (3.6-3) for  $\theta$ . Note that when the flight-path angle  $\gamma$  is zero, (3.6-5) reduces to

$$\tan \phi = \frac{\mathcal{G} \cos \beta}{\cos \alpha - \mathcal{G} \sin \alpha \sin \beta}, \quad (3.6-6)$$

and when  $\beta$  is small, this reduces to

$$\tan \phi = \frac{\mathcal{G}}{\cos \alpha} = \frac{\dot{\psi}}{g_D} \frac{V_T}{\cos \alpha} = \frac{\dot{\psi}}{g_D} \frac{V_T}{\cos \theta} \quad (3.6-7)$$

Equation (3.6-7) applies to a level, non-sideslipping turn and can be found from a simplified analysis given in standard texts. This completes the description of the flight-path constraints; we next show how a trim program may be constructed and provide examples of trimming the aircraft models.

## The Steady-State Trim Algorithm

The steady-state flight conditions are determined by solving the nonlinear state equations for the state and control vectors that make the state derivatives  $\dot{U}$ ,  $\dot{V}$ ,  $\dot{W}$  (or  $\dot{V}_T$ ,  $\dot{\alpha}$ ,  $\dot{\beta}$ ) and  $\dot{P}$ ,  $\dot{Q}$ ,  $\dot{R}$  identically zero. A convenient way to do this, with a readily available numerical algorithm, is to form a scalar *cost function* from the sum of the squares of the derivatives above. A function minimization algorithm can then be used to adjust the control variables and the appropriate state variables to minimize this scalar cost. Examples of suitable algorithms are the IMSL routine “ZXMW”

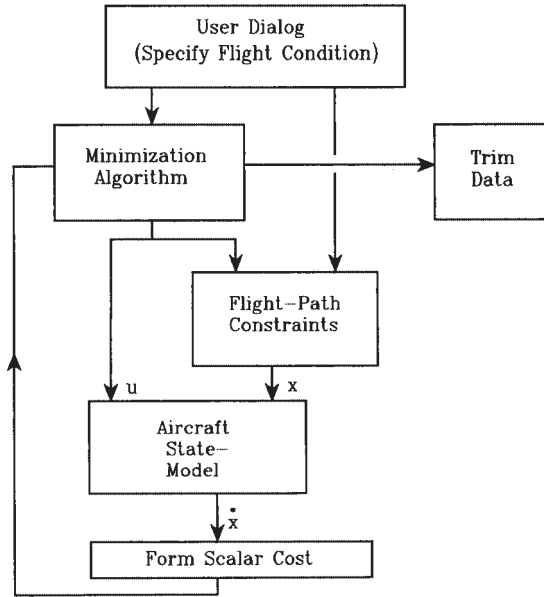


Figure 3.6-1 Steady-state trim flowchart.

(IMSL, 1980), and the SIMPLEX algorithm (Press et al., 1986; Nelder and Mead, 1964). Figure 3.6-1 illustrates how the complete trim algorithm may be organized. Only the cost function is tailored to a specific aircraft or set of state equations. We now give a simple trim example using the transport aircraft model.

**Example 3.6-1: Steady-State Trim for a 3-DoF Aircraft Model** In this example we will construct a simple 3-DoF trim program and use it on the transport aircraft model in Figure 3.5-1. It is only necessary to choose the speed and altitude, set the pitch rate state to zero, and adjust the throttle and elevator controls and the angle-of-attack state. Instead of the ROC constraint, we can specify the flight-path angle and constrain the pitch-attitude state to be equal to the angle of attack plus the flight-path angle. A simple MATLAB program is as follows:

```

% TRIM.m
clear all
global x u gamma
x(1)=input('Enter Vt : ');
x(5)= input('Enter h : ');
gamma=input('Enter Gamma (deg.) : ')/57.29578;
name= input('Name of Cost function file ? : ',' s');
cg= 0.25; land=1; % 0=clean 1=gear+flaps
u=[0.1 -10 cg land];
x(2)=.1; % Alpha, initial guess
x(3)=x(2) +gamma; % Theta

```

```
x(4)=0;    % Pitch rate
x(6)=0;
s0=[u(1) u(2) x(2)];
% Now initialize any other states and get initial cost
disp(['Initial cost = ',num2str( feval(name,s0) ) ])
[s,fval]=fminsearch(name,s0) ;
x(2)=s(3); x(3)=s(3)+gamma;
u(1)=s(1); u(2)=s(2) ;
disp(['minimum cost = ',num2str(fval)])
disp(['minimizing vector= ',num2str(s)])
temp=[length(x),length(u),x,u];
name= input('Name of output file ? : ',' s') ;
dlmwrite(name,temp);
```

and a cost function for the transport aircraft model is

```
% Cost Function for 3-DOF Aircraft
function [f]=cost(s);
global x u gamma
u(1)= s(1);
u(2)= s(2);
x(2)= s(3);
x(3)= x(2)+ gamma;
time= 0.0;
[xd]=transp(time,x,u);
f= xd(1)^2 + 100*xd(2)^2 + 10*xd(4)^2;
```

The MATLAB function “fminsearch” performs the minimization and is actually a Nelder and Mead Simplex algorithm. The results obtained for level flight with  $c_g = 0.25\bar{c}$  and flaps and landing gear retracted are shown in Table 3.6-1. The cost function can be reduced to less than 1E-30, but anything below about 1E-12 causes negligible changes in the states and controls. The weighting on the derivatives in the cost function was experimental and makes little difference to the results.

The trim program for Example 3.6-1 can easily be modified for other experiments, such as trimming for a specific alpha by varying the airspeed (Problem 3.6-4). We next consider the slightly more difficult problem of trimming a 6-DoF model, with additional dynamics such as an engine model that must also be put into a steady-state condition. This will be illustrated with the F-16 model using the Fortran code in Appendix B.

**TABLE 3.6-1 Trim Data for the Transport Aircraft Model**

Altitude (ft)	speed (ft/s)	initial cost	final cost	throttle	elevator (deg)	alpha (deg)
0	170	28.9	< 1E-20	0.297	-25.7	22.1
0	500	3.54	< 1E-20	0.293	2.46	0.580
30k	500	10.8	< 1E-20	0.204	-4.10	5.43





**Example 3.6-2: Steady-State Trim for a 6-DoF Model** The following *cost function* subprogram has been specifically tailored to the F-16 model but is representative of the 6-DoF case in general:

```
function cost(s)
parameter (nn=20)
real s(*)
common/state/x(nn),xd(nn)
common/controls/tht1,el,ail,rdr
tht1 = s(1)
el = s(2)
x(2) = s(3)
ail = s(4)
rdr = s(5)
x(3) = s(6)
x(13)= tgear(tht1)
call constr(x)
call f(time,x,xd)
cost = xd(1)**2 + 100*(xd(2)**2 + xd(3)**2) + 10*(xd(7)**2
& + xd(8)**2 + xd(9)**2)
return
end
```

This cost function is specific to the F-16 model because of the assignment statement for  $X_{13}$ . An examination of the F-16 model will show that this statement sets the derivative  $\dot{X}_{13}$  to zero and hence puts the engine dynamics into the steady state. Any other dynamics in the aircraft model besides the rigid-body dynamics must be put into the steady-state condition in this way. In our original large F-16 model, this was done for the leading-edge flap actuator and its phase-lead network.

In this cost function, unlike the previous case, the state variables  $X_4$  through  $X_9$  (excluding  $X_6$ ) are continually assigned new values in the constraint routine CONSTR. This routine implements the rate-of-climb and turn coordination constraints that were derived earlier. In the cost the aerodynamic angle rates  $\dot{\alpha}$  and  $\dot{\beta}$  have been weighted the most heavily, the angular rate derivatives  $\dot{P}$ ,  $\dot{Q}$ ,  $\dot{R}$  have medium weights, and the derivative  $\dot{V}_T$  has the least weight. Again, the weights are uncritical.

We will now use this cost function to determine the steady-state conditions in a coordinated turn performed by the F-16 model. The cg location of the model is at  $0.35\bar{7}$ , and the aircraft dynamics are unstable in pitch in the chosen flight condition. The turn would stress a pilot since it involves a sustained normal acceleration of 4.5 gs.

The trim program dialog and keyboard inputs are shown in Figure 3.6-2 as they would appear on a terminal display. Note that entering a “r” in response to a Fortran read statement causes the program to use the last values assigned to the variable. This allows the minimization to be picked up from where it was stopped if the final cost function was not low enough. In the run shown, the cost function was reduced by almost 10 orders of magnitude after 1000 function calls. Execution is very fast, and this is a reasonable number of calls.

The cost function can always be reduced to  $1 \times 10^{-10}$  or less; lower values are useful simply for checking consistency of results. The most effective way to use the simplex algorithm is to perform 500 to 1000 iterations and, if the cost is not

```

? Altitude (ft) : 0
? Air Speed (ft/s) and Climb Angle (deg) : 502,0
? Roll, Pull-Up, and Turn rates (rad/s) : 0,0,.3

Turn Radius (ft)= 1.6733E+03   Approx Roll Angle (deg)= 77.94
? Coordinated Turn (def. = Y) : /
? Required No. of Trim Iterations (def. =1000) : /

? Guess : Throttle, Elevator, Ailerons, Rudder : /
Computed : 8.35E-01 -1.48E+00 9.54E-02 -4.11E-01

    Angle of Attack 1.37E+01    Sideslip Angle 2.92E-02
    Pitch Angle 2.87E+00    Roll Angle 7.83E+01
Normal Acceleration 4.65E+00    Lateral Accn. -5.02E-06
Dynamic Pressure 3.00E+02    Mach Number 4.50E-01

Initial Cost Function 1.85E+01,    Final Cost Fn. 3.98E-09
? More Iterations (def = Y) : N

? Enter "M" to modify this trim
    "R" to restart
    "/" to file data/quit : /

? Name of Output File (def= None) : /

? Enter "M" for Menu
    "/" to quit : /

```

**Figure 3.6-2** Terminal display for trim.

acceptable, to reinitialize the step size of the minimization algorithm before each new set of iterations. More trim iterations were later performed on this example and the cost function reached a lower limit of  $5.52\text{E-}13$  (the trim program and model use only single-precision arithmetic); no significant changes occurred in the numerical values given above. The final state and control vectors placed in the output file were as follows:

$$\begin{aligned}
 X_1 &= 5.020000\text{E} + 02, & X_2 &= 2.392628\text{E} - 01, & X_3 &= 5.061803\text{E} - 04, \\
 X_4 &= 1.366289\text{E} + 00, & X_5 &= 5.000808\text{E} - 02, & X_6 &= 2.340769\text{E} - 01, \\
 X_7 &= -1.499617\text{E} - 02, & X_8 &= 2.933811\text{E} - 01, & X_9 &= 6.084932\text{E} - 02, \\
 X_{10} &= 0.000000\text{E} + 00, & X_{11} &= 0.000000\text{E} + 00, & X_{12} &= 0.000000\text{E} + 00, \\
 X_{13} &= 6.412363\text{E} + 01, \\
 U_1 &= 8.349601\text{E} - 01, & U_2 &= -1.481766\text{E} + 00, & U_3 &= 9.553108\text{E} - 02, \\
 U_4 &= -4.118124\text{E} - 01
 \end{aligned}$$

This trim will be used for a flight simulation example in a following subsection and in Section 3.7 to illustrate coupling effects in the aircraft dynamics. ■

Trimmed Conditions for Studying Aircraft Dynamics

The steady-state performance of an airplane can be investigated very thoroughly from a set of trimmed flight conditions. The specific fuel consumption, rate of climb, various critical speeds for takeoff and landing, radius of turn, and so on, can all be determined for a number of different flight conditions. We have not provided enough modeling detail for all of these investigations, but the model and the trim program could be further developed if required.

Here we will examine the trimmed level-flight conditions over a range of speed. The F-16 is balanced to minimize trim drag, and for straight and level flight across the speed range of our model, the change in the trimmed elevator deflection is very small and varies erratically. At very low speeds, and therefore low dynamic pressure, a high value of the lift coefficient is needed to support the aircraft weight. This causes high induced drag, and because of the large angle of attack, the engine thrust must support a large component of the aircraft weight. Therefore, the throttle setting must increase at low speeds. The throttle setting also increases as transonic speeds are approached because of the increasing drag, and thus the throttle-setting v. speed curve must pass through a minimum.

Data for trimmed level flight at sea level, with the nominal cg position, are given in Table 3.6-2. As the speed is lowered, the angle of attack increases, the leading-edge flap reaches its limit (at about  $\alpha = 18^\circ$ , although no longer visible in the data), and the trimmed throttle setting begins to increase from its very low value. The model can be trimmed until alpha reaches about  $45^\circ$ , when a rapid increase in trimmed elevator deflection occurs, quickly reaching the deflection limit.

Figure 3.6-3 shows throttle setting plotted against airspeed. This curve is not the same as the airplane “power-required” curve because the engine characteristics are also included in it. Nevertheless, we shall loosely refer to it as the *power curve*. It shows clearly the minimum throttle setting. For a propeller-driven plane this is the condition for *best endurance* (but not best range) at the given altitude. For a jet plane the fuel consumption is more strongly related to thrust than power, so this is no longer

TABLE 3.6-2 Trim Data for the F-16 Model

Speed	130	140	150	170	200	260	300	350	400
Throttle	0.816	0.736	0.619	0.464	0.287	0.148	0.122	0.107	0.108
AOA	45.6	40.3	34.6	27.2	19.7	11.6	8.49	5.87	4.16
Elevation	20.1	−1.36	0.173	0.621	0.723	−0.090	−0.591	−0.539	−0.591
Speed	440	500	540	600	640	700	800	ft/s	
Throttle	0.113	0.137	0.160	0.200	0.230	0.282	0.378	Per unit	
AOA	3.19	2.14	1.63	1.04	0.742	0.382	−0.045	degrees	
Elevation	−0.671	−0.756	−0.798	−0.846	−0.871	−0.900	−0.943	degrees	

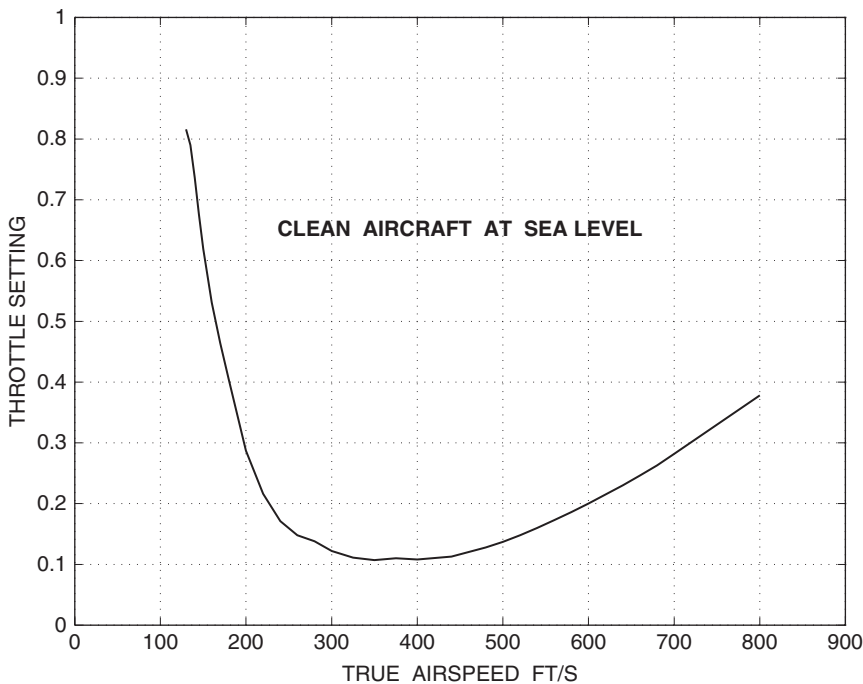


Figure 3.6-3 F-16 model, trimmed power curve.

true. For more details on the static performance information that can be derived from a power-available curve, see Dommasch et al. (1967).

The region to the left of the minimum of the power-required curve is known as the *back side of the power curve*. If the aircraft is operating on the back side of the power curve, opening the throttle produces an increase in altitude, *not* an increase in speed. The speed is then controlled by the elevator. This region of operation may be encountered in the landing phase of flight (e.g., carrier landings).

Table 3.6-3 presents another set of trimmed conditions for the F-16 model; these will be used for the simulation examples in this chapter and for controller design in subsequent chapters. The F-16 model aerodynamic data were referenced to the  $0.35\bar{x}$ -position, and this is the “nominal” position for the cg. The nominal speed and altitude were chosen to give a representative flight condition suitable for later examples and designs. The table contains data for the nominal condition, a forward-cg condition, an aft-cg condition, and steady-state turn and pull-up conditions with a forward cg. The forward- and aft-cg cases have been included for a later demonstration of the effect of cg position on stability. A forward-cg location has been used for the two maneuvering cases so that the effects of the maneuver can be illustrated without the additional complication of unstable dynamics.

**TABLE 3.6-3 Trimmed Flight Conditions for the F-16**Nominal Condition:  $h = 0$  ft,  $\bar{q} = 300$  psf,  $X_{cg} = .35\bar{c}$ ,  $\dot{\phi} = \dot{\theta} = \dot{\psi} = \gamma = 0$ 

variable	CONDITION				
	Nominal	$X_{cg} = 0.3\bar{c}$	$X_{cg} = +0.38\bar{c}$	$X_{cg} = +0.3\bar{c}$ $\dot{\psi} = 0.3$ r/s	$X_{cg} = -0.3\bar{c}$ $\dot{\theta} = 0.3$ r/s
$V_T$ (ft/s)	502.0	502.0	502.0	502.0	502.0
$\alpha$ (rad)	0.03691	0.03936	0.03544	0.2485	0.3006
$\beta$ (rad)	$-4.0E-9$	$4.1E-9$	$3.1E-8$	$4.8E-4$	$4.1E-5$
$\phi$ (rad)	0	0	0	1.367	0
$\theta$ (rad)	0.03691	0.03936	0.03544	0.05185	0.3006
$P$ (r/s)	0	0	0	$-0.01555$	0
$Q$ (r/s)	0	0	0	0.2934	0.3000
$R$ (r/s)	0	0	0	0.06071	0
THTL(0-1)	0.1385	0.1485	0.1325	0.8499	1.023
EL(deg)	$-0.7588$	$-1.931$	$-0.05590$	$-6.256$	$-7.082$
AIL(deg)	$-1.2E-7$	$-7.0E-8$	$-5.1E-7$	0.09891	$-6.2E-4$
RDR(deg)	$6.2E-7$	$8.3E-7$	$4.3E-6$	$-0.4218$	0.01655

### Flight Simulation Examples

Here we give two flight simulation examples using the MATLAB simulation program from Section 3.4 with the transport aircraft model and one example using the F-16 model with a Fortran version of the simulation program.

**Example 3.6-3: Simulated Response to an Elevator Pulse** The transport aircraft model was trimmed for level flight in the “clean” condition at sea level, with  $x_{cg} = 0.25$  and a true airspeed of 250 ft/s, using the trim program given in this section. The state and control vectors were

$$U^T = [0.1845 \quad -9.2184]; \quad X^T = [250 \quad 0.16192 \quad 0.16192 \quad 0 \quad 0]$$

A time-history simulation was performed using the program NLSIM.m, as given in Example 3.4-1, and with the above initial conditions. RK4 integration with a step size of 20 ms was used. An elevator-*doublet* pulse of  $2^\circ$  from 1 to 1.5 s and  $-2^\circ$  from 1.5 to 2 s was superimposed on the trimmed elevator deflection using the code that was shown disabled in Example 3.4-1. A doublet is bidirectional with a mean value of zero and is intended to restore the original flight conditions when it ends.

Figure 3.6-4 shows the pitch-attitude and angle-of-attack responses to the elevator doublet. The initial pitch responses do not match (in shape or duration) the elevator disturbance that caused them. Instead, the responses are characteristic of the aircraft and represent a *natural mode* of the aircraft dynamics, in which alpha and theta vary

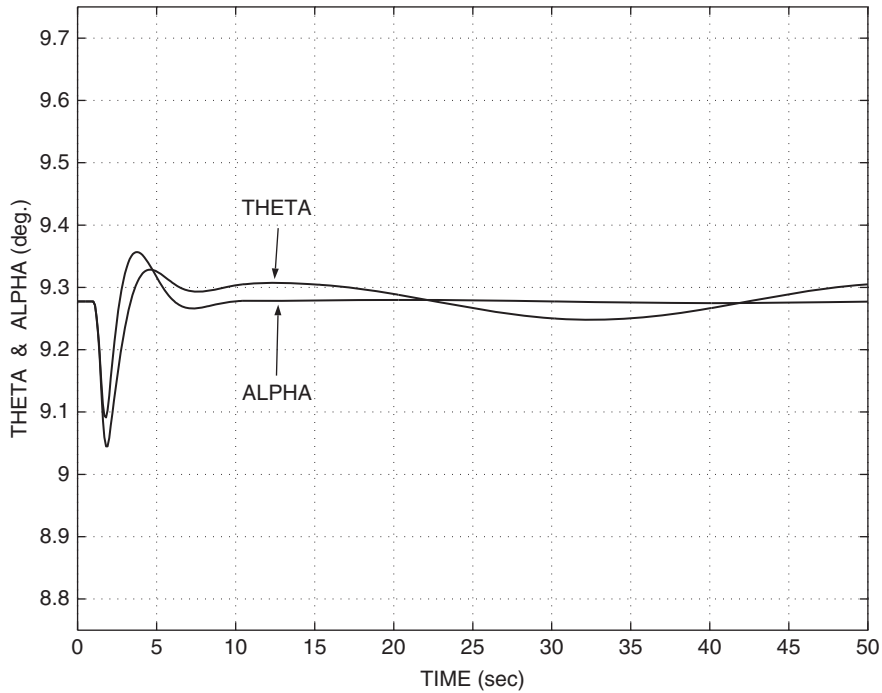


**Figure 3.6-4** Transport aircraft, elevator-doublet response.

together, thus causing very little change in the flight-path angle. This mode is known as the *short-period mode*. If we inspect the other longitudinal variables, we will find that airspeed and altitude are almost constant, and only alpha, theta, and pitch rate vary. When the short-period response dies out, at about 10 s, alpha becomes constant and pitch rate becomes zero. There remains a small-amplitude, very lightly damped oscillation in which the aircraft gains altitude, with increasing pitch attitude and a positive flight-path angle and decreasing speed, and then reverses this motion. This is the *phugoid mode* of an aircraft. The short-duration elevator doublet may cause very little excitation of the phugoid mode if that mode is better damped than is the case here. ■

**Example 3.6-4: Simulated Response to a Throttle Pulse** In this example we will use the transport aircraft with the same trim conditions as Example 3.6-3 and superimpose a doublet pulse on the steady-state throttle setting. The doublet will have the value 0.1 from 1 to 4 s and  $-0.1$  from 4 to 7 s. Figure 3.6-5 shows the response. The angle of attack is barely affected, but the pitch attitude exhibits the phugoid oscillation that was observed in Example 3.6-3. An examination of the speed, altitude, and flight-path

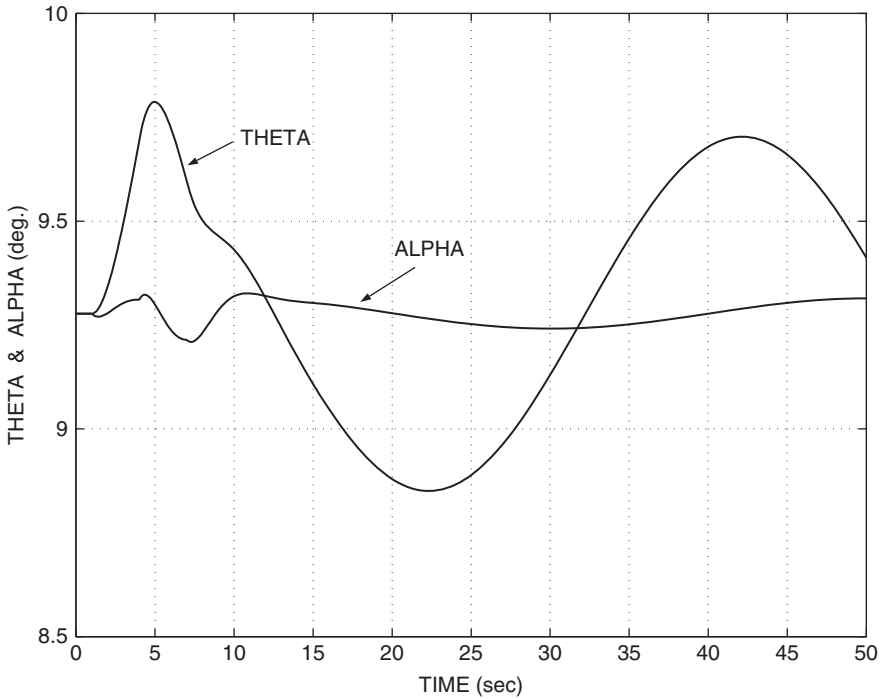


**Figure 3.6-5** Transport aircraft, throttle-doublet response.

angle variables shows that they vary in unison with theta. Therefore, we conclude that the thrust disturbance has excited the phugoid mode, with very little effect on the short-period mode.

■

**Example 3.6-5: Simulation of a Coordinated Turn** This example is a time-history simulation of a steady-state coordinated turn using the F-16 model with the trim data from Example 3.6-2. The simulation data from the TRESP program are presented in Figure 3.6-6. The aircraft is turning at 0.3 rad/s and therefore turns through 54 rad or about 8.6 revolutions in the 180-s simulation.

Figure 3.6-7 shows the ground track of the aircraft and shows that the eight circles fall exactly over each other. In Section 3.8 we will see that the aircraft dynamics have quite a wide spread of time constants, and in this flight condition, there is an unstable mode with a time constant of about 1.7 s. Unless the integration time step is reduced below about 0.02 s, the fourth-order Runge-Kutta routine eventually diverges when integrating this example.

```
Initial condition filename ? (def.= none): EX362

Number of states and outputs to be recorded ?
# States (def.= 0) : 2
Which ones ? : 10 11
# Outputs (def.= 0) : /
Variable (V) or fixed (F) step integration ? (def= F) : /
Length of run (sec) ? : 180
Print time-interval (on screen) ? : 10
Plotting time-interval ? : .5
Sample period (integration step) ? : .01

      TIME      X-10      X-11
0.00E+00  0.00E+00  0.00E+00
1.00E+01  2.36E+02  3.33E+03
2.00E+01 -4.68E+02  6.65E+01
3.00E+01  6.90E+02  3.20E+03
4.00E+01 -8.97E+02  2.61E+02
5.00E+01  1.09E+03  2.94E+03
6.00E+01 -1.26E+03  5.68E+02
7.00E+01  1.40E+03  2.59E+03
8.00E+01 -1.51E+03  9.62E+02
9.00E+01  1.60E+03  2.16E+03
1.00E+02 -1.65E+03  1.41E+03
1.10E+02  1.67E+03  1.70E+03
1.20E+02 -1.66E+03  1.89E+03
1.30E+02  1.61E+03  1.22E+03
1.40E+02 -1.53E+03  2.35E+03
1.50E+02  1.42E+03  7.87E+02
1.60E+02 -1.28E+03  2.76E+03
1.70E+02  1.11E+03  4.22E+02
1.80E+02 -9.21E+02  3.07E+03

Enter  0 to file data      1 to quit
       2 to restart        3 to pick other states
       4 to change integration  5 to change run time :
```

Figure 3.6-6    Simulation results for F-16 model.

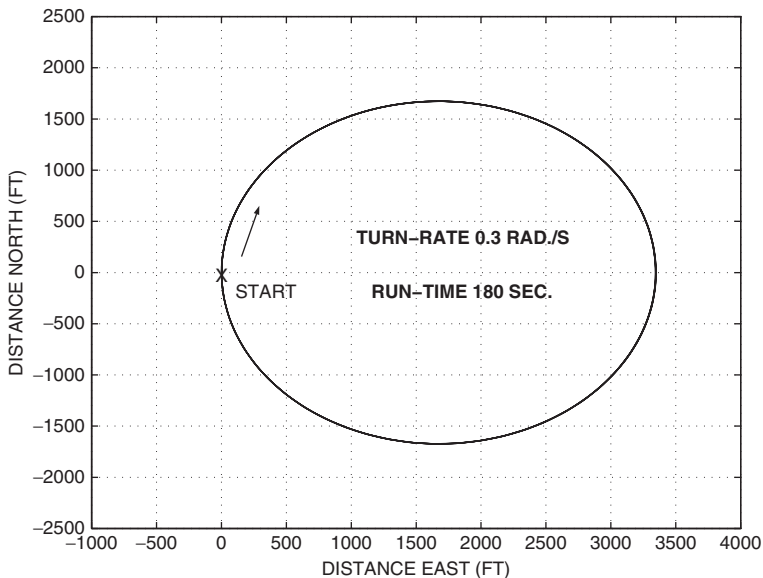


Figure 3.6-7    The ground track of a coordinated turn.



The foregoing examples have illustrated digital simulation using nonlinear continuous-time dynamic equations, with control inputs applied in discrete time (i.e., changing only at the sampling instants). In the next section we will derive linear dynamic equations; these offer no advantages for simulation but do allow a variety of analytical tools to be applied to the dynamics.

### 3.7 NUMERICAL LINEARIZATION

#### Theory of Linearization

In Section 2.6 we linearized the aircraft implicit nonlinear state equations algebraically and obtained LTI state equations corresponding to a given flight condition. This linearization was specific to aircraft equations and was only tractable under the restrictions of wings-level, non-sideslipping steady-state flight. Now we will introduce a numerical linearization algorithm that can be applied to any nonlinear model in the same explicit state-space form that was used with numerical integration.

A multivariate Taylor series expansion of the explicit state equations (3.4-1b) around a point  $(X_e, U_e)$  gives

$$\dot{X} + \delta\dot{X} = f(X_e, U_e) + \frac{\partial f}{\partial X}\delta X + \frac{\partial f}{\partial U}\delta U + \text{h.o.t.},$$

where the partial derivative terms denote Jacobian matrices (as in Section 2.6) and the perturbations

$$\delta X \equiv (X - X_e), \quad \delta U \equiv (U - U_e)$$

are “small.” In the series “h.o.t.” denotes higher-order terms, which will be neglected. If  $X_e$  and  $U_e$  are equilibrium solutions obtained from the trim program, then

$$0 = \dot{X} = f(X_e, U_e)$$

and so

$$\delta\dot{X} = \frac{\partial f}{\partial X}\delta X + \frac{\partial f}{\partial U}\delta U \quad (3.7-1)$$

This equation is in the form of the LTI state equation,

$$\dot{x} = Ax + Bu, \quad (3.7-2)$$

where the lowercase symbols denote perturbations from the equilibrium, but  $\dot{x}$  is the actual value of the derivative vector.

The method of estimating the first partial derivatives, which make up the Jacobian matrices, will be illustrated with a function of a single variable  $z = g(v)$ . Using Taylor series expansions of  $g$  around  $v = v_e$ , we obtain

$$\begin{aligned} z_1 \equiv g(v_e + h) &= g(v_e) + h \frac{\partial g}{\partial v}(v_e) + \frac{h^2}{2!} \frac{\partial^2 g}{\partial v^2}(v_e) + \text{h.o.t.} \\ z_{-1} \equiv g(v_e - h) &= g(v_e) - h \frac{\partial g}{\partial v}(v_e) + \dots \end{aligned}$$

Then it is easy to see that

$$\left. \frac{\partial g}{\partial v} \right|_{v=v_e} = \frac{z_1 - z_{-1}}{2h} - \frac{h^2}{3!} \frac{\partial^3 g}{\partial v^3}(v_e) - \text{h.o.t.} \quad (3.7-3)$$

and neglecting terms of order  $h^2$  and higher leaves a very simple approximation for the first partial derivative.

A higher-order approximation can be found by writing the Taylor series for

$$z_2 = g(v_e + 2h)$$

and

$$z_{-2} = g(v_e - 2h)$$

It can then be shown that

$$\left. \frac{\partial g}{\partial v} \right|_{v=v_e} = \frac{8(z_1 - z_{-1}) - (z_2 - z_{-2})}{12h} + O(h^4) \quad (3.7-4)$$

Therefore, by using four values of the function  $g$ , we can obtain an estimate of the first partial derivative that includes Taylor series terms through  $h^3$ .

## Algorithm and Examples

When turning the formulae for the partial derivatives into a numerical algorithm, one must determine what size of perturbation can be considered “small” in Equation (3.7-1). The perturbations may often be around an equilibrium value of zero, so it is not always possible to choose some fraction of the equilibrium value. Instead, one can start with a fairly arbitrary initial perturbation and progressively reduce it until the algorithm obtained from (3.7-3) or (3.7-4) converges on some value for the derivative. Figure 3.7-1 shows a flowchart for numerical linearization, and a simple MATLAB program is given below.

```
% File LINZE.m
clear all
name = input('Enter Name of State Eqns. File : ','s');
tfile= input('Enter Name of Trim File : ','s');
tmp= dlmread(tfile,',' );
n=tmp(1); m=tmp(2); x=tmp(3:n+2);
u=tmp(n+3:m+n+2); tol=1e-6; time=0.;
mm= input('Number of control inputs to be used ? : ');
dx=0.1*x;
for i=1:n % Set Perturbations
    if dx(i)==0.0;
        dx(i)=0.1;
    end
end
last=zeros(n,1); a=zeros(n,n);
for j=1:n
```

```

xt=x;
for i=1:10
    xt(j)=x(j)+dx(j);
    xd1= feval (name,time,xt,u);
    xt(j)=x(j)-dx(j);
    xd2= feval (name,time,xt,u);
    a(:,j)= (xd1-xd2)'/(2*dx(j));
    if max( abs(a(:,j))-last)./abs( a(:,j) + 1e-12 )<tol;
        break
    end
    dx(j)= 0.5*dx(j);
    last = a(:,j);
end
%column=j
iteration=i;
if iteration==10
    disp('not converged on A, column',num2str(j))
end
end
end
dlmwrite('A.dat',a);
    
```

This program computes one column of  $A$  at a time; a fractional error is computed for each element of the column array, and the largest fractional error must satisfy a convergence tolerance. If the algorithm has not converged after dividing the initial perturbation by  $2^9$ , the user is informed and must deal with the problem by increasing the tolerance or linearizing at a slightly different flight condition. To save space, the

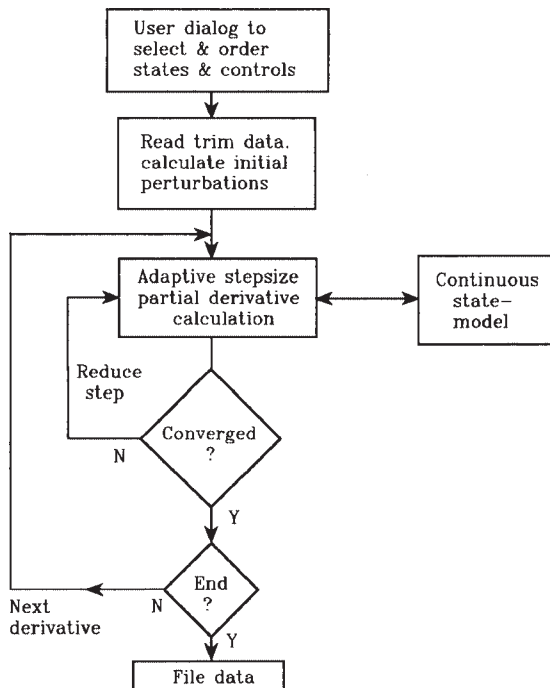


**Figure 3.7-1** Flowchart for linearization.

calculation of the  $B$ -matrix is not shown; note that not all of the control variables should be perturbed (e.g., the landing gear switch) so the user must enter a value for the variable  $mm$ .

For a differentiable function, perturbations that are too large produce a (Taylor series) truncation error, while perturbations that are too small cause a round-off error due to the finite-precision computer arithmetic. Many simulations are written with single-precision arithmetic, and round-off error will then be much more significant than with MATLAB double-precision arithmetic. Difficulties are also caused by discontinuities in the function or its derivative. For example, if a simulation variable has reached a “hard” limit, this will cause a discontinuity in its derivative. A more sophisticated linearization algorithm may be designed to find an optimal-size perturbation and to detect discontinuities (see, for example, Taylor and Antonioti, 1993). The student should add the calculations for the  $B$ -,  $C$ -, and  $D$ -matrices to the above program (see Problem 3.7-2). A linearization program “Jacob” for the Fortran model is given in Appendix B.

**Example 3.7-1: Comparison of Algebraic and Numerical Linearization** This example uses the transport aircraft longitudinal model of Section 3.5. The model contains an alpha-dot contribution to the pitching moment, the thrust vector is offset from the cg by the amount  $ZE$ , and the engine thrust varies with speed. It therefore provides a good check on the results of the algebraic linearization in Section 2.6.

A short program was written to evaluate the longitudinal state equation coefficient matrices (2.6-29) using the formulae in Tables 2.6-1 to 2.6-3 (see Problem 3.7-3). The program contains the dimensionless stability derivatives given in the transport aircraft model and reads the steady-state trim data from a data file. It calculates the  $A$ - and  $B$ -matrices in (2.6-30) and then premultiplies them by the inverse of the  $E$ -matrix. The new  $A$ - and  $B$ -matrices were printed out for comparison with numerical linearization results.

The model was trimmed in the clean condition at a large angle of attack and in climbing flight, so that  $\sin \alpha$  and  $\sin \gamma$  terms contributed significantly to the results. The trim condition was  $cg = 0.25\bar{c}$ ,  $h = 0$  ft,  $V_T = 200$  ft/s, and  $\gamma = 15^\circ$ . This condition required an angle of attack of  $13.9^\circ$  and a throttle setting of 1.01 (i.e., slightly beyond maximum power!). The algebraic linearization program gave

$$E^{-1}A = \begin{array}{c} \begin{array}{cccc} v_T & \alpha & \theta & q \end{array} \\ \begin{bmatrix} -2.7337E-02 & 1.6853E+01 & -3.1074E+01 & 0.0000E+00 \\ -1.4167E-03 & -5.1234E-01 & -4.1631E-02 & 1.0000E+00 \\ 0.0000E+00 & 0.0000E+00 & 0.0000E+00 & 1.0000E+00 \\ -1.1415E-04 & -4.9581E-01 & 4.8119E-03 & -4.2381E-01 \end{bmatrix} \end{array}$$

$$E^{-1}B = \begin{array}{c} \begin{array}{cc} \delta_i & \delta_e \end{array} \\ \begin{bmatrix} 1.0173E+01 & 0.0000E+00 \\ -1.2596E-02 & 0.0000E+00 \\ 0.0000E+00 & 0.0000E+00 \\ 2.7017E-02 & -7.0452E-03 \end{bmatrix} \end{array}$$

The algebraic linearization did not account for an altitude state and the consequent coupling of the equations through the atmosphere model. Therefore, only the first four states were selected when the numerical linearization was performed. The numerical linearization produced the following results:

$$A = \begin{bmatrix} -2.7337E-02 & 1.6852E+01 & -3.1073E+01 & 0.0000E+00 \\ -1.4168E-03 & -5.1232E-01 & -4.1630E-02 & 1.0000E+00 \\ 0.0000E+00 & 0.0000E+00 & 0.0000E+00 & 1.0000E+00 \\ -1.1415E-04 & -4.9583E-01 & 4.8118E-03 & -4.2381E-01 \end{bmatrix}$$

$$B = \begin{bmatrix} 1.0173E+01 & 0.0000E+00 \\ -1.2596E-02 & 0.0000E+00 \\ 0.0000E+00 & 0.0000E+00 \\ 2.7017E-02 & -7.0452E-03 \end{bmatrix}$$

These results are in very close agreement with the algebraic linearization results; the largest discrepancy is a difference of 2 in the fifth digit. ■

The stability derivatives and numerical linearization play complementary roles. The stability derivatives are useful for preliminary design; they can be estimated from a geometrical description of an aircraft and can be used to calculate the modes and stability of the aircraft. When an aircraft configuration has been chosen and enough data have been gathered to build a mathematical model, numerical linearization can be used to perform control system design and to obtain a dynamic description of the aircraft in other than wings-level non-sideslipping flight.

**Example 3.7-2: Linearization of the F-16 Model** In Chapter 2 it was shown that under the conditions of small perturbations from steady-state, wings-level, non-sideslipping flight, the rigid-aircraft equations of motion could be split into two uncoupled sets. These were the longitudinal equations that involve the variables speed, alpha, pitch attitude, and pitch rate and the lateral-directional equations that involve beta, roll angle, and roll and yaw rates. The Jacob program makes it easy to demonstrate this decoupling and to show that coupling occurs when the sideslip and roll angles are nonzero. A good example is provided by two steady-state flight conditions that differ only in terms of roll angle. In Table 3.6-3, the wings-level pull-up with  $\dot{\theta} = 0.3$  rad/s and the coordinated turn at 0.3 rad/s are both at 300 psf dynamic pressure with zero sideslip and similar angles of attack (and almost identical normal acceleration). The Jacobian matrices for these two steady-state conditions will now be compared.

The Fortran linearization program makes provision for reordering states and for choosing subsets of states. The north and east geographic position states and the geographic heading state  $\psi$  have no effect on the dynamic behavior; their derivatives are a function of the other states, but these states themselves are not coupled back into the state equations. Also, the altitude state only enters the aircraft equations through the atmosphere model and dynamic pressure, and in this case it has negligible coupling to the other states. Therefore, we will not select these state variables for the LTI model.

To illustrate decoupling, Jacob was used to reorder the remaining nine states into longitudinal states  $v_T$ ,  $\alpha$ ,  $\theta$ ,  $q$  and the engine power state (POW), followed by lateral directional states  $\beta$ ,  $\phi$ ,  $p$ ,  $r$ . The inputs were ordered as  $\delta_t$ ,  $\delta_e$ ,  $\delta_a$ ,  $\delta_r$  and the outputs as  $a_n$ ,  $q$ ,  $\alpha$ . The results for the steady-state pull-up are shown in Figure 3.7-2.

These results are rounded to three significant digits, except for numbers less than 0.001, which are rounded to only one significant digit. The  $A$ - and  $B$ -matrices have been partitioned to separate the longitudinal and lateral states and controls, and it is evident that the expected decoupling does indeed exist. In the  $A$ -matrix, the exact relationship  $\dot{\theta} = q$ , when  $\phi = 0$ , is evident on the third row. There is a small amount of coupling of  $\dot{V}_T$  to  $\beta$  and  $\phi$  and of  $\dot{q}$  to  $r$ , but the other terms are one to two orders of magnitude smaller. The  $B$ -matrix shows that the aileron and rudder have essentially no effect on the longitudinal states and the throttle and elevator have no effect on the lateral-directional states.

The  $D$ -matrix has a nonzero entry, corresponding to the elevator to normal acceleration transfer function, because accelerations are directly coupled to forces and therefore to control surface deflection. Other expected features are the reciprocal of the engine time constant (at full power) as the only nonzero entry on the fifth row

$$\begin{aligned}
 A = & \begin{array}{c} \begin{array}{ccccccccc} v_T & \alpha & \theta & q & \text{pow} & \beta & \phi & p & r \end{array} \\ \left[ \begin{array}{ccccccccc} -.127 & -.235 & -32.2 & -9.51 & .314 & : & -.0028 & .00126 & 5E-5 & 2E-4 \\ -7E-4 & -.969 & 0 & .908 & -2E-4 & : & 1.5E-5 & 0 & -4E-5 & -1E-5 \\ 0 & 0 & 0 & 1 & 0 & : & 0 & 0 & 0 & 0 \\ 9E-4 & -4.56 & 0 & -1.58 & 0 & : & 9.2E-5 & 0 & 0 & -.00287 \\ 0 & 0 & 0 & 0 & -5.00 & : & 0 & 0 & 0 & 0 \end{array} \right. \\ \hline & \left[ \begin{array}{ccccccccc} 1E-8 & 2E-5 & 3E-6 & 8E-7 & -3E-8 & : & -.322 & .0612 & .298 & -.948 \\ 0 & 0 & 0 & 0 & 0 & : & 0 & .0930 & 1.00 & .310 \\ -3E-7 & -.00248 & 0 & 3E-4 & 0 & : & -62.5 & 0 & -3.00 & 1.99 \\ -3E-6 & -.00188 & 0 & .00254 & 0 & : & 7.67 & 0 & -.262 & -.629 \end{array} \right] \end{array} \\
B = & \begin{array}{c} \begin{array}{cccc} \delta_t & \delta_e & \delta_a & \delta_r \end{array} \\ \left[ \begin{array}{cccc} 0 & -.244 & : & 6E-6 & 2E-5 \\ 0 & -.00209 & : & 0 & 0 \\ 0 & 0 & : & 0 & 0 \\ 0 & -.199 & : & 0 & 0 \\ 1087 & 0 & : & 0 & 0 \end{array} \right. \\ \hline & \left[ \begin{array}{cccc} 0 & 2E-8 & : & 3E-4 & 8E-4 \\ 0 & 0 & : & 0 & 0 \\ 0 & 0 & : & -.645 & .126 \\ 0 & 0 & : & -.0180 & -.0657 \end{array} \right] \end{array} \\
D = & \begin{array}{c} \left[ \begin{array}{cccc} 0 & .0333 & 0 & 0 \\ 0 & 0 & 0 & 0 \\ 0 & 0 & 0 & 0 \end{array} \right] \end{array} \\
C = & \begin{array}{c} \left[ \begin{array}{ccccccccc} .0208 & 15.2 & 0 & 1.45 & 0 & -4.5E-4 & 0 & 0 & 0 \\ 0 & 0 & 0 & 1.00 & 0 & 0 & 0 & 0 & 0 \\ 0 & 57.3 & 0 & 0 & 0 & 0 & 0 & 0 & 0 \end{array} \right] \begin{array}{c} a_n \\ q \\ \alpha \end{array} \end{array}
\end{aligned}$$

Figure 3.7-2 Jacobian matrices for a pull-up.

$$A = \begin{bmatrix} -.090 & -.169 & -.31.2 & -.7.75 & .318 & : & 31.4 & -.7.73 & 5E-4 & 2E-3 \\ -5E-4 & -.1.05 & .0151 & .903 & -2E-4 & : & 3E-4 & -.0607 & -5E-4 & -1E-4 \\ 0 & 0 & 0 & .203 & 0 & : & 0 & -.300 & 0 & -.979 \\ 1E-3 & 1.26 & 0 & -1.66 & 0 & : & 1E-3 & 0 & .0589 & -.0157 \\ 0 & 0 & 0 & 0 & -5.00 & : & 0 & 0 & 0 & 0 \\ \hline -1E-4 & 1.4E-4 & -.0032 & 7E-6 & -3E-7 & : & -.322 & .0130 & .248 & -.961 \\ 0 & 0 & .300 & .0508 & 0 & : & 0 & 0 & 1.00 & .0105 \\ -3E-4 & .0578 & 0 & -.0469 & 0 & : & -59.4 & 0 & -3.19 & 1.64 \\ 5E-5 & -.0617 & 0 & .0123 & 0 & : & 8.88 & 0 & -.299 & -.564 \end{bmatrix}$$

Figure 3.7-3 Jacobian matrix for 4.5 g turn.

of the  $A$ -matrix and the value of  $g$  appearing in the (1, 3) position. The reader should compare these results with the state equations derived in Chapter 2 and determine the significance of the numerical values.

If we next use the Jacobian program to determine the  $A$ -matrix for the 4.5  $g$  coordinated turn, we obtain the matrix shown in Figure 3.7-3. A comparison of this matrix with the previous  $A$ -matrix shows that several strong coupling terms have now appeared in the upper right block. Less pronounced coupling has appeared in the lower left block. These couplings can be understood by referring to the nonlinear equations (2.5-19), the nonlinear moment equations, and the Euler angle equations (1.4-5), with  $\phi$  nonzero. In the next section we develop the tools to determine how the dynamic behavior is changed by this coupling, and in Chapter 4 we consider the implications of these changes in the dynamics. ■

### 3.8 AIRCRAFT DYNAMIC BEHAVIOR

In Examples 3.6-3 and 3.6-4 two different characteristic modes of the aircraft dynamics were excited separately by applying different inputs. One of the variables ( $\theta$ ) observed in the simulation was found to be involved in both modes; the other observed variable ( $\alpha$ ) was essentially involved in only one. In this section we will study the dynamic behavior analytically through modal decomposition and analysis of the transfer functions.

#### Modal Decomposition Applied to Aircraft Dynamics

In Section 3.6 the classical phugoid and short-period aircraft modes were illustrated by nonlinear simulation. The complete set of modes of a conventional aircraft will now be illustrated by modal decomposition using a linear F-16 model. The second set of trim conditions in Table 3.6-3 will be used, that is, straight and level flight with stable dynamics. A Jacobian  $A$ -matrix must first be found for this flight condition, and not all of the thirteen states in the full  $A$ -matrix will be needed.

Once again we will drop the north and east geographic position states and the geographic heading state, which do not affect the dynamics. These states

correspond to the integrals of linear combinations of other states and, if retained in the  $A$ -matrix, will produce zero eigenvalues (poles at the origin). The engine power state couples into the dynamics (through  $V_T$ ) but is not influenced by any other states. Left in the  $A$ -matrix, it will produce an eigenvalue of  $-1.0$ , corresponding to the reciprocal of the 1-s engine time constant, and again does not affect the aircraft modes.

There is also clear decoupling of the lateral and longitudinal dynamics in this flight condition. Therefore, the modal decomposition will be demonstrated using two separate reduced Jacobian matrices. Note that the method of deriving the  $A$ -matrix by perturbing the state variables assumes that the control inputs are constant. Therefore, the modes derived in the analysis are “stick-fixed” modes, that is, the control surfaces are implicitly assumed to be locked in position. This assumption will hold most accurately for fully powered (as opposed to power-boosted or unpowered) control surfaces; these control systems are called *irreversible*.

**Example 3.8-1: F-16 Longitudinal Modes** The IMSL eigenvalue subroutine EIGRF (IMSL, 1980), with double precision, was used to produce the following results. Other sources of eigenvalue/eigenvector routines are readily available (Press et al., 1986; MATLAB, 1990). A simple driver program was written, and each pair of eigenvectors was normalized by dividing all elements by the complex number corresponding to the element of greatest magnitude. The longitudinal dynamics Jacobian matrix for the F-16 model in straight and level flight at 502.0 ft/s with a cg position of  $0.3\bar{c}$  is given by

$$A = \begin{matrix} & \begin{matrix} v_T & \alpha & \theta & q \end{matrix} \\ \begin{bmatrix} -2.0244E - 02 & 7.8763E + 00 & -3.2170E + 01 & -6.5020E - 01 \\ -2.5372E - 04 & -1.0190E + 00 & 0.0000E + 00 & 9.0484E - 01 \\ 0.0000E + 00 & 0.0000E + 00 & 0.0000E + 00 & 1.0000E + 00 \\ 7.9472E - 11 & -2.4982E + 00 & 0.0000E + 00 & -1.3861E + 00 \end{bmatrix} \end{matrix}$$

The four states give rise to two complex conjugate pairs of eigenvalues, which correspond to two stable oscillatory modes. The eigenvalues are

$$\begin{aligned} & -1.2039 \pm j1.4922 && (\text{short-period mode, } T = 4.21\text{s, } \zeta = 0.628) \\ & -0.0087297 \pm j0.073966 && (\text{phugoid mode, } T = 84.9\text{s, } \zeta = 0.117) \end{aligned}$$

The periods of these modes are separated by more than an order of magnitude, so they are easily identifiable as the short-period and phugoid modes. The phugoid mode is very lightly damped ( $\zeta = 0.117$ ), but its period is so long that a pilot would have no difficulty in damping out a phugoid oscillation. The short-period mode is reasonably well damped in this particular flight condition, and the aircraft response to elevator commands would be acceptable to the pilot.



The corresponding eigenvectors are two complex conjugate pairs given by

<i>short-period</i>	<i>phugoid</i>
$\begin{bmatrix} 1.0 \\ 0.090 \\ 0.059 \\ 0.0092 \end{bmatrix} \pm j \begin{bmatrix} 0 \\ 0.017 \\ 0.054 \\ 0.15 \end{bmatrix}$	$\begin{bmatrix} 1.0 \\ -9.6E-5 \\ -3.8E-4 \\ 1.7E-4 \end{bmatrix} \pm j \begin{bmatrix} 0 \\ 5.0E-7 \\ 2.3E-3 \\ 8.4E-6 \end{bmatrix} \begin{matrix} v_T \\ \alpha \\ \theta \\ q \end{matrix}$

Both pairs of eigenvectors are dominated by the element corresponding to airspeed, and the relative involvement of the other variables is difficult to assess. Nevertheless, the results show that the variables  $\alpha$  and  $q$  are involved relatively weakly in the phugoid mode as compared to the short period, and the phugoid mode involves mostly  $V_T$  and  $\theta$ . This agrees with the conclusions drawn from the nonlinear simulation examples.

The relative involvement of different variables in the dynamic modes can be determined more precisely if the dynamic equations are made dimensionless, so that the eigenvectors are also dimensionless. This requires the introduction of time scaling (Etkin, 1972). Additional information can be extracted from the eigenvectors if they are plotted in the complex plane so that their phase relationships can be observed (Etkin, 1972). ■

**Example 3.8-2: F-16 Lateral-Directional Modes** The Jacobian matrix for the lateral-directional dynamics of the F-16 model in straight and level flight at 502.0 ft/s with a cg position of  $0.3\bar{c}$  is given by

$$A = \begin{matrix} & \beta & \phi & p & r \\ \begin{bmatrix} -3.2200E-01 & 6.4032E-02 & 3.8904E-02 & -9.9156E-01 \\ 0.0000E+00 & 0.0000E+00 & 1.0000E+00 & 3.9385E-02 \\ -3.0919E+01 & 0.0000E+00 & -3.6730E+00 & 6.7425E-01 \\ 9.4724E+00 & 0.0000E+00 & -2.6358E-02 & -4.9849E-01 \end{bmatrix} \end{matrix}$$

This time there are two real eigenvalues and a complex conjugate pair. They are

$-0.4399 \pm j3.220$	(dutch roll mode, $T = 1.95s, \zeta = 0.135$ )
$-3.601$	(roll subsidence mode, $\tau = 0.28 \text{ s}$ )
$-0.0128$	(spiral mode, $\tau = 77.9 \text{ s}$ )

The eigenvectors are

<i>Dutch Roll Mode</i>	<i>Roll Mode</i>	<i>Spiral Mode</i>
$\begin{bmatrix} -0.11 \\ -0.037 \\ 1.0 \\ -0.29 \end{bmatrix} \pm j \begin{bmatrix} -0.097 \\ -0.30 \\ 0 \\ 0.33 \end{bmatrix}$	$\begin{bmatrix} -0.0020 \\ -0.28 \\ 1 \\ 0.015 \end{bmatrix}$	$\begin{bmatrix} 0.0032 \\ 1 \\ -0.015 \\ 0.063 \end{bmatrix} \begin{matrix} \beta \\ \phi \\ p \\ r \end{matrix}$

The oscillatory mode involves all of the variables and is a rolling and yawing motion with some sideslipping. This motion has been likened to the motion of a drunken skater and is called the *dutch roll mode*. The aircraft rudder produces both rolling and yawing moments, and a rudder pulse will excite this mode. The eigenvalues show that the dutch roll period is quite short ( $T = 1.95$  s) and the oscillation is very lightly damped ( $\zeta = 0.135$ ). This would make landing in gusty wind conditions difficult for the pilot, and in a passenger aircraft, passengers sitting near the tail would be very uncomfortable in turbulent conditions.

The second mode is simply a stable exponential mode and clearly involves mostly roll rate and a corresponding roll angle; it is known as the *roll subsidence mode*. The aircraft roll angle response to lateral control inputs is an important part of the handling qualities requirements. This mode, derived from the linear model, will not allow the aircraft maximum roll rate to be calculated but does give a good idea of how quickly the aircraft will start to roll. In this case the time constant of 0.28 s indicates a fast roll response.

The third mode is also a stable exponential mode but is distinguished by a much longer time constant (78 s). It involves more roll angle and yaw rate than the roll mode and is known as the *spiral mode*. The small amount of sideslip shows that the spiral mode can be a coordinated motion. In some aircraft the spiral mode may be unstable, and stability can be built into a design by using wing dihedral (see Chapter 2). An unstable spiral mode can cause an aircraft to get into an ever-steeper, but coordinated, spiral dive. ■

## Interpretation of Aircraft Transfer Functions

We now look at the aircraft dynamic behavior through various transfer functions. More specifically, we will look for pole-zero cancellations to determine what modes remain involved in a particular response. We will also look at the frequency response of a transfer function in order to improve our understanding of the correlation between the frequency and time domains.

**Example 3.8-3: F-16 Elevator-to-Pitch-Rate Transfer Function** For this example a full thirteen-state Jacobian  $A$ -matrix was obtained for the straight and level flight conditions used in Examples 3.8-1 and 3.8-2. The  $B$  and  $C$  Jacobian matrices were also obtained, and from these matrices the elevator-to-pitch-rate transfer function was selected. The  $D$ -matrix is  $1 \times 1$  and is null, meaning that the transfer function has a relative degree of unity or greater.

Table 3.8-1 shows the static loop sensitivity and poles and zeros resulting from double-precision computations rounded to seven digits. The poles and zeros have been ordered to suit the purposes of this example. Because of the straight and level flight condition of the symmetrical aircraft, all of the lateral-directional poles will be canceled by zeros. There will be three poles at the origin, corresponding to integration of north and east velocity components, and integration of heading rate. These will also be canceled by zeros since those states are not involved in the dynamics. The throttle input is not being used and so the 1-s engine lag will be canceled by a zero.

**TABLE 3.8-1 F-16 Model, Elevator-to-Pitch-Rate Transfer Function**

Static Loop Sensitivity = -10.453 (deg. units)				
ZEROS		POLES		
Real Part	Imaginary Part	Real Part	Imaginary Part	
0.0000E + 00	0.0000E + 00	0.0000E + 00	0.0000E + 00	N
0.0000E + 00	0.0000E + 00	0.0000E + 00	0.0000E + 00	E
0.0000E + 00	0.0000E + 00	0.0000E + 00	0.0000E + 00	$\psi$
-4.3987E-01	3.2200E + 00	-4.3987E-01	3.2200E + 00	dutch
-4.3987E-01	-3.2200E + 00	-4.3987E-01	-3.2200E + 00	dutch
-3.6009E + 00	0.0000E + 00	-3.6009E + 00	0.0000E + 00	roll
-1.2835E-02	0.0000E + 00	-1.2835E-02	0.0000E + 00	spiral
-8.8010E-04	0.0000E + 00	-2.0874E-03	0.0000E + 00	Alt.
-1.0000E + 00	0.0000E + 00	-1.0000E + 00	0.0000E + 00	Engine
0.0000E + 00	0.0000E + 00	-1.2040E + 00	1.4923E + 00	SP
-2.1785E-02	0.0000E + 00	-1.2040E + 00	-1.4923E + 00	SP
-9.8713E-01	0.0000E + 00	-7.6538E-03	7.8119E-02	PHUG
		-7.6538E-03	-7.8119E-02	PHUG

The table shows that all of these cancellations are exact within the precision of the calculations. The remaining poles correspond to the phugoid and short-period modes and the altitude pole. The altitude pole is a very slow pole and is only weakly involved in the transfer function because of the nearby zero, so that the elevator-to-pitch-rate transfer function is approximately given by

$$\frac{q}{\delta_e} = \frac{-10.45s(s + 0.9871)(s + 0.02179)}{(s + 1.204 \pm j1.492)(s + 0.007654 \pm j0.07812)} \frac{\text{deg/s}}{\text{deg}}$$

The phugoid mode has a natural frequency of 0.079 rad/s and a damping ratio of 0.10; the corresponding figures for the short-period mode are 1.9 rad/s and 0.63. This transfer function has a dc gain of zero (because of the zero at the origin), indicating that a constant elevator deflection will not sustain a steady pitch rate. If the phugoid poles are canceled with the zero at the origin and the zero at  $s = -0.02$ , a *short-period approximation* transfer function is obtained:

$$\frac{q}{\delta_e} = \frac{-10.45(s + 0.9871)}{(s + 1.204 \pm j1.492)} \frac{\text{deg/s}}{\text{deg}}$$

This transfer function has a finite dc gain and shows that constant elevator deflection tends to produce constant pitch rate over an interval of time that is short compared to the phugoid period. The short-period approximation will be used in controller designs in Chapter 4, and its validity will be demonstrated. In the next example the short-period approximation will be examined in the frequency domain. ■

**Example 3.8-4: F-16 Elevator-to-Pitch-Rate Frequency Response** The poles and zeros of the elevator-to-pitch-rate transfer function, given in Example 3.8-3, will now

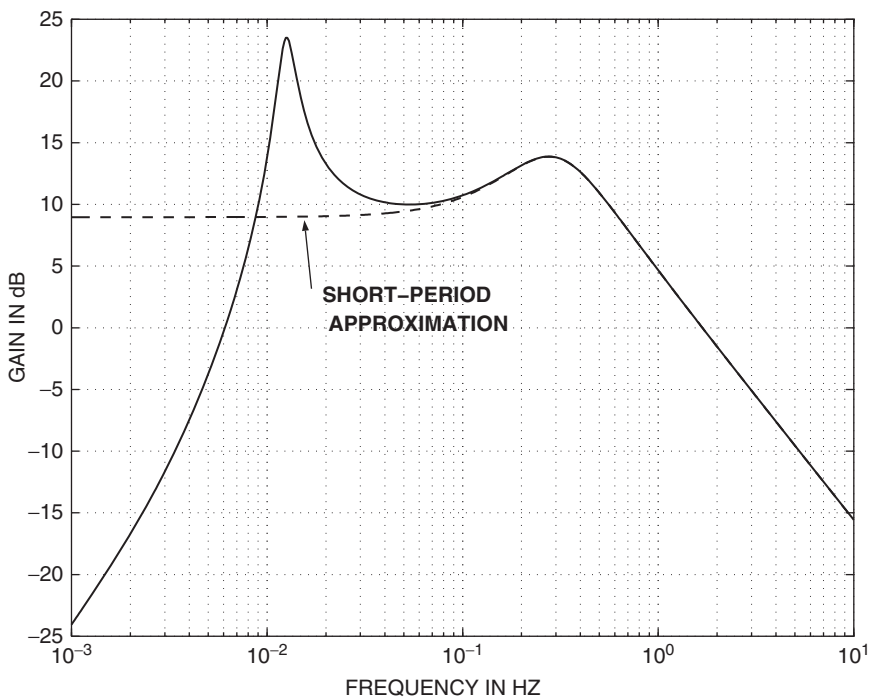


**Figure 3.8-1a** Bode gain plot, elevator to pitch rate.

be used to generate the corresponding frequency-response plots. Figure 3.8-1a shows a Bode plot of the magnitude response of both the complete transfer function and the short-period approximation. The phase plots are shown in Figure 3.8-1b. The magnitude plot shows a large peak in the response at a frequency close to the natural frequency of the lightly damped phugoid mode and a smaller peak due to the more heavily damped short-period mode.

Both the magnitude and phase plots show that the short-period approximation is a good approximation to the pitch-rate transfer function at frequencies above about 0.03 Hz. The upper *cutoff* or *corner* frequency of the short-period transfer function is about 0.8 Hz, and this gives some feel for the speed of response in pitch when different aircraft are compared. Note that the exact phase plot starts at  $+90^\circ$  due to the zero at the origin, rises toward  $180^\circ$  because of the additional phase lead of the zero at  $s = -0.02$ , and then falls back rapidly because of the  $180^\circ$  lag effect of the phugoid poles. The zero at  $s = -0.99$  causes another small lead effect before the lag of the short-period poles takes over; the high-frequency asymptotic phase shift is  $-90^\circ$  because the relative degree of the transfer function is unity.

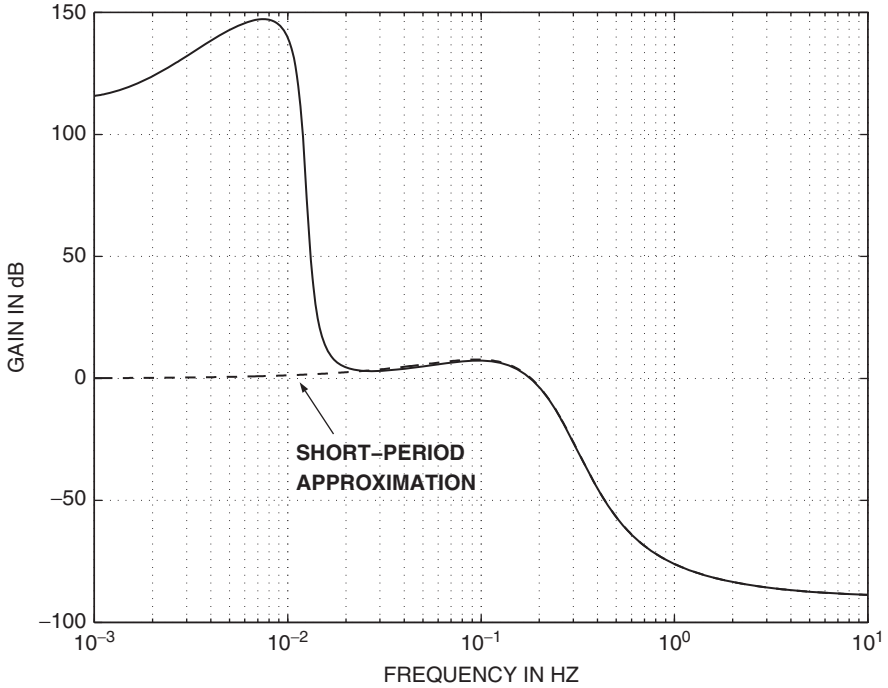


**Figure 3.8-1b** Bode phase plot of the pitch-rate transfer function. ■

**Example 3.8-5: Transport Aircraft Throttle Response** In this example we examine the throttle-to-speed transfer function for the transport aircraft model in Section 3.5 using the same flight condition as Examples 3.6-3 and 3.6-4. The model was trimmed for level flight at sea level in the clean configuration, with  $x_{cg} = 0.25\bar{c}$  and a true airspeed of 250 ft/s, and the following Jacobian matrices were determined:

$$A = \begin{bmatrix} v_T & \alpha & \theta & q & h \\ -1.6096E-02 & 1.8832E+01 & -3.2170E+01 & 0.0000E+00 & 5.4000E-05 \\ -1.0189E-03 & -6.3537E-01 & 0.0000E+00 & 1.0000E+00 & 3.7000E-06 \\ 0.0000E+00 & 0.0000E+00 & 0.0000E+00 & 1.0000E+00 & 0.0000E+00 \\ 1.0744E-04 & -7.7544E-01 & 0.0000E+00 & -5.2977E-01 & -4.1000E-07 \\ 0.0000E+00 & -2.5000E+02 & 2.5000E+02 & 0.0000E+00 & 0.0000E+00 \end{bmatrix}$$

$$B = \begin{bmatrix} 9.9679E+00 \\ -6.5130E-03 \\ 0.0000E+00 \\ 2.5575E-02 \\ 0.0000E+00 \end{bmatrix}, \quad C = [1 \ 0 \ 0 \ 0 \ 0], \quad D = 0$$

The altitude state  $h$  has very small coupling to the other states and was initially neglected. The throttle-to-speed transfer function (with the elevator fixed), as determined from the states  $v_T$ ,  $\alpha$ ,  $\theta$ ,  $q$ , was found to be

$$\frac{V_T}{\delta_t} = \frac{9.968(s - 0.0601)(s + 0.6065 \pm j0.8811)}{(s + 2.277E - 4 \pm j0.1567)(s + 0.5904 \pm j0.8811)} \quad (1)$$

As expected, this transfer function essentially involves only the phugoid mode, and when the short-period poles are canceled with the nearby complex zeros, we are left with the approximation

$$\frac{V_T}{\delta_t} = \frac{9.968(s - 0.0601)}{(s + 2.277E - 4 \pm j0.1567)} \quad (2)$$

The poles and zeros of (2) are quite close to the origin and the relative degree is unity, so throttle inputs are initially integrated. However, the phugoid mode will soon take over and hide this effect under a very lightly damped oscillation in speed. In addition, the NMP zero indicates that there are competing physical mechanisms at work. It may be remembered that the engine thrust line is offset below the cg, and this will cause the aircraft to tend to pitch up and consequently slow down in response to a sudden increase in throttle. Furthermore, at this relatively low speed the aircraft is trimmed with a large amount of “up elevator,” so that any initial increase in speed tends to create an increase in the nose-up pitching moment and again counteract the increase in speed. These facts can be confirmed by changing the engine offset and by trimming the model at higher speeds where less elevator is required. The NMP zero can thus be made to move to the origin and into the left-half plane.

In general, when the throttle is opened, the extra thrust may produce an increase in speed and/or a gain in altitude, and the phugoid mode is associated with the subsequent interchange of potential and kinetic energy. In this case we see that the positive static loop sensitivity and single NMP zero correspond to a negative dc gain. Therefore, when the throttle is opened, a very lightly damped phugoid oscillation will be initiated, starting with an increase in speed but with a mean value corresponding to a lower speed. The increased thrust will therefore be converted to an increase in altitude. This can be confirmed with a time-history simulation by applying a step throttle input to the linear model from which transfer function (1) was obtained.

Now we consider a more accurate transfer function model of the aircraft. If the aircraft altitude state is included in the A-matrix, it is found that because of the atmosphere model, there are small coupling terms from altitude to several other states. The transfer function corresponding to (1) then becomes

$$\frac{V_T}{\delta_t} = \frac{9.968(s - 0.01506)(s - 0.04528)(s + 0.6066 \pm j0.8814)}{(s + 3.305E - 5)(s + 0.5905 \pm j0.8813)(s + 6.788E - 5 \pm j0.1588)} \quad (3)$$

The very slow altitude pole (at  $s = -3E - 5$ ) has now appeared in the transfer function. An additional NMP zero is also present, and the dc gain of the transfer function is now positive. The physical explanation is that since the decrease in atmospheric

density with altitude is now modeled, the tendency to gain altitude is reduced and the speed will now increase in response to a throttle increase.

Simulation results (see Problem 3.8-2) show that for the linear model without the altitude state the average airspeed (averaged over the phugoid period) decreases in response to a throttle step. When the altitude state is included, the average airspeed decreases at first and then increases. The altitude increases in either case. The response of the nonlinear model with a relatively small throttle step increment (10% increase) agrees closely with the linear model with altitude included. ■

### 3.9 FEEDBACK CONTROL

#### Introduction

A major portion of this book is concerned with performing feedback control design on aircraft dynamics, and in this section we review the relevant classical control theory and design techniques.

In the context of controlling dynamic systems, feedback is defined as returning to the input of a system a signal obtained from its output, as shown in Figure 3.9-1. If the signal is fed back with the intention of canceling the effect of an input that produced it, we have negative feedback, as indicated by the minus sign at the *summing junction* in the figure. The system to be controlled is called the *plant*, denoted by  $G_p$ , and the feedback connection forms a *closed loop* around the plant. Components that are added to make the feedback control work effectively are represented by the *compensator*  $G_c$ . The block labeled  $H$  may represent additional compensation and/or a measurement transducer; thus the output of  $H$  may be the electrical analog of the physical *output variable*  $y$ . The *command input*  $r$  may be a different physical variable (e.g.,  $r$  may be the pilot's control stick force or deflection and  $y$  may be gs) and the *command prefilter*  $H_r$  will have a conversion factor such that the same kinds of physical quantity are compared at the summing junction.

When  $r$  and  $y$  are the same physical quantities, they can still have different scale factors, for example, a system may be designed to make  $y = 10r$ . A general definition of *control error*,  $e$ , is

$$e = r - y \quad (3.9-1)$$

Very often  $H_r$  and  $H$  will have different dynamics but the same low-frequency gain. Then the control error is independent of input amplitude and is a more practical

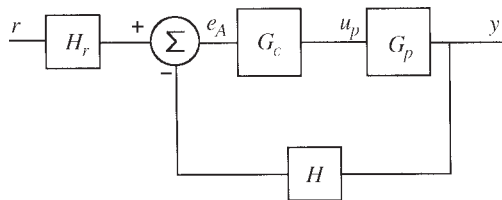


**Figure 3.9-1** Feedback control: single-loop configuration.

measure of performance. In addition, when the dynamic effects in  $H$  and  $H_r$  lie outside the frequency range of interest for the plant and compensator, they can be replaced by identity transformations. If  $H$  is replaced by the identity operation, the system is said to have *unity feedback*. The output of the summing junction is the “actuating” signal  $e_A$ , and in a well-designed control system it will normally be very small compared to the summed inputs. When  $H$  and  $H_r$  can be replaced by identity operations,  $e_A$  is identical to the control error.

One of the reasons for using negative feedback is to “regulate” the output of the plant, that is, to hold the output constant at a “set point,” as in an aircraft “altitude-hold” autopilot. Another reason is to make the output “track” (i.e., follow) a changing command, as in making an aircraft track the pilot’s pitch-rate command. In these *regulator* and *tracker* applications, negative feedback can change the nature of the plant behavior, for example, the plant may exhibit integrating behavior (e.g., as in steering a vehicle) whereas the closed-loop system simply follows its commands. Also, negative feedback can stabilize an unstable plant (e.g., the X-29 and F-117 aircraft), improve an unsatisfactory system response, allow us to trade gain for increased bandwidth and better linearity, and reduce the effects of extraneous inputs (i.e., “disturbances”). The closed-loop transient response can be made to have dominant modes that are known to provide acceptable *handling qualities* for a human operator (from back-hoe operator to aircraft pilot) or even make one aircraft simulate another (e.g., Gulfstream trainer for space shuttle pilots). To achieve these benefits, it is usually necessary to include some additional compensator dynamics within the feedback loop. In the rest of this section we will see how to choose a suitable type of compensator, how to perform a design with the compensator in place, and how to evaluate the control system design.

## Feedback Configurations and Closed-Loop Equations

We will analyze feedback configurations of the form shown in Figure 3.9-1 and with additional loops as in Figure 3.9-2. In Figure 3.9-2 the dynamics  $G_c$ , in the *forward path*, represent a *cascade compensator* (i.e., in “series” with the plant). The “inner-loop” feedback  $H_i$  represents *feedback compensation* and may correspond to *rate feedback* from a tachometer or a rate gyro when  $y$  is an angular position.

In Figure 3.9-2, the individual dynamics may be described by transfer functions or state equations, and from these we need to be able to construct a dynamic description

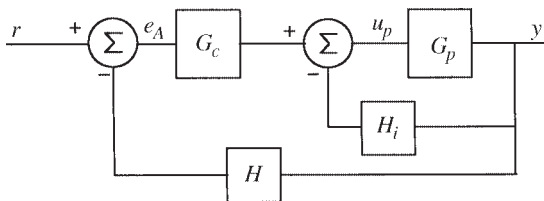


**Figure 3.9-2** Feedback control with an inner loop.



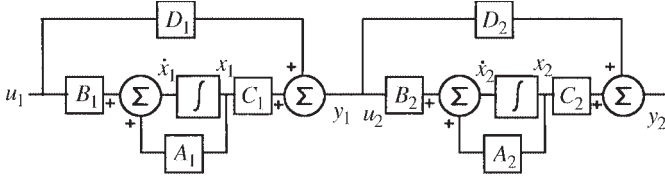


**Figure 3.9-3** Cascaded state-space systems.

of the complete system, with input  $r$  and output  $y$ . To achieve this, we must first reduce the inner loop to a single transfer function or state-space description, cascade the result with the dynamics  $G_c$ , and then reduce the outer loop by the same method as the inner loop.

First, consider the basic problem of cascading two dynamic systems. We already know that systems described by transfer functions may be cascaded by multiplying together the transfer functions and, in matrix form, we must ensure compatible dimensions in the matrix multiplication. We will now derive a formula for cascading state-space dynamic equations. In Figure 3.9-3, state-space system “1” is followed by system “2” in cascade. If we include both sets of state variables in one “augmented” state vector, an inspection of the block diagram gives the following equations:

$$\begin{bmatrix} \dot{x}_1 \\ \dot{x}_2 \end{bmatrix} = \begin{bmatrix} A_1 & 0 \\ B_2 C_1 & A_2 \end{bmatrix} \begin{bmatrix} x_1 \\ x_2 \end{bmatrix} + \begin{bmatrix} B_1 \\ B_2 D_1 \end{bmatrix} u_1 \quad (3.9-2a)$$

$$y_2 = [D_2 C_1 \quad C_2] \begin{bmatrix} x_1 \\ x_2 \end{bmatrix} + [D_2 D_1] u_1 \quad (3.9-2b)$$

These operations are numerically stable and easy to perform or incorporate in software design tools (e.g., MATLAB “Series” command).

Next, consider a single feedback loop with forward path dynamics  $G$  and feedback-path dynamics  $H$  (Figure 3.9-1 with  $H_r = I$  and  $G_c G_p$  combined as  $G$ ). Let  $G$  represent a  $(p \times m)$  transfer function matrix and  $H$  a  $(m \times p)$  transfer function matrix.  $H(s)$  may have some null rows or columns, depending on the choice of feedback connections. Simple matrix algebra gives the relationships

$$E_A(s) = R - HGE_A \quad (3.9-3a)$$

$$Y(s) = GE_A = G(I + HG)^{-1}R(s) \quad (3.9-3b)$$

so the closed-loop transfer function matrix is

$$G_{CL}(s) = G(I + GH)^{-1} \quad (3.9-4a)$$

and in the SISO case,

$$G_{CL}(s) = \frac{G}{1 + GH}, \quad (3.9-4b)$$

where  $G(s)H(s)$  is called the *loop transfer function*. For frequency ranges over which the SISO loop transfer function has large magnitude, the closed-loop transfer function is given by

$$G_{CL}(s) \approx \frac{1}{H} \quad (3.9-4c)$$

and this property is used to provide a precisely defined transfer function when  $G$  is large in magnitude but not well defined (e.g., operational amplifiers).

In the state-space case, if we draw diagrams of the form used in Figure 3.9-3 for both  $G$  and  $H$ , it is easy to derive the following closed-loop state equations:

$$\begin{bmatrix} \dot{x}_G \\ \dot{x}_H \end{bmatrix} = \begin{bmatrix} A_G - B_G D_H C_G & -B_G C_H \\ B_H C_G & A_H \end{bmatrix} \begin{bmatrix} x_G \\ x_H \end{bmatrix} + \begin{bmatrix} B_G \\ 0 \end{bmatrix} r \quad (3.9-5a)$$

$$y = [C_G \quad 0] \begin{bmatrix} x_G \\ x_H \end{bmatrix} + [0] u \quad (3.9-5b)$$

Here the subscripts  $G$  and  $H$  indicate, respectively, the forward-path and feedback-path dynamics. We have also taken the special case of  $D_G \equiv 0$  since the plant dynamics are normally low pass. Again, these operations are very simple numerically and are preferable to working with polynomials (the MATLAB command “feedback” will perform these operations).

The forward-path dynamics may include a cascade compensator and a plant and, in the special case where the feedback path contains only a gain matrix  $K$ , the above equations reduce to

$$\dot{x} = (A_G - B_G K C_G)x + B_G r \quad (3.9-6a)$$

$$y = C_G x \quad (3.9-6b)$$

The closed-loop  $A$ -matrix  $A_{CL}$  is given by

$$A_{CL} = (A_G - B_G K C_G), \quad (3.9-6c)$$

and the other matrices are unchanged.

Design software is usually arranged to produce a value for the feedback gain  $K$ . If we wish to obtain a unity-feedback design, we must scale the command  $r$  by the same gain as the feedback (i.e.,  $K$ ). The closed-loop system is then equivalent to a unity-feedback system with a gain  $K$  in the error path; this is illustrated in Figure 3.9-4. The closed-loop equations, with  $D \equiv 0$ , are easily seen to be

$$\dot{x} = (A - BKC)x + BKr \quad (3.9-7a)$$

$$y = Cx \quad (3.9-7b)$$

Therefore, we can design unity-feedback systems with the same software as long as we finally postmultiply the original  $B$ -matrix by  $K$ .

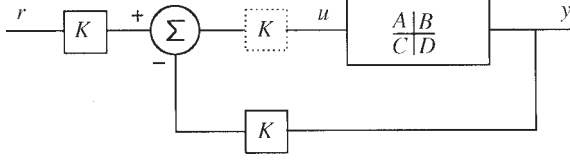


**Figure 3.9-4** Transforming to unity feedback.

In Chapter 4 we will perform a classical control design on a MIMO plant, namely, the aircraft lateral-directional dynamics. These have two inputs, aileron and rudder deflections, and two or more outputs. The classical design approach is iterative, closing one loop at a time and then repeating the process until the design is satisfactory. Here we will note how the loops can interact. The closed-loop MIMO transfer function is given in Equation (3.9-4a) and, closing any individual SISO loop through  $GH$ , in general, changes both the poles and zeros of any other SISO transfer function in  $G_{CL}$ . Various types of zeros are defined for a transfer function matrix (MacFarlane and Karcianias, 1976; Desoer and Schulman, 1974), and different subsets of these zeros will appear in the various SISO transfer functions. The zeros of a particular element of the transfer function matrix will not all appear in the corresponding SISO transfer function because of pole-zero cancellations. The actual SISO zeros can be found by the method of “coupling numerators” (McRuer et al., 1973).

Now let us return to the SISO case, with the closed-loop transfer function (3.9-4b). Also, let  $G$  and  $H$  be represented by monic polynomials as

$$G(s) = k_G \frac{N_G(s)}{D_G(s)}, \quad H(s) = k_H \frac{N_H(s)}{D_H(s)}$$

Then

$$\frac{Y(s)}{R(s)} = \frac{G}{1 + GH} = \frac{k_G N_G D_H}{D_G D_H + k_G k_H N_G N_H} \quad (3.9-8)$$

and  $K = k_G k_H$  is the static loop sensitivity of the loop transfer function  $G(s)H(s)$ . We will often simply refer to  $K$  as the loop gain. Equation (3.9-8) shows that the closed-loop zeros are the combined zeros of  $G$  and poles of  $H$ . The closed-loop poles are given by the zeros of the *characteristic equation*

$$1 + G(s)H(s) = 0, \quad (3.9-9a)$$

that is, the roots of the *characteristic polynomial*

$$D_G D_H + K N_G N_H \quad (3.9-9b)$$

Therefore, the positions of the closed-loop poles vary with  $K$ . The frequency response of the loop transfer function  $GH$  and the behavior, with  $K$ , of the roots of the characteristic polynomial are the basis of the two common design techniques of classical control theory. These will be described shortly.

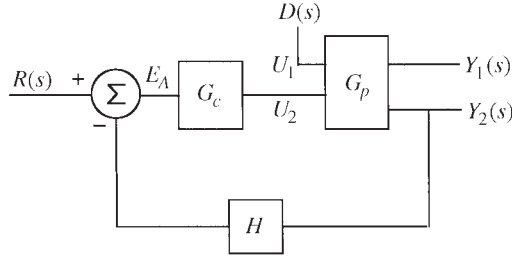


**Figure 3.9-5** Disturbance input, transfer function description.

This subsection has examined the closed-loop equations in various forms. Our last development will be the closed-loop equations for signals, other than the command, injected into the loop. An example is an aircraft model with control inputs applied to the control surfaces and wind gusts entering into the aerodynamic calculations as disturbances. In general, a MIMO plant model will be required with inputs for both disturbances and controls. Figure 3.9-5 shows an example where the plant  $G_p$  is treated as a two-input, two-output system. One input-output pair is used by the feedback loop (e.g., for feedback of angle of attack to the elevator), and the other pair has been created to determine the effect of the disturbance on some other output variable (e.g., effect of wind gusts on normal acceleration).

Referring to Figure 3.9-5, the transfer function equations are

$$Y(s) = G_p \begin{bmatrix} 1 \\ 0 \end{bmatrix} D(s) + G_p \begin{bmatrix} 0 \\ 1 \end{bmatrix} (G_c R(s) - [0 \quad G_c H] Y(s))$$

or, solving for  $Y(s)$ ,

$$Y(s) = \left( I + G_p \begin{bmatrix} 0 & 0 \\ 0 & G_c H \end{bmatrix} \right)^{-1} G_p \left( \begin{bmatrix} 1 \\ 0 \end{bmatrix} D + \begin{bmatrix} 1 \\ G_c \end{bmatrix} R \right) \quad (3.9-10)$$

Control inputs are multiplied by  $G_c$ , and higher gain in  $G_c$  will give better rejection of disturbance inputs. Equation (3.9-10) requires an inversion of a polynomial matrix and is inconvenient for numerical computations.

Figure 3.9-6 shows a state-space description of a compensator cascaded with a plant and a disturbance input to the plant. An analysis of the diagram is greatly simplified by the absence of a direct feedthrough path in the compensator, and this matches the aircraft situation if the control surface actuators are included with the compensator model. By inspection, the state equations are

$$\begin{bmatrix} \dot{x}_p \\ \dot{x}_c \end{bmatrix} = \begin{bmatrix} A_p & B_p C_c \\ -B_c C_p & A_c - B_c D_p C_c \end{bmatrix} \begin{bmatrix} x_p \\ x_c \end{bmatrix} + \begin{bmatrix} B_p \\ -B_c D_p \end{bmatrix} d + \begin{bmatrix} 0 \\ B_c \end{bmatrix} r \quad (3.9-11a)$$

$$y = [C_p \quad D_p C_c] \begin{bmatrix} x_p \\ x_c \end{bmatrix} + [D_p] d \quad (3.9-11b)$$

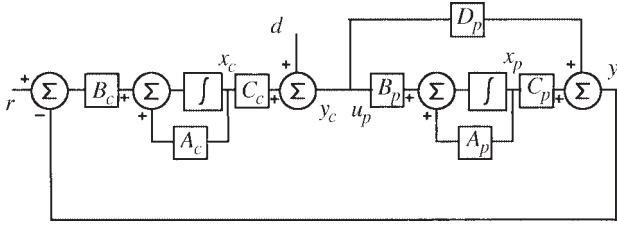


**Figure 3.9-6** Disturbance input, state-space description.

These equations can be used to determine the transfer function (or poles and zeros or frequency response) from the disturbance input to the response variable of interest. Aircraft in flight are subjected to random disturbances from discrete wind gusts and continuous turbulence, and these types of disturbances are modeled with a *power spectral density function* (PSDF) (see MIL-F-8785C). A measure of a stationary (statistics independent of time) random signal is its *root-mean-square* (rms) value, and this can be calculated from the area under the PSDF (Brown and Hwang, 1997). The aircraft response PSDF must be calculated from the squared magnitude of the appropriate transfer function multiplied by the PSDF of the disturbance. Alternatively, a model of the disturbance can be included in the nonlinear state equations, and the response to the disturbance can be found by simulation.

### Steady-State Error and System Type

An analysis of Figure 3.9-1 with SISO transfer functions  $G$  and  $H$  in the forward and feedback paths (with  $H_r = I$  and  $G = G_c G_p$ ) using the error definition (3.9-1) gives the error transfer function

$$\frac{E(s)}{R(s)} = \frac{1 + G(H - 1)}{1 + GH} \quad (3.9-12a)$$

With unity feedback, this reduces to

$$\frac{E(s)}{R(s)} = \frac{1}{1 + G} \quad (3.9-12b)$$

First consider the unity-feedback case and think of a regulator where “steady state” implies a constant output. If the forward-path transfer function exhibits integrating action, then a steady-state error cannot exist. Electronic operational amplifier circuits can provide almost perfect integration and so, if necessary, we may decide to include an integrator in the error path. In the case of a tracker, the steady-state error will depend on the type of command input and so we must analyze this situation.

In (3.9-12b) let there be  $q$  pure integrations in  $G$ , after any cancellations with zeros at the origin, and let  $G = s^{-q} G'$ . Then,

$$\frac{E(s)}{R(s)} = \frac{1}{1 + G} = \frac{s^q}{s^q + G'}, \quad (3.9-13)$$

where  $G'(0)$  is finite. Let the system be stable and have a polynomial input  $(t^n/n!)$   $U_{-1}(t)$  with Laplace transform  $1/s^{n+1}$ . Then the final-value theorem gives the following expression for the steady-state control error:

$$e_{ss}(t) = \lim_{s \rightarrow 0} sE(s) = \lim_{s \rightarrow 0} \frac{s^{q-n}}{(s^q + G')} \quad (3.9-14)$$

Therefore, in order to track a polynomial input of degree  $n$ , with finite steady-state error, the control system must have  $n$  pure integrations in the forward path. Such a system is called a *type- $n$*  control system. An additional integration will reduce the steady-state error to zero, while one less integration will cause the steady-state error to grow without bound. Each integration adds  $90^\circ$  of phase lag and makes the control system progressively more difficult to stabilize, so that systems are restricted to type 2 or lower in practice. The value of the finite steady-state error is

$$\begin{aligned} \text{when } q = n = 0 \text{ (step input),} \quad e_{ss} &= \frac{1}{(1 + G(0))} \\ \text{when } q = n \geq 1 \text{ (ramp, parabola, etc.),} \quad e_{ss} &= 1/G'(0) \end{aligned} \quad (3.9-15)$$

The step, ramp, and parabolic *error coefficients* are defined as

$$\begin{aligned} K_p &\equiv \lim_{s \rightarrow 0} G(s) \text{ and error to a unit step} = \frac{1}{(1 + k_p)} \\ K_v &\equiv \lim_{s \rightarrow 0} sG(s) \text{ and error to a unit ramp} = \frac{1}{K_v} \\ K_a &\equiv \lim_{s \rightarrow 0} s^2 G(s) \text{ and error to a unit parabola} = \frac{1}{K_a} \end{aligned} \quad (3.9-16)$$

and are used to specify performance requirements. Now consider the nonunity-feedback case and, as discussed in connection with (3.9-1), let  $H(0) = 1$ . The formula corresponding to (3.9-14) is

$$e_{ss}(t) = \lim_{s \rightarrow 0} \frac{s^{q-n} + G'(H-1)/s^n}{s^q + G'H} \quad (3.9-17)$$

and for comparison with the unity-feedback case, let  $q = n$ . Then, if  $q = n = 0$ ,

$$e_{ss} = \left[ \frac{1 + G(H-1)}{(1 + GH)} \right]_{s=0} = \frac{1}{1 + G(0)} \quad (3.9-18a)$$

and if  $q = n > 0$ ,

$$e_{ss} = \lim_{s \rightarrow 0} \left[ \frac{1 + G'(H-1)/s^n}{G'H} \right] \quad (3.9-18b)$$

Because of the condition  $H(0) = 1$ , the steady-state error with a constant input, Equation (3.9-18a), is the same as the unity-feedback case. With polynomial

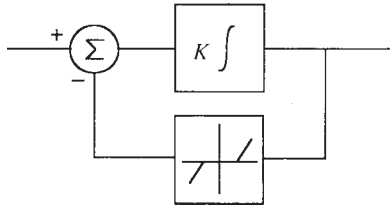


**Figure 3.9-7** Integrator windup protection.

inputs, Equation (3.9-18b) shows that the steady-state error depends on the limit of  $(H - 1)/s^n$  as  $s$  becomes zero. If  $H(s)$  is written as a ratio of polynomials, then  $H(0) = 1$  guarantees that  $H - 1$  has at least one free  $s$  to cancel with  $s^n$ . Therefore, unlike the unity-feedback case, the error can become infinite with a parabolic input ( $n = 2$ ). This is illustrated in Example 3.9-6.

Practical command inputs may contain derivatives of all orders for short periods of time, so that the tracking error may grow and then decrease again. System-type requirements and error coefficients are preliminary design considerations, and these ideas are used later in the design examples and in Chapter 4.

System type can be misleading in nonlinear situations. If, for example, the plant includes an electric motor, the integration of motor speed to angular position is a “kinematic” integration. If there are no other integrations in the forward path, the error signal must become large enough to overcome the static frictional torques of the motor and load before the motor will begin to turn. Therefore, this system will not behave like a type-1 system.

Another problem encountered with integral control of real systems is *integrator windup*. An electronic integrator *saturates* when its output gets close to the circuit positive or negative supply voltages. If the plant becomes temporarily nonlinear (e.g., “rate saturation”) before saturation occurs in the integrator, then depending on the command signal, the integrator may begin to integrate a large error signal that takes its output farther beyond the plant saturation level. When the plant comes out of saturation or the command reverses, it may take some significant time before this excessive output is removed and linear control is regained. Figure 3.9-7 shows an anti-windup arrangement. When the output of the integrator reaches the plant saturation value, it exceeds the threshold of the dead-zone device. The resulting feedback turns the integrator into a fast lag transfer function. Anti-windup arrangements are used in both analog and digital aircraft flight control systems. A related problem can occur when switching between different control system modes. All energy storage elements must be initialized so that unwanted sudden movements of the control surfaces do not occur.

## Stability

A familiar example of feedback causing instability is provided by the public address (PA) system of an auditorium. When an acoustical signal from the loudspeakers is

received at the microphone and the gain and phase around the acoustical path are such that the signal reinforces itself, the loudspeakers produce a loud whistle. This is probably the most natural intuitive way to understand feedback stability. Thus, we might examine the frequency response of the loop transfer function  $GH$  to determine if the gain is greater than unity when the phase lag has reached  $180^\circ$ ; that is, we must look for the condition  $GH(j\omega) = -1$ . This corresponds to finding a root of  $(1 + GH) = 0$  on the  $s$ -plane  $j\omega$ -axis, which is the stability boundary.

In 1932 H. Nyquist used the *principle of the argument* from complex variable theory (Phillips, 1961), applied to  $F(s) = 1 + GH(s)$ , to develop a test for stability. A semicircular “test” contour of “infinite” radius is used to enclose the right-half  $s$ -plane. According to the principle of argument, as  $s$  traverses the closed test contour in a clockwise direction, the increment in the argument of  $F(s)$  is  $N \times (2\pi)$ , where  $N = (P - Z)$ , and  $P$  and  $Z$  are, respectively, the number of poles and zeros of  $F(s)$  inside the test contour. We see that poles and zeros of  $F(s) = 1 + GH(s)$  are, respectively, the open-loop and closed-loop poles, and  $N$  is the number of counterclockwise encirclements of the  $s$ -plane origin.

Rather than count the encirclements of the origin by  $1 + GH$ , we can, more conveniently, count the encirclements of the *critical point*  $(-1 + j0)$  by  $GH(s)$ . In general,  $P$  and  $Z$  are both greater than or equal to zero, and so  $N$  may be a positive or a negative integer. Since the test contour encloses the whole right-half  $s$ -plane, we have a closed-loop stability test by finding  $Z$ , given by

$$Z = P - N \quad (3.9-19)$$

or

$$\# \text{ unstable } CL \text{ poles} = \# \text{ unstable } OL \text{ poles} - \# CCW \text{ encirclements}$$

The test contour, known as the *Nyquist D-contour*, can be indented with infinitesimal semicircles to exclude open-loop poles on the  $j\omega$ -axis. Note that some authors define  $N$  to be the number of clockwise encirclements, and they reverse the sign of  $N$  in (3.9-19).

**Example 3.9-1: An Example of Nyquist’s Stability Criterion** Let the open-loop transfer function be given by

$$G(s)H(s) = \frac{K(s+2)(s+4)}{s(s^2 - 4s + 13)}, \quad k > 0$$

Figure 3.9-8a shows the Nyquist D-contour, indented with a semicircle to avoid the pole at the origin. Figure 3.9-8b shows the Nyquist plot; letters have been used to mark corresponding points on the two plots. The indentation can be represented by the equation  $s = re^{j\theta}$ , with  $r \rightarrow 0$  and  $-\pi/2 \leq \theta \leq \pi/2$ , as an aid to establishing the corresponding points. Imagine  $G(s)H(s)$  represented by vectors drawn from the poles and zeros to a starting point at  $a$  on the D-contour. When  $s = a$ , the net angle of the vectors is zero and the magnitude of  $GH(a)$  approaches infinity as  $r$  becomes zero; this gives the corresponding point  $a'$  on the  $GH$  plot. When  $s = b$ , the angle of the



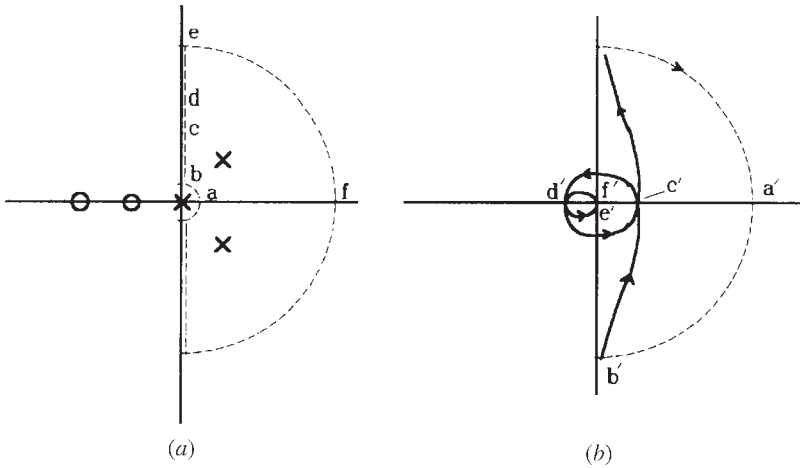


**Figure 3.9-8** (a) A Nyquist D-contour; (b) a Nyquist plot.

vector from the pole at the origin has become  $90^\circ$ , but the net angle of the other vectors is close to zero; this gives the point  $b'$ . The part of the D-contour from  $b$  to  $e$  corresponds to real frequencies, and the frequency response  $GH(j\omega)$  could be measured with test equipment if the system were not unstable. The relative degree is unity so, as  $\omega$  increases,  $GH(j\omega)$  approaches zero magnitude with a phase angle of  $-90^\circ$  (or  $+270^\circ$ ). Let  $s = c$  and  $d$  be the points where the phase of  $GH$  passes through zero and  $180^\circ$ , respectively. From  $s = e$  to  $s = f$ , the phase of  $GH(s)$  returns to zero, while the magnitude remains infinitesimal. The remainder of the D-contour uses conjugate values of  $s$ , and the remaining half of the Nyquist plot is the conjugate of the part already drawn.

The D-contour shows that  $P = 2$ , and the Nyquist plot shows that the number of counterclockwise encirclements of the critical point is  $N = 0$  or  $N = 2$ , depending on the magnitude of  $GH(j\omega)$  at  $d'$ . This, in turn, depends on the loop gain  $K$ , and so

$$\text{small } K \rightarrow Z = 2 - 0 = 2 \quad (\text{closed-loop unstable})$$

$$\text{large } K \rightarrow Z = 2 - 2 = 0 \quad (\text{closed-loop stable})$$

This is the opposite of the common behavior, in which a system becomes unstable when the gain is increased too much, and this behavior is known as *conditional stability*. At  $s = c$  and  $d'$ ,  $\text{Im}[GH(j\omega)] = 0$ ; then solving  $\text{Re}[GH(j\omega)] = -1$ , evaluated at the higher value of  $\omega$ , gives the value of  $K$  at the stability boundary. A Nyquist plot can be obtained with the following MATLAB code:

```
num=[1 6 8]; den=[1 -4 13 0];
w= logspace(-1,1,400);
k= 6;
nyquist(k*num,den,2*pi*w)
```

% 0.1 Hz to 10 Hz, 400 points  
% Stable k

Most practical control systems are open-loop stable, so that  $Z = -N$ , and therefore we require  $N = 0$  for stability. Also, we need only consider the positive  $j\omega$ -axis of the D-contour, since the negative  $j\omega$ -axis gives a conjugate locus in the  $GH$ -plane, and the infinite semicircle maps to the origin of the  $GH$ -plane (because the relative degree of the transfer function of a real compensator and plant is greater than zero). A few rough sketches will show that, under these conditions, *if the locus of  $GH$  is plotted as the frequency is varied from  $\omega = 0$  to  $\omega = \infty$ , the closed-loop system is unstable if the critical point lies to the right of the locus*. An example of the Nyquist plot of a stable type-1, relative-degree-3 system is shown in Figure 3.9-13. These restricted conditions for stability agree with the intuitive criterion that the magnitude of the loop transfer function should be less than unity when its phase lag is  $180^\circ$ .

Stability criteria, other than Nyquist's test, mostly involve testing the characteristic equation (CE) directly for roots in the right-half  $s$ -plane. A necessary but not sufficient condition for stability is that all of the coefficients of the CE should have the same sign and be nonzero [see also Descartes' rule of signs (D'Azzo and Houpis, 1988)]. Routh's test (Dorf and Bishop, 2001) uses the coefficients of the CE and provides more information, in that the number of right-half-plane roots and the stability boundary can be determined. In the state-space context the roots of the CE are the eigenvalues of the  $A$ -matrix, but then we must go to the trouble of solving the characteristic equation.

## Types of Compensation

The discussion of stability and some Nyquist sketches for simple systems that are open-loop stable should lead to some ideas about the frequency-domain properties required of a compensator. Alternatively, we might look at a compensator as a means of adding extra terms to the system characteristic equation so that the roots can be moved to desirable locations in the left-half  $s$ -plane. In frequency-domain terms, a compensator should produce phase lead in a frequency range where the lag of the plant is approaching  $180^\circ$  and the gain is near unity or it should cut the gain when the phase lag is approaching  $180^\circ$ . For a minimum-phase transfer function phase lead is associated with rising gain, and this approximates the characteristics of a differentiator. Differentiation accentuates the noise on a signal, and so practical compensators should be designed to produce phase lead and rising gain only over a limited frequency range.

Let us now examine a compensator with a single differentiation, a proportional-plus-derivative (PD) compensator, which can be approximated in real systems. The transfer function is

$$G_c(s) = K_P + K_D s \quad (3.9-20)$$

Equation (3.9-4b) gives the unity-feedback closed-loop transfer function as

$$\frac{Y}{R} = \frac{(K_P + K_D s)G_p}{1 + (K_P + K_D s)G_p} \quad (3.9-21)$$

The characteristic equation now contains the proportional and derivative terms  $K_p$  and  $K_D$ , and it may be possible to achieve satisfactory closed-loop poles. However, in addition to the noise problem, there is now a closed-loop zero at  $s = -K_p/K_D$ , and this zero can cause a large overshoot in the step response unless the plant poles are heavily damped.

As an alternative to PD compensation, consider Figure 3.9-2 with unity feedback, simple proportional control, and inner-loop rate feedback:

$$G_c = K_p; \quad H_i = K_r s$$

Then, using (3.9-4b) to close the inner loop first, the overall closed-loop transfer function is found to be

$$\frac{Y}{R} = \frac{K_p G_p}{1 + (K_p + K_r s) G_p} \quad (3.9-22)$$

Therefore, with rate feedback, we can achieve the same closed-loop poles as PD control, but without accentuating noise in the error channel and without the troublesome closed-loop zero.

A practical cascade compensator that only approximates PD control and satisfies the practical requirement of relative degree greater than or equal to zero is the simple “phase-lead” compensator shown in Table 3.3-1. The numerator  $(s + z)$ , on its own, represents a derivative term plus a proportional term, which is equivalent to a zero at  $s = -z$ . The pole is at  $s = -p$ , with  $p > z$ , and if we were to compare the Bode plots of  $(s/z + 1)$  and  $(s/z + 1)/(s/p + 1)$  we would see that the derivative action begins to disappear as the second corner frequency  $\omega = p$  is approached. The practical limit  $(p/z) < 10$  is usually observed to avoid greatly accentuating noise.

Phase-lead compensation is effective and inexpensive; inner-loop rate feedback incurs the cost of a rate sensor and may not be physically appropriate for a particular plant. A practical rate sensor also has limited bandwidth, and its transfer function pole(s) will appear as closed-loop zeros. However, these zeros are likely to be much farther from the  $s$ -plane origin than the lead compensator zero and therefore less troublesome in terms of causing overshoot.

The subsection on steady-state error and system type explained the need for “integral control.” Unfortunately, “pure” integral control has some detrimental effects on closed-loop transient response. First, a pole at the  $s$ -plane origin is destabilizing because it adds a constant  $90^\circ$  phase lag to the loop transfer function. Second, an open-loop pole at the origin may become a slow closed-loop pole (see the root-locus section). To overcome the phase-lag problem we use “proportional plus integral” (PI) control in the cascade compensator. The compensator transfer function is  $(k_p + k_i/s)$  or, equivalently,  $k_p(s + k_i/k_p)/s$ . The Bode plot of this transfer function shows that the phase lag disappears at high frequency.

If we use Figure 3.9-1 with unity feedback,  $H_r = 1$ , and a cascaded PI compensator, the closed-loop transfer function is

$$\frac{Y}{R} = \frac{(sK_p + K_i)G_p}{s + (sK_p + K_i)G_p} \quad (3.9-23)$$

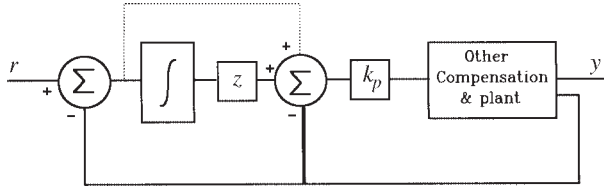


**Figure 3.9-9** PI compensation with no closed-loop zero.

The PI control has introduced a closed-loop zero at  $s = -K_i/K_p$ , and again this may cause an excessive overshoot in the step response. To see what inner-loop feedback can do for us, in Figure 3.9-2 let

$$G_c = K_i/s; \quad H_i = K_f; \quad H = 1$$

so that the closed-loop transfer function becomes

$$\frac{Y}{R} = \frac{K_i G_p}{s + (sK_f + K_i)G_p} \quad (3.9-24)$$

The inner-loop proportional feedback, combined with pure integral control, has the same characteristic equation as PI control but has eliminated the closed-loop PI zero. Another way of looking at this is shown in Figure 3.9-9. The signal fed back to the plant input is unchanged if the PI proportional path (lightly dotted line) is removed and the feedback path shown with the heavy line is added. The overall closed-loop transfer function has changed because the input signal,  $r$ , no longer sees a proportional path. We can also see that the inner-loop feedback would remove the effect of an integration in the plant, and so this modification may reduce the system type. Proportional-plus-derivative control can be interpreted in a similar manner.

A lag compensator is also shown in Table 3.3-1; it has a pole and a zero, with the pole closer to the origin. If the pole is placed very close to the origin, it can be thought of as an approximation to PI compensation, although we usually choose the zero position in a different way from PI compensation. By using the  $s$ -plane vector interpretation of the lag compensator or drawing its Bode plots, we see that it provides a reduction in gain at high frequency (hf) without the  $90^\circ$  asymptotic phase lag. It can be thought of as a way of alleviating stability problems caused by phase lag at hf or of boosting low-frequency (lf) gain relative to hf gain in order to improve the position error coefficient in a type-0 system.

The compensators described above may be used in combination and, for example, two stages of phase-lead compensation can provide more lead than a single stage for the same increase in gain.

## SISO Root-Locus Design

In this subsection we introduce our first classical design technique: *root-locus* design, devised by W. R. Evans in 1948. The root-locus technique provides a

graphical method of plotting the locii of the roots of a polynomial, in the complex plane, when a coefficient in the polynomial is varied. It can be applied directly to the characteristic equation of a closed-loop control system to determine when any poles become lightly damped or unstable and to determine the effects of adding compensator poles and zeros.

Consider the following polynomial equation in the complex variable  $s$ ,

$$s^n + a_{n-1}s^{n-1} + \cdots + a_js^j + \cdots + a_1s + a_0 = 0$$

Suppose that we wish to examine the movement of the roots when the coefficient  $a_j$  is varied. The root-locus rules of construction can be applied by writing the equation as

$$1 + \frac{a_js}{(s^n + \cdots + a_0) - a_js} = 0 \quad (3.9-25)$$

The characteristic equation (3.9-9a) can be written in this form as

$$1 + \frac{K N(s)}{D(s)} = 0, \quad (3.9-26)$$

where the monic polynomials  $N(s)$  and  $D(s)$  contain, respectively, the known open-loop zeros and poles ( $n$  poles and  $m$  zeros) and the static loop sensitivity  $K$  is to be varied.

Equation (3.9-26) is the equation that is satisfied on the locii of the closed-loop poles, that is, on the “branches” of a *root-locus plot*. It can be rewritten as

$$\frac{K N(s)}{D(s)} = -1 \quad (3.9-27)$$

from which we get the “angle condition”

$$\angle N(s) - \angle D(s) = \begin{cases} (2r+1)\pi, & K > 0 \\ r(2\pi), & K < 0 \end{cases} \quad r = 0, \pm 1, \pm 2, \dots \quad (3.9-28)$$

and the “magnitude condition”

$$|K| = \frac{|D(s)|}{|N(s)|} = \frac{\Pi (\text{lengths of vectors from poles})}{\Pi (\text{lengths of vectors from zeros})} \quad (3.9-29)$$

When there are no zeros, the denominator of (3.9-29) is unity. These two conditions are the basis of most of the root-locus rules, which are now enumerated:

1. Number of branches = number of open-loop poles ( $n$ ).
2. The root-locus plot is symmetrical about the  $s$ -plane real axis.

3. For  $K > 0$ , sections of the real axis to the left of an odd number of poles and zeros are part of the locus. When  $K$  is negative, we have the so-called *zero-angle root locus*, which is on the axis to the left of an even number of poles and zeros.
4. The  $n$  branches start (when  $K = 0$ ) at the open-loop poles and end (when  $K = \infty$ ) on the  $m$  open-loop zeros, or at infinity (if  $n > m$ ).
5. Branches that go to infinity approach asymptotes given by

$$\angle \text{asymptotes} = \pm \frac{(2r+1)\pi}{(n-m)}, \quad r = 0, \pm 1, \pm 2, \dots$$

$$\text{real-axis intersection of asymptotes} = \frac{\Sigma(\text{finite poles}) - \Sigma(\text{finite zeros})}{(n-m)}$$

6. If two real-axis branches meet as  $K$  is increased, they will break away to form a complex pair of poles. Similarly, two complex branches may arrive at the same real-axis point and become a real pair. Break-away and arrival points can be found by solving (3.9-27) for  $K$  and then finding the values of  $s$  that satisfy  $\partial K / \partial s = 0$  with  $s$  treated as a real variable.
7. Root-locus branches meet or leave the real axis at  $90^\circ$ .
8. If a “test point” is very close to a complex pole or zero, all of the vectors from the other poles and zeros can be approximated by drawing them to that pole or zero. The angle of the remaining vector, found from the angle condition (3.9-28), gives the angle of departure or arrival of the root-locus branch for the pole or zero in question.
9. Imaginary-axis crossing points can be found by replacing  $s$  by  $j\omega$  in the characteristic equation and solving the separate real and imaginary conditions that result. Alternatively, the root-locus angle condition can be applied or a standard test for stability (e.g., Routh-Hurwitz) can be used.
10. Constant net damping: When the relative degree  $(n - m)$  of the loop transfer function is greater than unity, then, if some branches are moving left, others must be moving right.

Software is available to construct root-locus plots (e.g., MATLAB “rlocus” and “rltool”), but the above rules allow us to anticipate the effects of proposed compensators. We will now illustrate root-locus design by means of some examples.

**Example 3.9-2: Root-Locus Design Using a Lead Compensator** In this example we will show how a phase-lead compensator can stabilize an unstable system, but the compensator will be chosen to illustrate the root-locus rules rather than to produce the “best” control system design. This example can be done more easily using transfer functions, but we wish to develop familiarity with the state-space approach, for later applications.

Let the plant be type 2 with transfer function

$$G(s) = \frac{100}{s^2(s+10)}$$

In yet another technique for obtaining state equations, the transfer function was expanded as a sum of partial fraction terms, and state variables were chosen to be the integrator outputs in the simulation diagram representation of each partial fraction term, as in Section 3.2. The plant  $A$ -,  $B$ -,  $C$ -, and  $D$ -matrices are

$$ap = \begin{bmatrix} 0 & 1 & 0 \\ 0 & 0 & 0 \\ 0 & 0 & -10 \end{bmatrix} \quad bp = \begin{bmatrix} 0 \\ 1 \\ 1 \end{bmatrix} \quad cp = [10 \quad -1 \quad 1] \quad dp = [0]$$

The compensator state-space description is given in Table 3.3-1. Equations (3.9-2) can easily be used to cascade the compensator with the plant, but here we will illustrate the use of the “series” command in a MATLAB program:

```
ap= [ 0 1 0; 0 0 0; 0 0 -10];
bp= [0; 1; 1]; cp= [10 -1 1]; dp= [0];           % Plant
z=.6; p= 9;                                       % Compr. Zero & pole
ac= [-p]; bc= [1]; cc= [z-p]; dc= [1];          % Lead comp.
[a b c d] = series(ac,bc,cc,dc,ap,bp,cp,0);      % Comp. + plant
k= linspace(0,10,2000);
r= rlocus(a,b,c,d,k); plot(r)
grid on
```

The root-locus plot is shown in Figure 3.9-10, with the compensator pole at  $s = -9$  and the zero at  $s = -0.6$ . Without the compensator the two branches from the double

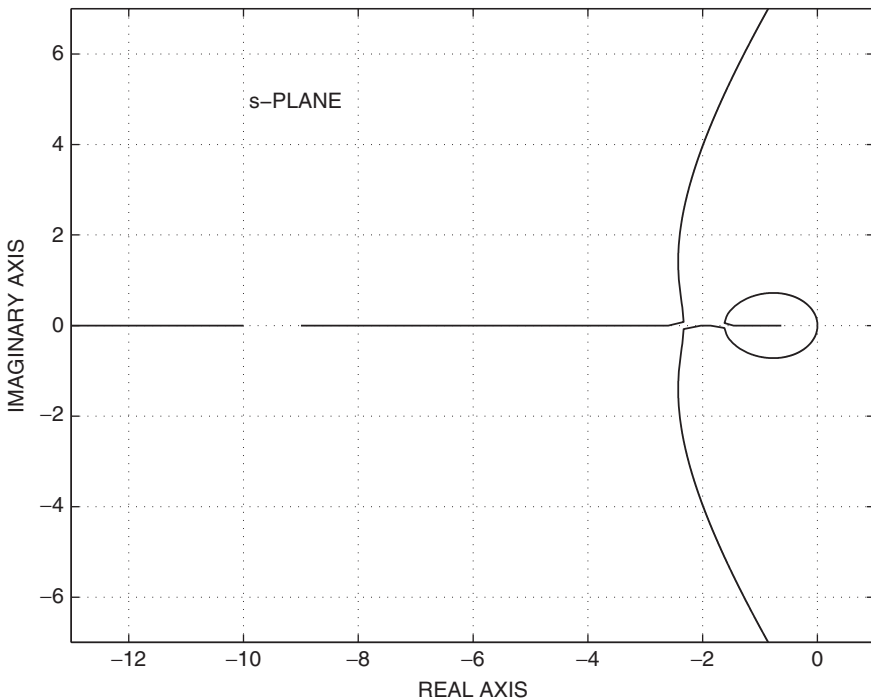


**Figure 3.9-10** Lead compensation on the root-locus plot.

pole at the origin would immediately move into the right-half  $s$ -plane, while the real pole at  $s = -10$  moves left (i.e., constant net damping). The effect of placing the compensator zero near the origin, with its pole well to the left, is strong enough to pull the two branches from the origin into the real axis. The branch that approaches the compensator zero represents a closed-loop pole close to the origin and hence a slow closed-loop mode. The “strength” of this mode (i.e., residue in the pole) will depend on how close the pole gets to the zero, but in a practical design the compensator zero would be placed farther to the left. The other branch from the origin moves left and meets the compensator pole. They break away from the real axis and move toward the right-half plane (i.e., constant net damping again) and approach  $60^\circ$  asymptotes. It is worthwhile to check the root-locus rules, one by one, against this example. All of the rules are illustrated except the “angle-of-departure” rule. ■

This phase-lead example will be repeated as Example 3.9-5, done in the frequency domain, and with more emphasis on practical design considerations. In general, possible root-locus design techniques include placing the compensator zero on or to the left of the second real plant pole from the origin or placing it at the real part of a desired complex pair. The compensator pole position may then be adjusted to give a closed-loop dominant pair a desired frequency or damping. The closed-loop step response should be checked and the design may be modified by moving the pole position or by moving both the pole and zero keeping the ratio  $p/z$  constant.

PI compensator design will be illustrated next by the following root-locus example.

**Example 3.9-3: Root-Locus Design of a PI Compensator** Let the plant and PI compensator transfer functions be

$$G_p = \frac{1}{(s+3)(s+6)} \quad G_c = \frac{K(s+z)}{s}$$

The design goals will be to obtain a dominant complex pole pair with damping ratio of  $1/\sqrt{2}$  together with the highest possible ramp error coefficient. The root-locus plot will show the trade-offs in the design, and a simulation will be used to check that the closed-loop step response is like that of a quadratic lag with  $\zeta = 1/\sqrt{2}$ . A MATLAB program is:

```
z = 2; num= [1 z]; den= [1 9 18 0]; % Choose z
[a,b,c,d]= tf2ss(num,den); % Compr. + Plant
k= linspace(0,50,2000);
r= rlocus(a,b,c,d,k); plot(r), grid on % Root locus

sgrid(.707,0)
axis([-8,1,-8,8])
rlocfind(a,b,c,d) % Find K for zeta=.707

sys1= ss(a,18*b,c,d); % K=18
sys2= feedback(sys1,1,-1); % Close loop
step(sys2,3) % Step response
grid on
```



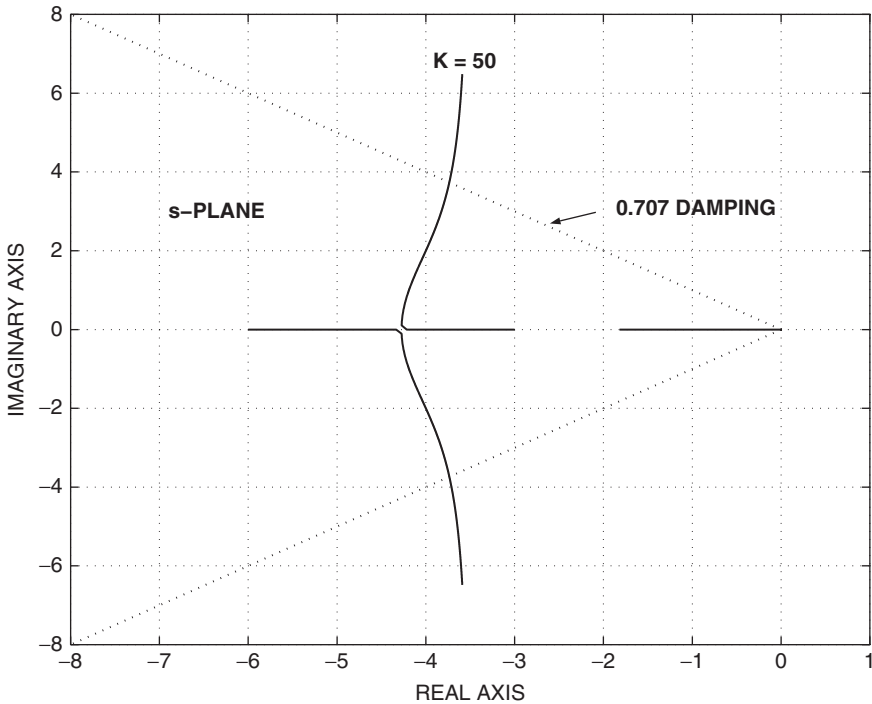


**Figure 3.9-11** PI compensation on the root-locus plot.

Figure 3.9-11 is the root-locus plot with  $z = 2$ . The relative degree of the loop transfer function is 2, and so the asymptotes are at  $90^\circ$  to the real axis. The damping of the complex poles can become very small, but the system can never become unstable. The ramp error coefficient is

$$K_v = \lim_{s \rightarrow 0} sG(s) = \frac{Kz}{(3)(6)}$$

If we make  $z$  small, the error coefficient will be small. In addition, the root-locus plot shows that there will be a slow closed-loop pole trapped near the origin. If we place the PI zero to the left of the plant pole at  $s = -3$ , the complex poles will break away from the axis between  $s = 0$  and  $s = -3$ . This could produce a dominant pair of poles, but they may be too close to the origin for a fast, well-damped response. Therefore, we might try  $1 < z < 4$  while adjusting  $K$  to give a damping ratio  $\zeta = 0.707$  and checking  $K_v$ . When this is done,  $K_v$  is found to peak when  $z = 3$  and  $K = 18$ . The zero then cancels the slowest plant pole and the closed-loop dynamics are second order with the desired damping ratio. The step response is shown in Figure 3.9-12. In general, the best position for the zero should be determined on a case-by-case basis using considerations similar to those above.

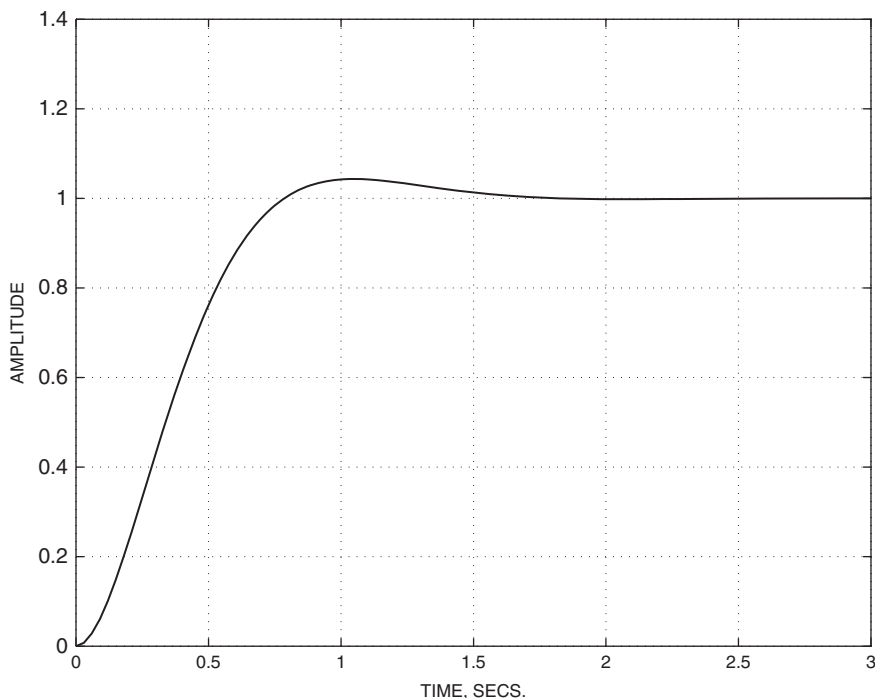


**Figure 3.9-12** Step response with PI compensation. ■

A lag compensator (see Table 3.3-1) can be used to increase the value of a control system error coefficient ( $K_p, K_v, K_a, \dots$ ), without appreciably affecting stability. The lag compensator pole can be placed close to the origin and the lag compensator zero placed not far to the left of the pole. At low frequencies, the compensator gain is given by the length of the zero vector divided by that of the pole vector. Time constants up to about 100 s are practicable, so the pole could be placed at  $s = -0.01$ . Then, placing the zero at  $s = -0.1$  will give a low-frequency gain of 10.0. At high frequency these two pole and zero vectors are close together and have little effect on the dynamics. This technique traps a slow pole near the origin, as was noted in Example 3.9-2. Note that to get greater than unity low-frequency compensator gain, an amplifier is required. An alternative approach to lag compensation is to increase the loop gain as much as possible and solve problems of high-frequency instability by using the lag compensator to cut the high-frequency gain without adding much phase lag. The term *lag compensator* is unfortunate in that, unlike a simple lag transfer function, its ultimate phase lag is zero. This technique is useful in situations where “unmodeled” high-frequency dynamics are causing instability, and trial-and-error compensation is used. Lag compensation is better illustrated in the frequency domain than on the root-locus plot.

In summary, the root-locus technique works well with low-order dynamics and is especially useful as a “back-of-the-envelope” analysis or design technique.

With a large number of poles and zeros it becomes necessary to switch to the frequency-domain techniques illustrated in the next subsection.

## Frequency-Domain Design

In frequency-domain design we plot the frequency response of the loop transfer function and use ideas related to Nyquist, Bode, and Nichols plots (Franklin et al., 2002) to arrive at appropriate parameters for one of the standard compensator transfer functions.

The Nyquist stability test leads to useful analysis and design ideas. Some control loops contain pure delay effects, for example, signal propagation delays in a transmission medium or “transport delays” due to piping, belt-feed devices, and so on. In the aircraft case, we have computational delays in a flight control computer and decision and reaction time delays in the human pilot. A pure delay  $T$  has the transcendental transfer function  $ke^{-sT}$ . This function can easily be plotted in a graphical frequency-response design format but, for root-locus design, it can only be approximated as a rational polynomial function (Franklin et al., 2002). In the case of nonlinear plants, the *describing function* technique allows us to analyze stability and *limit cycle* oscillations by using a movable critical point on the Nyquist plot (West, 1960). Other important Nyquist-related design tools are the *gain* and *phase margins*; these will be illustrated here and applied in Chapter 4.

If the open-loop frequency-response locus passes close to the point  $(-1 + j0)$ , the stability boundary is being approached and the system transient response is likely to be underdamped. The gain margin of a feedback loop is the increase in gain that can be allowed before the loop becomes unstable. It can be calculated by finding the gain at the phase crossover frequency, as illustrated in Figure 3.9-13. The phase margin is the number of degrees by which the phase angle of  $GH$  exceeds  $-180^\circ$  when  $|GH| = 1.0$ . It can be calculated from the gain crossover shown in Figure 3.9-13. As a rule of thumb a phase margin of  $30^\circ$  to  $60^\circ$  will be required to obtain a good closed-loop transient response, and this should be accompanied by a gain margin of 6 to 15 dB. When closing a feedback loop produces only an underdamped complex pair of poles, the closed-loop damping ratio is related to the phase margin by  $\zeta \approx PM^0/100$  for phase margins up to about  $70^\circ$  (Franklin et al., 2002). This relationship also holds approximately if the closed dynamics are dominated by a complex pair.

In classical frequency-domain design, lead, lag, and PI cascade compensators are used, in conjunction with gain and phase margins, to achieve satisfactory closed-loop designs. We will first review the frequency-domain properties of these compensators. Table 3.3-1 shows passive networks that implement lead and lag compensation (see also Section 3.3), and the lead and lag transfer functions can both be written (apart from a gain constant) as

$$G_C(s) = \frac{s+z}{s+p} \quad \begin{array}{l} p > z \equiv \text{lead} \\ p < z \equiv \text{lag} \end{array} \quad (3.9-30)$$

Inspection of this transfer function shows that the hf gain is 1.0 and the lf gain is  $z/p$ , with a phase angle of zero in both cases. The polar plot of  $G_C(j\omega)$  is a semicircle

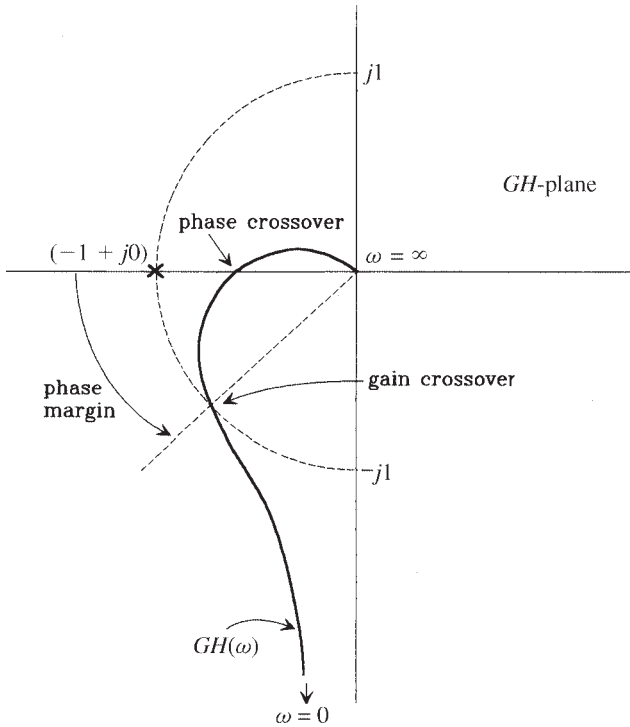


**Figure 3.9-13** Stability margins on the Nyquist plot.

above (lead) or below (lag) the positive real axis, with its diameter determined by the lf and hf gains (Problem 3.9-9). This is shown in Figure 3.9-14 for the lead transfer function. The figure shows that the maximum lead angle  $\phi_M$  and the corresponding gain are given by

$$\sin \phi_M = \frac{1 - z/p}{1 + z/p} \quad (3.9-31a)$$

$$|G(\phi = \phi_M)| = \sqrt{(z/p)} \quad (3.9-31b)$$

For the passive lag compensator this gain must be multiplied by  $p/z$ , giving

$$|G(\phi = \phi_M)| = \sqrt{(p/z)} \quad (\text{lag comp.}) \quad (3.9-31c)$$

The Bode plot shows that the frequency of maximum lead or lag is the geometrical mean of the corner frequencies:

$$\omega_{\phi_M} = \sqrt{(pz)} \quad (3.9-31d)$$

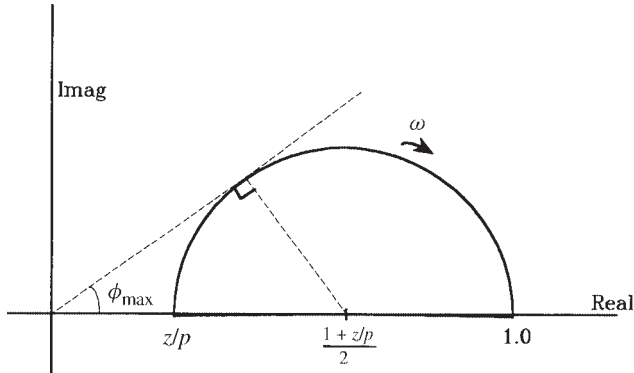


Figure 3.9-14 Lead compensator polar plot.

The design techniques with these compensators are illustrated in the following examples.

**Example 3.9-4: Design of a Passive Lag Compensator** This system has unity feedback, with a loop transfer function

$$G_c(s)G_p(s) = \frac{p_c (s + z_c)}{z_c (s + p_c)} \frac{K}{s(s+1)(s+15)(s+20)},$$

and the closed-loop requirements will be a velocity error coefficient of  $K_v \geq 13$  and a phase margin of  $25^\circ$ .

A loop gain of  $K = 4000$  meets the  $K_v$  requirement. Also, the Bode plot of  $G_p$  shows that the phase angle is  $-150^\circ$  at a frequency  $\omega_1 = 1.25$  rad/s. If the compensated loop transfer function has unit magnitude at this frequency and the compensator produces only about  $5^\circ$  lag, then the phase margin requirement will be satisfied. A passive lag compensator has a gain close to  $p_c/z_c$  and about  $5^\circ$  lag at one decade above the upper corner frequency. Therefore, we now choose the compensator zero to be  $Z_c = 0.1\omega_1 = 0.125$  rad/s. At  $\omega_1$  the magnitude of the plant transfer function is 6.5, and so we require  $p_c/z_c = 1/6.5$ . This gives the compensator pole frequency as  $p_c = 0.125/6.5$ , or about 0.02.

Parts of the following MATLAB code were used to produce the Bode and Nyquist plots shown in Figures 3.9-15a and b and also a step response.

```
den= conv([1 1 0],[1 35 300]); num=[4000];           % Plant
nc= conv([1.125], num);
dc=conv(6.5*[1.02],den);                             % Plant + Compr.
margin(num,den); hold on margin(nc,dc)                % Margins

w= 2*pi*logspace(-.5,1,400);                          % Code for Nyquist Plots
[re,im]=nyquist(num,den,w);                          % Uncompensated
plot(re,im)
```

```

grid on
axis([-4,.5,-1,.4])
hold on
w=2*pi*logspace(-.8,1,400);
[re,im]=nyquist(nc,dc,w);           % Compensated
plot(re,im)

sys=tf(nc,dc);                     % Code for closed loop step
sys2=feedback(sys,1,-1);           % close loop
step(sys2)

```

The Bode plots in Figure 3.9-15a show that, above about 0.1 rad/s, the lag compensator has cut the gain by a constant amount and, at the gain crossover frequency (1.27 rad/s), it adds negligible phase lag. This stabilizes the system, and the compensated phase margin is almost exactly equal to the design value of 25°. The phase lag of the compensator can be seen to be concentrated in the range 0.01 to 0.5 rad/s. The Nyquist plots in Figure 3.9-15b show the unstable uncompensated system and the stable compensated system. Because of the small phase margin, the closed-loop step response is lightly damped (overshoot > 50%), and the design could easily be repeated to increase the phase margin.

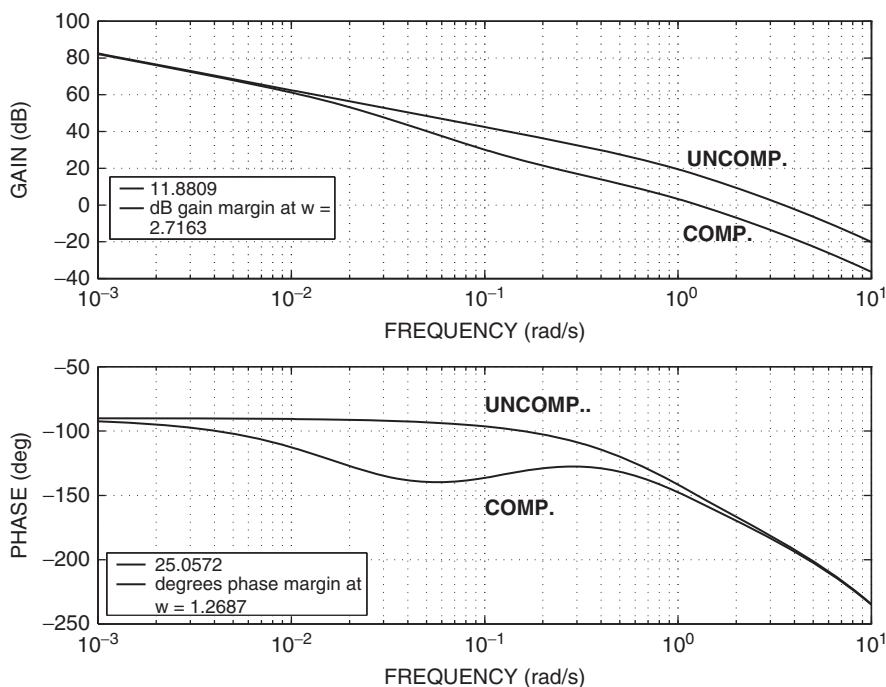


**Figure 3.9-15a** Lag-compensated Bode plots.

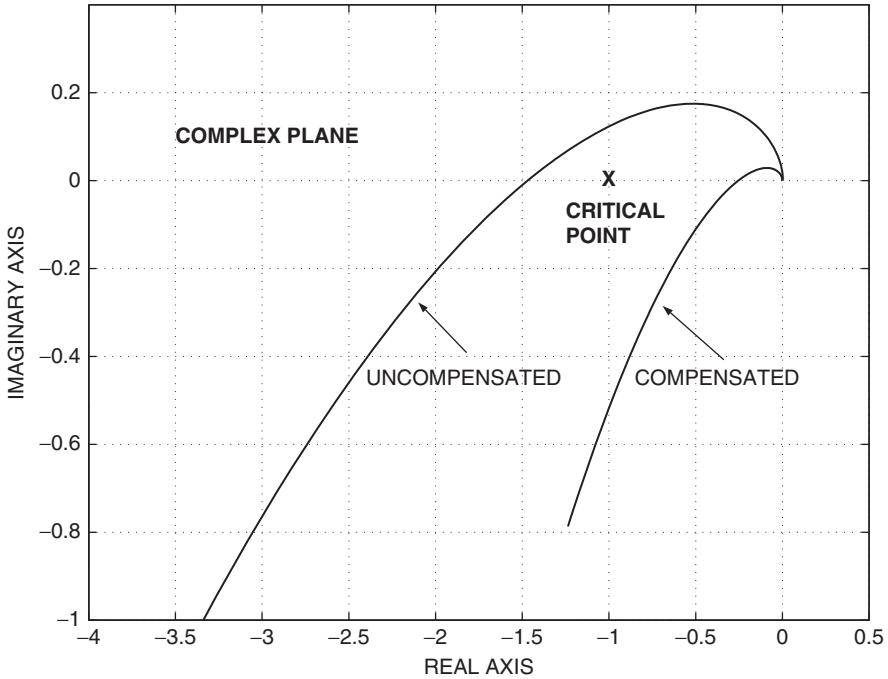


Figure 3.9-15b Lag-compensated Nyquist plot. ■

**Example 3.9-5: Design of a Passive Lead Compensator** In this example we will use a passive lead compensator to stabilize an unstable type-2 system. The design specifications will be to achieve a phase margin of  $45^\circ$  with the highest possible acceleration error coefficient  $K_a$  and a compensator pole-zero ratio not greater than 10. Using the passive lead transfer function from Table 3.3-1, the loop transfer function will be

$$G_c(s)G_p(s) = \frac{(s + z_c)}{(s + p_c)} \frac{K}{s^2(s + 5)}$$

The usual starting point for lead compensator design is to choose the frequency of maximum lead to be equal to the phase margin frequency of the plant. A Bode plot of the plant only, with  $K = 1$ , shows that the phase margin frequency and the phase margin are, respectively,

$$\omega_\phi = 0.45 \text{ rad/s}$$

$$\phi_M = -5.1^\circ \text{ (unstable)}$$

The required compensator phase lead is obtained from the design specification, with an allowance of an extra  $5^\circ$ :

$$\phi_{MAX} = (45^\circ - (-5.1^\circ)) + 5^\circ \approx 55^\circ$$

Therefore, from (3.9-31a), the compensator zero-pole ratio is

$$\frac{z_c}{p_c} = \frac{1 - \sin(\phi_{MAX})}{1 + \sin(\phi_{MAX})} = 10.05$$

By setting

$$\omega_{\phi M} = \omega_{\phi}$$

as noted above, the compensator equation (3.9-31d) gives

$$z_c = \omega_{\phi} \sqrt{z_c/p_c} = 0.142 \text{ rad/s}$$

$$p_c = 10z_c = 1.42 \text{ rad/s}$$

The compensated phase margin can now be checked, and Figure 3.9-16 shows the compensated and uncompensated Bode plots as well as the gain and phase margins. The phase margin is only 42.3° but, if we adjust the compensator to move the peak of the phase curve to the left, it will coincide with the gain crossover and the phase margin will be adequate. It is also evident that the gain margin is bigger than required and, if we raise the loop gain, the phase margin will improve without changing the compensator. For the next design iteration  $K = 3$  was used, and the peak of the phase curve occurred exactly at the gain crossover, with a phase margin of 50° and gain margin of 22.4 dB.

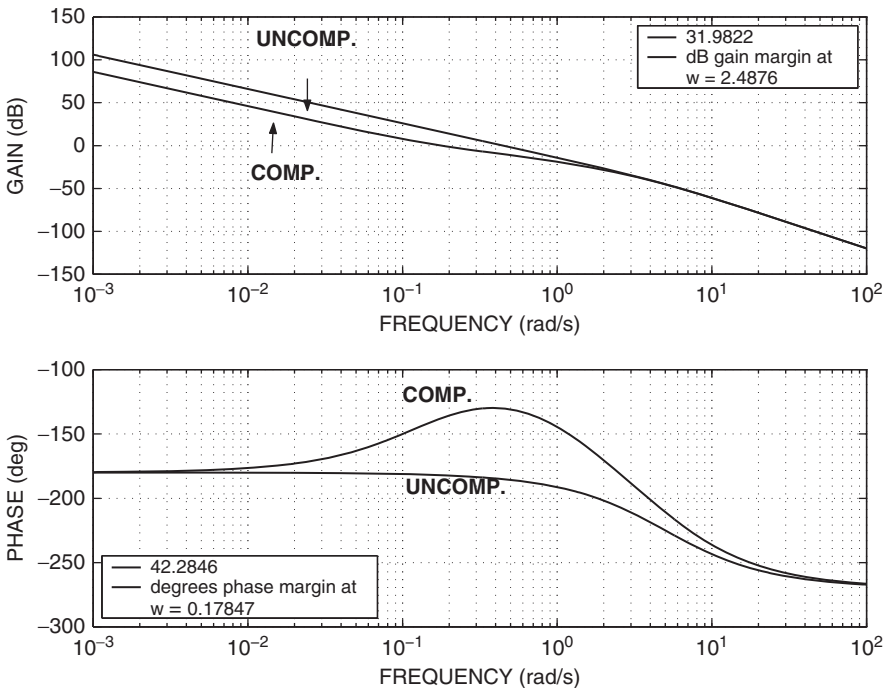


**Figure 3.9-16** Lead-compensated Bode plots.



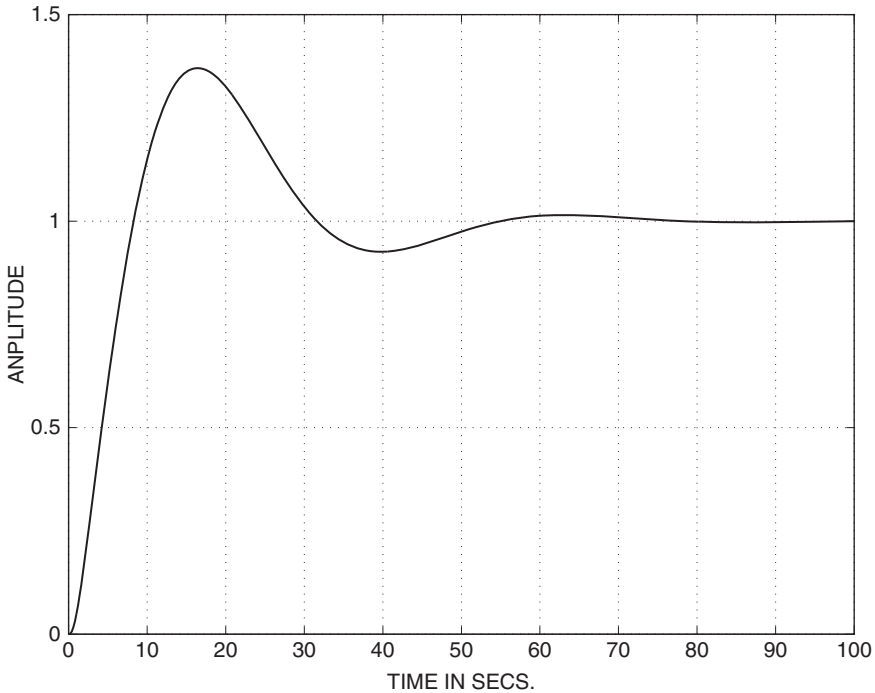


**Figure 3.9-17** Lead-compensated step response.

The phase margin of  $50^\circ$  is greater than required by our specification, and we could either retain  $K = 3$  and retune the compensator using a reduced  $p/z$  ratio or increase  $K$  and retune the compensator using the same  $p/z$  ratio. For example, we can achieve  $\phi_M = 45^\circ$  with  $K = 13$  if we keep  $(p_c/z_c) = 10$  and use  $z_c = 0.31$ . Another consideration is that the acceleration error coefficient is given by

$$K_a = \frac{z_c}{p_c} \frac{K}{5}$$

and should be checked as we trade gain  $K$  with compensator pole-zero ratio. However, even with the generous margins of  $50^\circ$  in phase and 22.4 dB in gain, the step response, plotted in Figure 3.9-17, has a large overshoot. The next example illustrates a way to overcome this problem. ■

In summary, a phase-lead cascade compensator has the effect of increasing closed-loop bandwidth, thereby producing a faster system. It usually provides a moderate increase in error coefficient and an overshoot in the closed-loop step response.

The frequency-domain design techniques that have been illustrated above do not distinguish between transfer functions in the forward path or in the feedback path. If the cascade compensator is in the forward path, its zeros appear as zeros of the closed-loop transfer function. If it is in the feedback path, its poles will appear as

closed-loop zeros. In the above example, the lead compensator zero, close to the origin, caused a large overshoot in the step response. If the same compensator is moved to the feedback path, the resulting closed-loop zero will be much farther to the left and the overshoot will be reduced. This technique has been used in aircraft and missile control systems.

Another technique that can be used to overcome the effect of the closed-loop zero is to cancel it with a pole of the prefilter  $H_r$ . Alternatively, instead of forward-path lead compensation, another compensation technique that similarly speeds up the system response can be used, for example, inner-loop rate feedback.

**Example 3.9-6: Feedback Compensation with a Phase-Lead Network** Here we will use the results of Example 3.9-5 with the lead compensator in the feedback path. To demonstrate the effectiveness of this technique the loop gain has been increased to  $K = 106$  when the phase margin is only  $30^\circ$  (the optimum compensator is now  $z_c = 0.93$ ,  $p_c = 9.3$ ). The compensator dc gain has been increased to unity by multiplying the  $B$ - and  $D$ -matrices by  $p/z$  and, to maintain  $K = 106$ , the plant gain has been reduced by  $z/p$ . The following MATLAB code will generate step, ramp, and parabolic responses:

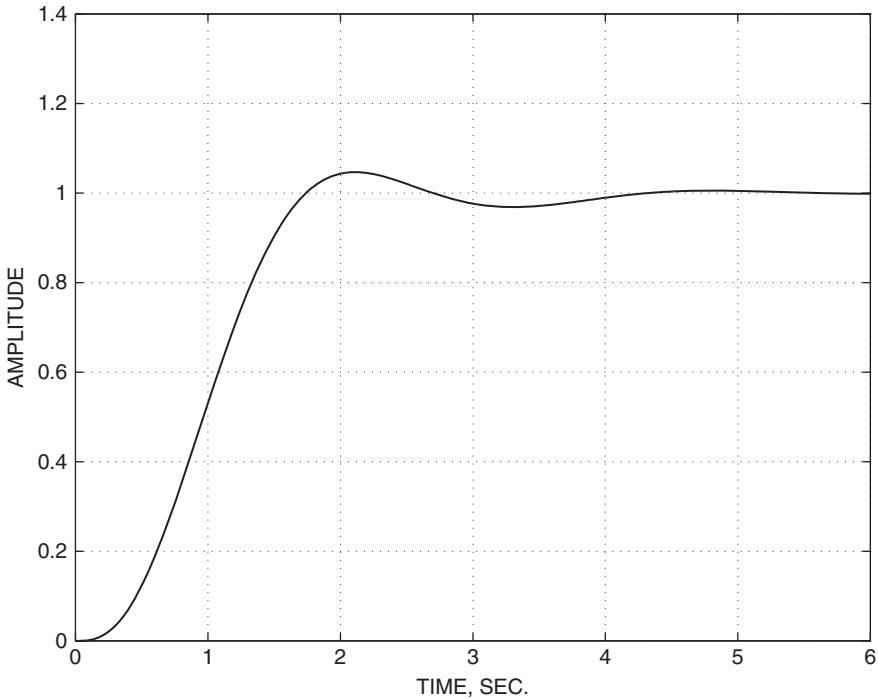
```
ap=[0 1 0; 0 0 1; 0 0 -5];      k=106;                % Plant
bp=[0; 0; k*z/p];  cp=[1 0 0];  dp=[0];
p=9.3;  z=.93;                % Compensator
ac=[-p];  bc=[p/z];  cc=[z-p];  dc=[p/z];
[a,b,c,d]= feedback(ap,bp,cp,dp,ac,bc,cc,dc,-1);    % Close loop
t=[0:.005:6];
u=ones(length(t),1);          % Step Input
%u=t';                        % Ramp Input
%u=[0.5*t.^2]';               % Parabolic Input
[y,x]=lsim(a,b,c,d,u,t);      % Time history
plot(t,y,t,u)
```

Figure 3.9-18 shows the unit-step response. The overshoot is about 5%, compared to 55% when the compensator is in the forward path, and the speed of response is about the same in each case.

When Equation (3.9-17) is applied, with  $q = 2$ , we find

$$\begin{aligned} \text{step input, } n = 0 : \quad & e_{ss} = 0 \\ \text{ramp input, } n = 1 : \quad & e_{ss} = (p/z - 1)/p = 0.968 \\ \text{parabolic input, } n = 2 : \quad & e_{ss} = \infty \end{aligned}$$

These results can be confirmed by simulation using the code given above. Therefore the system has effectively been reduced to a type-1 system. Depending on the design specifications, this may be perfectly acceptable.



**Figure 3.9-18** Step response with feedback lead compensation. ■

### 3.10 SUMMARY

In this chapter we have developed all of the components shown in Figure 3.1-1. Two nonlinear state-space aircraft models have been provided in the form of source code. Programs for trimming, linearization, and time-response simulation have been described, and some source code is given in Appendix B. All of the development has been illustrated with applications to aircraft, so that the reader should be well prepared for aircraft control system design in Chapter 4. Our review of linear systems and feedback control has been limited to theory and techniques that we use in the text. For additional background material, the reader should consult some of the current control theory texts (Kailath, 1980; Kuo, 1987; D’Azzo and Houpis, 1988; Brogan, 1991; Nise, 1995; Dorf and Bishop, 2001; Ogata, 2002; Franklin et al., 2002).

### REFERENCES

- Brogan, W. L. *Modern Control Theory*. 3d ed. Englewood Cliffs, N.J.: Prentice Hall, 1991.
- Brown, R. G., and P. Y. C. Hwang. *Introduction to Random Signals and Applied Kalman Filtering*. 3d ed. New York: Wiley, 1997.

- D'Azzo, J. J., and C. H. Houpis. *Linear Control System Analysis and Design*. 3d ed. New York: McGraw-Hill, 1988.
- Desoer, C. A., and J. D. Schulman. "Zeros and Poles of Matrix Transfer Functions and Their Dynamical Interpretation." *IEEE Transactions on Circuits and Systems* CAS-21 (1974): 3–8.
- DeRusso, P. M., R. J. Roy, and C. M. Close. *State Variables for Engineers*. New York: Wiley, 1965, p. 397.
- Dommasch, D. O., S. S. Sherby, and T. F. Connolly. *Airplane Aerodynamics*. 4th ed. Belmont, Calif.: Pitman, 1967.
- Dorf, R. C., and R. H. Bishop. *Modern Control Systems*. 9th ed. Upper Saddle River, N.J.: Prentice Hall, 2001.
- Emami-Naeini, A., and P. Van Dooren. "Computation of Zeros of Linear Multivariable Systems." *Automatica* 18, no. 4 (1982): 415–430.
- Etkin, B. *Dynamics of Atmospheric Flight*. New York: Wiley, 1972.
- Franklin, G. F., J. D. Powell, and A. Emami Naeini. *Feedback Control of Dynamic Systems*. 4th ed. Upper Saddle River, N.J.: Prentice Hall, 2002.
- Gear, C. W. *Numerical Initial Value Problems in Ordinary Differential Equations*. Englewood Cliffs, N.J.: Prentice Hall, 1971.
- Hamming, R. W. *Numerical Methods for Scientists and Engineers*. New York: McGraw-Hill, 1962.
- Healey, M. "Study of Methods of Computing Transition Matrices." *Proceedings of the IEE* 120, no. 8 (August 1973): 905–912.
- Hindmarsh, A. C. "Large Ordinary Differential Equation Systems and Software." *IEEE Control Systems Magazine* (December 1982): 24–30.
- IMSL. *Library Contents Document*. 8th ed. Houston, Tx.: International Mathematical and Statistical Libraries, 1980.
- Isaacson, E., and H. B. Keller. *Analysis of Numerical Methods*. New York: Wiley, 1966.
- Kailath, T. *Linear Systems*. Englewood Cliffs, N.J.: Prentice Hall, 1980.
- Kuo, B. C. *Automatic Control Systems*. Englewood Cliffs, N.J.: Prentice Hall, 1987.
- Laning, J. H., and R. H. Battin. *Random Processes in Automatic Control*. New York: McGraw-Hill, 1956, Appendix C.
- MacFarlane, A. G. J., and N. Karcianas. "Poles and Zeros of Linear Multivariable Systems, A Survey of the Algebraic, Geometric, and Complex-variable Theory." *International Journal of Control* 24 (1976): 33–74.
- MATLAB User's Guide*. Natick, Mass.: MathWorks, Inc., 1990.
- McRuer, D., I. Ashkenas, and D. Graham. *Aircraft Dynamics and Automatic Control*. Princeton, N.J.: Princeton University Press, 1973.
- MIL-F-8785C*. "U.S. Dept. of Defense Military Specification: Flying Qualities of Piloted Airplanes," November 5, 1980.
- Moler, C., and C. Van Loan. "Nineteen Dubious Ways to Compute the Exponential of a Matrix." *SIAM Review* 20, no. 4 (October 1978): 801–836.
- Nelder, J. A., and R. Mead. "A Simplex Method for Function Minimization." *Computer Journal* 7 (1964): 308–313.
- Nguyen, L. T., et al. "Simulator Study of Stall/Post-Stall Characteristics of a Fighter Airplane with Relaxed Longitudinal Static Stability." *NASA Technical Paper 1538*. Washington, D.C.: NASA, December 1979.

- Nise, N. S. *Control Systems Engineering*. 2d ed. Menlo Park, Calif.: Addison-Wesley, 1995.
- Ogata, K. *System Dynamics*. 3d ed. Upper Saddle River, N.J.: Prentice Hall, 1998.
- *Modern Control Engineering*. 4th ed. Upper Saddle River, N.J.: Prentice Hall, 2002.
- Phillips, E. G. *Functions of a Complex Variable*. 8th ed. Edinburgh: Oliver and Boyd, 1961.
- Press, W. H., B. P. Flannery, S. A. Teukolsky, and W. T. Vetterling. *Numerical Recipes: The Art of Scientific Computing*. New York: Cambridge University Press, 1986.
- Ralston, A. *A First Course in Numerical Analysis*. New York: McGraw-Hill, 1965.
- Shampine, L. F., and M. K. Gordon. *Solution of Ordinary Differential Equations: The Initial Value Problem*. San Francisco: W. H. Freeman, 1975.
- Taylor, J. H., and A. J. Antoniotti. "Linearization Algorithm for Computer-Aided Control Engineering." *IEEE Control Systems Magazine* 13, no. 2 (April 1993): 58–64.
- Van Loan, C. F. "Computing Integrals Involving the Matrix Exponential." *IEEE Transactions on Automatic Control* AC-23, no. 3 (June 1978): 395–404.
- West, J. C. *Analytical Techniques for Nonlinear Control Systems*. London: The English Universities Press, 1960.
- Yuan, S. W. *Foundations of Fluid Mechanics*. Englewood Cliffs, N.J.: Prentice Hall, 1967.
- Zakian, V. "Rational Approximants to the Matrix Exponential." *Electronics Letters* 6, no. 5 (December 10, 1970): 814–815.

## PROBLEMS

### Section 3.2

- 3.2-1** Given the mechanical system in Figure 3.2-1, add another mass,  $m_2$ , at the junction of  $k_2$  and  $d_2$ . Let the mass have negligible friction to ground (other than  $d_2$ ). Find a set of state equations for this system and write out the  $A$ ,  $B$ ,  $C$ ,  $D$  coefficient matrices. The input is  $u$ , and there are two outputs:  $y$  and  $w$ .
- 3.2-2** Repeat Problem 3.2-1 with an additional spring,  $k_3$ , connected from  $m_1$  to ground.
- 3.2-3** For the bridged-T circuit shown in Figure 3.2-2, follow the method given in Example 3.2-2 and find expressions for the rest of the elements of the  $A$ -,  $B$ -,  $C$ -, and  $D$ -matrices.
- 3.2-4** Use the technique from Example 3.2-2 to find a set of state and output equations for the quadratic-lag circuit in Table 3.3-1.
- 3.2-5** Given the differential equation

$$2\ddot{y} + 3\dot{y} + 4y = 4\ddot{u} + 6\dot{u} + u$$

turn it into an integral equation for  $y$ , draw a simulation diagram, assign state variables to the outputs of the integrators, and find a set of coefficient matrices  $A$ ,  $B$ ,  $C$ ,  $D$  for the state equations. Show that your  $A$ - and  $B$ -matrices agree with Equation (3.2-6).

**3.2-6** Apply Equation (3.2-9) to two sample periods and use Simpson's rule to obtain an approximation to the integral. Then obtain a recursion formula for  $x(k)$ .

**3.2-7** Given the  $A$ -matrix

$$A = \begin{bmatrix} 0 & 1 & 0 \\ 0 & 0 & 1 \\ -2 & -4 & -3 \end{bmatrix}$$

find, by hand, the eigenvalues, eigenvectors, and a modal matrix. Use (3.2-12) to find the matrix  $e^{At}$ .

**3.2-8** Use the formula (3.2-18) to find  $e^{At}$ , in its simplest form, for the  $A$ -matrix

$$A = \begin{bmatrix} 0 & 1 \\ -1 & -1 \end{bmatrix}$$

**3.2-9** Use the Laplace transform to solve the following ODE, with  $\alpha$  as a parameter and zero initial conditions. Reduce the solution to its simplest form (i.e., one trigonometric function, not two).

$$\dot{y} + y = \sin(10t + \alpha)U_{-1}(t), \quad 0 \leq \alpha \leq \pi/2$$

Plot a few graphs (e.g., in MATLAB) of the solution, for  $0 \leq t \leq 5$  s, and use these to explain the effect of different values of  $\alpha$ . Suggest a practical situation that this model describes.

**3.2-10 (a)** Put the following ODE into state-space form and solve the state equations by Laplace transform:

$$\ddot{y} + 2\dot{y} + 25y = 10 \sin(\omega_1 t)U_{-1}(t)$$

**(b)** Construct a plot of the amplitude of the particular solution,  $y_p$ , as  $\omega_1$  is varied from 1 to 20 rad/s.

### Section 3.3

**3.3-1** Given the following  $A$ - and  $B$ -matrices, use Cramer's rule to find the transfer function  $X_2(s)/U(s)$ :

$$A = \begin{bmatrix} 1 & 0 & 1 \\ 0 & 0 & 2 \\ -1 & -3 & -2 \end{bmatrix} \quad B = \begin{bmatrix} 0 \\ 1 \\ 1 \end{bmatrix}$$

**3.3-2** Use the Laplace transform to find the step response of the transfer function

$$\frac{s + \alpha}{s^2 + s + 1}$$

with  $\alpha$  as a parameter. Program the answer and obtain plots of the step response for positive and negative  $\alpha$ . Describe the effect of the zero on the system step response.

- 3.3-3** Use the Laplace transform to find the step response of the simple-lead transfer function  $s\tau / (s\tau + 1)$ .
- 3.3-4** Use the Laplace transform to find the unit impulse response of a standard form quadratic-lag transfer function.
- 3.3-5** (a) Show that the Laplace transform of a periodic function  $f(t) \equiv f(t + kT)$ ,  $k = \text{integer}$ , is given by

$$F(s) = \frac{\mathcal{L}[f_1(t)]}{(1 - e^{-Ts})} \quad \text{where } f_1(t) \equiv \begin{cases} f(t) & 0 \leq t \leq T \\ 0, & \text{elsewhere} \end{cases}$$

(b) Sketch the poles and zeros of  $F(s)$ , assuming a set for  $F_1(s)$ .

- 3.3-6** (a) The transfer function of a zero-order hold is given by

$$G(s) = \frac{1 - e^{-Ts}}{s}$$

Explain the effect of the factor  $(1 - e^{-Ts})$  and contrast it with the same factor in Problem 3.3-5.

(b) Sketch all of the poles and zeros of  $G(s)$ .

## Section 3.4

- 3.4-1** Program the second-order ABM formula, Equation (3.4-14), as an M-file. Use it to integrate the Van der Pol equation (Example 3.4-1) and perform an execution speed versus accuracy comparison with the RK4 integration.
- 3.4-2** Simulate the Lorenz equations

$$\begin{aligned}\dot{x} &= 10(y - x) \\ \dot{y} &= (r - z)x - y \\ \dot{z} &= xy - 8z/3\end{aligned}$$

using the format of Example 3.4-1. Choose a set of initial conditions, ( $X^T(0) = [-0.1, 0.1, -0.1], [-1, -1, 100], [0, 5, 75]$  is suggested) and investigate the dynamic behavior for  $0 < r < 170$ . Plot waveforms (time histories) and 2D and 3D phase portraits. Make provision to view only the last several seconds of a phase portrait so that asymptotically stable periodic orbits can be seen.

### Section 3.5

- 3.5-1** (a) Program the transport aircraft model in Section 3.5.  
 (b) Check your model using the data in Table 3.6-1; calculate the weighted sum of squares of the derivatives for each test case.  
 (c) Find, in the textbook, the source of each of the state equations. Show source equation numbers and give any algebraic derivation.
- 3.5-2** (a) Program the F-16 model given in Section 3.5.  
 (b) Make a plot of  $CM(\alpha, \epsilon)$  with “ $\epsilon$ ” as a parameter.  
 (c) Plot  $CZ(\alpha, \beta, \epsilon)$  to best display its 3D nature.  
 (d) Make a driver program for your model in part (a) and obtain the test case results given in Table 3.5-2.

### Section 3.6

- 3.6-1** (a) With the transport aircraft model from Problem 3.5-1, use the TRIM.m program to reproduce the steady-state trim conditions given in Table 3.6-1.  
 (b) Use the trim program to find out how steeply the aircraft (in clean configuration, with  $x_{cg} = 0.25\bar{c}$ ) can climb for a range of speeds from 200 to 500 ft/s at sea level. Compute the rate of climb (ROC) for each speed and determine the speed at which the ROC is a maximum.
- 3.6-2** Devise a trim algorithm or use the program in the Appendix B1 to trim the F-16 model. Duplicate some longitudinal trims from Tables 3.6-2 and 3.6-3.
- 3.6-3** (a) Derive Equation (3.6-3) for the pitch attitude in terms of the flight-path angle.  
 (b) Derive Equation (3.6-5).
- 3.6-4** Modify the trim program used in Problem 3.6-1 to trim the transport aircraft for a prescribed angle of attack by varying  $V_T$ . Derive a trim condition for  $\alpha = 15^\circ$  at 10,000 ft.
- 3.6-5** Use the trim and time-history programs to duplicate the results of Examples 3.6-3 and 3.6-4.

### Section 3.7

- 3.7-1** Given the nonlinear state equations

$$\dot{x}_1 = x_1^3 - x_2^2 + 8$$

$$\dot{x}_2 = x_1 x_2$$

- (a) Find all of the singular (equilibrium) points.  
 (b) Linearize the equations and find the algebraic “A-matrix.”



- (c) Find the numerical  $A$ -matrix and its eigenvalues (by hand) at each singular point and describe the type of perturbed behavior that you would expect near each point.
- 3.7-2** Program the MATLAB linearization algorithm given in Section 3.7 and add a calculation of the  $B$ -matrix. Use this to confirm the results of Example 3.7-1.
- 3.7-3** Write a program to compute the matrices  $E^{-1}A$  and  $E^{-1}B$  for the decoupled longitudinal equations given in Section 2.6 from the stability derivatives. Test it on the transport aircraft model and compare the results with those given in Example 3.7-1.
- 3.7-4** (a) Derive the result given in Equation (3.7-4).  
 (b) Incorporate Equation (3.7-4) in the linearization program and compare its performance with the original algorithm on the transport aircraft model.

### Section 3.8

- 3.8-1** Find and identify the eigenvalues and eigenvectors of the transport aircraft  $A$ -matrix given in Example 3.8-5. Use the modal expansion [Equation (3.2-15)] to determine what variables are chiefly involved in each mode.
- 3.8-2** Run linear and nonlinear time-history simulations of a step throttle input to the transport aircraft model using the data of Example 3.8-5. Compare the various speed and altitude responses and confirm the points made in Example 3.8-5 about the transfer functions.
- 3.8-3** (a) Obtain magnitude and phase Bode plots for the transport aircraft throttle-to-speed transfer function using the data of Example 3.8-5.  
 (b) Repeat part (a) for the throttle-to-altitude transfer function. Explain how the features of the plots match the transfer function factors and identify all asymptotes.
- 3.8-4** (a) Use the transport aircraft dynamics in Example 3.8-5 to find the Bode magnitude and phase plots of the elevator-to-pitch-rate transfer function.  
 (b) Determine a short-period approximation and show it on the same plots as in part (a).  
 (c) Repeat part (a) using the elevator-to-pitch-attitude transfer function and explain the difference between the two sets of graphs.

### Section 3.9

- 3.9-1** (a) A unity-feedback control system has the forward-path transfer function  $G(s) = 18(s + 2) / [s(s + 3)(s + 6)]$ . Calculate, by hand, the steady-state error when the reference input is a unit-ramp function.  
 (b) Confirm the answer to part (a) by means of a simulation and plot.

- 3.9-2** (a) A feedback control system has forward-path SISO transfer functions  $G_1$  followed by  $G_2$  in cascade and a feedback transfer function  $H$ . An additive disturbance  $D(s)$  is injected between  $G_1$  and  $G_2$ . Find the transfer functions from  $D$  to the output  $Y$  and to the error  $(R - Y)$ .
- (b) If  $G_1 = 10/s$ ,  $G_2 = 1/[s(s + 5)]$ , and  $H = 10(s + .9)/(s + 9.0)$ , find the error as a function of time when the disturbance is a unit step.
- (c) If we are free to redistribute the gain in the forward path, how can the error be reduced?
- 3.9-3** (a) A unity-feedback control system has  $G_c = k(s + z)/s$  and  $G_p = 10/[s(s + 10)]$ . Determine the compensator parameters  $k$  and  $z$  to achieve closed-loop poles with  $\zeta = 1/\sqrt{5}$  and the highest possible error constant.
- (b) This system controls the azimuth rotation of a radar antenna. The antenna is tracking a target with a velocity vector  $[2000, 0, 0]^T$  starting from an initial position of  $[-10000, 2000, 0]^T$  at  $t = 0$  (coordinate origin at the radar, right handed with  $x$  and  $y$  in the horizontal plane, and  $y$  pointing to the closest approach point of the target). Use MATLAB “Isim” to obtain a plot of the tracking error as the target goes past the radar. Use a state-space model and calculate an initial-condition vector to avoid a large transient.
- 3.9-4** Repeat Example 3.9-1 and obtain your own Nyquist plot. Calculate, by hand, the value of  $K$  at the stability boundary.
- 3.9-5** (a) A feedback control system has the loop transfer function

$$G(s)H(s) = \frac{K}{(s + 1)(s + 2)(s + 4)}, \quad K > 0$$

Sketch the Nyquist D-contour and the Nyquist plot and label all of the significant corresponding points.

- (b) Solve, by hand, the equation  $\text{Im}[GH(j\omega)] = 0$  to find the value of  $K$  that gives neutral stability.
- 3.9-6** A feedback control system has the loop transfer function

$$G(s)H(s) = \frac{K(s + 6)}{s(s + 4)(s^2 + 4s + 8)}, \quad K > 0$$

- (a) Make a rough sketch of the expected root-locus plot.
- (b) Calculate, by hand, any real-axis breakaway and entry points and the angles and real-axis intersection points of any asymptotes.
- (c) Use any available commercial software to get an accurate root-locus plot.
- 3.9-7** Redesign Example 3.9-2 with root locus to try to get dominant poles with  $\zeta = 1/\sqrt{2}$  and  $p/z$  not greater than 10.

- 3.9-8** Given the loop transfer function  $G(s)H(s) = K(s + 1)/[s(s - 1)]$ , with  $K > 0$ :
- (a) Draw the D-contour and Nyquist plot and identify corresponding points on each.
  - (b) Calculate the value of  $K$  that gives marginal stability.
  - (c) Find the gain and phase margins when  $K = 2$ .
- 3.9-9** (a) Show that the polar plot of the transfer function  $G(s) = (s + z)/(s + p)$  is a semicircle with its diameter on the real axis.
- (b) Derive the expression for the maximum phase lead or phase lag, the frequency at which this occurs, and the gain at this frequency.
  - (c) Sketch the polar plot for the phase-lag case.
- 3.9-10** Design a lead compensator for the unity-feedback control system in Example 3.9-2 [forward-path transfer function  $100/(s^2(s + 10))$ ]. Use a lead compensator with a pole-to-zero ratio of 10. Design for the largest possible loop gain consistent with a gain margin of at least 12 dB and (a) a  $30^\circ$  phase margin and (b) a  $45^\circ$  phase margin. Derive the state equations with the compensator included (as in Example 3.9-2), close the loop with the appropriate gain matrix, and compare the step responses of these two designs.

## CHAPTER 4

---

# AIRCRAFT DYNAMICS AND CLASSICAL CONTROL DESIGN

---

### 4.1 INTRODUCTION

In the previous chapters we have developed mathematical tools, realistic aircraft models, and algorithms for performing flight simulation and flight control design. Before we attempt to use all of these tools, models, and algorithms, we must have a clear idea of their applicability and the rationale and design goals for automatic flight control systems. Some idea of the history of the development of automatic flight controls is helpful in this respect.

#### Historical Perspective

The success of the Wright brothers in achieving the first powered flight in December 1903 has been attributed to both their systematic design approach (they built and used a wind tunnel) and the emphasis they placed on making their aircraft controllable by the pilot rather than inherently stable. However, the difficulties of controlling the early aircraft and the progress toward longer flight times led quickly to the development of an automatic control system. Thus, in 1912 an autopilot was developed by the Sperry Gyroscope Company and tested on a Curtiss flying boat. By 1914 the “Sperry Aeroplane Stabilizer” had reached such a state of development that a public flying demonstration was given in which the mechanic walked along the wing while the pilot raised his hands from the controls.

World War I (1914–1918) provided the impetus for great progress in aircraft design. However, a human pilot was perfectly capable of providing the normal stabilizing and control functions for the aircraft of this era, and the time was not ripe for rapid developments in automatic control. The small-perturbation theory of aircraft

dynamics had been developed (Bryan, 1911), and in the 1920s stability derivatives were measured and calculated and the theory was confirmed by flight tests. Little practical use was made of the theory because even the problem of finding the roots of a quartic equation was difficult at the time. Development of autopilots continued, using gyroscopes as the reference sensor and pneumatic servomechanisms to position the control surfaces. A Sperry autopilot also helped Wiley Post to fly around the world in less than eight days in 1933.

In the late 1930s classical control theory began to develop. The need to design stable telephone repeater amplifiers with closely controlled gain led to the work of Black in “regeneration theory” and to Nyquist’s frequency-domain stability criterion. The same stimuli also led to Bode’s complex-frequency-domain theory for the relationships between gain and phase and his logarithmic plots of gain and phase. World War II (1939–1945) led to further developments in control theory because of the need for radar tracking and the development of servomechanisms for positioning guns and radar antennas. Once again wartime spurred improvements in aircraft design. The large expansion of the speed-altitude envelope and the need to carry and dispose of large payloads led to large variations in the aircraft dynamics, thus creating a need to analyze the dynamic behavior. Larger aircraft required power-booster control surfaces, and developments in hydraulic servomechanisms resulted. Also, the need to fly at night and in bad weather conditions led to developments in radio navigation aids and a need to couple these aids to the autopilot. Thus, in 1947, a U.S. Air Force C-53 made a transatlantic flight, including takeoff and landing, completely under the control of an autopilot.

By the late 1940s the concepts of frequency response and transfer functions had become more generally known and the first analog computers were becoming available. The root-locus technique, published by W. R. Evans in 1948, was a major development in analyzing and designing control systems (it is even more useful in the computer age!). Analyses of the stability and performance of aircraft under automatic control began to be performed more commonly by the aircraft companies. The aircraft altitude-speed envelope was being expanded rapidly by the first jet fighters and by a series of research aircraft (the “x” series in the United States).

The rocket-powered Bell X-1 aircraft made its first flight in January 1946; in October 1947 it achieved supersonic flight, and in August 1949 an altitude of nearly 72,000 ft was reached. The envelope was extended further by the next generation of X-planes, X-1A through X-1D. After reaching Mach 2.44 and 75,000 ft altitude, *inertia coupling* (see Chapter 1 Section Angular Motion and Section Control Augmentation Systems) caused the X-1A to spin around all three axes, almost killing the pilot, Major Charles Yeager. Inertia coupling effects were encountered because these aircraft had the basic form of a modern jet fighter with short stubby wings, most of the mass concentrated along the longitudinal axis, and relatively small tail surfaces for directional stability. Before the problem was fully understood, a number of aircraft of the period suffered inertia coupling effects, sometimes with disastrous results. These included the X-2 and X-3 and the F-100 jet fighter during the course of its production program in 1953.

Many other factors besides inertia coupling contributed to the need for a more analytical approach to aircraft stability and control problems. The changes in aircraft

mass properties, together with the need to reduce the area of the aerodynamic surfaces (for lower drag at high speed), caused changes in the natural modes of the aircraft, so that they were no longer easily controllable by the pilot. In addition, the damping of the natural modes tended to decrease as the altitude limits of the airplanes were expanded; these factors made it more important to predict the frequency and damping of the modes analytically. Also, the expansion of the aircraft speed-altitude envelope meant that much greater variations in the dynamics of the aircraft were encountered.

Power-boosted or fully powered control surfaces were introduced because of the increasing aerodynamic loads associated with greater performance and larger aircraft and because they could eliminate the many hours of flight test needed to balance the control surfaces carefully. Properly balanced control surfaces were previously necessary to provide a suitable feel to the pilot's controls. With power-boosted controls the feel could be modified with springs and bobweights, and with fully powered irreversible controls the feel could be provided completely artificially. Thus, the "handling qualities" of the aircraft could be adjusted to be satisfactory over a very wide envelope. Power-boosted controls also made possible the use of *stability augmentation*, in which signals from angular rate sensors could be fed to the control surface actuators to modify the natural modes of the aircraft. In addition, they facilitated the use of more complex autopilots.

The year 1949 saw the first flight of the de Havilland Comet, the aircraft that essentially defined the modern jet transport aircraft. In the early 1950s the problems of supersonic flight up to Mach 3 and beyond were beginning to be investigated. The Lockheed X-7 unmanned rocket plane was built to provide a testbed for a ramjet engine. During a five-year test program beginning in 1951, it also provided information on high-speed aerodynamics, aerothermodynamics, special fuels, and special materials. Data from programs such as this undoubtedly contributed to the design of aircraft such as the F-104 and the SR-71. The X-15 rocket plane, which first flew in 1959, expanded the envelope for manned flight to beyond Mach 6 and above 300,000 ft. This aircraft was equipped with a Honeywell-designed adaptive control system that provided three-axis stability augmentation and a transition from aerodynamic control to reaction control as the aerodynamic controls became ineffective at high altitude.

In the early 1960s small fighter aircraft were approaching Mach 2 speeds; a French Mirage achieved Mach 2.3, and later an F-4 Phantom made a record-breaking Mach 2.4 flight. In the civil aviation field, this was the time of the Boeing 707 and Douglas DC8 passenger jets and the development of the Aerospatiale-British Aerospace Concorde SST. The digital computer was beginning to have a major impact on engineering, the techniques of numerical analysis assumed greater importance, and this stimulated the growth of modern control theory in the mid-1960s.

A great deal of hypersonic aerodynamics knowledge was gained from the X-15 program and from hypersonic wind tunnel studies in the late 1950s. The X-20 (Dyna-Soar) vehicle, to be built by Boeing under a 1960 contract, was to be a rocket-launched unpowered glider that would gather data to solve the problems of pilot-controlled reentry from orbit. The final design was a unique V-shaped vehicle with a thick wing and upturned wing tips. Although the program was canceled

before completion of the first vehicle, it pioneered the technology for the U.S. space shuttle. Later, the unmanned ASSET (1963–1965) and PRIME (X-23A; 1966–1967) vehicles provided flight data on structures, materials, control systems, and other technologies for maneuvering reentry. This was followed in 1969 and the early 1970s by the X-24 manned, blunt lifting body vehicles. These provided data on the low-speed characteristics of maneuverable reentry vehicles, including stability characteristics, pilot experience for comparison with simulators, man-vehicle interface data, and much control system information.

Because of the digital computer, the 1970s saw great strides in computational fluid dynamics, structural and flutter (structural divergence) analysis, simulation of complex dynamical systems, and the application of guidance and control theory in real-time onboard digital computers. Simulation techniques made possible realistic pilot training on the ground, and the automatic flight control system on board an aircraft allowed the dynamic behavior of an entirely different aircraft to be simulated. Thus, space shuttle pilots trained on a Gulfstream-II aircraft that simulated the feel of the space shuttle.

In the 1970s, flight control technology advances allowed the F-16 aircraft to be designed for “relaxed static stability” and all-electric (full “fly-by-wire”) control. Previous aircraft had used “high-authority” electrical control superimposed on the basic electrohydraulic system (e.g., the F-111) or, as in the case of the Concorde, an electrical system with mechanical backup. The processing of electrical signals for automatic flight control systems was still in analog rather than digital form.

The 1980s saw the flight testing of aircraft with additional aerodynamic control surfaces that provided direct-lift control or direct sideforce control (such as the AFTI F-16 and the Grumman forward-swept wing X-29A aircraft) and with digital flight control systems (e.g., McDonnell F-15E and F-18). The AFTI F-16 aircraft allowed the use of sideforce control through a ventral fin and direct-lift control through the combination of the horizontal tail and wing leading-edge flaps. The *decoupled motions* provided by this control were evaluated for possible use in combat situations. The X-29A research aircraft is unstable in pitch (–35% static margin at low speed) and has three-surface pitch control (canards, wing flaperons, and strake flaps). The flight control system is a triply redundant digital system (three digital processors with “voting” to eliminate a faulty channel) with analog backup for each processor. These aircraft raise interesting multivariable control problems for modern control theory.

The U.S. space shuttle made its first flight in March 1981. There was also a resurgence of interest in hypersonic flight during the 1980s. Single-stage-to-orbit vehicles were studied, including the British HOTOL (horizontal takeoff and landing) unmanned satellite launch vehicle and the U.S. TAV (Trans-Atmospheric Vehicle)—fully reusable rapid-turnaround vehicles for manned reconnaissance, weapon delivery, and delivery of large payloads to orbit. These were followed in the United States by the NASP (National Aerospace Plane) study contracts on a manned single-stage-to-orbit vehicle. Other studies looked at boosted vehicles; these included the French HERMES vehicle (similar to the space shuttle, manned) and a number of U.S. BGVs (boost-glide vehicles).

Many lessons were learned about the control of hypersonic vehicles. The trajectories must be carefully controlled because the frictional heating in the atmosphere can create temperatures of a few thousand degrees Fahrenheit at critical points on the vehicle. A change in flight conditions can cause localized changes in the airflow, from laminar to turbulent flow, and this can lead to a rapid increase in temperature at some point on the surface of the vehicle. Manual control is difficult or not feasible in most flight phases and, if attempted, would limit the performance. The trajectory can be controlled by feedback comparison with a precomputed reference trajectory or with real-time trajectory prediction calculations (as in the case of the space shuttle).

There can be large uncertainties in the aerodynamic coefficients of the hypersonic vehicles, and this complicates the design of the automatic control systems and limits their performance. The control systems must be adapted (gain scheduled, or self-adaptive) in flight to allow for the wide variations in vehicle dynamics over the large flight envelope. If fixed “scheduling” is used, difficulties are encountered in sensing the flight conditions. External probes sensing “air data” (dynamic pressure and Mach) can only be used at low Mach numbers, and the air data must be derived from the navigation system and a stored model of the atmosphere. The real atmosphere can show large, unpredictable variations in density; therefore, the control systems must be designed to tolerate these variations.

The era of true “aerospace” vehicles introduces many new challenges for the control engineer. He or she must now think in terms of guidance and control, algorithms and simulation, and numerical methods and digital implementation. Many relatively new analytical techniques are required, including numerical optimization, analysis of sensitivity and robustness to parameter variations, adaptive techniques, and multi-variable control. Furthermore, the control engineer can no longer work in isolation; many other technologies will be closely integrated into a design, and constraints will be imposed on the designs from a variety of sources (e.g., structural, thermal, propulsion, energy management and performance, and human factors).

## The Need for Automatic Control Systems

The evolution of modern aircraft created a need for power-driven aerodynamic control surfaces and automatic pilot control systems, as described in the preceding subsection. In addition, the widening performance envelope created a need to augment the stability of the aircraft dynamics over some parts of the envelope. This need for stability augmentation is now described in more detail.

Figure 4.1-1 shows the altitude-Mach envelope of a modern high-performance aircraft; the boundaries of this envelope are determined by a number of factors. The low-speed limit is set by the maximum lift that can be generated (the alpha limit in the figure), and the high-speed limit follows a constant dynamic pressure contour (because of structural limits, including temperature). At the higher altitudes the speed becomes limited by the maximum engine thrust (which has fallen off with altitude). The altitude limit imposed on the envelope is where the combination of airframe and engine characteristics can no longer produce a certain minimum rate of climb (this is the “service ceiling”).



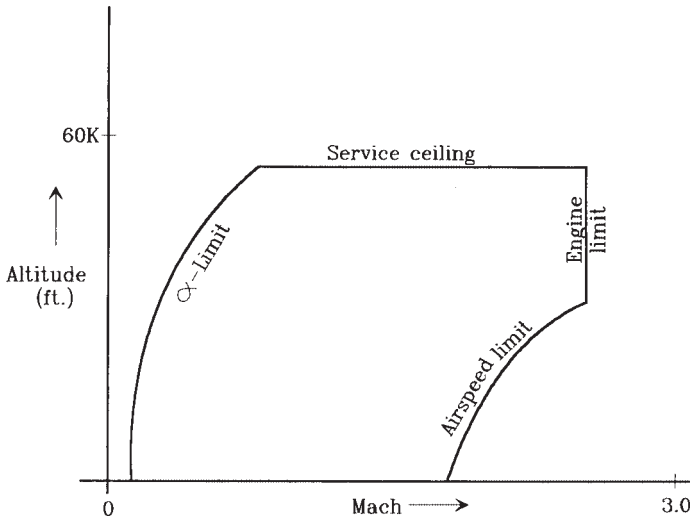


**Figure 4.1-1** Aircraft altitude-Mach envelope.

The aircraft envelope covers a very wide range of dynamic pressure. For example, in the landing phase the dynamic pressure may be as low as 50 psf, whereas at Mach 1.2 at sea level the dynamic pressure is 2150 psf. Large variations in dynamic pressure cause correspondingly large variations in the coefficients of the dynamic equations. Other factors also contribute to changes in the aircraft dynamics. The basic aerodynamic coefficients change with Mach number and as functions of the aerodynamic angles, and the mass properties change with different payloads and changing fuel load.

Because of the large changes in aircraft dynamics, a dynamic mode that is stable and adequately damped in one flight condition may become unstable, or at least inadequately damped, in another flight condition. A lightly damped oscillatory mode may cause a great deal of discomfort to passengers or make it difficult for the pilot to control the trajectory precisely. These problems are overcome by using feedback control to modify the aircraft dynamics. The aircraft motion variables are sensed and used to generate signals that can be fed into the aircraft control surface actuators, thus modifying the dynamic behavior. This feedback must be adjusted according to the flight condition. The adjustment process is called *gain scheduling* because, in its simplest form, it involves only changing the amount of feedback as a function of a “scheduling” variable. These scheduling variables will normally be measured dynamic pressure and/or Mach number.

In the case of low-performance aircraft with relatively narrow envelopes and control surfaces that are not power driven, an unsatisfactory dynamic mode must be corrected by modifying the basic design. As in the case of the high-performance aircraft, this requires an understanding of the dynamic modes and their dependence on the aerodynamic coefficients and aerodynamic derivatives.

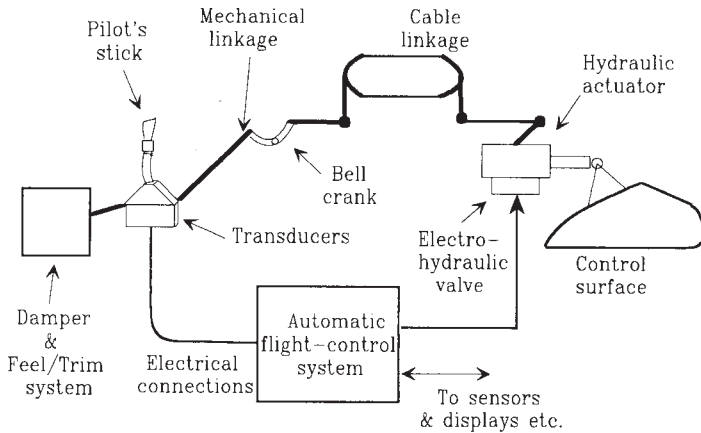


**Figure 4.1-2** An electromechanical control system.

Figure 4.1-2 shows how a fully powered aircraft control system might be implemented with mechanical, hydraulic, and electrical components. Because the control surfaces are fully power driven, there is no force or motion feedback to the pilot's control stick. This is called an *irreversible* control system, and bob weights and springs (or electrical or hydraulic devices) must be added to the control stick to provide some "feel" to the pilot. The stick and rudder pedals are shown linked to the actuators by a combination of mechanical links and bell cranks and control wires. The control surfaces are driven by a hydraulic servomechanism that has a follow-up action; that is, the high-power output shaft is driven until its position corresponds to the position of the low-power input shaft.

Augmentation signals are conveniently added to the system of Figure 4.1-2 by electrical means. The signals from rate gyros (angular rate measuring devices), accelerometers, the air data computer, and other sources are processed by the flight control computer. The electrical output of the flight control computer (converted to analog form) is used to drive electrohydraulic valves, and these superimpose additional motion on the hydromechanical control system.

## The Functions of the Automatic Control Systems

The descriptions and analyses of aircraft modes in Chapters 3 and 4 show that they can be divided into different categories. One category includes modes that involve mainly the rotational degrees of freedom; these are the short-period, roll, and dutch roll modes. Their natural frequencies (or time constants, if purely exponential) are determined by the moments of inertia of the aircraft and the moments generated by the aerodynamic surfaces; their damping is determined by the rate-dependent aerodynamic moments. The remaining modes (phugoid and spiral) involve changes in the flight path and are much slower modes. The phugoid mode involves the translational degrees of freedom and is dependent on the aerodynamic forces of lift and drag and

their variation with speed. The spiral mode depends on aerodynamic moments, but only weak aerodynamic forces are involved.

The responsiveness of an aircraft to maneuvering commands is determined in part by the speed of the rotational modes. The frequencies of these modes tend to be sufficiently high that a pilot would find it difficult or impossible to control the aircraft if the modes were lightly damped or unstable. Therefore, it is necessary to provide automatic control systems to give these modes suitable damping and natural frequencies. Such control systems are known as *stability augmentation systems* (SASs). If the augmentation system is intended to control the mode and to provide the pilot with a particular type of response to the control inputs, it is known as a *control augmentation system* (CAS). An example of this is a normal acceleration CAS, in which the pilot’s inputs are intended to control the acceleration generated along the negative z-axis.

The slow modes (phugoid and spiral) are controllable by a pilot. But since it is undesirable for a pilot to have to pay continuous attention to controlling these modes, an automatic control system is needed to provide “pilot relief.” An *autopilot* is an automatic control system that provides both pilot relief functions and special functions such as automatic landing.

The common types of SAS, CAS, and autopilot functions can be listed as follows:

SAS	CAS	Autopilots
Roll damper	Roll rate	Pitch-attitude hold
Pitch damper	Pitch rate	Altitude hold
Yaw damper	Normal acceleration	Speed/Mach hold
	Lateral/directional	Automatic landing
		Roll angle hold
		Turn coordination
		Heading hold/VOR hold

These control systems are described and illustrated by numerical examples in Sections 4.4 through 4.7.

4.2 AIRCRAFT RIGID-BODY MODES

In this section algebraic expressions for the rigid-body modes will be derived so that their dependence on the stability derivatives and on the flight conditions can be examined and conditions for stability can be deduced. When decoupling of the longitudinal and lateral-directional dynamics occurs (“lat-long” decoupling), it becomes feasible to manipulate the aircraft transformed state equations algebraically. Both the longitudinal and lateral-directional dynamics are still fourth order, so the modes are obtained from the roots of a fourth-order characteristic polynomial. Algebraic solution of a quartic equation is not practicable, but with some simplifying assumptions based on knowledge of the stability derivatives and the physics of flight, this problem can be bypassed.

## Algebraic Derivation of Longitudinal Transfer Functions and Modes

The coefficient matrices for the decoupled longitudinal state equations are given in (2.6-29). The SISO transfer functions can be derived very easily by applying Cramer's rule to the Laplace transformed state equations as follows. The matrix  $(sE - A)$  is given by

$$(sE - A) = \begin{bmatrix} s(V_{T_e} - Z_{\dot{\alpha}}) - Z_{\alpha} & -(V_{T_e} + Z_q) & -Z_V + X_{T_V} \sin(\alpha_e + \alpha_T) & g_D \sin \gamma_e \\ -sM_{\dot{\alpha}} - M_{\alpha} - M_{T_{\alpha}} & s - M_q & -(M_V + M_{T_V}) & 0 \\ -X_{\alpha} & 0 & s - X_V - X_{T_V} \cos(\alpha_e + \alpha_T) & g_D \cos \gamma_e \\ 0 & -1 & 0 & s \end{bmatrix} \quad (4.2-1)$$

and the  $B$ -matrix is

$$B = \begin{bmatrix} Z_{\delta_e} & -X_{\delta_t} \sin(\alpha_e + \alpha_T) \\ M_{\delta_e} & M_{\delta_t} \\ X_{\delta_e} & X_{\delta_t} \cos(\alpha_e + \alpha_T) \\ 0 & 0 \end{bmatrix}$$

If, for example, the  $q/\delta_e$  transfer function is required, the  $\delta_e$  column of  $B$  must be substituted for the  $q$  column of  $|sE - A|$ . The transfer function is

$$\frac{q}{\delta_e} = \frac{1}{|sE - A|} \begin{vmatrix} S(V_{T_e} - Z_{\dot{\alpha}}) - Z_{\alpha} & Z_{\delta_e} & -Z_V + X_{T_V} \sin(\alpha_e + \alpha_T) & g_D \sin \gamma_e \\ -sM_{\dot{\alpha}} - M_{\alpha} - M_{T_{\alpha}} & M_{\delta_e} & -(M_V + M_{T_V}) & 0 \\ -X_{\alpha} & X_{\delta_e} & s - X_V - X_{T_V} \cos(\alpha_e + \alpha_T) & g_D \cos \gamma_e \\ 0 & 0 & 0 & s \end{vmatrix} \quad (4.2-2)$$

It is evident from inspection of the determinant that this transfer function is of the form

$$\frac{q(s)}{\delta_e(s)} = \frac{s(b_2 s^2 + b_1 s + b_0)}{a_4 s^4 + a_3 s^3 + a_2 s^2 + a_1 s + a_0} \quad (4.2-3)$$

Expressions for the numerator and denominator coefficients can be derived in a straightforward way by expanding the determinants. However, the coefficients are complicated functions of the dimensional derivatives and are tedious to evaluate without a digital computer. This is a feasible method of deriving transfer functions from the stability derivatives, but it relies on lat-long decoupling and provides very little insight. We will now examine various approximations that lead to transfer functions that are simple enough to provide some insight into the dynamic behavior.

Consider the decoupled longitudinal dynamics; a time-history simulation in Section 3.6 showed that it was possible to excite separately the short-period and phugoid modes. In the phugoid case speed and theta varied, with alpha and  $q$  almost constant; while in the short-period case alpha,  $q$ , and theta varied, with speed

constant. This implies additional decoupling in the dynamic equations that will now be investigated.

Returning to the longitudinal coefficient matrices (2.6-29), with state and control vectors

$$x = [\alpha \ q \ v_T \ \theta]^T \quad u = [\delta_e \ \delta_t]^T \quad (4.2-4)$$

partition the state equations as

$$\begin{bmatrix} E_1 & 0 \\ 0 & I \end{bmatrix} \dot{x} = \begin{bmatrix} A_{11} & A_{12} \\ A_{21} & A_{22} \end{bmatrix} x + \begin{bmatrix} B_{11} & B_{12} \\ B_{21} & B_{22} \end{bmatrix} u, \quad (4.2-5)$$

with  $E_1(2 \times 2)$ ,  $A_{ij}(2 \times 2)$ , and  $B_{ij}(2 \times 1)$ . Now if it is to be possible for  $v_T$  and  $\theta$  to vary, without significant changes in  $\alpha$  and  $q$ , the submatrix  $A_{12}$  must introduce very little coupling from the second set of equations into the first. An examination of the appropriate terms of the matrix  $E^{-1}A$  in Example 3.7-2 shows that this is the case in that particular example. More generally, the  $a_{14}$  term is null when the flight-path angle is zero, and  $a_{24}$  is identically zero. The  $a_{23}$  term is insignificant when the tuck derivative and the thrust derivative  $M_{T_V}$  are negligible. The tuck derivative is negligible at low Mach numbers, and the thrust derivative is often negligible because the thrust vector passes close to the cg. When the  $a_{13}$  term is expanded in terms of dimensionless derivatives, components due to  $2g_D/V_{T_e}$ ,  $C_{L_V}$ , and  $C_{T_V}$  are found. The gravity term is small at normal airspeeds, and the variation of lift coefficient with airspeed is negligible at low Mach numbers. The thrust derivative depends on the type of propulsion, but it is found to be multiplied by  $\sin(\alpha_e + \alpha_T)$  and is then usually small under normal flight conditions. In summary, the conditions for decoupling in the  $A$ -matrix include small flight path angle, small angle of attack, and low Mach number.

If the control stick is held fixed and there are no feedback control systems operating, the input  $u$  is null and we can ignore the  $B$ -matrix. The eigenvalues of the  $A$ -matrix then yield *stick-fixed modes* of the aircraft. Here we will look for decoupling in the  $B$ -matrix and find a transfer function for the decoupled equations. The  $B_{12}$  block in (4.2-5) includes the variation of the thrust and pitching moment coefficients with throttle changes. The thrust coefficient term is multiplied by  $\sin(\alpha_e + \alpha_T)$  and may often be neglected; the pitching moment term is negligible when the thrust vector passes close to the cm.

We will now neglect the  $A_{12}$  and  $B_{12}$  terms in (4.2-5) and extract the alpha and pitch-rate equations from the complete dynamics to obtain a short-period transfer function.

## The Short-Period Approximation

The short-period approximation obtained from (4.2-5) is

$$\begin{bmatrix} V_{T_e} - Z_{\dot{\alpha}} & 0 \\ -M_{\dot{\alpha}} & 1 \end{bmatrix} \begin{bmatrix} \dot{\alpha} \\ \dot{q} \end{bmatrix} = \begin{bmatrix} Z_{\alpha} & V_{T_e} + Z_q \\ M_{\alpha} & M_q \end{bmatrix} \begin{bmatrix} \alpha \\ q \end{bmatrix} + \begin{bmatrix} Z_{\delta_e} \\ M_{\delta_e} \end{bmatrix} \delta_e, \quad (4.2-6)$$

where, for compactness,  $M_\alpha$  will be assumed to include  $M_{T_e}$ . The transfer function matrix is given by

$$C(sE - A)^{-1}B = \frac{C}{\Delta_{sp}} \begin{bmatrix} (s - M_q) Z_{\delta e} + (V_{T_e} + Z_q) M_{\delta e} \\ (s M_{\dot{\alpha}} + M_\alpha) Z_{\delta e} + [s(V_{T_e} - Z_{\dot{\alpha}}) - Z_\alpha] M_{\delta e} \end{bmatrix},$$

where  $C$  is the appropriate coupling matrix for  $\alpha$  or  $q$  and  $\Delta_{sp}$  is the short-period characteristic polynomial:

$$\begin{aligned} \Delta_{sp} = & (V_{T_e} - Z_{\dot{\alpha}})s^2 - [Z_\alpha + (V_{T_e} - Z_{\dot{\alpha}})M_q + (V_{T_e} + Z_q)M_{\dot{\alpha}}]s \\ & + M_q Z_\alpha - (V_{T_e} + Z_q)M_\alpha \end{aligned} \quad (4.2-7)$$

The individual transfer functions are

$$\frac{\alpha}{\delta_e} = \frac{Z_{\delta e}s + (V_{T_e} + Z_q)M_{\delta e} - M_q Z_{\delta e}}{\Delta_{sp}} \quad (4.2-8)$$

$$\frac{q}{\delta_e} = \frac{[(V_{T_e} - Z_{\dot{\alpha}})M_{\delta e} + Z_{\delta e}M_{\dot{\alpha}}]s + M_\alpha Z_{\delta e} - Z_\alpha M_{\delta e}}{\Delta_{sp}} \quad (4.2-9)$$

The short-period mode is normally complex, so comparing the denominator with the quadratic standard form (3.3-16) gives

$$\omega_{n_{sp}}^2 = \frac{M_q Z_\alpha - M_\alpha (V_{T_e} + Z_q)}{V_{T_e} - Z_{\dot{\alpha}}} \quad (4.2-10a)$$

$$-2\zeta_{sp}\omega_{n_{sp}} = M_q + \frac{M_{\dot{\alpha}}(V_{T_e} + Z_q) + Z_\alpha}{V_{T_e} - Z_{\dot{\alpha}}} \quad (4.2-10b)$$

The derivatives  $Z_q$  and  $Z_{\dot{\alpha}}$  are normally small compared to  $V_{T_e}$  and will be dropped from these equations. Then, when the dimensionless derivatives are substituted and the approximation  $C_D \ll C_{L_\alpha}$  is used, the results are

$$\omega_{n_{sp}}^2 = \frac{\bar{q}S\bar{c}}{J_y} \left[ -C_{m_\alpha} - \frac{\rho S\bar{c}}{4m} C_{m_q} C_{L_\alpha} \right] \quad (4.2-11)$$

$$\zeta_{sp} = \frac{1}{4\sqrt{2}} \left[ \frac{(\rho S\bar{c})\bar{c}^2}{J_y} \right]^{1/2} \frac{\left[ -C_{m_q} - C_{m_{\dot{\alpha}}} + \frac{2J_y}{m\bar{c}^2} C_{L_\alpha} \right]}{\left[ -C_{m_\alpha} - \frac{\rho S\bar{c}}{4m} C_{m_q} C_{L_\alpha} \right]^{1/2}} \quad (4.2-12)$$

In both equations the term  $\rho S\bar{c}/4m$  is a mass ratio, typically on the order of 0.001 and decreasing with altitude. However,  $C_{m_q} C_{L_\alpha}$  may be quite large and so, compared to  $C_{m_\alpha}$ , we may not be able to neglect this term. In the natural frequency formula these terms are multiplied by dynamic pressure so, without any assumptions about

the mass ratio term, we can say that the natural frequency is directly proportional to airspeed and tends to decrease with air density (i.e., with altitude).

The inertia ratio  $2J_Y/m\bar{c}^2$  that occurs in the damping formula is equal to twice the square of the quantity: pitching radius of gyration over mean chord, which may be around unity. Therefore, it is difficult to say anything about a dominant term in the numerator, though we do expect the pitch damping derivative to be important. The inertia ratio  $(\rho S \bar{c}) \bar{c}^2 / J_Y$  will cause the damping ratio to *decrease as the square root of the air density* (unless the pitch stiffness is near zero, so that the density term in the denominator cancels this effect).

It must be emphasized again that the above results are only valid at low Mach numbers where the stability derivatives are reasonably constant. Also, the above analysis assumed a damped, oscillatory short-period mode; different behavior will be illustrated later.

## The Phugoid Approximation

Approximations for the natural frequency and damping of the phugoid mode will be developed by extending the approach used to derive the short-period results. Refer again to (4.2-5) and assume that only the phugoid mode has been excited. If the derivatives  $\dot{\alpha}$  and  $\dot{q}$  are then neglected, the first pair of equations reduce to algebraic equations that act as a constraint on the remaining differential equations in the phugoid variables. Therefore, we have

$$\begin{aligned} 0 &= A_{11} \begin{bmatrix} \alpha \\ q \end{bmatrix} + A_{12} \begin{bmatrix} v_T \\ \theta \end{bmatrix} \\ \begin{bmatrix} \dot{v}_T \\ \dot{\theta} \end{bmatrix} &= A_{21} \begin{bmatrix} \alpha \\ q \end{bmatrix} + A_{22} \begin{bmatrix} v_T \\ \theta \end{bmatrix} \end{aligned}$$

When the algebraic equations are used to eliminate  $\alpha$  and  $q$  from the differential equations, the following equations for the phugoid variables are obtained:

$$\begin{bmatrix} \dot{v}_T \\ \dot{\theta} \end{bmatrix} = (A_{22} - A_{21}A_{11}^{-1}A_{12}) \begin{bmatrix} v_T \\ \theta \end{bmatrix} \quad (4.2-13)$$

In order to evaluate the coefficient matrix, we will make the usual assumption that  $\gamma_e = 0$ . This greatly simplifies the derivation, but as we will see later,  $\gamma$  has a significant effect on the phugoid mode. Equation (4.2-13) now becomes

$$\begin{bmatrix} \dot{v}_T \\ \dot{\theta} \end{bmatrix} = \begin{bmatrix} X'_V - \frac{X_\alpha [M_q(Z_V - X_{TV} \sin(\alpha_e + \alpha_T)) - (V_{Te} + Z_q)(M_V + M_{TV})]}{\Delta_p} & -g_D \\ \frac{M_\alpha(Z_V - X_{TV} \sin(\alpha_e + \alpha_T)) - Z_\alpha(M_V + M_{TV})}{\Delta_p} & 0 \end{bmatrix} \begin{bmatrix} v_T \\ \theta \end{bmatrix} \quad (4.2-14)$$

where

$$X'_V = X_V + X_{T_V} \cos(\alpha_e + \alpha_T)$$

$$\Delta_p = M_q Z_\alpha - M_\alpha (V_{T_e} + Z_q)$$

The characteristic equation can now be found from  $|sI - A|$ , and a comparison with the quadratic standard form gives the following expressions for the phugoid natural frequency and damping:

$$\omega_{np}^2 = g_D \frac{M_\alpha (Z_V - X_{T_V} \sin(\alpha_e + \alpha_T)) - Z_\alpha (M_V + M_{T_V})}{M_q Z_\alpha - M_\alpha (V_{T_e} + Z_q)} \quad (4.2-15a)$$

$$2\zeta_p \omega_{np} = -X'_V + \frac{X_\alpha [M_q (Z_V - X_{T_V} \sin(\alpha_e + \alpha_T)) - (V_{T_e} + Z_q)(M_V + M_{T_V})]}{M_q Z_\alpha - M_\alpha (V_{T_e} + Z_q)} \quad (4.2-15b)$$

These expressions are considerably more complicated than those for the short-period mode; nevertheless, some conclusions can be drawn from them.

Consider the expression for the phugoid frequency, and for simplicity neglect the thrust derivatives and  $Z_q$ . Then insert dimensionless derivatives, with  $C_{m_e} = 0$  and  $C_{D_e} \ll C_{L_\alpha}$ ; the result is

$$\omega_{np}^2 = \frac{2g_D}{\bar{c}} \frac{C_{m_\alpha} (2C_{L_e} + C_{L_V}) - C_{L_\alpha} C_{m_V}}{C_{m_q} C_{L_\alpha} + \frac{4m}{\rho S \bar{c}} C_{m_\alpha}} \quad (4.2-16)$$

This is the equation that will be used to calculate the phugoid frequency, but the variation with flight conditions can be illustrated as follows. The numerator contains the compressibility effects  $C_{L_V}$  and  $C_{m_V}$  and the equilibrium lift  $C_{L_e}$ . The denominator is the same as the square-bracket term in the short-period equation (4.2-11), except that the whole expression is now multiplied by  $4m/(\rho S \bar{c})$ , ( $\approx 10^3$ ). If the mass ratio times pitch stiffness does dominate the denominator, and if we also neglect the compressibility terms in the numerator, we get a very simple expression for the phugoid frequency:

$$\omega_{np}^2 \approx \frac{2g_D}{\bar{c}} \frac{\rho S \bar{c}}{4m} (2C_{L_e}) = \frac{2g_D^2}{V_{T_e}^2} \frac{\bar{q} S C_{L_e}}{mg_D} \quad (4.2-17a)$$

In level flight, with a small angle of attack, the lift is approximately equal to the weight, and this equation reduces to

$$\omega_{np} \approx \frac{g_D}{V_T} \sqrt{2} \quad (4.2-17b)$$

Therefore, phugoid frequency is inversely proportional to airspeed, other things being equal. For a given speed, at higher altitude,  $\alpha$  will be bigger and so the thrust will



provide a larger component of the total vertical force, and a smaller aerodynamic lift component will be needed. Therefore, according to (4.2-17a), the frequency will be lower at higher altitude. The result given in Equation (4.2-17b) was found by F. W. Lanchester in 1908 and can be derived for large-amplitude motion from energy considerations.

It is more difficult to derive simple expressions for the damping of the phugoid and, furthermore, in the next subsection, the damping equation (4.2-15b) is shown to be quite inaccurate. Nevertheless it is still worthwhile to examine this equation to understand what factors influence the phugoid damping. The second term in the equation is often much smaller than the first, and analyzing only the first term gives

$$2\zeta_p\omega_{n_p} \approx -[X_V + X_{T_V} \cos(\alpha_e + \alpha_T)]$$

The dimensional derivatives on the right-hand side contain the equilibrium values of drag and thrust, and we will substitute the steady-state condition (2.4-1a) for these quantities, thus

$$2\zeta_p\omega_{n_p} \approx \frac{-2g_D \sin \gamma_e}{V_{T_e}} + \frac{\bar{q}S}{mV_{T_e}}[C_{D_V} - C_{T_V} \cos(\alpha_e + \alpha_T)]$$

Now consider the level flight case; use (4.2-17a) to substitute for  $\omega_{n_p}$  and equate lift to weight,

$$\zeta_p = \frac{1}{2\sqrt{2}} \frac{[C_{D_V} - C_{T_V} \cos(\alpha_e + \alpha_T)]}{C_{L_e}} \quad (4.2-18)$$

The phugoid mode involves changes in speed, and this equation shows that the damping depends on the changes in drag and thrust with speed. The speed damping derivative  $C_{D_V}$  is small until the transonic drag rise begins and then usually negative in the supersonic regime. Therefore, (4.2-18) indicates the possibility of an unstable phugoid (negative damping) in the supersonic regime, depending on the way in which thrust varies with Mach. Roskam (1979) provides (approximate) comparative analyses of the derivative  $C_{T_V}$  for jets, propeller aircraft, rocket aircraft, and unpowered aircraft. However, we should remember that even Equation (4.2-15b) does not necessarily give very accurate results for the phugoid damping. More accurate numerical results given in the next subsection show that at subsonic speeds *the phugoid damping ratio increases with airspeed and decreases with altitude*. Example 4.2-2 shows, in addition, that the damping decreases rapidly with flight-path angle.

### Accuracy of the Short-Period and Phugoid Approximations

The short-period approximation almost always gives a good approximation for the  $\alpha$  and  $q$  response to elevator inputs with constant throttle setting, and it will play an important role in the numerical designs in this chapter. The phugoid approximation usually gives good accuracy for the period of the phugoid oscillation but not for the damping ratio. These facts are borne out by the transport aircraft model.

The dimensional-derivative evaluation program used in Example 3.7-1 was extended to calculate the short-period and phugoid properties from (4.2-7) and (4.2-14), respectively. Thus, the characteristic roots (or the frequencies and damping ratios) could be calculated for the transport aircraft from any given set of steady-state flight conditions. The program also calculated the matrix  $E^{-1}A$  (as used in Example 3.7-1) so that “exact” dynamic modes could be obtained from this matrix using an eigenvalue program. The flight conditions were level flight at sea level, with different airspeeds and cg positions. Table 4.2-1 shows the results of these calculations. An asterisk in the table indicates characteristic roots instead of period and damping ratio.

The first three sets of entries show the effect of varying airspeed; the last four sets show the effect of moving the cg position further aft with speed held constant. The short-period approximation is seen to be a very good approximation for the first five cases. The phugoid approximation gives accurate results for the period; the damping ratio is quite inaccurate but the accuracy appears to improve when the period is large. Note that the phugoid mode is unstable at low airspeed (200 ft/s).

When the cg is moved aft, the short-period roots move onto the real axis, and then one real root moves toward the phugoid roots. The short-period and phugoid approximations break down and one real root moves into the right-half plane. At the same time a new oscillatory mode appears that has a phugoid-like period with a short-period damping ratio. This mode is sometimes known as the *third oscillatory mode*, and it is characteristic of a statically unstable airplane. Also, the fact that one real root becomes unstable signals an exponential instability in pitch (a pitch “departure”) rather than an oscillatory instability. This is the kind of instability that might be intuitively associated with the loss of positive pitch stiffness.

**TABLE 4.2-1 Accuracy of Short-Period and Phugoid Formulas**

Airspeed/cg		Calculation	$T_{SP}$	$\zeta_{SP}$	$T_p$	$\zeta_p$
200,	0.25	Approximate	7.44	0.555	32.3	0.102
		Exact	7.33	0.565	32.7	-0.0129
400,	0.25	Approximate	3.73	0.551	63.5	0.064
		Exact	3.72	0.551	63.6	0.035
600,	0.25	Approximate	2.48	0.551	96.5	0.112
		Exact	2.48	0.551	96.6	0.099
400,	0.30	Approximate	4.04	0.598	65.4	0.067
		Exact	4.04	0.524	65.5	0.033
400,	0.40	Approximate	5.04	0.744	74.1	0.083
		Exact	5.02	0.652	74.3	0.036
400,	0.50	Approximate	(-0.523, -1.33)*		476	0.691
		Exact	(-0.810 $\pm j0.200$ )*		476	0.630
400,	0.55	Approximate	(-1.70, -0.158, -0.158, 0.128)*			
		Exact	(-1.44, 0.100, -0.150 $\pm j0.123$ )*			

In the example, the stability boundary for the aft-cg location occurs when the cg lies between  $0.501 \bar{c}$  and  $0.502 \bar{c}$ . It is evident that the characteristic equation of the short-period approximation cannot be used as an accurate means of calculating this cg position. However, the condition for a single real root to move into the right-half plane can be derived quite easily from the complete longitudinal dynamics, as we now show.

## Pitch Stability

Sections 2.2 and 2.4 described the concept of positive pitch stiffness and pointed out that positive stiffness was not sufficient to guarantee stability of the longitudinal motion. The stability of the longitudinal motion will now be investigated by means of a dynamic analysis.

The characteristic polynomial of the decoupled longitudinal dynamics can be obtained from the determinant  $|sE - A|$ , with the  $E$ - and  $A$ -matrices as given in (2.6-29). The constant term in the characteristic polynomial is equal to the product of the roots, and therefore the constant term will vanish when a real root reaches the origin, as the pitch-stability limit is reached. This constant term is obtained by putting  $s = 0$  in  $|sE - A|$ , and therefore the stability boundary is given by  $|A| = 0$ . If the determinant obtained from (2.6-29) is expanded about the (4, 2) element, with  $\gamma_e = 0$ , the result is

$$\begin{aligned} 0 = |A| &= \begin{vmatrix} Z_\alpha Z_V - X_{TV} \sin(\alpha_e + \alpha_T) & 0 \\ M_\alpha + M_{T_\alpha} M_V + M_{TV} & 0 \\ X_\alpha X_V + X_{TV} \cos(\alpha_e + \alpha_T) & -g_D \end{vmatrix} \\ &= -g_D \begin{vmatrix} Z_\alpha Z_V & -X_{TV} \sin(\alpha_e + \alpha_T) \\ M_\alpha + M_{T_\alpha} & M_V + M_{TV} \end{vmatrix} \end{aligned}$$

or

$$Z_\alpha(M_V + M_{TV}) - (M_\alpha + M_{T_\alpha})(Z_V - X_{TV} \sin(\alpha_e + \alpha_T)) = 0$$

When the dimensionless derivatives are substituted into this equation, the factors  $(\bar{q}S/m)$ ,  $(\bar{q}S\bar{c}/J_y)$ , and  $(1/V_{T_e})$  are removed, and the equilibrium condition  $(C_{M_e} + C_{M_{T_e}}) = 0$  is applied, the stability boundary becomes

$$\begin{aligned} &(C_{D_e} + C_{L_\alpha})(C_{m_V} + C_{m_{TV}}) \\ &- (C_{m_\alpha} + C_{m_{T_\alpha}})[2C_{L_e} + C_{L_V} + (2C_{T_e} + C_{TV}) \sin(\alpha_e + \alpha_T)] = 0 \end{aligned}$$

This equation can be simplified by using (2.4-1b) to get the following relationship for steady-state level flight:

$$2C_{T_e} \sin(\alpha_e + \alpha_T) + 2C_{L_e} = 2mg_D/(\bar{q}S) \equiv 2C_{W_e},$$

where  $C_W (\approx C_L)$  is the aircraft weight made dimensionless in the usual way. Substituting this result into the stability boundary condition, we get

$$(C_{D_e} + C_{L_\alpha})(C_{m_V} + C_{m_{T_V}}) - (C_{m_\alpha} + C_{m_{T_\alpha}})[2C_{W_e} + C_{L_V} + C_{T_V} \sin(\alpha_e + \alpha_T)] = 0$$

To further simplify the expression, neglect the drag coefficient compared to the lift-curve slope, and let the thrust and aerodynamic moment derivatives be included in a single derivative. Then,

$$0 = C_{L_\alpha} C_{m_V} - C_{m_\alpha} [2C_{W_e} + C_{L_V} + C_{T_V} \sin(\alpha_e + \alpha_T)] \quad (4.2-19)$$

This condition still holds when the last two terms on the right are negligible and, knowing that  $C_{W_e}$  and  $C_{L_\alpha}$  are always positive, we can deduce that the condition for pitch stability is

$$C_{m_\alpha} < \frac{C_{L_\alpha} C_{m_V}}{2C_{W_e} + C_{L_V} + C_{T_V} \sin(\alpha_e + \alpha_T)} \quad (4.2-20)$$

When the tuck derivative is zero, (4.2-20) reduces to the static stability condition [see, for example, (2.4-19)]. When the aircraft has an unstable tuck ( $C_{m_V} < 0$ ) at high subsonic Mach numbers, a greater low-speed static margin is required to maintain pitch stability at those Mach numbers. Roskam (1979) points out that the pitch divergence of most subsonic jet transports is rather slow and not necessarily objectionable.

### Algebraic Derivation of Lateral-Directional Transfer Functions

The lateral-directional coefficient matrices are given by (2.6-31). We will eliminate the  $E$ -matrix by dividing the first lateral equation by  $V_{T_e}$ ; the characteristic polynomial is then

$$|sI - A| = \begin{vmatrix} s - \frac{Y_\beta}{V_{T_e}} & \frac{-g_D \cos \theta_e}{V_{T_e}} & \frac{-Y_p}{V_{T_e}} & 1 - \frac{Y_r}{V_{T_e}} \\ 0 & s & -c\gamma_e/c\theta_e & -s\gamma_e/c\theta_e \\ -L'_\beta & 0 & s - L'_p & -L'_r \\ -N'_\beta & 0 & -N'_p & s - N'_r \end{vmatrix} \quad (4.2-21)$$

and the  $B$ -matrix is

$$B = \begin{bmatrix} \frac{Y_{\delta a}}{V_{T_e}} & \frac{Y_{\delta r}}{V_{T_e}} \\ 0 & 0 \\ L'_{\delta a} & L'_{\delta r} \\ N'_{\delta a} & N'_{\delta r} \end{bmatrix} \quad (4.2-22)$$

Cramer's rule can now be used to find any particular transfer function. It is usual to make the lateral-directional equations manageable by assuming level flight ( $\gamma_e = 0$ ). Then, for example, the aileron-to-roll-rate transfer function is

$$\frac{p(s)}{\delta_a(s)} = \frac{1}{|sI - A|} \begin{vmatrix} s - \frac{Y_\beta}{V_{T_e}} & \frac{-g_D \cos \theta_e}{V_{T_e}} & \frac{Y_{\delta a}}{V_{T_e}} & 1 - \frac{Y_r}{V_{T_e}} \\ 0 & s & 0 & 0 \\ -L'_\beta & 0 & L'_{\delta a} & -L'_r \\ -N'_\beta & 0 & N'_{\delta a} & s - N'_r \end{vmatrix}, \quad (4.2-23)$$

which is of the form

$$\frac{p(s)}{\delta_a(s)} = \frac{ks(s^2 + 2\zeta_\phi \omega_\phi s + \omega_\phi^2)}{a_4 s^4 + a_3 s^3 + a_2 s^2 + a_1 s + a_0} \quad (4.2-24)$$

The subscript  $\phi$  has been used on the numerator quadratic because the same factor appears in the roll angle transfer function, and the notation is in common use.

Once again, the polynomial coefficients are complicated functions of the dimensional derivatives, but some simplifications are possible. If the sideforce and yawing effects of the ailerons are neglected (i.e., neglect  $Y_{\delta a}/V_{T_e}$  and  $N'_{\delta a}$ ), the determinant in (4.2-23) has a simple expansion about the third column. Then assuming that  $Y_r/V_{T_e} \ll 1.0$ , the numerator of (4.2-24) can be written as

$$ks(s^2 + 2\zeta_\phi \omega_\phi s + \omega_\phi^2) = sL'_{\delta a}[s^2 - s(N'_r + Y_\beta/V_{T_e}) + (N'_\beta + Y_\beta N'_r/V_{T_e})] \quad (4.2-25)$$

When the aircraft has negligible *roll-yaw coupling*, the quadratic factor on the right-hand side of (4.2-25) also appears in the lateral-directional characteristic polynomial. This is shown in the next subsection. The resulting cancellation leaves a particularly simple expression for the aileron-to-roll-rate transfer function.

The lateral-directional characteristic equation does not separate into factors that clearly define each mode. Approximations will be derived that may describe an individual mode reasonably well, but they must be checked for applicability in any given case. Nevertheless, these approximations do provide useful insight into the dynamic behavior, and they will be derived for this reason. We start with the dutch roll approximation.

## The Dutch Roll Approximation

The dihedral derivative  $C_{l_\beta}$  determines the amount of rolling in the dutch roll mode, and when this derivative is small, the mode will consist mainly of sideslipping and yawing. The dihedral derivative tends to be large in modern swept-wing aircraft and so it will be neglected only for the purpose of deriving the traditional "3-DoF dutch roll approximation." A more modern approximation will then be given.

The coefficient of the roll angle in the beta-dot equation is the gravity term in the characteristic determinant (4.2-21). When this element is neglected, the determinant has a simple reduction about the second column. The reduction of the subsequent third-order determinant can be further simplified if the terms  $Y_p/V_{T_e}$  and  $Y_r/V_{T_e}$  can be dropped ( $Y_p$  is often zero, and  $Y_r/V_{T_e} \ll 1.0$ ). The cross-derivative term  $N'_p$  (yawing moment due to roll rate) is also often negligible. The dihedral derivative then no longer appears in the characteristic polynomial, which is given by

$$|sI - A| = s(s - L'_p)[s^2 - s(N'_r + Y_\beta/V_{T_e}) + (N'_\beta + Y_\beta N'_r/V_{T_e})] \quad (4.2-26)$$

This polynomial has a root at the origin and at  $s = L'_p$ , which respectively approximate the spiral pole and the roll subsidence pole. The quadratic factor contains the dutch roll poles, and it exactly matches the numerator quadratic of the roll-rate transfer function (4.2-25). Therefore, an approximation to the aileron-to-roll-rate transfer function (4.2-24) is given by

$$\frac{p(s)}{\delta_a(s)} = \frac{L'_{\delta a}}{(s - L'_p)} \quad (4.2-27)$$

Equation (4.2-26) gives the dutch roll approximations as

$$\begin{aligned} \omega_{nd}^2 &= N'_\beta + (Y_\beta/V_{T_e})N'_r \\ \zeta_d &= -(N'_r + Y_\beta/V_{T_e})/(2\omega_{nd}) \end{aligned} \quad (4.2-28a)$$

A more recent approximation (Ananthkrishnan and Unnikrishnan, 2001) is

$$\omega_{nd}^2 = N'_\beta + \frac{Y_\beta}{V_{T_e}}N'_r + \frac{g_D}{V_{T_e}}\frac{L'_\beta}{L'_p} - \left( L'_\beta + \frac{Y_\beta}{V_{T_e}}L'_r \right) \frac{N'_p}{L'_p}, \quad (4.2-28b)$$

whose first two terms agree with (4.2-28a). The damping equation in (4.2-28a) is unchanged, and so improved accuracy in the damping calculation will only come via the more accurate natural frequency.

We will now substitute dimensionless stability derivatives into the traditional dutch roll formulas and examine the dependence on flight conditions. The derivative  $N'_\beta$  is given by

$$N'_\beta = \frac{N_\beta + (J'_{XZ}/J'_Z)L_\beta}{1 - J'^2_{XZ}/(J'_X J'_Z)} \quad (4.2-29)$$

The stability-axes cross-product of inertia  $J'_{XZ}$  varies rapidly with the equilibrium angle of attack, typically changing from a small positive value at low alpha to a much larger negative value at high alpha. This larger value is still relatively small compared to  $J'_Z$ , so the primed derivatives are normally quite close to their unprimed values. It is possible for  $N_\beta$  to decrease and even change sign at high alpha, but then the linear equations are unlikely to be valid.

If we simply use the unprimed derivative  $N_\beta$  in the formula for the dutch roll frequency and then substitute the dimensionless derivatives, we obtain

$$\omega_{n_d}^2 = \frac{\bar{q}Sb}{J'_z} \left[ C_{n_\beta} + \frac{\rho S b}{4m} C_{Y_\beta} C_{n_r} \right] \quad (4.2-30)$$

The  $C_{n_r}$  term is usually negligible compared to  $C_{n_\beta}$ , and this equation shows that the dutch roll frequency is proportional to the square root of dynamic pressure, assuming constant  $C_{n_\beta}$ . Therefore, at constant altitude, the *frequency increases in proportion to the airspeed*, and for a given speed the *frequency decreases with altitude*.

When unprimed derivatives are substituted into the damping formula, followed by dimensionless derivatives and the natural frequency expression from (4.2-28a), the damping ratio is given by

$$\zeta_d = -\frac{1}{4} \left[ \frac{(\rho S b) b^2}{2J'_z} \right]^{1/2} \frac{C_{n_r} + (2J'_z / mb^2) C_{Y_\beta}}{[C_{n_\beta} + (\rho S b / 4m) C_{n_r} C_{Y_\beta}]^{1/2}} \quad (4.2-31)$$

This expression indicates that the dutch roll damping is independent of dynamic pressure. *It will be proportional to the square root of density* since the second term of the denominator is usually negligible.

The dutch roll natural frequency formula tends to be quite accurate if the dihedral derivative is small, although the damping formula is not. This is illustrated in Example 4.2-1. Finally, note that the approximation to the roll subsidence pole,  $s = L'_p$ , is not very accurate, and a more accurate approximation will be derived next.

## The Spiral and Roll Subsidence Approximations

The rolling and spiral modes usually involve very little sideslip. The rolling mode is almost pure rolling motion around the  $x$ -stability axis, and the spiral mode consists of yawing motion with some roll. It is common for the spiral mode to be unstable, and the motion then consists of increasing yaw and roll angles in a tightening downward spiral.

These facts allow approximations to be devised by modifying the  $\beta$  equation and leaving the moment equations unchanged. Sideforce due to sideslip is eliminated from the equation,  $\beta$  is neglected, and the gravity force is balanced against the force component associated with yaw rate. Thus, in the characteristic determinant (4.2-21) the term  $s - Y_\beta/V_{T_e}$  is eliminated, and the  $Y_p/V_{T_e}$  term is again neglected. Because the gravity force is intimately involved in the spiral mode, the mode is dependent on flight-path angle. Unfortunately, the assumption of level flight is needed to allow a reasonably simple analysis and will therefore be used here. The effect of flight-path angle will be investigated numerically in Example 4.2-2. When the simplified determinant is expanded, the following second-order characteristic equation is obtained:

$$N'_\beta s^2 + (L'_\beta N'_p - L'_p N'_\beta - L'_\beta g_D / V_{T_e}) s + (L'_\beta N'_r - N'_\beta L'_r) g_D / V_{T_e} = 0 \quad (4.2-32)$$

The roots of this quadratic equation are usually real, stable, and widely separated because the spiral pole is very much closer to the origin than the roll pole. Therefore, the sum of the roots (given by the negative of the coefficient of  $s$  when the quadratic is made monic) is approximately equal to the reciprocal of the roll time constant  $\tau_R$ ,

$$\tau_R \approx \frac{N'_\beta}{L'_\beta N'_p - L'_p N'_\beta - L'_\beta g_D / V_{T_e}} \quad (4.2-33)$$

The quadratic constant term (i.e., the product of the roots) divided by the roll root gives the reciprocal of the spiral time constant  $\tau_S$ ,

$$\tau_S \approx \frac{L'_\beta N'_p - L'_p N'_\beta - L'_\beta g_D / V_{T_e}}{(L'_\beta N'_r - N'_\beta L'_r) g_D / V_{T_e}} \quad (4.2-34)$$

Note that a negative value for the time constant will simply mean an unstable exponential mode. A slightly more accurate formula for  $\tau_S$  is given by Ananthkrishnan and Unnikrishnan (2001), but the difference is usually negligible. In the denominator of the roll time constant equation, the first term contains cross-derivatives and is usually negligible; the second term usually dominates the third, and under these conditions,

$$\tau_R \approx \frac{1}{L'_p} = -\frac{b}{V_T} \frac{4J'_X}{(\rho S b) b^2} \frac{1}{C_{\ell_p}} \text{ secs.} \quad (4.2-35)$$

This equation indicates that *the roll time constant will vary inversely as the product of density and speed*, given the above approximations, and a constant roll damping derivative.

The numerator of the spiral equation is the same as the denominator of the roll equation, and making the same approximation as above,

$$\tau_S \approx \frac{-L'_p N'_\beta}{(L'_\beta N'_r - L'_r N'_\beta)} = \frac{-C_{\ell_p} C_{n_\beta}}{(C_{\ell_\beta} C_{n_r} - C_{\ell_r} C_{n_\beta})} \frac{V_{T_e}}{g_D} \quad (4.2-36)$$

This equation indicates that the spiral time constant is proportional to speed, given the earlier approximations, and that the stability derivatives remain constant.

## Spiral Stability

The condition for a pole at the origin is given by  $|A| = 0$ , and in the case of the lateral dynamics this normally represents the spiral pole becoming neutrally stable. From the characteristic determinant (4.2-21), we obtain

$$|A| = \begin{vmatrix} \frac{Y_\beta}{V_{T_e}} & \frac{(g_D \cos \theta_e)}{V_{T_e}} & \frac{Y_p}{V_{T_e}} & -1 + \frac{Y_r}{V_{T_e}} \\ 0 & 0 & c\gamma_e / c\theta_e & s\gamma_e / c\theta_e \\ L'_\beta & 0 & L'_p & L'_r \\ N'_\beta & 0 & N'_p & N'_r \end{vmatrix}$$



When the determinant is expanded, the spiral stability boundary is found to be given by

$$(L'_\beta N'_r - N'_\beta L'_r) \cos \gamma_e + (L'_p N'_\beta - L'_\beta N'_p) \sin \gamma_e = 0 \quad (4.2-37)$$

This equation shows that spiral stability is dependent on flight-path angle, as noted earlier.

### Accuracy of the Lateral-Mode Approximations

The accuracy of the lateral-mode formulas is often quite good apart from the dutch roll damping. The spiral time constant is also accurately predicted when this mode is unstable. This accuracy will be demonstrated in the following example using a model of a business jet in a cruising flight condition.

**Example 4.2-1: Lateral Modes of a Business Jet** The following lateral-directional data for a business jet are taken from Roskam (1979).

Flight Condition:

$$W = 13,000 \text{ lb}, \quad g = 32.17, \quad h = 40,000 \text{ ft} \quad (\rho = 0.000588 \text{ slug/ft}^3)$$

$$V_T = 675 \text{ ft/s}, \quad \gamma = 0 \text{ deg}, \quad \alpha = 2.7 \text{ deg}$$

$$J_x = 28,000; \quad J_z = 47,000; \quad J_{xz} = 1,350 \text{ slug-ft}^2 \quad (\text{body axes})$$

$$\text{Geometrical Data: } S = 232 \text{ ft}^2, \quad b = 34.2 \text{ ft}$$

Stability Derivatives:

$$C_{y_\beta} = -0.730, \quad C_{y_p} = 0, \quad C_{y_r} = +0.400$$

$$C_{l_\beta} = -0.110, \quad C_{l_p} = -0.453, \quad C_{l_r} = +0.163$$

$$C_{n_\beta} = +0.127, \quad C_{n_p} = +0.008, \quad C_{n_r} = -0.201$$

A short program was written to convert the moments of inertia to stability axes, calculate the elements of the decoupled  $A$ -matrix, and evaluate the approximate equations for the modal characteristics [from (4.2-28a) and (4.2-32)–(4.2-34)]. Some intermediate results are:

Stability-Axes Moments of Inertia:

$$J'_X = 27,915 \quad J'_Z = 47,085 \quad J'_{XZ} = 450.0$$

Dimensional Derivatives:

$$Y_\beta = -56.14, \quad Y_p = 0, \quad Y_r = 0.7793$$

$$L_\beta = -4.188, \quad L_p = -0.4369, \quad L_r = 0.1572$$

$$N_\beta = 2.867, \quad N_p = 0.004575, \quad N_r = -0.1149$$

Primed Dimensional Derivatives:

$$\begin{aligned} L'_\beta &= -4.143; \quad L'_p = -0.4369; \quad L'_r = 0.1554 \\ N'_\beta &= 2.827; \quad N'_p = 0.0003991; \quad N'_r = -0.1135 \end{aligned}$$

The full  $A$ -matrix was calculated from (4.2-21) so that an eigenvalue program could be used to determine the modes “exactly.” The exact and approximate results are as follows:

Dutch Roll Mode:

$$\text{Exact: } \omega_n = 1.689 \text{ rad/s, } \zeta = 0.03878$$

$$\text{Equations (4.2-28a): } \omega_n = 1.684 \text{ rad/s, } \zeta = 0.05837$$

Roll Subsidence Mode:

$$\text{Exact: } \tau_R = 1.994$$

$$\text{Equation (4.2-32): } \tau_R = 1.980$$

$$\text{Equation (4.2-33): } \tau_R = 1.976$$

Spiral Mode:

$$\text{Exact: } \tau_S = 978.4$$

$$\text{Equation (4.2-32): } \tau_S = 976.7$$

$$\text{Equation (4.2-33): } \tau_S = 978.6$$

These results are in remarkably good agreement, apart from the dutch roll damping. ■

## Mode Variation from the Nonlinear Model

It is not very realistic to use a fixed set of stability derivatives to show the variation of the modal characteristics with flight conditions. Therefore, as a final example we will use the completely numerical approach to calculate the modes of the nonlinear F-16 model at different flight conditions. The modes will only be calculated accurately since the numerical linearization is set up to produce the state equation coefficient matrices, not the stability derivatives. The variation of the modes with flight-path angle will also be determined, since this could not easily be done with the approximate formulas.

**Example 4.2-2: Mode Dependence from the Nonlinear Model** The nonlinear F-16 model allows a realistic examination of the dependence of the modes on flight conditions, since it is not built from a fixed set of aerodynamic derivatives. The following results were obtained by trimming and numerically linearizing the model at the desired flight condition and then using an eigenvalue program to determine the modes

TABLE 4.2-2 Effect of Flight-Path Angle on F-16 Modes

$\gamma$	-5	0	5	10	15	20	deg
$T_D$	1.934	1.933	1.934	1.937	1.941	1.946	s
$\zeta_D$	0.1346	0.1353	0.1360	0.1366	0.1371	0.1375	
$\tau_S$	55.33	77.91	133.0	461.9	-312.3	-117.0	s
$\tau_R$	0.2777	0.2777	0.2775	0.2772	0.2766	0.2760	s
$T_{SP}$	3.281	3.277	3.273	3.269	3.266	3.262	s
$\zeta_{SP}$	0.6277	0.6279	0.6281	0.6282	0.6283	0.6283	
$T_P$	79.60	80.05	80.93	82.39	84.36	86.82	s
$\zeta_P$	0.1297	0.09751	0.06557	0.03396	0.00227	-0.0298	

from the full thirteen-state  $A$ -matrix. Virtually identical results could be obtained by using the decoupled lat-long matrices.

The effect of flight-path angle was investigated by trimming the model according to the second set of conditions in Table 3.6-3 (502 ft/s,  $h = 0$  ft,  $cg = 0.3 \bar{c}$ ) but with different values of  $\gamma$ . The modes are shown in Table 4.2-2. It is evident from these results that the “rotational” modes are almost independent of  $\gamma$ . Weak but consistent trends are visible in the dutch roll and roll subsidence modes and in the short period. Overall, the properties of the rotational modes are remarkably constant, considering the nature of the tabular aerodynamic data and the numerical processing (trimming and linearization) required to obtain them. The “flight-path” modes, phugoid and spiral, are strongly influenced by the flight-path angle. The spiral time constant initially increases as the flight-path angle increases, becomes infinite as the stability boundary is approached, and then decreases with flight-path angle when the mode is unstable. The phugoid period is only weakly affected by  $\gamma$  but increases as  $\gamma$  increases. Phugoid damping is more strongly affected; it decreases with increasing  $\gamma$  and the phugoid becomes unstable at a quite modest flight-path angle.

In Table 4.2-3 the model is trimmed in level flight with various combinations of speed and altitude to illustrate the effect of these two variables on the modes. The  $cg$  position is again at  $0.3 \bar{c}$ . The flight conditions have been chosen to compare different speeds at the same altitude, the same speed at different altitudes, high and low dynamic pressures at the same altitude, and the same dynamic pressure at two greatly different altitudes. The first trim condition (50,000 ft, 900 ft/s) corresponds to 0.93 Mach and is therefore strictly outside the valid Mach range of the model; this is also true to a lesser extent for the third case (0.81 Mach). We do not have a model that includes compressibility effects, and we will simply consider this example as illustrating the variation of the modes when compressibility is not important. The second trim condition (50,000 ft, 600 ft/s) corresponds to full throttle, while the first case (higher speed) corresponds to only 0.765 throttle. Therefore, a dive-and-climb maneuver would be needed to get from the second to the first flight condition. The longitudinal dynamics are unstable in the second case. In the fourth flight condition trial-and-error adjustment of the speed was used to make the dynamic pressure the same as the first case.

**TABLE 4.2-3 Effect of Speed and Altitude on F-16 Modes**

Altitude/speed (dyn. pres)	50k, 900 (160)	50k, 600 (71)	0, 900 (963)	0, 367 (160)	ft, ft/s lb/ft <sup>2</sup>
$T_D$	2.365	2.735	1.143	2.396	s
$\zeta_D$	0.06480	0.07722	0.1272	0.1470	
$\tau_S$	179.2	138.7	122.1	73.52	s
$\tau_R$	1.050	2.230	0.1487	0.4160	s
$T_{SP}$	4.507	u/s	2.372	4.023	s
$\zeta_{SP}$	0.2615	u/s	0.8175	0.5735	
$T_P$	102.1	u/s	183.4	56.93	s
$\zeta_P$	0.005453	u/s	0.3242	0.06240	

The tabulated results show that, as expected, the dutch roll has almost the same period at two widely different speed-altitude combinations with the same dynamic pressure. They also show the expected increase in period with altitude (at constant speed) and the decrease in period with airspeed (at constant altitude). The dutch roll damping does tend to be independent of dynamic pressure and to decrease with altitude, as predicted by the theory.

The spiral time constant is expected to vary directly with  $V_T$  if the third numerator term in (4.2-36) is negligible and to vary as  $V_T/\bar{q}$  if that term is dominant. The results indicate that the actual variation is somewhere in between these two trends. This is not unexpected because the F-16 has swept wings, and  $C_{l_\beta}$  can be expected to play a significant part in (4.2-36).

The time constant of the roll subsidence mode is approximately proportional to  $V_T/\bar{q}$ , as predicted. The short-period mode also shows the expected trends; the period is roughly the same at the two equal dynamic pressure conditions and is much smaller at the high dynamic pressure condition. As predicted, the damping is much more strongly affected by altitude than by dynamic pressure.

In the case of the phugoid period the two sea-level results show that the sixfold increase in dynamic pressure causes an increase in the period of 3.2 times (compared to the prediction of  $\sqrt{6}$ ). At constant dynamic pressure the period increases with altitude, as expected. The phugoid damping also shows the expected trend, increasing with airspeed and decreasing with altitude. ■

### 4.3 THE HANDLING QUALITIES REQUIREMENTS

#### Background

Control law design can only be performed satisfactorily if a set of design requirements or performance criteria is available. In the case of control systems for piloted aircraft, generally applicable quantitative design criteria are very difficult to obtain. The reason for this is that the ultimate evaluation of a human operator control system

is necessarily subjective and, with aircraft, the pilot evaluates the aircraft in different ways depending on the type of aircraft and phase of flight. For example, in a dynamic maneuvering situation the pilot may be concerned mainly with the control forces that must be exerted and the resulting 6-DoF translational and angular accelerations. In a task requiring precision tracking the pilot's evaluation will be more influenced by visual cues and the response of the aircraft to turbulence.

Also, a pilot's opinion of the *handling qualities* of an aircraft is inevitably influenced by factors other than the obvious control system considerations of response to control inputs and response to disturbance inputs (e.g., turbulence). He or she will be influenced by the ergonomic design of the cockpit controls, the visibility from the cockpit, the weather conditions, the mission requirements, and physical and emotional factors. The variability introduced by all these factors can only be reduced by averaging test results over many flights and many pilots.

A systematic approach to handling qualities evaluation is available through *pilot opinion rating* scales such as the Cooper-Harper scale (Cooper and Harper, 1969). This rating scale is shown in Table 4.3-1. Once a rating scale like this has been

**TABLE 4.3-1 Pilot Opinion Rating and Flying Qualities Level**

Aircraft Characteristics	Demands on Pilot in Selected Task or Required Operation	Pilot Rating	Flying Qualities Level
Excellent; highly desirable	Pilot compensation not a factor for desired performance	1	1
Good; negligible deficiencies	as above	2	
Fair; some mildly unpleasant deficiencies	Minimal pilot compensation required for desired performance	3	
Minor but annoying deficiencies	Desired performance requires moderate pilot compensation	4	2
Moderately objectionable deficiencies	Adequate performance requires considerable pilot compensation	5	
Very objectionable but tolerable deficiencies	Adequate performance requires extensive pilot compensation	6	
Major deficiencies	Adequate performance not attainable with maximum tolerable pilot compensation controllability not in question	7	3
Major deficiencies	Considerable pilot compensation required for control	8	
Major deficiencies	Intense pilot compensation required to retain control	9	
Major deficiencies	Control will be lost during some portion of required operation	10	

established, it is possible to begin correlating the pilot opinion rating with the properties of the aircraft dynamic model and hence derive some analytical specifications that will guarantee good handling qualities. Although this may seem simple in principle, it has proven remarkably difficult to achieve in practice, and after many years of handling qualities research it is still not possible to precisely specify design criteria for control systems intended to modify the aircraft dynamics. A survey and a large bibliography covering twenty-five years of handling qualities research has been given by Ashkenas (1984). The “background information and user guides” for the military flying qualities specifications MIL-F-8785B and MIL-F-8785C (Chalk et al., 1969; Moorhouse and Woodcock, 1982) also provide much useful information.

We first consider some possible ways in which requirements for dynamic response may be specified. The aircraft model may be linearized in a particular flight condition and the poles and zeros, or frequency response, of a particular transfer function compared with a specification. Alternatively, certain time responses may be derived from the nonlinear model, in a particular flight condition, and compared with specifications. Yet another alternative is to model the human operator as an element in a closed control loop containing the aircraft dynamics and determine what requirements are placed on the operator if the closed-loop control is to have a satisfactory command or disturbance response. All of these techniques have been or are being considered by workers in the field, and we will examine some of the ideas in more detail.

## Pole-Zero Specifications

Suppose that lat-long decoupling is assumed and the pitch axis is considered. In addition, assume linear dynamic behavior. Then if a transfer function shows that the dynamic response is dominated by a single pair of complex poles (e.g., the short-period poles), the pilot’s opinion of the aircraft handling qualities should correlate with the position of these poles. A number of studies have provided data to link pole positions to pilot opinion rating.

In one of the early studies, O’Hara (1967) produced iso-opinion contours for the location of the short-period poles; these were plotted on axes of undamped natural frequency versus damping ratio. They showed that the most satisfactory pilot opinion rating corresponded to poles inside a closed contour bounded by about 2.4 and 3.8 rad/s and by damping ratios of about 0.4 and 1.0, with its center at about 3.0 rad/s and  $\zeta = 0.65$ . This and other similar results form the basis of current pole position handling qualities criteria.

Unfortunately for the pole position criterion, even if the decoupling and linearity assumptions are justified, there are at least two reasons why this approach may not work well. The first is that transfer function zeros are also important (they have a strong effect on step-response overshoot). Second, the aircraft and control system dynamics may include quite a lot of poles that contribute significantly to the time response. Pilots are very sensitive to additional dynamics, and the difficulties of specifying requirements on more than just a single pair of poles quickly become prohibitive. The problem of transfer function zeros will be considered first.

The short-period elevator-to-pitch-rate transfer function (4.2-9) plays an important role in the pilot's assessment of the longitudinal-axis flying qualities. In this transfer function the  $Z_{\delta_e}$ ,  $Z_{\dot{\alpha}}$ , and  $Z_q$  terms can usually be neglected, with the following result:

$$\frac{q}{\delta_e} = \frac{Z_\alpha M_{\delta_e} (s V_{T_e} / Z_\alpha - 1)}{V_{T_e} s^2 - (Z_\alpha + V_{T_e} M_q + V_{T_e} M_{\dot{\alpha}}) s + M_q Z_\alpha - V_{T_e} M_\alpha} \quad (4.3-1)$$

In the handling qualities literature the dimensional derivative  $L_\alpha (\equiv \partial L / \partial \alpha \approx -m Z_\alpha, C_D \ll C_{L_\alpha})$  is often used instead of  $Z_\alpha$ , and the time constant associated with the transfer function zero is given the symbol  $T_{\theta_2}$  ( $T_{\theta_1}$  is associated with the phugoid mode). Therefore, we see that

$$T_{\theta_2} = -V_{T_e} / Z_\alpha \approx m V_{T_e} / L_\alpha \quad (4.3-2)$$

This time constant is also often expressed in terms of the aircraft load factor response to angle of attack,  $n_\alpha$ . Aircraft *load factor*,  $n$ , is defined as lift ( $L$ ) divided by the weight ( $W$ ), and  $n_\alpha$  is the gradient of this quantity with respect to alpha [ $n_\alpha = (\partial L / \partial \alpha) / W$ ]. Therefore, we have

$$T_{\theta_2} = V_{T_e} / (g_D n_\alpha) \quad (4.3-3)$$

The position of the pitch-rate transfer function zero has been shown to correlate with pilot opinion ratings of the flying qualities (Chalk, 1963). Shomber and Gertsen (1967) derived iso-opinion curves involving the short-period frequency and damping,  $T_{\theta_2}$ , and  $n_\alpha$ . When  $n_\alpha$  was less than 15 g/rad, they found that pilot opinion correlated well with  $1/(\omega_n T_{\theta_2})$  and  $\zeta$ , with the optimum conditions being around  $1/(\omega_n T_{\theta_2}) = 0.45$ ,  $\zeta = 0.7$ . When  $n_\alpha$  was greater than 15, they found that the correlation was with  $n_\alpha / \omega_n$  (i.e.,  $T_{\theta_2}$  no longer fixed) and  $\zeta$ , with the optimum conditions near  $n_\alpha / \omega_n = 10$ ,  $\zeta = 0.7$ . The military flying qualities requirements (see later) specify the short-period natural frequency in terms of  $n_\alpha$ , and there is still a division of opinion over the importance of  $T_{\theta_2}$  versus  $n_\alpha$ .

The lateral-directional dynamics have proved somewhat less critical than the longitudinal dynamics from the point of view of handling qualities. The normally required changes in the aircraft trajectory can be achieved by a combination of rolling and pitching. O'Hara (1967) used iso-opinion curves to show that lateral dynamics would receive a good rating if the maximum roll acceleration was appropriate for the roll time constant. Both of these quantities are transfer function parameters. Regardless of these studies the current military requirements provide only specifications for the roll time constant and the time to reach a given roll angle. The latter quantity must be obtained from a flight test or a nonlinear simulation.

The dutch roll mode is an unwanted complication in this simple picture; it should be fast and adequately damped (see later) so that the airplane will quickly reorient itself after a directional disturbance. Ideally, the dutch roll should have very little involvement in the lateral dynamics and should therefore almost cancel out of the lateral transfer functions. This requires that quantities  $\omega_\phi$  and  $\zeta_\phi$  for the complex zeros [see (4.2-24)] should coincide with  $\omega_d$  and  $\zeta_d$  for the dutch roll poles. The

ratio  $\omega_\phi/\omega_d$  is the most important quantity in this respect, and iso-opinion curves of  $\omega_\phi/\omega_d$  versus  $\zeta_d$  have been plotted (Ashkenas, 1966).

As might be expected, the optimum value of  $\omega_\phi/\omega_d$  is close to unity for a stable dutch roll. However, there is a subtlety in these results; it can be shown that favorable yaw is generated in a turn when  $\omega_\phi/\omega_d > 1$ , and the converse is true. We will refer to this again in connection with the lateral-directional control augmentation system in Section 4.5.

Finally, consider the case of highly augmented aircraft, where the control systems contribute a number of poles and zeros in addition to those associated with the basic rigid-body transfer functions. Specifications placed on poles and zeros quickly become unmanageable and, as in the case of control system design, one must resort to frequency-response techniques. One way in which frequency-domain ideas have been applied to handling qualities specifications is described in the next subsection.

### Frequency-Response Specifications

In general, the goal of an aircraft control system design should be to produce dominant closed-loop poles that resemble the basic rigid-body poles, with satisfactory damping and natural frequency. The effect of the additional dynamics resulting from the control system compensation networks, and possibly the lower-frequency flexible modes, can be allowed for by determining an “equivalent low-order system” (Craig and Ashkenas, 1971; Hodgkinson, 1979; Bischoff, 1981; Gentry, 1982).

In this concept the coefficients are determined for a low-order transfer function that matches the frequency response of the actual transfer function over a limited frequency range. The gain and phase are matched simultaneously by adjusting the coefficients of the low-order transfer function to minimize a cost function of the form

$$\text{COST} = \frac{20}{n} \sum_{i=1}^{i=n} \left[ \Delta G(\omega_i)^2 + \frac{\Delta P(\omega_i)^2}{57.3} \right] \quad (4.3-4)$$

Here  $n$  is the number of discrete frequencies ( $\omega_i$ ) used,  $\Delta G(\omega_i)$  is the difference in gain (in decibels) between the transfer functions at the frequency  $\omega_i$ , and  $\Delta P(\omega_i)$  is the difference in phase (in degrees) at  $\omega_i$ . The frequency range used is nominally 0.3 to 10 rad/s, and 20 to 30 discrete frequencies are needed. The upper frequency limit is based on the maximum control frequencies that pilots have been observed to use. The lower limit is based on observations that pilots do not provide continuous closed-loop control at very low frequencies, and the value given does not provide for matching the phugoid mode. The cost function is minimized with a multivariable search routine, in the same way that we obtained steady-state trim in Chapter 3.

The stick-force-to-pitch-rate transfer function is typically used to evaluate the longitudinal dynamics. To compare a particular aircraft with both the short-period and phugoid specifications in the military flying qualities specifications, the assumed form of this transfer function is

$$\frac{q}{F_s} = \frac{K(s + 1/T_{\theta_1})(s + 1/T_{\theta_2})e^{-\tau s}}{\left(s^2 + 2\zeta_p\omega_{n_p}s + \omega_{n_p}^2\right)\left(s^2 + 2\zeta_{sp}\omega_{n_{sp}}s + \omega_{n_{sp}}^2\right)} \frac{\text{rad/s}}{\text{lb}} \quad (4.3-5)$$



Here the subscripts  $p$  and  $sp$  indicate, respectively, the phugoid and short-period modes. The frequency range for matching the transfer functions should be extended down to about 0.01 rad/s when the phugoid is included.

The term  $e^{-\tau s}$  is included in the low-order model to provide an equivalent time delay for matching high-frequency effects from, for example, actuator modes, structural modes and mode filters, and noise filters. The time delay term contributes only a phase shift to the transfer function; this is consistent with the fact that the phase variations from high-frequency dynamics extend over a larger frequency range than gain variations. The military requirements suggest that for level-1 handling qualities, the maximum allowable value of the equivalent time delay should be 10.0 ms.

If a good fit to an equivalent low-order system is obtained (e.g., a cost of 10.0 or less), the pole-zero criteria can be applied to this equivalent system. If low values of the cost function cannot be obtained, other criteria must be used.

Another example of frequency-domain specifications applied to aircraft control systems (but not directly to handling qualities) is the military standard requirement document for the design, installation, and test of flight control systems (*MIL-F-9490*, 1975). This provides stability criteria by specifying the minimum gain and phase margins that must be achieved in any actuator path, with all other feedback paths closed. Typical values are a 6-dB gain margin and 30° phase margin.

## Time-Response Specifications

Placing handling qualities requirements on the time response has the advantage that a time response can readily be obtained from the full nonlinear model dynamics. It does, however, raise the problems of what type of test input to apply and which output variable to observe. In the case of the longitudinal dynamics, it is natural once again to specify requirements on the pitch-rate response. However, fighter aircraft control systems are normally designed to give the pilot control over pitch rate at low speed and normal acceleration (acceleration measured along the body negative  $z$ -axis) at high speed. The latter gives direct control over the variable that stresses the pilot. The two control schemes must be smoothly blended together (see, e.g., Toles, 1985).

Efforts to develop time-response criteria have mostly been linked to the decoupled longitudinal dynamics and have made use of the short-period approximation. They have attempted to define an envelope inside which the pitch rate, angle of attack, or normal acceleration response to an elevator step input should lie. As early as 1963 a step-response envelope for angle of attack was derived from the short-period iso-opinion curves (Rynaski, 1985). Envelope criteria have been published for the pitch-rate response of an SST and of the space shuttle (see Rynaski, 1985).

A time-history envelope criterion,  $C^*(t)$ , called “C-star,” was published in 1965 (Tobie et al., 1966) and is still in use. The  $C^*$  criterion uses a linear combination of pitch rate and normal acceleration at the pilot’s station:

$$C^*(t) = a_{n_p} + 12.4q, \quad (4.3-6)$$

where  $a_{n_p}$  is the normal acceleration in  $g$ 's (approximately zero  $g$ 's = level flight) and  $q$  is the pitch rate in radians per second. The envelope for the  $C^*$  criterion is shown in

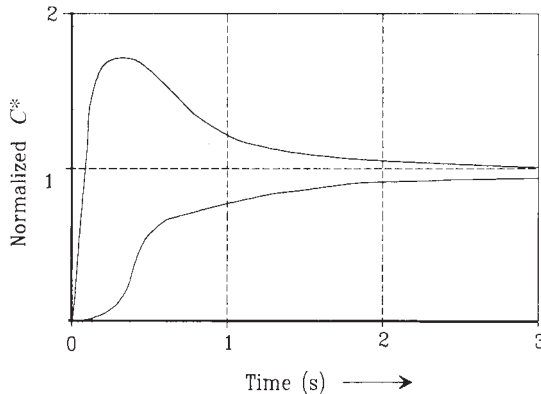


**Figure 4.3-1** The  $C^*$ -star envelope.

Figure 4.3-1. If the response  $C^*(t)$  to an elevator step input falls inside the envelope, level-1 flying qualities on the pitch axis will hopefully be obtained. A more recent time-domain criterion than  $C^*$  relates pilot opinion ratings to target tracking error and time on target for a step target tracking task (Onstott and Faulkner, 1978).

The cited envelope criteria often give conflicting results and may disagree with the pilot ratings for specific aircraft. Pitch-rate responses having large overshoots and poor settling times have often corresponded to good pilot opinion ratings. It is known that for fighter aircraft air combat modes a pitch-rate overshoot is required for good gross acquisition of targets, and a deadbeat pitch-rate response is required for good fine tracking. Rynaski (1985) has argued that angle of attack should be the basic response variable, and it appears that the angle-of-attack response corresponding to good handling qualities may be more like a good conventional step response (i.e., small overshoot and fast nonoscillatory settling).

A time-response criterion, called  $D^*$  (or coordination perception parameter), has been devised for the lateral-directional response (Kisslinger and Wendle, 1971). The idea is similar to  $C^*$  in that the coordination perception parameter is a blend of lateral acceleration and sideslip angle, and envelope limits for acceptable performance are specified.

## Requirements Based on Human Operator Models

For certain types of control tasks it is possible to model a human operator with linear differential equations or a transfer function. An example of such a task is a compensatory tracking task with a random input, that is, a control task in which the operator uses only tracking *error* information to track an unpredictable target. This information may be presented by instruments such as a pilot's artificial horizon display. The human operator model consists of the transfer function and an added nonanalytic output signal called the *remnant*. The purpose of the remnant is to account for the discrepancies between experimental results with a human operator and analyses using the model. The transfer function model is often given the name *human operator*

*describing function* (not to be confused with the describing function of nonlinear control theory).

The human operator transfer function model for the compensatory tracking task is usually assumed to be

$$Y(s) = \frac{K_p e^{-ds} (\tau_\ell s + 1)}{(\tau_i s + 1)(\tau_n s + 1)} \quad (4.3-7)$$

In this transfer function the pure delay,  $d$ , may be taken to represent the motor control functions in the cerebellum and the neuromuscular delay, while the lag  $\tau_n$  models the mechanical properties of the muscles and limbs. It is known that the speed of response is severely limited by the delay term rather than the lag, and the latter is neglected in many applications. The gain,  $K_p$ , lead time constant,  $\tau_\ell$ , and lag time constant,  $\tau_i$ , represent the capability of the human operator to optimize his or her control of a given task. Thus, the operator may use lag compensation to achieve high gain and fine control in some low-bandwidth tasks or lead compensation to achieve high bandwidth.

This model has been applied to aircraft piloting tasks, and hypotheses (the *adjustment rules*) have been developed for the way in which the adaptive parameters will be “chosen” by the pilot (McRuer et al., 1965). It is also used as the basis of a transfer function method of assessing flying qualities (Neal and Smith, 1970). Interesting examples of the transfer function model applied to a pilot controlling roll angle are given by Etkin (1972) and Roskam (1979).

In the Neal-Smith method the model (4.3-7) is used in conjunction with the aircraft stick-force-to-pitch-attitude transfer function in a closed pitch-attitude control loop. It is assumed that the human pilot adjusts the lead, lag, and gain, so that the *droop* and *peak magnification* of the closed-loop frequency response are minimized, as shown in Figure 4.3-2. Therefore, this process is duplicated with the models, the lag  $\tau_n$  is neglected, and the delay is taken as  $d = 0.3$  s. The lead and lag time constants are adjusted, according to the adjustment rules, to optimize the closed-loop frequency response. When this has been done, the maximum lead or lag provided by the pilot

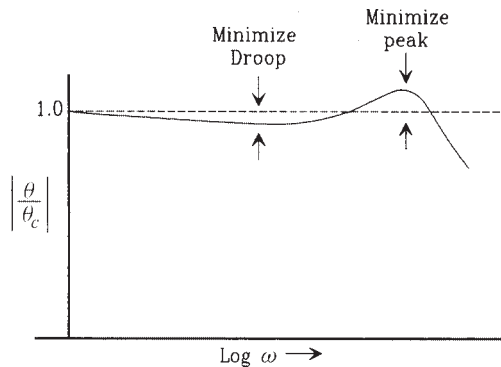


**Figure 4.3-2** Closed-loop frequency response for Neal-Smith criterion.

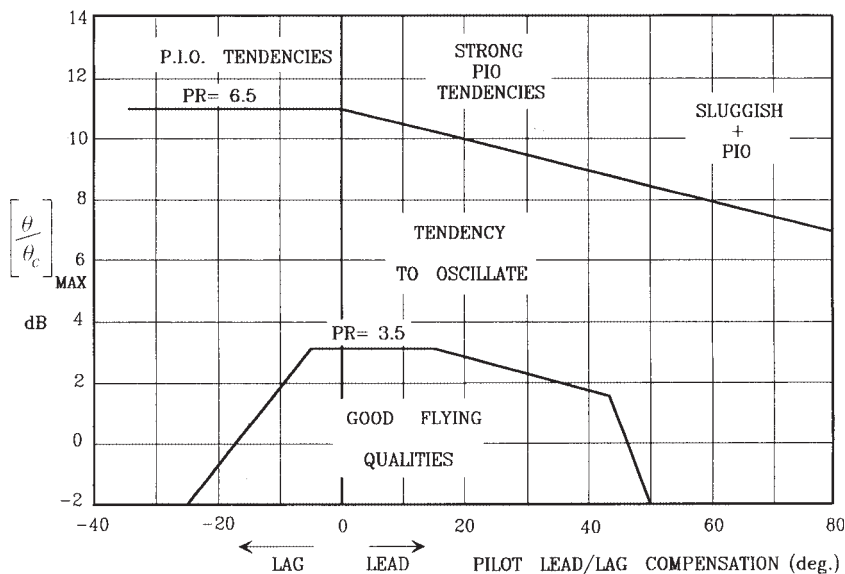


Figure 4.3-3 Neal-Smith evaluation chart.

model is determined, together with the value of the peak magnification. The pilot opinion rating is then determined from a plot like that shown in Figure 4.3-3.

A later development than the transfer function model of the human operator is the *optimal control model* (OCM), attributable mainly to Baron, Kleinman, and Levison (Kleinman et al., 1970, p. 358). It uses a state-variable formulation and optimal control theory and is based on the assumption that “a well-motivated, well-trained human operator behaves in a near optimal manner, subject to his inherent limitations and constraints and his control task.” A description of this model is outside the scope of this chapter, since it has not found its way directly into flying qualities specifications. More information can be found in the book by Sheridan and Ferrell (1974) and in the references cited. A summary of work in human operator modeling, with a fairly comprehensive bibliography, has been given by Gerlach (1977).

Human operator modeling applied to a pilot performing compensatory tracking tasks has now accumulated quite a long history, and attention has turned to modeling the human operator performing other piloting tasks. In a modern fighter aircraft the workload involved in operating all of the different systems (flight control, navigation, radar, weapons, etc.) can be overwhelming, and modeling the human decision-making process has become important. A survey of the relationship of flying qualities specifications to task performance and the use of pilot models has been given by George and Moorhouse (1982).

## Other Requirements

The preceding subsections described ways in which the dynamic response of an aircraft and its control systems can be characterized and how these may lead to handling

qualities criteria. There are a number of other requirements that must be satisfied for an aircraft to receive a good handling qualities rating. Some of these have no direct effect on control system design, but they are “inside the loop” that is closed by the pilot. They will be briefly described because of their importance.

One of the more important characteristics of the pilot’s controls is the *control feel*, that is, the force and deflection characteristics of the control stick during a particular maneuver. Aircraft whose control surfaces are not power boosted require much careful balancing of the control surfaces and the addition of a mass and springs to the control stick in order to obtain satisfactory feel. Aircraft with fully powered, irreversible controls require an artificial-feel system.

Artificial feel may take the form of centering springs, an electromechanical damper, and, for longitudinal control, a mechanical or hydraulic system that provides a stick reaction force proportional to the normal acceleration in  $g$ s during a pull-up maneuver. Iso-opinion studies have shown that the amount of stick force per  $g$  is quite critical and there is an associated optimum value of stick deflection. Stick-force-per- $g$  requirements are given in the military aircraft specifications, in addition to the control forces required in various flight phases.

Another factor that influences a pilot’s opinion of handling qualities, particularly in the landing phase, is speed stability. The aircraft response to a speed disturbance is an exponential change, and this response will typically be rated as satisfactory if it is stable with a time constant of less than about 50 s. An unstable exponential response may be acceptable under some conditions provided that the time constant is greater than about 25 s.

## The Military Flying Qualities Specifications

In the preceding subsections we attempted to convey some idea of the difficulty of specifying analytical performance criteria for the dynamic behavior of piloted aircraft. The civil and military aviation authorities of various countries are also faced with this problem. In general, their requirements documents are not very analytical and do not provide any way out of our difficulty. However, the U.S. “Military Specification for the Flying Qualities of Piloted Airplanes” (*MIL-F-8785C*, 1980) does provide some analytical specifications that must be met by U.S. military aircraft. A background document and user guide, containing much useful information and a large bibliography, is also available (Chalk et al., 1969). These documents are readily available, and only the mode specifications of *MIL-F-8785C* will be summarized here. (Note that *MIL-F-8785C* has now been superseded by *MIL 1797*, which contains additional information, but this document has limited circulation.)

The military specification defines airplane classes, flight phases, and flying qualities levels, so that different modes can be specified for the various combinations. These are defined in Table 4.3-2; the flying qualities levels are linked to the Cooper-Harper ratings as shown in Table 4.3-1. The specifications for the aircraft modes are as follows.

**TABLE 4.3-2 Definitions—Flying Qualities Specifications***Airplane Classes*

- Class I: Small, light airplanes.  
 Class II: Medium weight, low-to-medium-maneuverability airplanes.  
 Class III: Large, heavy, low-to-medium-maneuverability airplanes.  
 Class IV: High-maneuverability airplanes.

*Flight Phases*

- Category A: Nonterminal flight phases generally requiring rapid maneuvering.  
 Category B: Nonterminal flight phases normally accomplished using gradual maneuvers without precision tracking, although accurate flight-path control may be required.  
 Category C: Terminal flight phases normally accomplished using gradual maneuvers and usually requiring accurate flight-path control.

*Flying Qualities Levels*

- Level 1: Flying qualities adequate for the mission flight phase.  
 Level 2: Flying qualities adequate to accomplish the mission flight phase, but some increase in pilot workload or degradation in mission effectiveness exists.  
 Level 3: Flying qualities such that the airplane can be controlled safely, but pilot workload is excessive, or mission effectiveness is inadequate, or both.

**Phugoid Specifications** The military specification dictates that for the different levels of flying qualities the damping  $\zeta_p$  and natural frequency  $\omega_{n_p}$  of the phugoid mode will satisfy the following requirements:

$$\text{Level 1: } \zeta_p \geq 0.04$$

$$\text{Level 2: } \zeta_p \geq 0.0$$

$$\text{Level 3: } T_{2p} \geq 55.0 \text{ s}$$

In the level-3 requirement the mode is assumed to be unstable, and  $T_2$  denotes the time required for the mode to double in amplitude. For an exponentially growing sinusoidal mode this time is given by

$$T_2 = \log_e 2 / (-\zeta \omega_n) \quad (\zeta \text{ has negative values})$$

These requirements apply with the pitch control free or fixed; they need not be met transonically in certain cases.

**Short-Period Specifications** The short-period requirements are specified in terms of the natural frequency and damping of the “short-period mode” of the equivalent low-order system (as defined earlier). The adequacy of the equivalent system

**TABLE 4.3-3a Short-Period Damping Ratio Limits**

Level	Cat. A & C Flight Phases		Cat. B Flight Phases	
	Minimum	Maximum	Minimum	Maximum
1	0.35	1.30	0.30	2.00
2	0.25	2.00	0.20	2.00
3	0.15*	no limit	0.15*	no limit

\*May be reduced at altitude > 20,000 ft with approval.

**TABLE 4.3-3b Limits on  $\omega_{n_{sp}}^2 / (n/\alpha)$**

Level	Cat. A Phases		Cat. B Phases		Cat. C Phases	
	Min.	Max.	Min.	Max.	Min.	Max.
1	0.28	3.60	0.085	3.60	0.16	3.60
	$\omega_n \geq 1.0$				$\omega_n \geq 0.7$	
2	0.16	10.0	0.038	10.0	0.096	10.0
	$\omega_n \geq 0.6$				$\omega_n \geq 0.4$	
3	0.16	no limit	0.038	no limit	0.096	no limit

There are some additional limits on the minimum value of  $n/\alpha$  and the minimum value of  $\omega_n$  for different classes of airplane in category C.

approximation is to be judged by the procuring agency. Table 4.3-3a shows the requirements on the equivalent short-period damping ratio  $\zeta_{sp}$ .

The requirements on equivalent undamped natural frequency ( $\omega_{n_{sp}}$ ) are given in Table 4.3-3b and are specified indirectly, in terms of the quantity  $\omega_{n_{sp}}^2 / (n/\alpha)$ . The denominator ( $n/\alpha$ ) of this term is the aircraft load factor response to angle of attack in  $g$ 's per radian, as explained in the subsection on pole-zero specifications.

**Roll-Mode Specifications** The maximum allowable value of the roll-subsidence-mode time constant is given in Table 4.3-4. In addition to these time constant specifications there is a comprehensive set of requirements on the time required to achieve various (large) changes in roll angle following an abrupt roll command. For example, for air-to-air combat (a flight phase within category A for class IV airplanes) the minimum allowable time to achieve a certain roll angle depends on airspeed, but for level-1 flying qualities may be as short as 1.0 s for 90° roll and 2.8 s for 360° roll.

**Spiral-Mode Specifications** The spiral mode is allowed to be unstable, but limits are placed on the minimum time for the mode to double in amplitude, as shown in Table 4.3-5. These requirements must be met following a roll angle disturbance of up to 20° from trimmed-for-zero-yaw-rate wings-level flight, with the cockpit controls free.

**TABLE 4.3-4 Maximum Roll-Mode Time Constant (s)**

Flight Phase Category	Class	Level		
		1	2	3
A	I, IV	1.0	1.4	no limit
	II, III	1.4	3.0	no limit
B	All	1.4	3.0	10
C	I, II-C, IV	1.0	1.4	no limit
	II-L, III	1.4	3.0	no limit

**TABLE 4.3-5 Spiral-Mode Minimum Doubling Time**

Flight Phase Category	Level 1	Level 2	Level 3
A & C	12 s	8 s	4 s
B	20 s	8 s	4 s

**TABLE 4.3-6 Dutch-Roll-Mode Specifications**

Level	Flight Phase Category	Class	min $\zeta_d$	min $\zeta_d \omega_{n_d}$	min $\omega_{n_d}$
1	A	I, IV	0.19	0.35	1.0
		II, III	0.19	0.35	0.4
	B	all	0.08	0.15	0.4
	C	I, II-C, IV	0.08	0.15	1.0
		II-L, III	0.08	0.15	0.4
2	all	all	0.02	0.05	0.4
3	all	all	0.02	no limit	0.04

**Dutch-Roll-Mode Specifications** The frequency  $\omega_{n_d}$  and damping ratio  $\zeta_d$  of the dutch roll mode must exceed the minimum values given in Table 4.3-6. Note that the quantity  $\zeta \omega_n$  is the  $s$ -plane real-axis coordinate of the roots, and  $\omega_n$  is the radial distance from the origin for complex roots. Therefore, these requirements define an area of the  $s$ -plane in which the dutch roll roots must lie.

The lower limit on  $\zeta_d$  is the larger of the two values that come from the table, except that a value of 0.7 need not be exceeded for class III. Also, class III airplanes may be exempted from some of the minimum  $\omega_d$  requirements. Airplanes that have a large amount of roll-yaw coupling, as measured by the ratio of the maximum roll angle to the maximum value of sideslip in a dutch roll oscillation, are subject to a more stringent requirement on  $\zeta_d \omega_{n_d}$  (see *MIL-F-8785C*).



The military requirements document specifies dynamic response mainly through the pole-zero requirements. These have been summarized here so that the reader may evaluate some of the controller designs described later. Much additional information covering other aspects of flying qualities is available in the requirements document, and it is essential reading for anyone with other than a casual interest in this field.

#### 4.4 STABILITY AUGMENTATION

Most high-performance commercial and military aircraft require some form of stability augmentation. Some military aircraft are actually unstable and would be virtually impossible to fly without an automatic control system. The SAS typically uses sensors to measure the body-axes angular rates of the vehicle and feeds back processed versions of these signals to servomechanisms that drive the aerodynamic control surfaces. In this way an aerodynamic moment proportional to angular velocity and its derivatives can be generated and used to produce a damping effect on the motion. If the basic mode is unstable or if it is desired to change both damping and natural frequency independently, additional feedback signals will be required, as we will see.

Stability augmentation systems are conventionally designed separately for the longitudinal dynamics and the lateral-directional dynamics, and this is made possible by the decoupling of the aircraft dynamics in most flight conditions. In the next two subsections aircraft model dynamics will be used to describe the design of the various augmentation systems.

##### Pitch-Axis Stability Augmentation

The purpose of a pitch SAS is to provide satisfactory natural frequency and damping for the short-period mode. This mode involves the variables alpha and pitch rate; feedback of these variables to the elevator actuator will modify the frequency and damping. Figure 4.4-1 shows the arrangement; if the short-period mode is lightly damped but otherwise adequate, only pitch-rate feedback is required. If the frequency and damping are both unsatisfactory or the mode is unstable, alpha feedback is necessary. The phugoid mode will be largely unaffected by this feedback. Outer feedback

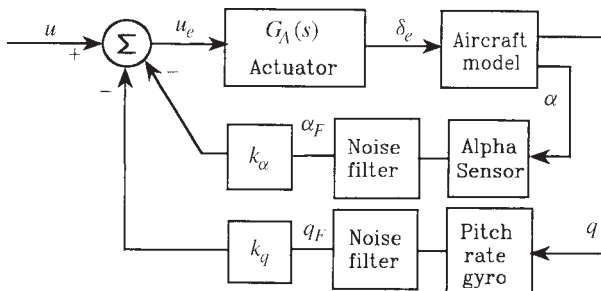


Figure 4.4-1 Pitch-axis stability augmentation.

control loops will often be closed around the pitch SAS to provide, for example, autopilot functions. Automatic adjustment of the augmentation (inner) loop feedback gains may be arranged when the outer feedback loops are engaged, so that the overall performance is optimal.

A physical understanding of the effect of alpha feedback follows from the explanation of pitch stiffness in Chapter 2. A statically unstable aircraft has a pitching moment curve with a positive slope over some range(s) of alpha. If perturbations in alpha are sensed and fed back to the elevator servo to generate a restoring pitching moment, the slope of the pitching moment curve can be made more negative in the region around the operating angle of attack. Furthermore, the overall pitching moment curve and the trimmed elevator deflection will not be affected, thus preserving the trim-drag and maneuverability characteristics that the designer built into the basic airplane design.

The angle-of-attack measurement may be obtained from the pitot-static air data system, or a small “wind vane” mounted on the side of the aircraft forebody and positioned (after much testing and calibration) to measure alpha over a wide range of flight conditions. Two sensors may be used, on opposite sides of the aircraft, to provide redundancy and possibly to average out measurement errors caused by sideslipping. In addition, it may be necessary to compute (in real time) a “true” angle of attack from the “indicated angle of attack,” airspeed, and Mach number, in order to relate the freestream angle of attack of the airframe to the direction of the flowfield at the sensor position. The signal from the alpha sensor is usually noisy because of turbulence, and a noise filter is used to reduce the amount of noise injected into the control system.

Alpha feedback is avoided if possible because of the difficulty of getting an accurate, rapidly responding, noise-free measurement and because of the vulnerability of the sensor to mechanical damage. Noise from the alpha sensor can make it difficult to achieve precise pointing (e.g., for targeting), so the amount of alpha feedback is normally restricted.

The pitch-rate sensor is normally a mechanical gyroscopic device arranged to measure the (inertial) angular rate around the pitch axis. The location of the gyro must be chosen very carefully to avoid picking up the vibrations of the aircraft structure. At a node of an idealized structural oscillation there is angular motion but no displacement, and at an antinode the converse is true. Thus, the first choice for the rate gyro location is an antinode corresponding to the most important structural mode. Flight tests must then be used to adjust the position of the gyros. A bad choice of gyro locations can adversely affect handling qualities or, in extreme cases, cause oscillations in the flight control systems (AFWAL-TR-84-3105, 1984). The gyro filter shown in Figure 4.4-1 is usually necessary to remove noise and/or cancel structural-mode vibrations.

The sign convention that has been adopted in this book (see Chapter 3) means that a positive elevator deflection leads to a negative pitching moment. Therefore, for convenience, a phase reversal will be included between the elevator actuator and the control surface in each example, so that the positive-gain root-locus algorithm can be used for design.

**Example 4.4-1: The Effects of Pitch Rate and Alpha Feedback** The longitudinal (four-state) Jacobian matrices for the F-16 model in the nominal flight condition in Table 3.6-3 are

$$\begin{aligned}
 A &= \begin{matrix} & v_T & \alpha & \theta & q \\ \begin{bmatrix} -1.9311E-02 & 8.8157E+00 & -3.2170E+01 & -5.7499E-01 \\ -2.5389E-04 & -1.0189E+00 & 0.0000E+00 & 9.0506E-01 \\ 0.0000E+00 & 0.0000E+00 & 0.0000E+00 & 1.0000E+00 \\ 2.9465E-12 & 8.2225E-01 & 0.0000E+00 & -1.0774E+00 \end{bmatrix} \end{matrix} \\
 B &= \begin{matrix} \delta_e \\ \begin{bmatrix} 1.7370E-01 \\ -2.1499E-03 \\ 0.0000E+00 \\ -1.7555E-01 \end{bmatrix} \end{matrix} \quad (1) \\
 C &= \begin{bmatrix} 0.000000E+00 & 5.729578E+01 & 0.000000E+00 & 0.000000E+00 \\ 0.000000E+00 & 0.000000E+00 & 0.000000E+00 & 5.729578E+01 \end{bmatrix} \begin{matrix} \alpha \\ q \end{matrix}
 \end{aligned}$$

The single input is the elevator deflection,  $\delta_e$ , in degrees, and the two outputs are the appropriate feedback signals: alpha and pitch rate. The entries in the  $C$ -matrix are the conversions to units of degrees for consistency with the input.

Either of the two SISO transfer functions obtained from the coefficient matrices will exhibit the dynamic modes for this flight condition; the elevator-to-alpha transfer function is

$$\frac{\alpha}{\delta_e} = \frac{-0.1232(s + 75.00)(s + 0.009820 \pm j0.09379)}{(s - 0.09755)(s + 1.912)(s + 0.1507 \pm j0.1153)} \quad (2)$$

Unlike the transfer functions for stable cg positions (e.g.,  $x_{CG} = 0.3 \bar{c}$ ) in Chapter 3, this transfer function does not exhibit the usual phugoid and short-period poles. The pole at  $s \approx .098$  indicates an unstable exponential mode with a time constant of about 10 s. The complex pole pair corresponds to an oscillatory mode with a period of 33 s and damping ratio of 0.79; this is like a phugoid period with a short-period damping ratio. This mode is the “third oscillatory mode” of the statically unstable airplane (see Section Aircraft Rigid-Body Modes).

The modes described above obviously do not satisfy the requirements for good handling qualities, and providing continuous control of the unstable mode would be a very demanding job for a pilot. We will now show that alpha and pitch-rate feedback together will restore stability and provide virtually complete control of the position of the short-period poles.

The configuration shown in Figure 4.4-1 will be used with an alpha filter but, for simplicity, no pitch-rate filter. The actuator and alpha filter models are taken from the original F-16 model report (Nguyen et al., 1979) and are both simple-lag filters with

time constants  $\tau_a = 1/20.2$  s and  $\tau_F = 0.1$  s, respectively. The aircraft state-space model (1) augmented with these models, is

$$\dot{x} = \begin{bmatrix} & & & : & & : & 0 \\ & & & : & & : & 0 \\ & A & & : & -B & : & 0 \\ & & & : & & : & 0 \\ \hline 0 & 0 & 0 & 0 & : & -20.2 & : & 0 \\ 0 & 10.0 & 0 & 0 & : & 0 & : & -10.0 \end{bmatrix} \begin{bmatrix} v_T \\ \alpha \\ \theta \\ q \\ \hline x_a \\ x_F \end{bmatrix} + \begin{bmatrix} 0 \\ 0 \\ 0 \\ 0 \\ \hline 20.2 \\ 0 \end{bmatrix} u_e \quad (3a)$$

$$y = \begin{bmatrix} \alpha \\ q \\ \hline \alpha_F \end{bmatrix} = \begin{bmatrix} & C & & : & 0 & & 0 \\ & & & : & 0 & & 0 \\ \hline 0 & 0 & 0 & 0 & : & 0 & 57.29578 \end{bmatrix} x \quad (3b)$$

Notice that the original state equations are still satisfied and the original  $\delta_e$  input is now connected to the actuator state  $x_a$  through the phase reversal. The actuator is driven by a new input,  $u_e$ . Also, the  $\alpha$  filter is driven by the  $\alpha$  state of the aircraft dynamics, and an additional output has been created so that the filtered signal  $\alpha_F$  is available for feedback. These state equations could also have been created by simulating the filters as part of the aircraft model and running the linearization program again. In the rest of this chapter the augmented matrices will be created by the MATLAB “series” command, as used in Chapter 3.

The state equations (3) can now be used to obtain the loop transfer functions needed for root-locus design. In the case of the innermost (alpha) loop, we already know that the  $\alpha$ -loop transfer function will consist of Equation (2) with the two lag filters in cascade, and the effect of the feedback  $k_\alpha$  can be anticipated using a sketch of the pole and zero positions. The goal of the alpha feedback is to pull the unstable pole, at  $s = 0.098$ , back into the left-half  $s$ -plane. Let the augmented coefficient matrices in Equation (3) be denoted by  $aa$ ,  $ba$ , and  $ca$ . Then the following MATLAB commands can be used to obtain the root locus:

```
k= logspace(-2,1,2000);
r= rlocus(aa,ba,ca(3,:),0,k);    % 3rd row of C
plot(r)
grid on
axis([-20,1,-10,10])
```

Figures 4.4-2a and b show the root-locus plot for the inner loop on two different scales. The expanded scale near the origin (Figure 4.4-2b) shows that the effect of the alpha feedback is to make the loci from the third-mode poles come together on the real axis (near  $s = -0.2$ ). The branch going to the right then meets the locus coming from the unstable pole, and they leave the real axis to terminate on the complex zeros near the origin. This provides a pair of closed-loop poles that correspond to a

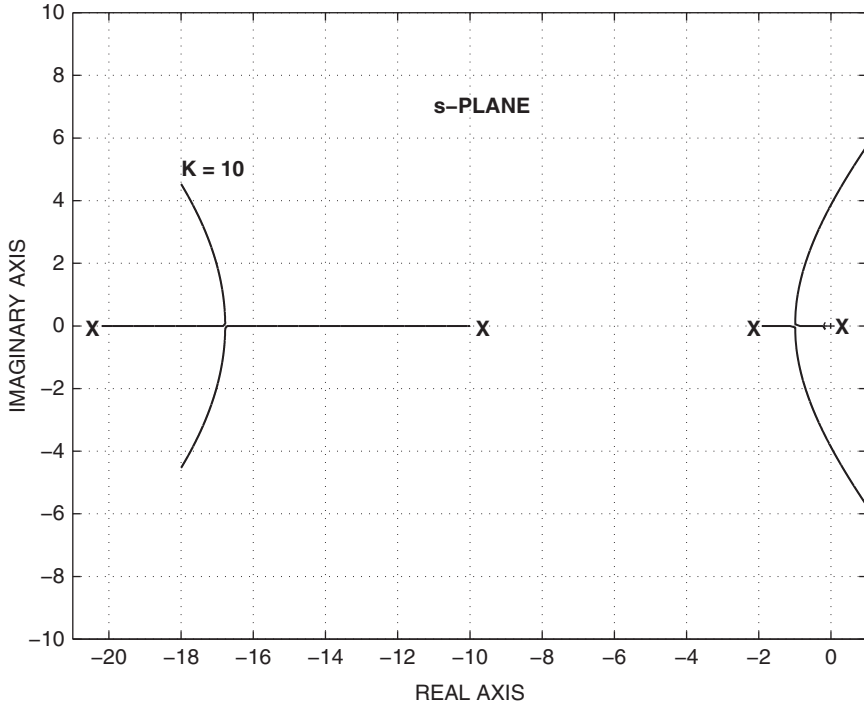


**Figure 4.4-2a** Inner-loop root-locus plot for pitch SAS.

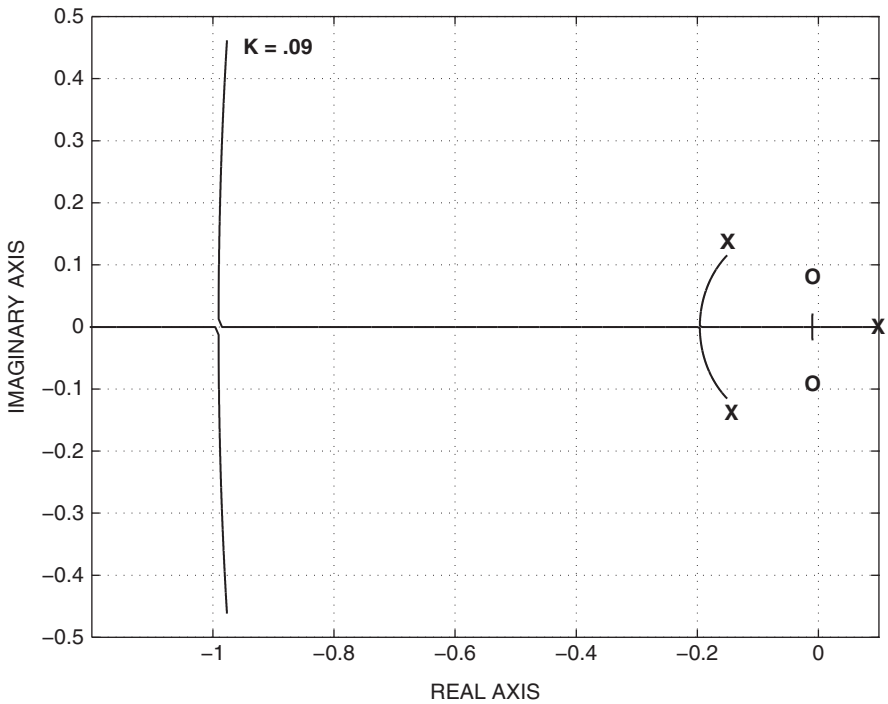


**Figure 4.4-2b** Expanded inner-loop root-locus plot for pitch SAS.

phugoid mode. The left branch from the third-mode poles meets the locus from the pole at  $s = -1.9$ , and they leave the axis near  $s = -1$  to form a short-period mode. Alpha feedback has therefore produced the anticipated effect: The aircraft is stable with conventional longitudinal modes.

The larger-scale plot (Figure 4.4-2a) shows that as the magnitude of the alpha feedback is increased, the frequency of the new short-period poles increases and they move toward the right-half plane. The movement toward the right-half plane is in accordance with the constant net damping rule and the filter and actuator poles moving left. A slower (less expensive) actuator would place the actuator pole closer to the origin and cause the short-period poles to have a lower frequency at a given damping ratio. The position of the short-period poles for  $k_\alpha = 0.5$  is  $-0.70 \pm j2.0$ . At this position the natural frequency is about 2.2 rad/s, which is acceptable according to the flying qualities requirements, but the damping ratio ( $\zeta = 0.33$ ) is quite low.

A root-locus plot will now show the effect of varying  $k_q$ , with  $k_\alpha$  fixed at 0.5. The following MATLAB commands can be used:

```
ac1= aa- ba*k_alpha*ca(3,:);          % Choose k_alpha
% [z,p,k]= ss2zp(ac1,ba,ca(2,:),0)    % q/u transf. fn
r= rlocus(ac1,ba,ca(2,:),0);
plot(r)
```

The  $q/u$  transfer function with  $k_\alpha = 0.5$  and  $k_q = 0$  is

$$\frac{q}{u} = \frac{203.2s(s + 10.0)(s + 1.027)(s + 0.02174)}{(s + 20.01)(s + 10.89)(s + 0.6990 \pm j2.030)(s + 0.008458 \pm j0.08269)} \quad (4)$$

Note that the zeros of this transfer function are the  $1/T_{\theta_1}$  and  $1/T_{\theta_2}$  unaugmented open-loop zeros, with the addition of a zero at  $s = -10$ . This zero has appeared because of the MIMO dynamics (two outputs, one input). It originally canceled the alpha filter pole out of the pitch-rate transfer function, but the inner-loop feedback has now moved the alpha filter pole to  $s = -10.89$ .

Figure 4.4-3 shows the root-locus plot for variable  $k_q$ . The phugoid poles move very slightly but are not visible on the plot. The short-period poles follow a circular arc around  $s = -1$  (roughly constant natural frequency) as the pitch-rate feedback is increased. The poles become real for quite low values of  $k_q$  and, with larger values, a new higher-frequency oscillatory mode is created by the filter and actuator poles. Such a mode would be objectionable to the pilot, and we look for lower values of  $k_q$  that make the short-period poles match the flying qualities requirements, with no additional oscillatory mode. The value  $k_q = 0.25$  places the short-period poles at  $s = -2.02 \pm j1.94$ . This corresponds to a natural frequency of 2.8 rad/s and a damping ratio of  $\zeta = 0.72$ . The corresponding closed-loop transfer function for pitch rate is given by

$$\frac{q}{u} = \frac{203.2s(s + 10.0)(s + 1.027)(s + 0.02174)}{(s + 16.39)(s + 11.88)(s + 2.018 \pm j1.945)(s + 0.008781 \pm j0.06681)} \quad (5)$$

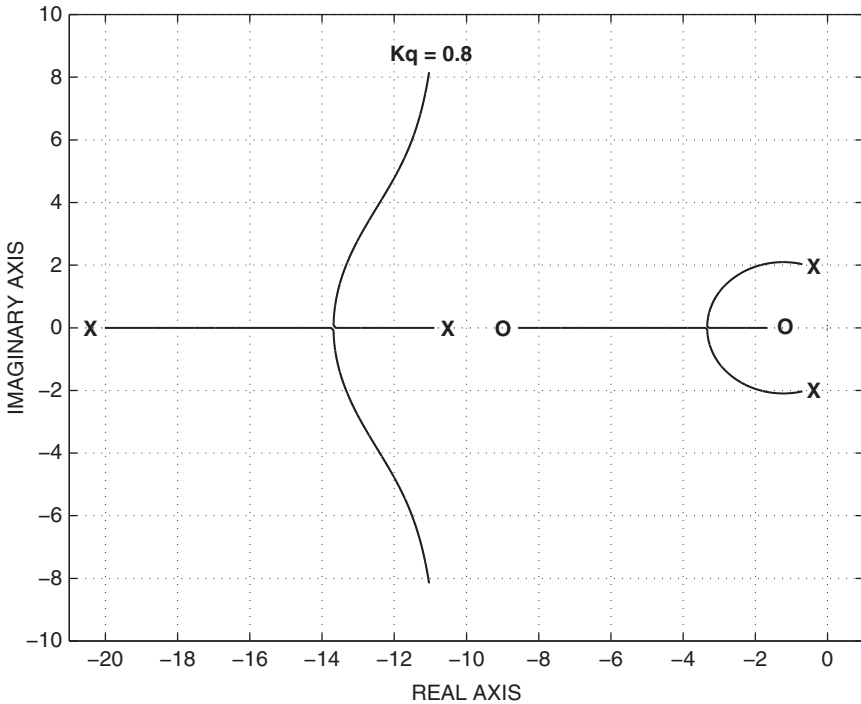


**Figure 4.4-3** Outer-loop root-locus plot for pitch SAS.

The original actuator pole has moved from  $s = -20.2$  to  $s = -16.39$ , and the  $\alpha$ -filter pole has moved from  $s = -10$  to  $s = -11.88$ . Apart from these factors, this transfer function is very similar to the stable-cg transfer function in Example 3.8-3 but with improved short-period pole positions. ■

Example 4.4-1 shows that alpha feedback stabilizes the unstable short-period mode and determines its natural frequency, while the pitch-rate feedback mainly determines the damping. The amount of alpha feedback needed to get a satisfactory natural frequency was  $0.5^\circ$  of elevator deflection per degree of alpha. The alpha signal is noisy and sometimes unreliable, and this large amount of alpha feedback is preferably avoided. In the second root-locus plot it can be seen that, as the pitch-rate feedback is varied, the locus of the short-period poles circles around the  $1/T_{\theta_2}$  zero. Therefore, by moving the zero to the left, a higher natural frequency can be achieved, or the same natural frequency can be achieved with less alpha feedback. This will be demonstrated in the next example.

**Example 4.4-2: A Pitch-SAS Design** The coefficient matrices  $aa$ ,  $bb$ ,  $cc$  from Example 4.4-1 are used again here, and the alpha feedback gain will be reduced to  $k_\alpha = 0.1$ . A lag compensator with a pole at  $s = -1$  and a zero at  $s = -3$  will be

cascaded with the plant to effectively move the  $1/T_{\theta_2}$  zero to  $s = -3$ . The MATLAB commands are

```
ac1= aa - ba*0.1*ca(3,:);           % Close alpha loop,  $K_\alpha=.1$ 
qfb= ss(ac1,ba,ca(2,:),0);          % SISO system for q f.b.
z=3; p=1;
lag= ss(-p,1,z-p,1);                % Lag compensator
csys= series(lag,qfb);               % Cascade Comp. before plant
[a,b,c,d]= ssdata(csys);
k= logspace(-2,0,2000);
r= rlocus(a,b,c,d,k);
plot(r)
grid on
axis([-20,1,-10,10])
```

The root-locus plot is the same shape as Figure 4.4-3, and when the pitch-rate feedback gain is  $k_q = 0.2$ , the closed-loop transfer function is

$$\frac{q}{u} = \frac{203.2s(s+10.0)(s+1.027)(s+0.0217)(s+3)}{(s+18.02)(s+10.3)(s+1.025)(s+1.98 \pm j2.01)(s+0.0107 \pm j0.0093)} \quad (1)$$

When the pole and zero close to  $s = -1$  are canceled out, this transfer function is essentially the same as in Example 4.4-1 except that there is a zero at  $s = -3$  instead of  $s = -1$ . This zero can be replaced by a zero at  $s = -1$  once again, by placing the lag compensator in the feedback path. However, a zero at  $s = -1$  produces a much bigger overshoot in the step response than the zero at  $s = -3$ . Therefore the flying qualities requirements on  $T_{\theta_2}$  should be checked (see Section The Handling Qualities Requirements) to obtain some guidance on the position of the zero.

This example shows that the same short-period mode, as in Example 4.4-1, can be achieved with much less alpha feedback and less pitch-rate feedback. Also, the transfer function (1) shows that no additional modes are introduced. A dynamic compensator is the price paid for this. Section 4.3 shows that the  $1/T_{\theta_2}$  zero will move with flight conditions, and so the compensator parameters may have to be changed with flight conditions. ■

## Lateral-Directional Stability Augmentation/Yaw Damper

Figure 4.4-4 shows the most basic augmentation system for the lateral-directional dynamics. Body-axis roll rate is fed back to the ailerons to modify the roll subsidence mode, and yaw rate is fed back to the rudder to modify the dutch roll mode (yaw damper feedback). The lateral (rolling) motion is not, in general, decoupled from the yawing and sideslipping (directional) motions. Therefore, the augmentation systems will be analyzed with the aid of the multivariable state equations (two inputs, ailerons and rudder, and two or more outputs), as implied by the figure. This analysis will be restricted to the simple feedback scheme shown in the figure; in a later section additional feedback couplings will be introduced between the roll and yaw channels.



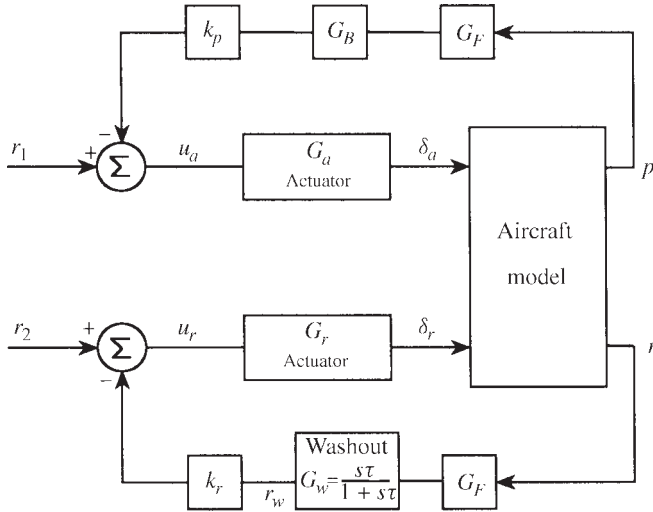


**Figure 4.4-4** Lateral-directional augmentation.

The purpose of the yaw damper feedback is to use the rudder to generate a yawing moment that opposes any yaw rate that builds up from the dutch roll mode. This raises a difficulty; in a coordinated steady-state turn the yaw rate has a constant nonzero value (see Table 3.6-3 and the subsection on turn coordination) which the yaw-rate feedback will try to oppose. Therefore, with the yaw damper operating, the pilot must apply larger than normal rudder pedal inputs to overcome the action of the yaw damper and coordinate a turn. This has been found to be very objectionable to pilots. A simple control system solution to the problem is to use “transient rate feedback,” in which the feedback signal is differentiated (approximately) so that it vanishes during steady-state conditions. The approximate differentiation can be accomplished with a simple first-order high-pass filter (see Table 3.3-1), called a “washout filter” in this kind of application.

In Figure 4.4-4,  $G_w$  is the washout filter, the transfer function  $G_a$  represents an equivalent transfer function for differential actuation of the left and right ailerons, and  $G_r$  is the rudder actuator. The transfer functions  $G_F$  represent noise filtering and any effective lag at the output of the roll-rate and yaw-rate gyros, and  $G_B$  is a *bending-mode filter*. The bending-mode filter is needed because the moments generated by the ailerons are transmitted through the flexible-beam structure of the wing, and their effect is sensed by the roll-rate gyro in the fuselage. The transfer function of this path corresponds to a general low-pass filtering effect, with resonances occurring at the bending modes of the wing. Because the wing bending modes are relatively low in frequency, they can contribute significant phase shift, and possibly gain changes, within the bandwidth of the roll-rate loop. The bending-mode filter is designed to compensate for these phase and gain changes.

To understand the purpose of the roll-rate feedback, consider the following facts. In Section 4.2 the variation of the roll time constant with flight conditions was

analyzed, and in Chapter 2 the change of aileron effectiveness with angle of attack was described. These effects cause large, undesirable variations in aircraft roll performance that result in the pilot flying the aircraft less precisely. Closed-loop control of roll rate is used to reduce the variation of roll performance with flight conditions.

While the roll time constant is a feature of the linear small-perturbation model and gives no indication of the maximum roll rate or time to roll through a large angle, it is relevant to the initial speed of response and control of smaller-amplitude motion. Figure 4.4-5 shows a plot of the reciprocal of the F-16 roll time constant versus alpha and indicates that this time constant may become unacceptably slow at high angles of attack. The plot was derived by trimming the F-16 model in straight and level flight at sea level, with the nominal cg position, over a range of speeds. At angles of attack greater than about  $20^\circ$  the roll pole coupled with the spiral pole to form a complex pair.

Landing approach takes place at a relatively high angle of attack, and the roll-rate feedback may be needed to ensure good roll response. Also, satisfactory damping of the dutch roll mode is particularly important during landing approach in gusty crosswind conditions. Our F-16 model does not include flaps and landing gear, so the design of the augmentation loops will simply be illustrated on a low-speed, low-altitude flight condition. If we take the F-16 model dynamics at zero altitude,

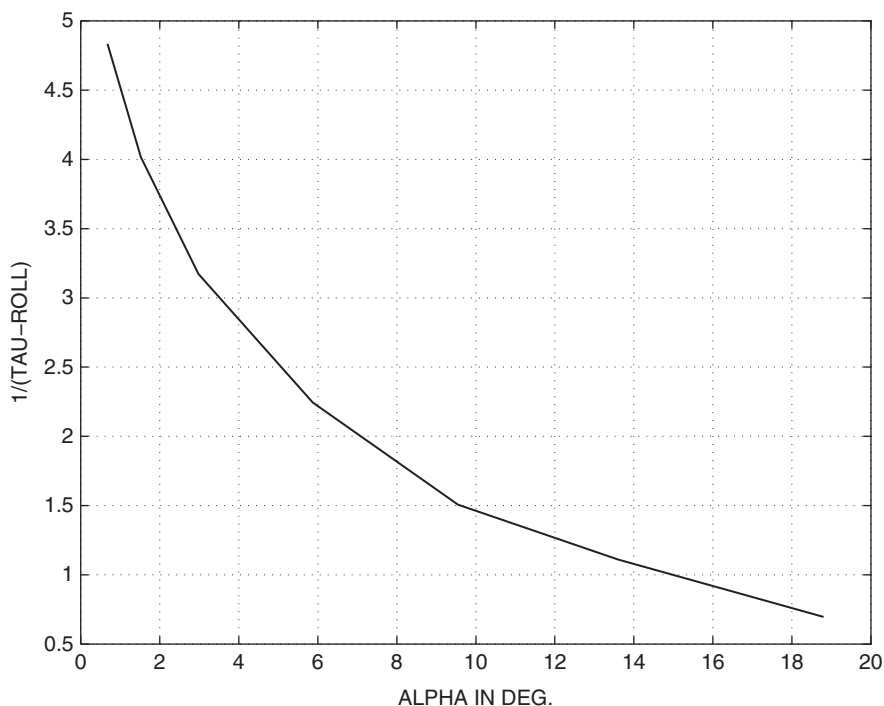


**Figure 4.4-5** F-16 model roll time constant versus alpha in degrees.

with the nominal cg position and an airspeed of 205.0 ft/s ( $\alpha = 18.8^\circ$ ), the roll pole is real and quite slow ( $\tau = 1.44$  s), and the dutch roll is very lightly damped ( $\zeta = 0.2$ ). The state equations can be found by linearization, and a five-state set of lateral-directional equations can be decoupled from the full thirteen-state set. The coefficient matrices are found to be

$$A = \begin{bmatrix} \beta & \phi & \psi & p & r \\ -0.13150 & 0.14858 & 0.0 & 0.32434 & -0.93964 \\ 0.0 & 0.0 & 0.0 & 1.0 & 0.33976 \\ 0.0 & 0.0 & 0.0 & 0.0 & 1.0561 \\ -10.614 & 0.0 & 0.0 & -1.1793 & 1.0023 \\ 0.99655 & 0.0 & 0.0 & -0.0018174 & -0.25855 \end{bmatrix}$$

$$B = \begin{bmatrix} \delta_a & \delta_r \\ 0.00012049 & 0.00032897 \\ 0.0 & 0.0 \\ 0.0 & 0.0 \\ -0.1031578 & 0.020987 \\ -0.0021330 & -0.010715 \end{bmatrix} \quad (4.4-1a)$$

$$C = \begin{bmatrix} 0.0 & 0.0 & 0.0 & 57.29578 & 0.0 \\ 0.0 & 0.0 & 0.0 & 0.0 & 57.29578 \end{bmatrix} \begin{matrix} p \\ r \end{matrix} \quad D = \begin{bmatrix} 0 & 0 \\ 0 & 0 \end{bmatrix} \quad (4.4-1b)$$

The null column in the  $A$ -matrix shows that the state  $\psi$  is not coupled back to any other states, and it can be omitted from the state equations when designing an augmentation system. The  $C$ -matrix has been used to convert the output quantities to degrees, to match the control surface inputs. The transfer functions of primary interest are

$$\frac{p}{\delta_a} = \frac{-5.911(s - 0.05092)(s + 0.2370 \pm j1.072)}{(s + 0.06789)(s + 0.6960)(s + 0.4027 \pm j2.012)} \quad (4.4-2)$$

$$\frac{r}{\delta_a} = \frac{-0.1222(s + 0.4642)(s + 0.3512 \pm j4.325)}{(s + 0.06789)(s + 0.6960)(s + 0.4027 \pm j2.012)} \quad (4.4-3)$$

$$\frac{p}{\delta_r} = \frac{+1.202(s - 0.05280)(s - 2.177)(s + 1.942)}{(s + 0.06789)(s + 0.6960)(s + 0.4027 \pm j2.012)} \quad (4.4-4)$$

$$\frac{r}{\delta_r} = \frac{-0.6139(s + 0.5078)(s + 0.3880 \pm j1.5439)}{(s + 0.06789)(s + 0.6960)(s + 0.4027 \pm j2.012)} \quad (4.4-5)$$

The dutch roll poles are not canceled out of the  $p/\delta_a$  transfer function by the complex zeros. Therefore, coupling exists between the rolling and yawing motions, and the dutch roll mode will involve some rolling motion. These transfer functions validate the decision to use the MIMO state equations for the analysis. At lower angles of

attack the dutch roll poles will typically be largely canceled out of the  $p/\delta_a$  transfer function, leaving only the roll subsidence and spiral poles.

The two roll-rate transfer functions given above contain NMP zeros close to the origin. This is because gravity will cause the aircraft to begin to sideslip as it rolls. Then, if the dihedral derivative  $C_{l\beta}$  is negative (positive roll stiffness), the aircraft will have a tendency to roll in the opposite direction. This effect will be more pronounced in a slow roll when the sideslip has a chance to build up.

The rudder-to-roll-rate transfer function has another NMP zero farther away from the origin, corresponding to faster-acting NMP effects. A positive deflection of the rudder directly produces a positive rolling moment (see Table 3.5-1) and a negative yawing moment. The negative yawing moment rapidly leads to positive sideslip, which will in turn produce a negative rolling moment if the aircraft has positive roll stiffness. This effect tends to cancel the initial positive roll, and the NMP zero is the transfer function manifestation of these competing effects.

**Example 4.4-3: A Roll Damper/Yaw Damper Design** In Figure 4.4-4 the aileron and rudder actuators will be taken as simple lags with a corner frequency of 20.2 rad/s (as in the original model), and the bending mode filter will be omitted. The coefficient matrices for the plant will be (4.4-1) with the  $\psi$  state removed and denoted by  $ap$ ,  $bp$ ,  $cp$ ,  $dp$ . Positive deflections of the control surfaces lead to negative values for the principal moments (Table 3.5-1) so, in order to use the positive-gain root locus for design, we will insert a phase reversal at the output of the control surface actuators (in the  $C$ -matrix). The aileron and rudder actuators will be combined into one two-input, two-output state model and cascaded with the plant as follows:

```
aa= [-20.2 0; 0 -20.2];      ba= [20.2 0; 0 20.2];      % Actuator
ca= [-1 0; 0 -1];           da= [0 0; 0 0];           % SIGN CHANGE
actua= ss(aa,ba,ca,da);      % u1=  $\delta_a$ , u2=  $\delta_r$ 
plant= ss(ap,bp,cp,dp);      % x1=beta, x2=phi, x3=p, x4=r
sys1 = series(actua,plant);   % y1=p, y2=r (degrees)
```

The washout filter will be incorporated in a two-input, two-output model, with the first input-output pair being a direct connection:

```
aw= [-1/ $\tau_w$ ];              bw= [0 1/ $\tau_w$ ];              %  $\tau_w$  to be defined
cw= [0;-1];                 dw= [1 0; 0 1];              % y1=p y2=washed-r
wash= ss(aw,bw,cw,dw);
sys2= series(sys1,wash);     % x1=wash, x2=beta, ..., x6=ail, x7=rdr
```

The washout filter time constant is a compromise; too large a value is undesirable since the yaw damper will then interfere with the entry into turns. The following root-locus design plots can also be used to show that too small a value will reduce the achievable dutch roll damping (see Problem 4.4-3). The time constant is normally of the order of 1 s, and  $\tau_w = 1.0$  s is used here.

Experience shows that the roll damping loop is the less critical loop, and it is conveniently closed first. The  $p/u_a$  transfer function is the same as (4.4-2) with an

additional pole at  $s = -20.2$  and the static loop sensitivity changed to 119 (i.e., 20.2 times the original value of 5.91). The MATLAB commands to obtain a root-locus plot and to close the loop are:

```
[a,b,c,d]= ssdata(sys2);
k= linspace(0, .9, 3000);
r= rlocus(a,b(:,1),c(1,:),0,k);
plot(r) % Roll channel root locus
grid on
axis([-12,1,-5,5])
```

Figure 4.4-6 is the root-locus plot for positive  $k_p$ . It shows that the feedback has had the desired effect of speeding up the roll subsidence pole, which moves to the left in the  $s$ -plane and eventually combines with the actuator pole to form a complex pair. The spiral pole (not visible) moves a little to the right toward the NMP zero at  $s = 0.05$ , and the dutch roll poles change significantly as they move toward the open-loop complex zeros. If the feedback gain is made too high in this design, it will be found to be excessive at lower angles of attack. Furthermore, a high value will simply cause the aileron actuators to reach their rate and deflection limits more rapidly, as they become less effective at the higher angles of attack. A feedback gain

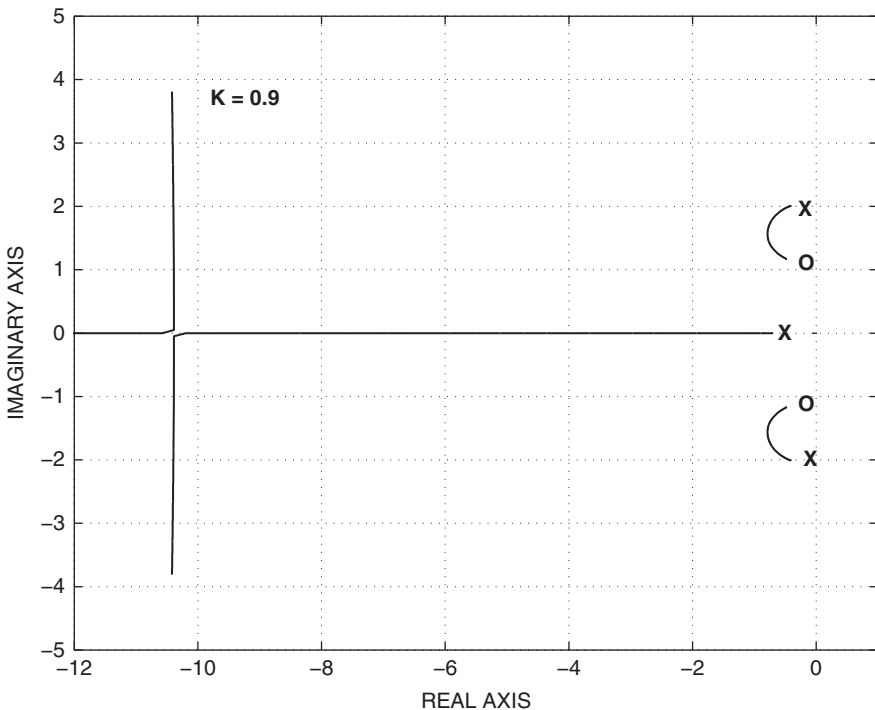


Figure 4.4-6 Root-locus plot for the roll damping loop.

of  $k_p = 0.2$  puts the roll subsidence pole at  $s = -1.37$ , which is about twice as fast as the open-loop value. This is a suitable starting value for investigating the effect of closing the yaw damper loop:

```
ac11= a - b(:,1)*kp*c(1,:);           % Close roll loop
[z,p,kl]= ss2zp(ac11,b(:,2),c(2,:),0) % Yaw tr. fn. + wash
r= rlocus( ac11,b(:,2),c(2,:),0,k);
plot(r)                                % Yaw channel root locus
```

The transfer function  $r_w/u_r$  (with  $k_p = 0.2$ ) is

$$\frac{r_w}{u_r} = \frac{12.40s(s + 18.8)(s + 0.760)(s + 0.961 \pm j0.947)}{(s + 1)(s + 18.9)(s + 1.37)(s + 0.0280)(s + 20.2)(s + 0.752 \pm j1.719)} \quad (1)$$

A root-locus plot for closing the yaw-rate loop through the feedback gain  $k_r$  is shown in Figure 4.4-7. Although not shown in the figure, one of the actuator poles is effectively canceled by the zero at  $s = -18.8$ ; the remaining actuator pole moves to the right to meet the roll pole and form a new complex pair. As the magnitude of  $k_r$  is increased, the spiral pole moves slightly closer to the washout zero at the origin, and the washout pole moves toward the zero at  $s = -0.76$ . At first the dutch roll poles

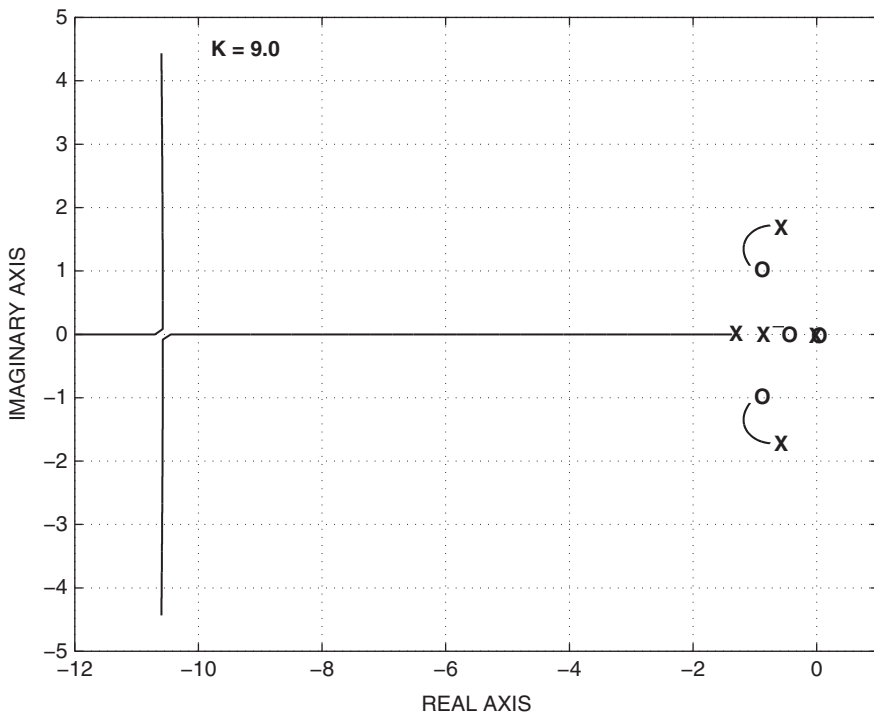


Figure 4.4-7 Root-locus plot for the yaw-rate loop.

move around an arc of constant natural frequency (approximately), and increasing damping ratio, toward the complex zeros. After  $k_r$  reaches about 3.5, the natural frequency begins to decrease and the damping ratio tends to remain constant. This feedback gain was considered to be the optimum value for the dutch roll poles, and so the yaw-rate loop was closed:

```
ac12= a - b* [.2 0; 0 3.5]*c;
[z,p,k1]= ss2zp(ac12,b(:,1),c(1,:),0) % c.l. roll-rate t.f.
```

The principal transfer functions were found to be

$$\frac{p}{r_1} = \frac{119.4(s + 17.4)(s - 0.0502)(s + 3.74)(s + 0.262 \pm j0.557)}{(s + 18.7)(s + 17.7)(s + 0.0174)(s + 3.29)(s + 0.861)(s + 1.18 \pm j1.33)} \quad (2)$$

$$\frac{r}{r_2} = \frac{12.4(s + 18.8)(s + 1.00)(s + 0.760)(s + 0.961 \pm j0.947)}{(s + 17.7)(s + 18.7)(s + 3.29)(s + 0.861)(s + 0.0174)(s + 1.18 \pm j1.33)}, \quad (3)$$

where  $r_1$  and  $r_2$  are the roll-rate and yaw-rate reference inputs, as shown in Figure 4.4-4.

Transfer functions (2) and (3) show that the dutch roll poles and the washout pole (at  $s = -0.861$ ) do not cancel out of the  $p/r_1$  transfer function, so there is still strong coupling between the roll and yaw channels. The dutch roll natural frequency and damping ( $\omega_n = 1.78$  rad/s,  $\zeta = 0.67$ ) are now satisfactory, but the appearance of the relatively slow washout pole in the lateral dynamics may mean that the roll response is not much improved. Since we no longer have a simple dominant poles situation, a time response simulation is needed to assess the design. Before this is undertaken, the effect of a higher gain in the roll-rate loop will be considered.

If the roll-rate loop is closed, with  $k_p = 0.4$ , the roll subsidence pole moves out to  $s = -3.08$ , and the zero in the yaw-rate loop transfer function (1) moves from  $s = -0.76$  to  $s = -3.40$ . This causes different behavior in the root-locus plot for the yaw-rate loop, as shown in Figure 4.4-8. The washout pole now moves to the left instead of the right. A comparison of Figures 4.4-7 and 4.4-8 shows that the price paid for this potential improvement in roll response is that the maximum dutch roll frequency is reduced. If the yaw-rate loop is closed with  $k_r = 1.3$ , to obtain the highest possible damped frequency for the dutch roll poles, the closed-loop transfer functions are

$$\frac{p}{r_1} = \frac{119.4(s + 19.27)(s + 1.74)(s - 0.0507)(s + 0.334 \pm j0.787)}{(s + 19.25)(s + 17.4)(s + 0.00767)(s + 2.82)(s + 1.57)(s + 0.987 \pm j0.984)} \quad (4)$$

$$\frac{r}{r_2} = \frac{12.40(s + 1.00)(s + 17.1)(s + 3.40)(s + 0.486 \pm j0.459)}{(s + 19.25)(s + 17.4)(s + 0.00767)(s + 2.82)(s + 1.57)(s + 0.987 \pm j0.984)} \quad (5)$$

The dutch roll frequency has decreased to  $\omega_n = 1.39$  rad/s, and the damping has increased to  $\zeta = 0.71$ ; these values still represent good flying qualities (see Table 4.3-6). An improvement in the roll response should have been obtained since the slow washout pole is nearly canceled by the zero at  $s = -1.74$ , and the roll

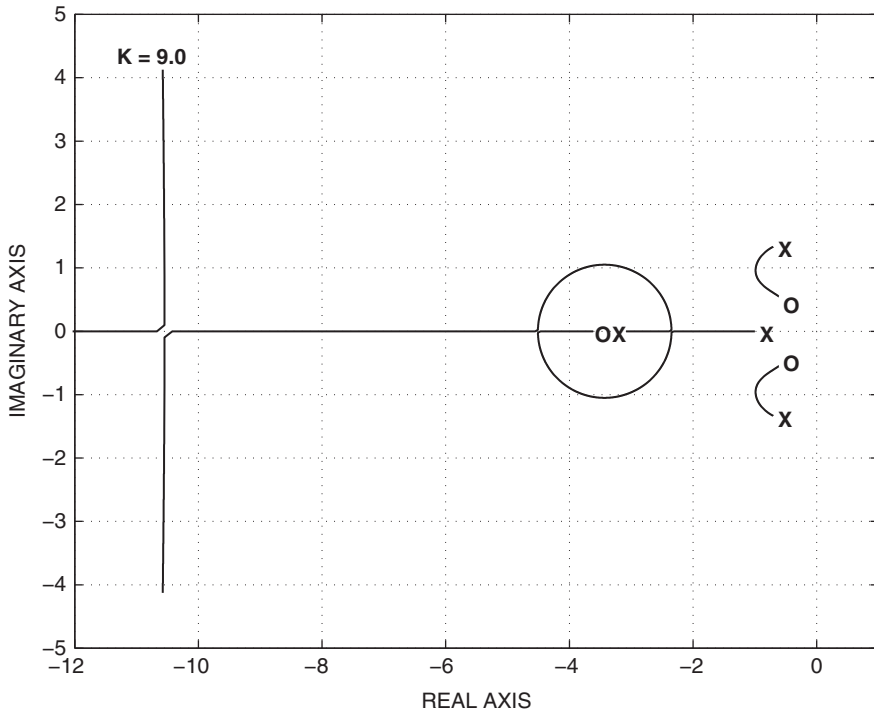


Figure 4.4-8 Alternate yaw-rate root locus.

subsidence pole (at  $s = -2.82$ ) may now dominate the roll response. Note the way in which one actuator pole almost cancels out of each transfer function. Also, in the yaw-rate response, note the zero at  $s = -1$  that originally canceled the washout pole. The transfer functions still show significant roll-yaw coupling.

The roll response of this design can only be assessed with a simulation, and because of the presence of the slow spiral pole in the transfer functions, a doublet pulse should be used as the input. The time responses were obtained by closing the yaw-rate and roll-rate loops with the feedback gains above ( $k_p = 0.4$ ,  $k_r = 1.3$ ) and using the following commands:

```
ac12= a - b*[.4 0; 0 1.3]*c;           % Close roll & yaw
t= [0:.02:10];                         % 501 points for plot
u= [-1.8*ones(1,51),1.8*ones(1,50),zeros(1,400)]'; % Doublet
[y,x]= lsim(ac12,b(:,1),c(1,:),0,u,t); % Linear simulation
plot(t,y,t,u)
grid on
```

Figure 4.4-9 compares the roll-rate response of the open-loop dynamics (augmented with the actuators) with the closed-loop response. The doublet input is negative for 1 s, positive for 1 s, then zero, with unit amplitude in the open-loop case. In the



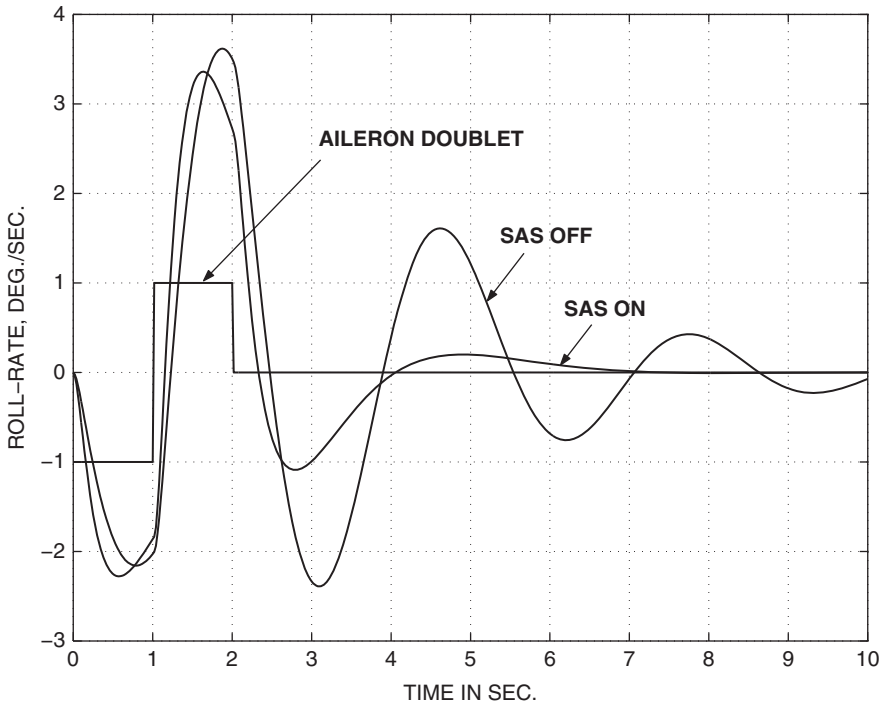


**Figure 4.4-9** Roll-rate response to an aileron doublet.

closed-loop case the overall gain is different, and the doublet was adjusted to  $1.8^\circ$  so that the responses were of similar amplitude. The figure exhibits the major improvement in the dutch roll damping and the small but significant improvement in the roll-rate speed of response. ■

This example indicates the difficulties of multivariable design when significant cross-coupling is present in the dynamics. It also shows the difficulty of obtaining a good roll response at low dynamic pressure and high  $\alpha$ . The design could be pursued further by investigating the effect of changing the washout time constant and using compensation networks, such as a phase lead, in the yaw-rate feedback loop. As pointed out earlier, increasing the bandwidth of the control loops may simply lead to saturation of the control surface actuators, and the limitations of the basic aircraft must be considered first.

## 4.5 CONTROL AUGMENTATION SYSTEMS

When an aircraft is under manual control (as opposed to autopilot control), the stability augmentation systems of the preceding section are, in most cases, the only automatic flight control systems needed. But in the case of high-performance military

aircraft, where the pilot may have to maneuver the aircraft to its performance limits and perform tasks such as precision tracking of targets, specialized CASs are needed. Flight control technology has advanced to the point where the flight control system (FCS) can provide the pilot with selectable “task-tailored control laws.” For example, although the role of a fighter aircraft has changed to include launching missiles from long range, the importance of the classical dogfight is still recognized. A dogfight places a premium on high maneuverability and “agility” (ability to change maneuvers quickly) in the aircraft and a control system that allows the pilot to take advantage of this maneuverability. In this situation a suitable controlled variable for the pitch axis is the *normal acceleration* of the aircraft. This is the component of acceleration in the negative direction of the body-fixed  $z$ -axis. It is directly relevant to performing a maximum-rate turn and must be controllable up to the structural limits of the airframe or the pilot’s physical limits. Therefore, for a dogfight, a “ $g$ -command” control system is an appropriate mode of operation of the flight control system. Other reasons for using this type of system will be described when we come to consider an example.

Another common mode of operation for a pitch-axis control augmentation system is as a pitch-rate command system. When a situation requires precise tracking of a target, by means of a sighting device, it has been found that a deadbeat response to pitch-rate commands is well suited to the task. Control of pitch rate is also the preferred system for approach and landing. Systems have been designed (Toles, 1985) which blend together the control of pitch rate and normal acceleration.

With respect to lateral-directional control, the most prevalent control augmentation system is a roll-rate command system. This system may be designed to roll the aircraft around its own velocity vector rather than the body axis. The reasons for this are described in the following sections.

### Pitch-Rate Control Augmentation Systems

Figure 4.5-1 is a block diagram of a pitch-rate CAS. Type-0 control is not very satisfactory because the control inputs to the plant may be quite large (e.g., several degrees of elevator deflection) while the gains in the error channel are not usually very high

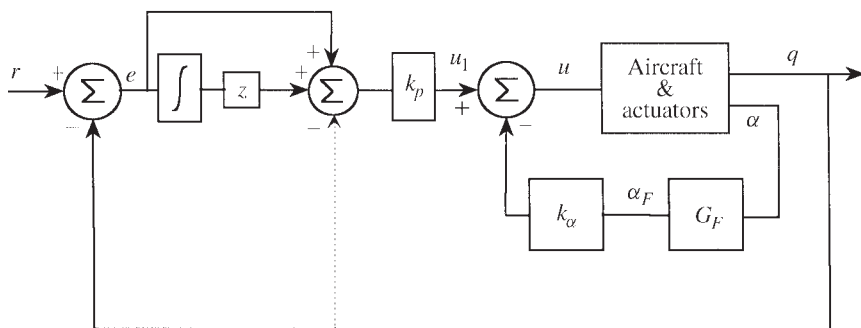


Figure 4.5-1 Pitch-rate control augmentation.

and entail large control errors. Therefore, proportional-plus-integral compensation is used to provide more precise control. Inner-loop alpha feedback is used, as in Example 4.4-1, when the pitch stiffness is inadequate.

The proportional path of the PI compensator can be replaced by an equivalent inner-loop pitch-rate feedback shown as a dotted line. This leaves the closed-loop poles unchanged but removes the PI zero from the closed-loop transfer function, thus reducing step-response overshoot [see Equation (3.9-24)]. It will be shown to be convenient to keep the PI zero while performing root-locus design.

The design of the pitch-rate CAS will now be illustrated by an example. It will be shown that the design can be performed on the short-period dynamics, but some caution must be used.

**Example 4.5-1: A Pitch-Rate CAS Design** The F-16 longitudinal dynamics corresponding to the nominal flight condition in Table 3.6-3 will be used once again. The  $A$ ,  $B$ ,  $C$  coefficient matrices are given in Example 4.4-1. These equations do not exhibit a short-period mode, but the  $\alpha$  and  $q$  equations are only loosely coupled to  $v_T$  and  $\theta$  and can be extracted as in Section 4.2. The final design will be verified on the complete dynamics. The elevator actuator and  $\alpha$ -filter dynamics will be those used in Section 4.4, and a sign change will be incorporated at the actuator output.

The design procedure will be to close the alpha loop, then inspect the actuator to pitch-rate transfer function and choose a position for the PI zero that is likely to yield a satisfactory root-locus plot. This procedure will be illustrated by MATLAB statements.

We first define the plant matrices, cascade the actuator and filter, and close the alpha feedback loop:

```
ap=[-1.0189 0.90506; 0.82225 -1.0774]; % x1= alpha x2=q
bp=[-2.1499E-3; -1.7555E-1]; % Elevator input
cp=[57.29578 0; 0 57.29578]; % y1= alpha, y2= q
dp=[0 0];
sysp= ss(ap,bp,cp,dp); % Plant
sysa= ss(-20.2, 20.2, -1, 0); % Actuator & SIGN CHANGE
[sys1]= series(sysa,sysp); % Actuator then Plant
sysf= ss(-10,[10 0],[1; 0],[0 0; 0 1]); % Alpha Filter
[sys2]= series(sys1,sysf); % Actuator+Plant+Filter
[a b c d]= ssdata(sys2); % Extract a,b,c,d
acl= a - b*[k $\alpha$  0]*c; % Close Alpha-loop
[z,p,k]= sszp(acl,b,c(2,:),0) % q/u1 transf. fn.
```

The filter has been defined with two inputs and two outputs, and one input-output pair is a direct connection so that  $q$  is available as output 2. When the inner-loop feedback gain  $k_\alpha$  is chosen, the zeros, poles, and gain of the  $q/u_1$  transfer function will be calculated.

The final design will be relatively slow unless the integrator pole can be moved well to the left or made to coincide with a zero. Some trial designs show that this demands a smaller amount of alpha feedback than that used in Example 4.4-1; this will be demonstrated by comparing two different values of  $k_\alpha$ .

Consider first the situation with  $k_\alpha = 0.20$ . The  $q/u_1$  transfer function is then given by

$$\frac{q}{u_1} = \frac{203.2(s + 10.0)(s + 1.029)}{(s + 10.38)(s + 20.13)(s + 0.8957 \pm j1.152)}$$

The behavior of the outer-loop root locus with the added PI compensator can now be anticipated. As  $k_p$  is varied, the integrator pole will move toward the zero at  $-1.029$ ; the compensator zero should be placed to the left of this zero, and the short-period poles will circle around the compensator zero. The following commands will add the PI compensator and plot the root loci:

```
sys3= ss(ac1,b,c,[0;0]);           % Alpha-loop closed
sysi= ss(0,3,1,1);                 % PI= (s+3)/s
sys4= series(sysi,sys3);            % x1=alpha-f,, x5= PI
[aa,bb,cc,dd]= ssdata(sys4);
k= linspace(0,.9,1000);
r= rlocus(aa,bb,cc(2,:),0,k);
plot(r)
axis([-16,0,-8,8])
grid on
```

The root locus is shown in Figure 4.5-2 for a compensator zero at  $s = -3.0$ . When  $k_p$  reaches about 0.5, the filter and actuator poles form a second complex pair, the integrator pole has moved to  $s = -0.91$ , and the short-period poles are at  $s = -3.2 \pm j3.4$ . Increasing  $k_p$  causes the second complex pair to quickly become less damped, while the integrator pole moves only slightly farther left. If the amount of alpha feedback is reduced, the integrator pole can be moved closer to the zero at  $s = -1.029$  before the second complex pole pair appears, while maintaining a satisfactory short-period pair.

The alpha feedback was eventually reduced to  $k_\alpha = 0.08$ , and the compensator zero was retained at  $s = -3.0$  with the intention of causing the short-period poles to pass near  $s = -4 \pm j3$  ( $\omega_n = 5, \zeta = 0.8$ ). The root-locus plot was the same shape as Figure 4.5-2. With  $k_p = 0.5$  the slow integrator pole reached  $s = -1.02$  and stopped moving left, the short-period poles reached  $s = -3.4 \pm j3$ , and the actuator and filter poles were still short of combining to form a complex pair. The closed-loop (unity-feedback) transfer function was

$$\frac{q}{r} = \frac{101.6(s + 3.00)(s + 10.0)(s + 1.029)}{(s + 10.7)(s + 13.7)(s + 1.02)(s + 3.43 \pm j3.03)}$$

This was considered to be a promising design and the closed-loop step response was simulated with the following code:

```
ac12= aa- bb*0.5*cc(2,:);          % close outer loop
sys= ss(ac12,0.5*bb,cc(2,:),0);     % unity feedback
step(sys,3)
```

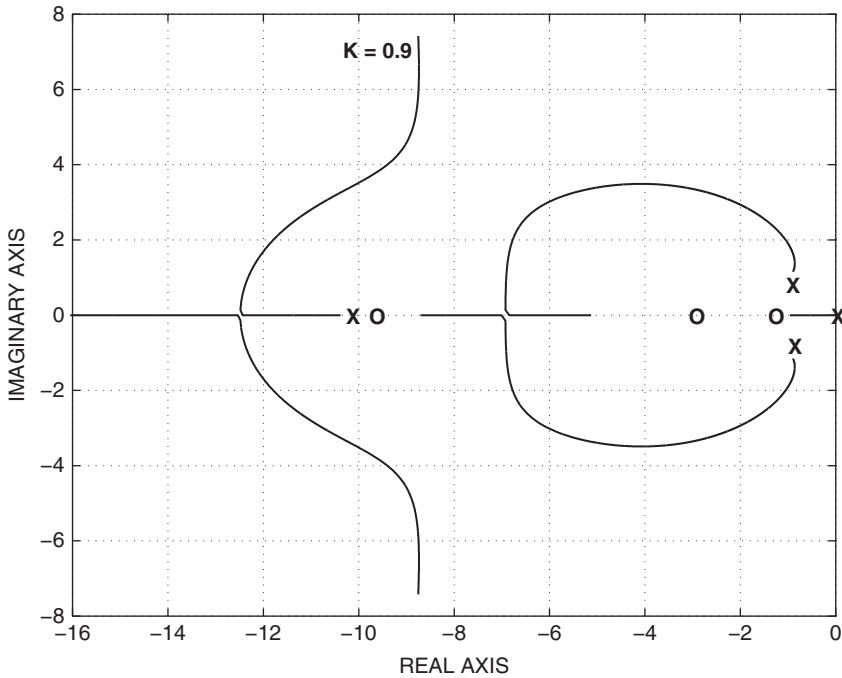


**Figure 4.5-2** Root-locus plot for the pitch-rate CAS.

Figure 4.5-3 shows the step response. This response has a fast rise time and a large overshoot (almost 20%) and does not satisfy the “deadbeat” requirement. The other curve shows the pitch-rate step response when the compensator zero is removed. The rise time is now longer, but the settling time is about the same and the overshoot is only about 2%. This is potentially a good design, and we will move on to apply the same feedback gains to the complete longitudinal dynamics.

When the feedback gains  $k_\alpha = 0.08$  and  $k_p = 0.5$  are used on the full dynamics given in Example 4.4-1, the closed-loop transfer function is

$$\frac{q}{r} = \frac{304.8(s + 10.0)(s + 1.027)(s + 0.02174)s}{(s + 10.75)(s + 13.67)(s + 1.016)(s + 3.430 \pm j3.032)(s + 0.02173)s}$$

Observe that this transfer function contains the subset of poles and zeros given by the short-period approximation and the phugoid mode has degenerated to two real poles with this small amount of alpha feedback. Also, the phugoid poles are canceled by zeros and so would play no part in the pitch-rate response in this case.

This example illustrates some of the features of a pitch-rate CAS. An actual design can only be optimized by careful comparison with the flying qualities

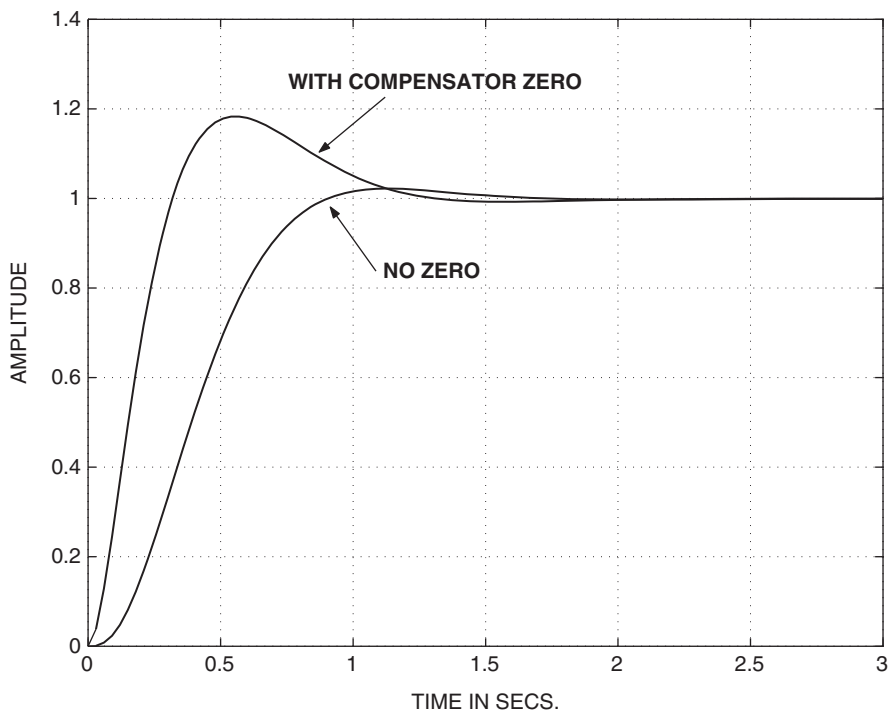


**Figure 4.5-3** Step response of the pitch-rate CAS.

requirements, piloted simulation, and flight test. During the design process nominal designs must be performed at several points throughout the speed-altitude envelope, and the feedback gains will be a function of some “scheduling” parameters, such as dynamic pressure. ■

### Normal Acceleration Control Augmentation Systems

In a fighter aircraft, if an accelerometer is placed close to the pilot’s station, aligned along the body  $z$ -axis, and used as the feedback sensor for control of the elevator, the pilot has precise control over his  $z$ -axis  $g$ -load during high- $g$  maneuvers. If  $1\ g$  is subtracted from the accelerometer output, the control system will hold the aircraft approximately in level flight with no control input from the pilot. If the pilot blacks out from the  $g$ -load and relaxes any force on the control stick, the aircraft will return to  $1\ g$  flight. Other useful features of this system are that the accelerometer output contains a component proportional to  $\alpha$  and can inherently stabilize an unstable short-period mode, and the accelerometer is an internal sensor that is less noisy and more reliable than an  $\alpha$  sensor.

Section 1.5 shows that the acceleration at a position  $P$  (the pilot's station here) is related to the acceleration at another fixed point (the aircraft cm) in the rigid aircraft, frame  $b$ , by a transport acceleration equation:

$$\mathbf{a}_{p/i} = \mathbf{a}_{cm/i} + \dot{\boldsymbol{\omega}}_{b/i} \times \mathbf{r}_{p/cm} + \boldsymbol{\omega}_{b/i} \times (\boldsymbol{\omega}_{b/i} \times \mathbf{r}_{p/cm})$$

where  $\mathbf{r}_{p/cm}$  is the accelerometer position vector from the cm. If the accelerometer is on the aircraft longitudinal axis ( $x$ -axis) and aligned parallel to the  $z$ -axis, "positive up," then the *normal acceleration* is

$$a_n \equiv -\mathbf{a}_{p/i}^z = -(\mathbf{a}_{cm/i}^z - \dot{Q}x_a + PRx_a) \quad (4.5-1a)$$

where the  $z$  superscript indicates the *frd*  $z$ -component and  $x_a$  is the *frd*  $x$ -position of the accelerometer. In a wings-level pull-up only the first two terms on the right-hand side are nonzero. In turning flight, the next subsection shows that a fighter aircraft control system should be designed to roll the aircraft around the  $x$  stability axis, and then  $PR = P^2 \tan \alpha$ . Therefore, if the aircraft is rolled rapidly at high  $\alpha$ , the  $PR$  term can be quite large and contributes negatively to the normal acceleration, as the aircraft nose moves along a circular arc around the  $x$  stability axis. Here, we will only illustrate the wings-level case.

In the real aircraft  $a_n$  must be obtained from the specific force sensed by an accelerometer, and is given by (see Chapter 1 Section Geodesy, Coordinate Systems, Gravity)

$$a_n = f_n + (-G_D^{ned} \cos \theta \cos \phi) \quad (4.5-1b)$$

If we define  $n_z = a_n/g_D$  as the normal acceleration in  $g$  units, the ratio  $|\mathbf{G}|/g_D$  is very close to unity, and

$$n_z \approx f_n - \cos \theta \cos \phi \quad g - \text{units} \quad (4.5-1c)$$

In level flight, at small angles of attack, the feedback signal for the control system is

$$n_z \approx f_n - 1.0 \quad g - \text{units} \quad (4.5-1d)$$

so this normal acceleration is approximately zero in steady level flight; it is often called the "incremental" normal acceleration.

If Equation (4.5-1a) is included in the nonlinear aircraft model, numerical linearization will yield a linear equation for  $a_n$  as a perturbation from its near-zero steady level flight value. A linear equation can also be obtained algebraically by finding the increment in the aerodynamic and thrust forces due to perturbations in the state and control variables, and this involves the  $Z$ -derivatives (see, for example, McRuer et al., 1973). For the nonlinear F-16 model numerically linearized at the nominal level flight condition in Table 3.6-3, the output equation for normal acceleration at the cg ( $x_a = 0$ ) is found to be

$$a_n = 0.003981v_T + 15.88\alpha + 1.481q + 0.03333\delta_e, \quad (4.5-2)$$

where  $\alpha$  and  $q$  are in radians and  $\delta_e$  is in degrees.

The normal acceleration in (4.5-2) depends on  $v_T$ ,  $\alpha$ , and  $q$  (the quantities that define the longitudinal aerodynamic forces) and on elevator deflection, which produces aerodynamic forces directly. This direct-feed term was also noted in Example 3.7-2 and leads to a transfer function of relative degree zero. Note that  $a_n$  is insensitive to the pitch attitude when  $\theta$  is small.

The elevator-to-normal-acceleration transfer function corresponding to (4.5-2) can be found from the Jacobian matrices and is

$$\frac{a_n}{\delta_e} = \frac{0.03333(s - 0.003038)(s + 0.01675)(s + 6.432)(s - 13.14)}{(s - 0.09756)(s + 1.912)(s + 0.1507 \pm j0.1153)} \quad (4.5-3)$$

This transfer function has the same poles that were noted in Example 4.4-1. Because of the NMP zero at  $s = 13.14$ , the normal acceleration response to a negative step elevator command (aircraft nose-up) will be an initial negative acceleration, quickly followed by the expected positive normal acceleration.

The physical explanation for the NMP behavior is that when the elevator control surface is deflected trailing edge upward to produce a positive normal acceleration, this creates a downward increment of force on the tail. The result is that the cg of the aircraft may drop momentarily during the pitch-up, so the normal acceleration may briefly become negative before it builds up positively. At the pilot's station ahead of the cg, the normal acceleration also depends on the pitch angular acceleration about the cg, so only a positive normal acceleration may be felt in a pitch-up. Table 4.5-1 shows the elevator-to-normal-acceleration transfer function zeros for a range of accelerometer positions, from the cg forward. The zeros close to the origin do not change significantly from the positions given in (4.5-3), and only the static loop sensitivity and the remaining zeros are shown.

Table 4.5-1 shows that as the accelerometer position is moved forward, the NMP zero moves out toward infinity and the static loop sensitivity decreases, thus keeping the transfer function dc gain constant. Eventually the static loop sensitivity changes sign and a zero comes in from infinity along the negative real axis, finally combining with the other real zero to form a complex pair. At a position near 6.1 ft forward of the cg the NMP effect disappears, and this point corresponds to an "instantaneous center of rotation" when an elevator input is suddenly applied. Note that in the case

**TABLE 4.5-1 Transfer Function Zeros versus Accelerometer Position**

$x_a$ (ft)	Static Loop Sensitivity and Numerator Factors		
0	0.03333	$(s + 6.432)$	$(s - 13.14)$
5	0.006042	$(s + 9.171)$	$(s - 50.82)$
6	0.0005847	$(s + 10.68)$	$(s - 450.7)$
6.1	0.00004005	$(s + 10.90)$	$(s - 6448.2)$
7	-0.004872	$(s + 14.73)$	$(s + 39.23)$
15	-0.04852	$(s + 3.175 \pm j6.925)$	



of the real F-16 aircraft, the pilot's station is approximately 15 ft ahead of the cg and is therefore not close to the instantaneous center of rotation.

It is also important to place the accelerometer close to a node of the most important fuselage bending mode. If this is not done, structural oscillations will be coupled into the rigid-body control system and may degrade the handling qualities or even lead to an "aeroservoelastic" limit cycle oscillation (see, e.g., AFWAL-TR-84-3105). Inevitably, the design of a normal acceleration control system to achieve good handling qualities is difficult and can require a good deal of refinement based on flight test results. A control system that has a good normal acceleration step response may have a pitch-rate response with a very large overshoot, and conversely, a reduction in the pitch-rate overshoot may lead to a sluggish normal acceleration response. The  $C^*$  criterion is appropriate for initial evaluation of the control system, since it is based on a blend of normal acceleration at the pilot's station and pitch rate.

Finally, note that an accelerometer is an internal (within the fuselage) sensor, with higher reliability and lower noise than the external alpha sensor. However, both accelerometers and alpha sensors are typically employed on modern fighter aircraft, and this reduces the dependence on the alpha sensor. A disadvantage of normal acceleration feedback is that the gain of the transfer function (4.5-3) varies widely with dynamic pressure. Accelerometer noise may become a problem if, at low dynamic pressure, the gain has to be greatly boosted to achieve a desirable closed-loop response. We will now investigate the features of the normal acceleration CAS by means of a design example.

**Example 4.5-2: A Normal Acceleration CAS Design** The configuration shown in Figure 4.5-4 will be used. The dynamics will be the same as Example 4.5-1, but an output equation for normal acceleration must be determined. Therefore, using numerical linearization of the F-16 model with the accelerometer 15 ft forward of the cg (i.e., at the pilot's station) and the nominal flight condition from Table 3.6-3, the output equation is found to be

$$a_n = 0.0039813v_T + 16.262\alpha + 0.97877q - 0.048523\delta_e \quad (1)$$

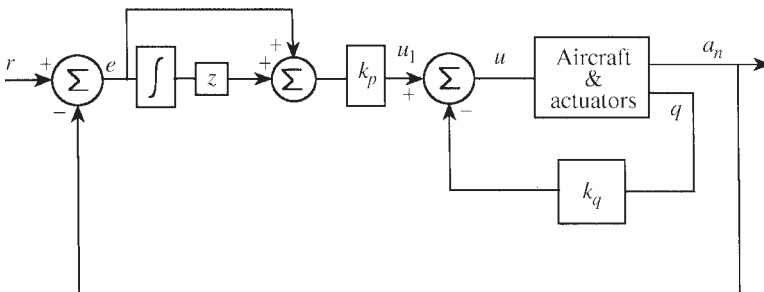


Figure 4.5-4 Normal acceleration control augmentation.

In (1) the dependence on  $v_T$  is quite weak, so the states  $V_T$  and  $\theta$  will be dropped, with the final results checked on the complete dynamics. The MATLAB commands to cascade the actuator with the plant and close the pitch-rate loop are:

```
ap=[-1.0189  0.90506;  0.82225  -1.0774]; % x1= alpha x2=q
bp=[-2.1499E-3; -1.7555E-1]; % Elevator input
cp=[0  57.29578; 16.262  0.97877]; % y1=q y2= an
dp=[0; -0.048523];
sysp= ss(ap,bp,cp,dp); % Plant
sysa= ss(-20.2, 20.2, -1,0); % Actuator, SIGN CHANGE
[sys1]= series(sysa,sysp); % Actuator then Plant
[a,b,c,d]= ssdata(sys1); % a_n/u transfer fn.
acl= a - b*[0.4 0]*c; % Close q loop
[z,p,k]= ss2zp(acl,b,c(2,:),d) % a_n/u_1 transfer fn.
```

The plant transfer function from elevator actuator input to normal acceleration is found to be

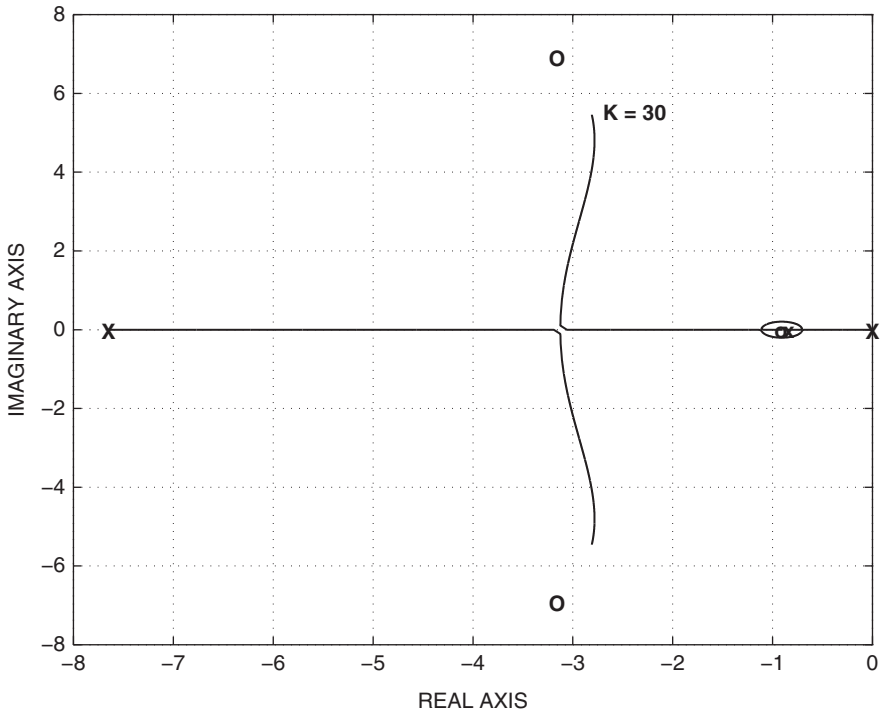
$$\frac{a_n}{u} = \frac{.9802(s + 3.179 \pm j6.922)}{(s + 20.20)(s + 1.911)(s + 0.1850)} \quad (2)$$

The effect of the inner-loop pitch-rate feedback is to speed up the two slow poles, and at quite low gain the pole from  $s = -1.911$  combines with the actuator pole to form a complex pair. Speeding up these poles is desirable for a fast time response, but as noted previously, the amount of pitch-rate feedback is limited by practical considerations (pickup of structural noise). The value  $k_q = 0.4$  (degrees of elevator deflection per degree per second of pitch rate) is in line with our past experience (0.25 to 0.5) and leads to the following closed-loop transfer function:

$$\frac{a_n}{u_1} = \frac{0.9802(s + 3.179 \pm j6.922)}{(s + 13.78)(s + 7.661)(s + 0.8601)} \quad (3)$$

The outer-loop root locus with the added PI compensator can now be anticipated. The compensator pole (at  $s = 0$ ) will combine with the pole at  $s = -0.8601$  to form a complex pair, and these poles will move toward the complex zeros of (3). This behavior will be modified depending on the position of the compensator zero. If the compensator zero is well to the left of  $s = -0.8601$ , these branches will be deflected only slightly to the left before landing on the complex zeros. At the same time the pole at  $s = -7.661$  will move toward the compensator zero, creating a potential slow-pole problem. The complex zeros are not well damped and it is difficult to achieve fast, well-damped, complex poles together with a fast real pole.

The alternative is to place the compensator zero close to the pole at  $s = -0.8601$  so that this pole is effectively canceled. The loci for the short-period poles will then break away from the real axis somewhere closer to the pole at  $s = -7.661$  before proceeding to the complex zeros. Some trial and error shows that this approach leads to a better time response, and it will be followed here. In practice, the sensitivity of the poles to gain variations, noise pickup, and possible advantages of additional compensator poles and zeros would have to be considered.



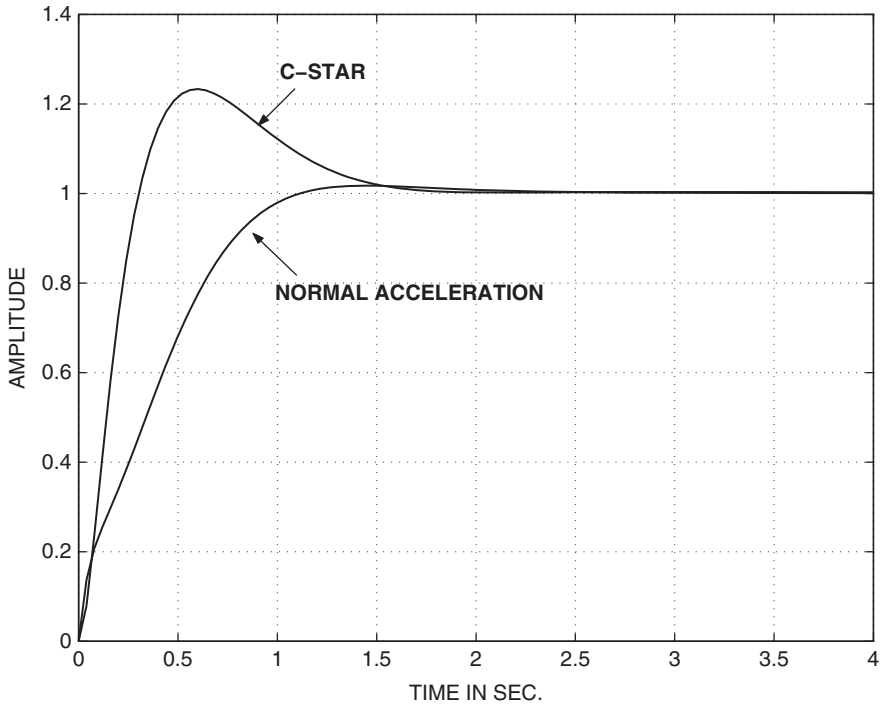
**Figure 4.5-5** Root-locus plot for the normal acceleration CAS.

Figure 4.5-5 shows the outer-loop root locus (i.e.,  $k_p$  varied) when the PI compensator zero is placed at  $s = -0.9$  (to demonstrate that exact cancellation is not required). The effect of the imperfect cancellation is visible near  $s = -0.9$ , and the locus of the short-period poles shows that satisfactory damping and natural frequency can be achieved without the use of an additional lead compensator.

The short-period poles should be made well damped because the compensator zero can be anticipated to cause an overshoot in the closed-loop step response. When the root locus is calibrated with a few values of  $k_p$ , a value  $k_p = 5$  puts the short-period poles at  $s = -3.00 \pm j2.18$  ( $\omega_n = 3.7$ ,  $\zeta = 0.81$ ). The closed-loop transfer function is then

$$\frac{a_n}{r} = \frac{4.901(s + 0.9000)(s + 3.179 \pm j6.922)}{(s + 20.28)(s + 0.9176)(s + 3.000 \pm j2.180)} \quad (4)$$

Figure 4.5-6 shows the closed-loop step response corresponding to this transfer function and the normalized  $C^*$  response. The  $a_n$  response is fast and well damped; the initial rate of rise is particularly fast because of the pitch acceleration component of the response. The rate limitations of the elevator actuator would modify this response slightly. The associated pitch-rate response (not illustrated) shows an overshoot of approximately 100%, but the  $C^*$  response falls almost exactly in the middle



**Figure 4.5-6** Normal acceleration CAS; step and C-star responses.

of the level-1 envelope (see Section The Handling Qualities Requirements). The  $C^*$  values were computed by adding the component  $12.4q$  to the normal acceleration output equation in the closed-loop Jacobian matrices. An initial time-response run was performed so that the steady-state value of  $C^*$  could be determined for use in normalizing the response.

The closed-loop transfer function obtained by applying the same feedback gains to the complete longitudinal dynamics (i.e., phugoid included) is

$$\frac{a_n}{r} = \frac{4.901(s + 0.900)(s + 3.175 \pm j6.925)(s + 0.01685)(s - 0.003139)}{(s + 20.28)(s + 0.9194)(s + 3.000 \pm j2.186)(s + 0.01637)(s - 0.003219)} \quad (5)$$

Notice that this transfer function contains, to a very good approximation, the poles and zeros of (4), thereby justifying the use of the short-period approximation. In (5) the phugoid mode is degenerate (two real poles) and one pole is unstable, whereas in Section 4.4 a stable phugoid was achieved with the basic stability augmentation system. This is because the normal acceleration equation (1) contains a component due to  $v_T$ , and this component is being fed back in a positive sense (positive  $\delta_e$  gives positive  $v_T$ ). The phugoid mode is almost canceled by the transfer function zeros in this case, and the unstable pole is very slow. An unstable phugoid pole is probably immaterial in this flight control (dogfight) mode, but the instability could

be avoided by retaining some inner-loop alpha feedback and using less gain in the normal acceleration loop. An alternative possibility is to modify the feedback signal by subtracting  $\cos \theta \cos \phi$  from the accelerometer output, as in (4.5-1b), to remove the gravity component. If this is done, the feedback signal will contain a  $\theta$ -component that will be in the correct sense to provide a stabilizing effect on the phugoid mode. This control system would hold a steady climb or dive with no control stick deflection and needs little input in a coordinated turn. It would probably prove objectionable to pilots. ■

## Lateral-Directional Control Augmentation

The roll/yaw stability augmentation system described in Section 4.4 is adequate for most aircraft, but for aircraft that must maneuver rapidly at high angles of attack, a more refined lateral-directional control augmentation system is required. The lateral aerodynamic control surfaces (ailerons and differential elevator) tend to cause the aircraft to roll about its longitudinal axis, and at high alpha, this can lead to some highly undesirable effects.

Consider the effect of a rapid  $90^\circ$  body-axis roll at high alpha. It is easy to visualize that the angle of attack will be converted immediately, and almost entirely, to a sideslip angle. This is referred to as *kinematic coupling* of alpha and beta. Because of this rapid elimination of the angle of attack, the body-axis roll is counterproductive. The most important purpose of a roll is to initiate a turn, which is then achieved by using angle of attack to produce the lift that will subsequently generate the required centripetal acceleration.

The sideslip created by kinematic coupling is referred to as *adverse sideslip* because it will tend to oppose the roll (remember that  $C_{l_\beta}$  is normally negative; a right roll will generate positive beta through kinematic coupling and hence a negative rolling moment). The sideslip will exist until the aircraft has yawed into the wind once more, and then if the angle of attack must be reestablished, the result will be an inefficient turn entry. Most modern fighters therefore use automatic control systems designed to roll the aircraft about the stability  $x$ -axis, thus maintaining the initial angle of attack.

Finally, large sideslip angles are undesirable for several important reasons. The effectiveness of the aerodynamic control surfaces may be greatly reduced; directional stability may be lost so that, in some cases, aircraft have been known to “swap ends” in flight. Even if directional stability is maintained, a large sideforce can be developed that may possibly break the vertical tail.

Another important effect that occurs during a roll is *inertia coupling*. Suppose that the aircraft has been designed to roll around the stability  $x$ -axis with no sideslip. Then the transformations in Section 2.3 can be used to determine the body-axes roll and yaw rates that result in a stability-axes roll rate  $P_s$  with zero yaw rate  $R_s$ . The relevant equations are

$$P_s = P \cos \alpha + R \sin \alpha \quad (4.5-4a)$$

$$0 = R_s = -P \sin \alpha + R \cos \alpha \quad (4.5-4b)$$

or

$$R = P \tan \alpha \quad (4.5-4c)$$

When alpha is positive,  $R$  and  $P$  must have the same sign, and if alpha is large, body-axes yaw rates comparable to the body-axes roll rate must be generated. Therefore, in a rapid high-alpha roll, gyroscopic (inertia coupling) effects will generate a significant body-axes pitching moment. Euler's equations of motion (1.5-6) illustrate the inertia coupling effects when the cross-products of inertia can be neglected. Using these equations, the pitching moment,  $M_{IC}$ , due to inertia coupling is given by

$$M_{IC} = \dot{Q}J_Y = (J_Z - J_X)PR \quad (4.5-5)$$

For modern fighter aircraft with stubby wings and engine(s) on or near the longitudinal axis, the moment of inertia,  $J_X$ , is usually small compared to  $J_Z$  (while  $J_Z$  and  $J_Y$  are comparable in magnitude). Therefore, a rapid roll (right or left) about the stability  $x$ -axis, at large positive alpha, can produce a strong nose-up pitching moment. To avoid a "pitch departure," the pitch-axis control augmentation system must cause the horizontal tail to generate an opposing aerodynamic moment. At high alpha it may be difficult to obtain the necessary aerodynamic pitching moment because of the horizontal-tail stalling. Even when adequate pitching moment is available, the required yawing moment may be unachievable because the rudder is blanketed by the wings. Conventional aircraft therefore have greatly degraded roll response at high alpha, and furthermore, the control systems must often be designed to limit the commanded roll rate to avoid a pitch departure.

Figure 4.5-7 illustrates the essential features of a lateral-directional CAS for a modern fighter aircraft; compensation networks, limiters, and so on, are added as necessary. The aileron control channel is the same as that shown in Figure 4.4-4 for the lateral-directional SAS, except that the aileron-actuator input now has a cross-connection to the rudder actuator via an alpha-dependent gain (also Mach dependent in general). This cross-connection, known as the *aileron-rudder interconnect* (ARI), may be implemented hydromechanically on some aircraft or electrically on others. Its purpose is to provide the component of yaw rate necessary to achieve a stability-axis roll.

The ARI gain must be determined, as a function of alpha and Mach number, to achieve the exact amount of yaw rate required to satisfy the constraint equation (4.5-4c). The gain is typically estimated from the known aerodynamic data and adjusted using nonlinear simulation. We can avoid this by incorporating the constraint  $R = P \tan \alpha$  in our steady-state trim program and trimming the aircraft for a "steady-state" roll (see Chapter 3 Section Steady-State Flight). Table 4.5-2 shows an abridged set of trim data for different roll rates and two different pitch rates; the angular units are all in degrees. The trim program has driven the lateral acceleration  $a_y$  (along the body  $y$ -axis) to essentially zero (about  $10^{-6}$  gs) with a small sideslip angle.

The table shows that angle of attack is almost independent of the roll rate, but it is dependent on pitch rate. Therefore, the second half of the table is for a pitch

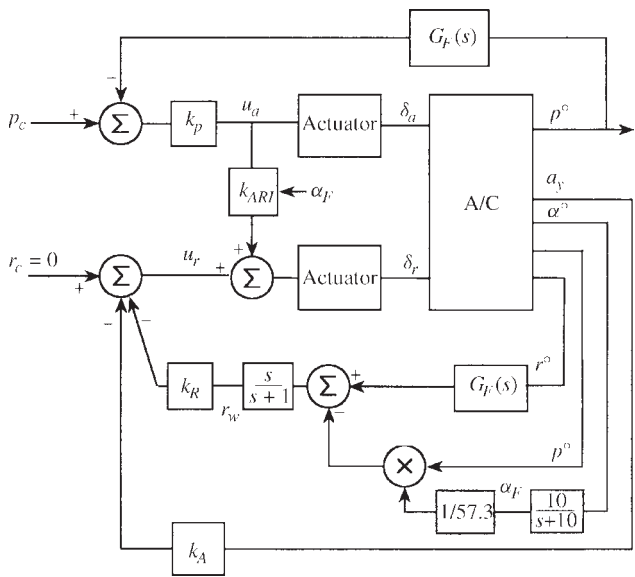


Figure 4.5-7 A lateral-directional CAS.

TABLE 4.5-2 Trim Conditions for Determining ARI Gain

$cg = 0.35\bar{c}, V_T = 502, h = 0, \bar{q} = 300, M = 0.450$							
	$P$	$\alpha$	$\beta$	$a_y$	aileron	rudder	rdr/ail
$Q = 0$	10	2.12	-0.012	0	-0.813	0.269	-0.331
	20	2.12	-0.023	0	-1.63	0.537	-0.329
	45	2.15	-0.050	0	-3.66	1.20	-0.328
	60	2.17	-0.065	0	-4.88	1.60	-0.328
	90	2.22	-0.091	0	-7.32	2.38	-0.325
	120	2.28	-0.112	0	-9.76	3.14	-0.322
	180	2.39	-0.139	0	-14.6	4.63	-0.317
$Q = 5$	10	6.53	0.012	0	-0.835	-0.0948	0.114
	20	6.52	0.022	0	-1.67	-0.195	0.117
	45	6.46	0.046	0	-3.76	-0.445	0.118
	60	6.41	0.058	0	-5.01	-0.595	0.119
	90	6.28	0.071	0	-7.52	-0.897	0.119
	180	5.87	0.048	0	-15.0	-1.83	0.122

rate of 5 deg/s and serves to provide data for a higher alpha condition (6.5°). Pitch rates of 10, 15, and 20 deg/s were used to provide additional data; maximum engine thrust is reached in between the last two conditions. The table indicates that for a stability-axis roll under the conditions shown (i.e.,  $M = 0.45$ , etc.), the required ratio of rudder deflection to aileron deflection is -0.33 at  $\alpha = 2.2^\circ$  and 0.12 at  $\alpha = 6.5^\circ$ .

Using the additional data for other angles of attack showed that the ratio of rudder to aileron deflection,  $k_{ARI}$ , was a good fit to the straight line:

$$k_{ARI} = 0.13\alpha - 0.7, \quad (\alpha \text{ in degrees}) \quad (4.5-6)$$

In a practical design the effect of Mach number must also be determined, and a two-dimensional lookup table might be constructed for  $k_{ARI}$ . Because of time and space limitations, (4.5-6) will be used here, and the design example will not involve large variations of Mach number.

The ARI alone would be an open-loop attempt to achieve a stability-axis roll and, to improve on this, feedback control is used to drive the lateral acceleration to zero (as in Table 4.5-2). Figure 4.5-7 shows how lateral acceleration is fed back and compared with a null reference input, and the error signal is used to drive the rudder actuator. This is also known as a *turn coordination* scheme and can be used in autopilot systems to respond to radio navigation steering signals or relieve the pilot of the need to coordinate turns.

Like the normal acceleration CAS, lateral acceleration feedback suffers from a wide variation of sensitivity. High values of feedback gain are needed at low speed, and this may cause problems with accelerometer noise. At low speed ( $M < 0.3$ ) sideslip angle feedback is normally used instead of lateral acceleration but has the disadvantage that a beta sensor is less reliable than an accelerometer.

The inner feedback loop in the rudder channel provides dutch roll damping by feeding back an approximation to the stability-axis yaw rate [Equation (4.5-4b)] to the rudder. Thus, the filtered alpha signal, converted to radians (as necessary), is used as an approximation to  $\sin \alpha$  multiplied by the roll rate and subtracted from the yaw rate. The stability-axis yaw rate is washed out so that it operates only transiently and does not contribute to a control error when a steady yaw rate is present. Note that, according to (2.5-29), the yaw-rate feedback is equivalent to a combination of beta and beta-dot feedback.

When necessary the pilot can still sideslip the airplane, because rudder inputs are applied directly to the rudder actuator. The control system will tend to reject this disturbance input, so the desirable effect of limiting the sideslipping capability will be achieved.

A practical lateral-directional CAS, based on the concept above, will be a complex system involving gain scheduling (with angle of attack and dynamic pressure or Mach), multipliers and limiters, and discrete switching (to change the control laws automatically at the alpha limits). It is a particularly good illustration of the fact that aircraft control systems incorporate many nonlinear and time-varying effects and the “tuning” of a design is often done by trial and error using computer simulation as a tool together with piloted simulation and flight tests. An example of a lateral-directional CAS design based on Figure 4.5-7 will now be given.

**Example 4.5-3: A Lateral-Directional CAS Design** This design will be performed on the F-16 model in the nominal flight condition of Table 3.6-3 (level flight at sea level,  $\alpha = 2.115^\circ$ ) and will follow Figure 4.5-7. The lateral accelerometer is at



the aircraft cg, and the coefficient matrices found by linearizing the aircraft model lateral-directional dynamics are, in MATLAB format,

```
ap= [-3.2201E-01  6.4040E-02  3.6382E-02  -9.9167E-01;    % x1= $\beta$ 
      0.0          0.0          1.0          3.6928E-02;    % x2= $\varphi$ 
      -3.0649E+01  0.0          -3.6784E+00  6.6461E-01;    % x3= $p$ 
      8.5395E+00   0.0          -2.5435E-02  -4.7637E-01 ]; % x4= $r$ 
bp= [ 2.9506E-04   8.0557E-04;
      0.0          0.0;                                     % input-1 =  $\delta_a$ 
      -7.3331E-01  1.3154E-01;                               % input-2 =  $\delta_r$ 
      -3.1865E-02  -6.2017E-02 ];
cp= [-5.0249E+00  0.0      -8.1179E-03  1.1932E-01;    % y1=  $a_y$ 
      0.0          0.0      5.7296E+01  0.0;           % y2=  $p$ 
      0.0          0.0      0.0          5.7296E+01 ]; % y3=  $r$ 
dp= [ 4.6043E-03  1.2571E-02;
      0.0          0.0;
      0.0          0.0 ];
```

The control surface actuator dynamics will be the same as Example 4.4-3. The filtered alpha signal is fixed at the trim value, and ARI and roll-rate feedback equations are linearized around this value:

```
kari=.13*2.115 -0.7;
aa= [-20.2 0; 0 -20.2]; % Two Actuators
ba= [20.2 0; 20.2*kari 20.2]; % Inp-1= Ail., Inp-2=ARI & rdr
ca= [-1 0; 0 -1]; da= [0 0; 0 0]; % SIGN CHANGE in C
actua= ss(aa,ba,ca,da);
plant= ss(ap,bp,cp,dp); % x1= $\beta$ , x2= $\phi$ , x3= $p$ , x4= $r$ 
sys1 = series(actua,plant); % x5= aileron x6= rudder
```

The washout filter has a time constant of 1 s and is included in a three-input, three-output state-space model with direct connections for the  $p$  and  $a_y$  signals. This model is cascaded at the output of the plant:

```
km= 2.115/57.3; % Multiply p by alpha in rads.
aw= [-1]; bw= [0 -km 1]; % Washout filter
cw= [0; 0; -1]; % outputs  $a_y, p, r$ 
dw= [1 0 0; 0 1 0; 0 -km 1]; % inputs  $a_y, p, r$ 
wash= ss(aw,bw,cw,dw);
sys2= series(sys1,wash); % x1=wash x2= $\beta$ , etc
[a,b,c,d]= ssdata(sys2); % Complete augmented system
```

The ARI affects only the  $B$ -matrix, and when the poles and zeros of the principal transfer functions are checked, it is found, as expected, that the effect of the ARI is to move only the zeros of transfer functions from the  $u_a$  input. The open-loop transfer function from actuator input to roll rate, with the ARI connected, is given by

$$\frac{p}{u_a} = \frac{913.4(s + 0.4018 \pm j2.945)(s - 0.002343)}{(s + 0.4235 \pm j3.064)(s + 3.616)(s + 0.01433)(s + 20.20)} \quad (1)$$

The roll subsidence pole is at  $s = -3.615$ , the spiral pole is stable at  $s = -0.01433$ , and the dutch roll poles are lightly damped and almost cancel out of this transfer function. Positive  $u_a$  inputs ( $-\delta_a$ ) will initially produce a positive roll rate, and the “slow” NMP zero indicates that this will disappear as the spiral trajectory becomes established.

A root-locus plot for the roll-rate loop showed that the dutch roll poles moved toward the canceling zeros. The spiral pole moved toward the NMP zero at  $s = 0.0023$ , and the roll subsidence pole joined with the actuator pole to form a high-frequency complex pair whose damping decreased as the feedback gain was increased. A fast roll-rate response was desired so it was decided to allow this complex pair but keep them well damped. Roll-rate gains close to those used in Example 4.4-3 were tried and the gain  $k_p = 0.2$  was chosen, which produced a damping ratio of about 0.7 for the complex pair and a stable spiral mode. The roll-rate loop was closed and the transfer function  $r_w/u_r$  was found with the following commands:

```
ac1= a - b*[0 0.2 0; 0 0 0]*c; % close roll loop
[z,p,k]= ss2zp(ac1,b(:,2),c(3,:),0) % rw/ur transf. fn.
```

giving

$$\frac{r_w}{u_r} = \frac{77.40s(s + 0.1030 \pm j0.2272)(s + 11.84 \pm j10.10)}{(s + 1)(s + 20.2)(s + 0.0027)(s + 0.4323 \pm j2.976)(s + 11.90 \pm j10.70)} \quad (2)$$

A root-locus plot for this loop shows that the dutch roll poles have their highest natural frequency and good damping when  $k_r = 0.8$ , and this gain was used as the initial gain for investigating the lateral acceleration feedback loop:

```
ac1= a- b*[0 0.2 0; 0 0 0.8]*c; % Close roll & yaw loops
[z,p,k]= ss2zp(ac1,b(:,2),c(1,:),0) % ay/uy transfer fn.
```

After removing an approximate cancellation of two complex pairs of poles and zeros, the lateral acceleration transfer function is

$$\frac{a_y}{r_c} = \frac{-0.2539(s + 1)(s - 4.157)(s + 4.00)(s - 0.0002)}{(s + 16.54)(s + 2.168)(s + 0.0026)(s + 1.701 \pm j1.486)} \quad (3)$$

The NMP zero at  $s = 4.157$  is analogous to the NMP zero in the elevator-to-normal-acceleration transfer function. Ignoring for the moment the “slow” NMP zero at  $s = 0.0002$ , the Laplace transform final-value theorem shows that a positive-step  $r_c$  (negative rudder deflection) produces positive lateral acceleration, but the NMP zero at  $s = 4.157$  indicates that this acceleration will initially be negative. The explanation is that negative rudder deflection immediately produces a negative sideforce contribution from the tail, but then, as negative sideslip builds up, the sideforce at the cg will become positive.

If the dihedral derivative is negative (positive stiffness), the aircraft will next begin to roll right, and negative sideforce will again occur as its weight starts a positive sideslipping motion. This is the cause of the “slow” NMP zero at  $s = 0.0002$ . The

purpose of the lateral acceleration feedback is to cancel the sideslip that is causing the short-term lateral acceleration, so lateral acceleration must be fed back negatively to  $u_r$ . The following commands will give the root-locus plot for the lateral acceleration feedback, with the roll- and yaw-rate loops closed:

```
k= linspace(0,100,2000);
r= rlocus(acl,b(:,2),c(1,:),0,k);
plot(r)
grid on
axis([-23.5,.5,-12,12])
```

The root-locus plot, Figure 4.5-8, shows that increasing the lateral acceleration feedback causes the dutch roll poles to circle around in the left-half  $s$ -plane, before terminating in the right-half plane on the NMP zero and at infinity. Increasing the inner-loop yaw-rate feedback causes the dutch roll poles to circle farther to the left in the  $s$ -plane and allows more lateral acceleration feedback to be used. However, using large amounts of lateral acceleration feedback creates a slow real pole by pulling the washout pole back to the right (it was moved left by the rate feedback) and makes the dutch roll pole positions quite sensitive to gain changes.

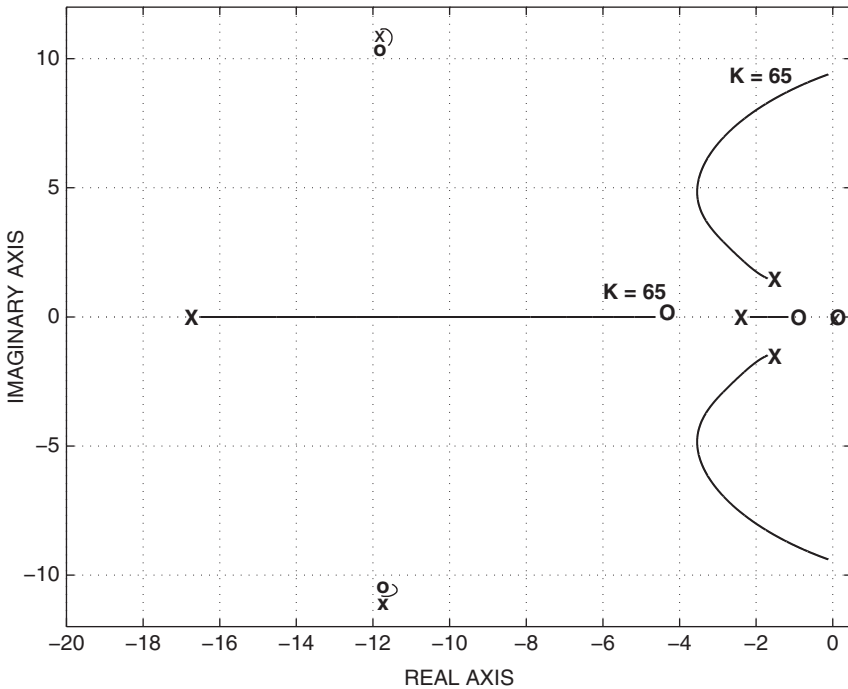


**Figure 4.5-8** Root-locus plot for lateral acceleration feedback.

A conservative choice,  $k_r = 0.8$ ,  $k_a = 10$ , was made for the yaw rate and acceleration feedback gains. The relevant closed-loop transfer functions are

$$\frac{p}{p_c} = \frac{182.7(s + 13.10)(s + 2.428 \pm j2.243)(s + 1.538)(s - 0.002347)}{(s + 13.42)(s + 2.386 \pm j2.231)(s + 1.575)(s + 0.002116)(s + 11.78 \pm j10.96)} \quad (4)$$

$$\frac{a_y}{r_c} = \frac{-0.2539(s - 4.157)(s + 4.00)(s + 11.92 \pm j10.58)(s + 1.00)(s - 0.0001965)}{(s + 13.42)(s + 2.386 \pm j2.231)(s + 1.575)(s + 0.002116)(s + 11.78 \pm j10.96)} \quad (5)$$

A number of poles and zeros can be canceled out of the transfer functions, and there is good decoupling between the two channels. The static loop sensitivity of the first transfer function has changed because the feedback gain  $k_p$  has been moved into the forward path, as shown in Figure 4.5-6. Note that the dutch roll mode is satisfactory, and the spiral mode is stable but with an increased time constant. ■

## 4.6 AUTOPILOTS

Most of the flying qualities specifications do not apply directly to autopilot design. In the case of pilot relief autopilot modes, the autopilot must be designed to meet specifications on steady-state error and disturbance rejection, with less emphasis on dynamic response. In addition, special consideration must be given to the way in which the autopilot is engaged and disengaged, so that uncomfortable or dangerous transient motions are not produced. For example, the altitude-hold autopilot that we will design could not be engaged directly at a few hundred feet below the commanded altitude. Otherwise the result would be a very steep climb, possibly leading to a stall if the engine thrust was not increased.

On the other hand, navigation-coupled autopilot modes must be designed to have a dynamic response that is appropriate to their function. For example, in an automatic terrain-following mode an autopilot must track a randomly changing input of quite wide bandwidth, without significant overshoots in its response. A number of autopilot designs will now be illustrated using the transport aircraft and F-16 dynamic models.

### Pitch-Attitude Hold

This autopilot is normally used only when the aircraft is in wings-level flight. The controlled variable is  $\theta$  ( $\theta = \gamma + \alpha$ ) and the sensor is an attitude reference gyro (which provides an error signal proportional to the deviation from a preset orientation in inertial space). The controller does not hold the flight-path angle,  $\gamma$ , constant because the angle of attack changes with flight conditions. Thus, if thrust is increased,  $\alpha$  will tend to decrease and the aircraft will climb, and as aircraft weight decreases (as fuel is burned),  $\alpha$  will decrease, also causing a gradual climb. Similarly, a preset climb will gradually level out as decreasing air density causes  $\alpha$  to increase. Because of these characteristics the pitch-attitude-hold autopilot is not very important in its own right. However, the same feedback configuration is used in the inner loops of other autopilots, such as altitude hold and automatic landing.

The block diagram of an attitude-hold autopilot is shown in Figure 4.6-1. Dynamic compensation,  $G_c(s)$ , is necessary if a small steady-state error and good transient

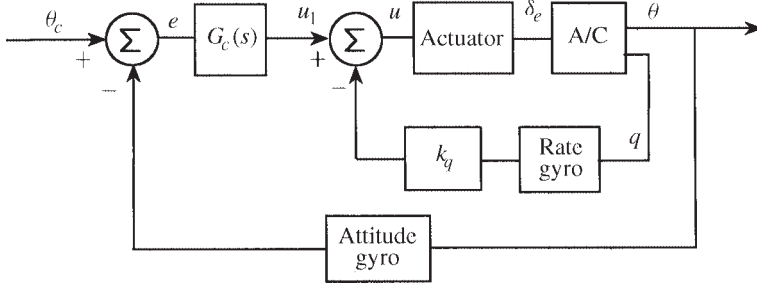


**Figure 4.6-1** A pitch-attitude autopilot.

response are required. Inner-loop rate feedback is used to provide additional design freedom and to promote good short-period damping. If the principles are investigated by using only the short-period approximation for the aircraft dynamics, adding an integrator to obtain pitch from pitch rate and a lag model for the elevator actuator, some root-locus sketches will show that the pitch-attitude feedback reduces the damping of the short-period mode and eventually makes it unstable. Pitch attitude is one of the variables involved in the phugoid mode, and an analysis using the complete pitch dynamics will show that the pitch-attitude feedback increases the phugoid damping and eventually produces two stable real poles. An accurate analysis of the effect on the phugoid mode requires that the attitude state also be included in the plant dynamics.

Two design examples will be given, with and without a dynamic compensator, and these designs will be used later as parts of more complex autopilots. The first example will be for a high-altitude cruise condition and the second for a landing condition.

**Example 4.6-1: A Simple Pitch-Attitude-Hold Autopilot** This example will demonstrate the basic characteristics with no dynamic compensation, so  $G_c$  will be simply a gain  $k_\theta$ . We will also neglect the dynamics of the gyros. The dynamics of the transport aircraft model in a level flight cruise condition at 25,000 ft, 500 ft/s true airspeed, and  $x_{cg} = 0.25\bar{c}$  are given by

$$A = \begin{bmatrix} v_T & \alpha & \theta & q & h \\ -0.0082354 & 18.938 & -32.170 & 0.0 & 5.9022E-05 \\ -0.00025617 & -0.56761 & 0.0 & 1.0 & 2.2633E-06 \\ 0.0 & 0.0 & 0.0 & 1.0 & 0.0 \\ 1.3114E-05 & -1.4847 & 0.0 & -0.47599 & -1.4947E-07 \\ 0.0 & -500.00 & 500.00 & 0.0 & 0.0 \end{bmatrix} \quad (1)$$

$$B^T = \begin{bmatrix} 0 & 0 & 0 & -0.019781 & 0 \end{bmatrix} \quad (\text{single input } \delta_e)$$

$$C = \begin{bmatrix} 0 & 0 & 57.296 & 0 & 0 \\ 0 & 0 & 0 & 57.296 & 0 \end{bmatrix} \begin{matrix} \theta \\ q \end{matrix} \quad D = \begin{bmatrix} 0 \\ 0 \end{bmatrix}$$

These plant matrices will be renamed  $ap$ ,  $bp$ , and so on and augmented with a simple-lag elevator-actuator model of time constant 0.1 s. The plant sign change

needed to make positive pitch rate correspond to positive elevator deflection will be incorporated in the actuator dynamics. The design procedure will yield values for  $k_q$  and  $k_\theta$ . The MATLAB commands are:

```
plant= ss(ap,bp,cp,dp);
aa= [-10]; ba= [10];           % Actuator
ca= [-1]; da= [0];           % sign change for plant
actua= ss(aa,ba,ca,da);
sys1 = series(actua,plant);
[a,b,c,d]= ssdata(sys1);
```

The transfer function from  $\delta_e$  to  $\theta$  is found to be

$$\frac{\theta}{\delta_e} = \frac{-1.133(s + 0.5567)(s + 0.01897)(s + 1.666E - 4)}{(s + 0.5234 \pm j1.217)(s + 0.002471 \pm j0.08988)(s + 1.892E - 4)} \quad (2)$$

All of the modes are stable, but the complex modes are quite lightly damped ( $\zeta_{sp} = 0.395$ ,  $\zeta_p = 0.027$ ) in this flight condition. The altitude pole is almost canceled by a zero, but omitting the altitude state will cause a noticeable error in the phugoid parameters. The effect of pitch-attitude feedback on this transfer function can be deduced from the root-locus rules. The altitude pole will move to the nearby zero, and the phugoid poles will move to the real axis and eventually terminate on the two remaining zeros. When the effect of the actuator pole is accounted for, the short-period poles must move toward the right-half plane (approaching  $60^\circ$  asymptotes). Thus, the short-period mode becomes less well damped as the phugoid damping increases.

The steady-state pitch-attitude error can be minimized by making the compensator gain as large as possible. A simple design procedure is to fix  $k_\theta$  and then use a root-locus plot to adjust  $k_q$  for best short-period damping. If the damping is more than adequate, then  $k_\theta$  can be increased further. The MATLAB commands are:

```
acl= a - b*[k_theta 0]*c;           % Choose k_theta
k= linspace(0,10,1000);
r= rlocus(acl,b,c(2,:),0,k)         % Root locus for k_q
plot(r)
```

Figure 4.6-2 shows the root-locus plot for  $k_q$  when  $k_\theta = 4.0$  (elevator degrees per degree of pitch). All of the poles except the short-period poles are on the real axis, and the damping of the short-period poles passes through a maximum as  $k_q$  varies. The upper branch of the loci will move upward and to the right as  $k_\theta$  is increased, thus reducing the maximum damping that can be attained.

The maximum short-period damping in Figure 4.6-2 is more than adequate, and a gain ( $k_q = 2.5$ ) corresponding to lower damping and reduced natural frequency ( $\zeta = 0.64$ ,  $\omega_n = 3.12$ ) was selected. The gains  $k_q = 2.5$  and  $k_\theta = 4.0$  and the following MATLAB commands will give the closed-loop transfer function:

```
acl= a - b*[4 2.5]*c;           % Close both loops
[z,p,k]= sszpz(acl,4*b,c(1,:),0) % Closed-loop, Unity fb
```

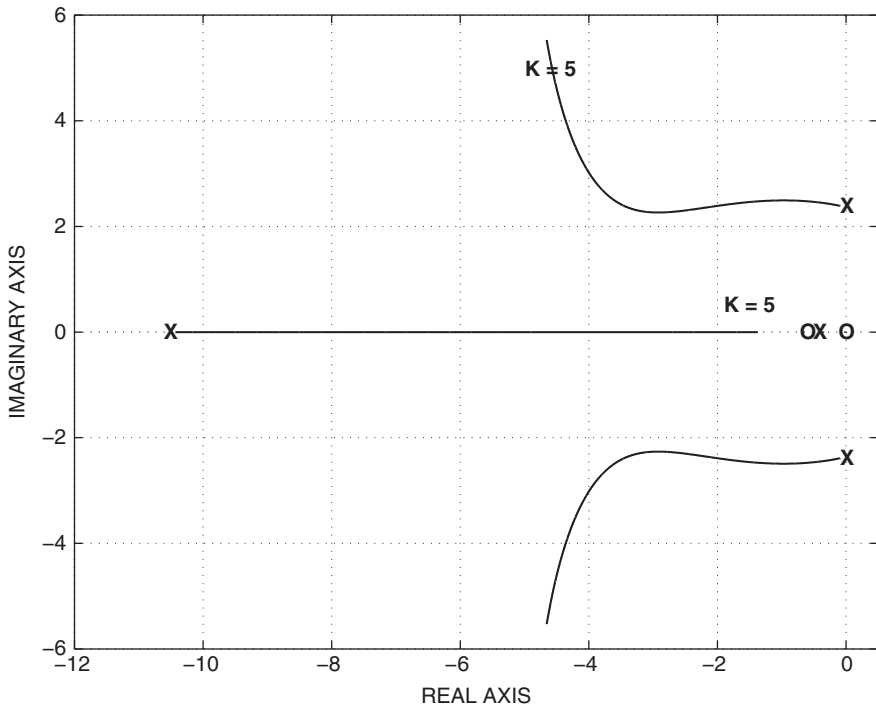


**Figure 4.6-2** Root-locus plot for pitch-rate feedback.

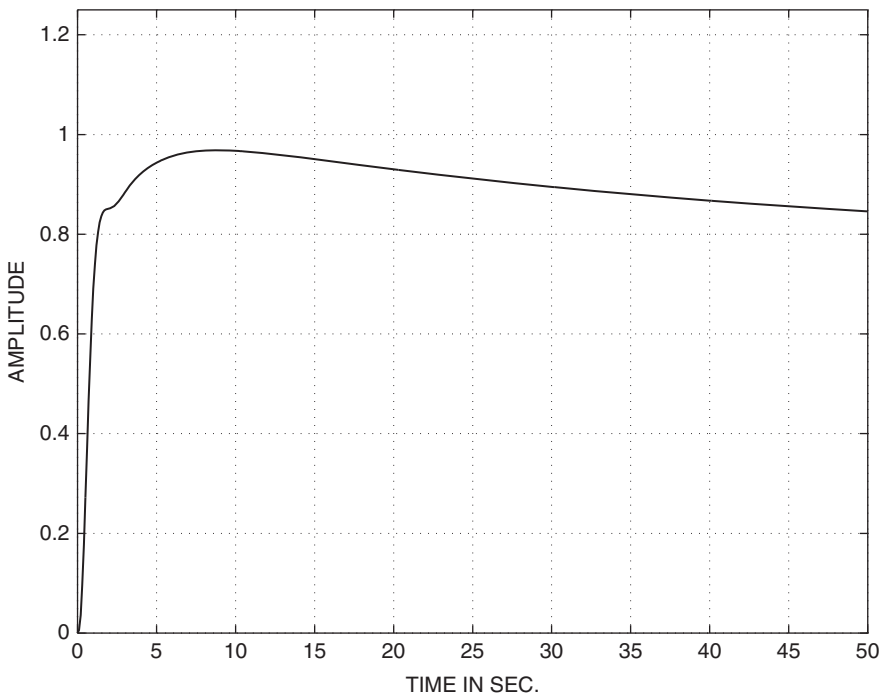


**Figure 4.6-3** Step response of the pitch-attitude controller.

The closed-loop transfer function is

$$\frac{\theta}{\theta_c} = \frac{45.33(s + 0.5567)(s + 0.01897)(s + 1.666E - 4)}{(s + 1.999 \pm j2.389)(s + 6.646)(s + 0.3815)(s + 0.02522)(s + 1.718E - 4)} \quad (3)$$

The altitude pole is almost canceled by a zero, but the cancellation of the degenerate phugoid poles is less exact and they are readily apparent in the step response, shown in Figure 4.6-3. The step response also has a large steady-state error and eventually settles at about 0.77.

This design has the disadvantage that as  $k_\theta$  is increased to reduce the steady-state error, large values of  $k_q$  (i.e.,  $k_q > 2.5^\circ$  of elevator per degree per second of pitch rate) must be used to obtain adequate damping of the short-period poles. This is likely to cause problems with rate sensor noise or structural-mode feedback. ■

In the next example dynamic compensation will be used to provide fast-responding, more precise control of pitch attitude, so that the controller can be used for the flare and touchdown of an automatic landing system.

**Example 4.6-2: A Pitch-Attitude Hold with Dynamic Compensation** When the transport aircraft model is trimmed with landing gear and flaps deployed, at  $V_T = 250$  ft/s,  $h = 50$  ft,  $\gamma = -2.5^\circ$ , and  $x_{cg} = 0.25\bar{c}$ , the dynamics are described by

$$A = \begin{bmatrix} v_T & \alpha & \theta & q \\ -3.8916E - 02 & 1.8992E + 01 & -3.2139E + 01 & 0.0000E + 00 \\ -1.0285E - 03 & -6.4537E - 01 & 5.6129E - 03 & 1.0000E + 00 \\ 0.0000E + 00 & 0.0000E + 00 & 0.0000E + 00 & 1.0000E + 00 \\ 8.0847E - 05 & -7.7287E - 01 & -8.0979E - 04 & -5.2900E - 01 \end{bmatrix} \quad (1)$$

$$B^T = \begin{bmatrix} 0 & 0 & 0 & -0.010992 \end{bmatrix} (\delta_e)$$

$$C = \begin{bmatrix} 0 & 0 & 57.296 & 0 \\ 0 & 0 & 0 & 57.296 \end{bmatrix} \begin{matrix} \theta \\ q \end{matrix} \quad D = \begin{bmatrix} 0 \\ 0 \end{bmatrix}$$

For simplicity the altitude state has been omitted, since its effect on the design is negligible. Once again the plant matrices will be renamed  $ap$ ,  $bp$ , and so on, and the same actuator dynamics as Example 4.6-1 will be used:

```
plant= ss(ap,bp,cp,dp);
aa= [-10]; ba= [10]; % Actuator
ca= [-1]; da= [0]; % sign change for plant
actua= ss(aa,ba,ca,da);
sys1 = series(actua,plant); % Actuator & Plant
[a,b,c,d]= ssdata(sys1);
acl= a- b*[0 k_q]*c; % Close Pitch-rate fb
% [z,p,k]= ss2zp(acl,b,c(1,:),0)
qclosed= ss(acl,b,c(1,:),0); % SISO system for theta
```



The pitch-rate feedback gain,  $k_q$ , will be limited to a smaller value than Example 4.6-1 for the reasons mentioned there. A gain  $k_q = 1.0$  results in a short-period damping ratio of  $\zeta_{sp} = 0.74$ ; the elevator-input-to-pitch-attitude transfer function is then

$$\frac{\theta}{u_1} = \frac{6.298(s + 0.6112)(s + 0.07305)}{(s + 0.9442 \pm j0.8674)(s + 0.01836 \pm j0.1328)(s + 9.288)} \quad (2)$$

and this value of  $k_q$  will be used for the rest of the design. A PI compensator will be used to remove the steady-state pitch error. The PI zero will be placed between the zeros at  $s = -0.07$  and  $s = -0.6$ , so that the PI pole will move toward  $s = -0.07$ . The phugoid poles will move toward the real axis between the other two zeros and become heavily damped. The following commands can be used to add the PI compensator, determine the gain and phase margins, close the pitch attitude loop, and test the step response:

```

zero= ?                               % Choose a PI zero position
picomp= ss([0],[zero],[1],[1]);       % PI Compensator
syspi = series(picomp,qclosed);       % PI comp & system
[a,b,c,d]= ssdata(syspi);
k1= ?                                 % Choose Proportional Gain
% margin(a,k1*b,c,0);                 % Gain & Phase Margins
acl= a - b*k1*c;                     % Close Pitch Loop
closd= ss(acl,k1*b,c,0);              % Scale b for unity feedback
step(closd,50)                        % Cl.-loop step response
    
```

Some trial and error with the step response led to a PI zero at  $s = -0.2$  and  $k_1 \approx 2$ . The resulting step response still exhibits an overshoot with a small short-period oscillation superimposed on a well-damped phugoid oscillation, which takes a long time to settle. A large increase in loop gain should reduce the residues in the slow poles but will degrade the short-period damping unless an additional compensator is used.

A root-locus sketch using transfer function (2), with the PI pole and zero added, shows that a phase-lead zero to the left of the short-period poles should pull the poles to the left and allow higher loop gain for a given damping. The phase-lead compensator was given a pole-to-zero ratio of 10 (the maximum recommended), and the pole frequency was adjusted to maximize the gain and phase margins while progressively raising the loop gain. The relevant code is:

```

pole= ?                               % Choose a pole position
lead= ss(-pole,pole,-.9,1);           % Lead compensator
sysall= series(lead,syspi);           % PI + Lead + Plant
[a,b,c,d]= ssdata(sysall);
k1= ?                                 % Choose Proportional Gain
margin(a,k1*b,c,0);                   % Gain & Phase Margins
    
```

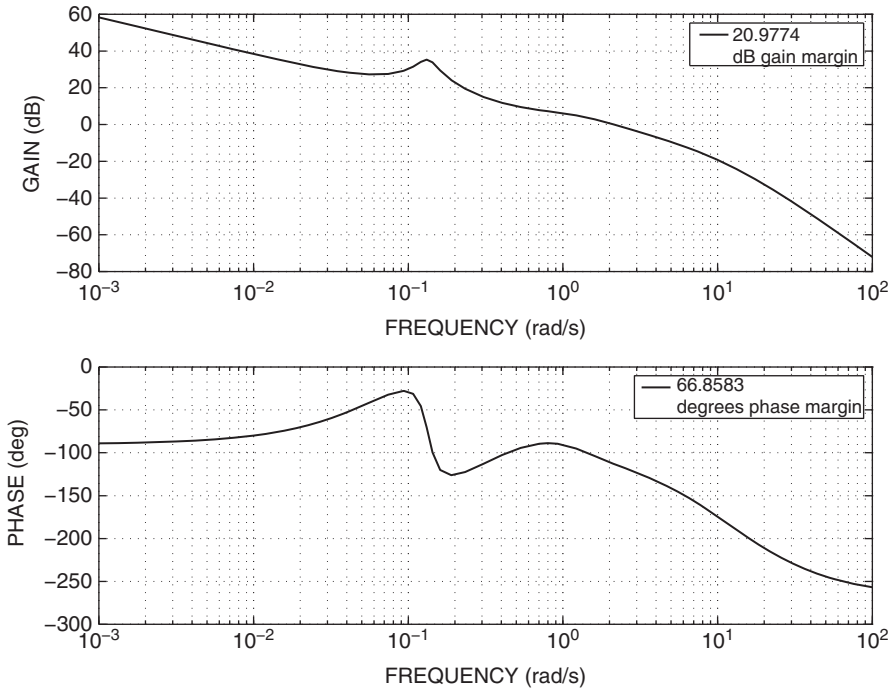


**Figure 4.6-4** Bode plots for the pitch-attitude controller.

The compensator

$$G_c = 40 \frac{s + 0.2}{s} \frac{s + 1.4}{s + 14} \quad (3)$$

gives a phase margin of  $66.8^\circ$  at 0.33 Hz and a gain margin of 21 dB at 1.75 Hz. The phase and gain margin plots with this compensator are shown in Figure 4.6-4. The closed-loop pitch attitude transfer function, with unity feedback, is given by

$$\frac{\theta}{\theta_c} = \frac{251.9(s + 0.6112)(s + 0.07305)(s + 1.40)(s + 0.20)}{(s + 2.121 \pm j1.762)(s + 0.2717 \pm j0.1516)(s + 0.06335)(s + 4.170)(s + 16.19)} \quad (4)$$

In the transfer function (4) the short-period mode has increased in frequency [compared to (2)], and the phugoid mode has increased in frequency and become more damped. The step response, shown in Figure 4.6-5, has a fast rise time but is slow to settle and contains an undesirable undershoot at about 2 s. If the PI compensator closed-loop zero is removed, by the modification shown in Figure 3.9-9, the rise time will be slower but a response that resembles that of a dominant complex pair can be obtained. This is also shown in Figure 4.6-5.

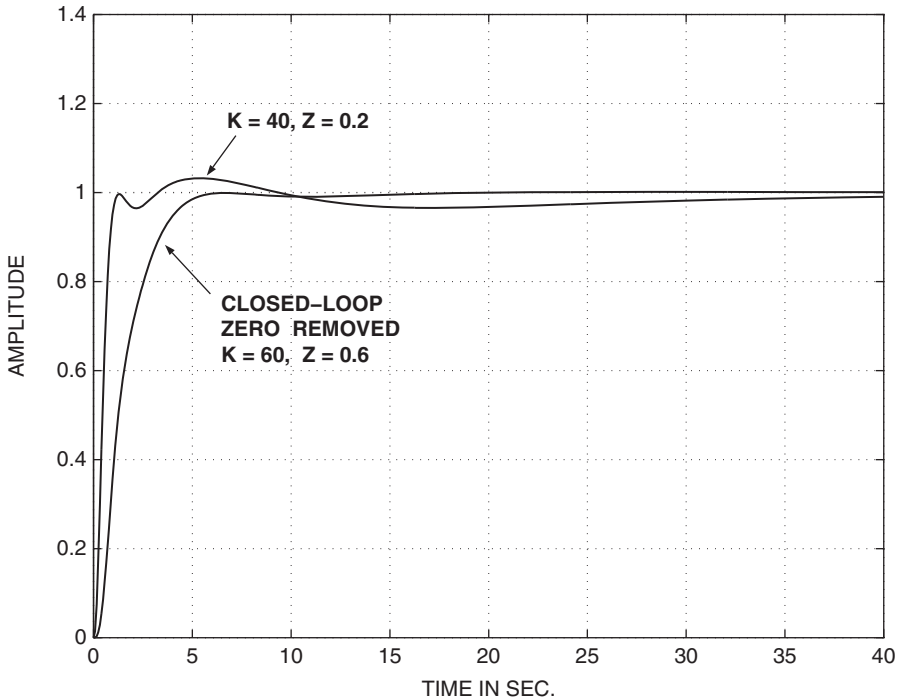


Figure 4.6-5 Step response of the pitch-attitude controller.

### Altitude Hold/Mach Hold

Altitude hold is an important pilot relief mode; it allows an aircraft to be held at a fixed altitude in an air route corridor to meet air traffic control requirements. The sensed altitude is normally the *pressure altitude*, that is, altitude computed in the air data computer from external pressure measurements. In a modern passenger aircraft the altitude hold will typically hold the aircraft well within  $\pm 200$  ft and provide a warning signal if the deviation exceeds  $\pm 100$  ft. The system will have *limited authority* over the horizontal control surfaces and will again warn the pilot if the control limits have been reached. These situations will often occur, for example, in rapidly rising air currents deflected upward by mountain ranges (“mountain waves”). A modern system may also have an “easy-on” or “fly-up, fly-down” feature that allows the autopilot to take the aircraft to an assigned altitude without exceeding certain rate-of-climb and pitch-attitude limits (e.g., 2000 to 3000 ft/min,  $20^\circ$  pitch attitude).

The Mach-hold autopilot is chiefly used on commercial passenger jets during climb and descent. During a climb the throttles may be set at a fairly high power level, and feedback of Mach number to the elevator will be used to achieve a constant-Mach climb. The speed will vary over the range of altitude, but the constant Mach number will provide the best fuel efficiency. Similarly, a descent will be flown at constant Mach with the throttles near idle. At the cruising altitude, control of both the throttle

and elevator will be used to provide altitude hold and speed hold for pilot relief and efficient cruising. In the following example an altitude-hold design will be illustrated.

**Example 4.6-3: An Altitude-Hold Autopilot Design** The altitude-hold configuration is shown in Figure 4.6-6, where  $G_c$  is a compensator and  $G_F$  is the effective lag of the pressure-altitude measurement. In the interest of simplicity the altitude sensor lag will be omitted from this example. Again for simplicity, the basic pitch-attitude autopilot from Example 4.6-1 will be used to provide the inner loops of the design, and the compensator  $G_c$  will still allow good altitude control to be achieved. The first design goal will be to achieve a high loop gain for good rejection of low-frequency (lf) altitude disturbances and small altitude error. Second, an altitude response that is deadbeat and relatively slow will be required for energy efficiency and passenger comfort.

Altitude is one of the state variables, and by adding an appropriate row to the C-matrix in Example 4.6-1, the transfer function from the pitch-attitude command to altitude can be determined. The altitude feedback has a strong effect on the phugoid poles and a relatively weak effect on the short-period poles. Therefore, the damping of the short-period mode will initially be set close to the desired final value. Thus, based on the experience of Example 4.6-1, the pitch-rate and pitch-attitude feedback loops will be closed by gains  $k_q = 2.5$  and  $k_p = 3.0$ . Starting from “sys1” in Example 4.6-1, we have

```
[a b c d]= ssdata(sys1)           % Actuators & Plant
acl= a- b*[3 2.5]*c;             % Close  $k_p$  and  $k_q$  loops
ch= [0 0 0 0 1 0]               % C matrix for Altitude
[z,p,k]= ss2zp(acl,3*b,ch,0)     % Transfer fn.  $h/\theta_c$ 
```

The transfer function from  $\theta_c$  to  $h$ , with unity feedback of  $\theta$ , is

$$\frac{h}{\theta_c} = \frac{168.4(s + 0.002264)}{(s + 2.261 \pm j1.936)(s + 6.170)(s + 0.3333)(s + 0.02750)(s + 1.731E - 4)} \quad (1)$$

with a short-period damping ratio of 0.76.

A root-locus sketch shows that the poles from  $s = -0.028$  and  $s = -0.333$  will break away from the real axis to form phugoid poles. The phugoid poles will move toward the right-half plane, while the short-period poles and the pole from  $s = -6.17$

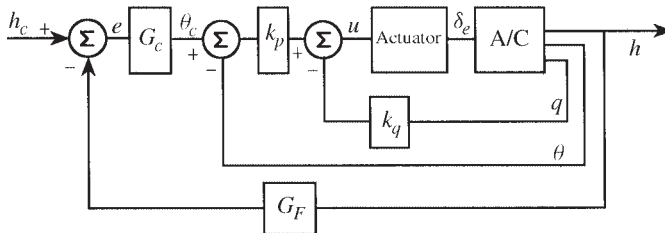


Figure 4.6-6 An altitude-hold autopilot.

move left. A phase-lead compensator with its zero close to  $s = -0.333$  will improve the gain and phase margins. A compensator pole-to-zero ratio of 8 was chosen (a compromise between noise accentuation and too little phase lead), and the pole frequency was adjusted for the best margins each time the gain was raised. A deadbeat step response was found to require a large phase margin ( $\approx 70^\circ$ ). The commands were:

```
sys2= ss(ac1,3*b,ch,0);
pole= ? % Choose Lead-Comp. Pole
lead= ss(-pole,pole,-.875,1); % Lead-compensator
sys3= series(lead,sys2); % Cascade with c.l. system
[a,b,c,d]= ssdata(sys3);
k= ? % Choose loop gain
margin(a,k*b,c,0) % Check Margins
```

and the lead compensator

$$G_c = \frac{s + 0.3}{3(s + 2.4)} \quad (2)$$

gives gain and phase margins of 13.3 dB and  $71.2^\circ$ , respectively. Unfortunately, the lead compensator reduces the lf loop gain. The transfer function (1) has an lf gain of about 72.8 dB (or 4380) and the compensator (2) reduces this by 27.6 dB (i.e.,  $1/24$ ). The final loop gain of 45.2 dB (or 182) would allow a steady-state altitude error of 1 ft per 183 ft, a rather poor performance. The performance can be improved by adding a lag compensator that boosts the lf gain, while adding negligible phase lag in the frequency range of the lead compensator. The same effect can be achieved by using a PI compensator to make the altitude control loop type 1 and placing the PI zero close to the origin. A simple lag compensator has the advantage that it can be implemented with passive components (see Table 3.3-1), provided that the time constant is not too large. Modern electronics has diminished this advantage but, for an analog design, a lag compensator is still simpler and more reliable than a PI compensator, and its use will be illustrated here.

Practical considerations limit the maximum time constant of an analog lag compensator to about 100 s (pole at  $s = -0.01$ ). If the compensator zero is chosen to give a large lf gain increase, then it will be found that in the closed-loop transfer function the slow poles (from  $s = -0.0275$  and  $s = -0.01$ ) have relatively large residues (i.e., do not cancel with zeros). If the lag compensator zero is placed near  $s = -0.05$  (i.e., an lf gain increase of 5) these slow poles will have a relatively small effect on the closed-loop time response. There will also be less phase lag in the frequency range where the lead compensator is to be added. Therefore, the lag compensator zero was placed at  $s = -0.05$ . The commands were:

```
lag= ss(-.01,.01,4,1);
sys4= series(lag,sys3);
[a,b,c,d]= ssdata(sys4);
margin(a,.3333*b,c,0);
ac1= a-.3333*b*c;
closed= ss(ac1,.3333*b,c,0);
step(closed,30)
```

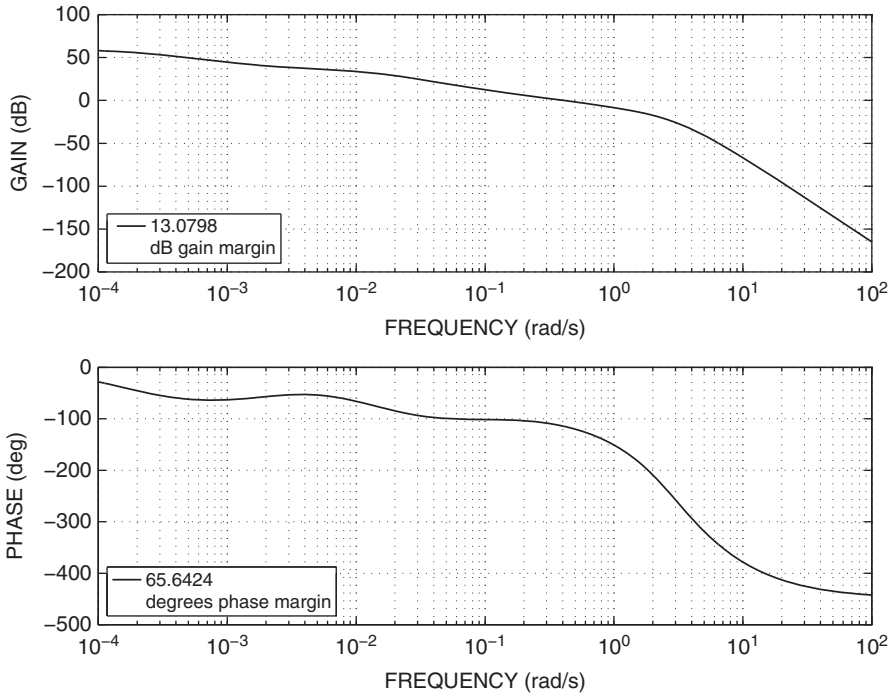


**Figure 4.6-7** Bode plots for the altitude-hold controller.

The gain and phase margins with both compensators are 13.1 dB and 65.7°, respectively. The If loop gain is 913, which is adequate. Figure 4.6-7 shows the phase and gain margin Bode plots.

The closed-loop altitude transfer function is

$$\frac{h}{h_c} = \frac{56.14(s + 0.30)(s + 0.050)(s + 0.002264)}{(s + 6.29)(s + 2.75 \pm j2.03)(s + 0.673 \pm j0.604)(s + 0.267)(s + 0.053)(s + 0.00224)} \quad (3)$$

A comparison with transfer function (1) shows that the fast poles have not moved significantly, the three slowest poles essentially cancel out of the transfer function, and a new complex pair has been created.

The step response is shown in Figure 4.6-8. The effect of the slow poles is visible as a small, slowly decaying displacement from the final value. The steady-state error will be negligible because of the high value of the If loop gain. The response is essentially deadbeat and is considerably slower than a pitch-axis response. It could be slowed down further by reduction of the loop gain or by using additional lag compensation but is considered to be satisfactory. As pointed out earlier, it is obvious that this autopilot would not normally be directly engaged with a large altitude error.

The reader may wish to consider repeating this design for cruising conditions at, say, 35,000 ft, to determine the need for scheduling of the controller gains.

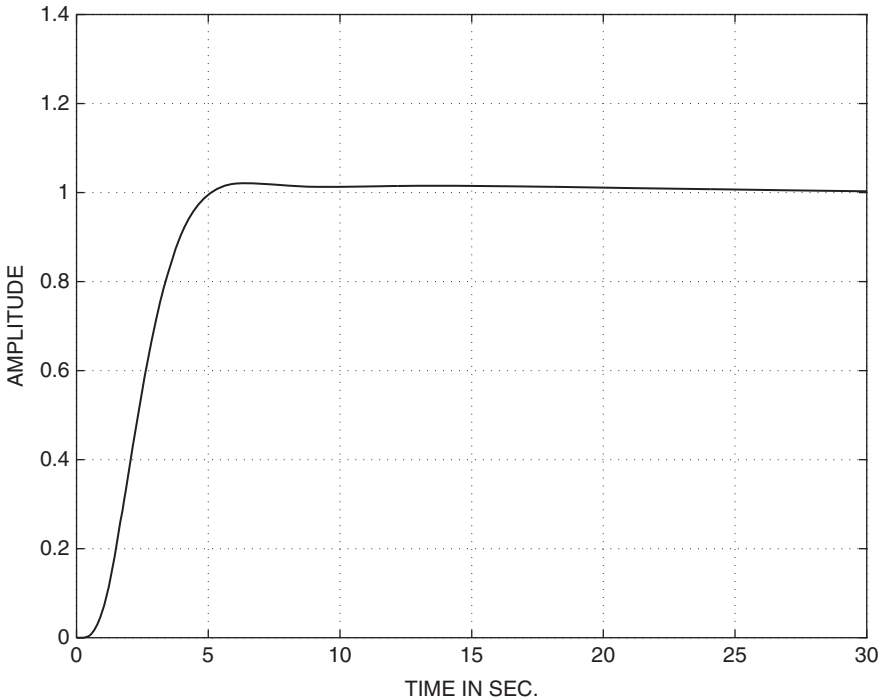


**Figure 4.6-8** Step-response of the altitude-hold controller. ■

## Automatic Landing Systems

In Section 4.1 we referred to the need for automatic control in situations where controlling the trajectory of an air vehicle was too difficult a task for a human pilot. A particular case of this is the landing phase in conditions such as bad weather or limited visibility. Landing in limited visibility may be achieved by providing the pilot with instruments to determine the aircraft's position relative to a reference trajectory, but a landing in more difficult conditions requires full automatic control with the pilot playing only a supervisory role.

Automatic control of the longitudinal trajectory requires simultaneous control of engine thrust and pitch attitude because, for example, using only the elevator to attempt to gain altitude may result in a loss of speed and an eventual stall. If the landing speed is such that the aircraft is on the “back side” of the power curve (see Chapter 3 Section Steady-State Flight), the throttle controls altitude and the elevator controls airspeed (increased power causes a gain in altitude, down elevator causes a gain in speed).

An aircraft is normally *reconfigured* for landing and takeoff by deploying wing leading- and trailing-edge devices (slats, flaps) so that the wing effectively has more camber and area. This provides more lift at low speed and increased drag; the wing is thereby optimized for a low-speed landing. The reconfiguration has the effect of

moving the minimum of the power curve to lower speed. Thus, most aircraft do not operate on the back side of the power curve, although naval aviators are routinely taught to fly in this regime for aircraft carrier operations. The reconfigured wing and extended landing gear produce a strong nose-down moment, which in turn leads to a trim with a large amount of “up” elevator. We will see this effect in our transport aircraft model in the following example, and these conditions play a role in determining the elevator size and deflection limit during the aircraft design.

A typical automatic landing system uses a radio beam directed upward from the ground at  $3^\circ$ , with equipment onboard the aircraft to measure the angular deviation from the beam and compute the perpendicular displacement of the aircraft from the *glide path*. Additional equipment is used to provide azimuth information, so that the aircraft can be lined up with the runway. The glide path must usually be intercepted at, at least, 3000 ft altitude (over the outer marker), and the aircraft will descend with an airspeed of 130 to 150 knots (220 to 253 ft/s) under automatic control.

Figure 4.6-9 shows an elevation view of a descending trajectory with velocity  $V_A$  (in tangent-plane coordinates) and flight-path angle  $\gamma$ . The reference trajectory has an angle  $\gamma_R$ , and the radio beam equipment is at the position  $Q$ . Assume that the aircraft passes through the radio beam at point  $P$  and time  $t_1$  and the descent is too gradual (as shown). The resulting positive glide-path deviation that builds up is denoted by  $d$ . The automatic landing equipment measures the angular deviation  $\delta$  and the range  $R$  and calculates  $d$  from

$$d = R \sin \delta \quad (4.6-1)$$

An onboard automatic control system is used to maneuver the aircraft so that  $d$  is driven back to zero.

To design a control system we must relate  $d$  to the aircraft trajectory. The geometry of the figure shows that the derivative of  $d$  is given by

$$\dot{d} = V_A \sin(\gamma - \gamma_R) \quad (4.6-2)$$

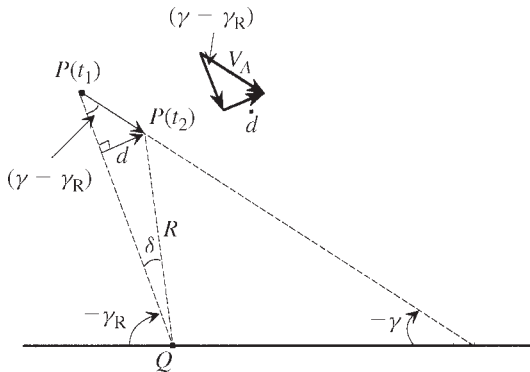


**Figure 4.6-9** Glide-slope geometry for autoland.



Therefore,  $d(t)$  can be derived by integrating this equation with the aircraft state equations, with the initial condition  $d(t_1) = 0$  applied at the time  $t_1$  at which the aircraft intersects the glide path. Note that when  $d$  is computed from (4.6-1), the sensitivity of  $d$  to flight-path changes will depend on the range  $R$ . This effect will be assumed to be compensated for in the onboard computer, so that an automatic control system can be designed for some nominal value of the range. The design of the longitudinal control system for automatic landing will now be presented as an example.

**Example 4.6-4: Longitudinal Control for Automatic Landing.** Figure 4.6-10 is a block diagram of the autoland control system. The transport aircraft model in the landing configuration will be used. The throttle servo and engine response will be modeled by a single 5-s lag and the elevator servo by a 0.1-s lag, as shown; sensor lags have been neglected. The compensators that must be designed are  $G_1$  and  $G_2$ , and the pitch-attitude controller will be taken from Example 4.6-2.

Equation (4.6-2) was added to the transport aircraft model, with  $\gamma_R$  as a model input and  $d$  as an additional state. The model was trimmed with gear down and landing flap settings for the conditions  $V_T = 250$  ft/s,  $\gamma = -2.5^\circ$ ,  $x_{cg} = 0.25 \bar{c}$ , and  $h = 750$  ft. The  $A$  and  $B$  Jacobian matrices for this flight condition are

$$ap = \begin{matrix} & v_T & \alpha & \theta & q & h & d \\ \begin{bmatrix} -0.038580 & 18.984 & -32.139 & 0 & 1.3233E-4 & 0 \\ -0.0010280 & -0.63253 & 0.0056129 & 1.0 & 3.7553E-6 & 0 \\ 0 & 0 & 0 & 1.0 & 0 & 0 \\ 7.8601E-5 & -0.75905 & -0.00079341 & -0.51830 & -3.0808E-7 & 0 \\ -0.043620 & -249.76 & 249.76 & 0 & 0 & 0 \\ 0 & -250.00 & 250.00 & 0 & 0 & 0 \end{bmatrix} & ; \end{matrix}$$

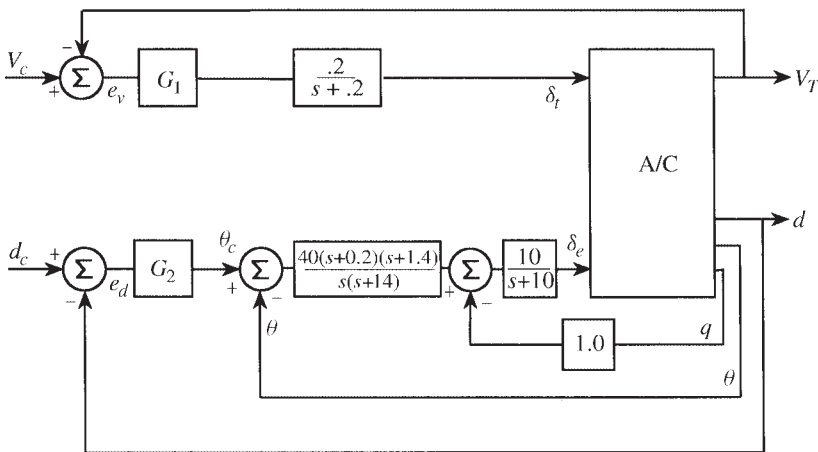


Figure 4.6-10 Control system for automatic landing.

$$bp = \begin{bmatrix} \delta_t & \delta_e \\ 10.100 & 0 \\ -1.5446E-4 & 0 \\ 0 & 0 \\ 0.024656 & -0.010770 \\ 0 & 0 \\ 0 & 0 \end{bmatrix}$$

The classical design procedure will be, as usual, to close one loop at a time. In this example there are four loops to be closed. Each loop closure changes both the poles and zeros for the other loop transfer functions. Preferably, the loops should be closed in a sequence that minimizes the number of design iterations. The pitch-attitude control loops are inner loops that we might logically expect to close first. If the effects of thrust and speed on pitching moment are not strong, then the pitch-attitude loops will be affected only by the change in angle of attack with speed. When the pitch-attitude loop is closed, changes in speed will cause changes in the angle of attack and therefore in the flight-path angle and  $\dot{d}$ . The pitch-attitude control thus determines the interaction of the speed loop on the  $d$ -loop. We will close the pitch-attitude loops first using the controller from Example 4.6-2. The  $d$  control loop cannot hold the required trajectory without closing the speed (auto-throttle) loop, but the speed loop can function independently of the  $d$ -loop. Therefore, the speed loop should logically be closed next.

Following Example 4.6-2, the pitch-attitude controller can be applied with the following commands:

```
cp= [ 0 0 57.29578 0 0 0; 0 0 0 57.29578 0 0]; % theta & q
dp= [0, 0];
plant= ss(ap,bp(:,2),cp,dp); % Elev. input
actua= ss(-10,10,-1,0) % Change sign at output
sys1 = series(actua,plant); % 1 i/p, 2 o/p
[a,b,c,d]= ssdata(sys1);
acl= a- b*[0 1]*c; % Close q-loop, kq=1
qclosed= ss(acl,b,c(1,:),0); % SISO
lead= ss(-14,14,-.9,1); % Lead compensator
sys2= series(lead,qclosed);
picomp = ss(0,0.2,1,1); % PI compensator
sys3= series(picomp,sys2);
[a,bt,c,d]= ssdata(sys3);
acl= a- bt*40*c(1,:); % Close theta loop
```

The closed-loop zero of the PI compensator has been retained because additional zeros provide more phase lead when compensating the outer loops. The transfer function from throttle to speed can now be found:

```
cvt= [1 0 0 0 0 0 0 0]; % C-matrix for VT
bth= [bp(:,1);0;0;0]; % B-matrix for Throttle i/p
[z,p,k]= ss2zp(acl,bth,cvt,0); % Get poles and zeros
```

After canceling some very close pole-zero pairs, the throttle-to-speed transfer function is

$$\frac{v_t}{\delta_t} \approx \frac{10.10(s + 0.2736 \pm j0.1116)(s + 0.001484)}{(s + 0.2674 \pm j0.1552)(s + 0.0002005)(s + 0.06449)} \quad (1)$$

A root-locus sketch of transfer function (1) (not shown) shows that the pole from  $s = -0.06$  will move left to meet the pole from the throttle servo (when added), and they will break away from the real axis to approach  $90^\circ$  asymptotes. Given the slow response of the throttle servo and engine lag, we may try to speed up the auto-throttle loop with a phase-lead compensator, although this may cause the throttle servo to saturate frequently. Adding the throttle servo and closing the loop with no additional gain show an infinite gain margin and a phase margin of about  $10^\circ$ . The low-frequency loop gain is about 60 dB and the resulting small steady-state error will be acceptable. Therefore, a lead compensator was chosen to improve the phase margin of this loop.

The compensator

$$G_1(s) = \frac{10(s + 1)}{s + 10} \quad (2)$$

gives a phase margin of about  $60^\circ$  and retains the same lf loop gain. The speed control loop can now be closed:

```
th2vt = ss(ac1,bth,cvt,0);           % SISO, throttle to speed
servo = ss(-.2,.2,1,0);             % Throttle servo & Eng. lag
ut2vt = series(servo,th2vt);
splead= ss(-10,10,-.9,1);           % Phase lead
comp sp= series(splead,ut2vt);       % Compensator & plant
[a,b,c,d]= ssdata(comp sp);
ac1= a- b*10*c;                     % Close auto-throttle loop
```

With the speed loop closed, the  $d/\theta_c$  transfer function for the final loop closure is found from:

```
btheta= [40*bt; 0; 0];              % B-matrix for unity f.b. theta-loop
cd = [0 0 0 0 0 1 0 0 0 0];        % C-matrix for d output
[z,p,k]= ss2zp(ac1,btheta,cd,0)    % d/θc transfer fn.
```

After removing some canceling pole-zero pairs, the transfer function reduces to

$$\frac{d}{\theta_c} = \frac{675.2(s + 1.40)(s + 0.20)}{(s + 2.021 \pm j1.770)(s + 0.2725 \pm j0.1114)(s + 4.409)(s + 16.16)(s + 0.001475)} \quad (3)$$

Notice that the zeros were created by the compensators in the pitch-attitude controller. A sketch of the root-locus plot will show that the poles at  $s \approx (-0.27 \pm j0.11)$  move into the right-half plane as the loop gain is increased, and the margin command shows that with unity feedback the gain and phase margins would be negative. In addition, a Bode plot shows that the lf gain levels out at 69 dB (2818). Using the margin command to optimize a phase-lead compensator, we find that  $2(s + 0.6)/(s + 6)$

will provide a phase margin of  $58.4^\circ$  and a gain margin of 11.1 dB, but the  $l_f$  gain is then reduced to  $2818/5$ , or 563. It is desirable to follow the glide slope closely when near the ground; therefore, we will make the controller type 1 by adding a PI compensator, as well as the phase lead.

When a PI controller and lead compensator are cascaded with transfer function (3), a root-locus sketch shows that the integrator pole and the pole from  $s = -0.0015$  will circle to the left in the  $s$ -plane to terminate eventually on the PI zero and the zero at  $s = -0.20$ . By placing the PI zero near the zero at  $s = -0.2$  and, using high gain, we will hope to get small residues in these slow poles and avoid a very sluggish closed-loop response. Note that the zero at  $s = -0.20$  from the pitch-attitude controller is now partly responsible for determining the speed of response of the  $d$  loop.

The compensator

$$G_2(s) = 1.0 \times \frac{(s + 0.18)(s + 0.5)}{s(s + 5)} \quad (4)$$

was derived by examining the effect of the PI zero on the closed-loop poles and zeros and the step response. The lead compensator was adjusted to obtain a compromise between the gain and phase margins, and these were, respectively, 14.7 dB and  $51.6^\circ$ . Figures 4.6-11a and b show the Bode plots; note that the pole at  $s = -0.0015$

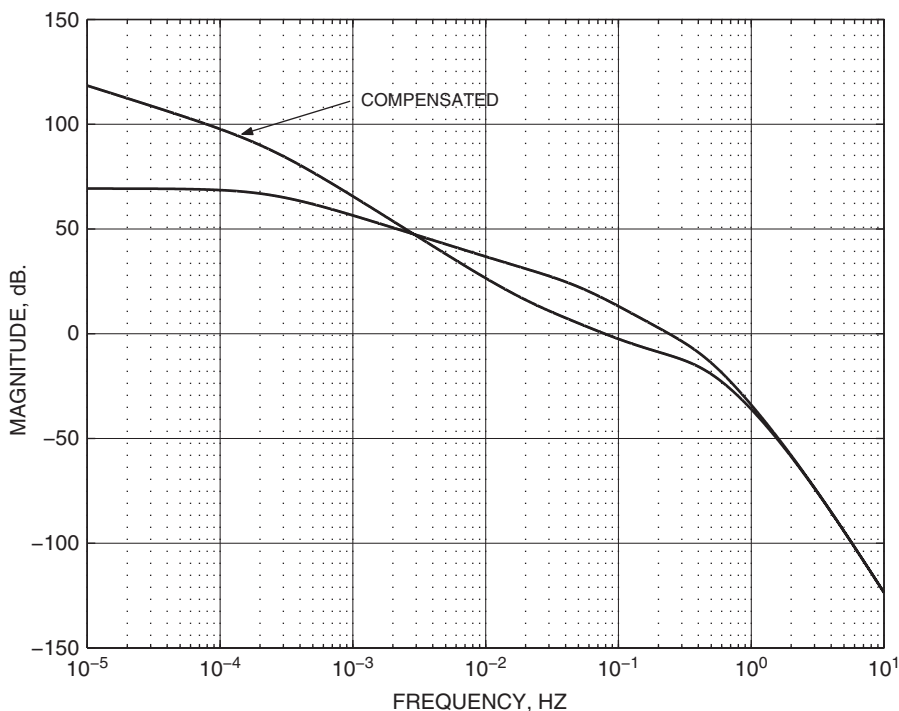


**Figure 4.6-11a** Bode gain plot for the automatic-landing  $d$ -loop.

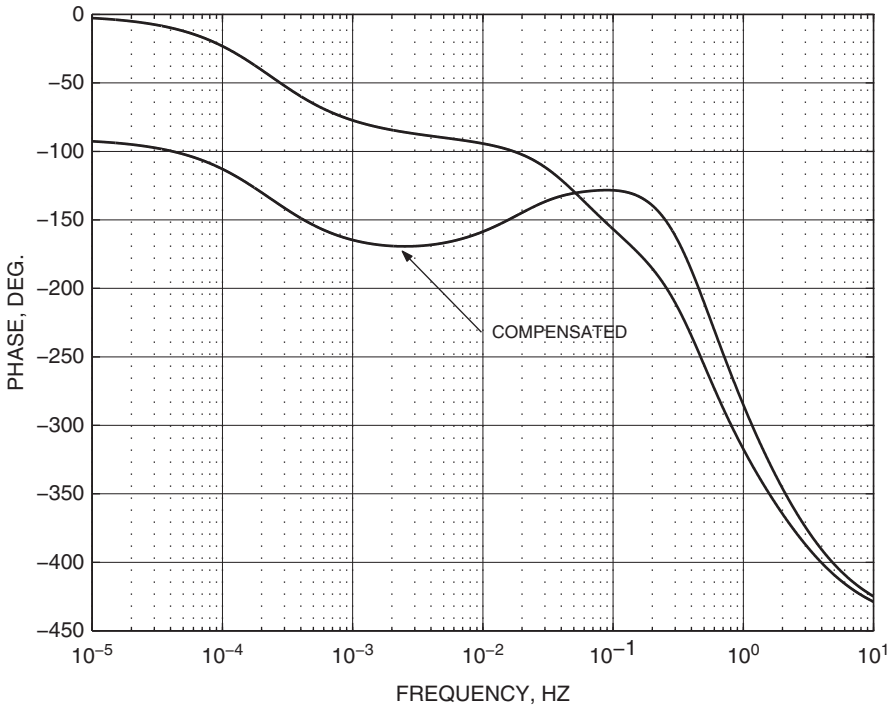


**Figure 4.6-11b** Bode phase plot for the automatic-landing  $d$ -loop.

causes the low-frequency phase lag to approach  $-180^\circ$  (like a type-2 system) before the lead compensation begins to take effect.

When some close poles and zeros are canceled, the principal closed-loop transfer functions are

$$\frac{v_T}{v_c} \approx \frac{20.20(s+1)}{(s+7.627)(s+1.280 \pm j0.9480)} \quad (5)$$

$$\frac{d}{d_c} \approx \frac{677.0(s+1.40)(s+0.50)(s+0.20)(s+0.180)}{(s+16.2)(s+5.16 \pm j1.65)(s+1.38 \pm j1.69)(s+0.292 \pm j0.348)(s+0.179 \pm j0.0764)} \quad (6)$$

Note that in the  $d$  transfer function the slowest pair of complex poles is close to terminating on the zeros at  $s = -0.18$  and  $s = -0.20$ . The step responses could be evaluated by a linear simulation using the closed-loop state equations. Instead a nonlinear simulation of the glide-path descent will be illustrated in Section 4.7. ■

## Roll-Angle-Hold Autopilots

In its simplest form, as a wing leveler, the roll angle autopilot has a history going back to the experiments of Elmer Sperry (see Section Introduction). A sensor incorporating

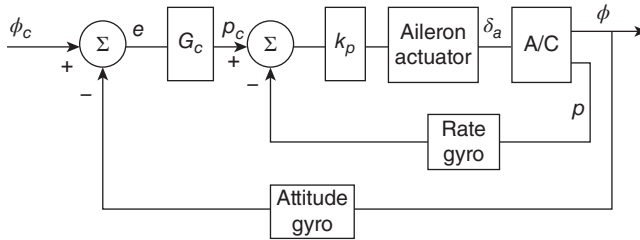


**Figure 4.6-12** A roll angle control system.

an attitude reference, such as a gyroscope, is used to sense deviations from the vertical. Feedback of the deviation signal in the aircraft  $y$ - $z$  plane to the ailerons can then be used to control the roll angle of the aircraft. The autopilot will hold the wings level and thus provide a pilot relief function for long flights and eliminate the danger of the pilot being caught unaware in a coordinated spiral motion toward the ground.

If the aircraft is held at some attitude other than wings level, additional control systems must be used to control sideslip and pitch rate, so that a coordinated turning motion is produced. Depending on the commanded pitch rate, the aircraft may gain or lose altitude in a turn. If a means of varying the roll reference is provided, the aircraft can be steered in any direction by a single control. These control systems can provide the inner loops for other autopilots that allow an aircraft to fly on a fixed compass heading or follow a radio navigational beam in the presence of cross-winds. Such systems will be described later.

Figure 4.6-12 shows a block diagram of a roll-angle-hold autopilot. High-performance aircraft virtually always have available a roll-rate gyro for use by a SAS or CAS, and this can be used to provide inner-loop rate damping for the autopilot. If the roll-rate gyro is not available, then for good performance, a compensator is needed in the roll angle error path. There is usually no requirement for precise tracking of roll angle commands, so type-0 roll angle control can be used. By the same token, the *velocity error* due to straight roll-rate feedback (i.e., no washout) is not important, particularly since the roll rate is not usually sustained for very long.

If the aircraft has strong roll-yaw coupling, the roll-angle-to-aileron feedback must be considered as part of a multivariable design, as in Sections 4.4 and 4.5. This is often not the case, and in the lateral transfer function, the poles associated with the directional controls are approximately canceled by zeros. The transfer function for the roll angle loop is then determined by the roll subsidence pole, the spiral pole, and the actuator and compensator (if any) poles. If roll-rate feedback is used, in conjunction with the roll angle feedback, there is good control over the position of the closed-loop poles and quite large amounts of feedback can be used. A roll angle autopilot design will now be illustrated.

**Example 4.6-5: A Roll Angle-Hold Autopilot** This example will use the controller subroutine from the lateral-directional CAS in Example 4.5-3 and with the same flight conditions. In Figure 4.6-12 the dynamics of the gyros will be neglected. With

$k_p = 0.2$ , the closed-loop transfer function from the roll-rate command,  $p_c$ , to the roll angle in Figure 4.6-12 is found to be

$$\frac{\phi}{p_c} = \frac{182.7(s + 13.09)(s + 2.429 \pm j2.241)(s + 1.540)}{(s + 13.42)(s + 2.386 \pm j2.231)(s + 1.575)(s + 0.002116)(s + 11.78 \pm j10.96)} \quad (1)$$

or, approximately,

$$\frac{\phi}{p_c} = \frac{182.7}{(s + 11.78 \pm j10.96)(s + 0.002116)} \quad (2)$$

In this transfer function the complex pole pair arose from the actuator pole and the roll subsidence pole, and the real pole is the spiral pole. The spiral pole is close to the origin and approximates an integration between the roll rate and the roll angle. When the roll angle feedback loop is closed, the spiral pole moves to the left and the complex poles move to the right. The root-locus plot is shown in Figure 4.6-13.

A proportional gain (for  $G_c$ ) of  $k_\phi = 5.0$  gave the complex poles a damping ratio of  $\zeta = 0.71$  (at  $s = -8.88 \pm j8.93$ ), and the real pole was at  $s = -5.4$ . The roll angle control loop is well damped but unrealistically fast. The commanded attitude will be more tightly controlled in the steady state, but the aileron actuators may be driven

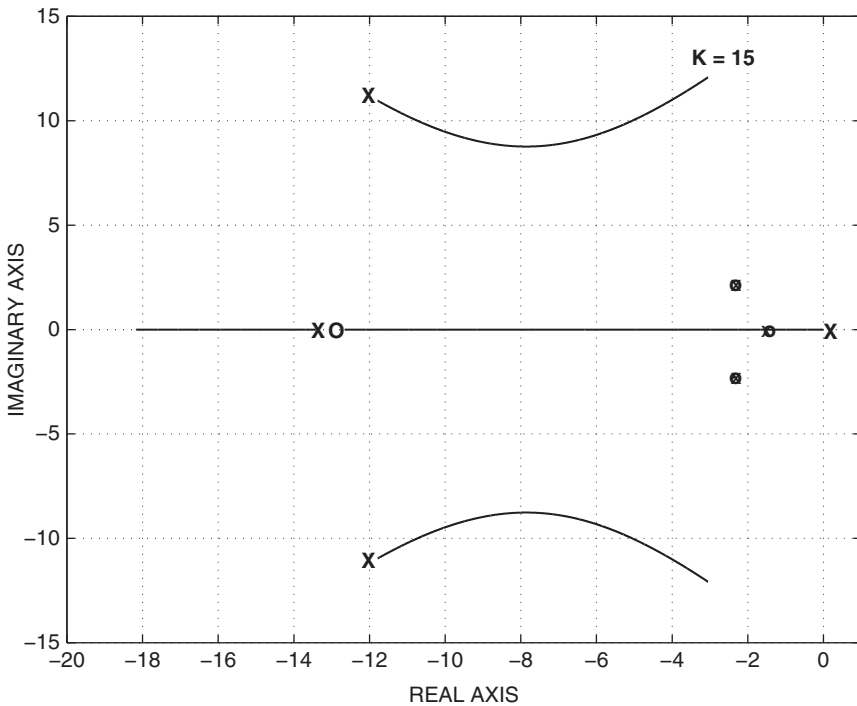


**Figure 4.6-13** Root-locus plot for roll-angle-hold controller.

into rate limiting if abrupt roll angle commands are applied. This control system will be used in the next subsection in a nonlinear simulation. ■

## Turn Coordination and Turn Compensation

A coordinated turn is defined as zero lateral acceleration of the aircraft cg (i.e., zero component of inertial acceleration on the body  $y$ -axis). In a symmetrical aircraft the components of acceleration in the plane of symmetry need not be zero, and so the coordinated turn need not be a steady-state condition. In an asymmetrical aircraft the sideslip angle may not be exactly zero in a coordinated turn because of, for example, asymmetric thrust or the effects of the angular momentum of spinning rotors. Turn coordination is desirable for passenger comfort and, in a fighter aircraft, it allows the pilot to function more effectively. In addition, by minimizing sideslip, it maintains maximum aerodynamic efficiency and also minimizes undesirable aerodynamic loading of the structure. Automatic turn coordination is also useful for a remotely piloted vehicle performing video surveillance or targeting.

In a coordinated turn, level or otherwise, the aircraft maintains the same pitch and roll attitude with respect to the reference coordinate system, but its heading changes continuously at a constant rate. Therefore, the Euler angle rates  $\dot{\phi}$  and  $\dot{\theta}$  are identically zero, and  $\dot{\psi}$  is the turn rate. The Euler kinematical equations (1.3-21) show that, under these conditions, the body-axes components of the angular velocity are

$$\begin{aligned} P &= -\dot{\psi} \sin \theta \\ Q &= \dot{\psi} \sin \phi \cos \theta \\ R &= \dot{\psi} \cos \phi \cos \theta \end{aligned} \quad (4.6-3)$$

If the aircraft is equipped with angular rate control systems on each axis these rates can be computed, and then they can be used as the controller commands to produce a coordinated turn. In level flight, with small sideslip, the turn coordination constraint is given by Equation (3.6-7):

$$\tan \phi = \frac{\dot{\psi}}{g_D} \frac{V_T}{\cos \theta} \quad (4.6-4)$$

If  $\cos \theta \approx 1.0$ , then, for a specified turn rate  $\dot{\psi}$ , the required pitch and yaw rates can be calculated and the roll rate can be neglected. This produces a quite satisfactory level turn.

Alternative coordination schemes include feedback of sideslip or lateral acceleration to the rudder or computing just a yaw-rate command as a function of measured roll angle [see Blakelock (1965) for details]. If, in addition, a pitch-rate command is calculated from the above equations as a function of roll angle, the turn can be held level. This is referred to as “turn compensation” (Blakelock, 1965); it can also be achieved by using altitude feedback to the elevator. An example of turn coordination is given in Example 4.7-5.



## Autopilot Navigational Modes

Automatic navigation is an important autopilot function for both military and civil aircraft, and the most important systems will be briefly summarized. A *heading-hold* autopilot is designed to hold the aircraft on a given compass heading. The conventional method of implementing this autopilot is to close an additional yaw angle feedback loop around the roll angle control system (including turn compensation) that was illustrated above. Figure 4.6-14 shows the arrangement. The transfer function relating heading angle to roll angle uses the linearized equation obtained from (4.6-4) when  $\phi$  is small and  $\cos \theta \approx 1$ . Note that the transfer function gain is inversely proportional to speed. An investigation of the root locus for the heading angle loop and the effects of flight conditions will be left to the reader [see also Blakelock (1965) and Roskam (1979)].

A *VOR-hold* (VHF Omni Range) autopilot is an autopilot designed to home on an omnidirectional radio beacon. The heading-angle-hold system (including, e.g., turn compensation) is used to implement this autopilot, and Figure 4.6-15 shows how this is done. The transfer function derived from the geometry of the beam following is similar to that derived for the automatic-landing longitudinal control system. The system normally requires proportional-plus-integral compensation and possibly lead compensation also. Again, it is left to the reader to investigate further (Blakelock, 1965; Roskam, 1979).

A specialized military autopilot that is particularly interesting is a *terrain-following, terrain avoidance* (TFTA) autopilot. This system uses the aircraft's radar

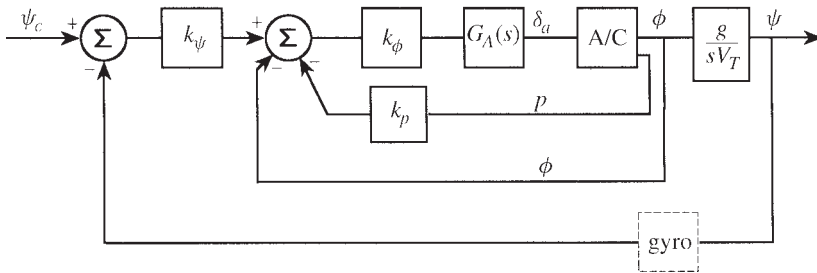


Figure 4.6-14 A heading-hold control system.

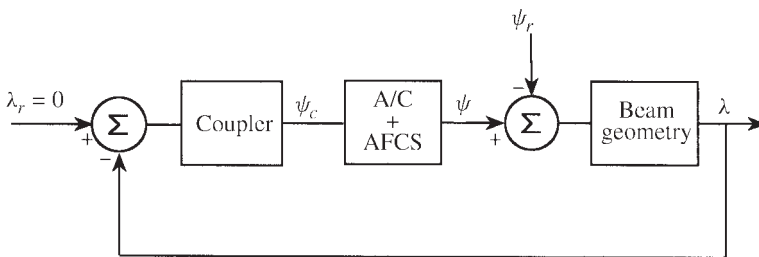


Figure 4.6-15 A VOR-hold autopilot.

or a separate radar carried underneath the aircraft (as in the LANTIRN system). The radar provides guidance commands to fly at constant height (e.g., 100 to 400 ft) above Earth's surface at high speed. The fly-up, fly-down commands are usually applied to a  $g$ -command control system as described in Section 4.5, and the lateral-directional guidance commands are applied to a roll angle steering control system as in Example 4.7-5.

## 4.7 NONLINEAR SIMULATION

The linear designs illustrated in previous sections are only the first stage in the design of complete aircraft control systems. At the second stage the control systems must be evaluated on a nonlinear model of the aircraft, with larger amplitude maneuvers and over a larger portion of the envelope. To perform this evaluation, nonlinear control system elements must be modeled (e.g., any multipliers or nonlinear calculations in the control system equations and rate limiting and deflection limiting in the control surface actuators). Actuator performance will be strongly affected by the aerodynamic loads on the control surface, further complicating the nonlinear behavior. During this second stage the nonlinear simulation can be done with preprogrammed commands or with a desktop flight simulator with no cockpit, rudimentary controls, and limited video display capabilities. At a later stage the nonlinear simulation will be performed with a cockpit mock-up and out-of-the-window video displays and used for piloted evaluation of the aircraft. This will eventually be followed by pilot training in the simulator.

In nonlinear simulation it is highly desirable to separate the control system equations from the equations of motion and from the aerodynamic database. If this is done, errors are easier to find, different controller designs can be substituted easily, there is less chance of corrupting unrelated computer code, and not all of the code has to be recompiled when changes are made. In a big organization different groups of people are responsible for the aerodynamic database and the control systems, and this partitioning of the computer software is very appropriate. The state-space formulation greatly facilitates the achievement of this objective. State variables that are needed for the controllers can be numbered independently of state variables needed for the equations of motion or any other equation set, and at compilation time or during code interpretation, all of the state variables can be placed in one large array for numerical solution purposes. This is like a parallel operation on all of the state variables simultaneously, and there is no question of different variables being of different age. In this section examples of nonlinear simulation will be provided using the transport aircraft in MATLAB code and the F-16 model in Fortran.

**Example 4.7-1: Pitch-Rate CAS Nonlinear Simulation** In this example the pitch-rate controller designed in Example 4.5-1 will be converted to a subprogram (i.e., a function subprogram or a subroutine subprogram) that can be linked with a nonlinear aircraft model, an integration routine, and a driver program to perform flight simulation. This subprogram must have access to the output variables of the aircraft model and the controller command inputs (e.g., as formal parameters, as “global” variables,

or through a “common” allocation of memory). A set of controller state variables that can be appended to the array of aircraft state variables must be used. The output of this subprogram is an array of derivatives, and they must be appended to the array of derivatives from the aircraft model.

The first statements in the controller subprogram are specific to the programming language and must define the variable types and how they are to be passed to and from the subprogram. The rest of the subprogram is essentially independent of the programming language and consists of the matrix state equations of Example 4.5-1 translated into individual state equations, as in Table 3.3-1. The aircraft model has thirteen state variables so here the controller states will be numbered from fourteen on and appended to the aircraft state vector. In Fortran, the code is:

```

subroutine FC(time,x,xdot)           ! x in, x-dot out
dimension x(*), xdot(*)             ! assumed-size arrays
common/controls/thtl,el,ail,rdr,qcom ! controls & commands
common/output/an,alat,ax,qbar,amach,vt,alpha,theta,q ! from a/c
el=-x(14)                           ! actuator state-->elevator
call f16(time,x,xdot)               ! Aircraft model
xdot(15)= 10.0*(alpha-x(15) )       ! Alpha filter
xdot(16)= qcom - q                  ! PI integrator input
u= 1.5*x(16) - .5*q-.08*x(15)       ! Control law
xdot(14)= 20.2*(u - x(14) )         ! Elevator actuator
return
end

```

Values have already been assigned to the state variables when this subroutine is called, but the longitudinal control inputs must be assigned before the aircraft model equations can be executed. Therefore, the elevator control is assigned to the actuator state before calling the aircraft model. The lateral-directional controls and states will not be changed from their trim values. Throttle commands and the pitch-rate command “qcom” will be assigned in a separate subprogram. Control surface rate and deflection limits are not modeled; this will be done in later examples. Note that this controller and the aircraft model can be numerically linearized when linked together, and the Jacobian matrices will agree very accurately with the closed-loop matrices in Example 4.5-1. This provides a check for correct operation.

Accurate initialization will allow the longitudinal dynamics to be exercised without waiting for an initial transient to die out. The alpha filter state should be initialized with the trim value of alpha and the elevator state with the trim value of elevator deflection (both in degrees). The initial value of the error integrator state can be calculated as follows. From Figure 4.5-1 we see that the steady-state (no integrator input) elevator deflection is given by

$$-\delta_e = k_p z x_i - k_a \alpha$$

When the trim values are inserted in this equation, the trim value of the integrator output is found to be  $x_i = 0.6186$ . The aircraft trim data file can now be augmented with the initial conditions for the three controller states.

A simulation of the F-16 aircraft model, with this controller, will now be used to illustrate some points about controller design. The following discrete-time subprogram was used to provide simulation commands.

```

subroutine DISCRETE(time,TS,x,xdot,)
dimension x(*), xdot(*)
common/controls/thtl,el,ail,rdr,qcom

if (time.lt. 10.0) then
  qcom= 0.0
else if (time.lt. 20.0) then
  qcom= 8.65
  thtl= 1.0
else if (time.lt. 50.0) then
  qcom= 0.0
else
  qcom= 10.0
end if
return
end

```

Figure 4.7-1 shows the vertical-plane trajectory produced by the commands, and Figure 4.7-2 shows the pitch-rate response. The aircraft is given full throttle and a

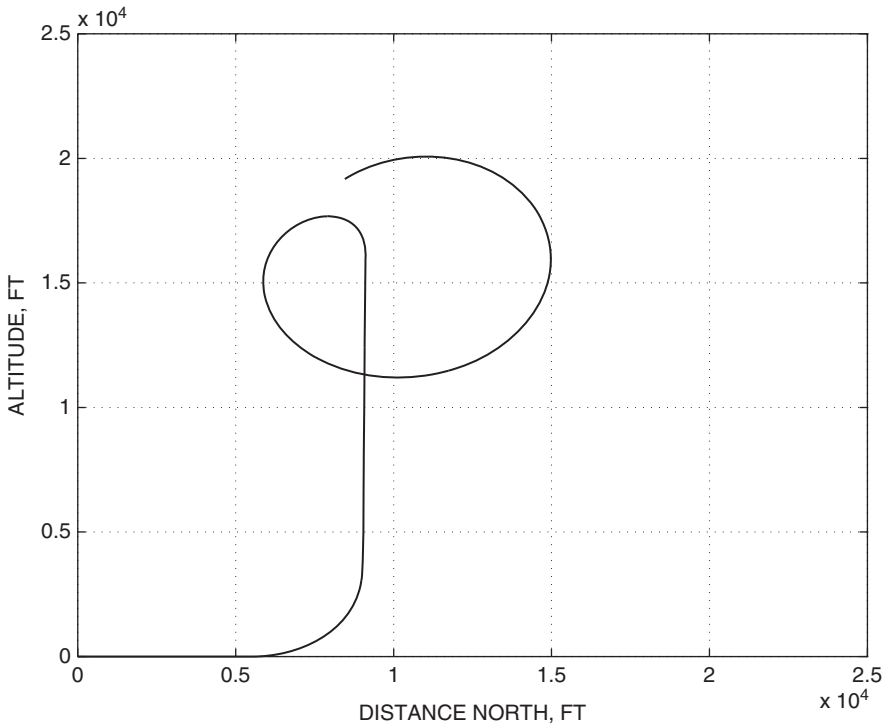


**Figure 4.7-1** Aircraft trajectory in the vertical plane.

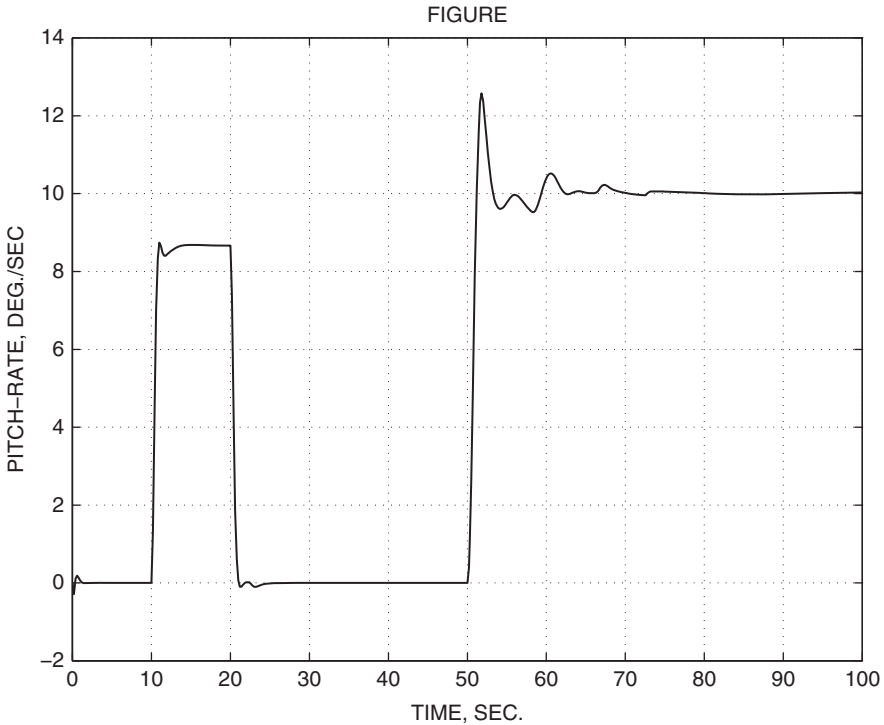


**Figure 4.7-2** Aircraft pitch-rate response along the trajectory.

pitch-up command at  $t = 10$  s; the pitch-rate command has been adjusted to bring the aircraft vertical at  $t = 20$  s. At  $t = 50$  s the airspeed has fallen to about 300 ft/s and the altitude is approximately 16,000 ft; therefore, the flight conditions are greatly different from the controller design conditions (sea level and 502 ft/s). The pitch-rate response has a large overshoot at  $t = 50$  s because of the off-nominal design conditions. The aircraft dynamics change with flight conditions as described in Section 4.2, and in a practical controller design, the gain coefficients would be “*gain scheduled*” as functions of dynamic pressure and/or Mach number. The time of flight was 100 s for the trajectory shown, and the lateral-directional dynamics did not become significantly involved in the motion. The sideslip angle peaked up to about  $0.1^\circ$  after the pitch-over command at  $t = 50$  s but then returned to very small values. The angle of attack reached a peak of approximately  $15^\circ$  at  $t = 55$  s. ■

**Example 4.7-2: Lateral-Directional CAS Nonlinear Simulation.** In this example the lateral-directional controller designed in Example 4.5-3 is programmed for nonlinear simulation and used, together with the pitch-rate controller from Example 4.7-1, to provide complete 6-DoF control. The controller code is:

```
subroutine FC(time,x,xd)
dimension x(*), xd(*)
real m
```

```

common/controls/thtl,el,ail,rdr,pcom,qcom,rcom
common/output/an,ay,ax,qbar,m,alpha,beta,phid,thtad,
    & pd,qd,rd                                ! d means degree units
el =-x(1)                                     ! actuator state-> el
ail=-x(4)                                     ! : : : : :-> ail
rdr=-x(5)                                     ! : : : : :-> rdr
call fl6(time,x(7),xd(7))                    ! aircraft dynamics
xd(3)= qcom- qd                              ! error integrator
u = 1.5*x(3)-.5*qd-.08*x(2)                 ! pitch control law
xd(1)= 20.2*(u-x(1))                        ! elevator actuator
xd(2)= 10.0*( alpha- x(2) )                 ! alpha filter
ua = 0.2*(pcom-pd)                          ! roll control law
xd(4)= 20.2*( ua- x(4) )                    ! aileron actuators
ari = (0.13*x(2)- 0.7)*ua                   ! ARI
rs = rd- pd*x(2)/57.3                       ! yaw-rate feedback
xd(6)= rs- x(6)                             ! washout
err= rcom -.8*xd(6)- 10.0*ay                ! yaw control law
xd(5)= 20.2*( err + ari- x(5) )             ! rudder actuator
return
end

```

This time the controller states are numbered first and the aircraft states are appended to these. The nominal flight condition of Table 3.6-3 was used, and the six compensator states were included in the trim data file. The actuator states must be set to the trimmed values of the corresponding aircraft controls, and the alpha filter state to the value of alpha in degrees. The other controller states can be set to zero since the rest of the controller is linear.

A nonlinear simulation was chosen that would exercise the ARI through high-alpha and fast roll rates yet be easily preprogrammed for non-real-time simulation. The trajectory chosen was a pull-up into a vertical loop, with a 180° roll at the top of the loop and continuing into a second vertical loop. The preprogrammed commands were:

```

subroutine DISCRETE(time,ts,x,xd)
dimension x(*),xd(*)
common/controls/thtl,el,ail,rdr,pcom,qcom,rcom

if (time.lt. 5.0) then
    qcom= 0.0
    pcom= 0.0
    rcom= 0.0
else if (time.lt. 15.0) then
    qcom= 15.0                                ! Pull up at 15 deg/s
    thtl= 1.0                                ! at full throttle
else if (time.lt. 17.0) then
    pcom= 150.0                              ! rolling for 2 sec.
else
    pcom= 0.0
end if
return
end

```

The alpha filter and actuator states were initialized exactly with the correct initial conditions, but the other controller states were left uninitialized, so the first 5 s of the flight was used to let any transients die away. Full throttle and a 15-deg/s pitch-rate command are applied at  $t = 5$  s, and then a roll-rate command pulse is applied between 15 s and 17 s. The desired roll rate is therefore 90 deg/s, but because of the finite error of the type-0 roll-rate loop, the rate command had to be adjusted by trial and error to achieve the 180° roll.

An elevation view of the trajectory is shown in Figure 4.7-3a. The first loop corresponds to a normal acceleration of about 4 g, and the aircraft speed decreases roughly linearly from 500 ft/s at 5.0 s to 270 ft/s at 24 s (near the top of the second loop). Figures 4.7-3b and c show angle of attack, roll attitude, and pitch attitude. Alpha increases rapidly as the loop is started, remains roughly constant to provide the centripetal acceleration while the pitch attitude is between 45° and 90°, and then starts to fall off as gravity helps to provide the centripetal acceleration. During the second loop alpha rises to a larger peak, because the airspeed has dropped considerably by then.

The roll angle of 0° suddenly becomes a roll angle of 180° as the aircraft passes through the vertical-attitude condition, and this wings-level attitude is held until the roll is started at 15 s. The attitude angles are computed by integrating the angular rates

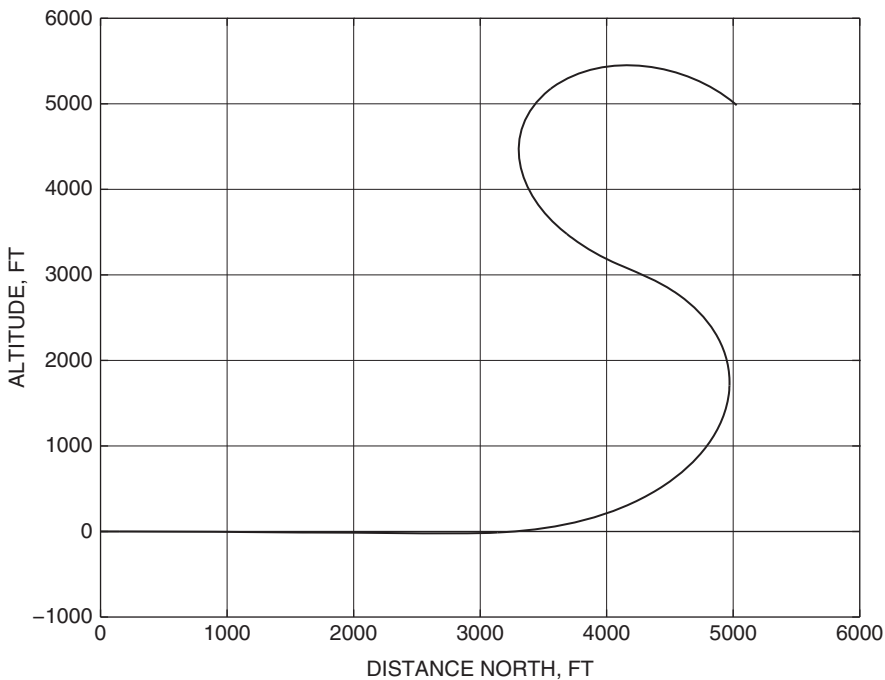


**Figure 4.7-3a** Aircraft trajectory in the vertical plane.

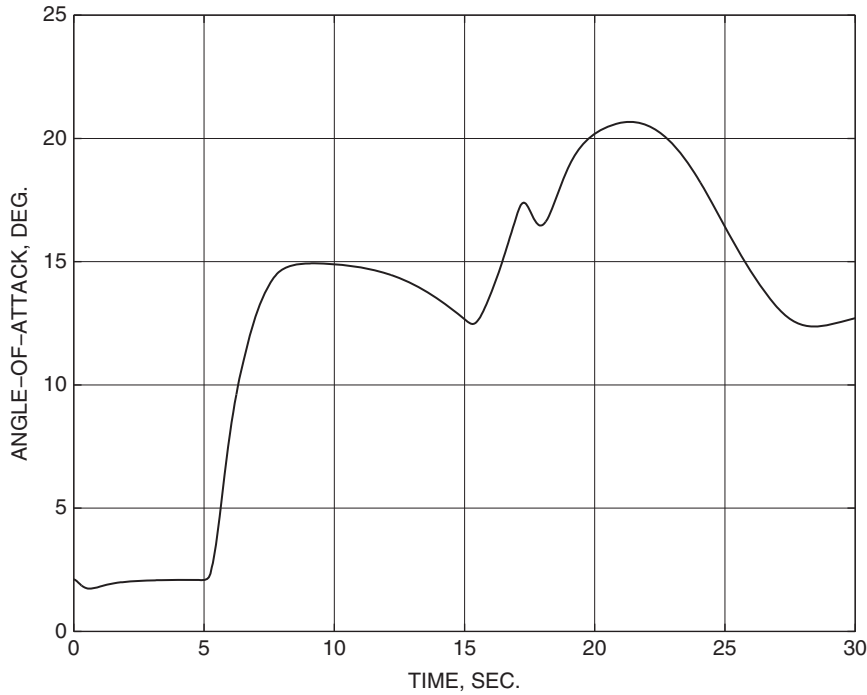


**Figure 4.7-3b** Angle of attack versus time.

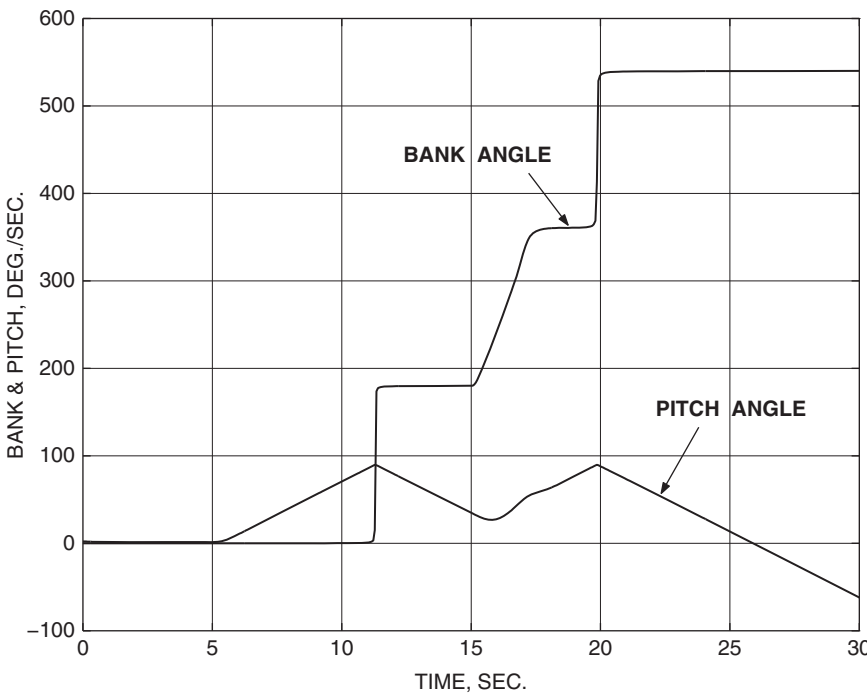


**Figure 4.7-3c** Aircraft roll and pitch angles along trajectory.



(state derivatives), not from trigonometric functions, so the roll angle may contain multiple  $360^\circ$  ambiguities, depending on how the angular rates behave.

Figure 4.7-3*d* shows the fast roll-rate response and the corresponding yaw rate that is generated by the ARI. The pitch rate undergoes a positive perturbation during the roll, and this is due to the nose-up pitching moment generated by inertia coupling. Figure 4.7-3*e* shows the positive increment in elevator deflection that is generated by the longitudinal control system to counteract the inertia-coupling moment. As stated earlier, a major problem when rolling rapidly at still higher angles of attack is that the longitudinal control surfaces may be unable to generate a large enough nose-down moment.

In this example the elevator deflections are quite small, but the aileron and rudder deflections are large. This is due to the combination of high demanded roll rate and low aileron effectiveness (because of the high  $\alpha$  and relatively low dynamic pressure). It is also partly due to the fact that while the rudder is generating the required yaw rate, it is also generating a rolling moment that opposes the aileron rolling moment. The large peak deflections are due to the instantaneous demand for the high roll rate. Note that the aileron and rudder deflection rates may have reached or exceeded the capabilities of their actuators; this concern is addressed later.

Figure 4.7-3*f* shows that the control system has done an excellent job of keeping the sideslip angle small during this demanding maneuver. The sideslip excursions are

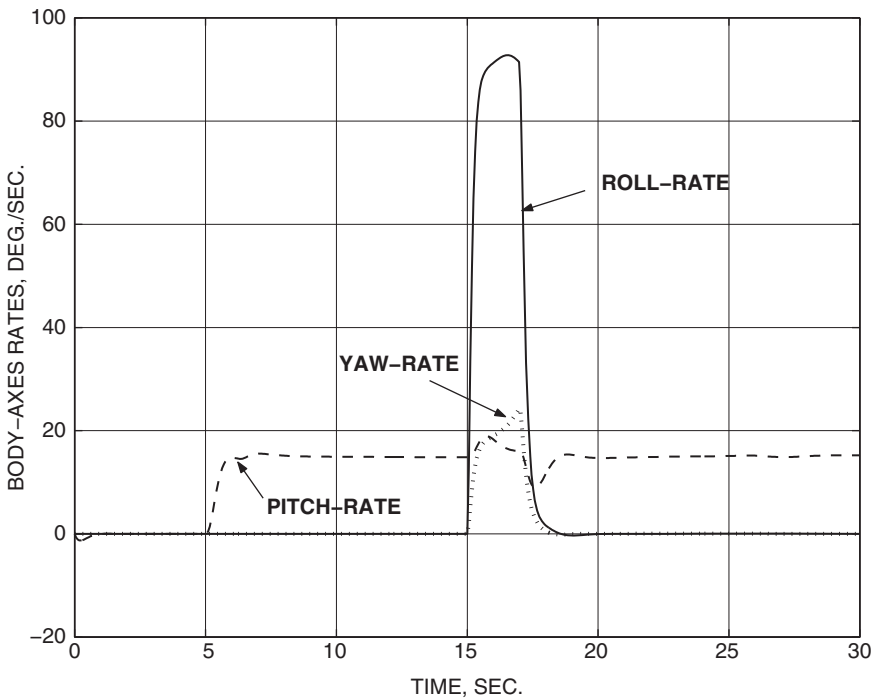


**Figure 4.7-3*d*** Aircraft body-axes angular rates along trajectory.

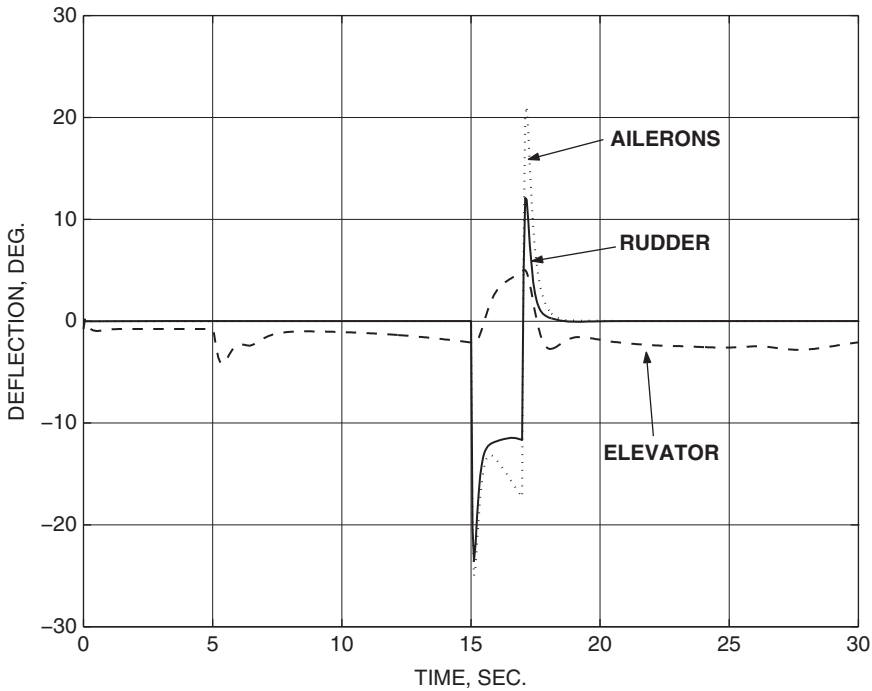


Figure 4.7-3e Control surface deflections along trajectory.

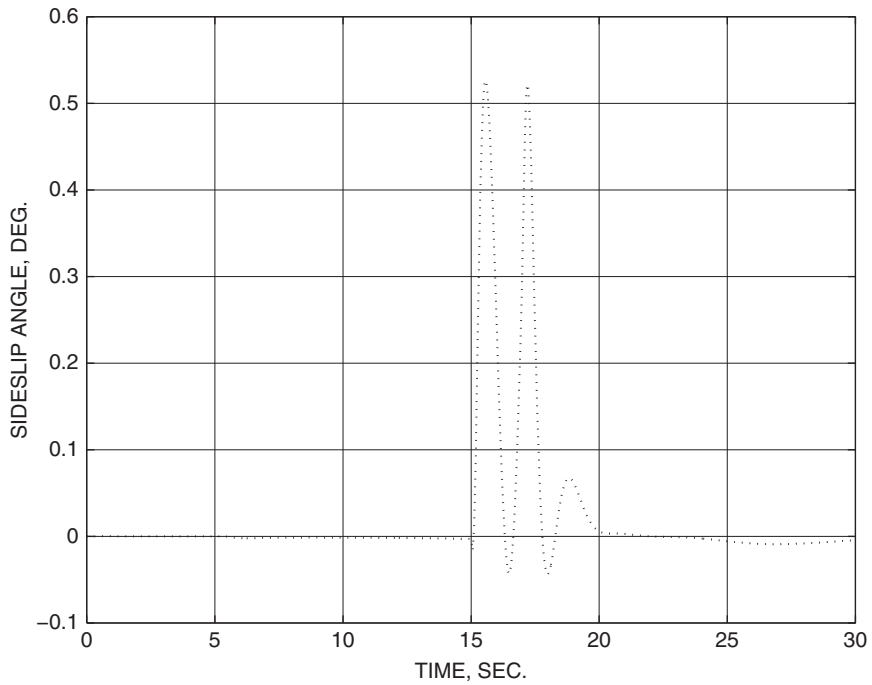
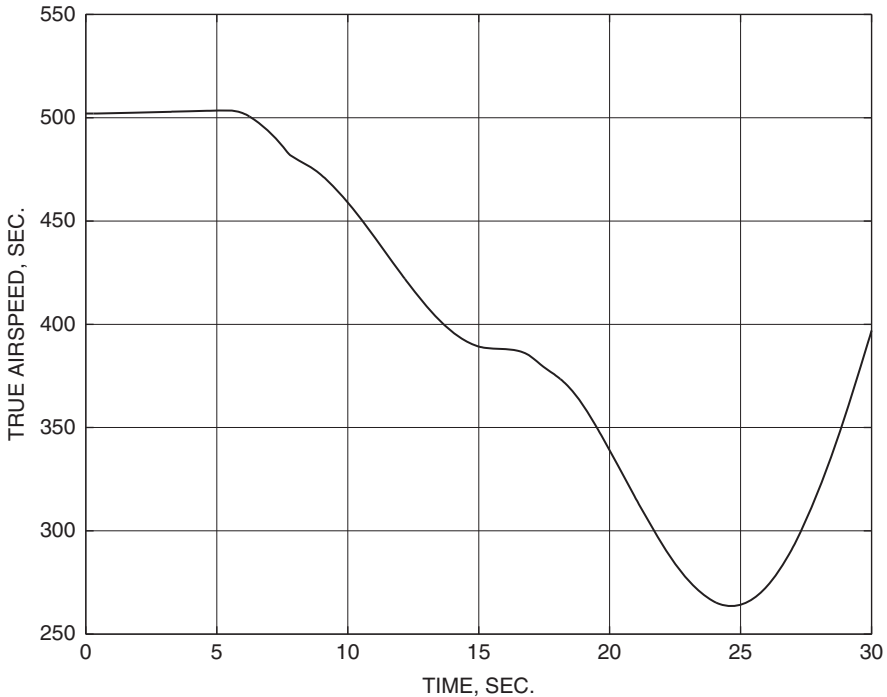


Figure 4.7-3f Sideslip angle variation along trajectory.



**Figure 4.7-3g** True airspeed variation along trajectory.

biased positively, that is, toward adverse beta. This is desirable in general; a combination of adverse and proverse beta tends to excite the dutch roll mode. The ARI gain is quite critical, and the values used are close to optimal. Larger values will produce a single negative beta excursion and a single positive beta excursion that are more nearly symmetrical about zero but considerably larger in magnitude. Figure 4.7-3g shows the variation of airspeed with time. The maneuvers have caused the speed to fall continuously until the top of the second loop is passed, despite full throttle being used throughout. The twofold reduction in speed will cause a fourfold reduction in dynamic pressure.

Finally, note that the performance may appear satisfactory for these flight conditions, but the design must be evaluated at other altitude/speed combinations. Gain scheduling with Mach number will probably be required, and much more comprehensive simulation is necessary before the design can be considered practical. ■

**Example 4.7-3: Simulation of Automatic Landing** This example will simulate longitudinal control for an automatic landing of the transport aircraft model using the longitudinal controller designed in Example 4.6-4. The MATLAB controller code

can be constructed quite easily from the code in Example 4.6-4 with the help of Figure 4.6-10 and Table 3.3-1:

```
% GLIDE.M Glide-Slope Controller for Ex. 4.7-3
function [xd]= glide(time,x,u)
global xd
u(2) = -x(8); % set elevator
u(1) = x(11); % set throttle
[xd] = transp(time,x,u); % call aircraft
xd(14)= 0.0 - x(7); % d-loop error
dpi = xd(14) +.18*x(14); % PI compensation
xd(13)= dpi - 5.0*x(13); % Phase Lead
thcom = xd(13) + 0.5*x(13); % theta command

xd(9) = thcom - 57.29578*x(3); % Pitch error
tpi = xd(9) + 0.2*x(9); % PI integrator
xd(10)= tpi - 14.0*x(10); % Phase Lead
qcom = 40.0*(xd(10) + 1.4*x(10)); % Pitch-rate command
qerr = qcom - 57.29578*x(4); % q error
xd(8) = 10.0*(qerr-x(8)); % El. actuator

ev = 250 - x(1); % speed error
xd(12)= ev - 10.0*x(12); % lead compensator
ut = 10.0*(ev - 9.0*x(12)); % lead comp.
xd(11)= 0.2*(ut - x(11)); % throttle lag
```

and the sequence of .M files involved in the simulation is:

```
NLSIM.M - Nonlinear simulation from Chap. 3
RK4 - Fourth-order Runge-Kutta from Ch. 3
GLIDE.M - Controller routine above
TRANSP.M - Transport-Aircraft model from Ch. 3
ADC.M - Atmosphere model for Transp. Aircraft
```

The chosen initial conditions were level flight at  $V_T = 250$  ft/s,  $h = 1500$  ft, with flaps and gear deployed, and  $x_{cg} = 0.25$ . An initial-condition data file can be obtained by using TRIM.M (Chapter 3), as follows. In the steady state all of the integrator inputs in Figure 4.6-10 are zero, and it is easy to write algebraic equations for all of the controller variables in terms of the aircraft states and controls. When these equations are included in the cost function, the trim program will produce an initial condition file for all fourteen controller and aircraft states (see Example 4.7-4). In the transport aircraft model the reference flight-path angle was programmed to change from zero to  $-2.5^\circ$  at  $t = 15$  s to represent glide-path capture.

Figure 4.7-4a shows the trajectory for 50 s of simulated flight; the aircraft starts out in level flight with no transient because the controller was accurately initialized. Figure 4.7-4b shows the deviation from the glide path. Figure 4.7-4c shows the

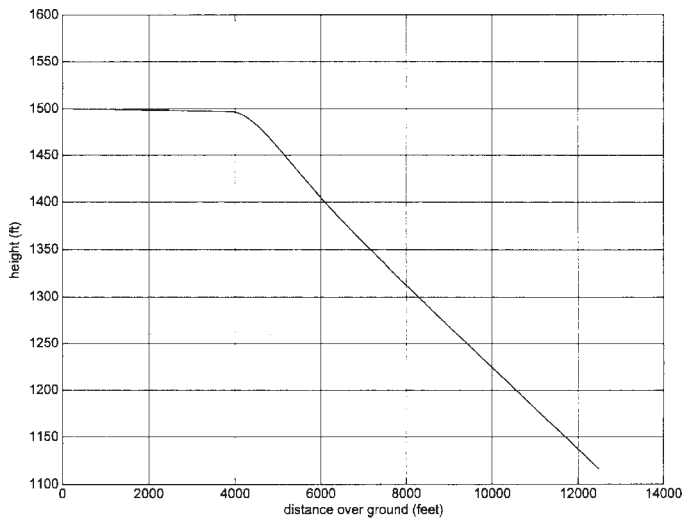


Figure 4.7-4a Automatic landing; elevation profile.

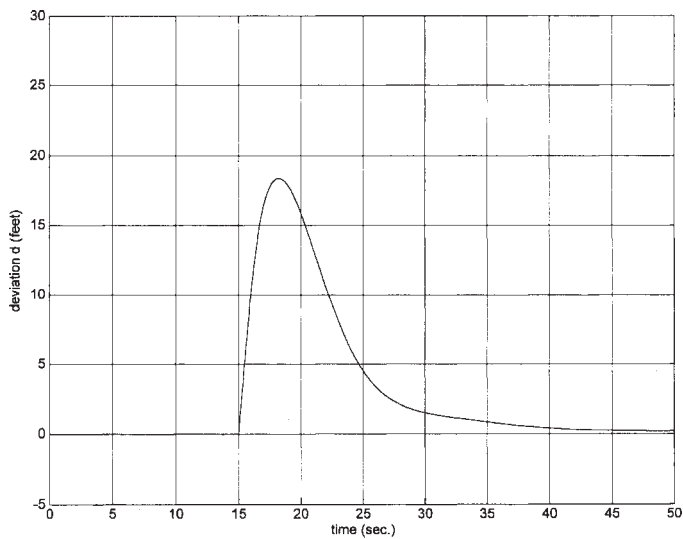


Figure 4.7-4b Automatic landing; deviation from glide path.

behavior of  $\alpha$ , pitch attitude, and elevator deflection, and Figures 4.7-4*d* and *e* show, respectively, the corresponding variation of throttle position and airspeed. It is evident that the airplane is driven onto the glide path quickly and smoothly, without large excursions in pitch attitude. Airspeed is held very nearly constant and the throttle is changed smoothly and gently. Because of the tight control,

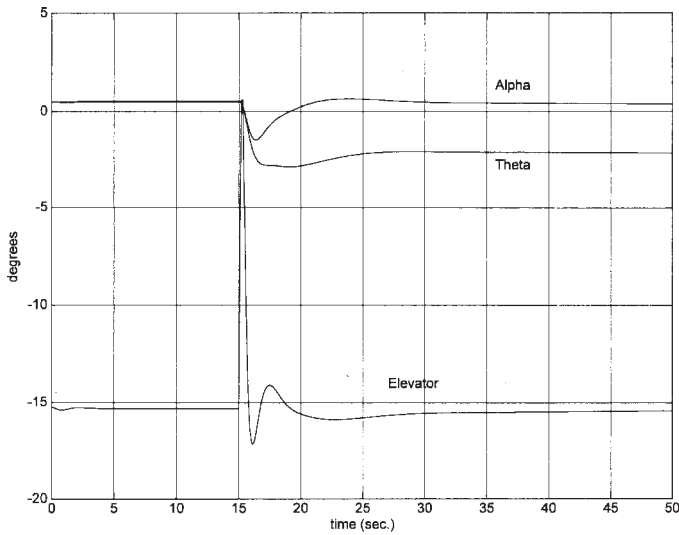


Figure 4.7-4c Automatic landing; controlled variables.

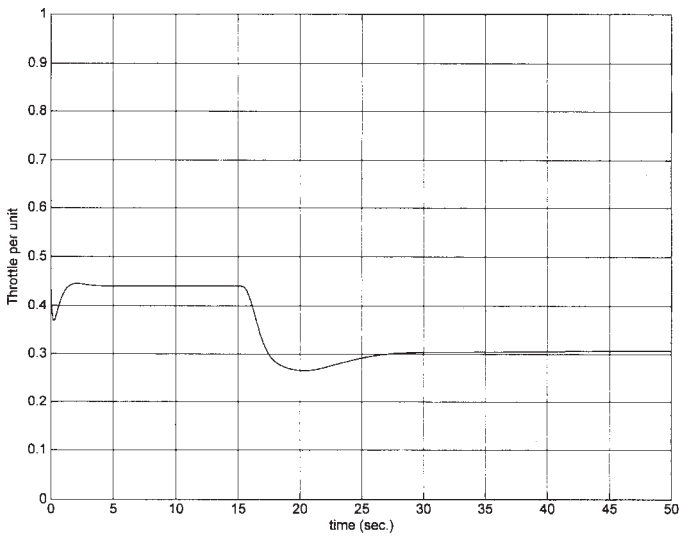


Figure 4.7-4d Automatic landing; throttle variation.

the elevator shows some rapid excursions, which could cause rate limiting in a real actuator.

The final component of this design is the automatic “flare” control that makes the aircraft begin to level out as the altitude approaches zero and touch down with an acceptably small rate of descent. This is described in the following subsection.

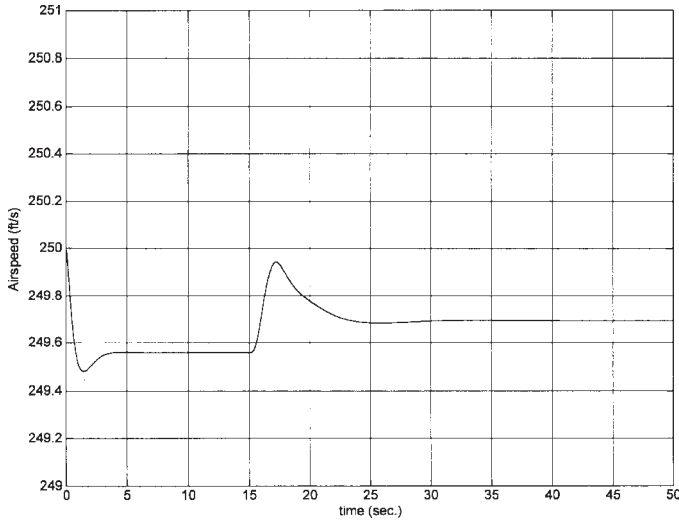


Figure 4.7-4e Automatic landing: airspeed variation.

## Flare Control

At an altitude of about 50 ft above the runway the automatic landing system must start to reduce the rate of descent of the aircraft, achieve the correct pitch attitude for landing, and begin to reduce the airspeed. This portion of the trajectory is called the landing flare, and the geometry of the flare is illustrated in Figure 4.7-5. On the glide path the aircraft is descending at a rate of 10 ft/s or greater and will hit the ground hard if the flare is not executed. The rate of descent must be reduced to less than about 2.0 ft/s by touchdown. The pitch attitude angle will depend on the airspeed and will be only a few degrees for a large jetliner; military aircraft may land with large pitch angles to make use of aerodynamic braking. Altitude rate ( $\dot{h} = V_T \sin \gamma$ ) is a natural choice for the controlled variable since it determines the impact, can be derived in the radar altimeter, makes the control system independent of ground effect and wind disturbances, and involves control of one less plant integration than altitude.

Modern digital-controller-based automatic landing systems can yaw the aircraft to deal with cross-winds while lining up the runway, decrab the aircraft and dip a wing

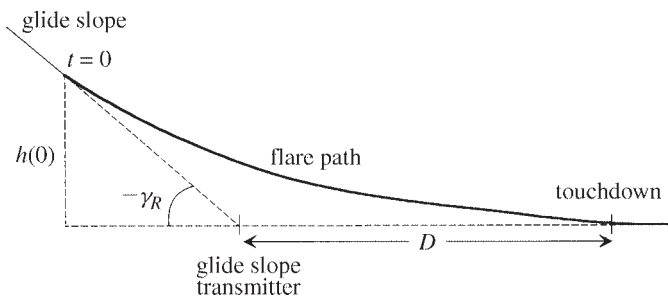


Figure 4.7-5 Landing-flare geometry

to keep the lateral velocity component small, and level the wings immediately before touchdown.

**Example 4.7-4: Automatic Flare Control** In this example we will use altitude rate from the aircraft model as the controlled variable and switch from the glide-path controller to the flare controller when the altitude reaches 50 ft. The speed loop will continue to operate with the same command input. Switching from one controller to another can cause large transients in the aircraft states, which is disconcerting and dangerous so close to the ground. To avoid this, the flare controller must be initialized with the final conditions on the glide slope and then commanded to go smoothly to the new altitude rate. Here we have used only a simple controller with one additional state,  $x(15)$ , which is initialized to zero. Thus, the following code shows only a PI compensator and a gain, with a step command of  $-2$  ft/s, for the altitude-rate controller. Some logic (variable “MODE”) is used to ensure that control does not momentarily switch back to the glide-path controller if integration errors or transients cause a fluctuation in altitude at changeover. The airspeed on the glide path was chosen to give the aircraft a slightly pitched-up attitude at touchdown and was 235 ft/s (139 knots). The controller code is as follows:

```
% FLARE.M Glide-Slope & Flare Controller
function [xd]= flare(time,x,u);
global xd mode
u(2) = -x(8); % set elevator
u(1) = x(11); % set throttle
[xd] = transp(time,x,u); % call aircraft
h = x(5); % altitude
vcom=235; % commanded speed
if time<1
    mode=0; % glideslope mode
end
if h>50 & mode==0 % d-controller
    xd(14)= 0.0 - x(7); % integrate d-error
    dpi= xd(14) + .18*x(14); % PI comp.
    xd(13)= dpi - 5.0*x(13); % lead compensation
    thcom = xd(13) + 0.5*x(13); % theta command
    xd(15)=0.; % for flare controller
elseif h<=50 | mode==2 % roll-out mode
    mode=2;
    xd=zeros(1,15);
    thcom=0;
elseif h<=50 | mode==1 % flare controller
    mode=1; % lock out other modes
    hdot=-2; % sink-rate command
    xd(15)= ( hdot - xd(5) ); % PI integrator
    thcom=.1*( xd(15) +.5*x(15) ); % C. L. Zero at-.5
    xd(13)=0;
end
xd(9) = thcom - 57.29578*x(3); % integrate pitch error
tpi = xd(9) + 0.2*x(9); % PI compensation
xd(10)= tpi - 14.0*x(10); % phase-lead comp.
qcom = 40*( xd(10) + 1.4*x(10) ); % pitch-rate command
```



```

qerr = qcom - 57.29578*x(4);           % pitch-rate error
xd(8) = 10.0 * (qerr - x(8) );         % Elevator actuator

ev = vcom - x(1);                      % Autothrottle code
xd(12)= ev - 10.0*x(12);               % phase-lead pole
ut = 10.0*(ev - 9.0*x(12) );           % phase-lead zero
xd(11)= 0.2*(ut - x(11));              % throttle servo

```

and the cost function used with the trim program was:

```

% Cost Function for 3-DOF Aircraft
function [f]=ssland(s);
global x u gamma
u(1)= s(1);           % throttle
u(2)= s(2);           % elevator
x(2)= s(3);           % alpha
x(3)= x(2) + gamma;   % theta
x(8)= -u(2);
x(10)= x(8)/(40*1.4);
x(9)= 14*x(10)/.2;
x(13)= 57.29578*x(3)/.5;
x(14)= 5*x(13)/.18;
x(11)= u(1);
x(12)= x(11)/10;
x(15)= 0.0;           % flare control state
time= 0.0;
[xd]=transp(time,x,u);
f= xd(1)^2 + 100*xd(2)^2 + 10*xd(4)^2;

```

A nonlinear simulation of the controller, with the transport aircraft model, was started from an initial state corresponding to an altitude of 300 ft on the glide-path simulation of Example 4.7-3. Figures 4.7-6a through *c* show the trajectory,

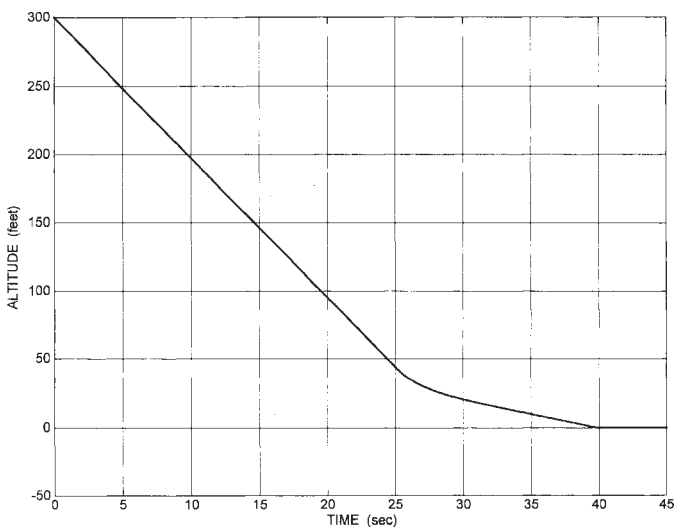


**Figure 4.7-6a** Automatic landing; glide slope and flare trajectory.

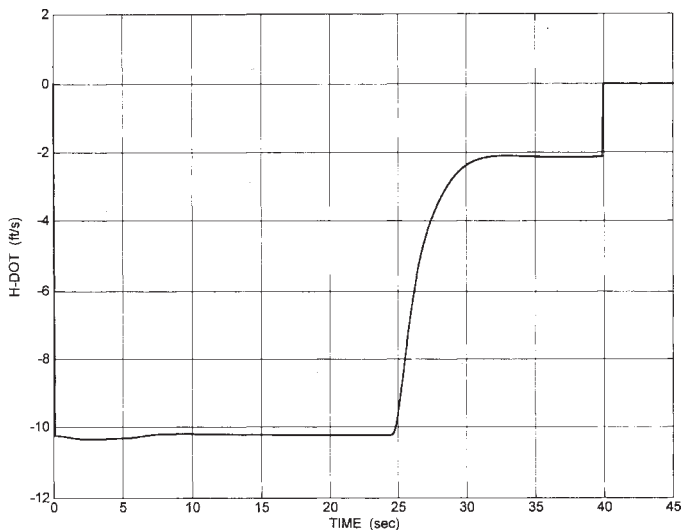


Figure 4.7-6b Altitude rate during flare.

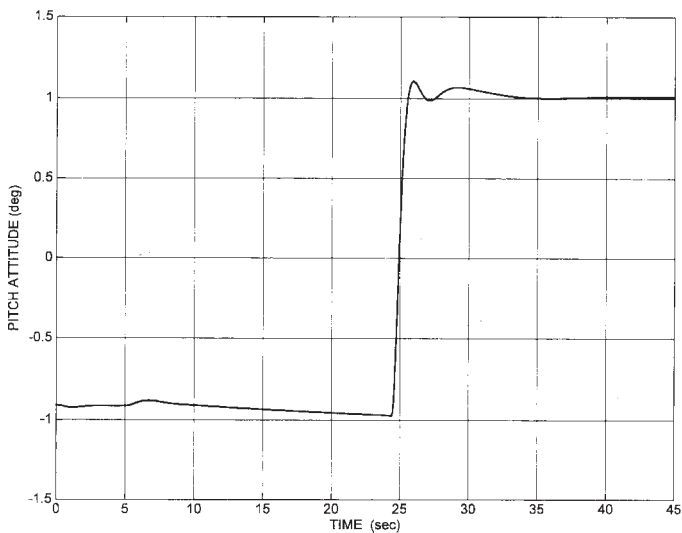


Figure 4.7-6c Pitch attitude during flare.

vertical speed, and pitch attitude. The vertical speed and pitch attitude have reached the desired values well before touchdown. The pitch-attitude change is faster than necessary; the small well-damped oscillation in pitch would be barely noticeable to the passengers. ■

**Example 4.7-5: A Roll-Angle-Steering Control System** The controller routine for the lateral-directional CAS is easily modified to include the roll angle feedback and the turn compensation. The controller and command Fortran routines are shown below.

```

subroutine FC(time,x,xd)
dimension x(*), xd(*)
real m
common/controls/thtl,el,ail,rdr,bank,qcom,rcom
common/output/an,ay,ax,qbar,m,alpha,beta,phid,thtad,
& pd,qd,rd
el = -x(1)
ail= -x(4)
rdr= -x(5)
call f16(time,x(7),xd(7))
qcom= rd*tan(phid/57.29578)      ! turn compensation
xd(3)= qcom - qd
u= 1.5*x(3) - .5*qd - .08*x(2)
xd(1)= 20.2*(u-x(1))
xd(2)= 10.0*( alpha - x(2) )
ua = 1.0*(bank-phid -.2*pd)      ! bank angle control law
xd(4)= 20.2*( ua - x(4) )
ari = (0.13*x(2) - 0.7)*ua
rs = rd - pd*x(2)/57.3
xd(6)= rs - x(6)
err= rcom - .8*xd(6) - 10.0*ay
xd(5)= 20.2*( err + ari - x(5) )
return
end

subroutine DISCRETE(time,ts,x,xd)
dimension x(*),xd(*)
common/controls/thtl,el,ail,rdr,bank,qcom,rcom
if (time.ge. 20.0) Then
    bank= -70.0
else if (time.ge. 5.0) Then
    bank= 70.0
else
    bank = 0.0
    qcom = 0.0
    rcom = 0.0
end if
return
end

```

The same initial-condition data used for the lateral-directional CAS were used with this controller, and a simulation was flown using the discrete-time commands shown above. Figure 4.7-7a shows the ground track of the aircraft in response to these commands. The altitude decreased by about 600 ft during the 30-s simulation because of

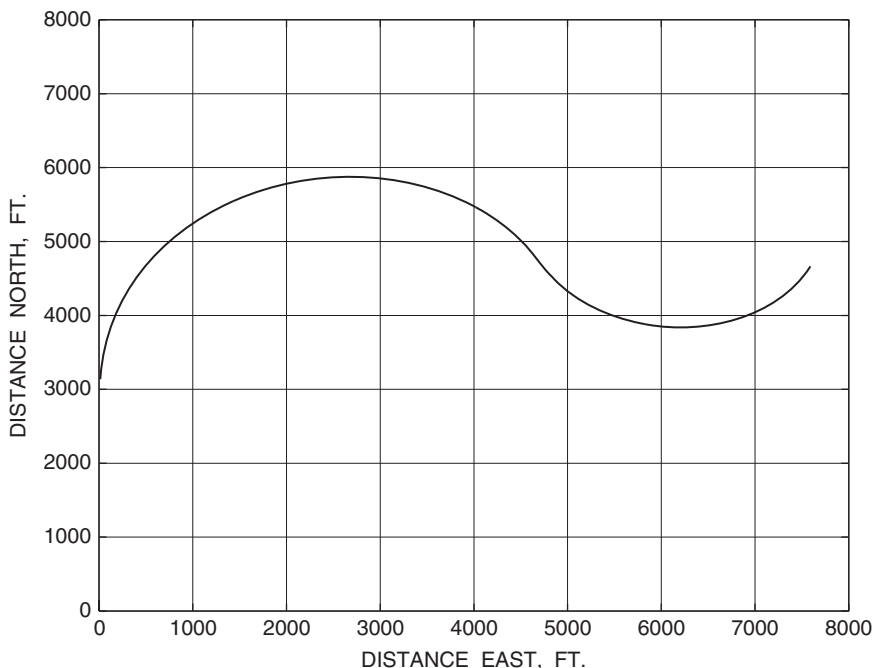


**Figure 4.7-7a** Ground track during roll angle steering.

the open-loop turn compensation and the finite control error of the lateral-directional control systems. The speed decreased by about 200 ft/s during the simulation, because of the maneuvers.

Figures 4.7-7*b*, *c*, and *d* show, respectively, the fast well-damped roll angle response, the angle of attack, and the sideslip angle. The aileron and rudder deflections are shown in Figures 4.7-7*e* and *f*; these show short-duration deflections that are well beyond the limits of the control surfaces and raise the following important points.

First, the simulation results may be unrealistic if the control surface rate and deflection limits are not modeled. Second, control system limiting will be caused by the abrupt large-amplitude commands and the high gains that have been used in the roll angle control. This is not necessarily a problem if the system response is still acceptable, since the fastest possible roll response may be desired, and the high gains also provide a small control error for low-amplitude inputs. Third, the airplane handling qualities are the most important consideration, and in this situation the stick prefilter and the maximum roll rate of the airframe will play a major part in determining the pilot's opinion of the roll performance.

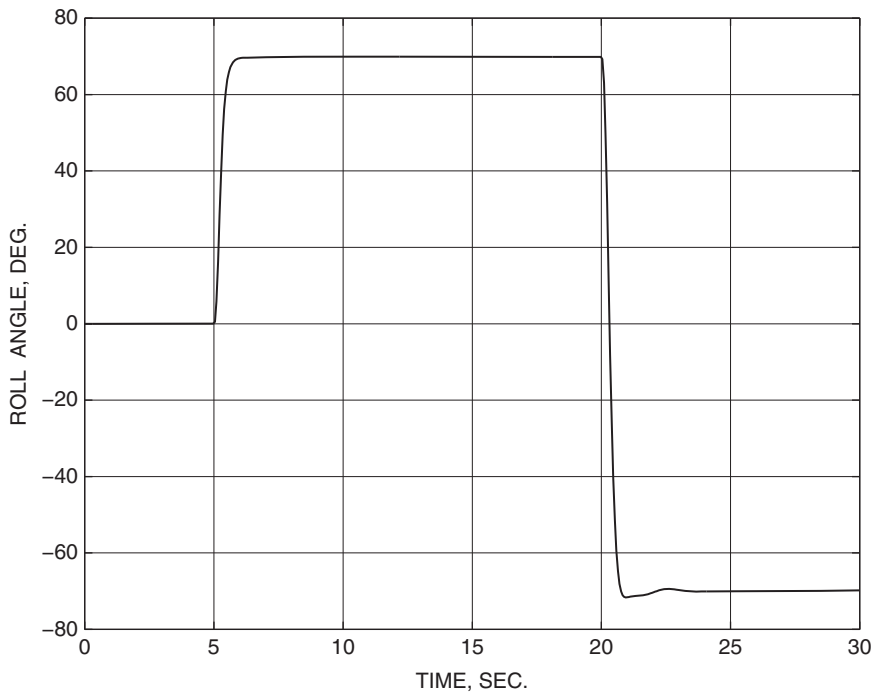


Figure 4.7-7b Bank angle during roll angle steering.

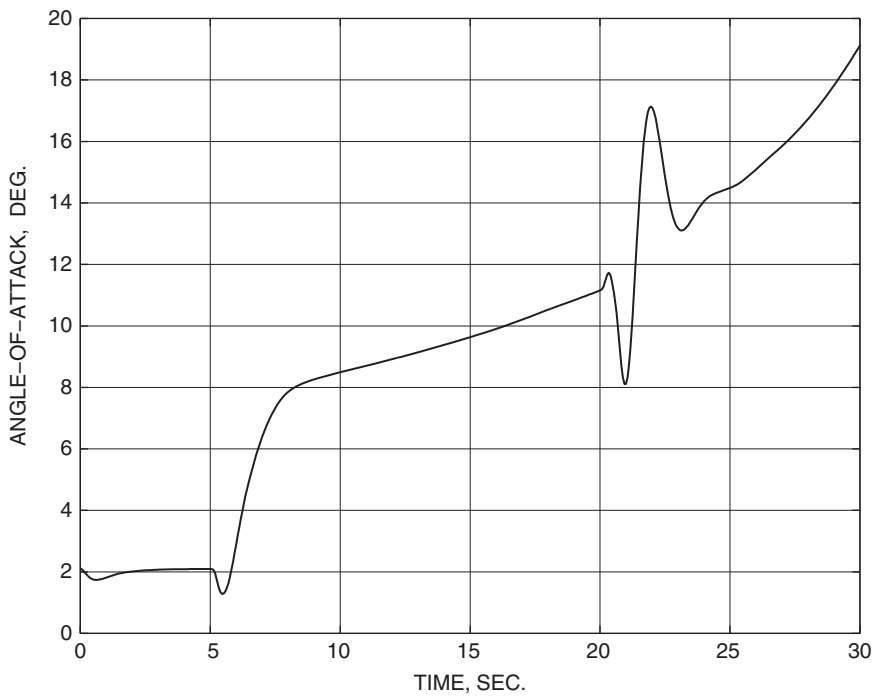


Figure 4.7-7c Angle of attack during roll angle steering.

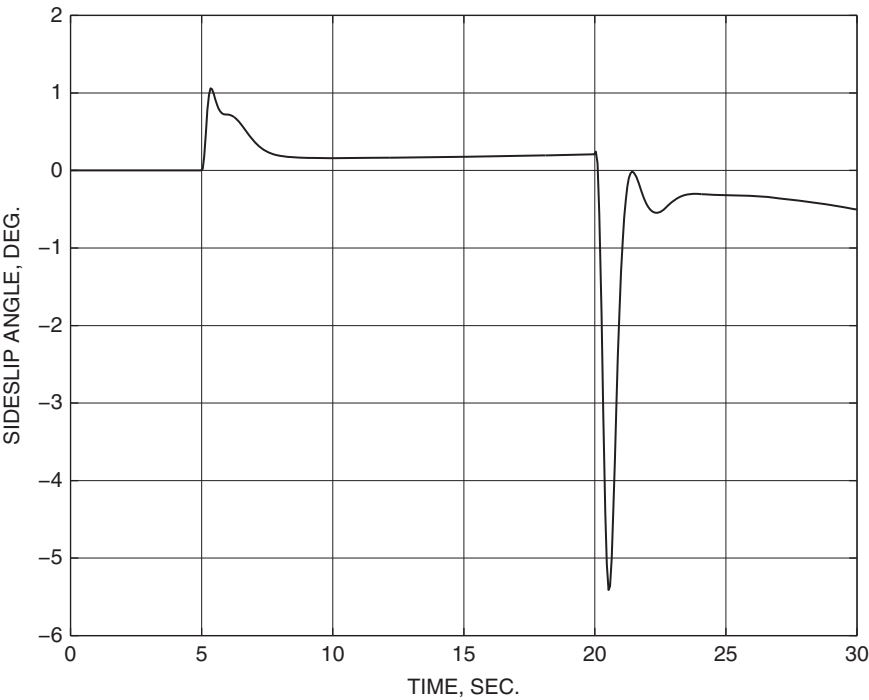


Figure 4.7-7d Sideslip angle during roll angle steering.

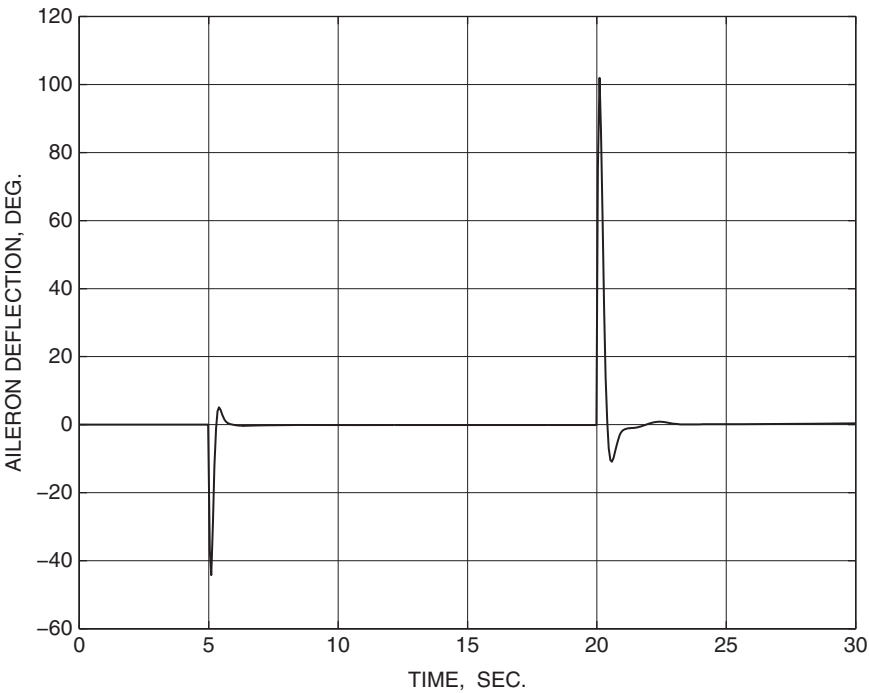
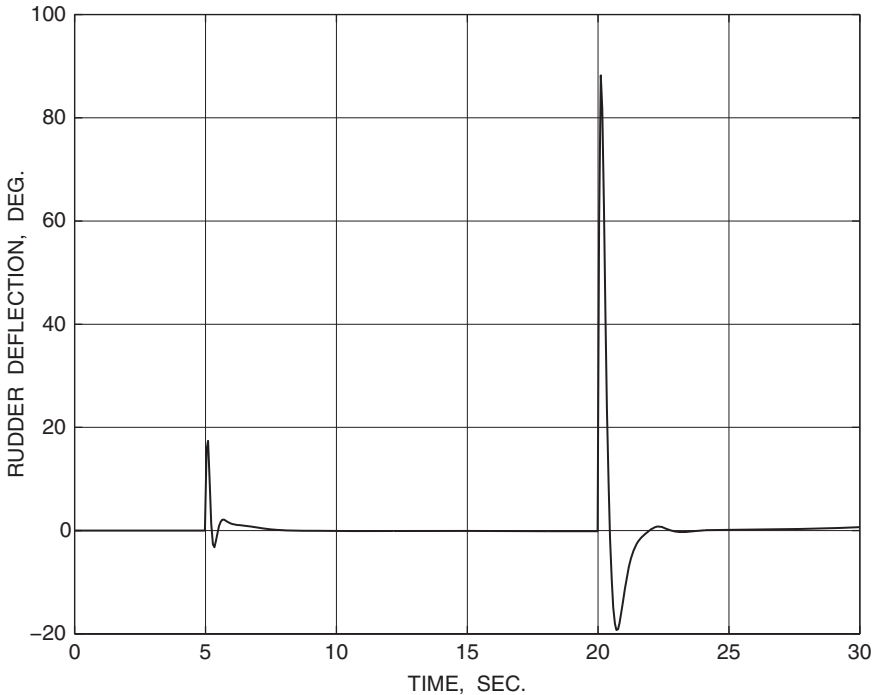


Figure 4.7-7e Aileron deflection during roll angle steering.



**Figure 4.7-7f** Rudder deflection during roll angle steering.

**Example 4.7-6: Simulation of a Controller with Limiters** Here we deal with “hard limiting” as distinct from merely nonlinear behavior. To simulate limiting behavior the control variables, state variables, and state derivatives must be modified when the limiting occurs. Other variables are essentially dummy variables that are assigned according to the states and controls. Rate limiting can be simulated by simply “clamping” the appropriate state derivative when its maximum value is reached. State-variable limits must be dealt with by modifying their derivatives also. When a state variable reaches a limit, a nonzero derivative is allowed only if it is in the direction that takes the state variable off the limit. This is related to the integrator wind-up problem described in Chapter 3. In this example, the code used for Example 4.7-2 has been modified by the addition of rate and deflection limits and is shown below. In-line comments have been added to explain the details.

The behavior of the controller, with limiters, is illustrated by a time-history simulation similar to that of Example 4.7-2, and the discrete-time commands are shown below. The integration step size was reduced to 1 ms in this simulation to capture the action of the limiters with sufficient accuracy. This can make the execution quite slow.

```

subroutine FC(time,x,xd)
dimension x(*), xd(*)
real m
common/controls/tht1,el,ail,rdr,pcom,qcom,rcom
common/output/an,ay,ax,qbar,m,alpha,beta,phid,thtad,pd,qd,
& rd
data erl,edl,arl,adl,rrl,rdl/60.0,25.0,80.0,21.5,120.0,30.0/
el = -x(1)
ail= -x(4)
rdr= -x(5)
call fl6(time,x(7),xd(7))
xd(2)= 10.0*( alpha - x(2) )
xd(3)= qcom - qd
u= 1.5*x(3) - .5*qd - .08*x(2)
xd(1)= 20.2*(u-x(1))

if( abs(xd(1)) .gt. erl) then
    xd(1)= sign(erl, xd(1))          ! Elevator rate limit
end if
if(x(1) .gt. edl) then
    x(1)= edl                      ! Elevator + deflection limit
    if(xd(1) .gt. 0.0) xd(1)= 0.0   ! Stop integrating positively
    if(xd(3) .lt. 0.0) xd(3)= 0.0   ! clamp error integrator
else if (x(1) .lt. -edl) then
    x(1)= -edl                    ! Elevator - deflection limit
    if(xd(1) .lt. 0.0) xd(1)= 0.0   ! stop integrating negatively
    If(xd(3) .gt. 0.0) xd(3)= 0.0   ! clamp error integrator
else
    continue
end if

ua  = 0.2*(pcom-pd)
xd(4)= 20.2*( ua - x(4) )
if( abs(xd(4)) .gt. arl) then
    xd(4)= sign(arl, xd(4))          ! Aileron rate limit
end if
if(x(4) .gt. adl) then
    x(4)= adl                      ! Aileron deflection limit
    if(xd(4).gt. 0.0) xd(4)= 0.0
else if (x(4) .lt. -adl) then
    x(4)= -adl
    if(xd(4) .lt. 0.0) xd(4)= 0.0
else
    continue
end if

temp= ua
if (abs(temp).gt. adl) then
    temp= sign(adl,temp)            ! limit ARI to aileron limit
end if
ari = (0.13*x(2) - 0.7)*temp
rs  = rd - pd*x(2)/57.3
xd(6)= rs - x(6)

```



```

err= rcom - .8*xd(6) - 10.0*ay
xd(5)= 20.2*( err + ari - x(5) )

if( abs(xd(5)) .gt. rrl) then
    xd(5)= sign(rrl, xd(5))          ! Rudder rate limit
end if
if(x(5).gt. rdl) then
    x(5)= rdl
    if(xd(5).gt. 0.0) xd(5)= 0.0
else if (x(5) .lt. -rdl) then
    x(5)= -rdl
    if(xd(5) .lt. 0.0) xd(5)= 0.0
else
    continue
end if
return
end

subroutine DISCRETE(time,ts,x,xd)
parameter (ll=20)
dimension x(*),xd(*)
common/controls/thtl,el,ail,rdr,pcom,qcom,rcom
common/output/op(ll)
if (time.lt. 5.0) then
    qcom= 0.0
    pcom= 0.0
    rcom= 0.0
else if (time.lt. 12.0) then
    qcom= 20.0
    thtl= 1.0
else if (time.lt. 16.0) then
    qcom= 0.0
    pcom= 300.0
else
    pcom = 0.0
    qcom = 0.0
end if
return
end

```

A pull-up at 20 deg/s is simulated, so that the angle of attack attains quite large values. When  $\alpha$  reaches about  $23^\circ$  (Figure 4.7-8a), a large roll-rate command is applied; this causes the aileron and rudder actuators to saturate almost immediately (Figure 4.7-8b). The directional controls are then unable to control the sideslip tightly, and some of the angle of attack is rapidly converted to sideslip (Figure 4.7-8c) through kinematic coupling. As the roll and yaw rates build up (Figure 4.7-8d), the inertia coupling moment becomes strong. The elevator deflection then goes from a small negative value to its positive limit, as it tries to oppose the inertia coupling moment. Figure 4.7-8e shows the roll-angle variation, Figure 4.7-8f shows pitch attitude, and Figure 4.7-8g shows the decrease in airspeed during the maneuvers.

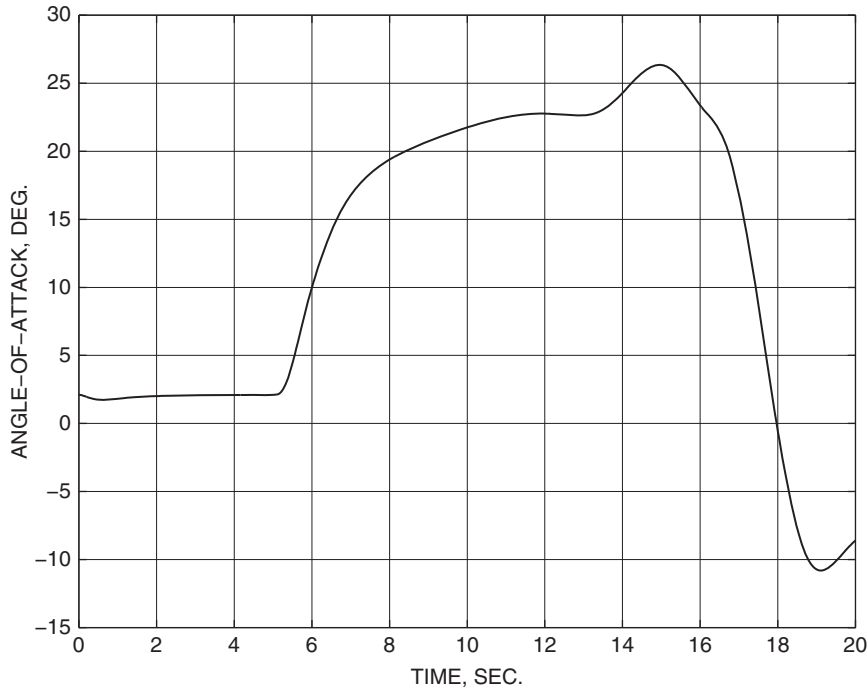


Figure 4.7-8a Simulation of limiting; alpha variation.

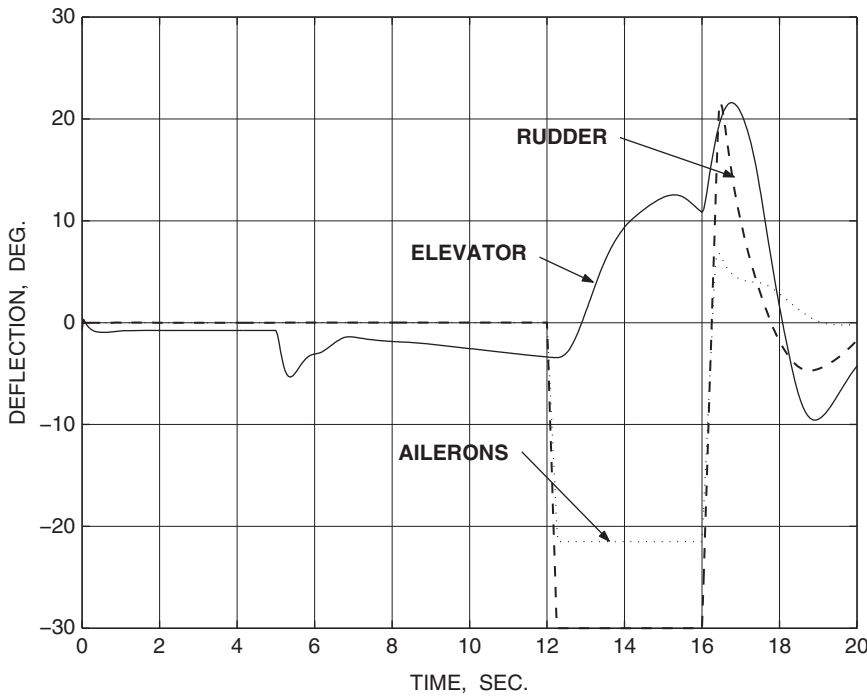


Figure 4.7-8b Simulation of limiting; control surface deflections.

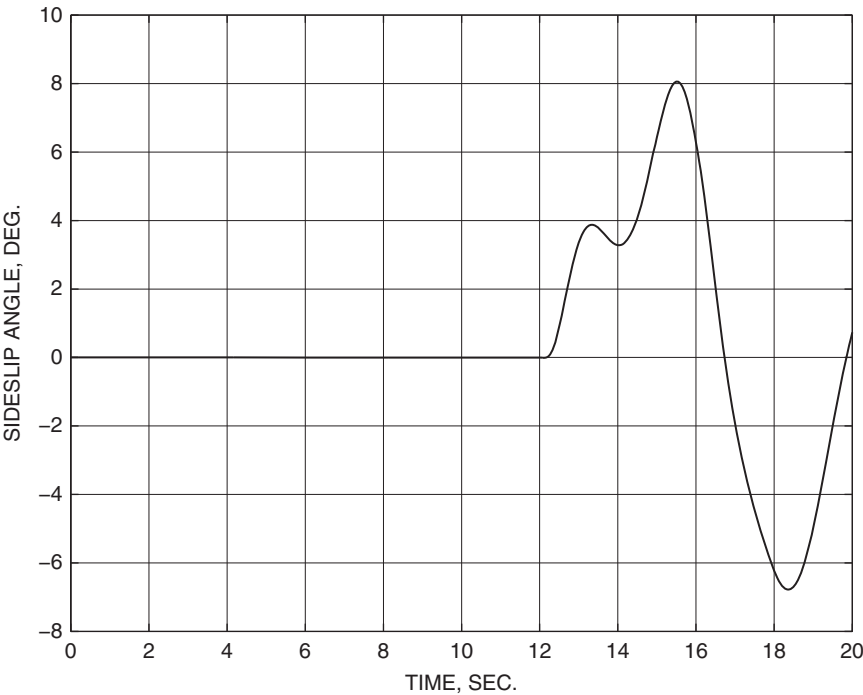


Figure 4.7-8c Simulation of limiting; sideslip variation.

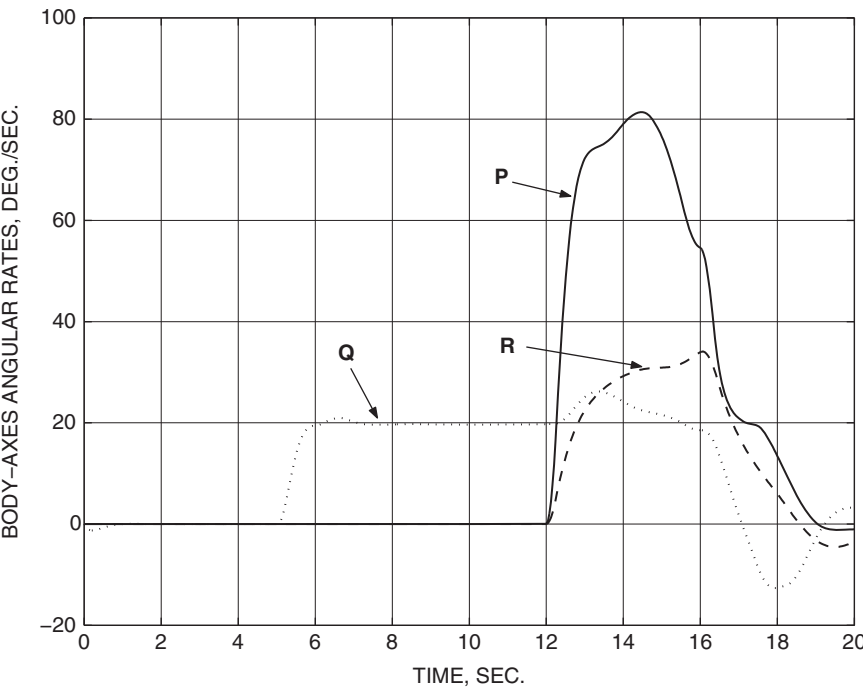


Figure 4.7-8d Simulation of limiting; aircraft angular rates.

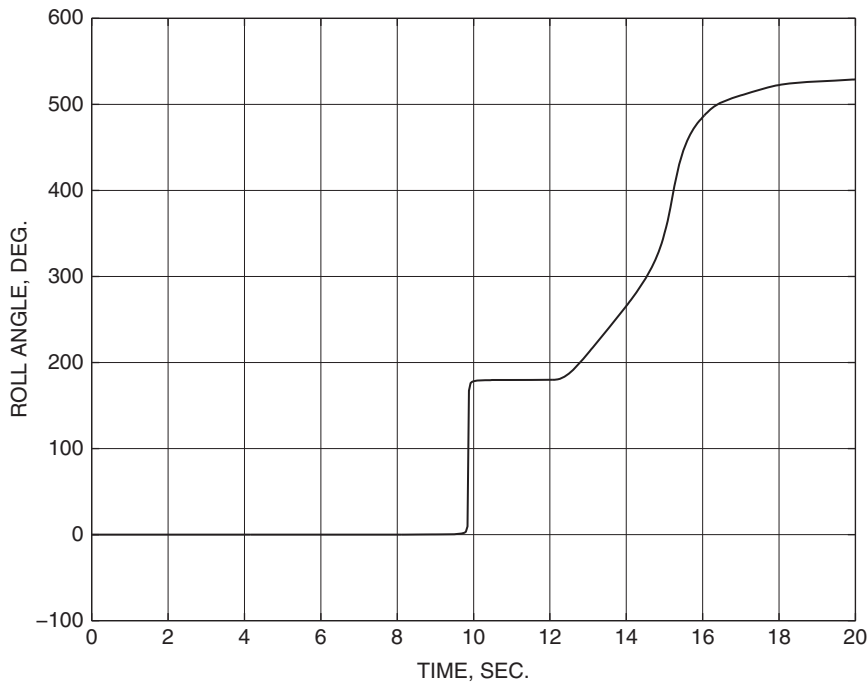


Figure 4.7-8e Simulation of limiting; roll angle variation.

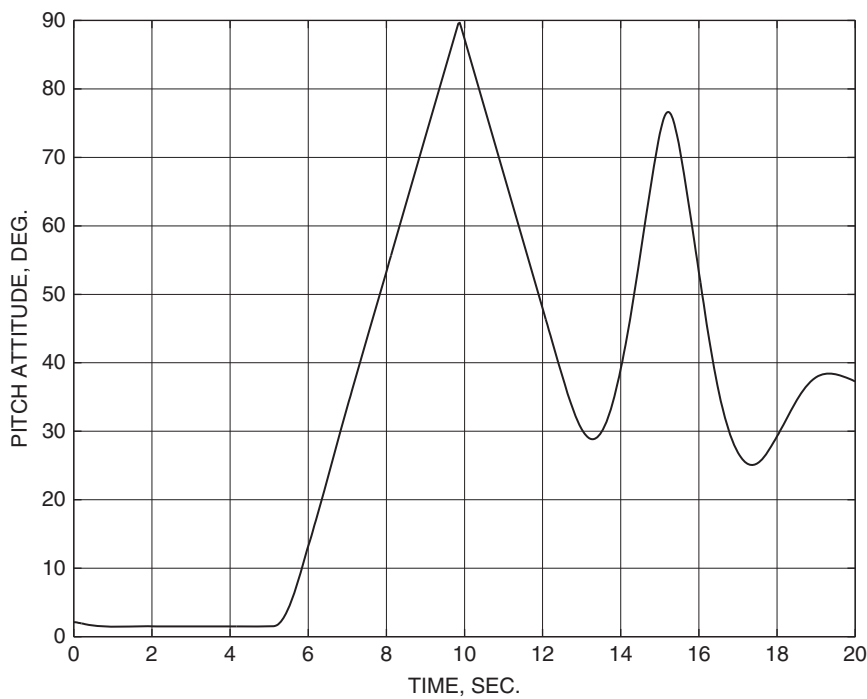
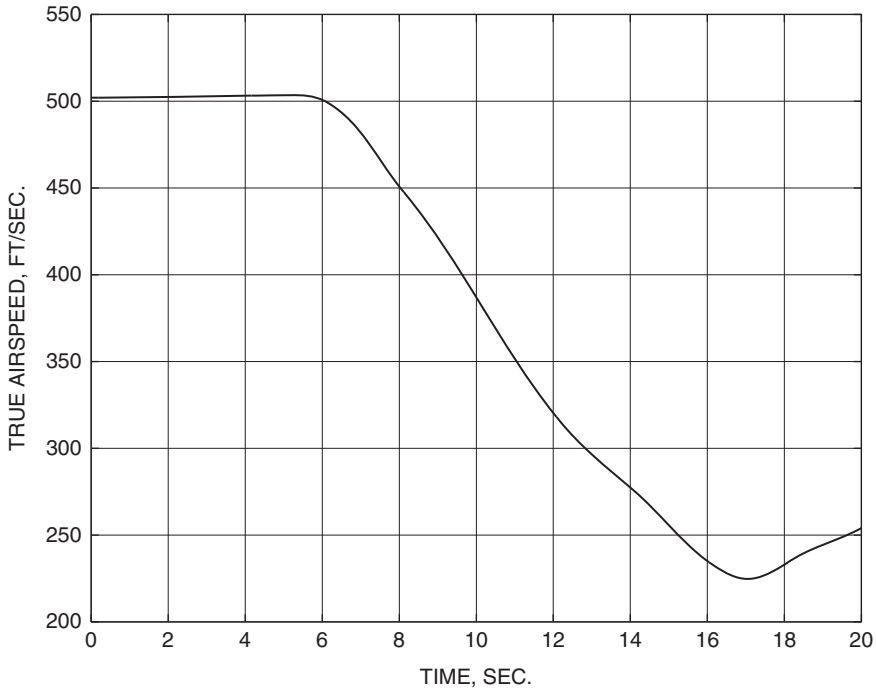


Figure 4.7-8f Simulation of limiting; pitch-attitude variation.



**Figure 4.7-8g** Simulation of limiting; airspeed variation.

In the flight condition illustrated, the available roll and yaw rates are insufficient to cause a pitch departure (due to inertia coupling), but the elevator saturation means that there is no longitudinal control available for 2 or 3 s. For this aircraft, pitch departure appears to be a problem only at very low dynamic pressure and high  $\alpha$ , and more details can be found in the work of Nguyen et al. (1979). These types of problems are usually solved by using command limiters to limit the roll rate that the pilot can command or the angle of attack that can be reached through the longitudinal controls. The limiting values must be made functions of the flight conditions, and the design process is a lengthy one involving much nonlinear simulation. ■

## 4.8 SUMMARY

In this chapter we have described the effect of flight conditions on the aircraft modes, presented some background in handling qualities and control design criteria, and described the purpose and design requirements of a large number of commonly used control systems. The design examples are quite realistic, having been performed on nonlinear aircraft models that are quite accurately representative of two very different types of aircraft. An infinite number of variations on the designs are possible and some of these are suggested in the chapter problems. Time and space limitations have

not allowed the control designs to be gain scheduled over the aircraft envelope and to be evaluated thoroughly in terms of the handling qualities requirements, but the necessary capabilities have been developed.

The state-space formulation of modern control has provided an exceptionally convenient framework for the software and the use of classical design techniques. It should be evident that a primary requirement for successful design of aircraft control systems is an understanding of the physics of flight and that interpreting the results of simulations is a vital aspect of this. Classical control theory fits extremely well into this picture because it relates very closely to the physics of the problems and usually provides clues to the modifications needed to make the design successful. In the following chapters modern design techniques will be introduced. These techniques will come into their own in situations that we found difficult to handle up to this point, such as shaping the closed-loop time response when a number of poles and zeros all contribute significantly.

## REFERENCES

- AFWAL-TR-84-3105. *Proceedings of the Aeroservoelastic Specialists Meeting*, October 2-3, 1984, vols. I and II. Wright-Patterson AFB, Ohio: USAF Flight Dynamics Laboratory.
- Ananthkrishnan, N., and S. Unnikrishnan. "Literal Approximations to Aircraft Dynamic Modes." *Journal of Guidance, Control, and Dynamics* 24, no. 6 (November–December 2001): 1196–1203.
- Ashkenas, I. L. "Some Open and Closed-Loop Aspects of Airplane Lateral-Directional Handling Qualities." *AGARD Report* 533, 1966.
- . "Twenty-Five Years of Handling Qualities Research." *AIAA Journal of Aircraft* 21, no. 5 (May 1984): 289–301.
- Bischoff, D. E. "Longitudinal Equivalent Systems Analysis of Navy Tactical Aircraft." AIAA paper 81-1775. *AIAA Guidance and Control Conference*, Albuquerque, NM, August 19–21, 1981.
- Blakelock, J. H. *Automatic Control of Aircraft and Missiles*. New York: Wiley, 1965.
- Bryan, G. H. *Stability in Aviation*. London: Macmillan, 1911.
- Chalk, C. R. "Fixed-Base Simulator Investigation of the Effects of  $L_a$  and True Speed on Pilot Opinion Rating of Longitudinal Flying Qualities." *USAF ASD-TDR-63-399*. Wright-Patterson AFB, Ohio: USAF Flight Dynamics Laboratory, November 1963.
- Chalk, C. R., T. P. Neal, and T. M. Harris. *Background Information and User Guide for MIL-F-8785B (ASG)*. Buffalo, N.Y.: Cornell Aeronautical Laboratories Inc., August 1969 (AFFDL-TR-69-72; AD860856).
- Cooper, G. E., and R. P. Harper, Jr. "The Use of Pilot Rating in the Evaluation of Aircraft Handling Qualities." *NASA Technical Note D-5153*. Washington, D.C.: NASA, 1969.
- Craig, S. J., and I. L. Ashkenas. *Background Data and Recommended Revisions for MIL-8785B (ASG), "Military Specification—Flying Qualities of Piloted Airplanes."* Technical Report TR-189-1. Hawthorne, Calif.: Systems Technology Inc., March 1971.
- Etkin, B. *Dynamics of Atmospheric Flight*. New York: Wiley, 1972.

- Gentry, T. A. "Guidance for the Use of Equivalent Systems with MIL-F-8785C." Paper 82-1355. *AIAA Atmospheric Flight Mechanics Conference*, San Diego, 1982.
- George, F. L., and D. J. Moorhouse. "Relationship of the Flying Qualities Specification to Task Performance." *AFFTC/NASA-Dryden/AIAA Workshop Flight Testing to Identify Pilot Workload and Pilot Dynamics*. Edwards AFB, Calif., January 19-21, 1982.
- Gerlach, O. H. "Developments in Mathematical Models of Human Pilot Behavior." *Aeronautical Journal* (July 1977): 293-305.
- Hodgkinson, J. "Equivalent Systems Approach for Flying Qualities Specification." MCAIR 79-017. Paper presented at *SAE Aerospace Control and Guidance Systems Committee Meeting*, Denver, Colo., March 7-9, 1979.
- Kisslinger, R. L., and M. J. Wendle. "Survivable Flight Control System Interim Report," No. 1, "Studies Analysis and Approach, Supplement for Control Criteria Studies." Technical Report AFFDL-TR-71-20, suppl. 1. Wright-Patterson AFB, Ohio: Air Force Flight Dynamics Laboratory, May 1971.
- Kleinman, D. L., S. Baron, and W. H. Levison. "An Optimal Control Model of Human Response." Part I: Theory and Validation; Part II: Prediction of Human Performance in a Complex Task. *Automatica* 6 (1970): 357-369.
- McRuer, D. T., D. Graham, E. Krendel, and W. Reisner, Jr. *Human Pilot Dynamics in Compensatory Systems*. AFFDL-TR-65-15. USAF, Wright-Patterson AFB, Ohio: Air Force Flight Dynamics Laboratory, 1965.
- McRuer, D., I. Ashkenas, and D. Graham. *Aircraft Dynamics and Automatic Control*. Princeton, N.J.: Princeton University Press, 1973.
- MIL-F-8785C*. "U.S. Dept. of Defense Military Specification: Flying Qualities of Piloted Airplanes." November 5, 1980.
- MIL-F-9490D*. "Flight Control Systems: Design, Installation, and Test of, Piloted Aircraft, General Specification for." USAF, June 1975.
- Moorhouse, D. J., and R. J. Woodcock. "Background Information and User Guide for MIL-F-8785C." *AFWAL-TR-81-3109 (AD-A119-421)*. Wright-Patterson AFB, Ohio: Air Force Wright Aeronautical Laboratories, July 1982.
- Neal, T. P., and R. E. Smith. "An In-flight Investigation to Develop Control System Design Criteria for Fighter Airplanes." *AFFDL-TR-70-74*, vols. I and II. Wright-Patterson AFB, Ohio, Air Force Flight Dynamics Laboratory, December 1970.
- Nguyen, L. T., et al. "Simulator Study of Stall/Post-Stall Characteristics of a Fighter Airplane with Relaxed Longitudinal Static Stability." *NASA Tech. Paper 1538*. Washington, D.C.: NASA December 1979.
- O'Hara, F. "Handling Criteria." *Journal of the Royal Aeronautical Society* 71, no. 676 (1967): 271-291.
- Onstott, E. D., and W. H. Faulkner. "Production Evaluation and Specification of Closed-Loop and Multi-Axis Flying Qualities." *AFFDL-TR-78-3*. Wright-Patterson AFB, Ohio: Air Force Flight Dynamics Laboratory, February 1978.
- Roskam, J. *Airplane Flight Dynamics and Automatic Flight Controls*. Lawrence, Kans.: Roskam Aviation and Engineering Corp., 1979.
- Rynaski, E. G. "Flying Qualities in the Time Domain." AIAA paper 85-1849. *AIAA Guidance, Navigation and Control Conference*, Snowmass, Colo., August 1985.
- Sheridan, T. B., and W. R. Ferrell. *Man-Machine Systems: Information, Control, and Decision Models of Human Operator Performance*. Cambridge, Mass.: MIT Press, 1974.

Shomber, H. A., and W. M. Gertsen. "Longitudinal Handling Qualities Criteria: An Evaluation." *Journal of Aircraft* 4, no. 4 (1967): 371–376.

Tobie, H. N., E. M. Elliot, and L. G. Malcom. "A New Longitudinal Handling Qualities Criterion." *Proceedings of the National Aerospace Electronics Conference*, Dayton, Ohio, May 16–18, 1966, pp. 93–99.

Toles, R. D. "Application of Digital Multi-Input/Multi-Output Control Law with Command Path Blended Gains for the Pitch Axis Task-Tailored Air Combat Mode of the AFTI/F-16." *Proceedings of the 1985 American Control Conference*, Boston, June 1985, p. 1475.

## PROBLEMS

### Section 4.2

**4.2-1** Use the results of Section 4.2 to write a program that will calculate the damping and natural frequency of the phugoid and short-period modes from the dimensionless longitudinal stability derivatives. Use it to check the results given in Table 4.2-1.

**4.2-2** Write a program to determine the lateral-directional modes from the appropriate dimensionless derivatives and use it to check the results of Example 4.2-1. Determine both the approximate values from the equations in Section 4.2 and accurate values from the eigenvalues of the coefficient matrices.

### Section 4.4

**4.4-1** When the F-16 model is trimmed for level flight at 30,000 ft and 820 ft/s, the dynamic pressure and angle of attack are the same as those of the nominal sea-level condition in Table 3.6-3. The  $A$ - and  $B$ -matrices are given by

$$A = \begin{array}{c} v_T \qquad \alpha \qquad \theta \qquad q \\ \left[ \begin{array}{cccc} -5.9172E-03 & 8.8482E+00 & -3.2170E+01 & -3.5136E-01 \\ -9.5423E-05 & -6.2426E-01 & 0.0000E+00 & 9.6439E-01 \\ 0.0000E+00 & 0.0000E+00 & 0.0000E+00 & 1.0000E+00 \\ 2.4638E-11 & 8.2290E-01 & 0.0000E+00 & -6.6011E-01 \end{array} \right] \end{array}$$

$$B = \begin{array}{c} \delta_e \\ \left[ \begin{array}{c} 1.7391E-01 \\ -1.3172E-03 \\ 0.0 \\ -1.7569E-01 \end{array} \right] \end{array}$$

Explain how and why these dynamic equations differ from those in Example 4.4-1. Augment these dynamics with the same alpha filter and elevator actuator as in the example and find  $\alpha$  and  $q$  feedback gains that will



yield closed-loop longitudinal dynamics as close as possible to those obtained in Example 4.4-1.

- 4.4-2** Using the same flight conditions as in Problem 4.4-1, the lateral-directional dynamics of the F-16 model are

$$A = \begin{array}{c} \begin{array}{cccc} \beta & \phi & p & r \\ \begin{bmatrix} -0.19729 & 0.039205 & 0.036657 & -0.99645 \\ 0 & 0 & 1.0 & 0.036878 \\ -30.666 & 0 & -2.2538 & 0.40705 \\ 8.5461 & 0 & -0.015556 & -0.29186 \end{bmatrix} \end{array} \\ \\ \begin{array}{cc} \delta_a & \delta_r \\ \begin{bmatrix} 1.8078E-04 & 4.9356E-04 \\ 0 & 0 \\ -0.73388 & 0.13165 \\ -0.031891 & -0.062067 \end{bmatrix} \end{array} \end{array}$$

Determine and identify the modes. Find suitable feedback gains for basic lateral-directional stability augmentation, as in Example 4.4-3. Compare the roll-rate response to an aileron doublet with the response shown in Example 4.4-3.

- 4.4-3** Repeat Example 4.4-3 with washout time constants of 0.5 s and 2.0 s and describe the difference in behavior and the effect on the dutch roll damping.
- 4.4-4** Repeat Example 4.4-2 using the F-16 dynamics given in Problem 4.4-1. Is the lag compensator still useful?

## Section 4.5

- 4.5-1** Repeat the pitch-CAS design (Example 4.5-1) using the F-16 dynamics given in Problem 4.4-1. Does the position of the PI zero need to be changed? Could this design be made to work, over at least the low-Mach part of the envelope, by changing only the proportional gain? Is it possible to say anything about the need for gain scheduling the controller? Determine the step response with and without the PI zero.
- 4.5-2** Repeat the design of the normal acceleration CAS in Example 4.5-2, but with the accelerometer placed at the aircraft cg. Attempt to obtain a step response that is fast but well damped and similar to that shown in Figure 4.5-6.
- 4.5-3** Use the MATLAB program NLSIM from Chapter 3 to simulate some maneuvers with the lateral-directional CAS from Example 4.5-3. In the state equation MATLAB function, use linear state equations for the longitudinal and lateral-directional dynamics but model the nonlinear ARI and yaw-rate feedback. Compare the results with and without the ARI operating.

## Section 4.6

- 4.6-1** Redesign the pitch-attitude hold in Example 4.6-1 using the short-period approximation, with an additional integrator to produce pitch from pitch rate. Evaluate the design with a step-response simulation performed on the full dynamics.
- 4.6-2** Redesign the pitch-attitude hold in Example 4.6-2 with the PI zero placed at  $s = -0.1$ ; compare the step response with that given in the text. Can this design be performed using the short-period approximation?
- 4.6-3** Attempt to design a Mach-hold autopilot using the same dynamics as in Example 4.6-3 and Figure 4.6-6, but with Mach as the controlled variable. Show that the throttle-to-Mach transfer function contains an NMP zero that makes this difficult or impossible. What is the way out of this difficulty?
- 4.6-4** Redesign the  $d$ -loop of the glide-slope controller in Example 4.6-4 with the PI zero at  $s = -0.1$ . Also attempt to design the lead compensator so that the elevator is less active during the acquisition of the glide slope. Compare the simulation results with those given in the text.
- 4.6-5** Modify Example 4.6-5 to use PI control and lead compensation (if necessary) so that zero steady-state roll angle error can be achieved.

## Section 4.7

- 4.7-1** Use NLSIM to repeat the pitch CAS nonlinear simulation in Example 4.7-1 but, instead of the nonlinear F-16 model, use the linear state equations for the nominal flight condition. Show graphs for comparison with those in Example 4.7-1 and discuss the differences.
- 4.7-2** Reproduce the glide-path and flare simulations described in Examples 4.7-3 and 4.7-4. Add code to simulate rate limiting in the elevator actuator and determine how low the maximum elevator slew rate can be before the results are significantly changed.

## CHAPTER 5

---

# MODERN DESIGN TECHNIQUES

---

### 5.1 INTRODUCTION

Modern control theory has made a significant impact on the aircraft industry in recent years. Bryson (e.g., 1985; Ly et al., 1985) pioneered in applying it to aircraft control. Boeing (Gangsaas et al., 1986) has implemented control systems designed using modern techniques, for instance, in the Boeing 767 autopilot. Honeywell has promoted modern robust design (Doyle and Stein, 1981). Linear quadratic methods were used by General Dynamics in the control system of the AFTI/F-16 (*AFWAL-TR-84-308*, 1984).

Therefore, in aircraft control systems design it is essential to have an understanding of modern control theory. Unfortunately, the traditional modern design techniques based on state-variable feedback that are available in current texts are not suitable for aircraft control design. This is due to several things, one of which is their dependence on selecting large numbers of design parameters—namely, the performance index weighting matrices. Any design method for aircraft controls should eliminate the need for this trial-and-error selection. Thus, the techniques by Ly et al. (1985), Gangsaas et al. (1986), Davison and Ferguson (1981), and Moerder and Calise (1985) all rely on modified design techniques that use output feedback or order reduction techniques in conjunction with the minimization of a nonstandard performance index.

In the remainder of the book we focus on modern design techniques that are suitable for use in aircraft control. Included are such approaches as eigenstructure assignment, model-following, dynamic inversion, linear quadratic regulator/loop transfer recovery (LQG/LTR), and linear quadratic (LQ) output feedback design. Each of these techniques has its proponents, and each has its advantages and disadvantages, as we will attempt to demonstrate. We will focus on output feedback

design, with performance criteria that are more general than the usual integral quadratic form. Using this approach it is straightforward to design controllers that have a sensible structure from the point of view of the experience within the aircraft industry without the trial-and-error selection of a large number of design parameters.

Our strategy in the next chapters will be different than in the first part of the book due to the different character of the material to be covered. We will first develop each modern design technique and then present examples showing how it is used in aircraft controls. In several instances we will consider the same examples presented in Chapter 4; this will afford an opportunity to contrast the classical and modern approaches to design. We now discuss some basic philosophy of modern control design.

### Limitations of Classical Control

In Chapter 4 we showed how to design aircraft control systems using classical control techniques. The essence of classical design was *successive loop closure* guided by a good deal of intuition and experience that assisted in selecting the control system structure. For instance, we knew it was desirable to provide inner rate feedback loops around a plant to reduce the effect of plant parameter variations. In conjunction with this we used standard compensator structures designed to approximate derivative action to stabilize the system or integral action to eliminate steady-state error.

The one-loop-at-a-time design approach was aided by such tools as root locus, Bode and Nyquist plots, and so on, that enabled us to visualize how the system dynamics were being modified. However, the design procedure became increasingly difficult as more loops were added and did not guarantee success when the dynamics were multivariable, that is, when there were multiple inputs, multiple outputs, or multiple feedback loops.

### Philosophy of Modern Control

Two concepts are central to modern control system design. The first is that *the design is based directly on the state-variable model*, which contains more information about the system than the input-output (black box) description. The state-variable model was introduced into system theory, along with matrix algebra, by R. Kalman (1958, 1960). Since we have already seen how to extract state equations from the nonlinear aircraft dynamics and use them for analysis, we are at this point in a good position to use them for control design.

The second central concept is *the expression of performance specifications in terms of a mathematically precise performance criterion* which then yields *matrix equations for the control gains*. These matrix equations are solved using readily available computer software. The classical successive-loop-closure approach means that the control gains are selected individually. In complete contrast, solving matrix equations allows *all the control gains to be computed simultaneously* so that all loops are closed at the same time. This simultaneous design means that we will have greater insight into the design freedom than is possible when the system has more than one

input and/or output or multiple control loops. Moreover, using modern control theory we are able to design control systems more quickly and directly than when using classical techniques.

As in classical control, we are able with modern techniques to select the structure of the control system using the intuition developed in the aircraft industry. Thus, it is straightforward to include washout circuits, integral control, and so on. The key to this is the use of *output feedback* design techniques, introduced in Section 5.3 and used throughout the chapter.

The modern control formulation means that the trial and error of one-loop-at-a-time design disappears. Instead, the fundamental engineering decision is *the selection of a suitable performance criterion*. Let us now discuss some important design problems and their associated performance criteria.

## Fundamental Design Problems

***Pole Placement/Eigenvector Assignment*** Modern control techniques are available for assigning the poles in multi-input/multi-output (MIMO) systems to desired locations *in one step* by solving equations for the feedback gains. These are called *pole placement techniques*. Once we move away from classical one-loop-at-a-time design and obtain the capability to compute all the feedback gains simultaneously, it will become clear that in the MIMO case *it is possible to do more than simply assign the poles*. In fact, the closed-loop eigenvectors may also be selected within limits.

Desirable pole locations for aircraft design may be found in the military flying qualities specifications (see Section 4.3). However, while discussing flying qualities requirements, we noted that the time response depends not only on the pole locations but also on the zeros of the individual single-input/single-output (SISO) transfer functions, or equivalently on the eigenvectors (see the discussion on system modes in Chapter 3). Thus, the capability of modern control design to select both the closed-loop poles and eigenvectors is relevant in aircraft design.

In this design approach, the performance criterion is to achieve specified pole locations and eigenvectors. We will discuss pole placement/eigenstructure assignment in Section 5.2.

***Regulator Problem*** A fundamental design problem is the *regulator problem*, where it is necessary to regulate the outputs of the system to zero while ensuring that they exhibit desirable time-response characteristics. The regulator problem is important in the design of stability augmentation systems and autopilots.

Stable regulation of systems implies closed-loop stability, but using modern control we may do more than simply ensure stability. To exercise our design freedom, we select as our performance criterion an *integral-squared performance index (PI)* similar to those used in classical design (D’Azzo and Houpis, 1988). That is, the squares of the states and inputs are integrated to obtain the PI. The control gains that minimize the PI are found by solving matrix equations using computer programs. Note that if the integral of the squares of the states is made small, then in some sense the states themselves are forced to stay near zero. Selecting different weighting coefficients in

the PI for the various state components results in different time-domain behavior in the closed-loop system. Thus, modern control regulator design is fundamentally a *time-domain design technique* useful in shaping the closed-loop response. This is in contrast to classical controls, where most techniques are in the frequency domain.

We will discuss the regulator problem in Section 5.3. A deficiency of the traditional approach to modern regulator design using state feedback and the standard quadratic PI is that, to obtain suitable responses, one must select a large number of design parameters—namely, the PI weighting matrices. To avoid such trial-and-error approaches, we use modified PIs (Section 5.5) that are more suitable for aircraft control system design.

**Tracker Problem** Another fundamental design problem is the *tracker problem*, where it is desired for an aircraft to follow or track a command signal. The command may be either constant or time varying. This is also referred to as the *servo design problem*. The tracker problem is important in the design of control augmentation systems, where, for instance, the command signal may be a desired pitch rate or normal acceleration command. The tracker problem also relies on the selection of an integral-squared PI. However, now it is desired to keep the outputs not at zero but near the reference command signals.

The modern control technique we will use for tracker design is not the standard one—it has been modified in several respects to make it more suitable for the purpose of aircraft control design. Specifically, we select a general PI that can easily be modified to attain different performance objectives. The result is a convenient technique for aircraft control design that does not involve the trial-and-error tuning of large numbers of parameters. This design approach is described in Sections 5.4 and 5.5.

**Model Following** An important approach to control design is *model following*, where it is desired for the aircraft to perform like an ideal model with desirable flying qualities. We have seen in Chapter 4 that one way to specify good flying qualities is to prescribe a low-order model (e.g., with one zero and a complex pole pair) whose response the closed-loop system should match. In this design technique the performance criterion is some measure of the difference between the model and controlled aircraft responses. We cover model-following design in Section 5.6, showing how to design controllers that make the aircraft behave like the model.

As another application, we show that model-following design offers a very straightforward approach to the design of an automatic flare control system. Note that in flare control it is desired for the aircraft to follow an exponential path to a smooth touchdown—here, the model is just the desired trajectory.

**Dynamic Inversion** The aircraft is fundamentally a nonlinear system. Unfortunately, it is very difficult to design control systems directly for nonlinear systems. Therefore, most aircraft control systems are based on linear systems design at a given operating point. This requires that different controllers be designed for different operating points. Using gain scheduling, the linear controllers are then combined to provide control effectiveness over an operating envelope. One technique that can be applied

to nonlinear systems is *dynamic inversion*. This is based on the technique of *feedback linearization*. Dynamic inversion control requires that the controller have a full model of the nonlinearities of the aircraft. Using modern high-power computers, this is possible. In Section 5.8 we cover dynamic inversion, which has gained in popularity in recent years for aircraft control design.

**Robust Design** It is important to incorporate notions from classical control theory into modern design. Particularly vital is the frequency-domain approach to robustness analysis. However, it is well known that in a multivariable system individual gain and phase margins between different pairs of inputs and outputs mean little from the point of view of overall robustness. Therefore, in Chapter 6 we generalize frequency-domain robustness analysis techniques to MIMO systems using the concept of the *singular value*. There, we also present the LQG/LTR technique, which has recently gained popularity in aircraft controls design.

**Observers, Kalman Filter, and Regulators** In Chapter 6 we also cover the design of observers and the Kalman filter, which are dynamical systems that estimate the full state from measurements of the outputs. By using feedback of these state estimates in conjunction with the observer dynamics, we are able to design a dynamic linear quadratic regulator, which is just a compensator similar to those obtained using classical techniques. In the modern approach, however, a convenient design method for *multivariable systems* is achieved by solving matrix equations to guarantee specified performance.

**Digital Control** The control systems of modern aircraft are implemented on digital microprocessors. Examples are the F-15E, F18, and late models of the F-16. The advantages of digital control include the ability to implement complicated multi-loop control systems, reprogram the controller gains and structure (e.g., for gain scheduling), obtain redundancy for failure tolerance, and use digital signal processing techniques to filter the control signals.

Digital control design introduces some new problems, such as the need to account for the delays associated with the sampling and hold processes and control computation. Also important is the development of design techniques that overcome the drawbacks associated with  $z$ -plane design, where the need arises for extreme accuracy in placing the poles within the unit circle. Implementation problems include accounting for actuator saturation and the effects of computer finite word length, roundoff error, overflow, and so on. We discuss the basics of digital control in Chapter 7.

## 5.2 ASSIGNMENT OF CLOSED-LOOP DYNAMICS

Classical design techniques such as root locus and Bode analysis are directly applicable only to SISO systems. Using such techniques a single feedback gain may be selected to place the closed-loop poles to guarantee desirable time responses and robustness qualities. In the case of multiple inputs and outputs or multiple control

loops, the classical techniques require successive closures of individual loops and involve a significant amount of trial and error.

In the MIMO case it is possible to do more than simply place the poles. This extra freedom is difficult to appreciate from the point of view of classical control theory due to the successive SISO design approach. In this section we want to show how modern control theory can be used in the multivariable case to place the poles as well as to *take advantage of the extra freedom arising from multiple inputs* to assign the closed-loop eigenvectors. This is important since, as we saw in Sections 3.8 and 4.3, the time response of a multivariable system depends not only on the poles but also on the zeros of the individual SISO transfer functions or equivalently on the eigenvectors.

The *eigenstructure assignment* technique discussed in this section offers good insight and is especially useful for the design of *decoupling controllers*, as we will show in an example. As far as obtaining suitable time responses for multivariable systems goes, linear quadratic approaches like those in Sections 5.3 to 5.7 and 6.5 have generally been found more appropriate in the aircraft industry.

We will now discuss some basic feedback concepts from the point of view of modern control theory.

## State Feedback and Output Feedback

We have shown that the linearized equations of motion of an aircraft may be written in the state-space form

$$\dot{x} = Ax + Bu \quad (5.2-1)$$

$$y = Cx, \quad (5.2-2)$$

with  $x(t) \in \mathbf{R}^n$  the state,  $u(t) \in \mathbf{R}^m$  the control input, and  $y(t) \in \mathbf{R}^p$  the measured output.

Let us select a feedback control input of the form

$$u = -Kx + v, \quad (5.2-3)$$

where  $v(t)$  is an auxiliary input which might be, for instance, the pilot's command and  $K$  is an  $m \times n$  gain matrix to be determined. This is called a *state-variable feedback* since all of the state components are fed back. The feedback gain  $K$  is an  $m \times n$  matrix of scalar control gains.

Substituting the control into the state equation yields the closed-loop system

$$\dot{x} = (A - BK)x + Bv \quad (5.2-4)$$

The closed-loop plant matrix is  $(A - BK)$ , and we would like to select the feedback gain  $K$  for good closed-loop performance.

It is a fundamental result of modern control theory that if the system is *controllable*, all of the closed-loop poles may be assigned to desired locations by



selection of  $K$ . Controllability means that the control input  $u(t)$  independently affects all the system modes. It can be tested for by examining the controllability matrix (Kailath, 1980)

$$U = [B \quad AB \quad A^2B \quad \cdots \quad A^{n-1}B] \quad (5.2-5)$$

The system is controllable if  $U$  has full rank of  $n$ , that is, if  $U$  has  $n$  linearly independent columns. This is equivalent to the nonsingularity of the Gramian  $UU^T$ , which is a square  $n \times n$  matrix whose determinant can be evaluated.

In the next subsection we will see that if there is more than one control loop, corresponding to more than one control gain, we can not only place the poles but also to a certain extent select the eigenvectors.

Unfortunately, in aircraft control systems it is usually not possible or economically feasible to measure all the states accurately. It is possible to design a dynamic observer or Kalman filter to provide estimates  $\hat{x}(t)$  of the states  $x(t)$  and then use *feedback of the estimates* by modifying (5.2-3) to read  $u = -K\hat{x} + v$ . Indeed, we do discuss this approach in Section 6.4, since we need it to cover the LQG/LTR robust design technique in Section 6.5. However, since the aircraft dynamics are nonlinear, all the parameters of any linear observer would need to be gain scheduled. This is inconvenient if the order of the observer is large.

Therefore, to obtain realistic aircraft control schemes, we should feed back not the entire state  $x(t)$  but only the measurable outputs  $y(t)$ . The *output feedback* control law is

$$u = -Ky + v = -KCx + v, \quad (5.2-6)$$

which on substitution into (5.2-1) yields the closed-loop system

$$\dot{x} = (A - BKC)x + Bv \quad (5.2-7)$$

Now the closed-loop plant matrix is  $(A - BKC)$ . The output feedback matrix  $K$  is an  $m \times p$  matrix of scalar gains. Thus, since  $p$  is generally less than  $n$ , there are fewer scalar control gains to select in output feedback design than in state feedback design.

An important advantage of output feedback, as we will see, is that it allows us to *incorporate a compensator of desired form into the feedback system*. In aircraft control, there is a wealth of experience that often dictates the form of the control system. For instance, a washout filter may be required or a PI controller may be needed for zero steady-state error.

Unlike the state feedback case, there is no convenient test to determine for a given system if the closed-loop poles may be independently assigned using output feedback. Pole placement using output feedback is more difficult to accomplish than using state feedback. The basic thrust of this chapter is to investigate the selection of the output feedback gain matrix  $K$  to obtain desirable closed-loop characteristics. Note that this will involve more than simply placing the poles, since desirable time responses depend on the poles as well as the zeros of the individual SISO transfer functions. These zeros can also be influenced using feedback if there is more than one input and output.

The gain matrix  $K$  is  $m \times n$  for state feedback and  $m \times p$  for output feedback. In the MIMO case there could be many gain elements, each corresponding to a feedback path. In classical control theory the individual gains must be separately selected using trial-and-error successive loop closure design. By contrast, using modern controls design *all the elements of  $K$  are selected simultaneously*. Thus, all the feedback loops in a complicated control system can be closed at the same time with a modern control approach.

We will now discuss the selection of  $K$  to yield desired closed-loop poles and eigenvectors—that is, to assign the closed-loop eigenstructure. Both state feedback and output feedback will be considered. First, let us recall the importance of the eigenvectors in the system response.

### Modal Decomposition

We have discussed the importance of the system modes in Sections 3.8 and 4.2. Let us now carry that discussion a bit further. Let  $\lambda_i$  be an eigenvalue with right eigenvector  $v_i$  and left eigenvector  $w_i$ , so that

$$Av_i = \lambda_i v_i, \quad w_i^T A = \lambda_i w_i^T \quad (5.2-8)$$

Since  $y = Cx$ , we may use the results of Section 3.8 to write the output as

$$y(t) = \sum_{i=1}^n (w_i^T x_0) C v_i e^{\lambda_i t} + \sum_{i=1}^n C v_i \int_0^t e^{\lambda_i(t-\tau)} w_i^T B u(\tau) d\tau \quad (5.2-9)$$

The initial condition is  $x(0) = x_0$ . This equation is valid when the Jordan form of matrix  $A$  is diagonal.

From this equation we may note that  $C v_i$  is a direction in the output space associated with  $\lambda_i$ , while the influence of the control input  $u(t)$  on eigenvalue  $\lambda_i$  is determined by  $w_i^T B$ .

If  $C v_i = 0$ , motion in the direction  $v_i$  cannot be observed in the output and we say that  $\lambda_i$  is *unobservable*. If  $w_i^T B = 0$ , the control input  $u(t)$  can never contribute to the motion in the direction  $v_i$  and we say that  $\lambda_i$  is *uncontrollable*.

Clearly, we may affect the coupling between the inputs, states, and outputs by selecting the vectors  $v_i$  and  $w_i$  in the closed-loop system; that is, we can influence the *numerators* of the individual SISO transfer functions as well as the poles. To see this clearly, examine the transfer function

$$H(s) = C(sI - A)^{-1} B \quad (5.2-10)$$

Let the Jordan matrix  $J$  and matrix of eigenvectors  $M$  be

$$J = \text{diag} \{ \lambda_i \}, \quad M = [v_1 \quad v_2 \quad \cdots \quad v_n]^T, \quad (5.2-11)$$

so that

$$M^{-1} = [w_1 \quad w_2 \quad \cdots \quad w_n]^T \quad (5.2-12)$$

Now recall that  $A = MJM^{-1}$  and use the fact that  $(QP)^{-1} = P^{-1}Q^{-1}$  for any two compatible square matrices  $P$  and  $Q$  to write (5.2-10) as

$$H(s) = CM(sI - J)^{-1}M^{-1}B,$$

or, since  $(sI - J)^{-1}$  is diagonal with elements like  $1/(s - \lambda_i)$ , as

$$H(s) = \sum_{i=1}^n \frac{Cv_i w_i^T B}{s - \lambda_i} \quad (5.2-13)$$

This equation gives the partial fraction expansion of  $H(s)$  in terms of the eigenstructure of  $A$  when  $A$  is diagonalizable.

Several things may be said at this point. First, if  $\lambda_i$  is unobservable or uncontrollable, its contribution to the partial fraction expansion of  $H(s)$  is zero. In this case we say that the state-space description (5.2-1), (5.2-2) is *not minimal*. Second, the terms  $Cv_i$  and  $w_i^T B$  determine the residues of the poles and hence the *zeros* of the individual SISO transfer functions in the  $p \times m$  matrix  $H(s)$ . By proposing a technique for selecting the closed-loop eigenvectors by feedback, we are therefore proposing a method of shaping the time response that goes beyond what is possible using only pole placement.

In the next subsections we will show how to design feedback gains that achieve desired closed-loop eigenvectors using both state feedback and output feedback. Meanwhile, in the following example we give some insight on desirable eigenvectors from the point of view of aircraft behavior, recalling some results from Sections 3.8 and 4.2. We also show that the eigenvectors may be selected to obtain *decoupling between the system modes*.

**Example 5.2-1: Selecting Eigenvectors for Decoupling** In Sections 3.8 and 4.2 we studied the aircraft longitudinal and lateral modes, showing which states are involved in each one. To ensure that the controlled aircraft exhibits suitable flying qualities, we should take care to design the control system so that this basic modal structure is preserved (Sobel and Shapiro, 1985; Andry et al., 1983).

In this example we idealize the findings of Sections 3.8 and 4.2 a bit. That is, we make more categorical statements about the mode couplings in order to obtain concrete design objectives.

**(a) Longitudinal Axis.** Assuming that the state equations are augmented by a simple-lag elevator actuator model, in the linearized perturbed longitudinal equations of an aircraft the state can be taken as

$$x = \begin{bmatrix} \alpha \\ q \\ \theta \\ v_T \\ \delta_e \end{bmatrix} \quad (1)$$

The states are angle of attack,  $\alpha$ , pitch rate,  $q$ , pitch angle,  $\theta$ , total velocity,  $v_T$ , and elevator actuator state,  $\delta_e$ , the elevator deflection. We have ordered the states this way to make the upcoming discussion clearer [see (2)].

The short-period mode is due primarily to a coupling of energy between  $\alpha$  and  $q$ . The phugoid mode is due primarily to a coupling between  $\theta$  and  $v_T$ . It is desirable for the forward velocity to be unaffected by short-period oscillations, while the phugoid oscillations should have no influence on angle of attack.

To achieve this behavior, we could select the closed-loop eigenvectors as

$$v_1 = \begin{bmatrix} 1 \\ -1 \\ 0 \\ 0 \\ x \end{bmatrix} + j \begin{bmatrix} -1 \\ 1 \\ 0 \\ 0 \\ x \end{bmatrix}, \quad v_3 = \begin{bmatrix} 0 \\ 0 \\ 1 \\ -1 \\ x \end{bmatrix} + j \begin{bmatrix} 0 \\ 0 \\ -1 \\ 1 \\ x \end{bmatrix}, \quad (2)$$

with  $v_2$  and  $v_4$  the complex conjugates of  $v_1$  and  $v_3$ , respectively. Components whose values we do not care about are denoted by  $x$ . Then one oscillatory mode, the one with directions specified by  $v_1$  and  $v_2$ , will involve the first two components of the state vector but will not inject energy into components 3 and 4. This will be a “good” short-period mode. Similarly, the phugoid mode, described by the eigenvectors  $v_3$  and  $v_4$ , will involve components 3 and 4 but will not affect components 1 and 2.

A good design will have these closed-loop eigenvectors. The closed-loop poles should also be specified to attain the desired frequency and damping of the short-period and phugoid modes. The former will be defined by  $\lambda_1$  and  $\lambda_2$ , while the latter will be determined by  $\lambda_3$  and  $\lambda_4$ .

It may be necessary to modify the  $A$ -matrix to a form that involves the nondimensional time to make the modal coupling of the eigenvectors more apparent (McRuer et al., 1973). That is, the modified  $A$ -matrix should have the eigenvectors in (2).

**(b) Lateral Axis.** In the linearized perturbed lateral equations of an aircraft the state can be taken as

$$x = \begin{bmatrix} r \\ \beta \\ p \\ \phi \\ \delta_r \\ \delta_a \end{bmatrix}, \quad (3)$$

where we have assumed first-order lags for the rudder and aileron actuators. The states are yaw rate,  $r$ , sideslip angle,  $\beta$ , roll rate,  $p$ , bank angle,  $\phi$ , and the actuator states,  $\delta_r$ , the rudder deflection, and  $\delta_a$ , the aileron deflection.

Roll commands should not excite the dutch roll mode. Thus let us associate  $r$  and  $\beta$  in the closed-loop system with the dutch roll mode (see Section 4.2). Then the roll

subsidence mode, which involves  $p$ , should not influence  $r$  and  $\beta$ . Similarly, the dutch roll oscillation should have no effect on roll rate or bank angle. Desirable eigenvectors to achieve this decoupling between modes are given by

$$v_1 = \begin{bmatrix} 1 \\ -1 \\ 0 \\ 0 \\ x \\ x \end{bmatrix} + j \begin{bmatrix} -1 \\ 1 \\ 0 \\ 0 \\ x \\ x \end{bmatrix}, \quad v_3 = \begin{bmatrix} 0 \\ 0 \\ 1 \\ x \\ x \\ x \end{bmatrix}, \quad (4)$$

with  $v_2$  the complex conjugate of  $v_1$  and  $x$  denoting entries whose values we are not concerned about. The closed-loop poles should also be selected for desirable time response:  $\lambda_1$  and  $\lambda_2$  for the dutch roll mode and  $\lambda_3$  for the roll subsidence mode. The desired closed-loop spiral mode may be selected as  $\lambda_4$ . ■

### Eigenstructure Assignment by Full State Feedback

Now that we have seen what the eigenvectors mean from the point of view of the aircraft behavior, we will discuss the assignment of both the closed-loop poles and eigenvectors, first by full state feedback and then in the next subsection by output feedback. This represents an extension of classical control theory in several ways. First, we are able to deal in a natural fashion with MIMO systems, *selecting all the control gains simultaneously for suitable performance*. Second, we will be able to use the extra freedom in systems with more than one input and output to assign the eigenvectors as well as the poles, thus directly influencing the *zeros* of the individual SISO transfer functions. Third, we will be able to address the problem of *decoupling of the modes* through considerations like those in Example 5.2-1.

**Matrix Equation for Eigenstructure Assignment** For ease of presentation we will assume that  $B$  and  $C$  have full rank  $m$  and  $p$ , respectively. Our discussion will be based on the polynomial matrix

$$C(s) = [sI - A \quad B], \quad (5.2-14)$$

with  $s$  a complex variable and  $A$  and  $B$  the system plant and input matrices.

In this subsection we follow Moore (1975) and consider full state feedback of the form

$$u = -Kx \quad (5.2-15)$$

Under the influence of this control input the closed-loop system becomes

$$\dot{x} = (A - BK)x \quad (5.2-16)$$

To select  $K$  so that a desired eigenvalue  $\lambda_i$  and associated eigenvector  $v_i$  are assigned to the closed-loop system, suppose that we can find a vector  $u_i \in \mathbf{R}^m$  to satisfy the equation

$$[\lambda_i I - A \quad B] \begin{bmatrix} v_i \\ u_i \end{bmatrix} = 0 \quad (5.2-17)$$

Now, choose the feedback gain  $K$  to satisfy

$$Kv_i = u_i \quad (5.2-18)$$

Using the last two equations, we may write

$$0 = (\lambda_i I - A)v_i + Bu_i \quad (5.2-19)$$

$$0 = [\lambda_i I - (A - BK)]v_i, \quad (5.2-20)$$

so that according to (5.2-8),  $v_i$  is assigned as a closed-loop eigenvector for eigenvalue  $\lambda_i$ .

As  $Cv_i$  was shown in the preceding subsection to be a direction in the output space  $\mathbf{R}^p$  associated with  $v_i$ , so  $u_i$  is the associated direction in the input space  $\mathbf{R}^m$ . That is, motions of  $u(t)$  in the direction of  $u_i$  will cause motions of  $x(t)$  in the direction of  $v_i$ , resulting in motions of  $y(t)$  in the direction of  $Cv_i$ .

To complete the picture, suppose that  $n$  eigenvalues  $\lambda_i$  and associated eigenvectors  $v_i$  are chosen and in each case we have found a vector  $u_i$  that satisfies (5.2-17). Then we may define  $K$  by

$$K[v_1 \quad v_2 \quad \cdots \quad v_n] = [u_1 \quad u_2 \quad \cdots \quad u_n] \quad (5.2-21)$$

or by appropriate definition of the matrices  $V$  and  $U$ ,

$$KV = U \quad (5.2-22)$$

Then, for each value of  $i = 1, \dots, n$ , (5.2-20) will hold, so that each  $\lambda_i$  will be assigned as a closed-loop pole with associated eigenvector  $v_i$ . This is the design technique for eigenstructure assignment using full state feedback. It remains only to discuss a few points.

**Design Considerations** Since, by definition, the closed-loop eigenvectors must be linearly independent, it is necessary to select  $v_i$  as linearly independent vectors. Then (5.2-22) may be solved for  $K$  to give

$$K = UV^{-1} \quad (5.2-23)$$

Another issue is that the closed-loop system and feedback gain must be real and not complex. Thus, if a complex closed-loop pole  $\lambda_i$  is selected, it is also necessary to select as a closed-loop pole its complex conjugate  $\lambda_i^*$ . Moreover, if  $v_i$  is to be the closed-loop eigenvector associated with a complex pole  $\lambda_i$ , then in order for (5.2-21) to have a real solution  $K$ , it is necessary to select  $v_i^*$  (i.e., the complex conjugate of  $v_i$ ) as the eigenvector for  $\lambda_i^*$ .

To see that under these circumstances (5.2-22) indeed has a real solution  $K$ , note first that if  $u_i$  solves (5.2-19) for a given  $\lambda_i$  and  $v_i$ , then  $u_i^*$  solves the equation for their complex conjugates. Therefore, if  $u_i = u_R + ju_I$  and  $v_i = v_R + jv_I$ , then to assign the desired eigenstructure,  $K$  must satisfy

$$K \begin{bmatrix} v_R + jv_I & v_R - jv_I \end{bmatrix} = \begin{bmatrix} u_R + ju_I & u_R - ju_I \end{bmatrix} \quad (5.2-24)$$

Postmultiplying both sides of this equation by

$$M = \frac{1}{2} \begin{bmatrix} 1 & -j \\ 1 & j \end{bmatrix},$$

it is seen that this equation is equivalent to the real equation

$$K \begin{bmatrix} v_R & v_I \end{bmatrix} = \begin{bmatrix} u_R & u_I \end{bmatrix}, \quad (5.2-25)$$

which clearly has as a solution a real gain matrix  $K$ . Thus, if  $v_i$  is complex, then to obtain a real value for  $K$  it is only necessary to use not  $v_i$  and  $v_i^*$  (respectively  $u_i$  and  $u_i^*$ ) in (5.2-21) but the real and imaginary parts of  $v_i$  (respectively  $u_i$ ).

Finally, we must investigate the conditions for existence of a solution to (5.2-17). It is unfortunately not usually possible to specify independently an arbitrary  $\lambda_i$  and  $v_i$  and obtain a solution  $u_i$  to this equation. Indeed, assuming that  $\lambda_i$  is not an open-loop pole, we have

$$v_i = -(\lambda_i I - A)^{-1} B u_i \quad (5.2-26)$$

Thus, for the existence of a solution  $u_i$ , the desired  $v_i$  must be a linear combination of the  $m$  columns of the linear operator

$$L_i = (\lambda_i I - A)^{-1} B \quad (5.2-27)$$

Since  $B$  has full rank  $m$  by assumption, the matrix  $L_i$  also has rank  $m$ . Thus,  $v_i$  must lie in an  $m$ -dimensional subspace of  $\mathbf{R}^n$  that depends on the choice of  $\lambda_i$ . This means that we have  *$m$  degrees of freedom in selecting the closed-loop eigenvector  $v_i$  once  $\lambda_i$  has been selected.*

This last point is the crucial difference between classical SISO design and multi-variable eigenstructure assignment. If  $m = 1$ , which corresponds to the single-input case, then eigenvector  $v_i$  has only one degree of freedom once the desired eigenvalue  $\lambda_i$  has been selected; that is, there is no additional freedom to choose the eigenvector. However, in the multi-input case where  $m > 1$ , we can have additional freedom

to specify the internal structure of the closed-loop system by selecting  $m$  degrees of freedom of  $v_i$  arbitrarily. In the preceding subsection we have seen the importance of this in terms of design performance.

The successive-loop-closure approach of classical control, where only one feedback gain is selected at a time, obscures the extra design freedom arising from multiple inputs. In modern control, where all gains are selected simultaneously, this freedom is clearly revealed.

**Design Procedure** The following design procedure for eigenstructure assignment is suggested. For a desired closed-loop pole/vector pair of  $\lambda_i$  and  $v_i^d$ , solve the equation

$$\begin{bmatrix} \lambda_i I - A & B \\ d & 0 \end{bmatrix} \begin{bmatrix} v_i \\ u_i \end{bmatrix} = \begin{bmatrix} 0 \\ v_i^d \end{bmatrix} \quad (5.2-28)$$

for  $u_i$  and the *achievable eigenvector*  $v_i$ . Repeat for  $i = 1, \dots, n$  to select  $n$  closed-loop poles. If the  $v_i$ s are not linearly independent, modify the choices for  $\lambda_i$  and/or  $v_i^d$  and repeat. Finally, determine the required state-variable feedback gain  $K$  using (5.2-23).

The design matrix  $D$  may be chosen for several different design objectives:

1.  $D = I$ . This is the case where the desired vectors  $v_i^d$  are eigenvectors (as in Example 5.2-1).
2.  $D = C$ . This is the case where the desired vectors are directions in the output space  $\mathbf{R}^p$ , so that we desire  $Cv_i = v_i^d$ .
3. If certain components of  $v_i$  are of no concern (see Example 5.2-1), the corresponding columns of  $D$  should be selected as zero. The remaining columns should be selected as columns from the  $d \times d$  identity matrix, with  $d$  the number of rows of  $D$ . The elements of  $v_i$  that they multiply should be as specified by the elements of  $v_i^d$ . We illustrate further in Example 5.2-3.

We have seen that (5.2-28) may not have an exact solution  $v_i, u_i$ . It is necessary to find a solution so that (1) the first  $n$  equations hold exactly [i.e., (5.2-19) must hold exactly] and (2) the second block equation  $Dv_i = v_i^d$  holds as closely as possible (then our design objectives are most closely matched). Subroutine LLBQF in the IMSL library (IMSL) allows us to do this. It gives a least-squares solution to the second equation in the sense that  $\|Dv_i - v_i^d\|^2$  is minimized over all possible  $v_i$  for which there exists a  $u_i$  that satisfies (5.2-19) (where  $\|w\|$  is the Euclidean norm of vector  $w$ ).

An interactive design technique is suggested wherein:

1. Given the desired  $\lambda_i$  and  $v_i^d$ , (5.2-28) is solved for the pair  $v_i, u_i$  meeting the requirements above.
2. The achievable eigenvector  $v_i$  is compared with the desired eigenvector and if it is unsatisfactory either  $v_i^d$  or  $\lambda_i$  may be modified and step 1 repeated.



### Eigenstructure Assignment by Output Feedback

In an aircraft control system, all of the states are not generally available for measurement. Instead, only selected outputs are available for control purposes. It is not difficult to modify the eigenstructure assignment technique so that the admissible controls are of the form

$$u = -Ky, \quad (5.2-29)$$

with output  $y(t) \in \mathbf{R}^p$  given by (5.2-2) (Srinathkumar, 1978). In this case, we will show that  $p$  eigenvalues may easily be assigned, with  $m$  degrees of freedom in the choice of the associated eigenvectors.

**Matrix Equation for Eigenstructure Assignment** In the case of output feedback the closed-loop system is

$$\dot{x} = (A - BKC)x \quad (5.2-30)$$

and it is only necessary to replace (5.2-18) by

$$KCv_i = u_i \quad (5.2-31)$$

Then, according to (5.2-17),

$$0 = (\lambda_i I - (A - BKC))v_i, \quad (5.2-32)$$

so that  $v_i$  is assigned as a closed-loop eigenvector for eigenvalue  $\lambda_i$ . In this case, (5.2-21) for  $K$  is replaced by

$$KC[v_1 \ v_2 \ \cdots \ v_r] = [u_1 \ u_2 \ \cdots \ u_r], \quad (5.2-33)$$

where  $r$  is the number of closed-loop eigenvalues selected.

If  $r = p$  and the vectors  $Cv_i$  are linearly independent, we may define

$$V = [v_1 \ v_2 \ \cdots \ v_r], \quad U = [u_1 \ u_2 \ \cdots \ u_r] \quad (5.2-34)$$

and solve for  $K$  using

$$K = U(CV)^{-1} \quad (5.2-35)$$

Thus, it is clear what is lost by using incomplete state information for feedback purposes, for we can in general no longer assign  $n$  poles arbitrarily.

**Extensions** What we have demonstrated is a technique for assigning by output feedback  $p$  closed-loop poles, with  $m$  degrees of freedom in specifying the components of each associated closed-loop eigenvector (where  $m$  is the number of inputs).

If  $m \leq p$ , so that the number of inputs is greater than or equal to the number of outputs, the technique just presented is suitable. However, if  $m > p$ , we must use the technique on the “dual” system. That is,  $(A, B, C)$  is replaced by  $(A^T, C^T, B^T)$  and the design is performed to find  $K^T$ . In this case we may assign  $m$  closed-loop poles, with  $p$  degrees of freedom in assigning the associated eigenvectors.

A problem with eigenstructure assignment using output feedback is that it is not possible to tell what happens to the  $n - p$  poles that are not assigned. Indeed, some of them may become unstable, even though the original plant was stable. If this occurs, or if some closed-loop poles are too lightly damped, the design should be repeated using different values for  $\lambda_i$  or  $v_i^d$ . Generally, it is found that if one does not ask for too much in terms of modifying the original plant behavior, that is, if most of the desired closed-loop poles are not too different from the open-loop poles, instability of the unassigned poles is not a problem (as long as they are open-loop stable).

Srinathkumar shows that it is possible to assign an almost arbitrary set of  $\min(n, m + p - 1)$  eigenvalues, but we will not go into details here. Kwon and Youn (1987) show that it may be possible to assign  $m + p$  poles in some examples.

The next concept is quite important, so we will illustrate it by an example.

**Example 5.2-2: Eigenstructure Assignment Using Dynamic Regulator** We have shown how to select constant-feedback gains to assign the closed-loop eigenstructure. However, it is possible to obtain a desired modal structure by using a dynamic compensator. This example shows how to design a dynamic compensator for eigenstructure assignment.

Consider the plant

$$\dot{x} = Ax + Bu \quad (1)$$

$$y = Cx \quad (2)$$

with the regulator dynamics defined by

$$\dot{z} = Fz + Gy \quad (3)$$

$$u = Hz + Jy \quad (4)$$

This corresponds to the situation in Figure 5.2-1. Matrices  $F$ ,  $G$ ,  $H$ , and  $J$  are to be selected to yield a desired closed-loop eigenstructure.

Show that by defining the augmented plant, input, and output matrices

$$\begin{bmatrix} A & 0 \\ 0 & 0 \end{bmatrix}, \quad \begin{bmatrix} B & 0 \\ 0 & I \end{bmatrix}, \quad \begin{bmatrix} C & 0 \\ 0 & I \end{bmatrix} \quad (5)$$

and the gain matrix

$$K = \begin{bmatrix} -J & -H \\ -G & -F \end{bmatrix} \quad (6)$$

the problem of determining  $F$ ,  $G$ ,  $H$ , and  $J$  to yield desired closed-loop poles  $\lambda_i$  and eigenvectors  $v_i^d$  may be solved by using the techniques of this section to determine  $K$ .

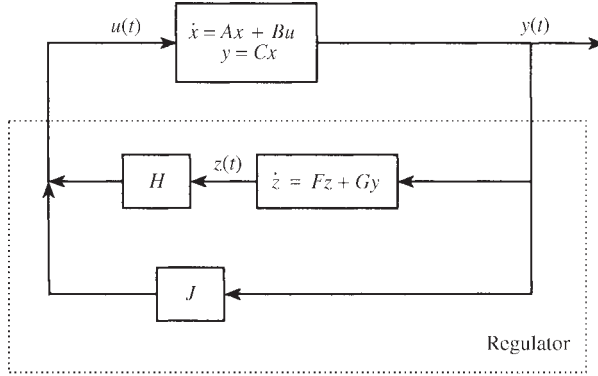


**Figure 5.2-1** Plant with regulator.

*Note:* A problem with this approach is that the regulator matrix  $F$  cannot be guaranteed stable. An alternative approach to regulator/observer design is given by Andry et al. (1984). ■

**Example 5.2-3: Eigenstructure Design of Longitudinal Pitch Pointing Control.** This example is taken from the work of Sobel and Shapiro (1985). A linearized model of the short-period dynamics of an advanced (CCV-type) fighter aircraft is given. These dynamics are augmented by elevator and flaperon actuator dynamics given by the simplified model  $20/(s + 20)$  so that the state vector is

$$x = \begin{bmatrix} \alpha \\ q \\ \gamma \\ \delta_e \\ \delta_f \end{bmatrix}, \quad (1)$$

where the state components are, respectively, angle of attack, pitch rate, flight-path angle, elevator deflection, and flaperon deflection. The control inputs are elevator and flaperon commands so that

$$u = \begin{bmatrix} \delta_{e_c} \\ \delta_{f_c} \end{bmatrix} \quad (2)$$

The plant and control matrices are

$$A = \begin{bmatrix} -1.341 & 0.9933 & 0 & -0.1689 & -0.2518 \\ 43.223 & -0.8693 & 0 & -17.251 & -1.5766 \\ 1.341 & 0.0067 & 0 & 0.1689 & 0.2518 \\ 0 & 0 & 0 & -20 & 0 \\ 0 & 0 & 0 & 0 & -20 \end{bmatrix}$$

$$B = \begin{bmatrix} 0 & 0 \\ 0 & 0 \\ 0 & 0 \\ 20 & 0 \\ 0 & 20 \end{bmatrix} \quad (3)$$

and the open-loop eigenvalues are

$$\begin{aligned}
 \lambda_1 = 5.452 & \quad \left. \begin{array}{l} \lambda_2 = -7.662 \end{array} \right\} \text{unstable short-period mode} \\
 \lambda_3 = 0.0 & \quad \text{pitch-attitude mode} \\
 \lambda_4 = -20 & \quad \text{elevator actuator mode} \\
 \lambda_5 = -20 & \quad \text{flaperon actuator mode}
 \end{aligned} \tag{4}$$

The measured output available for control purposes is

$$y = \begin{bmatrix} q \\ n_{zp} \\ \gamma \\ \delta_e \\ \delta_f \end{bmatrix}, \tag{5}$$

where  $n_{zp}$  is normal acceleration at the pilot's station. The altitude rate  $\dot{h}$  is obtained from the air data computer and the flight-path angle is then computed using

$$\gamma = \frac{\dot{h}}{TAS} \tag{6}$$

with  $T$  as the true airspeed. The control surface deflections are measured using linear variable differential transformers (LVDTs). The relation between  $y(t)$  and  $x(t)$  is given by

$$y = \begin{bmatrix} 0 & 1 & 0 & 0 & 0 \\ 47.76 & -0.268 & 0 & -4.56 & 4.45 \\ 0 & 0 & 1 & 0 & 0 \\ 0 & 0 & 0 & 1 & 0 \\ 0 & 0 & 0 & 0 & 1 \end{bmatrix} x \equiv Cx \tag{7}$$

Since there are five outputs and two control inputs, we may place all the closed-loop poles as well as assign the eigenvectors within two-dimensional subspaces. This roughly corresponds to selecting two components of each eigenvector arbitrarily.

The desired closed-loop short-period poles are chosen to meet military specifications for category A, level-1 flight (*Mil. Spec. 1797*, 1987) (see Section 4.3). Thus, the desired short-period damping ratio and frequency are 0.8 and 7 rad/s, respectively.

For stability, we specify that the desired closed-loop pitch-attitude mode should decay exponentially with a time constant of 1, so that the pole should be at  $s = -1$ . The actuator poles should be near  $-20$ ; however, selecting repeated poles

can yield problems with the design algorithm. The desired eigenvalues are thus selected as

$$\left. \begin{aligned} \lambda_1 &= -5.6 + j4.2 \\ \lambda_2 &= -5.6 - j4.2 \end{aligned} \right\} \text{short-period mode}$$

$$\begin{aligned} \lambda_3 &= -1.0 && \text{pitch-attitude mode} \\ \lambda_4 &= -19.0 && \text{elevator actuator mode} \\ \lambda_5 &= -19.5 && \text{flaperon actuator mode} \end{aligned} \quad (8)$$

In pitch pointing, the control objective is to allow pitch-attitude control while maintaining constant flight-path angle. To achieve this we select the desired closed-loop eigenvectors to decouple pitch-rate and flight-path angle. Thus, an attitude command should be prevented from causing a significant flight-path change. The desired closed-loop eigenvectors are shown in Table 5.2-1, where  $x$  denotes elements of no concern to us. Recall that  $\alpha$  and  $q$  are associated with the short-period mode.

We now discuss the design procedure and the selection of the  $D$ -matrix in the design equation (5.2-28). We must determine the vectors  $v_i$  and  $u_i$  for use in (5.2-33) to solve for the feedback gain matrix  $K$ . To accomplish this, first consider the desired structure of the short-period mode. According to Table 5.2-1, the required short-period eigenvectors have two “don’t care” entries. Define  $v_1^d$  in terms of the required eigenvector as

$$v_1^d = \begin{bmatrix} 1 & 0 & 0 & 0 & 0 \\ 0 & 1 & 0 & 0 & 0 \\ 0 & 0 & 1 & 0 & 0 \end{bmatrix} \left[ \begin{bmatrix} 1 \\ -1 \\ 0 \\ x \\ x \end{bmatrix} + j \begin{bmatrix} -1 \\ 1 \\ 0 \\ x \\ x \end{bmatrix} \right] = \begin{bmatrix} 1 \\ -1 \\ 0 \end{bmatrix} + j \begin{bmatrix} -1 \\ 1 \\ 0 \end{bmatrix} \quad (9)$$

to be the desired vector associated with  $\lambda_1 = -5.6 + j4.2$  and select  $D$  as the  $3 \times 6$  coefficient matrix in (9). Then (5.2-28) may be solved for  $v_1$  and  $u_1$ . Then the vectors

**TABLE 5.2-1 Desired and Achievable Eigenvectors**

<i>Desired Eigenvectors</i>						<i>Achievable Eigenvectors</i>				
$\begin{bmatrix} 1 \\ -1 \\ 0 \\ x \\ x \end{bmatrix}$	$+j \begin{bmatrix} -1 \\ 1 \\ 0 \\ x \\ x \end{bmatrix}$	$\begin{bmatrix} x \\ 0 \\ 1 \\ x \\ x \end{bmatrix}$	$\begin{bmatrix} x \\ x \\ x \\ 1 \\ x \end{bmatrix}$	$\begin{bmatrix} x \\ x \\ x \\ x \\ 1 \end{bmatrix}$	$\begin{matrix} \alpha \\ q \\ \gamma \\ \delta_e \\ \delta_f \end{matrix}$	$\begin{bmatrix} -0.93 \\ 1 \\ 0 \\ -5.13 \\ 8.36 \end{bmatrix}$	$+j \begin{bmatrix} 1 \\ -9.5 \\ 0 \\ 0.129 \\ -5.16 \end{bmatrix}$	$\begin{bmatrix} -1 \\ 0 \\ 1 \\ -2.8 \\ 3.23 \end{bmatrix}$	$\begin{bmatrix} -0.051 \\ 1.07 \\ -0.006 \\ 1 \\ 0 \end{bmatrix}$	$\begin{bmatrix} 0.01 \\ 0.06 \\ -0.014 \\ 0 \\ 1 \end{bmatrix}$
$\alpha/q$		$\gamma$	$\delta_e$	$\delta_f$		$\alpha/q$		$\gamma$	$\delta_e$	$\delta_f$
Short period						Short period				

associated with  $\lambda_2 = \lambda_1^*$  are  $v_2 = v_1^*$ ,  $u_2 = u_1^*$ . The achievable eigenvectors  $v_1$  and  $v_2$  associated with the short-period mode are shown in Table 5.2-1.

To determine whether the results to this point are satisfactory, the achievable eigenvectors  $v_1$  and  $v_2$  are compared with the desired eigenvectors. They are satisfactory since there is no coupling to state component 3. Note that although we attempted to select three components of the eigenvectors knowing that there are only two degrees of freedom in this selection, we have nevertheless been fortunate in attaining our design objectives. Had we not been so lucky, it would have been necessary to try different desired eigenvectors or else slightly different values for the closed-loop poles.

Moving on to the desired structure of  $\lambda_3$ , examine Table 5.2-1 to define

$$v_3^d = \begin{bmatrix} 0 & 1 & 0 & 0 & 0 \\ 0 & 0 & 1 & 0 & 0 \end{bmatrix} \begin{bmatrix} x \\ 0 \\ 1 \\ x \\ x \end{bmatrix} = \begin{bmatrix} 0 \\ 1 \end{bmatrix} \quad (10)$$

to be the desired vector associated with  $\lambda_3 = -1.0$  and select  $D$  as the  $2 \times 6$  coefficient matrix in (10). Then (5.2-28) may be solved for  $v_3$  and  $u_3$ . The result is the achievable eigenvector  $v_3$  shown in Table 5.2-1; again, it is suitable.

To design for the desired structure of  $\lambda_4$ , examine Table 5.2-1 to define

$$v_4^d = \begin{bmatrix} 0 & 0 & 0 & 1 & 0 \end{bmatrix} \begin{bmatrix} x \\ x \\ x \\ 1 \\ x \end{bmatrix} = 1 \quad (11)$$

to be the desired vector associated with  $\lambda_4 = -19.0$  and select  $D$  as the  $1 \times 6$  coefficient matrix in (11). Then (5.2-28) may be solved for  $v_4$  and  $u_4$ . The results are in the table. Similar procedures apply for  $\lambda_5$ .

Now that all the requisite vectors  $v_i$  and  $u_i$ ,  $i = 1, 2, 3, 4, 5$ , have been computed, they are used, along with the  $C$ -matrix from (7), to solve for the feedback gain using (5.2-33). The result is

$$K = \begin{bmatrix} -0.931 & -0.149 & -3.25 & -0.153 & 0.747 \\ 0.954 & 0.210 & 6.10 & 0.537 & -1.04 \end{bmatrix} \quad (12)$$

To check the design, a computer simulation was performed. The closed-loop system was excited with an initial condition of 0.2 rad in angle of attack. Note from Figure 5.2-2 that this excited the short-period mode but had negligible effect on the flight-path angle.

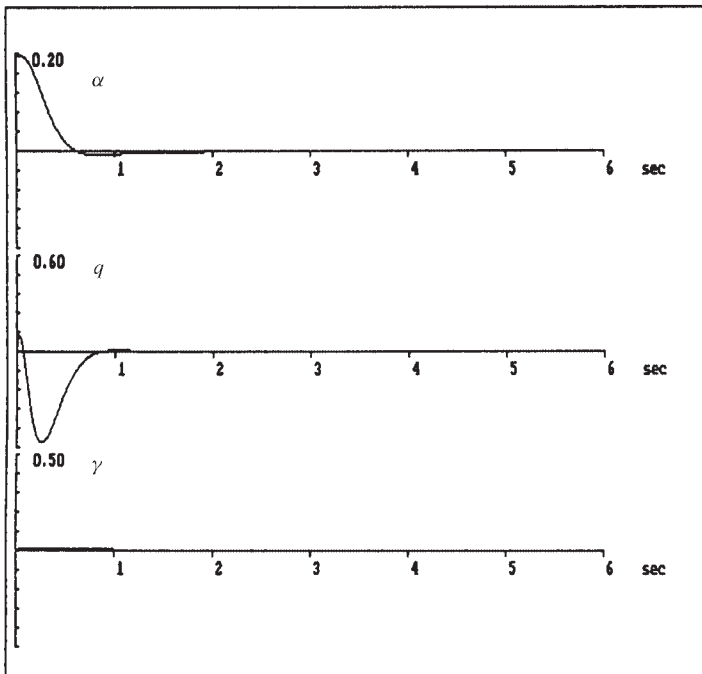


Figure 5.2-2 Closed-loop response to angle-of-attack initial condition. ■

### 5.3 LINEAR QUADRATIC REGULATOR WITH OUTPUT FEEDBACK

Our objective in this section is to show how to use modern techniques to design stability augmentation systems (SASs) and autopilots. This is accomplished by regulating certain states of the aircraft to zero while obtaining desirable closed-loop response characteristics. It involves the problem of stabilizing the aircraft by placing the closed-loop poles at desirable locations.

Using classical control theory, we were forced to take a one-loop-at-a-time approach to designing multivariable SASs and autopilots. In this section we will select a performance criterion that reflects our concern with closed-loop stability and good time responses and then derive matrix equations that may be solved for *all the control gains simultaneously*. These matrix equations are solved using digital computer programs (see Appendix B). This approach thus closes all the loops simultaneously and results in a simplified design strategy for MIMO systems or SISO systems with multiple feedback loops.

Once the performance criterion has been selected, the control gains are explicitly computed by matrix design equations, and closed-loop stability will generally be guaranteed. This means that *the engineering judgment in modern control enters into the selection of the performance criterion*. Different criteria will result in different closed-loop time responses and robustness properties.

We assume the plant is given by the linear time-invariant state-variable model

$$\dot{x} = Ax + Bu \quad (5.3-1)$$

$$y = Cx, \quad (5.3-2)$$

with  $x(t) \in \mathbf{R}^n$  the state,  $u(t) \in \mathbf{R}^m$  the control input, and  $y(t) \in \mathbf{R}^p$  the measured output. The controls will be output feedbacks of the form

$$u = -Ky, \quad (5.3-3)$$

where  $K$  is an  $m \times p$  matrix of constant-feedback coefficients to be determined by the design procedure. Since the regulator problem only involves stabilizing the aircraft and inducing good closed-loop time responses,  $u(t)$  will be taken as a pure feedback with no auxiliary input (see Section 5.2).

As we will see in Section 5.4, output feedback will allow us to design aircraft controllers of any desired structure. This is one reason for preferring it over full state feedback.

In the regulator problem, we are interested in obtaining good time responses as well as in the stability of the closed-loop system. Therefore, we will select a performance criterion *in the time domain*. Let us now present this criterion.

### Quadratic Performance Index

The objective of state regulation for the aircraft is to drive any initial condition error to zero, thus guaranteeing stability. This may be achieved by selecting the control input  $u(t)$  to minimize a quadratic *cost* or *performance index (PI)* of the type

$$J = \frac{1}{2} \int_0^\infty (x^T Q x + u^T R u) dt, \quad (5.3-4)$$

where  $Q$  and  $R$  are symmetric positive-semidefinite *weighting matrices*. Positive semidefiniteness of a square matrix  $M$  (denoted  $M \geq 0$ ) is equivalent to all its eigenvalues being nonnegative and also to the requirement that the quadratic form  $x^T M x$  be nonnegative for all vectors  $x$ . Therefore, the definiteness assumptions on  $Q$  and  $R$  guarantee that  $J$  is nonnegative and lead to a sensible minimization problem. This quadratic PI is a vector version of an integral-squared PI of the sort used in classical control (D'Azzo and Houpis, 1988).

To understand the motivation for the choice of (5.3-4), consider the following. If the square root  $\sqrt{M}$  of a positive-semidefinite matrix  $M$  is defined by

$$M = \sqrt{M}^T \sqrt{M}, \quad (5.3-5)$$

we may write (5.3-4) as

$$J = \frac{1}{2} \int_0^\infty \left( \|\sqrt{Q}x\|^2 + \|\sqrt{R}u\|^2 \right) dt, \quad (5.3-6)$$



with  $\|w\|$  the Euclidean norm of a vector  $w$  (i.e.,  $\|w\|^2 = w^T w$ ). If we are able to select the control input  $u(t)$  so that  $J$  takes on a minimum finite value, certainly the integrand must become zero for large time. This means that both the linear combination  $\sqrt{Q}x(t)$  of the states and the linear combination  $\sqrt{R}u(t)$  of the controls must go to zero. In different designs we may select  $Q$  and  $R$  for different performance requirements, corresponding to specified functions of the state and input. In particular, if  $Q$  and  $R$  are both chosen nonsingular, the entire state vector  $x(t)$  and all the controls  $u(t)$  will go to zero with time if  $J$  has a finite value.

Since a bounded value for  $J$  will guarantee that  $\sqrt{Q}x(t)$  and  $\sqrt{R}u(t)$  go to zero with time, this formulation for the PI is appropriate for the regulator problem as any initial condition errors will be driven to zero.

If the state vector  $x(t)$  consists of capacitor voltages  $v(t)$  and inductor currents  $i(t)$ , then  $\|x\|^2$  will contain terms like  $v^2(t)$  and  $i^2(t)$ . Similarly, if velocity  $s(t)$  is a state component,  $\|x\|^2$  will contain terms like  $s^2(t)$ . Therefore, the minimization of the PI (5.3.4) is a generalized *minimum-energy* problem. We are concerned with minimizing the energy in the states without using too much control energy.

The relative magnitudes of  $Q$  and  $R$  may be selected to trade off requirements on the smallness of the state against requirements on the smallness of the input. For instance, a larger control-weighting matrix  $R$  will make it necessary for  $u(t)$  to be smaller to ensure that  $\sqrt{R}u(t)$  is near zero. We say that a larger  $R$  *penalizes* the controls more, so that they will be smaller in norm relative to the state vector. On the other hand, to make  $x(t)$  go to zero more quickly with time, we may select a larger  $Q$ .

As a final remark on the PI, we will see that the positions of the closed-loop poles depend on the choices for the weighting matrices  $Q$  and  $R$ . That is,  $Q$  and  $R$  may be chosen to yield good time responses in the closed-loop system.

Let us now derive matrix design equations that may be used to solve for the control gain  $K$  that minimizes the PI. The result will be the design equations in Table 5.3-1. Software to solve these equations for  $K$  is described in Appendix B.

## Solution of the LQR Problem

The LQR problem with output feedback is the following. Given the linear system (5.3-1), (5.3-2), find the feedback coefficient matrix  $K$  in the control input (5.3-3) that minimizes the value of the quadratic PI (5.3-4). In contrast with most of the classical control techniques given in earlier chapters, this is a *time-domain* design technique.

By substituting the control (5.3-3) into (5.3-1) the closed-loop system equations are found to be

$$\dot{x} = (A - BKC)x \equiv A_c x \quad (5.3-7)$$

The PI may be expressed in terms of  $K$  as

$$J = \frac{1}{2} \int_0^\infty x^T (Q + C^T K^T R K C) x dt \quad (5.3-8)$$

The design problem is now to select the gain  $K$  so that  $J$  is minimized subject to the dynamical constraint (5.3-7).

This *dynamical* optimization problem may be converted into an equivalent *static* one that is easier to solve as follows. Suppose that we can find a constant, symmetric, positive-semidefinite matrix  $P$  so that

$$\frac{d}{dt}(x^T Px) = -x^T(Q + C^T K^T R K C)x \quad (5.3-9)$$

Then  $J$  may be written as

$$J = \frac{1}{2}x^T(0)Px(0) - \frac{1}{2}\lim_{t \rightarrow \infty} x^T(t)Px(t) \quad (5.3-10)$$

Assuming that the closed-loop system is asymptotically stable so that  $x(t)$  vanishes with time, this becomes

$$J = \frac{1}{2}x^T(0)Px(0) \quad (5.3-11)$$

If  $P$  satisfies (5.3-9), we may use (5.3-7) to see that

$$\begin{aligned} -x^T(Q + C^T K^T R K C)x &= \frac{d}{dt}(x^T Px) = \dot{x}^T Px + x^T P \dot{x} \\ &= x^T(A_c^T P + P A_c)x \end{aligned} \quad (5.3-12)$$

Since this must hold for all initial conditions and hence for all state trajectories  $x(t)$ , we may write

$$g = A_c^T P + P A_c + C^T K^T R K C + Q = 0 \quad (5.3-13)$$

If  $K$  and  $Q$  are given and  $P$  is to be solved for, this is called a *Lyapunov equation*. (A Lyapunov equation is a symmetric linear matrix equation. Note that the equation does not change if its transpose is taken.)

In summary, for any fixed feedback matrix  $K$ , if there exists a constant, symmetric, positive-semidefinite matrix  $P$  that satisfies (5.3-13) and if the closed-loop system is stable, the cost  $J$  is given in terms of  $P$  by (5.3-11). This is an important result in that the  $n \times n$  auxiliary matrix  $P$  is independent of the state. Given a feedback matrix  $K$ ,  $P$  may be computed from the Lyapunov equation (5.3-13). Then only the initial condition  $x(0)$  is required to compute the closed-loop cost under the influence of the feedback control  $u = -Ky$  *before we actually apply it*.

It is now necessary to use this result to compute the gain  $K$  that minimizes the PI. By using the trace identity

$$\text{tr}(AB) = \text{tr}(BA) \quad (5.3-14)$$

for any compatibly dimensioned matrices  $A$  and  $B$  (with the trace of a matrix the sum of its diagonal elements), we may write (5.3-11) as

$$J = \frac{1}{2}\text{tr}(PX), \quad (5.3-15)$$

where the  $n \times n$  symmetric matrix  $X$  is defined by

$$X \equiv x(0)x^T(0) \quad (5.3-16)$$

It is now clear that the problem of selecting  $K$  to minimize (5.3-8) subject to the dynamical constraint (5.3-7) on the states is equivalent to the *algebraic* problem of selecting  $K$  to minimize (5.3-15) subject to the constraint (5.3-13) on the auxiliary matrix  $P$ .

To solve this modified problem, we use the Lagrange multiplier approach (Lewis, 1986) to modify the problem yet again. Thus, adjoin the constraint to the PI by defining the Hamiltonian

$$\mathcal{H} = \text{tr}(PX) + \text{tr}(gS) \quad (5.3-17)$$

with  $S$  a symmetric  $n \times n$  matrix of Lagrange multipliers that still needs to be determined. Then our constrained optimization problem is equivalent to the simpler problem of minimizing (5.3-17) without constraints. To accomplish this we need only set the partial derivatives of  $\mathcal{H}$  with respect to all the independent variables  $P$ ,  $S$ , and  $K$  equal to zero. Using the facts that for any compatibly dimensioned matrices  $A$ ,  $B$ , and  $C$  and any scalar  $y$ ,

$$\frac{\partial}{\partial B} \text{tr}(ABC) = A^T C^T \quad (5.3-18)$$

and

$$\frac{\partial y}{\partial B^T} = \left[ \frac{\partial y}{\partial B} \right]^T, \quad (5.3-19)$$

the necessary conditions for the solution of the LQR problem with output feedback are given by

$$0 = \frac{\partial \mathcal{H}}{\partial S} = g = A_c^T P + P A_c + C^T K^T B K C + Q \quad (5.3-20)$$

$$0 = \frac{\partial \mathcal{H}}{\partial P} = A_c S + S A_c^T + X \quad (5.3-21)$$

$$0 = \frac{1}{2} \frac{\partial \mathcal{H}}{\partial K} = R K C S C^T - B^T P S C^T \quad (5.3-22)$$

The first two of these are Lyapunov equations and the third is an equation for the gain  $K$ . If  $R$  is positive definite (i.e., all eigenvalues greater than zero, which implies nonsingularity; denoted  $R > 0$ ) and  $C S C^T$  is nonsingular, then (5.3-22) may be solved for  $K$  to obtain

$$K = R^{-1} B^T P S C^T (C S C^T)^{-1} \quad (5.3-23)$$

To obtain the output feedback gain  $K$  minimizing the PI (5.3-4), we need to solve the three coupled equations (5.3-20), (5.3-21), and (5.3-23). This situation is quite strange, for to find  $K$  we must determine along the way the values of two auxiliary and apparently unnecessary  $n \times n$  matrices,  $P$  and  $S$ . These auxiliary quantities may, however, not be as unnecessary as it appears, for note that the optimal cost may be determined directly from  $P$  and the initial state by using (5.3-11).

**The Initial-Condition Problem** Unfortunately, the dependence of  $X$  in (5.3-16) on the initial state  $x(0)$  is undesirable, since it makes the optimal gain dependent on the initial state through Equation (5.3-21). In many applications  $x(0)$  may not be known. This dependence is typical of output feedback design. We will see at the end of this chapter that in the case of state feedback it does not occur. Meanwhile, it is usual (Levine and Athans, 1970) to sidestep this problem by minimizing not the PI (5.3-4) but its *expected value*, that is,  $E\{J\}$ . Then (5.3-11) and (5.3-16) are replaced by

$$E\{J\} = \frac{1}{2}E\{x^T(0)Px(0)\} = \frac{1}{2}\text{tr}(PX), \quad (5.3-24)$$

where the symmetric  $n \times n$  matrix

$$X \equiv E\{x(0)x^T(0)\} \quad (5.3-25)$$

is the initial autocorrelation of the state. It is usual to assume that nothing is known of  $x(0)$  except that it is uniformly distributed on a surface described by  $X$ . That is, we assume that the actual initial state is unknown but it is nonzero with a certain expected Euclidean norm. For instance, if the initial states are assumed to be uniformly distributed on the unit sphere, then  $X = I$ , the identity. This is a sensible assumption for the regulator problem, where we are trying to drive arbitrary nonzero initial states to zero.

The design equations for the LQR with output feedback are collected in Table 5.3-1 for convenient reference. We will now discuss their solution for  $K$ .

### Determining the Optimal Feedback Gain

The importance of this modern LQ approach to control design is that the matrix equations in Table 5.3-1 are used to solve for all the  $m \times p$  elements of  $K$  at once. This corresponds to closing all the feedback loops simultaneously. Moreover, as long as certain reasonable conditions (to be discussed) on the plant and PI weighting matrices hold, *the closed-loop system is generally guaranteed to be stable*. In view of the trial-and-error successive-loop-closure approach used in stabilizing multivariable systems using classical approaches, this is quite important.

The equations for  $P$ ,  $S$ , and  $K$  are coupled nonlinear matrix equations in three unknowns. It is important to discuss some aspects of their solution for the optimal feedback gain matrix  $K$ .

**Numerical Solution Techniques** There are three basic numerical techniques for determining the optimal output feedback gain  $K$ . First, we may use a numerical optimization routine such as the Simplex algorithm by Nelder and Mead (1964) and Press et al. (1986). This algorithm would use only (5.3-26) and (5.3-29). For a given value of  $K$ , it would solve the Lyapunov equation for  $P$  and then use  $P$  in the second equation to determine  $E\{J\}$ . Based on this, it would vary the elements of  $K$  to minimize  $E\{J\}$ . The Lyapunov equation may be solved using, for instance, subroutine ATXPXA (Bartels and Stewart, 1972). See also the NASA controls design package ORACLS (Armstrong, 1980).

**TABLE 5.3-1 LQR with Output Feedback***System Model*

$$\dot{x} = Ax + Bu$$

$$y = Cx$$

*Control*

$$u = -Ky$$

*Performance Index*

$$J = \frac{1}{2}E \left[ \int_0^\infty (x^T Qx + u^T Ru) dt \right]$$

with

$$Q \geq 0, \quad R > 0$$

*Optimal Gain Design Equations*

$$0 = A_c^T P + P A_c + C^T K^T R K C + Q \quad (5.3-26)$$

$$0 = A_c S + S A_c^T + X \quad (5.3-27)$$

$$K = R^{-1} B^T P S C^T (C S C^T)^{-1} \quad (5.3-28)$$

where

$$A_c = A - B K C, \quad X = E\{x(0)x^T(0)\}$$

*Optimal Cost*

$$J = \frac{1}{2}\text{tr}(PX) \quad (5.3-29)$$

A second approach for computing  $K$  is to use a gradient-based routine such as Davidon-Fletcher-Powell (Press et al., 1986). This routine would use all of the design equations in Table 5.3-1. For a given value of  $K$ , it would solve the two Lyapunov equations to find the auxiliary matrices  $P$  and  $S$ . Then it would use the third design equation in the form (5.3-22). Note that if  $P$  satisfies the first Lyapunov equation, then  $\dot{g} = 0$  so that [see (5.3-17)]  $E\{J\} = \frac{1}{2}E\{H\}$  and  $\partial E\{J\}/\partial K = \frac{1}{2}\partial E\{H\}/\partial K$ . Thus, the third design equation gives the gradient of  $E\{J\}$  with respect to  $K$ , which would be used by the routine to update the value of  $K$ .

Finally, an iterative solution algorithm was presented by Moerder and Calise (1985). It is given in Table 5.3-2. It was shown by Moerder and Calise (1985) that the algorithm converges to a local minimum for  $J$  if the following conditions hold.

### Conditions for Convergence of the LQ Solution Algorithm

1. There exists a gain  $K$  such that  $A_c$  is stable. If this is true, we call the system (5.3-1)/(5.3-2) *output stabilizable*.
2. The output matrix  $C$  has full row rank  $p$ .

**TABLE 5.3-2 Optimal Output Feedback Solution Algorithm**


---

1. Initialize:

Set  $k = 0$ .

Determine a gain  $K_0$  so that  $A - BK_0C$  is asymptotically stable.

2.  $k$ th iteration:

Set  $A_k = A - BK_kC$ .

Solve for  $P_k$  and  $S_k$  in

$$0 = A_k^T P_k + P_k A_k + C^T K_k^T R K_k C + Q$$

$$0 = A_k S_k + S_k A_k^T + X$$

Set  $J_k = \frac{1}{2} \text{tr}(P_k X)$ .

Evaluate the gain update direction

$$\Delta K = R^{-1} B^T P S C^T (C S C^T)^{-1} - K_k$$

Update the gain by

$$K_{k+1} = K_k + \alpha \Delta K$$

where  $\alpha$  is chosen so that

$A - BK_{k+1}C$  is asymptotically stable

$$J_{k+1} \equiv \frac{1}{2} \text{tr}(P_{k+1} X) \leq J_k$$

If  $J_{k+1}$  and  $J_k$  are close enough to each other, go to 3.

Otherwise, set  $k = k + 1$  and go to 2.

3. Terminate:

Set  $K = K_{k+1}$ ,  $J = J_{k+1}$ .

Stop.

---

3. Control weighting matrix  $R$  is positive definite. This means that all the control inputs should be weighted in the PI.

4.  $Q$  is positive semidefinite and  $(\sqrt{Q}, A)$  is *detectable*. That is, the observability matrix polynomial

$$O(s) \equiv \begin{bmatrix} sI - A \\ -\sqrt{Q} \end{bmatrix} \quad (5.3-30)$$

has full rank  $n$  for all values of the complex variable  $s$  not contained in the left-half plane (Kailath, 1980).

If these conditions hold, the algorithm finds an output feedback gain that stabilizes the plant and minimizes the PI. The detectability condition means that any unstable system modes must be observable in the PI. Then if the PI is bounded, which it is if the optimization algorithm is successful, signals associated with the unstable modes must go to zero as  $t$  becomes large, that is, they are stabilized in the closed-loop system.

**Initial Stabilizing Gain** Since all three algorithms for solving the matrix equations in Table 5.3-1 for  $K$  are iterative in nature, a basic issue for all of them is the selection of an initial stabilizing output feedback gain  $K_0$ . That is, to start the algorithms, it is necessary to provide a  $K_0$  such that  $(A - BK_0C)$  is stable. See, for instance, Table 5.3-2.

One technique for finding such a gain is given by Broussard and Halyo (1983). Another possibility is to use the eigenstructure assignment techniques of the preceding section to determine an initial gain for the LQ solution algorithm. We could even select a stabilizing gain using the classical techniques of Chapter 4 and then use modern design techniques to tune the control gains for optimal performance.

A quite convenient technique for finding an initial stabilizing gain  $K_0$  is discussed in Section 5.5. This involves finding a full  $m \times n$  state-variable feedback matrix and then zeroing the entries that are not needed in the  $m \times p$  output feedback matrix for the given measured outputs. Note that there are many techniques for finding a full state feedback that stabilizes a system given  $A$  and  $B$  [see Section 5.7 and Lewis (1986)].

**Iterative Design** Software that solves for the optimal output feedback gain  $K$  is described in Appendix B. Given good software, design using the LQ approach is straightforward. A design procedure would involve selecting the *design parameters*  $Q$  and  $R$ , determining the optimal gain  $K$ , and simulating the closed-loop response and frequency-domain characteristics. If the results are not suitable, different matrices  $Q$  and  $R$  are chosen and the design is repeated. Good software makes a design iteration take only a few minutes.

This approach introduces the notion of *tuning the design parameters  $Q$  and  $R$  for good performance*. In the next two sections we will present sensible techniques for obtaining suitable PI weighting matrices  $Q$  and  $R$  that do not depend on individually selecting all of their entries.

Example 5.3-1 will illustrate these notions.

## Selection of the PI Weighting Matrices

Once the PI weighting matrices  $Q$  and  $R$  have been selected, the determination of the optimal feedback gain  $K$  is a formal procedure relying on the solution of nonlinear coupled matrix equations. Therefore, the engineering judgment in modern LQ design appears in the selection of  $Q$  and  $R$ . There are some guidelines for this which we will now discuss.

**Observability in the Choice of  $Q$**  For stabilizing solutions to the output feedback problem, it is necessary for  $(\sqrt{Q}, A)$  to be detectable. The detectability condition basically means that  $Q$  should be chosen so that all unstable states are weighted in the PI. Then, if  $J$  is bounded so that  $\sqrt{Q}x(t)$  vanishes for large  $t$ , the open-loop unstable states will be forced to zero through the action of the control. This means exactly that the unstable poles must have been stabilized by the feedback control gain.

A stronger condition than detectability is *observability*, which amounts to the full rank of  $O(s)$  for all values of  $s$ . Observability is easier to check than detectability since it is equivalent to the full rank  $n$  of the *observability matrix*

$$O \equiv \begin{bmatrix} \sqrt{Q} \\ \sqrt{Q}A \\ \vdots \\ \sqrt{Q}A^{n-1} \end{bmatrix}, \quad (5.3-31)$$

which is a constant matrix and so easier to deal with than  $O(s)$ . In fact,  $O$  has full rank  $n$  if and only if the observability Gramian  $O^T O$  is nonsingular. Since the Gramian is an  $n \times n$  matrix, its determinant is easily examined using available software [e.g., singular-value decomposition/condition number (IMSL)]. The observability of  $(\sqrt{Q}, A)$  means basically that *all* states are weighted in the PI.

From a numerical point of view, if  $(\sqrt{Q}, A)$  is observable, a positive-definite solution  $P$  to (5.3-26) results; otherwise,  $P$  may be singular. Since  $P$  helps determine  $K$  through (5.3-28), it is found that if  $P$  is singular, it may result in some zero-gain elements in  $K$ . That is, if  $(\sqrt{Q}, A)$  is not observable, the LQ algorithm can refuse to close some of the feedback loops.

This observability condition amounts to a restriction on the selection of  $Q$  and is a drawback of modern control (see Example 5.3-1). In Section 5.5 we will show how to avoid this condition by using a modified PI.

**The Structure of  $Q$**  The choice of  $Q$  can be confronted more easily by considering the performance objectives of the LQR. Suppose that a *performance output*

$$z = Hx \quad (5.3-32)$$

is required to be small in the closed-loop system. For instance, in an aircraft lateral regulator it is desired for the sideslip angle, yaw rate, roll angle, and roll rate to be small (see Example 5.3-1). Therefore, we might select  $z = [\beta \ r \ \phi \ p]^T$ . Once  $z(t)$  has been chosen, the performance output matrix  $H$  may be formally written down.

The signal  $z(t)$  may be made small by LQR design by selecting the PI

$$J = \frac{1}{2} \int_0^\infty (z^T z + u^T R u) dt, \quad (5.3-33)$$

which amounts to using the PI in Table 5.3-1 with  $Q = H^T H$ , so that  $Q$  may be computed from  $H$ . That is, by weighting *performance outputs* in the PI,  $Q$  is directly given.

**Maximum Desired Values of  $z(t)$  and  $u(t)$**  A convenient guideline for selecting  $Q$  and  $R$  is given by Bryson and Ho (1975). Suppose that the performance output (5.3-32) has been defined so that  $H$  is given. Consider the PI

$$J = \frac{1}{2} \int_0^\infty (z^T \bar{Q} z + u^T R u) dt \quad (5.3-34)$$



Then, in Table 5.3-1 we have  $Q = H^T \bar{Q} H$ . To select  $\bar{Q}$  and  $R$ , one might proceed as follows using the *maximum allowable deviations* in  $z(t)$  and  $u(t)$ .

Define the maximum allowable deviation in component  $z_i(t)$  of  $z(t)$  as  $z_{iM}$  and the maximum allowable deviation in component  $u_i(t)$  of the control input  $u(t)$  as  $u_{iM}$ . Then  $\bar{Q}$  and  $R$  may be selected as  $\bar{Q} = \text{diag}\{q_i\}$ ,  $R = \text{diag}\{r_i\}$ , with

$$q_i = \frac{1}{z_{iM}^2}, \quad r_i = \frac{1}{u_{iM}^2} \quad (5.3-35)$$

The rationale for this choice is easy to understand. For instance, as the allowed limits  $z_{iM}$  on  $z_i(t)$  decrease, the weighting in the PI placed on  $z_i(t)$  increases, which requires smaller excursions in  $z_i(t)$  in the closed-loop system.

**Implicit Model Following** The implicit model-following design technique in Section 5.6 shows how to select  $Q$  and  $R$  so that the closed-loop system behaves like a prescribed ideal model. The ideal model may be selected according to flying qualities requirements (see Section 4.3). It should be selected so that its poles and zeros correspond to the desired closed-loop time-response characteristics.

**Asymptotic Properties of the LQR** Consider the PI

$$J = \frac{1}{2} \int_0^\infty (x^T Q x + \rho u^T R u) dt, \quad (5.3-36)$$

where  $\rho$  is a scalar design parameter. There are some quite nice results that describe the asymptotic performance of the LQR as  $\rho$  becomes small and as  $\rho$  becomes large (Kwakernaak and Sivan, 1972; Harvey and Stein, 1978; Grimble and Johnson, 1988).

These results detail the asymptotic closed-loop eigenstructure of the LQR and are of some assistance in selecting  $Q$  and  $R$ . Unfortunately, they are only well developed for the case of full state-variable feedback, where  $C = I$  and all the states are allowed for feedback. Thus, they are appropriate in connection with the discussion in Section 5.7.

**Example 5.3-1: LQR Design for F-16 Lateral Regulator** In Chapter 4 we designed a roll damper/yaw damper for a low-speed flight condition of the F-16. Successive loop closures were used to perform the design using the root-locus approach. In this example we should like to demonstrate the power of the LQ design equations in Table 5.3-1 by designing a lateral regulator.

In our approach we will select the design parameters  $Q$  and  $R$  in the table and then use the design equations there to close all the feedback loops simultaneously by computing  $K$ . The objective is to design a closed-loop controller to provide for the function of a lateral SAS as well as the closure of the roll-attitude loop. This objective involves the design of two feedback channels with multiple loops, but it is straightforward to deal with using modern control techniques. The simplicity of MIMO design using the LQR will be evident.

(a) **Aircraft State Equations.** We used the F-16 linearized lateral dynamics at the nominal flight condition in Table 3.6-3 ( $V_T = 502$  ft/s, 300 psf dynamic pressure, cg at  $0.35 \bar{c}$ ), retaining the lateral states sideslip,  $\beta$ , bank angle,  $\phi$ , roll rate,  $p$ , and yaw rate,  $r$ . Additional states  $\delta_a$  and  $\delta_r$  are introduced by the aileron and rudder actuators

$$\delta_a = \frac{20.2}{s + 20.2} u_a, \quad \delta_r = \frac{20.2}{s + 20.2} u_r \quad (1)$$

A washout filter

$$r_w = \frac{s}{s + 1} r \quad (2)$$

is used, with  $r$  the yaw rate and  $r_w$  the washed-out yaw rate. The washout filter state is denoted  $x_w$ . Thus, the entire state vector is

$$x = [\beta \quad \phi \quad p \quad r \quad \delta_a \quad \delta_r \quad x_w]^T \quad (3)$$

The full-state-variable model of the aircraft plus actuators, washout filter, and control dynamics is of the form

$$\dot{x} = Ax + Bu, \quad (4)$$

with

$$A = \begin{bmatrix} -0.3220 & 0.0640 & 0.0364 & -0.9917 & 0.0003 & 0.0008 & 0 \\ 0 & 0 & 1 & 0.0037 & 0 & 0 & 0 \\ -30.6492 & 0 & -3.6784 & 0.6646 & -0.7333 & 0.1315 & 0 \\ 8.5396 & 0 & -0.0254 & -0.4764 & -0.0319 & -0.0620 & 0 \\ 0 & 0 & 0 & 0 & -20.2 & 0 & 0 \\ 0 & 0 & 0 & 0 & 0 & -20.2 & 0 \\ 0 & 0 & 0 & 57.2958 & 0 & 0 & -1 \end{bmatrix}$$

$$B = \begin{bmatrix} 0 & 0 \\ 0 & 0 \\ 0 & 0 \\ 0 & 0 \\ 20.2 & 0 \\ 0 & 20.2 \\ 0 & 0 \end{bmatrix} \quad (5)$$

The control inputs are the rudder and aileron servo inputs so that

$$u = \begin{bmatrix} u_a \\ u_r \end{bmatrix} \quad (6)$$

and the output is

$$y = \begin{bmatrix} r_w \\ p \\ \beta \\ \phi \end{bmatrix} \quad (7)$$

Thus,  $y = Cx$  with

$$C = \begin{bmatrix} 0 & 0 & 0 & 57.2958 & 0 & 0 & -1 \\ 0 & 0 & 57.2958 & 0 & 0 & 0 & 0 \\ 57.2958 & 0 & 0 & 0 & 0 & 0 & 0 \\ 0 & 57.2958 & 0 & 0 & 0 & 0 & 0 \end{bmatrix} \quad (8)$$

The factor of 57.2958 converts radians to degrees. The feedback control will be output feedback of the form  $u = Ky$ , so that  $K$  is a  $2 \times 4$  matrix. That is, we will select eight feedback gains.

For this system the open-loop dutch roll mode has poles at  $-0.4425 \pm j3.063$  and so has insufficient damping. The spiral mode has a pole at  $-0.01631$ .

**(b) LQR Output Feedback Design.** For the computation of the feedback gain  $K$ , it is necessary to select PI weighting matrices  $Q$  and  $R$  in Table 5.3-1. Then the software described in Appendix B is used to compute the optimal gain  $K$  using the design equations in the table. Our philosophy for selecting  $Q$  and  $R$  follows.

First, let us discuss the choice of  $Q$ . It is desired to obtain good stability of the dutch roll mode, so that  $\beta^2$  and  $r^2$  should be weighted in the PI by factors of  $q_{dr}$ . To obtain stability of the roll mode, which in closed-loop will consist primarily of  $p$  and  $\phi$ , we may weight  $p^2$  and  $\phi^2$  in the PI by factors of  $q_r$ . We do not care about  $\delta_a$  and  $\delta_r$ , so it is not necessary to weight them in the PI; the control weighting matrix  $R$  will prevent unreasonably large control inputs. Thus, so far we have

$$Q = \text{diag}\{q_{dr}, \quad q_r, \quad q_r, \quad q_{dr}, \quad 0, \quad 0, \quad 0\} \quad (9)$$

We do not care directly about  $x_w$ ; however, it is necessary to weight it in the PI. This is because omitting it would cause problems with the observability condition. A square root of  $Q$  in (9) is

$$\sqrt{Q} = \begin{bmatrix} \sqrt{q_{dr}} & \sqrt{q_r} & \sqrt{q_r} & \sqrt{q_{dr}} & 0 & 0 & 0 \end{bmatrix} \quad (10)$$

Consequently, the observability matrix (5.3-31) has a right-hand column of zero; hence the system is unobservable. This may be noted in simpler fashion by examining the  $A$ -matrix in (5), where the seventh state  $x_w$  is seen to have no influence on the states that are weighted in (9). To correct this potential problem, we chose

$$Q = \text{diag}\{q_{dr}, q_r, q_r, q_{dr}, 0, 0, 1\} \quad (11)$$

As far as the  $R$ -matrix goes, it is generally satisfactory to select it as

$$R = \rho I, \quad (12)$$

with  $I$  the identity matrix and  $\rho$  a scalar design parameter.

Now the design equations in Table 5.3-1 were solved using the software described in Appendix B for several choices of  $\rho$ ,  $q_{dr}$ ,  $q_r$ . After a few trials, we obtained a good result using  $\rho = 0.1$ ,  $q_{qr} = 50$ ,  $q_r = 100$ . For this selection the optimal feedback gain was

$$K = \begin{bmatrix} -0.56 & -0.44 & 0.11 & -0.35 \\ -1.19 & -0.21 & -0.44 & 0.26 \end{bmatrix} \quad (13)$$

The resulting closed-loop poles were at

$$\begin{aligned} s &= -3.13 \pm j0.83 && \text{dutch roll mode}(r, \beta) \\ &-0.82 \pm j0.11 && \text{roll mode}(p, \varphi) \\ &-11.47 \pm j17.18, -15.02 \end{aligned} \quad (14)$$

To verify the design, a simulation was performed. The initial state was selected as  $x(0) = [1 \ 0 \ 0 \ 0 \ 0 \ 0 \ 0]^T$ ; that is, we chose  $\beta(0) = 1$ . Figure 5.3-1 shows the results. Part *a* shows the dutch roll mode and part *b* the roll mode. Note that the responses correspond to the poles in (14), where the dutch roll is the faster mode. Compare to the results of Example 4.4-3.

This design has two deficiencies. First, it uses eight feedback gains in (13). This is undesirable for two reasons: (1) it requires the gain scheduling of all eight gains and (2) the control system has no structure. That is, all outputs are fed back to both inputs; zeroing some of the gains would give the controller more structure in terms of feeding back certain outputs to only one or the other of the inputs.

The second deficiency is that it was necessary to juggle the entries of  $Q$  to obtain a good solution. Actually, due to our weighting of  $\beta^2$  and  $r^2$  by  $q_{dr}$  and  $\varphi^2$  and  $p^2$  by  $q_r$ , the design was fairly straightforward and took about half an hour in all. It was, however, necessary to weight the washout filter state  $x_w$ , which is not obvious without considering the observability question.

In Section 5.5 we will show how to overcome both of these deficiencies: the former using “constrained output feedback” and the latter using time weighting like  $t^k$  in the PI.

**(c) Effect of Weighting Parameters.** It is interesting to examine more closely the effects of the design parameters, namely, the entries of the PI weighting matrices  $Q$  and  $R$ . Using the same  $Q$  as above, we show the sideslip response in Figure 5.3-2a for control weightings of  $\rho = 0.1, 0.5$ , and 1. Increased control weighting in the PI generally suppresses the control signals in the closed-loop system; that is, less control effort is allowed. As less control effort is allowed, the control is less effective in controlling the modes. Indeed, according to the figure, as  $\rho$  increases, the undershoot in  $\beta$  increases. Moreover, with increasing  $\rho$  the control is also less effective in suppressing the undesirable oscillations in the dutch roll mode which were noted in the open-loop system.

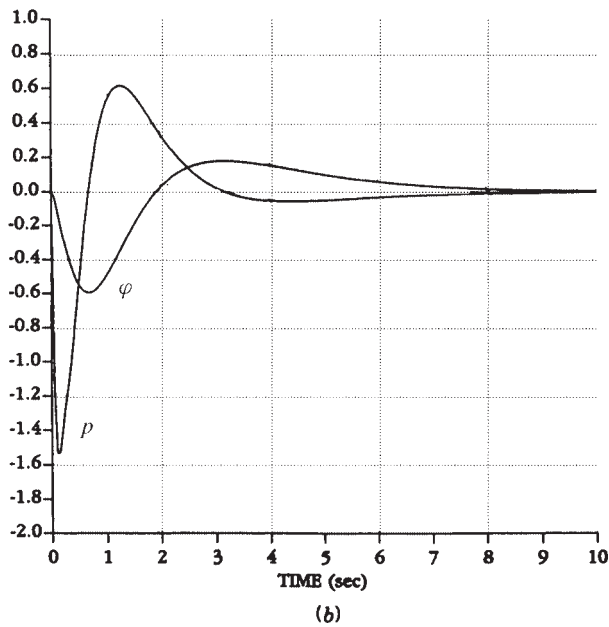
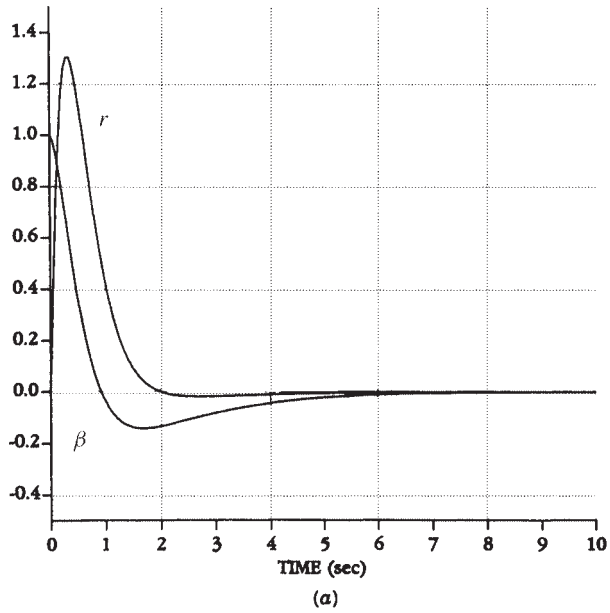


**Figure 5.3-1** Closed-loop lateral response: (a) dutch roll states  $\beta$  and  $r$ ; (b) roll-mode states  $\phi$  and  $p$ .

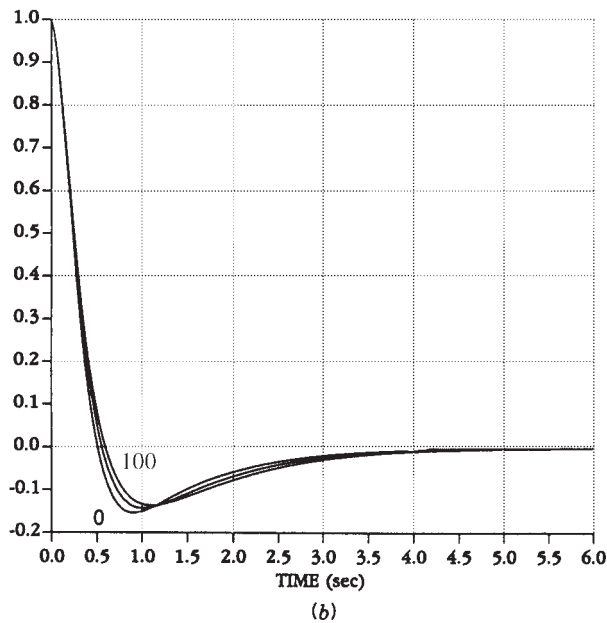
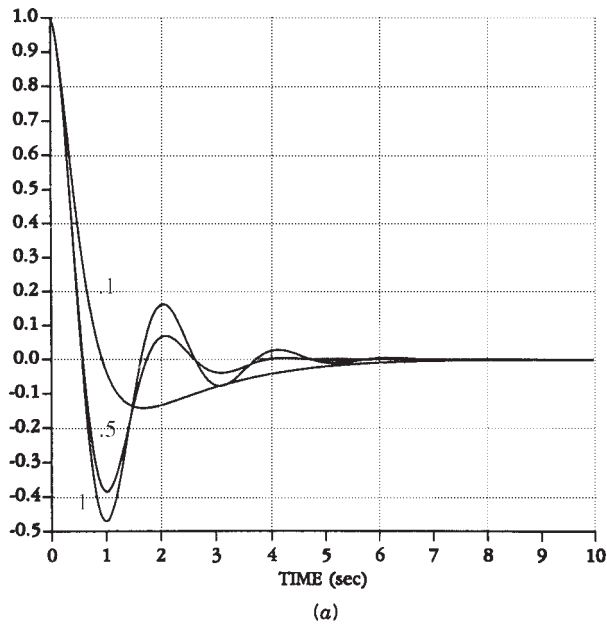


**Figure 5.3-2** Effect of PI weighting parameters: (a) sideslip as a function of  $\rho$  ( $\rho = 0.1, 0.5, 1$ ); (b) sideslip as a function of  $q_{dr}$  ( $q_{dr} = 0.50, 100$ ).

As far as the effect of the dutch roll weighting  $q_{dr}$  goes, examine Figure 5.3-2b, where  $\rho = 0.1$  and  $q_r = 100$  as in part a, but the sideslip response is shown for  $q_{dr} = 0, 50$ , and 100. As  $q_{dr}$  increases, the undershoot decreases, reflecting the fact that increased weighting on  $\beta^2$  in the PI will result in smaller excursions in  $\beta$  in closed loop.

One last point is worth noting. The open-loop system is stable; therefore, it is clear that it is detectable, since all the unstable modes are observable for any choice of  $Q$  (there are no unstable modes). Thus, the design would work if we omitted the weighting on  $x_w^2$  in the  $Q$ -matrix (although, it turns out, the closed-loop poles are not as good). In general, however, the detectability condition is difficult to check in large systems that are open-loop unstable; thus, the observability condition is used instead. Failing to weight an undetectable state can lead to some zero elements of  $K$ , meaning that some feedback loops are not closed. Thus, to guarantee that this does not occur,  $Q$  should be selected so that  $(\sqrt{Q}, A)$  is observable.

To avoid all this discussion on observability, we may simply use a modified non-standard PI with weighting like  $t^k$ . Such a PI is introduced in Section 5.5 and leads to a simplified design procedure.

**(d) Gain Scheduling.** For implementation on an aircraft, the control gains in (13) should be gain scheduled. To accomplish this, the nonlinear aircraft equations are linearized at several equilibrium flight conditions over the desired flight envelope to obtain state-variable models like (4) with different  $A$ - and  $B$ -matrices. Then the LQR design is repeated for those different systems.

A major advantage of LQR design will quickly be apparent, for once the control structure has been selected, it takes only a minute or two to run the software to find the optimal gains for a new  $A$  and  $B$  using the design equations in Table 5.3-1. Note that the optimal gains for one point in the gain schedule can be used as initial stabilizing gains in the LQ solution algorithm for the next point.

It is important, however, to be aware of an additional consideration. The optimal gains at each gain-scheduling point should guarantee *robust stability and performance*; that is, they should guarantee stability and good performance at points *near* the design equilibrium point. Such robust stability can be verified after the LQ design by using multivariable frequency-domain techniques. These techniques are developed in Section 6.2, where the remarks on robustness to plant parameter variations are particularly relevant to gain scheduling. ■

## 5.4 TRACKING A COMMAND

In aircraft control we are often interested not in regulating the state near zero, which we discussed in the preceding section, but in *following a nonzero reference command signal*. For example, we may be interested in designing a control system for optimal step-response shaping. This reference input tracking or *servodesign* problem is important in the design of command augmentation systems (CASs), where the reference command may be, for instance, desired pitch rate or normal acceleration. In this section and the next we cover tracker design.

It should be mentioned that the *optimal* LQ tracker of modern control is not a causal system (Lewis, 1986). It depends on solving an “adjoint” system of differential equations backward in time and so is impossible to implement. A suboptimal “steady-state” tracker using full state-variable feedback is available, but it offers no convenient structure for the control system in terms of desired dynamics such as PI control, washout filters, and so on. Thus, there have been problems with using it in aircraft control.

Modified versions of the LQ tracker have been presented by Davison and Ferguson (1981) and Gangsaas et al. (1986). There, controllers of desired structure can be designed since the approaches are output feedback based. The optimal gains are determined numerically to minimize a PI with, possibly, some constraints.

It is possible to design a tracker by first designing a regulator using, for instance, Table 5.3-1. Then some feedforward terms are added to guarantee perfect tracking (Kwakernaak and Sivan, 1972). The problem with this technique is that the resulting tracker has no convenient structure and often requires derivatives of the reference command input. Moreover, servosystems designed using this approach depend on knowing the dc gain exactly. If the dc gain is not known exactly, the performance deteriorates. That is, the design is *not robust* to uncertainties in the model.

Here we discuss an approach to the design of tracking control systems which is more useful in aircraft control applications (Stevens et al., 1992). This approach will allow us to design a servo control system that has any structure desired. This structure will include a unity-gain outer loop that feeds the performance output back and subtracts it from the reference command, thus defining a tracker error  $e(t)$  which should be kept small (see Figure 5.4-1). It can also include compensator dynamics such as a washout filter or an integral controller. The control gains are chosen to minimize a quadratic PI. We are able to give explicit design equations for the control gains (see Table 5.4-1), which may be solved using the software described in Appendix B.

A problem with the tracker developed in this section is the need to select the design parameters  $Q$  and  $R$  in the PI in Table 5.4-1, given in a later subsection. There are

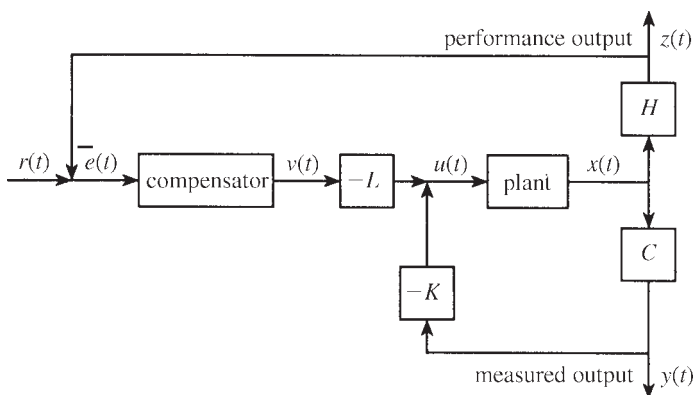


**Figure 5.4-1** Plant with compensator of desired structure.



some intuitive techniques available for choosing these parameters (see Section 5.3); however, in Section 5.5 we will show how modified PIs may be used to make the selection of  $Q$  and  $R$  almost transparent, yielding tracker design techniques that are very convenient for use in aircraft control systems design. We will show, in fact, that *the key to achieving required performance using modern design strategies is in selecting an appropriate PI.*

## Tracker with Desired Structure

In aircraft control design there is a wealth of experience and knowledge that dictates in many situations what sort of compensator dynamics yield good performance from the point of view of both the control engineer and the pilot. For example, a washout circuit may be required, or it may be necessary to augment some feedforward channels with integrators to obtain a steady-state error of exactly zero.

The control system structures used in classical aircraft design also give good *robustness properties*. That is, they perform well even if there are disturbances or uncertainties in the system. Thus, the multivariable approach developed here usually affords this robustness. Formal techniques for verifying closed-loop robustness for multivariable control systems are given in Chapter 6.

Our approach to tracker design allows controller dynamics of any desired structure and then determines the control gains that minimize a quadratic PI over that structure. Before discussing the tracker design, let us recall from Chapter 3 how compensator dynamics may be incorporated into the aircraft state equations.

A dynamic compensator of prescribed structure may be incorporated into the system description as follows.

Consider the situation in Figure 5.4-1, where the plant is described by

$$\dot{x} = Ax + Bu \quad (5.4-1)$$

$$y = Cx, \quad (5.4-2)$$

with state  $x(t)$ , control input  $u(t)$ , and  $y(t)$  the *measured output* available for feedback purposes. In addition,

$$z = Hx \quad (5.4-3)$$

is a *performance output*, which must track the given *reference input*  $z(t)$ . The performance output  $z(t)$  is not generally equal to  $y(t)$ .

It is important to realize that for perfect tracking it is necessary to have as many control inputs in vector  $u(t)$  as there are command signals to track in  $r(t)$  (Kwakernaak and Sivan, 1972).

The dynamic compensator has the form

$$\begin{aligned} \dot{w} &= Fw + Ge \\ v &= Dw + Je, \end{aligned} \quad (5.4-4)$$

with state  $w(t)$ , output  $v(t)$ , and input equal to the *tracking error*

$$e(t) = r(t) - z(t) \quad (5.4-5)$$

$F$ ,  $G$ ,  $D$ , and  $J$  are known matrices chosen to include the desired structure in the compensator.

The allowed form for the plant control input is

$$u = -Ky - Lv, \quad (5.4-6)$$

where the constant gain matrices  $K$  and  $L$  are to be chosen in the control design step to result in satisfactory tracking of  $r(t)$ . This formulation allows for both feedback and feedforward compensator dynamics.

As we have seen in Chapter 3, these dynamics and output equations may be written in augmented form as

$$\frac{d}{dt} \begin{bmatrix} x \\ w \end{bmatrix} = \begin{bmatrix} A & 0 \\ -GH & F \end{bmatrix} \begin{bmatrix} x \\ w \end{bmatrix} + \begin{bmatrix} B \\ 0 \end{bmatrix} u + \begin{bmatrix} 0 \\ G \end{bmatrix} r \quad (5.4-7)$$

$$\begin{bmatrix} y \\ v \end{bmatrix} = \begin{bmatrix} C & 0 \\ -JH & D \end{bmatrix} \begin{bmatrix} x \\ w \end{bmatrix} + \begin{bmatrix} 0 \\ J \end{bmatrix} r \quad (5.4-8)$$

$$z = [H \ 0] \begin{bmatrix} y \\ w \end{bmatrix}, \quad (5.4-9)$$

and the control input may be expressed as

$$u = -[K \ L] \begin{bmatrix} y \\ v \end{bmatrix} \quad (5.4-10)$$

Note that in terms of the augmented plant/compensator state description, the admissible controls are represented as a *constant output feedback*  $[K \ L]$ . In the augmented description, all matrices are known except the gains  $K$  and  $L$ , which need to be selected to yield acceptable closed-loop performance.

A comment on the compensator matrices  $F$ ,  $G$ ,  $D$ , and  $J$  is in order. Often, these matrices are completely specified by the structure of the compensator. Such is the case, for instance, if the compensator contains integrators. However, if it is desired to include a washout or a lead-lag, it may not be clear exactly how to select the time constants. In such cases, engineering judgment will usually give some insight. However, it may sometimes be necessary to go through the design to be proposed and then, if required, return to readjust  $F$ ,  $G$ ,  $D$ , and  $J$  and reperform the design.

## LQ Formulation of the Tracker Problem

By redefining the state, the output, and the matrix variables to streamline the notation, we see that the augmented equations (5.4-7) to (5.4-9) that contain the dynamics of both the aircraft and the compensator are of the form

$$\dot{x} = Ax + Bu + Gr \quad (5.4-11)$$

$$y = Cx + Fr \quad (5.4-12)$$

$$z = Hx \quad (5.4-13)$$

In this description, let us take the state  $x(t) \in \mathbf{R}^n$ , control input  $u(t) \in \mathbf{R}^m$ , reference input  $r(t) \in \mathbf{R}^q$ , performance output  $z(t) \in \mathbf{R}^q$ , and measured output  $y(t) \in \mathbf{R}^p$ . The admissible controls (5.4-10) are proportional output feedbacks of the form

$$u = -Ky = -KCx - KFr \quad (5.4-14)$$

with constant gain  $K$  to be determined. This situation corresponds to the block diagram in Figure 5.4-2. Since  $K$  is an  $m \times p$  matrix, we intend to close all the feedback loops simultaneously by computing  $K$ .

Using these equations the closed-loop system is found to be

$$\begin{aligned} \dot{x} &= (A - BKC)x + (G - BKF)r \\ &\equiv A_c x + B_c r \end{aligned} \quad (5.4-15)$$

In the remainder of this subsection, we will use the formulation (5.4-11) to (5.4-14), assuming that the compensator, if required, has already been included in the system dynamics and demonstrating how to select the constant output feedback gain matrix  $K$  using LQ techniques.

Our formulation differs sharply from the traditional formulations of the optimal tracker problem (Kwakernaak and Sivan, 1972; Lewis, 1986). Note that (5.4-14) includes both feedback and feedforward terms, so that both the closed-loop poles and compensator zeros may be affected by varying the gain  $K$  (see Example 5.4-1). Thus, we should expect better success in shaping the step response than by placing only the poles.

Since the performance specifications of aircraft are often given in terms of time-domain criteria (*Mil. Spec. 1797*, 1987) (see Section 4.3) and these criteria are

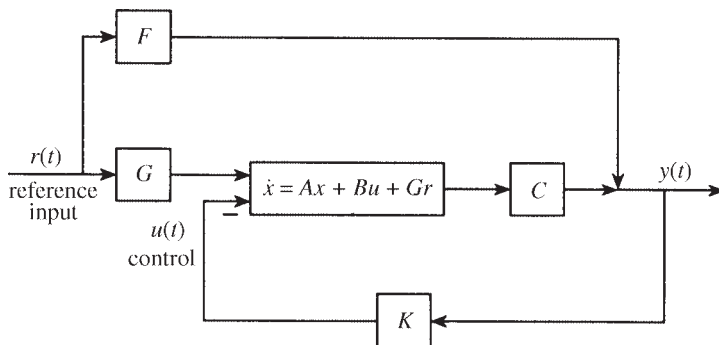


**Figure 5.4-2** Plant/feedback structure.

closely related to the step response, we will assume henceforth that the reference input  $r(t)$  is a step command with magnitude  $r_0$ . Designing for such a command will yield suitable time-response characteristics. Although our design is based on step-response shaping, it should be clearly realized that the resulting control system, if properly designed, will give good time responses for *any arbitrary reference command signal*  $r(t)$ .

Let us now formulate an optimal control problem for selecting the control gain  $K$  to guarantee tracking of  $r(t)$ . Then we will derive the design equations in Table 5.4-1, which are used to determine the optimal  $K$ . These equations are solved using software like that described in Appendix B.

**The Deviation System** Denote steady-state values by overbars and deviations from the steady-state values by tildes. Then the state, output, and control deviations are given by

$$\tilde{x}(t) = x(t) - \bar{x} \quad (5.4-16)$$

$$\tilde{y}(t) = y(t) - \bar{y} = C\tilde{x} \quad (5.4-17)$$

$$\tilde{z}(t) = z(t) - \bar{z} = H\tilde{x} \quad (5.4-18)$$

$$\tilde{u}(t) = u(t) - \bar{u} = -KCx - KFr_0 - (-KC\tilde{x} - KFr_0) = -KC\tilde{x}(t)$$

or

$$\tilde{u} = -K\tilde{y} \quad (5.4-19)$$

The tracking error  $e(t) = r(t) - z(t)$  is given by

$$e(t) = \tilde{e}(t) + \bar{e} \quad (5.4-20)$$

with the error deviation given by

$$\tilde{e}(t) = e(t) - \bar{e} = (r_0 - Hx) - (r_0 - H\tilde{x}) = -H\tilde{x}$$

or

$$\tilde{e} = -\tilde{z} \quad (5.4-21)$$

Since in any acceptable design the closed-loop plant will be asymptotically stable,  $A_c$  is nonsingular. According to (5.4-15), at steady state

$$0 = A_c\bar{x} + B_xr_0, \quad (5.4-22)$$

so that the steady-state response  $\bar{x}$  is

$$x = -A_c^{-1}B_xr_0 \quad (5.4-23)$$

and the steady-state error is

$$\bar{e} = r_0 - H\bar{x} = (1 + HA_c^{-1}B_c)r_0 \quad (5.4-24)$$

To understand this expression, note that the closed-loop transfer function from  $r_0$  to  $z$  [see (5.4-15) and (5.4-13)] is

$$H(s) = H(sI - A_c)^{-1}B_c \quad (5.4-25)$$

The steady-state behavior may be investigated by considering the dc value of  $H(s)$  (i.e.,  $s = 0$ ); this is just  $-HA_c^{-1}B_c$ , the term appearing in (5.4-24).

Using (5.4-16), (5.4-19), and (5.4-23) in (5.4-15) the closed-loop dynamics of the state deviation are seen to be

$$\dot{\tilde{x}} = A_c \tilde{x} \quad (5.4-26)$$

$$\tilde{y} = C \tilde{x} \quad (5.4-27)$$

$$\tilde{z} = H \tilde{x} = -\tilde{e} \quad (5.4-28)$$

and the control input to the deviation system (5.4-26) is (5.4-19). Thus, the step-response shaping problem has been converted to a *regulator problem* for the deviation system

$$\dot{\tilde{x}} = A \tilde{x} + B \tilde{u} \quad (5.4-29)$$

Again, we emphasize the difference between our approach and traditional ones (e.g., Kwakernaak and Sivan, 1972). Once the gain  $K$  in (5.4-19) has been found, the control for the plant is given by (5.4-14), which inherently has both feedback and feedforward terms. Thus, no extra feedforward term need be added to make  $\bar{e}$  zero.

**Performance Index** To make the tracking error  $e(t)$  in (5.4-20) small, we propose to attack two equivalent problems: the problem of regulating the error deviation  $\tilde{e}(t) = -\tilde{z}(t)$  to zero and the problem of making the steady-state error  $\bar{e}$  small.

Note that we do not assume a type-1 system, which would force  $\bar{e}$  to be equal to zero. This can be important in aircraft control, where it may not be desirable to force the system to be of type 1 by augmenting all control channels with integrators. This augmentation complicates the servo structure. Moreover, it is well known from classical control theory that suitable step responses may often be obtained without resorting to inserting integrators in all the feedforward channels.

To make both the error deviation  $\tilde{e}(t) = -H\tilde{x}(t)$  and the steady-state error  $\bar{e}$  small, we propose selecting  $K$  to minimize the PI

$$J = \frac{1}{2} \int_0^\infty (\tilde{e}^T \tilde{e} + \tilde{u}^T R \tilde{u}) dt + \frac{1}{2} \bar{e}^T V \bar{e}, \quad (5.4-30)$$

with  $R > 0$ ,  $V \geq 0$ , design parameters. The integrand is the standard quadratic PI with, however, a weighting  $V$  included on the steady-state error. Note that the PI weights the control *deviations* and not the controls themselves. If the system is of type 1, containing integrators in all the feedforward paths, then  $V$  may be set to zero since the steady-state error is automatically zero.

Making the error deviation  $\tilde{e}(t)$  small improves the transient response, while making the steady-state error  $\bar{e}(t)$  small improves the steady-state response. If the system is of type 0, these effects involve a trade-off, so that then there is a design trade-off involved in selecting the size of  $V$ .

We can generally select  $R = rI$  and  $V = vI$ , with  $r$  and  $v$  scalars. This simplifies the design since now only a few parameters must be tuned during the interactive design process.

According to (5.4-21),  $\tilde{e}^T \tilde{e} = \tilde{x}^T H^T H \tilde{x}$ . Referring to Table 5.3-1, therefore, it follows that the matrix  $Q$  there is equal to  $H^T H$ , where  $H$  is known. That is, weighting the error deviation in the PI has already shown us how to select the design parameter  $Q$ , affording a considerable simplification.

The problem we now have to solve is how to select the control gains  $K$  to minimize the PI  $J$  for the deviation system (5.4-29). Then the tracker control for the original system is given by (5.4-14).

We should point out that the proposed approach is suboptimal in the sense that minimizing the PI does not necessarily minimize a quadratic function of the total error  $e(t) = \bar{e} + \tilde{e}(t)$ . It does, however, guarantee that both  $\tilde{e}(t)$  and  $\bar{e}$  are small in the closed-loop system, which is a design goal.

### Solution of the LQ Tracker Problem

It is now necessary to solve for the optimal feedback gain  $K$  that minimizes the PI. The design equations needed are now derived. They appear in Table 5.4-1.

By using (5.4-26) and a technique like the one used in Section 5.3 (see the problems at the end of the chapter), the optimal cost is found to satisfy

$$J = \frac{1}{2} \tilde{x}^T(0) P \tilde{x}(0) + \frac{1}{2} \bar{e}^T V \bar{e}, \quad (5.4-31)$$

with  $P \geq 0$  the solution to

$$0 = g \equiv A_c^T P + P A_c + Q + C^T K^T R K C, \quad (5.4-32)$$

with  $Q = H^T H$  and  $\bar{e}$  given by (5.4-24).

In our discussion of the linear quadratic regulator we assumed that the initial conditions were uniformly distributed on a surface with known characteristics. While this is satisfactory for the regulator problem, it is an unsatisfactory assumption for the tracker problem. In the latter situation the system starts at rest and must achieve a given final state that is dependent on the reference input, namely (5.4-23). To find the correct value of  $\tilde{x}(0)$ , we note that since the plant starts at rest [i.e.,  $x(0) = 0$ ], according to (5.4-16),

$$\tilde{x}(0) = -\tilde{x}, \quad (5.4-33)$$

so that the optimal cost (5.4-31) becomes

$$J = \frac{1}{2}\bar{x}^T P \bar{x} + \frac{1}{2}\bar{e}^T V \bar{e} = \frac{1}{2}\text{tr}(PX) + \frac{1}{2}\bar{e}^T V \bar{e}, \quad (5.4-34)$$

with  $P$  given by (5.4-32),  $\bar{e}$  given by (5.4-24), and

$$X \equiv \bar{x}\bar{x}^T = A_c^{-1} B_c r_0 r_0^T B_c^T A_c^{-T}, \quad (5.4-35)$$

with  $A_c^{-T} = (A_c^{-1})^T$ .

The optimal solution to the unit-step tracking problem, with (5.4-11) initially at rest, may now be determined by minimizing  $J$  in (5.4-34) over the gains  $K$ , subject to the constraint (5.4-32) and Equations (5.4-24) and (5.4-35).

This algebraic optimization problem can be solved by any well-known numerical method (see Press et al., 1986; Söderström, 1978). A good approach for a fairly small number ( $mp \leq 10$ ) of gain elements in  $K$  is the Simplex minimization routine (Nelder and Mead, 1964). To evaluate the PI for each fixed value of  $K$  in the iterative solution procedure, one may solve (5.4-32) for  $P$  using subroutine ATXPXA (Bartels and Stewart, 1972) and then employ (5.4-34). Software for determining the optimal control gains  $K$  is described in Appendix B.

**Design Equations for Gradient-Based Solution** As an alternative solution procedure, one may use gradient-based techniques [e.g., the Davidon-Fletcher-Powell algorithm (Press et al., 1986)], which are generally faster than non-gradient-based approaches.

To find the gradient of the PI with respect to the gains, define the Hamiltonian

$$\mathcal{H} = \frac{1}{2}\text{tr}(PX) + \frac{1}{2}\text{tr}(gS) + \frac{1}{2}\bar{e}^T V \bar{e}, \quad (5.4-36)$$

with  $S$  a Lagrange multiplier. Now, using the basic matrix calculus identities,

$$\frac{\partial Y^{-1}}{\partial x} = -Y^{-1} \frac{\partial Y}{\partial x} Y^{-1} \quad (5.4-37)$$

$$\frac{\partial UV}{\partial x} = \frac{\partial U}{\partial x} V + U \frac{\partial V}{\partial x} \quad (5.4-38)$$

$$\frac{\partial y}{\partial x} = \text{tr} \left[ \frac{\partial y}{\partial z} \cdot \frac{\partial z^T}{\partial x} \right], \quad (5.4-39)$$

we may proceed as in the preceding section, with, however, a little more patience due to the extra terms (see the problems!), to obtain the necessary conditions for a solution given in Table 5.4-1.

To find  $K$  by a gradient minimization algorithm, it is necessary to provide the algorithm with the values of  $J$  and  $\partial J / \partial K$  for a given  $K$ . The value of  $J$  is given by the expression in Table 5.4-1 for the optimal cost. To find  $\partial J / \partial K$  given  $K$ , solve (5.4-40) and (5.4-41) for  $P$  and  $S$ . Then since these equations hold,  $\partial J / \partial K = \partial \mathcal{H} / \partial K$ , which may be found using (5.4-42). These equations should be compared to those in Table 5.3-1. Note that the dependence of  $X$  on the gain  $K$  [see (5.4-45)] and the presence of  $\bar{e}$  in the PI have resulted in extra terms being added in (5.4-42).

**TABLE 5.4-1 LQ Tracker with Output Feedback***System Model*

$$\dot{x} = Ax + Bu + Gr$$

$$y = Cx + Fr$$

$$z = Hx$$

*Control*

$$u = -Ky$$

*Performance Index*

$$J = \frac{1}{2} \int_0^\infty (\tilde{x}^T Q \tilde{x} + \tilde{u}^T R \tilde{u}) dt + \frac{1}{2} \tilde{e}^T V \tilde{e}, \text{ with } Q = H^T H$$

*Optimal Output Feedback Gain*

$$0 = \frac{\partial \mathcal{H}}{\partial S} = A_c^T P + P A_c + Q + C^T K^T R K C \quad (5.4-40)$$

$$0 = \frac{\partial \mathcal{H}}{\partial P} = A_c S + S A_c^T + X \quad (5.4-41)$$

$$0 = \frac{\partial \mathcal{H}}{\partial K} = R K C S C^T - B^T P S C^T + B^T A_c^{-T} (P + H^T V H) \bar{x} \bar{y}^T - B^T A_c^{-T} H^T V r_0 \bar{y}^T. \quad (5.4-42)$$

with  $r$  a unit step of magnitude  $r_0$  and

$$\bar{x} = -A_c^{-1} B_c r_0 \quad (5.4-43)$$

$$\bar{y} = C \bar{x} + F r_0 \quad (5.4-44)$$

$$X = \bar{x} \bar{x}^T = A_c^{-1} B_c r_0 r_0^T B_c^T A_c^{-T} \quad (5.4-45)$$

where

$$A_c = A - B K C, \quad B_c = G - B K F$$

*Optimal Cost*

$$J = \frac{1}{2} \text{tr}(P X) + \frac{1}{2} \tilde{e}^T V \tilde{e}$$

**Determining the Optimal Feedback Gain**

The issues in finding the optimal output feedback gain  $K$  in the tracker problem of Table 5.4-1 are the same as those discussed in connection with the regulator problem of Table 5.3-1. They are choice of  $Q$  to satisfy detectability, choice of solution technique, finding an initial stabilizing gain, and iterative design by tuning  $Q$  and  $R$ .



We emphasize that there are only a few design parameters in our approach, namely,  $r$  and  $v$  (since we can generally select  $R = rI$ ,  $V = vI$ ). Thus, it is not difficult or time consuming to come up with good designs. Much of the simplicity of our approach derives from the fact that  $-Q$  in the PI is equal to  $H^T H$ , which is known.

Let us now illustrate the servo design procedure by an example.

**Example 5.4-1: Normal Acceleration CAS** In Chapter 4 we designed a normal acceleration CAS using classical control theory. In that example, successive loop closures were used with root-locus design to obtain the feedback gains. Here we will show that using the LQ design equations in Table 5.4-1 we can close all the loops simultaneously. Thus, the design procedure is more straightforward. We will also demonstrate that using LQ design *the algorithm automatically selects the zero of the compensator for optimal performance.*

**(a) Control System Structure.** The normal acceleration control system is shown in Figure 5.4-3, where  $r$  is a reference step input in  $g$ s and  $u(t)$  is the elevator actuator voltage. An integrator has been added in the feedforward path to achieve zero steady-state error. The performance output that should track the reference command  $r$  is  $z = n_z$ , so that the tracking error is  $e = r - n_z$ . The state and measured outputs are

$$x = \begin{bmatrix} \alpha \\ q \\ \delta_e \\ \alpha_F \\ \epsilon \end{bmatrix}, \quad y = \begin{bmatrix} \alpha_F \\ q \\ e \\ \epsilon \end{bmatrix}, \quad (1)$$

with  $\epsilon(t)$  the integrator output and  $\alpha_F$  the filtered measurements of angle of attack.

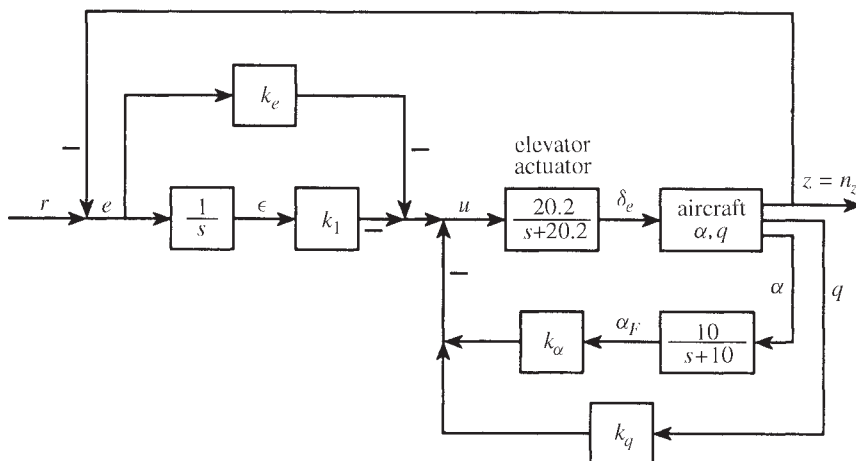


Figure 5.4-3 G-command system.

Exactly as in Chapter 4, we linearized the F-16 dynamics about the nominal flight condition in Table 3.6-3 (502 ft/s, level flight, dynamic pressure of 300 psf,  $x_{cg} = 0.35\bar{c}$ ) and augmented the dynamics to include the elevator actuator, angle-of-attack filter, and compensator dynamics. The result is

$$\dot{x} = Ax + Bu + Gr \quad (2)$$

$$y = Cx + Fr \quad (3)$$

$$z = Hx, \quad (4)$$

with

$$A = \begin{bmatrix} -1.01887 & 0.90506 & -0.00215 & 0 & 0 \\ 0.8225 & -1.07741 & -0.17555 & 0 & 0 \\ 0 & 0 & -20.2 & 0 & 0 \\ 10 & 0 & 0 & -10 & 0 \\ -16.26 & -0.9788 & 0.04852 & 0 & 0 \end{bmatrix}$$

$$B = \begin{bmatrix} 0 \\ 0 \\ 20.2 \\ 0 \\ 0 \end{bmatrix} \quad G = \begin{bmatrix} 0 \\ 0 \\ 0 \\ 0 \\ 1 \end{bmatrix} \quad (5a)$$

$$C = \begin{bmatrix} 0 & 0 & 0 & 57.2988 & 0 \\ 0 & 57.2958 & 0 & 0 & 0 \\ -16.26 & -0.9788 & 0.04852 & 0 & 0 \\ 0 & 0 & 0 & 0 & 1 \end{bmatrix} \quad F = \begin{bmatrix} 0 \\ 0 \\ 1 \\ 0 \end{bmatrix} \quad (5b)$$

$$H = [16.26 \quad 0.9788 \quad 0.04852 \quad 0 \quad 0] \quad (5c)$$

The factor of 57.2958 is added to convert angles from radians to degrees.

The control input is

$$u = -Ky = -[k_\alpha \quad k_q \quad k_e \quad k_I]y = -k_\alpha \alpha_F - k_q q - k_e e - k_I e \quad (6)$$

It is desired to select the four control gains to guarantee a good response to a step command  $r$ . Note that  $k_\alpha$  and  $k_q$  are feedback gains, while  $k_e$  and  $k_I$  are feedforward gains.

Note that the proportional-plus-integral compensator is given by

$$k_e + \frac{k_I}{s} = k_e \frac{s + k_I/k_e}{s}, \quad (7)$$

which has a zero at  $s = -k_I/k_e$ . Since the LQ design algorithm will select all four control gains, it will *automatically select the optimal location for the compensator zero*.

(b) *Performance Index and Determination of the Control Gains.* Due to the integrator, the system is of type 1. Therefore, the steady-state error  $\tilde{e}$  is automatically equal to zero. A natural PI thus seems to be

$$J = \frac{1}{2} \int_0^\infty (\tilde{e}^2 + \rho \tilde{u}^2) dt \quad (8)$$

with  $\rho$  a scalar weighting parameter. Since  $\tilde{e} = H\tilde{x}$ , this corresponds to the PI in Table 5.4-1 with

$$Q = H^T H = \begin{bmatrix} 264 & 16 & 1 & 0 & 0 \\ 16 & 1 & 0 & 0 & 0 \\ 1 & 0 & 0 & 0 & 0 \\ 0 & 0 & 0 & 0 & 0 \\ 0 & 0 & 0 & 0 & 0 \end{bmatrix} \quad (9)$$

This is, unfortunately, not a suitable  $Q$ -matrix since  $(H, A)$  is not observable in open loop. Indeed, according to Figure 5.4-3, observing the first two states  $\alpha$  and  $q$  can never give information about  $\epsilon$  in the open-loop configuration (where the control gains are zero). Thus, the integrator state is unobservable in the PI. Since the integrator pole is at  $s = 0$ ,  $(H, A)$  is undetectable (unstable unobservable pole), so that any design based on (9) would, in fact, yield a value for the integral gain of  $k_I = 0$ .

We will show in Section 5.5 a very convenient way to correct problems like this. There we will introduce a time weighting of  $t^k$  into the PI. In the meantime, to correct the observability problem here, let us select

$$Q = \begin{bmatrix} 264 & 16 & 1 & 0 & 0 \\ 16 & 1 & 0 & 0 & 0 \\ 1 & 0 & 0 & 0 & 0 \\ 0 & 0 & 0 & 0 & 0 \\ 0 & 0 & 0 & 0 & 1 \end{bmatrix}, \quad (10)$$

where we include a weighting on  $\epsilon(t)$  to make it observable in the PI.

Now, we selected  $\rho = 1$  and solved the design equations in Table 5.4-1 for the optimal control gain  $K$  using the software described in Appendix B. For this  $Q$  and  $\rho$  the feedback matrix was

$$K = [0.006 \quad -0.152 \quad 1.17 \quad 0.996] \quad (11)$$

and the closed-loop poles were

$$s = -1.15 \pm j0.69 \quad (12)$$

$$-1.60, -9.98, -19.54$$

These yield a system that is not fast enough; the complex pair is also unsuitable in terms of flying qualities requirements.

After repeating the design using several different  $Q$  and  $\rho$ , we decided on

$$Q = \begin{bmatrix} 264 & 16 & 1 & 0 & 0 \\ 16 & 60 & 0 & 0 & 0 \\ 1 & 0 & 0 & 0 & 0 \\ 0 & 0 & 0 & 0 & 0 \\ 0 & 0 & 0 & 0 & 100 \end{bmatrix}, \quad (13)$$

$\rho = 0.01$ . The decreased control weighting  $\rho$  has the effect of allowing larger control effort and so speeding up the response. The increased weighting on the integrator output  $\epsilon(t)$  has the effect of forcing  $n_z$  to its final value of  $r$  more quickly, hence also speeding up the response. The increased weighting on the second state component  $q$  has the effect of regulating excursions in  $\tilde{q}(t)$  closer to zero and hence of providing increased damping.

With this  $Q$  and  $\rho$  the control matrix was

$$K = [-1.629 \quad -1.316 \quad 18.56 \quad 77.6] \quad (14)$$

and the closed-loop poles were at

$$\begin{aligned} s &= -2.98 \pm j3.17, \\ &\quad -19.31 \pm j4.64 \\ &\quad -5.91 \end{aligned} \quad (15)$$

The closed-loop step response is shown in Figure 5.4-4; it is fairly fast with an overshoot of 6%. Note the hump in the initial response due to the non-minimum-phase zero. Further tuning of the elements of  $Q$  and  $R$  could provide less overshoot, a faster response, and a smaller gain for the angle-of-attack feedback. (It is worth noting that we will obtain a far better response with more reasonable gains in Example 5.5-2, where we use a PI with time-dependent weighting like  $t^k$ .)

According to (7), the compensator zero has been placed by the LQ algorithm at

$$s = -\frac{k_1}{k_e} = -4.18 \quad (16)$$

Using the software described in Appendix B, the entire design, including determining  $K$  for different choices of  $Q$  and  $\rho$  until a suitable design was reached, took about 30 minutes.

(c) *Discussion.* We can now emphasize an important aspect of modern LQ design. As long as  $Q \geq 0$ ,  $R > 0$ , and  $(\sqrt{Q}, A)$  is observable, the closed-loop system designed using Table 5.4-1 is generally stable. Thus, the LQ theory has allowed us to tie the control system design to some *design parameters* which may be tuned to obtain acceptable behavior—namely, the elements of weighting matrices  $Q$  and  $R$ . Using the software described in Appendix B, for a given  $Q$  and  $R$  the optimal

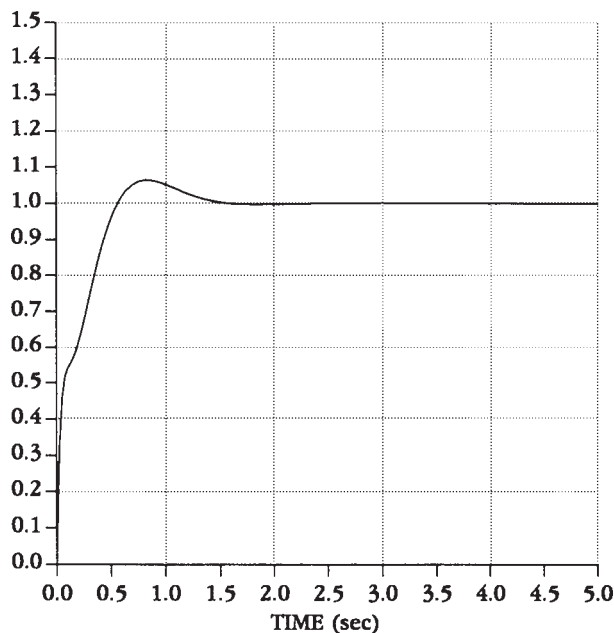


Figure 5.4-4 Normal acceleration step response.

gain  $K$  is easily found. If it is not suitable in terms of time responses and closed-loop poles, the elements of  $Q$  and  $R$  can be changed and the design repeated. The importance of this is that for admissible  $Q$  and  $R$  *closed-loop stability is guaranteed*.

A disadvantage of the design equations in Table 5.4-1 is the need to try different  $Q$  and  $R$  until suitable performance is obtained as well as the need for  $(H, A)$  to be observable. In Section 5.5 we will introduce a different PI with time weighting of  $t^k$  which eliminates these deficiencies.

Another point needs to be made. Using the control (6)/(3) in (2) yields the closed-loop plant

$$\dot{x} = (A - BKC)x + (G - BKF)r \quad (17)$$

whence the closed-loop transfer function from  $r(t)$  to  $z(t)$  is

$$H(s) = H(sI - (A - BKC))^{-1}(G - BKF) \quad (18)$$

Note that the transfer function numerator depends on the optimal gain  $K$ . That is, this scheme uses optimal positioning of *both the poles and zeros* to attain step-response shaping.

**(d) Selection of Initial Stabilizing Gain.** In order to initialize the algorithm that determines the optimal  $K$  by solving the design equations in Table 5.4-1, it is necessary to find an initial gain that stabilizes the system. In this example we simply

selected gains with signs corresponding to the static loop sensitivity of the individual transfer functions, since this corresponds to negative feedback. The static loop sensitivities from  $u$  to  $\alpha$  and from  $u$  to  $q$  are negative, so negative gains were chosen for these loops. The initial gain used was

$$K = [-0.1 \quad -0.1 \quad 1 \quad 1] \quad (19)$$

■

## 5.5 MODIFYING THE PERFORMANCE INDEX

Modern control theory affords us the ability to close all the feedback loops simultaneously by solving matrix equations for the gain matrix  $K$ . With a sensible problem formulation, it also *guarantees the stability of the closed-loop system*. These two fundamental properties make modern design very useful for aircraft control systems. One should recall the difficulty in guaranteeing closed-loop stability in multiloop control systems using one-loop-at-a-time design (Chapter 4).

An additional important advantage is as follows. The standard aircraft control system structures used in classical design have been developed to yield good *robustness properties*. That is, they yield good performance even if there are disturbances in the systems or modeling inaccuracies such as plant parameter variations or high-frequency unmodeled dynamics (e.g., flexible aircraft modes). Since the approach described here allows these standard structures to be incorporated into the control system, it generally yields robust control systems. We will discuss procedures for formally verifying robustness in Chapter 6.

In the LQ regulator design method of Section 5.3 and the LQ tracker design method of Section 5.4, it was necessary to select the PI weighting matrices  $Q$  and  $R$  as design parameters. Moreover, it was necessary to satisfy an observability property in selecting  $Q$ . There are some good approaches that give guidance in selecting  $Q$ , such as Bryson's approach (see Section 5.3). Note also that, in Table 5.4-1,  $Q=H^TH$ , where  $H$  is known. However, due to the observability requirement the design parameters  $Q$  and  $R$  do not necessarily correspond to actual performance objectives.

In this section we show how to modify the PI to considerably simplify the selection of the weighting matrices  $Q$  and  $R$  in Table 5.4-1. The observability of  $(\sqrt{Q}, A)$  will be unnecessary. The PIs shown in this section correspond to actual performance objectives and involve only a few design parameters, even for systems with many states and many control gains to determine. These facts, coupled with the capability already demonstrated of employing a compensator with any desired structure, will result in a powerful and convenient approach to the design of multivariable aircraft control systems.

A wide range of performance objectives may be attained by using modifications of the PI. We will consider several modifications, all of which are useful depending on the performance objectives. The important concept to grasp is that *the key to obtaining suitable closed-loop behavior using LQ design lies in selecting a suitable PI for the problem at hand*. At the end of the section we present several examples in aircraft control design to demonstrate this issue as well as the directness of the approach.

We will again be concerned with the system plus compensator

$$\dot{x} = Ax + Bu + Gr \quad (5.5-1)$$

We are trying to determine controls that are static output feedbacks of the form

$$u = -Ky \quad (5.5-2)$$

with

$$y = Cx + Fr \quad (5.5-3)$$

the measured output and

$$z = Hx \quad (5.5-4)$$

the performance output, which is to track the reference command  $r$ . If we are interested in regulation and not tracking, then  $G$  and  $F$  do not appear in the equations and  $z$  is not defined.

### Constrained Feedback Matrix

In many applications it is desired for certain elements of the feedback gain matrix  $K$  to be zero to avoid coupling between certain output-input pairs. Zeroing certain gains allows us to specify the detailed structure of the control system. For instance, it may be desired that the error in channel 1 of the controller not be coupled to the control input in channel 2. Zeroing some gains also simplifies the gain-scheduling problem by reducing the number of nonzero gains requiring tabulation. This is called *constrained* output feedback design.

**Gain Element Weighting** Certain elements  $k_{ij}$  of  $K$  can be made small simply by weighting them in the performance index, that is, by selecting a PI like

$$J = \frac{1}{2} \int_0^\infty (\tilde{x}^T Q \tilde{x} + \tilde{u}^T R \tilde{u}) dt + \sum_i \sum_j g_{ij} k_{ij}^2 \quad (5.5-5)$$

Gain element weight  $g_{ij}$  is chosen large to make the  $(i, j)$ th element  $k_{ij}$  of the feedback matrix  $K$  small in the final design. Then, in implementing the controller, the small elements of  $K$  may simply be set to zero.

The design problem is now to minimize

$$J = \frac{1}{2} \text{tr}(PX) + \sum_i \sum_j g_{ij} k_{ij}^2, \quad (5.5-6)$$

with  $P$  satisfying the matrix equation in Table 5.3-1 or Table 5.4-1, as appropriate. This may be accomplished by using the equations in Table 5.3-1 (if we are interested

in regulation) or Table 5.4-1 (if we are interested in tracking) to numerically minimize the PI, but with the extra term involving the gain weighting that appears in (5.5-6) (Moerder and Calise, 1985).

**Computing an Initial Stabilizing Gain** The iterative algorithms that solve the design equations in Tables 5.3-1 and 5.4-1 require initial stabilizing gains. Unfortunately, stabilizing output feedback gains can be complicated to find in large multivariable systems. A few ways to find  $K_0$  so that  $(A - BK_0C)$  is stable were mentioned in Section 5.3 and Example 5.4-1d. Gain element weighting can be used to solve the problem of determining an initial stabilizing output feedback gain, as we now see.

There are many techniques for finding a stabilizing *state-variable* feedback given the plant system matrix  $A$  and control matrix  $B$  [see Kailath (1980) as well as Section 5.7]. That is, it is straightforward to find a  $K_0$  so that  $(A - BK_0)$  is stable. Routines that perform this are available in standard software packages such as ORACLS (Armstrong, 1980). Unfortunately, for flight control purposes, state feedback design is unsuitable for reasons such as those we have discussed. However, suppose that an  $m \times n$  stabilizing state feedback gain has been found. Then, to determine an  $m \times p$  output feedback gain, it is only necessary to weight in the PI the elements of the state feedback matrix that do not correspond to measured outputs. The algorithm will then provide a suitable output feedback gain matrix by driving these elements to zero.

**Gain Element Fixing** There is an attractive alternative to gain element weighting for fixing gain matrix elements. If a numerical technique such as Simplex (Press et al., 1986) is used to determine the optimal control by varying  $K$  and directly evaluating  $J$ , we may simply fix certain elements of  $K$  and not allow the Simplex to vary them. This allows the fixed elements to be retained at any desired (possibly nonzero) value and takes far fewer computations than gain element weighting, especially if many elements of  $K$  are fixed.

If, on the other hand, a gradient-based routine such as Davidon-Fletcher-Powell (Press et al., 1986) is used in conjunction with the design equations in Tables 5.3-1 or 5.4-1, it is easy to modify the gradient  $\partial J / \partial K$  to leave certain elements of  $K$  fixed. Indeed, to fix element  $(i, j)$  of  $K$ , one need only set element  $(i, j)$  of  $\partial J / \partial K$  equal to zero.

These approaches require fewer operations than the gain weighting approach based on (5.5-5) and are incorporated in the software described in Appendix B, which is called program LQ. Illustrations of control design using constrained output feedback are provided in the examples.

## Derivative Weighting

As we will soon show in an example, it is often convenient to weight in the PI not the states themselves but their derivatives. This is because rates of change of the states can in some design specifications be more important than the values of the states. For



instance, elevator rate of change has a closer connection with required control energy than does elevator deflection. To accomodate such situations, we may consider the PI

$$J = \frac{1}{2} \int_0^\infty \dot{x}^T Q \dot{x} dt \quad (5.5-7)$$

One way to formulate this optimization problem is to convert this PI to one that weights the states and inputs but has a state/input cross-weighting term [simply substitute (5.4-29) into  $J$ ]. This optimization problem is solved by Lewis (1986).

An alternative (see the problems) is to minimize

$$J = \frac{1}{2} \text{tr} \left[ P \tilde{x}(0) \tilde{x}^T(0) \right], \quad (5.5-8)$$

with  $P$  the solution to

$$A_c^T P + P A_c + Q = 0 \quad (5.5-9)$$

Again, any optimization technique may be used. More details on this formulation may be found in the work of Quintana et al. (1976).

In the step-response shaping problem, the value of the initial state derivative vector to use in (5.5-8) is easy to determine since  $x(0) = 0$  and  $\tilde{x}$  is a constant, so that according to (5.4-16) and (5.4-15)

$$\dot{\tilde{x}}(0) = B_c r_0 \quad (5.5-10)$$

### Time-Dependent Weighting

One final form of the PI remains to be discussed. A step response that is apparently good (i.e., fast, with acceptable overshoot and settling time) may contain a slow pole(s) with small residue, so that the response creeps for a long time as it nears its final value. The quadratic performance criterion penalizes small errors relatively lightly and so does not tend to suppress this kind of behavior.

Thus, in the spirit of the classical (ITAE, ISTSE, etc.) performance indices (D'Azzo and Houpis, 1988) we define a PI that contains a time-weighted component:

$$J = \frac{1}{2} \int_0^\infty (t^k \tilde{x}^T P \tilde{x} + \tilde{x}^T Q \tilde{x}) dt \quad (5.5-11)$$

If we are interested in including a control-weighting term  $\tilde{u}^T R \tilde{u}$  in (5.5-11) and in using the output feedback (5.5-2), we may add the term  $C^T K^T R K C$  (since  $\tilde{u}^T R \tilde{u} = \tilde{x}^T C^T K^T R K C \tilde{x}$ ) to the appropriate state-weighting matrix  $P$  or  $Q$ , depending on whether we wish to multiply the control-weighting term by  $t^k$ . For instance, if the control input term is not to be weighted by  $t^k$ , the PI (5.5-11) takes on the form

$$J = \frac{1}{2} \int_0^\infty [t^k \tilde{x}^T P \tilde{x} + \tilde{x}^T (Q + C^T K^T R K C) \tilde{x}] dt \quad (5.5-12)$$

If it is desired to have the control weighting multiplied by  $t^k$ , the term  $C^T K^T R K C$  should be added to  $P$  instead of  $Q$ .

Whether or not the control effort should be time weighted is a matter for experiment with the particular design. The time-varying weighting in the PI places a heavy penalty on errors that occur late in the response and is thus very effective in suppressing the effect of a slow pole as well as in eliminating lightly damped settling behavior.

Due to the factor  $t^k$ , the optimal gain  $K$  that minimizes  $J$  is time varying. However, to obtain useful designs we will determine the suboptimal solution that assumes a time-invariant control gain  $K$ . Note that time-varying gains would be very difficult to gain schedule.

We may successively integrate by parts (see the problems) to show that the value of (5.5-12) for a given value of  $K$  is given by successively solving the nested Lyapunov equations

$$\begin{aligned} 0 &= g_0 \equiv A_c^T P_0 + P_0 A_c + P \\ 0 &= g_1 \equiv A_c^T P_1 + P_1 A_c + P_0 \\ &\vdots \\ 0 &= g_{k-1} \equiv A_c^T P_{k-1} + P_{k-1} A_c + P_{k-2} \\ 0 &= g_k \equiv A_c^T P_k A_c + k! P_{k-1} + Q + C^T K^T R K C \end{aligned} \quad (5.5-13)$$

Then

$$J = \frac{1}{2} \tilde{x}^T(0) P_k \tilde{x}(0) = \frac{1}{2} \bar{x}^T P_k \bar{x} = \frac{1}{2} \text{tr}(P_k X) \quad (5.5-14)$$

A minimization routine such as Simplex (Nelder and Mead, 1964; Press et al., 1986) can be used to find the optimal gains using (5.5-13) and (5.5-14) to evaluate the PI for a specified value of the gain  $K$ .

Alternatively, to use a faster gradient-based routine, we may determine the gradient of  $J$  with respect to  $K$ . To do so, define the Hamiltonian

$$\mathcal{H} = \frac{1}{2} \text{tr}(P_k X) + \frac{1}{2} \text{tr}(g_0 S_0) + \dots + \frac{1}{2} \text{tr}(g_k S_k), \quad (5.5-15)$$

where  $S_i \geq 0$  are matrices of undetermined Lagrange multipliers. Then, by differentiating  $\mathcal{H}$  with respect to all variables, necessary conditions for a minimum may be found (see the Problems). These design equations for the LQ tracker with time weighting are summarized in Table 5.5-1.

To use a gradient-based optimization routine such as Davidon-Fletcher-Powell (Press et al., 1986), we may proceed as follows. For a given  $K$ , solve the nested Lyapunov equations for  $P_i$  and  $S_i$ . Since the  $g_i$  are then all zero, (5.5-15) shows that  $J = \mathcal{H}$ . Then (5.5-23) gives the gradient of  $J$  with respect to  $K$ , which is used by the gradient-based routine to find the updated value of  $K$ .

If it is desired to use LQ *regulator* design (as opposed to tracker design, that is, Table 5.3-1) with time-dependent weighting, one need only set  $X = I$  (assuming that  $E\{x(0)x^T(0)\} = I$ ) and  $\bar{x} = 0$  in the tracker design equations of Table 5.5-1.

**TABLE 5.5-1 LQ Tracker with Time-Weighted PI***System Model*

$$\begin{aligned}\dot{x} &= Ax + Bu + Gr \\ y &= Cx + Fr\end{aligned}$$

*Control*

$$u = -Ky$$

*Performance Index*

$$J = \frac{1}{2} \int_0^\infty \left[ t^k \tilde{x}^T P \tilde{x} + \tilde{x}^T (Q + C^T K^T R K C) \tilde{x} \right] dt$$

*Optimal Output Feedback Control*

$$\begin{aligned}0 &= g_0 \equiv A_c^T P_0 + P_0 A_c + P \\ 0 &= g_1 \equiv A_c^T P_1 + P_1 A_c + P_0 \\ &\vdots \\ 0 &= g_{k-1} \equiv A_c^T P_{k-1} + P_{k-1} A_c + P_{k-2}\end{aligned} \tag{5.5-21}$$

$$\begin{aligned}0 &= g_k \equiv A_c^T P_k + P_k A_c + k! P_{k-1} + Q + C^T K^T R K C \\ 0 &= A_c S_k + S_k A_c^T + X \\ 0 &= A_c S_{k-1} + S_{k-1} A_c^T + k! S_k \\ 0 &= A_c S_{k-2} + S_{k-2} A_c^T + S_{k-1} \\ &\vdots\end{aligned} \tag{5.5-22}$$

$$\begin{aligned}0 &= A_c S_0 + S_0 A_c^T + S_1 \\ 0 &= \frac{\partial \mathcal{H}}{\partial K} = R K C S_k C^T - B^T (P_0 S_0 + \cdots + P_k S_k) C^T + B^T A_c^{-T} P_k \bar{x} \bar{y}^T\end{aligned} \tag{5.5-23}$$

with  $r$  a unit step of magnitude  $r_0$  and

$$\bar{x} = -A_c^{-1} B_c r_0 \tag{5.5-24}$$

$$\bar{y} = C \bar{x} + F r_0 \tag{5.5-25}$$

$$X = \bar{x} \bar{x}^T = A_c^{-1} B_c r_0 r_0^T B_c^T A_c^{-T} \tag{5.5-26}$$

where

$$A_c = A - B K C, \quad B_c = G - B K F$$

*Optimal Cost*

$$J = \frac{1}{2} \text{tr}(P_k X)$$

Software to determine the optimal value of  $K$  given the design parameters  $k$ ,  $Q$ , and  $R$  (for both the regulator and tracker) is described in Appendix B. It is called program LQ.

A combination of derivative and time-dependent weighting occurs in the PI:

$$J = \frac{1}{2} \int_0^\infty \left( t^k \tilde{x}^T P \tilde{x} + \tilde{x}^T Q \tilde{x} \right) dt \quad (5.5-16)$$

The optimal gains in this situation may be determined by minimizing

$$J = \frac{1}{2} \tilde{x}^T(0) P_k \tilde{x}(0) = \frac{1}{2} r_0^T B_c^T P_k B_c r_0 \quad (5.5-17)$$

subject to (5.5-13) with  $R = 0$ .

### A Fundamental Design Property

We now mention a fact of key importance in connection with time-dependent weighting. We will be very concerned to use PIs that are sensible from a design point of view. That is, we will not be content to select  $P$  and  $Q$  in Table 5.5-1 as  $n \times n$  matrices and juggle their entries until a suitable design occurs. This sort of approach is one of the fundamental flaws of modern LQ design.

A sensible PI is one of the form

$$J = \frac{1}{2} \int_0^\infty \left( t^k \tilde{e}^T \tilde{e} + r \tilde{u}^T \tilde{u} \right) dt, \quad (5.5-18)$$

where, according to Section 5.4, the error deviation is given by

$$\tilde{e} = -H\tilde{x}, \quad (5.5-19)$$

with  $z = Hx$  the performance output. This PI corresponds to our desire to make the error small without too much control energy. Since  $\tilde{e}^T \tilde{e} = \tilde{x}^T H^T H \tilde{x}$ , it amounts to using the PI in Table 5.5-1 with  $Q = 0$ ,  $R = rI$ , and  $P = H^T H$ .

However, if  $(H, A)$  is not observable and if  $k = 0$ , there may be problems with any LQ design (Lewis, 1986). Specifically, in this case the Lyapunov equation

$$A_c^T P + P A_c + H^T H + C^T K^T R K C = 0 \quad (5.5-20)$$

may not have a positive-definite solution  $P$ . This could result in some of the feedback gains being set to zero in the LQ optimal solution.

To correct this, we could add a term like  $\tilde{x}^T Q \tilde{x}$  in the PI, with  $(\sqrt{Q}, A)$  observable. This, however, is exactly what we are trying to avoid, since it will give us all of the elements of  $Q$  as design parameters that should be varied until a suitable  $K$

results. To avoid this counterintuitive approach, we need only select  $k > 0$  in the PI in Table 5.5-1. To see why, consider the case  $Q = 0$  and examine Table 5.5-1. Note that even if  $(\sqrt{P}, A)$  is not observable,  $[(k!P_{k-1})^{1/2}, A]$  may be observable for some  $k > 0$ . If so, the last Lyapunov equation in (5.5-21) will have a positive-definite solution  $P_k$ , which will correct the observability problem. That is, by using time weighting, the LQ observability problem is corrected. We will illustrate this point in Example 5.5-2.

**Example 5.5-1: Constrained Feedback Control for F-16 Lateral Dynamics** In Example 5.3-1 we showed how to design a lateral stability augmentation system for an F-16. The resulting gain matrix  $K$  had eight nonzero entries. It would be desirable to avoid gain scheduling such a large number of gains as well as to avoid feedback from roll rate and bank angle to rudder and from washed-out yaw rate and sideslip to aileron. That is, the gain matrix should have the form

$$K = \begin{bmatrix} 0 & x & 0 & x \\ x & 0 & x & 0 \end{bmatrix} \quad (1)$$

This *constrained output feedback* regulator is quite easy to design using the techniques just discussed. Indeed, select a PI of the form (5.5-5) with  $g_{11} = 1000$ ,  $g_{13} = 1000$ ,  $g_{12} = 1000$ ,  $g_{24} = 1000$  in order to weight the unwanted entries of  $K = [k_{ij}]$ . Then the algorithm of Table 5.3-1, with the modified equation (5.5-6) used to evaluate the PI in a numerical minimization scheme, yields the feedback gain matrix

$$K = \begin{bmatrix} -1E-3 & -0.55 & 1E-3 & -0.49 \\ -1.14 & -1E-3 & 0.05 & 1E-3 \end{bmatrix} \approx \begin{bmatrix} 0 & -0.55 & 0 & -0.49 \\ -1.14 & 0 & 0.55 & 0 \end{bmatrix} \quad (2)$$

The same  $Q$  and  $R$  were used as in Example 5.3-1. The resulting closed-loop poles are

$$\begin{aligned} s &= -1.16 \pm j0.99 && \text{dutch roll mode } (r, \beta) \\ &-0.79 && \text{spiral mode} \\ &-7.42 && \text{roll subsidence mode} \\ &-11.54 \pm j19.51, -12.27 && \end{aligned} \quad (3)$$

■

Note that the spiral and roll subsidence modes now consist of two real poles so that the complex roll mode is absent. The closed-loop response is shown in Figure 5.5-1. It should be compared to the response obtained in Example 5.3-1 as well as in examples in Chapter 4.

An alternative design technique is simply to use the option in program LQ of instructing the program to leave certain elements of  $K$  fixed at zero during the minimization procedure.

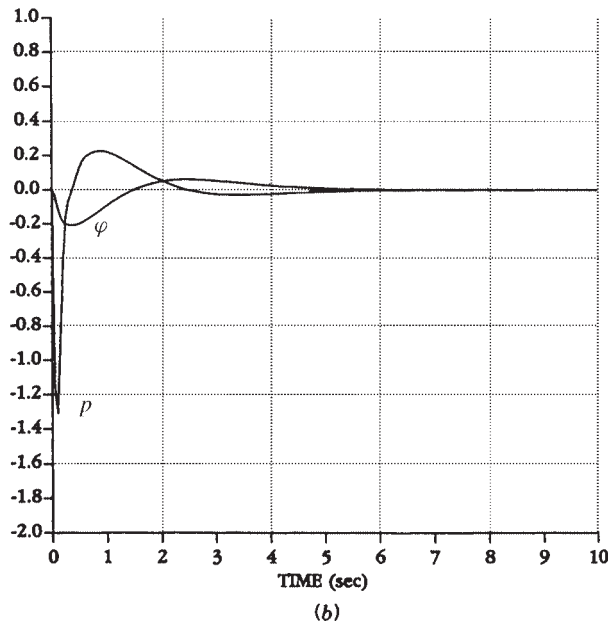
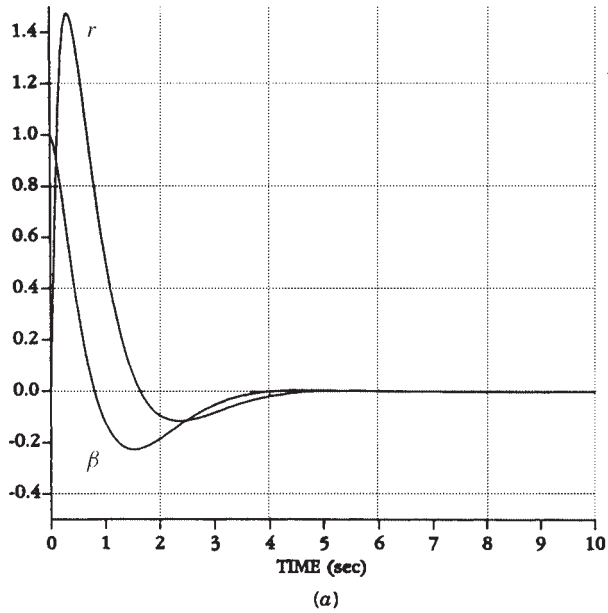


**Figure 5.5-1** Closed-loop lateral response: (a) dutch roll states  $\beta$  and  $r$ ; (b) spiral and roll subsidence states  $\phi$  and  $p$ .

**Example 5.5-2: Time-Dependent Weighting Design of Normal Acceleration CAS** In Example 5.4-1 we designed a normal acceleration CAS. A deficiency with that approach was the need to check for the observability of  $(\sqrt{Q}, A)$ ; there, unobservability led us to weight the integrator output in  $Q$ . In this example we show how to avoid the observability issue by using time-dependent weighting in the PI.

The aircraft and controller dynamics are the same as in Example 5.4-1. Here, however, we will select the time-weighted PI

$$J = \frac{1}{2} \int_0^{\infty} (t^2 \tilde{e}^2 + \rho \tilde{u}^2) dt, \quad (1)$$

which is entirely sensible from a performance point of view and contains only one design parameter to be tuned. This corresponds to the PI in Table 5.5-1 with  $P = H^T H$ ,  $Q = 0$ ,  $R = \rho$ .

Selecting  $\rho = 0.05$  and using program LQ, we obtained the control gains

$$K = [-0.847 \quad -0.452 \quad 1.647 \quad 8.602], \quad (2)$$

the closed-loop poles

$$\begin{aligned} s &= -1.90 \pm j2.58 \\ &\quad -2.35 \\ &\quad -13.88 \pm j13.12, \end{aligned} \quad (3)$$

and the step response shown in Figure 5.5-2. It is much better than the result of Example 5.4-1 and was obtained without juggling the elements of the  $Q$ -matrix or

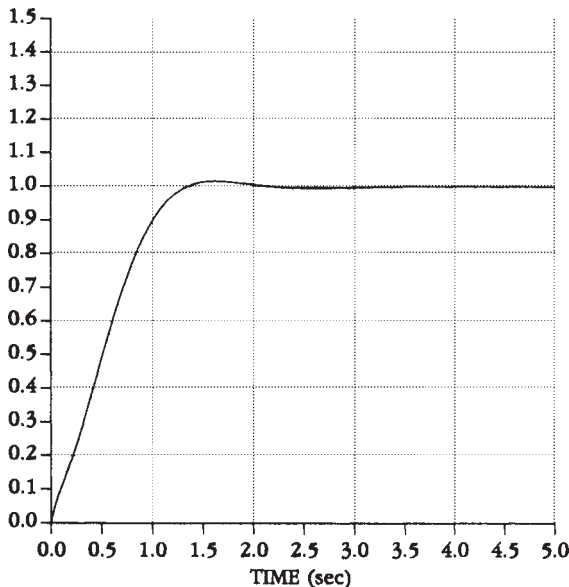


Figure 5.5-2 Normal acceleration step response.

worrying about observability issues. By using time weighting in the PI, we have formulated a design problem that has only one design parameter that needs to be varied, namely, the control weighting,  $\rho$ . This entire design took 5 minutes. Contrast to Example 4.5-3. ■

**Example 5.5-3: Pitch-Rate Control System Using LQ Design** In this example we reconsider pitch-rate control system design using LQ techniques. The approach to be used here should be compared to the classical approach used in Chapter 4. It will be demonstrated how two of the PIs just developed can simplify the control system design, since they have *only one design parameter that must be tuned to obtain good performance*. This LQ technique is therefore in sharp contrast to the classical approach, where we had to vary all three elements of the gain matrix in successive-loop-closure design. It is also in contrast to the traditional modern LQ approaches, where all the elements of the PI weighting matrices must generally be tuned to obtain good performance and where the observability properties of the PI must be considered in selecting the state-weighting matrix.

Since we are using a modern LQ-based approach, a sensible formulation of the problem should result in closed-loop stability for all selections of the design parameter. This is an extremely important property of modern control design techniques and in complete contrast to classical techniques, where stability in multiloop systems can be difficult to achieve.

(a) *Aircraft and Control System Dynamics.* The pitch control system is shown in Figure 5.5-3, where the control input is elevator actuator voltage  $u(t)$  and  $r$  is a reference step input corresponding to the desired pitch command. Thus, the performance output,  $z(t)$ , is the pitch rate,  $q$ . The measured outputs  $y(t)$  are pitch,  $q$ , and angle of attack,  $\alpha$ ; however, since  $\alpha$  measurements are quite noisy, a low-pass filter with a

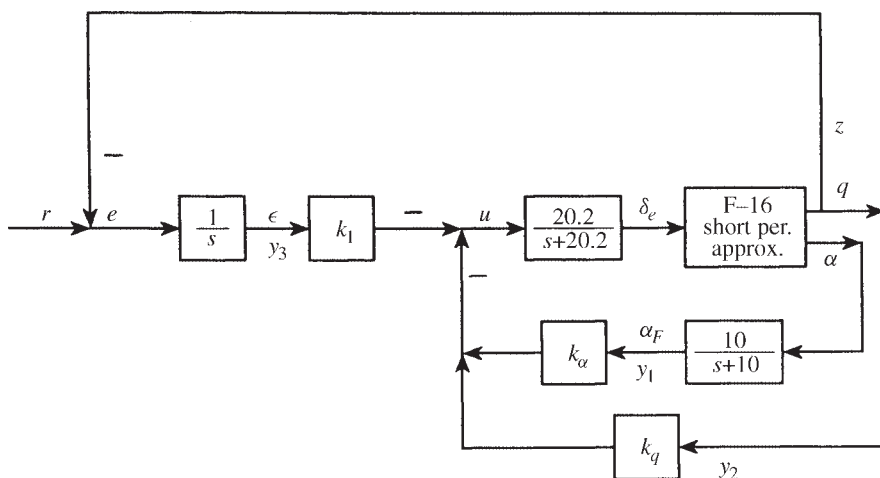


Figure 5.5-3 Pitch-rate control system.



cutoff frequency of 10 rad/s is used to provide filtered measurements  $\alpha_F$  of the angle of attack. To ensure zero steady-state error an integrator was added in the feedforward channel; this corresponds to the compensator dynamics. The integrator output is  $\epsilon$ .

We used the short-period approximation to the F-16 dynamics linearized about the nominal flight condition in Table 3.6-3 (502 ft/s, 0 ft altitude, level flight, with the cg at  $0.35\bar{c}$ ). Thus, the basic aircraft states of interest are  $\alpha$  and  $q$ . An additional state is introduced by the elevator actuator. The elevator deflection is  $\delta_e$ .

The states and outputs of the plant plus compensator are

$$x = \begin{bmatrix} \alpha \\ q \\ \delta_e \\ \alpha_F \\ \epsilon \end{bmatrix}, \quad y = \begin{bmatrix} \alpha_F \\ q \\ \epsilon \end{bmatrix} \quad (1)$$

and the system dynamics are described by

$$\dot{x} = Ax + Bu + Gr \quad (2)$$

$$y = Cx + Fr \quad (3)$$

$$z = Hx \quad (4)$$

with

$$A = \begin{bmatrix} -1.01887 & 0.90506 & -0.00215 & 0 & 0 \\ 0.82225 & -1.07741 & -0.17555 & 0 & 0 \\ 0 & 0 & -20.2 & 0 & 0 \\ 10 & 0 & 0 & -10 & 0 \\ 0 & -57.2958 & 0 & 0 & 0 \end{bmatrix}$$

$$B = \begin{bmatrix} 0 \\ 0 \\ 20.2 \\ 0 \\ 0 \end{bmatrix} \quad G = \begin{bmatrix} 0 \\ 0 \\ 0 \\ 0 \\ 1 \end{bmatrix}$$

$$C = \begin{bmatrix} 0 & 0 & 0 & 57.2958 & 0 \\ 0 & 57.2958 & 0 & 0 & 0 \\ 0 & 0 & 0 & 0 & 1 \end{bmatrix} \quad F = \begin{bmatrix} 0 \\ 0 \\ 0 \end{bmatrix}$$

$$H = [0 \quad 57.2958 \quad 0 \quad 0 \quad 0]$$

The factor of 57.2958 is added to convert angles from radians to degrees.

The control input is

$$u = -Ky = -[k_\alpha \quad k_q \quad k_I]y = -k_\alpha \alpha_F - k_q q - k_I \epsilon \quad (5)$$

It is required to select the feedback gains to yield good closed-loop response to a step input at  $r$ , which corresponds to a single-input/multi-output design problem.

Now consider two LQ designs based on two different performance indices. The modified PIs introduced in this section will mean that we do not need to worry about observability issues and that *only one design parameter will appear*. This is significant in view of the fact that there are five states and three control gains to find.

Since the integrator makes the system type 1, the steady-state error  $\bar{e}$  is equal to zero and

$$e(t) = \tilde{e}(t) \quad (6)$$

Thus, the PI term involving  $\bar{e}$  in Section 5.4 is not required.

(b) *Time-Dependent Weighting Design.* Consider the PI

$$J = \frac{1}{2} \int_0^\infty (t^2 \tilde{e}^2 + \rho \tilde{u}^2) dt \quad (7)$$

This is a natural PI that corresponds to the actual performance requirements of keeping the tracking error small without using too much control energy and also has the important advantage of requiring the adjustment of only one design parameter  $\rho$ . It amounts to using  $P = H^T H$ ,  $Q = 0$ ,  $R = \rho$  in Table 5.5-1.

Program LQ was used to solve the design equations in Table 5.5-1 for several values of  $\rho$ . A good step response was found with  $\rho = 1$ , which yielded optimal gains of

$$K = [-0.046 \quad -1.072 \quad 3.381] \quad (8)$$

closed-loop poles of  $s = -8.67 \pm j9.72$ ,  $-9.85$ ,  $-4.07$ , and  $-1.04$ , and the step response in Figure 5.5-4. Compare to the results of Example 4.5-1.

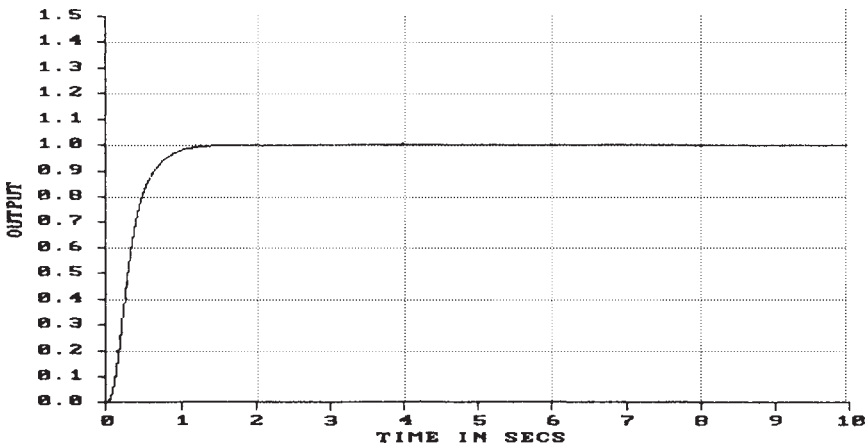


Figure 5.5-4 Pitch-rate step response using time-dependent weighting design.

(c) *Derivative Weighting Design.* Since elevator actuator *rate* has a stronger intuitive connection to “control activity” than does elevator displacement, let us illustrate derivative weighting by repeating the design. Select the PI

$$J = \frac{1}{2} \int_0^{\infty} (pt^2 e^2 + \dot{\delta}_e^2) dt \quad (9)$$

Since  $e(t) = \dot{\epsilon}(t)$ , this may be written

$$J = \frac{1}{2} \int_0^{\infty} (pt^2 \dot{\epsilon}^2 + \delta_e^2) dt, \quad (10)$$

with  $\epsilon(t)$  and  $\delta_e(t)$  the deviations in the integrator output and elevator deflection. This is exactly the derivative weighting PI (5.5-16) with  $P = \text{diag}\{0, 0, 0, 0, p\}$  and  $Q = \text{diag}\{0, 0, 1, 0, 0\}$ .

It should be emphasized that we have again been careful to formulate the problem in such a way that only one design parameter, namely,  $p$ , needs to be adjusted in the iterative design phase.

The software described in Appendix B was used to minimize (5.5-17) subject to (5.5-13) for several values of  $p$ . The weight  $p = 10$  led to a good step response, as shown in Figure 5.5-5. The feedback gain matrix was

$$K = [-0.0807 \quad -0.475 \quad 1.361] \quad (11)$$

and the closed-loop poles were at  $s = -3.26 \pm j2.83$ ,  $-1.02$ ,  $-10.67$ , and  $-14.09$ . These poles are virtually identical to those obtained in Example 4.5-1. Compare the design process in this example with the design process in that example.

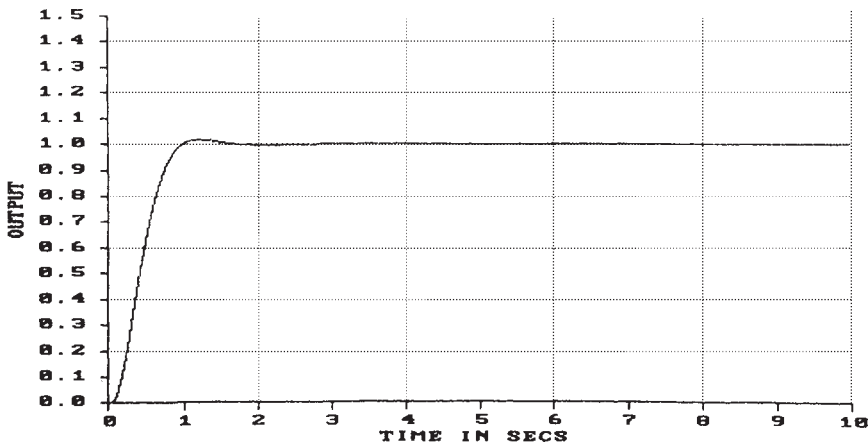


Figure 5.5-5 Pitch-rate step response using derivative weighting design. ■

**Example 5.5-4: Multivariable Wing Leveler** In this example, we will illustrate a multi-input/multi-output (MIMO) design using the LQ approach developed in this chapter. This example should be compared with Chapter 4, where we designed a two-input/two-output roll damper/yaw damper using classical control by successive loop closures.

**(a) Control System Structure.** The control system shown in Figure 5.5-6 is meant to hold the aircraft's wing level while providing yaw damping by holding washed-out yaw rate,  $r_w$ , at zero. It is a two-channel system. In the upper channel there is an outer-loop unity-gain feedback of bank angle,  $\phi$ , with an inner-loop feedback of roll rate,  $p$ . This channel has a PI compensator to make the system type 1 to achieve zero steady-state bank angle error. The control input for the upper channel is aileron deflection,  $\delta_a$ . The lower channel has a feedback of washed-out yaw rate,  $r_w$ ; in this channel the control input is rudder deflection,  $\delta_r$ .

The reference command is  $r_c = [r_\phi \quad r_r]^T$ . The tracking control system should hold  $\phi$  at the commanded value of  $r_\phi$ , and  $r_w$  at the commanded value of  $r_r$ , which is equal to zero. To hold the wing level,  $r_\phi$  is set equal to zero, although it could be any commanded bank angle. The tracking error is  $e = [e_\phi \quad e_r]^T$  with

$$\begin{aligned} e_\phi &= r_\phi - \phi \\ e_r &= r_r - r_w \end{aligned} \quad (1)$$

**(b) State Equations for Aircraft and Control Dynamics.** As in Example 5.3-1, we used the F-16 linearized lateral dynamics at the nominal flight condition in Table 3.6-3 ( $V_T = 502 \text{ ft/s}$ , 300 psf dynamic pressure, cg at  $0.35\bar{c}$ ) retaining the lateral states sideslip,  $\beta$ , bank angle,  $\phi$ , roll rate,  $p$ , and yaw rate,  $r$ . Additional states  $\delta_a$  and  $\delta_r$  are introduced by the aileron and rudder actuators. The washout filter state is called  $x_w$ .

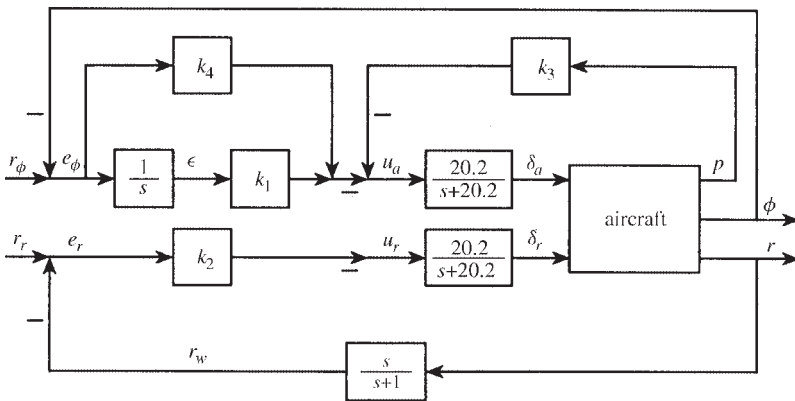


**Figure 5.5-6** Wing-leveler lateral control system.

We denote by  $\epsilon$  the output of the controller integrator in the upper channel. Thus, the entire state vector is

$$x = [\beta \quad \phi \quad p \quad r \quad \delta_a \quad \delta_r \quad x_w \quad \epsilon]^T \quad (2)$$

The full state-variable model of the aircraft plus actuators, washout filter, and control dynamics is of the form

$$\dot{x} = Ax + Bu + Gr_c \quad (3)$$

with

$$A = \begin{bmatrix} -0.3220 & 0.0640 & 0.0364 & -0.9917 & 0.0003 & 0.0008 & 0 & 0 \\ 0 & 0 & 1 & 0.0037 & 0 & 0 & 0 & 0 \\ -30.6492 & 0 & -3.6784 & 0.6646 & -0.7333 & 0.1315 & 0 & 0 \\ 8.5395 & 0 & -0.0254 & -0.4764 & -0.0319 & -0.0620 & 0 & 0 \\ 0 & 0 & 0 & 0 & -20.2 & 0 & 0 & 0 \\ 0 & 0 & 0 & 0 & 0 & -20.2 & 0 & 0 \\ 0 & 0 & 0 & 57.2958 & 0 & 0 & -1 & 0 \\ 0 & -1 & 0 & 0 & 0 & 0 & 0 & 0 \end{bmatrix}$$

$$B = \begin{bmatrix} 0 & 0 \\ 0 & 0 \\ 0 & 0 \\ 0 & 0 \\ 20.2 & 0 \\ 0 & 20.2 \\ 0 & 0 \\ 0 & 0 \end{bmatrix} \quad G = \begin{bmatrix} 0 & 0 \\ 0 & 0 \\ 0 & 0 \\ 0 & 0 \\ 0 & 0 \\ 0 & 0 \\ 0 & 0 \\ 1 & 0 \end{bmatrix} \quad (4)$$

The performance output that should follow the reference input  $[r_\phi \quad r_r]^T$  is

$$z = \begin{bmatrix} \phi \\ r_w \end{bmatrix} = \begin{bmatrix} 0 & 1 & 0 & 0 & 0 & 0 & 0 & 0 \\ 0 & 0 & 0 & 57.2958 & 0 & 0 & -1 & 0 \end{bmatrix} x = Hx, \quad (5)$$

where the factor 57.2958 converts radians to degrees. According to the figure, if we define the measured output as

$$y = \begin{bmatrix} \epsilon \\ e_r \\ p \\ e_\phi \end{bmatrix} = Cx + Fr_c \quad (6)$$

with

$$c = \begin{bmatrix} 0 & 0 & 0 & 0 & 0 & 0 & 0 & 1 \\ 0 & 0 & 0 & -57.2958 & 0 & 0 & 1 & 0 \\ 0 & 0 & 1 & 0 & 0 & 0 & 0 & 0 \\ 0 & -1 & 0 & 0 & 0 & 0 & 0 & 0 \end{bmatrix}$$

$$F = \begin{bmatrix} 0 & 0 \\ 0 & 1 \\ 0 & 0 \\ 1 & 0 \end{bmatrix} \quad (7)$$

the control input  $u = [u_a \ u_r]^T$  may be expressed as

$$u = -Ky \quad (8)$$

with

$$K = \begin{bmatrix} k_1 & 0 & k_3 & k_4 \\ 0 & k_2 & 0 & 0 \end{bmatrix} \quad (9)$$

The control gains,  $k_i$ , must now be determined for satisfactory closed-loop response. Therefore, this is an output feedback design problem exactly of the form addressed in this chapter. Note that some of the entries of  $K$  must be constrained to zero to yield the desired control structure shown in Figure 5.5-6.

(c) *LQ Output Feedback Design.* To guarantee tracking by  $z(t)$  of the reference command  $r_c(t)$ , we may select the PI

$$J = \frac{1}{2} \int \left( \tilde{x}^T P \tilde{x} + \tilde{u}^T \tilde{u} \right) dt + \frac{1}{2} \tilde{v} \tilde{e}^T \tilde{e} \quad (10)$$

with  $\tilde{x}(t)$  and  $\tilde{u}(t)$  the state and control deviations defined in Section 5.4 and  $\tilde{e}$  the steady-state error. Although the integrator in the upper control channel guarantees that  $\tilde{e}_\phi$  will be zero, the steady-state error weighting  $\tilde{v}$  is required to ensure that  $\tilde{e}_r$  is small. Note that  $\tilde{v}$  is a scalar.

The design equations for  $K$  using this PI are given in Table 5.5-1, with, however, the extra terms from Table 5.4-1 added to (5.5-23) due to the steady-state error weighting  $\tilde{v}$ . Thus,  $K$  is easily determined using program LQ.

Several attempts were made to obtain suitable closed-loop behavior using different values for  $\tilde{v}$  and  $P$ . Finally, it was found that good behavior was obtained with  $\tilde{v} = 10$  and  $P$  selected to weight the states  $\beta, \phi, p, r$  and  $\epsilon$ , as well as the cross-term in  $\phi r$ . That is,

$$p_{11} = p_{22} = p_{33} = p_{44} = p_{88} = 100, \quad p_{24} = p_{42} = 10 \quad (11)$$

The motivation for the  $p_{24}$  cross-weighting is that, after a few design attempts with different  $P$ , it was found that there were always several barely stable and badly damped complex pole pairs in the closed-loop system. The  $p_{24}, p_{42}$  cross-weighting

penalizes the dutch roll mode, which was one of the ones yielding problems. The motivation for selecting  $p_{88}$  weighting is that good results are generally obtained if the integrator output is weighted.

Using the final selection of  $v$  and  $P$ , the control gains were found to be

$$\begin{aligned} k_1 &= 15.04, & k_2 &= 0.1822, \\ k_3 &= -5.348, & k_4 &= 22.52, \end{aligned} \quad (12)$$

yielding closed-loop poles of

$$\begin{aligned} &-0.72 \pm j3.03 \\ &-1.12 \pm j0.07 \\ &-2.43, -5.05 \\ &-15.3, -19.4 \end{aligned} \quad (13)$$

(d) *Simulation.* The closed-loop response to a reference command of  $r_\phi = 1$ ,  $r_r = 0$  is shown in Figure 5.5-7. The transient response and steady-state errors are both quite satisfactory. This is despite the presence of an underdamped pole pair at  $-0.72 \pm j3.03$ . One should recall the discussion in Chapter 4, where the strong

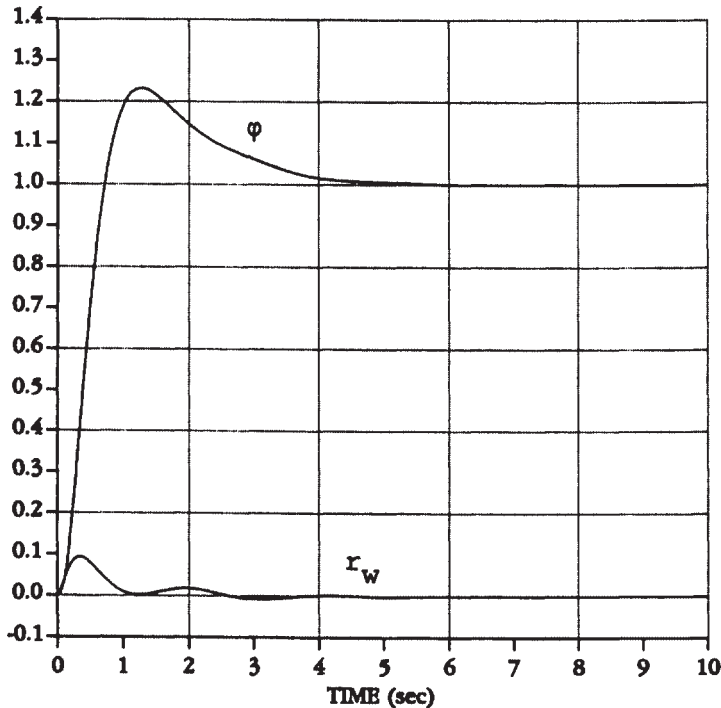


**Figure 5.5-7** Closed-loop response to a command of  $r_\phi = 1$ ,  $r_r = 0$ . Bank angle  $\phi$  (rad) and washed-out yaw rate (rad/s).

coupling between the aircraft roll and yaw channels was emphasized. Despite this, Figure 5.5-7 shows that we have been quite successful in decoupling the yaw rate from the bank angle. ■

**Example 5.5-5: Glide-Slope Coupler** A glide-slope coupler is part of an automatic landing system—it guides an aircraft down a predetermined flight path to the end of a runway. At the end of the descent another control system, the automatic flare control (Example 5.6-1), is switched in to cause the aircraft to flare to a landing.

In this example we design a glide-slope coupler for the longitudinal dynamics of a medium-sized transport aircraft. Our approach should be compared to the frequency-domain approach in Example 4.6-4. See also Blakelock (1965).

**(a) Aircraft Dynamics.** The important inputs are both elevator and throttle for this problem, since both are needed to fly down a glide path in a coordinated manner. Exactly as in Example 4.6-4, the longitudinal dynamics of the aircraft were linearized about a velocity of  $V_T = 250 \text{ ft/s}$  with the cg at  $0.25\bar{c}$  and including throttle and elevator actuators. The state and control inputs are

$$x = [v_t \quad \alpha \quad \theta \quad q \quad \delta_t \quad \delta_e]^T, \quad u = [u_t \quad u_e]^T, \quad (1)$$

with  $v_T$  the deviation from trim velocity. The dynamics are described by

$$\dot{x} = Ax + Bu, \quad (2)$$

where  $A$  and  $B$  may be found by referring to Example 4.6-4. (In finding the  $A$  and  $B$  in (2) from the matrices in Example 4.6-4, note our selection of states.)

At this point it is worthwhile to examine Figure 5.5-8, which we are starting to construct.

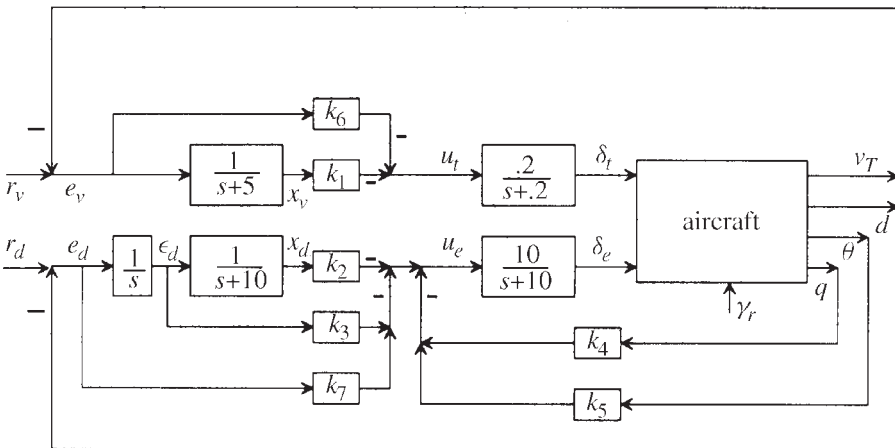


Figure 5.5-8 Glide-slope coupler.



(b) *Glide-Slope Geometry.* The glide-slope geometry is discussed in Example 4.6-4. The commanded or reference flight-path angle  $-\gamma_r$  is generally  $2.5^\circ$ . The perpendicular distance from the glide path is  $d(t)$ .

Our control objectives in the glide-slope coupler are to regulate to zero the off-glide-path distance,  $d$ , and the deviation from trim velocity,  $v_T$ . Then the aircraft will remain on the glide path with the nominal velocity of  $V_T = 250$  ft/s. To accomplish this, the two control inputs are throttle and elevator. The outputs available for feedback are pitch rate,  $q$ , pitch angle,  $\theta$ ,  $v_T$ , and  $d$ , which is available from measurements taken from the ground.

The component of velocity perpendicular to the glide path is given by

$$\dot{d} = V_T \sin(\gamma - \gamma_r) \approx V_T(\gamma - \gamma_r) \quad (3)$$

when  $(\gamma - \gamma_r)$  is small. We will assume that the velocity deviation  $v_T$  is small and take  $v_T$  in (3) as the trim velocity 250 ft/s. To follow the glide path, we require  $d = 0$ , so that the flight-path angle  $\gamma$  should be equal to  $\gamma_r$ . Then the aircraft will descend at an angle of  $\gamma_r = -2.5^\circ$ .

In terms of variables in the state vector in (1), we may use  $\gamma = \theta - \alpha$  to write

$$d = V_T\theta - V_T\alpha - \frac{V_T}{57.2958}\gamma_r = V_T\theta - V_T\alpha - 4.3633\gamma_r, \quad (4)$$

with  $\theta$  and  $\alpha$  in radians and  $\gamma_r$  in degrees. Therefore, we may include the off-glide-path distance  $d$  as a state in (1) by redefining

$$x = [v_T \quad \alpha \quad \theta \quad q \quad d \quad \delta_t \quad \delta_e]^T \quad (5)$$

(c) *Control System Structure.* Our objective is to regulate  $v_T$  and  $d$  to zero. Thus, we may define the performance output as

$$z = \begin{bmatrix} v_T \\ d \end{bmatrix} = Hx \quad (6)$$

Now examine Figure 5.5-8, which we have drawn to show that this may be considered as a tracking problem with reference commands  $r_v$  and  $r_d$  of zero. The tracking error is  $e = [e_v \quad e_d]^T$  with

$$\begin{aligned} e_v &= r_v - v_T \\ e_d &= r_d - d \end{aligned} \quad (7)$$

To obtain zero steady-state error in  $v_T(t)$  and  $d(t)$ , we could add integrators in each of the forward error paths. However, according to the open-loop dynamics in Example 4.6-4 there are already several poles near the origin. Adding more poles near the origin makes the problem of stabilization more difficult.

Since we are more concerned about keeping  $d$  exactly zero, let us only add an integrator in the forward path corresponding to the tracking error in  $d$ . We can then obtain

a small enough error in  $v_T$  without a forward-path integrator by using weighting of the steady-state error, as we will soon see.

An additional consideration for including a forward-path integrator in the  $d$  channel is the following. Note from (4) and Figure 5.5-8 that the commanded glide-path angle  $\gamma_r$  acts as a constant disturbance of magnitude  $-2.5^\circ$  into the system. The disturbance affects  $d$ . To reject this constant disturbance, we need a type-1 system with respect to  $d$ , which requires the integrator in the  $d$  feedforward path.

We can gain considerable insight by having root-locus design techniques in mind during a design by modern control. Thus, to pull the closed-loop poles into the left-half plane, we may add compensator zeros in the left-half plane. To implement the compensators without pure differentiation, we should add poles relatively far in the left-half plane, where they will not appreciably affect the root locus. Thus, let us propose a lead compensator in each forward channel (see Figure 5.5-8).

The compensators we propose are of the form

$$\begin{aligned}\frac{w_v}{e_v} &= \frac{k_1}{s+5} + k_6 = k_6 \frac{s + (5 + k_1/k_6)}{s+5} \\ u_t &= -w_v\end{aligned}\tag{8}$$

and

$$\begin{aligned}\frac{w_d}{e_d} &= \frac{k_2}{s(s+10)} \frac{k_3}{s} + k_7 \\ &= k_7 \frac{s^2 + (10 + k_3/k_7)s + (k_2 + 10k_3)/k_7}{s(s+10)} \\ u_e &= -w_d\end{aligned}\tag{9}$$

The important point to note is that, by varying the control gains, we may adjust *both the compensator gain and its zeros*. Thus, the *LQ optimization routine can adjust the zeros of the compensators*, presumably inducing lead compensation where it is required. We have selected the throttle compensator pole at  $s = -5$  and the distance compensator pole at  $s = -10$ ; however, any poles far to the left compared to the aircraft poles would suffice.

As we have seen in Example 4.6-4, selecting multiple control gains by classical techniques requires a successive-loop-closure approach. We hope to show that finding suitable gains using modern control theory is far easier, given a sensible problem formulation.

To formulate the controller so that the gains may be determined by our output feedback LQ approach, note that state-variable representations of (8) and (9) are given by

$$\dot{x}_v = -5x_v + e_v = -5x_v - v_T + r_v\tag{10}$$

$$u_t = -k_1x_v - k_6e_v = -k_1x_v - k_6(v_T + r_v)\tag{11}$$

and

$$\dot{e}_d = e_d = -d + r_d \quad (12)$$

$$\dot{x}_d = -10x_d + \epsilon_d \quad (13)$$

$$u_e = -k_2x_d - k_3\epsilon_d - k_7e_d = -k_2x_d - k_3\epsilon_d - k_7(-d + r_d) \quad (14)$$

The dynamical equations (4), (10), (12), and (13) may be incorporated into the system description by defining the augmented state

$$x = [v_T \quad \alpha \quad \theta \quad q \quad d \quad \delta_t \quad \delta_e \quad x_v \quad x_d \quad \epsilon_d]^T \quad (15)$$

Then the augmented system is described by

$$\dot{x} = Ax + Bu + Gr \quad (16)$$

with

$$A = \begin{bmatrix} -0.04 & 19.0096 & -32.1689 & 0 & 0 & 10.1 & 0 & 0 & 0 & 0 \\ -0.001 & -0.64627 & 0 & 1 & 0 & 0 & 0 & 0 & 0 & 0 \\ 0 & 0 & 0 & 1 & 0 & 0 & 0 & 0 & 0 & 0 \\ 0 & -0.7739 & 0 & -0.529765 & 0 & 0.02463 & -0.011 & 0 & 0 & 0 \\ 0 & -250 & 250 & 0 & 0 & 0 & 0 & 0 & 0 & 0 \\ 0 & 0 & 0 & 0 & 0 & -0.2 & 0 & 0 & 0 & 0 \\ 0 & 0 & 0 & 0 & 0 & 0 & -10 & 0 & 0 & 0 \\ -1 & 0 & 0 & 0 & 0 & 0 & 0 & -5 & 0 & 0 \\ 0 & 0 & 0 & 0 & 0 & 0 & 0 & 0 & -10 & 1 \\ 0 & 0 & 0 & 0 & -1 & 0 & 0 & 0 & 0 & 0 \end{bmatrix}$$

$$B = \begin{bmatrix} 0 & 0 & 0 \\ 0 & 0 & 0 \\ 0 & 0 & 0 \\ 0 & 0 & 0 \\ 0 & 0 & -4.3633 \\ 0.2 & 0 & 0 \\ 0 & 10 & 0 \\ 0 & 0 & 0 \\ 0 & 0 & 0 \\ 0 & 0 & 0 \end{bmatrix}, \quad G = \begin{bmatrix} 0 & 0 \\ 0 & 0 \\ 0 & 0 \\ 0 & 0 \\ 0 & 0 \\ 0 & 0 \\ 0 & 0 \\ 1 & 0 \\ 0 & 0 \\ 0 & 1 \end{bmatrix} \quad (17)$$

To incorporate the constant disturbance  $\gamma_r$  required in (4), we have defined an augmented input

$$u' = [u^T \quad \gamma_r]^T = [u_i \quad u_e \quad \gamma_r]^T \quad (18)$$

Inputs such as  $\gamma_r$ , which are not actual controls, or reference signals  $r(t)$  in the usual tracking system sense, are called *exogenous inputs*. Although they play the role of disturbances in the system, they are crucial in guaranteeing the desired system behavior.

Indeed, were we to ignore  $\gamma_r$ , the glide-slope coupler would always make the aircraft fly a horizontal path!

It should be clearly understood that for the design of the control system only the control input  $u(t)$  is used. The full input  $u'(t)$  will be required only in the simulation state, where  $\gamma_r$  will be set equal to  $-2.5^\circ$  to obtain the desired landing approach behavior.

In (16)/(17) the reference input is defined as

$$r = [r_v \quad r_d]^T, \quad (19)$$

which is zero for the glide-slope coupler.

The equations (11) and (14) may be incorporated by defining a new measured output as

$$y = [x_v \quad x_d \quad e_d \quad q \quad \theta \quad e_v \quad e_d]^T \quad (20)$$

Then

$$y = Cx = Fr \quad (21)$$

with

$$C = \begin{bmatrix} 0 & 0 & 0 & 0 & 0 & 0 & 0 & 1 & 0 & 0 \\ 0 & 0 & 0 & 0 & 0 & 0 & 0 & 0 & 1 & 0 \\ 0 & 0 & 0 & 0 & 0 & 0 & 0 & 0 & 0 & 1 \\ 0 & 0 & 0 & 57.2958 & 0 & 0 & 0 & 0 & 0 & 0 \\ 0 & 0 & 57.2958 & 0 & 0 & 0 & 0 & 0 & 0 & 0 \\ -1 & 0 & 0 & 0 & 0 & 0 & 0 & 0 & 0 & 0 \\ 0 & 0 & 0 & 0 & -1 & 0 & 0 & 0 & 0 & 0 \end{bmatrix}$$

$$F = \begin{bmatrix} 0 & 0 \\ 0 & 0 \\ 0 & 0 \\ 0 & 0 \\ 0 & 0 \\ 0 & 0 \\ 0 & 0 \\ 1 & 0 \\ 0 & 1 \end{bmatrix} \quad (22)$$

Now, according to Figure 5.5-8, the control vector  $u(t)$  is given by the output feedback

$$u \begin{bmatrix} u_r \\ u_e \end{bmatrix} = - \begin{bmatrix} k_1 & 0 & 0 & 0 & 0 & k_6 & 0 \\ 0 & k_2 & k_3 & k_4 & k_5 & 0 & k_7 \end{bmatrix} y = -Ky, \quad (23)$$

which has some elements constrained to zero.

According to (6), we may write

$$z = \begin{bmatrix} v_T \\ d \end{bmatrix} = \begin{bmatrix} 1 & 0 & 0 & 0 & 0 & 0 & 0 & 0 & 0 & 0 \\ 0 & 0 & 0 & 0 & 1 & 0 & 0 & 0 & 0 & 0 \end{bmatrix} x = Hx \quad (24)$$

At this point we have succeeded in casting the glide-slope coupler design problem into the formulation required in Tables 5.4-1 and 5.5-1.

It is important to understand the construction of the matrices in (17), (22), and (24), for this problem formulation stage is one of the most important phases in the LQ design technique.

(d) *PI and Control Design.* The other important phase in LQ design is the selection of an appropriate PI. Since the loop gain around the velocity loop is not of type 1, we will require weighting of the steady-state error to force  $v_T$  to go to zero at steady state. Thus, let us propose the PI

$$J = \frac{1}{2} \int_0^\infty (qt^2 \tilde{e}^T \tilde{e} + \tilde{u}^T \tilde{u}) dt + \frac{1}{2} v \bar{e}^T \bar{e} \quad (25)$$

The motivation for the weighting  $t^2$  follows. Weighting  $\tilde{e}$  in the PI makes practical sense since we want it to vanish. However,  $\tilde{e}^T \tilde{e} = \tilde{x}^T H^T H \tilde{x}$ , and  $(H, A)$  is not observable. In fact, the compensator states are not observable through  $z = Hx$ . An LQ design without the weighting  $t^2$  would, therefore, fail. To correct the situation, we could weight the entire state in the PI by using a term like  $\tilde{x}^T Q \tilde{x}$ . However, this would give us too many design parameters (i.e., the elements of  $Q$ ) and lead to a counterintuitive situation.

We prefer to work with sensible PIs, and in this situation we want to retain the weighting of  $\tilde{e}(t)$ , which is the variable of direct concern to us. Therefore, we use  $t^2$  weighting to correct the observability problem. See the discussion preceding Example 5.5-1.

With  $t^2$  weighting, a large value of the scalar  $q$  will result in a closed-loop system that is too fast. After several design iterations, it was found that suitable values for the PI design parameters were  $q = 0.001$ ,  $v = 100$ . We employed program LQ to solve for the optimal gain  $K$  using the design equations of Table 5.5-1, including the steady-state error weighting from Table 5.4-1. We selected the option of fixing seven of the gain elements to zero as required by (23).

With  $q = 0.001$ ,  $v = 100$ , the optimal control gains were

$$K = \begin{bmatrix} 2.598 & 0 & 0 & 0 & 0 & -0.9927 & 0 \\ 0 & 583.7 & -58.33 & -2.054 & -1.375 & 0 & 6.1 \end{bmatrix} \quad (26)$$

and the closed-loop poles were at

$$\begin{aligned} & -0.27 \pm j1.01 \\ & -0.36 \pm j0.49 \\ & -0.37 \pm j0.09 \\ & -1.18, -4.78, -8.38, -10.09 \end{aligned} \quad (27)$$

Thus, the slowest time constant is  $1/0.27 \approx 4$  s.

(e) *Simulation and Discussion.* A simulation of the glide-slope coupler appears in Figure 5.5-9. The aircraft was initialized in level flight at 1500 ft. The glide-slope coupler was switched on as the aircraft crossed through the glide path.

For simulation purposes, we used the exogenous input  $\gamma_r = -2.5^\circ$  (the desired glide-path angle) and reference commands of  $r_v = 0$ ,  $r_d = 0$ . Altitude  $h$  was added as a state using the equation for vertical velocity

$$\dot{h} = V_T \sin \gamma \approx V_T(\theta - \alpha), \quad (28)$$

with  $V_T$  assumed to be the trim velocity of 250 ft/s.

According to the altitude plot in Figure 5.5-9a, after a small transient lasting about 20 s, the aircraft settles down onto the glide path and follows it down. Touchdown occurred at 137.5 s. Figure 5.5-9b shows the off-glide-path error  $d$ .

Figure 5.5-9c shows angle of attack and pitch angle. Note that after the transient the flight-path angle is given by  $\gamma = \theta - \alpha = -2.5^\circ$ . Since in the descending configuration the aircraft is no longer at the original trim condition, a small angle of attack  $\alpha$  of  $-0.18^\circ$  remains at steady state. The final pitch angle  $\theta$  is  $-2.68^\circ$ .

According to Figure 5.5-9d, the velocity deviation  $v_T$  settles out at 0.29 ft/s. This is a consequence of the fact that there is no integrator in the forward  $e_v$  path in Figure 5.5-8. Thus, the steady-state velocity on the glide path is  $V_T = 250.29$  ft/s; this is very suitable from a performance point of view. The smallness of the steady-state deviation despite the fact that the  $v_T$  loop is of type 0 is a consequence of the steady-state error weighting  $v$  in the PI (25).

Finally, the elevator and throttle control efforts  $\delta e$  and  $\delta t$  are shown in Figure 5.5-9e. Note the coordinated control achieved in this two-input system using the LQ approach. Since the descent down the glide path does not represent the original trim condition, the steady-state values of the control efforts are not zero. Intuitively, less throttle is required to maintain 250 ft/s if the aircraft is descending.

Figure 5.5-9 shows that, as the aircraft passes through the glide path, the elevator is pushed forward and the throttle is cut. As a result, the angle of attack and pitch angle decrease. After a slight positive position error,  $d$ , and an initial increase in velocity,  $v_T$ , further control effort stabilizes the aircraft on the glide path.

It is interesting to note the fundamental mechanism behind the glide-slope coupler. Namely, we regulate  $d$  in (3) and (4) to zero so that  $\gamma = \gamma_r = -2.5^\circ$ . Then, according to (28),  $\dot{h} = V_T \sin \gamma_r$ , the appropriate descent rate to stay on the glide path.

With the optimal gains in (26), according to (8) the velocity channel compensator is

$$\frac{w_v}{e_v} = -0.9927 \frac{s + 2.38}{s + 5}, \quad (29)$$

which is a lead compensator as anticipated. The zeros in the  $d$  channel compensator could similarly be found. It is important to note that our formulation has resulted in the *compensator zeros being selected in an optimal fashion*. This is an improvement over root-locus design, where the zeros are determined using the engineering judgment that actually only applies for single-input/single-output systems.

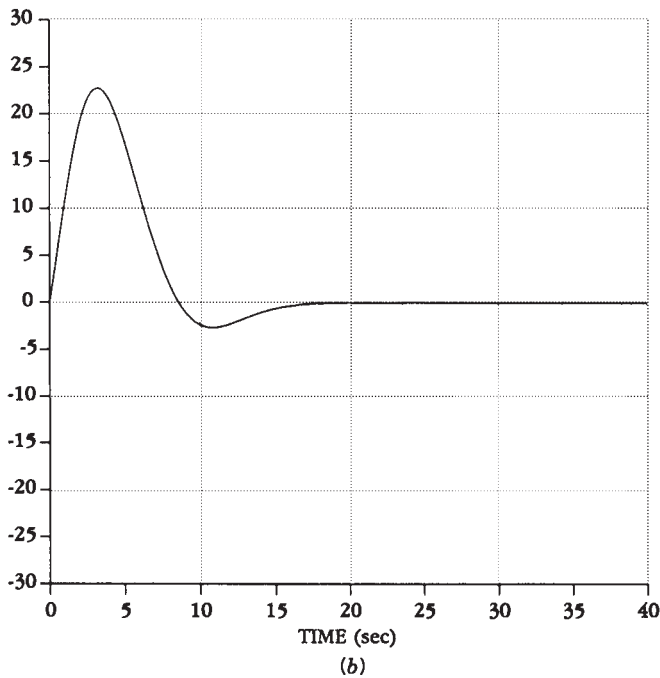
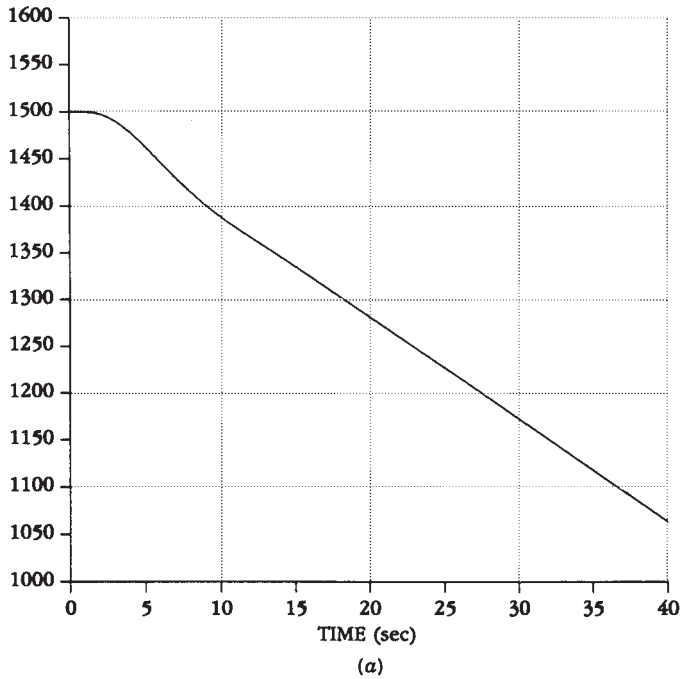


**Figure 5.5-9** Glide-slope coupler responses: (a) altitude  $h$  (ft); (b) off-glide path distance  $d$  (ft). (c) Angle of attack  $\alpha$  and pitch angle  $\theta$  (deg); (d) velocity deviation  $v_T$  (ft/s). (e) Control efforts  $\delta_e$  (rad) and  $\delta_i$  (per unit).

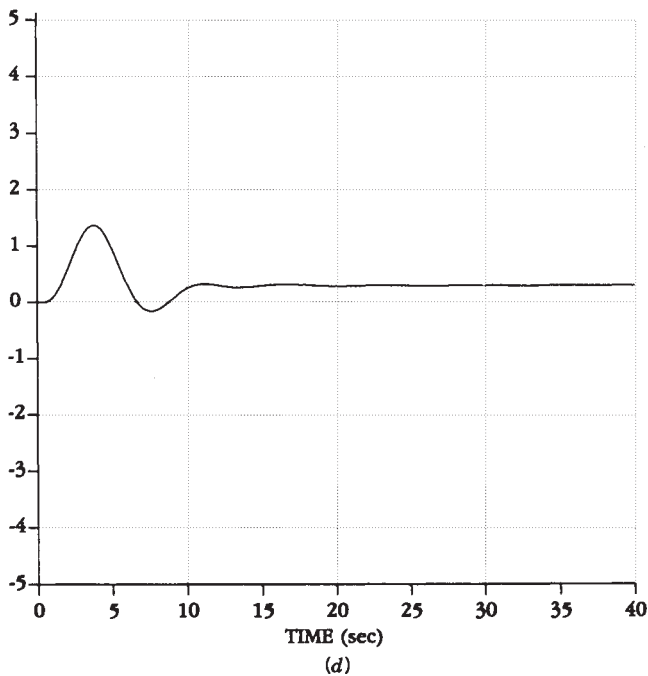
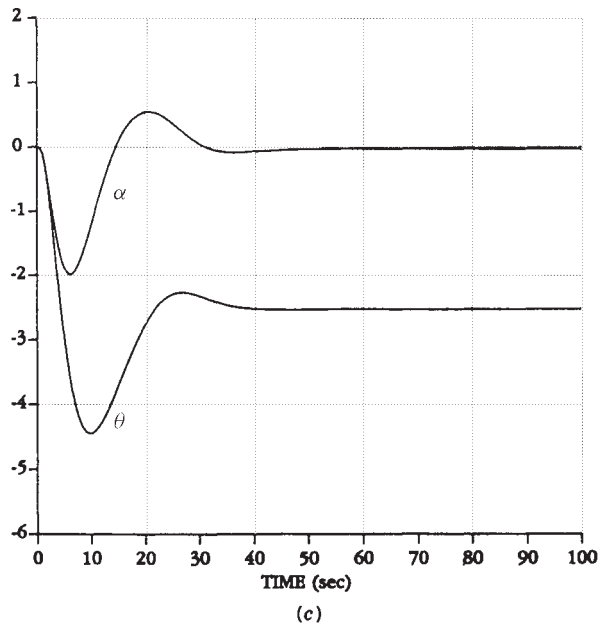


Figure 5.5-9 (continued)



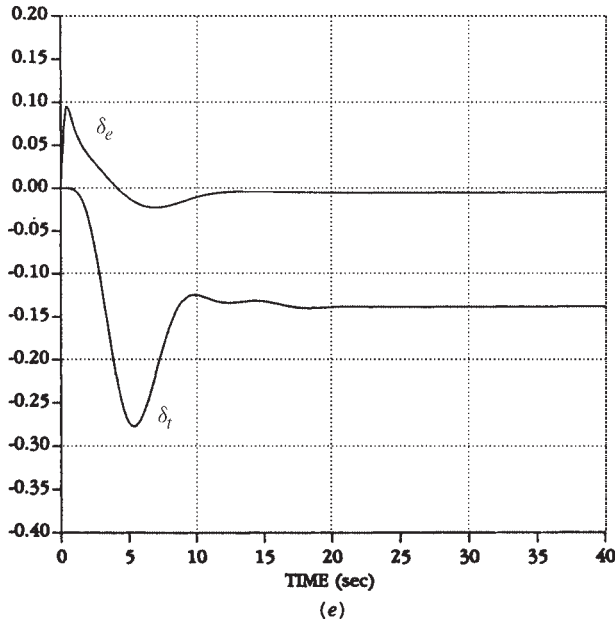


Figure 5.5-9 (continued)

It should be mentioned that determining an initial stabilizing gain  $K_0$  for program LQ is not easy. In this example, we used the root-locus techniques from Chapter 4 to find the initial gain. Other approaches were discussed earlier in the subsection entitled “Constrained Feedback Matrix.” ■

## 5.6 MODEL-FOLLOWING DESIGN

In Section 4.3 we discussed flying qualities and gave the military flying qualities specifications for the various aircraft modes. These desirable flying qualities could be viewed as constituting an *ideal model with good performance* which we would like to reproduce in the actual aircraft. For instance, to obtain good longitudinal performance we could select suitable short-period and phugoid poles from the flying qualities specifications tabulated in Section 4.3. Then we could determine a state-variable realization of an ideal model with this behavior (see Stern and Henke, 1971). Finally, we could design a control system to make the actual aircraft behave like this ideal model.

This approach to control system design is the powerful model-following design technique. In this section we show how to design controllers that make the aircraft behave like a desired model. We will discuss two fundamentally different sorts of model-following control, “explicit” and “implicit,” which result in controllers of different structure (Armstrong, 1980; Kreindler and Rothschild, 1976; O’Brien and Broussard, 1978).

## Explicit Model-Following Control

**Regulation with Model-Following Behavior** First, we will consider the regulator problem, where the objective is to drive the plant state to zero. Then we will treat the more difficult tracker or servo problem, where the plant is to follow a reference command with behavior like the prescribed model. Let the plant be described in state-variable form by

$$\dot{x} = Ax + Bu \quad (5.6-1)$$

$$y = Cx \quad (5.6-2)$$

$$z = Hx, \quad (5.6-3)$$

with state  $x(t) \in \mathbf{R}^n$  and control input  $u(t) \in \mathbf{R}^m$ . The measured output  $y(t)$  is available for feedback purposes.

A model is prescribed with dynamics

$$\dot{\underline{x}} = \underline{A}x \quad (5.6-4)$$

$$\underline{z} = \underline{H}x, \quad (5.6-5)$$

where the model matrix  $\underline{A}$  reflects a system with desirable handling qualities such as speed of response, overshoot, and so on. The model states suitable for feedback purposes are given by

$$\underline{y} = \underline{C}x \quad (5.6-6)$$

Model quantities will be denoted by underbars or the subscript  $m$ .

Notice that the model has no reference input, since we are considering the regulator problem here. That is, the plant should have the same unforced response as the model, which translates into suitable locations of the poles.

It is desired to select the plant control  $u(t)$  so that the plant performance output  $z(t)$  matches the model output  $\underline{z}(t)$ , for then the plant will exhibit the desirable time response of the model. That is, we should like to minimize the *model mismatch error*

$$e = \underline{z} - z = \underline{H}x - Hx \quad (5.6-7)$$

To achieve this control objective, let us select the performance index

$$J = \frac{1}{2} \int_0^\infty (e^T Q e + u^T R u) dt, \quad (5.6-8)$$

with  $Q > 0$  (to ensure that all components of the error vanish) and  $R > 0$ .

We can cast this model-matching problem into the form of the regulator problem whose solution appears in Table 5.3-1 as follows.

Define the augmented state  $x' = [x^T \quad \underline{x}^T]^T$  and the augmented system

$$\dot{x}' \begin{bmatrix} A & 0 \\ 0 & \underline{A} \end{bmatrix} x' + \begin{bmatrix} B \\ 0 \end{bmatrix} u \equiv A'x' + B'u \quad (5.6-9)$$

$$y' = \begin{bmatrix} y \\ \underline{y} \end{bmatrix} = \begin{bmatrix} C & 0 \\ 0 & \underline{C} \end{bmatrix} x' \equiv C'x', \quad (5.6-10)$$

so that

$$e = [-H \quad \underline{H}] x' \equiv H'x' \quad (5.6-11)$$

Then the PI (5.6-8) may be written

$$J = \frac{1}{2} \int_0^\infty ((x')^T Q' x' + u^T R u) dt, \quad (5.6-12)$$

with

$$Q' = \begin{bmatrix} H^T Q H & -H^T Q \underline{H} \\ -\underline{H}^T Q H & \underline{H}^T Q \underline{H} \end{bmatrix} \quad (5.6-13)$$

At this point it is clear that the design equations of Table 5.3-1 can be used to select  $u(t)$  if the primed quantities  $A'$ ,  $B'$ ,  $C'$ ,  $Q'$  are used there. The conditions for convergence of the algorithm in Table 5.3-2 require that  $(A', B', C')$  be output stabilizable and  $(\sqrt{Q'}, A')$  be detectable. Since the model matrix  $\underline{A}$  is certainly stable, the block-diagonal form of  $A'$  and  $C'$  shows that output stabilizability of the plant  $(A, B, C)$  is required. The second condition requires detectability of the plant  $(H, A)$ .

The form of the resulting output feedback control law is quite interesting. Indeed, the optimal feedback is of the form

$$u = -K'y' \equiv -[K_p \quad K_m] y' = -K_p y - K_m \underline{y} \quad (5.6-14)$$

Thus, not only the plant output but also the *model* output is required. That is, the model acts as a *compensator* to drive the plant states to zero in such a fashion that the performance output  $z(t)$  follows the model output  $\underline{z}(t)$ .

**Tracking with Model-Following Behavior** Unfortunately, while the model-following regulator problem has a direct solution that is easy to obtain, the model-following *tracker* problem is not so easy. In this situation, we should like the plant (5.6-1) to (5.6-3) to behave like the model

$$\dot{\underline{x}} = \underline{A}\underline{x} + \underline{B}r \quad (5.6-15)$$

$$\underline{z} = \underline{H}\underline{x}, \quad (5.6-16)$$

which is *driven by the reference input*  $r(t)$ . The approach above yields

$$\dot{x}' = \begin{bmatrix} A & 0 \\ 0 & \underline{A} \end{bmatrix} x' + \begin{bmatrix} B \\ 0 \end{bmatrix} u + \begin{bmatrix} 0 \\ B \end{bmatrix} r \equiv A'x' + B'u + G'r, \quad (5.6-17)$$

and thus the derivation in Section 5.3 results in a PI that contains a term in  $r(t)$ , for which the determination of the optimal feedback gains is not easy (Lewis, 1986).

A convenient technique for designing a practical tracker is the *command generator tracker (CGT)* technique, where the tracking problem is converted into a regulator problem (Franklin et al., 1986). In this approach, a generator system is assumed for the reference input. We will apply it here.

Thus, suppose that for some initial conditions the reference command  $r(t)$  satisfies the differential equation

$$r^{(d)} + a_1 r^{(d-1)} + \cdots + a_d r = 0 \quad (5.6-18)$$

for a given degree  $d$  and set of coefficients  $a_i$ . Most command signals of interest satisfy such an equation. For instance, the unit step of magnitude  $r_0$  satisfies

$$\dot{r} = 0, \quad (5.6-19)$$

with  $r(0) = r_0$ , while the ramp (velocity command) with slope  $v_0$  satisfies

$$\ddot{r} = 0, \quad (5.6-20)$$

with  $r(0) = 0$ ,  $\dot{r}(0) = v_0$ . We call (5.6-18) the *command generator system*.

Define the command generator characteristic polynomial as

$$\Delta(s) = s^d + a_1 s^{d-1} + \cdots + a_d \quad (5.6-21)$$

Then denoting  $d/dt$  in the time domain by  $D$ , we may write

$$\Delta(D)r = 0 \quad (5.6-22)$$

Multiplying the augmented dynamics (5.6-17) by  $\Delta(D)$  results in the modified system

$$\dot{\xi} = A'\xi + B'\mu, \quad (5.6-23)$$

where the modified state and control input are

$$\xi = \Delta(D)x' = (x')^{(d)} + a_1 (x')^{(d-1)} + \cdots + a_d x' \quad (5.6-24)$$

$$\mu = \Delta(D)u = u^{(d)} + a_1 u^{(d-1)} + \cdots + a_d u \quad (5.6-25)$$

The reason for these manipulations is that because of (5.6-22), the reference command  $r(t)$  does not appear in (5.6-23). Let us partition  $\xi$  as

$$\xi = \begin{bmatrix} \xi_p \\ \xi_m \end{bmatrix} \quad (5.6-26)$$

Applying  $\Delta(D)$  to the model mismatch error (5.6-7) results in

$$\Delta(D)e = \begin{bmatrix} -H & \underline{H} \end{bmatrix} \xi = H' \xi \quad (5.6-27)$$

This may be expressed in terms of state variables using the observability canonical form (Kailath, 1980), which for scalar  $e(t)$  and  $d = 3$ , for instance, is

$$\dot{\epsilon} = \begin{bmatrix} 0 & 1 & 0 \\ 0 & 0 & 1 \\ -a_3 & -a_2 & -a_1 \end{bmatrix} \epsilon + \begin{bmatrix} 0 \\ 0 \\ H' \end{bmatrix} \xi \equiv F\epsilon + \begin{bmatrix} 0 \\ 0 \\ H' \end{bmatrix} \xi \quad (5.6-28)$$

$$e = \begin{bmatrix} 1 & 0 & 0 \end{bmatrix} \epsilon, \quad (5.6-29)$$

where  $\epsilon(t) = [e \ \dot{e} \ \cdots \ e^{(d-1)}]^T$  is the vector of the error and its first  $d - 1$  derivatives.

Collecting all the dynamics (5.6-23) to (5.6-28) into one system yields

$$\frac{d}{dt} \begin{bmatrix} \epsilon \\ \xi \end{bmatrix} = \left[ \begin{array}{c|c} F & 0 \\ \hline 0 & A' \end{array} \right] \begin{bmatrix} \epsilon \\ \xi \end{bmatrix} + \begin{bmatrix} 0 \\ B' \end{bmatrix} \mu \quad (5.6-30)$$

Let us now note what we have achieved. Using the command generator polynomial  $\Delta(s)$ , we have prefiltered the augmented state, control input, and error to obtain a system (5.6-30) *that is not driven by the reference input  $r(t)$* . Using this system we may now perform an LQ *regulator* design, since if its state goes to zero, the tracking error  $e(t)$  vanishes. That is, by performing a regulator design (using Table 5.3-1) for (5.6-30), we may design a *tracker* control system that causes the original plant to follow the reference command with performance like that of the ideal model.

For the regulator design, we will take the outputs available for feedback in (5.6-30) as

$$v = \begin{bmatrix} I & 0 & 0 \\ 0 & C & 0 \\ 0 & 0 & \underline{C} \end{bmatrix} \begin{bmatrix} \epsilon \\ \xi_p \\ \xi_m \end{bmatrix} \quad (5.6-31)$$

To achieve small error without using too much control energy, we may select the PI (5.6-8) (with  $u(t)$  replaced by  $\mu(t)$ ). According to (5.6-29), the error is given in terms of the state of (5.6-30) by

$$e = h \begin{bmatrix} \epsilon \\ \xi \end{bmatrix}, \quad (5.6-32)$$

with  $h = [1 \ 0 \ \cdots \ 0]$  the first row of the identity matrix. Therefore, in the PI we should weight the state of (5.6-30) using

$$Q' = h^T Q h \quad (5.6-33)$$

Since the observability canonical form is always observable, the augmented system (5.6-30) is detectable if the plant  $(H, A)$  and the model  $(\underline{H}, \underline{A})$  are both detectable.

Now, by applying the equations of Table 5.3-1 to the system (5.6-30) with outputs (5.6-31) and PI weights  $Q'$  and  $R$ , we may compute the control gains in the control law

$$\mu = -[K_\epsilon \quad K_p \quad K_m] \begin{bmatrix} \epsilon \\ C\xi_p \\ C\xi_m \end{bmatrix} \quad (5.6-34)$$

or

$$\Delta(s)u = -K_\epsilon \epsilon - K_p C \Delta(s)x - K_m \underline{C} \Delta(s)\underline{x} \quad (5.6-35)$$

To determine the optimal tracking control input  $u(t)$  for the original system, write this as

$$\Delta(s)(u + K_p y + K_m \underline{y}) = -K_\epsilon \epsilon \equiv -[K_d \quad \cdots \quad K_2 \quad K_1] \begin{bmatrix} e \\ \dot{e} \\ \vdots \\ e^{(d-1)} \end{bmatrix} \quad (5.6-36)$$

Thus, we obtain the transfer function

$$\frac{u + K_p y + K_m \underline{y}}{e} = -\frac{K_1 s^{d-1} + \cdots + K_{d-1} s + K_d}{s^d + a_1 s^{d-1} + \cdots + a_d}, \quad (5.6-37)$$

which may be implemented in reachability canonical form (Kailath, 1980) to obtain the control structure shown in Figure 5.6-1.

**CGT Structure** The structure of this *model-following command generator tracker* (CGT) is very interesting. It consists of an output feedback  $K_p$ , a feedforward compensator that is nothing but the reference model with a gain of  $K_m$ , and an additional feedforward filter in the error channel that guarantees perfect tracking. Note that if  $d = 1$  so that  $r(t)$  is a unit step, the error filter is a PI controller. If  $d = 2$  so that  $r(t)$

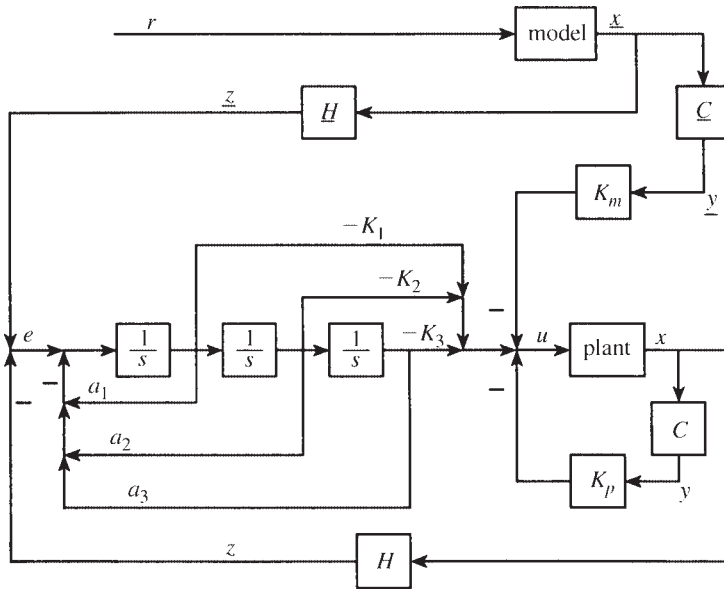


**Figure 5.6-1** Explicit model-following command generator tracker for  $d = 3$ .

is a ramp, the error filter consists of two integrators, resulting in a type-2 system that gives zero steady-state error. What this means is the CGT design *automatically adds the compensator of appropriate structure to guarantee that the system has the correct type for perfect tracking*.

It is extremely interesting to note that the augmented state description (5.6-30) is nothing but the state description of Figure 5.6-1. It should be emphasized that this technique is extremely direct to apply. Indeed, given the prescribed model and the command generator polynomial  $\Delta(s)$ , the system (5.6-30)/(5.6-31) may be written down immediately and the equations in Table 5.3-1 used to select the feedback gains.

A word on the command generator assumption (5.6-22) is in order. In point of fact, for aircraft applications  $r(t)$  is usually the pilot's command input. For control system design it is not necessary to determine the actual coefficients  $a_i$  that describe the pilot command, although this is one approach (Kreindler and Rothschild, 1976). Instead, the performance objectives should be taken into account to select  $\Delta(s)$ . For instance, if it is desired for the aircraft to follow a position command, we may select the command generator  $\dot{r} = 0$ . On the other hand, if the aircraft should follow a rate (velocity) command, we may select  $\ddot{r} = 0$ . Then when the actual command input  $r(t)$  is applied (which may be neither a unit step nor a unit ramp), the aircraft will exhibit the appropriate closed-loop behavior.

### Implicit Model-Following Control

We will now discuss a formulation that results in a radically different sort of control scheme. In explicit model following, which is also called *model in the system control*,

the model explicitly appeared in the controller as a feedforward compensator. On the other hand, implicit model following, also called *model in the performance index*, is a completely different approach in which the model does not appear in the control structure. Indeed, implicit model following can be viewed simply as a technique for selecting the weighting matrices in the PI in a meaningful way [see Armstrong (1980) and Kreindler and Rothschild (1976)].

Suppose that the performance output  $z(t)$  of the plant prescribed by (5.6-1) to (5.6-3) is required to follow the model given by

$$\dot{z} = \underline{A}z \quad (5.6-38)$$

The model matrix  $\underline{A}$  has poles corresponding to desirable handling qualities of the plant, such as may be found in *Mil. Spec. 1797* (1987) and Stern and Henke (1971).

When the control objective is met, the performance output will satisfy the differential equation (5.6-38). Thus, we may define an error by

$$e = \dot{z} - \underline{A}z \quad (5.6-39)$$

This is a different sort of error than we have seen before.

To make  $e(t)$  small without using too much control energy, we may choose  $u(t)$  to minimize the PI (5.6-8). Since  $\dot{z} = HAx + HBu$ , this becomes

$$J = \frac{1}{2} \int_0^\infty [(HAx + HBu - \underline{A}Hx)^T Q (HAx + HBu - \underline{A}Hx) + u^T R u] dt \quad (5.6-40)$$

or

$$J = \frac{1}{2} \int_0^\infty (x^T Q' x + 2x^T W u + u^T R' u) dt, \quad (5.6-41)$$

where

$$\begin{aligned} Q' &= (HA - \underline{A}H)^T Q (HA - \underline{A}H) \\ W &= (HA - \underline{A}H)^T Q HB, \quad R' = (B^T H^T Q HB + R) \end{aligned} \quad (5.6-42)$$

The additional term in  $W$  is a *cross-weighting* between  $u(t)$  and  $x(t)$ .

In Table 5.3-1 we have given the LQ regulator design equations to determine the optimal output feedback gains for the case  $W = 0$ . By using techniques like those in that derivation (see the problems), we may derive the modified design equations for the case of  $W \neq 0$ . They are

$$0 = A_c^T P + P A_c + Q + C^T K^T R K C - W^T K C - C^T K^T W^T \quad (5.6-43)$$

$$0 = A_c S + S A_c^T + X \quad (5.6-44)$$

$$0 = R K C S C^T - (P B + W)^T S C^T, \quad (5.6-45)$$

where

$$A_c = A - B K C \quad (5.6-46)$$



The optimal cost is still given by

$$J - \frac{1}{2}\text{tr}(PX) \quad (5.6-47)$$

To find the optimal output feedback gains in

$$u = -Ky \quad (5.6-48)$$

for implicit model following, it is only necessary to solve these design equations using  $Q'$ ,  $W$ , and  $R'$ . For this, a technique like that in Table 5.3-2 may be used. Alternatively, algorithms such as the Simplex or Davidon-Fletcher-Powell may be employed.

Note that implicit model following in the regulator case is nothing but a convenient technique for selecting the PI weighting matrices  $Q'$ ,  $R'$  (and  $W$ ) to guarantee desirable behavior, since the right-hand sides of (5.6-42) are known. Indeed, it is reasonable to select  $R = \rho I$  and  $Q = I$ .

It is possible to design a tracking control system using implicit model following by using the CGT approach. However, this system has an undesirable structure from the point of view of aircraft control since it generally requires derivatives of the performance output  $z(t)$ .

**Example 5.6-1: Automatic Flare Control by Model-Following Design.** Model-following design may be used to design a control system that makes the aircraft behave like an ideal model (Kreindler and Rothschild, 1976). Such a model may be constructed using the military flying qualities requirements discussed in Section 4.3 so that it has good performance. However, this is not the only use for model-following design in aircraft controls.

In this example, we complete the design of the automatic landing system that was begun in Example 5.5-5. There, we constructed a glide-slope coupler whose function is to conduct an aircraft down a glide path toward the runway. Here we will show that explicit model-following design may be used to design the automatic flare control system whose function is to cause the aircraft to flare gently to a touchdown.

(a) *Determining the Reference Model.* The control system is basically an altitude-hold system with a time-varying reference or commanded altitude  $\underline{h}t$ . A gentle flare is described by an exponential, so that the commanded altitude should obey the differential equation

$$\dot{\underline{h}} = -\frac{1}{\tau}\underline{h} + r, \quad \text{initial condition } \underline{h}(0) = \underline{h}_0, \quad (1)$$

where  $\tau$  and  $\underline{h}_0$  are chosen for the desired flare characteristics. Equation (1) is the reference model (see 5.6-15)

$$\begin{aligned} \dot{\underline{x}} &= \underline{A}\underline{x} + \underline{B}r \\ \underline{z} &= \underline{H}\underline{x}, \end{aligned} \quad (2)$$

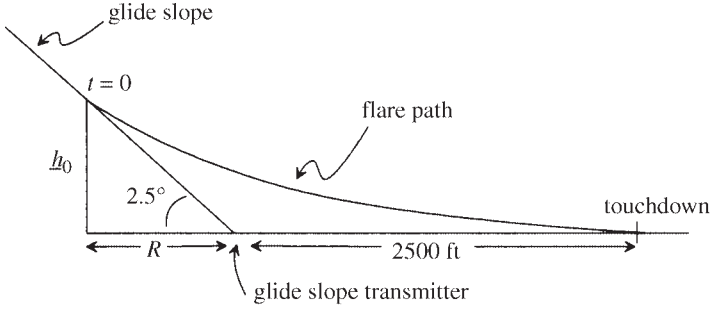


**Figure 5.6-2** Flare-path geometry.

with  $\underline{A} = -1/\tau$ ,  $\underline{B} = 1$ ,  $\underline{H} = 1$ . Thus,  $\underline{z} = \underline{x} = \underline{h}$ . The model reference input is  $r(t)$ , which is equal to the constant value of zero in this example. Then

$$\underline{h}(t) = \underline{h}_0 e^{-t/\tau} \quad (3)$$

The geometry of the flare path shown in Figure 5.6-2 may be used to determine the flare time constant  $\tau$  and initial altitude  $\underline{h}_0$  (see Blakelock, 1965). In Example 5.5-5 we designed a glide-slope coupler for a total velocity of  $V_T = 250 \text{ ft/s}$ . Thus, on the glide path the rate of descent is

$$\dot{h} = V_T \sin(-2.5^\circ) \approx -V_T \frac{2.5}{57.2958} = -10.91 \text{ ft/s} \quad (4)$$

The flare control system is turned on at time  $t = 0$  shown in the figure. Therefore, for (1) we obtain  $\dot{\underline{h}}(0) = -10.91$ , and

$$\underline{h}_0 = -\tau \dot{\underline{h}}(0) = 10.91 \tau \text{ ft} \quad (5)$$

The distance  $R$  is thus given by

$$R = \frac{\underline{h}_0}{\tan(2.5^\circ)} \approx \underline{h}_0 \times \frac{57.2958}{2.5} = V_T \tau \text{ ft} \quad (6)$$

If it is desired to touch down 2500 ft beyond the glide-slope transmitter, and if we assume that  $\underline{h}(t)$  given in (1) vanishes in  $4\tau$  seconds, then

$$4\tau V_T = R + 2500 = V_T \tau + 2500 \quad (7)$$

or

$$3\tau V_T = 2500, \quad (8)$$

so that

$$\tau = 3.333 \text{ s} \quad (9)$$

This yields the reference model

$$\dot{h} = -0.3h + r, \quad h_0 = 36.37 \text{ ft}, \quad (10)$$

with reference input  $r(t)$  taking the constant value of zero.

**(b) Basic Aircraft and Controller.** The flare control system is shown in Figure 5.6-3. For small flight-path angles the aircraft altitude is given by

$$\dot{h} = V_T \sin \gamma = V_T \sin(\theta - \alpha) \approx V_T \theta - V_T \alpha, \quad (11)$$

which is the same as the equation in Example 5.5-5 for  $\dot{d}$  (with  $d$  the off-glide path distance) without the term in  $\gamma_r$ . What this means is that an altitude-hold system is given by the lower  $d$ -hold channel in the glide-slope coupler in Figure 5.5-8, with  $d$  replaced everywhere by  $h$  and  $\gamma_r$  removed. Indeed, the control gains in that system were used as an initial stabilizing guess in the LQ design for this example.

In this example we want to illustrate the model-following design procedure for the  $h$  control channel only. A complete design would include a second velocity-hold channel exactly as in the glide-scope coupler.

We used low-velocity longitudinal Jacobians for a medium-sized transport linearized about  $V_T = 250$  ft/s,  $cg = 0.25\bar{c}$ , as in Example 5.5-5. For the flare control system  $h$  channel, we may use the short-period approximation, with, however,  $\theta$  retained due to the need to compute the altitude using (11).

The state of the aircraft plus the lead compensator is

$$x = [\alpha \quad \theta \quad q \quad h \quad \delta_e \quad x_1]^T \quad (12)$$

with  $x_1$  the compensator state (see Figure 5.6-3). The performance output is

$$z = h = [0 \quad 0 \quad 0 \quad 1 \quad 0 \quad 0]x = Hx \quad (13)$$

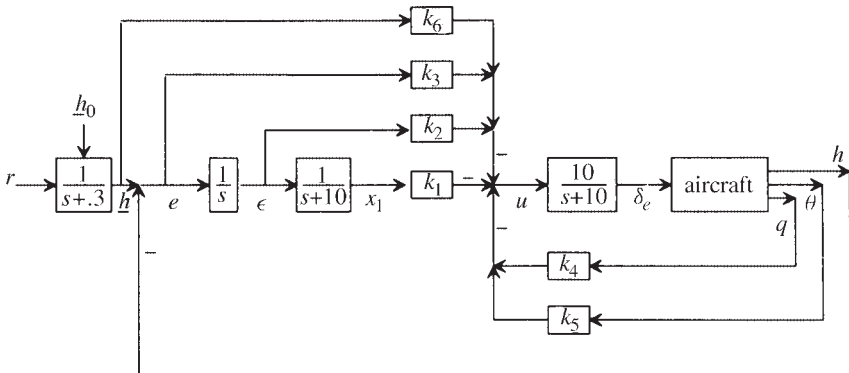


Figure 5.6-3 Automatic flare control system.

and the control input  $u(t)$  is the elevator servo command. According to the figure, the measured outputs corresponding to the aircraft and the lead compensator are

$$y = [x_1 \quad q \quad \theta]^T \quad (14)$$

(c) *Explicit Model-Following Control.* We should like the reference output  $z(t)$  to follow the model altitude  $\underline{h}(t)$  given by (2)/(10). Since the model's reference input  $r(t)$  has the constant value of zero,  $r(t)$  satisfies the differential equation

$$\dot{r} = 0, \quad (15)$$

so that the command generator polynomial (5.6-21) is given by

$$\Delta(s) = s \quad (16)$$

The model mismatch latitude error (5.6-7) is given by

$$e = \underline{h} - h \quad (17)$$

Therefore, the observability canonical form realization (5.6-28) is

$$\dot{\epsilon} = [-H \quad \underline{H}] \xi = [0 \quad 0 \quad 0 \quad -1 \quad 0 \quad 0 \mid 1] \xi, \quad (18)$$

with  $\xi(t)$  the modified state  $\Delta(s)[x^T \quad \underline{x}]^T$ .

According to (18),  $F = 0$  in the augmented system (5.6-30). Thus, we are required to incorporate an integrator in the control system [see (5.6-37) and Figure 5.6-1]. This we have already done in Figure 5.6-3.

The overall dynamics of the modified system (5.6-30) are given by

$$\begin{aligned} \dot{X} &= AX + Bu \\ y &= CX, \end{aligned} \quad (19)$$

with  $X$  the augmented state that contains the basic aircraft and compensator dynamics, the model dynamics (10), and the integrator required by (18). For convenience, we will order the states differently than in (5.6-30), taking

$$X = [\alpha \quad \theta \quad q \quad h \quad \delta_e \quad x_1 \quad \epsilon \quad \underline{h}]^T \quad (20)$$

According to Figure 5.6-3, the outputs are

$$Y = [x_1 \quad \epsilon \quad e \quad q \quad \theta \quad \underline{h}]^T \quad (21)$$

The model state  $\underline{h}$  is included as an output due to the development leading to (5.6-37).

With this structure, the plant matrices are given by

$$A = \begin{bmatrix} -0.64627 & 0 & 1 & 0 & 0 & 0 & 0 & 0 \\ 0 & 0 & 1 & 0 & 0 & 0 & 0 & 0 \\ -0.7739 & 0 & -0.52977 & 0 & -0.011 & 0 & 0 & 0 \\ -250 & 250 & 0 & 0 & 0 & 0 & 0 & 0 \\ 0 & 0 & 0 & 0 & -10 & 0 & 0 & 0 \\ 0 & 0 & 0 & 0 & 0 & -10 & 1 & 0 \\ 0 & 0 & 0 & -1 & 0 & 0 & 0 & 1 \\ 0 & 0 & 0 & 0 & 0 & 0 & 0 & -0.3 \end{bmatrix} \quad (22)$$

$$B = \begin{bmatrix} 0 \\ 0 \\ 0 \\ 0 \\ 10 \\ 0 \\ 0 \\ 0 \\ 0 \end{bmatrix} \quad (23)$$

$$C = \begin{bmatrix} 0 & 0 & 0 & 0 & 0 & 1 & 0 & 0 \\ 0 & 0 & 0 & 0 & 0 & 0 & 1 & 0 \\ 0 & 0 & 0 & -1 & 0 & 0 & 0 & 1 \\ 0 & 0 & 57.2958 & 0 & 0 & 0 & 0 & 0 \\ 0 & 57.2958 & 0 & 0 & 0 & 0 & 0 & 0 \\ 0 & 0 & 0 & 0 & 0 & 0 & 0 & 1 \end{bmatrix} \quad (24)$$

Then, according to Figure 5.6-3, the control input  $u(t)$  is given by

$$u = -Ky = (k_1x_1 + k_2e + k_3\dot{e} + k_4q + k_5\theta + k_6\dot{h}) \quad (25)$$

The control structure shown in Figure 5.6-3 and described here is nothing but the structure required for model following according to Figure 5.6-1.

(d) *PI and LQ Control Gain Design.* Although the explicit model-following design technique discussed in this section involves using the LQ *regulator* design equations from Table 5.3-1 on the augmented system (5.6-30), we have found that the results are generally better using LQ *tracker design with time-weighted PI*. Thus, we used the design equations in Table 5.5-1 with the auxiliary matrices

$$\begin{aligned} G &= [0 \ 0 \ 0 \ 0 \ 0 \ 0 \ 0 \ 0 \ 1]^T \\ F &= [0 \ 0 \ 0 \ 0 \ 0 \ 0 \ 0]^T \\ H &= [0 \ 0 \ 0 \ -1 \ 0 \ 0 \ 0 \ 1]^T, \end{aligned} \quad (26)$$

which were determined from Figure 5.6-3. (Note the redefinition of the matrix  $H$ .)

The PI was selected as

$$J = \frac{1}{2} \int_0^\infty (qt^2\tilde{e}^2 + \tilde{u}^2)dt \quad (27)$$

It is important to note that a sensible formulation of the problem has resulted in the appearance of *only one design parameter,  $q$ , in the PI*. Thus, we will not be faced with tuning many design parameters in an effort to obtain suitable responses. In view of the fact that there are eight states and six control gains to determine, this is quite significant. No steady-state error weighting is used in the PI since the plant is of type 1.

After several design iterations using the software of Appendix B to solve for  $K$  using the design equations in Table 5.5-1, we decided on  $q = 0.001$  and obtained the control gains

$$K = [593.4 \quad -59.30 \quad 6.154 \quad -0.56 \quad -1.00 \quad -0.01852] \quad (28)$$

The closed-loop poles were at

$$\begin{aligned} & -0.15 \pm j0.23 \\ & -0.15 \pm j1.02 \\ & -0.30, -0.92 \\ & -9.43, -10.22 \end{aligned} \quad (29)$$

Note that the model pole of  $s = -0.3$  has not moved since it is uncontrollable.

(e) *Simulation and Discussion.* The controlled flare is shown in Figure 5.6-4—it matches the desired flare  $\underline{h}(t)$  very well. To obtain this graph it is necessary to use initial conditions  $x(0)$  corresponding to the equilibrium state on the glide slope from Example 5.5-5. The flight-path angle  $\gamma$  is shown in Figure 5.6-5a. Shown in Figure 5.6-5b is the elevator command,  $\delta_e$ ; in examining this figure recall that upward elevator deflection (i.e., back stick) is defined as negative.

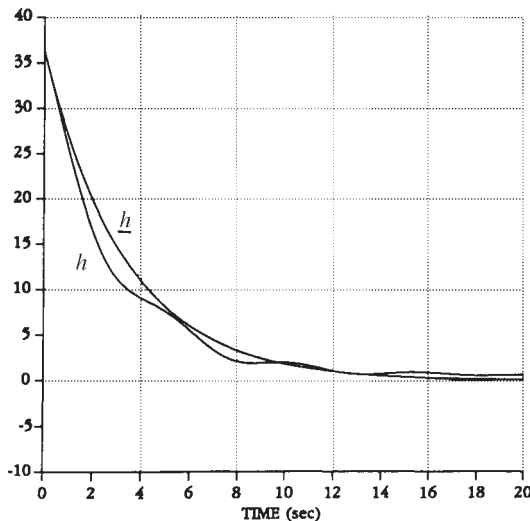
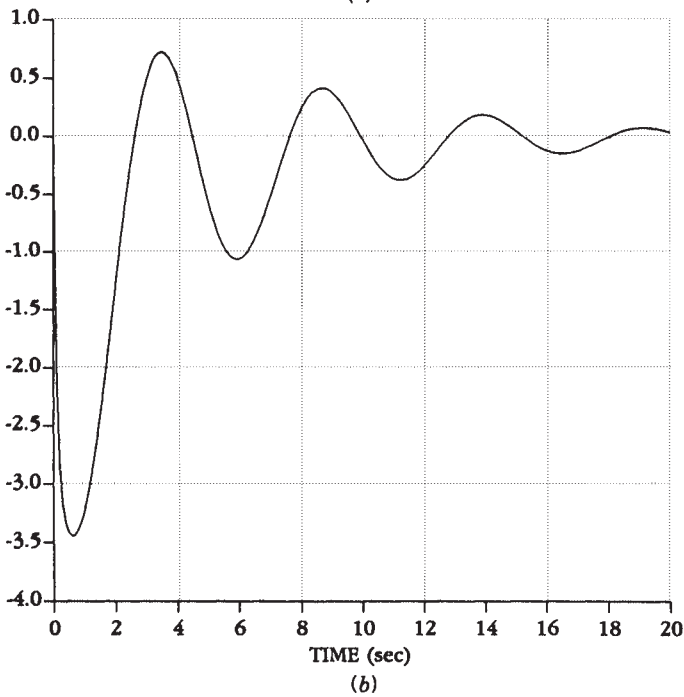
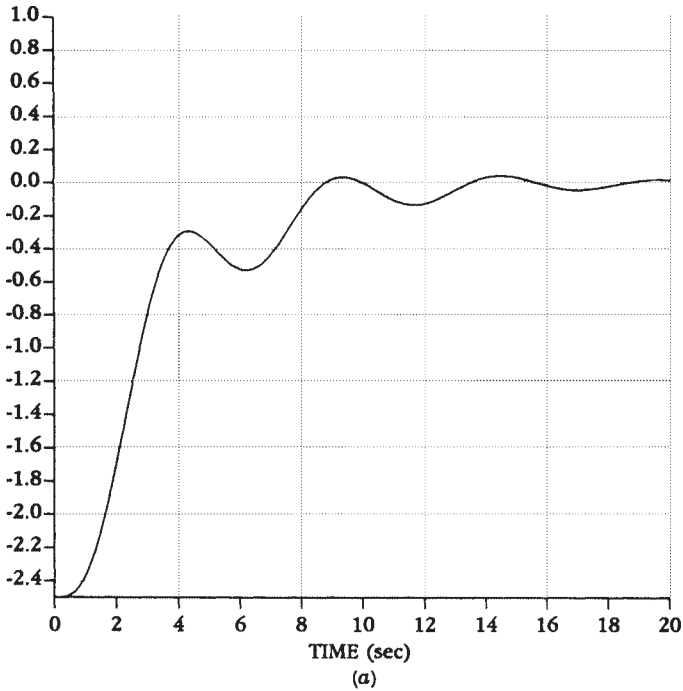


Figure 5.6-4 Controlled flare, altitude in feet.



**Figure 5.6-5** Aircraft response during controlled flare: (a) flight-path angle  $\gamma$  (deg); (b) elevator command  $\delta_e$  (deg).

The poles in (29) are quite slow and there is one badly damped pair. However, the time responses are acceptable. This is because the flare control system is engaged with the aircraft on the glide path, so that there are no sudden reference command changes to excite the underdamped mode. Moreover, the flare is gentle, so that the time scale of the desired motion is on the order of the time scale of the closed-loop poles.

Although the control gain from the model state  $\underline{h}$  to elevator servo command  $u$  is small, it plays a very important function. As may be seen in Blakelock (1965), the tendency of the flare control system without model state feedforward is to lag behind the desired response. This results in a flare that is always below the desired path and requires a modification in the design flare time constant  $\tau$ . The feedforward of  $h$  corrects this problem in a simple manner.

Using the gains in (28), the compensator in the forward error channel of Figure 5.6-3 has the transfer function

$$\frac{k_1}{s(s+10)} + \frac{k_2}{s} + k_3 = \frac{6.154(s+0.364)}{s+10}, \quad (30)$$

where the pole at  $s = 0$  has been canceled by a zero at  $s = 0$  to yield a simplified compensator. Thus, there is no integrator in the feedforward path, and the model-following behavior does not rely on the system being of type 1. The ratio of the zero to the poles in the lead compensator is excessive, and the design may be repeated using, for instance, a compensator pole at  $s = -5$  instead of  $s = -10$  (and no integrator). ■

## 5.7 LINEAR QUADRATIC DESIGN WITH FULL STATE FEEDBACK

In the previous sections of this chapter we have seen how to design control systems using a variety of modern control techniques that rely only on measuring a system *output*. These output feedback approaches are very suitable for aircraft control design since they allow us to design a compensator with any desired dynamical structure. This cannot be accomplished using full state feedback.

In this section we intend to explore full state-variable feedback in the linear quadratic regulator (LQR) for the insight it provides. That is, for the system

$$\dot{x} = Ax + Bu, \quad (5.7-1)$$

with  $x \in \mathbf{R}^n$ ,  $u \in \mathbf{R}^m$ , we want to examine control laws of the form

$$u = -Kx, \quad (5.7-2)$$

which result in the closed-loop system

$$\dot{x} = (A - BK)x \equiv A_c x \quad (5.7-3)$$

In the previous sections we defined the measurable output

$$y = Cx \quad (5.7-4)$$



and restricted ourselves to controls of the form

$$u = -Ky = -KCx \quad (5.7-5)$$

Here we plan to examine the simplifications in the control design equations that come about when  $C = I$ . As we will see, we can draw some conclusions that will give more insight into modern control theory.

### The Relevance of State Feedback

Although all the states are seldom measurable in aircraft control systems, we have several objectives for looking at state-variable feedback design in this section. First, it is clear that state feedback is just the special case of output feedback with  $C = I$ . That is, it assumes that all the states can be measured. Thus, the theory for state-variable feedback will tell us *the best performance that we can expect* in the closed-loop system by using static output feedback, where all of the states are not available as measurements.

Second, the output feedback design equations in Tables 5.3-1, 5.4-1, and 5.5-1 are not the LQR equations with which the reader may be familiar. We would like to show how they relate to the more traditional Riccati equation.

If all the states are involved in the feedback, there are some very powerful stability results of which the reader should be aware. Indeed, under some reasonable assumptions it is possible to *guarantee the stability of the closed-loop system* using the optimal LQ state feedback gain. Similar theoretical results for output feedback have not yet been discovered.

Finally, we will need state feedback in Chapter 6 when we discuss dynamic regulators and LQR/LTR robust design. A limitation of state feedback is that all the states are not generally available, but only the outputs are measured. However, we can design a full state feedback  $u = -Kx$  and then a dynamic observer to estimate the states from the measured outputs. Then the state *estimates*  $\hat{x}$  may be fed back, instead of the states themselves, in a control law such as  $u = -K\hat{x}$ . The combination of state feedback plus an observer is called a *dynamic regulator*. It is a compensator of the sort used in classical control, but it is easy to design for multivariable systems, overcoming a deficiency of the classical approach, where multiloop and MIMO systems are hard to deal with.

### The Riccati Equation and Kalman Gain

By setting  $C = I$  all of our work in Sections 5.3 and 5.4 applies to state feedback. That is, all the work of deriving the control design equations for state feedback has already been done. Let us see how the LQR design equations simplify in the case of full state feedback.

To regulate the performance output

$$z = Hx \quad (5.7-6)$$

to zero, let us select the PI

$$J = \frac{1}{2} \int_0^{\infty} (x^T Q x + u^T R u) dt, \quad (5.7-7)$$

with  $Q = H^T H \geq 0$ ,  $R > 0$ .

The output feedback gain  $K$  in (5.7-5) that minimizes the PI may be found using the design equations in Table 5.3-1. To obtain the optimal state feedback in (5.7-2), we may simply set  $C = I$  in the table. The results are

$$0 = A_c^T P + P A_c + Q + K^T R K \quad (5.7-8)$$

$$0 = A_c S + S A_c^T + X \quad (5.7-9)$$

$$K = R^{-1} B^T P S S^{-1}, \quad (5.7-10)$$

where the initial state autocorrelation is

$$X = E\{x(0)x^T(0)\} \quad (5.7-11)$$

The problems in computing the output feedback gains include the need to know  $X$  and the selection of an initial stabilizing gain  $K_0$  for the algorithm in Table 5.3-2. Moreover, although we gave conditions for the convergence to a local minimum of the algorithm in that table, little is known about the necessary and sufficient conditions for the existence of an output feedback gain that satisfies the design equations and stabilizes the plant.

All of these problems vanish in the case of state feedback, as we will now show. According to (5.7-10),

$$K = R^{-1} B^T P, \quad (5.7-12)$$

that is, the solution  $S$  to (5.7-9) *is not needed to solve for the optimal state feedback gain*. The gain  $K$  is called the *Kalman gain*. Using (5.7-12) in (5.7-8) yields

$$0 = A_c^T P + P A_c + Q + P B R^{-1} B^T P \quad (5.7-13)$$

or, according to (5.7-3),

$$\begin{aligned} 0 &= (A - B R^{-1} B^T P)^T P + P(A - B R^{-1} B^T P) \\ &\quad + Q + P B R^{-1} B^T P \\ 0 &= A^T P + P A + Q - P B R^{-1} B^T P \end{aligned} \quad (5.7-14)$$

This matrix quadratic equation is called the *algebraic Riccati equation (ARE)*. It is named after Count J. F. Riccati, who used a related equation in the study of heat flow (Riccati, 1724). Since the equation is equal to its own transpose (verify!), the solution  $P$  is symmetric ( $P = P^T$ ).

Since  $S$  is not needed to find the optimal state feedback gain  $K$ , this gain does not depend on  $X$  in (5.7-9). That is, contrary to the case with output feedback, to compute the optimal state feedback gains *no information about the initial state  $x(0)$  is needed*. Thus, it is not required to take expected values of the PI as we did in Section 5.3. Therefore, according to the development in that section, the optimal cost is given by

$$J = \frac{1}{2}x^T(0)Px(0) \quad (5.7-15)$$

The state feedback LQR is summarized in Table 5.7-1.

Setting  $C = I$  has allowed us to replace the solution of three coupled matrix equations by the solution of *one nonlinear matrix equation* for  $P$ . Then the Kalman gain is given in terms of  $P$  by (5.7-17). The importance of this is that there are many good techniques for solving the Riccati equation using *standard software packages* [e.g., ORACLS (Armstrong, 1980), MATRIX<sub>x</sub> (1989), PC-MATLAB (Moler et al., 1987), and IMSL (1980)]. On the other hand, the specialized software for solving the output feedback problem in Tables 5.3-1, 5.4-1, or 5.5-1 can be used to solve the full state feedback problem by setting  $C = I$ .

### Guaranteed Closed-Loop Stability

The theory for the LQ regulator with state feedback is well developed. In fact, the next stability result is so fundamental that we set it apart as a theorem (Lewis, 1986). The notion of detectability was introduced while discussing Table 5.3-2. We say that  $(A, H)$  is detectable if there exists an  $L$  so that  $A - LH$  is stable; this amounts to

**TABLE 5.7-1 LQR with State Feedback**

---

*System Model*

$$\dot{x} = Ax + Bu$$

*Control*

$$u = -Kx$$

*Performance Index*

$$J = \frac{1}{2} \int_0^\infty (x^T Q x + u^T R u) dt$$

*Optimal LQ Design Equations*

- Algebraic Riccati equation (ARE)

$$0 = A^T P + PA + Q - PBR^{-1}B^T P \quad (5.7-16)$$

- Kalman gain

$$K = R^{-1}B^T P \quad (5.7-17)$$

*Optimal Cost*

$$J = \frac{1}{2}x^T(0)Px(0)$$


---

the observability of the unstable modes of  $A$ . We say that  $(A, B)$  is *stabilizable* if there exists a feedback gain  $K$  such that  $A_c = A - BK$  is stable. This amounts to the controllability of the unstable modes of  $A$ .

**Theorem.** Let  $H$  be any matrix so that  $Q = H^T H$ . Suppose that  $(H, A)$  is detectable. Then  $(A, B)$  is stabilizable if and only if:

- (a) There exists a unique positive-semidefinite solution  $P$  to the Riccati equation.
- (b) The closed-loop system (5.7-3) is asymptotically stable if the Kalman gain  $K$  is computed using (5.7-17) in terms of this positive-semidefinite solution  $P$ . ■

This result is at the heart of modern control theory. Exactly as in classical control, it allows us to examine *open-loop* properties (i.e., detectability and stabilizability) and draw conclusions about the closed-loop system. As long as  $(H, A)$  is detectable, so that all the unstable modes appear in the PI, and  $(A, B)$  is stabilizable, so that the control  $u(t)$  has sufficient influence on the system, the LQ regulator using state feedback will *guarantee* a stable closed-loop system. A similar easily understandable result has not yet been discovered for output feedback.

Detectability is implied by the stronger condition of observability, which is easy to check by verifying that the observability matrix has full rank  $n$  (see Section 5.3). Stabilizability is implied by controllability, which is easy to check by verifying that the controllability matrix has full rank  $n$  (see Section 5.2). Thus, the controllability of  $(A, B)$  and the observability of  $(H, A)$  guarantee closed-loop stability of the LQ regulator with state feedback.

This theorem, coupled with the availability of good software for solving the ARE, means that it is always straightforward to find a state-variable feedback gain  $K$  that stabilizes any stabilizable plant, no matter how many inputs or outputs it has.

Since output feedback amounts to a partial state feedback, it is clear that if the conditions of the theorem do not hold, we should not expect to be able to stabilize the plant using any output feedback (unless time-dependent weighting of the form  $t^k$  is used in the PI to avoid the observability requirement; see Section 5.5). Thus, in the case of output feedback design these conditions should hold *as a minimum*. In fact, we saw that the algorithm of Table 5.3-2 requires the detectability of  $(\sqrt{Q}, A)$  and the output stabilizability of the system. Output stabilizability is a stronger condition than stabilizability.

In the case of a full state feedback, it is possible in simple examples to give a direct correlation between the PI weighting matrices and the closed-loop poles. Let us investigate this connection for systems obeying Newton's laws.

**Example 5.7-1: LQR with State Feedback for Systems Obeying Newton's Laws** In this example we will see that in the case of full state feedback for simple systems there is a direct connection between the PI weights and the closed-loop damping ratio and natural frequency.

Systems obeying Newton's laws may be described by the state equation

$$\dot{x} = \begin{bmatrix} 0 & 1 \\ 0 & 0 \end{bmatrix} x + \begin{bmatrix} 0 \\ 1 \end{bmatrix} u = Ax + Bu, \quad (1)$$

where the state is  $x = [d \quad v]^T$  with  $d(t)$  the position and  $v(t)$  the velocity and the control  $(u)t$  is an acceleration input. Indeed, note that (1) says nothing other than  $\ddot{d} = u$ , or  $a = F/m$ .

Let the PI be

$$J = \frac{1}{2} \int_0^\infty (x^T Q x + u^2) dt, \quad (2)$$

with  $Q = \text{diag}\{q_d^2, q_v\}$ . In this example, we will see the effect of  $q_d$  and  $q_v$ . Note that it is not useful to include a separate control weighting  $r$ , since only the ratios  $q_d^2/r$  and  $q_v/r$  are important in  $J$ .

Since the Riccati solution  $P$  is symmetric, we may assume that

$$P = \begin{bmatrix} p_1 & p_2 \\ p_2 & p_3 \end{bmatrix} \quad (3)$$

for some scalars  $p_1, p_2, p_3$  to be determined. Using  $A, B, Q$ , and  $r = 1$  in the Riccati equation in Table 5.7-1 yields

$$\begin{aligned} 0 = & \begin{bmatrix} 0 & 0 \\ 1 & 0 \end{bmatrix} \begin{bmatrix} p_1 & p_2 \\ p_2 & p_3 \end{bmatrix} + \begin{bmatrix} p_1 & p_2 \\ p_2 & p_3 \end{bmatrix} \begin{bmatrix} 0 & 0 \\ 1 & 0 \end{bmatrix} + \begin{bmatrix} q_d^2 & 0 \\ 1 & q_v \end{bmatrix} \\ & - \begin{bmatrix} p_1 & p_2 \\ p_2 & p_3 \end{bmatrix} \begin{bmatrix} 0 & 0 \\ 1 & 0 \end{bmatrix} \begin{bmatrix} p_1 & p_2 \\ p_2 & p_3 \end{bmatrix} \end{aligned} \quad (4)$$

The reader should verify that this may be multiplied out to obtain the three scalar equations

$$0 = -p_2^2 + q_d^2 \quad (5a)$$

$$0 = p_1 - p_2 p_3 \quad (5b)$$

$$0 = 2p_2 - p_3^2 + q_v \quad (5c)$$

Solving these equations in the order (5a), (5c), (5b) gives

$$p_2 = q_d \quad (6a)$$

$$p_3 = \sqrt{2} \sqrt{q_d + \frac{q_v}{2}} \quad (6b)$$

$$p_1 = q_d \sqrt{2} \sqrt{q_d + \frac{q_v}{2}}, \quad (6c)$$

where we have selected the signs that make  $P$  positive definite.

According to Table 5.7-1, the Kalman gain is equal to

$$K + R^{-1}B^T P = \begin{bmatrix} 0 & 1 \end{bmatrix} \begin{bmatrix} p_1 & p_2 \\ p_2 & p_3 \end{bmatrix} = \begin{bmatrix} p_2 & p_3 \end{bmatrix} \quad (7)$$

Therefore,

$$K = \begin{bmatrix} q_d & \sqrt{2}\sqrt{q_d + \frac{q_v}{2}} \end{bmatrix} \quad (8)$$

It should be emphasized that in the case of state feedback we have been able to find an *explicit expression* for  $K$  in terms of the PI weights. This is not possible for output feedback.

Using (8), the closed-loop system matrix is found to be

$$A_c = (A - BK) = \begin{bmatrix} 0 & 1 \\ -q_d & -\sqrt{2}\sqrt{q_d + \frac{q_v}{2}} \end{bmatrix} \quad (9)$$

Therefore, the closed-loop characteristic polynomial is

$$\Delta_c(s) = |sI - A_c| = s^2 + 2\zeta\omega s + \omega^2, \quad (10)$$

with the optimal natural frequency  $\omega$  and damping ratio  $\zeta$  given by

$$\omega = \sqrt{q_d}, \quad \zeta = \frac{1}{\sqrt{2}}\sqrt{1 + \frac{q_v}{2q_d}} \quad (11)$$

It is now clear how selection of the weights in the PI affects the closed-loop behavior. Note that if no velocity weighting  $q_v$  is used, the damping ratio becomes the familiar  $1/\sqrt{2}$ .

Note that  $(A, B)$  is reachable since

$$U = \begin{bmatrix} B & AB \end{bmatrix} = \begin{bmatrix} 0 & 1 \\ 1 & 0 \end{bmatrix} \quad (12)$$

is nonsingular. The observability matrix is

$$O = \begin{bmatrix} \sqrt{Q} \\ \sqrt{QA} \end{bmatrix} = \begin{bmatrix} q_d & 0 \\ 0 & \sqrt{d_v} \\ 0 & q_d \\ 0 & 0 \end{bmatrix} \quad (13)$$

Therefore, observability is guaranteed if and only if the position weighting  $q_d$  is greater than zero. Then the theorem says that we should be able to rely on a stable closed-loop system. Examining (11) makes it clear that this is indeed the case. ■

## 5.8 DYNAMIC INVERSION DESIGN

In this chapter we have presented some basic tools of modern control design for linear systems. Since aircraft are inherently nonlinear systems, applying these linear design tools means that one must design several linear controllers and then gain schedule them over the operating regime of the aircraft (see Problem 5.4-9). There are alternative techniques that can deal directly with the known nonlinearities of the aircraft dynamics using these nonlinearities in the controller to improve the system performance. These techniques are generally based on the *feedback* linearization approach (Slotine and Li, 1991) developed by Hunt et al. (1983) and Jacubczyk and Respondek (1980).

In this section we introduce the technique known as *dynamic inversion*, which has grown popular in recent years (Adams and Banda, 1993; Lane and Stengel, 1988; Enns et al., 1994; Tomlin et al., 1995; Wright Laboratory Report, 1996). The dynamic inversion controller takes into account the nonlinearities of the aircraft and thus does not require gain scheduling. As such it is suitable for a wide range of operating conditions, including high-angle-of-attack and hypervelocity design. To simulate the dynamic inversion control scheme, we use the technique of computer simulation for nonlinear dynamical systems given in Section 3.3. For this, we use the MATLAB software (*MATLAB Reference Guide*, 1994).

Though dynamics inversion is used for nonlinear systems and shows its true power there, we will start this section with a linear derivation and design example to get a feel for how it works. Then, we will study dynamic inversion controls design and simulation for a nonlinear aircraft.

### Dynamic Inversion for Linear Systems

**Derivation of Dynamic Inversion Controller** Let the plant be described in state-variable form by

$$\dot{x} = Ax + Bu \quad (5.8-1)$$

$$y = Cx, \quad (5.8-2)$$

with state  $x(t) \in \mathbf{R}^n$ , control input  $u(t) \in \mathbf{R}^m$ , and output  $y(t) \in \mathbf{R}^p$ . The entire state  $x(t)$  is available for feedback purposes.

It is assumed that the system is *square*, that is, the number of inputs  $m$  is equal to the number of outputs  $p$  so that vectors  $u(t)$  and  $y(t)$  have the same dimension. This often occurs for aircraft systems, since there is often one control actuator per degree of freedom. If this is not the case, we may make some amendments to the following procedure. For instance, in modern high-performance aircraft, there may be more actuators than degrees of freedom (e.g., elevators, horizontal stabilators, and thrust vectoring for longitudinal dynamics). In this event, the control dimension may be reduced to obtain a square system by several techniques, including ganging, pseudo control, and daisy chaining (Wright Laboratory Report, 1996). These

are all techniques for *allocating control effectiveness* among several redundant actuators.

For a square system, then, it is desired to control the output  $y(t)$  so that it follows a desired reference trajectory  $r(t)$ . Define the tracking error as

$$e(t) = r(t) - y(t) \quad (5.8-3)$$

In dynamic inversion, one differentiates the output  $y(t)$  until the control  $u(t)$  appears in the expression for the derivative. This is known technically as *input-output feedback linearization* (Slotine and Li, 1991). Taking the first derivative yields

$$\dot{y} = C\dot{x} = CAx + CBu, \quad (5.8-4)$$

where  $u(t)$  appears if matrix  $CB$  is not zero. In this case, since the system is square, so is matrix  $CB$ . If  $CB$  is nonsingular, then we are done. If  $CB = 0$ , then we continue to differentiate, obtaining

$$\ddot{y} = C\dot{x} = CA\dot{x} + CB\dot{u} = CA^2x + CABu \quad (5.8-5)$$

If matrix  $CAB$  is nonsingular, we are done. If  $CAB = 0$ , we differentiate again, continuing until the coefficient multiplying  $u(t)$  is nonzero.

For aircraft, it is generally the case that  $CB$  is nonsingular. This is because of the way in which the control actuators enter into the aircraft dynamics equations, with one actuator for each degree of freedom. Then, we may stop at (5.8-4). Define an auxiliary input  $v(t)$  by

$$v = CBu + CAx - \dot{r} \quad (5.8-6)$$

so that

$$u = (CB)^{-1}(\dot{r} - CAx + v) \quad (5.8-7)$$

Substituting this expression for  $u(t)$  into (5.8-4) yields

$$\begin{aligned} \dot{y} &= CAx + CB[(CB)^{-1}(\dot{r} - CAx + v)] \\ &= CAx + \dot{r} - CAx + v \end{aligned} \quad (5.8-8)$$

or

$$\dot{e} = -v \quad (5.8-9)$$

The auxiliary input  $v(t)$  was selected to make expression (5.8-7) hold in order to cancel the term  $CAx$  and so that  $CB$  does not appear in (5.8-9).

System (5.8-9) is the *error dynamics*. To complete the design, it is only necessary to select  $v(t)$  so that this system is stable. Due to the way in which  $v(t)$  was defined by (5.8-7), the error dynamics have a very simple form; indeed, the error system



has  $p$  poles at  $s = 0$ . This means that it is very easy to select  $v(t)$  to stabilize this system. A variety of techniques may be used, including robust control, LQR/LTR (see Chapter 6), and other linear system design techniques (Adams and Banda, 1993; Lane and Stengel, 1988; Enns et al., 1994; Tomlin et al., 1995; Wright Laboratory Report, 1996).

A simple choice for  $v(t)$  is

$$v = Ke \quad (5.8-10)$$

Then, one has the closed-loop error dynamics given by

$$\dot{e} = -Ke, \quad (5.8-11)$$

which is a stable system as long as gain matrix  $K$  is positive definite. In practice, one usually selects  $K$  diagonal to keep the control channels in the outer loop decoupled. The gain  $K$  should be selected so that the closed-loop system satisfied MILSPEC flying qualities requirements.

The overall dynamic inversion control input is given by

$$u = (CB)^{-1}(\dot{r} + Ke - CAx) \quad (5.8-12)$$

The control scheme given by this is shown in Figure 5.8-1. Note that (5.8-10) is simply an *outer proportional feedback tracking loop*, while (5.8-7) is an *inner control loop* using full state-variable feedback. This inner loop is called the *feedback linearization loop*. Its function is to make the system from  $v(t)$  to  $y(t)$  appear like a linear system with poles at the origin (5.8-9). This greatly simplifies the design of the outer tracking loop. There is also a feedforward term involving  $\dot{r}(t)$ , which is known as *velocity feedforward*. This greatly improves the tracking accuracy of the closed-loop system.

Note that to implement the dynamic inversion control algorithm (5.8-12) one must know  $CA$  and  $CB$ . That is, *a model of the aircraft dynamics is actually built into the controller*. This is what makes the outer control loop design so simple. Moreover, full state feedback is required for the inner loop.

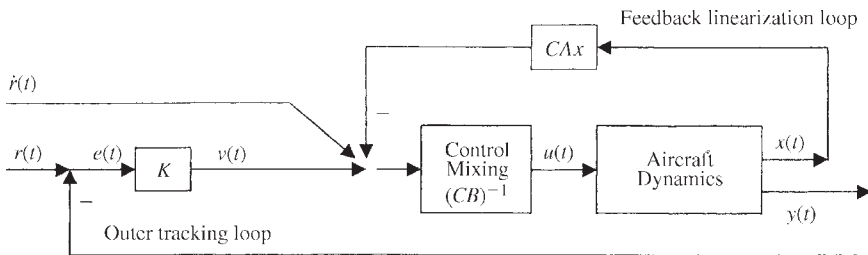


**Figure 5.8-1** Dynamic inversion controller.

This completes the design of the dynamic inversion controller. The full power of this approach will be seen in the next subsection when we apply the technique to nonlinear aircraft systems.

**Zero Dynamics** Equation (5.8-11) only gives the error dynamics of the output  $y(t)$ . The full closed-loop system is obtained by substituting the control (5.8-7) into the state equation (5.8-1). This yields

$$\begin{aligned}\dot{x} &= Ax + B(CB)^{-1}(\dot{r} - CAx + v) \\ \dot{x} &= [I - B(CB)^{-1}]Ax + B(CB)^{-1}(\dot{r} + v)\end{aligned}\quad (5.8-13)$$

The *zero dynamics* are defined as the dynamics of the system when the input  $v(t)$  is selected to give an output  $y(t)$  equal to zero. Since  $y(t) = 0$ , then  $\dot{y}(t) = 0$ , so that (5.8-9) shows that

$$v = -\dot{e} = \dot{y} - \dot{r} = -\dot{r}$$

Substituting this value for  $v(t)$  into (5.8-13) yields the zero dynamics

$$\dot{x} = [I - B(CB)^{-1}C]Ax \equiv A_z x \quad (5.8-14)$$

Note that the dimension of the entire state is  $n$ , while the dimension of the error dynamics (5.8-11) is  $p < n$ . The error dynamics are guaranteed stable by the choice of  $v(t)$ ; however, there remain  $n-p$  poles that may or may not be stable. These poles are unobservable selecting the output  $y(t)$ , and so they cannot be moved using the dynamic inversion controller. These  $n-p$  poles are exactly given by the zero dynamics. If some of these internal zeros are NMP, then the closed-loop system designed by dynamic inversion will be unstable.

The poles of the matrix  $A_z$  consist of  $p$  poles at the origin [namely, the poles of error dynamics system (5.8-9)] plus the  $n-p$  internal zeros. Define the operator

$$P \equiv I - B(CB)^{-1}C \quad (5.8-15)$$

Note that  $P^2 = P$  so that  $P$  is a projection. Furthermore,  $PB \equiv [I - B(CB)^{-1}C]B = 0$  and  $CP \equiv C[I - B(CB)^{-1}C] = 0$ , so that  $P$  is the projection on the null space of  $C$  along the range of  $B$ . Thus,  $A_z = PA$  describes those dynamics that are both in the null space of  $C$  and in range perpendicular of  $B$ . These are precisely the modes that are unobservable using the output  $y(t)$  and cannot be controlled using the dynamic inversion approach.

**Selection of Controlled Variables** For dynamic inversion to be successful, it is necessary to *select the controlled variable (CV)  $y(t)$  so that the zero dynamics are stable.*

This may be checked by computing  $A_z$  for the selected output matrix  $C$  and finding its poles. If they are not stable, then a new  $C$ -matrix must be selected. Once a suitable  $C$ -matrix has been found, the  $p$  poles of the error dynamics may be selected using (5.8-10).

The outputs to be controlled in fighter aircraft are usually selected as:

$$\begin{aligned} \text{pitch axis CV: } & q + n_{zp}/V_{CO} \\ \text{roll axis CV: } & p + \alpha r \\ \text{yaw axis CV: } & r - \alpha p - (g \sin \phi \cos \theta)/V + k\beta \end{aligned} \quad (5.8-16)$$

Discussion of these controlled variables may be found in the work of Enns et al. (1994). These CVs are suitable for most conventional flight regimes and piloting tasks. They may need modifications for high- $\alpha$  or very-low-speed flight.

The pitch-axis CV is motivated by the  $C$ -star criterion  $C^*$ . See the discussion in Section 4.3 on  $C^*$ . One uses the normal acceleration at the pilot's station  $n_{zp}$  and not  $n_z$  at the center of gravity of the aircraft since the latter yields unstable zero dynamics. The crossover velocity  $V_{CO}$  of the CV should be selected to match the MILSPEC requirements on  $n_{zp}$  and pitch rate  $q$ . Even using this CV, dynamic inversion design can destabilize the phugoid mode. This problem may be avoided by adding a small airspeed term to the pitch-axis CV (Enns et al., 1994) to obtain

$$\text{pitch axis CV: } q + n_{zp}/V_{CO} + kv_T \quad (5.8-17)$$

The gain  $k$  is selected so that the zero dynamics are stable. This is illustrated in the next example. The roll- and yaw-axis CVs generally do not have such a stability problem.

In the next example we show how to select CVs and design a dynamic inversion controller for linearized longitudinal dynamics. To verify the performance of the controller, we employ MATLAB using the technique for computer simulation of systems that was introduced in Section 3.3. This technique applies for linear or non-linear systems and employs directly the actual controller. Once the simulation results are satisfactory, this controller can simply be cut out of the code and programmed into the aircraft computer.

**Example 5.8-1: Dynamic Inversion Design for Linear F-16 Longitudinal Dynamics** Consider the linearized F-16 longitudinal dynamics of Chapter 3. Including an elevator actuator, the states are given by

$$x = [v_T \quad \alpha \quad \theta \quad q \quad \delta_e]^T \quad (1)$$

The control input is the elevator input  $u_e$ . The  $A$ - and  $B$ -matrices are given by

$$A = \begin{bmatrix} -0.1270 & -235.0000 & -32.2000 & -9.5100 & -0.2440 \\ 0 & -0.9690 & 0 & 0.9080 & -0.0020 \\ 0 & 0 & 0 & 1.0000 & 0 \\ 0 & -4.5600 & 0 & -1.5800 & -0.2000 \\ 0 & 0 & 0 & 0 & -20.2000 \end{bmatrix} \quad B = \begin{bmatrix} 0 \\ 0 \\ 0 \\ 0 \\ 20.2 \end{bmatrix} \quad (2)$$

In Chapter 4 both the normal acceleration  $n_z$  at the cg and the normal acceleration  $n_{zp}$  at the pilot's station are given. One has

$$n_z = [0.004 \quad 15.88 \quad 0 \quad 1.481 \quad 0.33]x \quad (3)$$

$$n_{zp} = [0.004 \quad 16.2620 \quad 0 \quad 0.9780 \quad -0.0485]x \quad (4)$$

Computing  $C^* = n_{zp} + 12.4q$  as in Chapter 4 yields

$$C^* = [0.004 \quad 16.2620 \quad 0 \quad 13.3780 \quad -0.0485]x \quad (5)$$

(a) *Zero Dynamics for Different Controlled Variables.* To find a suitable CV, one may compute the zero dynamics  $A_z = [I - B(CB)^{-1}C]A$  for the above outputs. Then, the eigenvalues of  $A_z$  may be determined. One notes that all these computations are very easy using the MATLAB software.

For  $y(t) = n_z$  one obtains

$$13.8346, -65717, -0.1242, 0.0633, 0$$

Since the number of inputs and outputs is  $p = 1$ , one obtains one pole at zero, corresponding to the error dynamics (5.8-9). The remaining poles of  $A_z$  are the zero dynamics. Since there are unstable zeros, performing dynamic inversion design using  $n_z$  as the CV would destabilize the system.

For  $y(t) = n_{zp}$  one obtains the poles of  $A_z$  as

$$-3.6652 \pm 7.6280i, \quad -0.1244, \quad 0.0550, \quad 0$$

One has the pole at zero of the error dynamics, plus the internal zeros using this choice for  $y(t)$ . The situation is better, and there is only one slightly unstable pole in the zero dynamics.

For  $y(t) = C^*$  one obtains

$$-56.3022, \quad -2.1389, \quad -0.1252, \quad 0.0325, \quad 0,$$

which still reveals a slightly unstable zero dynamics pole.

Accordingly, none of these would be appropriate choices for the CV for dynamic inversion design, though  $n_{zp}$  and  $C^*$  are both better than  $n_z$ . The trouble is the velocity term in  $n_{zp}$  and  $C^*$ . One may correct the problem by adding a small airspeed term to  $n_{zp}$  or  $C^*$  (Enns et al., 1994). After a few tries, we decided on

$$y(t) = C^* - 0.014v_T = n_{zp} + 12.4q - 0.014v_T, \quad (6)$$

which yields

$$y(t) = [-.01 \quad 16.2620 \quad 0 \quad 13.3780 \quad -0.0485]x = Cx \quad (7)$$

Computing now  $A_z$  and finding its eigenvalues yield

$$-56.2243, \quad -2.0209, \quad -0.1423, \quad -0.0758, \quad 0$$

The unstable zero dynamics pole is gone and so we proceed to simulate the dynamic inversion controller.

**(b) Simulation of the Dynamic Inversion Controller.** To simulate the dynamic inversion controller given in Figure 5.8-1, we use a method of computer simulation that is based on the nonlinear state equation  $\dot{x} = f(x, u)$ . This technique was detailed in Section 3.3 and works for either linear or nonlinear systems. MATLAB has a built-in function that performs Runge-Kutta integration and is very convenient to use here.

The third-order Runge-Kutta integrator in MATLAB is called *ode23*, and it requires a MATLAB M file containing the nonlinear state dynamics. This M file is given in Figure 5.8-2. The form of this M file is very important. Note that one first computes the dynamic inverse controller (5.8-12), and then computes the state equation derivatives for the aircraft. Thus, the first portion of the M file is exactly the code required to implement the controller on the actual aircraft.

It is important to note that the dynamic inversion controller must know the aircraft dynamics  $A, B, C$ . That is, the controller must contain a model of the aircraft dynamics.

We selected the desired trajectory  $r(t)$  equal to a unit step, since if the step response of the controlled aircraft is suitable, then the controller has a good performance for a wide range of pilot input commands.

The MATLAB command lines required to run the simulation are given by

```
» [t,x]=ode23('F16LinDynInv',[0 5],[0 0 0 0 0]');
» y=x*cstarmodd';
» plot(t,y)
```

```

% Inverse Dynamics Controller for F16 Linear Dynamics

function xdot=F16LinDynInv(t,x)
global y
%      VT= x(1);      ! True airspeed
%      ALPH= x(2);    ! Angle of Attack in rads.
%      THTA= x(3);    ! Pitch attitude in rads.
%      Q   = x(4);    ! Pitch rate rad/s
%      elev= x(5);    ! elevator actuator
% Inverse Dynamics Controller

% Model of aircraft

a= [ -0.1270  -235.0000  -32.2000  -9.5100  -0.2440
      0       -0.9690      0       0.9080  -0.0020
      0         0         0         0       1.0000      0
      0       -4.5600      0       -1.5800  -0.2000
      0         0         0         0         0      -20.2000 ];
b= [ 0 0 0 0 20.20 ]';
c= [ -0.01  16.2620      0  13.3780  -0.0485 ];
& % y=cstar' modified

% command input

r= 1 ; % check step response
rdot= 0 ;

% controller parameters

K= 10;

% plant outputs, tracking errors, and control inputs

y= c*x ; % y= cstar' modified
e= r-y ;
v= K*e ;
w= rdot - c*a*x + v ;
u= inv(c*b) * w ;
tht1=0
uelev= u ;

% Aircraft State Equations

xdot(1)= -0.1270*x(1) -235.0*x(2) -32.3*x(3) -9.51*x(4) -0.244*x(5) +62.8*tht1 ;
xdot(2)= -0.9690*x(2) +0.908*x(4) -0.002*x(5) -0.04*tht1 ;
xdot(3)= x(4) ;
xdot(4)= -4.56*x(2) -1.58*x(4) -0.2*x(5) ;
xdot(5)= -0.20*x(5) +20.2*uelev;

xdot=xdot' ;

```

**Figure 5.8-2** Dynamic inversion controller and simulation code.

where *cstarmodd* is the *C*-matrix defined by (7). The second argument in *ode23* specifies the integration time interval 0 to 5 s, and the third argument specifies zero initial conditions  $x(0)$ .

The output  $y(t)$  is shown in Figure 5.8-3. If the time constant is not suitable according to MILSPEC requirements, one may simply select another value of  $K$  in (5.8-12) and repeat the simulation. The pitch rate is shown in Figure 5.8-4.

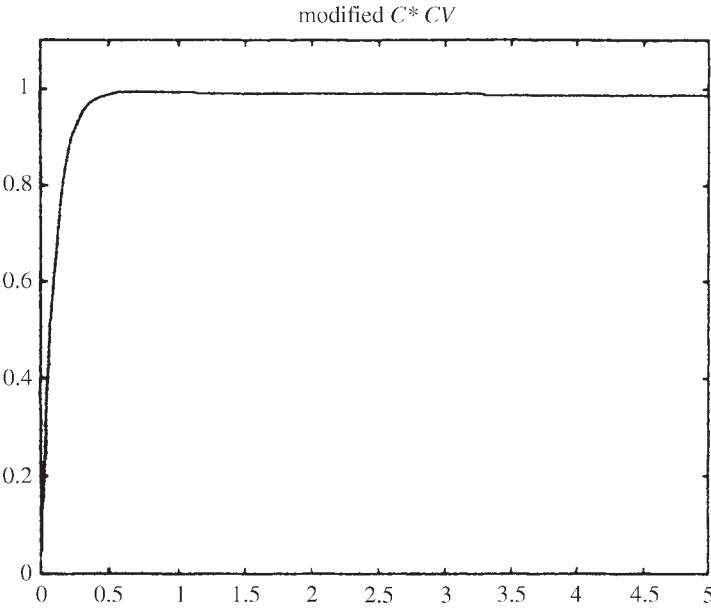


Figure 5.8-3 Modified  $C^*$  controlled variable.

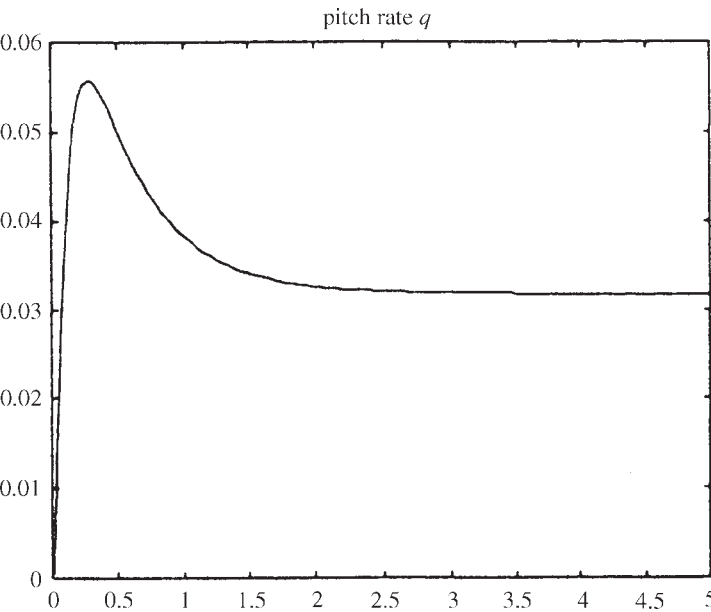


Figure 5.8-4 Pitch rate  $q(t)$ .



**A Pathological Case** In aircraft control one generally has  $CB$  nonsingular in (5.8-4). If  $CB = 0$  one may proceed as discussed there. However, in pathological situations it may occur that  $CB$  is neither zero nor nonsingular. Then one must proceed as follows.

Differentiating repeatedly one obtains

$$\begin{aligned}\ddot{y} &= C\ddot{x} = CA\dot{x} + CB\dot{u} = CA^2x + CB\dot{u} + CABu = CA^2x + C[B \quad AB] \begin{bmatrix} \dot{u} \\ u \end{bmatrix} \\ \ddot{y} &= C\ddot{x} = CA^3x + C[B \quad AB \quad A^2B] \begin{bmatrix} \ddot{u} \\ \dot{u} \\ u \end{bmatrix}\end{aligned}$$

Continuing for  $n$  steps, with  $n$  the number of states, one obtains the  $n$ th derivative of  $y(t)$  as

$$y^{(n)}(t) = CA^n x(t) + CU_n \underline{u}(t), \quad (5.8-18)$$

where the controllability matrix is

$$U_n = [B \quad AB \quad \cdots \quad A^{n-1}B] \quad (5.8-19)$$

and  $\underline{u}(t)$  is a vector of  $u(t)$  and its first  $n - 1$  derivatives.

Now, if the system is controllable, then  $U_n$  has rank  $n$ . If in addition the  $C$ -matrix has rank  $p$ , then  $CU_n$  has rank  $p$ . In this case, though  $CU_n$  is not square, it has a right inverse given by

$$(CU_n)^+ = (CU_n)^T [(CU_n)(CU_n)^T]^{-1} \quad (5.8-20)$$

for note that  $(CU_n)(CU_n)^+ = I$ , the  $p \times p$  identity matrix. Thus, one may define

$$\underline{u} = (CU_n)^+(r^{(n)} - CA^n x + v) \quad (5.8-21)$$

and substitute into (5.8-18) to obtain

$$y^{(n)}(t) = CA^n x(t) + CU_n \underline{u}(t) = CA^n x(t) + CU_n [(CU_n)^+(r^{(n)} - CA^n x + v)],$$

which yields

$$y^{(n)}(t) = r^{(n)} + v \quad (5.8-22)$$

or

$$e^{(n)} = -v \quad (5.8-23)$$

This is the error dynamics. It has  $p$  poles at the origin.

Selecting now the outer loop structure given by

$$v = K_{n-1}e^{(n-1)} + \cdots + K_0 e \quad (5.8-24)$$



gives the closed-loop error dynamics

$$e^{(n)} + K_{n-1}e^{(n-1)} + \cdots + K_0e = 0 \quad (5.8-25)$$

The gains  $K_i$  can be selected to make this system stable. Note that this requires feed-forward of the tracking error  $e(t)$  and its derivatives.

In this pathological case, the inverse dynamics controller is given by (5.8-21) and (5.8-24). A dynamical system can then be employed to extract the control input  $u(t)$  from its derivative vector  $\underline{u}(t)$ .

## Dynamic Inversion for Nonlinear Systems

Since the aircraft is inherently a nonlinear system, we will now discuss dynamic inversion control for nonlinear systems (Slotine and Li, 1991; Enns et al., 1994; Wright Laboratory Report, 1996). Dynamic inversion is one of few control techniques that can directly be extended to nonlinear systems.

**Derivation of Dynamic Inversion Controller** Let the plant be described in nonlinear state-variable form by

$$\dot{x} = f(x) + g(x)u \quad (5.8-26)$$

$$y = h(x), \quad (5.8-27)$$

with state  $x(t) \in R^n$ , control input  $u(t) \in R^m$ , and output  $y(t) \in R^p$ . The entire state  $x(t)$  is available for feedback purposes. It is assumed that the system is *square*, that is, the number of inputs  $m$  is equal to the number of outputs  $p$  so that vectors  $u(t)$  and  $y(t)$  have the same dimension.

Note that the system is linear in the control input  $u(t)$ . This generally holds for aircraft systems, though if it does not and one has instead the more general state equation

$$\dot{x} = f(x, u),$$

one can use a modified form of the upcoming development (Enns et al., 1994).

To make the system follow a desired trajectory  $r(t)$ , the tracking error is defined as

$$e(t) = r(t) - y(t) \quad (5.8-28)$$

Differentiate the output to obtain

$$\dot{y} = \frac{\partial h}{\partial x} \dot{x} = \frac{\partial h}{\partial x} f(x) + \frac{\partial h}{\partial x} g(x)u \equiv F(x) + G(x)u \quad (5.8-29)$$

Define now the control input by

$$u = G^{-1}(x)[-F(x) + \dot{r} + v] \quad (5.8-30)$$

with  $v(t)$  an auxiliary input to be defined. Substituting this expression into (5.8-29) yields the error dynamics

$$\dot{e} = -v \quad (5.8-31)$$

Now, any linear design technique, including robust control techniques, LQR/LTR, and so on, can be used to select  $v(t)$  to stabilize this linear system with  $p$  poles at the origin. One convenient choice is simply

$$v = Ke \quad (5.8-32)$$

with  $K$  positive definite.

The overall dynamic inversion controller is given by

$$u = G^{-1}(x)[-F(x) + \dot{r} + Ke] \quad (5.8-33)$$

This controller is depicted in Figure 5.8-5. It requires full state feedback for the inner loop.

Note that the control  $u(t)$  has been selected to make the plant from  $v(t)$  to  $y(t)$  be simply a linear system with  $p$  poles at the origin. This is accomplished by the inner feedback linearization loop, which is now nonlinear. Then, an outer tracking loop is closed to complete the design. Any linear design technique, including robust control, H-infinity, or LQG/LTR, may be used for this outer-loop design.

It is important to note that the control (5.8-33) contains a model of the aircraft dynamics, since it requires  $F(x)$  and  $G(x)$ . Therefore, to implement it, one must know the nonlinear functions in the aircraft equation. In the upcoming example, this amounts to including the nonlinear aircraft functions in the controller, but in practice it usually entails including *full lookup tables* in the controller. This can become cumbersome but is possible with today's computing systems.

In aircraft systems,  $G(x)$  is usually nonsingular. If  $G(x)$  is not nonsingular, then one must take more steps to derive the controller. If  $G(x) = 0$ , one may proceed as in Slotine and Li (1991), repeatedly differentiating  $y(t)$  using Lie derivatives.

The CVs are selected as detailed for linear systems, though nonlinear versions of the controlled outputs may be used. For instance, for the roll axis one might use the nonlinear version  $p \cos \alpha + r \sin \alpha$  (Enns et al., 1994).

In the nonlinear case, it is more difficult to test the selected controlled variables than in the linear case, since one does not have the artifice of the zero dynamic matrix  $A_z$ . However, one may linearize the nonlinearities and use a version of the technique presented for linear systems. Specifically, the full closed-loop dynamics are given by

$$\begin{aligned} \dot{x} &= f(x) + g(x)G^{-1}(x)[-F(x) + \dot{r} + v] \\ &= \left[ I - gG^{-1} \frac{\partial h}{\partial x} \right] f(x) + gG^{-1}[\dot{r} + v] \end{aligned} \quad (5.8-34)$$

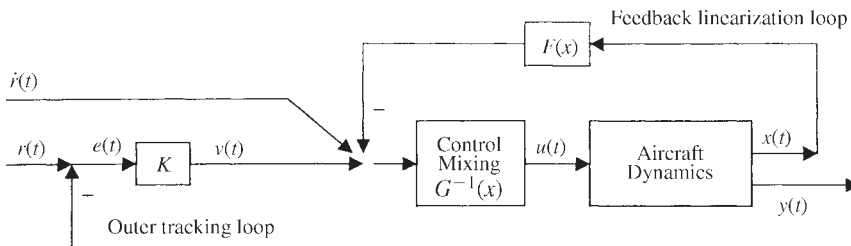


Figure 5.8-5 Nonlinear dynamic inversion controller.

The zero dynamics are given by

$$\dot{x} = \left[ I - gG^{-1} \frac{\partial h}{\partial x} \right] f(x) \quad (5.8-35)$$

These may be linearized to determine the suitability of the CV at a specific operating point. Stability may also be checked by simulation. Simply simulate (5.8-35) in MATLAB, selecting different initial conditions and verifying that the state converges to zero in each case. This amounts to plotting a phase portrait of the zero dynamics (Tomlin et al., 1995).

**Example 5.8-2: Dynamic Inversion Design for Nonlinear Longitudinal Dynamics** We now present a nonlinear version of Example 5.8-1. A longitudinal model  $\dot{x} = f(x) + g(x)u$  of an aircraft similar to that resented in Chapter 3 is given in Figure 5.8-6. The states are

$$x = [v_T \quad \alpha \quad \theta \quad q \quad \delta_e]^T \quad (1)$$

and the control input is the elevator actuator input  $u_e$ .

The normal acceleration is given by

$$n_z = \bar{q}S(C_L \cos \alpha + C_D \sin \alpha)/mg \quad (2)$$

and the normal acceleration at the pilot's station is

$$n_{zp} = n_z + 15\dot{q}/g = \bar{q}S(C_L \cos \alpha + C_D \sin \alpha)/mg + 15M/gI_{yy}, \quad (3)$$

with  $M$  the pitching moment (MOM in Figure 5.8-6). The output is selected as

$$y = C^* = n_{zp} + 12.4q \equiv h(x) \quad (4)$$

We aim to apply (5.8-33) to compute the dynamic inversion controller. To do this, we must determine

$$F(x) = \frac{\partial h}{\partial x} f(x) \quad \text{and} \quad G(x) = \frac{\partial h}{\partial x} g(x) \quad (5)$$

$f(x)$  and  $g(x)$  are easily determined from the nonlinear dynamics and are given in Figure 5.8-7. Finding  $\partial h/\partial x$  is tedious and the results are as follows. First,  $\partial n_z/\partial x$  is given as

$$\begin{aligned} \frac{\partial n_z}{\partial v_T} &= \rho v_T S(C_L \cos \alpha + C_D \sin \alpha)/mg \\ \frac{\partial n_z}{\partial \alpha} &= \bar{q}S[(C_D + 4.58) \cos \alpha - 0.515C_L \sin \alpha]/mg \\ \frac{\partial n_z}{\partial \theta} &= 0, \quad \frac{\partial n_z}{\partial q} = 0, \quad \frac{\partial n_z}{\partial \delta_e} = 0 \end{aligned} \quad (6)$$

```

% Nonlinear Longitudinal Aircraft Model (for small airplane)
% B. Stevens file modified by F. Lewis on 8 May 2000

function xdot=NonLinDynInv(t,x);

% Definition of some constants for the aircraft used for simulation;
WEIGHT = 2300.0; G=32.2; MASS=WEIGHT/G;
IYY = 2094.;
RHO = 2.377E-3;
S = 175.0;
CBAR = 4.89;
CMQ = -12.0;
RTOD = 57.29578;      ! radians to degrees

VT= x(1);      ! True airspeed
ALPH= x(2);    ! Angle of Attack in rads.
THTA= x(3);    ! Pitch attitude in rads
Q  = x(4);    ! Pitch rate rad/s
EL= x(5);      ! elevator actuator

% Computed control inputs are thtl (throttle) and uelev (elev. act. command)

GAM= THTA - ALPH;
CBV= 0.5*CBAR/VT;
CL = 0.25 + 4.58*ALPH;      ! Linear lift curve
CM = 0.015 - 0.75*ALPH - 0.9*x(5); ! Linear pitching moment
CD = .038 + .053*CL*CL;    ! Parabolic drag
QBAR= 0.5*RHO*VT*VT;      ! Dynamic pressure
LIFT= QBAR*S*CL;
DRAG= QBAR*S*CD;
MOM = QBAR*S*CBAR*(CM + CBV*CMQ*Q); ! Added pitch damping
FT= (338.02 + 1.5651*vt - .00884*vt**2 ) * thtl; ! Nonlinear Thrust

% State Equations

xdot(1)= (FT*cos(ALPH) - DRAG - WEIGHT*sin(GAM) )/MASS;
xdot(2)= (-FT*sin(ALPH) - LIFT + WEIGHT*cos(GAM) )/(MASS*VT) + Q;
xdot(3)= Q;
xdot(4)= MOM/IYY;
xdot(5)= -20.2*x(5) + 20.2*uelev;

% outputs

nz= QBAR*S*(CL*cos(ALPH) + CD*sin(ALPH)) / (G*MASS) ! Normal accel.
nzp= nz + 15*MOM/(g*IYY) ! Normal accel. at pilot's station
cstar= nzp - 12.4q ! controlled variable

```

**Figure 5.8-6** Nonlinear model of aircraft longitudinal dynamics.

Next, one has  $\partial M/\partial x$  given by

$$\begin{aligned}
 \frac{\partial M}{\partial v_T} &= \rho v_T S \bar{c} C_M + \frac{S \bar{c}^2}{4} \rho q C_{mq} \\
 \frac{\partial M}{\partial \alpha} &= -0.75 \bar{q} \bar{c} S \\
 \frac{\partial M}{\partial \theta} &= 0 \\
 \frac{\partial M}{\partial q} &= \frac{S \bar{c}^2 \bar{q}}{2 v_T} C_{mq} \\
 \frac{\partial M}{\partial \delta_e} &= -0.9 \bar{q} \bar{c} S
 \end{aligned} \tag{7}$$

Finally, one has

$$\frac{\partial C^*}{\partial x} = \frac{\partial n_z}{\partial x} + \frac{15}{gI_{yy}} \frac{\partial M}{\partial x} + k,$$

where  $k = [0 \ 0 \ 0 \ 12.40]^T$ . All of these are included finally in Figure 5.8-7.

To simulate the dynamic inversion controller, one may write a single MATLAB M file containing both the controller in Figure 5.8-7 and the aircraft dynamics in Figure 5.8-6. The form of this M file will be similar in spirit to that used in Example 5.8-1. This is left for the enterprising reader.

It is very important to note that the dynamic inversion controller in Figure 5.8-7 requires full knowledge of all the nonlinear dynamics of the aircraft. In this example this entails including all the analytic expressions used in the aircraft model. However, in practice, it generally involves including full aircraft lookup tables in the controller. In this example, the Jacobian  $\partial h/\partial x$  was computed analytically. In practice, one may use a numerical differentiation routine as part of the controller.

```
% Nonlinear Longitudinal Dynamic Inversion Controller
function xdot=NonLinDynInvCtrlr(t,x);

% MODEL OF AIRCRAFT DYNAMICS USED IN CONTROLLER

% Definition of some constants for the aircraft used for simulation;
WEIGHT = 2300.0; G=32.2; MASS=WEIGHT/G;
IYY = 2094.;
RHO = 2.377E-3;
S = 175.0;
CBAR = 4.89;
CMQ = -12.0;
RTOD = 57.29578;      % radians to degrees

VT= x(1);      % True airspeed
ALPH= x(2);    % Angle of Attack in rads.
THTA= x(3);    % Pitch attitude in rads.
Q  = x(4);    % Pitch rate rad/s
EL= x(5);      % elevator actuator

% Computed control inputs are thtl (throttle) and EL (elevator command)
GAM= THTA - ALPH;
CBV= 0.5*CBAR/VT;
CL = 0.25 + 4.58*ALPH;      % Linear lift curve
CM = 0.015 - 0.75*ALPH - 0.9*x(5); % Linear pitching moment
CD = .038 + 0.53*CL*CL;    % Parabolic drag
QBAR= 0.5*RHO*VT*VT;      % Dynamic pressure
LIFT= QBAR*S*CL;
DRAG= QBAR*S*CD;
MOM = QBAR*S*CBAR*(CM + CBV*CMQ*Q); % Added pitch damping
FT= (338.02 + 1.5651*vt - .00884*vt**2 ) * thtl; % Nonlinear Thrust

% function f(x)
f1= (FT*cos(ALPH) - DRAG - WEIGHT*sin(GAM) )/MASS;
f2= (-FT*sin(ALPH) - LIFT + WEIGHT*cos(GAM) )/(MASS*VT) + Q;
f3= Q;
f4= MOM/IYY;
f5= -20.2*x(5);

% function g(x)
g=[0 0 0 0 20.2]';
```

**Figure 5.8-7** Nonlinear dynamic inversion controller (Part I). Nonlinear dynamic inversion controller (Part II).

## 5.9 SUMMARY

In this chapter we showed how to use modern control techniques to design multi-variable and multiloop aircraft flight control systems. The approach is based on the state-variable model and a mathematical performance criterion selected according to the performance objectives. The matrix of control gains is determined by solving explicit matrix equations using computer software. Using such an approach, all the feedback loops are closed simultaneously to yield the guaranteed performance desired. This is in contrast to the classical techniques of Chapter 4, which relied on trial-and-error successive loop closures to find the control gains individually.

Two basic modern design techniques were covered. In Section 5.2 we discussed eigenstructure assignment techniques that take advantage of the freedom inherent in design for systems with more than one input and/or output to assign the closed-loop poles and eigenvectors. In the remainder of the chapter we covered linear quadratic (LQ) techniques, where the control gains are selected to minimize generalized quadratic performance indices (PIs). Design equations were derived for the control gains minimizing these PIs and listed in tabular form for easy reference. The design equations may be solved for the control gains using software like that described in Appendix B.

In Section 5.5 the thrust was to introduce modified nonstandard PIs allowing LQ designs with only a small number of design parameters that require tuning for suitable performance. The point was made that successful control system design hinges on the selection of a suitable PI.

Our primary thrust was to use output feedback to allow the design of a compensator with any desired structure. The PI was an integral of the squares of the states and control inputs; thus the LQ techniques used in this chapter are *time-domain* techniques.

In Section 5.8 we discussed dynamic inversion design, which results in a controller with an inner feedback linearization loop and an outer tracking loop.

## REFERENCES

- Adams, R.J., and S. S. Banda. "Robust Flight Control Design Using Dynamic Inversion and Structured Singular Value Synthesis." *IEEE Transactions on Control System Technology* 1, no. 2 (June 1993): 80–92.
- AFWAL-TR-84-3008. "AFTI/F-16 Development and Integration Program, DFCS Phase Final Technical Report." Fort Worth, Tex.: General Dynamics, December 1984.
- Andry, A. N., Jr., E. Y. Shapiro, and J. C. Chung. "Eigenstructure Assignment for Linear Systems." *IEEE Transactions on Aerospace and Electronic Systems* AES-19, no. 5 (September 1983): 711–729.
- Andry, A. N., Jr., J. C. Chung, and E. Y. Shapiro. "Modalized Observers." *IEEE Transactions on Automatic Control* AC-29, no. 7 (July 1984): 669–672.
- Armstrong, E. S. *ORACLs: A Design System for Linear Multivariable Control*. New York: Marcel Dekker, 1980.

- Bartels, R. H., and G. W. Stewart. "Solution of the Matrix Equation  $AX + XB = C$ ." *Communications of the ACM* 15, no. 9 (September 1972): 820–826.
- Blakelock, J. H. *Automatic Control of Aircraft and Missiles*. New York: Wiley, 1965.
- Broussard, J., and N. Halyo. "Active Flutter Control using Discrete Optimal Constrained Dynamic Compensators." *Proceedings of the American Control Conference*, June 1983, pp. 1026–1034.
- Bryson, A. E., Jr. "New Concepts in Control Theory, 1959–1984." *Journal of Guidance* 8, no. 4 (July–August 1985): 417–425.
- Bryson, A. E., Jr., and Y.-C. Ho. *Applied Optimal Control*. New York: Hemisphere, 1975.
- Davison, E. J., and I. J. Ferguson. "The Design of Controllers for the Multivariable Robust Servomechanism Problem Using Parameter Optimization Methods." *IEEE Transactions on Automatic Control* AC-26, no. 1 (February 1981): 93–110.
- D'Azzo, J. J., and C. H. Houpis. *Linear Control System Analysis and Design*. New York: McGraw-Hill, 1988.
- Doyle, J. C., and G. Stein. "Multivariable Feedback Design: Concepts for a Classical/Modern Synthesis." *IEEE Transactions on Automatic Control* AC-26, no. 1 (February 1981): 4–16.
- Enns, D., D. Bugajski, R. Hendrick, and G. Stein. "Dynamic Inversion: An Evolving Methodology for Flight Control Design." *International Journal of Control* 59, no. 1 (1994): 71–91.
- Franklin, G. F., J. D. Powell, and A. Emami-Naeini. *Feedback Control of Dynamic Systems*. Reading, Mass.: Addison-Wesley, 1986.
- Gangsaas, D., K. R. Bruce, J. D. Blight, and U.-L. Ly. "Application of Modern Synthesis to Aircraft Control: Three Case Studies." *IEEE Transactions on Automatic Control* AC-31, no. 11 (November 1986): 995–1014.
- Grimble, M. J., and M. A. Johnson. *Optimal Control and Stochastic Estimation: Theory and Applications*. Vol. 1. New York: Wiley, 1988.
- Harvey, C. A., and G. Stein. "Quadratic Weights for Asymptotic Regulator Properties." *IEEE Transactions on Automatic Control* AC-23, no. 3 (1978): 378–387.
- Hunt, L. R., R. Su, and G. Meyer. "Global Transformations of Nonlinear Systems." *IEEE Transactions on Automatic Control* 28 (1983): 24–31.
- IMSL. *Library Contents Document*. 8th ed. Houston, Tex.: International Mathematical and Statistical Libraries, Inc., 1980.
- Jacubczyk, B., and W. Respondek. "On Linearization of Control Systems." *Bulletin Academie Polonaise de Science et Mathematique* 28 (1980): 517–522.
- Kailath, T. *Linear Systems*. Englewood Cliffs, N.J.: Prentice Hall, 1980.
- Kalman, R. "Contributions to the Theory of Optimal Control." *Boletin de la Sociedad de Matematica Mexicana* 5 (1958): 102–119.
- Kalman, R. E. "A New Approach to Linear Filtering and Prediction Problems." *Transactions of the ASME Journal of Basic Engineering* 82 (1960): 34–35.
- Kreindler, E., and D. Rothschild. "Model-Following in Linear-Quadratic Optimization." *American Institute of Aeronautics and Astronautics Journal* 14, no. 7 (July 1976): 835–842.
- Kwakernaak, H., and R. Sivan. *Linear Optimal Control Systems*. New York: Wiley, 1972.
- Kwon, B.-H., and M.-J. Youn. "Eigenvalue-Generalized Eigenvector Assignment by Output Feedback." *IEEE Transactions on Automatic Control* AC-32, no. 5 (May 1987): 417–421.
- Lane, S. H., and R. F. Stengel. "Flight Control Using Non-Linear Inverse Dynamics." *Automatica* 24, no. 4 (1988): 471–483.

- Levine, W. S., and M. Athans. "On the Determination of the Optimal Constant Output Feedback Gains for Linear Multivariable Systems." *IEEE Transactions on Automatic Control* AC-15, no. 1 (February 1970): 44–48.
- Lewis, F. L. *Optimal Control*. New York: Wiley, 1986.
- Ly, U.-L., A. E. Bryson, and R. H. Cannon. "Design of Low-Order Compensators Using Parameter Optimization." *Automatica* 21, no. 3 (1985): 315–318.
- MacFarlane, A.G.J. "The Calculation of Functionals of the Time and Frequency Response of a Linear Constant Coefficient Dynamical System." *Quarterly Journal of Mechanical Applied Mathematics* 16, pt. 2 (1963): 259–271.
- MATLAB Reference Guide*. Natick, Mass.: The MathWorks, 1994.
- MATRIX<sub>x</sub>. Santa Clara, Calif.: Integrated Systems, Inc., 1989.
- McRuer, D., I. Ashkenas, and D. Graham. *Aircraft Dynamics and Automatic Control*. Princeton N.J.: Princeton University Press, 1973.
- Mil. Spec. 1797*. "Flying Qualities of Piloted Vehicles." 1987.
- Moerder, D. D., and A. J. Calise. "Convergence of a Numerical Algorithm for Calculating Optimal Output Feedback Gains." *IEEE Transactions on Automatic Control* AC-30, no. 9 (September 1985): 900–903.
- Moler, C., J. Little, and S. Bangert. *PC-Matlab*. Sherborn, Mass.: The Mathworks, Inc., 1987.
- Moore, Bruce C. "On the flexibility offered by state feedback in multivariable systems beyond closed loop eigenvalue assignment." Decision and Control including the 14th Symposium on Adaptive Processes, 1975 IEEE Conference on. IEEE, 1975.
- Nelder, J. A., and R. Mead. "A Simplex Method for Function Minimization." *Computing Journal* 7 (1964): 308–313.
- O'Brien, M. J., and J. R. Broussard. "Feedforward control to track the output of a forced model." Decision and Control including the 17th Symposium on Adaptive Processes, 1978 IEEE Conference on. IEEE, 1979.
- Press, W. H., B. P. Flannery, S. A. Teukolsky, and W. T. Vetterling. *Numerical Recipes: The Art of Scientific Computing*. New York: Cambridge University Press, 1986.
- Quintana, V. H., M. A. Zohdy, and J. H. Anderson. "On the Design of Output Feedback Excitation Controllers of Synchronous Machines." *IEEE Transactions of Power Apparatus Systems* PAS-95, no. 3 (1976): 954–961.
- Riccati, J. F. "Animadversiones in aequationes differentiales secundi gradus." *Actorum Eruditorum quae Lipsiae publicantur, Suppl.* 8 (1724): 66–73.
- Shahian, B., and M. Hassul. *Control System Design Using MATLAB*. Englewood Cliffs, N.J.: Prentice-Hall, 1993.
- Slotine, J.-J. E., and W. Li. *Applied Nonlinear Control*. Englewood Cliffs, N.J.: Prentice Hall, 1991.
- Sobel, K., and E. Shapiro. "Eigenstructure assignment for design of multimode flight control systems." *IEEE Control Systems Magazine* 5.2 (1985): 9–15.
- Söderström, T. "On Some Algorithms for Design of Optimal Constrained Regulators." *IEEE Transactions on Automatic Control* AC-23, no. 6 (December 1978): 1100–1101.
- Srinathkumar, S. "Eigenvalue/Eigenvector Assignment Using Output Feedback." *IEEE Transactions on Automatic Control* AC-23, no. 1 (February 1978): 79–81.
- Stern, G., and H. A. Henke. "A Design Procedure and Handling-Quality Criteria for Lateral-Directional Flight Control Systems." *AF-FDL-TR-70-152*. Wright-Patterson AFB, Ohio: Air Force Flight Dynamics Laboratory, May 1971.



Stevens, B. L., F. L. Lewis, and F. Al-Sunni. "Aircraft Flight Controls Design Using Output Feedback." *Journal of Guidance, Control, and Dynamics*, 15, no. 1 (January–February 1992): 238–246.

Tomlin, C., J. Lygeros, L. Benvenuti, and S. Sastry. "Output Tracking for a Non-Minimum Phase Dynamic CTOL Aircraft Model." *Proceedings of the Conference on Decision and Control*, New Orleans, December 1995, pp. 1867–1872.

Wright Laboratory Report WL-TR-96-3099. Wright-Patterson AFB, Ohio, May 1996.

## PROBLEMS

### Section 5.2

**5.2-1 Eigenstructure Assignment with Full State Feedback.** The short-period approximation of an aircraft with the cg far aft might be described by

$$\dot{x} = \begin{bmatrix} -1.10188 & 0.90528 & -0.00212 \\ 4.0639 & -0.77013 & -0.169190 \\ 0 & 0 & -10 \end{bmatrix} x + \begin{bmatrix} 0 & 0 \\ 0 & 1 \\ 10 & 0 \end{bmatrix} u, \quad (1)$$

which includes an elevator actuator of  $10/(s+10)$ . The state is  $x = [\alpha \ q \ \delta_e]^T$ . An extra control input  $u_2$  has been added to illustrate the extra design freedom available in multivariable systems.

(a) Find the poles.

(b) To conform to flying qualities specifications, it is desired to assign closed-loop short-period eigenvalues  $\lambda_1$  and  $\lambda_2$  of  $-2 \pm j2$ . The actuator pole does not matter but may be assigned to  $s = -15$  to speed up its response. The desired closed-loop eigenvectors are

$$v_1 = v_2^* = [0.20 + j0.35 \ -0.98 + j0.07 \ 0]^T, \\ v_3 = [0 \ 0 \ 1]^T$$

Find the state feedback gain  $K$  in  $u = -Kx$  to assign the desired eigenstructure.

**5.2-2 Eigenstructure Assignment with Output Feedback.** In Problem 5.2-1, a more realistic situation occurs when only measurements of  $\alpha$  and  $q$  are taken. Then the control is  $u = -Ky$  with  $y = [\alpha \ q]^T$ . Only two poles may now be assigned. Select desired closed-loop poles as  $\lambda_1$  and  $\lambda_2$  in Problem 5.1, with the same eigenvectors  $v_1$  and  $v_2$ . Find the required output feedback gain  $K$ . Find the closed-loop poles. What happens to the actuator pole?

**5.2-3** In Problem 5.2-1, change the control input to  $B = [0 \ 0 \ 10]^T$  and use feedback of the output  $y = [\alpha \ q]^T$ . Now two poles can be assigned, but there is no freedom in selecting the eigenvectors. Select the desired closed-loop poles  $\lambda_1 = \lambda_2^* = -2 + j2$ . Find the achievable associated eigenvectors  $v_1$  and  $v_2$ . Find the feedback gain  $K$ . Find the closed-loop actuator pole.

## Section 5.3

**5.3-1** Fill in the details in the derivation of the design equations in Table 5.3-1.

### 5.3-2 Output Feedback Design for Scalar Systems

(a) Consider the case where  $x(t)$ ,  $u(t)$ ,  $y(t)$  are all scalars. Show that the solution  $S$  to the second Lyapunov equation in Table 5.3-1 is not needed to determine the output feedback gain  $K$ . Find an explicit solution for  $P$  and hence for the optimal gain  $K$ .

(b) Repeat for the case where  $x(t)$  and  $y(t)$  are scalars but  $u(t)$  is an  $m$ -vector.

**5.3-3** Use (5.3-28) to eliminate  $K$  in the Lyapunov equations of Table 5.3-1, hence deriving two coupled nonlinear equations that may be solved for the optimal auxiliary matrices  $S$  and  $P$ . Does this simplify the solution of the output feedback design problem?

**5.3-4 Software for Output Feedback Design.** Write a program that finds the gain  $K$  minimizing the PI in Table 5.3-1 using the Simplex algorithm of Press et al. (1986). Use it to verify the results of Example 5.3-1. Can you tune the elements of  $Q$  and  $R$  to obtain better closed-loop responses than the ones given?

**5.3-5** For the system

$$\dot{x} \begin{bmatrix} 0 & 1 \\ 0 & 0 \end{bmatrix} x + \begin{bmatrix} 0 \\ 1 \end{bmatrix} u, \quad y = [1 \quad 1]x \quad (1)$$

find the output feedback gain that minimizes the PI in Table 5.3-1 with  $Q = I$ . Try various values of  $R$  to obtain a good response. You will need the software from Problem 5.3-4. The closed-loop step response may be plotted using the software described in Appendix B. (Note that system (1) is nothing but Newton's law, since if  $x = [p \quad v]^T$ , then  $\ddot{p} = u$ , where  $u(t)$  may be interpreted as an acceleration input  $F/m$ .)

**5.3-6 Gradient-Based Software for Output Feedback Design.** Write a program that finds the gain  $K$  minimizing the PI in Table 5.3-1 using the Davidon-Fletcher-Powell algorithm (Press et al., 1986). Use it to verify the results of Example 5.3-1.

## Section 5.4

**5.4-1** Derive (5.4-31).

**5.4-2** Derive the necessary conditions in Table 5.4-1.

**5.4-3** In Example 5.4-1, use the observability matrix to verify that the original proposed value of  $Q = H^T H$  has  $(\sqrt{Q}, A)$  unobservable while the  $Q$  that contains a (5,5) element has  $(\sqrt{Q}, A)$  observable.

**5.4-4 Software for LQ Output Feedback Design.** Write a program to solve for the optimal gain  $K$  in Table 5.4-1 using the Simplex algorithm (Press et al., 1986). Use it to verify Example 5.4-1.

- 5.4-5** In Example 5.4-1 we used an output with four components. There is an extra degree of freedom in the choice of control gains that may not be needed. Redo the example using the software from Problem 5.4-4, with the output defined as  $y = [\alpha_F \quad q \quad e]^T$ .
- 5.4-6** To see whether the angle-of-attack filter in Example 5.4-1 complicates the design, redo the example using  $y = [\alpha \quad q \quad e \quad \epsilon]^T$ .
- 5.4-7** Redo Example 5.4-1 using root-locus techniques like those in Chapter 4. Based on this, are the gains selected by the LQ algorithm sensible from the point of view of classical control theory?
- 5.4-8 Gradient-Based Software for LQ Output Feedback Design.** Write a program to solve for the optimal gain  $K$  in Table 5.4-1 using the Davidon-Fletcher-Powell algorithms (Press et al., 1986). Use it to verify Example 5.4-1.
- 5.4-9 Gain Scheduling.** To implement a control law on an aircraft, it must be gain scheduled over the flight envelope where it will be used. In Section 3.5 a software longitudinal model was given for a transport aircraft. In Section 3.6 it was shown how to use a trim program to obtain linearized state-variable models at different trim conditions. Using the trim software, obtain three state-variable models for the short-period approximation at 0 ft altitude for speeds of 170, 220, and 300 ft/s. Redo the normal acceleration CAS in Example 5.4-1 for each of these three state-space models. The result is three sets of control gains, each of which is valid for one of the trim conditions. To implement the gain-scheduled control law, write a simple program that selects between the control gains depending on the actual measured speed of the aircraft. Use linear interpolation between the three gain element values for points between the three equilibrium conditions.

## Section 5.5

- 5.5-1** Show the validity of (5.5-8) and (5.5-9).
- 5.5-2** Use a technique like that employed in Section 5.3 to derive the expression for the optimal cost in terms of  $P_k$  that appears in Table 5.5-1. You will need to successively integrate by parts (MacFarlane, 1963).
- 5.5-3** Derive the necessary conditions in Table 5.5-1.
- 5.5-4 Software for Output Feedback LQR Design.** Write a program that finds the gain  $K$  minimizing the PI in Table 5.3-1 using the Simplex algorithm (Press et al., 1986). Include gain element weighting using (5.5-6). Use this software to verify the results of Example 5.5-1.
- 5.5-5 Software for Output Feedback LQ Tracker Design.** Write a program that finds the gain  $K$  minimizing the PI in Table 5.4-1 using the Simplex algorithm (Press et al., 1986). Include gain element weighting using (5.5-6).

- 5.5-6** In Example 5.4-1 we used an output with four components. There is an extra degree of freedom in the choice of control gains which may not be needed. Using the gain element weighting software from Problem 5.5-5, redo the example with a large weight on the gain element multiplying  $e(t)$  to drive it to zero. Is the performance as good? Try tuning the performance index weights for better performance.
- 5.5-7 Software for Time-Weighted Output Feedback Tracker Design.** Write a program that finds the gain  $K$  minimizing the PI in Table 5.5-1 using the Simplex algorithm (Press et al., 1986). Include gain element weighting using (5.5-6). Use this software to verify the results of Example 5.5-2. Redo the design using weighting of  $t^3$ ,  $t^4$ . Is there any significant difference from the  $t^2$  case?
- 5.5-8 Root-Locus Design.** Redo Example 5.5-3, finding the control gains using root-locus techniques like those in Chapter 4. Compare this procedure to modern design using software that solves the design equations in Table 5.5-1.

## Section 5.6

- 5.6-1** Derive the implicit model-following design equations (5.6-43) to (5.6-45).
- 5.6-2** Using the control gains found in the flare control system of Example 5.6-1, determine the compensator zeros in Figure 5.6-3.
- 5.6-3** A system obeying Newton's laws is described by the state equations

$$\dot{x} = \begin{bmatrix} 0 & 1 \\ 0 & 0 \end{bmatrix} x + \begin{bmatrix} 0 \\ 1 \end{bmatrix} u, \quad y = [1 \quad 1]x$$

The state is  $x = [p \quad v]^T$ , with  $p(t)$  the position and  $v(t)$  the velocity. Using the CGT approach, design an explicit model-following controller that makes the position follow a quadratic input command  $r(t) = r_0 + r_1 t + r_2 t^2$ .

- 5.6-4** It is desired to make the scalar plant

$$\dot{x} = x + u, \quad y = x, \quad z = x$$

behave like the scalar model

$$\dot{\underline{x}} = -2\underline{x} + r, \quad \underline{y} = \underline{x}, \quad \underline{z} = \underline{x}$$

with reference input  $r$  equal to the unit step. Use explicit model following to design a servosystem:

- Draw the controller structure.
- Select the control gains using LQR design on the augmented system.

## Section 5.7

**5.7-1 Damped Harmonic Oscillator.** The damped harmonic oscillator is described by

$$\dot{x} = \begin{bmatrix} 0 & 1 \\ -\omega_n^2 & -2\zeta\omega_n \end{bmatrix} x + \begin{bmatrix} 0 \\ 1 \end{bmatrix} u,$$

with  $\zeta$  the damping ratio and  $\omega_n$  the natural frequency. This system is useful in modeling systems with an oscillatory mode (e.g., short-period mode, fuel slosh).

- (a) Repeat Example 5.7-1 for this system.
- (b) For several choices of the PI weighting parameters, find the optimal gain and simulate the closed-loop response. (You can check your results using the software written to solve the design equations in Table 5.3-1, 5.4-1, or 5.5-1 by setting  $C = I$  there.)

## Section 5.8

**5.8-1** A basic helicopter model (Shahian and Hassul, 1993) is given by

$$\dot{x} = \begin{bmatrix} -0.4 & 0 & -0.01 \\ 1 & 0 & 0 \\ -1.4 & 9.8 & -0.02 \end{bmatrix} x + \begin{bmatrix} 6.3 \\ 0 \\ 9.8 \end{bmatrix} \delta,$$

where the state is  $x = [q \ \theta \ v]$ , with  $q$  = pitch rate,  $\theta$  = pitch angle, and  $v$  = horizontal velocity. The control input is the rotor tilt angle  $\delta$ .

- (a) Select different controlled variables as outputs and investigate the stability of the zero dynamics.
- (b) Select a CV that yields stable zero dynamics. Design the dynamic inversion controller. Simulate using MATLAB.

**5.8-2** A nonlinear system is given by

$$\begin{aligned} \dot{x}_1 &= x_1 x_2 + x_3 \\ \dot{x}_2 &= -2x_2 + x_1 u \\ \dot{x}_3 &= \sin x_1 + 2x_1 x_2 + u \end{aligned}$$

- (a) Select  $y(t) = x_1(t)$  as the controlled variable. Investigate the stability of the zero dynamics.
- (b) Design the dynamic inversion controller. Simulate using MATLAB.

**5.8-3** Perform the full simulation in Example 5.8-2. That is, combine the dynamic inversion controller and the aircraft into one M file and plot the outputs using MATLAB as done in Example 5.8-1.

## CHAPTER 6

---

# ROBUSTNESS AND MULTIVARIABLE FREQUENCY-DOMAIN TECHNIQUES

---

### 6.1 INTRODUCTION

#### Modeling Errors and Stability Robustness

In the design of aircraft control systems it is important to realize that the rigid-body equations that are the basis for design in Chapters 4 and 5 are only an approximation to the nonlinear aircraft dynamics. An aircraft has flexible modes that are important at high frequencies; we neglected these in our rigid-body design model. These *unmodeled high-frequency dynamics* can act to destabilize a control system that may have quite suitable behavior in terms only of the rigid-body model.

Moreover, as the aircraft changes its equilibrium flight condition, the linearized rigid-body model describing its perturbed behavior changes. This *parameter variation* is a low-frequency effect that can also act to destabilize the system. To compensate for this variation, one may determine suitable controller gains for linearized models at several design equilibrium points over a flight envelope. Then, these design gains may be scheduled in computer lookup tables for suitable controller performance over the whole envelope. For gain scheduling to work, it is essential for the controller gains at each design equilibrium point to guarantee stability for actual flight conditions near that equilibrium point. Thus, it is important to design controllers that have *stability robustness*, which is the ability to provide stability in spite of modeling errors due to high-frequency unmodeled dynamics and plant parameter variations.

#### Disturbances and Performance Robustness

It is often important to account for disturbances such as wind gusts and sensor measurement noise. Disturbances can often act to cause unsatisfactory performance in a

system that has been designed without taking them into account. Thus, it is important to design controllers that have *performance robustness*, which is the ability to guarantee acceptable performance (in terms of percent overshoot, settling time, etc.) even though the system may be subject to disturbances.

## Classical Robust Design

In classical control, robustness may be designed into the system from the beginning by providing sufficient gain and phase margin to counteract the effects of inaccurate modeling or disturbances. In terms of the Bode magnitude plot, it is known that the loop gain should be high at low frequencies for performance robustness but low at high frequencies, where unmodeled dynamics may be present, for stability robustness. The concept of bandwidth is important in this connection, as is the concept of the sensitivity function.

Classical control design techniques are generally in the frequency domain, so they afford a convenient approach to robust design for single-input/single-output (SISO) systems. However, it is well known that the individual gain margins, phase margins, and sensitivities of all the SISO transfer functions in a multivariable or multiloop system have little to do with its overall robustness. Thus, there have been problems in extending classical robust design notions to multi-input/multi-output (MIMO) systems.

## Modern Robust Design

Modern control techniques provide a direct way to design multiloop controllers for MIMO systems by closing all the loops simultaneously. Performance is guaranteed in terms of minimizing a quadratic performance index (PI) which, with a sensible problem formulation, generally implies closed-loop stability as well. However, all our work in Chapter 5 assumed that the aircraft model is exactly known and that there are no disturbances. In fact, this is rarely the case.

In this chapter we show that the classical frequency-domain robustness measures are easily extended to MIMO systems in a rigorous fashion by using the notion of the *singular value*. In Section 6.2 we develop the *multivariable loop gain and sensitivity* and describe the *multivariable Bode magnitude plot*. In terms of this plot, we present bounds that *guarantee* both robust stability and robust performance for multivariable systems, deriving notions that are entirely analogous to those in classical control.

In Section 6.3 we give a design technique for robust multivariable controllers using modern output feedback theory, showing how robustness may be guaranteed. The approach is a straightforward extension of classical techniques. To yield both suitable time-domain performance and robustness, an iterative approach is described that is simple and direct using the software described in Appendix B. We illustrate by designing a pitch-rate control system that has good performance despite the presence of flexible modes and wind gusts.

A popular modern approach to the design of robust controllers is *linear quadratic Gaussian/loop transfer recovery* (LQG/LTR). This approach has been used extensively by Honeywell in the design of advanced multivariable aircraft control

systems. LQG/LTR relies on the *separation principle*, which involves designing a full-state-variable feedback (as in Section 5.7) and then an *observer* to provide the state estimates for feedback purposes. The result is a dynamic compensator that is similar to those resulting from classical control approaches. The importance of the separation principle is that compensators can be designed for *multivariable systems* in a straightforward manner by solving matrix equations. In Section 6.4 we discuss observers and the Kalman filter. In Section 6.5 we cover LQG/LTR design.

A recent approach to modern robust design is  $H$ -infinity design (Francis et al., 1984; Doyle et al., 1989; Kaminer et al., 1990). However, using  $H$ -infinity design it is difficult to obtain a controller with a desired structure. For this reason, as well as due to space limitations, we will not cover  $H$ -infinity design.

## 6.2 MULTIVARIABLE FREQUENCY-DOMAIN ANALYSIS

We will deal with system uncertainties, as in classical control, using robust design techniques which are conveniently examined in the frequency domain. To this point, our work in modern control has been in the time domain, since the LQ performance index is a time-domain criterion.

One problem that arises immediately for MIMO systems is that of extending the SISO Bode magnitude plot. We are not interested in making several individual SISO frequency plots for various combinations of the inputs and outputs in the MIMO system and examining gain and phase margins. Such approaches have been tried and may not always yield much insight into the true behavior of the MIMO system. This is due to the coupling that generally exists between *all* inputs and *all* outputs of a MIMO system.

Thus, in this section we introduce the *multivariable loop gain and sensitivity* and the *multivariable Bode magnitude plot*, which will be nothing but the plot versus frequency of the *singular values* of the transfer function matrix. This basic tool allows much of the rich experience of classical control theory to be applied to MIMO systems. Thus, we will discover that for robust performance the minimum singular value of the loop gain should be large at low frequencies, where disturbances are present. On the other hand, for robust stability the maximum singular value of the loop gain should be small at high frequencies, where there are significant modeling inaccuracies. We will also see that to guarantee stability despite parameter variations in the linearized model due to operating point changes, the maximum singular value should be below an upper limit.

### Sensitivity and Cosensitivity

Figure 6.2-1 shows a standard feedback system of the sort that we have seen several times in our work to date. The plant is  $G(s)$ , and  $K(s)$  is the feedback/feedforward compensator which can be designed by any of the techniques we have covered. The plant output is  $z(t) \in \mathbf{R}^q$ , the plant control input is  $u(t) \in \mathbf{R}^m$ , and the reference input is  $r(t) \in \mathbf{R}^q$ .



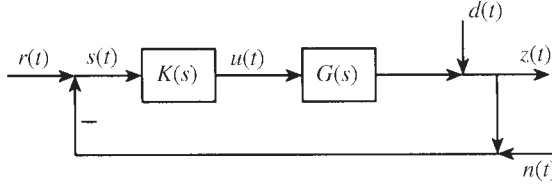


**Figure 6.2-1** Standard feedback configuration.

We have mentioned in Section 5.4 that perfect tracking may not be achieved unless the number  $m$  of control inputs  $u(t)$  is greater than or equal to the number  $q$  of performance outputs  $z(t)$  (Kwakernaak and Sivan, 1972). Therefore, we will assume that  $m = q$  so that the plant  $G(s)$  and compensator  $K(s)$  are square. This is only a consequence of sensible design, not a restriction on the sorts of plants that may be considered.

We have added a few items to the figure to characterize uncertainties. The signal  $d(t)$  represents a *disturbance* acting on the system of the sort appearing in classical control. This could represent, for instance, wind gusts. The *sensor measurement noise* or errors are represented by  $n(t)$ . Both of these signals are generally vectors of dimension  $q$ . Typically, the disturbances occur at low frequencies, say below some  $\omega_d$ , while the measurement noise  $n(t)$  has its predominant effect at high frequencies, say above some value  $\omega_n$ . Typical Bode plots for the magnitudes of these terms appear in Figure 6.2-2 for the case that  $d(t)$  and  $n(t)$  are scalars. The reference input is generally also a low-frequency signal (e.g., the unit step).

The tracking error is

$$e(t) \equiv r(t) - z(t) \quad (6.2-1)$$

Due to the presence of  $n(t)$ ,  $e(t)$  may not be symbolized in Figure 6.2-1. The signal  $s(t)$  is in fact given by

$$s(t) = r(t) - z(t) - n(t) = e(t) - n(t) \quad (6.2-2)$$

Let us perform a frequency-domain analysis on the system to see the effects of the uncertainties on system performance. In terms of Laplace transforms we may write

$$Z(s) = G(s)K(s)S(s) + D(s) \quad (6.2-3)$$

$$S(s) = R(s) - Z(s) - N(s) \quad (6.2-4)$$

$$E(s) = R(s) - Z(s) \quad (6.2-5)$$

Now we may solve for  $Z(s)$  and  $E(s)$ , obtaining the closed-loop transfer function relations (see the problems at the end of the chapter)

$$Z(s) = (I + GK)^{-1}GK(R - N) + (I + GK)^{-1}D \quad (6.2-6)$$

$$E(s) = [I - (I + GK)^{-1}GK]R + (I + GK)^{-1}GKN - (I + GK)^{-1}D \quad (6.2-7)$$

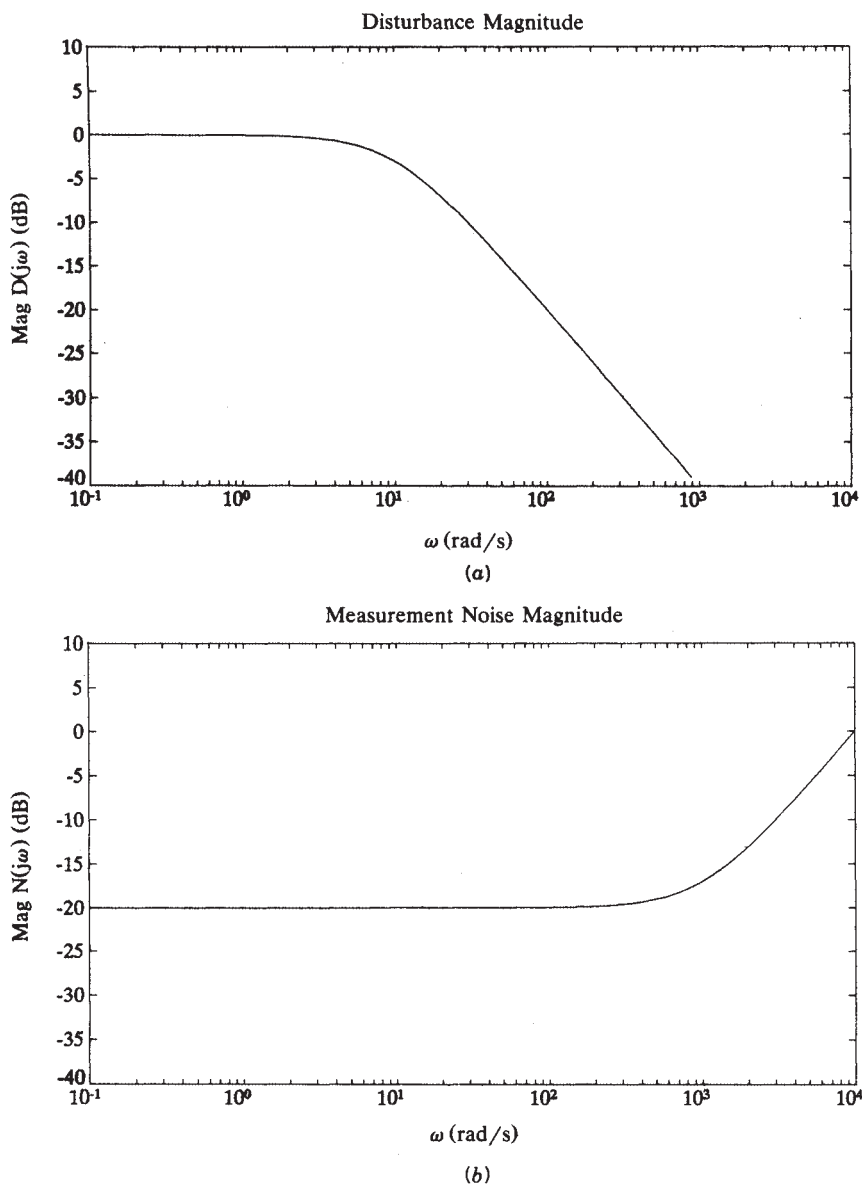


**Figure 6.2-2** Typical Bode plots for the uncertain signals in the system: (a) disturbance magnitude; (b) measurement noise magnitude.

It is important to note that, unlike the case for SISO systems, care must be taken to perform the matrix operations in the correct order (for instance,  $GK \neq KG$ ). The multiplications by matrix inverses must also be performed in the correct order.

We can put these equations into a more convenient form. According to the matrix inversion lemma, (6.2-7) may be written as

$$E(s) = (I + GK)^{-1}(R - D) + (I + GK)^{-1}GKN \quad (6.2-8)$$

Moreover, since  $GK$  is square and invertible, we can write

$$\begin{aligned} (I + GK)^{-1}GK &= [(GK)^{-1}(I + GK)]^{-1} = [(GK)^{-1} + I]^{-1} \\ &= [(I + GK)(GK)^{-1}]^{-1} = GK(I + GK)^{-1} \end{aligned} \quad (6.2-9)$$

Therefore, we may finally write  $Z(s)$  and  $E(s)$  as

$$Z(s) = GK(I + GK)^{-1}(R - N) + (I + GK)^{-1}D \quad (6.2-10)$$

$$E(s) = (I + GK)^{-1}(R - D) + GK(I + GK)^{-1}N \quad (6.2-11)$$

To simplify things a bit, define the *system sensitivity*

$$S(s) = (I + GK)^{-1} \quad (6.2-12)$$

and

$$T(s) = GK(I + GK)^{-1} = (I + GK)^{-1}GK \quad (6.2-13)$$

Since

$$S(s) + T(s) = (I + GK)(I + GK)^{-1} = I \quad (6.2-14)$$

we call  $T(s)$  the *complementary sensitivity*, or in short, the *cosensitivity*. Note that the *return difference*

$$L(s) = I + GK \quad (6.2-15)$$

is the inverse of the sensitivity. The *loop gain* is given by  $G(s)K(s)$ .

These expressions extend the classical notions of loop gain, return difference, and sensitivity to multivariable systems. They are generally square transfer function matrices of dimension  $q \times q$ . In terms of these new quantities, we have

$$Z(s) = T(s)(R(s) - N(s)) + S(s)D(s) \quad (6.2-16)$$

$$E(s) = S(s)(R(s) - D(s)) + T(s)N(s) \quad (6.2-17)$$

According to the second equation, to ensure small tracking errors, we must have  $S(j\omega)$  small at those frequencies  $\omega$  where the reference input  $r(t)$  and disturbance  $d(t)$  are large. This will yield good *disturbance rejection*. On the other hand, for

satisfactory *sensor noise rejection*, we should have  $T(j\omega)$  small at those frequencies  $\omega$  where  $n(t)$  is large.

Unfortunately, a glance at (6.2-14) reveals that  $S(j\omega)$  and  $T(j\omega)$  cannot simultaneously be small at any one frequency  $\omega$ . According to Figure 6.2-2, we should like to have  $S(j\omega)$  small at low frequencies, where  $r(t)$  and  $d(t)$  dominate, and  $T(j\omega)$  small at high frequencies, where  $n(t)$  dominates.

These are nothing but the multivariable generalizations of the well-known SISO classical notion that a large loop gain  $GK(j\omega)$  is required at low frequencies for satisfactory performance and small errors, but a small loop gain is required at high frequencies where sensor noises are present.

### Multivariable Bode Plot

These notions are not difficult to understand on a heuristic level. Unfortunately, it is not so straightforward to determine a clear measure for the “smallness” of  $S(j\omega)$  and  $T(j\omega)$ . These are both square matrices of dimension  $q \times q$ , with  $q$  the number of performance outputs  $z(t)$  and reference inputs  $r(t)$ . They are complex functions of the frequency. Clearly, the classical notion of the Bode magnitude plot, which is defined only for *scalar* complex functions of  $\omega$ , must be extended to the MIMO case.

Some work was done early on using the frequency-dependent eigenvalues of a square complex matrix as a measure of smallness (Rosenbrock, 1974; MacFarlane, 1970; MacFarlane and Kouvaritakis, 1977). However, note that the matrix

$$M = \begin{bmatrix} 0.1 & 100 \\ 0 & 0.1 \end{bmatrix} \quad (6.2-18)$$

has large and small components, but its eigenvalues are both at 0.1.

A better measure of the magnitude of square matrices is the *singular value (SV)* (Strang, 1980). Given any matrix  $M$  we may write its *singular value decomposition (SVD)* as

$$M = U\Sigma V^*, \quad (6.2-19)$$

with  $*$  denoting complex conjugate transpose,  $U$  and  $V$  square unitary matrices (i.e.,  $V^{-1} = V^*$ , the complex conjugate transpose of  $V$ ), and

$$\Sigma = \begin{bmatrix} \sigma_1 & & & & & \\ & \sigma_2 & & & & \\ & & \ddots & & & \\ & & & \sigma_r & & \\ & & & & 0 & \\ & & & & & \ddots \\ & & & & & & 0 \end{bmatrix}, \quad (6.2-20)$$

with  $r = \text{rank}(M)$ . The singular values are the  $\sigma_i$ , which are ordered so that  $\sigma_1 \geq \sigma_2 \geq \dots \geq \sigma_r$ . The SVD may loosely be thought of as the extension to general matrices

(which may be nonsquare or complex) of the Jordan form. If  $M$  is a function of  $j\omega$ , so are  $U$ ,  $\sigma_i$ , and  $V$ .

Since  $MM^* = U\Sigma V^*V\Sigma^T U^* = U\Sigma^2 U^*$ , it follows that the singular values of  $M$  are simply the (positive) square roots of the nonzero eigenvalues of  $MM^*$ . A similar proof shows that the nonzero eigenvalues of  $MM^*$  and those of  $M^*M$  are the same.

We note that the  $M$  given above has two singular values,  $\sigma_1 = 100.0001$  and  $\sigma_2 = 0.0001$ . Thus, this measure indicates that  $M$  has a large and a small component. Indeed, note that

$$\begin{bmatrix} 0.1 & 100 \\ 0 & 0.1 \end{bmatrix} \begin{bmatrix} -1 \\ 0.001 \end{bmatrix} = \begin{bmatrix} 0 \\ 0.0001 \end{bmatrix} \quad (6.2-21)$$

while

$$\begin{bmatrix} 0.1 & 100 \\ 0 & 0.1 \end{bmatrix} \begin{bmatrix} 0.001 \\ 1 \end{bmatrix} = \begin{bmatrix} 100.0001 \\ 0.1 \end{bmatrix} \quad (6.2-22)$$

Thus, the singular value  $\sigma_2$  has the *input direction*

$$\begin{bmatrix} -1 \\ 0.001 \end{bmatrix}$$

associated with it for which the output contains the value  $\sigma_2$ . On the other hand, the singular value  $\sigma_1$  has an associated input direction of

$$\begin{bmatrix} 0.001 \\ 1 \end{bmatrix}$$

for which the output contains the value  $\sigma_1$ .

There are many nice properties of the singular value that make it a suitable choice for defining the magnitude of matrix functions. Among these is the fact that the maximum singular value is an *induced matrix norm*, and norms have several useful attributes. The use of the SVs in the context of modern control was explored by Doyle and Stein (1981) and Safonov et al. (1981).

A major factor is that there are many good software packages that have good routines for computing the singular value [e.g., subroutine LSVDF in IMSL (1980) or Moler et al. (1987)]. Thus, plots like those we will present may easily be obtained by writing only a computer program to drive the available subroutines. Indeed, since the SVD uses unitary matrices, its computation is numerically stable. An efficient technique for obtaining the SVs of a complex matrix as a function of frequency  $\omega$  is given by Laub (1981).

We note that a complete picture of the behavior of a complex matrix versus  $\omega$  must take into account the magnitudes of the SVs as well as the *multivariable phase*, which may also be obtained from the SVD (Postlethwaite et al., 1981). Thus, complete MIMO generalizations of the Bode magnitude *and* phase plots are available. However, the theory relating to the phase portion of the plot is more difficult to use in a practical design technique, although a MIMO generalization of the Bode gain-phase relation is available (Doyle and Stein, 1981). Therefore, we will only employ plots of the SVs versus frequency, which correspond to the Bode magnitude plot for MIMO systems.

The magnitude of a square transfer function matrix  $H(j\omega)$  at any frequency  $\omega$  depends on the direction of the input excitation. Inputs in a certain direction in the input space will excite only the SV(s) associated with that direction. However, for any input, the magnitude of the transfer function  $H(j\omega)$  at any given frequency  $\omega$  may be bounded above by its *maximum singular value*, denoted  $\bar{\sigma}(H(j\omega))$  and below by its *minimum singular value*, denoted  $\underline{\sigma}(H(j\omega))$ . Therefore, all our results, as well as the plots we will give, need take into account only these two bounding values of “magnitude.”

**Example 6.2-1: MIMO Bode Magnitude Plots** Here, we consider a simple non-aircraft system to make some points about the SV plots. Consider the multivariable system

$$\dot{x} = \begin{bmatrix} -1 & -1 & 0 & 0 \\ 1 & -1 & 0 & 0 \\ 0 & 0 & -2 & 6 \\ 0 & 0 & -6 & -2 \end{bmatrix} x + \begin{bmatrix} 1 & 0 \\ 0 & 0 \\ 0 & 1 \\ 0 & 0 \end{bmatrix} u = Ax + Bu \quad (1)$$

$$z = \begin{bmatrix} 1 & 0 & 0 & 0 \\ 0 & 0 & 1 & 0 \end{bmatrix} x = Hx, \quad (2)$$

which as a  $2 \times 2$  MIMO transfer function of

$$H(s) = H(sI - A)^{-1}B = \frac{M(s)}{\Delta(s)}, \quad (3)$$

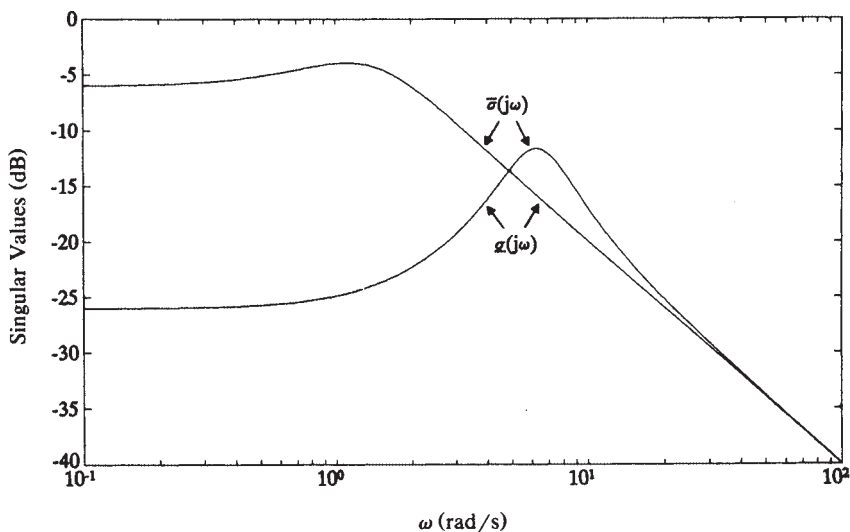


Figure 6.2-3 MIMO Bode magnitude plot of SVs versus frequency.

with

$$\Delta(s) = s^4 + 6s^3 + 50s^2 + 88s + 80$$

$$M(s) = \begin{bmatrix} 1 & 0 \\ 0 & 1 \end{bmatrix} s^3 + \begin{bmatrix} 5 & 0 \\ 0 & 4 \end{bmatrix} s^2 + \begin{bmatrix} 44 & 0 \\ 0 & 6 \end{bmatrix} s + \begin{bmatrix} 40 & 0 \\ 0 & 4 \end{bmatrix} \quad (4)$$

By writing a driver program that calls standard software (e.g., subroutine LSVD in IMSL, 1980) to evaluate the SVs at closely spaced values of frequency  $\omega$ , we may obtain the SV plots versus frequency shown in Figure 6.2-3. We call this the *multivariable Bode magnitude plot* for the MIMO transfer function  $H(s)$ .

Since  $H(s)$  is  $2 \times 2$ , it has two SVs. Note that although each SV is continuous, the maximum and minimum SVs are not. This is due to the fact that the SVs can cross over each other, as the figure illustrates. ■

**Example 6.2-2: Singular-Value Plots for F-16 Lateral Dynamics.** To illustrate the difference between the SV plots and the individual SISO Bode plots of a multivariable system, let us consider the F-16 lateral dynamics of Examples 5.3-1 and 5.5-4. In the latter example, we designed a wing leveler. For convenience, refer to the figure there showing the control system structure. Using the system matrices  $A$  and  $B$  in that example, which include an integrator in the  $\phi$  channel as well as actuator dynamics and a washout filter, take as the control inputs  $u = [u_a \ u_r]^T$ , with  $u_a$  the aileron servo input and  $u_r$  the rudder servo input. Select as outputs  $z = [\epsilon \ r_w]^T$ , with  $\epsilon$  the integrator output in the  $\phi$  channel and  $r_w$  the washed-out yaw rate.

The individual SISO transfer functions in this two-input/two-output open-loop system are

$$H_{11} = \frac{\epsilon}{u_a} = \frac{14.8}{s(s + 0.0163)(s + 3.615)(s + 20.2)} \quad (1)$$

$$H_{12} = \frac{r_w}{u_a} = \frac{-36.9s(s + 2.237) [(s + 0.55)^2 + 2.49^2]}{(s + 0.0163)(s + 1)(s + 3.165)(s + 20.2) [s + 0.4225)^2 + 3.063^2]} \quad (2)$$

$$H_{21} = \frac{\epsilon}{u_r} = \frac{-2.65(s + 2.573)(s - 2.283)}{s(s + 0.0163)(s + 3.615)(s + 20.2) [(s + 0.4225)^2 + 3.063^2]} \quad (3)$$

$$H_{22} = \frac{r_w}{u_r} = \frac{-0.718s [(s + 0.139)^2 + 0.446^2]}{(s + 0.0163)(s + 1)(s + 20.2) [s + 0.4225)^2 + 3.063^2]} \quad (4)$$

The standard Bode magnitude plots for these SISO transfer functions are shown in Figure 6.2-4. Clearly visible are the resonance due to the dutch roll mode as well as the integrator in the upper  $\phi$  channel in the figure in Example 5.5-4.

On the other hand, shown in Figure 6.2-5 are the SVs of this multivariable system. Note that it is not immediately evident how they relate to the SISO plots in Figure 6.2-4. In the next section we will see that bounds for guaranteed robustness are given for MIMO systems in terms of the minimum SV being large at low

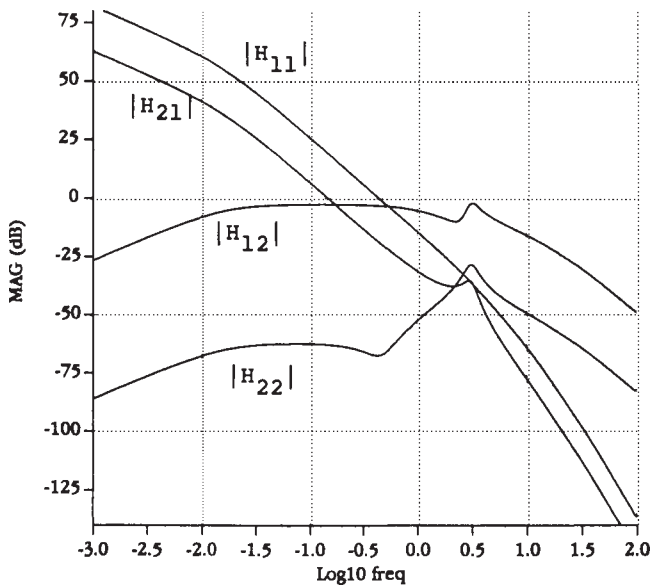


Figure 6.2-4 SISO Bode magnitude plots for F-16 lateral dynamics.

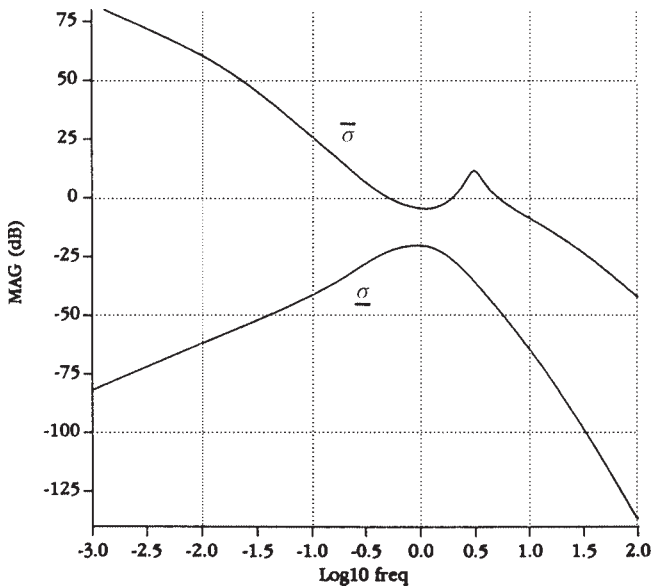


Figure 6.2-5 Singular values for F-16 lateral dynamics.



frequencies (for performance robustness) and the maximum SV being small at high frequencies (for stability robustness). The lack of any clear correspondence between Figures 6.2-4 and 6.2-5 shows that these bounds cannot be expressed in terms of the individual SISO Bode plots. ■

## Frequency-Domain Performance Specifications

We have seen how to make a multivariable Bode magnitude plot of a square transfer function matrix. It is now necessary to discuss *performance specifications* in the frequency domain in order to determine what a “desirable” Bode plot means in the MIMO case. The important point is that the low-frequency requirements are generally in terms of the *minimum* SV being *large*, while the high-frequency requirements are in terms of the *maximum* SV being *small*.

First, let us point out that the classical notion of *bandwidth* holds in the MIMO case. This is the frequency  $\omega_c$  for which the loop gain  $GK(j\omega)$  passes through a value of 1, or 0 dB. If the bandwidth should be limited due to high-frequency noise considerations, the *largest* SV should satisfy  $\overline{\sigma}(GK(j\omega)) = 1$  at the specified cutoff frequency  $\omega_c$ .

**$L_2$  Operator Gain** To relate frequency-domain behavior to time-domain behavior, we may take into account the following considerations (Morari and Zafiriou, 1989). Define the  $L_2$  norm of a vector time function  $s(t)$  by

$$\|s\|_2 = \left[ \int_0^\infty s^T(t) s(t) dt \right]^{1/2} \quad (6.2-23)$$

This is related to the total energy in  $s(t)$  and should be compared to the LQ performance index.

A linear time-invariant system has input  $u(t)$  and output  $z(t)$  related by the convolution integral

$$z(t) = \int_{-\infty}^\infty h(t - \tau) u(\tau) d\tau, \quad (6.2-24)$$

with  $h(t)$  the impulse response. The  $L_2$  operator gain, denoted  $\|H\|_2$ , of such a system is defined as the smallest value of  $\gamma$  such that

$$\|z\|_2 \leq \gamma \|u\|_2 \quad (6.2-25)$$

This is just the operator norm induced by the  $L_2$  vector norm. An important result is that the  $L_2$  operator gain is given by

$$\|H\|_2 = \max_{\omega} [\overline{\sigma}(H(j\omega))], \quad (6.2-26)$$

with  $H(s)$  the system transfer function. That is,  $\|H\|_2$  is nothing but the *maximum value* over  $\omega$  of the maximum SV of  $H(j\omega)$ . Thus,  $\|H\|_2$  is an *H-infinity norm* in the frequency domain.

This result gives increased importance to  $\bar{\sigma}(H(j\omega))$ , for if we are interested in keeping  $z(t)$  small over a range of frequencies, we should take care that  $\bar{\sigma}(H(j\omega))$  is small over that range.

It is now necessary to see how this result may be used in deriving frequency-domain performance specifications. Some facts we will use in this discussion are

$$\underline{\sigma}(GK) - 1 \leq \underline{\sigma}(I + GK) \leq \underline{\sigma}(GK) + 1 \quad (6.2-27)$$

$$\bar{\sigma}(M) = \frac{1}{\underline{\sigma}(M^{-1})}, \quad (6.2-28)$$

$$\bar{\sigma}(AB) \leq \bar{\sigma}(A)\bar{\sigma}(B) \quad (6.2-29)$$

for any matrices  $A, B, GK, M$ , with  $M$  nonsingular.

Before we begin a discussion of performance specifications, let us note the following. If  $S(j\omega)$  is small, as desired at low frequencies, then

$$\bar{\sigma}(S) = \bar{\sigma}[(I + GK)^{-1}] = \frac{1}{\underline{\sigma}(I + GK)} \approx \frac{1}{\underline{\sigma}(GK)} \quad (6.2-30)$$

That is, a large value of  $\underline{\sigma}(GK)$  guarantees a small value of  $\bar{\sigma}(s)$ .

On the other hand, if  $T(j\omega)$  is small, as is desired at high frequencies, then

$$\bar{\sigma}(T) = \bar{\sigma}[GK(I + GK)^{-1}] \approx \bar{\sigma}(GK) \quad (6.2-31)$$

That is, a small value of  $\bar{\sigma}(GK)$  guarantees a small value of  $\bar{\sigma}(T)$ .

This means that specifications that  $S(j\omega)$  be small at low frequencies and  $T(j\omega)$  be small at high frequencies may equally well be formulated in terms of  $\underline{\sigma}(GK)$  being large at low frequencies and  $\bar{\sigma}(GK)$  being small at high frequencies. Thus, all of our performance specifications will be in terms of the *minimum and maximum SVs of the loop gain  $GK(j\omega)$* . The practical significance of this is that we need only compute the SVs of  $GK(j\omega)$ , not those of  $S(j\omega)$  and  $T(j\omega)$ . These notions are symbolized in Figure 6.2-6, where it should be recalled that  $S + T = I$ .

Now, we will first consider low-frequency specifications on the SV plot and then high-frequency specifications. According to our discussion relating to (6.2-17), the former will involve the reference input  $r(t)$  and disturbances  $d(t)$ , while the latter will involve the sensor noise  $n(t)$ .

**Low-Frequency Specifications** For low frequencies let us suppose that the sensor noise  $n(t)$  is zero so that (6.2-17) becomes

$$E(s) = S(s)(R(s) - D(s)) \quad (6.2-32)$$

Thus, to keep  $\|e(t)\|_2$  small, it is only necessary to ensure that the  $L_2$  operator norm  $\|S\|_2$  is small at all frequencies where  $R(j\omega)$  and  $D(j\omega)$  are appreciable. This may be achieved by ensuring that, at such frequencies,  $\bar{\sigma}(S(j\omega))$  is small. As we have just seen, this may be guaranteed if we select

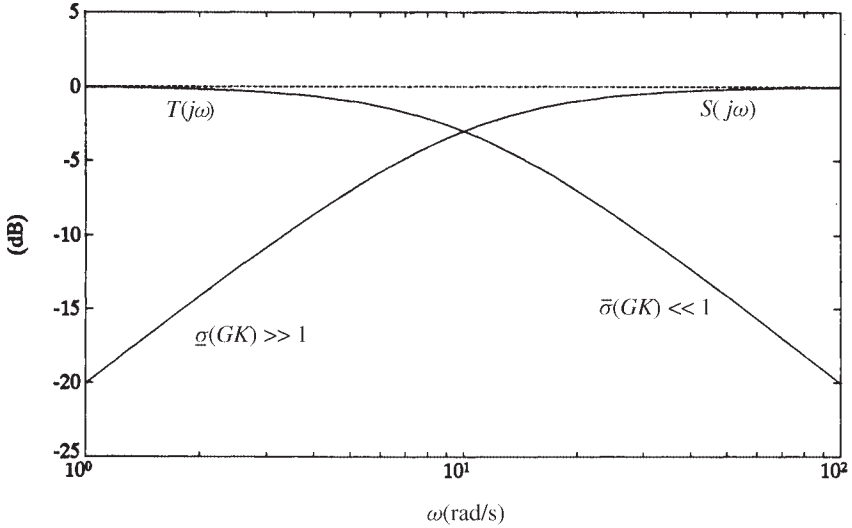


**Figure 6.2-6** Magnitude specifications on  $S(j\omega)$ ,  $T(j\omega)$ , and  $GK(j\omega_0)$ .

$$\underline{\sigma}(GK(j\omega)) \gg 1 \quad \text{for } \omega \leq \omega_d, \quad (6.2-33)$$

where  $D(s)$  and  $R(s)$  are appreciable for  $\omega \leq \omega_d$ .

Thus, exactly as in the classical case (Franklin et al., 1986), we are able to specify a low-frequency performance bound that guarantees *performance robustness*, that is, good performance in the face of low-frequency disturbances. For instance, to ensure that disturbances are attenuated by a factor of 0.01, we should ensure  $\underline{\sigma}(GK(j\omega))$  is greater than 40 dB at low frequencies  $\omega \leq \omega_d$ .

At this point it is worth examining Figure 6.2-9 below, which illustrates the frequency-domain performance specifications we are beginning to derive. Another low-frequency performance bound may be derived from steady-state error considerations. Thus, suppose that  $d(t) = 0$  and the reference input is a unit step of magnitude  $r$  so that  $R(s) = r/s$ . Then, according to (6.2-32) and the final-value theorem (Franklin et al., 1986), the steady-state error  $e_\infty$  is given by

$$e_\infty = \lim_{s \rightarrow 0} sE(s) = rS(0) \quad (6.2-34)$$

To ensure that the largest component of  $e_\infty$  is less than a prescribed small acceptable value  $\delta_\infty$ , we should therefore select

$$\underline{\sigma}(GK(0)) > \frac{r}{\delta_\infty} \quad (6.2-35)$$

The ultimate objective of all our concerns is to manufacture a compensator  $K(s)$  in Figure 6.2-1 that gives desirable performance. Let us now mention two low-frequency

considerations that are important in the initial stages of the design of the compensator  $K(s)$ .

To make the steady-state error in response to a unit step at  $r(t)$  exactly equal to zero, we may ensure that there is an integrator in *each path* of the system  $G(s)$  so that it is of type 1 (Franklin et al., 1986). Thus, suppose that the system to be controlled is given by

$$\begin{aligned}\dot{x} &= Ax + Bv \\ z &= Hx\end{aligned}\tag{6.2-36}$$

To add an integrator to each control path, we may augment the dynamics so that

$$\frac{d}{dt} \begin{bmatrix} x \\ \epsilon \end{bmatrix} = \begin{bmatrix} A & B \\ 0 & 0 \end{bmatrix} \begin{bmatrix} x \\ \epsilon \end{bmatrix} + \begin{bmatrix} 0 \\ I \end{bmatrix} u,\tag{6.2-37}$$

with  $\epsilon$  the integrator outputs (see Figure 6.2-7). The system  $G(s)$  in Figure 6.2-1 should now be taken as (6.2-37), which contains the integrators as a precompensator.

Although augmenting each control path with an integrator results in zero steady-state error, in some applications this may result in an unnecessarily complicated compensator. Note that the steady-state error may be made as small as desired without integrators by selecting  $K(s)$  so that (6.2-35) holds.

A final concern about the low-frequency behavior of  $G(s)$  needs to be addressed. It is desirable in many situations to have  $\underline{\sigma}(GK)$  and  $\overline{\sigma}(GK)$  close to the same value. Then the speed of the responses will be nearly the same in all channels of the system. This is called the issue of *balancing the SVs at low frequency*. The SVs of  $G(s)$  in Figure 6.2-1 may be balanced at low frequencies, as follows.

Suppose that the plant has the state-variable description (6.2-36), and let us add a square constant precompensator gain matrix  $P$ , so that

$$v = Pu\tag{6.2-38}$$

is the relation between the control input  $u(t)$  in Figure 6.2-1 and the actual plant input  $v(t)$ . The transfer function of the plant plus precompensator is now

$$G(s) = H(sI - A)^{-1}BP\tag{6.2-39}$$

As  $s$  goes to zero, this approaches

$$G(0) = H(-A)^{-1}BP,$$

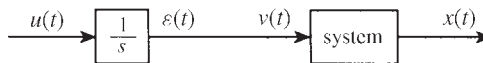


**Figure 6.2-7** Plant augmented with integrators.

as long as  $A$  has no poles at the origin. Therefore, we may ensure that  $G(0)$  has all SVs equal to a prescribed value of  $\gamma$  by selecting

$$P = \gamma[H(-A)^{-1}B]^{-1}, \quad (6.2-40)$$

for then  $G(0) = \gamma I$ .

The transfer function of (6.2-36) is

$$H(s) = H(sI - A)^{-1}B, \quad (6.2-41)$$

whence we see that the required value of the precompensator gain is

$$P = \gamma H^{-1}(0) \quad (6.2-42)$$

This is nothing but the (scaled) reciprocal dc gain.

**Example 6.2-3: Precompensator for Balancing and Zero Steady-State Error** Let us design a precompensator for the system in Example 6.2-1 using the notions just discussed. Substituting the values of  $A$ ,  $B$ , and  $H$  in (6.2-40) with  $\gamma = 1$  yields

$$P = [H(-A)^{-1}B]^{-1} = \begin{bmatrix} 2 & 0 \\ 0 & 20 \end{bmatrix} \quad (1)$$

To ensure zero-steady-state error as well as equal SVs at low frequencies, we may incorporate integrators in each input channel along with the gain matrix  $P$  by writing the augmented system

$$\frac{d}{dt} \begin{bmatrix} x \\ e \end{bmatrix} = \begin{bmatrix} A & B \\ 0 & 0 \end{bmatrix} \begin{bmatrix} x \\ e \end{bmatrix} + \begin{bmatrix} 0 \\ P \end{bmatrix} u \quad (2)$$

The SV plots for this plant plus precompensator appear in Figure 6.2-8. At low frequencies there is now a slope of  $-20$  dB/decade as well as equality of  $\underline{\sigma}$  and  $\bar{\sigma}$ . Thus, the augmented system is both balanced and of type 1. Compare Figure 6.2-8 to the SV plot of the uncompensated system in Figure 6.2-3. The remaining step is the selection of the feedback gain matrix for the augmented plant (2) so that the desired performance is achieved. ■

**High-Frequency Specifications** We now turn to a discussion of high-frequency performance specifications. The sensor noise is generally appreciable at frequencies above some known value  $\omega_n$  (see Figure 6.2-2). Thus, according to (6.2-17), to keep the tracking error norm  $\|e\|_2$  small in the face of measurement noise, we should ensure that the operator norm  $\|T\|_2$  is small at high frequencies above this value. By (6.2-31) this may be guaranteed if

$$\bar{\sigma}(GK(j\omega)) \ll 1 \quad \text{for } \omega \geq \omega_n \quad (6.2-43)$$

(see Figure 6.2-9). For instance, to ensure that sensor noise is attenuated by a factor of 0.1, we should guarantee that  $\bar{\sigma}(GK(j\omega)) < -20$  dB for  $\omega \geq \omega_n$ .

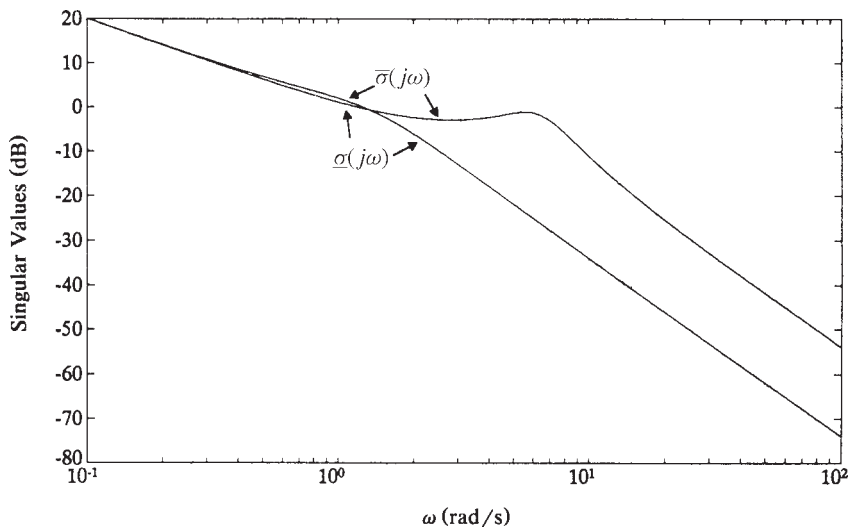


Figure 6.2-8 MIMO Bode magnitude plot for augmented plant.

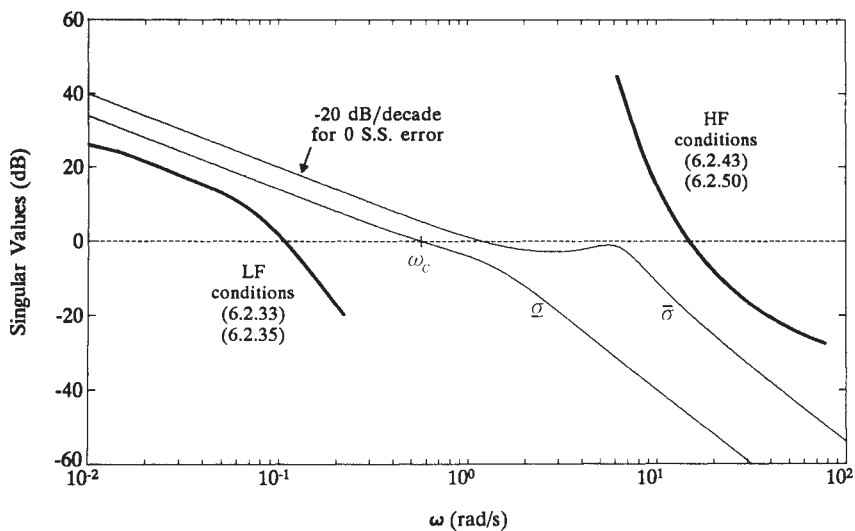


Figure 6.2-9 Frequency-domain performance specifications.

One final high-frequency robustness consideration needs to be mentioned. It is unusual for the plant model to be exactly known. There are two basic sorts of modeling inaccuracies that concern us in aircraft controls. The first is plant parameter variation due to changes in the linearization equilibrium point of the nonlinear model. This is a low-frequency phenomenon and will be discussed in the next subsection.

The second sort of inaccuracy is due to unmodeled high-frequency dynamics; this we discuss here.

We are assuming a rigid-body aircraft model for the purpose of control design and in so doing are neglecting flexible and vibrational modes at high frequencies. Thus, although our design may guarantee closed-loop stability for the *assumed mathematical model*  $G(s)$ , stability is not assured for the *actual plant*  $G'(s)$  with flexible modes. To guarantee *stability robustness* in the face of plant parameter uncertainty, we may proceed as follows.

The model uncertainties may be of two types. The actual plant model  $G'$  and the assumed plant model  $G$  may differ by *additive uncertainties* so that

$$G'(j\omega) = G(j\omega) + \Delta G(j\omega), \quad (6.2-44)$$

where the unknown discrepancy satisfies a known bound

$$\overline{\sigma}(\Delta G(j\omega)) < a(\omega), \quad (6.2-45)$$

with  $a(\omega)$  known for all  $\omega$ .

On the other hand, the actual plant model  $G'(s)$  and the assumed plant model  $G(s)$  may differ by *multiplicative uncertainties* so that

$$G'(j\omega) = [I + M(j\omega)]G(j\omega), \quad (6.2-46)$$

where the unknown discrepancy satisfies a known bound

$$\overline{\sigma}(M(j\omega)) < M(\omega), \quad (6.2-47)$$

with  $m(\omega)$  known for all  $\omega$ . We will show several ways of finding the bound  $m(\omega)$ . In Example 6.2-4 we show how to construct a reduced-order model for the system, which may then be used for control design. There  $m(\omega)$  is determined from the neglected dynamics. In Example 6.3-1 we show how  $m(\omega)$  may be determined in terms of the aircraft's neglected flexible modes. In the next subsection we show how to determine  $m(\omega)$  in terms of plant parameter variations in the linearized model due to operating point changes.

Since we may write (6.2-44) as

$$G'(j\omega) = [I + \Delta G(j\omega)G^{-1}(j\omega)]G(j\omega) \equiv [I + M(j\omega)]G(j\omega), \quad (6.2-48)$$

we will confine ourselves to a discussion of multiplicative uncertainties, following Doyle and Stein (1981).

Suppose that we have designed a compensator  $K(s)$  so that the closed-loop system in Figure 6.2-1 is stable. We should now like to derive a frequency-domain condition that guarantees the stability of the *actual* closed-loop system, which contains not  $G(s)$ ,

but  $G'(s)$ , satisfying (6.2-46)/(6.2-47). For this, the multivariable Nyquist condition (Rosenbrock, 1974) may be used.

Thus, it is required that the encirclement count of the map  $|I + G'K|$  be equal to the negative number of unstable open-loop poles of  $G'K$ . By assumption, this number is the same as that of  $GK$ . Thus, the number of encirclements of  $|I + G'K|$  must remain unchanged for all  $G'$  allowed by (6.2-47). This is assured if and only if  $|I + G'K|$  remains nonzero as  $G$  is warped continuously toward  $G'$ , or equivalently,

$$0 < \underline{\sigma}[I + [I + \epsilon M(s)]G(s)K(s)]$$

for all  $0 \leq \epsilon \leq 1$ , all  $M(s)$  satisfying (6.2-47) and all  $s$  on the standard Nyquist contour.

Since  $G'$  vanishes on the infinite radius segment of the Nyquist contour, and assuming for simplicity that no indentations are required along the  $j\omega$ -axis portion, this reduces to the following equivalent conditions:

$$0 < \underline{\sigma}[I + G(j\omega)K(j\omega) + \epsilon M(j\omega)G(j\omega)K(j\omega)]$$

for all  $0 \leq \epsilon \leq 1$ ,  $0 \leq \omega < \infty$ , all  $M$ ,

$$\text{iff} \quad 0 < \underline{\sigma}[\{I + \epsilon MGK(I + GK)^{-1}\} (I + GK)]$$

$$\text{iff} \quad 0 < \underline{\sigma}[I + MGK(I + GK)^{-1}]$$

$$\text{all} \quad 0 \leq \omega < \infty, \text{ and all } M,$$

$$\text{iff} \quad \overline{\sigma}[GK(I + GK)^{-1}] < \frac{1}{m(\omega)} \quad (6.2-49)$$

for all  $0 \leq \omega < \infty$ . Thus, stability robustness translates into a requirement that the cosensitivity  $T(j\omega)$  be bounded above by the reciprocal of the multiplicative modeling discrepancy bound  $m(\omega)$ .

In the case of high-frequency unmodeled dynamics,  $1/m(\omega)$  is small at high  $\omega$ , so that according to (6.2-31), we may simplify (6.2-49) by writing it in terms of the loop gain as

$$\overline{\sigma}(GK(j\omega)) < \frac{1}{m(\omega)} \quad (6.2-50)$$

for all  $\omega$  such that  $m(\omega) \gg 1$ .

This bound for stability robustness is illustrated in Figure 6.2-9.

An example will be useful at this point.

**Example 6.2-4: Model Reduction and Stability Robustness** In some situations we have a high-order aircraft model that is inconvenient to use for controller design. Examples occur in engine control and spacecraft control. In such situations, it is possible to compute a reduced-order model of the system which may then be used for controller design. Here we will show a convenient technique for model reduction as



well as an illustration of the stability robustness bound  $m(\omega)$ . The technique described here is from Athans et al. (1986).

(a) *Model Reduction by Partial Fraction Expansion.* Suppose that the actual plant is described by

$$\dot{x} = Ax + Bu \quad (1a)$$

$$z = Hx, \quad (1b)$$

with  $x \in \mathbf{R}^n$ . If  $A$  is simple with eigenvalues  $\lambda_i$ , right eigenvectors  $u_i$ , and left eigenvectors  $v_i$  so that

$$Au_i = \lambda_i u_i, \quad v_i^T A = \lambda_i v_i^T, \quad (2)$$

then the transfer function

$$G'(s) = H(sI - A)^{-1}B \quad (3)$$

may be written as the partial fraction expansion (Section 5.2)

$$G'(s) = \sum_{i=1}^n \frac{R_i}{s - \lambda_i}, \quad (4)$$

with residue matrices given by

$$R_i = H u_i v_i^T B \quad (5)$$

If the value of  $n$  is large, it may be desirable to find a *reduced-order approximation* to (1) for which a simplified compensator  $K(s)$  in Figure 6.2-1 may be designed. Then, if the approximation is a good one, the compensator  $K(s)$  should work well when used on the actual plant  $G'(s)$ .

To find a reduced-order approximation  $G(s)$  to the plant, we may proceed as follows. Decide which of the eigenvalues  $\lambda_i$  in (4) are to be retained in  $G(s)$ . This may be done using engineering judgment, by omitting high-frequency modes, by omitting terms in (4) that have small residues, and so on. Let the  $r$  eigenvalues to be retained in  $G(s)$  be  $\lambda_i, \lambda_2, \dots, \lambda_r$ .

Define the matrix

$$Q = \text{diag} \{Q_i\}, \quad (6)$$

where  $Q$  is an  $r \times r$  matrix and the blocks  $Q_i$  are defined as

$$Q_i = \begin{cases} 1, & \text{for each real eigenvalue retained} \\ \begin{bmatrix} \frac{1}{2} & -\frac{j}{2} \\ \frac{j}{2} & \frac{1}{2} \end{bmatrix}, & \text{for each complex pair retained} \end{cases} \quad (7)$$

Compute the matrices

$$V \equiv Q^{-1} \begin{bmatrix} v_i^T \\ \vdots \\ v_r^T \end{bmatrix} \quad (8)$$

$$U \equiv [u_1 \quad \cdots \quad u_r] Q \quad (9)$$

In terms of these constructions, the reduced-order system is nothing but a projection of (1) onto a space of dimension  $r$  with state defined by

$$w = Vx \quad (10)$$

The system matrices in the reduced-order approximate system

$$\dot{w} = Fw + Gu \quad (11a)$$

$$z = Jw + Du \quad (11b)$$

are given by

$$F = VAU$$

$$G = VB$$

$$J = HU, \quad (12)$$

with the direct-feed matrix given in terms of the residues of the neglected eigenvalues as

$$D = \sum_{i=r+1}^n \frac{R_i}{\lambda_i} \quad (13)$$

The motivation for selecting such a  $D$ -matrix is as follows. The transfer function

$$G(s) = J(sI - F)^{-1}G + D$$

of the reduced system (11) is given as (verify!)

$$G(s) = \sum_{i=1}^r \frac{R_i}{s - \lambda_i} + \sum_{i=r+1}^n \frac{R_i}{\lambda_i} \quad (14)$$

Evaluating  $G(j\omega)$  and  $G'(j\omega)$  at  $\omega = 0$ , it is seen that they are equal to dc. Thus, the modeling errors induced by taking  $G(s)$  instead of the actual  $G'(s)$  occur at higher frequencies. Indeed, they depend on the frequencies of the neglected eigenvalues of (1).

To determine the  $M(s)$  in (6.2-46) that is induced by the order reduction, note that

$$G' = (I + M)G \quad (15)$$

so that

$$M = (G' - G)G^{-1} \quad (16)$$

or

$$M(s) = \left[ \sum_{i=r+1}^n \frac{R_i}{\lambda_i} \frac{s}{s - \lambda_i} \right] G^{-1}(s) \quad (17)$$

Then the high-frequency robustness bound is given in terms of

$$m(j\omega) = \overline{\sigma}(M(j\omega)) \quad (18)$$

Note that  $M(j\omega)$  tends to zero as  $\omega$  becomes small, reflecting our perfect certainty of the actual plant at dc.

(b) *An Example.* Let us use an example to illustrate the model reduction procedure and show also how to compute the upper bound  $m(\omega)$  in (6.2-46)/(6.2-47) on the high-frequency modeling errors thereby induced. To make it easy to see what is going on, we will take a Jordan form system.

Let there be prescribed the MIMO system

$$\dot{x} = \begin{bmatrix} -1 & 0 & 0 \\ 0 & -2 & 0 \\ 0 & 0 & -10 \end{bmatrix} x + \begin{bmatrix} 1 & 0 \\ 0 & 1 \\ 2 & 0 \end{bmatrix} u = Ax + Bu \quad (19a)$$

$$z = \begin{bmatrix} 1 & 0 & 0 \\ 0 & 1 & 1 \end{bmatrix} x = Cx \quad (19b)$$

The eigenvectors are given by  $u_i = e_i$ ,  $v_i = e_i$ ,  $i = 1, 2, 3$ , with  $e_i$  the  $i$ th column of the  $3 \times 3$  identity matrix. Thus, the transfer function is given by the partial fraction expansion

$$G'(s) = \frac{R_1}{s+1} + \frac{R_2}{s+2} + \frac{R_3}{s+10}, \quad (20)$$

with

$$R_1 = \begin{bmatrix} 1 & 0 \\ 0 & 0 \end{bmatrix}, \quad R_2 = \begin{bmatrix} 0 & 0 \\ 0 & 1 \end{bmatrix}, \quad R_3 = \begin{bmatrix} 0 & 0 \\ 2 & 0 \end{bmatrix} \quad (21)$$

To find the reduced-order system that retains the poles at  $\lambda = -1$  and  $\lambda = -2$ , define

$$Q = \begin{bmatrix} 1 & 0 \\ 0 & 1 \end{bmatrix}, \quad V = \begin{bmatrix} 1 & 0 & 0 \\ 0 & 1 & 0 \end{bmatrix}, \quad U = \begin{bmatrix} 1 & 0 \\ 0 & 1 \\ 0 & 0 \end{bmatrix} \quad (22)$$

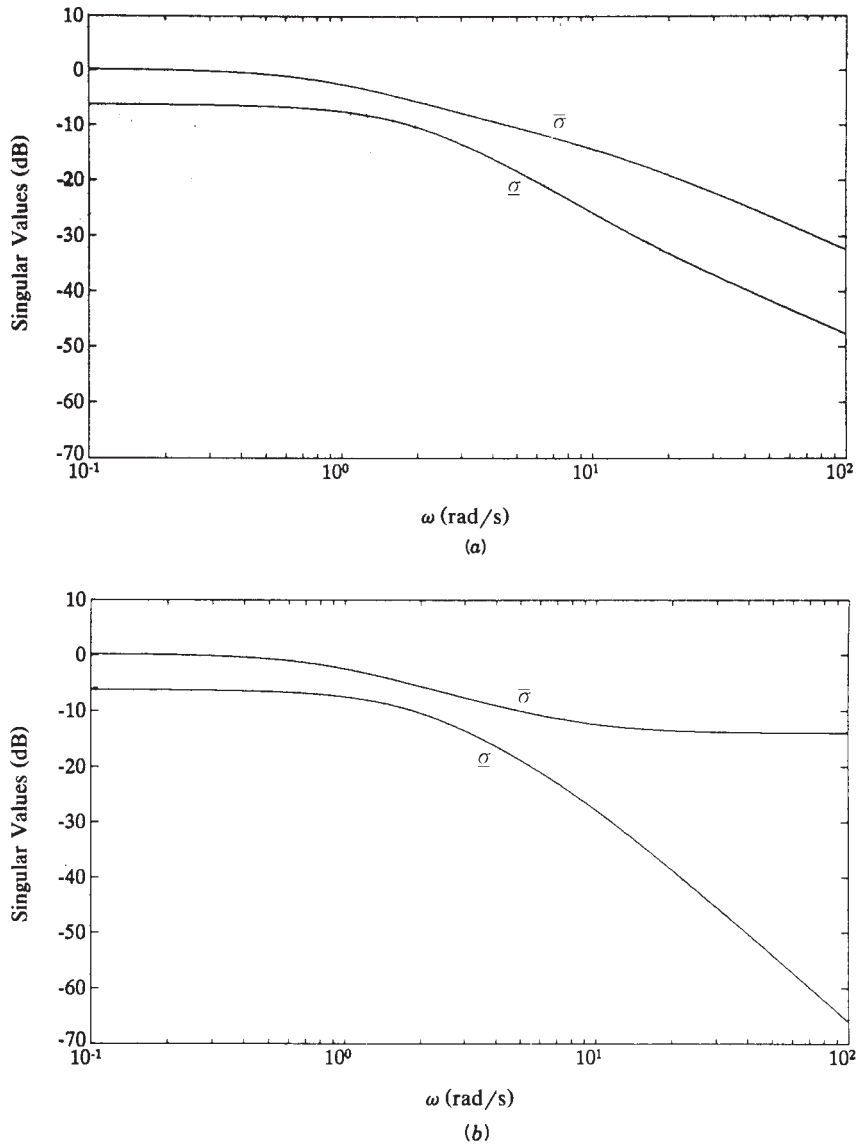


**Figure 6.2-10** MIMO Bode magnitude plots of SVs: (a) actual plant; (b) reduced-order approximation.

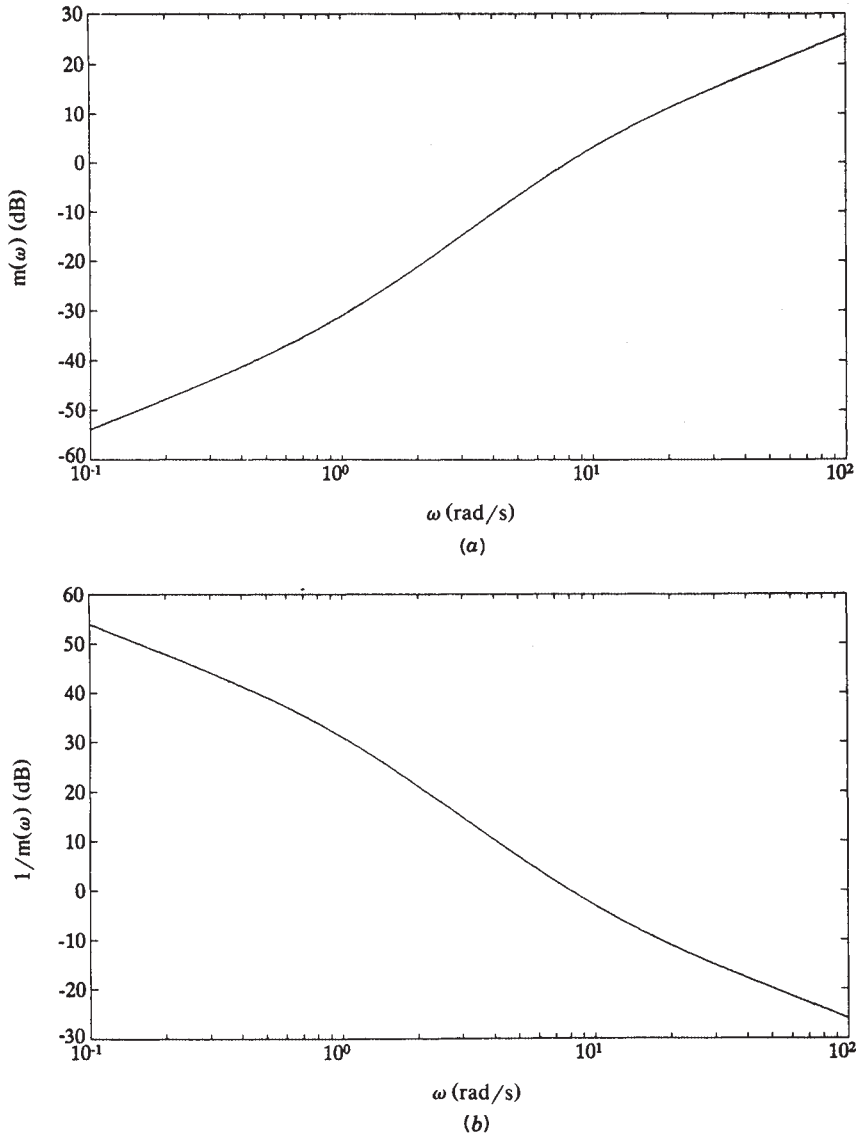


**Figure 6.2-11** High-frequency stability robustness bound: (a)  $m(\omega)$ ; (b)  $1/m(\omega)$ .

and compute the approximate system

$$\dot{w} = \begin{bmatrix} -1 & 0 \\ 0 & -2 \end{bmatrix} w + \begin{bmatrix} 1 & 0 \\ 0 & 1 \end{bmatrix} u = Fw + Gu \quad (23a)$$

$$z = \begin{bmatrix} 1 & 0 \\ 0 & 1 \end{bmatrix} w + \begin{bmatrix} 0 & 0 \\ 0.2 & 0 \end{bmatrix} u = Jw + Du \quad (23b)$$

This has a transfer function of

$$G(s) = \frac{R_1}{s+1} + \frac{R_2}{s+2} + D \quad (24)$$

Singular-value plots of the actual plant (19) and the reduced-order approximation (23) are shown in Figure 6.2-10.

The multiplicative error is given by

$$M = (G' - G)G^{-1} = \begin{bmatrix} 0 & 0 \\ -\frac{0.2s(s+1)}{s+10} & 0 \end{bmatrix}, \quad (25)$$

whence

$$m(\omega) = \bar{\sigma}(M(j(\omega))) = \frac{0.2\omega\sqrt{\omega^2 + 1}}{\sqrt{\omega^2 + 100}}, \quad (26)$$

and the high-frequency bound on the loop gain  $GK(j\omega)$  is given by

$$\frac{1}{m(j\omega)} = \frac{5\sqrt{\omega^2 + 100}}{\omega\sqrt{\omega^2 + 1}} \quad (28)$$

This bound is plotted in Figure 6.2-11. Note that the modeling errors become appreciable (i.e., of magnitude 1) at a frequency of 8.0 rad/s. Above this frequency, we should ensure that constraint (6.2-50) on the loop gain magnitude holds to guarantee stability robustness. This will be a restriction on any compensator  $K(s)$  designed using the reduced-order plant (23). ■

## Robustness Bounds for Plant Parameter Variations

The aircraft is nonlinear, but for controller design we use linearized models obtained at some operating point. In practice, it is necessary to determine linear models at several design operating points over a specified flight envelope and determine optimal control gains for each one. Then these design control gains are tabulated and scheduled using microprocessors, so that the gains most appropriate for the actual operating point of the aircraft are used in the controller. It is usual to determine which of the design operating points are closest to the actual operating point and use some sort of linear combination of the control gains corresponding to these design points.

It is important for the control gains to stabilize the aircraft at all points near the design operating point for this gain-scheduling procedure to be effective. In passing

from operating point to operating point, the parameters of the state-variable model vary. Using (6.2-49), we may design controllers that guarantee robust stability despite plant parameter variations.

Suppose that the nominal perturbed model used for design is

$$\begin{aligned}\dot{x} &= Ax + Bu \\ y &= Cx\end{aligned}\tag{6.2-51}$$

which has the transfer function

$$G(s) = C(sI - A)^{-1}B\tag{6.2-52}$$

However, due to operating point changes the actual aircraft perturbed motion is described by

$$\begin{aligned}\dot{x} &= (A + \Delta A)x + (B + \Delta B)u \\ y &= (C + \Delta C)x,\end{aligned}\tag{6.2-53}$$

where the plant parameter variation matrices are  $\Delta A$ ,  $\Delta B$ ,  $\Delta C$ . It is not difficult to show [see Stevens et al. (1987) and the problems at the end of this chapter] that this results in the transfer function

$$G'(s) = G(s) + \Delta G(s),$$

with

$$\begin{aligned}\Delta G(s) &= C(sI - A)^{-1}\Delta B + \Delta C (sI - A)^{-1}B \\ &\quad + C(sI - A)^{-1}\Delta A(sI - A)^{-1}B,\end{aligned}\tag{6.2-54}$$

where second-order effects have been neglected. Hence (6.2-48) may be used to determine the multiplicative uncertainty bound  $m(\omega)$ . The cosensitivity  $T(j\omega)$  should then satisfy the upper bound (6.2-49) for guaranteed stability in the face of the parameter variations  $\Delta A$ ,  $\Delta B$ ,  $\Delta C$ .

Since  $(sI - A)^{-1}$  has a relative degree of at least 1, the high-frequency roll-off of  $\Delta G(j\omega)$  is at least  $-20$  dB/decade. Thus, plant parameter variations yield an upper bound for the cosensitivity at low frequencies.

Using (6.2-54) it is possible to design robust controllers over a range of operating points that do not require gain scheduling. Compare with Minto et al. (1990).

### 6.3 ROBUST OUTPUT FEEDBACK DESIGN

We should now like to incorporate the robustness concepts introduced in Section 6.2 into the LQ output feedback design procedure for aircraft control systems. This may be accomplished using the following steps:

1. If necessary, augment the plant with added dynamics to achieve the required steady-state error behavior or to achieve balanced SVs at dc. Use the techniques of Example 6.2-3.
2. Select a performance index, the PI weighting matrices  $Q$  and  $R$ , and, if applicable, the time weighting factor  $k$  in  $t^k$ .
3. Determine the optimal output feedback gain  $K$  using, for instance, Table 5.4-1 or 5.5-1.
4. Simulate the time responses of the closed-loop system to verify that they are satisfactory. If not, select different  $Q$ ,  $R$ , and  $k$  and return to step 3.
5. Determine the low-frequency and high-frequency bounds required for performance robustness and stability robustness. Plot the loop gain SVs to verify that the bounds are satisfied. If they are not, select new  $Q$ ,  $R$ , and  $k$  and return to step 3.

An example will illustrate the robust output feedback design procedure.

**Example 6.3-1: Pitch-Rate Control System Robust to Wind Gusts and Unmodeled Flexible Mode** Here we will illustrate the design of a pitch-rate control system that is robust in the presence of vertical wind gusts and the unmodeled dynamics associated with a flexible mode. It would be worthwhile first to review the pitch-rate CAS designed in Examples 4.5-1 and 5.5-3.

(a) *Control System Structure.* The pitch-rate CAS system is described in Example 5.5-3. The state and measured outputs are

$$x = \begin{bmatrix} \alpha \\ q \\ \delta_e \\ \alpha_F \\ \epsilon \end{bmatrix}, \quad y = \begin{bmatrix} \alpha_F \\ q \\ \epsilon \end{bmatrix}, \quad (1)$$

with  $\alpha_F$  the filtered angle of attack and  $\epsilon$  the output of the integrator added to ensure zero steady-state error. The performance output  $z(t)$  that should track the reference input  $r(t)$  is  $q(t)$ .

Linearizing the F-16 dynamics about the nominal flight condition in Table 3.6-3 (502 ft/s, level flight,  $x_{cg} = 0.35 \bar{\tau}$ ) yields

$$\dot{x} = Ax + Bu + Gr \quad (2)$$

$$y = Cx + Fr \quad (3)$$

$$z = Hx, \quad (4)$$

with the system matrices given in Example 5.5-3.



The control input is

$$u = -Ky = -\begin{bmatrix} k_\alpha & k_q & k_1 \end{bmatrix} y = -k_\alpha \alpha_F - k_q q - k_1 \epsilon \quad (5)$$

It is desired to select the control gains to guarantee a good response to a step command  $r$  in the presence of vertical wind gusts and the unmodeled dynamics of the first flexible mode.

(b) *Frequency-Domain Robustness Bounds.* According to *Mil. Spec. 1797* (1987), the vertical wind gust noise has a spectral density given in Dryden form as

$$\Phi_w(\omega) = 2L\sigma^2 \frac{1 + 3L^2\omega^2}{(1 + L^2\omega^2)^2}, \quad (6)$$

with  $\omega$  the frequency in rad/s,  $\sigma$  the turbulence intensity, and  $L$  the turbulence scale length divided by true airspeed. Assuming that the vertical gust velocity is a disturbance input that changes the angle of attack, the software described in Chapter 3 can be used to find a control input matrix from gust velocity to  $x$ . Then, using stochastic techniques like those in Example 6.4-2, the magnitude of the gust disturbance versus frequency can be found. It is shown in Figure 6.3-1. We took  $\sigma = 10$  ft/s and  $L = (1700 \text{ ft}) / (502 \text{ ft/s}) = 3.49$  s.

Let the transfer function of the rigid dynamics from  $u(t)$  to  $z(t)$  be denoted by  $G(s)$ . Then the transfer function including the first flexible mode is given by Blakelock (1965):

$$G'(s) = G(s)F(s), \quad (7)$$

where

$$F(s) = \frac{\omega_n^2}{s^2 + 2\zeta\omega_n s + \omega_n^2}, \quad (8)$$

with  $\omega_n = 40$  rad/s and  $\zeta = 0.3$ . According to Section 6.2, therefore, the multiplicative uncertainty is given by

$$M(s) = F(s) - I = \frac{-s(s + 2\zeta\omega_n)}{s^2 + 2\zeta\omega_n s + \omega_n^2} \quad (9)$$

The magnitude of  $1/M(j\omega)$  is shown in Figure 6.3-1.

We should like to perform our control design using only the rigid dynamics  $G(s)$ . Then, for performance robustness in the face of the gust disturbance and stability robustness in the face of the first flexible mode, the loop gain SVs should lie within the bounds implied by the gust disturbance magnitude and  $1/|M(j\omega)|$ .

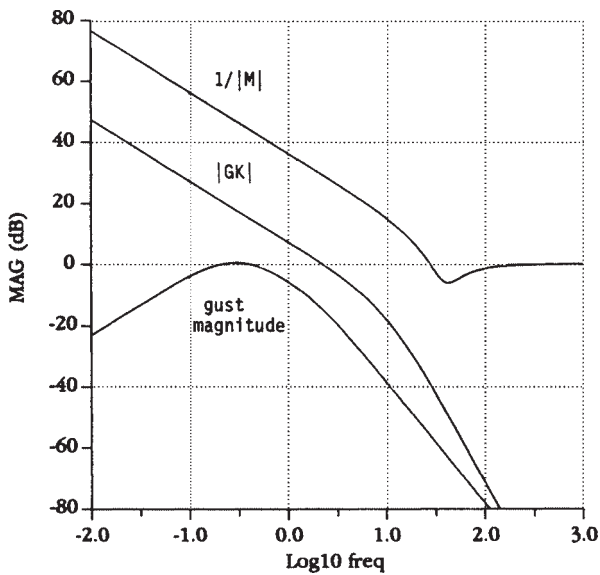


Figure 6.3-1 Frequency-domain magnitude plots and robustness bounds.

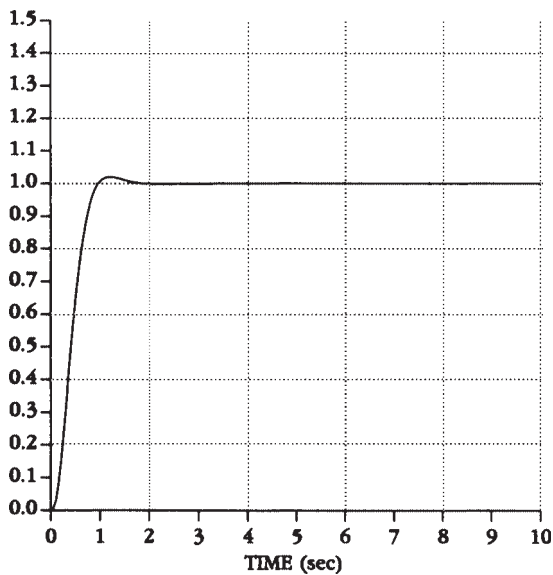


Figure 6.3-2 Optimal pitch-rate step response.

(c) *Controls Design and Robustness Verification.* In Example 5.5-3(c) we performed a derivative-weighting design and obtained the control gains

$$K = \begin{bmatrix} -0.0807 & -0.475 & 1.361 \end{bmatrix} \quad (10)$$

The resulting step response is reproduced in Figure 6.3-2, and the closed-loop poles were

$$\begin{aligned} s &= -3.26 \pm j2.83 \\ &- 1.02 \\ &- 10.67, -14.09 \end{aligned} \quad (11)$$

To verify that the robustness bounds hold for this design, it is necessary to find the loop gain  $GK(s)$  of the closed-loop system. Thus, in the figure of Example 5.5-3 it is necessary to find the loop transfer function from  $e(t)$  around to  $e(t)$  [i.e., from  $e(t)$  to  $-z(t)$ ]. With respect to this loop gain, note that some of the elements in (10) are feedforward gains while some are feedback gains.

The magnitude of  $GK(j\omega)$  is plotted in Figure 6.3-1. Note that the robustness bounds are satisfied. Therefore, this design is robust in the presence of vertical turbulence velocities up to 10 ft/s as well as the first flexible mode. ■

## 6.4 OBSERVERS AND THE KALMAN FILTER

The central theme in Chapter 5 was control design using partial state or output feedback. We saw in Section 5.4 that by using output feedback a compensator of any desired structure may be used, with the feedback gains being selected by modern LQ techniques. Thus, output feedback design is very suitable for aircraft control. In Section 6.3 we saw how to verify the robustness of the closed-loop system using multivariable Bode plots.

On the other hand, in Section 5.7 we saw that the design equations for full-state-variable feedback were simpler than those for output feedback. In fact, in state-variable design it is only necessary to solve the matrix Riccati equation, for which there are many good techniques [ORACLS (Armstrong, 1980), PC-MATLAB (Moler et al., 1987), and MATRIX<sub>x</sub> (1989)]. By contrast, in output feedback design it is necessary to solve three coupled nonlinear equations (see Table 5.3-1), which must generally be done using iterative techniques (Moerder and Calise, 1985; Press et al., 1986).

Moreover, in the case of full state feedback, if the system  $(A, B)$  is reachable and  $(\sqrt{Q}, A)$  is observable (with  $Q$  the state weighting in the PI), the Kalman gain is guaranteed to stabilize the plant and yield a global minimum value for the PI. This is a fundamental result of modern control theory, and no such result yet exists for output feedback. The best that may be said is that if the plant is output stabilizable, the algorithm of Table 5.3-2 yields a local minimum for the PI and a stable plant.

Another issue is that the LQ regulator with full state feedback enjoys some important robustness properties that are not guaranteed using output feedback. Specifically, as we will see in Section 6.5, it has an infinite gain margin and 60% of phase margin.

Thus, state feedback design offers some advantages over output feedback if the structure of the compensator is of no concern. Although this is rarely the case in aircraft controls, it is nevertheless instructive to pursue a compensator design technique based on state feedback.

Since all the states are seldom available, the first order of business is to estimate the full state  $x(t)$  given only partial information in the form of the measured outputs  $y(t)$ . This is the *observer design* problem. Having estimated the state, we may then use the *estimate* of the state for feedback purposes, designing a feedback gain *as if* all the states were measurable. The combination of the observer and the state feedback gain is then a dynamic regulator similar to those used in classical control, as we will show in the last portion of this section. In the modern approach, however, it is straightforward to design multivariable regulators with desirable properties by solving matrix equations due to the fundamental *separation principle*, which states that the feedback gain and observer may be designed separately and then concatenated.

One of our prime objectives in this section and the next is to discuss the LQG/LTR technique for control design. This is an important modern technique for the design of robust aircraft control systems. It relies on full-state-feedback design, followed by the design of an observer that allows full recovery of the guaranteed robustness properties of the LQ regulator with state feedback.

Of course, observers and filters have important applications in aircraft in their own right. For instance, the angle of attack is difficult to measure accurately; however, using an observer or Kalman filter, it is not difficult to estimate the angle of attack very precisely by measuring pitch rate and normal acceleration (see Example 6.4-2).

## Observer Design

In aircraft control, all of the states are rarely available for feedback purposes. Instead, only the measured outputs are available. Using modern control theory, if the measured outputs capture enough information about the dynamics of the system, it is possible to use them to *estimate* or *observe* all the states. Then these state estimates may be used for feedback purposes.

To see how a state observer can be constructed, consider the aircraft equations in state-space form

$$\dot{x} = Ax + Bu \quad (6.4-1)$$

$$y = Cx, \quad (6.4-2)$$

with  $x(t) \in \mathbf{R}^n$  the state,  $u(t) \in \mathbf{R}^m$  the control input, and  $y(t) \in \mathbf{R}^p$  the available measured outputs.

Let the estimate of  $x(t)$  be  $\hat{x}(t)$ . We claim that the state observer is a dynamical system described by

$$\dot{\hat{x}} = A\hat{x} + Bu + L(y - C\hat{x}) \quad (6.4-3)$$

or

$$\dot{\hat{x}} = (A - LC)\hat{x} + Bu + Ly \equiv A_0\hat{x} + Bu + Ly \quad (6.4-4)$$

That is, the observer is a system with two inputs, namely,  $u(t)$  and  $y(t)$ , both of which are known.

Since  $\hat{x}(t)$  is the state estimate, we could call

$$\hat{y} = C\hat{x} \quad (6.4-5)$$

the estimated output. It is desired that  $\hat{x}(t)$  be close to  $x(t)$ . Thus, if the observer is working properly, the quantity  $y - \hat{y}$  that appears in (6.4-3) should be small. In fact,

$$\tilde{y} = y - \hat{y} \quad (6.4-6)$$

is the *output estimation error*.

It is worth examining Figure 6.4-1, which depicts the state observer. Note that the observer consists of two parts: a *model of the system* involving  $(A, B, C)$  and an *error-correcting portion* that involves the output error multiplied by  $L$ . We call matrix  $L$  the *observer gain*.

To demonstrate that the proposed dynamical system is indeed an observer, it is necessary to show that it manufactures an estimate  $\hat{x}(t)$  that is close to the actual state  $x(t)$ . For this purpose, define the (*state*) *estimation error* as

$$\tilde{x} = x - \hat{x} \quad (6.4-7)$$

By differentiating (6.4-7) and using (6.4-1) and (6.4-4), it is seen that the estimation error has dynamics given by

$$\dot{\tilde{x}} = (A - LC)\tilde{x} = A_0\tilde{x} \quad (6.4-8)$$

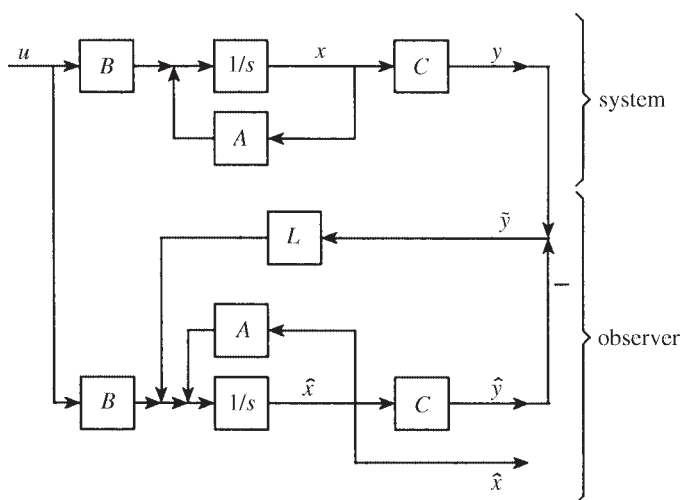


Figure 6.4-1 State observer.

The initial estimation error is  $\tilde{x}(0) = x(0) - \hat{x}(0)$ , with  $\hat{x}(0)$  the initial estimate, which is generally taken as zero.

It is required that the estimation error vanish with time for any  $\tilde{x}(0)$ , for then  $\hat{x}(t)$  will approach  $x(t)$ . This will occur if  $A_0 = (A - LC)$  is asymptotically stable. Therefore, as long as we select the observer gain  $L$  so that  $(A - LC)$  is stable, (6.4-3) is indeed an observer for the state in (6.4-1). The observer design problem is to select  $L$  so that the error vanishes suitably quickly. It is a well-known result of modern control theory that the poles of  $(A - LC)$  may be arbitrarily assigned to desired locations if and only if  $(C, A)$  is observable.

Since, according to Figure 6.4-1, we are injecting the output into the state derivative,  $L$  is called an *output injection*. Observers of the sort we are mentioning here are called *output injection observers*, and their design could be called output injection design.

It is important to discuss the output injection problem of selecting  $L$  so that  $(A - LC)$  is stable, for it is a problem we have already solved under a different guise. The state feedback control law for system (6.4-1) is

$$u = -Kx, \quad (6.4-9)$$

which results in the closed-loop system

$$\dot{x} = (A - BK)x \quad (6.4-10)$$

The state feedback design problem is to select  $K$  for desired closed-loop properties. We have shown how this may be accomplished in Section 5.7. Thus, if we select the feedback gain as the Kalman gain

$$K = R^{-1}B^T P, \quad (6.4-11)$$

with  $P$  the positive-definite solution to the algebraic Riccati equation (ARE)

$$0 = A^T P + PA + Q - PBR^{-1}B^T P, \quad (6.4-12)$$

then if  $(A, B)$  is reachable and  $(\sqrt{Q}, A)$  is observable, the closed-loop system is guaranteed to be stable. The matrices  $Q$  and  $R$  are design parameters that will determine the closed-loop dynamics, as we have seen in the examples of Chapter 5.

Now, compare (6.4-8) and (6.4-10). They are very similar. In fact,

$$(A - LC)^T = A^T - C^T L^T, \quad (6.4-13)$$

which has the free matrix  $L^T$  to the right, exactly as in the state feedback problem involving  $(A - BK)$ . This important fact is called *duality*, that is, state feedback and output injection are duals. [Note that  $A - LC$  and  $(A - LC)^T$  have the same poles.]

The important result of duality for us is that *the same theory we have developed for selecting the state feedback gain may be used to select the output injection gain  $L$ .*

In fact, compare (6.4-13) to  $(A - BK)$ . Now, in the design equations (6.4-11) and (6.4-12) let us replace  $A$ ,  $B$ , and  $K$  everywhere they occur by  $A^T$ ,  $C^T$ , and  $L^T$ , respectively. The result is

$$\begin{aligned} L^T &= R^{-1}CP \\ 0 &= AP + PA^T + Q - PC^T R^{-1}CP \end{aligned} \quad (6.4-14)$$

The first of these may be rewritten as

$$L = P C^T R^{-1} \quad (6.4-15)$$

We call (6.4-14) the *observer ARE*.

Let us note the following connection between reachability and observability. Taking the transpose of the reachability matrix yields

$$\begin{aligned} U^T &= [B \quad AB \quad A^2B \quad \cdots \quad A^{n-1}B]^T \\ &= \begin{bmatrix} B^T \\ B^T A \\ \vdots \\ B^T (A^T)^{n-1} \end{bmatrix} \end{aligned} \quad (6.4-16)$$

However, the observability matrix is

$$V = \begin{bmatrix} C \\ CA \\ \vdots \\ CA^{n-1} \end{bmatrix} \quad (6.4-17)$$

Comparing  $U^T$  and  $V$ , it is apparent that they have the same form. In fact, since  $U$  and  $U^T$  have the same rank, it is evident that  $(A, B)$  is reachable if and only if  $(B^T, A^T)$  is observable. This is another aspect of duality.

Taking into account these notions, an essential result of output injection is the following. It is the dual of the guaranteed stability using the Kalman gain discussed in Section 5.7. Due to its importance, we formulate it as a theorem.

**Theorem.** *Let  $(C, A)$  be observable and  $(A, \sqrt{Q})$  be reachable. Then the error system (6.4-8) using the gain  $L$  given by (6.4-15), with  $P$  the unique positive-definite solution to (6.4-14), is asymptotically stable. ■*

Stability of the error system guarantees that the state estimate  $\hat{x}(t)$  will approach the actual state  $x(t)$ . By selecting  $L$  to place the poles of  $(A - LC)$  far enough to the left in the  $s$ -plane, the estimation error  $\tilde{x}(t)$  can be made to vanish as quickly as desired.

The power of this theorem is that we may treat  $Q$  and  $R$  as design parameters that may be turned until suitable observer behavior results for the gain computed from the

observer ARE. As long as we select  $Q$  and  $R$  to satisfy the theorem, observer stability is assured. An additional factor, of course, is that software for solving the observer ARE is readily available [e.g., ORACLS (Armstrong, 1980), PC-MATLAB (Moler et al., 1987), and MATRIX<sub>x</sub> (1989)].

We have assumed that the system matrices  $(A, B, C)$  are exactly known. Unfortunately, in reality this is rarely the case. In aircraft control, for instance, (6.4-1) and (6.4-2) represent a model of a nonlinear system at an equilibrium point. Variations in the operating point will result in variations in the elements of  $A$ ,  $B$ , and  $C$ . However, if the poles of  $(A - LC)$  are selected far enough to the left in the  $s$ -plane (i.e., fast enough), the estimation error will be small despite uncertainties in the system matrices. That is, the observer has some robustness to modeling inaccuracies.

It is worth mentioning that there are many other techniques for the selection of the observer gain  $L$ . In the single-output case the observability matrix  $V$  is square. Then Ackermann's formula (Franklin et al., 1986) may be used to compute  $L$ . If

$$\Delta_{(0)}(s) = |sI - (A - LC)| \quad (6.4-18)$$

is the desired observer characteristic polynomial, the required observer gain is given by

$$L = \Delta_0(A)V^{-1}e_n, \quad (6.4-19)$$

with  $e_n = [0 \cdots 0 \ 1]^T$  the last column of the  $n \times n$  identity matrix.

A general rule of thumb is that for suitable accuracy in the state estimate  $\hat{x}(t)$ , the slowest observer pole should have a real part 5 to 10 times larger than the real part of the fastest system pole. That is, the observer time constants should be 5 to 10 times larger than the system time constants.

**Example 6.4-1: Observer Design for Double Integrator System** In Example 5.7-1 we discussed state feedback design for systems obeying Newton's laws,

$$\dot{x} = \begin{bmatrix} 0 & 1 \\ 0 & 0 \end{bmatrix} x + \begin{bmatrix} 0 \\ 1 \end{bmatrix} u = Ax + Bu, \quad (1)$$

where the state is  $x = [d \ v]^T$ , with  $d(t)$  the position and  $v(t)$  the velocity, and the control  $u(t)$  is an acceleration input. Let us take position measurements so that the measured output is

$$y = [1 \ 0]x = Cx \quad (2)$$

We should like to design an observer that will reconstruct the full state  $x(t)$  given only position measurements. Let us note that simple differentiation of  $y(t) = d(t)$  to obtain  $v(t)$  is unsatisfactory, since differentiation increases sensor noise. In fact, the observer is a *low-pass* filter that provides estimates while rejecting high-frequency noise. We will discuss two techniques for observer design.



(a) *Riccati Equation Design.* There is good software available in standard design packages for solving the observer ARE [e.g., ORACLS (Armstrong, 1980) and PCMATLAB (Moler et al., 1987)]. However, in this example we want to solve the ARE analytically to show the relation between the design parameters  $Q$  and  $R$  and the observer poles.

Selecting  $R = 1$  and  $Q = \text{diag}\{q_d, q_v^2\}$  with  $q_d$  and  $q_v$  nonnegative, we may assume that

$$P = \begin{bmatrix} p_1 & p_2 \\ p_2 & p_3 \end{bmatrix} \quad (3)$$

for some scalars  $p_1, p_2$ , and  $p_3$  to be determined. The observer ARE (6.4-14) becomes

$$\begin{aligned} 0 = & \begin{bmatrix} 0 & 1 \\ 0 & 0 \end{bmatrix} \begin{bmatrix} p_1 & p_2 \\ p_2 & p_3 \end{bmatrix} + \begin{bmatrix} p_1 & p_2 \\ p_2 & p_3 \end{bmatrix} \begin{bmatrix} 0 & 0 \\ 1 & 0 \end{bmatrix} + \begin{bmatrix} q_d & 0 \\ 0 & q_v^2 \end{bmatrix} \\ & - \begin{bmatrix} p_1 & p_2 \\ p_2 & p_3 \end{bmatrix} \begin{bmatrix} 1 & 0 \\ 0 & 0 \end{bmatrix} \begin{bmatrix} p_1 & p_2 \\ p_2 & p_3 \end{bmatrix}, \end{aligned} \quad (4)$$

which may be multiplied out to obtain the three scalar equations

$$0 = 2p_2 - p_1^2 + q_d \quad (5a)$$

$$0 = p_3 - p_1 p_2 \quad (5b)$$

$$0 = p_2^2 + q_v^2 \quad (5c)$$

Solving these equations gives

$$p_2 = q_v \quad (6a)$$

$$p_1 = \sqrt{2} \sqrt{q_v + \frac{q_d}{2}} \quad (6b)$$

$$p_3 = q_v \sqrt{2} \sqrt{q_v + \frac{q_d}{2}}, \quad (6c)$$

where we have selected the signs that make  $P$  positive definite.

According to (6.4-15), the observer gain is equal to

$$L = \begin{bmatrix} p_1 & p_2 \\ p_2 & p_3 \end{bmatrix} \begin{bmatrix} 1 \\ 0 \end{bmatrix} = \begin{bmatrix} p_1 \\ p_2 \end{bmatrix} \quad (7)$$

Therefore,

$$L = \begin{bmatrix} \sqrt{2} \sqrt{q_v + \frac{q_d}{2}} \\ q_v \end{bmatrix} \quad (8)$$

Using (8), the error system matrix is found to be

$$A_0 = (A - LC) = \begin{bmatrix} -\sqrt{2}\sqrt{q_v + \frac{q_d}{2}} & 1 \\ -q_v & 0 \end{bmatrix} \quad (9)$$

Therefore, the observer characteristic polynomial is

$$\Delta_0(s) = |sI - A_0| = s^2 + 2\zeta\omega s + \omega^2, \quad (10)$$

with the observer natural frequency  $\omega$  and damping ratio  $\zeta$  given by

$$\omega = \sqrt{q_v}, \quad \zeta = \frac{1}{\sqrt{2}}\sqrt{1 + \frac{q_d}{2q_v}} \quad (11)$$

It is now clear how selection of  $Q$  affects the observer behavior. Note that if  $q_d = 0$ , the damping ratio becomes the familiar  $1/\sqrt{2}$ .

The reader should verify that the system is observable and that  $(A, \sqrt{Q})$  is reachable as long as  $q_v \neq 0$ . A comparison with Example 5.7-1, where a state feedback was designed for Newton's system, reveals some interesting aspects of duality.

(b) *Ackermann's Formula Design.* Riccati equation observer design is useful whether the plant has only one or multiple outputs. If there is only one output, we may use Ackermann's formula (6.4-19).

Let the desired observer polynomial be

$$\Delta_0(s) = s^2 + 2\zeta\omega s + \omega^2 \quad (12)$$

for some specified damping ratio  $\zeta$  and natural frequency  $\omega$ . Then

$$\Delta_0(A) = A^2 + 2\zeta\omega A + \omega^2 I = \begin{bmatrix} \omega_2 & 2\zeta\omega \\ 0 & \omega^2 \end{bmatrix} \quad (13)$$

$$V = \begin{bmatrix} C \\ CA \end{bmatrix} = I, \quad (14)$$

so that the observer gain is

$$L = \begin{bmatrix} 2\zeta\omega \\ \omega_2 \end{bmatrix} \quad (15)$$

One may verify that the characteristic polynomial of  $A_0 = A - LC$  is indeed (12).

(c) *Simulation.* To design an observer with a complex pole pair having damping ratio of  $\zeta = 1/\sqrt{2}$  and natural frequency of  $\omega = 1$  rad/s, the observer gain was selected as

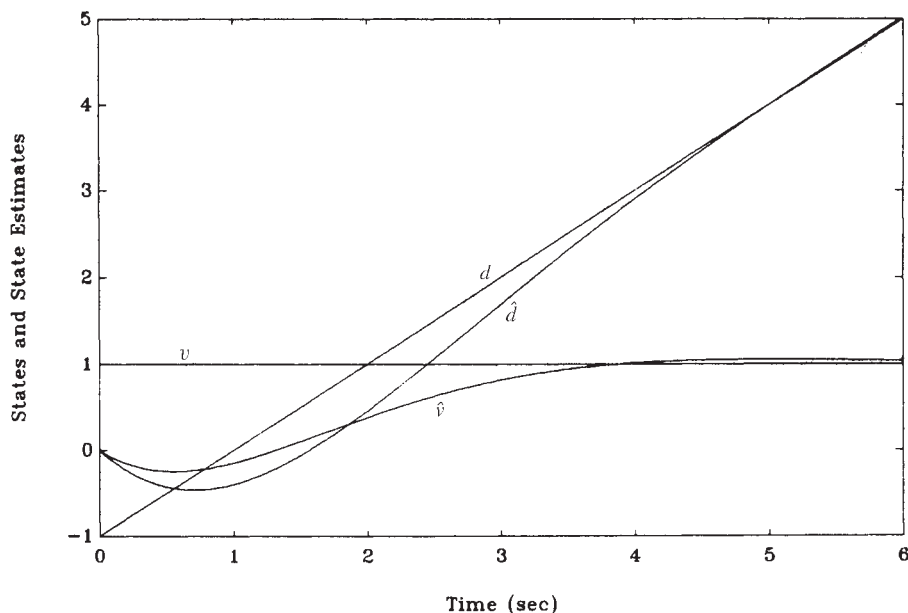


Figure 6.4-2 Actual and estimated states.

$$L = \begin{bmatrix} \sqrt{2} \\ 1 \end{bmatrix} \quad (16)$$

A simulation was performed. The time histories of the actual states and their estimates are shown in Figure 6.4-2. The initial conditions were  $d(0) = -1$ ,  $v(0) = 1$  and the input was  $u(t) = 0$ . The observer was started with initial states of  $\hat{d}(0) = 0$ ,  $\hat{v}(0) = 0$ . ■

## The Kalman Filter

Throughout Chapter 5 we assumed that the system is exactly known and that no modeling inaccuracies, disturbances, or noises are present. In fact, nature is seldom so cooperative. In Sections 6.2 and 6.3 we showed how to take account of uncertainties in the model and the environment using a robust frequency-domain approach. An alternative is to treat uncertainties using *probability theory*.

In this subsection we develop the Kalman filter, which is based on a probabilistic treatment of process and measurement noises. The Kalman filter is an observer that is used for navigation and other applications that require the reconstruction of the state from noisy measurements. Since it is fundamentally a low-pass filter, it has good noise rejection capabilities. In Example 6.4-2 we show how to use the Kalman filter to estimate the angle of attack in the face of gust disturbances. In Section 6.5 we show how to use a state-variable feedback and a Kalman filter to design robust aircraft controllers by using the LQG/LTR technique.

We begin with a brief review of probability theory. It is not necessary to follow the derivation to use the Kalman filter: It is only necessary to solve the design equations in Table 6.4-1 below. Thus, one could skip the review that follows. However, an understanding of the theory will result in more sensible application of the filter. Supplemental references are Gelb (1974) and Lewis (1986b).

**A Brief Review of Probability Theory** Suppose that the plant is described by the stochastic dynamical equation

$$\dot{x} = Ax + Bu + Gw \quad (6.4-20)$$

$$y = Cx + v, \quad (6.4-21)$$

with state  $x(t) \in \mathbf{R}^n$ , control input  $u(t) \in \mathbf{R}^m$ , and measured output  $y(t) \in \mathbf{R}^p$ . Signal  $w(t)$  is an unknown *process noise* that acts to disturb the plant. It could represent the effects of wind gusts, for instance, or unmodeled high-frequency plant dynamics. Signal  $v(t)$  is an unknown *measurement noise* that acts to impair the measurements; it could represent sensor noise.

Since (6.4-20) is driven by process noise, the state  $x(t)$  is now also a random process, as is  $y(t)$ . To investigate average properties of random processes, we will require several concepts from probability theory (Papoulis, 1984). The point is that although  $w(t)$  and  $v(t)$  represent unknown random processes, we do in fact know something about them which can help us in control design. For instance, we may know their average values or total energy content. The concepts we will now define allow us to incorporate this general sort of knowledge into our theory.

Given a random vector  $z \in \mathbf{R}^n$ , we denote by  $f_z(\zeta)$  the *probability density function (PDF)* of  $z$ . The PDF represents the probability that  $z$  takes on a value within the differential region  $d\zeta$  centered at  $\zeta$ . Although the value of  $z$  may be unknown, it is quite common in many situations to have a good feel for its PDF.

The *expected value* of a function  $g(z)$  of a random vector  $z$  is defined as

$$E\{g(z)\} = \int_{-\infty}^{\infty} g(\zeta)f_z(\zeta)d\zeta \quad (6.4-22)$$

The *mean* or *expected value* of  $z$  is defined by

$$E\{z\} = \int_{-\infty}^{\infty} \zeta f_z(\zeta)d\zeta, \quad (6.4-23)$$

which we will symbolize by  $\bar{z}$  to economize on notation. Note that  $\bar{z} \in \mathbf{R}^n$ .

The covariance of  $z$  is given by

$$P_z = E\{(z - \bar{z})(z - \bar{z})^T\} \quad (6.4-24)$$

Note that  $P_z$  is an  $n \times n$  constant matrix.

An important class of random vectors is characterized by the *Gaussian* or *normal* PDF

$$f_z(\zeta) = \frac{1}{\sqrt{(2\pi)^n |P_z|}} e^{-(\zeta - \bar{z})^T P_z^{-1} (\zeta - \bar{z})/2} \quad (6.4-25)$$

In the scalar case  $n = 1$  this reduces to the more familiar

$$f_z(\zeta) = \frac{1}{\sqrt{2\pi P_z}} e^{-(\zeta - \bar{z})^2 / 2P_z}, \quad (6.4-26)$$

which is illustrated in Figure 6.4-3. Such random vectors take on values near the mean  $\bar{z}$  with greatest probability and have a decreasing probability of taking on values farther away from  $\bar{z}$ . Many naturally occurring random variables are Gaussian.

If the random vector is a time function, it is called a *random process*, symbolized as  $z(t)$ . Then the PDF may also be time varying and we write  $f_z(\zeta, t)$ . One can imagine the PDF in Figure 6.4-3 changing with time. In this situation, the expected value and covariance matrix are also functions of time, so we write  $\bar{z}(t)$  and  $P_z(t)$ .

Many random processes  $z(t)$  of interest to us have a time-invariant PDF. These are *stationary* processes and, even though they are random time functions, they have a constant mean and covariance.

To characterize the relation between two random processes  $z(t)$  and  $x(t)$ , we employ the *joint PDF*  $f_{zx}(\zeta, \xi, t_1, t_2)$ , which represents the probability that  $(z(t_1), x(t_2))$  is within the differential area  $d\zeta \times d\xi$  centered at  $(\zeta, \xi)$ . For our purposes, we will assume that the processes  $z(t)$  and  $x(t)$  are *jointly stationary*, that is, the joint PDF is not a function of both times  $t_1$  and  $t_2$  but depends only on the difference  $(t_1 - t_2)$ .

In the stationary case, the expected value of the function of two variables  $g(z, x)$  is defined as

$$E\{g(z(t_1), x(t_2))\} = \int_{-\infty}^{\infty} g(\zeta, \xi) f_{zx}(\zeta, \xi, t_1 - t_2) d\zeta d\xi \quad (6.4-27)$$

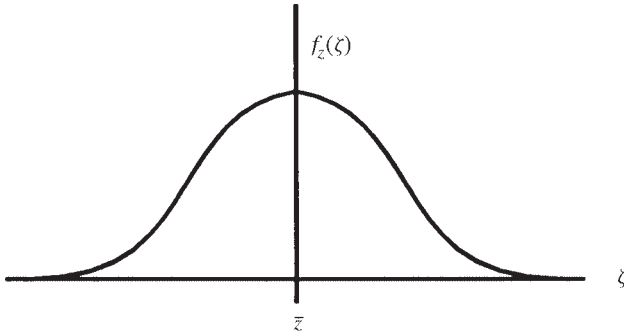


**Figure 6.4-3** Gaussian PDF.

In particular, the *cross-correlation matrix* is defined by

$$R_{zx}(\tau) = E\{z(t + \tau)x^T(t)\} \quad (6.4-28)$$

In the sequel, we will briefly require the cross-correlation matrix of two nonstationary processes, which is defined as

$$R_{zx}(t, \tau) = E\{z(t)x^T(\tau)\} \quad (6.4-29)$$

Considering  $z(t_1)$  and  $z(t_2)$  as two jointly distributed random stationary processes, we may define the *autocorrelation function* of  $z(t)$  as

$$R_z(\tau) = E\{z(t + \tau)z^T(t)\} \quad (6.4-30)$$

The autocorrelation function gives us some important information about the random process  $z(t)$ . For instance,

$$\text{tr}[R_z(0)] = \text{tr}[E\{z(t)z^T(t)\}] = E\{\|z(t)\|^2\}$$

is equal to the total energy in the process  $z(t)$ . (In writing this equation recall that, for any compatible matrices  $M$  and  $N$ ,  $\text{tr}(MN) = \text{tr}(NM)$ .)

If

$$R_{zx}(\tau) = 0, \quad (6.4-31)$$

we call  $z(t)$  and  $x(t)$  *orthogonal*. If

$$R_z(\tau) = P\delta(\tau), \quad (6.4-32)$$

where  $P$  is a constant matrix and  $\delta(t)$  is the Dirac delta, then  $z(t)$  is orthogonal to  $z(t + \tau)$  for any  $\tau \neq 0$ . What this means is that the value of the process  $z(t)$  at one time  $t$  is unrelated to its value at another time  $\tau \neq t$ . Such a process is called *white noise*. An example is the thermal noise in an electric circuit, which is due to the thermal agitation of the electrons in the resistors.

Note that  $P\delta(0)$  is the covariance of  $z(t)$ , which is unbounded. We call  $P$  a *spectral density matrix*. It is sometimes loosely referred to as a covariance matrix.

**Derivation of the Kalman Filter** We may now return to system (6.4-20)/(6.4-21). Neither the initial state  $x(0)$ , the process noise  $w(t)$ , nor the measurement noise  $v(t)$  is exactly known. However, in practice we may have some feeling for their general characteristics. Using the concepts we have just discussed, we may formalize this general knowledge so that it may be used in control design.

The process noise is due to some sort of system disturbance, such as wind gusts; the measurement noise is due to sensor inaccuracies; and the initial state is uncertain

because of our ignorance. Since these are all unrelated, it is reasonable to assume that  $x(0)$ ,  $w(t)$ , and  $v(t)$  are mutually orthogonal. Some feeling for  $x(0)$  may be present in that we may know its mean  $\bar{x}_0$  and covariance  $P_0$ . We symbolize this as

$$x(0) \sim (\bar{x}_0, P_0) \quad (6.4-33)$$

It is not unreasonable to assume that  $w(t)$  and  $v(t)$  have means of zero, since, for instance, there should be no bias on the measuring instruments. We will also assume that the process noise and measurement noise are white noise processes, so that

$$R_w(\tau) = E\{w(t + \tau)w^T(t)\} = Q\delta(\tau) \quad (6.4-34)$$

$$R_v(\tau) = E\{v(t + \tau)v^T(t)\} = R\delta(\tau) \quad (6.4-35)$$

Spectral density matrices  $Q$  and  $R$  will be assumed known. [Often, we have a good feeling for the standard deviations of  $w(t)$  and  $v(t)$ .] According to (6.4-30),  $Q$  and  $R$  are positive semidefinite. We will assume in addition that  $R$  is nonsingular. In summary, we will assume that

$$w(t) \sim (0, Q), \quad Q \geq 0 \quad (6.4-36)$$

$$v(t) \sim (0, R), \quad R > 0 \quad (6.4-37)$$

The assumption that  $w(t)$  and  $v(t)$  are white may in some applications be a bad one. For instance, wind gust noise is generally of low frequency. However, suppose that  $w(t)$  is not white. Then we can determine a system description

$$\dot{x}_w = A_w x_w + B_w n \quad (6.4-38)$$

$$w = C_w x_w + D_w n, \quad (6.4-39)$$

which has a white noise input  $n(t)$  and output  $w(t)$ . This is called a *noise-shaping filter*. These dynamics may be combined with the plant equations (6.4-20) and (6.4-21) to obtain the augmented dynamics

$$\begin{bmatrix} \dot{x} \\ \dot{x}_w \end{bmatrix} = \begin{bmatrix} A & GC_w \\ 0 & A_w \end{bmatrix} \begin{bmatrix} x \\ x_w \end{bmatrix} + \begin{bmatrix} B \\ 0 \end{bmatrix} u + \begin{bmatrix} CD_w \\ B_w \end{bmatrix} n \quad (6.4-40)$$

$$y = \begin{bmatrix} C & 0 \end{bmatrix} \begin{bmatrix} x \\ x_w \end{bmatrix} + v \quad (6.4-41)$$

This augmented system does have a white process noise  $n(t)$ . A similar procedure may be followed if  $v(t)$  is nonwhite. Thus, we can generally describe a plant with non-white noises in terms of an augmented system with white process and measurement noises.

The determination of a system (6.4-38)/(6.4-39) that describes nonwhite noise  $w(t)$  [or  $v(t)$ ] is based on factoring the spectral density of the noise  $w(t)$ . For details, see Lewis (1986b). We will illustrate the procedure in Example 6.4-2.

We should now like to design an estimator for the stochastic system (6.4-20)/(6.4-21) under the assumptions just listed. We will propose the output injection observer, which has the form

$$\dot{\hat{x}} = A\hat{x} + Bu + L(y - \hat{y}) \quad (6.4-42)$$

or

$$\dot{\hat{x}} = (A - LC)\hat{x} + Bu + Ly \quad (6.4-43)$$

The time function  $\hat{x}(t)$  is the state estimate and

$$\hat{y} = E\{Cx + v\} = C\hat{x} \quad (6.4-44)$$

is the estimate of the output  $y(t)$ . [This expected value is actually the *conditional* mean given the previous measurements; see Lewis (1986b).]

The estimator gain  $L$  must be selected to provide an optimal estimate in the presence of the noises  $w(t)$  and  $v(t)$ . To select  $L$ , we will need to define the estimation error

$$\tilde{x}(t) = x(t) - \hat{x}(t) \quad (6.4-45)$$

Using (6.4-20) and (6.4-42), we may derive the error dynamics to be

$$\begin{aligned} \dot{\tilde{x}} &= (A - LC)\tilde{x} + Gw - Lv \\ &\equiv A_0\tilde{x} + Gw - Lv \end{aligned} \quad (6.4-46)$$

Note that the error system is driven by both the process and measurement noise. The output of the error system may be taken as  $\tilde{y} = y - \hat{y}$  so that

$$\tilde{y} = C\tilde{x} + v \quad (6.4-47)$$

The *error covariance* is given by

$$P(t) = E\{\tilde{x}\tilde{x}^T\}, \quad (6.4-48)$$

which is time varying. Thus,  $\tilde{x}(t)$  is a nonstationary random process. The error covariance is a measure of the *uncertainty* in the estimate. Smaller values for  $P(t)$  mean that the estimate is better, since the error is more closely distributed about its mean value of zero if  $P(t)$  is smaller.

If the observer is asymptotically stable and  $w(t)$  and  $v(t)$  are stationary processes, the error  $\tilde{x}(t)$  will eventually reach a *steady state* in which it is also stationary with constant mean and covariance. The gain  $L$  will be chosen to minimize the *steady-state error covariance*  $P$ . Thus, the optimal gain  $L$  will be a constant matrix of observer gains.



Before determining the optimal gain  $L$ , let us compute the mean and covariance of the estimation error  $\tilde{x}(t)$ . Using (6.4-46) and the linearity of the expectation operator,

$$E\{\dot{\tilde{x}}\} = A_0 E\{\tilde{x}\} + GE\{w\} - LE\{v\}, \quad (6.4-49)$$

so that

$$\frac{d}{dt}E\{\tilde{x}\} = A_0 E\{\tilde{x}\} \quad (6.4-50)$$

Thus,  $E\{\tilde{x}\}$  is a deterministic time-varying quantity that obeys a differential equation with system matrix  $A_0$ . If  $A_0 = A - LC$  is stable, then  $E\{\tilde{x}\}$  eventually stabilizes at a steady-state value of zero, since the process and measurement noises are of zero mean. Since

$$E\{\hat{x}\} = E\{x\} - E\{\tilde{x}\} = E\{x\} - \hat{x}, \quad (6.4-51)$$

it follows that in this case the estimate  $\hat{x}(t)$  approaches  $E\{x(t)\}$ . Then the estimate is said to be *unbiased*. According also to (6.4-51), the mean of the initial error  $\hat{x}(0)$  is equal to zero if the observer (6.4-43) is initialized to  $\hat{x}(0) = x_0$ , with  $\bar{x}_0$  the mean of  $x(0)$ .

If the process noise  $w(t)$  and/or measurement noise  $v(t)$  have means that are not zero, then according to (6.4-49), the steady-state value of  $E\{\tilde{x}\}$  is not equal to zero. In this case,  $\hat{x}(t)$  does not tend asymptotically to the true state  $x(t)$  but is offset from it by the constant value  $-E\{\tilde{x}\}$ . Then the estimates are said to be biased (see the problems).

To determine the error covariance, note that the solution of (6.4-46) is given by

$$\tilde{x}(t) = e^{A_0 t} \tilde{x}(0) - \int_0^t e^{A_0(t-\tau)} L v(\tau) d\tau + \int_0^t e^{A_0(t-\tau)} G w(\tau) d\tau \quad (6.4-52)$$

We will soon require the cross-correlation matrices  $R_{v\tilde{x}}(t, t)$  and  $R_{w\tilde{x}}(t, t)$ . To find them, use (6.4-52) and the assumption that  $x(0)$  [and hence  $\tilde{x}(0)$ ],  $w(t)$ , and  $v(t)$  are orthogonal. Thus,

$$\begin{aligned} R_{v\tilde{x}}(t, t) &= E\{v(t)\tilde{x}^T(t)\} \\ &= - \int_0^t E\{v(t)v^T(\tau)\} L^T e^{A_0^T(t-\tau)} d\tau \end{aligned} \quad (6.4-53)$$

Note that

$$R_v(t, \tau) = R\delta(t - \tau) \quad (6.4-54)$$

but the integral in (6.4-53) has an upper limit of  $t$ . Recall that the unit impulse can be expressed as

$$\delta(t) = \lim_{T \rightarrow 0} \frac{1}{T} \prod \left( \frac{t}{T} \right), \quad (6.4-55)$$

where the rectangle function

$$\frac{1}{T} \Pi\left(\frac{t}{T}\right) = \begin{cases} \frac{1}{T}, & |t| < \frac{T}{2} \\ 0 & \text{otherwise} \end{cases} \quad (6.4-56)$$

is centered at  $t = 0$ . Therefore, only half the area of  $\delta(t - \tau)$  should be considered as being to the left of  $\tau = t$ . Hence, (6.4-53) is

$$R_{v\tilde{x}}(t, t) = -\frac{1}{2}RL^T \quad (6.4-57)$$

Similarly,

$$\begin{aligned} R_{w\tilde{x}}(t, t) &= E\{w(t)\tilde{x}^T(t)\} \\ &= \int_0^t E\{w(t)w^T(\tau)\}G^T e^{A_0^T(t-\tau)} d\tau \end{aligned} \quad (6.4-58)$$

or

$$R_{w\tilde{x}}(t, t) = \frac{1}{2}QG^T \quad (6.4-59)$$

To find a differential equation for  $P(t) = E\{\tilde{x}\tilde{x}^T\}$ , write

$$\dot{P}(t) = E\left\{\frac{d\tilde{x}}{dt}\tilde{x}^T\right\} + E\left\{\tilde{x}\frac{d\tilde{x}^T}{dt}\right\} \quad (6.4-60)$$

According to the error dynamics (6.4-46) the first term is equal to

$$E\left\{\frac{d\tilde{x}}{dt}\tilde{x}^T\right\} = (A - LC)P + \frac{1}{2}LRL^T + \frac{1}{2}GQG^T, \quad (6.4-61)$$

where we have used (6.4-57) and (6.4-59). To this equation add its transpose to obtain

$$\dot{P} = A_0P + PA_0^T + LRL^T + GQG^T \quad (6.4-62)$$

What we have derived in (6.4-62) is an expression for the error covariance when the observer (6.4-43) is used with a specific gain  $L$ . Given any  $L$  such that  $(A - LC)$  is stable, we may solve (6.4-62) for  $P(t)$  using as initial condition  $P(0) = P_0$ , with  $P_0$  the covariance of the initial state, which represents the uncertainty in the initial estimate  $\hat{x}(0) = \bar{x}_0$ .

Clearly, gains that result in smaller error covariances  $P(t)$  are better, for then the error  $\tilde{x}(t)$  is generally closer to its mean of zero. That is, the error covariance is a measure of the performance of the observer, and smaller covariance matrices are

indicative of better observers. We say that  $P$  is a measure of the uncertainty in the estimate. [Given symmetric positive-semidefinite matrices  $P_1$  and  $P_2$ ,  $P_1$  is less than  $P_2$  if  $(P_2 - P_1) \geq 0$ .]

The error covariance  $P(t)$  reaches a bounded steady-state value  $P$  as  $t \rightarrow \infty$  as long as  $A_0$  is asymptotically stable. At steady state,  $\dot{P} = 0$  so that (6.4-62) becomes the algebraic equation

$$0 = A_0 P + P A_0^T + L R L^T + G Q G^T \quad (6.4-63)$$

The steady-state error covariance is the positive-(semi)definite solution to (6.4-63). To obtain a constant observer gain, we may select  $L$  to *minimize the steady-state error covariance*  $P$ . Necessary conditions for  $L$  are now easily obtained after the same fashion that the output feedback gain  $K$  was obtained in Section 5.3.

Thus, define a performance index (PI)

$$J = \frac{1}{2} \text{tr}(P) \quad (6.4-64)$$

[Note that  $\text{tr}(P)$  is the sum of the eigenvalues of  $P$ . Thus, a small  $J$  corresponds to a small  $P$ .] To select  $L$  so that  $J$  is minimized subject to the constraint (6.4-63), define the Hamiltonian

$$\mathcal{H} = \frac{1}{2} \text{tr}(P) + \frac{1}{2} \text{tr}(gS), \quad (6.4-65)$$

where

$$g = A_0 P + P A_0^T + L R L^T + G Q G^T \quad (6.4-66)$$

and  $S$  is an  $n \times n$  undetermined (Lagrange) multiplier.

To minimize  $J$  subject to the constraint  $g = 0$ , we may equivalently minimize  $\mathcal{H}$  with no constraints. Necessary conditions for a minimum are therefore given by

$$\frac{\partial \mathcal{H}}{\partial S} = A_0 P + P A_0^T + L R L^T + G Q G^T = 0 \quad (6.4-67)$$

$$\frac{\partial \mathcal{H}}{\partial P} = A_0^T S + S A_0 + I = 0 \quad (6.4-68)$$

$$\frac{1}{2} \frac{\partial \mathcal{H}}{\partial L} = S L R - S P C^T = 0 \quad (6.4-69)$$

If  $A_0$  is stable, the solution  $S$  to (6.4-68) is positive definite. Then, according to (6.4-69),

$$L = P C^T R^{-1} \quad (6.4-70)$$

Substituting this value for  $L$  into (6.4-67) yields

$$(A - P C^T R^{-1} C) P + P (A - P C^T R^{-1} C)^T + P C^T R^{-1} C P + G Q G^T = 0 \quad (6.4-71)$$

or

$$AP + PA^T + GQG^T - PC^TR^{-1}CP = 0 \quad (6.4-72)$$

To determine the optimal observer gain  $L$ , we may therefore proceed by solving (6.4-72) for the error covariance  $P$  and then using (6.4-70) to compute  $L$ . The matrix quadratic equation (6.4-72) is called the *algebraic (filter) Riccati equation* (ARE). There are several efficient techniques for solving the ARE for  $P$  [e.g., Armstrong, 1980; IMSL, 1980; MATRIX<sub>x</sub>, 1989; MATLAB (Moler et al., 1987)].

The optimal gain  $L$  determined using (6.4-70) is called the *steady-state Kalman gain*, and the observer so constructed is called the *steady-state Kalman filter*. The term *steady state* refers to the fact that although the optimal gain that minimizes  $P(t)$  is generally time varying, we have selected the optimal gain that minimizes the *steady-state* error covariance in order to obtain a constant observer gain. Since the gain must eventually be gain scheduled in actual flight control applications, we require a constant gain to keep the number of parameters to be scheduled within reason.

The design equations for the Kalman filter are collected in Table 6.4-1. A block diagram appears in Figure 6.4-1. The steady-state Kalman filter is the best estimator with constant gains that has the dynamics of the form in the table. Such a filter is said to be *linear*. It can be shown (Lewis, 1986*b*) that if the process noise  $w(t)$  and measurement noise  $v(t)$  are *Gaussian*, this is also *the optimal* steady-state estimator of any form.

The quantity

$$\tilde{y}(t) = y(t) - \hat{y}(t) = y(t) - C\hat{x}(t) \quad (6.4-73)$$

**TABLE 6.4-1 The Kalman Filter**

---

*System Model*

$$\dot{x} = Ax + Bu + Gw$$

$$y = Cx + v$$

$$x(0) \sim (\bar{x}_0, P_0), \quad w(t) \sim (0, Q), \quad v(t) \sim (0, R)$$

*Assumptions*

$w(t)$  and  $v(t)$  are white noise processes orthogonal to each other and to  $x(0)$ .

*Initialization*

$$\hat{x}(0) = \bar{x}_0$$

*Error Covariance ARE*

$$AP + PA^T + GQG^T - PC^TR^{-1}CP = 0$$

*Kalman Gain*

$$L = PC^TR^{-1}$$

*Estimate Dynamics (Filter Dynamics)*

$$\dot{\hat{x}} = A\hat{x} + Bu + L(y - C\hat{x})$$


---

that drives the filter dynamics in the table is called the residual. For more information on the Kalman filter, see the work of Bryson and Ho (1975), Kwakernaak and Sivan (1972), and Lewis (1986b).

The filter ARE should be compared to the ARE we discussed at the beginning of this section in connection with output injection design. There, no particular meaning was given to the auxiliary matrix  $P$ . In this stochastic setting, we have discovered that it is nothing but the error covariance. Small values of  $P$  generally indicate a filter with good estimation performance.

The theorem offered in connection with output injection observer design also holds here. Thus, suppose that  $(C, A)$  is observable and  $(A, G\sqrt{Q})$  is reachable. Then the ARE has a unique positive-definite solution  $P$ . Moreover, error system (6.4-46) using the gain Kalman gain  $L$  given by (6.4-70), with  $P$  the unique positive-definite solution to the ARE, is asymptotically stable.

One might be inclined to believe that the less noise in the system, the better. However, the actual situation is quite surprising. For the existence of the Kalman filter it was necessary to assume that  $R > 0$ , that is, that *the measurement noise corrupts all the measurements*. If there are some noise-free measurements, a more complicated filter known as the *Deyst filter* must be used. Moreover, the assumption that  $(A, G\sqrt{Q})$  is reachable means that *the process noise should excite all the states*.

**Example 6.4-2: Kalman Filter Estimation of Angle of Attack in Gust Noise** The short-period approximation to the F-16 longitudinal dynamics is

$$\dot{x} = Ax + B\delta_e + Gw_g, \quad (1)$$

with  $x = [\alpha \quad q]^T$ ,  $\alpha$  the angle of attack,  $q$  the pitch rate, control input  $\delta_e$  the elevator deflection, and  $w_g$  the vertical wind gust disturbance velocity. Using the software described in Chapter 3 to linearize the F-16 dynamics about the nominal flight condition in Table 3.6-3 (true airspeed of 502 ft/s, dynamic pressure of 300 psf, and cg at 0.35  $\bar{c}$ ), the plant matrices are found to be

$$A = \begin{bmatrix} -1.01887 & 0.90506 \\ 0.82225 & -1.07741 \end{bmatrix}, \quad B = \begin{bmatrix} -0.00215 \\ -0.17555 \end{bmatrix}, \quad G = \begin{bmatrix} 0.00203 \\ -0.00164 \end{bmatrix} \quad (2)$$

The vertical wind gust noise is not white but according to *Mil. Spec. 1797* (1987) has a spectral density given in Dryden form as

$$\Phi_w(\omega) = 2L\sigma^2 \frac{1 + 3L^2\omega^2}{(1 + L^2\omega^2)^2}, \quad (3)$$

with  $\omega$  the frequency in rad/s,  $\sigma$  the turbulence intensity, and  $L$  the turbulence scale length divided by true airspeed. Taking  $\sigma = 10$  ft/s and  $L = (1750 \text{ ft}) / (502 \text{ ft/s}) = 3.49$  s (see *Mil. Spec. 1797*, 1987) the gust spectral density is shown in Figure 6.4-4.

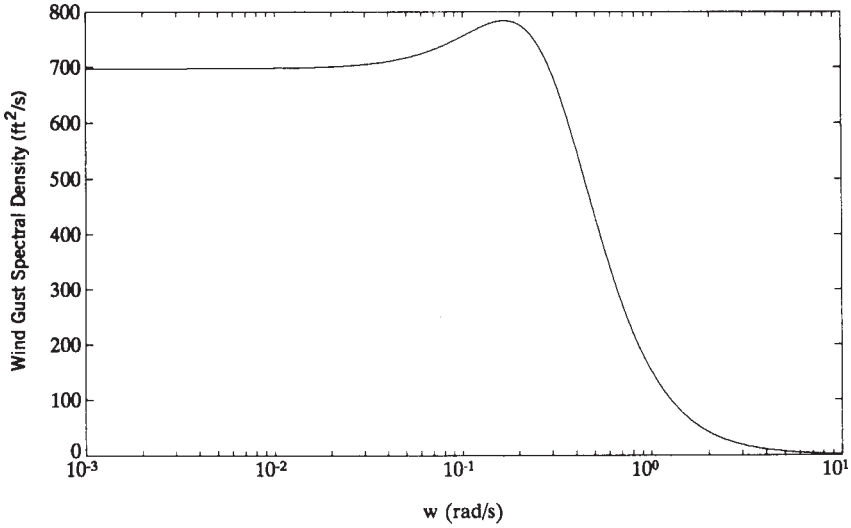


**Figure 6.4-4** Vertical wind gust spectral density.

(a) *Determination of Gust-Shaping Filter.* Since  $w_g$  is not white, a noise-shaping filter of the form of (6.4-38), (6.4-39) must be determined by factoring  $\Phi_w(s)$  (Lewis, 1986b). Note that

$$\Phi_w(\omega) = 2L\sigma^2 \frac{(1 + \sqrt{3}Lj\omega)(1 - \sqrt{3}Lj\omega)}{(1 + Lj\omega)^2(1 - Lj\omega)^2}, \quad (4)$$

so that

$$\Phi_w(s) = H_w(s)H_w(-s) \quad (5)$$

with

$$H_w(s) = \sigma \sqrt{\frac{6}{L}} \frac{s + 1/L\sqrt{3}}{L(s + 1/L)^2} \quad (6)$$

$$H_w(s) = \sigma \sqrt{\frac{6}{L}} \frac{s + 1/L\sqrt{3}}{s^2 + 2s/L + 1/L^2} \quad (7)$$

Now a reachable canonical form realization of  $H_w(s)$  (Kailath, 1980) is given by

$$\dot{z} = \begin{bmatrix} 0 & 1 \\ -\frac{1}{L^2} & -\frac{2}{L} \end{bmatrix} z + \begin{bmatrix} 0 \\ 1 \end{bmatrix} w \quad (8)$$

$$w_g = \gamma \begin{bmatrix} \frac{1}{L\sqrt{3}} & 1 \end{bmatrix} z, \quad (9)$$

where the gain is  $\gamma = \sigma\sqrt{g/L}$ . Using  $\sigma = 10$ ,  $L = 3.49$  yields

$$\dot{z} = \begin{bmatrix} 0 & 1 \\ -0.0823 & -0.5737 \end{bmatrix} z + \begin{bmatrix} 0 \\ 1 \end{bmatrix} w \approx A_w z + B_w w \quad (10)$$

$$w_g = [2.1728 \quad 13.1192] z \equiv C_w z \quad (11)$$

The shaping filter (10)/(11) is a system driven by the *white* noise input  $w(t) \sim (0, 1)$  that generates the gust noise  $w_g(t)$  with spectral density given by (3).

(b) *Augmented Plant Dynamics.* The overall system, driven by the white noise input  $w(t) \sim (0, 1)$  and including an elevator actuator with transfer function  $20.2/(s + 20.2)$ , is given by [see (6.4-40)]

$$\frac{d}{dt} \begin{bmatrix} \alpha \\ q \\ z_1 \\ z_2 \\ \delta_e \end{bmatrix} = \begin{bmatrix} -1.01887 & 0.90506 & 0.00441 & 0.02663 & -0.00215 \\ 0.82225 & -1.07741 & -0.00356 & -0.02152 & -0.17555 \\ 0 & 0 & 0 & 1 & 0 \\ 0 & 0 & -0.0823 & -0.5737 & 0 \\ 0 & 0 & 0 & 0 & -20.2 \end{bmatrix} \begin{bmatrix} \alpha \\ q \\ z_1 \\ z_2 \\ \delta_e \end{bmatrix} + \begin{bmatrix} 0 \\ 0 \\ 0 \\ 0 \\ 20.2 \end{bmatrix} u + \begin{bmatrix} 0 \\ 0 \\ 0 \\ 1 \\ 0 \end{bmatrix} w \quad (12)$$

with  $u(t)$  the elevator actuator input. To economize on notation, let us symbolize this augmented system as

$$\dot{x} = Ax + Bu + Gw \quad (13)$$

(c) *Estimating Angle of Attack.* Direct measurements of angle of attack  $\alpha$  are noisy and biased. However, pitch rate  $q$  and normal acceleration  $n_z$  are convenient to measure. Using the software in Chapter 3 it is determined that

$$n_z = 15.87875\alpha + 1.48113q \quad (14)$$

Therefore, let us select the measured output as

$$y = \begin{bmatrix} n_z \\ q \end{bmatrix} = \begin{bmatrix} 15.87875 & 1.48113 & 0 & 0 & 0 \\ 0 & 1 & 0 & 0 & 0 \end{bmatrix} x + v \equiv Cx + v, \quad (15)$$

where  $v(t)$  is measurement noise. A reasonable measurement noise covariance is

$$R = \begin{bmatrix} \frac{1}{20} & 0 \\ 0 & \frac{1}{60} \end{bmatrix} \quad (16)$$

Now the algebraic Riccati equation in Table 6.4-1 may be solved using standard available software [e.g., ORACLS (Armstrong, 1980; IMSL, 1980), PC-MATLAB (Moler et al., 1987), and MATRIX<sub>x</sub> (1989)] to obtain the Kalman gain

$$L = \begin{bmatrix} 0.0375 & -0.0041 \\ -0.0202 & 0.0029 \\ 3.5981 & -0.2426 \\ 1.9061 & -0.2872 \\ 0 & 0 \end{bmatrix}, \quad (17)$$

whence the Kalman filter is given by

$$\dot{\hat{x}} = (A - LC)\hat{x} + Bu + Ly \quad (18)$$

Note that the Kalman gain corresponding to the fifth state  $\delta_e$  is zero. This is due to the fact that, according to (12), the gust noise  $w(t)$  does not excite the actuator motor.

To implement the estimator we could use the state formulation (18) in a subroutine or compute the transfer function to the angle-of-attack estimate given by

$$H_\alpha(s) = \begin{bmatrix} 1 & 0 & \cdots & 0 \end{bmatrix} [sI - (A - LC)]^{-1} \begin{bmatrix} B & L \end{bmatrix} \quad (19)$$

(Note that  $\alpha$  is the first component of  $x$ .) Then the angle-of-attack estimate is given by

$$\hat{\alpha}(s) = H(s) \begin{bmatrix} U(s) \\ Y(s) \end{bmatrix}, \quad (20)$$

so that  $\alpha(t)$  may be estimated using  $u(t)$  and  $y(t)$ , both of which are known.

Similarly, the estimate of the wind gust velocity  $w_g(t)$  may be recovered. ■

## Dynamic Regulator Design Using the Separation Principle

The fundamental approach to regulator and compensator design in this book involves selecting the compensator dynamics using the intuition of classical control and traditional aircraft design. Then the adjustable compensator gains are computed using the output feedback design equations in Table 5.3-1, 5.4-1, or 5.5-1. The advantages of this approach include:

1. Good software for solving the design equations is available [e.g., the Davidon-Fletcher-Powell algorithm (Press et al., 1986)]. See Appendix B.
2. General multi-input/multi-output control design is straightforward.



3. All the intuition in classical control design in the aircraft industry can be used to select the compensator structure.
4. Complicated compensator structures are avoided, which is important from the point of view of the pilot's feel for the aircraft and also simplifies the gain-scheduling problem.

However, in complicated modern systems (e.g., aircraft engines) there may be no a priori guidelines for selecting the compensator structure. In this case, a combination of LQ state feedback and observer/filter design proves very useful for controller design. This combination is known as linear quadratic Gaussian (LQG) design and is explored next. In Section 6.5 we discuss the LQG/LTR technique for robust design, which has become popular in some aspects of aircraft control.

**Linear Quadratic Gaussian Design** The linear quadratic regulator (LQR) and the Kalman filter can be used together to design a dynamic regulator. This procedure is called linear quadratic Gaussian (LQG) design and will now be described. An important advantage of LQG design is that the compensator structure is given by the procedure, so that it need not be known beforehand. This makes LQG design useful in the control of complicated modern-day systems (e.g., space structures, aircraft engines), where an appropriate compensator structure may not be known.

Suppose that the plant and measured outputs are given by

$$\dot{x} = Ax + Bu + Gw \quad (6.4-74)$$

$$y = Cx + v, \quad (6.4-75)$$

with  $x(t) \in \mathbf{R}^n$ ,  $u(t)$  the control input,  $w(t)$  the process noise, and  $v(t)$  the measurement noise. Suppose that the full-state-feedback control

$$u = -Kx + r \quad (6.4-76)$$

has been designed, with  $r(t)$  the pilot's input command. That is, the state feedback gain  $K$  has been selected by some technique, such as the LQR technique in Section 5.7. If the control (6.4-76) is substituted into (6.4-74), the closed-loop system is found to be

$$\dot{x} = (A - BK)x + Br + Gw \quad (6.4-77)$$

Full-state-feedback design is attractive because if the conditions in Section 5.7 hold, the closed-loop system is guaranteed stable. Such a strong result has not yet been shown for output feedback. Moreover, using full state feedback all the poles of  $(A - BK)$  may be placed arbitrarily as desired. Finally, the state feedback design equations are simpler than those for output feedback and may be solved using standard available routines [e.g., ORACLS (Armstrong, 1980; IMSL, 1980), PCMATLAB (Moler et al., 1987), and MATRIX<sub>x</sub> (1989)]. However, the control law (6.4-76) cannot be implemented since all the states are usually not available as measurements.

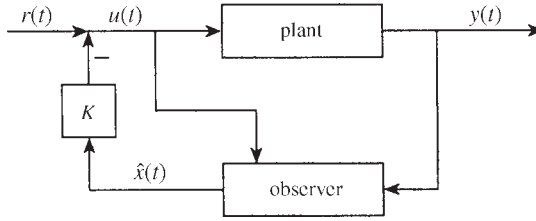


**Figure 6.4-5** Regulator design using observer and full state feedback.

Now, suppose that an observer or Kalman filter

$$\dot{\hat{x}} = (A - LC)\hat{x} + Bu + Ly \quad (6.4-78)$$

has been designed. That is, the filter gain  $L$  has been selected by any of the techniques discussed in this section to provide state estimates. Then, since all the states are not measurable and the control (6.4-76) cannot be implemented in practice, we propose to feed back the *estimate*  $\hat{x}(t)$  instead of the actual state  $x(t)$ . That is, let us examine the feedback law

$$u = -K\hat{x} + r \quad (6.4-79)$$

The closed-loop structure using this controller is shown in Figure 6.4-5. Due to the fact that the observer is a dynamical system, the proposed controller is nothing but a dynamical regulator of the sort seen in classical control theory. However, in contrast to classical design, the theory makes it easy to design *multivariable regulators with guaranteed stability even for complicated MIMO systems*.

If  $K$  is selected using the LQR Riccati equation in Section 5.7 and  $L$  is selected using the Kalman filter Riccati equation in Table 6.4-1, this procedure is called LQG design.

We propose to show that using this control:

1. The closed-loop poles are the same as if the full state feedback (6.4-76) had been used.
2. The transfer function from  $r(t)$  to  $y(t)$  is the same as if (6.4-76) had been used.

The importance of these results is that the state feedback  $K$  and the observer gain  $L$  may be designed *separately* to yield desired closed-loop plant behavior and observer behavior. This is the *separation principle*, which is at the heart of modern control design. Two important ramifications of the separation principle are that closed-loop stability is guaranteed and good software is available to solve the matrix design equations that yield  $K$  and  $L$ .

**The Separation Principle** To show the two important results just mentioned, define the estimation error (6.4-45) and examine the error dynamics (6.4-46). In terms of

$\tilde{x}(t)$ , we may write (6.4-79) as

$$u = -Kx + K\tilde{x} + r, \quad (6.4-80)$$

which, when used in (6.4-74), yields

$$\dot{x} = (A - BK)x + BK\tilde{x} + Br + Gw \quad (6.4-81)$$

Now, write (6.4-81) and (6.4-46) as the augmented system

$$\frac{d}{dt} \begin{bmatrix} x \\ \tilde{x} \end{bmatrix} = \begin{bmatrix} A - BK & BK \\ 0 & A - LC \end{bmatrix} \begin{bmatrix} x \\ \tilde{x} \end{bmatrix} + \begin{bmatrix} B \\ 0 \end{bmatrix} r + \begin{bmatrix} G \\ L \end{bmatrix} w - \begin{bmatrix} 0 \\ L \end{bmatrix} v \quad (6.4-82)$$

$$y = \begin{bmatrix} C & 0 \end{bmatrix} \begin{bmatrix} x \\ \tilde{x} \end{bmatrix} + v \quad (6.4-83)$$

This represents the complete dynamics of Figure 6.4-5.

Since the augmented system is block triangular, the closed-loop characteristic equation is

$$\Delta(s) = |sI - (A - BK)| \cdot |sI - (A - LC)| = 0 \quad (6.4-84)$$

That is, the closed-loop poles are nothing but the plant poles that result by choosing  $K$  and the desired observer poles that result by choosing  $L$ . Thus, the state feedback gain  $K$  and observer gain  $L$  may be selected separately for desirable closed-loop behavior.

The closed-loop transfer function from  $r(t)$  to  $y(t)$  is given by

$$H_c(s) = \begin{bmatrix} C & 0 \end{bmatrix} \begin{bmatrix} A - BK & BK \\ 0 & A - LC \end{bmatrix}^{-1} \begin{bmatrix} B \\ 0 \end{bmatrix},$$

and the triangular form of the system matrix makes it easy to see that

$$H_c(s) = C [sI - (A - BK)]^{-1} B \quad (6.4-85)$$

This, however, is exactly what results if the full state feedback (6.4-76) is used.

Of course, the initial conditions also affect the output  $y(t)$ . However, since the observer is stable, the effects of the initial error  $\tilde{x}(0)$  will vanish with time. The observer poles [i.e., those of  $(A - LC)$ ] should be chosen 5 to 10 times faster than the desired closed-loop plant poles [i.e., those of  $(A - BK)$ ] for good closed-loop behavior.

**Discussion** From our point of view, when possible it is usually better to design compensators using output feedback as we have demonstrated in the previous chapters than to use separation principle design. To see why, let us examine the structure of the dynamic compensator in Figure 6.4-5 in more detail.

The control input  $u(t)$  may be expressed as

$$U(s) = H_y(s)Y(s) + H_u(s)U(s) + R(s), \quad (6.4-86)$$

where, according to (6.4-79) and (6.4-78), the transfer function from  $y(t)$  to  $u(t)$  is

$$H_y(s) = -K[sI - (A - LC)]^{-1} L \quad (6.4-87)$$

and the transfer function from  $u(t)$  to  $u(t)$  is

$$H_u(s) = -K[sI - (A - LC)]^{-1} B \quad (6.4-88)$$

Now, note that the compensator designed by this technique has order equal to the order  $n$  of the plant. This means that it has too many parameters to be conveniently gain scheduled. Moreover, it has no special structure. This means that none of the classical control intuition available in the aircraft industry has been used in its design.

It is possible to design *reduced-order* compensators using the separation principle. Three possible approaches are:

1. Find a reduced-order model of the plant, then design a compensator for this reduced-order model.
2. Design a compensator for the full plant, then reduce the order of the compensator.
3. Design the reduced-order compensator directly from the full-order plant.

One technique for order reduction is the partial fraction expansion technique in Example 6.2-3. Other techniques include principal-component analysis (Moore, 1982) and the frequency-weighted technique by Anderson and Liu (1989). A very convenient approach is given by Ly et al. (1985).

It is important to realize that although the plant is minimal (i.e., reachable and observable), the LQ regulator may not be. That is, it may have unreachable or unobservable states. A technique for reducing the regulator to minimal form is given by Yousuff and Skelton (1984).

In Section 6.5 we illustrate the design of a LQ regulator in robust design using the LQG/LTR approach.

## 6.5 LINEAR QUADRATIC GAUSSIAN/LOOP TRANSFER RECOVERY

We saw in Sections 6.2 and 6.3 how to use the multivariable Bode plot to design controllers guaranteeing performance robustness and stability robustness using output feedback. In Section 6.4 we discussed the Kalman filter. In this section we propose to cover the LQG/LTR design technique for robust controllers. This approach is quite popular in the current literature and has been used extensively by Honeywell and others to design multivariable aircraft flight control systems (Doyle and Stein, 1981; Athans, 1986). It is based on the fact that the linear quadratic regulator (LQR) using state-variable feedback has certain *guaranteed robustness properties*.

Thus, suppose that a state feedback gain  $K$  has been computed using the ARE as in Section 5.7. This state feedback cannot be implemented since all of the states are not available as measurements; however, it can be used as the basis for the design of a dynamic LQR by using a Kalman filter to provide state estimates for feedback purposes. We would like to discuss two issues. First, we will show that, in contrast to output feedback, state feedback has certain guaranteed robustness properties in terms of gain and phase margins. Then we will see that the Kalman filter may be designed so that the dynamic regulator recovers the desirable robustness properties of full state feedback.

### Guaranteed Robustness of the LQR

We have discussed conditions for performance robustness and stability robustness for the general feedback configuration of the form shown in Figure 6.2-1, where  $G(s)$  is the plant and  $K(s)$  is the compensator. The LQR using *state feedback* has many important properties, as we have seen in Section 5.7. In this subsection we should like to return to the LQR to show that it has certain *guaranteed robustness properties* that make it even more useful (Safonov and Athans, 1977).

Thus, suppose that in Figure 6.2-1,  $K(s) = K$ , the constant optimal LQ state feedback gain determined using the ARE as in Table 5.7-1. Suppose, moreover, that

$$G(s) = (sI - A)^{-1}B \quad (6.5-1)$$

is a plant in state-variable formulation.

For this subsection, it will be necessary to consider the loop gain *referred to the control input*  $u(t)$  in Figure 6.2-1. This is in contrast to the work in Section 6.2, where we referred the loop gain to the output  $z(t)$ , or equivalently to the signal  $s(t)$  in the figure. Breaking the loop at  $u(t)$  yields the loop gain

$$KG(s) = K(sI - A)^{-1}B \quad (6.5-2)$$

Our discussion will be based on the *optimal return difference relation* that holds for the LQR with state feedback (Lewis, 1986a; Grimble and Johnson, 1988; Kwakernaak and Sivan, 1972), namely,

$$\begin{aligned} & [I + K(-sI - A)^{-1}B]^T [I + K(sI - A)^{-1}B] \\ &= I + \frac{1}{\rho} B^T (-sI - A)^{-T} Q (sI - A)^{-1} B, \end{aligned} \quad (6.5-3)$$

where “ $-T$ ” means the inverse transposal. We have selected  $R = P_I$ .

Denoting the  $i$ th SV of a matrix  $M$  as  $\sigma_i(M)$ , we note that, by definition

$$\sigma_i(M) = \sqrt{\lambda_i(M^*M)}, \quad (6.5-4)$$

with  $\lambda_i(M^*M)$  the  $i$ th eigenvalue of matrix  $M^*M$  and  $M^*$  the complex conjugate transpose of  $M$ . Therefore, according to (6.5-3), there results (Doyle and Stein, 1981)

$$\begin{aligned}\sigma_i[I + KG(j\omega)] &= \left[ \lambda_i \left[ I + \frac{1}{\rho} B^T (-j\omega I - A)^{-T} Q (j\omega I - A)^{-1} B \right] \right]^{1/2} \\ &= \left[ 1 + \frac{1}{\rho} \lambda_i \left[ B^T (-j\omega I - A)^{-T} Q (j\omega I - A)^{-1} B \right] \right]^{1/2}\end{aligned}$$

or

$$\sigma_i[I + KG(j\omega)] = \left[ 1 + \frac{1}{\rho} \sigma_i^2 [H(j\omega)] \right]^{1/2}, \quad (6.5-5)$$

with

$$H(s) = H(sI - A)^{-1}B \quad (6.5-6)$$

and  $Q = H^T H$ .

We could call (6.5-5) the *optimal SV relation* of the LQR. It is important due to the fact that the right-hand side is known in terms of open-loop quantities *before the optimal feedback gain is found* by solution of the ARE, while the left-hand side is the closed-loop return difference. Thus, exactly as in classical control, we are able to derive properties of the closed-loop system in terms of properties of the open-loop system.

According to this relation, for all  $\omega$  the minimum SV satisfies the *LQ optimal SV constraint*

$$\underline{\sigma}[I + KG(j\omega)] \geq 1 \quad (6.5-7)$$

Thus, the LQ regulator always results in a *decreased sensitivity*.

Some important conclusions on the guaranteed robustness of the LQR may now be discovered using the *multivariable Nyquist criterion* (Postlethwaite et al., 1981), which we will refer to as the polar plot of the return difference  $I + KG(s)$ , where the origin is the critical point (Grimble and Johnson, 1988). [Usual usage is to refer the criterion to the polar plot of the loop gain  $KG(s)$  where  $-1$  is the critical point.]

A typical polar plot of  $\underline{\sigma}(I + KG(j\omega))$  is shown in Figure 6.5-1, where the optimal SV constraint appears as the condition that *all the SVs remain outside the unit disc*. To see how the end points of the plots were discovered, note that since  $K(sI - A)^{-1}B$  has relative degree of at least 1, its limiting value for  $s = j\omega$  as  $\omega \rightarrow \infty$  is zero. Thus, in this limit,  $I + KG(j\omega)$  tends to  $I$ . On the other hand, as  $\omega \rightarrow 0$ , the limiting value of  $I + KG(j\omega)$  is determined by the dc loop gain, which should be large.

The multivariable Nyquist criterion says that the closed-loop system is stable if none of the SV plots of  $I + KG(j\omega)$  encircle the origin in the figure. Clearly, due to the optimal SV constraint, no encirclements are possible. This constitutes a proof of the *guaranteed stability* of the LQR.

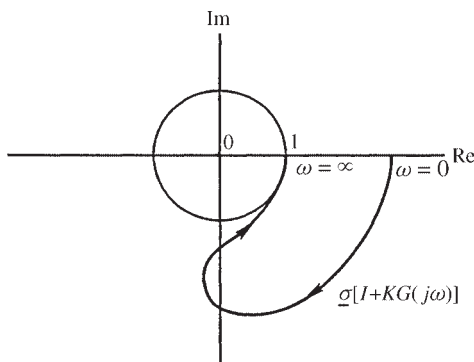


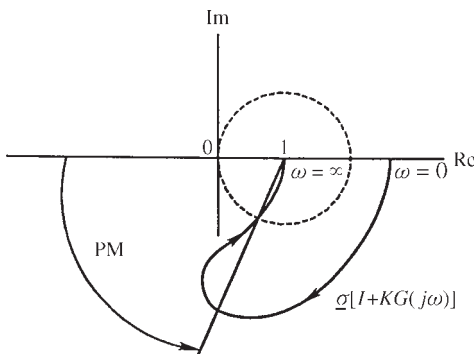
**Figure 6.5-1** Typical polar plot for optimal LQ return difference (referred to the plant input).

Multiplying the optimal feedback  $K$  by any positive scalar gain  $k$  results in a loop gain of  $kKG(s)$ , which has a minimum SV plot identical to the one in Figure 6.5-1 except that it is scaled outward. That is, the  $\omega \rightarrow 0$  limit (i.e., the dc gain) will be larger, but the  $\omega \rightarrow \infty$  limit will still be 1. Thus, the closed-loop system will still be stable. In classical terms, the LQR has an *infinite gain margin*.

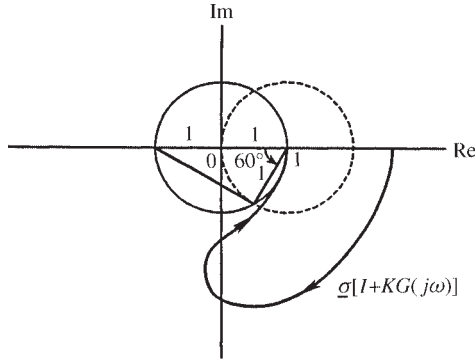
The *phase margin* may be defined for multivariable systems as the angle marked “PM” in Figure 6.5-2. As in the classical case, it is the angle through which the polar plot of  $\sigma[I + KG(j\omega)]$  must be rotated (about the point 1) clockwise to make the plot go through the origin.

Figure 6.5-3 combines Figures 6.5-1 and 6.5-2. By using some simple geometry, we may find the value of the angle indicated as  $60^\circ$ . Therefore, due to the LQ SV constraint, the plot of  $\sigma[I + KG(j\omega)]$  must be rotated through at least  $60^\circ$  to make it pass through the origin. The LQR thus has a *guaranteed phase margin of at least  $60^\circ$* .

This means that a phase shift of up to  $60^\circ$  may be introduced in any of the  $m$  paths in Figure 6.2-1 or in all paths simultaneously as long as the paths are not coupled to each other in the process.



**Figure 6.5-2** Definition of multivariable phase margin.



**Figure 6.5-3** Guaranteed phase margin of the LQR.

This phase margin is excessive; it is higher than that normally required in classical control system design. This overdesign means that in other performance aspects the LQR may have some deficiencies. One of these turns out to be that at the crossover frequency (loop gain = 1), the slope of the multivariable. The Bode plot is  $-20\text{dB/decade}$ , which is a relatively slow attenuation rate (Doyle and Stein, 1981). By allowing a  $Q$  weighting matrix in the PI that is not positive semidefinite, it is possible to obtain better LQ designs that have higher roll-off rates at high frequencies (Shin and Chen, 1974; Ohta et al., 1990; Al-Sunni et al., 1992).

A stability robustness bound like (6.2-49) may be obtained for the loop gain referred to the input  $u(t)$ . It is

$$\overline{\sigma}[KG(I + KG)^{-1}] < \frac{1}{m(\omega)} \quad (6.5-8)$$

The inverse of this is

$$m(\omega) < \frac{1}{\overline{\sigma}[KG(I + KG)^{-1}]} = \underline{\sigma}[I + (KG)^{-1}] \quad (6.5-9)$$

It can be shown (see the problems) that (6.5-7) implies that

$$\underline{\sigma}[I + (KG(j\omega))^{-1}] \geq \frac{1}{2} \quad (6.5-10)$$

Therefore, the LQR remains stable for all multiplicative uncertainties in the plant transfer function which satisfy  $m(\omega) < \frac{1}{2}$ .

### Loop Transfer Recovery

The control design techniques we discussed in Chapter 5 involve selecting a desirable compensator structure using classical aircraft control intuition. Then the compensator



gains are adjusted using output feedback design for suitable performance. Robustness may be guaranteed using the multivariable Bode plot as shown in Sections 6.2 and 6.3.

However, in some cases, the plant may be so complex that there is little intuition available for selecting the compensator structure. This can be the case, for instance, for a jet engine (Athans et al., 1986). In this event, the technique to be presented in this section may be useful for controller design, since it yields a suitable compensator structure automatically.

Let us examine here the plant

$$\dot{x} = Ax + Bu + Gw \quad (6.5-11)$$

$$y = Cx + v, \quad (6.5-12)$$

with process noise  $w(t) \sim (0, M)$  and measurement  $n(t) \sim (0, v^2 N)$  both white,  $M > 0$ ,  $N > 0$ , and  $v$  a scalar parameter.

We have seen that the full-state-feedback control

$$u = -Kx \quad (6.5-13)$$

has some extremely attractive features, including simplified design equations (Section 5.7) and some important guaranteed robustness properties. Unfortunately, *these are not shared by an output feedback control law*, where the robustness must be checked independently. However, state feedback is usually impossible to use since all the states are seldom available for feedback in any practical application.

According to Figure 6.5-4a, where the plant transfer function is

$$\Phi(s)B = (sI - A)^{-1}B, \quad (6.5-14)$$

the loop gain, breaking the loop at the input  $u(t)$ , is

$$L_s(s) = K\Phi B \quad (6.5-15)$$

According to Section 6.4, if an observer or Kalman filter is used to produce a state estimate  $\hat{x}(t)$ , which is then used in the control law

$$u = -K\hat{x}, \quad (6.5-16)$$

the result is a regulator which, due to the separation principle, has the same transfer function as the state feedback controller. However, it is known that the guaranteed robustness properties of the full-state-feedback controller are generally lost (Doyle, 1978).

In this section we will assume that a state feedback gain  $K$  has already been determined using, for instance, the ARE design technique in Section 5.7. This  $K$  yields suitable robustness properties of  $K\Phi B$ . We should like to present a technique for

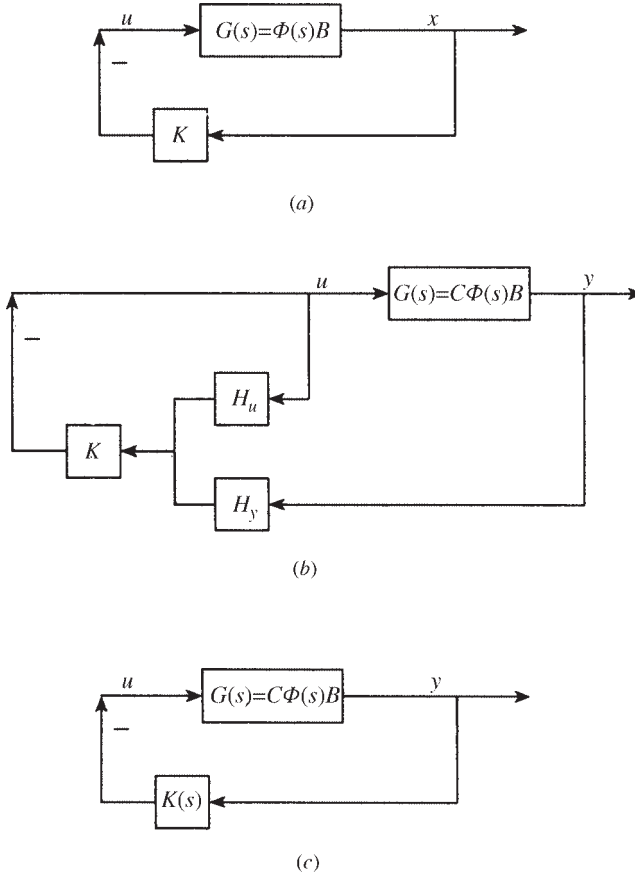


**Figure 6.5-4** (a) Loop gain with full state feedback; (b) regulator using observer and estimate feedback; (c) regulator loop gain.

designing a Kalman filter that results in a regulator that *recovers* the guaranteed robustness properties of the full-state-feedback control law as the design parameter  $\nu$  goes to zero. The technique is called linear quadratic Gaussian/loop transfer recovery (LQG/LTR), since the loop gain (i.e., loop transfer function)  $K\Phi B$  of full state feedback is recovered in the regulator as  $\nu \rightarrow 0$ . As we will see, the key to robustness using a stochastic regulator is in the selection of the noise spectral densities  $M$  and  $N$ .

**Regulator Loop Gain** Using an observer or Kalman filter, the closed-loop system appears in Figure 6.5-4b, where the regulator is given by (Section 6.4)

$$\begin{aligned}
 U(s) &= -K[sI - (A - LC)]^{-1}BU(s) - K[sI - (A - LC)]^{-1}LY(s) \\
 &= -H_u(s)U(s) - H_y(s)Y(s)
 \end{aligned} \tag{6.5-17}$$

and  $L$  is the observer or Kalman gain. Denoting the observer resolvent matrix as

$$\Phi_0(s) = [sI - (A - LC)]^{-1} \quad (6.5-18)$$

we write

$$H_u = K\Phi_0 B, \quad H_y = K\Phi_0 L \quad (6.5-19)$$

To find an expression for  $K(s)$  in Figure 6.5-4c using the regulator, note that  $(I + H_u)U = -H_y Y$ , so that

$$U = -(I + H_u)^{-1} H_y Y = -K(s)Y \quad (6.5-20)$$

However,

$$\begin{aligned} (I + H_u)^{-1} K &= [I + K(sI - (A - LC))^{-1} B]^{-1} K \\ &= [I - K(sI - (A - BK - LC))^{-1} B] \\ &= K(sI - (A - BK - LC))^{-1} [(sI - (A - BK - LC)) - BK] \\ &= K(sI - (A - BK - LC))^{-1} \Phi_0^{-1}, \end{aligned}$$

where the matrix inversion lemma was used in the second step. Therefore,

$$\begin{aligned} K(s) &= (I + H_u)^{-1} H_y \\ &= K[sI - (A - BK - LC)]^{-1} \Phi_0^{-1} \Phi_0 L \end{aligned}$$

or

$$K(s) = K[sI - (A - BK - LC)]^{-1} L \equiv K\Phi_r L, \quad (6.5-21)$$

with  $\Phi_r(s)$  the regulator resolvent matrix.

We will now show how to make the loop gain (at the input) using the regulator

$$L_r(s) = K(s)G(s) = K\Phi_r LC\Phi B \quad (6.5-22)$$

approach the loop gain  $L_s(s) = K\Phi B$  using full state feedback, which is guaranteed to be robust.

**Recovery of State Feedback Loop Gain at the Input** To design the Kalman filter so that the regulator loop gain at the input  $L_r(s)$  is the same as the state feedback loop gain  $L_s(s)$ , we will need to assume that the plant  $C\Phi B$  is *minimum phase* (i.e., with stable zeros), with  $B$  and  $C$  of full rank and  $\dim(u) = \dim(y)$ . The references for this subsection are Doyle and Stein (1979, 1981), Athans (1986), Stein and Athans (1987), and Birdwell (1989).

Let us propose  $G = I$  and the process noise spectral density matrix

$$M = \nu^2 M_0 + BB^T, \quad (6.5-23)$$

with  $M_0 > 0$ . Then, according to Table 6.4-1,

$$L = PC^T(\nu^2 N)^{-1} \quad (6.5-24)$$

and the Kalman filter ARE becomes

$$0 = AP + PA^T + (\nu^2 M_0 + BB^T) - PC^T(\nu^2 N)^{-1}CP \quad (6.5-25)$$

According to Kwakernaak and Sivan (1972), if the aforementioned assumptions hold, then  $P \rightarrow 0$  as  $\nu \rightarrow 0$ , so that

$$L(\nu^2 N)L^T = PC^T(\nu^2 N)^{-1}CP \rightarrow BB^T$$

The general solution of this equation is

$$L \rightarrow \frac{1}{\nu} B U N^{-1/2}, \quad (6.5-26)$$

with  $U$  any unitary matrix.

We claim that in this situation  $L_r(s) \rightarrow L_s(s)$  as  $\nu \rightarrow 0$ . Indeed, defining the full-state-feedback resolvent as

$$\Phi_c(s) = (sI - (A - BK))^{-1} \quad (6.5-27)$$

we may write

$$\begin{aligned} L_r(s) &= K(s)G(s) = K[sI - (A - BK - LC)^{-1}]LC\Phi B \\ &= K[\Phi_c^{-1} + LC]^{-1}LC\Phi B \\ &= K[\Phi_c - \Phi_c L(I + C\Phi_c L)^{-1}C\Phi_c]LC\Phi B \\ &= K\Phi_c L[I - (I + C\Phi_c L)^{-1}C\Phi_c L]C\Phi B \\ &= K\Phi_c L[(I + C\Phi_c L) - C\Phi_c L](I + C\Phi_c L)^{-1}C\Phi B \\ &= K\Phi_c L(I + C\Phi_c L)^{-1}C\Phi B \\ &\rightarrow K\Phi_c B(C\Phi_c B)^{-1}C\Phi B \\ &= K\Phi B(1 + K\Phi B)^{-1}[C\Phi B(I + K\Phi B)^{-1}]^{-1}C\Phi B \\ &= [K\Phi B(C\Phi B)^{-1}]C\Phi B = K\Phi B \end{aligned} \quad (6.5-28)$$

The matrix inversion lemma was used in going from line 2 to line 3 and from line 7 to line 8. The limiting value (6.5-26) for  $L$  was used at the arrow.

What we have shown is that using  $G = I$  and the process noise given by (6.5-23), as  $\nu \rightarrow 0$ , the regulator loop gain using a Kalman filter approaches the loop gain using full state feedback. This means that as  $\nu \rightarrow 0$ , all the robustness properties of the full-state-feedback control law are recovered in the stochastic regulator.

The *LQG/LTR design procedure* is thus as follows:

1. Use the control ARE in Table 5.7-1 to design a state feedback gain  $K$  with desirable properties. This may involve iterative design varying the PI weighting matrices  $Q$  and  $R$ .
2. Select  $G = I$ , process noise spectral density  $M = \nu^2 M_0 + BB^T$  and noise spectral density  $\nu^2 N$  for some  $M_0 > 0$  and  $N > 0$ . Fix the design parameter  $\nu$  and use the Kalman filter ARE to solve for the Kalman gain  $L$ .
3. Plot the maximum and minimum SVs of the regulator loop gain  $L_r(s)$  and verify that the robustness bounds are satisfied. If they are not, decrease  $\nu$  and return to 2.

A *reduced-order* regulator with suitable robustness properties may be designed by the LQG/LTR approach using the notions at the end of Section 6.4. That is, either a regulator may be designed for a reduced-order model of the plant or the regulator designed for the full-order plant may then have its order reduced. In using the first approach, a high-frequency bound characterizing the unmodeled dynamics should be used to guarantee stability robustness.

An interesting aspect of the LQR/LTR approach is that the recovery process may be viewed as a *frequency-domain linear quadratic* technique that trades off the smallness of the sensitivity  $S(j\omega)$  and the cosensitivity  $T(j\omega)$  at various frequencies. These notions are explored by Stein and Athans (1987) and Safonov et al. (1981).

***Non-Minimum-Phase Plants and Parameter Variations*** The limiting value of  $K(s)$  is given by the bracketed term in (6.5-28). Clearly, as  $\nu \rightarrow 0$  the regulator *inverts the plant transfer function*  $C\phi B$ . If the plant is of minimum phase, with very stable zeros, the LQG/LTR approach generally gives good results. On the other hand, if the plant is non-minimum-phase or has stable zeros with large time constants, the approach can be unsuitable.

In some applications, however, even if the plant is non-minimum-phase, the LQG/LTR technique can produce satisfactory results (Athans, 1986). In this situation, better performance may result if the design parameter  $\nu$  is not nearly zero. If the right-half-plane zeros occur at high frequencies where the loop gain is small, the LQG/LTR approach works quite well.

An additional defect of the LQG/LTR approach appears when there are plant parameter variations. As seen in Section 6.2, stability in the presence of parameter variations requires that the loop gain SVs be below some upper bound at low frequencies. However, this bound is not taken into account in the LQG/LTR derivation. Thus, LQG/LTR can yield problems for aircraft control design, where gain scheduling

is required. The  $H$ -infinity design approach (Francis et al., 1984; Doyle et al., 1989) has been used with success to overcome this problem.

**Recovery of Robust Loop Gain at the Output** We have shown that, by designing the state feedback first and then computing the Kalman filter gain using a specific choice of noise spectral densities, the stochastic regulator recovers the robustness of the loop gain  $K(s)G(s)$  referred to the input  $u(t)$  in Figure 6.5-4. However, in Section 6.2 we saw that for a small tracking error the robustness should be studied in terms of the loop gain  $G(s)K(s)$  referred to the error or equivalently to the system *output*.

Here we should like to show how to design a stochastic regulator that recovers a robust loop gain  $G(s)K(s)$ . This yields a second LQG/LTR design algorithm.

Thus, suppose that we *first design a Kalman filter* with gain  $L$  using Table 6.4-1. By duality theory, one may see that the Kalman filter loop gain

$$L_k(s) = C\Phi L \quad (6.5-29)$$

enjoys exactly the same guaranteed robustness properties as the state feedback loop gain  $K\Phi B$  that were described earlier in this section:

$$L_r^o(s) = G(s)K(s) = C\Phi BK\Phi_r L \quad (6.5-30)$$

Thus, we should like to determine how to design a state feedback gain  $K$  so that  $L_r^o(s)$  approaches  $C\Phi L$ . As we will see, the key to this is in the selection of the PI weighting matrices  $Q$  and  $R$  in Table 5.7-1.

To determine  $K$ , let us propose the PI

$$J = \frac{1}{2} \int_0^\infty (x^T Q x + \rho^2 u^T R u) dt \quad (6.5-31)$$

where

$$Q = \rho^2 Q_0 + C^T C, \quad (6.5-32)$$

with  $Q_0 > 0$ . By using techniques dual to those above, we may demonstrate that as  $\rho \rightarrow 0$  the state feedback gain determined using Table 5.7-1 approaches

$$K \rightarrow \frac{1}{\rho} R^{-1/2} W C, \quad (6.5-33)$$

with  $W$  a unitary matrix. Using this fact, it may be shown that

$$L_r^o(s) = G(s)K(s) \rightarrow C\Phi L \quad (6.5-34)$$

The LQR/LTR design technique for loop gain recovery at the output is therefore exactly dual to that for recovery at the input. Specifically, the Kalman gain  $L$  is first

determined using Table 6.4-1 for desired robustness properties. Then  $Q$  and  $R$  are selected, with  $Q$  of the special form (6.5-32). For a small value of  $\rho$ , the state feedback gain  $K$  is determined using Table 5.7-1. If the SV Bode plots of  $L_r^\rho(s)$  do not show acceptable robustness,  $\rho$  is decreased and a new  $K$  is determined.

If the plant  $C\Phi B$  is minimum phase, all is well as  $\rho$  is decreased. However, if there are zeros in the right-half plane, there could be problems as  $\rho$  becomes too small, although with care the LQG/LTR technique often still produces good results for suitable  $\rho$ .

**Example 6.5-1: LQG/LTR Design of Aircraft Lateral Control System** We will illustrate the loop transfer recovery technique on a lateral aircraft CAS design. This example should be compared with examples in Chapter 4 and Example 5.5-4. All computations, including solving for the state feedback gains and Kalman filter gains, were carried out very easily using MATLAB (Moler et al., 1987).

(a) *Control Objective.* The tracking control system shown in Figure 6.5-5 is meant to provide coordinated turns by causing the bank angle  $\phi(t)$  to follow a desired command while maintaining the sideslip angle  $\beta(t)$  at zero. It is a two-channel system with control input  $u = [u_\phi \ u_\beta]^T$ .

The reference command is  $r = [r_\phi \ r_\beta]^T$ . The control system should hold  $\phi$  at the commanded value of  $r_\phi$  and  $\beta(t)$  at the commanded value of  $r_\beta$ , which is equal to zero. The tracking error is  $e = [e_\phi \ e_\beta]^T$  with

$$\begin{aligned} e_\phi &= r_\phi - \phi \\ e_\beta &= r_\beta - \beta \end{aligned} \tag{1}$$

The negatives of the errors appear in the figure since a minus sign appears in  $u = -K\hat{x}$  as is standard for LQG design.

(b) *State Equations of Aircraft and Basic Compensator Dynamics.* To obtain the basic aircraft dynamics, the nonlinear F-16 model was linearized at the nominal flight

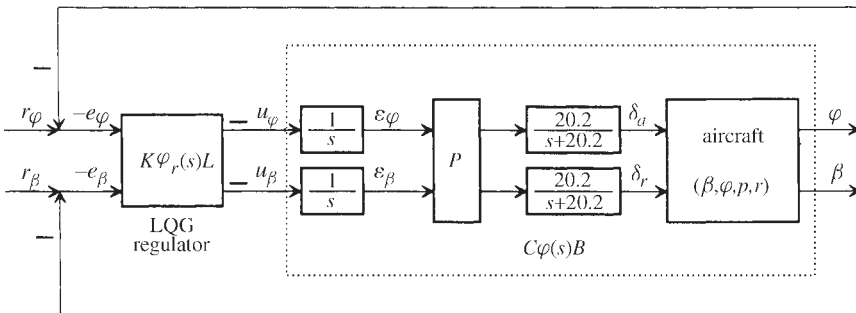


**Figure 6.5-5** Aircraft turn coordinator control system.

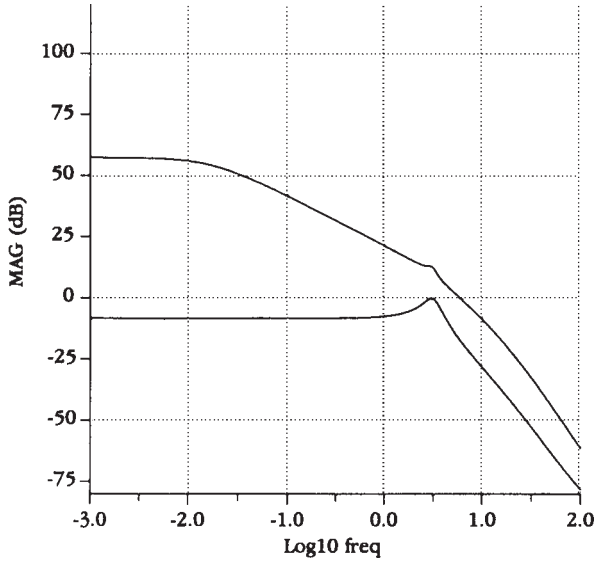


Figure 6.5-6 Singular values of the basic aircraft dynamics.

condition in Table 3.6-3 ( $V_T = 502$  ft/s, 0 ft altitude, 300 psf dynamic pressure, cg at  $0.35\bar{c}$ ) retaining the state sideslip  $\beta$ , bank angle  $\phi$ , roll rate  $p$ , and yaw rate  $r$ . Additional states  $\delta_a$  and  $\delta_r$  are introduced by the aileron and rudder actuators, both of which are modeled as having approximate transfer functions of  $20.2/(s + 20.2)$ . The aileron deflection is  $\delta_a$  and the rudder deflection is  $\delta_r$ .

The SVs versus frequency of the basic aircraft with actuators are shown in Figure 6.5-6. Clearly, the steady-state error will be large in the closed loop since the loop gain has neither integrator behavior nor large SVs at dc. Moreover, the SVs are widely separated at dc, so that they are not balanced.

To correct these deficiencies we may use the techniques of Example 6.2-3. The dc gain of the system is given by

$$H(0) = \begin{bmatrix} -727.37 & -76.94 \\ -2.36 & 0.14 \end{bmatrix} \quad (2)$$

First, the dynamics are augmented by integrators in each control channel. We denote the integrator outputs by  $\epsilon_\phi$  and  $\epsilon_\beta$ . The SV plots including the integrators are shown in Figure 6.5-7. The dc slope is now  $-20$  dB/decade, so that the closed-loop steady-state error will be zero. Next, the system was augmented by  $P = H^{-1}(0)$  to balance the SVs at dc. The net result is shown in Figure 6.5-8, which is very suitable.

The entire state vector, including aircraft states and integrator states, is

$$x = [\beta \ \phi \ p \ r \ \delta_a \ \delta_r \ \epsilon_\phi \ \epsilon_\beta]^T \quad (3)$$





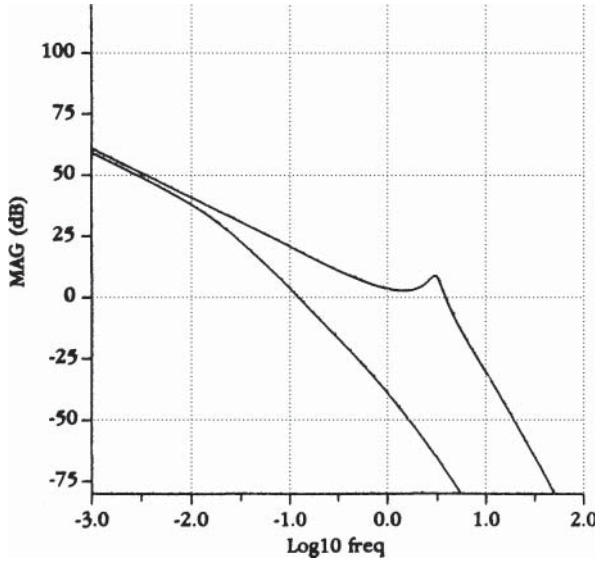


**Figure 6.5-8** Singular values of aircraft augmented by integrators and inverse dc gain matrix  $P$ .

where the factor of 57.2958 converts radians to degrees. Then

$$e = r - y \quad (8)$$

(c) *Frequency-Domain Robustness Bounds.* We now derive the bounds on the loop gain MIMO Bode magnitude plot that guarantee robustness of the closed-loop system. Consider first the high-frequency bound. Let us assume that the aircraft model is accurate to within 10% up to a frequency of 2 rad/s, after which the uncertainty grows without bound at the rate of 20 dB/decade. The uncertainty could be due to actuator modeling inaccuracies, aircraft flexible modes, and so on. This behavior is modeled by

$$m(\omega) = \frac{s + 2}{20} \quad (9)$$

We assume  $m(\omega)$  to be a bound on the multiplicative uncertainty in the aircraft transfer function (Section 6.2).

For stability robustness, despite the modeling errors, we saw in Section 6.2 that the loop gain referred to the output should satisfy

$$\overline{\sigma}(GK(j\omega)) < \frac{1}{m(\omega)} = \left| \frac{20}{s + 2} \right| \quad (10)$$

when  $1/m(\omega) \ll 1$ . The function  $1/m(\omega)$  is plotted in Figure 6.5-9.

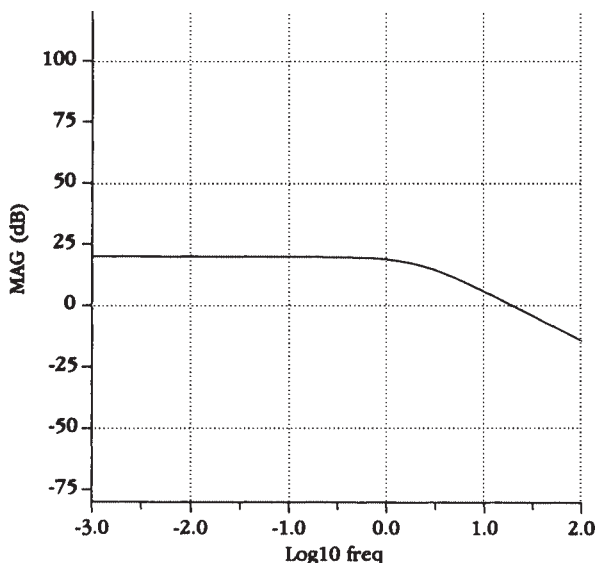


**Figure 6.5-9** Multiplicative uncertainty bound  $1/m(\omega)$  for the aircraft dynamical model.

Turning to the low-frequency bound on the closed-loop gain, the closed-loop system should be robust to wind gust disturbances. Using techniques like those in Examples 6.3-1, the gust magnitude plot shown in Figure 6.5-10a may be obtained. According to Section 6.2, for robust performance despite wind gusts, the minimum loop gain  $\text{SV } \underline{g}(GK(j\omega))$  should be above this bound.

(d) *Target Feedback Loop Design.* The robustness bounds just derived are expressed in terms of the SV plots referred to  $e(t)$ . To recover the loop gain  $GK(j\omega)$  at  $e(t)$ , or equivalently at the output, the Kalman filter should be designed first, so that we should employ LQG/LTR algorithm 2. Then  $C\Phi(s)L$  is the target feedback loop which should be recovered in the state feedback design phase.

In standard applications of the LQG/LTR technique, the regulator is designed for robustness, but the time responses are not even examined until the design has been completed. It is difficult to obtain decent time responses using this approach. In this example we should like to emphasize the fact that *it is not difficult to obtain good time responses as well as robustness using LQG/LTR*. It is only necessary to select the Kalman gain  $L$  in Table 6.4-1 for good robustness properties as well as *suitable step responses* of the target feedback loop  $C\Phi(s)L$ , where  $\Phi(s) = (sI - A)^{-1}$ .

Using MATLAB, the Kalman filter design equations in Table 6.4-1 were solved using

$$Q = \text{diag}\{0.01, 0.01, 0.01, 0.01, 0, 0, 1, 1\}, \quad (11)$$

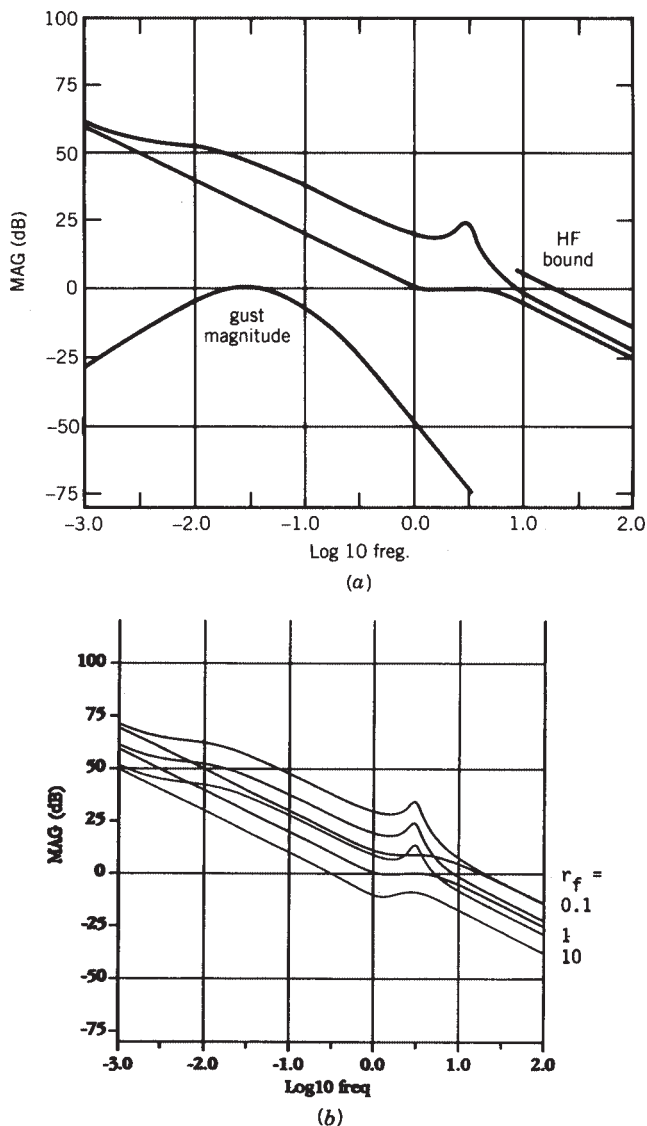
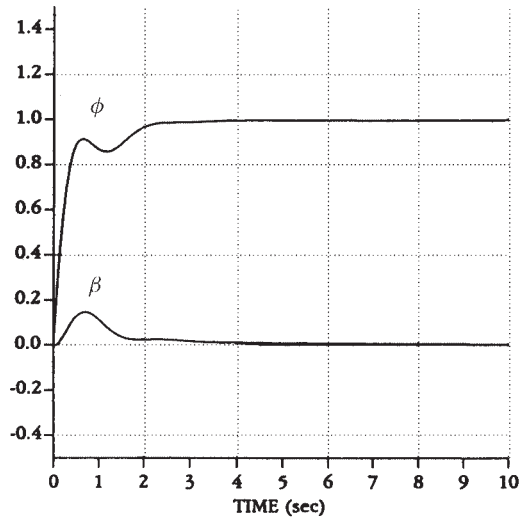
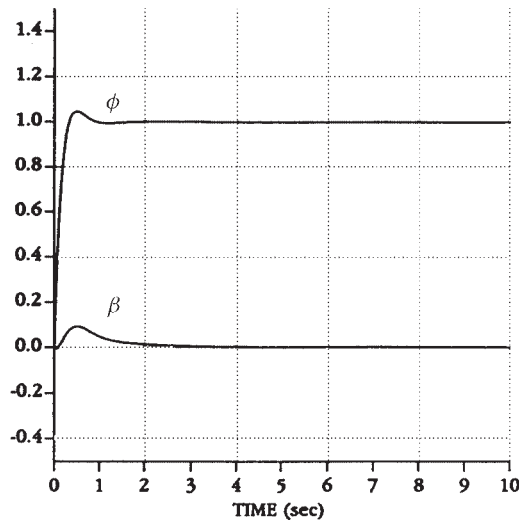


**Figure 6.5-10** Singular values of Kalman filter open-loop gain  $C\Phi(s)L$ : (a) for  $r_f = 1$ , including robustness bounds; (b) for various values of  $r_f$ .

$R = r_f I$ , and various values of  $r_f$ . The maximum and minimum SVs of the filter open-loop gain  $C = \Phi(s)L$  for  $r_f = 1$  are shown in Figure 6.5-10a, which also depicts the robustness bounds. The SVs for several values of  $r_f$  are shown in Figure 6.5-10b. Note how the SV magnitudes increase as  $r_f$  decreases, reflecting improved rejection of low-frequency disturbances. The figures show that the robustness bounds are



(a)



(b)

**Figure 6.5-11** Step responses of target feedback loop  $C\Phi(s)L$ : (a)  $r_f = 10$ ; (b)  $r_f = 1$ ; (c)  $r_f = 0.1$ .

satisfied for  $r_f = 1$  and  $r_f = 10$  but the high-frequency bound is violated for  $r_f = 0.1$ .

The associated step responses of  $C = \Phi(s)L$  with reference commands of  $r_\phi = 1$ ,  $r_\beta = 0$  are shown in Figure 6.5-11. The response for  $r_f = 10$  is unsuitable, while the response for  $r_f = 0.1$  is too fast and would not be appreciated by the pilot.

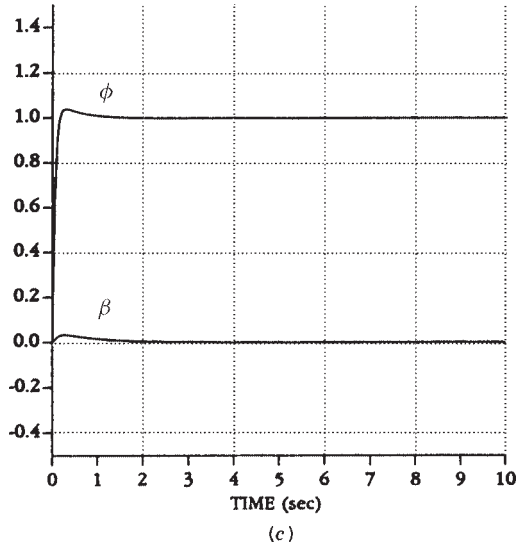


Figure 6.5-11 (continued)

On the other hand, the response for  $r_f = 1$  shows suitable time of response and overshoot characteristics as well as good decoupling between the bank angle  $\phi(t)$  and the sideslip  $\beta(t)$ .

Therefore, the target feedback loop was selected as  $C = \Phi(s)L$  with  $r_f = 1$ , since this results in a design that has suitable robustness properties and step responses. The corresponding Kalman gain is given by

$$L = \begin{bmatrix} -0.007 & 0.097 \\ 0.130 & -0.007 \\ 0.199 & -0.198 \\ -0.093 & -0.020 \\ -0.197 & -0.185 \\ 1.858 & 1.757 \\ 0.685 & -0.729 \\ 0.729 & 0.684 \end{bmatrix} \quad (12)$$

The Kalman filter poles (e.g., those of  $A - LC$ ) are given by

$$\begin{aligned} s = & -0.002, -0.879, -1.470, \\ & -3.952 \pm j3.589, \\ & -7.205, -20.2, -20.2 \end{aligned} \quad (13)$$

Although there is a slow pole, the step response is good, so this pole evidently has a small residue.

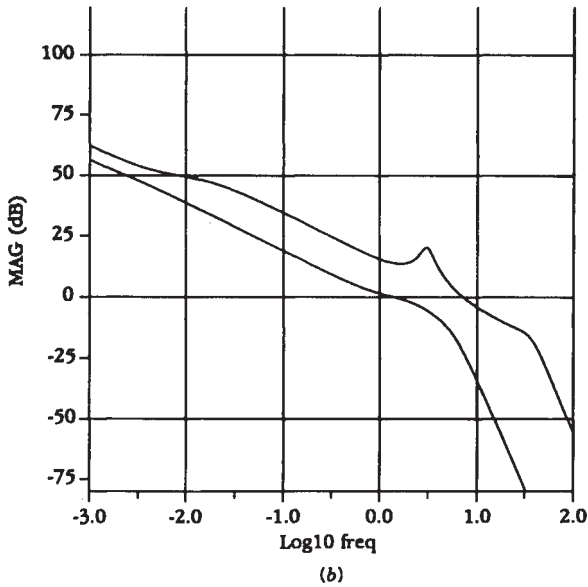
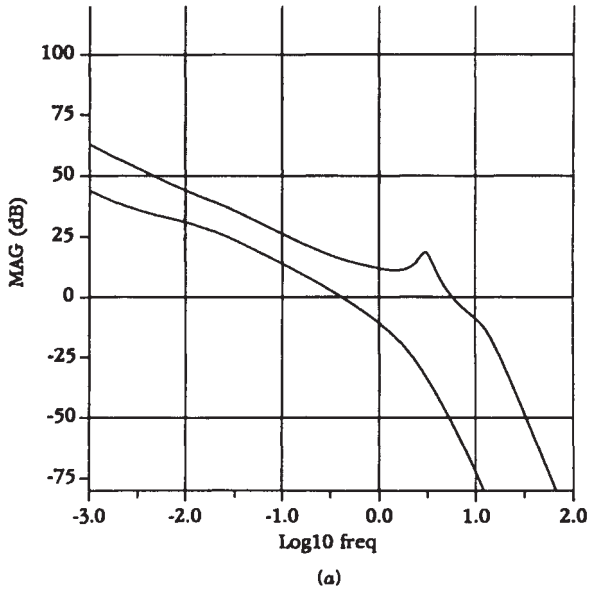


**Figure 6.5-12** Singular-value plots for the LQG regulator: (a) LQG with  $r_c = 10^{-3}$ ; (b) LQG with  $r_c = 10^{-7}$ ; (c) LQG with  $r_c = 10^{-11}$ , including robustness bounds.

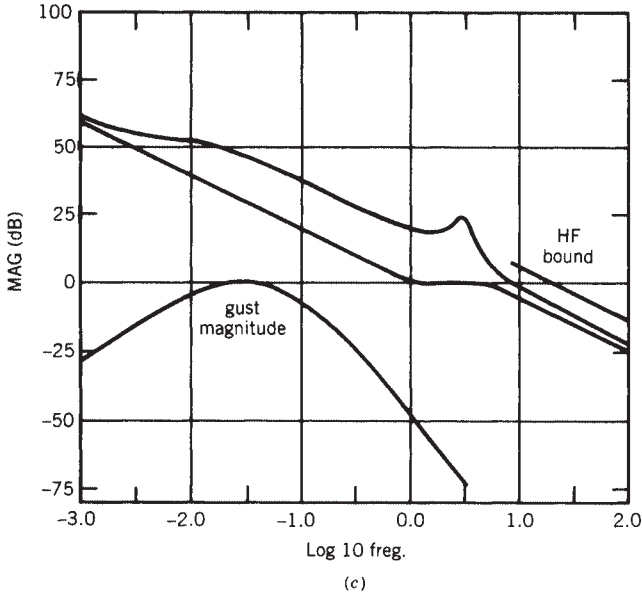


Figure 6.5-12 (continued)

It is of interest to discuss how the frequency and time responses were plotted. For the frequency response, we used the open-loop system

$$\begin{aligned}\dot{\hat{x}} &= A\hat{x} + Le \\ \hat{y} &= C\hat{x},\end{aligned}\quad (14)$$

which has a transfer function of  $C\Phi(s)L = C(sI - A)^{-1}L$ . A program was written which plots the SVs versus frequency for a system given in state-space form. This yielded Figure 6.5-10.

For the step response, it is necessary to examine the closed-loop system. In this case, the loop is closed by using  $e = r - \hat{y}$  in (14), obtaining

$$\begin{aligned}\dot{\hat{x}} &= (A - LC)\hat{x} + Lr \\ \hat{y} &= C\hat{x}\end{aligned}\quad (15)$$

Using these dynamics in program TRESP (Appendix B) with  $r = [1 \ 0]^T$  produces the step-response plot.

A word on the choice for  $Q$  is in order. The design parameters  $Q$  and  $R$  should be selected so that the target feedback loop  $C = \Phi(s)L$  has good robustness and time-response properties. It is traditional to select  $Q = BB^T$ , which accounts for the last two diagonal entries of (11). However, in this example it was impossible to obtain good step responses using this selection for  $Q$ . Motivated by the fact that the process



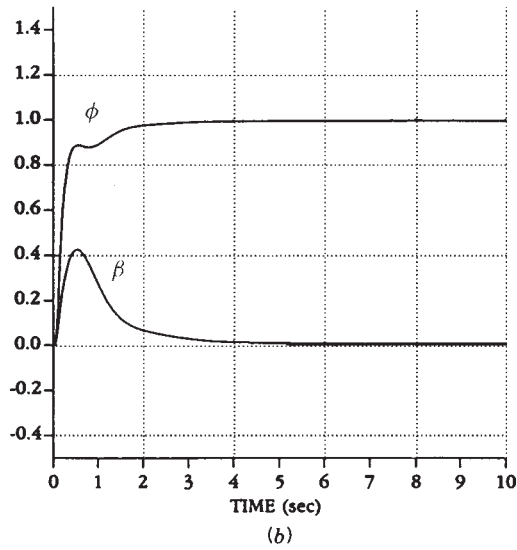
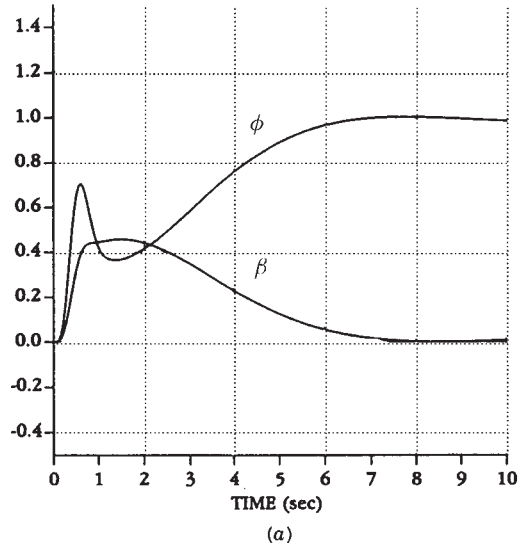


**Figure 6.5-13** Closed-loop step responses of the LQG regulator: (a) LQG with  $r_c = 10^{-3}$ ; (b) LQG with  $r_c = 10^{-7}$ ; (c) LQG with  $r_c = 10^{-11}$ .

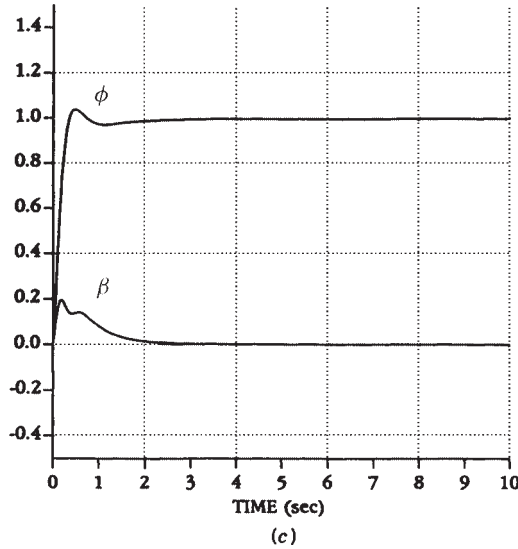


Figure 6.5-13 (continued)

noise in the aircraft excites the first four states as well, we experimented with different values for  $Q$ , plotting in each case the SVs and step responses. After a few iterations, the final choice (11) was made.

(e) *Loop Transfer Recovery at the Output*. The target feedback loop  $C\Phi(s)L$  using  $r_f = 1$  has good properties in both the frequency and time domains. Unfortunately, the closed-loop system with the LQG regulator has a loop gain referred to the output of  $C\Phi(s)BK\Phi_r(s)L$ , with the regulator resolvent given by

$$\Phi_r(s) = [sI - (A - LC - BK)]^{-1} \quad (16)$$

On the other hand, LQG/LTR algorithm 2 shows how to select a state feedback gain  $K$  so that the LQG regulator loop gain approaches the ideal loop gain  $C\Phi(s)L$ . Let us now select such a feedback gain matrix.

Using MATLAB, the LQR design problem in Table 5.7-1 was solved with  $Q = C^T C$ ,  $R = \rho^2 I$ , and various values of  $r_c \equiv \rho^2$  to obtain different feedback gains  $K$ . Some representative SVs of the LQG loop gain  $C\Phi(s)BK\Phi_r(s)L$  are plotted in Figure 6.5-12, where  $L$  is the target loop Kalman gain (12). Note how the actual SVs approach the target SVs in Figure 6.5-10a as  $r_c$  decreases. A good match is obtained for  $r_c = 10^{-11}$ .

Figure 6.5-12c also depicts the robustness bounds, which are satisfied for this choice of  $r_c = 10^{-11}$ . The corresponding step responses are given in Figure 6.5-13. A suitable step response that matches well the target response of Figure 6.5-11b results when  $r_c = 10^{-11}$ .

It is of interest to discuss how these plots were obtained. For the LQG SV plots, the complete dynamics are given by

$$\begin{aligned}\dot{x} &= Ax + Bu \\ \dot{\hat{x}} &= (A - LC)\hat{x} + Bu + Lw \\ u &= -K\hat{x},\end{aligned}\tag{17}$$

where  $w(t) = -e(t)$ . These may be combined into the augmented system

$$\begin{bmatrix} \dot{x} \\ \dot{\hat{x}} \end{bmatrix} = \begin{bmatrix} A & -BK \\ 0 & A - LC - BK \end{bmatrix} \begin{bmatrix} x \\ \hat{x} \end{bmatrix} + \begin{bmatrix} 0 \\ L \end{bmatrix} w\tag{18}$$

$$y = \begin{bmatrix} C & 0 \end{bmatrix} \begin{bmatrix} x \\ \hat{x} \end{bmatrix},\tag{19}$$

which has transfer function  $C\Phi(s)BK\Phi_r(s)L$ . The SVs are now easily plotted.

For the step responses, the closed-loop system must be studied. To close the loop, set  $w = y - r$  in (18) to obtain the closed-loop dynamics

$$\begin{bmatrix} \dot{x} \\ \dot{\hat{x}} \end{bmatrix} = \begin{bmatrix} A & -BK \\ LC & A - LC - BK \end{bmatrix} \begin{bmatrix} x \\ \hat{x} \end{bmatrix} + \begin{bmatrix} 0 \\ -L \end{bmatrix} r\tag{20}$$

$$y = \begin{bmatrix} C & 0 \end{bmatrix} \begin{bmatrix} x \\ \hat{x} \end{bmatrix}\tag{21}$$

These are used with program TRESP in Appendix B to obtain Figure 6.5-13.

The final LQG regulator is given by the Kalman gain  $L$  in (12) and the feedback gain  $K$  corresponding to  $r_c = 10^{-11}$ .

(f) *Reduced-Order Regulator.* The LQG regulator just designed has order  $n = 8$ , the same as the plant. This is excessive for an aircraft lateral control system. A reduced-order regulator that produces very good results may easily be determined using the partial-fraction-expansion approach in Example 6.2-4, principal-component analysis (Moore, 1982), or other techniques. This is easily accomplished using MATLAB. The SV plots and step response using the reduced-order regulator should be examined to verify robustness and suitable performance. ■

## 6.6 SUMMARY

In Section 6.2 we extended some classical frequency-domain analysis techniques to multivariable systems using the notion of the SV. We defined the multivariable loop gain, return difference, and sensitivity and showed that the multivariable Bode magnitude plot is just the plot of the maximum and minimum SVs of the loop gain versus frequency. To guarantee stability robustness to unmodeled high-frequency dynamics

and plant parameter variations, as well as performance robustness in the presence of disturbances, we derived various frequency-domain bounds that the SVs of the loop gain must satisfy.

A convenient robust output feedback design approach was presented in Section 6.3 that results in acceptable time-domain performance with guaranteed robustness.

In Section 6.4 we covered the design of multivariable observers for estimating the full state of the aircraft model from the measured outputs. We discussed the Kalman filter, showing an example of its use by reconstructing the angle of attack from normal acceleration and pitch-rate measurements in the presence of wind gust noise. We showed how to use full state feedback and an observer to design a dynamic regulator.

Finally, in Section 6.5 we covered the popular LQG/LTR robust design technique, illustrating with the design of a multivariable lateral control system.

## REFERENCES

- Al-Sunni, F. M., B. L. Stevens, and F. L. Lewis. "Negative State Weighting in the Linear Quadratic Regulator for Aircraft Control," *Journal of Guidance, Control, and Dynamics*, 15, no. 5 (September–October, 1992): 1279–1281.
- Anderson, B.D.O., and Y. Liu. "Controller Reduction: Concepts and Approaches," *IEEE Transactions on Automatic Control* AC-34, no. 8 (August 1989): 802–812.
- Armstrong, E. S. *ORACLs: A Design System for Linear Multivariable Control*. New York: Marcel Dekker, 1980.
- Athans, M. "A Tutorial on the LQG/LTR Method." *Proceedings of the American Control Conference*, June 1986, pp. 1289–1296.
- Athans, M., P. Kapsouris, E. Kappos, and H. A. Spang III. "Linear-Quadratic Gaussian with Loop-Transfer Recovery Methodology for the F-100 Engine." *Journal of Guidance, Control, and Dynamics* 9, no. 1 (January–February 1986): 45–52.
- Birdwell, J. D. "Evolution of a Design Methodology for LQG/LTR." *IEEE Control Systems Magazine* 9(3) (April 1989): 73–77.
- Blakelock, J. H. *Automatic Control of Aircraft and Missiles*. New York: Wiley, 1965.
- Bryson, A. E., Jr., and Y.-C. Ho. *Applied Optimal Control*. New York: Hemisphere, 1975.
- Doyle, J. C. "Guaranteed Margins for LQG Regulators." *IEEE Transactions on Automatic Control* (August 1978): 756–757.
- Doyle, J. C., and G. Stein. "Robustness with Observers." *IEEE Transactions on Automatic Control* AC-24, no. 4 (August 1979): 607–611.
- . "Multivariable Feedback Design: Concepts for a Classical/Modern Synthesis." *IEEE Transactions on Automatic Control* AC-26, no. 1 (February 1981): 4–16.
- Doyle, J. C., K. Glover, P. P. Khargonekar, and B. Francis. "State-Space Solutions to Standard  $H_2$  and  $H_\infty$  Control Problems." *IEEE Transactions on Automatic Control* AC-34, no. 8 (August 1989): 831–847.
- Francis, B., J. W. Helton, and G. Zames. " $H_\infty$  Optimal Feedback Controllers for Linear Multivariable Systems." *IEEE Transactions on Automatic Control* AC-29, no. 10 (October 1984): 888–900.

- Franklin, G. F., J. D. Powell, and A. Emami-Naeini. *Feedback Control of Dynamic Systems*. Reading, Mass.: Addison-Wesley, 1986.
- Gelb, A., ed. *Applied Optimal Estimation*. Cambridge, Mass.: MIT Press, 1974.
- Grimble, M. J., and M. A. Johnson. *Optimal Control and Stochastic Estimation: Theory and Applications*, vol. 1. New York: Wiley, 1988.
- IMSL. *Library Contents Document*. 8th ed. Houston, Tex.: International Mathematical and Statistical Libraries, Inc., 1980.
- Kailath, T. *Linear Systems*. Englewood Cliffs, N.J.: Prentice Hall, 1980.
- Kaminer, I., P. P. Khargonekar, and G. Robel. "Design of Localizer Capture and Track Modes for a Lateral Autopilot Using H-infinity Synthesis." *IEEE Control Systems Magazine* 10, no. 4 (June 1990): 13–21.
- Kwakernaak, H., and R. Sivan. *Linear Optimal Control Systems*. New York: Wiley, 1972.
- Laub, A. J. "An Inequality and Some Computations Related to the Robust Stability of Linear Dynamic Systems." *IEEE Transactions on Automatic Control* AC-24, no. 2 (April 1979): 318–320.
- . "Efficient Multivariable Frequency Response Computations." *IEEE Transactions on Automatic Control* AC-26, no. 2 (April 1981): 407–408.
- Lewis, F. L. *Optimal Control*. New York: Wiley, 1986a.
- . *Optimal Estimation*. New York: Wiley, 1986b.
- Ly, U.-L., A. E. Bryson, and R. H. Cannon. "Design of Low-Order Compensators Using Parameter Optimization." *Automatica* 21, no. 3 (1985): 315–318.
- MacFarlane, A.G.J. "Return-Difference and Return-Ratio Matrices and Their Use in the Analysis and Design of Multivariable Feedback Control Systems." *Proceedings of the Institute of Electrical Engineering* 117, no. 10 (October 1970): 2037–2049.
- MacFarlane, A.G.J., and B. Kouvaritakis. "A Design Technique for Linear Multivariable Feedback Systems." *International Journal of Control* 25 (1977): 837–874.
- MATRIX<sub>x</sub>. Santa Clara, Calif.: Integrated Systems, Inc., 1989.
- Mil. Spec. 1797*. "Flying Qualities of Piloted Vehicles." 1987.
- Minto, K. D., J. H. Chow, and J. W. Beseler. "An Explicit Model-Matching Approach to Lateral-Axis Autopilot Design." *IEEE Control Systems Magazine* 10, no. 4 (June 1990): 22–28.
- Moerder, D. D., and A. J. Calise. "Convergence of a Numerical Algorithm for Calculating Optimal Output Feedback Gains." *IEEE Transactions on Automatic Control* AC-30, no. 9 (September 1985): 900–903.
- Moler, C., J. Little, and S. Bangert. *PC-Matlab*. Sherborn, Mass.: The Mathworks, Inc., 1987.
- Moore, B. C. "Principal Component Analysis in Linear Systems: Controllability, Observability, and Model Reduction." *IEEE Transactions on Automatic Control* AC-26, no. 1 (1982): 17–32.
- Morari, M., and E. Zafiriou. *Robust Process Control*. Englewood Cliffs, N.J.: Prentice Hall, 1989.
- Ohta, H., P. N. Nikiforuk, and M. Kakinuma. "Use of negative weights in linear quadratic regulator synthesis." *Journal of Guidance, Control, and Dynamics* 14.4 (1991): 791–796.
- Papoulis, A. *Probability, Random Variables, and Stochastic Processes*. 2d ed. New York: McGraw-Hill, 1984.

- Postlethwaite, I., J. M. Edmunds, and A.G.J. MacFarlane. "Principal Gains and Principal Phases in the Analysis of Linear Multivariable Systems." *IEEE Transactions on Automatic Control* AC-26, no. 1 (February 1981): 32–46.
- Press, W. H., B. P. Flannery, S. A. Teukolsky, and W. T. Vetterling. *Numerical Recipes: The Art of Scientific Computing*. New York: Cambridge University Press, 1986.
- Rosenbrock, H. H. *Computer-Aided Control System Design*. New York: Academic, 1974.
- Safonov, M. G., and M. Athans. "Gain and Phase Margin for Multiloop LQG Regulators." *IEEE Transactions on Automatic Control* AC-22, no. 2 (April 1977): 173–178.
- Safonov, M. G., A. J. Laub, and G. L. Hartmann. "Feedback Properties of Multivariable Systems: The Role and Use of the Return Difference Matrix." *IEEE Transactions on Automatic Control* AC-26, no. 1 (February 1981): 47–65.
- Shin, V., and C. Chen. "On the Weighting Factors of the Quadratic Criterion in Optimal Control." *International Journal of Control* 19 (May 1974): 947–955.
- Stein, G., and M. Athans. "The LQG/LTR Procedure for Multivariable Feedback Control Design." *IEEE Transactions on Automatic Control* AC-32, no. 2 (February 1987): 105–114.
- Stevens, B. L., P. Vesty, B. S. Heck, and F. L. Lewis. "Loop Shaping with Output Feedback." *Proceedings of the American Control Conference* (June 1987): 146–149.
- Strang, G. *Linear Algebra and Its Applications*. 2d ed. New York: Academic, 1980.
- Yousuff, A., and R. E. Skelton. "A Note on Balanced Controller Reduction." *IEEE Transactions on Automatic Control* AC-29, no. 3 (March 1984): 254–257.

## PROBLEMS

### Section 6.2

- 6.2-1** Derive in detail the multivariable expressions (6.2-16) and (6.2-17) for the performance output and the tracking error.
- 6.2-2** Prove (6.2-54). You will need to neglect any terms that contain second-order terms in the parameter variation matrices and use the fact that, for small  $X$ ,  $(I - X)^{-1} \approx (I + X)$ .
- 6.2-3 Multivariable Closed-Loop Transfer Relations.** In Figure 6.2-1, let the plant  $G(s)$  be described by

$$\dot{x} = \begin{bmatrix} 0 & 1 & 0 \\ 0 & -3 & 0 \\ 0 & 0 & 0 \end{bmatrix} x + \begin{bmatrix} 0 & 0 \\ 1 & 0 \\ 0 & 1 \end{bmatrix} u, \quad z = \begin{bmatrix} 1 & 0 & 0 \\ 0 & 0 & 1 \end{bmatrix} x$$

and the compensator is  $K(s) = 2I_2$ .

- (a) Find the multivariable loop gain and return difference.
- (b) Find the sensitivity and cosensitivity.
- (c) Find the closed-loop transfer function from  $r(t)$  to  $z(t)$  and hence the closed-loop poles.

- 6.2-4** For the continuous-time system in Example 6.2-1, plot the individual SISO Bode magnitude plots from input 1 to outputs 1 and 2 and from input 2 to outputs 1 and 2. Compare them to the MIMO Bode plot to see that there is no obvious relation. Thus, the robustness bounds cannot be given in terms of the individual SISO Bode plots.
- 6.2-5 Software for MIMO Bode Magnitude Plot.** Write a computer program to plot the Bode magnitude plot for a multivariable system given in state-space form  $\dot{x} = Ax + Bu$ ,  $y = Cx + Du$ . Your program should read in  $A$ ,  $B$ ,  $C$ ,  $D$ . You may use a SVD routine [e.g., IMSL (1980) and Press et al. (1986)] or the technique by Laub (1979). Use the software to verify Examples 6.2-1 and 6.2-2.
- 6.2-6 Multivariable Bode Plot.** For the system in Problem 6.2-3, plot the multivariable Bode magnitude plots for:
- (a) The loop gain  $GK$
  - (b) The sensitivity  $S$  and cosensitivity  $T$ . For which frequency ranges do the plots for  $GK(j\omega)$  match those for  $S(j\omega)$ ? For  $T(j\omega)$ ?
- 6.2-7 Bode Plots for F-16 Lateral Regulator.** Plot the loop gain multivariable Bode magnitude plot for the F-16 lateral regulator designed in Example 5.3-1.
- 6.2-8 Balancing and Zero Steady-State Error.** Find a precompensator for balancing the SVs at low frequency and ensuring zero steady-state error for the system

$$\dot{x} = \begin{bmatrix} 0 & 1 & 0 \\ -2 & -3 & 0 \\ 0 & 0 & -3 \end{bmatrix} x + \begin{bmatrix} 0 & 0 \\ 1 & 0 \\ 0 & 1 \end{bmatrix} u, \quad z = \begin{bmatrix} 1 & 0 & 0 \\ 0 & 0 & 1 \end{bmatrix} x$$

Plot the SVs of the original and precompensated system.

## Section 6.3

- 6.3-1 Model Reduction and Neglected High-Frequency Modes.** An unstable system influenced by high-frequency parasitics is given by

$$\dot{x} = \begin{bmatrix} 0 & 1 & 0 \\ 1 & 0 & 1 \\ 0 & 0 & -10 \end{bmatrix} x + \begin{bmatrix} 0 & 0 \\ 0 & 1 \\ 1 & 0 \end{bmatrix} u, \quad z = \begin{bmatrix} 1 & 0 & 0 \end{bmatrix} x$$

- (a) Use the technique of Example 6.2-4 to find a reduced-order model that neglects the high-frequency mode at  $s = 10$  rad/s. Find the bound  $m(j\omega)$  on the magnitude of the neglected portion.
- (b) Using techniques like those in Sections 5.4 and 5.5, design a servo control system for the reduced-order model. Try a lead compensator whose gains are varied by the LQ algorithm, as used in Example 5.5-5. Verify the step response of the closed-loop system by performing a simulation on the reduced-order system.

- (c) Find the loop gain of the closed-loop system and plot its SVs. Do they fall below the bound  $1/m(j\omega)$ , thus guaranteeing robustness to the neglected mode? If not, return to part (b) and find other gains that do guarantee stability robustness.
- (d) Simulate your controller on the full system, including the high-frequency mode. How does the step response look?
- (e) A better controller results if high-frequency dynamics are not neglected in the design stage. Design a servo control system for the full third-order system. It may be necessary to use a more complicated controller. Verify the step response of the closed-loop system by performing a simulation. Compare to the results of part (d).

**6.3-2 Gain-Scheduling Robustness.** In the problems for Section 5.4 a gain-scheduled normal acceleration CAS was designed for a transport aircraft using three equilibrium points. Using the results at the end of Section 6.2, we want to check the design for robustness to plant parameter variations. Call the systems at the three equilibrium points  $(A_i, B_i, C_i)$ ,  $i = 1, 2, 3$ .

- (a) In Problem 6.2-5 you wrote a program to plot the MIMO Bode magnitude plots for a state-variable system. Note that a state-space realization of  $\Delta G(s)$  in (6.2-54) is given by

$$\dot{x} = \begin{bmatrix} A & -\Delta A \\ 0 & A \end{bmatrix} x + \begin{bmatrix} \Delta B \\ b \end{bmatrix} u, \quad y = \begin{bmatrix} C & \Delta C \end{bmatrix} x$$

That is, this system has transfer function of  $\Delta G$ . Define  $\Delta G_{ij}(s)$  as being computed using  $\Delta A = A_i - A_j$ ,  $\Delta B = B_i - B_j$ ,  $\Delta C = C_i - C_j$ . Use these facts combined with (6.2-48) to obtain low-frequency bounds for robustness to the gain-scheduling plant parameter variations.

- (b) Find the loop gain SVs of your design for the gain-scheduled CAS. Do they fall below the robustness bounds? If not, select new PI weights and try to improve the design. If this fails, you will need to select more closely spaced equilibrium points for the gain-scheduled design.

## Section 6.4

**6.4-1 Nonzero-Mean Noise.** Use (6.4-49) to write down the best estimate for  $x(t)$  in terms of the filter state  $\hat{x}(t)$  if the process noise  $w(t)$  and measurement noise  $v(t)$  have nonzero means of  $\bar{w}$  and  $\bar{v}$ , respectively.

**6.4-2 Observer for Angle of Attack.** In Example 5.5-3 a low-pass filter of  $10/(s + 10)$  was used to smooth out the angle-of-attack measurements to design a pitch-rate CAS. An alternative is to use an observer to reconstruct  $\alpha$ . This completely avoids measurements of the angle of attack.

- (a) Considering only the  $2 \times 2$  short-period approximation, design an observer that uses measurements of  $q(t)$  to provide estimates of  $\alpha(t)$ . The



observer should have  $\zeta = 1/\sqrt{2}$  and  $\omega_n = 10$  rad/s. Use Ackermann's formula to find the output injection matrix  $L$ .

- (b) Delete the  $\alpha$ -filter in Example 5.5-3, replacing it by the dynamics of the second-order observer just designed. With the new augmented dynamics, perform the LQ design of Example 5.5-3. Compare the performance of this pitch-rate CAS to the one using the  $\alpha$ -filter.

**6.4-3 Dynamic LQ Regulator for Pitch-Rate CAS.** In Example 5.5-3 and Problem 6.4-2, output feedback design was used to build a pitch-rate CAS. In this problem we would like to use LQG theory to perform the design.

- (a) Design an observer for  $\alpha$  using  $q$  measurements, as described in the previous problem.
- (b) Neglect the elevator actuator, considering only the  $2 \times 2$  short-period approximation in Example 5.5-3 plus the feedforward-path integrator. Find the state feedback gain  $K$  to place the poles at  $\zeta = 1/\sqrt{2}$ ,  $\omega_n = 3.5$  rad/s; this yields good flying qualities for the short-period mode. Use Ackermann's formula or the design software for Table 5.3-1 with  $C = I$ .
- (c) Using the  $2 \times 2$  observer and the state feedback  $K$ , construct a dynamic pitch-rate CAS. Verify its performance by plotting the step response.

**6.4-4 Kalman Filter.** Software for solving the Kalman filter ARE is available in Armstrong (1980) and IMSL (1980); also MATRIX<sub>x</sub> (1989) and MATLAB (Moler et al., 1987). Alternatively, the Kalman filter gain  $L$  can be found using the software for Table 5.3-1 on the dual plant  $(A^T, C^T, B^T)$  with  $B = I$ . Repeat Example 6.4-2 if the wind gusts have a turbulence intensity of 20 ft/s.

## Section 6.5

**6.5-1** Show that (6.5-7) implies (6.5-10) (see Laub, 1979).

**6.5-2 LQG/LTR Design.** Note that the state feedback gain  $K$  can be found using the software for Table 5.3-1 with  $C = I$ . Likewise, the Kalman filter gain  $L$  can be found using the software for Table 5.3-1 on the dual plant  $(A^T, C^T, B^T)$ , with  $B = I$ .

- (a) In Problem 6.4-3(b), plot the loop gain SVs assuming full state feedback.
- (b) Now angle-of-attack measurements are not allowed. Design a Kalman filter for various values of the design parameter  $\nu$ . In each case, plot the closed-loop step response as well as the loop gain SVs. Compare the step response and the SVs to the case for full state feedback as  $\nu$  becomes small.

## CHAPTER 7

---

# DIGITAL CONTROL

---

### 7.1 INTRODUCTION

In Chapters 4 through 6 we have shown how to design continuous-time controllers for aircraft. However, with microprocessors so fast, light, and economical, control laws are usually implemented on modern aircraft in digital form. In view of the requirement for gain scheduling of aircraft controllers, digital control schemes are especially useful, for gain scheduling is very easy on a digital computer.

To provide reliability in the event of failures, modern aircraft control schemes are redundant, with two or three control laws for each application. The actual control to be applied is selected by “voting”; that is, there should be good agreement between two out of three controllers. Such schemes are more conveniently implemented on a microprocessor, where the comparison and voting logic reside.

In this chapter we address the design of digital, or discrete-time, controllers, since the design of such controllers involves some extra considerations of which one should be aware. In Section 7.2 we discuss the *simulation* of digital controllers on a digital computer. Then in Sections 7.3 and 7.4 two approaches to digital control *design* are examined. Finally, some aspects of the actual *implementation* are mentioned in Section 7.5.

In the first approach to digital control design, covered in Section 7.3, we show how to convert an already designed continuous-time controller to a discrete-time controller using, for instance, the bilinear transform (BLT). An advantage of this *continuous controller redesign* approach is that the sample period  $T$  does not have to be selected until after the continuous controller has been designed.

Unfortunately, controller discretization schemes based on transformations such as the BLT are approximations. Consequently, the sampling period  $T$  must be

small to ensure that the digital controller performs like the continuous version from which it was designed. Therefore, in Section 7.4 we show how the design of the continuous-time controller may be *modified* to take into account some properties of the sampling process as well as computation delays. Discretization of such a modified continuous controller yields a digital control system with improved performance.

In Section 7.5 we discuss some implementation considerations, such as actuator saturation and controller structure.

There are many excellent references on digital control; some of them are listed at the end of the chapter. We will draw most heavily on the work of Franklin and Powell (1980), Åström and Wittenmark (1984), and Lewis (1992).

## 7.2 SIMULATION OF DIGITAL CONTROLLERS

A digital control scheme is shown in Figure 7.1-1. The plant  $G(s)$  is a continuous-time system, and  $K(z)$  is the dynamic digital controller, where  $s$  and  $z$  are, respectively, the Laplace and Z-transform variables (i.e.,  $1/s$  represents integration and  $z^{-1}$  represents a unit time delay). The digital controller  $K(z)$  is implemented using software code in a microprocessor.

The hold device in the figure is a digital-to-analog (D/A) converter that converts the discrete control samples  $u_k$  computed by the software controller  $K(z)$  into the continuous-time control  $u(t)$  required by the plant. It is a *data reconstruction* device. The input  $u_k$  and output  $u(t)$  for a *zero-order hold* (ZOH) are shown in Figure 7.2-2. Note that  $u(kT) = u_k$ , so that  $u(t)$  is continuous from the right. That is,  $u(t)$  is updated at times  $kT$ . The sampler with sample period  $T$  is an analog-to-digital (A/D) converter that takes the samples  $y_k = y(kT)$  of the output  $y(t)$  that are required by the software controller  $K(z)$ .

In this chapter we discuss the design of the digital controller  $K(z)$ . Once the controller has been designed, it is important to *simulate* it before it is implemented to determine if the closed-loop response is suitable. The simulation should provide the response at all times, including times between the samples.

To simulate a digital controller we may use the scheme shown in Figure 7.2-3. There the continuous dynamics  $G(s)$  are contained in the subroutine  $F(t, x, \dot{x})$ ; they are integrated using a Runge-Kutta integrator. Note that two time intervals are involved: the sampling period  $T$  and the *Runge-Kutta integration period*  $T_R \ll T$ .  $T_R$  should be selected as an integral divisor of  $T$ .

Several numerical integration schemes were discussed in Section 3.5. We have found that the Runge-Kutta routines are very suitable, while Adams-Bashforth

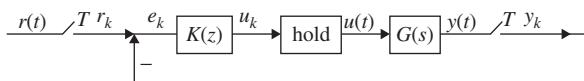
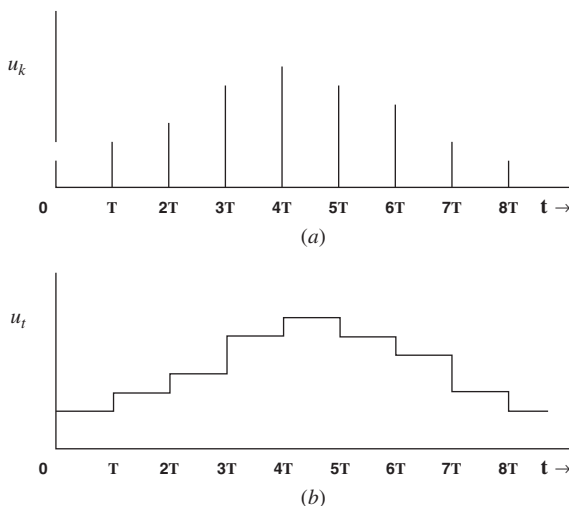
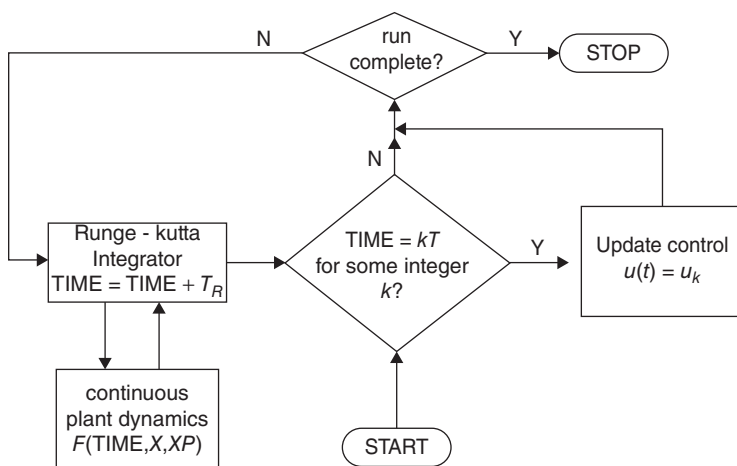


Figure 7.1-1 Digital controller.



**Figure 7.2-2** Data reconstruction using a ZOH: (a) discrete control sequence  $u_k$ ; (b) reconstructed continuous signal  $u(t)$ .

routines do not give enough accuracy for digital control purposes. This is especially true when advanced adaptive and parameter estimation techniques are used. For most purposes, the fixed-step-size Runge-Kutta algorithm in Appendix B is suitable if  $T_R$  is selected small enough. In rare instances it may be necessary to use an adaptive step size integrator such as Runge-Kutta-Fehlberg. In all the examples in this book, the fixed-step-size version was used.



**Figure 7.2-3** Digital control simulation scheme.

A driver program that realizes Figure 7.2-3 is given in Figure 7.2-4. It is written in a modular fashion to apply to a wide variety of situations and calls a Runge-Kutta integration routine such as the one in Appendix B. The Runge-Kutta integrator in turn calls subroutine F(TIME, X, XP) containing the continuous-time dynamics.

The digital controller is contained in subroutine DIG(T, X). Figure 7.2-3 assumes a ZOH; thus, the control input  $u(t)$  is updated to  $u_k$  at each time  $kT$  and then held constant until time  $(k + 1)T$ . The driver program in Figure 7.2-4 performs this.

It is important to realize that this simulation technique provides  $x(t)$  as a continuous function of time, even at values *between* the sampling instants [in fact, it provides  $x(t)$  at multiples of  $T_R$ ]. This is essential in verifying acceptable *intersample behavior* of the closed-loop system prior to implementing the digital controller on the actual

```

C  DRIVER PROGRAM TO COMPUTE AND SIMULATE DIGITAL CONTROL SCHEME
C  REQUIRES SUBROUTINES:
C    DIG(T,X) FOR DIGITAL CONTROL UPDATE AT SAMPLING INSTANTS
C    RUNKUT (TIME, TR, X, NSTATES) TO INTEGRATE CONTINUOUS DYNAMICS
C    F (TIME,X,XP) TO PROVIDE CONTINUOUS PLANT DYNAMICS

      PROGRAM DIGICON
      REAL X(1)
      COMMON/CONTROL/U(1)
      COMMON/OUTPUT/Y(1)

C  SET RUN TIME, SAMPLING PERIOD, RUNGE KUTTA STEP SIZE
      DATA TRUN,T,TR/5.,0.5,0.01/
C  SET INITIAL PLANT STATE
      DATA X(1)/0./

      TIME= 0.
      N= NINT (TRUN/T)
      NT= NINT (T/TR)

*  DIGITAL CONTROL SIMULATION RUN

      DO 10 K= 0,N-1
C    UPDATE DIGITAL CONTROL INPUT

      CALL DIG(T,X)

C    INTEGRATE CONTINUOUS DYNAMICS BETWEEN SAMPLES
      DO 10 I= 1,NT

C    WRITE TO FILE FOR PLOT
      WRITE(7,*) TIME,X(1),U

10  CALL RUNKUT (TIME,TR,X,1)
      WRITE(7,*) TIME,X(1),U
      STOP
      END

```

**Figure 7.2-4** Digital control simulation driver program.

plant. Even though the closed-loop behavior is acceptable at the sample points, with improper digital control system design there can be serious problems between the samples. The basic problem is that a badly designed controller can destroy observability, so that poor intersample behavior is not apparent at the sample points (Lewis, 1992). This simulation scheme allows the intersample behavior to be checked prior to actual implementation.

We will soon present several examples that demonstrate the simulation of digital controllers. First, it is necessary to discuss the design of digital controllers.

### 7.3 DISCRETIZATION OF CONTINUOUS CONTROLLERS

A digital control design approach that could directly use all of the continuous-time techniques of the previous chapters would be extremely appealing. Therefore, in this section we discuss the design of digital controllers by the redesign of existing continuous controllers. In this approach, the continuous controller is first designed using any desired technique. Then the controller is discretized using, for instance, the bilinear transform, to obtain the digital control law, which is finally programmed on the microprocessor.

An alternative approach to digital control design is given by Lewis (1992). In that approach, it is not necessary to design a continuous-time controller first, but a discrete-time controller is designed *directly* using a sampled version of the aircraft dynamics.

We now show how to discretize a continuous controller to obtain a digital controller. The idea is illustrated by designing a digital proportional-integral-derivative (PID) controller in Example 7.3-1 and a digital pitch-rate control system in Example 7.3-2.

Suppose that a continuous-time controller  $K^c(s)$  has been designed for the plant  $G(s)$  by some means, such as root-locus or LQ design. We will discuss two approximate schemes for converting  $K^c(s)$  into a discrete-time controller  $K(z)$  that can be implemented on a microprocessor. We discuss first the BLT and then the matched pole-zero (MPZ) technique.

The sample period is  $T$  seconds, so that the *sampling frequency* is

$$f_s = \frac{1}{T}, \omega_s = \frac{2\pi}{T} \quad (7.3-1)$$

#### Bilinear Transformation

A popular way to convert a continuous transfer function to a discrete one is the *bilinear transformation* or *Tustin's approximation*. On sampling (Franklin and Powell, 1980) the continuous poles are mapped to discrete poles according to  $z = e^{sT}$ . As may be seen by series expansion

$$z = e^{sT} \approx \frac{1 + sT/2}{1 - sT/2} \quad (7.3-2)$$

Therefore, to obtain an approximate sampling technique for continuous transfer functions, we may propose inverting this transformation and defining

$$s' = \frac{2}{T} \frac{z-1}{z+1} \quad (7.3-3)$$

An approximate discrete equivalent of the continuous transfer function is then given by

$$K(z) = K^c(s') \quad (7.3-4)$$

We call (7.3-3) the *bilinear transformation*, or BLT.

The BLT corresponds to approximating integration using the trapezoid rule, since if

$$\frac{Y(z)}{U(z)} = \frac{2}{T} \frac{z-1}{z+1} = \frac{2}{T} \frac{1-z^{-1}}{1+z^{-1}}$$

then (recall that  $z^{-1}$  is the unit delay in the time domain so that  $z^{-1}u_k = u_{k-1}$ )

$$u_k = u_{k-1} + \frac{T}{2}(y_k + y_{k-1}) \quad (7.3-5)$$

If the continuous transfer function is

$$K^c(s) = \frac{\prod_{i=1}^m (s + t_i)}{\prod_{i=1}^n (s + s_i)}, \quad (7.3-6)$$

with the relative degree  $r = n - m > 0$ , then the BLT yields the approximate discrete equivalent transfer function given by

$$\begin{aligned} K(z) &= \frac{\prod_{i=1}^m \left[ \frac{2(z-1)}{T(z+1)} + t_i \right]}{\prod_{i=1}^n \left[ \frac{2(z-1)}{T(z+1)} + s_i \right]} \\ K(z) &= \left[ \frac{T}{2} (z+1) \right]^r \frac{\prod_{i=1}^m [(z-1) + (z+1)t_i T/2]}{\prod_{i=1}^n [(z-1) + (z+1)s_i T/2]} \\ K(z) &= \left[ \frac{T}{2} (z+1) \right]^r \frac{\prod_{i=1}^m [(1 + t_i T/2)z - (1 - t_i T/2)]}{\prod_{i=1}^n [(1 + s_i T/2)z - (1 - s_i T/2)]} \end{aligned} \quad (7.3-7)$$

It can be seen that the poles and finite zeros map to the  $z$ -plane according to

$$z = \frac{1 + sT/2}{1 - sT/2}; \quad (7.3-8)$$

however, the  $r$  zeros at infinity in the  $s$ -plane map into zeros at  $z = -1$ . This is sensible since  $z = -1$  corresponds to the *Nyquist frequency*  $\omega_N$ , where  $z = e^{j\omega_N T} = -1$ , so that  $\omega_N T = \pi$  or

$$\omega_N = \frac{\pi}{T} = \frac{\omega_s}{2} \quad (7.3-9)$$

This is the highest frequency before folding of  $|K(e^{j\omega T})|$  occurs (see Figure 7.4-1). Since the BLT maps the left-half of the  $s$ -plane into the unit circle, it maps stable continuous systems  $K^c(s)$  into stable discrete  $K(z)$ .

According to (7.3-7), the BLT gives discretized transfer functions that have a relative degree of zero; that is, the degrees of the numerator and denominator are the same. If

$$K(z) = \frac{b_0 z^n + b_1 z^{n-1} + \cdots + b_n}{z^n + a_1 z^{n-1} + \cdots + a_n} \quad (7.3-10)$$

and  $Y(z) = K(z)U(z)$ , then the difference equation relation  $y_k$  and  $u_k$  is

$$y_k = -a_1 y_{k-1} - \cdots - a_n y_{k-n} + b_0 u_k + b_1 u_{k-1} + \cdots + b_n u_{k-n} \quad (7.3-11)$$

and the current output  $y_k$  depends on the current input  $u_k$ . This is usually an undesirable state of affairs, since it takes some computation time for the microprocessor to compute  $y_k$ . Techniques for including the computation time will be discussed later.

If the continuous-time controller is given in the state-space form

$$\begin{aligned} \dot{x} &= A^c x + B^c u \\ y &= Cx + Du, \end{aligned} \quad (7.3-12)$$

one may use the Laplace transform and (7.3-3) to show that the discretized system using the BLT is given by Hanselmann (1987) as

$$\begin{aligned} x_{k+1} &= Ax_k + B_1 u_{k+1} + B_0 u_k \\ y_k &= Cx_k + Du_k, \end{aligned} \quad (7.3-13)$$

with

$$\begin{aligned} A &= \left[ I - A^c \frac{T}{2} \right]^{-1} \left[ I + A^c \frac{T}{2} \right] \\ B_1 &= B_0 = \left[ I - A^c \frac{T}{2} \right]^{-1} \frac{T}{2} B^c \end{aligned} \quad (7.3-14)$$

Note that the discretized system is not a traditional state-space system since  $x_{k+1}$  depends on  $u_{k+1}$ . Aside from computation time delays, this is not a problem in our applications, since all we require of (7.3-13) is to implement it on a microprocessor. Since (7.3-13) is only a set of difference equations, this is easily accomplished. We illustrate how to discretize a continuous-time controller using the BLT in Examples 7.3-1 and 7.3-2, where we design a digital PID controller and a digital pitch-rate controller.



### Matched Pole Zero

The second popular approximation technique for converting a continuous transfer function to a discrete one is the MPZ method. Here, both the poles and finite zeros are mapped into the  $z$ -plane using the transformation  $e^{sT}$  as follows:

1. If  $K^c(s)$  has a pole (or finite zero) at  $s = s_i$ , then  $K(z)$  will have a pole (or finite zero) at

$$z_i = e^{s_i T} \quad (7.3-15)$$

2. If the relative degree of  $K^c(s)$  is  $r$ , so that it has  $r$  zeros at infinity,  $r$  zeros of  $K(z)$  are taken at  $z = -1$  by multiplying by the factor  $(1 + z)^r$ .
3. The gain of  $K(z)$  is selected so that the dc gains of  $K^c(s)$  and  $K(z)$  are the same, that is, so that

$$K(1) = K^c(0) \quad (7.3-16)$$

An alternative to step 2 is to map only  $r - 1$  of the infinite  $s$ -plane zeros into  $z = -1$ . This leaves the relative degree of  $K(z)$  equal to 1, which allows one sample period for control computation time. We will call this the *modified MPZ* method.

Thus, if

$$K^c(s) = \frac{\prod_{i=1}^m (s + t_i)}{\prod_{i=1}^n (s + s_i)} \quad (7.3-17)$$

and the relative degree is  $r = n - m$ , the MPZ discretized transfer function is

$$K(z) = k(z + 1)^{r-1} \frac{\prod_{i=1}^m (z - e^{-t_i T})}{\prod_{i=1}^n (z - e^{s_i T})}, \quad (7.3-18)$$

where the gain  $k$  is chosen to ensure (7.3-16). Note that if  $K^c(s)$  is stable, so is the  $K(z)$  obtained by the MPZ, since  $z = e^{sT}$  maps the left-half  $s$ -plane into the unit circle in the  $z$ -plane. Although the MPZ requires simpler algebra than the BLT, the latter is more popular in industry.

### Digital Design Examples

Now let us show some examples of digital controller design using the BLT and MPZ to discretize continuous controllers.

**Example 7.3-1: Discrete PID Controller** Since the continuous PID controller is so useful in aircraft control design, let us demonstrate how to discretize it to obtain a digital PID controller. A standard continuous-time PID controller has the transfer function (Åström and Wittenmark, 1984)

$$K^c(s) = k \left[ 1 + \frac{1}{T_I s} + \frac{T_D s}{1 + T_D s / N} \right], \quad (1)$$

where  $k$  is the proportional gain,  $T_I$  is the integration time constant or “reset” time, and  $T_D$  is the derivative time constant. Rather than use pure differentiation, a “filtered derivative” is used that has a pole far left in the  $s$ -plane at  $s = -N/T_D$ . A typical value for  $N$  is 3 to 10; it is usually fixed by the manufacturer of the controller.

Let us consider a few methods of discretizing (1) with sample period  $T$  seconds.

(a) *BLT*. Using the BLT, the discretized version of (1) is found to be

$$K(z) = k \left[ 1 + \frac{1}{T_I \frac{2(z-1)}{T(z+1)}} + \frac{T_D \frac{2(z-1)}{T(z+1)}}{1 + \frac{T_D}{N} \frac{2(z-1)}{T(z+1)}} \right] \quad (2)$$

or, on simplifying,

$$K(z) = k \left[ 1 + \frac{T}{T_{Id}} \frac{z+1}{z-1} + \frac{T_{Dd}}{T} \frac{z-1}{z-v} \right] \quad (3)$$

with the discrete integral and derivative time constants

$$T_{Id} = 2T_I \quad (4)$$

$$T_{Dd} = \frac{NT}{1 + NT/2T_D} \quad (5)$$

and the derivative-filtering pole at

$$v = \frac{1 - NT/2T_D}{1 + NT/2T_D} \quad (6)$$

(b) *MPZ*. Using the MPZ approach to discretize the PID controller yields

$$K(z) = k \left[ 1 + \frac{k_1(z+1)}{T_I(z-1)} + \frac{k_2 N(z-1)}{z - e^{-NT/T_D}} \right], \quad (7)$$

where  $k_1$  and  $k_2$  must be selected to match the dc gains. At dc, the  $D$  terms in (1) and (7) are both zero, so we may select  $k_2 = 1$ . The dc values of the  $I$  terms in (1) and (7) are unbounded. Therefore, to select  $k_1$  let us match the low-frequency gains. At low frequencies,  $e^{j\omega T} \approx 1 + j\omega T$ . Therefore, for small  $\omega$ , the  $I$  terms of (1) and (7) become

$$K^c(j\omega) = \frac{1}{j\omega T_I}$$

$$K(e^{j\omega T}) \approx \frac{2k_1}{T_I(j\omega T)},$$

and to match them, we require that  $k_1 = T/2$ .

Thus, using the MPZ the discretized PID controller again has the form (3), but now with

$$T_{ld} = 2T_I \quad (8)$$

$$T_{Dd} = NT \quad (9)$$

$$v = e^{-NT/T_D} \quad (10)$$

(c) *Modified MPZ.* If we use the modified MPZ method, then in the  $I$  term in (7) the factor  $(z + 1)$  does not appear. Then the normalizing gain  $k_1$  is computed to be  $T$ . In this case, the discretized PID controller takes on the form

$$K(z) = k \left[ 1 + \frac{T}{T_{ld}} \frac{1}{z-1} + \frac{T_{Dd}}{T} \frac{z-1}{z-v} \right], \quad (11)$$

with

$$T_{ld} = T_I \quad (12)$$

$$T_{Dd} = NT \quad (13)$$

$$v = e^{-NT/T_D} \quad (14)$$

Now, there is a control delay of one sample period ( $T$  s) in the integral term, which could be advantageous if there is a computation delay.

(d) *Difference Equation Implementation.* Let us illustrate how to implement the modified MPZ PID controller (11) using difference equations, which are easily placed into a software computer program. It is best from the point of view of numerical accuracy in the face of computer round-off error to implement digital controllers as several first- or second-order systems in parallel. Such a parallel implementation may be achieved as follows.

First, write  $K(z)$  in terms of  $z^{-1}$ , which is the unit delay in the time domain (i.e., a delay of  $T$  s, so that, for instance,  $z^{-1}u_k = u_{k-1}$ ), as

$$K(z^{-1}) = k \left[ 1 + \frac{T}{T_{ld}} \frac{z^{-1}}{1-z^{-1}} + \frac{T_{Dd}}{T} \frac{1-z^{-1}}{1-vz^{-1}} \right] \quad (15)$$

[*Note:* There is some abuse in notation in denoting (15) as  $K(z^{-1})$ ; this, we will accept.]

Now, suppose that the control input  $u_k$  is related to the tracking error as

$$u_k = K(z^{-1})e_k \quad (16)$$

Then,  $u_k$  may be computed from past and present values of  $e_k$  using auxiliary variables as follows:

$$v_k^I = v_{k-1}^I + \frac{T}{T_{Id}} e_{k-1} \quad (17)$$

$$v_k^D = v_{k-1}^D + \frac{T_{Dd}}{T} (e_k - e_{k-1}) \quad (18)$$

$$u_k = k(e_k + v_k^I + v_k^D) \quad (19)$$

The variables  $v_k^I$  and  $v_k^D$  represent the integral and derivative portions of the PID controller, respectively. For more discussion, see Åström and Wittenmark (1984). ■

**Example 7.3-2: Digital Pitch-Rate Controller via BLT** In Example 5.5-3 we designed a pitch-rate control system using LQ output feedback techniques. Here we demonstrate how to convert that continuous control system into a digital control system. The BLT is popular in industry; therefore, we will use it here.

The continuous controller is illustrated in Figure 7.3-1, where

$$K_1^c(s) = \frac{k_I}{s} \quad (1)$$

$$K_2^c(s) = \frac{10k_\alpha}{s + 10} \quad (2)$$

$$K_3^c(s) = k_q \quad (3)$$

The most suitable feedback gains in Example 5.5-3 were found using derivative weighting design to be

$$k_I = 1.361, \quad k_\alpha = -0.0807, \quad k_q = -0.475 \quad (4)$$

A digital control scheme with the same structure is shown in Figure 7.3-2. We have added samplers with period  $T$  to produce the samples of pitch rate,  $q$ , and angle

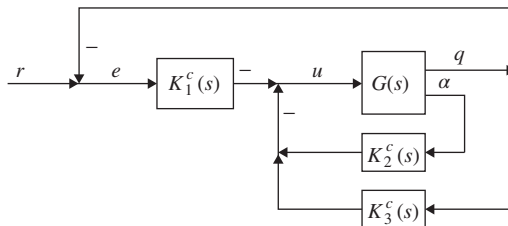


**Figure 7.3-1** Continuous pitch-rate controller.

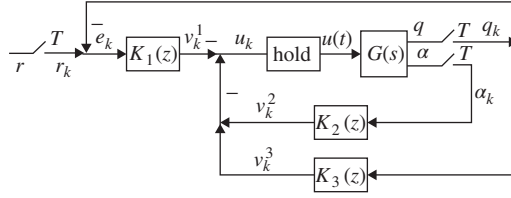


**Figure 7.3-2** Digital pitch-rate controller.

of attack,  $\alpha$ , as well as a hold device to convert the control samples  $u_k$  computed by the digital controller back to a continuous-time control input  $u(t)$  for the plant. Note that the reference input  $r(t)$  must also be sampled.

Since the integrator and alpha smoothing filter are part of the digital controller, the continuous dynamics  $G(s)$  in Figure 7.3-2 are given by  $\dot{x} = Ax + Bu$ ,  $y = Cx$ , with

$$A = \begin{bmatrix} -1.01887 & 0.90506 & -0.00215 \\ 0.82225 & -1.07741 & -0.17555 \\ 0 & 0 & -20.2 \end{bmatrix}, \quad B = \begin{bmatrix} 0 \\ 0 \\ 20.2 \end{bmatrix}$$

$$C = \begin{bmatrix} 57.2958 & 0 & 0 \\ 0 & 57.2958 & 0 \end{bmatrix}, \quad (5)$$

where

$$x = \begin{bmatrix} \alpha \\ q \\ \delta_e \end{bmatrix}, \quad y = \begin{bmatrix} \alpha \\ q \end{bmatrix} \quad (6)$$

Using the BLT, the discrete equivalents to (1) to (3) are found to be

$$K_1(z) = k_1 \frac{z+1}{z-1} \quad \text{with } k_1 = \frac{k_I T}{2} \quad (7)$$

$$K_2(z) = k_2 \frac{z+1}{z-\pi} \quad \text{with } k_2 = \frac{10k_\alpha T}{10T+2}, \quad \pi = \frac{1-10T/2}{1+10T/2} \quad (8)$$

$$K_3(z) = k_q \quad (9)$$

Defining the intermediate signals  $v_k^1, v_k^2, v_k^3$  shown in Figure 7.3-2 and denoting the unit delay in the time domain by  $z^{-1}$ , we may express (7) to (9) in terms of difference equations as follows:

$$e_k = r_k - q_k, \quad (10)$$

$$v_k^1 = k_1 \frac{1+z^{-1}}{1-z^{-1}} e_k$$

## C DIGITAL PITCH RATE CONTROLLER

```

SUBROUTINE DIG(IK,T,X)
REAL X(*), K(2), KI, KA, KQ
COMMON/CONTROL/U
COMMON/OUTPUT/AL,Q,UPLLOT
DATA REF, KI,KA,KQ/1., 1.361,-0.0807,-0.475/

K(1)= KI*T/2
K(2)= 10*KA*T/(10*T + 2)
P= (1 - 10*T/2) / (1 + 10*T/2)

E= REF - Q
V1= V1 + K(1)*(E + EKM1)
V2= P*V2 + K(2)*(AL + ALKM1)
V3= KQ*Q
U= -(V1 + V2 + V3)
UPLLOT= U

EKM1= E
ALKM1= AL

RETURN
END

```

## C CONTINUOUS SHORT PERIOD DYNAMICS

```

SUBROUTINE F(TIME,X,XP)
REAL X(*), XP(1)
COMMON/CONTROL/U
COMMON/OUTPUT/AL,Q
XP(1)= -1.01887*X(1) + 0.90506*X(2) - 0.00215*X(3)
XP(2)= 0.82225*X(1) - 1.07741*X(2) - 0.17555*X(3)
XP(3)= -20.2 *X(3) + 20.2*U

AL = 57.2958*X(1)
Q = 57.2958*X(2)

RETURN
END

```

**Figure 7.3-3** Digital simulation software: (a) FORTRAN subroutine to simulate digital pitch-rate controller; (b) subroutine  $F(t, x, \dot{x})$  to simulate continuous plant dynamics.

or

$$v_k^1 = v_{k-1}^1 + k_1(e_k + e_{k-1}), \quad (11)$$

$$v_k^2 = k_2 \frac{1 + z^{-1}}{1 - \pi z^{-1}} \alpha_k$$

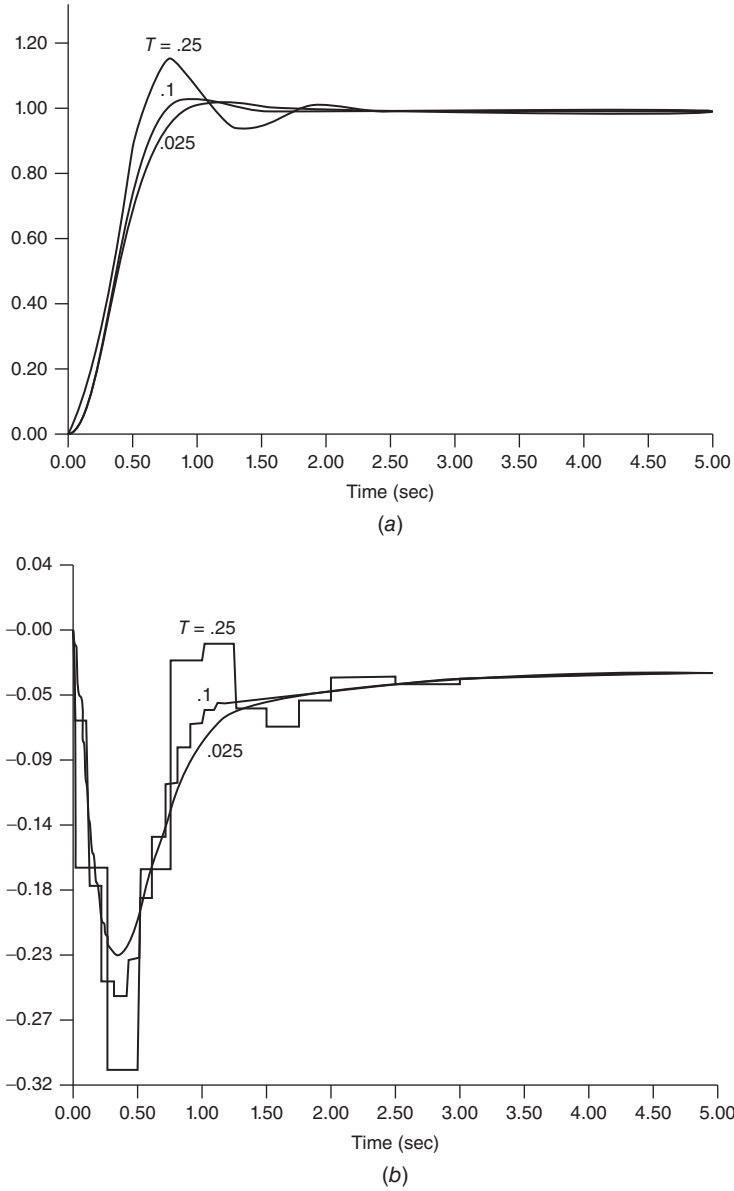


**Figure 7.3-4** Effect of sampling period: (a) step response  $q(t)$ ; (b) control input  $u(t)$ .

or

$$v_k^2 = \pi v_{k-1}^2 + k_2(\alpha_k + \alpha_{k-1}), \quad (12)$$

$$v_k^3 = k_q q_k \quad (13)$$

The control samples  $u_k$  are thus given by

$$u_k = -(v_k^1 + v_k^2 + v_k^3) \quad (14)$$

Note the low-pass filtering effects manifested by the averaging of  $e_k$  and  $\alpha_k$  that occurs in these equations. This will tend to average out any measurement noise.

These difference equations describe the digital controller and are easily implemented on a microprocessor. First, however, the controller should be simulated. The Fortran subroutine in Figure 7.3-3a may be used with the driver program in Figure 7.2-4 to simulate the digital control law. The subroutine  $F(t, x, \dot{x})$  required by the Runge-Kutta integrator for the continuous plant dynamics (5) is given in Figure 7.3-3b.

The step response using this digital controller was plotted for several sampling periods  $T$  in Figure 7.3-4. A zero-order hold was used. Note that the step response improves as  $T$  becomes small. Indeed, the response for  $T = 0.025$  s is indistinguishable from the response using a continuous controller in Example 5.5-3c.

The motivation for selecting  $T = 0.025$  s was as follows. The settling time of the continuous controller step response in Example 5.5-3c was  $t_s = 1$  s. The settling time is about four times the slowest time constant, which is thus 0.25 s. The sampling period should be selected about one-tenth of this for good performance. ■

## 7.4 MODIFIED CONTINUOUS DESIGN

In Section 7.3 we showed how to convert a continuous-time controller to a digital controller using the BLT and MPZ. However, that technique is only an approximate one that gives worse results as the sample period  $T$  increases. In this section we show how to *modify the design of the continuous controller* so that it yields a more suitable digital controller. This allows the use of larger sample periods. To do this we will take into account some properties of the zero-order-hold and sampling processes. Using modified continuous design, we are able to design in Example 7.4-1 a digital pitch-rate control system that works extremely well even for relatively large sample periods.

### Sampling, Hold Devices, and Computation Delays

We will examine some of the properties of the discretization and implementation processes to see how the continuous controller may be designed in a fashion that will yield an improved digital controller. Specifically, in the design of the continuous controller it is desirable to include the effects of sampling, hold devices, and computation delays.

**Sampling and Aliasing** We would like to gain some additional insight on the sampling process (Oppenheim and Schaffer, 1975; Franklin and Powell, 1980; Åström and Wittenmark, 1984). To do so, define the Nyquist frequency  $\omega_N = \omega_s / 2 = \pi / T$



and the sampling frequency  $\omega_s = 2\pi/T$  and picture the output  $y^*(t)$  of the sampler with input  $y(t)$  as the string of impulses

$$y^*(t) = \sum_{k=-\infty}^{\infty} y(t)\delta(t - kT), \quad (7.4-1)$$

where  $\delta(t)$  is the unit impulse. Since the impulse train is periodic, it has a Fourier series that may be computed to be

$$\sum_{k=-\infty}^{\infty} \delta(t - kT) = \frac{1}{T} \sum_{n=-\infty}^{\infty} e^{jn\omega_s t} \quad (7.4-2)$$

Using this in (7.4-1) and taking the Laplace transform yield

$$\begin{aligned} Y^*(s) &= \frac{1}{T} \int_{-\infty}^{\infty} y(t) \left[ \sum_{n=-\infty}^{\infty} e^{jn\omega_s t} \right] e^{-st} dt \\ Y^*(s) &= \frac{1}{T} \sum_{n=-\infty}^{\infty} \int_{-\infty}^{\infty} y(t) e^{-(s-jn\omega_s)t} dt \\ Y^*(s) &= \frac{1}{T} \sum_{n=-\infty}^{\infty} Y(s - jn\omega_s), \end{aligned} \quad (7.4-3)$$

where  $Y(s)$  is the Laplace transform of  $y(t)$  and  $Y^*(s)$  is the Laplace transform of the sampled signal  $y^*(t)$ . Due to the factor  $1/T$  appearing in (7.4-3), the sampler is said to have a *gain* of  $1/T$ .

Sketches of a typical  $Y(j\omega)$  and  $Y^*(j\omega)$  are shown in Figure 7.4-1, where  $\omega_H$  is the highest frequency contained in  $y(t)$ . Notice that the digital frequency response is symmetric with respect to  $\omega_N$  and periodic with respect to  $\omega_s$ . At frequencies less than  $\omega_N$ ,

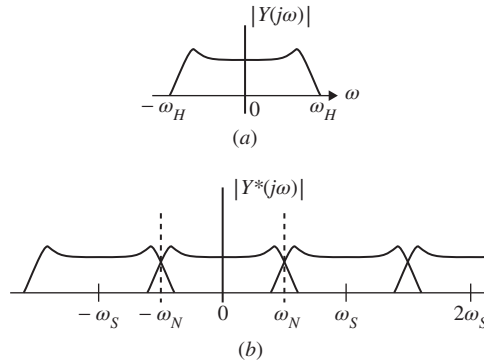


**Figure 7.4-1** Sampling in the frequency domain: (a) spectrum of  $y(t)$ ; (b) spectrum of sampled signal  $y^*(t)$ .

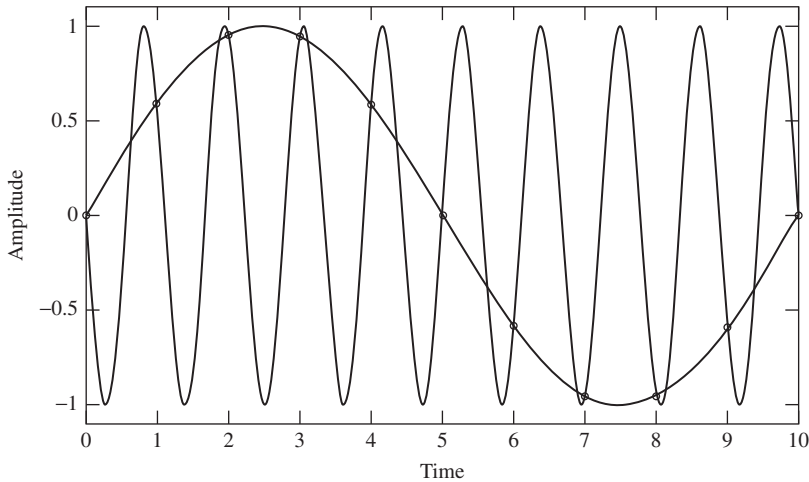


**Figure 7.4-2** Example of aliasing in the time domain.

the spectrum of  $Y^*(j\omega)$  has two parts: one part comes from  $Y(j\omega)$  and is the portion that should appear. However, there is an additional portion from  $Y(j(\omega - \omega_s))$ ; the “tail” of  $Y(j(\omega - \omega_s))$ , which contains high-frequency information about  $y(t)$ , is “folded” back or *aliased* into the lower frequencies of  $y^*(j\omega)$ . Thus, the high-frequency content of  $y(t)$  appears at low frequencies and can lead to problems in reconstructing  $y(t)$  from its samples.

If  $\omega_H < \omega_N$ , the tail of  $Y^*(j(\omega - \omega_s))$  does not appear to the right of  $\omega - \omega_N$  and  $y(t)$  can be uniquely reconstructed from its samples by low-pass filtering. This condition is equivalent to

$$\omega_s > 2\omega_H, \quad (7.4-4)$$

which is the sampling theorem of Shannon that guarantees aliasing does not occur.

It is interesting to see what the sampling theorem means in the time domain. In Figure 7.4-2, we show two continuous signals that have the same samples. If the original signal was the higher-frequency signal, the D/A reconstruction process will produce the lower-frequency signal from the samples of the higher-frequency signal. Thus, aliasing can result in *high-frequency signals being misinterpreted as low-frequency signals*. If the sampling frequency  $\omega_s$  is greater than twice the highest frequency  $\omega_H$  appearing in the continuous signal, the problem depicted in the figure does not occur and the signal can be accurately reconstructed from its samples.

**Selecting the Sampling Period** For control design, the sampling frequency  $\omega_s$  must generally be significantly greater than twice the highest frequency of any signal appearing in the system. That is, in control applications the sampling theorem does not usually provide much insight in selecting  $\omega_s$ . Some guides for selecting the sampling period  $T$  are now discussed.

If the continuous-time system has a single dominant complex pole pair with natural frequency of  $\omega$ , the rise time is given approximately by

$$t_r = \frac{1.8}{\omega} \quad (7.4-5)$$

It is reasonable to have at least two to four samples per rise time so that the error induced by ZOH reconstruction is not too great during the fastest variations of the continuous-time signal (Åström and Wittenmark, 1984). Then we have  $t_r = 1.8/\omega \geq 4T$ , or approximately

$$T \leq \frac{1}{2\omega} \quad (7.4-6)$$

However, if high-frequency components are present up to a frequency of  $\omega_H$  radians and it is desired to retain them in the sampled system, a rule of thumb is to select

$$T \leq \frac{1}{4\omega_H} \quad (7.4-7)$$

These formulas should be used with care, and to select a suitable  $T$  it may be necessary to perform digital control designs for several values of  $T$  for each case carrying out a computer simulation of the behavior of the plant under the influence of the proposed controller. Note particularly that using continuous redesign of digital controllers with the BLT or MPZ, even smaller sample periods may be required since the controller discretization technique is only an approximate one.

**Zero-Order Hold** The D/A hold device in Figure 7.1-1 is required to reconstruct the plant control input  $u(t)$  from the samples  $u_k$  provided by the digital control scheme. The ZOH is usually used. There, we take

$$u(t) = u(kT) = u_k, \quad kT \leq t < (k+1)T, \quad (7.4-8)$$

with  $u_k$  the  $k$ th sample of  $u(t)$ . The ZOH yields the sort of behavior in Figure 7.2-2 and has the impulse response shown in Figure 7.4-3. This impulse response may be written as

$$h(t) = u_{-1}(t) - u_{-1}(t - T),$$

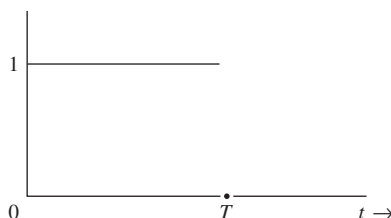


Figure 7.4-3 ZOH impulse response.

with  $u_{-1}(t)$  the unit step. Thus, the transfer function of the ZOH is

$$G_0(s) = \frac{1 - e^{-sT}}{s} \quad (7.4-9)$$

To determine the Bode magnitude and phase of  $G_0(s)$ , write

$$\begin{aligned} G_0(j\omega) &= \frac{1 - e^{-j\omega T}}{j\omega} = e^{-j\omega T/2} \frac{e^{j\omega T/2} - e^{-j\omega T/2}}{j\omega} \\ G_0(j\omega) &= T e^{-j\omega T/2} \frac{\sin(\omega T/2)}{\omega T/2} = T e^{-j\omega T/2} \operatorname{sinc} \frac{\omega}{\omega_s}, \end{aligned} \quad (7.4-10)$$

where  $\operatorname{sinc} x \equiv (\sin \pi x)/\pi x$ . The magnitude and phase of the ZOH are shown in Figure 7.4-4. Note that the ZOH is a low-pass filter of magnitude  $T|\operatorname{sinc}(\omega/\omega_s)|$  with a phase of

$$\angle \text{ZOH} = -\frac{\omega T}{2} + \theta = -\frac{\pi \omega}{\omega_s} + \theta, \quad \theta = \begin{cases} 0, & \sin \frac{\omega T}{2} > 0 \\ \pi, & \sin \frac{\omega T}{2} < 0 \end{cases} \quad (7.4-11)$$

According to (7.4-10), for frequencies  $\omega$  much smaller than  $\omega_s$ , the ZOH may be approximated by

$$G_0(s) \approx T e^{-sT/2}, \quad (7.4-12)$$

that is, by a pure delay of half the sampling period and a scale factor of  $T$ .

As we saw in the digital pitch-rate controller in Example 7.3-1, the performance of the digital controller deteriorates with increasing  $T$ , so that sample periods are required which may be too small. (We note that smaller values of  $T$  require faster computation to compute  $u_k$ ; thus a faster, and more expensive, microprocessor may be required for small  $T$ .) This deterioration is partly due to the delay introduced by the hold device. We will soon see how to take this delay into account *while designing the continuous controller*, so that discretization yields a digital controller that gives suitable performance for larger values of  $T$ .

**Computation Delay** If the microprocessor is fast so that the time  $\Delta$  required to compute the digital control law is negligible,  $\Delta$  will have little effect when a digital controller is implemented. However, if  $\Delta$  is appreciable, it can have a deleterious effect on the closed-loop response. Then it may be necessary to account for it.

If  $\Delta \leq T$ , the computation delay may be accounted for by ensuring that  $u_k$  depends only on *previous* values of the outputs. This may often be achieved by using the modified MPZ approach for digital controller design. However, the BLT is more popular and it always yields a  $u_k$  that depends on *current* values of the outputs [see (7.3-11)]. Moreover, the discrete PID controller (see Example 7.3-1) always has a dependence on the current outputs through the derivative term, even if the modified MPZ is used.

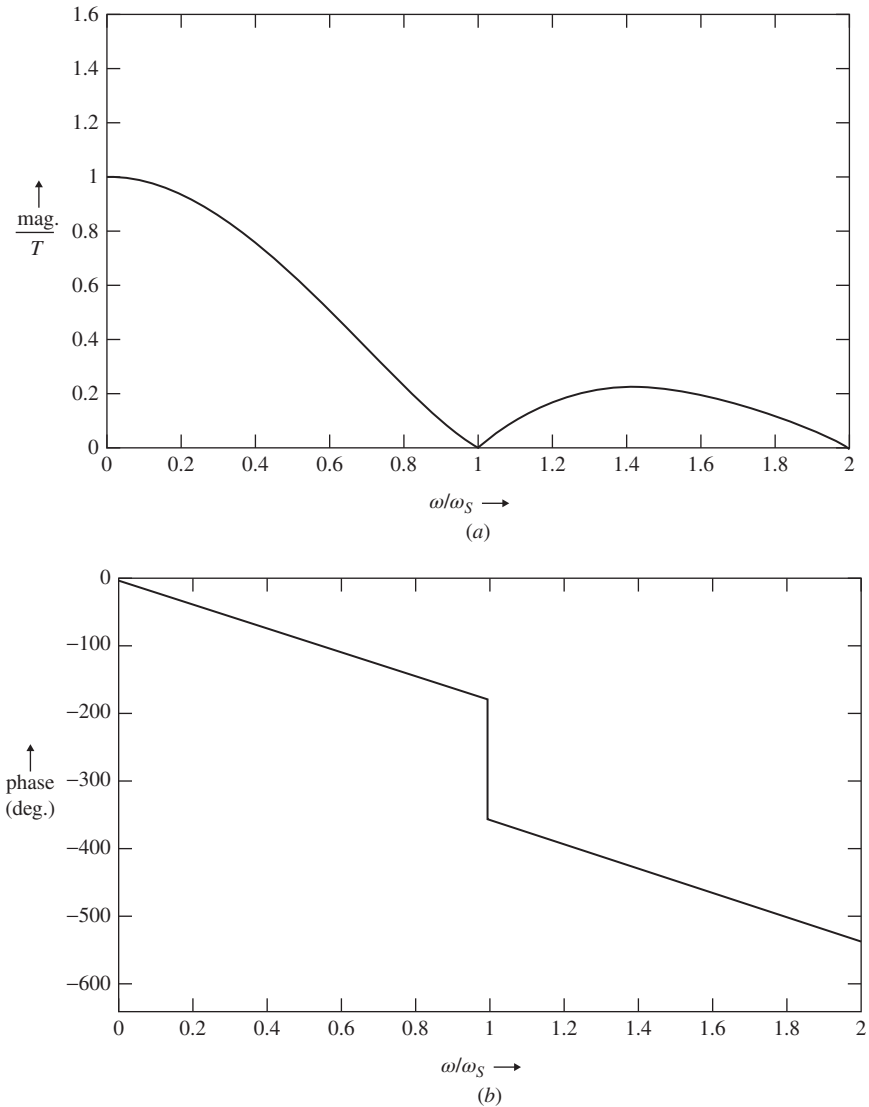


**Figure 7.4-4** ZOH Bode plots: (a) magnitude; (b) phase.

If the computation delay is not negligible but is only a fraction of  $T$ , it seems inefficient to allow it to cause a delay of a full  $T$  seconds in applying the control to the plant. If there is noise present in the system, then using outputs delayed by an entire sample period to compute  $u_k$  can, for large sample periods, lead to significant deterioration over using more recent outputs to compute  $u_k$ .

## Modified Continuous Design Procedures

We will now show how to account for the hold delay and computation delay *while designing the continuous controller*  $K^c(s)$  for discretization. Then, when the BLT or MPZ is used to discretize  $K^c(s)$ , a digital controller  $K(z)$  with improved performance will be obtained. We call this approach *modified continuous controller design for discretization*.

A disadvantage of modified continuous design techniques is that the sample period  $T$  must be selected prior to the continuous controller design. However, good software makes it easy to redesign the continuous controller with a different value of  $T$ . The advantage of the approach is that the effects of the sampling and hold operations, computation delay, and aliasing are apparent *while the continuous design is being performed*. Thus, they may be to some extent compensated for.

Modified continuous design can often allow significantly larger sample periods than direct application of the BLT or MPZ to a continuous controller designed with no consideration that the next step will be conversion to a digital control law. This will be illustrated in Example 7.4-1, where we design a pitch-rate control system by modified continuous design.

Let us discuss aliasing, computation delays, and then the ZOH.

**Aliasing** The plant  $G(s)$  is generally a low-pass filter. We have seen in Figure 7.4-1 that as long as the sampling frequency  $\omega_s$  is selected at least twice as large as the plant cutoff frequency  $\omega_H$ , the effects of aliasing will be small.

However, one type of signal appearing in the closed-loop system that may not be bandlimited is *measurement noise*. High-frequency measurement noise may be aliased down to lower frequencies that are within the plant bandwidth and thus have a detrimental effect on system performance. To avoid this, low-pass *anti-aliasing filters* of the form

$$H_a(s) = \frac{a}{s + a} \quad (7.4-13)$$

may be inserted after the measuring devices and before the samplers. The cutoff frequency  $a$  should be selected less than  $\omega_N = \omega_s/2$ , so that there is good attenuation beyond  $\omega_n$  rad/s.

If the cutoff frequency of the anti-aliasing filter is not much higher than the plant cutoff frequency, the filter will affect the closed-loop performance, and it should be appended to the plant *at the design stage* so that the continuous controller is designed taking it into account. See Figure 7.4-5, which represents the actual plant  $G(s)$  augmented by various filters, some still to be discussed, that should be taken into account in the design stage.

**Computation Delay** The delay associated with a computation time of  $\Delta$  has a transfer function of

$$G_{\text{comp}}(s) = e^{-s\Delta}, \quad (7.4-14)$$

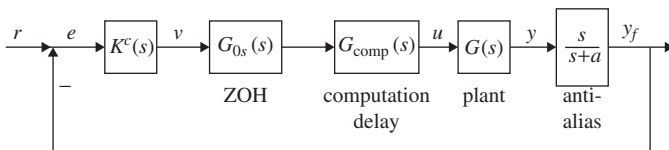


**Figure 7.4-5** Modified continuous plant with anti-aliasing filter and compensation to model hold device and computation delays.

which has a magnitude of 1 and a phase of  $-\omega\Delta$  radians. To account for this delay, we may perform the continuous controller design not on the plant  $G(s)$  but on  $G(s)e^{-s\Delta}$ . However, it is awkward to design a controller for a plant whose transfer function is not rational (Franklin et al., 1980). It is more convenient to approximate the delay with a rational transfer function.

For this purpose, we may use Padé approximants to  $e^{-s\Delta}$ , which match the first few terms of the Taylor series expansion (Su, 1971; Franklin et al., 1980). Table 7.4-1 gives several Padé approximants to  $e^{-s\Delta}$ . These approximants match the first  $n + m + 1$  terms of the Taylor series expansion, where  $n$  is the denominator degree and  $m$  the numerator degree.

To perform a modified continuous design that takes into account the computation delay  $\Delta$ , it is only necessary to incorporate a Padé approximant  $G_{\text{comp}}(s)$  to  $e^{-s\Delta}$  of suitable order into the plant as shown in Figure 7.4-5. The continuous controller  $K^c(s)$  designed for this modified plant is then discretized using the BLT or MPZ to produce a digital controller  $K(z)$ .

Notice that the Padé approximants in Table 7.4-1 having finite zeros are *non-minimum-phase*. This is a property of a pure time delay. The advantage of the modified continuous design approach is that the non-minimum-phase nature of the delayed plant manifests itself at the continuous controller design stage, so that the digital controller that results after using the BLT compensates for this problem automatically.

**Zero-Order Hold** Finally, let us discuss modified continuous design taking into account the ZOH. Since the sampler has a gain of  $1/T$ , the sampler plus ZOH has a transfer function of

$$G_{0s}(s) = \frac{1 - e^{-sT}}{sT} \quad (7.4-15)$$

Some useful approximants to  $G_{0s}(s)$  are given in Table 7.4-2. These have been computed using Padé approximants of  $e^{-sT}$ , so they are not strictly speaking Padé approximants, since they only match the first  $n + m$  terms of the Taylor series. They are, however, sufficiently accurate for our purposes. Note that the approximants to  $G_{0s}(s)$  have unstable zeros. Modified continuous controller design taking into account  $G_{0s}(s)$  involves designing a controller for  $G(s)G_{0s}(s)$  (see Figure 7.4-5).

TABLE 7.4-1 Padé Approximants to  $e^{-s\Delta}$  for Approximation of Computation Delay

$\frac{1}{1+s\Delta}$	$\frac{1-s\Delta/2}{1+s\Delta/2}$	
$\frac{1}{1+s\Delta+(s\Delta)^2/2}$	$\frac{1-s\Delta/3}{1+2s\Delta/3+(s\Delta)^2/6}$	$\frac{1-s\Delta/2+(s\Delta)^2/12}{1+s\Delta/2+(s\Delta)^2/12}$
$\frac{1}{1+s\Delta+(s\Delta)^2/2+(s\Delta)^3/6}$	$\frac{1-s\Delta/4}{1+3s\Delta/4+(s\Delta)^2/4+(s\Delta)^3/24}$	$\frac{1-2s\Delta/5+(s\Delta)^2/20}{1+3s\Delta/5+3(s\Delta)^2/20+(s\Delta)^3/60}$



**TABLE 7.4-2 Approximants to  $(1 - e^{-sT}) sT$  for Approximation of Hold Delay**

$\frac{1}{1 + sT/2}$
$\frac{1 - sT/6}{1 + sT/3}$
$\frac{1 - sT/10 + (sT)^2/60}{1 + 2sT/5 + (sT)^2/20}$
$\frac{1 - sT/14 + 23(sT)^2/840 - (sT)^3/840}{1 + 3sT/7 + (sT)^2/14 + (sT)^3/120}$

**Implementation** It is important to realize that the anti-aliasing filter should be implemented using analog circuitry as part of the plant  $G(s)$ . It should immediately precede the sampler. On the other hand,  $G_{comp}(s)$  is not implemented since it is a model of the computation delay;  $G_{0s}(s)$  is implemented by the ZOH and the sampler, and  $K^c(s)$  is discretized using the BLT or MPZ and becomes the digital controller  $K(z)$ .

The next example illustrates modified continuous design for discretization.

**Example 7.4-1: Digital Pitch-Rate Controller via Modified Continuous Design** In Example 5.5-3 we designed a continuous-time pitch-rate controller. In Example 7.3-2 we showed how to use the BLT to convert that controller into digital form. It was seen that the response was good for  $T = 0.025$  s, slightly worse for  $T = 0.1$  s, and unacceptable for  $T = 0.25$  s.

In this example let us design a modified continuous controller which, on discretization, will yield a better digital controller using larger sample periods than the one of Example 7.3-2. We will select the sampling period in this example to be  $T = 0.25$  s.

**(a) Modified Continuous-Time Plant.** To account for the effects of the hold delay we will incorporate a model of the sampling and hold processes into the continuous-time dynamical model of the aircraft as shown in Figure 7.4-5. Let us use a Padé approximant to (7.4-15). Specifically, examining Table 7.4-2, select

$$G_{0s}(s) = \frac{1 - sT/6}{1 + sT/3} = -\frac{1}{2} + \frac{9/2T}{s + 3/T} \quad (1)$$

According to Figure 7.4-5, the ZOH/sampler approximant should act as a filter on the plant control input  $u(t)$ . Thus, a state-variable representation of  $G_{0s}(s)$  is given by

$$\begin{aligned} \dot{x}_z &= -\frac{3}{T}x_z + \frac{9}{2T}v \\ u &= x_z - \frac{1}{2}v, \end{aligned} \quad (2)$$

where  $v(t)$  is the new input shown in Figure 7.4-5. With  $T = 0.25$  s this becomes

$$\begin{aligned}\dot{x}_z &= -12x_z + 18v \\ u &= x_z - 0.5v\end{aligned}\quad (3)$$

We should like to propose the same control structure used in Example 5.5-3. There, an angle-of-attack filter and an integrator in the feedforward channel were used. The ZOH/sampler dynamics (3) may be augmented into the system-plus-compensator state equations by defining the augmented state

$$x = [\alpha \quad q \quad \delta_e \quad \alpha_F \quad \varepsilon \quad x_z]^T \quad (4)$$

Then

$$\dot{x} = Ax + Bv + Er \quad (5)$$

$$y = Cx + Fr \quad (6)$$

$$z = Hx \quad (7)$$

with

$$\begin{aligned}A &= \begin{bmatrix} -1.01887 & 0.90506 & -0.00215 & 0 & 0 & 0 \\ 0.82225 & -1.07741 & -0.17555 & 0 & 0 & 0 \\ 0 & 0 & -20.2 & 0 & 0 & 20.2 \\ 10.0 & 0 & 0 & -10 & 0 & 0 \\ 0 & -57.2958 & 0 & 0 & 0 & 0 \\ 0 & 0 & 0 & 0 & 0 & -12 \end{bmatrix}, \\ B &= \begin{bmatrix} 0 \\ 0 \\ -10.1 \\ 0 \\ 0 \\ 18 \end{bmatrix}, \quad E = \begin{bmatrix} 0 \\ 0 \\ 0 \\ 0 \\ 1 \\ 0 \end{bmatrix} \\ C &= \begin{bmatrix} 0 & 0 & 0 & 57.2958 & 0 & 0 \\ 0 & 57.2958 & 0 & 0 & 0 & 0 \\ 0 & 0 & 0 & 0 & 1 & 0 \end{bmatrix}, \quad F = \begin{bmatrix} 0 \\ 0 \\ 0 \end{bmatrix} \\ H &= [0 \quad 57.2958 \quad 0 \quad 0 \quad 0 \quad 0]\end{aligned}$$

Then, according to Example 5.5-3, the control input  $v(t)$  is given by

$$v = -Ky = -[k_\alpha \quad k_q \quad k_I] y = -k_\alpha \alpha_F - k_q q - k_I \varepsilon \quad (8)$$

We are now in a position to perform the control design to select the control gains.

(b) *PI and Continuous Controls Design.* To design the continuous-time controller, let us select the performance index (PI)

$$J = \frac{1}{2} \int_0^{\infty} \left( q_5 t^2 e^2 + \delta_e^2 \right) dt \quad (9)$$

that weights elevator rate of change, since this is closely related to actuator energy. Since  $e(t) = \dot{\varepsilon}(t)$ , this may be written

$$J = \frac{1}{2} \int_0^{\infty} \left( q_5 t^2 \dot{\varepsilon}^2 + \delta_e^2 \right) dt, \quad (10)$$

with  $\varepsilon(t)$  and  $\delta_e(t)$  the deviations in the integrator output and elevator deflection. Thus, this is the PI with derivative weighting discussed in Section 5.5.

Using  $q_5 = 5$  and the software described in Appendix B, we computed the optimal gain matrix

$$K = \begin{bmatrix} -0.04238 & -0.4098 & 0.8426 \end{bmatrix}, \quad (11)$$

which gave the closed-loop poles

$$\begin{aligned} s &= -2.40 \pm j4.71 \\ &-1.08, -2.76 \\ &-9.86, -25.80 \end{aligned} \quad (12)$$

The closed-loop step response of the continuous-time controller is shown in Figure 7.4-6. Note that it is comparable to the responses shown in Example 5.5-3.

Let us note that the transfer function from  $v(t)$  to  $q(t)$  contains the approximate ZOH/sampler dynamics described by (1) and (3). These include a pole at  $s = -12$  which has no significant effect. However, they also include a non-minimum-phase zero at  $s = 24$ . This zero significantly changes the root locus, and the control gains (11) selected automatically by the LQ approach take this non-minimum-phase zero into account. Indeed, note the delay of approximately  $T = 0.25$  s in Figure 7.4-6.

It should also be realized that, in contrast to the situation in Example 7.3-2, which relied on the continuous design from Example 5.5-3, the sampling period is now needed to write the continuous dynamics (5) and hence to design the continuous-time controller.

(c) *Digital Controller.* The modified continuous controller just designed is described by exactly the same equations as in Example 7.3-2, with, however, the modified gain  $K$  given in (11). Thus, the new digital controller is exactly the same as the one described in that example, though using the modified gains.

To examine the performance of the modified digital controller, we may use the driver program described in Section 7.2, along with the continuous-time aircraft dynamics and the subroutine DIG(IK, T, X) from Example 7.3-2 with the gains in (11). The response for  $T = 0.25$  s is shown in Figure 7.4-7. Note that at this design sample period of  $T = 0.25$  s, the digital control response is much like the response

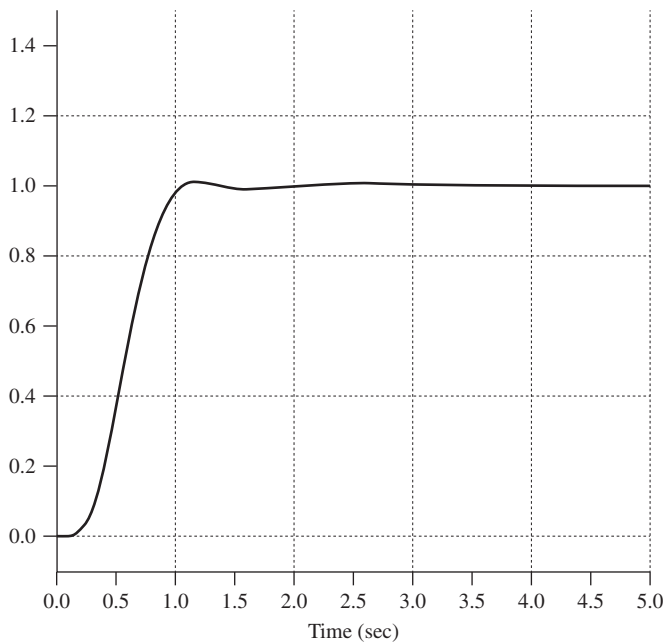


**Figure 7.4-6** Step response  $q(t)$  using modified continuous-time pitch-rate controller.

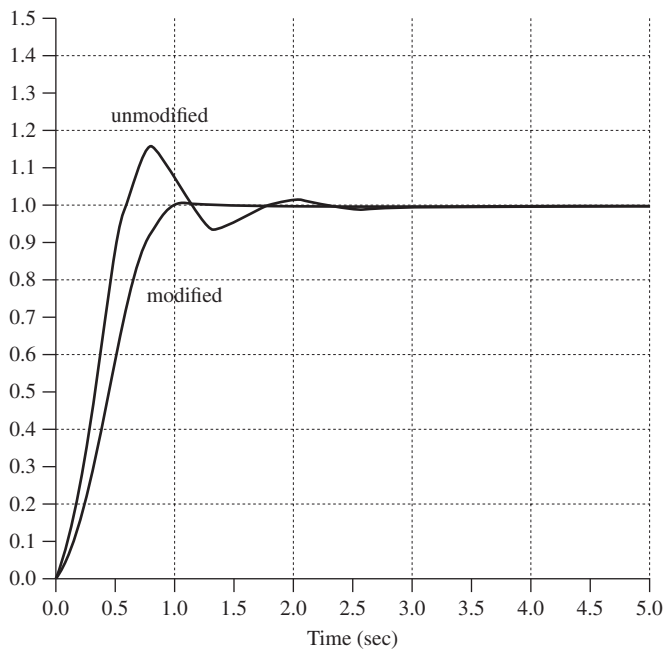


**Figure 7.4-7** Response of digital controller using modified and unmodified continuous-time design.

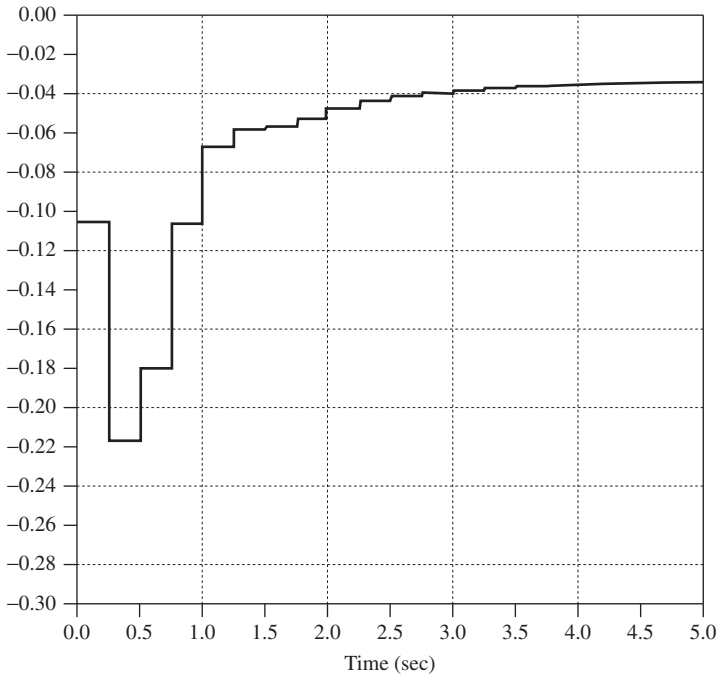


**Figure 7.4-8** Control input  $u(t)$  required for modified digital pitch-rate controller.

using the continuous-time controller shown in Figure 7.4-6. It is important to note, however, that, using the digital controller, the delay noted in Figure 7.4-6 does not appear.

For comparison we have also shown in Figure 7.4-7 the unacceptable response from Example 7.3-2 for  $T = 0.25$  s. This was the result of using a digital controller, obtained simply by applying the BLT to the unmodified continuous-time controller, which did not take into account the effects of the hold delay.

The control input  $u(t)$  required in the modified digital controller with  $T = 0.25$  s is shown in Figure 7.4-8. It may be compared to the control signals in Example 7.3-2.

Clearly, the response shown in Figure 7.4-7 obtained using modified continuous design is excellent. It far surpasses the digital control response in Example 7.3-2 for  $T = 0.25$  s. Thus, we have demonstrated that a sensible technique for taking into account some of the properties of the sample-and-hold process in the design stage of the continuous controller results in improved digital controllers that may be used with larger sample periods  $T$ . ■

## 7.5 IMPLEMENTATION CONSIDERATIONS

In this chapter we have discussed a design approach for digital controllers that is based on discretizing a continuous-time controller using the BLT or MPZ. It now

behooves us to look at some practical considerations involved with implementing the digital controller. Our discussion will necessarily be brief, giving only an indication of some of the issues. More detail may be discovered in the work of Åström and Wittenmark (1984), Franklin and Powell (1980), Franklin et al. (1980), Phillips and Nagle (1984), Hanselmann (1987), Lewis (1992), and Slivinsky and Borninski (1987). We will mention actuator saturation and windup and controller realization structures.

## Actuator Saturation and Windup

Actuator saturation is a problem that occurs in both continuous-time and digital control systems. Since it is easy to protect against by using a digital controller, we have placed it in this section.

A digital controller may be represented in the dynamic state-space form

$$x_{k+1} = Fx_k + Gw_k \quad (7.5-1)$$

$$u_k = Cx_k + Dw_k, \quad (7.5-2)$$

where  $x_k \in \mathbf{R}^n$  is the controller state and  $w_k$  the controller input, composed generally of the tracking error and the plant measured output.

We have assumed thus far that the plant control input  $u_k \in \mathbf{R}^m$  which is computed by the controller can actually be applied to the plant. However, in flight controls the plant inputs (such as elevator deflection  $\delta_e$ , throttle, and so on) are limited by *maximum* and *minimum* allowable values. Thus, the relation between the *desired plant input*  $v_k$  and the *actual plant input*  $u_k$  is given by the sort of behavior shown in Figure 7.5-1, where  $u_H$  and  $u_L$  represent, respectively, the maximum and minimum control effort allowed by the mechanical actuator. Thus, to describe the actual case in an aircraft flight control system, we are forced to include *nonlinear saturation functions* in the control channels as shown in Figure 7.5-2.

Consider the simple case where the controller is an integrator with input  $w_k$  and output  $v_k$ . Then all is well as long as  $v_k$  is between  $u_L$  and  $u_H$ , for in this region the aircraft input  $u_k$  equals  $v_k$ . However, if  $v_k$  exceeds  $u_H$ , then  $u_k$  is limited to its maximum value  $u_H$ . This in itself may not be a problem. The problem arises if  $w_k$

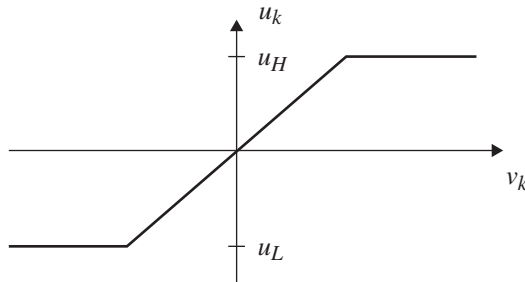


**Figure 7.5-1** Actuator saturation function.

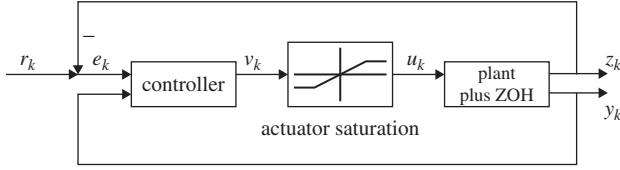


**Figure 7.5-2** Flight control system including actuator saturation.

remains positive, for then the integrator continues to integrate and  $v_k$  may increase well beyond  $u_H$ . Then, when  $w_k$  becomes negative, it may take considerable time for  $v_k$  to decrease below  $u_H$ . In the meantime,  $u_k$  is held at  $u_H$ , giving an incorrect control input to the aircraft. This effect of integrator saturation is called *windup*. It arises because the controllers we design are generally dynamical in nature, which means that they store information or energy.

To correct integrator windup, it is necessary to *limit the state of the controller* so that it is consistent with the saturation effects being experienced by the plant input  $u_k$ . This is not difficult to achieve (Åström and Wittenmark, 1984). Indeed, write (7.5-2) in the form

$$0 = u_k - Cx_k - Dw_k,$$

multiply it by  $L$ , which will soon be selected, and add it to (7.5-1) to obtain

$$x_{k+1} = (F - LC)x_k + (G - LD)w_k + Lu_k \quad (7.5-3)$$

This is the form in which the digital controller should be implemented to avoid windup, as we now argue. A little thought shows that actuator windup occurs in the form (7.5-1) when  $F$  is not asymptotically stable. For then, as long as  $w_k$  in (7.5-1) is nonzero,  $x_k$  will continue to increase. However, by selecting  $L$  so that

$$F_0 = F - LC \quad (7.5-4)$$

is asymptotically stable, this problem is averted.

A special case occurs when  $L$  is selected so that  $F_0$  has all poles at the origin. Then  $x_k$  displays *deadbeat behavior*; after  $n$  time steps it remains limited to an easily computed value dependent on the values of  $w_k$  and  $u_k$  (see the problems at the end of the chapter).

The *anti-windup gain*  $L$  may be selected to place the poles of  $F_0$  arbitrarily if  $(C, F)$  is observable. However, as long as  $(C, F)$  is *detectable* (i.e., has all its unstable poles observable), windup may be eliminated using this technique.

To complete the design for anti-windup protection, the digital controller should be implemented in the form (7.5-3) and the aircraft control input then selected according to

$$u_k = \text{sat} (Cx_k + Dw_k), \quad (7.5-5)$$

where the *saturation function* (shown in Figure 7.5-1) is defined for scalars as

$$\text{sat}(v) = \begin{cases} u_H, & v \geq u_H \\ v, & u_L < v < u_H \\ u_L, & v \leq u_L, \end{cases} \quad (7.5-6)$$

with  $u_H$  and  $u_L$  the maximum and minimum allowable values, respectively. For vectors, the saturation function is defined as

$$\text{sat}(v) = \begin{bmatrix} \text{sat}(v_1) \\ \text{sat}(v_2) \\ \vdots \\ \text{sat}(v_m) \end{bmatrix} \quad (7.5-7)$$

The values of  $u_H$  and  $u_L$  for each component  $v_i$  should be selected to correspond to the actual limits on the components of the plant input  $u_k$ .

Note that the limited signal  $u_k$  is used in (7.5-3), providing a feedback arrangement in the controller with anti-windup protection. What we have in effect done is include an *observer* with dynamics  $F_0$  in the digital controller. Since  $F_0$  is asymptotically stable, the observer will provide reasonable “estimates” even in the event of saturation.

Where  $u_k$  is not saturated, the controller with anti-windup compensation (7.5-3), (7.5-5) is identical to (7.5-1), (7.5-2).

If the controller is given in transfer function form

$$R(z^{-1})u_k = T(z^{-1})r_k - S(z^{-1})w_k, \quad (7.5-8)$$

where  $r_k$  is the reference command and  $z^{-1}$  is interpreted in the time domain as a unit delay of  $T$  seconds, anti-windup compensation may be incorporated as follows.

Select a desired stable observer polynomial  $A_0(z^{-1})$  and add  $A_0(z^{-1})u_k$  to both sides to obtain

$$A_0 u_k = T r_k - S w_k + (A_0 - R) u_k \quad (7.5-9)$$

A regulator with anti-windup compensation is then given by

$$A_0 v_k = T r_k - S w_k + (A_0 - R) u_k \quad (7.5-10)$$

$$u_k = \text{sat}(v_k) \quad (7.5-11)$$

**Example 7.5-1: Anti-Windup Compensation for Digital Proportional-Integral Controller** From Example 7.3-1 a general digital proportional-integral controller is given by

$$u_k = k \left[ 1 + \frac{T}{T_I} \frac{1}{z-1} \right] W_k, \quad (1)$$



where we have used design by the modified MPZ to obtain a delay of  $T$  seconds in the integrator to allow for computation time. The proportional gain is  $k$  and the reset time is  $T_I$ ; both are fixed in the design stage.

Multiply  $z^{-1}$  and write

$$(1 - z^{-1})u_k = k \left[ (1 - z^{-1}) + \frac{Tz^{-1}}{T_I} \right] w_k, \quad (2)$$

which is in the transfer function form (7.5-8). The corresponding difference equation form for implementation is

$$u_k = u_{k-1} + kw_k + k \left( -1 + \frac{T}{T_I} \right) w_{k-1} \quad (3)$$

This controller will experience windup problems since the autoregressive polynomial  $R = 1 - z^{-1}$  has a root at  $z = 1$ , making it marginally stable. Thus, when  $u_k$  is limited, the integrator will continue to integrate, “winding up” beyond the saturation level.

To correct this problem, select an observer polynomial of

$$A_0(z^{-1}) = 1 - \alpha z^{-1}, \quad (4)$$

which has a pole at some desirable location  $|\alpha| < 1$ . The design parameter  $\alpha$  may be selected by simulation studies. Then the controller with anti-windup protection (7.5-10)/(7.5-11) is given by

$$(1 - \alpha z^{-1})v_k = k \left[ 1 + \left( -1 + T/T_I \right) z^{-1} \right] w_k + (1 - \alpha)z^{-1}u_k \quad (5)$$

$$u_k = \text{sat}(v_k) \quad (6)$$

The corresponding difference equations for implementation are

$$v_k = kw_k + \alpha v_{k-1} + k \left( -1 + \frac{T}{T_I} \right) w_{k-1} + (1 - \alpha)u_{k-1} \quad (7)$$

$$u_k = \text{sat}(v_k) \quad (8)$$

A few lines of Fortran code implementing this digital controller are given in Figure 7.5-3. This subroutine may be used as the control update routine DIG with the digital simulation driver program in Section 7.2.

If  $\alpha = 1$ , we obtain the special case (2), which is called the *position form* and has no anti-windup compensation.

If  $\alpha = 0$ , we obtain the *deadbeat anti-windup compensation*

$$v_k = k \left[ 1 + \left( -1 + T/T_I \right) z^{-1} \right] w_k + u_{k-1}, \quad (9)$$

## C DIGITAL PI CONTROLLER WITH ANTIWINDUP COMPENSATION

```

SUBROUTINE CONUP(T)
REAL K
COMMON/CONTROL/U
COMMON/OUTPUT/Z
COMMON/REF/R
DATA K,AL,TI,ULOW,UHIGH/ 0.5, 0.2, 5., -0.5, 0.5/

E= R-Z
V= K*E + V
U= AMAX1(ULOW,V)
U= AMIN1(UHIGH,U)
V= AL*V + K*(-1 + T/TI)*E + (1-AL)*U

RETURN
END

```

**Figure 7.5-3** Fortran code implementing proportional-integral controller with anti-windup compensation.

with corresponding difference equation implementation

$$v_k = u_{k-1} + kw_k + \left(-1 + \frac{T}{T_I}\right) w_{k-1} \quad (10)$$

If  $u_k$  is not in saturation, this amounts to updating the plant control by adding the second and third terms in (10) to  $u_{k-1}$ . These terms are, therefore, nothing but  $u_k - u_{k-1}$ . The compensator with  $\alpha = 0$  is thus called the *velocity form* of the proportional-integral controller. ■

## Controller Realization Structures

Round-off errors can occur every time an arithmetic operation is performed. Moreover, since all the stable behavior of a discrete system is described by the location of the poles within the unit circle, great accuracy is required in the filter coefficients to obtain desired closed-loop pole locations.

A direct implementation of the digital filter would involve simply writing  $n$  difference equations describing (7.5-1)/(7.5-2) and would be virtually guaranteed to have severe numerical problems if  $n$  is larger. Specifically, the controller and observer canonical forms (Kailath, 1980) are notoriously unstable numerically. That is, their poles are very sensitive to small variations in their coefficients. It can be shown that the sensitivity to coefficient variations of the impulse response and frequency response is also high in direct implementations (Hanselmann, 1987). For good numerical performance with fixed-point arithmetic, digital filters should be implemented as *cascade or parallel combinations of first- and second-order filters*.

A state-space transformation may be used to place the digital filter into an appropriate form for implementation. To obtain real coefficients, the *real Jordan form*

is suitable (Phillips and Nagle, 1984; Hanselmann, 1987; Lewis, 1992). This is a block-diagonal form for (7.5-1), (7.5-2) having first- and second-order blocks in cascade and parallel. Corresponding to each real pole there will be first-order blocks, and corresponding to each complex pole there will be second-order blocks.

A form suitable for implementation may also be found by performing a partial fraction expansion (PFE) on the transfer function. A technique for doing this in terms of the eigenstructure is given in Section 5.2. However, a *real* PFE should be found which will have the form (in the case of a simple matrix  $F$ )

$$H(z) = D + \sum_{i=1}^r H_i(z), \quad (7.5-12)$$

where  $H_i(z)$  is first order for real poles and second order for complex poles. We are therefore concerned with implementing first-order filters of the form

$$H_1(z^{-1}) = \frac{b_1 z^{-1}}{1 + a_1 z^{-1}} \quad (7.5-13)$$

and second-order filters of the form

$$H_2(z^{-1}) = \frac{b_1 z^{-1} + b_2 z^{-2}}{1 + a_1 z^{-1} + a_2 z^{-2}} \quad (7.5-14)$$

To implement  $H_1(z^{-1})$ , we may write

$$\begin{aligned} y_k &= H_1(z^{-1})u_k \\ (1 + a_1 z^{-1})y_k &= b_1 z^{-1}u_k \\ y_k &= -a_1 y_{k-1} + b_1 u_{k-1}, \end{aligned} \quad (7.5-15)$$

which is a difference equation that may easily be programmed.

There are many ways to implement the second-order transfer function (Phillips and Nagle, 1984). Among these are *direct forms 1 through 4* (denoted D1, D2, D3, D4) and *cross-coupled forms 1 and 2* (denoted X1, X2).

In Figure 7.5-4 we show D1, D3, and X1. Forms D2, D4, and X2, respectively, are their duals (i.e., all arrows are reversed and the roles of the input and the output are interchanged). In Table 7.5-1 we give a comparison of the number of time delay elements, multipliers, and summing junctions for each form. Note that D1 and X1 conserve time delay elements, while D3 conserves summing junctions.

The difference equation implementations of these second-order modules are given in Table 7.5-2, with  $y_k = H_2(z^{-1})u_k$ . It is interesting that the difference equations for the X1 module may be written from the complex PFE (and hence, with a little manipulation, from the usual complex Jordan form).

When implementing these modules on a fixed-point microprocessor, it is important to incorporate overflow protection (Slivinsky and Borninski, 1987). When interconnecting them to produce  $H(z)$ , scaling may be introduced between the modules (Phillips and Nagle, 1984).

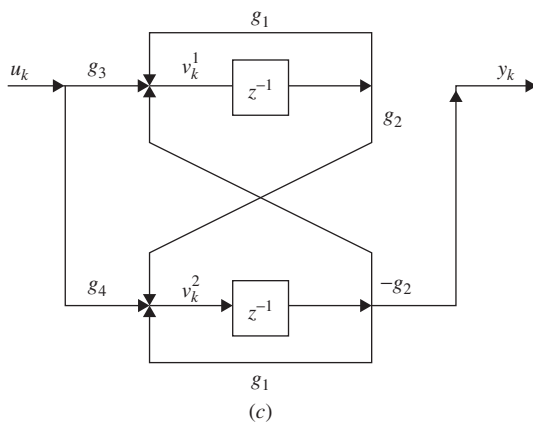
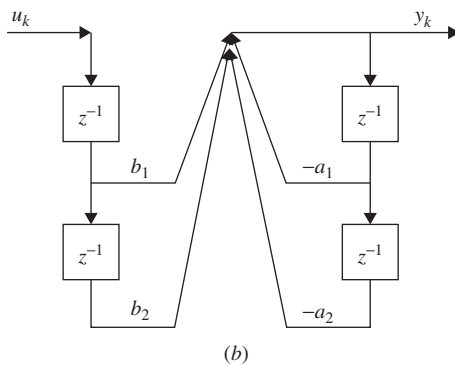
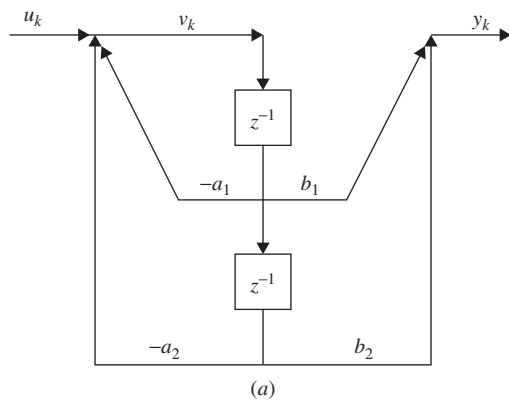


**Figure 7.5-4** Implementations of second-order digital filters: (a) direct form 1, D1; (b) direct form 3, D3; (c) cross-coupled form 1, X1.

**TABLE 7.5-1 Elements of Second-Order Modules**

	Structure		
	D1	D3	X1
Time delay elements	2	4	2
Multipliers	4	4	6
Summing junctions	2	1	2

**TABLE 7.5-2 Difference Equation Implementation of Second-Order Modules**

D1:

$$v_k = -a_1 v_{k-1} - a_2 v_{k-2} + u_k$$

$$y_k = b_1 v_{k-1} + b_2 v_{k-2}$$

D3:

$$y_k = -a_1 y_{k-1} - a_2 y_{k-2} + b_1 u_{k-1} + b_2 u_{k-2}$$

X1:

$$v_k^1 = g_1 v_{k-1}^1 - g_2 v_{k-1}^2 + g_3 u_k$$

$$v_k^2 = g_1 v_{k-1}^2 + g_2 v_{k-1}^1 + g_4 u_k$$

$$y_k = v_{k-1}^2$$

where  $g_i$  are defined by

$$H_2(z^{-1}) = \frac{Nz^{-1}}{1 + pz^{-1}} + \frac{N * z^{-1}}{1 + p * z^{-1}}$$

$$g_1 = -\text{Re}(p)$$

$$g_2 = -\text{Im}(p)$$

$$g_3 = 2 \text{Im}(N)$$

$$g_4 = 2 \text{Re}(N)$$

## 7.6 SUMMARY

Since most aircraft control systems are implemented using digital signal processors, in this chapter we have outlined the basics of digital control. In Section 7.2 we discussed how to simulate digital control schemes using a Runge-Kutta integrator on the continuous aircraft dynamics. This approach yields the time responses not only at the sample points but also between the samples. It is important to check the intersample performance of the closed-loop system before implementing a digital controller on an aircraft, since it can be unsatisfactory even though all is well at the sample points.

In Section 7.3 we gave a design technique for digital controllers that is based on *redesign of an existing continuous-time controller* by discretizing it using approximation techniques like the BLT and MPZ. This results in digital controllers that

require small sample periods to work properly. To overcome the requirement for unreasonably small sample periods, in Section 7.4 we showed how to modify the continuous-time controller so that, after discretization, a better digital controller is obtained that works for larger sample periods. This modification allowed the delay properties of the sample-and-hold process to be taken into account.

Finally, in Section 7.5 we mentioned some digital controller implementation considerations. We showed how to design controllers with anti-windup protection to overcome the problems of saturation of the control signals due to control limitations such as elevator deflection stops and throttle maximum limits. We gave some low-order controller structures that allow the implementation of digital controllers with maximum accuracy and efficiency.

## REFERENCES

- Åström, K. J., and B. Wittenmark. *Computer Controlled Systems*. Englewood Cliffs, N.J.: Prentice Hall, 1984.
- Franklin, G. F., and J. D. Powell. *Digital Control*. Reading, Mass.: Addison-Wesley, 1980.
- Franklin, G. F., J. D. Powell, and A. Emami-Naeini. *Feedback Control of Dynamic Systems*. Reading, Mass.: Addison-Wesley, 1980.
- Hanselmann, H. "Implementation of Digital Controllers: A Survey." *Automatica* 23, no. 1 (1987): 7–32.
- Kailath, T. *Linear Systems*. Englewood Cliffs, N.J.: Prentice Hall, 1980.
- Lewis, F. L. *Applied Optimal Control and Estimation*. Englewood Cliffs, N.J.: Prentice Hall, 1992.
- Oppenheim, A. V., and R. W. Schaffer. *Digital Signal Processing*. Englewood Cliffs, N.J.: Prentice Hall, 1975.
- Phillips, C. L., and H. T. Nagle, Jr. *Digital Control System Analysis and Design*. Englewood Cliffs, N.J.: Prentice Hall, 1984.
- Slivinsky, C., and J. Borninski. "Control System Compensation and Implementation with the TMS32010." In *Digital Signal Processing Applications*, ed. K.-S. Lin. Englewood Cliffs, N.J.: Prentice Hall, 1987.
- Su, K. L. *Time-Domain Synthesis of Linear Networks*. Englewood Cliffs, N.J.: Prentice Hall, 1971.

## PROBLEMS

### Section 7.3

- 7.3-1** Prove (7.3.13)/(7.3.14) by taking the Laplace transform of  $\dot{x} = Ax + Bu$  and then using the BLT.
- 7.3-2 Digital Pitch-Rate Controller.** Design a digital pitch-rate controller (see Example 7.3-2) using the MPZ technique. Simulate the step response for a few sample periods  $T$  and compare to the digital controller designed using the BLT.

**7.3-3 Digital Normal Acceleration CAS.** A normal acceleration CAS was designed in Example 5.4-1.

- (a) Using the BLT, design a digital normal acceleration CAS controller. Simulate the time response for various sampling periods.
- (b) Repeat using the modified MPZ.

**7.3-4 Digital Wing Leveler.** A wing leveler was designed in Example 5.5-4.

- (a) Using the BLT, design a digital wing leveler. Simulate the time response for various sampling periods.
- (b) Repeat using the modified MPZ.

## Section 7.4

**7.4-1** A Padé approximant for  $e^{-sT}$  is

$$G(s) = \frac{1 - 2sT/3 + (sT)^2/6}{1 + sT/3}$$

- (a) Use long division to determine how many terms of the Taylor series of  $e^{-sT}$  are matched by  $G(s)$ .
- (b) Use  $G(s)$  to derive one of the approximants for the ZOH plus sampler shown in Table 7.4-2. How many terms of the Taylor series are matched by this approximant?

**7.4-2 Digital Normal Acceleration CAS.** A normal acceleration CAS was designed in Example 5.4-1. Using the BLT, design a digital normal acceleration CAS controller. Use modified continuous design, including the hold delay. Use  $T = 0.1$  s. Simulate the time response and compare to the results of Problem 7.3-3.

**7.4-3 Digital Wing Leveler.** A wing leveler was designed in Example 5.5-4. Using the modified MPZ, design a digital wing leveler. Use modified continuous design, including the hold delay. Use  $T = 0.1$  s. Simulate the time response and compare to the results of Problem 7.3-4.

## Section 7.5

**7.5-1 Anti-Windup Compensator**

- (a) Write down the value of the state  $x_k$  in the anti-windup controller (7.5-3) for the deadbeat case where  $F_0$  has all poles at the origin. Assume that  $w_k$  and  $u_k$  are constant and that  $k > n$ . Note that if  $F_0$  has all poles at the origin, then  $F_0^n = 0$ , where  $n$  is the dimension of  $F_0$ .
- (b) Repeat for the case where the controller is just an integrator so that  $x_{k+1} = x_k + (T/T_I)w_k$ ,  $u_k = \text{sat}(x_k)$ . Simplify as far as possible.

- 7.5-2** Show how to determine the  $X1$  difference equations in Table 7.5-2 directly from the complex Jordan form blocks corresponding to a complex pair of poles.
- 7.5-3 Anti-Windup Protection for Normal Acceleration CAS.** In Example 5.4-1 a normal acceleration CAS was designed; it had a PI controller in the feedforward loop. In the problems for Section 7.3 this design was digitized.
- (a) Modify the digital normal acceleration CAS to add anti-windup protection.
  - (b) Now, set limits into the elevator actuator in your simulation program. Obtain time responses with and without the anti-windup protection.
- 7.5-4 Anti-Windup Protection for Pitch-Rate CAS.** Repeat the previous problem for the pitch-rate controller in Example 5.5-3, which was digitized in the problems for Section 7.3.



## CHAPTER 8

---

# MODELING AND SIMULATION OF MINIATURE AERIAL VEHICLES

---

### 8.1 INTRODUCTION

Successful flights with airplanes with no pilot onboard predate the first successful controlled airplane flights in 1903 by the Wright Brothers. In 1896, Samuel Pierpont Langley's team successfully flew a small steam-powered airplane model more than 3/4 of a mile (Anderson, 2008). Significantly, these first aircraft without a pilot onboard, a condition often referred to as *unmanned*, were not controlled. That is, their flight path was neither directed nor predictable. This limited the utility of such an airplane to verify design principles without putting a pilot at risk.

The decades that followed included several notable attempts at making an operationally useful unmanned aircraft. One area of considerable focus was the *cruise missile*. Here, an airplane is launched carrying a bomb that is directed on a one-way flight to a target. The Kettering Bug was developed in the United States and flew in 1918. The German V-1 flying bomb became the first cruise missile used in large numbers in 1944 to 1945, including many strikes directed at Britain. A second area of early usage of unmanned aircraft going on at the same time was as a *target drone*, where an unmanned aircraft was used for target practice or anti-aircraft weapons testing. These types of systems date back to 1935. The newest examples include unmanned variants of manned aircraft, such as a variant of the General Dynamics F-16 referred to as the QF-16.

As the guidance and control capabilities of these aircraft improved, the practical applications of unmanned airplanes expanded beyond the high-risk domains of aeronautics testing, target practice, and cruise missiles. Unmanned aircraft could now be precisely flown and recovered reliably. Communications capabilities also allowed them to be *remotely operated*, enabling real-time commands to be sent to the aircraft

and for the aircraft to send useful data to multiple users. By the 1990s systems such as the General Atomics MQ-1 Predator could be remotely operated via satellite for hours at a time and communicate high-quality video back to its operators. Following the attacks of September 11, 2001, an ongoing debate about the efficacy of using these types of aircraft to actually launch weapons ended. The result was the first systems capable of identifying, following, and then killing individuals from a single unmanned aircraft without putting the operators of the aircraft in harm's way. By many accounts, this was revolution in military affairs, changing the way wars are fought.

Recent decades have seen other areas of successful use of unmanned aircraft. The Yamaha RMAX is a small unmanned helicopter that has been used commercially since 1997 for widespread use in agriculture in Japan and other countries. Other application areas of interest include law enforcement, filmmaking, surveying, scientific research, logistics, and security.

No discussion of the use of small aircraft could be made without mentioning that flying small model aircraft for recreation also goes back to the dawn of aviation. The miniaturization and cost reduction of batteries, sensors, and processors associated with smartphones have led to a dramatic rise in the capabilities of small and inexpensive miniature unmanned aircraft since the mid-2000s. Very small and inexpensive airplanes and vertical take-off and landing (VTOL) aircraft can fly precisely, carry high-definition imagers, and be effectively remotely operated by an operator with limited training. Often first envisioned for recreational users, these types of systems have become good enough for many of the other application areas above. Aerial photography in particular is perhaps the most widespread commercial use of these small systems today.

A particular aircraft configuration that has been enabled by this trend in small electronics is the *multirotor*. This is a VTOL aircraft where several electric motors with propellers are mounted to a frame. Changing the power of the individual motors is used to change the velocity and attitude of the aircraft. When the multirotor specifically has four motors/propellers, it is often referred to as either a *quadrotor* or *quadcopter*; if it has six motors, as a *hexarotor* or *hexacopter*; and if it has eight motors, then as an *octorotor* or *octocopter*. Multirotors with other numbers of motors are also used.

From an aircraft performance standpoint, unmanned aircraft share many common characteristics with manned aircraft. Maximum range and endurance are key performance parameters dictated by the intended missions. Aircraft sizing dictates that a given aircraft design can be scaled larger to increase maximum range and endurance. Due to the energy density of fossil fuels vs. batteries available today, aircraft with very large range or endurance requirements tend to use internal combustion engines that burn fossil fuels. Electric propulsion is common today on aircraft that are very small and do not require long range or endurance. They benefit from the cost, simplicity, and low noise of electric propulsion. Aircraft that utilize solar energy collection are able to break out of this energy storage limitation and are an area of ongoing development.

A key challenge associated with all of these unmanned aircraft systems is achieving a desired level of reliability without a human pilot onboard to

control it. A remotely piloted aircraft relies on pilot inputs arriving via a wireless communication system. Such a system is subject to time delays, bandwidth limitations, and drop-outs that must be accounted for. Many successful systems provide the option of automated flight control and guidance to reduce operator workload and to account for potential loss of communication. Such a system is often described as having a higher degree of *autonomy* or *automation* due to this reduced reliance on the human operator. When flown by the human operator, many systems today also provide enough stability and control augmentation to make the handling qualities good enough that even an inexperienced pilot is able to effectively perform necessary flight maneuvers. So, although many of these miniature aircraft look simple, the underlying control and simulation problems are as complex as any other aircraft.

### Propellers vs. Rotors

Chapters 1 to 3 covered equations of motion and modeling of aircraft. In this chapter, that material is expanded upon for miniature aircraft. The models described for aerodynamic forces and moments apply here as well. For miniature aircraft, one key difference is the lower Reynolds numbers associated with the smaller size. This may imply somewhat different forces and moments for a given aerodynamic shape, but not a change in how we construct our aerodynamic models (Abbot and Von Doenhoff, 1959). Specifically, quantities like dynamic pressure and angle of attack will still be important inputs for our models of aerodynamic forces and moments. In order to effectively perform modeling and simulation of miniature aircraft, some additional topics are included here that relate to small aircraft (e.g., rotorcraft); including modeling propellers, rotors, and motors. This chapter also describes three miniature aircraft models: a small propeller-driven airplane, the Aeroworks 33% Edge 540T; a quadrotor aircraft (example of a multirotor), the AscTec Pelican; and a small helicopter, the Yamaha RMAX.

Typical terminology ascribes the name propeller to a rotating set of angled blades that provide thrust for an airplane. It is common to refer to the similar device on a helicopter or multirotor as a rotor. In this chapter, we will largely keep to this convention. From a modeling perspective, there are actually far more useful distinctions. Table 8.1-1 lists some key distinctions between propeller and rotor classes.

Starting with the fixed-pitch propeller, we see what is probably the simplest class (Figure 8.1-1): a solid object mounted to a shaft with a distinct shape so that it produces thrust when spinning. This is a common choice for propulsion on small airplanes as well as conventional multirotor configurations, including quadrotors. The primary means of increasing the thrust of this type of propeller as a means of control is to add additional power. This will cause the propeller to seek a new higher equilibrium RPM corresponding to a higher thrust and torque. Key characteristics of the fixed-pitch propeller include its diameter, pitch, number of blades, chord, stiffness, and mass properties.

For the multirotor configuration, complete attitude control can be obtained with, for example, four independent body-fixed motors/propellers, as illustrated in Figure 8.1-2 for a quadrotor. Each motor provides both thrust and a significant

**TABLE 8.1-1 Common Propeller and Rotor Classes**

Name	Description	Typical Uses
Fixed pitch	A single solid structure for the propeller/rotor, typical materials are wood, plastic, and carbon fiber	Airplane propeller, multirotor/quadrotor rotor
Variable pitch	Mechanism that enables the pitch of the blades to be varied in order to change thrust at constant RPM	Airplane propeller, helicopter tail rotor
Variable pitch and cyclic control	A mechanism that enables the pitch of the blades to be varied in order to change thrust as well as thrust tilting at constant RPM	Helicopter main rotor
Variable pitch and cyclic control with stabilizer bar	A mechanism to enable the pitch of the blades to be varied in order to change thrust as well as thrust tilting at constant RPM; a stabilizer bar to improve handling qualities	Helicopter main rotor



**Figure 8.1-1** Typical fixed-pitch propeller used for small airplanes and multirotors.

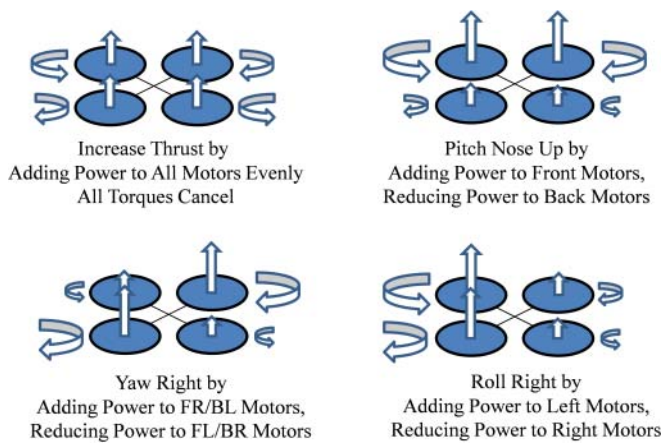


**Figure 8.1-2** A Multirotor with four fixed-pitch propellers (quadrotor) is able to independently control thrust, roll moment, pitch moment, and yaw moment.

reaction torque (corresponding to the lift and drag of the blades). When thrust goes up, so does torque. So, care must be taken to balance these effects when attempting to independently control thrust and individual moments, as shown in the figure. Because these changes in RPM of the individual motors are the primary means of flight control, it is important for multirotor models that the dynamics of propeller RPM be accounted for. Redundancy can be achieved by adding additional motors/propellers. Having an even number of motors allows half to spin in one direction and half to spin in the other, allowing yaw torque to be zero in hover with all motors producing the same thrust by symmetry.

For a helicopter tail rotor, it is typical to mechanically link the tail rotor drive to the main rotor drive. In order to change tail rotor thrust without changing the RPM of the tail rotor (or main rotor), a mechanism to vary the pitch of the blades is typically included, illustrated in Figure 8.1-3. From a modeling perspective, this mechanism is the primary difference between a typical helicopter tail rotor and a fixed-pitch propeller. That is, the propeller can change shape. Larger airplanes often utilize variable-pitch propellers in order to improve efficiency, to allow the blades to be “feathered” in order to minimize drag with a stopped engine, and sometimes to enable reverse thrust. A less common approach for the helicopter tail rotor is to utilize a fixed-pitch propeller with a separate motor to provide an independent control of RPM.

A conventional helicopter obtains primary roll and pitch control by tilting the thrust vector of the main rotor. This is typically accomplished, in conjunction with variable thrust, by adding the capability for the blades to take on different pitch angles as they make each revolution. This is illustrated in Figure 8.1-4. The slider mechanism used for the variable-pitch propeller has been replaced with a *swashplate*. The

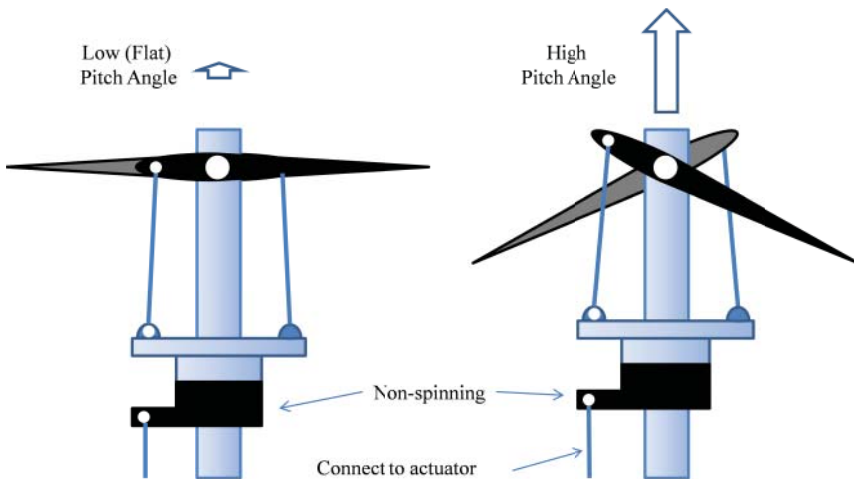


**Figure 8.1-3** Variable-pitch propeller mechanism schematic typical for a small helicopter tail rotor.

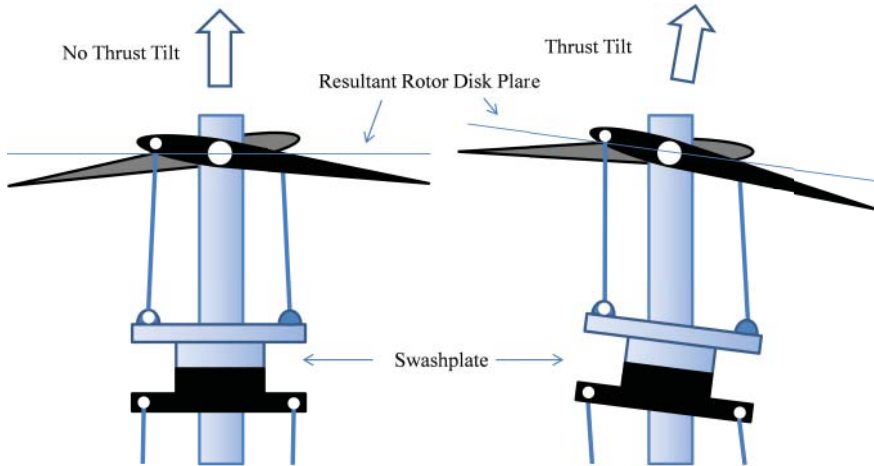


**Figure 8.1-4** Swashplate mechanism schematic typical for a helicopter main rotor.

swashplate has both a rotating and nonrotating element, allowing a transfer of information from the actuators to the rotor blade pitch angle. The swashplate is typically connected to at least three actuators, allowing the plate to both move up/down for variable thrust magnitude as well as tilt the thrust vector fore/aft and left/right. A single direction of tilt is illustrated in Figure 8.1-4. The tilting of the swashplate to the right in the figure causes the blade pitch to be maximum when the blade is pointing out of the page and minimum when it is pointing into the page. This thrust imbalance causes a moment that forces the spinning rotor (effectively a gyroscope) to tilt to the right. The rotor disk becomes tilted relative to the aircraft in a process called rotor flapping. This tilt of the rotor disk plane and the thrust vector generates a moment that can be used to rotate the aircraft. The sections below cover the modeling of these important flapping dynamics, key to describing the motion of helicopters.

Using the swashplate to increase or decrease total thrust by moving it directly up and down along the shaft is called collective pitch. Tilting the swashplate to generate thrust tilt is called cyclic pitch. In general, there are two directions of tilt: roll cyclic (to cause the aircraft to roll) and pitch cyclic (to cause the aircraft to pitch). These three independent actuation channels on the main rotor provide roll, pitch, and thrust control for the conventional helicopter. The tail rotor typically provides the yaw control. These actions are illustrated in Figure 8.1-5.

Some helicopter main rotors also include a stabilizer bar. This is essentially a small “rotor” on the same shaft as the first that exhibits different flapping dynamics than the main rotor, shown in Figure 8.1-6. As discussed below, the stabilizer bar normally responds slower than the main rotor. By mechanically interconnecting the stabilizer bar with the main rotor blade pitch, helicopter handling qualities can be improved by providing a form of feedback to attitude changes. The modeling of such a device can be viewed as an extension of handling main rotor flapping and is covered in this chapter below.

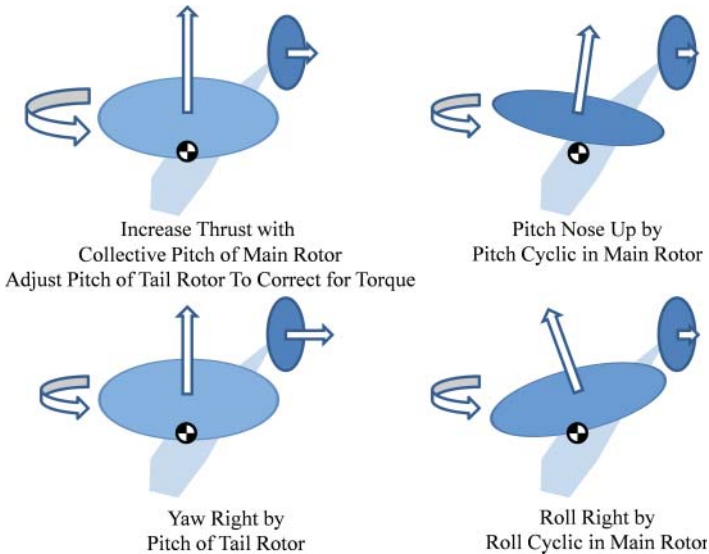


**Figure 8.1-5** A Helicopter is able to independently control thrust, roll moment, pitch moment, and yaw moment via the collective and cyclic pitch of the main rotor and the pitch of the tail rotor.



**Figure 8.1-6** Helicopter main rotor with a stabilizer bar.

Any of these propeller and rotor classes could also be placed inside a duct, creating another distinction to address from a modeling perspective. Properly designed, a true ducted propeller/rotor can have advantages in terms of aerodynamic efficiency. Some of the challenges include getting the flow to enter the duct smoothly, ensuring a small clearance between the propeller tips and the duct wall, and achieving this efficiency benefit across all required flight conditions (McCormick, 1998). Perhaps the most widespread and successful example of this is for helicopter tail rotors, such as seen on the Eurocopter AS365 Dauphin. However, it is still far less common than an unducted tail rotor. Rotor guards placed around the propellers/rotors on successful multirotors are typically there to address possible collisions with obstacles and are sufficiently

small and distant from the rotor itself to avoid the full complexities and efficiency benefits of duct modeling and design.

The sections that follow begin with computing the propeller/rotor forces and moments. This is followed by addressing rotor flapping dynamics. Following that is a discussion of the modeling of gas and electric motors. The chapter concludes with three aircraft model examples chosen to represent one aircraft from each major class of aircraft in common use today. Across the examples, we also see the building blocks for a potentially much larger number of possible aircraft configurations.

8.2    PROPELLER/ROTOR FORCES AND MOMENTS

In this subsection, models for the forces and moments due to propellers and rotors are described. One is typically concerned first and foremost with thrust and torque through the propeller shaft, and so this is covered first. An important distinction is made between models that include a degree of freedom (state) for the angular rate of the motor/propeller. For some aircraft, the RPM may be held tightly by a so-called governor or other system. When this is the case, propeller torques are effectively passed through to the aircraft itself. When this is not the case, it may be necessary to explicitly model the RPM or angular velocity of the propeller as it changes. The torques acting on the propeller/rotor are aerodynamic torque, typically opposing rotation, and engine/motor torque, typically causing rotation. The engine torque is imparted on the aircraft in the opposite direction as it applies to the propeller/rotor, as illustrated in Figure 8.2-1, that is, an equal and opposite reaction compared to the propeller/rotor. Because both engine/motor and aerodynamic torques are typically a function of propeller RPM, this model will be fully coupled.

For a fixed-pitch propeller, when an increase in thrust is desired, the pilot might increase the throttle input to the engine/motor. This will cause the engine torque to increase, which will increase the propeller RPM. As RPM climbs, propeller aerodynamic torque will increase until balance is restored. The propeller will now be at a higher RPM corresponding to a higher thrust level. Once RPM is constant again, the aerodynamic torque on the propeller will equal engine torque.

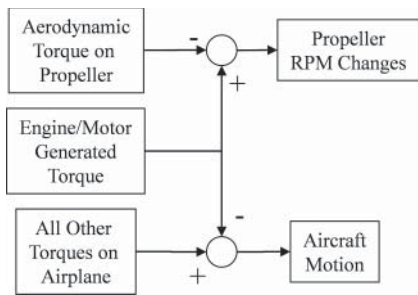


Figure 8.2-1    Modeling the rotational degree of freedom of a propeller.



The purpose of this section is to provide the tools necessary to model and simulate propellers and rotors in this manner. The level of detail is not sufficient to effectively design and develop propellers or rotor systems, as this is beyond the scope of this book.

A gyrocopter or a helicopter with a power loss represents a case where there is no engine torque into the main rotor, and so the aerodynamic rotor/propeller torques are dominant. So, a gyrocopter in steady flight or a helicopter performing an autorotation can encounter aerodynamic torque that is near zero or even negative by this convention.

### Thrust and Torque of a Propeller/Rotor

Throughout this section we will need to know the local flow properties at the propeller in order to effectively find thrust and torque. It is essential to address the fact that the velocity of the center of a propeller or rotor with respect to the air is not necessarily equal to the velocity of the aircraft itself. It is straightforward to account for the effect of aircraft body angular velocity. This is a dominant effect for helicopter tail rotors and multirotors given their displacement from the center of mass. For propeller  $P$ , the local velocity relative to the air can be found by

$$\mathbf{v}_{rel}^P = \mathbf{v}_{rel}^{bf} + \tilde{\boldsymbol{\omega}}_{b/i}^{bf} \mathbf{p}_{P/CM}^{bf} = [U^P \quad V^P \quad W^P]^T \quad (8.2-1)$$

$$V_T^P = |\mathbf{v}_{rel}^P| \quad (8.2-2)$$

where  $\mathbf{p}_{P/CM}^{bf}$  is the location of the propeller with respect to the aircraft center of mass and  $\mathbf{v}_{rel}^{bf}$  is the velocity of the aircraft with respect to the surrounding air. The speed of the propeller relative to the air is  $V_T^P$ . Beyond this correction factor for mounting location, some propellers and rotors are located within the wake or downwash of a wing or another rotor. Of particular concern here is a helicopter tail rotor, where the effect of the main rotor on the flow at the tail rotor can be significant.

A propeller produces thrust by imparting a change in velocity to the air that flows through it. The generated force (thrust) will be in the direction opposite the velocity change imparted on the air flowing through it. For the rotor of a hovering helicopter, this means the still surrounding air will be forced down in order to produce the upward thrust that keeps the helicopter in the air. For the propeller of an airplane in cruise, this means the air goes out the back of the airplane at a speed greater than it arrived at the airplane (from the perspective of an observer in the airplane). Focusing on the latter example, the air of higher speed will take up less area than the air of lower speed to the extent it is at approximately the same density. This effect is illustrated in Figure 8.2-2. In this idealized incompressible flow model, half of the velocity change happens prior to entering the propeller and half occurs after it passes through the propeller. The mass flow rate of the air passing through this propeller is

$$\dot{m} = \rho A (V_T^P + v_i) \quad (8.2-3)$$

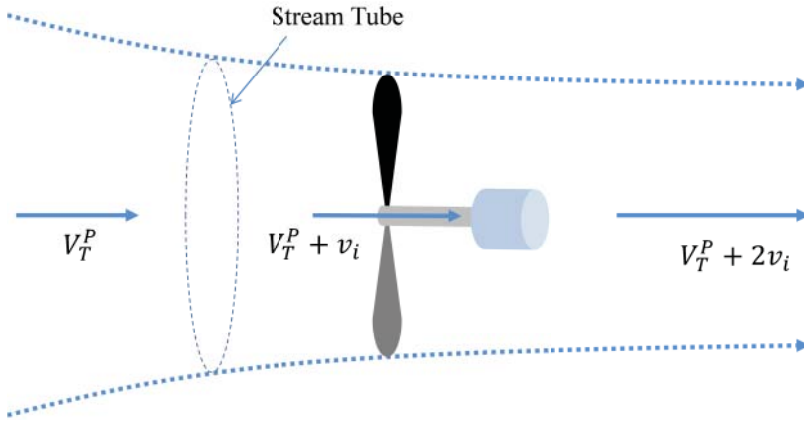


**Figure 8.2-2** Idealized flow through a propeller.

where  $A$  is the area of the propeller disk ( $A = \pi R^2$ ). The thrust is mass flow rate multiplied by the total change in velocity caused by the propeller, and is found by

$$T = \dot{m}2v_i = 2\rho A(V_T^P + v_i)v_i \quad (8.2-4)$$

As illustrated in Figure 8.2-2, the induced velocity changes the local flow at the propeller. This will change the effective angle of attack of the propeller blades. Determining propeller thrust, then, is tied to determining this induced velocity and vice versa. We need both a momentum relationship such as Equation (8.2-4) and one that relates thrust to the current angle of attack of the blades, which is itself a function of induced velocity.

Lieshman (2006) has pointed out that for very small rotors in hover the ideal wake contraction shown in Figure 8.2-2 is not fully achieved (perhaps around  $R < 8$  inches). This can reduce propulsive efficiency below what is presented here.

However, before we relate blade angle of attack with thrust, we need to deal with the general case where thrust and induced velocity are not aligned with the local flow. This would be the normal case for a helicopter in forward flight. A more general version would be

$$T = \dot{m}2v_i = 2\rho AV'v_i \quad (8.2-5)$$

where the effective speed of the flow at the rotor is

$$V' = \sqrt{U^2 + V^2 + (W^P - v_i)^2} \quad (8.2-6)$$

for the case where the thrust is directed along the body negative Z-axis, as would be the case for a conventional helicopter, illustrated in Figure 8.2-3 (Stepniewski and Keys, 1984, p. 62).

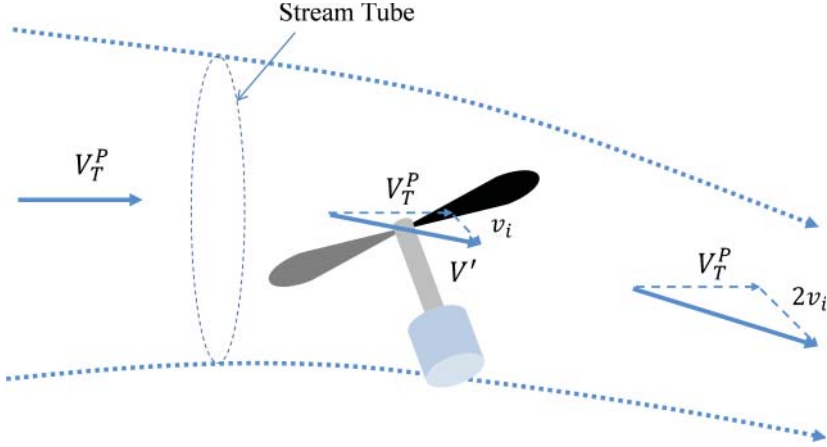


**Figure 8.2-3** Idealized flow through a rotor in forward flight.

The blade element method can be utilized to relate thrust to blade angle of attack and lift properties. Assuming ideal conditions (no blade stall, reverse flow) and a linear blade twist, the local blade angle of attack will be

$$\alpha(\psi, r) = \text{atan} \left( \frac{W^P - v_i}{\Omega r + U^P \sin \psi + V^P \cos \psi} \right) + \theta_0 + \theta_1 \frac{r}{R} \quad (8.2-7)$$

where  $\Omega$  is the angular rate of the rotor expressed in radians per second. Here, we are taking care to use  $[U^P \ V^P \ W^P]^T$  as the velocity of the propeller/rotor with respect to the air (undisturbed by the rotor itself) expressed in a frame where the rotor thrust is along the negative Z-axis, taking into account rotor disk flapping. Here,  $\theta_0$  represents the root blade angle, and  $\theta_1$  represents linear twist along the blade. More specifically, this is the angle the zero lift line of the airfoil makes relative to the rotor disk plane (Figure 8.1-4). The angle  $\psi$  is the current location of the blade as it travels around a single rotation, zero when pointing straight aft (negative X-axis). We take  $r$  to be the blade element location along the blade and  $R$  to be the total blade length (Figure 8.2-4).

To get lift per unit span of one blade, one uses

$$\frac{\Delta L(\psi, r)}{\Delta r} = \alpha(\psi, r) a \frac{\rho}{2} (\Omega r + U^P \sin \psi + V^P \cos \psi)^2 c \quad (8.2-8)$$

where  $a$  is the lift curve slope of the airfoil and  $c$  is the chord of the blade, both assumed constant. To get the total thrust, we integrate the lift along each blade. We integrate again to average that blade for one full rotation. Finally, we multiply by the number of blades ( $b$ ) to get total thrust:

$$T = \frac{b}{2\pi} \int_0^{2\pi} \int_0^R \frac{\Delta L(\psi, r)}{\Delta r} dr d\psi \quad (8.2-9)$$

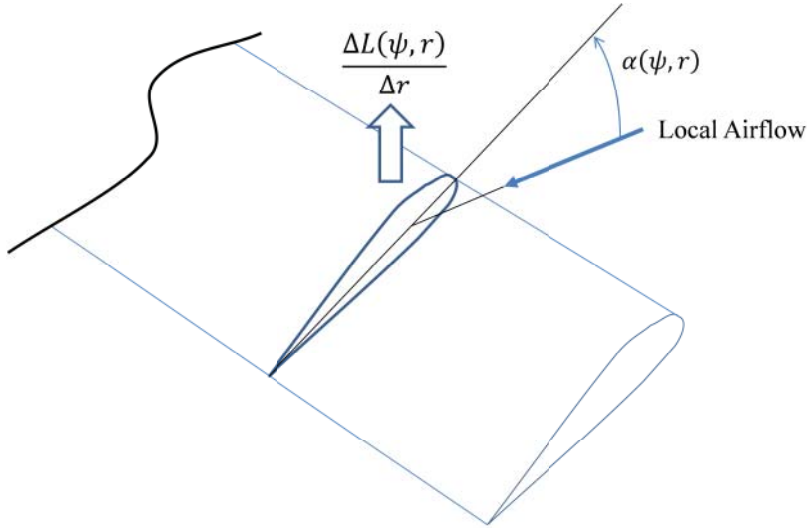


**Figure 8.2-4** Using the blade element method to estimate propeller/rotor thrust.

With these assumptions, it is possible to get a closed-form solution for this integral,

$$T = \frac{\rho abcR}{4} \left[ \begin{array}{l} (W^P - v_i)\Omega R + \frac{2}{3}(\Omega R)^2 \left( \theta_0 + \frac{3}{4}\theta_1 \right) + \dots \\ (U^{P^2} + V^{P^2}) \left( \theta_0 + \frac{1}{2}\theta_1 \right) \end{array} \right] \quad (8.2-10)$$

where a small-angle assumption was used to eliminate the  $\text{atan}$  function in Equation (8.2-7). This blade element method is sufficient for our purposes in this chapter. For a more complete treatment of this topic, including relaxing some of the key assumptions made, see the work of Prouty (1986).

Given the flight condition of the aircraft, the current collective pitch angle (which would be fixed for a fixed-pitch propeller), and rotor/propeller RPM, it is now possible to find the thrust, induced velocity, and flow speed at the propeller by simultaneously solving Equations (8.2-5), (8.2-6), and (8.2-10). A closed-form solution involves finding the roots of a fourth-order polynomial. A common approach is to simply solve it numerically within a simulation model (Figure 8.2-5).

It is also necessary to find the torque exerted by the air on the propeller/rotor. It is convenient to estimate the power first. Following this, one need only divide power by the shaft rate ( $\Omega$ ) to find torque. The first component is the induced power. Note that this contribution can be negative, even with a positive thrust, if the flow is going up through the bottom of the rotor ( $W^P > v_i$ ). It essentially represents the tilt of the lift vector due to the induced velocity:

$$P_{\text{induced}} = T(v_i - W^P) \quad (8.2-11)$$

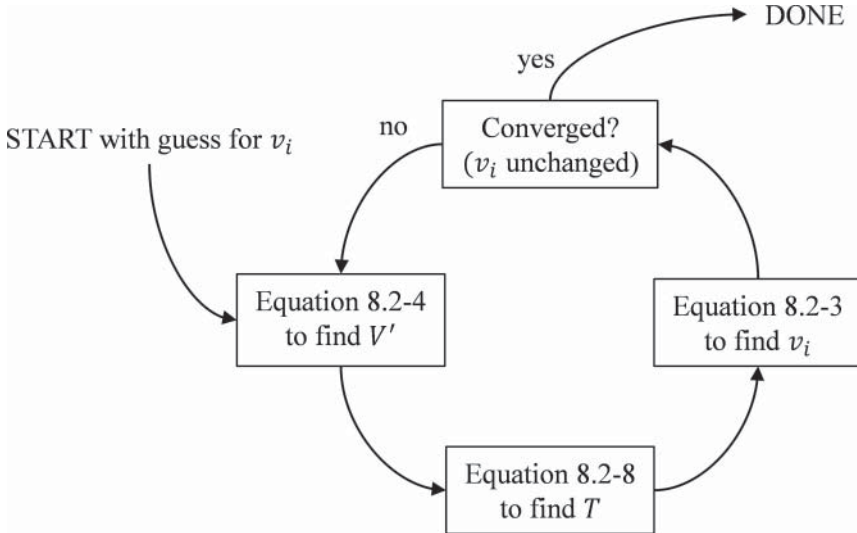


**Figure 8.2-5** Finding rotor thrust and induced velocity numerically.

The second contributor is profile power. This is the skin friction drag of the blades and is positive. This is found in a manner similar to thrust, with more complex versions available that include additional effects. Using the same assumptions we did for thrust (Prouty, 1986; Stepniewski and Keys, 1984, p. 127),

$$P_{profile} = \Omega \frac{b}{2\pi} \int_0^{2\pi} \int_0^R \frac{\Delta D(\psi, r)}{\Delta r} r dr d\psi \quad (8.2-12)$$

$$P_{profile} = \frac{\rho C_{d0} b c \Omega R^2}{8} \left[ (\Omega R)^2 + U^2 + V^2 \right] \quad (8.2-13)$$

where  $C_{d0}$  is the zero lift drag coefficient of the blade airfoil. Some sources include a factor of 4.6 on the velocity squared terms, which is effectively a correction factor to account for the effect of forward speed on both profile *and* induced power (Heffley and Mnich, 1987; Stepniewski and Keys, 1984, p. 134), which has already been accounted for here in the profile power directly. We are now ready to compute rotor aerodynamic torque,

$$Q_P = \frac{1}{\Omega} (P_{induced} + P_{profile}) \quad (8.2-14)$$

It is worth noting that we have also calculated the induced velocity of the propeller ( $v_i$ ) in the process of finding thrust and torque. The modeler may find this helpful in determining how the local flow properties have changed for aerodynamic surfaces (or other propellers/rotors) downstream of this propeller/rotor. The total change in the velocity of the flow will be approximately  $2v_i$  in a direction opposite to thrust, as

illustrated in Figure 8.2-3. To this level of approximation, the effect would be limited to those areas within the stream tube illustrated in the figure.

These relationships can be utilized to predict the thrust and torque for propellers/rotors mounted on the aircraft in any orientation with an appropriate coordinate transformation. This also includes the case where the direction is time varying due to rotor flapping dynamics or mechanical tilt such as for a tiltrotor aircraft.

An important limitation of the method described here for airplane propellers is the small-angle assumption made for blade angle of attack. This assumption can result in an erroneously large thrust (and low torque) for a typical airplane with a fixed-pitch propeller when the airplane itself is going much slower than the design cruise condition, such as on the ground when starting the takeoff roll. Here, the blade angle of attack may be high enough to result in a loss of lift near the root. To accurately predict thrust and torque for these conditions, such as for takeoff performance analysis, it may be advisable to work with propeller charts that provide thrust and torque coefficients as a nonlinear function of the ratio of blade tip speed to aircraft speed (Phillips, 2010).

**Fixed-Pitch Propeller Nomenclature** Small propellers/rotors are often specified by two numbers, such as the 9x7 propeller illustrated in Figure 8.1-1. These numbers indicate that the propeller has a diameter of 9 inches and a *pitch* of 7 inches. The pitch is the distance the propeller would travel if “screwed” one revolution. This can be related to the pitch angle of the blade as a function of location along the blade ( $r$ ):

$$\tan[\theta(r)] = \frac{\text{Distance Forward}}{\text{Distance Around}} = \frac{\text{pitch}}{2\pi r} \quad (8.2-15)$$

It is conventional to use  $r/R = 0.75$  in Equation (8.2-15) as the point of reference for determining the pitch of the propeller (Simons, 1999):

$$\text{Pitch} = \left(2\pi \frac{3}{4}R\right) \tan \left[\theta \left(\frac{3}{4}R\right)\right] \quad (8.2-16)$$

To continue with the linear twist assumption utilized in this section, we can approximately match this distribution by enforcing equality of blade pitch at  $r/R = 0.75$  and apply the linear twist through that same station:

$$\theta_0 = 2\text{atan}\left(\frac{\text{pitch}}{2\pi \frac{3}{4}R}\right), \theta_1 = -\frac{4}{3}\text{atan}\left(\frac{\text{pitch}}{2\pi \frac{3}{4}R}\right) \quad (8.2-17)$$

Note that most propellers have cambered airfoils. Thus, the actual collective pitch angle  $\theta_0$  is somewhat higher than the airfoil pitch angle to correctly account for the zero-lift angle of attack of the airfoil used.

## Computing Nonthrust Forces and Moments

Although thrust and torque around the prop shaft of a propeller or rotor are usually the dominant forces and moments, the remaining forces and moments can also be

significant. For example, they can cause some of the most important asymmetries for single-engine airplane flight. Here we cover accounting for some of the more important effects.

**Remaining Aerodynamic Forces and Moments** The most significant remaining force acting on a propeller is that acting perpendicular to thrust within a plane containing both the thrust and the relative velocity vector (Figure 8.2-6). This is the so-called H-force or hub force on a helicopter rotor. For an airplane propeller, it might be called the normal force (normal to thrust).

A closed-form solution can be found for this in a manner similar to thrust and torque. A version with similar assumptions to the thrust and torque relations provided above is

$$H = \frac{b}{2\pi} \int_0^{2\pi} \int_0^R \frac{\Delta D(\psi, r)}{\Delta r} \sin \psi dr d\psi \quad (8.2-18)$$

$$H = \frac{\rho C_{d_0} b c \Omega R^2}{4} \sqrt{U^2 + V^2} \quad (8.2-19)$$

For an airplane with a propeller, this moment can serve to add or subtract from the static stability (both directionally and longitudinally) depending on whether the propeller is mounted in front of or behind the center of mass (Perkins and Hage, 1949). The effect can be quite pronounced at low speed, given the fact that the moment scales with speed to the first power rather than speed to the second power, as would be the case for a vertical or horizontal fin. The effect can be pronounced even when the propeller is not producing thrust. It only needs to be spinning as found in Equation (8.2-19).

Beyond torque, the remaining aerodynamic moments would only be transferred to the aircraft itself directly for the case of a rigid rotor that is, not when separate flapping dynamics are to be included in the subsection below, where flapping motion is accounted for. When the propeller/rotor is treated as rigid, the moments that would normally cause rotor disk tilt are instead transferred directly to the aircraft itself. For an airplane, the dominant example is a phenomenon called P-factor, where, for example, an aircraft at high angle of attack experiences a yaw moment due to the thrust imbalance between the left and right sides of the propeller disk.

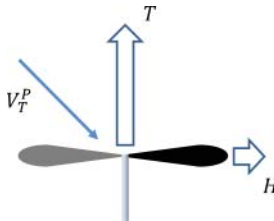


**Figure 8.2-6** H-force acting on a propeller/rotor.

To model these moments, the blade element method can be utilized, this time including the effect of angular velocity of the propeller/rotor:

$$\mathbf{\omega}_{P/r}^P = [P^P \quad Q^P \quad R^P]^T \quad (8.2-20)$$

To get a refined estimate for the angle of attack of the blade element,

$$\alpha(\psi, r) = \text{atan} \left( \frac{W^P - v_i + Q^P r \cos \psi + P^P r \sin \psi}{\Omega r + U^P \sin \psi + V^P \cos \psi} \right) + \theta_0 + \theta_1 \frac{r}{R} \quad (8.2-21)$$

Using a small-angle assumption to simplify the atan function in Equation (8.2-21), we can find rolling and pitching aerodynamic moments on the propeller/rotor (for a propeller/rotor spinning around the negative Z-axis, or counterclockwise as viewed from above):

$$L_{A-P} = -\rho abc R^2 \left[ \frac{\Omega R^2}{16} P^P + \left( \frac{(W^P - v_i)}{8} + \frac{\Omega R}{6} \theta_0 + \frac{\Omega R}{8} \theta_1 \right) U^P \right] \quad (8.2-22)$$

$$M_{A-P} = -\rho abc R^2 \left[ \frac{\Omega R^2}{16} Q^P + \left( \frac{(W^P - v_i)}{8} + \frac{\Omega R}{6} \theta_0 + \frac{\Omega R}{8} \theta_1 \right) V^P \right] \quad (8.2-23)$$

Notice that in both cases the propeller/rotor produces a damping effect, where there is a moment-resisting angular rate around that same axis. This is due to the fact any angular velocity will cause a blade lift distribution change that will tend to dampen motion.

For an airplane, the P-factor is predicted by rederiving Equations (8.2-22) and (8.2-23) for the case where the propeller rotor is spinning around the positive X-axis (clockwise as viewed from behind), a common choice for an airplane:

$$M_{A-P} = -\rho abc R^2 \left[ \frac{\Omega R^2}{16} Q^P + \left( \frac{(W^P - v_i)}{8} + \frac{\Omega R}{6} \theta_0 + \frac{\Omega R}{8} \theta_1 \right) V^P \right] \quad (8.2-24)$$

$$N_{A-P} = -\rho abc R^2 \left[ \frac{\Omega R^2}{16} R^P + \left( \frac{(W^P - v_i)}{8} + \frac{\Omega R}{6} \theta_0 + \frac{\Omega R}{8} \theta_1 \right) W^P \right] \quad (8.2-25)$$

So, if the aircraft is experiencing a large angle of attack,  $W^P$  will be large. With typical signs for the remaining parameters (in particular, that thrust is positive), the aircraft will experience a negative yaw moment,  $N_{A-P} < 0$ .

**Gyroscopic Moments** If treated as a rigid rotating subsystem, spinning propellers or rotors represent a spinning mass and thus can produce apparent moments. If treated as essentially a separate system with its own attitude motion, as would be the case when including flapping dynamics, then this will be accounted for within



the flapping dynamics themselves. In this section, we address the former case: We want to treat the propeller/rotor as a rigid rotating subsystem.

This is handled by accounting for the angular momentum of the spinning propeller when deriving the rigid-body dynamics of the aircraft. Equation (1.7-3) can be used to find the angular momentum of a rigid body:

$$\mathbf{h}_{cm/i}^{bf} = J_{b/i}^{bf} \boldsymbol{\omega}_{b/i}^{bf}$$

For a rotating subsystem spinning with angular velocity  $\boldsymbol{\omega}_{p/b}^{bf}$  and inertia matrix  $J_p^{bf}$ , the contribution of this subsystem can simply be added, to yield

$$\mathbf{h}_{cm/i}^{bf} = J_{b/i}^{bf} \boldsymbol{\omega}_{b/i}^{bf} + J_p^{bf} \boldsymbol{\omega}_{p/b}^{bf} \quad (8.2-26)$$

with a note that the inertia of the subsystem is included in the original  $J^{bf}$  as well. A new version of Equation (1.7-5), the state equation for angular velocity, can be found using this refined term for angular momentum:

$${}^b \dot{\boldsymbol{\omega}}_{b/i}^{bf} = (J^{bf})^{-1} \left[ \mathbf{M}^{bf} - \tilde{\boldsymbol{\omega}}_{b/i}^{bf} \left( J_{b/i}^{bf} \boldsymbol{\omega}_{b/i}^{bf} + J_p^{bf} \boldsymbol{\omega}_{p/b}^{bf} \right) \right] \quad (8.2-27)$$

Comparing Equations (8.2-27) and (1.7-5), one observes that the effect of the new term is equivalent to a moment, which we will refer to as the *gyroscopic moment*, a name inspired by the observation that this term is critical to the operation of mechanical gyroscopes. So, a good model for the gyroscopic moment of a spinning subsystem is

$$\mathbf{M}_{Gyro-P}^{bf} = -\tilde{\boldsymbol{\omega}}_{b/i}^{bf} J_p^{bf} \boldsymbol{\omega}_{p/b}^{bf} \quad (8.2-28)$$

which is effectively the cross product of the aircraft angular velocity with the angular momentum of the propeller/rotor. So, when an airplane with a single propeller spinning about the longitudinal axis pitches up, it will experience a yawing moment due to this term. The direction depends on the spin direction of the propeller.

This moment can be important for propeller-driven aircraft, particularly those with large propellers. This moment will also be important for multirotors. However, if as many propellers are spinning in one direction as the other, then the effects do tend to cancel each other. If the inertia of the propeller/rotor about the spin axis is the scalar  $J_p$  and the propeller/rotor is spinning around the positive body  $X$ -axis, then

$$\mathbf{M}_{Gyro-P}^{bf} = -\tilde{\boldsymbol{\omega}}_{b/i}^{bf} [J_p \Omega \quad 0 \quad 0]^T = J_p \Omega [0 \quad -R \quad Q]^T \quad (8.2-29)$$

It is also worth noting that some aircraft may experience significant gyroscopic moments from rotating parts other than propellers/rotors. Of particular concern may be the effect of the rotating elements of gas turbine engines, which may have a very high angular velocity.

### 8.3 MODELING ROTOR FLAPPING

The motion of a blade as it travels around a helicopter rotor is quite complex. To the extent that the motion is periodic at the frequency of rotor spin when the aircraft is in a steady-state flight condition, it is useful to consider steady (average) conditions separately from what is happening once per revolution, twice per revolution, and so on. If we are particularly concerned with the motion of the aircraft itself, then the average and once-per-revolution conditions typically dominate. Higher-fidelity simulation models would take into account these higher-order harmonics.

#### Tip Path Plane Equations of Motion

As introduced in Section 8.1, the swashplate mechanism can be used to intentionally tilt the rotor disk plane on a helicopter rotor. This has the effect of tilting the thrust vector and is the primary means of attitude control for the aircraft. However, the motion of the aircraft can also change the rotor disk plane tilt. As a result, it is necessary to model the tilt dynamics explicitly. That is, one may need to model the dynamics of the first-order harmonics of blade flapping. The typical symbol for blade flapping is beta, not to be confused with aircraft sideslip angle,

$$\beta(\psi) \cong a_0 - a_1 \cos \psi - b_1 \sin \psi \quad (8.3-1)$$

where  $a_0$  represents the coning angle (typically positive),  $a_1$  represents longitudinal tilt, and  $b_1$  represents lateral tilt, as shown in Figure 8.3-1.

**Coning Angle** The coning angle ( $a_0$ ) results from a balance between blade thrust load tending to increase the coning angle and centrifugal force tending to reduce it. Coning angle typically responds fast enough to changes in thrust and rotor RPM, so we can simply consider the response to be instantaneous for simulation purposes. An estimate for the opposing moments can be found in the literature (Prouty, 1986) for the case of ideal twist and blades with constant mass distribution. The coning angle is found by setting the sum of these two contributors to the flapping moment to zero,

$$\text{Flapping moment} = 0 = \frac{2}{3}TR - a_0 b I_{Bf} \Omega^2, \quad (8.3-2)$$

where  $I_{Bf}$  is the inertia of a single blade around the effective flapping hinge. To solve for the coning angle, one arrives at the approximation

$$a_0 = \frac{2}{3} \frac{TR}{b I_{Bf} \Omega^2} \quad (8.3-3)$$

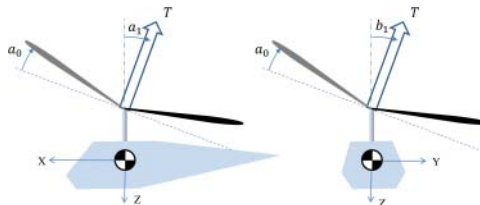


Figure 8.3-1 Blade first-order harmonic flapping motion (exaggerated).

However, this coning angle will normally not have a significant effect on low-speed motion. Tip path tilt, covered in the next subsection, will.

**Tip Path Tilt** Unlike the coning angle, the longitudinal and lateral tilt dynamics can couple with the rigid-body motion of the rest of the aircraft. Let us start by estimating the time constant of the response of the rotor if perturbed from an equilibrium tilt angle.

Here we distinguish between a teetering rotor, where the rotor can tilt on a pivot located at the center of rotation, and a rotor where the flapping hinge is offset from the spin axis. The latter case would also approximate a semirigid rotor, where there is a theoretical pivot location that is equivalent to blade behavior as it flexes (Figure 8.3-2).

Prouty (1986, p. 462) found the estimate for rotor flapping time constant in hover as

$$\tau = \frac{16}{\gamma\Omega} \frac{1}{\left(1 - \frac{e}{R}\right)^3 \left(1 + \frac{1}{3} \frac{e}{R}\right)} \quad (8.3-4)$$

Heffley et al. (1986) used a form that matches a Taylor series expansion of the above for small  $e$ :

$$\tau = \frac{16}{\gamma\Omega} \left(1 - \frac{8}{3} \frac{e}{R}\right)^{-1} \quad (8.3-5)$$

Fundamental to this time constant is the value for the Lock number,  $\gamma$ . This is a nondimensional parameter that characterizes the importance of aerodynamic forces vs. centrifugal forces acting on the blade. It is found by

$$\gamma = \frac{\rho ac R^4}{I_{Bf}} \quad (8.3-6)$$

where  $I_{Bf}$  is the blade inertia about the flapping axis rather than the spin axis, normally very nearly the same value as that about the spin axis. A blade with unusually high centrifugal forces, such as one with weights placed in the blade tips, would have a lower Lock number. A rotor with a high Lock number will have a small time constant for flapping motion. That is, it will respond faster.

It is worth noting that some rotor blades will change pitch as they flap, which is the so-called delta-3 effect. Like the hinge offset, this can also lead to a change in the rotor flapping time constant (Dreier, 2007).

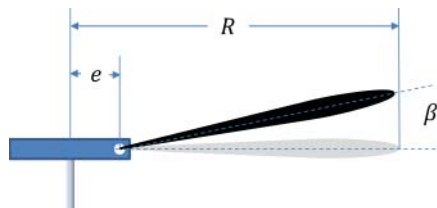


**Figure 8.3-2** Effective hinge offset of a rotor blade.

Now that the time constant of the response has been estimated, we turn to the prediction of the tip path motion, based on Heffley and Mnich (1987) with additional refinements from Mettler (2003):

$$\dot{a}_1 = \frac{1}{\tau} \left( \delta_{pitch} + P \frac{1}{\Omega} + F_c b_1 - F_V U^P - a_1 \right) - Q \quad (8.3-7)$$

$$\dot{b}_1 = \frac{1}{\tau} \left( \delta_{roll} - Q \frac{1}{\Omega} - F_c a_1 - F_V V^P - b_1 \right) - P \quad (8.3-8)$$

This represents a first-order response around each axis with a time constant for the response found above. The final term represents a direct input to the changes in tilt due to rigid-body motion. For high-speed flight, where the airspeed is greater than perhaps a third of the tip speed ( $\Omega R$ ), it is important to include additional speed effects (Prouty, 1986). The remaining terms deserve detailed discussion, which appears below. In each case a stability or control derivative is introduced with an estimate provided. Values for these sensitivities to motion variables could also be found experimentally. The following subsection extends this model to the case where the rotor has a stabilizer bar.

The  $\delta_{pitch}$  and  $\delta_{roll}$  terms represent cyclic pitch inputs. When all other terms are small (teetering rotor and no rigid-body motion), then  $a_1$  will approach  $\delta_{pitch}$ , as implied by Figure 8.1-4. Equations (8.3-7) and (8.3-8) imply that the tilt response to a cyclic step input would be exponential with time constant  $\tau$  if the aircraft was otherwise constrained not to move.

The  $P \frac{1}{\Omega}$  and  $Q \frac{1}{\Omega}$  terms are due to the change in the lift distribution of the blades due to vehicle rotation, similar to what was accounted for in the nonflapping rotor by Equations (8.2-22) and (8.2-23). Instead of providing damping, it causes the tip path plane to tilt off axis.

The  $F_c$  term, which is zero for a teetering rotor, couples longitudinal and lateral flapping. An estimate provided by Heffley and Mnich (1987) is

$$F_c = \frac{3}{4} \tau \Omega \frac{e}{R} \quad (8.3-9)$$

The  $F_V$  term is sometimes referred to as the dihedral effect for a rotor. The moments due to velocity components in the plane of the rotor disk [Equations (8.2-22) and (8.2-23)] are applied to the rotor disk, causing the tip path plane to tilt “away” from the incoming airflow. Based on the sensitivity in hover (Prouty, 1986, p. 564)

$$F_V = \frac{8}{3} \Omega R \left( \theta_0 + \frac{3}{4} \theta_1 \right) - 2v_i$$

Rewriting in terms of thrust, as done by Heffley et al. (1986), we obtain the alternate version

$$F_V = \frac{2}{\Omega R} \left( \frac{8T}{\rho a b c \Omega^2 R^3} + \sqrt{\frac{T}{2\rho\pi\Omega^2 R^4}} \right) \quad (8.3-10)$$

### Flapping Dynamics with a Stabilizer Bar

As described in Section 8.1, many small helicopters make use of a stabilizer bar (Figure 8.1-6). Our treatment of the flapping dynamics of the main rotor has given us the key necessary tools to model the stabilizer bar.

The stabilizer bar is essentially a second rotor that shares a common shaft with the main rotor. The key difference is that it has much slower flapping dynamics. As the aircraft rotates, the stabilizer bar will lag behind the main rotor. A mechanical interconnect of the stabilizer bar flapping to the cyclic main rotor is then used to create a feedback to resist this attitude displacement.

The typical stabilizer bar is a teetering rotor. So, the flapping time constant can be found, similar to (8.3-5), by

$$\tau_s = \frac{16}{\gamma_s \Omega} \quad (8.3-11)$$

where the Lock number of the stabilizer bar is  $\gamma_s$ . A complication is that the stabilizer bar is usually not of constant chord. Often it is “paddle” shaped, where the outer section contains a lifting airfoil (Figure 8.3-3). An appropriate relationship to find the Lock number for such a shape is (Mettler, 2003)

$$\gamma_s = \frac{\rho a_s c_s}{I_{sf}} (R_{s,outer}^4 - R_{s,inner}^4) \quad (8.3-12)$$

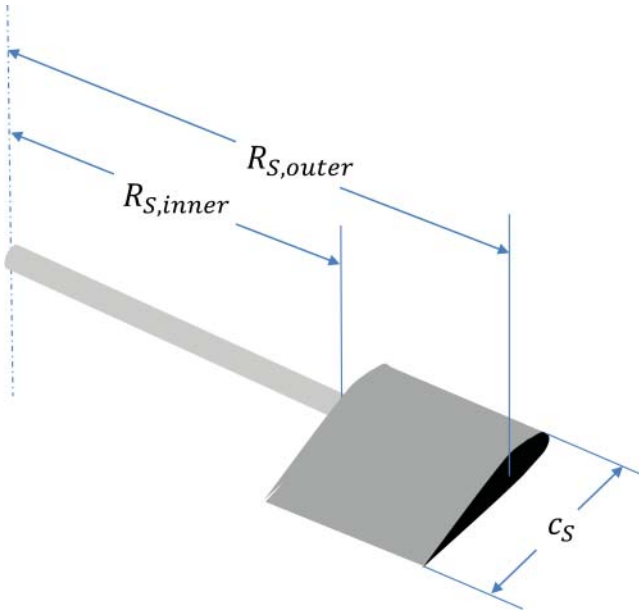


**Figure 8.3-3** Stabilizer bar geometry.

where  $a_s$ ,  $c_s$ , and  $I_{sf}$  are the lift curve slope, chord, and flapping inertia of the stabilizer bar, respectively, and  $R_{S-outer}$  and  $R_{S-inner}$  are the outer and inner radii of the lifting section of the paddle. Because of the diminished aerodynamic forces and the common presence of tip weights on the stabilizer bar, this time constant is normally much larger than the main rotor. So, even if the main rotor flapping could be neglected, the dynamics of a well-designed stabilizer bar could not be neglected when modeling aircraft motion.

In order for the stabilizer bar to enhance overall control effectiveness, it is often also given cyclic pitch commands proportional ( $K_{C \rightarrow S}$ ) to those sent to the main rotor and in the same manner, that is, via the swashplate. The flapping dynamics of the stabilizer bar can be written as

$$\dot{a}_{1S} = \frac{1}{\tau_S} \left( K_{C \rightarrow S} \delta_{pitch} + P \frac{1}{\Omega} - a_{1S} \right) - Q \quad (8.3-13)$$

$$\dot{b}_{1S} = \frac{1}{\tau_S} \left( K_{C \rightarrow S} \delta_{roll} - Q \frac{1}{\Omega} - b_{1S} \right) - P \quad (8.3-14)$$

Note that the  $\frac{1}{\Omega}$  off-axis terms are typically negligible for a stabilizer bar.

The final step is to modify the main rotor flapping dynamics to account for the presence of the stabilizer bar and the mechanical interconnect of the stabilizer bar flapping to cyclic pitch ( $K_{S \rightarrow C}$ ). The revised version has a new term associated with the stabilizer bar interconnect:

$$\dot{a}_1 = \frac{1}{\tau} \left( \delta_{pitch} + K_{S \rightarrow C} a_{1S} + P \frac{1}{\Omega} + F_c b_1 - F_V U^P - a_1 \right) - Q \quad (8.3-15)$$

$$\dot{b}_1 = \frac{1}{\tau} \left( \delta_{roll} + K_{S \rightarrow C} b_{1S} - Q \frac{1}{\Omega} - F_c a_1 - F_V V^P - b_1 \right) - P \quad (8.3-16)$$

### Forces and Moments on the Aircraft from a Flapping Rotor

In this subsection, the resultant thrust and flapping angles are utilized to estimate the total forces and moments acting on the aircraft itself. We start with thrust and torque, accounting for the thrust tilt. We must also account for the fact that the rotor is not, in general, mounted at the center of mass. There are also moments that pass through the hub for the nonteetering rotor. Normally, the effect of the stabilizer bar on body forces and moments can be neglected.

If a small-angle assumption is used for the flapping angles, one obtains for a rotor thrusting along the negative  $Z$ -axis with rotor spinning around the negative  $Z$ -axis:

$$\mathbf{F}_P^P = \begin{bmatrix} -T a_1 \\ T b_1 \\ -T \end{bmatrix} \quad (8.3-17)$$

$$\mathbf{M}_P^P = \begin{bmatrix} -T z_P b_1 - T y_P + F_\beta b_1 \\ -T z_P a_1 + T x_P + F_\beta a_1 \\ Q_E \end{bmatrix} \quad (8.3-18)$$

where  $[x_p \ y_p \ z_p]^T$  is the location of the rotor relative to the aircraft center of mass in the propeller/rotor frame and  $Q_E$  is engine torque discussed in the following subsection.

The rotor stiffness  $F_\beta$  can be estimated based on the equivalent hinge offset or otherwise determined experimentally. From Prouty (1986, p. 477) we find the commonly used estimate

$$F_\beta = \frac{3}{4} b I_{bf} \Omega^2 \frac{e}{R} \quad (8.3-19)$$

### More Advanced Modeling of Rotors

A variety of phenomena have been neglected in the modeling presented here, including issues such as retreating blade stall, tip and root losses, and more precise models for the shape of the wake. For the purposes of exploring aircraft motion, what we have here is often sufficient for miniature aircraft. For the detailed design of rotor systems, a more advanced treatment is needed; the reader is referred to many of the resources referenced in this chapter, particularly Prouty (1986).

In the modeling included here, we have assumed that the induced velocity will respond instantaneously to changes in the blade geometry and vehicle motion. In reality, it takes a finite amount of time for a real flowfield to adjust. This phenomenon can be important for rotorcraft that are going to be controlled at high bandwidth, particularly larger aircraft. This phenomenon is called dynamic inflow and can be effectively tackled by including an additional state or mode to account for this finite response (Chen and Hindson, 1986).

## 8.4 MOTOR MODELING

Here, we address the issue of modeling a motor or engine to provide power to a propeller or rotor. We limit this to basic/fundamental models suitable to answer questions about the delivery of power and torque within a larger simulation intended to predict aircraft motion, rather than what might be used for motor design.

For small aircraft, the two most common choices for providing mechanical power are the reciprocating internal combustion engine and the electric motor. In both cases, we will predict an engine torque, which will be delivered to the propeller/rotor. At the same time, an equal and opposite moment will go to the aircraft (Figure 8.2-1). With this engine torque computed ( $Q_E$ ), it is then possible to complete our differential equation for propeller/rotor angular rate:

$$\dot{\Omega} = \frac{1}{J_P} (Q_E - Q_P) \quad (8.4-1)$$

where  $J_P$  is the moment of inertia (scalar) of the propeller/rotor about its rotation/spin axis. Thus, angular rate  $\Omega$  constitutes an additional state to carry along with the rigid-body motion states when performing simulation and analysis.

## Internal Combustion Engine Modeling

The simplest relationship to predict internal combustion engine power is

$$P_E = V_d \frac{\Omega}{2\pi n_p} \bar{p}, \quad (8.4-2)$$

where  $V_d$  is the displacement of the engine,  $n_p$  is the number of revolutions per power stroke ( $n_p = 1$  for a two-stroke engine,  $n_p = 2$  for a four-stroke engine), and  $\bar{p}$  is the mean effective pressure of the engine (Anderson, 2008). Note that we are continuing to use  $\Omega$ , or angular velocity of the prop shaft. In many cases, there may be a transmission between the engine and the propeller/rotor, in which case these values would be distinct and related by a gear ratio.

The primary means of controlling engine power for an internal combustion engine is the throttle, which is used to adjust the mean effective pressure between lower and upper limits. When developing a model for simulation purposes, it is typical to have (at best) information about maximum engine power and/or torque as a function of RPM. For a typical engine, one finds that the maximum torque is approximately constant, which means the maximum mean effective pressure is also approximately constant in this case,

$$Q_E = \frac{P_E}{\Omega} = V_d \frac{1}{2\pi n_p} \bar{p} \quad (8.4-3)$$

This suggests that the simplest reasonable model for an internal combustion engine model would be to have it produce a power proportional to throttle (and therefore mean effective pressure) and shaft speed. The effect of density is expected to scale the mean effective pressure as well. The resulting form is

$$P_E(\delta_t, \Omega, \rho) = P_{E,max} \frac{\rho}{\rho_0} \frac{\min(\Omega, \Omega_{max})}{\Omega_{max}} \delta_t, \quad (8.4-4)$$

where  $\delta_t$  is the throttle setting with a value between near zero (corresponding to idle) and unity (corresponding to maximum). The angular rate  $\Omega_{max}$  corresponds to the RPM of maximum power, and so this term ensures that the engine does not produce power greater than  $P_{E-max}$ . A more complex model would replace Equation (8.4-3) with lookup tables for maximum power as a function of RPM, for example, as shown in Figure 8.4-1,

$$P_E(\delta_t, \Omega, \rho) = P_{E,max}(\Omega) \frac{\rho}{\rho_0} \delta_t \quad (8.4-5)$$

or even as a lookup table containing up to all three dependencies (density, shaft speed, and density). For a turbocharged engine, this mean effective pressure can be made higher to produce additional power, particularly at high altitude, with power taken from the engine output to generate this additional pressure.

If controlling engine/propeller RPM is of particular interest, then it may be appropriate to also include further dynamics in the response of the engine power found



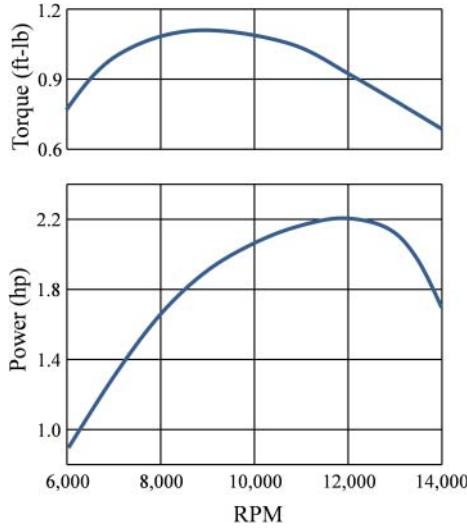


**Figure 8.4-1** Notional engine torque/power curves.

in Equation (8.4-5). These dynamics would normally be associated with mechanical movement of the throttle valve via a servo/actuator.

Fuel consumption can be effectively modeled as proportional to power, using the stated or estimated specific fuel consumption for the engine. That is, amount of fuel used per unit of time per unit of engine power (Anderson, 2008).

### Electric Motor Modeling

Electric motor torque can be effectively modeled as a torque proportional to an input signal and a reduction in torque that comes with increasing RPM (Stingu, 2011), or

$$Q_E(\delta_t, \Omega) = \frac{K_T}{R} \left( \delta_t - \frac{\Omega}{K_V} \right), \quad (8.4-6)$$

where constants  $K_T$ ,  $R$ , and  $K_V$  are properties of the motor (here,  $R$  is a resistance parameter, not to be confused with rotor radius). The input is  $\delta_t$ , using the same nomenclature as the internal combustion engine above. However, in this case the input would normally be measured in volts.

Modern electronic speed controllers (ESCs) are often used, which will regulate to a desired  $\Omega$  or RPM based on the commanded input by adjusting motor torque. The relationship between input and RPM may not be linear and may depend on the input voltage supplied to the ESC from a battery. Because propeller/rotor thrust tends to be proportional to  $\Omega^2$ , the command  $\Omega$  is often proportional to the square root of the input ( $\delta_t$ ) sent to the ESC.

Note that the ESC will achieve the commanded RPM only within the limits of available power and other constraints such as heat dissipation. For the power limit, we would use

$$Q_{E,max}(\Omega) = \frac{1}{\Omega} P_{E,max} \quad (8.4-7)$$

as the relevant torque limit.

## 8.5 SMALL AEROBATIC AIRPLANE MODEL

This subsection contains a medium-fidelity model of a small agile and aerobatic airplane. It is based on the Aeroworks 33% flying scale model of the Zivco Edge 540T, shown in Figure 8.5-1. The aircraft as modeled has been equipped with instrumentation that adds a small amount of weight to the aircraft. Although the aircraft has an outer shape that is a very close match to the full-size aircraft, the mass properties and engine power are not scaled. Unlike the full-scale aircraft, this model has a static-thrust-to-weight ratio greater than unity. Because of the geometry of the propeller prop wash relative to the full-span aileron, elevator, and rudder roll/pitch/yaw control is possible with the aircraft hovering with the nose straight up (Johnson et al., 2008). The aileron authority in hover is marginally enough to counter the torque from the propeller/engine. The example included here contains necessary elements to model this behavior, as well as many other elements of fully aerobatic flight.

The mass properties used for the small airplane example are given in Table 8.5-1. The product-of-inertia terms are assumed to be negligible.

The aerodynamic forces and moments of an airplane can be found using lookup tables. For the intended purpose, the tables need to include the full possible range of angle of attack and sideslip. That type of data is very difficult to obtain, often requiring several types of wind tunnel tests. The approach taken here was to specify the shape of these dependencies and then adjust the parameterization of these curves to match flight data at design conditions corresponding to hover and forward flight. The



**Figure 8.5-1** 33% Zivco Scale Edge 540T made by Aeroworks.

**TABLE 8.5-1 Aeroworks Edge Example Model Parameters: Mass Properties**

Parameter	Value
Weight , mg	29 lb
X-axis inertia, $J_x$	$0.32 \text{ slug} \cdot \text{ft}^2$
Y-axis inertia, $J_y$	$1.5 \text{ slug} \cdot \text{ft}^2$
Z-axis inertia, $J_z$	$2.3 \text{ slug} \cdot \text{ft}^2$

net result is a model that should not be considered quantitatively accurate outside of this narrow range yet be considered potentially useful to address basic questions about aircraft motion in these unusual flight conditions. The shape of the dependencies of motion variables will be based on estimating the effect of aircraft components individually and summing them, similar to that described by Dreier (2007).

To account for local flow differences, the effective velocity of each wing (left vs. right) with respect to the local airflow is estimated separately. Note that a term is included to account for the effect of the propeller. For the right wing, this is

$$\mathbf{v}_{rel,rw}^{bf} = \begin{bmatrix} U^{rw} \\ V^{rw} \\ W^{rw} \end{bmatrix} = \begin{bmatrix} U + Qz_{rw} - Ry_{rw} + \eta_w v_i \\ V + Rx_{rw} - Pz_{rw} \\ W + Py_{rw} - Qx_{rw} \end{bmatrix} \quad (8.5-1)$$

where  $\eta_w$  is a coefficient that accounts for the level of emersion of the wing in the propeller wash. The position vector  $[x_{rw} \ y_{rw} \ z_{rw}]^T$  is chosen to be approximately at the aerodynamic center of the wing panel. A similar velocity is found for the left wing.

The lift and drag of each wing panel are found separately. Continuing to use the right wing to illustrate the approach, the effective dynamic of the right wing is

$$\bar{q}'_{rw} = \frac{\rho}{2}(U^{rw2} + W^{rw2}) \quad (8.5-2)$$

Note that the lateral component  $U^{rw}$  has been remitted to approximately account for the effect of sideslip on the lift and drag forces to be calculated using this term. The prime included in the nomenclature is there to remind us of this. The angle of attack is next,

$$\alpha_{rw} = \text{atan2}(W^{rw}, U^{rw}) + \tau_a \delta_a \quad (8.5-3)$$

$$\alpha_{lw} = \text{atan2}(W^{lw}, U^{lw}) - \tau_a \delta_a, \quad (8.5-4)$$

where  $\text{atan2}(\cdot, \cdot)$  represents a four-quadrant inverse so that  $\alpha_{rw}$  can have the full range  $-\pi$  to  $+\pi$ . Note the inclusion of the effect of the aileron here. It modifies the effective angle of attack (with opposite sign for the left wing). The lift coefficient dependency on this angle of attack is found by first checking

$$C_{Lrw}(\alpha_{rw}) = a_w \alpha_{rw} + C_{L0,w} \quad (8.5-5)$$

to determine if it is in the linear range. The linear range is where

$$C_{Lmin,w} < C_{Lrw}(\alpha_{rw}) < C_{Lmax,w} \quad (8.5-6)$$

From the minimum and maximum lift coefficient points, linear interpolation is taken to be  $\alpha_{rw} = \pm\pi/2$  and  $C_{L_{rw}} = 0$ . This will cause the lift coefficient to fall to zero when the flow is normal to the plane of the wing. Over these same angle-of-attack ranges, a separation drag coefficient ( $C_{D,sep}$ ) is interpolated from zero to a flat-plate drag coefficient for the wing at  $\alpha_{rw} = \pm\pi/2$ . Rearward flight, corresponding to  $|\alpha_{rw}| > \pi/2$ , is approximated by

$$C_{L_{rw}}(\alpha_{rw}) = C_{Dfp,w} \sin(2\alpha_{rw}) \quad (8.5-7)$$

$$C_{D,sep_{rw}}(\alpha_{rw}) = C_{Dfp,w} \frac{1}{2} [1 - \cos(2\alpha_{rw})] \quad (8.5-8)$$

The drag coefficient consists of the separation drag as well as the profile and induced drag,

$$C_{D,sep_{rw}} = C_{D_{0,w}} + k_w \frac{1}{2} C_{L_{rw}}^2 + C_{D,sep_{rw}}(\alpha_{rw}), \quad (8.5-9)$$

where  $C_{D_{0,w}}$  is the zero lift drag coefficient of the wing and  $k_w$  is the induced drag coefficient. Because of the way they are subsequently dimensionalized, whole airplane parameters can be used here. We take the pitching moment coefficient to be zero for the symmetric airfoil used.

Forces and moments due to the wings can now be computed. Continuing with using the right wing as our example, the dimensionalized lift and drag are found by

$$L_{rw} = C_{L_{rw}} \frac{S}{2} \bar{q}'_{rw} \quad (8.5-10)$$

$$D_{rw} = C_{D_{rw}} \frac{S}{2} \bar{q}'_{rw}, \quad (8.5-11)$$

where  $S$  is the *total* reference wing area. It is important to resolve these into the body axes separately for each wing, as they could potentially be at very different angles of attack,

$$\mathbf{F}_{A,rw}^{bf} = \begin{bmatrix} X_{rw} \\ Y_{rw} \\ Z_{rw} \end{bmatrix} = \begin{bmatrix} +L_{rw} \sin(\alpha_{rw}) - D_{rw} \cos(\alpha_{rw}) \\ 0 \\ -L_{rw} \cos(\alpha_{rw}) - D_{rw} \sin(\alpha_{rw}) \end{bmatrix} \quad (8.5-12)$$

$$\mathbf{M}_{A,rw}^{bf} = \begin{bmatrix} L_{rw} \\ M_{rw} \\ N_{rw} \end{bmatrix} = \begin{bmatrix} y_{rw} Z_{rw} \\ -x_{rw} Z_{rw} + z_{rw} X_{rw} \\ -y_{rw} X_{rw} \end{bmatrix} \quad (8.5-13)$$

The parameters used for the wing are included in Table 8.5-2.

The horizontal tail is handled as a single panel with lift and drag. First the local velocity is found,

$$\mathbf{v}_{rel,ht}^{bf} = \begin{bmatrix} U^{ht} \\ V^{ht} \\ W^{ht} \end{bmatrix} = \begin{bmatrix} U + Qz_{ht} + \eta_{ht} v_i \\ V + Rx_{ht} - Pz_{ht} \\ W - Qx_{ht} - \eta_{w \rightarrow ht} v_{i,w} \end{bmatrix}, \quad (8.5-14)$$

**TABLE 8.5-2 Aeroworks Edge Example Model Parameters: Wing**

Parameter	Value
Wing area, $S$	13.0 ft <sup>2</sup>
Lift-curve slope, $a_w$	4.6
Lift coefficient at zero angle of attack, $C_{L0,w}$	0
Maximum lift coefficient, $C_{L_{max,w}}$	1.1
Minimum lift coefficient, $C_{L_{min,w}}$	-1.1
Zero lift drag coefficient of wing, $C_{D0,w}$	0.01
Induced drag coefficient of wing, $k_w$	0.060
Drag coefficient at $\alpha = 90^\circ$ , $C_{D_{fp,w}}$	1
Aileron deflection, $\delta_a$	-0.44 to 0.44
Flap effectiveness of ailerons, $\tau_a$	0.4
Effect of prop wash on wing, $\eta_w$	0.3
Effective center, body $X$ -direction, $x_w$	0.2 ft
Effective center, body $Y$ -direction, $y_w$	2.0 ft
Effective center, body $Z$ -direction, $z_w$	0 ft

where we have once again included a factor for prop wash. This time there is also the potential for downwash from the wing when  $U^{ht} > 0$ , approximated by estimating the induced velocity of the wing at the wing,

$$v_{i,w} = \max(0, U^h) \frac{1}{2} (C_{L_{rw}} + C_{L_{lw}}) k_w \quad (8.5-15)$$

and  $\eta_{w \rightarrow ht}$  adjusts for the location of the tail within the wing downwash. If fully immersed in the downwash, then the theoretical value would be 2. Effective dynamic pressure and angle of attack for the horizontal tail are given as

$$\bar{q}'_{ht} = \frac{\rho}{2} (U^{ht2} + W^{ht2}) \quad (8.5-16)$$

$$\alpha_{ht} = \text{atan2}(W^{ht}, U^{ht}) + \tau_e \delta_e \quad (8.5-17)$$

Lift and drag of the horizontal tail are handled in the same manner as for the wing, with different parameter choices. The parameters utilized are given in Table 8.5-3.

The vertical tail is handled very much like the horizontal tail, with the exception of velocity, dynamic pressure, and angle of attack. The vertical-tail angle of attack comes from sideslip of the aircraft:

$$\mathbf{v}_{rel,vt}^{bf} = \begin{bmatrix} U^{vt} \\ V^{vt} \\ W^{vt} \end{bmatrix} = \begin{bmatrix} U + Qz_{vt} + \eta_{vt}v_i \\ V + Rx_{vt} - Pz_{vt} \\ W - Qx_{vt} \end{bmatrix} \quad (8.5-18)$$

$$\bar{q}'_{vt} = \frac{\rho}{2} (U^{vt2} + V^{vt2}) \quad (8.5-19)$$

$$\alpha_{vt} = \text{atan2}(V^{vt}, U^{vt}) + \tau_r \delta_r \quad (8.5-20)$$

The parameters utilized for the vertical tail are given in Table 8.5-4.

**TABLE 8.5-3 Aeroworks Edge Example Model Parameters: Horizontal Tail**

Parameter	Value
Area, $S_{ht}$	3.0 ft <sup>2</sup>
Lift-curve slope, $a_{ht}$	3.6
Lift coefficient at zero angle of attack, $C_{L_{0,ht}}$	0
Maximum lift coefficient, $C_{L_{max,ht}}$	1.1
Minimum lift coefficient, $C_{L_{min,ht}}$	-1.1
Zero lift drag coefficient, $C_{D_{0,ht}}$	0.01
Induced drag coefficient, $k_{ht}$	0.080
Drag coefficient at $\alpha_{ht} = 90^\circ$ , $C_{D_{fp,ht}}$	1
Elevator deflection, $\delta_e$	-0.30 to 0.30
Flap effectiveness of elevator, $\tau_e$	0.5
Effect of prop wash on horizontal tail, $\eta_{ht}$	1.6
Effect of wing downwash wash on tail, $\eta_{w \rightarrow ht}$	2.0
Effective center, body X-direction, $x_{ht}$	-3.5 ft
Effective center, body Z-direction, $z_{ht}$	0 ft

**TABLE 8.5-4 Aeroworks Edge Example Model Parameters: Vertical Tail**

Parameter	Value
Area, $S_{vt}$	1.3 ft <sup>2</sup>
Lift-curve slope, $a_{vt}$	2.5
Lift coefficient at zero angle of attack, $C_{L_{0,vt}}$	0
Maximum lift coefficient, $C_{L_{max,vt}}$	1.1
Minimum lift coefficient, $C_{L_{min,vt}}$	-1.1
Zero lift drag coefficient, $C_{D_{0,vt}}$	0.01
Induced drag coefficient, $k_{vt}$	0.084
Drag coefficient at $\alpha_{vt} = 90^\circ$ , $C_{D_{fp,vt}}$	1
Rudder deflection, $\delta_r$	-0.50 to 0.50
Flap effectiveness of rudder, $\tau_r$	0.7
Effect of prop wash on vertical tail, $\eta_{vt}$	1.6
Effective center, body X-direction, $x_{vt}$	-4.1 ft
Effective center, body Z-direction, $z_{vt}$	-0.60 ft

The aerodynamic forces and moments of the fuselage are approximated in a manner similar to that used by Heffley and Mnich (1987) for a helicopter. This method is described in greater detail below in Section 8.7 for the helicopter example. Here, it is just capturing the drag of the fuselage. Using this approach, fuselage aerodynamic force is found by

$$\mathbf{F}_{A,fuse}^{bf} = \begin{bmatrix} X_{fuse} \\ Y_{fuse} \\ Z_{fuse} \end{bmatrix} = -\frac{\rho}{2} \begin{bmatrix} X_{fuse,u} |U + 2v_i| (U + 2v_i) \\ Y_{fuse,v} |V|V \\ Z_{fuse,w} |W|W \end{bmatrix}, \quad (8.5-21)$$

where  $X_{fuse,uu}$ ,  $Y_{fuse,vv}$ , and  $Z_{fuse,ww}$  are appropriate dimensional coefficients for each basis functions, and they are given in Table 8.5-5 for the example airplane. As formulated, they are the equivalent flat-plate area for flow in each of the three basis directions. Note that the local flow effect of the propeller, in this case assumed to be located well behind the propeller, is approximated. The corresponding moment is estimated by

$$\mathbf{M}_{A,fuse}^{bf} = \begin{bmatrix} L_{fuse} \\ M_{fuse} \\ N_{fuse} \end{bmatrix} = \begin{bmatrix} -z_{fuse} Y_{fuse} \\ -x_{fuse} Z_{fuse} + z_{fuse} X_{fuse} \\ x_{fuse} Y_{fuse} \end{bmatrix}, \quad (8.5-22)$$

where  $x_{fuse}$ ,  $z_{fuse}$  is the effective center of the fuselage expressed in the body frame.

The aircraft is equipped with a fixed-pitch propeller and a two-stroke internal combustion engine. The parameters for this combination are listed in Table 8.5-6. The propeller spins clockwise as viewed from behind. Gyroscopic torques can also be computed using the parameters included here.

**TABLE 8.5-5 Aeroworks Edge Example Model Parameters: Fuselage**

Parameter	Value
X-axis force coefficient, $X_{fuse,uu}$	0.15 ft <sup>2</sup>
Y-axis force coefficient, $Y_{fuse,vv}$	1.2 ft <sup>2</sup>
Z-axis force coefficient, $Y_{fuse,ww}$	1.0 ft <sup>2</sup>
Effective center, body X-direction, $x_{fuse}$	-1.5 ft
Effective center, body Z-direction, $z_{fuse}$	0 ft

**TABLE 8.5-6 Aeroworks Edge Example Model Parameters: Engine and Propeller**

Parameter	Value
<b>Engine</b>	
Maximum power, $P_{E,max}$	90% of rated 9.8 hp
Engine speed at best power, $\Omega_{max}$	1000 rad/s
<b>Propeller</b>	
Radius, $R$	1.1 ft
Lift-curve slope, $a$	5.9
Number of blades, $b$	2
Blade effective chord, $c$	0.17 ft
Effective zero lift drag coefficient, $C_{d_0}$	0.01
Root blade pitch, $\theta_0$	0.31
Blade twist, $\theta_1$	-0.21
Inertia of rotor about spin axis, $J_p$	0.0020 slug · ft <sup>2</sup>
Location, body X-direction, $x_p$	2.2 ft
Location, body Z-direction, $z_p$	0 ft

## 8.6 QUADROTOR MODEL

This subsection contains a medium-fidelity model of a quadrotor, or multirotor with four rotors. It represents a configuration of the AscTec Pelican aircraft, which is typically modified heavily for research purposes. The aircraft is shown in Figure 8.6-1 as utilized at the Georgia Institute of Technology for navigation research (Chowdhary et al., 2011).

The mass properties used for the multirotor example are given in Table 8.6-1. The product-of-inertia terms are assumed to be negligible.

The four rotors are treated as rigid, each with independent speed control. The rotors, speed controllers, and motors are identical, with the exception that two spin clockwise as viewed from above and two counterclockwise. The parameters are listed in Table 8.6-2 for the rotors.

The combination of the motor and electronic speed controller was modeled as a first-order system for rotor angular velocity. Here, we assume the speed controller is aggressively tracking the desired angular speed command  $\sqrt{\delta_t}$ . This would correspond to a motor torque of

$$Q_E(\delta_t, \Omega) = \min \left[ J_P \left( \sqrt{\delta_t} - \Omega \right) \frac{1}{\tau_{ESC}} + Q_P, \frac{1}{\Omega} P_{E,max} \right], \quad (8.6-1)$$

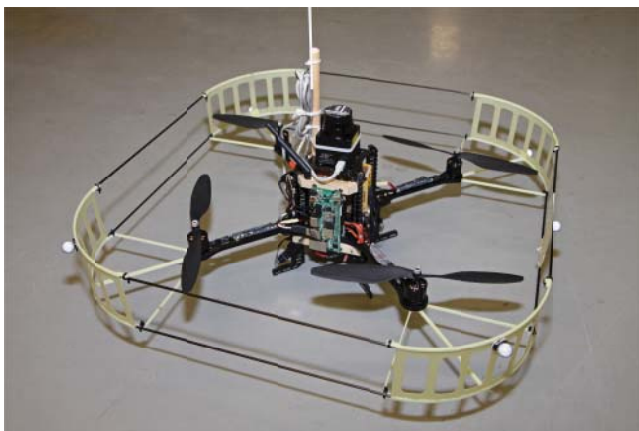


**Figure 8.6-1** Modified AscTec Pelican Quadrotor as configured at the Georgia Institute of Technology.

**TABLE 8.6-1 AscTec Pelican Example Model Parameters: Mass Properties**

Parameter	Value
Weight, $mg$	2.8 lb
X-axis Inertia, $J_x$	0.032 slug · ft <sup>2</sup>
Y-axis Inertia, $J_y$	0.032 slug · ft <sup>2</sup>
Z-axis Inertia, $J_z$	0.052 slug · ft <sup>2</sup>



**TABLE 8.6-2 AscTec Pelican Example Model Parameters: Rotor (each)**

Parameter	Value
Radius, $R$	0.42 ft
Lift-curve slope, $a$	5.7
Number of blades, $b$	2
Blade effective chord, $c$	0.09 ft
Effective zero lift drag coefficient, $C_{d0}$	0.01
Root blade pitch, $\theta_0$	0.49
Blade twist, $\theta_1$	-0.33
Inertia of rotor about spin axis, $J_p$	0.000030 slug · ft <sup>2</sup>
Location, body $X$ -direction, $x_p$	±0.49 ft
Location, body $Y$ -direction, $y_p$	±0.49 ft
Location, body $Z$ -direction, $z_p$	0 ft

**TABLE 8.6-3 AscTec Pelican Example Model Parameters: Motor and Speed Control (each)**

Parameter	Value
Maximum power, $P_{Emax}$	0.21 hp
Time constant for electronic speed control, $\tau_{ESC}$	0.05 s

which results in a first-order lag for angular speed tracking (if torque does not hit power limit) of the form

$$\dot{\Omega} = \left( \sqrt{\delta_t} - \Omega \right) \frac{1}{\tau_{ESC}} \quad (8.6-2)$$

The parameters used are listed in Table 8.6-3. In practice, the propeller/rotor torque  $Q_p$  in Equation (8.6-1) would come from the integration of tracking error within the speed controller. Because thrust tends to be proportional to  $\Omega^2$  rather than  $\Omega$ , this non-linearity is approximately accounted for by viewing  $\delta_t$  as the square of commanded angular speed. This is also handled by the speed controller.

## 8.7 SMALL HELICOPTER MODEL

This subsection contains a medium-fidelity model of a small helicopter based on a configuration of the Yamaha RMAX aircraft. It was specifically configured at the Georgia Institute of Technology as a research aircraft (Johnson and Schrage, 2004). This included the addition of instrumentation and processing capabilities. The aircraft is shown in Figure 8.7-1. The aircraft is primarily intended for agricultural applications. Simulation results utilizing this model are included in Section 9.5.

The mass properties used for the example are given in Table 8.7-1. The product-of-inertia terms are assumed to be negligible.



**Figure 8.7-1** Yamaha RMAX as configured at the George Institute of Technology.

**TABLE 8.7-1 Yamaha RMAX Example Model Parameters: Mass Properties**

Parameter	Value
Weight, $mg$	166 lb
X-axis Inertia, $J_x$	$2.3 \text{ slug} \cdot \text{ft}^2$
Y-axis Inertia, $J_y$	$8.3 \text{ slug} \cdot \text{ft}^2$
Z-axis Inertia, $J_z$	$7.3 \text{ slug} \cdot \text{ft}^2$

The main rotor is modeled with first-order flapping dynamics with a nonzero effective hinge offset. The parameters for this main rotor with stabilizer bar are given in Table 8.7-2. Note that this rotor spins clockwise as viewed from above.

The tail rotor is modeled as rigid, with parameters given in Table 8.7-3. Note the necessity to adapt the thrust calculations for the case where the rotor is pointed along the body  $Y$ -axis. The thrust is defined as positive to the left in this case, due to the clockwise spinning rotor. By making this choice, tail rotor thrust is normally positive. As is common for small helicopters, the yaw handling qualities are improved by providing a rate feedback to augment the tail rotor pitch command. Here, this is modeled with

$$\theta_{0,\text{augmented}} = \theta_0 - K_{SAS}R, \quad (8.7-1)$$

where  $R$  is the measured body-fixed axis yaw angular velocity and  $K_{SAS}$  is the fixed feedback gain.

**TABLE 8.7-2 Yamaha RMAX Example Model Parameters: Main Rotor**

Parameter	Value
<b>Main Rotor</b>	
Radius, $R$	5.1 ft
Normal rotor speed, $\Omega$	90 rad/s
Lift-curve slope, $a$	5.7
Number of blades, $b$	2
Blade effective chord, $c$	0.43 ft
Effective hinge offset, $e$	0.2 ft
Effective Inertia of a blade about flapping hinge, $I_{Bf}$	1.0 slug · ft <sup>2</sup>
Inertia of complete rotor system about spin axis, $J_P$	2.0 slug · ft <sup>2</sup>
Effective zero lift drag coefficient, $C_{d_0}$	0.01
Root blade pitch (collective) of zero lift line, $\theta_0$	0.12 to 0.30
Blade twist, $\theta_1$	−0.1
Cyclic pitch, $\delta_{pitch}$ or $\delta_{roll}$	−0.12 to 0.12
Location, body X-direction, $x_{P,mr}$	0 ft
Location, body Z-direction, $z_{P,mr}$	−1.4 ft
<b>Main Rotor Stabilizer Bar</b>	
Outer radius of paddle, $R_{S,outer}$	2.1 ft
Inner radius of paddle, $R_{S,inner}$	1.5 ft
Lift-curve slope, $a_S$	2.8
Blade effective chord, $c_S$	0.35 ft
Effective Inertia of a blade about flapping hinge, $I_{Sf}$	0.24 slug · ft <sup>2</sup>
Cyclic pitch of stabilizer bar per cyclic pitch to main rotor, $K_{C \rightarrow S}$	4.5
Cyclic pitch of main rotor per flap of the stabilizer bar, $K_{S \rightarrow C}$	0.33

**TABLE 8.7-3 Yamaha RMAX Example Model Parameters: Tail Rotor**

Parameter	Value
Radius, $R$	0.69 ft
Lift-curve slope, $a$	5.0
Number of blades, $b$	2
Blade effective chord, $c$	0.15 ft
Effective zero lift drag coefficient, $C_{d_0}$	0.01
Root blade pitch, $\theta_0$	0.0 to 0.30
Blade twist, $\theta_1$	0
Stability augmentation system gain, $K_{SAS}$	0.06 s
Location, body X-direction, $x_{P,tr}$	−6.04 ft
Location, body Z-direction, $z_{P,tr}$	−0.47 ft

**TABLE 8.7-4 Yamaha RMAX Example Model Parameters: Engine and Transmission**

Parameter	Value
Maximum power, $P_{E,max}$	90% of rated 21 hp
Engine speed at best power, $\Omega_{max}$	680 rad/s
Engine RPM per main rotor RPM	7.55 : 1
Tail rotor RPM per main rotor RPM	6.71 : 1

The aerodynamic forces and moments of the tail and fuselage can be modeled in the same manner as an airplane tail and fuselage. However, it is clearly important to include sideways and rearward flight. So, if lookup tables are to be used, then they need to include the full possible range of angle of attack and sideslip. To the extent that rotor forces and moments are expected to dominate, an appropriate medium-fidelity approach is used, inspired by Heffley and Mních (1987), which utilizes appropriate nonlinear basis functions. It is interesting to note that this is also a common approach to model airship or submarine hulls (Feldman, 1979).

Using this approach, fuselage aerodynamic force is found by

$$\mathbf{F}_{A,fuse}^b = \begin{bmatrix} X_{fuse} \\ Y_{fuse} \\ Z_{fuse} \end{bmatrix} = -\frac{\rho}{2} \begin{bmatrix} X_{fuse,uu} |U| U \\ Y_{fuse,vv} |V| V \\ Z_{fuse,ww} |W - v_i|(W - v_i) \end{bmatrix}, \quad (8.7-2)$$

where  $X_{fuse,uu}$ ,  $Y_{fuse,vv}$ , and  $Z_{fuse,ww}$  are appropriate dimensional coefficients for each basis function. As formulated, they are the equivalent flat-plate area for flow in each of the three basis directions. Note that the local flow effect of the main rotor, in this case assumed to be located just under the rotor, is approximated. The corresponding moment is estimated by

$$\mathbf{M}_{A,fuse}^b = \begin{bmatrix} L_{fuse} \\ M_{fuse} \\ N_{fuse} \end{bmatrix} = \begin{bmatrix} -z_{fuse} Y_{fuse} \\ -x_{fuse} Z_{fuse} + z_{fuse} X_{fuse} \\ x_{fuse} Y_{fuse} \end{bmatrix}, \quad (8.7-3)$$

where  $x_{fuse}$ ,  $z_{fuse}$  is the effective center of the fuselage expressed in the body frame.

This approach applied to a horizontal or vertical tail is just slightly more involved due to the lift generation of these surfaces. Although a conventional Yamaha RMAX does not have a horizontal tail, the equations are included here for completeness and because the Yamaha RMAX configuration documented here had a small horizontal tail added to it (Figure 8.7-1).

The velocity of the vertical tail with respect to the local airflow is approximated by

$$\begin{bmatrix} U^{vt} \\ V^{vt} \\ W^{vt} \end{bmatrix} = \begin{bmatrix} U + Qz_{vt} \\ V + Rx_{vt} - Pz_{vt} + v_{i,tr} \\ W - Qx_{vt} \end{bmatrix}, \quad (8.7-4)$$

where  $x_{vt}$ ,  $z_{vt}$  are the effective aerodynamic centers of the vertical tail expressed in the body frame. We have assumed that the vertical tail is close to the tail rotor and entirely within its downwash ( $v_{i,tr}$ ). Only the lateral component of the vertical-tail aerodynamic force is included here,

$$Y_{vt} = -\frac{\rho}{2}(Y_{vt,uv}|U^{vt}|V^{vt} + Y_{vt,vv}|V^{vt}|V^{vt}), \quad (8.7-5)$$

where  $Y_{vt,uv}$  acts as the product of the effective lift-curve slope and the area of the vertical tail and  $Y_{vt,vv}$  as the equivalent flat-plate area. To account for the potential of the vertical tail exceeding an angle of attack that would result in flow separation, the magnitude of this side force is further limited by

$$Y_{vt,limit} = \pm \frac{\rho}{2} Y_{vt,VV,max} (U^{vt2} + V^{vt2} + W^{vt2}), \quad (8.7-6)$$

where  $Y_{vt,VV,max}$  is effectively the product of the maximum lift coefficient and area of the vertical tail. The aerodynamic side force acting at the vertical tail results in the moment

$$\begin{bmatrix} L_{vt} \\ M_{vt} \\ N_{vt} \end{bmatrix} = \begin{bmatrix} -z_{vt} Y_{vt} \\ 0 \\ x_{vt} Y_{vt} \end{bmatrix} \quad (8.7-7)$$

The horizontal tail is handled in the same manner, with an appropriate change in axes:

$$\begin{bmatrix} U^{ht} \\ V^{ht} \\ W^{ht} \end{bmatrix} = \begin{bmatrix} U + Qz_{ht} \\ V + Rx_{ht} - Pz_{ht} \\ W - Qx_{ht} - v_i \end{bmatrix}, \quad (8.7-8)$$

where  $x_{ht}$ ,  $z_{ht}$  are the effective aerodynamic centers of the horizontal tail expressed in the body frame. Here, we assume the horizontal tail is located close to the main rotor and entirely within its downwash ( $v_i$ ). Only the vertical component of the horizontal-tail aerodynamic force is found by

$$Z_{ht} = -\frac{\rho}{2}(Z_{ht,uw}|U^{ht}|W^{ht} + Z_{ht,ww}|W^{ht}|W^{ht}) \quad (8.7-9)$$

Again, we verify this surface does not exceed the force limit

$$Z_{ht,limit} = \pm \frac{\rho}{2} Z_{ht,VV,max} (U^{ht2} + V^{ht2} + W^{ht2}) \quad (8.7-10)$$

This aerodynamic force component acting at the horizontal tail results in the moment

$$\begin{bmatrix} L_{ht} \\ M_{ht} \\ N_{ht} \end{bmatrix} = \begin{bmatrix} 0 \\ -x_{ht} Z_{ht} \\ 0 \end{bmatrix} \quad (8.7-11)$$

The parameters used to populate this aerodynamic model for the example are included in Table 8.7-5.

**TABLE 8.7-5 Yamaha RMAX Example Model Parameters: Fuselage and Tail**

Parameter	Value
<b>Fuselage</b>	
X-axis force coefficient, $X_{fuse,uu}$	2.3 ft <sup>2</sup>
Y-axis force coefficient, $Y_{fuse,vv}$	7.8 ft <sup>2</sup>
Z-axis force coefficient, $Y_{fuse,ww}$	7.0 ft <sup>2</sup>
Effective center, body X-direction, $x_{fuse}$	0 ft
Effective center, body Z-direction, $z_{fuse}$	0 ft
<b>Vertical Tail</b>	
Y-axis force coefficient, $Y_{vt,uv}$	0.69 ft <sup>2</sup>
Y-axis force coefficient, $Y_{vt,vv}$	0.23 ft <sup>2</sup>
Y-axis force coefficient, $Y_{vt,vv,limit}$	0.23 ft <sup>2</sup>
Effective center, body X-direction, $x_{vt}$	-6.2 ft
Effective center, body Z-direction, $z_{vt}$	-0.78 ft
<b>Horizontal Tail (not normally included on RMAX)</b>	
Z-axis force coefficient, $Z_{ht,uw}$	1.9 ft <sup>2</sup>
Z-axis force coefficient, $Z_{ht,ww}$	0.63 ft <sup>2</sup>
Z-axis force coefficient, $Z_{ht,vv,limit}$	0.63 ft <sup>2</sup>
Effective center, body X-direction, $x_{ht}$	-2.5 ft
Effective center, body Z-direction, $z_{ht}$	-0.59 ft

## 8.8 SUMMARY

This chapter expanded on the coverage of aerodynamic models for aircraft to include elements necessary to address miniature aircraft. This included coverage of the necessary concepts to understand typical small helicopters, airplanes, and multirotor configurations; computation of the thrust and force of propellers and rotors in hover as well as in forward flight; and modeling of motors and engines typical for small aircraft. There was coverage of the flapping dynamics of helicopter rotors and the use of the stabilizer bar.

Three specific small aircraft examples were provided that make use of the new elements introduced in the chapter.

The first example was the small aerobatic airplane. This airplane is able to transition to hover and act as a “tail sitter” configuration. A model for such a vehicle must address motion in every direction, including sitting still. This necessitated at least approximating the effect of slideslip and angle of attack for their full possible range.

The second example was a multirotor configuration. Here, a typical propeller model becomes a lifting rotor. It was necessary to handle four such rotors for the quadrotor presented. This example utilized electric motors.

The third example, a small unmanned helicopter, added the complexities of a flapping main rotor with a stabilizer bar and a tail rotor as well as the complexities of a transmission, where the modeler must keep track of multiple shaft rates.

## REFERENCES

- Abbot, I. H., and A. E. Von Doenhoff. *Theory of Wing Sections*. Mineola, NY: Dover, 1959.
- Anderson, J. D. *Introduction to Flight*. New York: McGraw-Hill, 2008.
- Chowdhary, G. V., et al. "Integrated Guidance Navigation and Control for a Fully Autonomous Indoor UAS." *Proceedings of the AIAA Guidance, Navigation, and Control Conference*. Washington, D.C.: AIAA, 2011.
- Chen, R. T. N., and W. S. Hindson. "Influence of Dynamic Inflow on the Helicopter Vertical Response." *NASA TM 88327*. Washington, D.C.: NASA, 1986.
- Dreier, M. E. *Introduction to Helicopter and Tiltrotor Flight Simulation*. Washington, D.C.: AIAA, 2007.
- Feldman, J. *DTNSRDC Revised Standard Submarine Equations of Motion*. SPD-0393-09. David W. Taylor Naval Ship Research and Development Center, 1979.
- Heffley, R. K., and M. A. Mnich. "Minimum-Complexity Helicopter Simulation Math Model" *NASA CR 177476 (and USAAVSCOM TR 87-A-7)*, Washington, D.C.: NASA, 1987.
- Heffley, R. K., S. M. Bourne, H. C. Curtis, W. S. Hindson, and R. A. Hess. "Study of Helicopter Roll Control Effectiveness Criteria." *NASA CR 177404 (and USAAVSCOM TR 85-A-5)*. Washington, D.C.: NASA, 1986.
- Johnson, E. N., and D. P. Schrage. "System Integration and Operation of a Research Unmanned Aerial Vehicle." *AIAA Journal of Aerospace Computing, Information, and Communication*, Washington, D.C.: AIAA, 1, no. 1 (January 2004): 5–18.
- Johnson, E. N., M. A. Turbe, A. D. Wu, S. K. Kannan, and J. C. Neidhoefer. "Flight Test Results of Autonomous Fixed-Wing Transition to and from Stationary Hover." *AIAA Journal of Guidance, Control, and Dynamics*, Washington, D.C.: AIAA, Vol. 31, no. 2 (March/April 2008): 358–370.
- Leishman, J. G. *Principles of Helicopter Aerodynamics*. Cambridge, U.K.: Cambridge University Press, 2006.
- McCormick, B. W. *Aerodynamics of V/STOL Flight*. Mineola, NY: Dover, 1998.
- Mettler, B. *Identification Modeling and Characteristics of Miniature Rotorcraft*. Dordrecht, the Netherlands: Kluwer Academic Publishers, 2003.
- Perkins, C. D., and R. E. Hage. *Airplane Performance Stability and Control*. New York: Wiley, 1949.
- Phillips, W. F. *Mechanics of Flight*. Hoboken, N.J.: Wiley, 2010.
- Prouty, R. W. *Helicopter Performance, Stability, and Control*. Malabar, FL: Krieger, 1986.
- Simons, M. *Model Aircraft Aerodynamics*. 4th ed., Poole, Dorset, U.K.: Nexus Special Interests, 1999.
- Stepniewski, W. Z., and C. N. Keys. *Rotary-Wing Aerodynamics*. Mineola, NY: Dover, 1984.
- Stingu, P. E. *Intelligent Control and Cooperation for Mobile Robots*. Ph.D. thesis. University of Texas at Arlington, 2011.

## PROBLEMS

### Section 8.1

- 8.1-1** (a) Describe the difference between a propeller and a rotor.  
 (b) Describe the difference between an engine and a motor.

- 8.1-2** Some multirotor configurations only have three rotors. Describe how they can achieve independent roll, pitch, yaw, and thrust control.

## Section 8.2

- 8.2-1** Using the thrust and induced power computations presented in this section, find an exact solution for thrust and power for the special case of hover over a fixed point with no wind.
- 8.2-2** The magnitude of the induced velocity of a rotor positively correlates with required power, noise, and (for a VTOL aircraft) kicking up dust and debris when hovering close to the ground. For a given thrust required, what parameter associated with the design of the aircraft do we expect to provide the greatest potential to reduce the induced velocity for a single-rotor helicopter? How about a multirotor?
- 8.2-3** A gyrocopter looks similar to a helicopter. It lacks a tail rotor and instead has an engine-driven propeller mounted longitudinally to provide forward thrust. The main rotor is not powered by the engine. For a helicopter, the main rotor disk is tilted forward as it flies. For a gyrocopter, the main rotor is tilted backward as it flies. Explain why this is so.
- 8.2-4** Derive Equations (8.2-17) and use them to determine an appropriate linear twist distribution ( $\theta_0$  and  $\theta_1$ ) for a 9x7 propeller.
- 8.2-5** Having a propeller in the back of an airplane leads to greater directional stability than having the propeller in the front. Estimate the equivalent change to the nondimensional stability derivative associated with directional static stability  $C_{n_\beta}$  due to the propeller, accounting for mounting location ( $x_p$ ).
- 8.2-6** Some aircraft in the early twentieth century had most of the engine, including all of the cylinders, rotate along with the propeller. This is sometimes called a *rotary* engine. This had a profound effect on the motion of the aircraft when turns were attempted, particularly on these light single-engine aircraft. Identify the source of the phenomenon and provide an estimate of the unexpected moments.

## Section 8.3

- 8.3-1** Observe that the first-order tip path dynamics presented in this section do not depend on the number of blades. This implies that one could increase the number of blades (perhaps to increase thrust) and do nothing to the flapping motion. Defend that this is possible. Would a single rotor (with a counterweight) have the same motion as well?
- 8.3-2** Using the first-order flapping dynamics for the stabilizer bar presented, derive a corresponding expression for the main rotor flapping angles using the approximation that the main rotor time constant is negligibly small. That is, we treat the main rotor flapping as responding instantly to input.



## Section 8.4

- 8.5-1 Estimate the power of a well-designed four-stroke internal combustion engine with 360 cubic inches of displacement running and 2500 RPM at sea level.
- 8.5-2 Explain what happens to torque when transferred from one shaft to another where the second is geared to turn twice as fast as the first. Explain what happens to power when going through the same transfer.

## Section 8.5

- 8.5-1 Defend the premise that the lift coefficient of a wing with an angle of attack of between  $90^\circ$  and  $180^\circ$  should be less than zero.
- 8.5-2 Provide an expression to use for gyroscopic torque to include in this model. Will it be significant?
- 8.5-3 Propeller wash over the fuselage can have a twist that leads to moments on the aircraft. Suggest a model change that might approximate the effect, perhaps with an appropriate unknown parameter to be determined by experiment.

## Section 8.6

- 8.6-1 Static thrust is the thrust when the aircraft is not moving. Estimate the total static thrust of the aircraft described in this section.
- 8.6-2 Some multirotor aircraft have the rotors canted/tilted slightly. The tilt is usually toward the center of the aircraft. Describe what effect this will have if the aircraft has forward speed.
- 8.6-3 Suggest a stability augmentation system (SAS) design for this example that utilizes only angular rate feedback. You may consider fixed gain or a dynamic compensator.

## Section 8.7

- 8.7-1 The Yamaha RMAX does not normally have a horizontal tail. One was added to an aircraft to hold an antenna and a sensor. Using the parameters provided as well as the methods included in this chapter, estimate the downward force on this surface in a hover.
- 8.7-2 Suggest an alternate design for the aircraft without the stabilizer bar and the addition of a stability augmentation system (SAS) that makes the aircraft behave as though it has a stabilizer bar. The emphasis should be on the design of the SAS, not the mechanics of the rotor head.

## CHAPTER 9

---

# ADAPTIVE CONTROL WITH APPLICATION TO MINIATURE AERIAL VEHICLES

---

### 9.1 INTRODUCTION

In this chapter, we build on nonlinear control methods introduced in Chapter 5 (Modern Control Techniques) by including ideas from adaptive control. We are motivated by the fact that many methods for control rely on an accurate model of the aircraft dynamics. The dynamic inversion methods introduced in Chapter 5 are an example, where an accurate model is required to achieve a desired reference model response. A highly accurate model is very difficult to achieve in practice. Allowing that model to be corrected and improved while the controller is in operation could address this issue.

A controller that automatically adjusts the feedforward or feedback gains is an *adaptive* controller. The basic idea that an adaptive controller could be adjusted automatically to maximize performance is nearly as old as automatic control itself. One of the early important examples of adaptive controllers being applied to flight control was an experimental controller tested as part of the NASA X-15 program in 1967 (Dydek et al., 2010). Test pilot Michael Adams was killed during one such test. Although the adaptive controller worked as intended during many flights, for this fatal flight the adaptive controller was partially implicated in the accident. So, although adaptation has the potential to increase reliability and performance, it clearly also has potential pitfalls. In the years that have followed, a large number of new potential adaptive control methods have been proposed and utilized for flight control. However, none has achieved anywhere near the level of trust in the aerospace community as nonadaptive flight control.

One method to increase trust in an adaptive control approach is to utilize methods that have an associated mathematical proof of stability or at least boundedness of

system signals. The existing examples tend to be highly conservative, to the point where the limits implied are of little practicality. However, the existence of a stability proof is clearly better than the absence of one. The methods discussed in this chapter are of this class. Because the approach focused on in this chapter has been applied to more than 1000 flights of many different types of miniature aircraft over twelve years of diverse flight operations, this method represents one of the most heavily verified adaptive flight control methods.

Although any control system could potentially benefit from an adaptive control perspective, unmanned aerial vehicle flight control can obtain several specific advantages that are uniquely important. The lack of a human pilot means that the ability of the human controller to provide adaptation is often not available. It may be possible to regain some of the reliability benefit by allowing adaptation within the control system itself. This need for adaptation may arise from either uncertainty in the vehicle behavior (itself perhaps typically larger for aircraft that are unmanned) or damage/faults.

In this chapter, deviations from a reference model are utilized to enable a dynamic inversion approach to adjust the controller response over time. Due to the fact that the controller gains are changing, we can recognize this is an adaptive control method. The basis of this gain adjustment depends upon a comparison between expected (reference) and actual responses. Due to this last property, this is also an example of model reference adaptive control (MRAC).

Within the realm of adding adaptation to a dynamic inversion flight control law, we will illustrate that we have effectively formulated a real-time nonlinear curve-fitting problem. We will then explore the specific case of utilizing artificial neural networks (NNs) as a proven method to perform this fitting.

The sections that follow will then cover a number of important realistic implementation issues that arise when attempting to implement an adaptive flight controller. This will start with the issue of limited authority (including input saturation) as well as accounting for a multiloop architecture that is common for automated guidance and flight control systems. For example, it is not unusual to see an attitude controller used by a position tracking guidance system. If one or both of these interconnected feedback control systems are adaptive, then this must be accounted for in the design.

A detailed example of adaptive guidance and flight control of a quadrotor and a small unmanned helicopter follows. This will include a discussion of several important implementation considerations, simulation results (using a model from Chapter 8), and flight test results. These implementation considerations will include observers for unmeasured states (Chapter 6) and digital control considerations from Chapter 7.

## **9.2 MODEL REFERENCE ADAPTIVE CONTROL BASED ON DYNAMIC INVERSION**

In Chapter 5.8, the method of dynamic inversion was described for control of nonlinear systems. For this method, the true dynamics of the aircraft were replaced

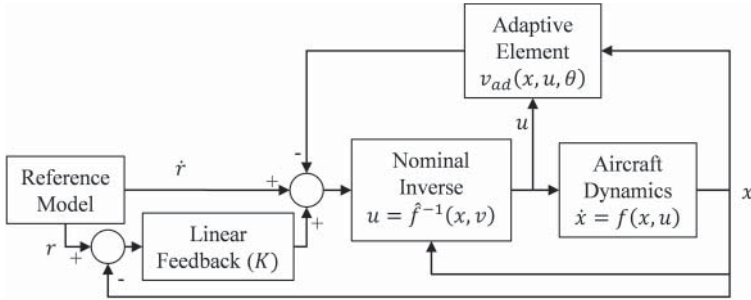


**Figure 9.2-1** Use of adaptation to correct model error in a dynamic inversion controller.

by desired dynamics through feedback. In this section, we look at addressing one of the most significant issues with this approach: the availability of an accurate model of the aircraft dynamics. Here, we attack the problem by refining the dynamics model used in the dynamic inversion controller in real time. This means that gains will be changing within the controller in response to changes in the aircraft (or differences between the true aircraft and the assumed model).

An illustration of such a controller is shown in Figure 9.2-1. Here, the architecture similar to that shown in Figure 5.8-5 is simplified to the special case of full state feedback and an adaptive component is added. This architecture includes a “nominal” controller based on the best available information about the aircraft dynamics embodied in the design. The adaptive element then works on the error in this nominal model and provides a correction. This correction can be an arbitrarily accurate correction given sufficient training information, sufficient inputs to the correction block in the form of states and inputs, and sufficient power in the adaptive element to curve fit this model error. Let the plant be described by

$$\dot{x} = f(x, u), \quad (9.2-1)$$

with state  $x \in R^n$  and  $u \in R^m$ . The nominal dynamic inverse needs to be of a similar form, but we distinguish here between the true plant dynamics in (9.2-1) and a known approximation to it of the form

$$v = \hat{f}(x, u), \quad (9.2-2)$$

with *pseudocontrol* signal  $v \in R^n$  as the “desired”  $\dot{x}$ . These dynamics are then inverted to find the plant input

$$u = \hat{f}^{-1}(x, v), \quad (9.2-3)$$

where the existence and uniqueness of this inverse are important points for further consideration below. For the moment, we will assume that there exists a set of inputs that will achieve our desired  $\dot{x}$  at the current state  $x$  and limit ourselves to the issue that  $f \neq \hat{f}$  in general.

When one introduces the adaptive element in the controller, it will ideally be a function of both the states and inputs of the original system [Equation (9.2-1)]. The total pseudocontrol input used in (9.2-3) will now have three components:

$$v = \dot{r} + Ke - v_{ad}(x, u, \theta), \quad (9.2-4)$$

where the  $\dot{r}$  term represents the desired response, the  $Ke$  term a linear feedback on the tracking error, and  $v_{ad}$  the new adaptive signal. In addition to all original system states and inputs, the latter includes internal parameters  $\theta$ .

By including  $v_{ad}$  in this way, a clear definition of  $v_{ad}$  emerges as the model error in the nominal controller design. To see this, we consider the reference model tracking error dynamics ( $e$ ). This can be written as

$$\begin{aligned} e &= r - x \\ \dot{e} &= \dot{r} - \dot{x} \end{aligned} \quad (9.2-5)$$

Substituting for  $\dot{x}$  using (9.2-1), (9.2-3), and (9.2-4) we find

$$\dot{e} = \dot{r} - f(x, u) = \dot{r} - \hat{f}(x, u) - f(x, u) + \hat{f}(x, u) \quad (9.2-6)$$

$$\dot{e} = -Ke + v_{ad}(x, u, \theta) - f(x, u) + \hat{f}(x, u) \quad (9.2-7)$$

We now have a useful definition for what we would like our adaptive controller to converge to. We seek to achieve the chosen linear tracking error dynamics ( $K$ ) by exact cancellation of the model error through adjustment of parameters  $\theta$ :

$$\dot{e} = -Ke \quad (9.2-8)$$

$$v_{ad}(x, u, \theta) = f(x, u) - \hat{f}(x, u) \quad (9.2-9)$$

We see explicitly in (9.2-9) that this is an exercise in nonlinear curve fitting. Specifically, we need to achieve a curve fit of the model error as a function of state and input.

This is a particularly powerful adaptive controller architecture in the sense that it can, in principle, adjust internal parameters in order to achieve desired dynamics for an unknown nonlinear system. As a practical matter, it is sufficient that the controller is able to fully correct for errors in the subset of the input and state space that the aircraft has experienced. We might also be satisfied in many cases with being able to adjust only to the recently experienced subset of the input and state space. That is, it may be acceptable for the controller to “forget” information about aspects of the aircraft no longer prevailing. One criterion for this being acceptable would be the ability of the controller to respond sufficiently fast when encountering new information. In this way, we distinguish between *long-term learning*, where we achieve improved performance if we return to a part of the state space that the vehicle has experienced before, and *short-term learning*, where the controller must readapt upon returning to previous portions of the state space.

In the next section, a specific method to achieve short-term learning is presented based on the concept of the artificial neural network. This construct has been used successfully in many curve-fitting applications. Within this adaptive control architecture, it could be referred to as neural network adaptive control.

### 9.3 NEURAL NETWORK ADAPTIVE CONTROL

A method that can be used to perform the curve fitting motivated in the previous section (9.2-9) is the artificial NN, of which there are many varieties. This section includes a description of several of the most common NN formulations utilized in adaptive control. For starters, a useful distinction for classifying these NN formulations is *parametric* NN vs. *nonparametric* NN (Lewis et al., 1999), as shown in Figure 9.3-1.

In the parametric NN, model error has a known basis function with one or more unknown parameters. For example, the functional form of the effectiveness of an airplane rudder may be known to sufficient accuracy, but the designer may want to account for an unknown scale and/or bias error. In this case, the adaptive signal can be written as

$$v_{ad}(x, u, \theta) = \sum_{i=1}^{Np} [\theta_i \Delta f_i(x, u)], \quad (9.3-1)$$

where  $Np$  is the number of basis functions and  $\Delta f_i(x, u)$  are the basis functions. Inclusion of a constant basis function would allow for the correction of a bias error. The inclusion of a basis function proportional to the rudder input would allow for the correction of a scale factor error.

In the nonparametric NN the designer does not explicitly include knowledge about the functional form of the model error. Here, sufficient parameterization is included to allow the NN to perform the curve fit to desired accuracy, even for a nonlinear system. One way to do this is inspired by how biological NNs work in the brain. In practice, the complexity level needed is small compared to that found in biology.

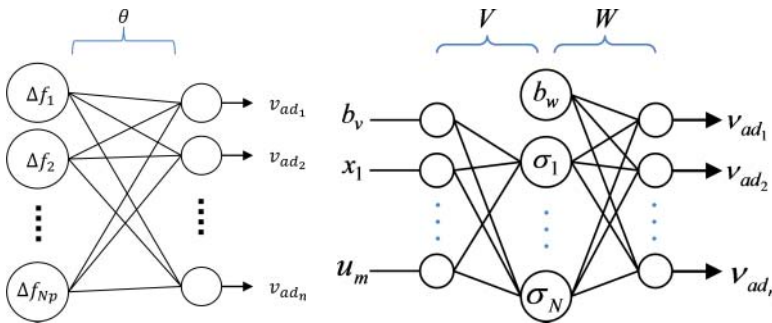


Figure 9.3-1 Parametric (left) and nonparametric (right) NN structures.

Specifically, biology inspires the idea of utilizing interconnections between *neurons* (Figure 9.3-1). In this case, the single hidden layer (SHL) NN is illustrated (Lewis et al., 1996, 1997). That is, there is one/single layer of neurons between the input layer and the output layer. Another important approach utilizes radial basis functions (RBFs) (Lavretsky and Wise, 2013). For the SHL, a *squashing function* is utilized at the hidden layer neurons, such as

$$\sigma_j(z) = \frac{1}{1 + e^{-a_j z}}, \quad (9.3-2)$$

for  $j = 1, \dots, N$ , with the value  $a_j$  chosen to be distinct for each  $j$ , where  $N$  is the number of hidden layer neurons. Using this, the full SHL NN can be written as

$$v_{ad}(x, u, \theta) = W^T \sigma(V^T \bar{x}), \quad (9.3-3)$$

where  $W \in R^{N \times n}$  are the output weights,  $V \in R^{n+m+1 \times N}$  are the input weights, and  $\bar{x} \in R^{n+m+1}$  is the input to the NN, normally the states  $x$ , plant inputs  $u$ , and a bias. The complete set of the elements of  $W$  and  $V$  are the NN adjustment parameters.

### Universal Approximation Theorem

One question that comes up is the choice of the number of hidden layer neurons ( $N$ ). With a very small number, it is clear by inspection that there may be insufficient capability to curve fit a reasonable model error function. Adding additional hidden layer neurons will certainly improve this curve-fitting capability. However, there will clearly be diminishing returns if the number increases beyond some level. In practice, it has been found that the incremental benefit is not particularly great beyond  $N = 5$  for the types of flight control problems addressed here, which is the number used in all work included in this chapter.

The *universal approximation theorem* for the SHL NN tells us that we can bound the fitting error within a compact set of states and plant inputs. Significantly, it can be achieved for any chosen error bound by adding additional middle layer neurons ( $N$ ) to the NN (Cybenko, 1989).

There are many examples in the literature of proofs of boundedness of all system signals for these types of controllers. These proofs typically involve a Lyapunov function candidate and invoking the universal approximation theorem to show that the Lyapunov candidate decreases outside of a compact set. This ensures convergence to a set containing zero tracking error (Yesildirek and Lewis, 1995; Kim and Lewis, 1998; Johnson and Calise, 2003; Lavretsky and Wise, 2013).

Very often, considerations of the proof of boundedness will inspire the adaptive laws themselves. A typical approach to training the NN that comes directly from a proof of boundedness is (Johnson and Calise, 2003)

$$\dot{W} = -[(\sigma - \sigma' V^T \bar{x})e^T + \lambda \|e\| W] \Gamma_W \quad (9.3-4)$$

$$\dot{V} = -\Gamma_V [\bar{x} e^T W^T \sigma' + \lambda \|e\| V], \quad (9.3-5)$$

where  $\Gamma_w$  and  $\Gamma_v$  are appropriately dimensioned diagonal matrices of learning rates. The matrix  $\sigma'$  is the gradient of  $\sigma$ . The e-modification scalar  $\lambda > 0$  is necessary for the associated boundedness theorem proof. Note the important role of tracking error ( $e$ ) here. When tracking error is zero, these parameters do not change.

**Example 9.3-1: Neural Network Adaptive Controller** In this example, a first-order system with significant model error is controlled using a SHL NN to provide adaptation. This corresponds to pitch-rate control of an aircraft with a significant unknown nonlinearity in pitch damping using the elevator. For the purposes of this example, the true dynamics are taken as

$$\dot{q} = M_q q + M_{\delta_e} \delta_e + \sin q, \quad (9.3-6)$$

where the last term,  $\sin q$ , represents an unanticipated fault as is entirely unknown during controller design. As a result, the approximate dynamic inverse is missing this term,

$$\delta_e = \frac{1}{M_{\delta_e}}(v - M_q q), \quad (9.3-7)$$

with pseudocontrol input corresponding to the derivative of pitch rate.

The following MATLAB code is able to simulate the results of such a controller:

```
% parameter choices
dt = 0.05; tfinal = 50; tswitch = 5;
Mdelta = -10; Mq = -1;
K = -1;
gammaw = 1; gammav = 10;
lambda = 0.01;
nmid = 5; nin = 3;
amin = 0.01; amax = 10;

% precompute activation potentials
a = zeros(nmid,1);
for i=1:nmid-1,
    a(i) = tan( atan(amin) + ( atan(amax) - atan(amin) )*(i+1)
               /nmid );
end;

% preallocate arrays
points = tfinal/dt + 1;
t = zeros(points,1); r = zeros(points,1);
x = zeros(points,1); u = zeros(points,1);
w = zeros(points,nmid); wdot = zeros(1,nmid);
v = zeros(points,nmid*nin); vdot = zeros(1,nmid*nin);
rdot = zeros(1,1); xdot = zeros(1,1);
Wdot = zeros(1,nmid); W = zeros(1,nmid);
Vdot = zeros(nmid,nin); V = zeros(nmid,nin);
xbar = zeros(nin,1);
sig = zeros(nmid,1); sigp = zeros(nmid,nmid);
```



```

for i=1:points,
    t(i)=(i-1)*dt;

    % external input
    if mod(t(i),2*tswitch)<tswitch, externalInput = 1;
    else                               externalInput = -1;
    end;

    % reference model
    rdot = -K*( externalInput - r(i,1) );

    % error signals
    e = r(i,1) - x(i,1);

    % NN inputs
    if i>1, oldu = u(i-1);
    else oldu = 0; end;
    xbar(1) = 1;
    xbar(2) = x(i,1);
    xbar(3) = oldu;

    % get weights from state vector
    W = w(i,:);
    for j=1:nmid,
        V(j,:) = v(i,(j-1)*nin+1:j*nin);
    end;

    % adaptive controller
    vx = V*xbar;
    for j=1:nmid-1,
        ez = exp( -a(j)*vx(j) );
        sig(j) = 1/( 1 + ez );
        sigp(j,j) = a(j)*ez*sig(j)*sig(j);
    end;
    sig(nmid) = 1;
    vad = W*sig;
    u(i) = ( rdot(1) - K*e - vad - Mq*x(i,1) )/Mdelta;

    % plant model
    xdot = sin( x(i,1) ) + Mdelta*u(i) + Mq*x(i,1);

    % learning law
    Wdot = -gammaw*( e*( sig' - xbar'*V'*sigp ) + lambda*norm
        ( e )*W );
    Vdot = -gammav*( sigp*W'*e*xbar' + lambda*norm
        ( e )*V );

    % put NN update in a vector
    wdot = Wdot;
    for j=1:nmid,
        vdot((j-1)*nin+1:j*nin) = Vdot(j,:);
    end;

```

```

% numerically integrate
if i==1,
x(i+1,:) = x(i,:) + xdot*dt;
r(i+1,:) = r(i,:) + rdot*dt;
w(i+1,:) = w(i,:) + wdot*dt;
v(i+1,:) = v(i,:) + vdot*dt;
elseif i<points,
x(i+1,:) = x(i,:) + ( 1.5*xdot - 0.5*oldxdot )*dt;
r(i+1,:) = r(i,:) + ( 1.5*rdot - 0.5*oldrdot )*dt;
w(i+1,:) = w(i,:) + ( 1.5*wdot - 0.5*oldwdot )*dt;
v(i+1,:) = v(i,:) + ( 1.5*vdot - 0.5*oldvdot )*dt;
end;
oldxdot = xdot; oldrdot = rdot;
oldwdot = wdot; oldvdot = vdot;
end;

```

The state history when the desired response is an aggressive square wave is shown in Figure 9.3-2. Here, we see that the controller performs better on each successive attempt at this maneuver, even though there was extreme error in the original model. In fact, the pitch-rate error is actually vanishing at these desired rates. The control effort (usage of elevator) is reasonable, as also seen in the figure.

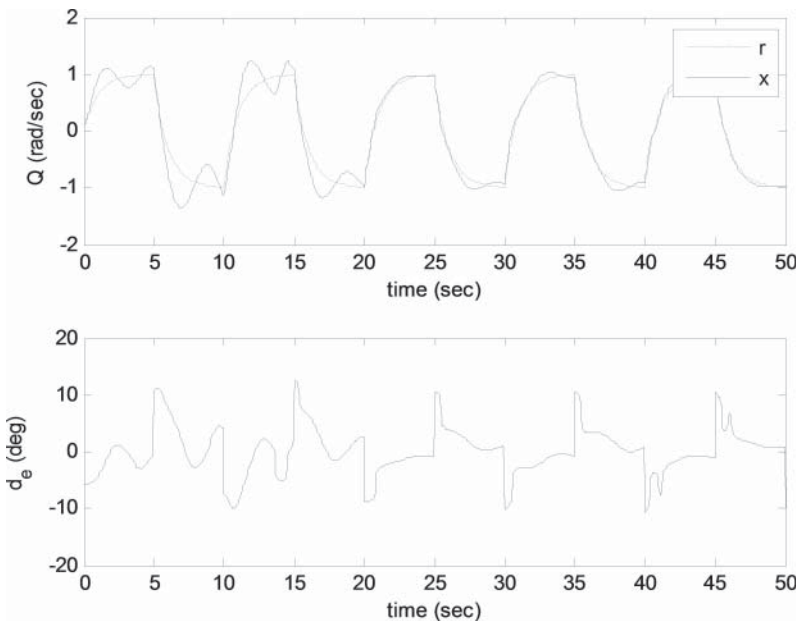


**Figure 9.3-2** State history (top) and input history (bottom) for Example 9.3-1.

Figure 9.3-3 shows the adaptive parameters. That is, all of the elements of  $V$  and  $W$  are plotted. After an initial transient, we see that the weights are settling in to nearly constant values, even though the vehicle is maneuvering rapidly. This, along with the low tracking error achieved, indicates successful adaptation.

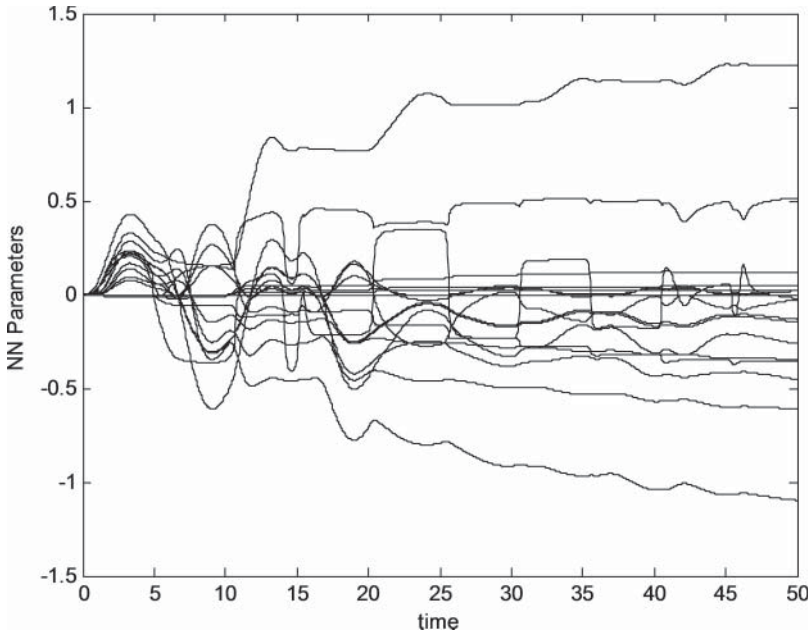


Figure 9.3-3 Neural network parameters for Example 9.3-1. ■

## 9.4 LIMITED AUTHORITY ADAPTIVE CONTROL

Input saturation and input rate saturation present a significant problem for adaptive control, even more so than for nonadaptive control (see Section 7.5 for a discussion of saturation and linear controllers). Saturation violates any *affine in control* assumption, which is common in the literature. It also violates the assumption that the sign of the effect of the control is locally known and nonzero, since the effect of any attempted additional control input is zero once saturation is encountered. The behavior is analogous to integrator windup in a linear controller but worse. Adaptation may attempt to correct for the unexpected effects of saturation, driving the system further into saturation. Like integrator windup, these effects can dramatically reduce the domain of attraction of a commanded equilibrium, in the worst case precluding any command or disturbance that would involve an input saturating for more than a brief period. However, it is possible for an adaptive law to function properly (as designed) even during input saturation, depending on the adaptation method used.

The notion that adaptation can continue even when the system is encountering input saturation is significant. An approach that halts adaptation when saturation is encountered, in order to prevent issues with input saturation, would be removing the benefit of adaptation during what is arguably the most important period to ensure reliable adaptation. That is because saturation is indicative of a transient response and/or a return from a higher gain condition. In either case, the flight control system designer would clearly prefer adaption to proceed at full effectiveness.

Another issue for adaptive control relates to the control of systems in *cascade*. This is where the state of one subsystem becomes the input to a second subsystem. An important example in flight control is the use of attitude to control velocity. To allow adaptation to take place for both of these interconnected subsystems, it is necessary to account for the response of the attitude subsystem when enabling adaptation for the velocity control (and vice versa). If the attitude subsystem is not able to respond fully for any reason, then the control system designer wants to ensure that the velocity subsystem adaptation can still proceed without issue.

### Pseudocontrol Hedging

Pseudocontrol hedging (PCH) is a method that can be applied to a dynamic inversion of a *limited authority* adaptive controller to achieve the goals outlined above. It involves feeding back expected system response to the reference model in order to allow adaptation to effectively proceed regardless of system response. This method requires finding the difference between commanded and predicted pseudocontrol and using this to modify the reference model response in such a way that (9.2-7) is satisfied. If (9.2-7) is still satisfied, then adaptive laws derived using it, such as (9.3-4 and 9.3-5), remain valid.

In developing a PCH design, the control system designer can select which system characteristics the system will attempt to correct for with adaptation. In this context, we expect the designer does not want the controller to attempt to correct for absolute input saturation or the response of subsystems that have their own adaptive process.

To formalize this in the context of input saturation only, let us introduce variable  $u_{cmd}$  to be the unsaturated input and  $u$  to be the saturated (limited) input to the system. The PCH controller is illustrated in Figure 9.4-1. Here, the PCH block is shown that computes the hedge signal

$$v_h = v - \hat{f}(x, u) \quad (9.4-1)$$

The reference model motion is modified by PCH in a specific way as described here. For the case where the original reference model is of the general form

$$\dot{r} = f_{rm}(r) \quad (9.4-2)$$

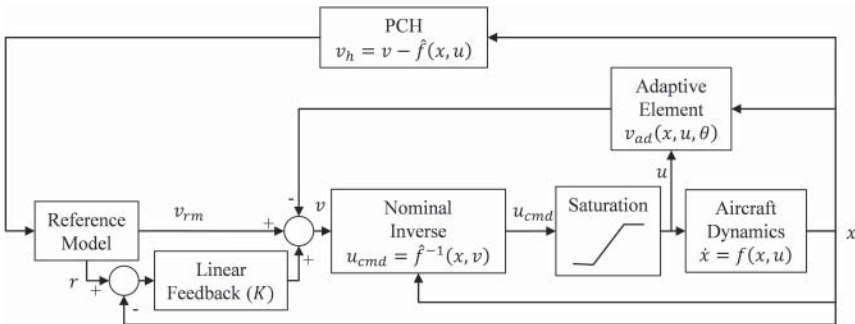


Figure 9.4-1 Use of PCH to address input saturation.

the modified form with PCH becomes

$$\dot{r} = f_{rm}(r) - v_h \quad (9.4-3a)$$

$$v_{rm} = f_{rm}(r), \quad (9.4-3b)$$

where  $v_{rm}$  is the feedforward signal from the reference model. Note that the PCH signal ( $v_h$ ) is integrated before it affects reference model output.

With PCH, if we rederive the reference model tracking error dynamics ( $e$ ), we find

$$\dot{e} = -Ke + v_{ad}(x, u, \theta) - f(x, u) + \hat{f}(x, u), \quad (9.4-4)$$

which is the same as (9.2-7) and one sees that  $u_{cmd}$  does not appear. As a result, adaptation is able to function properly and attempt to correct for the desired form of model error:  $f(x, u) - \hat{f}(x, u)$  as before.

**Example 9.4-1: Neural Network Adaptive Controller with PCH** In this example, a first-order system with significant model error from Example 9.3-1 is controlled using a SHL NN to provide adaptation. PCH is utilized to account for input saturation in the design. The true dynamics are once again taken as

$$\dot{q} = M_q q + M_{\delta_e} \delta_e + \sin q, \quad (9.4-5)$$

where the last term is considered entirely unknown. The input  $\delta_e$  is limited in magnitude. The approximate dynamic inverse is missing the unknown term and was designed ignoring the possibility of a saturated input,

$$\delta_{e cmd} = \frac{1}{M_{\delta_e}}(v - M_q q) \quad (9.4-6)$$

The elevator command from (9.4-6) is limited to the known limit before being sent to the elevator actuator. PCH is used to allow adaptation to proceed correctly even if the elevator command encounters saturation.

The following MATLAB code is able to simulate the results of such a controller:

```
% parameter choices
dt = 0.05; tfinal = 50; tswitch = 5;
Mdelta = -10; Mq = -1;
u_max = 0.1;
K = -1;
gammaw = 1; gammav = 10;
lambda = 0.01;
nmid = 5; nin = 3;
amin = 0.01; amax = 10;

% precompute activation potentials
a = zeros(nmid,1);
for i=1:nmid-1,
    a(i) = tan( atan(amin) + ( atan(amax) - atan(amin) )*(i+1)
              /nmid );
end;
```

```

% preallocate arrays
points = tfinal/dt + 1;
t = zeros(points,1); r = zeros(points,1);
x = zeros(points,1); u = zeros(points,1);
w = zeros(points,nmid); wdot = zeros(1,nmid);
v = zeros(points,nmid*nin); vdot = zeros(1,nmid*nin);
rdot = zeros(1,1); xdot = zeros(1,1);
Wdot = zeros(1,nmid); W = zeros(1,nmid);
Vdot = zeros(nmid,nin); V = zeros(nmid,nin);
xbar = zeros(nin,1);
sig = zeros(nmid,1); sigp = zeros(nmid,nmid);

for i=1:points,
    t(i)=(i-1)*dt;

    % external input
    if mod(t(i),2*tswitch)<tswitch, externalInput = 1;
    else externalInput = -1;
    end;

    % reference model
    vrm = -K*( externalInput - r(i,1) );

    % error signals
    e = r(i,1) - x(i,1);

    % NN inputs
    if i>1, oldu = u(i-1);
    else oldu = 0; end;
    xbar(1) = 1;
    xbar(2) = x(i,1);
    xbar(3) = oldu;

    % get weights from state vector
    W = w(i,:);
    for j=1:nmid,
        V(j,:) = v(i,(j-1)*nin+1:j*nin);
    end;

    % adaptive controller
    vx = V*xbar;
    for j=1:nmid-1,
        ez = exp( -a(j)*vx(j) );
        sig(j) = 1/( 1 + ez );
        sigp(j,j) = a(j)*ez*sig(j)*sig(j);
    end;
    sig(nmid) = 1;
    vad = W*sig;
    vv = vrm - K*e - vad;
    u_cmd = ( vv - Mq*x(i,1) )/Mdelta;
    if abs(u_cmd) > u_max, u(i) = u_max*sign(u_cmd);
    else u(i) = u_cmd;
end

```

```

% plant model
xdot = sin( x(i,1) ) + Mdelta*u(i) + Mq*x(i,1);

% hedge signal
vh = vv - ( Mdelta*u(i) + Mq*x(i,1) );

% reference model modified
rdot = vrm - vh;

% learning law
Wdot = -gammaw*( e*( sig' - xbar'*V'*sigp ) + lambda*norm
    ( e )*W );
Vdot = -gammav*( sigp*W'*e*xbar' + lambda*norm
    ( e )*V );

% put NN update in a vector
wdot = Wdot;
for j=1:nmid,
vdot((j-1)*nin+1:j*nin) = Vdot(j,:);
end;

% numerically integrate
if i==1,
x(i+1,:) = x(i,:) + xdot*dt;
r(i+1,:) = r(i,:) + rdot*dt;
w(i+1,:) = w(i,:) + wdot*dt;
v(i+1,:) = v(i,:) + vdot*dt;
elseif i<points,
x(i+1,:) = x(i,:) + ( 1.5*xdot - 0.5*oldxdot )*dt;
r(i+1,:) = r(i,:) + ( 1.5*rdot - 0.5*oldrdot )*dt;
w(i+1,:) = w(i,:) + ( 1.5*wdot - 0.5*oldwdot )*dt;
v(i+1,:) = v(i,:) + ( 1.5*vdot - 0.5*oldvdot )*dt;
end;
oldxdot = xdot; oldrdot = rdot;
oldwdot = wdot; oldvdot = vdot;
end;

```

The state history when the desired response is an aggressive square wave is shown in Figure 9.4-2. Here, we see that the controller still performs better on each successive attempt at this maneuver. This is true even though there is extreme error in the model and input saturation. As seen in the figure, the input is in fact at saturation for much of the response. Adaptation proceeds effectively despite significant input saturation (Figure 9.4-3). ■

## Adaptive Control for Cascaded Systems

The idea behind PCH can be expanded to allow systems in cascade to be controlled effectively. Here, adaptation in one subsystem is protected from interference by another subsystem which exists “downstream.” Here, this architecture is specifically applied to the case of controlling the position/velocity of an aircraft (one subsystem) utilizing attitude control (second subsystem). Clearly, what happens in terms of

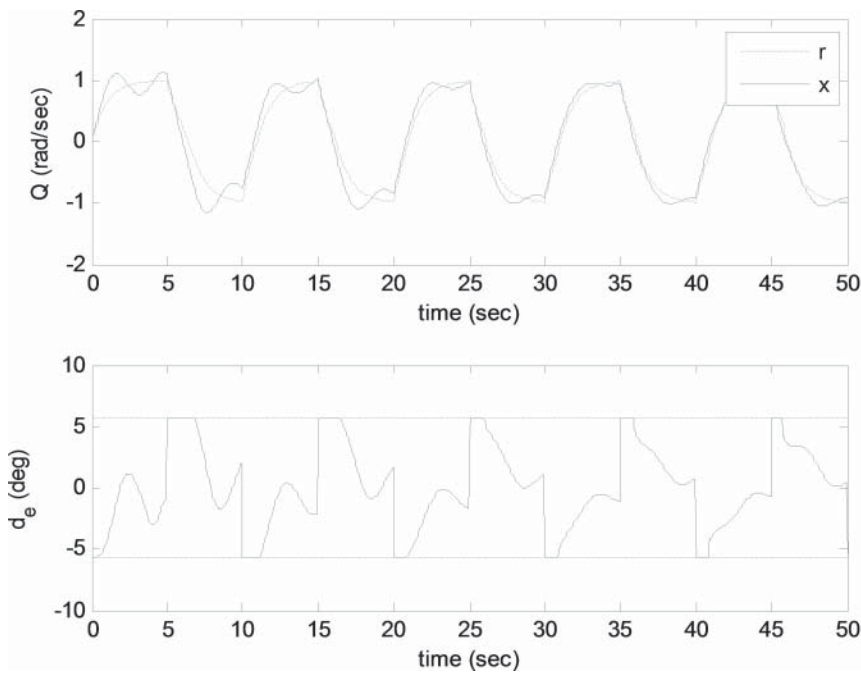


**Figure 9.4-2** State history (top) and input history (bottom) for Example 9.4-1.

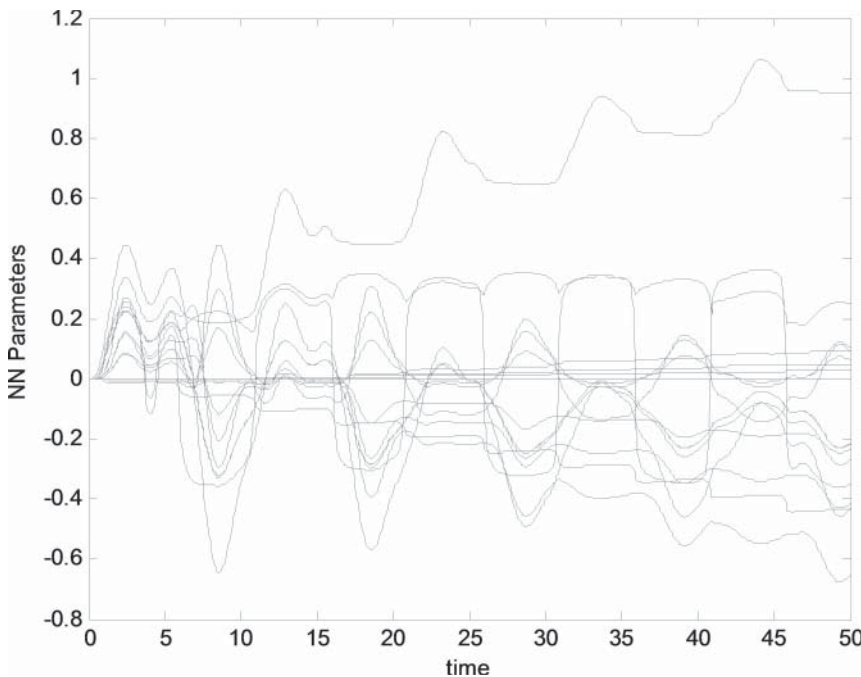


**Figure 9.4-3** Neural network parameter for Example 9.4-1.



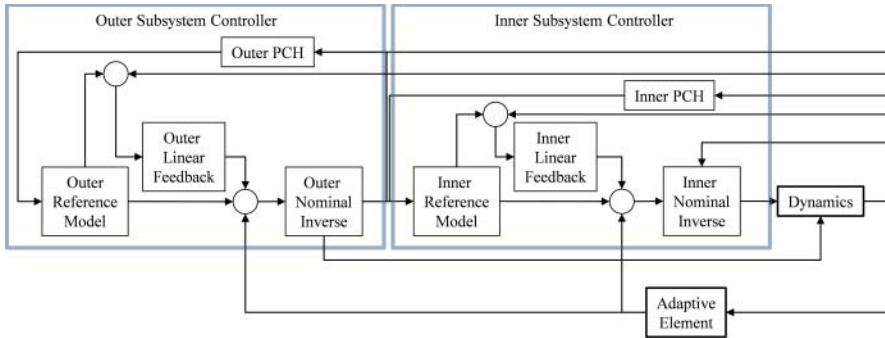


**Figure 9.4-4** Use of PCH to address systems in cascade (for clarity, full state/input feedback is not shown to all elements).

attitude on an aircraft will have a dramatic effect on velocity. Conceptually, PCH will be utilized to protect the outer loop (velocity) loop adaptation from the response of the inner loop (attitude). This architecture is shown in Figure 9.4-4.

Note that a single NN can provide the adaptation necessary to correct for all six degrees of freedom. That is, it can correct for model error in all three linear velocity components and all three angular velocity components. This allows the controller to utilize both direct force/moment controls as well as attitude changes to achieve desired accelerations. The design choices here would be specified by the two dynamic inversion blocks. In the following section, this architecture will be utilized as the basis for a small helicopter adaptive guidance and flight control system suitable for helicopters and multirotors/quadrotors. With minor modification, it can be utilized for airplanes.

## 9.5 NEURAL NETWORK ADAPTIVE CONTROL EXAMPLE

One early use of NN adaptive flight control was on the NASA X-36 unmanned aircraft (Brinker and Wise, 2001; Calise et al., 2001). Here, the approach was successfully applied to the attitude control of an unmanned airplane. There have been a variety of tests of similar adaptive controllers in a variety of programs in the years since. A notable example is the use on the Boeing Joint Direct Attack Munition (JDAM), for which operational benefits have been claimed (Sharma et al., 2000).

This section contains a detailed design of an adaptive guidance and flight control system applied to rotorcraft flight control, including helicopters (Johnson and Kannan, 2005) and multirotors/quadrotors. The aircraft included here are the AscTech Pelican quadrotor and the Yamaha RMAX small helicopter described in Chapter 8, with instrumentation and processing added to enable automatic flight. It combines concepts from this chapter as well as Chapters 5, 6, and 8. It has been utilized successfully to operate several other VTOL aircraft. With minor modification, it has also

been utilized to fly airplanes (Johnson et al., 2008) and other configurations (Johnson and Turbe, 2006).

### Description of an Adaptive Guidance, Navigation, and Control System for Miniature Aircraft

The position tracking of an aircraft is accomplished by utilizing the cascaded systems approach described in Section 9.4. This system utilizes attitude changes and direct force controls (such as rotor/propeller thrust) to achieve the desired position tracking. A state estimation system is utilized to generate estimates of vehicle state (angular velocity, attitude, linear velocity, and position) based on available sensors. The section below outlines the state estimation system that utilizes the Global Positioning Satellite System (GPS), an inertial measurement unit (IMU), and a magnetometer (heading). This configuration is illustrated in Figure 9.5-1. Using the common convention, the symbol  $\hat{x}$  is used to indicate an estimated actual state  $x$ . Section 6.4 covers state estimation systems, and the section below outlines the specific system estimation system utilized in this chapter.

**State Estimation** From Section 6.4 we find that the separation principle justifies designing the guidance/control system and the state estimation system separately. However, this principle only applies for the case of linear systems, which is clearly not the case here. In fact, the controller alone is nonlinear due to the adaptive process. So, validation of the closed-loop behavior of the entire system over the intended flight regimes is important.

The estimator is based on utilizing inertial measurements (accelerometers and gyros) in an IMU. The IMU data is integrated forward in time to propagate attitude, velocity, and position. An extended Kalman filter (EKF), based on the Kalman filter from Section 6.4, is utilized to incorporate other sensor inputs to reduce error and bound drift in this propagation. Estimates of accelerometer and gyro biases are also updated in this manner.

The state estimation system estimates the vehicle attitude quaternion,  $q_{frd/nd}$  seen in Chapter 1, Equation (1.8-16),

$$q_{frd/nd} = [q_0 \quad q_1 \quad q_2 \quad q_3]^T, \quad (9.5-1)$$

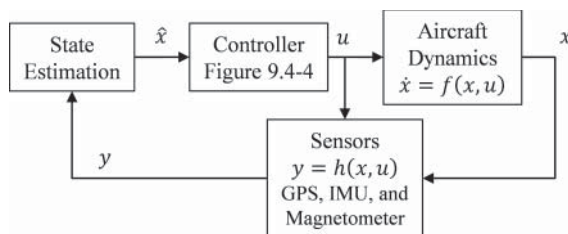


**Figure 9.5-1** Integrated adaptive guidance, navigation, and control systems.

the North/East/down (NED) position,

$$\begin{bmatrix} p_x & p_y & p_z \end{bmatrix}^T, \quad (9.5-2)$$

the NED velocity,

$$\begin{bmatrix} v_x & v_y & v_z \end{bmatrix}^T, \quad (9.5-3)$$

accelerometer biases,

$$\begin{bmatrix} b_{ax} & b_{ay} & b_{az} \end{bmatrix}^T, \quad (9.5-4)$$

and gyro biases,

$$\begin{bmatrix} b_{\omega x} & b_{\omega y} & b_{\omega z} \end{bmatrix}^T, \quad (9.5-5)$$

These are propagated utilizing inertial data for the gyros,

$$\begin{bmatrix} \omega_x & \omega_y & \omega_z \end{bmatrix}^T, \quad (9.5-6)$$

and accelerometers corrected to the cg (measuring nongravitational specific force),

$$\begin{bmatrix} s_x & s_y & s_z \end{bmatrix}^T, \quad (9.5-7)$$

with

$$\begin{bmatrix} \dot{q}_0 \\ \dot{q}_1 \\ \dot{q}_2 \\ \dot{q}_3 \end{bmatrix} = \begin{bmatrix} 0 & -\omega_x + b_{\omega x} & -\omega_y + b_{\omega y} & -\omega_z + b_{\omega z} \\ \omega_x - b_{\omega x} & 0 & \omega_z - b_{\omega z} & -\omega_y + b_{\omega y} \\ \omega_y - b_{\omega y} & -\omega_z + b_{\omega z} & 0 & \omega_x - b_{\omega x} \\ \omega_z - b_{\omega z} & \omega_y - b_{\omega y} & -\omega_x + b_{\omega x} & 0 \end{bmatrix} \begin{bmatrix} q_0 \\ q_1 \\ q_2 \\ q_3 \end{bmatrix} \quad (9.5-8)$$

$$\begin{bmatrix} \dot{p}_x \\ \dot{p}_y \\ \dot{p}_z \end{bmatrix} = \begin{bmatrix} v_x \\ v_y \\ v_z \end{bmatrix} \quad (9.5-9)$$

$$\begin{bmatrix} \dot{v}_x \\ \dot{v}_y \\ \dot{v}_z \end{bmatrix} = C_{ned/frd} \begin{bmatrix} s_x - b_{ax} \\ s_y - b_{ay} \\ s_z - b_{az} \end{bmatrix} + G, \quad (9.5-10)$$

where  $C_{ned/frd}$  is the transpose of  $C_{frd/ned}$ , itself dependent on the quaternion (9.5-1) via Equation (1.8-20), and

$$\begin{bmatrix} \dot{b}_{ax} \\ \dot{b}_{ay} \\ \dot{b}_{az} \end{bmatrix} = \begin{bmatrix} \dot{b}_{\omega x} \\ \dot{b}_{\omega y} \\ \dot{b}_{\omega z} \end{bmatrix} = 0 \quad (9.5-11)$$

Equations (9.5-8) through (9.5-11) represent the process model and can be written as a single function,

$$\frac{d}{dt} \hat{x} = f(\hat{x}, \omega_x, \omega_y, \omega_z, s_x, s_y, s_z) \quad (9.5-12)$$

Note that in (9.5-10)  $G$  is an estimate of the acceleration due to gravitation not measured by the accelerometers expressed in the NED frame, described in Section 1.6. The accelerometer data is corrected for mounting location by addressing the expression of acceleration in a rotating frame described in Section 1.5. Specifically, Equation (1.5-4) can be utilized to estimate what a theoretical set of accelerometers located at the center of mass of the aircraft would measure based on measures from a known location relative to the center of mass ( $\mathbf{p}_{P/Q}$ ):

$$\mathbf{s}_{CM/ned} = \mathbf{s}_{P/ned} - \boldsymbol{\alpha}_{frd/ned} \times \mathbf{p}_{P/Q} - \boldsymbol{\omega}_{frd/ned} \times (\boldsymbol{\omega}_{frd/ned} \times \mathbf{p}_{P/Q}) \quad (9.5-13)$$

To implement the EKF discrete update, it is also necessary to propagate a state estimate error covariance matrix  $P$ , appropriately initialized, with

$$\dot{P} = A^T P + P A + Q, \quad (9.5-14)$$

where

$$A = \frac{\partial f}{\partial \hat{x}} \quad (9.5-15)$$

is a matrix of partial derivatives of (9.5-12) and  $Q$  represents appropriate measurement noise covariance for the inertial measurements.

A discrete update of the state estimate and covariance matrix is made whenever any other sensor information is received using standard EKF methods (Gelb, 1974). For measurement  $y$  of the form

$$y = h(x) + v, \quad (9.5-16)$$

where  $v$  represents a zero mean measurement error with Gaussian distribution and variance  $R$ , the update is

$$C = \left. \frac{\partial h}{\partial x} \right|_{x=\hat{x}} \quad (9.5-17)$$

$$K = P C^T [C P C^T + R]^{-1} \quad (9.5-18)$$

$$\hat{x}^+ = \hat{x} + K [y - h(\hat{x})] \quad (9.5-19)$$

$$P^+ = [I - K C] P \quad (9.5-20)$$

For the results presented in this chapter, sensors are utilized and incorporated utilizing (9.5-17) to (9.5-20): a GPS receiver and a magnetometer. Both have a number of important issues described below.

For a tightly coupled filter, GPS data would require a clock bias estimate state, specifically a clock bias between the GPS constellation and the receiver clock. Then, each satellite measurement would be treated as the measurement of a single so-called *pseudorange* to each tracked satellite. In the loosely coupled design described here, the GPS receiver obtains estimates for clock bias, position, and

velocity utilizing tracked satellite signals. As a result, enough satellite pseudoranges must be available for the GPS receiver to independently estimate 3D position and clock bias. These four unknowns require four pseudoranges. For this loosely coupled design, Equation (9.5-17) for the GPS measurement contains six values, which correspond to the velocity and position of the GPS receiver antenna on the aircraft. It is necessary to account for the fact that the antenna is not necessarily located at the center of mass of the vehicle. It is also necessary to account for the time delay of the estimate coming from the GPS receiver. Here, this was done by keeping a buffer of expected GPS measurements  $[h(\hat{x})]$  from the past and using the stored values that correspond to the newly arrived GPS information (Christophersen et al., 2006). When performing the state estimate update for any sensor, it is critical that this buffer of expected measurements is also updated.

In this case a differential receiver is utilized that achieves position errors that are less than 1 ft more than 90% of the time. For a conventional GPS receiver, the accuracy is normally not sufficient for altitude control of a helicopter operating close to the ground. This altitude information might be augmented with a barometric altimeter or some other source of altitude measurement.

For the magnetometer, the sensor provides the direction and magnitude of the measured magnetic field resolved in a body-fixed coordinate system. In practice, the data only provide significant value in terms of aircraft heading. As a result, the measured data is utilized first to come up with a single measurement of aircraft heading utilizing a model of Earth's magnetic field as well as current aircraft roll/pitch angle estimates. So, (9.5-16) is simply the equation for aircraft heading. It is necessary when computing the difference between measured heading and estimated heading in (9.5-19) to take the angle between  $-180^\circ$  and  $180^\circ$  by adding or subtracting  $360^\circ$  to the difference as necessary.

***Integrated Adaptive Guidance and Control*** The update rate of the IMU for the Yamaha RMAX example described below is 100 Hz. The update rate of the control system is limited to 50 Hz by the actuator interface utilized. These update rates are quick enough to make any aliasing effects discussed in Chapter 7 unlikely to occur. The important exception would be higher-frequency structural vibrations, presumably induced by the rotor, becoming aliased going into the IMU. To prevent this issue, the IMU was carefully mounted within a vibration isolated structure. This is intended to suppress those vibrations that could produce aliased signals (low-frequency noise).

At several places in the overall system, there is time delay occurring. This includes sensor dynamics, sensor processing, communication delays, sensor fusion processing time, actuation dynamics, and more. To the extent that the state estimation system has gotten all signals to approximately the same time synchronization (e.g., to that of the IMU), it may be a reasonable assumption that each element of the system adds a nearly consistent time delay to all feedback signals that pass through it. Because pure time delay is a linear phenomenon, a system with the net total time delay around the entire feedback loop can be approximated as a single time delay at one point in the system. That is, it may be less important to know how much time delay occurs at every step than to have a good estimate of total loop time delay. The design of

the feedback control system should then account for this time delay and be robust to changes in it.

The total time delay was estimated by having the aircraft in an automatic hover and initiating a step response in the commanded horizontal position. A comparison was made between actuator command leaving the controller and sensed/estimated state arriving at the controller, with the most critical channel being cyclic pitch control and estimated angular velocity. Correlation between actuator command and resultant motion indicates a total of 160 ms of time delay around the feedback loop. It is important to realize that not all of this is likely pure time delay. Some of it is very likely other forms of higher-order dynamics, such as actuator motors and structural strain. Whatever the true source, it is important to ensure that the feedback controller can handle the full phase loss regardless of the source.

Processing requirements of this design are dominated by the state estimation system. The adaptive control scheme described here uses far less processing. The state estimation processing is itself dominated by propagating Equation (9.5-14). This involves multiplying two square matrices with a size equal to the number of states at every update rate of the filter, 100 Hz in this case. The numerical stability and accuracy of these calculations are critical to the performance of the filter. The results shown here actually propagate a factored version of  $P$  to improve accuracy, leading to a further increase in processing requirements (approximately double). Specifically, Bierman upper diagonal (UD) factorization is used (Bierman, 1977; Grewal and Andrews, 1993). A modern smartphone, personal computer, or laptop processor can easily handle these computations in real time. However, there may be an issue with some less capable and cheaper embedded processors utilized for miniature aircraft.

The architecture shown in Figure 9.4-4 requires a choice for reference models for both inner and outer subsystems. That is, we need to specify how we want the aircraft to try to move. An obvious choice is to look for a second-order response on each axis for attitude control (with selected frequency and damping ratios) as well as for each axis of position control. That is the choice made here. In the simplest version, we may want to achieve a natural frequency  $\omega$  and a damping ratio  $\zeta$ . In this case, the reference model dynamics would be

$$\ddot{r} = -K_D \dot{r} - K_P r, \quad (9.5-21)$$

where  $K_D = 2\zeta\omega$  and  $K_P = \omega^2$ .

However, there are two important issues. First, there may be coupling between the inner and outer loop responses. Second, the designer will likely desire internal limits on the states.

Coupling between the inner and outer loops can be expected if the desired frequency of response of the outer loop is not much slower than that of the inner loop. When this is not the case, a codesign of both loops is necessary. In order to achieve the more precise position control, it is necessary to take this step. To perform the codesign, the internal dynamics of the inner and outer loops are based on the two

sets of desired frequencies and damping ratios. Splitting up the inner and outer loop reference models into two sets is indicated here with subscripts:

$$\ddot{r}_i = -K_{D_i} \dot{r}_i - K_{P_i} r_i \quad (9.5-22)$$

$$\ddot{r}_o = -K_{D_o} \dot{r}_o - K_{P_o} r_o, \quad (9.5-23)$$

where the output of the outer loop controller ( $o$ ) is the external input to the inner loop controller ( $i$ ). One can then derive appropriate parameters for these reference models to achieve two chosen frequencies and damping ratios (now a fourth-order system). Here, we chose to make the damping ratios unity and the two frequencies equal. This is motivated by a desire to achieve the highest bandwidth position control within this architecture. The characteristic equation with four poles at  $-\omega$  looks like

$$(s + \omega)^4 = s^4 + K_{D_i} s^3 + K_{P_i} s^2 + K_{P_i} K_{D_o} s + K_{P_i} K_{P_o} = 0 \quad (9.5-24)$$

This can then be utilized to solve for the reference model parameters:

$$K_{P_i} = 6\omega^2, \quad K_{D_i} = 4\omega \quad (9.5-25)$$

$$K_{P_o} = \frac{\omega^2}{6}, \quad K_{D_o} = \frac{2\omega}{3} \quad (9.5-26)$$

The second issue is the potential need for internal limits. If the aircraft is asked to move a very large distance horizontally, the necessary velocities and attitudes to achieve a linear response will (with a sufficiently large distance) be inappropriate. For example, they may exceed the maximum possible speed of the aircraft. Internal limits on linear and angular velocity are included in the reference models in a similar manner to provide this functionality. First, a desired velocity component is found for each axis that seeks to eliminate position or attitude error:

$$v_{Unlimited} = -\frac{K_P}{K_D} r \quad (9.5-27)$$

This component is then limited as appropriate. For example, the norm of all three components might be limited while still maintaining the desired direction. The reference model motion is then computed by

$$\ddot{r} = K_D(v_{Limited} - \dot{r}) \quad (9.5-28)$$

In this way, we achieve the desired second-order response when the internal state is not limited. When it is limited, the system will track the limit. This reference model architecture is similar to nested saturation controllers (Teel, 1992), which can enable some important theoretical stability results to be stated (Johnson and Kannan, 2003).

In this design the linear feedback gains were chosen to be identical to the reference model feedback gains [Equations (9.5-21), (9.5-25), and (9.5-26)]. In some

applications, it might be desirable to make them somewhat faster than the reference model so that the motion of the reference model is the dominant response. Here, the reference model is of no special significance.

The inner loop (attitude) nominal dynamics were simplified as much as possible here. This is justified by having the adaptive controller able to address the many factors not included in this model. For each rotational axis, we introduce a diagonal element into a control effectiveness matrix  $B$  and a diagonal element into the rate damping term  $A$ :

$$\dot{x} = Ax + B\delta_i, \quad (9.5-29)$$

where  $x$  is the angular velocity components ( $P$ ,  $Q$ , and  $R$ ) and  $\delta_i$  are the attitude control inputs (roll, pitch, yaw). It is trivial to invert this model to find the  $\delta_i$  to achieve a desired angular acceleration as required by the controller.

For the outer loop (position control) nominal dynamic inverse included in Figure 9.4-4, the simplified model takes the multicopter or helicopter as simply a thrust vector (the main rotor or direction of multiple propellers) that can be pointed in any direction, after accounting for the effect of gravity. This is equivalent to neglecting other side forces and relying on adaptation to account for them. At a similar level of approximation as applied for the attitude control case, the thrust per unit mass (specific force), directed along the body-fixed down axis, is modeled by

$$s_z = Z_w W + Z_\delta \delta_o, \quad (9.5-30)$$

where  $W$  is the down body-fixed axis velocity component.

In order to realize this design, it is necessary to relate outer loop pseudocontrol (linear acceleration commands) to this thrust specific force and attitude commands. First, the total necessary specific force is found by

$$s_z = |\mathbf{v}_o - \mathbf{G}|, \quad (9.5-31)$$

where  $\mathbf{v}_o$  is outer loop pseudocontrol and  $\mathbf{G}$  is the estimated effect of gravitation. For example, if the outer loop pseudocontrol command ( $\mathbf{v}_o$ ) was zero (i.e., zero acceleration desired), then this would result in a commanded Z-axis specific force equal to the magnitude of gravitation. The angle that the body frame needs to be tilted is then found by first finding a unit vector in the direction of the desired specific force,

$$[-\mathbf{k}_{frd}]_{desired} = \hat{\mathbf{s}} = \frac{\mathbf{v}_o - \mathbf{G}}{|\mathbf{v}_o - \mathbf{G}|}, \quad (9.5-32)$$

which represents the desired negative body-fixed down axis direction. To use the same example again where  $\mathbf{v}_o$  is zero, this would result in the desired negative body-fixed down axis pointing in the opposite direction as gravitation, which again corresponds to hover.



One can also independently specify a desired heading for the aircraft  $\psi_{desired}$ , which need not be aligned with the flight path of the aircraft for a helicopter or multirotor. The desired body-fixed forward axis needs to be perpendicular to both the desired down direction and the NED unit vector,

$$\mathbf{j}_{ned} = [-\sin \psi_{desired} \quad \cos \psi_{desired} \quad 0]^T \quad (9.5-33)$$

Because it is perpendicular to both of the unit vectors obtained, the forward direction is found by normalizing the cross product of them

$$[\mathbf{i}_{frd}]_{desired} = \frac{\mathbf{j}_{ned} \times [\mathbf{k}_{frd}]_{desired}}{|\mathbf{j}_{ned} \times [\mathbf{k}_{frd}]_{desired}|} \quad (9.5-34)$$

and the right direction is perpendicular to both, or

$$[\mathbf{j}_{frd}]_{desired} = [\mathbf{k}_{frd}]_{desired} \times [\mathbf{i}_{frd}]_{desired} \quad (9.5-35)$$

The combination of Equations (9.5-32) to (9.5-35) provides the full direction cosine matrix of the desired body-fixed attitude with respect to NED. This becomes the desired attitude for the inner-loop controller. If converted into a quaternion as described in Section 1.8, the symbol  $q_{desired}$  would be appropriate.

Because attitude control is an inherently nonlinear problem, some additional development is required in order to relate desired and estimated attitude in order to produce an error angle that the inner-loop controller can track. There are many potential treatments of this problem found in the literature. Utilizing Euler angles to formulate this problem is one possibility (Das et al., 2009). Bach and Paielli (1993) present commonly used methods that utilize the direction cosine matrix as well as the quaternion to formulate this problem. Here, a commonly used quaternion error angle formulation is utilized to form a set of three error angles. This results in both the desired linear response for small perturbations and global stability under reasonable assumptions. The error angles are found by (Wie and Barba, 1985)

$$q_{desired} = [q_{d0} \quad q_{d1} \quad q_{d2} \quad q_{d3}]^T \quad (9.5-36)$$

$$q_{frd/ned} = [q_0 \quad q_1 \quad q_2 \quad q_3]^T \quad (9.5-37)$$

$$q_{desired} * [q_{frd/ned}]^{-1} = \begin{bmatrix} \Delta q_0 \\ \Delta q_1 \\ \Delta q_2 \\ \Delta q_3 \end{bmatrix} = \begin{bmatrix} q_{d0} & -q_{d1} & -q_{d2} & -q_{d3} \\ q_{d1} & q_{d0} & -q_{d3} & q_{d2} \\ q_{d2} & q_{d3} & q_{d0} & -q_{d1} \\ q_{d3} & -q_{d2} & q_{d1} & q_{d0} \end{bmatrix} \begin{bmatrix} q_0 \\ -q_1 \\ -q_2 \\ -q_3 \end{bmatrix} \quad (9.5-38)$$

$$\begin{bmatrix} \Delta \theta_f \\ \Delta \theta_r \\ \Delta \theta_d \end{bmatrix} = \frac{2\Delta q_0}{|\Delta q_0|} \begin{bmatrix} \Delta q_1 \\ \Delta q_2 \\ \Delta q_3 \end{bmatrix}, \quad (9.5-39)$$

where  $\Delta\theta_f$ ,  $\Delta\theta_r$ , and  $\Delta\theta_d$  are now the roll, pitch, and yaw attitude error angles, respectively, in the body-fixed frame suitable for tracking by the inner-loop controller [Equation (9.5-22)]. These angles take the role of  $r_i$  in the expression, and the linear form of (9.5-22) will be exact for small tracking error.

It is important to handle the case where desired thrust cannot be achieved. That is not an issue encountered in the results described later in this chapter, but it is important to shape the desired trajectory to appropriately account for priorities in position control in general. There are times when it may be reasonable to sacrifice horizontal position tracking in order to maintain altitude. There may be times when it may be preferred to sacrifice altitude control in order to maintain rotor rpm, such as in the early phase of a helicopter autorotation. These trade-offs could be handled by a higher-level planner that is able to shape the desired trajectory under these more complex contingencies.

The outputs of the controller at this point are roll, pitch, yaw, and thrust commands. For any particular aircraft configuration, these are then mapped into appropriate actuator commands. For the conventional helicopter, these would be proportional to cyclic, tail rotor collective, and main rotor collective. For the multirotor, these would map to throttle commands for the individual motors: for example, by inverting a linear mapping of forces and moments as a function of the desired thrust from each propeller of a quadrotor (Das et al., 2009). For the quadrotor arranged as an example in Section 8.6, this would be

$$\begin{bmatrix} \delta_o \\ \delta_{i_1} \\ \delta_{i_2} \\ \delta_{i_3} \end{bmatrix} = \begin{bmatrix} 1/m & 1/m & 1/m & 1/m \\ y_P/J_x & y_P/J_x & -y_P/J_x & -y_P/J_x \\ x_P/J_y & -x_P/J_y & -x_P/J_y & x_P/J_y \\ -C/J_z & C/J_z & -C/J_z & C/J_z \end{bmatrix} \begin{bmatrix} f_1 \\ f_2 \\ f_3 \\ f_4 \end{bmatrix}, \quad (9.5-40)$$

where  $f_1$ ,  $f_2$ ,  $f_3$ , and  $f_4$  are the desired thrust of each propeller and  $C$  is an assumed proportional relationship between the thrust and torque of the propeller.

There is one contingency similar to the above that can be addressed within the controller, at least in principle. In the development of this type of system, it is important that position control is still possible even when the heading control is not. That is, aircraft attitude changes utilized to hold position need not (and should not) assume that heading control is successful. Heading may not be maintained due to a saturated tail rotor, typically due to a wind or sideslip condition. For example, when attempting to fly sideways at an excessive speed the aircraft may not have enough tail rotor authority to maintain the sideslip. Fundamentally, this is achieved by utilizing current heading rather than desired heading when coming up with which way to roll/pitch to achieve desired position/velocity.

An important detail with this type of controller is what to do during takeoff and landing, specifically what to do with NN adaptation while the aircraft is on the ground. If this issue is ignored, then extreme control inputs may result on the ground as the controller attempts unsuccessfully to adapt to the fact that the aircraft is mechanically

constrained by ground contact. Similar to integrators in nonadaptive controllers, a common approach is to halt adaptation when the system detects that the aircraft is in contact with the ground. That method has been utilized here.

## Simulation Results

Simulation results for two different applications of the adaptive guidance and control methods described in this chapter are presented here. First, the trajectory-tracking flight of a quadrotor is described. Following this, more detailed results are provided for a small helicopter.

**Simulation of Quadrotor** Simulation tests were conducted for the guidance and control methods described above applied to the AscTec Pelican quadrotor described in Section 8.6. The relevant parameters are provided in Table 9.5-1. It is important to note that the “internal” limits are applied for capturing the desired state. The actual limits are determined when planning the desired trajectory itself. This controller was specifically optimized for indoor flight at relatively low speed but high precision. For this example, the simulation of the navigation (state estimation) system is dispensed with, and true values of aircraft state are utilized for feedback. Due to this fact, any transient or error is due entirely to the control system.

Figure 9.5-2 shows the position tracking for a rapidly flown small box pattern at constant altitude holding heading to zero. The desired trajectory consisted of

**TABLE 9.5-1 AscTec Pelican Controller Parameter Choices for the Results Presented in this Section**

Component	Parameter	Value
Reference model	Lateral pole locations ( $\omega$ )	2.5
	Longitudinal pole locations	2.5
	Altitude pole location	3.0
	Yaw pole location	2.5
	Reference model internal velocity limit	1.5 ft/s
	Reference model internal rate limit	2 rad/s
Adaptation	Outer layer learning rate ( $\Gamma_w$ )	1.0 (all)
	Inner layer learning rate ( $\Gamma_v$ )	5.0 (all)
	e-Modification ( $\lambda$ )	0.1 (all)
Nominal inverse	Roll control effectiveness ( $B$ )	10
	Pitch control effectiveness	10
	Yaw control effectiveness	6
	Roll damping ( $A$ )	0
	Pitch damping	0
	Yaw damping	0
	Thrust control effectiveness ( $Z_\delta$ )	-32
	Thrust damping ( $Z_w$ )	0

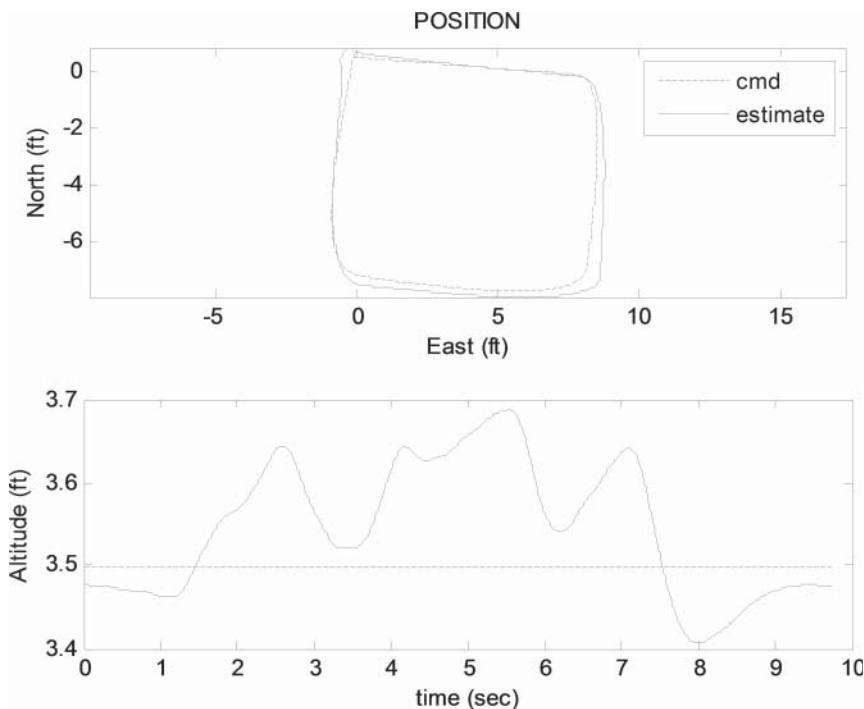


**Figure 9.5-2** Adaptive GNC position tracking for rapidly flown small box pattern from simulation of quadrotor.

acceleration/deceleration segments of  $10 \text{ ft/s}^2$  and a maximum speed of  $10 \text{ ft/s}$ . Figure 9.5-3 shows the corresponding attitude angles during the maneuvers. Roll and pitch rapidly change to around  $20^\circ$  to achieve the desired acceleration levels. Heading is held near zero. Figure 9.5-4 shows the revolution rate in RPM of each of the four propellers. Rapid changes are required to track this desired trajectory.

A video from this box pattern simulation is available at: [http://uav.ae.gatech.edu/videos/gtqS150131\\_square.mp4](http://uav.ae.gatech.edu/videos/gtqS150131_square.mp4)

**Simulation of Small Helicopter** Simulation tests were conducted for the system described above as applied to a small helicopter. In addition to the dynamic model of the Yamaha RMAX helicopter described in Section 8.5, appropriate models were introduced for the sensors: IMU, GPS, and magnetometer. These sensor models included the effects of mounting location, time delay, update rate, quantization, and noise. A screenshot of the visualization capability of the simulator is shown in Figure 9.5-5. The relevant parameters are provided in Table 9.5-2. It is important to note that the “internal” limits are applied for capturing the desired state. The actual limits are determined when planning the desired trajectory.

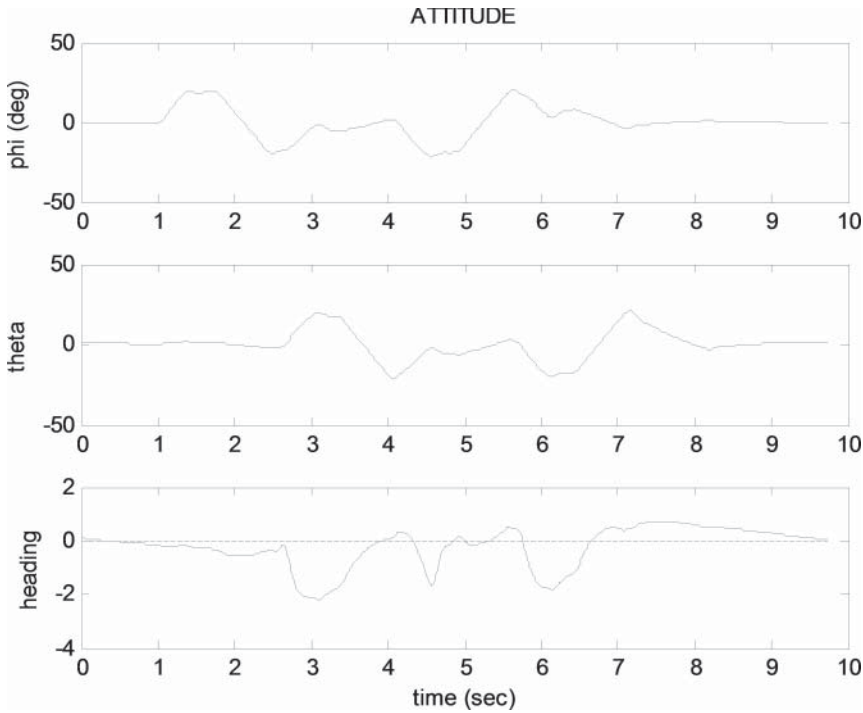


**Figure 9.5-3** Adaptive GNC attitude angles for rapidly flown small box pattern from simulation of quadrotor.

The results for step responses are described first. Note that in normal operational flight one would utilize smooth desired-trajectory commands. Here, we intentionally provide nonsmooth trajectory commands to verify tracking performance, including achieved bandwidth. In other words, normal flight would not involve inputs this aggressive for such small movements. This normal operation is illustrated in results that follow the step responses, showing more conventional flight operations.

It is important to note that plots of estimated vehicle state below are from the state estimate system driven by simulated measurements. It would be possible to also plot truth values for states to see the effect of both the controller and the state estimate components separately. However, due to the performance of the GPS utilized, there is very little difference between true state and estimated state in the simulator, typically within 0.2 ft. Given this fact and our interest in looking at controller performance primarily in this section, state estimates are plotted. This has the added benefit of allowing a more direct comparison of controller performance to the flight test results that follow, where true states are not known.

**Simulation of Small Helicopter Step Responses** Figure 9.5-6 shows the response for an instantaneous  $180^\circ$  change in the commanded heading. A bit more

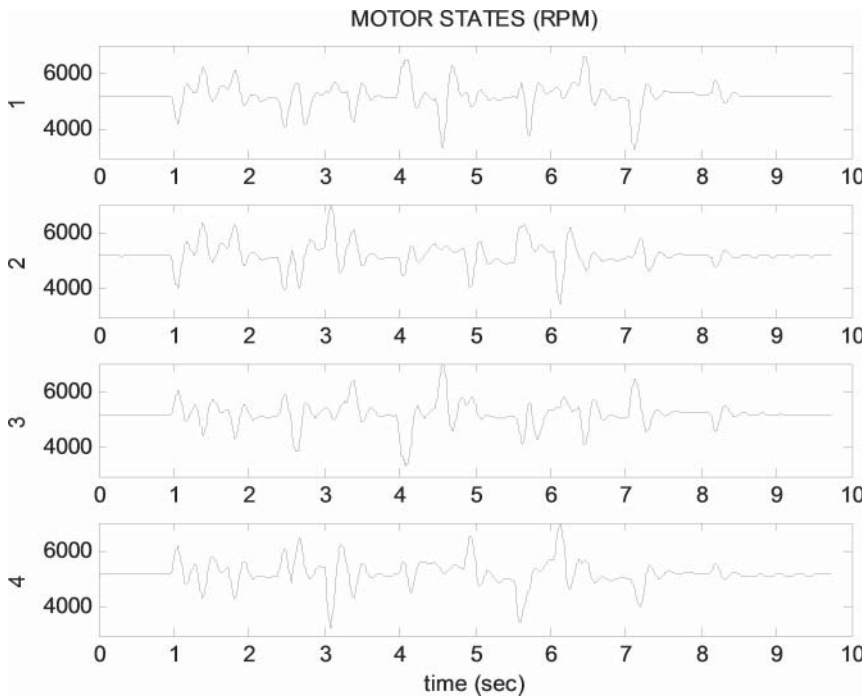


**Figure 9.5-4** Adaptive GNC motor states for rapidly flown small box pattern from simulation of quadrotor.

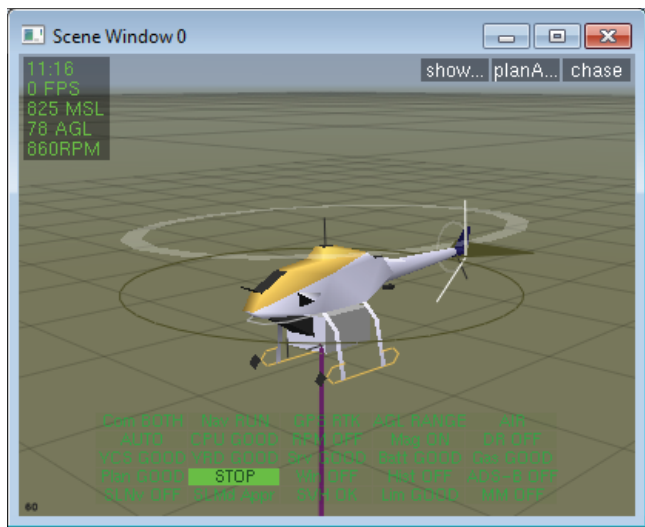


**Figure 9.5-5** Visualization of Yamaha RMAX in simulation environment.

**TABLE 9.5-2 Yamaha RMAX Controller Parameter Choices for the Results Presented in this Section**

Component	Parameter	Value
Reference model	Lateral pole locations ( $\omega$ )	2.5
	Longitudinal pole locations	2.0
	Altitude pole location	3.0
	Yaw pole location	3.0
	Reference model internal velocity limit	10 ft/s
	Reference model internal rate limit	2 rad/s
Adaptation	Outer layer learning rate ( $\Gamma_w$ )	1.0 (all)
	Inner layer learning rate ( $\Gamma_v$ )	5.0 (all)
	e-Modification ( $\lambda$ )	0.1 (all)
Nominal inverse	Roll control effectiveness ( $B$ )	15
	Pitch control effectiveness	10
	Yaw control effectiveness	15
	Roll damping ( $A$ )	-10
	Pitch damping	-8
	Yaw damping	-6
	Thrust control effectiveness ( $Z_\delta$ )	-25
	Thrust damping ( $Z_w$ )	0

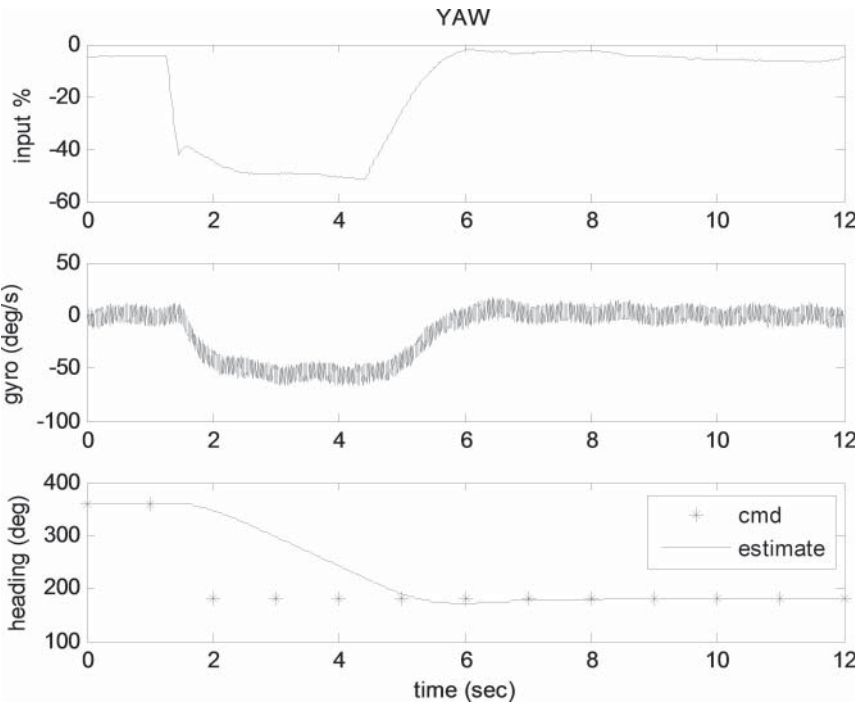


**Figure 9.5-6** Adaptive GNC 180° heading command step response (left) from simulation of RMAX.

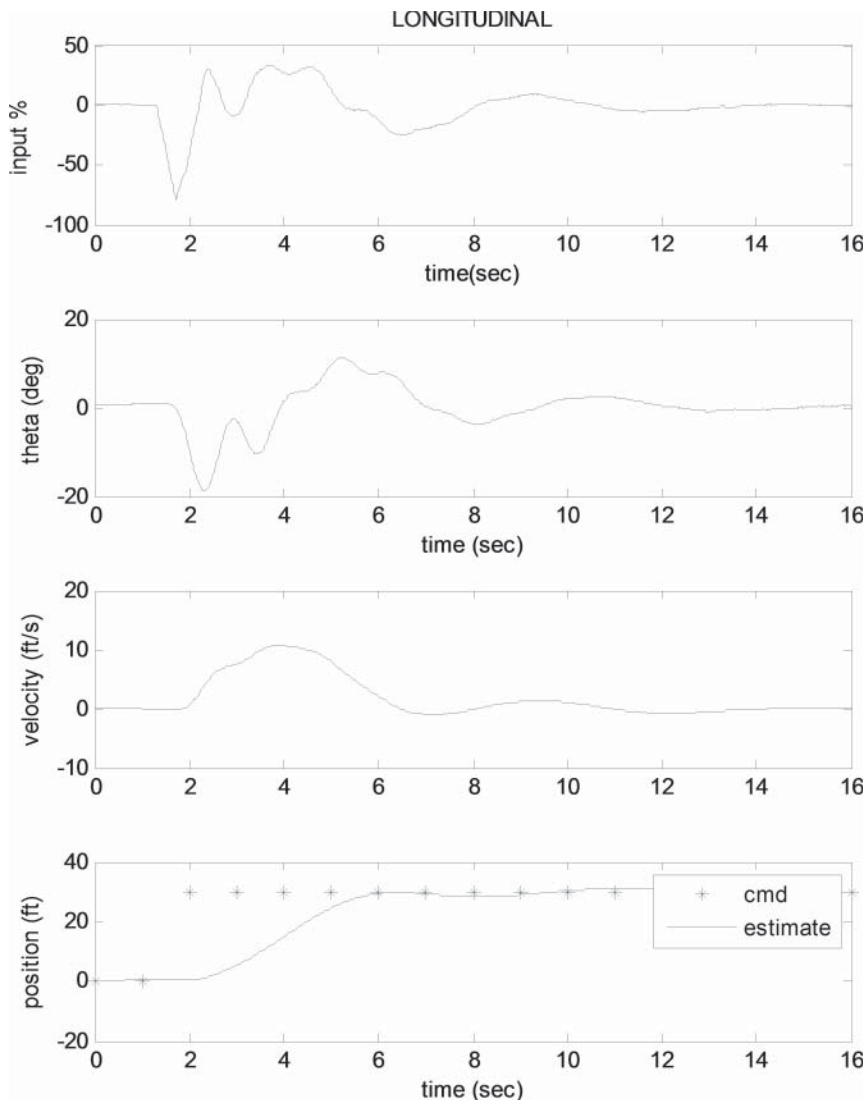


**Figure 9.5-7** Adaptive GNC 30 ft longitudinal position command step response (forward) from simulation of RMAX.

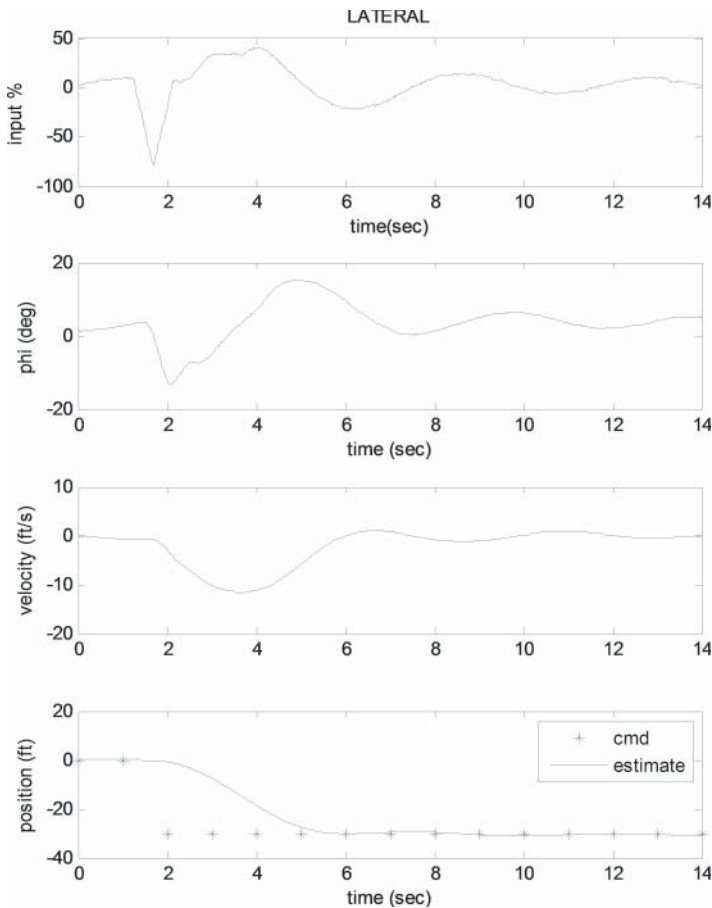
than 50% of maximum tail rotor authority is utilized to generate a maximum of approximately 50 deg/s of rotation, bringing the aircraft around for a total settling time of approximately 4 s. The raw yaw gyro is shown in the middle trace, and includes a significant once-per-rotor-revolution oscillation in this simulated raw measurement (about 14 Hz).

Figure 9.5-7 shows the longitudinal position response to a step input of 30 ft forward. This is accomplished primarily with longitudinal cyclic input. Approximately



75% of the full throw of the cyclic input is utilized to initiate the maneuver, quickly getting the aircraft up to the reference model internal rate limit of 10 ft/s. Note that this internal rate limit is only applied to intercepting the desired trajectory. The trajectory command has a much higher limit corresponding to the maximum speed of the aircraft. The position settling time of 5 s corresponds very well to the theoretical settling time of a fourth-order system with the desired frequencies specified here ( $\omega = 2$ ).

Figure 9.5-8 is the corresponding plot for lateral position response to a step input (to the left) of 30 ft. This is accomplished primarily with lateral cyclic input. Again, about 75% of full throw is utilized to start the maneuver. The internal rate limit is just reached (10 ft/s), and we see a settling time of approximately 4 s. This is close to the theoretical value based on the desired frequency ( $\omega = 2.5$ ).



**Figure 9.5-8** Adaptive GNC 30 ft lateral position command step response (left) from simulation of RMAX.

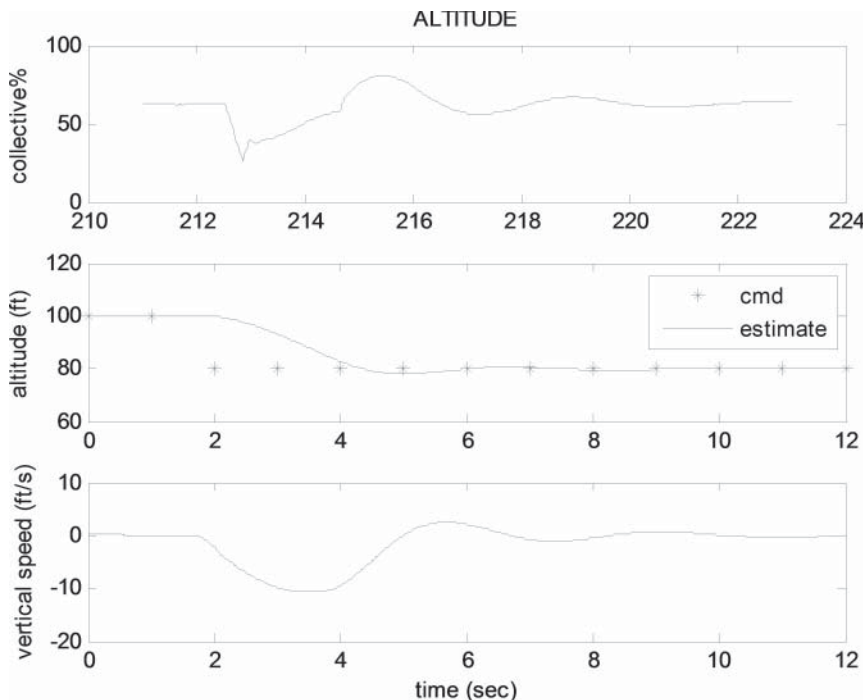
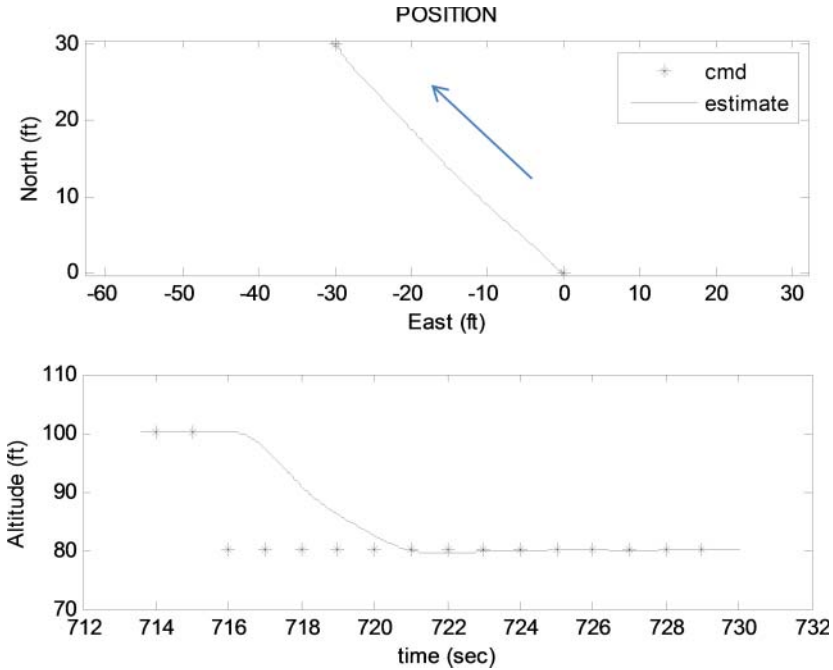


**Figure 9.5-9** Adaptive GNC 20 ft altitude command step response (down) from simulation of RMAX.

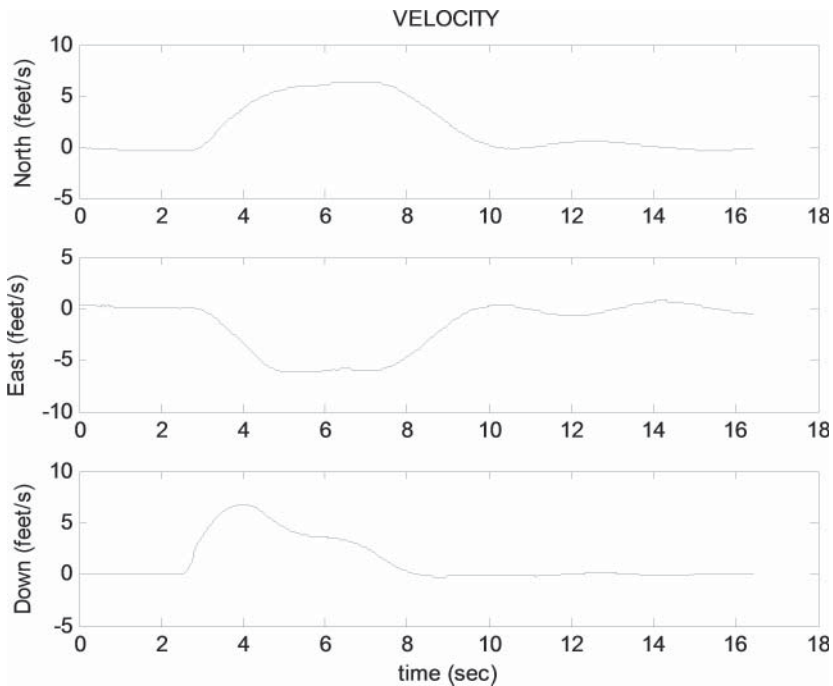
Figure 9.5-9 shows the altitude control response for a step input of 20 ft down. Again, about 50% of full throw of the collective pitch is utilized to start the descent and somewhat less in the reverse direction to stop it. The settling time is about 3 s, just reaching the internal rate limit of 10 ft/s (600 ft/min).

Figure 9.5-10 shows the position for the response to a “superstep” test of the system, where simultaneous position steps in all three directions (NED) and a 180° change in heading take place simultaneously. This maneuver is used to verify the performance of the system when there is movement on more than one axis. Essentially, this is a worst case transient response. Figure 9.5-11 shows velocity just approaching the internal limit of 10 ft/s in magnitude. Figure 9.5-12 shows the attitude during the maneuver. Notice that the initial reaction (nose down) is correct even though the aircraft is, at that moment, still 180° away from the desired heading. Figure 9.5-13 shows the inputs, utilizing between one-fourth and one-half of full throw in each axis.

A video from this superstep simulation is available at: [http://uav.ae.gatech.edu/videos/fgS141026\\_superstep.mp4](http://uav.ae.gatech.edu/videos/fgS141026_superstep.mp4)



**Figure 9.5-10** Adaptive GNC position and altitude tracking step response on all axes simultaneously from simulation of RMAX.



**Figure 9.5-11** Adaptive GNC velocity during step response on all axes simultaneously from simulation of RMAX.

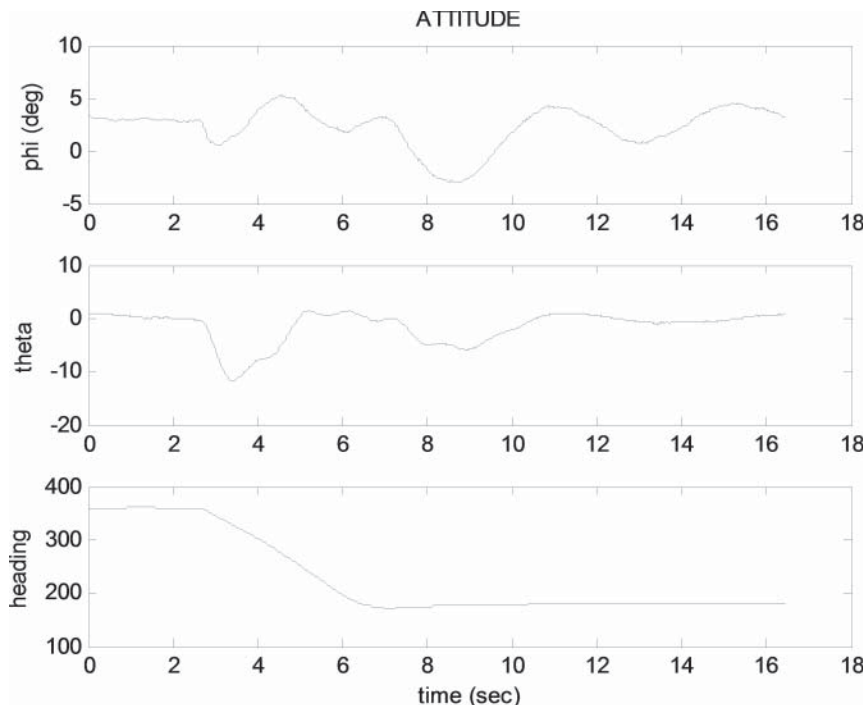


**Figure 9.5-12** Adaptive GNC attitude during step response on all axes simultaneously from simulation of RMAX.

**Simulation of Normal Small Helicopter Maneuvers** A complex flight pattern is utilized to exercise the system executing a series of maneuvers that might be used in normal flight. These maneuvers include acceleration from a hover, deceleration to a hover, sideways flight, rearward flight, and forward flight. Climbs and descents are also included. The test pattern lasts approximately 120 s, with the first half at low speed and the second half at a typical cruise speed.

Figure 9.5-14 shows the position tracking for a simulated test of these maneuvers. The right side of the figure shows a close-up of the low-speed portion of the flight. Tracking is good throughout. Note that the low-speed flight segment includes sideways flight (both ways) and rearward flight.

Figure 9.5-15 shows altitude and speed tracking. One can see that the low-speed portion includes speeds between zero and 15 ft/s. The high-speed segment is at 50 ft/s. Note that the deceleration chosen for the stop-to-hover at the end of the profile was a relatively high  $10 \text{ ft/s}^2$ , which does result in a few feet of altitude tracking error during the tail end of this relatively aggressive maneuver. We see that the maneuver resulted in  $20^\circ$  of nose-up pitch attitude in Figure 9.5-16. The high-speed turns were done at around  $20^\circ$  of bank in this case.

Figure 9.5-17 shows the inputs utilized during these same maneuvers. A significant fraction of the full collective pitch capability was utilized for the high-speed flight

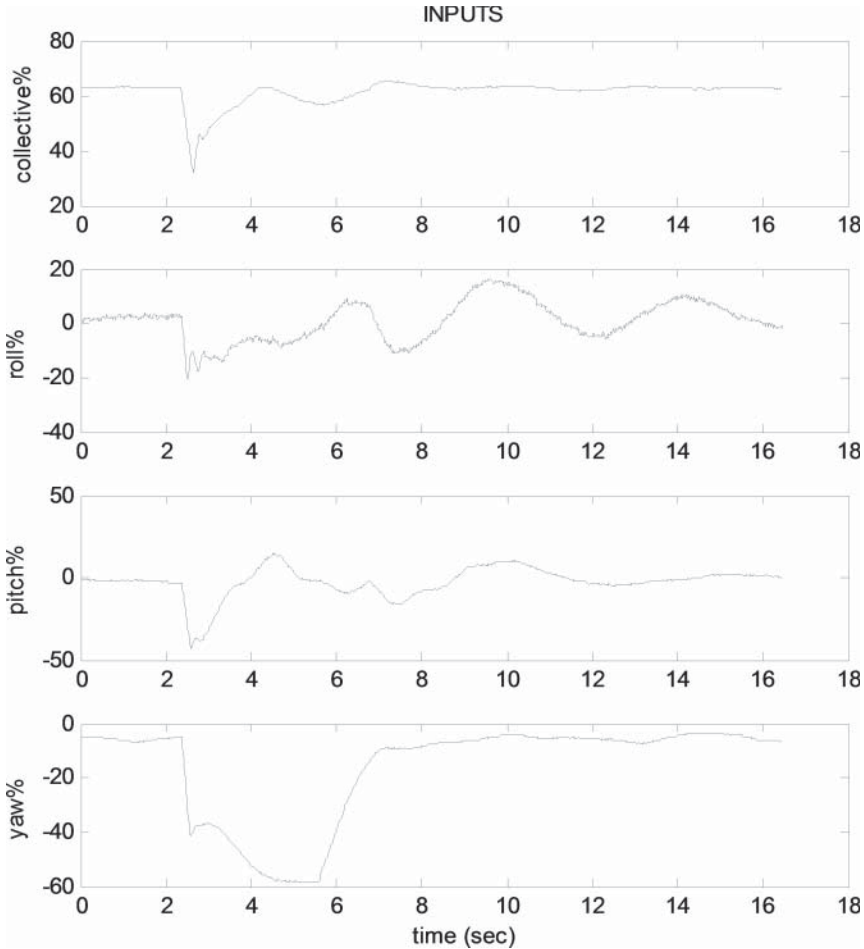


**Figure 9.5-13** Adaptive GNC inputs during step response on all axes simultaneously from simulation of RMAX.

segment. Approximately half of full throw was utilized for cyclic input (both in roll and pitch axes), and a slightly lesser amount of tail rotor authority was required.

A video from this simulation is available at: [http://uav.ae.gatech.edu/videos/fgS141026\\_exercises.mp4](http://uav.ae.gatech.edu/videos/fgS141026_exercises.mp4)

## Flight Test Results

A flight test of the above RMAX small helicopter system was conducted and is described here. The results for step responses are described first. Following this, normal operation is illustrated in the results that follow the step responses, showing a conventional oval racetrack flight path.

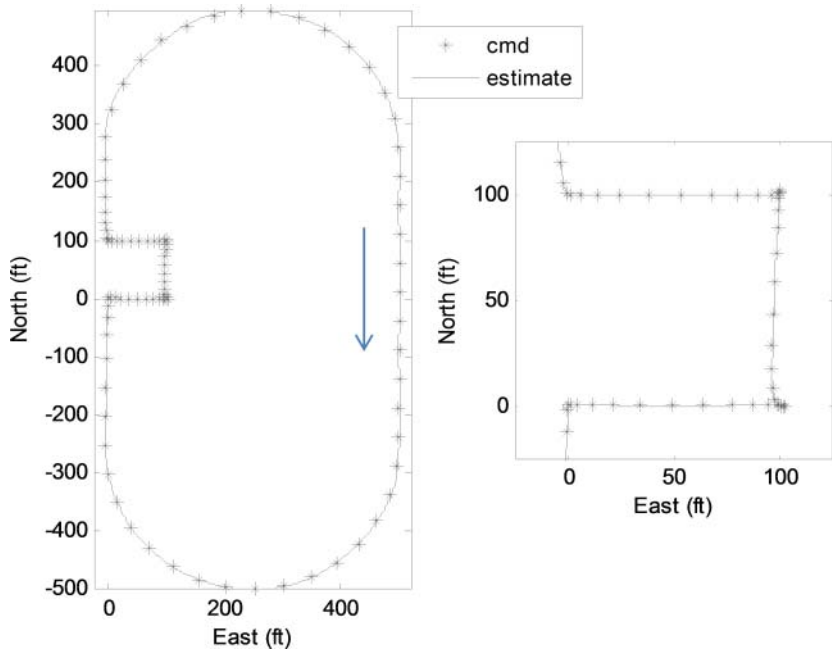


**Figure 9.5-14** Adaptive GNC position tracking during complex flight pattern from simulation of RMAX.

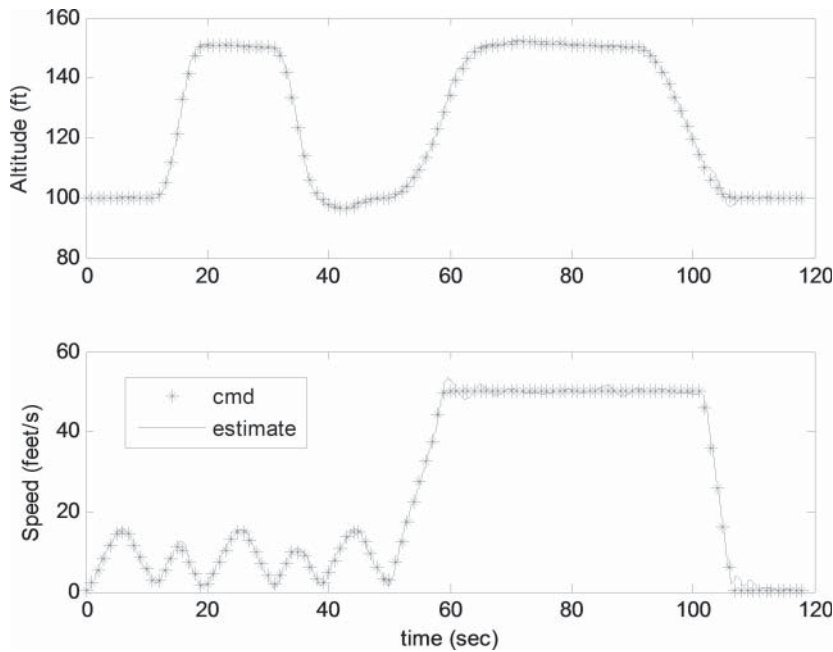


**Figure 9.5-15** Adaptive GNC altitude and speed tracking during complex flight pattern from simulation of RMAX.

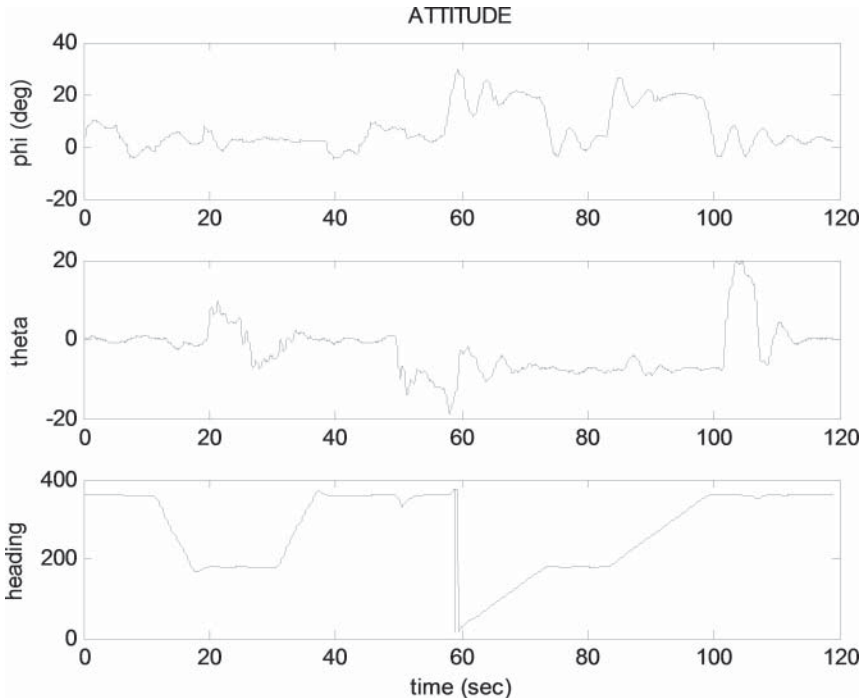


**Figure 9.5-16** Adaptive GNC altitude during complex flight pattern from simulation of RMAX.

**Flight Test of Step Responses** Figure 9.5-18 shows the response for an instantaneous  $180^\circ$  change in the commanded heading. A bit more than 50% of maximum tail rotor authority is utilized to generate a maximum of approximately 50 deg/s of rotation, bringing the aircraft around for a total settling time of approximately 5 s.

Figure 9.5-19 shows the longitudinal position response to a step input of 30 ft forward. This is accomplished primarily with longitudinal cyclic input. Approximately 50% of full throw of the cyclic input is utilized to initiate the maneuver, quickly getting the aircraft up to the reference model internal rate limit of 10 ft/s. The position settling time of 5 s corresponds very well to the theoretical settling time of a fourth-order system with the desired frequencies specified here ( $\omega = 2$ ).

Figure 9.5-20 is the corresponding plot for lateral position response to a step input (to the left) of 30 ft. This is accomplished primarily with lateral cyclic input. Again, about 50% of full throw is utilized to start the maneuver. The internal rate limit is just reached (10 ft/s), and we see a settling time of approximately 4 s. This is close to the theoretical value based on the desired frequency ( $\omega = 2.5$ ).

Figure 9.5-21 shows the altitude control response for a step input of 20 ft down. Again, about 50% of full throw of the collective pitch is utilized to start the descent

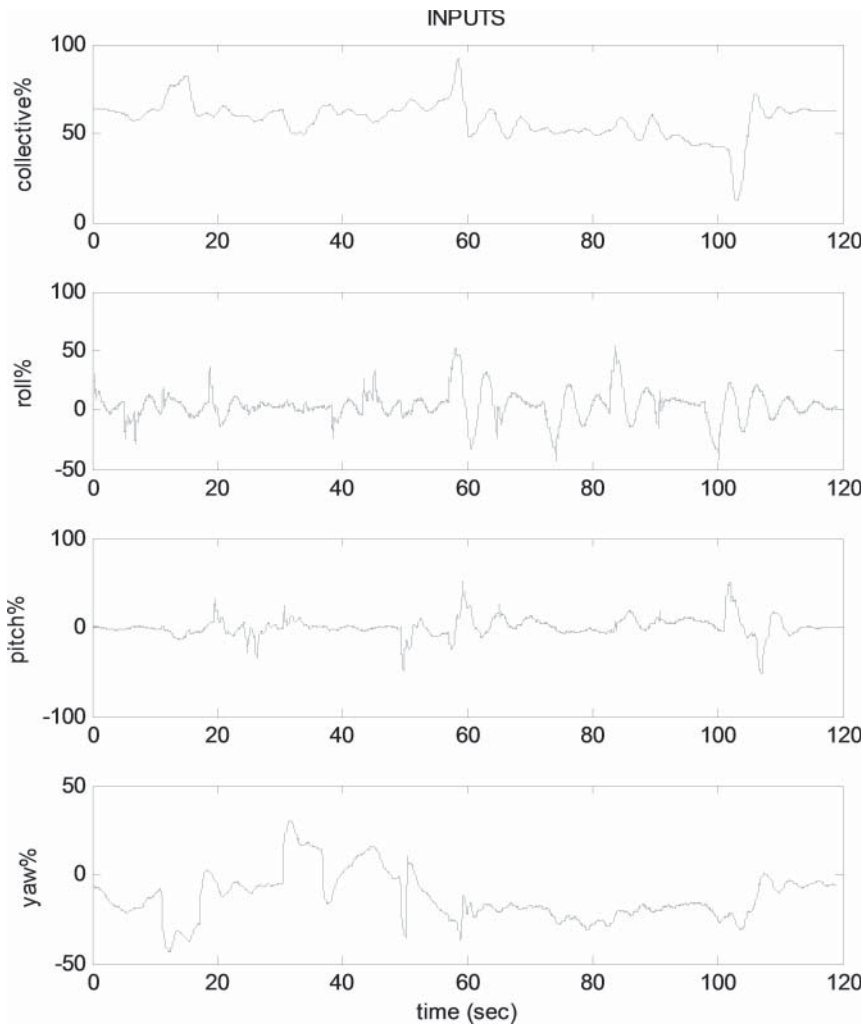


**Figure 9.5-17** Adaptive GNC inputs during complex flight pattern from simulation of RMAX.

and somewhat less in the reverse direction to stop it. The settling time is about 3 s, just reaching the internal rate limit of 10 ft/s (600 ft/min).

A video of the pitch response is available at: [http://uav.ae.gatech.edu/videos/g041222e2\\_30ftStep.mpg](http://uav.ae.gatech.edu/videos/g041222e2_30ftStep.mpg)

A video of the yaw response is available at: [http://uav.ae.gatech.edu/videos/g041222e3\\_180degStep.mpg](http://uav.ae.gatech.edu/videos/g041222e3_180degStep.mpg)



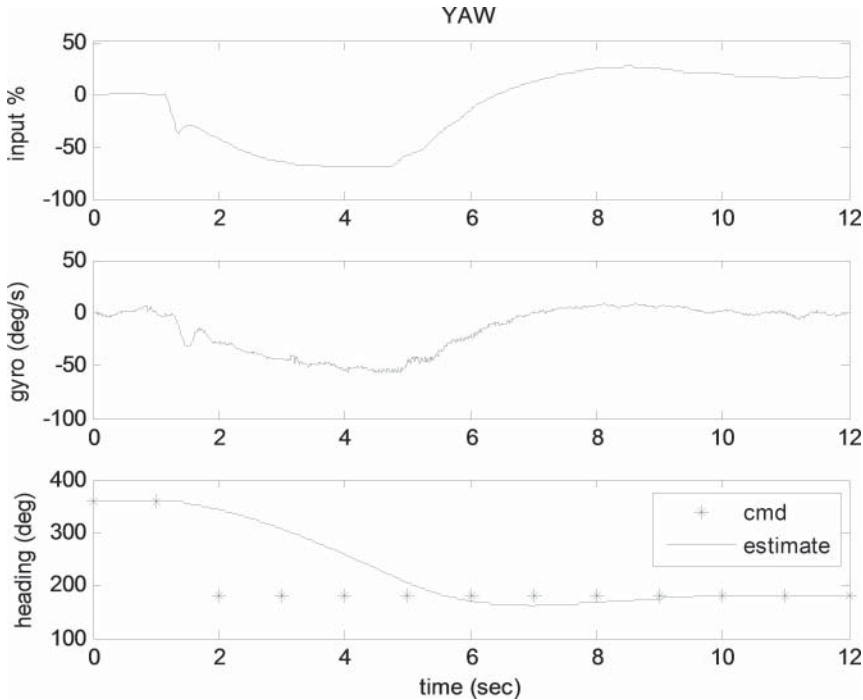
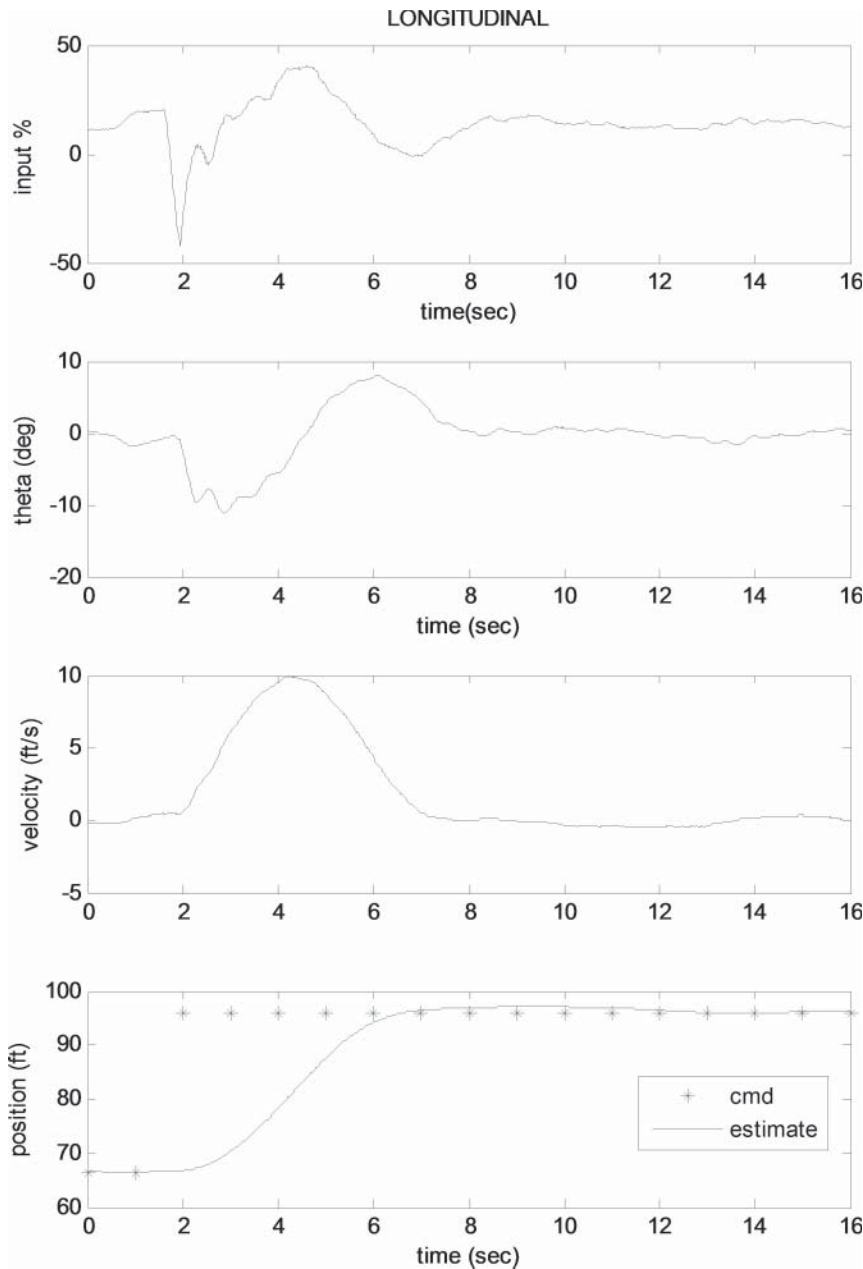


**Figure 9.5-18** Adaptive GNC 180° heading command step response (left) from flight test of RMAX.

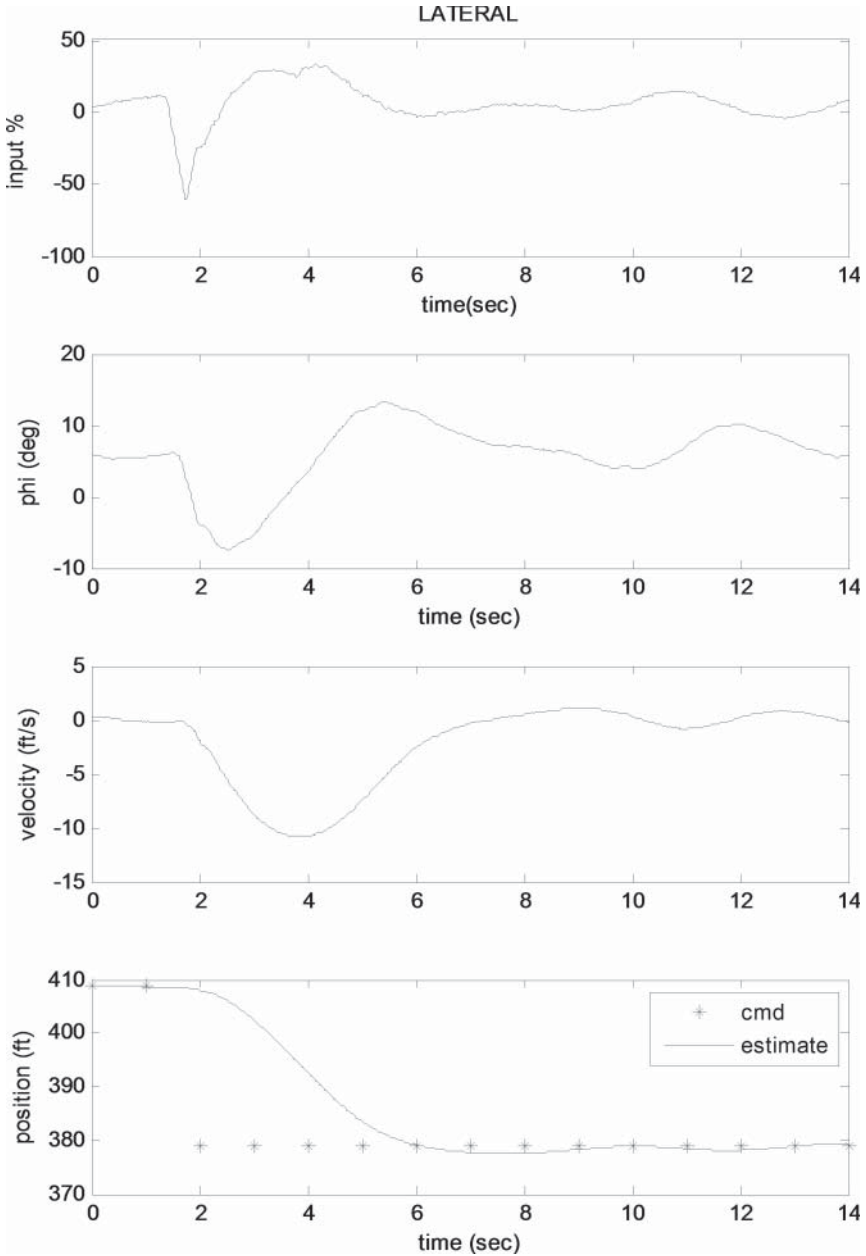
**Flight Test of a Conventional Flight Pattern** Figures 9.5-22 to 9.5-25 illustrate the response of the system when being utilized to fly a typical flight pattern consisting of accelerating, cruising, turning, and stopping. Figure 9.5-22 shows the position tracking. The aircraft starts near the origin and proceeds to the east, accelerating to 50 ft/s. It then turns right until it is heading west. It then turns right again so that it is heading toward where it started. It then proceeds to the starting location and stops. The commanded position shown in the figure is plotted once per second, providing an indication of the segment of flight that involved flight at a lower speed (near the origin).

Figure 9.5-23 shows the total speed of the aircraft during this maneuver. The desired acceleration was  $5 \text{ ft/s}^2$ , and so it requires 10 s to reach the intended speed. The reverse is true on the stop. The slight transient about halfway through the start occurred because the aircraft started the maneuver at the wrong heading and so was simultaneously making a large heading change and accelerating.

Figure 9.5-24 shows the estimated attitude during the maneuvers as standard Euler angles (Section 1.3). The roll angle is approximately  $20^\circ$  during the turns.



**Figure 9.5-19** Adaptive GNC 30 ft longitudinal position command step response (forward) from flight test of RMAX.



**Figure 9.5-20** Adaptive GNC 30 ft lateral position command step response (left) from flight test of RMAX.

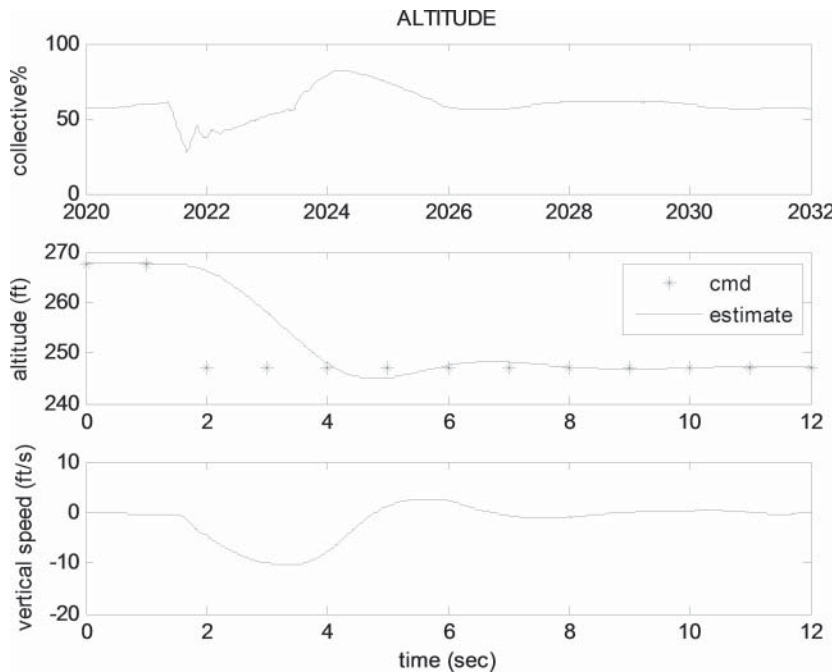


**Figure 9.5-21** Adaptive GNC 20 ft altitude command step response (down) from flight test of RMAX.

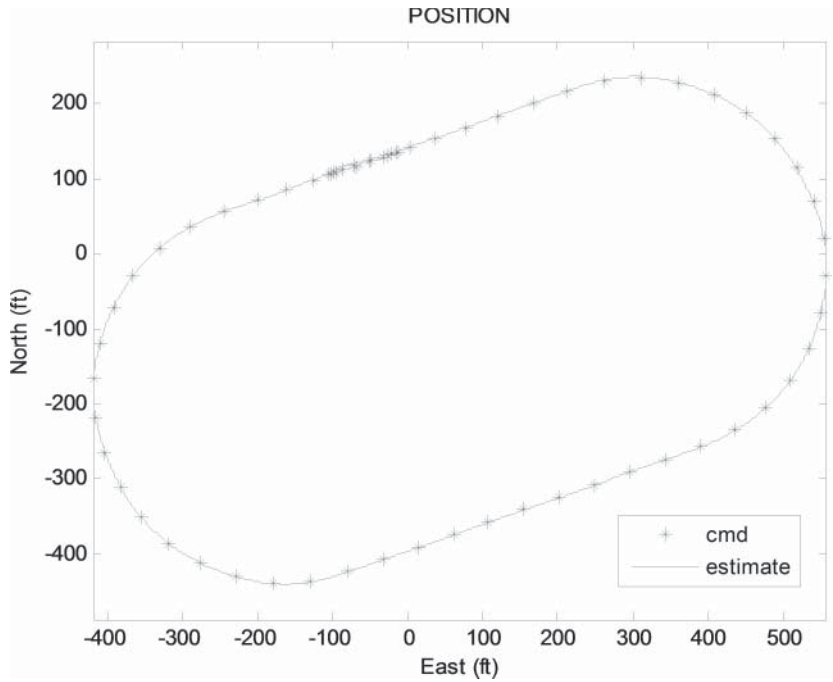


**Figure 9.5-22** Adaptive GNC tracking during racetrack pattern at 50 ft/s from flight test of RMAX.

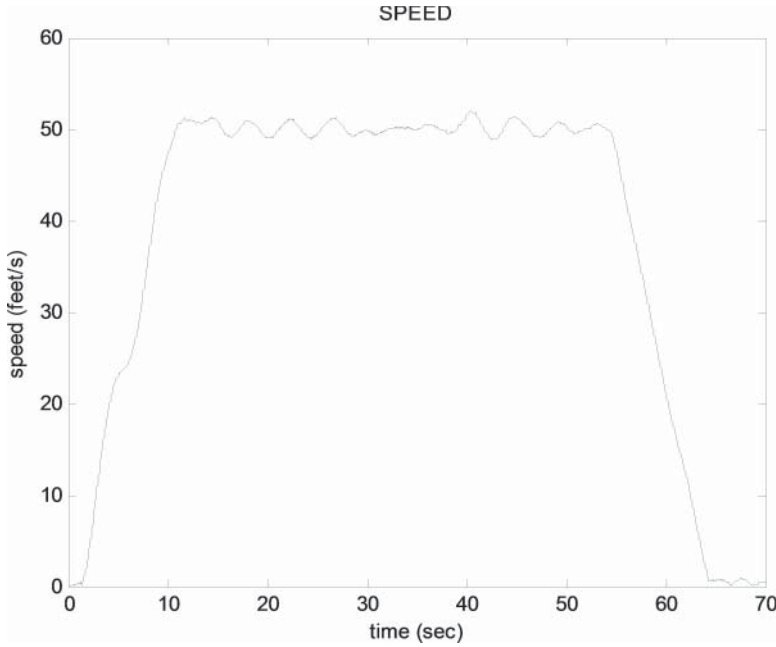


**Figure 9.5-23** Adaptive GNC speed during racetrack pattern from flight test of RMAX.

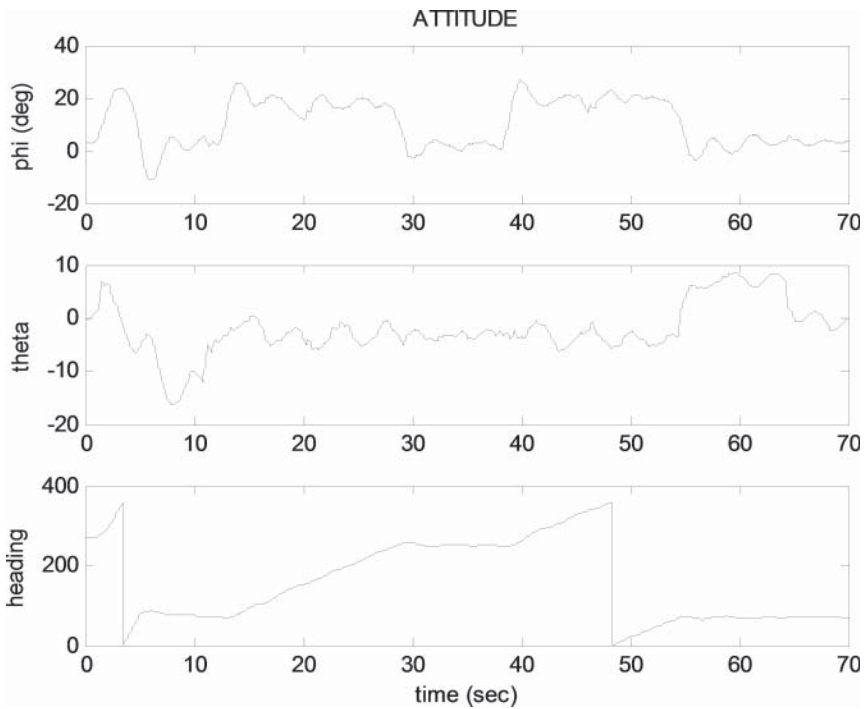


**Figure 9.5-24** Adaptive GNC altitude during racetrack pattern from flight test of RMAX.

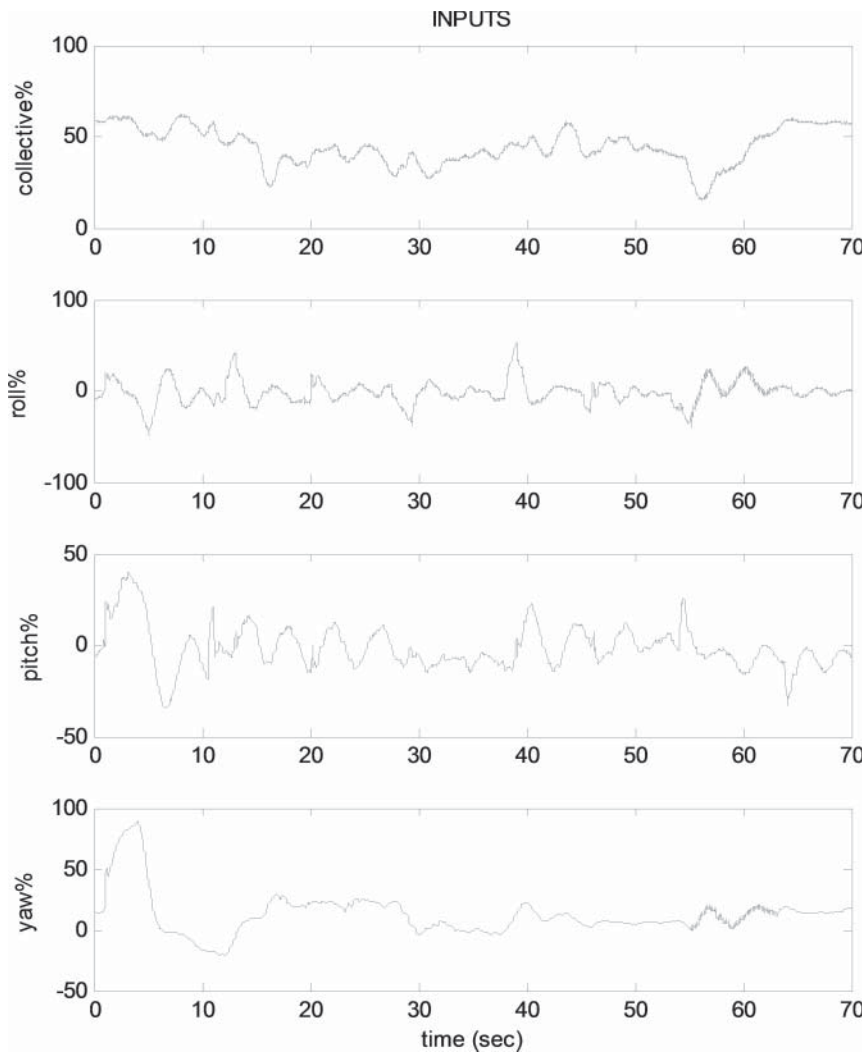


**Figure 9.5-25** Adaptive GNC inputs during racetrack pattern from flight test of RMAX.

This corresponds approximately to what should theoretically be necessary for the selected acceleration for the turns of  $10 \text{ ft/s}^2$ . Figure 9.5-25 shows the vehicle inputs during this pattern. The large yaw input at the start is due to the need to get the aircraft headed in the right direction. That is, the flight starts with a rapid change in the heading command.

A video of a racetrack pattern similar to the one corresponding to the data is available at: [http://uav.ae.gatech.edu/videos/f070911a1\\_racetrack50.wmv](http://uav.ae.gatech.edu/videos/f070911a1_racetrack50.wmv)

## 9.6 SUMMARY

In this chapter, we developed the concept of including adaptation of the vehicle dynamics model in the design of a control system. This was done specifically in the context of dynamic inversion. The resulting controller is an example of model reference adaptive control (MRAC). We utilized an artificial NN as a framework for performing an online curve fit of the model error in our nominal dynamic inversion.

Following this, we included a description of methods to handle some of the most significant issues in adaptive control: input saturation and enabling our control systems to have a cascaded structure. Taken together, these ideas allowed the development of an adaptive guidance and flight control system that not only is able to fly an aircraft in order to follow a prescribed position/velocity trajectory but also enables it to be adaptive in all six degrees of freedom.

This architecture was included in a full guidance, navigation, and control system design for a small helicopter, tying back to concepts from Chapters 5, 6, and 7. The discussion included issues of time delay, update rate, sensor mounting locations, sensor noise, and other related matters.

Simulation and the flight test results of this system were then covered, illustrating a system capable of high-bandwidth position tracking for normal aircraft maneuvers. The illustrated simulation and flight testing also included deliberate discontinuities in the desired trajectory command to verify the approach and implementation.

## REFERENCES

- Bierman, G. J. *Factorization Methods for Discrete Sequential Estimation*. Mineola, NY: Dover, 1977.
- Brinker, J., and K. Wise. "Flight Testing of a Reconfigurable Flight Control Law on the X-36 Tailless Fighter Aircraft." *AIAA Journal of Guidance, Control, and Dynamics*, Washington, D.C.: AIAA, 24, no. 5 (2001): 903–909.
- Calise, A., S. Lee, and M. Sharma. "Development of a Reconfigurable Flight Control Law for Tailless Aircraft." *AIAA Journal of Guidance, Control, and Dynamics*, Washington, D.C.: AIAA, 24, no. 5 (2001): 896–902.
- Christophersen, H. B., et al. "A Compact Guidance, Navigation, and Control System for Unmanned Aerial Vehicles." *AIAA Journal of Aerospace Computing, Information, and Communication*, Washington, D.C.: AIAA, 3, no. 5 (May 2006): 187–213.
- Cybenko, G. "Approximation by Superpositions of a Sigmoidal Function." *Mathematics of Control, Signals, and Systems* 2, no. 4 (1989): 303–314.
- Das, A., F. L. Lewis, and K. Subbarao. "Backstepping Approach for Controlling a Quadrotor using Lagrange Form Dynamics." *Journal of Intelligent and Robotic Systems* 56, nos. 1–2 (September 2009): 127–151.
- Dydek, Z. T., A. M. Annaswamy, and E. Lavretsky. "Adaptive Control and the NASA X-15-3 Flight Revisited." *IEEE Control Systems Magazine* (June 2010): 32–48.

- Gelb, A. *Applied Optimal Estimation*. Cambridge, Mass.: M.I.T. Press, 1974.
- Grewal, M. S., and A. P. Andrews. *Kalman Filtering Theory and Practice*. Englewood Cliffs, N.J.: Prentice Hall, 1993.
- Johnson, E. N., and A. J. Calise. "Limited Authority Adaptive Flight Control for Reusable Launch Vehicles." *AIAA Journal of Guidance, Control, and Dynamics*, Washington, D.C.: AIAA, 26, no. 6 (2003): 906–913.
- Johnson, E. N., and S. K. Kannan. "Adaptive Control with a Nested Saturation Reference Model." *Proceedings of the AIAA Guidance, Navigation, and Control Conference*, Washington, D.C.: AIAA, (August 2003): 1–11.
- Johnson, E. N., and S. K. Kannan. "Adaptive Trajectory Control for Autonomous Helicopters." *AIAA Journal of Guidance, Control, and Dynamics*, Washington, D.C.: AIAA, 28, no. 3 (May/June 2005): 524–538.
- Johnson, E. N., and M. A. Turbe. "Modeling, Control, and Flight Testing of a Small Ducted Fan Aircraft." *AIAA Journal of Guidance, Control, and Dynamics*, Washington, D.C.: AIAA, 29, no. 4 (July/August 2006): 769–779.
- Johnson, E. N., et al. "Flight Test Results of Autonomous Fixed-Wing Transition to and from Stationary Hover." *AIAA Journal of Guidance, Control, and Dynamics*, Washington, D.C.: AIAA, 31, no. 2 (March/April 2008): 358–370.
- Kim, Y. H., and F. L. Lewis. *High-Level Feedback Control with Neural Networks*. Singapore: World Scientific, 1998.
- Lavretsky, E., and K. A. Wise. *Robust and Adaptive Control*. Springer, 2013.
- Lewis, F. L., A. Yesildirek, and K. Liu. "Multilayer Neural-Net Robot Controller with Guaranteed Tracking Performance." *IEEE Transactions on Neural Networks* 7, no. 2 (March 1996): 388–399.
- Lewis, F. L., K. Liu, and A. Yesildirek. "Neural Net Robot Controller with Guaranteed Tracking Performance." *IEEE Transactions on Neural Networks* 6, no. 3 (May 1997).
- Lewis, F. L., S. Jagannathan, and A. Yesildirek. *Neural Network Control of Robot Manipulators and Nonlinear Systems*. Taylor & Francis, 1999.
- Sharma, M., A. Calise, and J. Corban. "Application of an Adaptive Autopilot Design to a Family of Guided Munitions." *Proceedings of the AIAA Guidance, Navigation, and Control Conference*, Washington, D.C.: AIAA, (August 2000): 1–9.
- Teel, A. R. "Global Stabilization and Restricted Tracking for Multiple Integrators with Bounded Controls." *Systems & Control Letters* 18 (1992): 165–171.
- Wie, B., and P. M. Barba. "Quaternion Feedback for Spacecraft Large Angle Maneuvers." *AIAA Journal of Guidance, Control, and Dynamics*, Washington, D.C.: AIAA, 8, no. 3 (1985): 360–365.
- Yesildirek, A., and F. Lewis. "Feedback Linearization Using Neural Networks." *Automatica* 31, no. 11 (1995): 1659–1664.

## PROBLEMS

### Section 9.2

- 9.2-1** Develop a controller design within the architecture described by Figure 9.2-1 for the case where the aircraft dynamics are known exactly and the adaptive



element is not necessary. The true dynamics are  $\dot{x} = u + \sin x$  using the same nomenclature as the figure. Your answer should include:

- (a) An appropriate reference model
- (b) An appropriate linear feedback
- (c) A nominal dynamic inverse

**9.2-2** Using your answer from Problem 9.2-1, simulate the system for a step input of the set point for the reference model.

**9.2-3** Using your answer from Problem 9.2-1, simulate the system for a step input of model error introduced as  $\Delta$  in the dynamics  $\dot{x} = u + \sin x + \Delta$ .

**9.2-4** Consider the case of a second order plant of the form  $m\ddot{x} = -kx - c\dot{x} + u$ , where  $m$ ,  $k$ , and  $c$  represent spring and damper coefficients as indicated. Treat pseudocontrol ( $v$ ) as desired  $\ddot{x}$ . Write the appropriate nominal inverse for this system with  $v$  and  $\dot{x}$  as inputs.

**9.2-5** In Chapter 4 (Equation 4.2-6), an approximation to the short-period mode was found to be

$$\begin{bmatrix} V_T & 0 \\ -M_\alpha & 1 \end{bmatrix} \begin{bmatrix} \dot{\alpha} \\ \dot{q} \end{bmatrix} = \begin{bmatrix} V_T & 0 \\ -M_\alpha & 1 \end{bmatrix} \begin{bmatrix} \alpha \\ q \end{bmatrix} + \begin{bmatrix} Z_{\delta_e} \\ M_{\delta_e} \end{bmatrix} \delta_e$$

Write an appropriate dynamic inverse with as inputs. Note that the pseudocontrol in this cases consists of both  $\dot{\alpha}$  and  $\dot{q}$ . The input to the system is elevator deflection,  $\delta_e$ .

### Section 9.3

**9.3-1** One method to train an artificial NN is to iteratively adjust the interconnection weights based on a set of training data. Consider the true function  $f(x) = \sin x$ . Train a nonparametric NN to approximate this function as close as possible using a training set with 100 randomly selected values for  $x$  between  $-\frac{\pi}{2}$  and  $\frac{\pi}{2}$ . Use an SHL structure with five hidden layer neurons. Use an initial guess of zero for all interconnection weights ( $W$  and  $V$ ). Then, go through each of the 100 points adjusting the weights. For each point, there is a model reconstruction error of  $r = W^T \sigma(V^T \bar{x}) - \sin x$ . Use this error as a basis to adjust the weights by the rule

$$\begin{aligned} \dot{W} &= -r \sigma^T \gamma_W \\ \dot{V} &= -\sigma' W^T r \bar{x}^T \gamma_V, \end{aligned}$$

where  $\gamma_W$  and  $\gamma_V$  are scalar learning rates to be chosen to optimize convergence. Repeat this process (an iteration) until convergence occurs. Make a plot of the total RMS reconstruction error across the 100 points as a function of iteration number. Plot the output of your final NN compared to the function above using your final “best” interconnection weights.

**9.3-2** Perform a trade study on Example 9.3-1 to confirm the choice of controller parameters. In each case, indicate any issues that arise with an extreme increase or decrease of that parameter. Make a final recommendation for each. Provide plots similar to Figures 9.3-2 and 9.3-3 for your final choices.

- (a) Outer layer learning rate  $\Gamma_W$
- (b) Inner layer learning rate  $\Gamma_V$
- (c) Number of hidden layer neurons  $N$

**9.3-3** Modify Example 9.3-1 to create a new related example that represents pitch *angle* control rather than pitch-rate control. This will make the system second order rather than first order. That is, pitch angle is just the integral of pitch rate. There is still only one pseudocontrol however. The linear feedback will now have two gains, of the form  $K_P e + K_D \dot{e}$ . An appropriate adaptive law to use is (Johnson and Calise, 2003)

$$\begin{aligned}\dot{W} &= -[(\sigma - \sigma' V^T \bar{x}) r^T + \lambda \|e\| W] \Gamma_W \\ \dot{V} &= -\Gamma_V [\bar{x} r^T W^T \sigma' + \lambda \|e\| V]\end{aligned}$$

with

$$r = \frac{K_P K_D e / 2 + K_P \dot{e}}{0.25(N - 1) + 1}$$

## Section 9.4

**9.4-1** Explain why it is not possible to do a simple dynamic inverse of a system that has an input saturation nonlinearity.

**9.4-2** Modify Example 9.4-1 to include an actuator rate limit of 0.1 rad/s. Include plots similar to Figures 9.4-2 and 9.4-3.

**9.4-3** Modify Example 9.4-1 for the case of *quantized* control. That is, the actuator can only take on values of  $u$  equal to  $-0.1, -0.05, 0, 0.05$ , and  $0.1$ . Implement this by leaving the nominal dynamic inverse alone and putting a filter after it to quantize the control (presumably by picking the value closest to the desired value). It may be necessary to modify the reference model and linear feedback to achieve good responses. Note that the resulting problem is similar to the use of a reaction control system for attitude control—typical for a spacecraft.

- (a) Provide plots similar to Figures 9.4-2 and 9.4-3 for your solution.
- (b) Add a plot that includes  $v_{ad}$  and  $f(x, u) - \hat{f}(x, u)$  as a function of time.

**9.4-4** PCH has some interesting properties when there is an error in the actuator limits. Repeat Example 9.4-1, but this time have the limit assumed in the controller be 0.12 and the true limit be 0.1 as before.

- (a) Provide plots similar to Figures 9.4-2 and 9.4-3 for your solution.
- (b) Add a plot that includes  $v_{ad}$  and  $f(x, u) - \hat{f}(x, u)$  as a function of time.

**Section 9.5**

- 9.5-1** Explain why the separation principle cannot be invoked in order to design the state estimation scheme and the adaptive controller utilized in this section separately.
- 9.5-2** In one system design, it takes 20 ms to get the sensor inputs, 20 ms to compute the actuator commands, and 50 ms to move the actuators. In a second design, it takes 50 ms to get the sensor inputs, 20 ms to compute the actuator commands, and 20 ms to move the actuators. Make the argument that these systems are equivalent in terms of analyzing the true motion of the aircraft that results.
- 9.5-3** Why is it important to halt NN adaptation when the aircraft is not flying (sitting still on the ground)?
- 9.5-4** The simulation and flight test results indicated good performance at both hover and high-speed flight with the same controller design. The normal practice is to develop more than one controller designs for different flight speeds for a helicopter. Discuss some reasons why it may not have been necessary in this instance.

# APPENDIX A

---

## F-16 MODEL

---

This appendix contains the remainder of the data for the F-16 aircraft model given in Chapter 3. The usage of the lookup tables will be made evident by referring to the aircraft model. These data, Appendix B, and the other programs used in this book can be obtained on a floppy disc, at a nominal cost, from Dr. B. L. Stevens, 1051 Park Manor Terr., Marietta, GA 30064.

### A.1 Mass Properties

$$\text{Weight (lbs) : } W = 20,500$$

$$\text{Moment of Intertia (slug-ft}^2\text{) : } J_{xx} = 9,456$$

$$J_{yy} = 55,814$$

$$J_{zz} = 63,100$$

$$J_{xz} = 982$$

### A.2 Wing Dimensions

$$\text{Span} = 30 \text{ ft}$$

$$\text{Area} = 300 \text{ ft}^2$$

$$\text{m.a.c} = 11.32 \text{ ft}$$

### A.3 Reference CG Location

$$X_{cg} = 0.35\bar{c}$$

## A.4 Control Surface Actuator Models

	deflection limit	rate limit	time const.
Elevator	$\pm 25.0^\circ$ ,	$60^\circ/\text{s}$ ,	0.0495 s lag
Ailerons	$\pm 21.5^\circ$ ,	$80^\circ/\text{s}$ ,	0.0495 s lag
Rudder	$\pm 30.0^\circ$ ,	$120^\circ/\text{s}$ ,	0.0495 s lag

## A.5 Engine Angular Momentum

Assumed fixed at 160 slug-ft<sup>2</sup>/s

## A.6 Standard Atmosphere Model

```

SUBROUTINE ADC(VT,ALT,AMACH,QBAR)      ! air data computer
DATA R0/2.377E-3/                      ! sea-level density
TFAC = 1.0 - 0.703E-5 * ALT
T      = 519.0 * TFAC                  ! temperature
IF (ALT .GE. 35000.0) T= 390.0
RHO = R0 * (TFAC**4.14)                ! density
AMACH= VT/SQRT(1.4*1716.3*T)           ! Mach number
QBAR = 0.5*RHO*VT*VT                  ! dynamic pressure
C      PS      = 1715.0 * RHO * T      ! static pressure
RETURN
END

```

## A.7 Engine Model

The F-16 engine power response is modeled by a first-order lag (in function PDOT, given below). The rest of the model consists of the throttle gearing (in TGEAR) and the lookup tables for thrust as a function of operating power level, altitude, and Mach (in THRUST). In the thrust lookup tables the rows correspond to a Mach number variation from 0 to 1.0 in increments of 0.2, and the columns correspond to altitudes from 0 to 50,000 ft in increments of 10,000 ft. There is a table for each of the power levels “idle,” “military,” and “maximum.” The accompanying linear interpolation algorithm can extrapolate beyond the boundaries of a table, but the results may not be realistic.

```

FUNCTION TGEAR(THTL) ! Power command v. thtl. relationship
IF (THTL.LE.0.77) THEN
TGEAR = 64.94*THTL
ELSE
TGEAR = 217.38*THTL-117.38
END IF
RETURN
END

FUNCTION PDOT(P3,P1) ! PDOT= rate of change of power
IF (P1.GE.50.0) THEN ! P3= actual power, P1= power command
IF (P3.GE.50.0) THEN
T=5.0
P2=P1

```

```

ELSE
P2=60.0
T=RTAU(P2-P3)
END IF
ELSE
IF (P3.GE.50.0) THEN
T=5.0
P2=40.0
ELSE
P2=P1
T=RTAU(P2-P3)
END IF
END IF
PDOT=T*(P2-P3)
RETURN
END
FUNCTION RTAU(DP)      ! used by function PDOT
IF (DP.LE.25.0) THEN
RTAU=1.0      ! reciprocal time constant
ELSE IF (DP.GE.50.0) THEN
RTAU=0.1
ELSE
RTAU=1.9-.036*DP
END IF
RETURN
END
FUNCTION THRUST(POW,ALT,RMACH)      ! Engine thrust model
REAL A(0:5,0:5), B(0:5,0:5), C(0:5,0:5)
DATA A/
+ 1060.0, 670.0, 880.0, 1140.0, 1500.0, 1860.0,
+ 635.0, 425.0, 690.0, 1010.0, 1330.0, 1700.0,
+ 60.0, 25.0, 345.0, 755.0, 1130.0, 1525.0,
+ -1020.0, -710.0, -300.0, 350.0, 910.0, 1360.0,
+ -2700.0, -1900.0, -1300.0, -247.0, 600.0, 1100.0,
+ -3600.0, -1400.0, -595.0, -342.0, -200.0, 700.0/
C      mil data now
DATA B/
+ 12680.0, 9150.0, 6200.0, 3950.0, 2450.0, 1400.0, + 12680.0,
9150.0, 6313.0, 4040.0, 2470.0, 1400.0, + 12610.0, 9312.0, 6610.0,
4290.0, 2600.0, 1560.0, + 12640.0, 9839.0, 7090.0, 4660.0, 2840.0,
1660.0, + 12390.0, 10176.0, 7750.0, 5320.0, 3250.0, 1930.0,
+ 11680.0, 9848.0, 8050.0, 6100.0, 3800.0, 2310.0/
C      max data now
DATA C/
+ 20000.0, 15000.0, 10800.0, 7000.0, 4000.0, 2500.0,
+ 21420.0, 15700.0, 11225.0, 7323.0, 4435.0, 2600.0,
+ 22700.0, 16860.0, 12250.0, 8154.0, 5000.0, 2835.0,
+ 24240.0, 18910.0, 13760.0, 9285.0, 5700.0, 3215.0,
+ 26070.0, 21075.0, 15975.0, 11115.0, 6860.0, 3950.0,
+ 28886.0, 23319.0, 18300.0, 13484.0, 8642.0, 5057.0/
C
H = .0001*ALT
I = INT(H)
IF (I.GE.5) I=4

```

```

DH= H-FLOAT(I)
RM= 5.0*RMACH
M = INT(RM)
IF(M.GE.5)M=4
DM= RM-FLOAT(M)
CDH=1.0-DH
S= B(I,M) *CDH + B(I+1,M) *DH
T= B(I,M+1)*CDH + B(I+1,M+1)*DH
TMIL= S + (T-S)*DM
IF( POW .LT. 50.0 ) THEN
S= A(I,M) *CDH + A(I+1,M) *DH
T= A(I,M+1)*CDH + A(I+1,M+1)*DH
TIDL= S + (T-S)*DM
THRUST=TIDL+(TMIL-TIDL)*POW*.02
ELSE
S= C(I,M) *CDH + C(I+1,M) *DH
T= C(I,M+1)*CDH + C(I+1,M+1)*DH
TMAX= S + (T-S)*DM
THRUST=TMIL+(TMAX-TMIL)*(POW-50.0)*.02
END IF
RETURN
END

```

## A.8 Aerodynamic Data

The aerodynamic data tables and associated interpolation algorithms, given below, will provide values for the body-axis dimensionless aerodynamic coefficients of the F-16 model at arbitrary values of the independent variables. The angle-of-attack range of the tables is from  $-10^\circ$  to  $45^\circ$  in  $5^\circ$  increments, and the sideslip angle range is from  $-30^\circ$  to  $30^\circ$  in either  $5^\circ$  or  $10^\circ$  increments. The given interpolation algorithm interpolates linearly between the data points; it will extrapolate beyond the table boundaries, but the results may be unrealistic.

```

SUBROUTINE DAMP(ALPHA, D) ! various damping coefficients
REAL A(-2:9,9),D(9)
DATA A/
& -.267, -.110, .308, 1.34, 2.08, 2.91, 2.76,
& 2.05, 1.50, 1.49, 1.83, 1.21,
& .882, .852, .876, .958, .962, .974, .819,
& .483, .590, 1.21, -.493, -1.04,
& -.108, -.108, -.188, .110, .258, .226, .344,
& .362, .611, .529, .298, -2.27,
& -8.80, -25.8, -28.9, -31.4, -31.2, -30.7, -27.7,
& -28.2, -29.0, -29.8, -38.3, -35.3,
& -.126, -.026, .063, .113, .208, .230, .319,
& .437, .680, .100, .447, -.330,
& -.360, -.359, -.443, -.420, -.383, -.375, -.329,
& -.294, -.230, -.210, -.120, -.100,
& -7.21, -.540, -5.23, -5.26, -6.11, -6.64, -5.69,
& -6.00, -6.20, -6.40, -6.60, -6.00,
& -.380, -.363, -.378, -.386, -.370, -.453, -.550,
& -.582, -.595, -.637, -1.02, -.840,

```

## 718 F-16 MODEL

```

& .061, .052, .052, -.012, -.013, -.024, .050,
& .150, .130, .158, .240, .150/
C
S= 0.2 * ALPHA
K= INT(S)
IF(K .LE. -2) K= -1
IF(K .GE. 9) K= 8
DA= S - FLOAT(K)
L = K + INT( SIGN(1.1,DA) )
DO 1, I= 1,9
1 D(I)= A(K,I) + ABS(DA) * (A(L,I) - A(K,I))
END
C
C D1= CXq; D2= CYr; D3= Cyp; D4= CZq; D5= Clr; D6= Clp
C D7= Cm q; D8= Cnr; D9= Cnp
FUNCTION CX(ALPHA,EL) ! x-axis aerodynamic force coeff.
REAL A(-2:9,-2:2)
DATA A/
& -.099, -.081, -.081, -.063, -.025, .044, .097,
& .113, .145, .167, .174, .166,
& -.048, -.038, -.040, -.021, .016, .083, .127,
& .137, .162, .177, .179, .167,
& -.022, -.020, -.021, -.004, .032, .094, .128,
& .130, .154, .161, .155, .138,
& -.040, -.038, -.039, -.025, .006, .062, .087,
& .085, .100, .110, .104, .091,
& -.083, -.073, -.076, -.072, -.046, .012, .024,
& .025, .043, .053, .047, .040/
C
S= 0.2 * ALPHA
K= INT(S)
IF(K .LE. -2) K= -1
IF(K .GE. 9) K= 8
DA= S - FLOAT(K)
L = K + INT( SIGN(1.1,DA) )
S= EL/12.0
M= INT(S)
IF(M .LE. -2) M= -1
IF(M .GE. 2) M= 1
DE= S - FLOAT(M)
N= M + INT( SIGN(1.1,DE) )
T= A(K,M)
U= A(K,N)
V= T + ABS(DA) * (A(L,M) - T)
W= U + ABS(DA) * (A(L,N) - U)
CX= V + (W-V) * ABS(DE)
RETURN
END
FUNCTION CY(BETA,AIL,RDR) ! sideforce coefficient
CY= -.02*BETA + .021*(AIL/20.0) + .086*(RDR/30.0)
END
FUNCTION CZ(ALPHA,BETA,EL) ! z-axis force coeff.
REAL A(-2:9)
DATA A/ .770, .241, -.100, -.416, -.731, -1.053,

```



```

& -1.366, -1.646, -1.917, -2.120, -2.248, -2.229/
S= 0.2 * ALPHA
K= INT(S)
IF(K .LE. -2) K= -1
IF(K .GE. 9) K= 8
DA= S - FLOAT(K)
L = K + INT( SIGN(1.1,DA) )
S= A(K) + ABS(DA) * (A(L) - A(K))
CZ= S*(1-(BETA/57.3)**2) - .19*(EL/25.0)
END
FUNCTION CM(ALPHA,EL) ! pitching moment coeff.
REAL A(-2:9,-2:2)
DATA A/
& .205, .168, .186, .196, .213, .251, .245,
& .238, .252, .231, .198, .192,
& .081, .077, .107, .110, .110, .141, .127,
& .119, .133, .108, .081, .093,
& -.046, -.020, -.009, -.005, -.006, .010, .006,
& -.001, .014, .000, -.013, .032,
& -.174, -.145, -.121, -.127, -.129, -.102, -.097,
& -.113, -.087, -.084, -.069, -.006,
& -.259, -.202, -.184, -.193, -.199, -.150, -.160,
& -.167, -.104, -.076, -.041, -.005/
C      SAME INTERPOLATION AS CX *****
C
FUNCTION CL(ALPHA,BETA) ! rolling moment coeff.
REAL A(-2:9,0:6)
DATA A/12*0,
& -.001, -.004, -.008, -.012, -.016, -.019, -.020,
& -.020, -.015, -.008, -.013, -.015,
& -.003, -.009, -.017, -.024, -.030, -.034, -.040,
& -.037, -.016, -.002, -.010, -.019,
& -.001, -.010, -.020, -.030, -.039, -.044, -.050,
& -.049, -.023, -.006, -.014, -.027,
& .000, -.010, -.022, -.034, -.047, -.046, -.059,
& -.061, -.033, -.036, -.035, -.035,
& .007, -.010, -.023, -.034, -.049, -.046, -.068,
& -.071, -.060, -.058, -.062, -.059,
& .009, -.011, -.023, -.037, -.050, -.047, -.074,
& -.079, -.091, -.076, -.077, -.076/
C
S= 0.2 * ALPHA
K= INT(S)
IF(K .LE. -2) K= -1
IF(K .GE. 9) K= 8
DA= S - FLOAT(K)
L = K + INT( SIGN(1.1,DA) )
S= .2* ABS(BETA)
M= INT(S)
IF(M .EQ. 0) M= 1
IF(M .GE. 6) M= 5
DB= S - FLOAT(M)

```

```

N= M + INT( SIGN(1.1,DB) )
T= A(K,M)
U= A(K,N)
V= T + ABS(DA) * (A(L,M) - T)
W= U + ABS(DA) * (A(L,N) - U)
DUM= V + (W-V) * ABS(DB)
CL= DUM + SIGN(1.0, BETA)
RETURN
END
FUNCTION CN(ALPHA,BETA)    ! yawing moment coeff.
REAL A(-2:9,0:6)
DATA A/12 *0,
& .018, .019, .018, .019, .019, .018, .013,
& .007, .004, -.014, -.017, -.033,
& .038, .042, .042, .042, .043, .039, .030,
& .017, .004, -.035, -.047, -.057,
& .056, .057, .059, .058, .058, .053, .032,
& .012, .002, -.046, -.071, -.073,
& .064, .077, .076, .074, .073, .057, .029,
& .007, .012, -.034, -.065, -.041,
& .074, .086, .093, .089, .080, .062, .049,
& .022, .028, -.012, -.002, -.013,
& .079, .090, .106, .106, .096, .080, .068,
& .030, .064, .015, .011, -.001/
C NOW USE SAME INTERPOLATION AS CL *****
C
FUNCTION DLDA(ALPHA,BETA) ! rolling mom. due to ailerons
REAL A(-2:9,-3:3)
DATA A/-.041, -.052, -.053, -.056, -.050, -.056, -.082,
& -.059, -.042, -.038, -.027, -.017,
& -.041, -.053, -.053, -.053, -.050, -.051, -.066,
& -.043, -.038, -.027, -.023, -.016,
& -.042, -.053, -.052, -.051, -.049, -.049, -.043,
& -.035, -.026, -.016, -.018, -.014,
& -.040, -.052, -.051, -.052, -.048, -.048, -.042,
& -.037, -.031, -.026, -.017, -.012,
& -.043, -.049, -.048, -.049, -.043, -.042, -.042,
& -.036, -.025, -.021, -.016, -.011,
& -.044, -.048, -.048, -.047, -.042, -.041, -.020,
& -.028, -.013, -.014, -.011, -.010,
& -.043, -.049, -.047, -.045, -.042, -.037, -.003,
& -.013, -.010, -.003, -.007, -.008/
S= 0.2 * ALPHA
K= INT(S)
IF(K .LE. -2) K= -1
IF(K .GE. 9) K= 8
DA= S - FLOAT(K)
L = K + INT( SIGN(1.1,DA) )
S= 0.1 * BETA
M= INT(S)
IF(M .eq. -3) M= -2
IF(M .GE. 3) M= 2

```

```

DB= S - FLOAT(M)
N= M + INT( SIGN(1.1,DB) )
T= A(K,M)
U= A(K,N)
V= T + ABS(DA) * (A(L,M) - T)
W= U + ABS(DA) * (A(L,N) - U)
DLDA= V + (W-V) * ABS(DB)
RETURN
END
FUNCTION DLDR(ALPHA,BETA) ! rolling moment due to rudder
REAL A(-2:9,-3:3) ! use same interpolation as DLDA
DATA A/ .005, .017, .014, .010, -.005, .009, .019,
& .005, -.000, -.005, -.011, .008,
& .007, .016, .014, .014, .013, .009, .012,
& .005, .000, .004, .009, .007,
& .013, .013, .011, .012, .011, .009, .008,
& .005, -.002, .005, .003, .005,
& .018, .015, .015, .014, .014, .014, .014,
& .015, .013, .011, .006, .001,
& .015, .014, .013, .013, .012, .011, .011,
& .010, .008, .008, .007, .003,
& .021, .011, .010, .011, .010, .009, .008,
& .010, .006, .005, .000, .001,
& .023, .010, .011, .011, .011, .010, .008,
& .010, .006, .014, .020, .000/
C
FUNCTION DNDA(ALPHA,BETA) ! yawing moment due to ailerons
REAL A(-2:9,-3:3) ! use same interpolation as DLDA *
DATA A/ .001, -.027, -.017, -.013, -.012, -.016, .001,
& .017, .011, .017, .008, .016,
& .002, -.014, -.016, -.016, -.014, -.019, -.021,
& .002, .012, .015, .015, .011,
& -.006, -.008, -.006, -.006, -.005, -.008, -.005,
& .007, .004, .007, .006, .006,
& -.011, -.011, -.010, -.009, -.008, -.006, .000,
& .004, .007, .010, .004, .010,
& -.015, -.015, -.014, -.012, -.011, -.008, -.002,
& .002, .006, .012, .011, .011,
& -.024, -.010, -.004, -.002, -.001, .003, .014,
& .006, -.001, .004, .004, .006,
& -.022, .002, -.003, -.005, -.003, -.001, -.009,
& -.009, -.001, .003, -.002, .001/
C
FUNCTION DNDR(ALPHA,BETA) ! yawing moment due to rudder
REAL A(-2:9,-3:3)
DATA A/ -.018, -.052, -.052, -.052, -.054, -.049, -.059,
& -.051, -.030, -.037, -.026, -.013,
& -.028, -.051, -.043, -.046, -.045, -.049, -.057,
& -.052, -.030, -.033, -.030, -.008,
& -.037, -.041, -.038, -.040, -.040, -.038, -.037,
& -.030, -.027, -.024, -.019, -.013,
& -.048, -.045, -.045, -.045, -.044, -.045, -.047,

```

**722** F-16 MODEL

```
& -.048, -.049, -.045, -.033, -.016,  
& -.043, -.044, -.041, -.041, -.040, -.038, -.034,  
& -.035, -.035, -.029, -.022, -.009,  
& -.052, -.034, -.036, -.036, -.035, -.028, -.024,  
& -.023, -.020, -.016, -.010, -.014,  
& -.062, -.034, -.027, -.028, -.027, -.027, -.023,  
& -.023, -.019, -.009, -.025, -.010/  
C NOW USE SAME INTERPOLATION AS DLDA *****
```

## APPENDIX B

---

### SOFTWARE

---

This appendix contains the Fortran code that is required to use the aircraft models given in the text and is not otherwise readily available. For the steady-state trim algorithm (Section B.1) we give the basic trimmer subroutine, part of the constraint subroutine, a cost function, and the Simplex minimization algorithm. The user must write a driver program and add additional flight-path constraints, as required. In Section B.2 a subroutine for numerical linearization is given, and the user need only add a driver program. Software for time-history simulation and control systems design is readily available from other sources and so, in the rest of this appendix, we have given only the Runge-Kutta algorithm that was used for most of the examples.

Appendix A, Appendix B, and the programs used in this book can be obtained on a floppy disc, at a nominal cost, from Dr. B. L. Stevens, 1051 Park Manor Terr., Marietta, GA 30064.

#### B.1 AIRCRAFT STEADY-STATE TRIM CODE

The subroutine “TRIMMER” (below) sets up a function minimization algorithm to determine a steady-state trim condition for either a 6-DoF or 3-DoF (longitudinal-only) aircraft model. The subroutine arguments are the number of degrees of freedom (NV) and the “COST” function (which must be declared “EXTERNAL” in the main program). Labeled COMMON storage is used to pass the state and control vectors to and from the main program and the cost function (and, in the case of the control vector, the aircraft model also).

The main program must initialize the state vector according to the trim condition required, and the control vector can simply be set to zero initially. It must also set the turn rate, roll rate, or pull up rate; set flags for coordinated turns or stability-axis roll;

and pass these through a common block ("CONSTRNT") to the constraint routine. A Simplex routine (given below) is used for function minimization, and it returns the coordinates of the cost function minimum in the Simplex vector S. The cost function is then called once more to set the state and control vectors to their final values, and these values are passed through COMMON to the main program to be placed in a data file. Subroutine "SMPLX" can easily be replaced by "ZXWMD" from the IMSL library, or "AMOEBA" from "Numerical Recipes" if desired. The author is indebted to Dr. P. Vesty for this Simplex routine.

```

SUBROUTINE TRIMMER (NV, COST)
PARAMETER (NN=20, MM=10)
EXTERNAL COST
CHARACTER*1 ANS
DIMENSION S(6), DS(6)
COMMON/ STATE/ X(NN)
COMMON/ CONTROLS/ U(MM)
COMMON/ OUTPUT/ AN,AY,AX,QBAR,AMACH ! common to aircraft
DATA RTOD /57.29577951/
S(1)= U(1)
S(2)= U(2)
S(3)= X(2)
IF(NV .LE. 3) GO TO 10
S(4)= U(3)
S(5)= U(4)
S(6)= X(3)
10      DS(1) = 0.2
        DS(2)= 1.0
        DS(3)= 0.02
IF(NV .LE. 3) GO TO 20
        DS(4)= 1.0
        DS(5)= 1.0
        DS(6)= 0.02
20      NC= 1000
WRITE(*,'(1X,A,$)') 'Reqd. # of trim iterations (def. = 1000) : '
READ(*,*,ERR=20) NC
SIGMA = -1.0
CALL SMPLX(COST,NV,S,DS,SIGMA,NC,F0,FFIN)
FFIN = COST(S)
IF (NV .GT. 3) THEN
WRITE(*,' (/11X,A)') 'Throttle      Elevator,      Ailerons,      Rud-
der'
WRITE(*,' (9X,4(1PE10.2,3X),/ )') U(1), U(2), U(3), U(4)
WRITE(*,99) 'Angle of attack',RTOD*X(2), 'Sideslip angle',RTOD*X(3)
WRITE(*,99) 'Pitch angle', RTOD*X(5), 'Bank angle', RTOD*X(4)
WRITE(*,99) 'Normal acceleration', AN, 'Lateral acceln', AY
WRITE(*,99) 'Dynamic pressure', QBAR, 'Mach number', AMACH
ELSE
WRITE(*,' (/1X,A)') 'Throttle      Elevator      Alpha Pitch'
WRITE(*,' (1X,4(1PE10.2,3X))') U(1),U(2),X(2)*RTOD,X(3)*RTOD
WRITE(*,' (/1X,A)') 'Normal acceleration Dynamic Pressure Mach '
WRITE(*,' (5X,3(1PE10.2,7X))') AN,QBAR,AMACH
END IF

```

```

WRITE(*,99)'Initial cost function ',F0,'Final cost function',FFIN
99      FORMAT(2(1X,A22,1PE10.2))
40      WRITE(*,' (/1X,A,$)') 'More Iterations ? (def= Y) : '
READ(*,' (A)',ERR= 40) ANS
IF (ANS .EQ. 'Y'.OR. ANS .EQ. 'y'.OR. ANS .EQ. '/') GO TO 10
IF (ANS .EQ. 'N'.OR. ANS .EQ. 'n') RETURN
GO TO 40
END
FUNCTION CLF16 (S)      ! F16 cost function (see text)
PARAMETER (NN=20)
REAL S(*), XD(NN)
COMMON/STATE/X(NN) ! common to main program
COMMON/CONTROLS/THTL,EL,AIL,RDR ! to aircraft
THTL = S(1)
EL = S(2)
X(2)= S(3)
AIL = S(4)
RDR = S(5)
X(3) = S(6)
X(13)= TGEAR (THTL)
CALL CONSTR (X)
CALL      F (TIME,X,XD)
CLF16 = XD(1)**2 + 100.0*( XD(2)**2 + XD(3)**2 )
&      + 10.0*( XD(7)**2 + XD(8)**2 + XD(9)**2 )
RETURN
END
SUBROUTINE CONSTR (X) ! used by COST, to apply constraints
DIMENSION X(*)
LOGICAL COORD, STAB
COMMON/CNSTRNT/RADGAM,SINGAM,RR,PR,TR,PHI,CPhi,SPHI,COORD,STAB
C common to main program.
CALPH = COS(X(2))
SALPH = SIN(X(2))
CBETA = COS(X(3))
SBETA = SIN(X(3))
IF (COORD) THEN
! coordinated turn logic here
ELSE IF (TR .NE. 0.0) THEN
! skidding turn logic here
ELSE      ! non-turning flight
X(4)= PHI
D = X(2)
IF(PHI .NE. 0.0) D = -X(2) ! inverted
IF( SINGAM .NE. 0.0 ) THEN ! climbing
SGOCB = SINGAM / CBETA
X(5)= D + ATAN( SGOCB/SQRT(1.0-SGOCB*SGOCB)) ! roc constraint
ELSE
X(5) = D      ! level
END IF
X(7)= RR
X(8)= PR
IF (STAB) THEN      ! stab.-axis roll
X(9)= RR*SALPH/CALPH

```

```

ELSE
X(9) = 0.0      ! body-axis roll
END IF
END IF
RETURN
END
SUBROUTINE SMPLX(FX,N,X,DX,SD,M,Y0,YL)
C This simplex algorithm minimizes FX(X), where X is (Nx1).
C DX contains the initial perturbations in X. SD should be set
  according
C to the tolerance required; when SD<0 the algorithm calls FX M
  times
REAL X(*), DX(*)
DIMENSION XX(32), XC(32), Y(33), V(32,32)
C
NV=N+1
DO 2 I=1,N
DO 1 J=1,NV
1      V(I,J)=X(I)
2      V(I,I+1)=X(I)+DX(I)
Y0=FX(X)
Y(1)=Y0
DO 3 J=2,NV
3      Y(J)=FX(V(1,J))
K=NV
4      YH=Y(1)
YL=Y(1)
NH=1
NL=1
DO 5 J=2,NV
IF(Y(J).GT.YH) THEN
YH=Y(J)
NH=J
ELSEIF(Y(J).LT.YL) THEN
YL=Y(J)
NL=J
ENDIF
5      CONTINUE
YB=Y(1)
DO 6 J=2,NV
6      YB=YB+Y(J)
YB=YB/NV
D=0.0
DO 7 J=1,NV
7      D=D+(Y(J)-YB)**2
SDA=SQRT(D/NV)
IF((K.GE.M).OR.(SDA.LE.SD)) THEN
SD=SDA
M=K
YL=Y(NL)
DO 8 I=1,N
8      X(I)=V(I,NL)

```



```

RETURN END IF
DO 10 I=1,N XC(I)=0.0
DO 9 J=1,NV
9      IF(J.NE.NH) XC(I)=XC(I)+V(I,J)
10     XC(I)=XC(I)/N
DO 11 I=1,N
11     X(I)=XC(I)+XC(I)-V(I,NH)
K=K+1
YR=FX(X)
IF(YR.LT.YL) THEN
DO 12 I=1,N
12     XX(I)=X(I)+X(I)-XC(I)
K=K+1
YE=FX(XX)
IF(YE.LT.YR) THEN
Y(NH)=YE
DO 13 I=1,N
13         V(I,NH)=XX(I)
ELSE
Y(NH)=YR
DO 14 I=1,N
14     V(I,NH)=X(I)
END IF
GOTO 4
ENDIF
Y2=Y(NL)
DO 15 J=1,NV
15     IF((J.NE.NL).AND.(J.NE.NH).AND.(Y(J).GT.Y2)) Y2=Y(J)
IF(YR.LT.YH) THEN
Y(NH)=YR
DO 16 I=1,N
16     V(I,NH)=X(I)
IF(YR.LT.Y2) GO TO 4
ENDIF
DO 17 I=1,N
17     XX(I)=0.5*(V(I,NH)+XC(I))
K=K+1
YC=FX(XX)
IF(YC.LT.YH) THEN
Y(NH)=YC
DO 18 I=1,N
18     V(I,NH)=XX(I)
ELSE
DO 20 J=1,NV
DO 19 I=1,N
19     V(I,J)=0.5*(V(I,J)+V(I,NL))
20     IF(J.NE.NL) Y(J)=FX(V(1,J))
K=K+N
ENDIF
GO TO 4
END

```

## B.2 NUMERICAL LINEARIZATION SUBROUTINE

Subroutine JACOB will calculate Jacobian matrices for the set of nonlinear state equations contained in the subroutine F (specified as an argument of JACOB). Subroutine F(TIME, X, XD) should contain "CONTROLS" and "OUTPUT" common blocks as used in the text. The argument FN is a double-precision function used to determine an approximation to each partial derivative that is required.

To calculate the  $A$ ,  $B$ ,  $C$ ,  $D$  matrices the main program should be designed to call JACOB four times, with FN replaced in turn by each of the partial derivative functions FDX, FDU, YDX, and YDU (given below). The partial derivative functions must be declared "EXTERNAL" in the main program. The vectors  $X$  and  $XD$  are, respectively, the state vector and its derivative. The vector  $V$  must contain the equilibrium condition and should be replaced by  $X$  or  $U$ , respectively, depending on whether the partial derivatives with respect to  $X$  or  $U$  are being calculated. The array  $IO$  is used to specify the set of integers corresponding to the rows of the Jacobian matrix, and  $JO$  is used to specify the set corresponding to the columns.  $NR$  and  $NC$  are, respectively, the number of rows and the number of columns in the Jacobian matrix and the linear array  $ABC$  contains the columns of the Jacobian matrix, stacked one after the other.

The linearization algorithm chooses smaller and smaller perturbations in the independent variable and compares three successive approximations to the particular partial derivative. If these approximations agree within a certain tolerance, then the size of the perturbation is reduced to determine if an even smaller tolerance can be satisfied. The algorithm terminates successfully when a tolerance TOLMIN is reached or if a tolerance of at least OKTOL can be achieved. If the algorithm does not terminate successfully, then the successive approximations are displayed and the user is asked to decide on the value of the partial derivative.

```
SUBROUTINE JACOB (FN,F,X,XD,V,IO,JO,ABC,NR,NC)
  DIMENSION X(*),XD(*),V(*),IO(*),JO(*),ABC(*)
  EXTERNAL FN,F
  LOGICAL FLAG, DIAGS
  CHARACTER*1 ANS
  REAL*8 FN,TDV
  DATA DEL,DMIN,TOLMIN,OKTOL /.01, .5, 3.3E-5, 8.1E-4/
  C
  DIAGS= .TRUE.
  PRINT ' (1X,A,$) ', 'DIAGNOSTICS ? (Y/N, "/"=N) '
  READ(*,' (A) ') ANS
  IF (ANS .EQ. '/' .OR. ANS .EQ. 'N' .OR. ANS .EQ. 'n') DIAGS=.FALSE.
  IJ= 1
  DO 40 J=1,NC
    DV= AMAX1( ABS( DEL*V(JO(J)) ), DMIN )
    DO 40 I=1,NR
      FLAG= .FALSE.
      1      TOL= 0.1
      OLTOL= TOL
      TDV= DBLE( DV )
      A2= 0.0
      A1= 0.0
```

```

A0= 0.0
B1= 0.0
B0= 0.0
D1= 0.0
D0= 0.0
IF (DIAGS .OR. FLAG) WRITE(*,' (/1X,A8,I2,A1,I2,11X,A12,8X,A5)')
& 'Element ',I,',',J, 'perturbation','slope'
DO 20 K= 1,18 ! iterations on TDV
A2= A1
A1= A0
B1= B0
D1= D0
A0= FN(F,XD,X,IO(I),JO(J),TDV)
Bφ= AMIN1( ABS(A0), ABS(A1) )
D0= ABS ( A0 - A1 )
IF (DIAGS .OR. FLAG) WRITE(*,' (20X,1P2E17.6)') TDV,A0
IF(K .LE. 2) GO TO 20
IF (A0 .EQ. A1 .AND. A1 .EQ. A2) THEN
ANS2= A1
GO TO 30
END IF
IF (A0 .EQ. 0.0) GO TO 25
10 IF( D0 .LE. TOL*B0 .AND. D1 .LE. TOL*B1) THEN
ANS2= A1
OLTOL= TOL
IF(DIAGS .OR. FLAG) WRITE(*,' (1X,A9,F8.7)') 'MET TOL= ',TOL
IF (TOL .LE. TOLMIN) THEN
GO TO 30
ELSE
TOL= 0.2*TOL
GO TO 10
END IF
END IF
20 TDV= 0.6D0*TDV
25 IF (OLTOL .LE. OKTOL) THEN
GO TO 30
ELSE IF (.NOT. FLAG) THEN
WRITE(*,' (/1X,A)') 'NO CONVERGENCE *****'
FLAG= .TRUE.
GO TO 1 ELSE
21 WRITE(*,' (1X,A,$)') 'Enter estimate : '
READ(*,*,ERR=21) ANS2
FLAG= .FALSE.
GO TO 30
END IF
30 ABC(IJ)= ANS2
IF (DIAGS) THEN
PRINT ' (27X,A5,1PE13.6)', 'Ans= ',ANS2
PAUSE 'Press "enter"'
END IF
40 IJ= IJ+1
RETURN END
DOUBLE PRECISION FUNCTION FDX(F,XD,X,I,J,DDX)
REAL*4 XD(*), X(*)

```

```

DOUBLE PRECISION T, DDX, XD1, XD2
EXTERNAL F
TIME= 0.0
T      = DBLE( X(J) )
X(J)= SNGL( T - DDX )
CALL F(TIME,X,XD)
XD1 = DBLE( XD(I) )
X(J)= SNGL( T + DDX )
CALL F(TIME,X,XD)
XD2 = DBLE( XD(I) )
FDX = (XD2-XD1)/(DDX+DDX)
X(J)= SNGL( T )
RETURN
END
DOUBLE PRECISION FUNCTION FDU(F,XD,X,I,J,DDU)
PARAMETER (NIN=10)
REAL*4 XD(*), X(*)
COMMON/CONTROLS/U(NIN)
DOUBLE PRECISION T, DDU, XD1, XD2
EXTERNAL F
TIME= 0.0
T      = DBLE( U(J) )
U(J)= SNGL( T - DDU )
CALL F(TIME,X,XD)
XD1 = DBLE( XD(I) )
U(J)= SNGL( T + DDU )
CALL F(TIME,X,XD)
XD2 = DBLE( XD(I) )
FDU = (XD2-XD1)/(DDU+DDU)
U(J)= SNGL( T )
RETURN
END
DOUBLE PRECISION FUNCTION YDX(F,XD,X,I,J,DDX)
PARAMETER (NOP=20)
REAL*4 XD(*), X(*)
COMMON/OUTPUT/Y/(NOP)
DOUBLE PRECISION T, DDX, YD1, YD2
EXTERNAL F
TIME= 0.0
T      = DBLE( X(J) )
X(J)= SNGL( T - DDX )
CALL F(TIME,X,XD)
YD1 = DBLE( Y(I) )
X(J)= SNGL( T + DDX )
CALL F(TIME,X,XD)
YD2 = DBLE( Y(I) )
YDX = (YD2-YD1)/(DDX+DDX)
X(J)= SNGL(T)
RETURN
END
DOUBLE PRECISION FUNCTION YDU(F,XD,X,I,J,DDU)
PARAMETER (NIN=10, NOP=20)

```

```

REAL*4 XD(*), X(*)
COMMON/CONTROLS/U(NIN)
COMMON/OUTPUT/Y(NOP)
DOUBLE PRECISION T, DDU, YD1, YD2
EXTERNAL F
TIME= 0.0
T      = DBLE( U(J) )
U(J)= SNGL( T - DDU )
CALL F(TIME,X,XD)
YD1 = DBLE( Y(I) )
U(J)= SNGL( T + DDU )
CALL F(TIME,X,XD)
YD2 = DBLE( Y(I) )
YDU = (YD2-YD1)/(DDU+DDU)
U(J)= SNGL(T)
RETURN
END

```

### B.3 RUNGE-KUTTA INTEGRATION

This subroutine implements “Runge’s fourth-order rule” as described in Chapter 3. Its arguments are the subroutine F containing the nonlinear state equations, the current time TT, the integration time step DT, the state and state derivative vectors XX and XD, and the number of state variables NX. Subroutine F should be declared EXTERNAL in the main program unit.

```

SUBROUTINE RK4 (F,TT,DT,XX,XD,NX)
PARAMETER (NN=30) ! same as main prog.
REAL*4 XX(*),XD(*),X(NN),XA(NN)
CALL F(TT,XX,XD)
DO 1 M=1,NX
XA (M)=XD (M) *DT
1      X (M)=XX (M) +0.5*XA (M)
T=TT+0.5*DT
CALL F (T,X,XD)
DO 2 M=1,NX
Q=XD (M) *DT
X (M)=XX (M) +0.5*Q
2      XA (M)=XA (M) +Q+Q
CALL F (T,X,XD)
DO 3 M=1,NX
Q=XD (M) *DT
X (M)=XX (M) +Q
3      XA (M)=XA (M) +Q+Q
TT=TT+DT
CALL F (TT,X,XD)
DO 4 M=1,NX
4      XX (M)=XX (M) + (XA (M) +XD (M) *DT) /6.0
RETURN
END

```

## B.4 OUTPUT FEEDBACK DESIGN

Output feedback design is not an easy problem. Finding the optimal output feedback gains to minimize a quadratic performance index (PI),

$$J = \frac{1}{2} \int_0^{\infty} (x^T Q x + u^T R u) dt, \quad (\text{B.7.1})$$

involves solving coupled nonlinear matrix design equations of the form (Chapter 5)

$$0 = \frac{\partial H}{\partial S} = A_c^T P + P A_c + C^T K^T R K C + Q \quad (\text{B.7.2})$$

$$0 = \frac{\partial H}{\partial P} = A_c S + S A_c^T + X \quad (\text{B.7.3})$$

$$0 = \frac{1}{2} \frac{\partial H}{\partial K} = R K C S C^T - B^T P S C^T, \quad (\text{B.7.4})$$

where

$$A_c = A - B K C, \quad X = x(0)x^T(0)$$

In the design of tracking systems, the equations are even worse.

We have used two general approaches to solving such equation sets. In the first, the PI  $J$  is computed based on (B.7.2) using

$$J = \frac{1}{2} \text{tr}(P X) \quad (\text{B.7.5})$$

The Simplex routine in Section B.1 was used to minimize  $J$ . In the second approach, a gradient algorithm (e.g., Davidon-Fletcher-Powell)<sup>\*</sup> was used. There, the gradient  $\partial J / \partial K$  is computed using all three design equations (B.7.2) to (B.7.4).

<sup>\*</sup>Press, W. H., B. P. Flannery, S. A. Teukolsky, and W. T. Vetterling, *Numerical Recipes*, New York: Cambridge, 1986.

# INDEX

---

Note: Page references in *italics* refer to figures and tables.

## A

- Acceleration derivatives, 81
- Accelerometers, 33–34
- Actuator saturation, *612*, 612–616, *613*
- Adaptive control. *See* Miniature aerial vehicles, adaptive control with application
- Aerodynamic angles, defined, 75–77, 76
- Aerodynamic coefficients
  - defined, 68
  - measurement and estimation, 82
- Aerodynamic derivatives
  - acceleration derivatives, 81
  - defined, 80
  - overview, 80–82, 121
- Aileron-rudder interconnect (ARI), 316
- Aircraft dynamic behavior, 205–213
  - interpretation of aircraft transfer functions, 208–213, *209*, *210*, *211*
  - modal decomposition applied to aircraft dynamics, 205–208
- Aircraft modeling, 63–141
  - aerodynamic coefficient measurement and estimation, 82
  - aerodynamic derivatives, 80–82
  - axes and angles, 75–77, 76
  - basic aerodynamics and, *64*, 64–75, *66*, *70*, *72*, *74*
  - component buildup, 83
  - data handling, *100*, 100–101
  - drag coefficient, 83, 83–86, 85
  - force and moment coefficients, 79–80
  - forces and moments, defined, 77–79, 78
  - lift coefficient, 86–90, 88, 89
  - linear models and stability
    - derivatives, 116–137, *121*, *124*, *130*, *131*, *132*, *135*, *136*
  - model building, overview, 63–64
  - nonlinear aircraft model, 108–116, *111*

Aircraft modeling, (*Continued*)

- pitching moment, 94–96, 95, 96
- pitching moment, control effects, 96–97
- problems, 139–141
- rolling moment, 91–93, 92
- rolling moment, control effects, 93–94, 94
- sideforce coefficient, 90, 90–91
- static analysis, 101–108, 102
- yaw, defined, 93
- yawing moment, 97–99, 98, 99

## Aircraft models for simulation, 179–184

- simple longitudinal model, 179–180
- simulation issues, 179
- six-degree-of-freedom nonlinear aircraft model, 180–184, 182–183, 184
- See also* Miniature aerial vehicles, modeling and simulation

## Airfoil section aerodynamics

- aircraft configurations, 73–75, 74
- airfoil, defined, 64, 64
- finite wings and, 71–73, 72
- overview, 64, 64–71, 66, 70

## Altitude hold/Mach hold, 329–332, 330, 332, 333

## American Institute of Aeronautics and Astronautics (AIAA), 75

## Angle of attack, 65, 75–77, 76, 88, 89

## Angular velocity vector, 1–2, 17

## Anhedral angle, 92

## Area rule, 84

## AscTec Pelican (quadrotor)

- miniature aerial vehicles, modeling and simulation, 654, 654–655, 655
- quadrotor, defined, 624

## simulation example, neural network adaptive control, 689–690, 689, 690

## Autonomy, of miniature aerial vehicles, 625

## Autopilot design

- altitude hold/Mach hold, 329–332, 330, 332, 333
- automatic landing systems, 333–339, 334, 335, 338, 339
- autopilot navigational modes, 343, 343–344

designing with modern techniques (*See* Linear quadratic regulator (LQR) with output feedback)

## function of automatic control systems and, 256–257

## historical perspective, 250–254

## need for automatic control systems and, 254–256, 255, 256

## overview, 322

## pitch-attitude hold, 322–328, 323, 325, 328, 329

## roll-angle-hold autopilots, 339–342, 340, 341

## turn coordination and turn compensation, 342

*See also* Classical control design

## Axial force, 77

**B**

## Back side of power curve, 194

## Bending-mode filter, 295

## Bilinear transformation, 588–590

## Bode plots, 164

## Body-axes equations, 109–111, 111

## Body-fixed coordinate system, 76

## Boeing, 252–253

## Bound vector, 3



## C

- Camber line, 65
- Cartesian/polar coordinate conversions, 29–31
- Cascaded systems, adaptive control for, 677, 680
- Celestial longitude, 26
- Centrifugal force, 22
- Centripetal acceleration, 20
- Chord line, 65
- Classical control design, 250–376
  - aircraft rigid-body modes, 257–274, 264, 273, 274
  - autopilot, 322–344, 323, 325, 328, 329, 330, 332, 333, 334, 335, 338, 339, 340, 341, 343
  - closed-loop control, 276, 278, 281, 283, 288–296, 291, 293, 378
  - control augmentation systems, 303–322, 304, 307, 308, 310, 311, 313, 314, 317, 321
  - feedback control and, 213, 217, 226
  - functions of automatic control systems, 256–257
  - handling qualities requirements, 274–287, 275, 280, 281, 282, 284, 285, 286
  - historical perspective, 250–254
  - limitations of, 378
  - need for automatic control systems, 254–256, 255, 256
  - nonlinear simulation, 344–371, 346, 347, 349, 350, 351, 352, 353, 355, 356, 357, 359, 360, 362, 363, 364, 365, 368, 369, 370, 371
  - overview, 250
  - problems, 374–376
  - stability augmentation, 287, 287–303, 291, 293, 295, 296, 299, 302, 303
- Closed-loop dynamics, classical design techniques, 381–396, 393, 395, 397
- Closed-loop feedback equations, 214, 214–219, 215, 217, 218, 219
- Command, tracking a. *See* Tracking a command
- Companion form, of linear state equations, 149
- Compensation, feedback control and, 224–226
- Compressibility effects, 69
- Conditional stability, 223
- Coning angle, 640–641
- Constrained feedback matrix, 429–430, 435, 436
- Continuous controller design
  - discretization of continuous controllers, 588–598, 594, 595, 596, 597
  - modified continuous design, 598–611, 599, 600, 601, 603, 605, 606, 607, 610, 611
  - overview, 584
  - See also* Digital control
- Control augmentation systems (CASs)
  - defined, 257
  - lateral-directional control augmentation, 315–322, 317, 321
  - normal acceleration CASs, 308–315, 310, 311, 313, 314
  - overview, 303–304
  - pitch-rate CASs, 304, 304–308, 307, 308
- Control feel, 283
- Control gains, modern control design and, 378–379
- Coordinate rotations, 7–16
  - cross-product matrix, 8
  - direct cosine matrix (DCM), overview, 8–10
  - eigenvalues and eigenvectors, 14–15
  - Euler rotations and DCM, 11–13
  - Euler's rotation theorem, 15–16

- Coordinate rotations, (*Continued*)
  - linear transformations, 13–14
  - scalar product, 7
- Coordinate system, defined, 3
- Coordination perception parameter, 280
- Coriolis acceleration, 20–22
- Critical Mach number, 69
- Cross-product matrix, 5, 8
- Cross-wind force, 77
- Cruise missiles, 623
- D**
- Data handling, efficiency of, 100, 100–101
- Decoupling
  - decoupled linear state equations, 126–128
  - of nonlinear equations/3-DOF
    - longitudinal model, 115–116
- De Havilland Comet, 252
- Department of Defense World Geodetic System 1984 (WGS-84)
  - defined, 23–25, 24
- Earth Gravitational Model 1996 (EGM96), 32
- Derivative of a vector, 16–17
- Derivatives. *See* Aerodynamic derivatives
- Derivative weighting, 430–431
- Deyst filter, 547
- Digital control, 584–622
  - defined, 381
  - discretization of continuous
    - controllers, 588–598, 594, 595, 596, 597
  - implementation considerations, 611–618, 612, 613, 616, 618, 619
  - modified continuous design, 598–611, 599, 600, 601, 603, 605, 606, 607, 610, 611
  - overview, 584–585
  - problems, 620–622
  - simulation of digital controllers, 585, 585–588, 586
- Dihedral angle, 92
- Dihedral derivative, 93, 136
- Dimensionless stability derivatives, 128–131, 130, 131
- Direct cosine matrix (DCM)
  - eigenvalues and eigenvectors, 14–15
  - Euler's rotation theorem, 11–13, 15–16
  - linear transformations, 13–14
  - overview, 8–10
  - from quaternion, 53
  - quaternion from, 53–54
- Direct-lift control, 253
- Discrete-time transition matrix, 152
- Dot product, 5
- Drag
  - defined, 65–66
  - drag coefficient, 70, 83, 83–86, 85
  - drag divergence Mach number, 69
  - drag due to lift, 83
  - drag polar, 86
- Dumping derivative, 81
- Dutch roll mode
  - classical control design and, 267–269, 286
  - yaw stiffness derivative and, 136–137
- Dynamic compensator, for
  - eigenstructure assignment, 392–393
- Dynamic inversion, 477–491
  - for linear systems, 477–487, 479, 484, 485
  - model reference adaptive control
    - based on, 665–668, 666 (*See also* Miniature aerial vehicles, adaptive control with application)
  - for nonlinear systems, 487–491, 488, 490, 491
  - overview, 380–381, 477
- Dynamic lift, 80
- Dynamic modes/stability, 67

Dynamic pressure, 68  
 Dynamic regulator design, using  
   separation principle, 550–554,  
   552

## E

Earth, spheroid model of. *See* Geodesy  
 Earth-centered-Earth-fixed (ECEF)  
   system, 25–26  
 Earth-centered-inertial (ECI) system,  
   25–26  
 Earth Gravitational Model 1996  
   (EGM96) (WGS-84), 32  
 Eccentricity, 25  
 Efficiency factor, 84  
 Eigenvalues/eigenvectors  
   defined, 14–15  
   eigenstructure assignment by full  
     state feedback, 387–390  
   eigenstructure assignment by output  
     feedback, 391–396, 393, 395,  
     397  
   modal decomposition, 152–153  
   *See also* Modern design techniques  
 Electric motor modeling, 647–648  
 Elevator control power, 96  
 Equation of Coriolis, 17–19, 18, 45  
 Euler angle kinematics, 19–20  
 Euler integration, 2, 171  
 Euler kinematical equations, defined,  
   120  
 Euler rotations, 11–13  
 Euler's rotation theorem, 15–16  
 Evans, W. R., 226, 251

## F

F-16  
   aircraft dynamic behavior (example),  
     208–210, 209  
   dynamic inversion design for linear  
     F-16 longitudinal dynamics  
       (example), 481–487  
   linearization, 203–205

LQR design for F-16 lateral regulator  
   (example), 407  
   modern design techniques and, 377,  
     381, 407–408, 424, 435, 439,  
     442, 481–487  
   mode variation, 272–274,  
     273, 274  
   singular-value plots for F-16  
     dynamics (example), 509–511,  
     510  
   six-degree-of-freedom nonlinear  
     aircraft model (example),  
     180–184, 182–183, 184  
 Feedback control design, 213–240  
   closed-loop equations, 214, 214–219,  
     215, 217, 218, 219  
   frequency-domain design, 233–240,  
     234, 235, 236, 237, 238,  
     239, 241  
   overview, 213, 213–214  
   robust output feedback design,  
     525–529, 528  
 SISO root-locus design, 226,  
   226–233, 229, 231, 232  
 stability, 221–224, 223  
 steady-state error and system type,  
   219–221  
 types of compensation, 224–226  
 Feedback linearization, dynamic  
   inversion and, 381  
 Feedback linearization loop, 479  
 Finite wings, 71–73, 72  
 Fixed-pitch propeller nomenclature, 636  
 Flare control, 357–371  
   automatic flare control (example),  
     358–360, 359, 360  
   overview, 357, 357–358  
   roll-angle steering control system  
     (example), 361–362, 362, 363,  
     364, 365  
   simulation of a controller with  
     limiters (example), 365–371,  
     368, 369, 370, 371

## Flat-Earth equations

- defined, 1
- matrix form, 41–43

## Flattening, 25

## Forces and moments

- aerodynamic coefficient measurement and estimation, 82
  - aerodynamic derivatives, 80–82
  - on aircraft from flapping rotor, 644–645
  - axes and angles, 75–77, 76
  - basic aerodynamics and, 64, 64–75, 66, 70, 72, 74
  - component buildup, 83
  - data handling, 100, 100–101
  - defined, 77–79, 78
  - drag coefficient, 83, 83–86, 85
  - force and moment coefficients, 79–80
  - lift coefficient, 86–90, 88, 89
  - linearization of force equations, 119–123, 121
  - linearization of moment equations, 123–126, 124
  - pitching moment, 94–96, 95, 96
  - pitching moment, control effects, 96–97
  - propeller/rotor forces and moments, 630, 630–639, 632, 633, 634, 635, 637
  - rolling moment, 91–94, 92, 94
  - sideforce coefficient, 90, 90–91
  - static analysis, 101–108, 102
  - wind- or stability-axes equations, 111–115
  - yawing moment, 97–99, 98, 99
- Frame of reference, defined, 3
- Freestream Mach number, 68–69
- Free vector, defined, 3
- Frequency-domain design, 233–240, 234, 235, 236, 237, 238, 239, 241
- Frequency-domain performance specifications, 511–524, 513, 516, 522, 523

- Frequency-response specifications, handling qualities requirements, 278–279

**G**

- Geocentric coordinates, 26
- Geodesy, 23–34
- Cartesian/polar coordinate conversions, 29–31
  - defined, 1
  - Earth-related coordinate transformations, 31
  - frames, Earth-centered coordinates, latitude and longitude, 25–27
  - geodetic coordinates, 26, 26–27
  - gravitation and accelerometers, 33–34
  - gravitation and gravity, 31–33
  - local coordinate systems, 27
  - overview, 23
  - radii of curvature, 27–28
  - shape of the Earth and Department of Defense World Geodetic System 1984 (WGS-84), 23–25, 24
  - trigonometric relationships for the spheroid, 29
- Geoid, 24
- Glide-slope coupler, 446, 446–455, 453, 454–455
- Global Positioning System (GPS), 24
- Gravitation, 23–34
- accelerometers and, 33–34
  - defined, 1, 31–33
  - Earth's gravitational field, defined, 23
  - geoid, 24
  - See also* Geodesy
- Greenwich Hour Angle (GHA), 31
- Gyroscopic moments, 638–639
- H**
- Hamilton, Sir William Rowan, 44, 45
- Handling qualities requirements, 274–287

background, 274–276, 275  
control feel, 283  
frequency-response specifications,  
278–279  
military flying qualities specifications,  
283  
pole-zero specifications, 276–278  
requirements based on human  
operator models, 280–282, 281,  
282  
speed stability, 283  
time-response specifications,  
279–280, 280  
Horizontal tail, 103–104  
Human operator describing function,  
280–281  
Hypersonic vehicles, history of,  
252–254

## I

Induced drag, 83  
Inertia coupling, 251, 315  
Inertial frame, defined, 3  
Inertial Navigation System (INS), 55  
Initial-value problem, 170  
Interference drag, 83  
Internal combustion engine modeling,  
646–647  
Irreversible control system, 256

## J

Jacobian matrices  
defined, 120  
for linearization, 199, 202, 203–205

## K

Kalman filter, 529–554  
derivation of, 540–547  
developing, 537–538  
dynamic regulator design using  
separation principle, 550–554,  
552

estimation of angle of attack in gust  
noise (example), 547–550, 548  
observer design problem and,  
530–537, 531  
overview, 381, 529–530  
probability theory and, 538–540, 539  
Kalman gain, 471–473  
Kinematic coupling, 315  
Kinematics and dynamics of aircraft  
motion, 1–62  
geodesy, coordinate systems, gravity,  
23–34, 24, 26  
kinematics, defined, 3  
matrix operations on vector  
coordinates, 7–16, 9  
overview, 1–3  
Poisson's kinematical equations  
(PKEs), 44–45  
quaternions, 45–58, 57  
rigid-body dynamics, 34–43  
rotational kinematics, 16–20, 18, 21  
vector operations, 3–7, 7

## L

Lag compensator, 232  
Landing systems, automatic, 333–339,  
334, 335, 338, 339  
Langley, Samuel Pierpont, 623  
Laplace transform (LT), 153–154  
Lateral-directional coefficients, 79  
Lateral-directional control  
augmentation, 315–322, 317,  
321  
Lateral-directional dimensionless  
derivatives, 136, 136–137  
Lateral-directional stability  
augmentation/yaw damper,  
294–303, 295, 296, 299, 300,  
302, 303  
Lateral-directional transfer functions  
accuracy of, 271–272  
algebraic derivation of, 266–267  
Latitude, 25–27

- Lead compensation, 225
- Life coefficient, 70
- Life-curve slope, 70
- Life-over-drag ratio, 71
- Lift
  - defined, 65–66
  - direct-lift control, 253
  - drag due to lift, 83
  - dynamic lift, 80
  - lift coefficient, 86–90, 88, 89
  - lift-curve slope, 132–133
  - vortex lift, 73–75
- Limit cycle, 176–178, 178
- Limited authority adaptive control, 673–679, 674, 677, 679
- Linear and time invariant (LTI) state equations
  - defined, 150
  - Laplace transform (LT) solution of, 153–154
  - time domain of, 150–152
- Linearization
  - algebraic compared to numerical linearization, 202–203
  - algorithm, 200–202, 201
  - of F-16 model, 203–205
  - numerical linearization, 199–205, 201, 204, 205
  - theory of, 199–200
- Linear models and stability derivatives
  - decoupled linear state equations, 126–128
  - dimensionless stability and control derivatives, 128–131, 130, 131
  - lateral-directional dimensionless derivatives, 136, 136–137
  - linearization, 119–126, 121, 124
  - longitudinal dimensionless derivatives, 131–135, 132, 135
  - overview, 116–117
  - singular points and steady-state flight, 117–118
- Linear multistep methods (LMMs), 170, 173–174, 175
- Linear quadratic Gaussian/loop transfer recovery (LQG/LTR), 554–577
  - for dynamic regulator, 551
  - Gaussian, defined, 546
  - guaranteed robustness of LQR, 554–558, 557, 558
  - loop transfer recovery, 558–577, 560, 565, 566, 567, 568, 569, 570, 571, 572, 573, 574, 575, 576
  - overview, 501, 554–555
- Linear quadratic regulator (LQR) with full state feedback, 470–476
  - guaranteed closed-loop stability, 473–476
  - overview, 470–471
  - Riccati equation and Kalman gain, 471–473
  - state feedback relevance, 471, 473
- Linear quadratic regulator (LQR) with output feedback, 397–413
  - determining optimal feedback gain, 402–405
  - overview, 397–398
  - quadratic performance index, 398–399
  - selection of PI weighting matrices, 405–413, 411, 412
  - solution of LQR problem, 399–402, 403, 404
- Linear state equation, 2
- Linear transformations, 13–14
- Local geocentric system (c-system), 28
- Lockheed X-7, 252
- Longitude, 25–27
- Longitudinal coefficients, 79
- Longitudinal dimensionless derivatives, 131–135, 132, 135, 136
- Longitudinal pitch pointing control, 393–396

Longitudinal transfer functions and  
modes, algebraic derivation of,  
258–259

Loop transfer function

feedback control, 215–217,  
222

robust design and LGQ/LTR,  
558–577, 560, 565, 566, 567,  
568, 569, 570, 571, 572, 573,  
574, 575, 576

*See also* Classical control design;  
Modeling, design, and simulation  
tools

## M

Mach-hold autopilot, 329–332, 330,  
332, 333

Mach number, 68–69

MATLAB

adaptive control, 670, 675  
classical control design, 290, 292,  
294, 299, 305, 312, 319, 324,  
344, 353  
dynamic inversion design, 477, 481,  
483, 489, 491  
feedback control, 216, 223, 228, 235  
(*See also* Feedback control  
design)

Kalman filter, 569

simulation tools, 176, 179, 181, 190,  
195

Mean line, 65

Meridian radius of curvature, 27–28

Miniature aerial vehicles, adaptive  
control with application,  
664–713

adaptive controller, defined, 664  
limited authority adaptive control,  
673–679, 674, 677, 678, 679  
model reference adaptive control  
based on dynamic inversion,  
665–668, 666

neural network adaptive control, 668,  
668–673, 672

neural network adaptive control  
(example), 679–708, 680, 689,  
690, 691, 692, 693, 694, 695,  
696, 697, 698, 699, 700, 701,  
702, 703, 704, 705, 706, 707, 708

overview, 664–665

Miniature aerial vehicles, modeling and  
simulation, 623–663

historical perspective, 623–624

modeling rotor flapping, 640,  
640–645, 641, 643

motor modeling, 645–648, 647

overview, 623–625

problems, 661–663

propeller/rotor forces and moments,  
630, 630–639, 632, 633, 634,  
635, 637

propellers vs. rotors, 625–630, 626,  
627, 628, 629

quadrotor model, 654, 654–655, 655

small aerobatic airplane model, 648,  
648–653, 649, 651, 652, 653

small helicopter model, 655–659,  
656, 657, 658, 660

Mission adaptive wing, 75

Modal decomposition

applied to aircraft dynamics, 205–208  
classical design techniques and,  
384–387

state-space models and, 152–153

Model building. *See* Aircraft modeling

Model-following design (modern design  
techniques), 455–470

explicit model-following control,  
456–461, 461

implicit model-following control,  
461–470, 464, 465, 468, 469

model following, defined,  
380

overview, 455

- Modeling, design, and simulation tools,  
142–249  
aircraft dynamic behavior, 205–213,  
209, 210, 211  
aircraft models for simulations,  
179–184, 180, 184, 185  
feedback control, 213, 213–240, 214,  
215, 217, 218, 219, 221, 223,  
226, 229, 231, 232, 234, 235,  
236, 237, 238, 239, 241  
numerical linearization, 199–205,  
201, 204, 205  
numerical solution of state equations,  
170–178, 176, 178  
overview, 142–143, 143  
problems, 243–249  
state-space models, overview,  
144–154, 145, 146, 148, 149,  
150  
steady-state flight, 185–199, 189,  
190, 192, 193, 194, 195, 196,  
197, 198  
transfer function models, 155–170,  
158, 161, 162, 165, 167, 168, 169  
*See also* Aircraft modeling; Miniature  
aerial vehicles, modeling and  
simulation
- Modern design techniques, 377–499  
assignment of closed-loop dynamics,  
381–396, 393, 395, 397  
dynamic inversion design, 477–491,  
479, 484, 485, 488, 490, 491  
fundamental design problems,  
379–381  
limitations of classical control, 378  
linear quadratic design with full state  
feedback, 470–476, 473  
linear quadratic regulator with output  
feedback, 397–413, 403, 404,  
411, 412  
model-following design, 455–470,  
461, 464, 465, 468, 469  
modifying performance index,  
428–455, 433, 436, 437, 438,  
440, 441, 442, 445, 446, 453,  
454, 455  
overview, 377–378  
philosophy of, 378–379  
problems, 495–499  
tracking a command, 413–428, 414,  
417, 422, 423, 427  
*See also* Miniature aerial vehicles,  
adaptive control with application
- Moment equations. *See* Forces and  
moments
- Motor modeling (miniature aerial  
vehicles), 645–648
- Multiple-input, multiple-output  
(MIMO) systems  
defined, 143  
feedback control, 217–218  
modern control techniques, 379
- Multivariable Bode plot, 506–511, 508,  
510
- Multivariable frequency-domain  
analysis, 502–525  
frequency-domain performance  
specifications, 511–524, 513,  
516, 522, 523  
multivariable Bode plot, 506–511,  
508, 510  
overview, 502  
robustness bounds for plant parameter  
variations, 524–525  
sensitivity and cosensitivity,  
502–506, 503, 504
- Multivariable wing leveler, 442,  
442–446, 445
- N**
- National Imagery and Mapping Agency  
(NIMA), 24
- Natural mode, 195
- Navigational modes, autopilot, 343,  
343–344



Neural network adaptive control  
  adaptive guidance and flight control  
    system applied to rotorcraft flight  
    control (example), 679–689, 680  
  overview, 668–669  
  quadrotor simulation, 689–690, 689,  
    690  
  small helicopter simulation, 690–697,  
    691, 692, 693, 694, 701, 702,  
    703, 704, 705, 706, 707, 708  
  universal approximation theorem,  
    669–673, 672

Neutral point, 107–108

Nonlinear aircraft model  
  body-axes equations, 109–111, 111  
  decoupling of nonlinear  
    equations/3-DOF longitudinal  
    model, 115–116  
  overview, 108–109  
  wind- or stability-axes equations,  
    111–115

Nonlinear simulation, 344–371  
  flare control, 357, 357–371, 359, 360,  
    362, 363, 364, 365, 368, 369,  
    370, 371  
  lateral-directional CAS nonlinear  
    simulation (example), 347,  
    347–353, 349, 350, 351, 352,  
    353  
  overview, 344  
  pitch-rate CAS nonlinear simulation  
    (example), 344–347, 346  
  simulation of automatic landing,  
    353–356, 355, 356, 357

Nonlinear state equation,  
  144–145

Normal acceleration control  
  augmentation systems (CASs),  
    308–315, 310, 311, 313, 314,  
    423, 423–428, 427

Normal force, 77

North-East-down (NED) system, 11

Numerical linearization, 199–205

Nyquist, H., 222

Nyquist-D contour, 222–224, 223

**O**

Oblate-rotating-Earth 6-DoF equations,  
  54–58, 57

Observer canonical form, of linear state  
  equations, 149

Optimal control model (OCM), 282

Ordinary differential equations (ODEs),  
  143, 143, 144. *See also*  
  State-space models

Output equation, 144–145

Output feedback design. *See* Feedback  
  control design

**P**

Padé approximants, 605

Parasite drag, 83

Performance index (PI) modification,  
  428–455  
  constrained feedback matrix,  
    429–430, 435, 436  
  derivative weighting, 430–431  
  glide-slope coupler, 446, 446–455,  
    453, 454–455  
  integral-squared PI, 379–380  
  multivariable wing leveler, 442,  
    442–446, 445  
  overview, 428–429  
  PI overview, 377–378  
  pitch-rate control system using LQ  
    design, 438, 438–441, 439, 441  
  quadratic PI, 398–399  
  time-dependent weighting, 431–435,  
    433, 437, 437–438, 440–441  
  *See also* Modern design techniques

Phase-lead compensation, 225

Phase portrait, 178

Phugoid approximation, 261–265, 264,  
  284

Pilot opinion rating scales, 275

Pitch-attitude hold, 322–328, 323, 325, 328, 329

Pitch-axis stability augmentation, 287–294, 291, 293

Pitch damping derivative, 133–134

Pitching moment

- coefficient, 70
- control effects, 96–97
- overview, 70, 94–96, 95, 96
- static stability analysis and, 102, 102, 104–107

Pitch-rate control augmentation systems (CASs), 304, 304–308, 307, 308, 526–529, 528

Pitch-rate control system, using LQ

- design, 438, 438–441, 439, 441

Pitch stability, 265–266

Pitch stiffness derivative, 133

Poisson's kinematical equations (PKEs)

- equation of Coriolis, 45
- overview, 44–45

Poles, transfer function models, 155–157, 158

Pole-zero specifications, classical

- control design, 276–278

Power spectral density function (PSDF), 219

Prandtl-Glauert correction factor, 72

Prandtl's lifting line theory, 72

Pressure altitude, 329

Prime vertical radius of curvature, 28

Principle of the argument, 222

Probability theory, Kalman filter and, 538–540, 539

Propellers

- fixed-pitch propeller nomenclature, 636
- propeller/rotor forces and moments, 630, 630–639, 632, 633, 634, 635, 637
- rotors vs., 625–630, 626, 627, 628, 629

Proportional plus integral (PI) compensator, 225

Pseudocontrol hedging (PCH), 674–677, 675, 677, 679

Pseudovectors, 4

## Q

Quadratic-lag circuit, 163, 165

Quadratic performance index, 398–399

Quadrotor

- defined, 624
- quadrotor model, 654, 654–655, 655
- simulation example, neural network

  - adaptive control, 689–691, 690, 691

Quaternions

- from direction cosine matrix, 53–54
- direction cosine matrix from, 53
- initializing, 51–52
- oblate-rotating-Earth 6-DoF

  - equations, 54–58, 57

- overview, 45–46
- quaternion coordinate rotation, 49–50
- quaternion kinematical equations, 50–51
- quaternion properties, 47–48
- vector rotation by, 48–49

## R

Radii of curvature, 27–28

Rate-of-climb (ROC) constraint, 186, 187

Regulator applications, 214

Regulator problem, 379–380

Relative wind, 43

Remnant, 280

Resonance, 158–159

Reynolds number, 68–69, 70–71, 625

Riccati equation, 471–473

Rigid-body dynamics

- angular motion, 35–39
- overview, 34–35

- translational motion of the center of mass, 39–43
- Rigid-body modes, 257–274
  - accuracy of lateral-mode
    - approximations, 271–272
  - accuracy of short-period and phugoid
    - approximations, 263–265, 264
  - algebraic derivation of
    - lateral-directional transfer functions, 266–267
  - algebraic derivation of longitudinal
    - transfer functions and modes, 258–259
  - dutch roll approximation, 267–269
  - mode variation from nonlinear model, 272–274, 273, 275
  - overview, 257
  - phugoid approximation, 261–263
  - pitch stability, 265–266
  - short-period approximation, 259–261
  - spiral and roll subsidence
    - approximations, 269–270
  - spiral stability, 270–271
- Rigidity, defined, 1
- Robust design
  - linear Gaussian quadratic/loop
    - transfer recovery, 554–577, 557, 558, 560, 565, 566, 567, 568, 569, 570, 571, 572, 573, 574, 575, 576
  - linear quadratic Gaussian/loop
    - transfer recovery (LQG/LTR), 501
  - multivariable frequency-domain
    - analysis, 502–525, 503, 504, 508, 510, 513, 514, 516, 522, 523
  - observers and Kalman filter, 529–554, 531, 537, 539, 546, 548, 552
  - overview, 377, 381, 500–502 (*See also* Modern design techniques)
  - problems, 580–583
  - robust output feedback design, 525–529, 528
- Roll-angle-hold autopilots, 339–342, 340, 341
- Roll control derivatives, 93
- Roll damping derivative, 137
- Rolling mode, 269–270, 285
- Rolling moment
  - control effects, 93–94, 94
  - overview, 91–93, 92
- Root-locus design, 226, 226–233, 229, 231, 232
- Rotational kinematics
  - angular velocity as a vector, 17
  - derivative of a vector, 16–17
  - Euler angle kinematics, 19–20
  - overview, 16
  - vector derivatives and rotation, 17–19, 18
- Rotation of vector
  - defined, 6–7, 7
  - quaternion coordinate rotation, 49–50
  - by quaternions, 48–49
- Rotors
  - forces and moments on aircraft from
    - flapping rotor, 644–645
  - modeling rotor flapping, 640, 640–645, 641, 643
  - propeller/rotor forces and moments, 630, 630–639, 632, 633, 634, 635, 637
  - propellers vs., 625–630, 626, 627, 628, 629
  - quadrotor, defined, 624
  - quadrotor model, 654, 654–655, 655
- Runge-Kutta (RK) methods, 170–172, 174–175, 585–588
- S
- Scalar product, 7
- Separation principle, 550–554, 552
- Short-period mode, 195, 259–261, 263–265, 264, 284–285

- Sideforce coefficient, 90, 90–91
- Sideslip angle, 75–77, 76. *See also*
  - Rolling moment
- Sign convention, for control surfaces, 184, 184, 288
- Simulation. *See* Miniature aerial vehicles, modeling and simulation; Modeling, design, and simulation tools
- Single-input, single-output (SISO) systems
  - defined, 143
  - feedback control, 215–217, 219
  - root-locus design, 226, 226–233, 229, 231, 232
  - SISO transfer function, 157–160
- Six-degrees-of-freedom (6-DoF) equations
  - defined, 16
  - Euler angle kinematics, 19
  - F-16 aircraft model for simulation (example), 180–184, 182–183, 184
  - quaternion, 54–58, 57
  - rigid-body dynamics, 34, 40, 42–43
  - translational kinematics, 20
- Skin friction, 65
- Small aerobatic airplane model, 648, 648–653, 649, 651, 652, 653
- Small helicopter
  - miniature aerial vehicles, modeling and simulation, 655–659, 656, 657, 658, 660
  - simulation example, neural network adaptive control, 691–698, 692, 693, 694, 695, 702, 703, 704, 705, 706, 707, 708
- Speed damping derivative, 135
- Speed stability, 283
- Sperry, Elmer, 339
- Sperry Gyroscope Company, 250
- Spiral mode, 208, 269–270, 285
- Spiral stability, 270–271
- Spoilers, 94
- Stability
  - feedback control and, 221, 221–224, 223
  - numerical algorithms and, 174
  - stability-axes coordinate system, 76
  - stability-axes equations, 111–115
  - stabilizer bars on rotors, 628, 643, 643–644
  - stable equilibrium, 66
- Stability augmentation systems (SASs), 287–303
  - defined, 257
  - designing with modern techniques (*See* Linear quadratic regulator (LQR) with output feedback)
  - lateral-directional stability
    - augmentation/yaw damper, 294–303, 295, 296, 299, 300, 302, 303
  - overview, 287
  - pitch-axis stability augmentation, 287–294, 291, 293
  - stability augmentation, defined, 252
- Stalled (airfoil), 70
- Standard atmosphere model, 67–68
- State feedback, LQR with, 470–476, 473
- State-space models, 144–154
  - classical design techniques and, 382–384
  - Laplace transform (LT) solution of LTI state equations, 153–154
  - modal decomposition, 152–153
  - models of mechanical and electrical systems, 144–147, 145, 146
  - nonlinear state and output equations, 144–145
  - ordinary differential equations (ODEs), 143, 143, 144
  - reduction of differential equations to state-space form, 147–150, 148, 149, 150

- time-domain solution of LTI state equations, 150–152
- See also* Modeling, design, and simulation tools
- State variables
  - overview, 2–3
  - state-variable model, 378
- Static coefficients, 80
- Static stability analysis
  - defined, 101
  - effect of horizontal tail, 103–104
  - neutral point, 107–108
  - static equilibrium, 101–103, 102
  - static stability analysis in pitch, 104–107
- Steady-state flight, 185–199
  - feedback and steady-state error, 219–221
  - flight simulation (examples), 195–199, 196, 197, 198
  - overview, 185–187
  - rate-of-climb constraint, 186, 187
  - steady state, defined, 546
  - trim algorithm, 188–192, 189, 190, 192
  - trimmed conditions for studying aircraft dynamics, 193, 193–194, 194, 195
  - turn coordination constraint, 187–188
- Stiff system, 174
- Strapdown equation, 45
- Streamlines, 64, 64
- Supersonic wave drag, 72
- T**
- Tail efficiency factor, 97
- Tangent-plane coordinate system, 27
- Target drones, 623
- Taylor series, 119, 170–173, 199–202, 605
- Terrain-following, terrain avoidance (TFTA) autopilot, 343
- Terrestrial longitude, 26
- 3-DOF longitudinal model, 115–116
- Thrust coefficient, 79, 87
- Thrust/torque, of propeller/rotor, 630, 631–639, 632, 633, 634, 635, 637
- Time-dependent weighting, 431–435, 433, 437, 437–438, 440–441
- Time-domain design technique, 399
- Time-history simulation, 175–178, 176
- Time step T, 170
- Tip path plane equations, of motion, 640–642
- Tracker applications, 214
- Tracker problem, 380
- Tracking a command, 413–428
  - determining optimal feedback gain, 422–428, 423, 427
  - LQ formulation of tracker problem, 416–420, 417
  - overview, 413–415, 414
  - solution of LQ tracker problem, 420–421, 422
  - tracker with desired structure, 415–416
- Transfer function models, 155–170
  - examples and standard forms, 160–163, 161
  - frequency response, 163–167, 165
  - poles and zeros, 155–157, 158
  - SISO transfer function, 157–160
  - time response, 167–170, 168, 169

Translational kinematics  
 acceleration relative to Earth,  
   22–23  
 overview, 20  
 velocity and acceleration in moving  
   frames, 20–22, 21

Transonic drag rise, 73

Transonic flow, 69

Trigonometric relationships for  
 spheroid, 29

Trim algorithm (for steady-state flight)  
 flowchart, 189  
 overview, 188–192, 189, 190, 192  
 for 3-DoF aircraft model, 189  
 trimmed conditions for studying  
   aircraft dynamics, 193, 193–194,  
   194, 195

Trimmed coefficients, 82

Tuck derivative, 134–135

Turbulence, 65

Turn coordination constraint,  
   187–188

Turn coordination/turn compensation,  
   342

Tustin's approximation, 588–590

**U**

Unity feedback, 214

Universal approximation theorem,  
   669–673, 672

Unmanned aircraft. *See* Miniature aerial  
 vehicles, modeling and  
 simulation

Unstable equilibrium, 67

Unsteady aerodynamic effects, 80

Untrimmed coefficients, 82

U.S. Department of Defense World  
 Geodetic System 1984 (WGS-84)  
 defined, 23–25, 24  
 Earth Gravitational Model 1996  
 (EGM96), 32

U.S. space shuttle, history of, 253

**V**

Van der Pol equation,  
   176–178, 178

Vector analysis  
 angular velocity vector, 1–2  
 matrix operations on vector  
   coordinates, 7–16  
 rotation of a vector, 6–7, 7  
 vector, defined, 3  
 vector operations, definitions and  
   notation, 3–4  
 vector properties, 4–6

Vector state equations, 39–41

Velocity feedforward, 479

Vertical take-off and landing (VTOL)  
 aircraft, 624

VOR-hold (VHF Omni Range)  
 autopilot, 343

Vortex lift, 73–75

Vortex sheet, 71

**W**

Wave drag, 83

Wetted area, 65

WGS. *See* Department of Defense  
 World Geodetic System 1984  
 (WGS-84)

Whitcomb, R. T., 84

Wind-axes equations,  
   111–115

Wing planform parameters,  
   72, 72–75

**Y**

Yamaha RMAX (small helicopter)  
 modeling and simulation,  
   655–659, 656, 657,  
   658, 660  
 simulation example, neural network  
 adaptive control, 691–698, 692,  
 693, 694, 695, 702, 703, 704,  
 705, 706, 707, 708

Yaw damping derivative,  
137  
Yawing moment  
control effects, 99  
overview, 97–99, 98, 99  
yaw, defined, 93  
yaw damping derivative,  
98  
Yaw stiffness derivative,  
136  
Yeager, Charles, 251

**Z**

Zero-order hold (ZUH), 585, 601–603,  
605  
Zeros  
pole-zero specifications, classical  
control design, 276–278  
Zeros, transfer function models,  
155–157, 158  
Zivco Edge 540T (small aerobatic  
airplane model), 648, 648–653,  
649, 651, 652, 653

# **WILEY END USER LICENSE AGREEMENT**

Go to [www.wiley.com/go/eula](http://www.wiley.com/go/eula) to access Wiley's ebook EULA.